SEISMICA

DECEMBER 2023 | VOL 2 | NO 2

ISSN 2816-9387

McGill | Library Bibliothèque

Issue 2, Volume 2, 2023

Aims and Scope

Seismica publishes original, novel, peer-reviewed research in the fields of seismology, earthquake science, and related disciplines. Seismica is a community-driven, diamond open-access journal. Articles are free to publish and free to read without a subscription, and authors retain full copyright.

Seismica strives to be **accessible**, **transparent**, **respectful**, **credible**, and **progressive**.

Seismica's scope includes a wide range of topics in seismological and earthquake sciences. A non-exhaustive list of topics that fall within the scope of Seismica includes: Fault-slip and earthquake source phenomena, Earthquake records, Imaging the Earth, Theoretical and computational seismology, Beyond Earth-tectonic applications, Techniques and instrumentation, Earthquake engineering and engineering seismology, Community engagement, communication and outreach.

For submission instructions, subscription and all other information visit: https://seismica.library.mcgill.ca/.
For editorial questions or issues, please contact info@seismica.org.
For technical assistance, please contact info@seismica.org.
For appeals, please contact appeals@seismica.org.

About the cover

Cover Caption In 2021, the National Institute of Seismology, Volcanology, Meteorology, and Hydrology (INSIVUMEH) of Guatemala carried out a significant expansion of the National Seismological Network (RSN) by installing 15 permanent seismic stations with real-time transmission. Each station was equipped with a broadband sensor and an accelerometer. These seismic stations notably enhanced seismic monitoring in Guatemala and were also shared with international seismological agencies, thereby serving a crucial role in earthquake and tsunami early warnings in the region. The image shows the installation work of the "Las Nubes (the clouds)" seismic station (GUSP code) located in San José Pinula, Guatemala Department (23 km from the Capital City). In the background (top of the photo), there is also a meteorological radar belonging to INSIVUMEH. Credit: INSIVUMEH staff.

Editorial Board

We warmly thank the following volunteers of the Editorial Board that have been involved in the issue.

Volunteers

We warmly thank the following volunteers that have been involved in the issue.

Issue 2, Volume 2, 2023

Table of Contents

Articles

Fast Reports

Editorials

Reports (excl. Fast Reports)

Opinion

doi:10.26443/seismica.v2i2.1086

SEISMICA

Red-light thresholds for induced seismicity in the UK

Ryan Schultz *[1], **Brian Baptie** [2], **Benjamin Edwards** [3], **Stefan Wiemer** [1]

[1]Department of Earth Sciences, Swiss Seismological Service, ETH Zürich, Zürich, Switzerland, [2]British Geological Survey, Edinburgh, United Kingdom, [3]School of Environmental Sciences, University of Liverpool, Liverpool, United Kingdom

Author contributions: *Conceptualization*: R. Schultz. *Data Curation*: R. Schultz, B. Baptie, B. Edwards. *Formal Analysis*: R. Schultz. *Funding Acquisition*: S. Wiemer. *Investigation*: R. Schultz. *Methodology*: R. Schultz, B. Edwards. *Project Administration*: R. Schultz. *Resources*: R. Schultz, B. Baptie. *Software*: R. Schultz, B. Edwards. *Supervision*: B. Baptie, S. Wiemer. *Validation*: R. Schultz. *Visualization*: R. Schultz. *Writing – original draft*: R. Schultz. *Writing – review & editing*: R. Schultz, B. Baptie, B. Edwards, S. Wiemer.

Abstract Induced earthquakes pose a serious hurdle to subsurface energy development. Concerns about induced seismicity led to terminal public opposition of hydraulic fracturing in the UK. Traffic light protocols (TLPs) are typically used to manage these risks, with the red-light designed as the last-possible stopping-point before exceeding a risk tolerance. We simulate trailing earthquake scenarios for the UK, focusing on three risk metrics: nuisance, damage, and local personal risk (LPR) – the likelihood of building collapse fatality for an individual. The severity of these risks can spatially vary (by orders-of-magnitude), depending on exposure. Estimated risks from the Preston New Road earthquakes are used to calibrate our UK earthquake risk tolerances, which we find to be comparable to Albertan (Canadian) tolerances. We find that nuisance and damage concerns supersede those from fatality and that the safest regions for Bowland Shale development would be along the east coast. A retrospective comparison of our TLP result with the Preston New Road case highlights the importance of red-light thresholds that adapt to new information. Overall, our findings provide recommendations for red-light thresholds (M_L 1.2-2.5) and proactive management of induced seismicity – regardless of anthropogenic source.

Non-technical summary Consideration of energy security briefly led the UK to reconsider its moratorium on shale gas hydraulic fracturing (HF) in 2022. HF has the potential to induce earthquakes, which originally led to the UK's moratorium, and could potentially threaten the future of other clean energy technologies. Based on these concerns, we model the potential for induced earthquake risks (nuisance impacts, building damage, and chance of fatality). We also use the experience from the previous earthquakes to calibrate the UK tolerance to these risks. These risk metrics/tolerances are combined to determine when an HF operation should stop: *i.e.*, the red-light threshold, reported as an earthquake magnitude. Our results suggest that the red-light threshold should change with location (M_L 1.2-2.5), primarily due to exposure from ground shaking varying with the distribution of population density. Nuisance and damage are likely the most important risk metrics to consider because they result in the lowest red-light magnitudes. We discuss how our approach could be used to choose HF locations and adapt to real-time information. Overall, our results provide a blueprint for the regulation of future induced earthquakes – including green technologies like geothermal or carbon/hydrogen storage.

Production Editor:
Gareth Funning
Handling Editor:
Stephen Hicks
Copy & Layout Editor:
Théa Ragon

Signed reviewer(s):
James Verdon

Received:
July 12, 2023
Accepted:
October 4, 2023
Published:
October 16, 2023

1 Introduction

Earthquakes can be induced by anthropogenic activities such as mining, wastewater disposal, and geothermal systems (Foulger et al., 2018). Hydraulic fracturing (HF), a petroleum extraction technique that stimulates fractures by injecting fluids into the subsurface under high pressure (Bickle et al., 2012), has also been documented to cause earthquakes (Atkinson et al., 2020; Schultz et al., 2022b). Yet, most HF operations do not cause noteworthy (*e.g.*, felt) earthquakes (Atkinson et al., 2016; Verdon and Rodríguez-Pradilla, 2023) and only susceptible regions appear to preferentially host larger induced events (Schultz et al., 2018; Pawley et al., 2018). Some cases of HF induced seismicity have hosted moderate magnitude events (M3+) that have been felt, or even damaging. For instance, the current largest documented case to date was the December 2018 M_L 5.7 event in the Sichuan Basin of China (Lei et al., 2019), which caused ~$7M USD in direct economic losses alongside human loss and injuries. Concerns around the risks of induced earthquakes have stymied resource development, in some cases even resulting in moratoriums or resource abandonment.

The UK has a controversial history of HF (Williams et al., 2017) and related induced earthquakes, despite prior tectonic (and coal mining induced) seismicity (Figure 1). The most prospective shale gas target in the UK is the Mississippian aged Bowland Shale (Smith et al., 2010; Andrews, 2013). The first shale gas exploration licenses were awarded in 2008, with the first well (Preese Hall 1, PH-1) targeting the Bowland Shale near Blackpool, Lancashire (Baptie et al., 2022). Stage stimu-

*Corresponding author: Ryan.Schultz@sed.ethz.ch

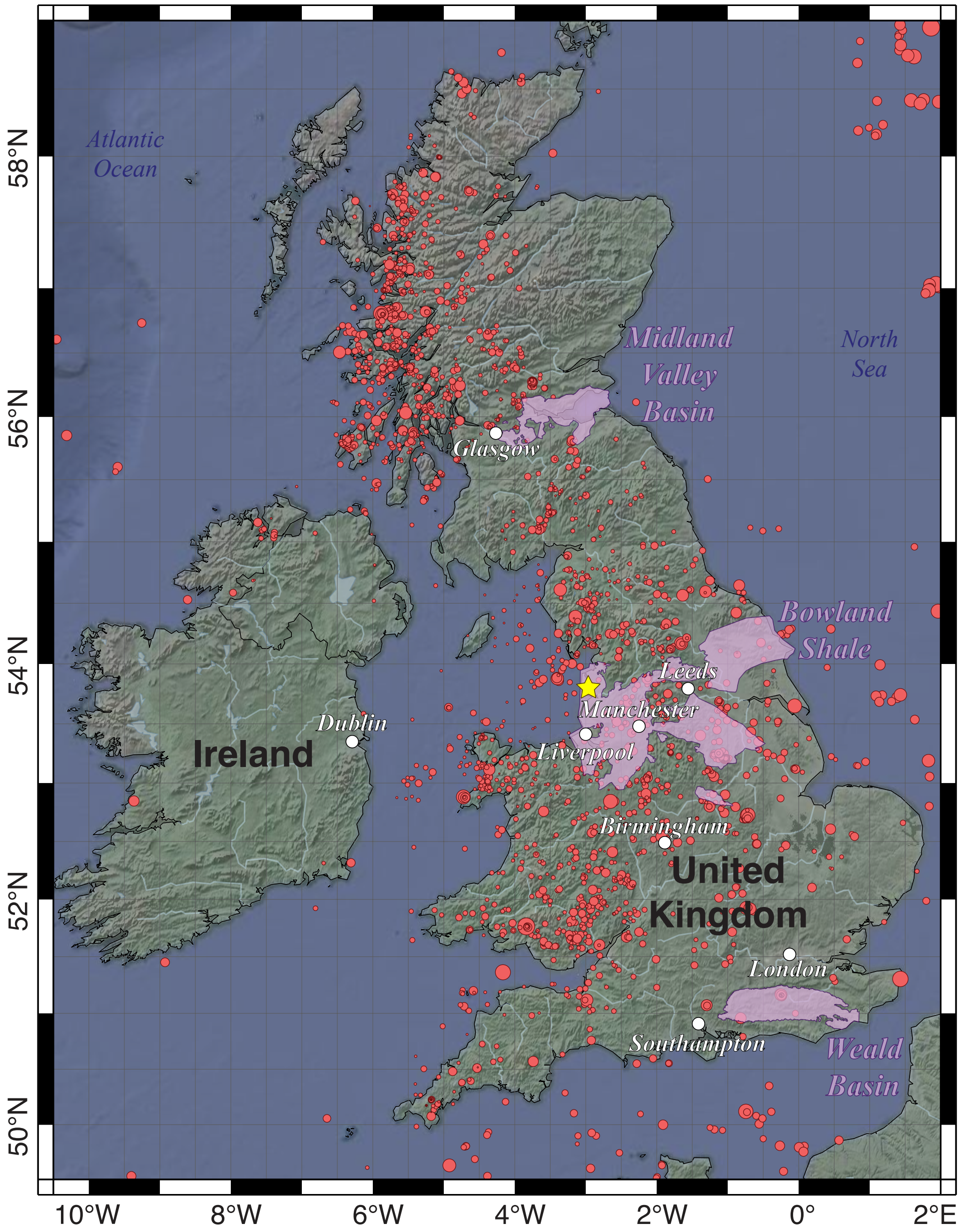

Figure 1 Map of the study area. Map of the UK including HF plays (purple polygons), HF wells (yellow star), earthquakes (red circles), and the largest municipalities (white circles).

lation at PH-1 during March-May of 2011 resulted in a series of induced earthquakes, the largest being the M_L 2.3 event on 1 April (de Pater and Baisch, 2011; Clarke et al., 2014). The induced events here were felt, leading to the suspension of the PH-1 operation, and an inquiry into the induced events (Green et al., 2012). The result of this inquiry was a regulatory roadmap that outlined monitoring requirements, seismic baseline assessment, fault avoidance strategies, mitigation measures, and a traffic light protocol (TLP) with a red-light threshold of M_L 0.5 (BEIS et al., 2013). Upon triggering a red-light, the operator must stop injection, reduce the pressure in the well, perform well integrity checks, and wait 18 hours before continuing stimulation (with regulatory approval).

A TLP is a regulatory control system designed with the intention of limiting the risks of induced seismicity (Majer et al., 2012). TLPs are typically designed with an escalating series of thresholds: green-light for unrestricted operation, yellow-light indicating when mitigation measures should be enacted, and the red-light for a regulatory intervention requiring the cessation of operation. Often (local) magnitude is used for delineating the yellow/red-light thresholds for practical reasons, like the simplicity of their estimation (Schultz et al., 2020a). The first case of a TLP used for induced seismicity hazard management was the Berlín geothermal project in El Salvador (Bommer et al., 2006). Since then, TLPs have been widely used for induced seismicity risk management (Ader et al., 2019; Schultz et al., 2020b) – including in the UK for HF.

The UK TLP was first put into a practical test in late-2018 with the Preston New Road 1z well (PNR-1z), targeting the Bowland Shale near Blackpool, Lancashire. HF operations at the PNR-1z well induced six events larger than M_L 0.5 that triggered the red-light, with the largest (M_L 1.6) event on 11 December 2018 being felt by some people nearby the epicentre (Clarke et al., 2019). Continuing nearly a year later (August 2019), the second

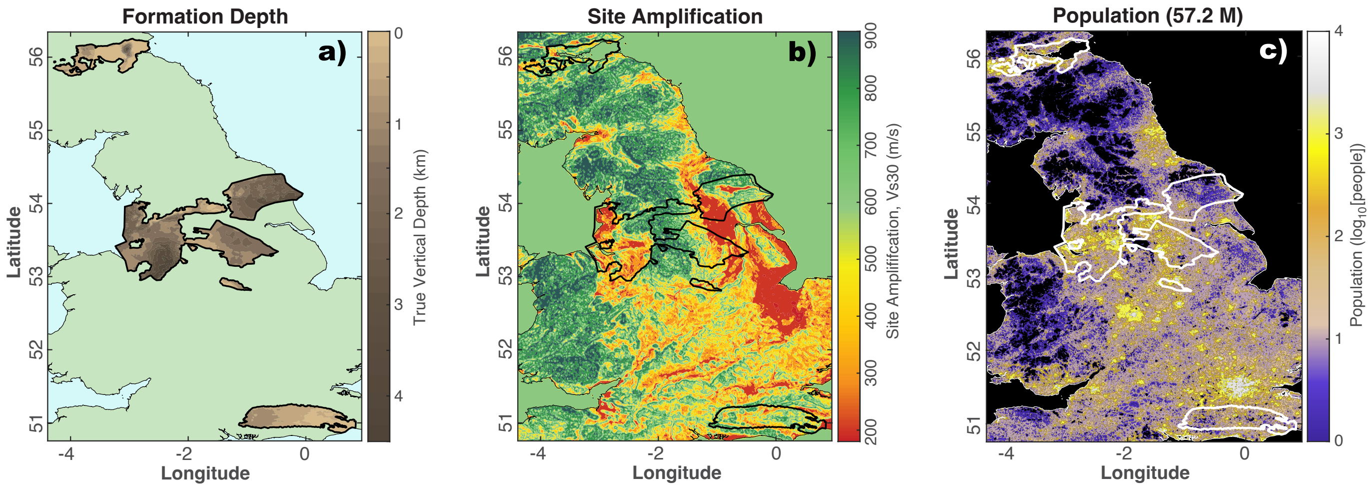

Figure 2 Maps of the input parameters for the UK. a) Depth contours for the target formation tops in the Midland Valley Basin, Bowland Shale, and Weald Basin (Andrews, 2013, 2014; Monaghan, 2014). b) Site amplification map, using slope-based V_{S30} as a proxy (Heath et al., 2020). c) Distribution of people throughout the UK (Rose et al., 2019). See also Figures S1, S2, & S3 for higher resolution versions.

lateral well (PNR-2) on the Preston New Road pad was hydraulically stimulated; the PNR-2 well also induced earthquakes, with the largest being M_L 2.9 on 26 August 2019. Notably, this event occurred more than 72 hours after the shut-in of the last stage (Kettlety et al., 2020) and was felt strongly near the epicentre (Edwards et al., 2021). This event led to the abandonment of this well, with only 7/47 planned stages being stimulated (Cuadrilla Resources Ltd, 2019). Consequently, this event triggered a review of the induced events (Oil and Gas Authority, 2018) and ultimately a moratorium on HF starting 2 November 2019. At the time of this study's publication the moratorium is ongoing.

Nevertheless, Russia's recent conflict against the Ukraine, and the knock-on effect of accompanying energy security needs in Europe, led the UK to reconsider their HF moratorium – prompting a report on recent HF induced seismicity understanding/management (Baptie et al., 2022). Previously, TLPs have been criticized for their inflexibility to consider events occurring after well shut-in and assumptions around the temporal sequence of largest magnitudes (Baisch et al., 2019). Since the UK moratorium, advancements have been made in understanding the earthquakes that follow well shut-in (Verdon and Bommer, 2020; Schultz et al., 2022a). As well, recent approaches have suggested translating seismic risks into equivalent red-light magnitude thresholds to better inform TLP designs (Schultz et al., 2020a, 2021a,b, 2022b).

In this study, we refine the *ad hoc* approaches of the past – instead, defining red-light thresholds using a risk-based approach. Like prior work, we find that risks vary spatially by orders of magnitude and that choosing a tolerance for risk allows for a fairer TLP design. In this case, we compare simulated risks from the 2019 PNR-2 M_L 2.9, 2.1, and 1.6 events to calibrate the UK tolerance for risk. These results indicate that red-light thresholds should vary from M_L 1.2-2.5, depending on exposure. Furthermore, we justify the importance of the risk metrics we considered and discuss their relevance for TLP design. Ultimately, a conscientious handling of induced seismicity risks will be important for the future of HF in the UK, especially considering the prior controversial history. Careful handling of HF risks will also be important for green energy development (like geothermal, carbon capture, or hydrogen storage), since 'perception spillover' can tarnish attitudes toward future industry (Westlake et al., 2023).

2 Data & Methods

Our TLP approach is based on risk evaluation and can be divided into three main categories: 1) determining the largest magnitude event following a HF operation, 2) estimating the resulting ground motion field, and 3) calculating the resulting seismic risks. Monte Carlo perturbations capture the variability within risk evaluations, which are repeated for all potential HF well locations in the UK (Figure 2). The details of each component are discussed in subsequent sections and have been described in previous works (Schultz et al., 2020a, 2021a,b, 2022b).

2.1 Trailing seismicity

Trailing seismicity refers to any earthquakes that occur after well injection stops. Sensitivity analysis has shown that these events are the most critical factor in designing a HF TLP (Schultz et al., 2021a). This is especially relevant, given that all the red-light events at the PNR-2 well occurred after stage stimulation was completed (Kettlety et al., 2020). Trailing magnitudes are estimated using a concept analogous to Båth's law (Båth, 1965), which states that the difference in magnitude between a mainshock and the largest aftershock ΔM depends on the count ratio R_S, the Gutenberg-Richter b-value, and confidence variables u_i (Schultz et al., 2022a).

$$\Delta M \approx \frac{1}{b}\log_{10}\left(\frac{1}{R_S}\right) + \frac{1}{b}\log_{10}\left(\frac{\ln(u_1)}{\ln(u_2)}\right) \quad (1)$$

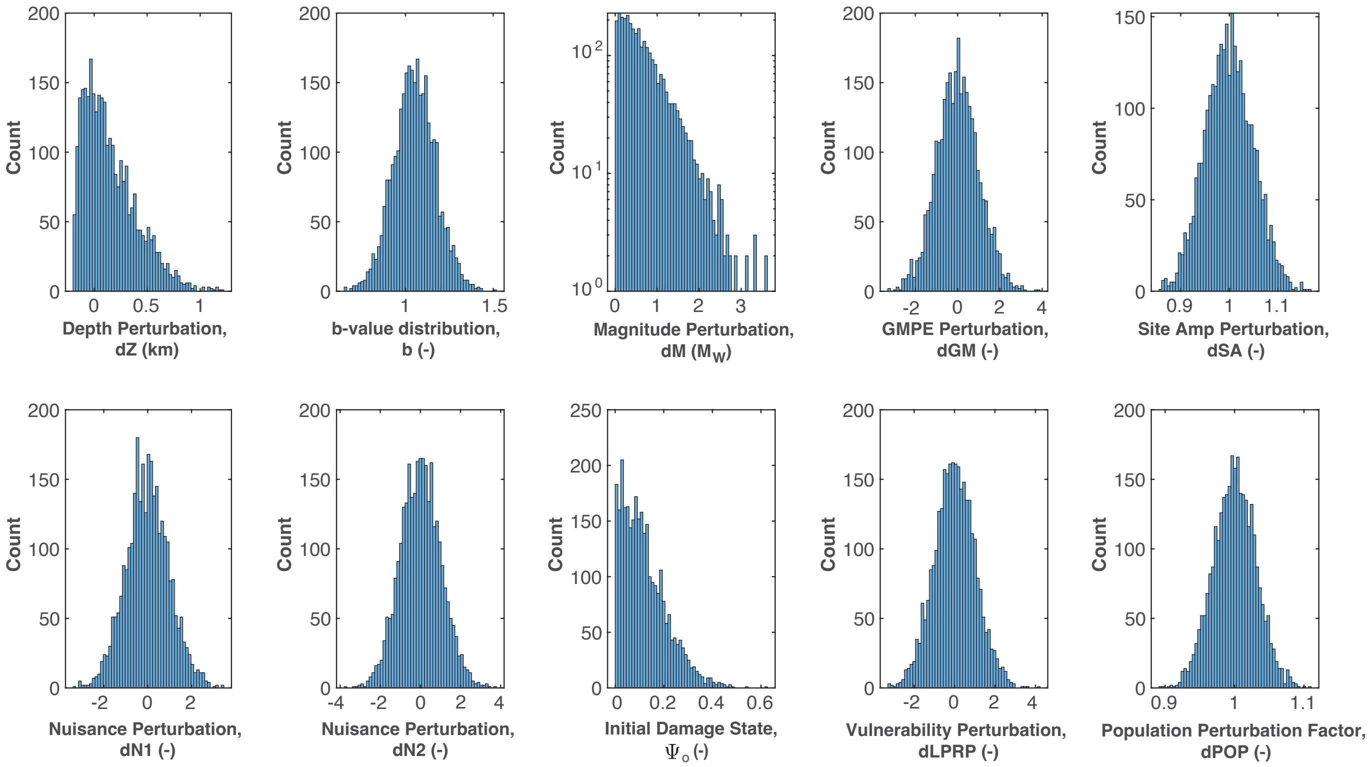

Figure 3 Perturbed input variables for the Monte Carlo analysis. Ten panels show histograms for each of the perturbed variables of interest: dZ – depth, b – *b*-value, dM – trailing magnitude, dGM – GMPE variability, dSA – site amplification perturbation factor, dN1 & dN2 – nuisance function variabilities, Ψ_o – initial damage state, dLPR – vulnerability function variability, and dPOP – population perturbation factor.

For the context of HF induced seismicity, we assume that a stimulation event (larger than the red-light) triggers a regulatory intervention that prompts well shut-in. Such an event is then followed by additional aftershock-like events trailing well shut-in. We inform our choice of *b*-value to be like those observed in the UK from various sources: prior tectonic seismicity baselines suggest values on the order of 1.01±0.06 (Mosca et al., 2022), while studies of the HF cases are closer to 1.10±0.10 (Kettlety et al., 2020) and 1.3 (Clarke et al., 2019). Each of these studies discerned significant variability in their *b*-values, depending on the subset of their data (Baptie et al., 2020). To encompass this range of *b*-values, we use a normal distribution with 1.05±0.12. The count ratio R_S represents the proportion of earthquakes occurring during stimulation to the total number of induced earthquakes. We use a distribution of R_S values based on the fit to the empirical data of short-term induced seismicity globally, like HF (Verdon and Bommer, 2020; Schultz et al., 2022a). This empirical R_S distribution has a mean and median value of 77% and 86%, respectively and was fit to a beta-distribution. As more information becomes available for induced seismicity caused by HF in the UK, this R_S distribution will be important to update as trailing seismicity is the most important factor in determining red-lights. In this sense, we can stochastically estimate the magnitude of the largest earthquake following a red-light (relative to the red-light) ΔM – by drawing random R_S and *b*-values from their distributions alongside uniform random values of u_1 and u_2. As well, we use a locally calibrated M_L-M_W conversion relationship (Edwards et al., 2021), a topic that has been extensively studied for the UK (Butcher et al., 2017; Luckett et al., 2018; Baptie et al., 2020; Roy et al., 2021). We refer readers to the prior study that details the statistical modelling of trailing earthquake magnitudes (Schultz et al., 2022a).

In addition to simulating the trailing event magnitudes, we also simulate the depth distribution of HF seismicity. The starting point for determining the depth is the top of the target formation, which provides the modal depth value and is based on geological assessments of shale targets in the UK. We use depths at formation tops to be conservative in our risk estimates. We consider the Limestone Coal Formation (Carboniferous) for the Midland Valley Basin (Monaghan, 2014), the Bowland Shale (Mississippian, Andrews, 2013), and the Kimmeridge Clay (Upper Jurassic) for the Weald Basin (Andrews, 2014, Figures 2a & S1). We do not account for UK legislation (UK Public General Acts, 2015) that prohibits HF operations shallower than 1000 m. We note that no exploration licenses have been awarded in Scotland, where a moratorium was imposed by the Scottish government in 2015. Additionally, no HF operations were completed in the Weald Basin. However, we include these basins to be comprehensive in our analysis and discussions. From the formation depth, the earthquakes are perturbed with a distribution that skews to deeper events (Figure 3). Typically, HF induced events occur near their stimulation interval, with some cases extending downwards into basement-rooted faults (Schultz et al., 2020b).

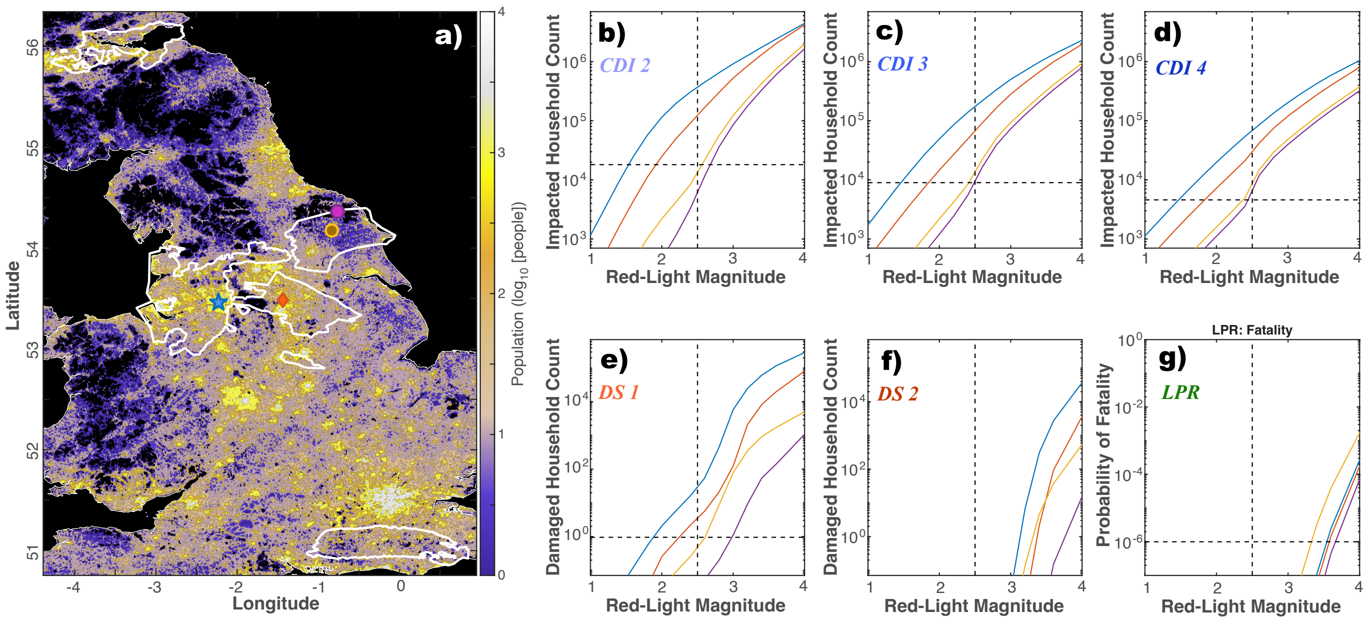

Figure 4 Risk curves for four locations. a) Population map of the UK showing the four locations sampled (coloured shapes) in the Bowland Shale. Median risk curves are plotted for nuisance at CDI 2 (b), CDI 3 (c), and CDI 4 (d) levels; damage at levels of DS 1 (e) and DS 2 (f); and LPR (g). Median risk curves are colour coordinated with their map locations. Iso-risk (horizontal dashed line) and iso-magnitude (vertical dashed line) are shown for reference.

2.2 Hazard Calculation

We use the simulated trailing earthquake scenarios to evaluate their hazards (Bommer, 2022) through a ground motion prediction equation (GMPE) – a formula that predicts the amplitude of earthquake ground motion based on factors such as magnitude, distance, depth, and site amplification. There are many GMPEs that are suitable for this region (Villani et al., 2019; Cremen et al., 2020), and we select one of them (Edwards et al., 2021). The effects of site amplification (Figures 2b & S2) are considered by using a global slope-based proxy for V_{S30} (Heath et al., 2020), corrected with non-linear NGA-West2 adjustments to the GMPE (Boore et al., 2014). The uncertainties in all inputs are perturbed via their standard errors, with ground motion also incorporating a spatially correlated intra-event error calibrated for European data (Esposito and Iervolino, 2012; Edwards et al., 2021). Our workflow primarily focuses on Peak Ground Velocity (PGV) as the key ground motion metric for nuisance and damage, but for building collapse assessment, we must use the geometric average of the spectral acceleration over various periods (Eads et al., 2015) – an important metric for assessing structural damage. The range of spectral acceleration periods averaged over (0.01s, 0.1s, 0.2s, 0.3s, 0.4s, 0.5s, 0.6s, 0.7s, 0.85s, & 1.0s) aligns with Groningen fatality risk studies (Crowley et al., 2017; Crowley and Pinho, 2020).

2.3 Risk Estimation

The estimated ground motion hazards are then translated into risk metrics like nuisance impacts, damage impacts, and chance of fatality. Risk metrics can be either aggregate (nuisance/damage) or local (individual chance of fatality). To compute the aggregate metrics, we use nuisance/fragility functions that define the chance of nuisance/damage as a function of ground motion (Figure S4). For this study, we use PGV-based North American nuisance functions (Schultz et al., 2021c) and Groningen fragility functions (Korswagen et al., 2019) to differentiate the degree of impact. Groningen fragility functions were chosen for their applicability to smaller to moderate magnitude (induced) seismicity, similar to prior studies in the UK (Edwards et al., 2021). For instance, degree of nuisance is categorized by Community Decimal Intensity (CDI, Wald et al., 2012) with levels ranging from 2-6 corresponding to subjective criteria of 'just felt', 'exciting', 'somewhat frightening', 'frightening', and 'extremely frightening', respectively. Similarly, the degree of damage is divided into damage states (DS, Korswagen et al., 2019), with levels 1-2 corresponding to visible light damage (>0.1 mm crack) and easily observable light damage (>1 mm crack), respectively. The third risk metric is a local risk that considers the chance of a specific type of fatality, known as local personal risk (LPR), which is the likelihood that a hypothetical person inside of a building for 95% of their time will suffer a building collapse death (SodM, Staatstoezicht op de Mijnen, 2014). To estimate this, we use the average Groningen vulnerability function (Crowley et al., 2017; Crowley and Pinho, 2020), which defines the chance of fatality as a function of period-averaged spectral acceleration. This vulnerability function is more conservative than the one used in PAGER's UK estimates (Figure S5) for global estimates of fatalities (Jaiswal et al., 2009; Caprio et al., 2015; Jaiswal and Wald, 2010). Our vulnerability and nuisance functions consider errors in these functions via a perturbation in their parameters (Figure S4), respectively (Figure 3). Our damage functions also include a building pre-damage term Ψ_o (Korswagen et al., 2019), which we assign a half Gaussian distribu-

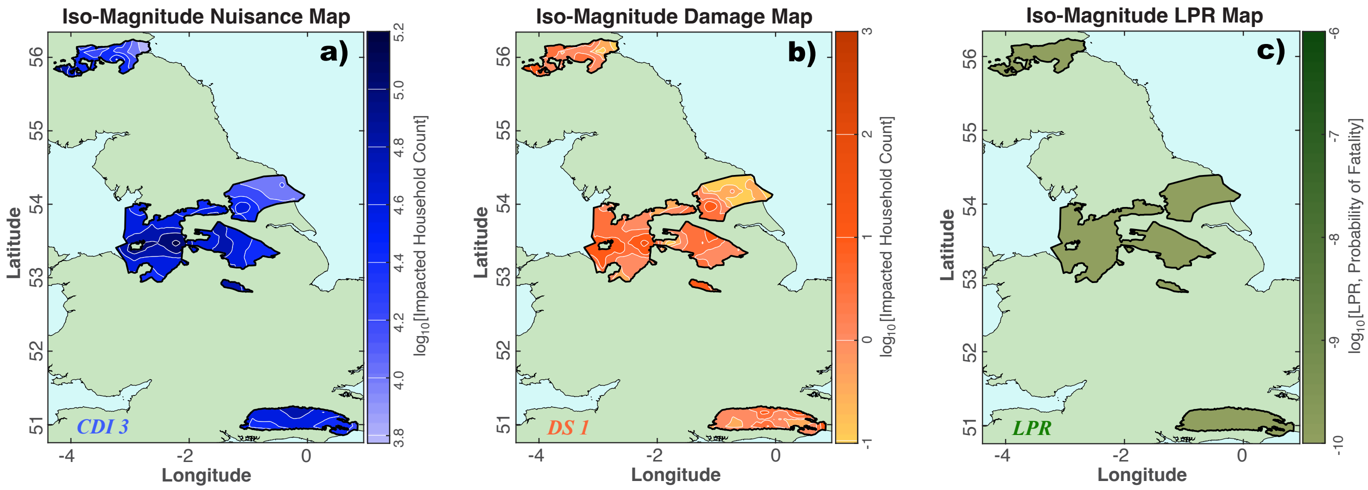

Figure 5 Iso-magnitude maps. a) Number of households impacted by CDI 3 nuisance. b) Number of households impacted by DS 1 damage. c) Map of LPR, the probability of loss of life. All maps use a red-light threshold of M_L 2.5. All maps have their risk metrics colored on a base-10 logarithmic scale. Damage and LPR maps are truncated at 10^{-1} and 10^{-10}, respectively.

tion (0.00+0.15) for perturbations (Figure 3). These error terms are included to account for uncertainties in estimating risk metrics via these simplified functions.

The severity of risk is then determined using an exposure model (Figures 2c & S3). The distribution of exposed population from the LandScan model (Rose et al., 2019) is gridded at ~1×1 km. Based on UK census data, we assume an average of 2.4 residents per household. The total number of homes affected by aggregate risk metrics is calculated by summing the expected number of homes affected at each 'shake grid' point (0.05×0.05°). As earthquakes of moderate magnitude have little to no far-reaching impact (Nievas et al., 2019), the simulation of nuisance and damage is limited to 400 and 40 km epicentral distance, respectively. The population maps are perturbed to account for variation in population distribution and uncertainties in our household inventory; each grid point is perturbed by a Poisson-like distribution (Gaussian with a mean of the grid point's value and a standard deviation of the square root of the value), to account for these uncertainties. LPR only considers the distance between the earthquake epicentre and the nearest populated grid point. When necessary, population is adjusted to reflect national temporal trends (Figure S6 U.N.-P.D., 2022).

2.4 Monte Carlo sampling

The final step is to account for the variabilities in individual components that will influence the output risk metrics. We use a 3000-trial Monte Carlo sampling approach in which all inputs are perturbed randomly via their previously described distributions (Figure 3). Inputs are sampled independently, with only nuisance parameter perturbations having a covariance (Schultz et al., 2021c). These repeated trials construct the statistical distribution of our risk metrics; by focusing on the median values, our red-light thresholds are the 50-50 chance of a given risk. We chose 3000-trials since this sample size produces stable median risk metrics estimates. For additional information on the workflow, we refer the reader to prior works on the subject (Schultz et al., 2020a, 2021a,b).

3 Results

With this approach (Section 2), we can now analyze the potential risk of HF cases in the UK. To do so, we begin by examining four test locations that are chosen to intentionally demonstrate the impact of exposure to our risk metrics (Figure 4). In each test location, risk increases monotonically as the red-light magnitude increases. However, the amount of risk in each location varies significantly for a constant red-light magnitude. We remind the reader that our approach quantifies the impacts that would happen following a red-light (including trailing seismicity) – it is unable to discern the likelihood of a red-light occurring, or the efficacy of an operator's mitigation procedures.

Our analysis begins by defining a single red-light threshold (*i.e.*, iso-magnitude) to examine how our three risk metrics vary with location. We then consider the impacts from prior UK HF seismicity to establish regional risk tolerances. Finally, we generate iso-risk maps that determine red-light thresholds based on these risk tolerances.

3.1 The iso-magnitude approach

First, we utilize our approach (Section 2) to determine the severity of risk for the geographic region of the UK. To do so, we create an 'earthquake grid' of 0.100×0.100° on which we simulate potential HF red-light earthquakes from a co-located HF operation. For each grid point, we assume a single red-light threshold of M_L 2.5. We choose this red-light threshold for two reasons: 1) this magnitude is below the 2019 M_L 2.9 PNR-2 earthquake and 2) this is slightly below the low end used for HF TLPs in North America (Schultz et al., 2021a). That said, we acknowledge that this choice is arbitrary.

Based on this premise, the impacts of our three estimated risk metrics (nuisance, damage, & LPR) are spatially heterogeneous and vary by orders of magnitude

Name/Place	Date	Magnitude (M_L)	Latitude	Longitude	Depth (km)	Tolerable?
HH-1	2019-02-27	3.2	51.160	-0.248	2.5	Intolerable
PNR-2	2019-08-26	2.9	53.787	-2.964	2.5	Intolerable
PH-1	2011-04-01	2.3	53.818	-2.950	2.3	Intolerable
PNR-2	2019-08-24	2.1	53.786	-2.969	2.1	Aggravating
PNR-2	2019-08-21	1.6	53.785	-2.971	2.1	Tolerable
PNR-1z	2018-12-11	1.6	53.787	-2.965	2.3	Tolerable

Table 1 Catalogue of the prominent (induced) events in the UK considered for our risk tolerance calibrations. See the text for a description on how event tolerability was chosen.

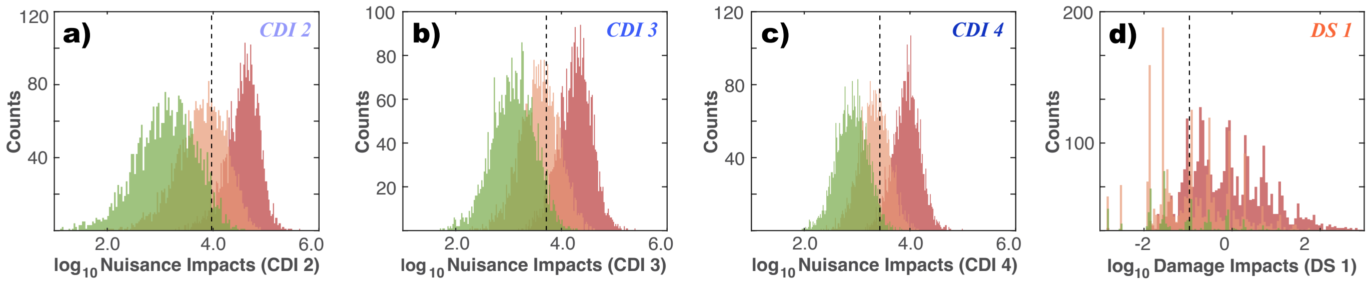

Figure 6 Modelled earthquake impact scenarios. Comparison of risk metrics between the M_L 1.6 (green bars), M_L 2.1 (orange bars) and M_L 2.9 PNR-2 events (red bars) alongside 50th percentile estimated tolerances for risk (dashed lines). Risk metrics of nuisance (a-c) and damage (d) are considered. All x-axis variables are in terms of the total number of homes impacted.

(Figure 5). The aggregate risk metrics (nuisance/damage impacts) follow the spatial population distribution, differing by their length scale. This difference in length scale has previously been explained by the typical range of damage/nuisance impacts for moderate magnitude earthquakes (*i.e.*, 10s/100s of kms, respectively). On the other hand, LPR appears to spatially correlate most strongly with the formation depth (Figures 2a & S1). This is because LPR is a local risk that we have estimated using the distance to the closest populated grid point. For the population distribution of the UK (Figures 2c & S3), effectively the epicentral distance is almost always 0 km, thus depth is effectively the only spatially varying input. This spatial variation in risk has previously been cited as a reason against iso-magnitude TLP designs (Schultz et al., 2021a,b).

3.2 Calibration of risk tolerances

In order to design fair TLPs, an iso-risk approach should be used. However, this approach requires making value-based decisions about acceptable risk tolerances, which can vary by region depending on the reputation of the operator and regulator (*i.e.*, the social license to operate, Smith and Richards, 2015; Thomas et al., 2017). To address this, we examine prior instances of HF-induced earthquakes in the UK to measure these tolerances empirically. We compare prominent (induced) earthquakes in the UK, that came under regulatory scrutiny (Table 1). For example, the HF induced events at PNR (Clarke et al., 2019; Kettlety et al., 2020) and PH-1 (Pater and Baisch, 2011; Clarke et al., 2014) are directly relevant for our study. We supplement this table with recent events near the Horse Hill well (HH-1), due to public concern (and regulatory scrutiny) that the events were induced hydrocarbon exploration. We emphasize that it is unlikely the Horse Hill earthquakes were induced (Hicks et al., 2019).

We use the known details of these events (Table 1) and a fit to the only free GMPE parameter (inter-event Z-score) based on observed shaking intensities. We do not use the trailing seismicity model in this case, since the event magnitude is known. From there, we proceed with the usual steps of our workflow, also utilizing 3000 Monte Carlo trials.

The estimation of the aggregate risk metrics is performed for all the significant (induced) events (Figures 6, S7, & S8). We separate the events into two bins: either having a tolerable or intolerable amount of risk, based on social/political reactions to the events. In this sense, we consider the M_L 2.9 PNR-2 event (and the Horse Hill or Preese Hall events) as the archetype of an intolerable amount of risk by UK standards, due to the public outrage and subsequent moratorium on HF development. The M_L 2.1 PNR-2 events are considered aggravating due to their public outrage and regulatory scrutiny, but operations were ultimately allowed to continue. All other events (Table 1) are considered tolerable (*e.g.*, M_L 1.6 PNR-2) because of a lack of social response (*e.g.*, regulatory change). Following this logic, we use these real events to 'bookend' UK tolerances to risks, by starting to constrain the upper/lower bounds to tolerances. For all three degrees of nuisance impacts (CDI 2-4), there is a clear separation between tolerable/intolerable event impacts (albeit with some overlap). For the damage impacts (DS 1-2), this separation is not as clear, with well-overlapping damage estimates from the three largest PNR-2 events.

From these observations, we begin to infer risk tolerances. We consider the intersection between the two PNR-2 (M_L 2.9 & 1.6) nuisance impacts as an empirical

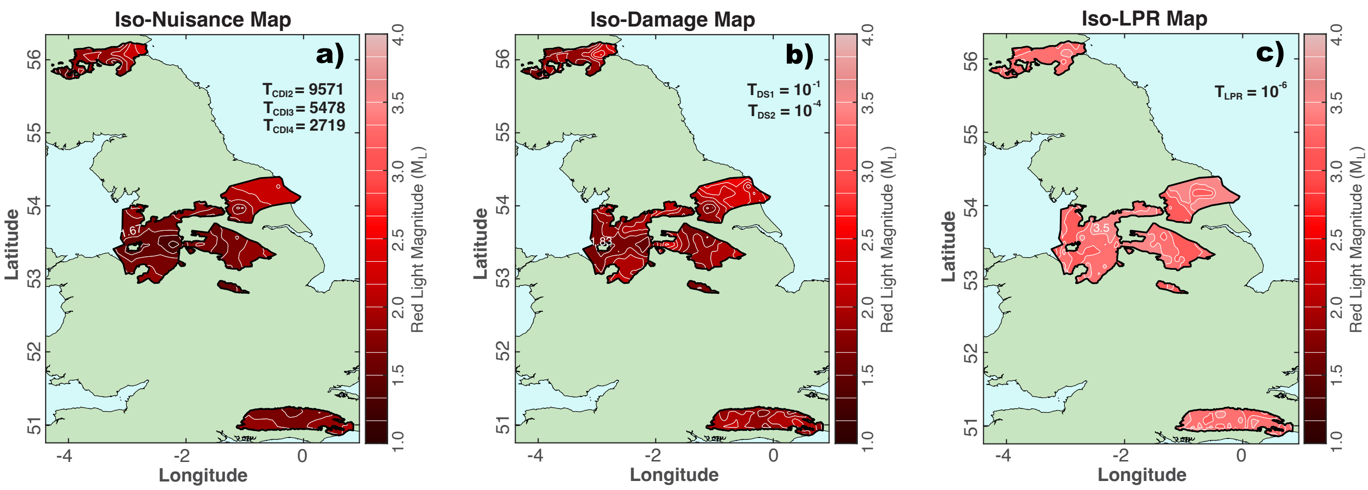

Figure 7 Iso-risk maps. a) Combination map of the three iso-nuisance maps (Figure S8). b) Combination map of the two iso-damage maps (Figure S9). c) Iso-LPR map. All maps have their tolerances for risk displayed as text.

measure of nuisance tolerance distribution. For damage tolerances, we consider the composite of the two PNR-2 damage impacts as an empirical measure of damage tolerance distribution. From these empirical tolerance distributions, we select the 50th percentile as our first choice for nuisance/damage tolerances. This 50th percentile choice results in nuisance tolerances roughly comparable to the modal/median value of the 2019 M_L 2.1 PNR-2 event (Figure 6). We note that estimates of tolerances from PNR-2 and PH-1 provide similar estimates (Figures 6 & S7), suggesting this approach is adequate for assessing a local populations tolerance to risks. Our 'bookending' approach estimated values of nuisance tolerance are T_{CDI2}=9571, T_{CDI3}=5478, T_{CDI4}=2719 impacted homes while damage tolerances are TDS1=10^{-1} and TDS2=10^{-4} impacted homes. Fatality risk tolerances are selected as 10^{-6} chance of occurring.

Last, we also provide a brief and qualitative comparison the 'Did You Feel it' reports collected by the British Geological Survey. Of all the earthquakes considered, we focus on the largest event (*i.e.*, the 2019 M_L 2.9 PNR-2 earthquake) which had 2266 submitted reports (*e.g.*, Edwards et al., 2021). Submitted reports indicated felt ground shaking intensities (EMS-98) of up to VI, although most are at V and IV; damage reports indicated 97 DS 1 and 50 DS 2 homes damaged. We emphasize that these felt/damage accounts are self-reported by the public, without expert verification. Our mean modelled values are 6249 CDI 2, 3298 CDI 3, and 1441 CDI 4 homes felt the event alongside 61 DS 1 and 0.01 DS 2 damaged homes. Taken at face-value, our modelled estimates of damage are approximately comparable to the reported values. We note that we intentionally use the modelled risk estimates of tolerance, rather than the reported metrics, to take advantage of estimation biases canceling out.

3.3 The iso-risk approach

We now apply an iso-risk approach using the empirically derived tolerances for aggregate risks in the UK (Section 3.2). Our tolerance for LPR is 10^{-6}, a conservative value for the range typically considered (Marzocchi et al., 2015; Commissie-Meijdam, 2015). Based on the previous risk curves (Section 3.1) and these risk tolerances, we then select red-light thresholds. We will discuss and justify the details and use of this risk tolerance later in the paper.

Prior research on nuisance has primarily focused on CDI 3, as tolerances to this metric are not well established (Schultz et al., 2021a,b). However, for the UK, we have empirically derived tolerances (Figures 6). We create separate iso-nuisance maps for each of the CDI 2-4 degrees (Figure S9). These individual maps are then combined into a single iso-nuisance map (Figure 7a), where the smallest red-light threshold from the three individual maps is selected at each grid point. In urban regions CDI 2 typically sets the threshold, while CDI 3 and CDI 4 control rural and remote regions, respectively (Figure S9). The differences between individual iso-nuisance maps are subtle, varying by no more than +0.4 M_L from the combination map. The iso-nuisance combination map has a spatial dependence on population distribution like the corresponding iso-magnitude map (Figure 5a).

We apply the same logic to the damage impacts risk metric, creating individual iso-damage maps that are then combined into a single iso-damage map (Figure S10). In this combined approach, the red-lights are entirely controlled by damage at the DS 1 level. It is worth noting that iso-damage combination exhibits a spatial dependence correlated with population distribution. The iso-damage map produces red-light thresholds that are roughly comparable to the iso-nuisance derived red-light thresholds.

Third, an iso-LPR map is produced using the same logic as the previous risk metrics (Figure 5c). Finally, we design TLP red-lights that will not exceed any of our risk metrics/tolerances by setting the smallest red-light threshold at each grid point (Figure 8). The median/mean values of this iso-risk combination map are M_L ~1.8, ranging between M_L 1.2-2.5, with 10th/90th percentiles at roughly M_L 1.6/2.2, respectively. When producing this combination map, nuisance and damage are roughly equivalent in concern (depending on location);

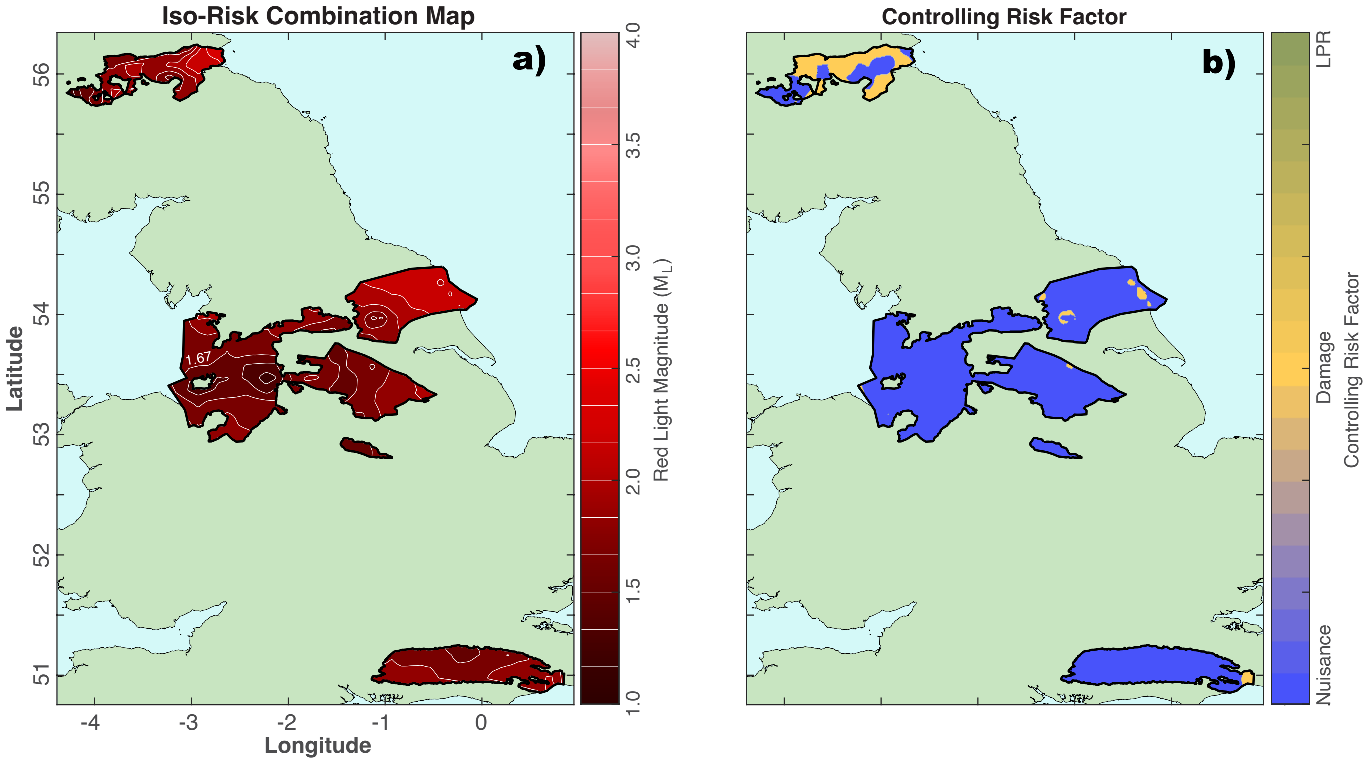

Figure 8 Combination map. a) Combination map of the three iso-risk maps (Figure 7). These three iso-risk maps are combined by taking the minimum red-light value at each grid point. b) Map showing which of the three iso-risk maps was the minimum red-light value for each grid point.

although, both nuisance and damage completely eclipse LPR concerns (Figure 8b).

4 Discussion

We discuss our results and their implications for effective TLP design in the UK.

4.1 Justification of risk metrics & risk tolerance choices

Here we briefly justify the use of our risks metrics and the tolerances derived for each metric. The use of LPR is much more straightforward than the other risks: there is an obvious need to keep citizens safe from harm and guidelines on tolerances to this risk (10^{-6}-10^{-4}) already exist, both for tectonic earthquakes (Marzocchi et al., 2015) and induced earthquakes (Commissie-Meijdam, 2015). This concern is relevant, since losses, both human and economic, have already resulted from HF induced earthquakes (Lei et al., 2019).

The inclusion of damage risks is also important, considering the aforementioned cases of damage. However, the exact handling of damage (and their tolerances) isn't quite as clear. One example is the Dutch handling of damage, where residents are entitled to compensation following a formal report and verify process – although there is a general feeling among the population that this handling is inadequate (van der Voort and Vanclay, 2015). In the case of the UK, our estimates suggest that residents are unwilling to accept any amount of damage, even at the DS 1 level (Figure 6d). This empirical estimate of damage tolerance has a tidy correspondence with the UK regulator's mandate, which is to "minimize the number of events felt at the surface by the public and to avoid the possibility of events capable of causing damage to nearby buildings or infrastructure" (Clarke et al., 2019; Oil and Gas Authority, 2018). Based on this information, we feel justified in our choice of (conservative) damage risk tolerances.

The inclusion of nuisance is the most nebulous risk metric: both because of the lack of prior consideration and predefined tolerances. Despite these limitations, previous 'good practice' guidelines have discussed the importance of nuisance (Majer et al., 2012) and legal frameworks often have liabilities defined around nuisance (Cypser and Davis, 1998). Building on this, many HF cases of regulatory intervention (*i.e.*, enacting a TLP, triggering a red-light, or ending the operation) have occurred without reports of damage or fatality (Schultz et al., 2021a,b). Furthermore, other studies on HF induced earthquakes in the UK have also highlighted the importance of quantifying/modelling nuisance (Cremen and Werner, 2020). Together, these points justify the inclusion of nuisance risks. The next step is to adequately choose nuisance tolerances. The definition of the red-light is the last-possible stopping-point before exceeding a tolerance to risk – *i.e.*, abandoning the operation to prevent taking an unacceptable risk. Based on this rationale, we have defined our nuisance tolerance to be between events that did/didn't trigger operation-ending regulatory interventions (Figure 6). In this sense, our selected nuisance tolerance threatens to end an operation (regardless of the existence of a predefined red-light). Last, we check these

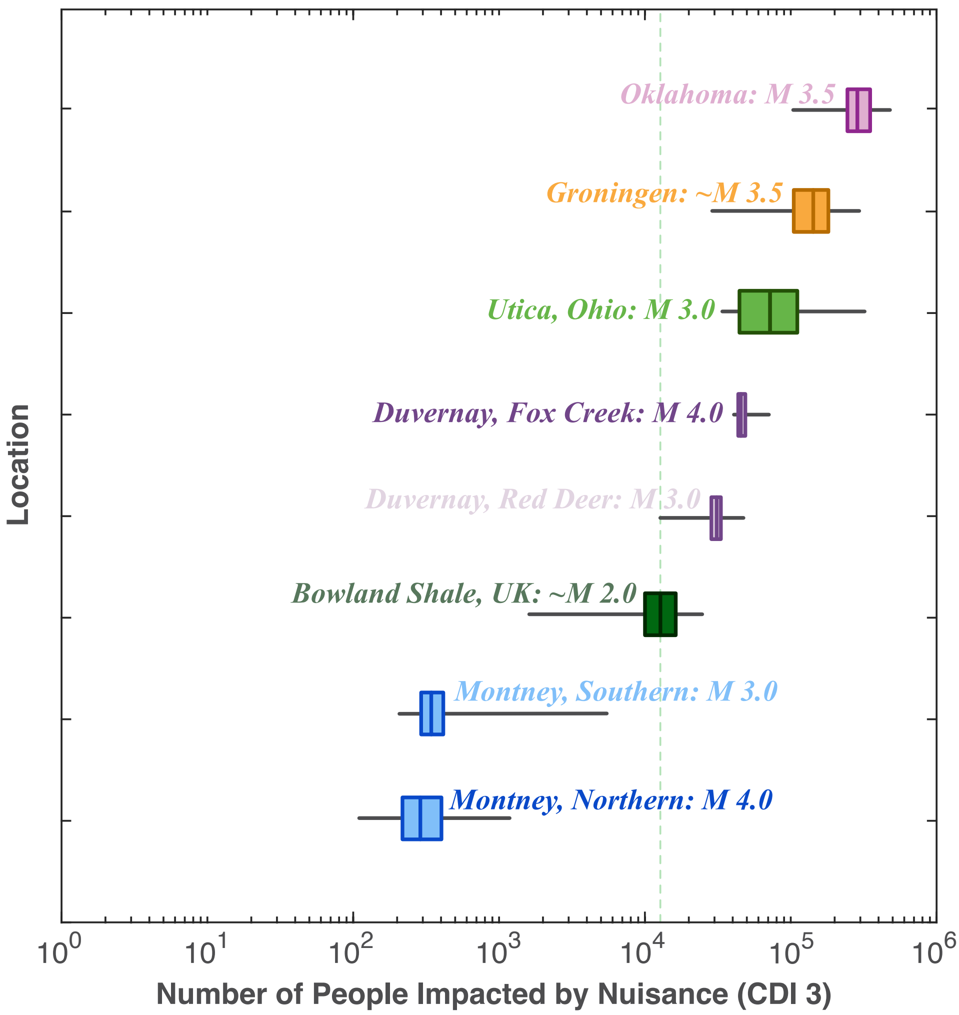

Figure 9 Worldwide nuisance tolerance estimates. The distribution of CDI 3 nuisance tolerance (box-and-whisker plots; boxes show 25-50-75 percentiles) for the UK (Figure 6) is compared to estimates in North America and the Netherlands (Schultz et al., 2021b, 2022b). The 50th percentile of the nuisance tolerance distribution, used to select the nuisance tolerance, is shown as green dashed line.

empirically derived nuisance tolerances against other measured tolerances (Figure 9, Schultz et al., 2022b, 2021b). We find that UK tolerances to nuisance are most like the risks implicitly taken by TLPs in Alberta, despite the significantly different red-light magnitude thresholds chosen there (*i.e.*, M_L 3.0 near Red Deer and M_L 4.0 near Fox Creek). Based on this, we feel that our inclusion of nuisance within the red-light design is justified. We note, however, that this approach can easily be repeated/updated using different tolerances as new information becomes available.

These tolerances result in red-light thresholds that vary spatially between M_L 1.2-2.5 (Figure 8). Comparatively, our thresholds are much smaller than the magnitudes of the largest recorded tectonic events onshore (M_L ~5) or offshore (M_L ~6, Musson, 2007, 2004) and smaller still than prior coal mining (M_L 3.1, Redmayne, 1988; Redmayne et al., 1998) or potash mining (1989 M_L 2.4, Browitt, 1991; Wilson et al., 2015) induced seismicity. These induced events were tolerated by the public, over a period of decades and in regions coincident with shale gas basins (Wilson et al., 2015). Cursory examination of temporal population trends (Figure S6, U.N.-P.D., 2022) suggests growth of ~10-20% since 1980, which can't account for the disparity between our red-lights and the previously accepted magnitudes. Similarly, our estimates of risk tolerances for the Horse Hill events (initially suspected as extraction-related, but found to be tectonic, Hicks et al., 2019) suggest tolerances approximately an order of magnitude larger than the ones derived for HF in the UK. We argue that these observations are not contradictory. Local tolerances are influenced by factors such as the type of risk, familiarity with the risk, consent to risk, geopolitical zeitgeist, personal needs, and past experiences (Marzocchi et al., 2015). In fact, surveys conducted in the UK indicate that local population are far less tolerant of earthquakes caused by HF compared to any other resource exploitation techniques (Evensen et al., 2022), supporting the differences of our tolerance estimates between HF and conventional hydrocarbon extraction (Figures 6, S7 & S8). If anything, this observation demonstrates the importance of maintaining a 'social license to operate' through effective outreach and communication (Majer et al., 2012).

In general, it is important to consider a combination

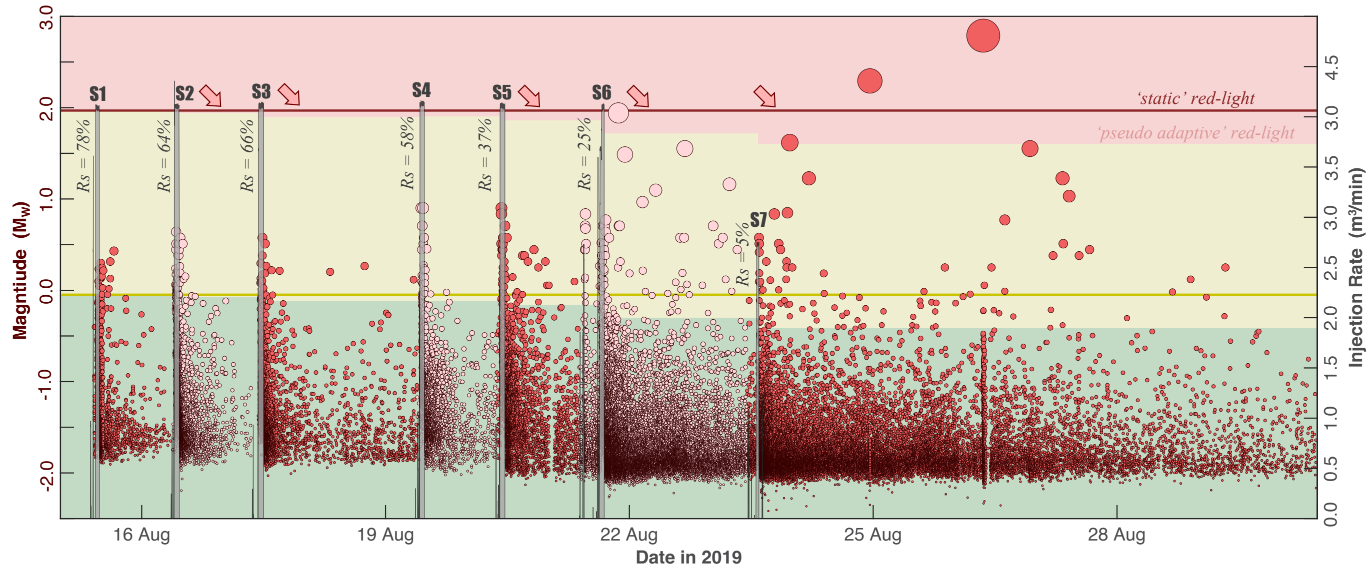

Figure 10 The proposed TLP retrospectively applied to PNR-2. Stimulation operations (grey areas) for the first seven stages (text labels) are shown alongside the induced earthquakes (red circles) and our proposed TLP thresholds: both 'static' *a priori* thresholds (solid-coloured lines) and 'pseudo adaptive' thresholds (coloured background) based on information from the previous stage stimulation. Red arrows indicate stages when the adaptive TLP red-light threshold sequentially decreases. Red-light moment magnitudes were estimated using an M_L-M_W conversion relationship (Edwards et al., 2021).

of all the risk metrics mentioned. Our approach offers the advantage of being able to simply combine multiple risk metrics (such as nuisance, damage, and fatality) and types (local or aggregate) by translating them into red-light thresholds. After defining the red-light, we can also link the design of yellow-light thresholds (Schultz et al., 2020a). Yellow-lights serve as a signal for operators to take appropriate mitigation measures before reaching the red-light threshold. However, magnitude 'jumps' (Verdon and Bommer, 2020) could create green-to-red transitions, rendering the yellow-light ineffective. Hence, setting an appropriate gap between yellow- and red-light thresholds is crucial to prevent this from happening. Previous studies (Schultz et al., 2020a) have suggested that yellow-light thresholds 2.0 magnitude units lower than the red-light is sufficient, although this depends on a jurisdiction's tolerance for triggering red-lights.

4.2 Retrospective comparison with the prior UK TLP

Our workflow enables a comparison with the prior TLP for the UK, which had a red-light set at M_L 0.5 that included an 18 hour pause (BEIS et al., 2013). Importantly, this differs from our definition of an operation-ending regulatory intervention for the red-light. By our standard, the prior UK 'red-light' is better defined as a yellow-light with prescriptive mitigation. In the location of the PH-1 well (Pater and Baisch, 2011; Clarke et al., 2014), which initially triggered the enactment of the prior TLP, our analysis suggests a red-light threshold of M_L ~1.7. If the aforementioned (Section 4.1) 2.0 magnitude gap between red-yellow is taken for a new TLP, this would indicate a yellow-light threshold of M_L -0.3, which is more conservative than the prior value of M_L 0.5. If we instead considered the old threshold as a proper red-light, we estimate that this scenario would only be weakly felt (CDI 2) at 10s of homes.

Our results also facilitate a retrospective analysis against known cases of HF induced earthquakes. In particular, the PNR-2 case is most relevant due to the 2019 M_L 2.9 event which prematurely ended operations (Kettlety et al., 2020). In this location, our results suggest a red-light threshold of M_L ~1.7. From the time history of events in this location, this red-light threshold would not have been triggered before the seventh (and final) stage of stimulation; the 26 August 2019 M_L 2.9 event occurred more than 72 hours after the completion of stage seven (Figure 10). The third largest event, which was induced from the sixth stage stimulation (21 August 2019 M_L 1.6), falls just below our red-light threshold (M_L 1.7). Following a similar comparison, our red-light thresholds would have been triggered for PH-1 (following the 2011 M_L 2.3 event) and would not have been triggered for PNR-1z (Figures S11 & S12) – as intended by our tolerance definitions.

The PNR-2 case highlights the need for updating of 'static' or *a priori* red-lights with incoming real-time information. Specific to PNR-2, we would expect that the red-light should decrease with time: the first six stages showed an anomalously high proportion of trailing seismicity (R_S=48%) compared to the global average (~86%) used to define our red-light (Schultz et al., 2020b, 2022a). Importantly, R_S is the most influential parameter for varying red-light thresholds (Schultz et al., 2021a). Similarly, the stage completions at PNR-1z (R_S=41%) and PH-1 (R_S=46%) also have a large proportion of trailing events compared to global averages (Schultz et al., 2022a). These systematically low values of R_S at PNR-1z and PNR-2 can explain the significant trailing seismicity observed for each well stage. Because of these trailing seismicity observations, we would expect that a dynamically updated red-light would have decreased from our static value as operations progressed.

To roughly demonstrate these dynamic red-light changes, we perform a pseudo adaptive update in response to the PNR-2 catalogue (Figure 10). Our simplistic approach assumes a change in the red-light threshold based entirely on the change of R_S value from the previous stage: essentially, we draw 10^6 trailing/red-light events for a given value of R_S , compute the median ΔM, and update the red-light in comparison to the difference from the global *a priori* median ΔM. This pseudo adaptive approach also demonstrates the sensitivity of red-lights to R_S changes. For example, stages five and six observed deviant R_S values of 37% and 25%, which reduce the red-light of subsequent stages by ~0.2 and ~0.4 M_W units (from the static red-light value), respectively. This simple updating process would have triggered a red-light following the 21 August 2019 M_L 1.6 event of stage six at PNR-2, ultimately ending the operation before the larger events of stage seven. Interestingly, this same process applied to PNR-1z still does not trigger a red-light, which is the intended goal for this case (Figure S11). Unfortunately, there are insufficient seismological data at the PH-1 case to adequately perform our pseudo adaptive TLP approach, so we are unable to assess if the M_L 2.3 event could have been avoided (Figure S12). Of course, this analysis has the benefit of hindsight; in practice, it is not well established how nearby stages are connected to seismogenic faults, linked in seismic response, and how well measured parameters (like R_S) would translate between stages – or how to forecast any of these considerations. While implementing a more rigorous updating of red-light values is beyond the scope of this paper (*e.g.*, Mignan et al., 2017), the HF events at PNR-2 appear to be an ideal case to test and develop this type of approach.

4.3 Prospective HF site recommendations

The design of a risk-based TLP for the UK provides a unique opportunity to begin discussing safer HF siting locations. The contentious history of HF in the UK (Williams et al., 2016) and induced earthquakes (Baptie et al., 2022) certainly makes this a significant concern. All of the basins have similar average risks (mean red-lights of M_L ~1.8); however, the Weald Basin (Figures 5, 7 & 8) is the most homogeneous, only ranging between M_L 1.6-2.0. The Bowland Shale has more disparate range M_L 1.2-2.3. The Midland Valley Basin has the most disparate ranges of red-lights, M_L 1.2-2.5 – largely due to the waterscapes where the Firth of Forth connects to the North Sea, near Edinburgh.

However, induced seismicity is not the only consideration: the anticipated productivity and the logistics/-costs of a prospective location also play a significant role in siting HF wells. The Bowland Shale has been considered the most prospective basin (Smith et al., 2010; Andrews, 2013), with operations targeting the western coast near Blackpool and Preston (e.g, PH-1, PNR-1z, & PNR-2 in Figure 1). These locations have red-light values near M_L 1.7, which is a location with slightly below average risk (owing to exposure). Highest risks are within the ~20 km vicinity of Manchester (M_L ~1.3), Liverpool, and York. The lowest Bowland Shale risks (M_L 2.3) are in a wide area near the eastern coast, from Bridlington to Scarborough. Depending on trade-offs for reduced productivity and logistical costs, this region could be a safer site choice (from the perspective of induced seismicity risks). Overall, our iso-risk red-light maps (Figure 8) facilitate comparisons and could be used to site prospective HF operations in the UK. We note that this approach focuses solely on the potential exposure to risks. Complementary siting approaches that consider the likelihood of induced seismicity, depending on the geological susceptibility to earthquakes (Pawley et al., 2018; Hicks et al., 2021), could also aid in choosing safer HF locations.

4.4 Limitations of our model and results

In this section, we briefly cover the limitations imposed by our model and the derived results. Firstly, components of our approach are based on models that were translated from other cases (*e.g.*, Groningen fragility and vulnerability functions). If more HF induced earthquakes occur, our model should be refined and updated accordingly. We want to emphasize that our workflow is adaptable and can incorporate new components or updates as needed. For example, if potential HF induced earthquakes in the UK are found to be only limited to a susceptible geographic region, a more targeted approach that utilizes known building inventories could improve risk assessments (Edwards et al., 2021). As well, risks posed to critical infrastructure could be included in the red-light determination, in relevant regions.

Our analysis has focused on the median risk values: *i.e.*, the 50-50 chance of a given risk impact. However, mean values are more informative being the expected risk impact. Our risk metrics have a heavy-tailed distribution, implying that the mean values will be strongly influenced by rare, high-consequence events with small likelihood. Therefore, using mean values instead of median would result in lower red-light thresholds. To better constrain these distributions, we would need a regional calibration of trailing count ratios (R_S), a better understanding of the maximum possible magnitudes, and component models that can extrapolate within appropriate ranges.

Finally, our approach has assumed static tolerances to risk, where a population suddenly changes their stance after risk value has been surpassed. Largely, this is due to the limited amount of data available to calibrate risk tolerances – our 'bookending' approach can only infer a range of values that the tolerance lies between. In reality, these tolerances may be time-dependent: such as by diurnal differences in tolerance, influenced by cumulative impacts from an operation, varying as the social license adjusts, or in response to growing urbanization/population increasing the amount of asset exposure. Much of our tolerance constraining approach has been restricted by the limitations of data/-case availability to make empirical inferences. To improve on these limitations would require methodological improvements for tolerance estimation, conceptual advances in modeling social change, or policy direction that explicitly defines agreeable risk tolerances.

5 Conclusions

To manage hypothetical induced seismicity in the UK, we have employed a risk-based design of TLP red-lights. We have relied on previously developed seismic hazard and risk research for the HF in the UK and the Groningen gas field (as a reasonable analogue). By contrasting the M_L 2.9, 2.1, and 1.6 PNR-2 events, we were able to empirically calibrate the UK tolerances to nuisance and damage risks. These calibrated tolerances are comparable to those established for HF in North America. Our findings indicate that nuisance and damage impacts impose more stringent red-lights than LPR. Based on our red-lights, we suggest potential sites where prospective HF wells could be drilled. The integration of these three risk metrics (nuisance impacts, damage impacts, and LPR) provides a quantitative basis for reference red-light thresholds to inform future HF TLPs in the UK, should the current moratorium be lifted. These results can also be adapted for other greener industries such as deep geothermal energy or carbon/hydrogen storage.

Acknowledgements

We would like to thank James Verdon and an anonymous reviewer for their critiques that helped improve this manuscript and Stephen Hicks for handling our manuscript as the editor. Grammatical editing of our manuscript was assisted by ChatGPT.

Data and code availability

Formation depths (Andrews, 2013, 2014; Monaghan, 2014), trailing seismicity model (Schultz et al., 2022a), GMPE model (Edwards et al., 2021), spatial noise correlation model (Esposito and Iervolino, 2012), site amplification (Heath et al., 2020), population density (Rose et al., 2019), nuisance function (Schultz et al., 2021c), fragility function (Korswagen et al., 2019), and vulnerability function (Crowley et al., 2017; Crowley and Pinho, 2020) are derived from prior studies. Earthquake catalogues and felt/damage reports are available online (https://earthquakes.bgs.ac.uk/earthquakes/dataSearch.html, https://www.nstauthority.co.uk/exploration-production/onshore/onshore-reports-and-data/preston-new-road-well-pnr2-data-studies/ & https://www.nstauthority.co.uk/exploration-production/onshore/onshore-reports-and-data/preston-new-road-pnr-1z-hydraulic-fracturing-operations-data/). Routines and publicly available data used to create the figures and results of this paper can be found online at GitHub https://github.com/RyanJamesSchultz/TLPuk or at Zenodo (https://doi.org/10.5281/zenodo.8416391). Additional materials on the workflow are also discussed in prior studies (Schultz et al., 2021a,b, 2022b).

Competing interests

The authors declare no competing interests.

References

Ader, T., Chendorain, M., Free, M., Saarno, T., Heikkinen, P., Malin, P. E., Leary, P., Kwiatek, G., Dresen, G., Bluemle, F., and Vuorinen, T. Design and implementation of a traffic light system for deep geothermal well stimulation in Finland. *Journal of Seismology*, 24(5):991–1014, Aug. 2019. doi: 10.1007/s10950-019-09853-y.

Andrews, I. The Carboniferous Bowland Shale gas study: geology and resource estimation. *British Geological Survey for Department of Energy and Climate Change*, page 64, 2013.

Andrews, I. The Jurassic shales of the Weald Basin: geology and shale oil and shale gas resource estimation. *British Geological Survey for Department of Energy and Climate Change*, page 89, 2014.

Atkinson, G. M., Eaton, D. W., Ghofrani, H., Walker, D., Cheadle, B., Schultz, R., Shcherbakov, R., Tiampo, K., Gu, J., Harrington, R. M., Liu, Y., van der Baan, M., and Kao, H. Hydraulic Fracturing and Seismicity in the Western Canada Sedimentary Basin. *Seismological Research Letters*, 87(3):631–647, Mar. 2016. doi: 10.1785/0220150263.

Atkinson, G. M., Eaton, D. W., and Igonin, N. Developments in understanding seismicity triggered by hydraulic fracturing. *Nature Reviews Earth & Environment*, 1(5):264–277, May 2020. doi: 10.1038/s43017-020-0049-7.

Baisch, S., Koch, C., and Muntendam-Bos, A. Traffic Light Systems: To What Extent Can Induced Seismicity Be Controlled? *Seismological Research Letters*, 90(3):1145–1154, Mar. 2019. doi: 10.1785/0220180337.

Baptie, B., Luckett, R., Butcher, A., and Werner, M. Robust relationships for magnitude conversion of PNR seismicity catalogues. *British Geological Survey Open-File Report*, 20(042):32, 2020.

Baptie, B., Segou, M., Hough, E., and Hennissen, J. Recent scientific advances in the understanding of induced seismicity from hydraulic fracturing of shales. *British Geological Survey Open Report*, 22(050):51, 2022.

Båth, M. Lateral inhomogeneities of the upper mantle. *Tectonophysics*, 2(6):483–514, Dec. 1965. doi: 10.1016/0040-1951(65)90003-x.

BEIS, D. f. B., Energy, and Strategy, I. Regulatory Roadmap: Onshore oil and gas exploration in the UK regulation and best practice, 2013. https://www.gov.uk/government/publications/regulatory-roadmap-onshore-oil-and-gas-.

Bickle, M., Goodman, D., Mair, R., Roberts, J., Selley, R., Shipton, Z., and Younger, P. Shale gas extraction in the UK: a review of hydraulic fracturing. In *The Royal Society and The Royal Academy of Engineering Report*, page 76. 2012.

Bommer, J. J. Earthquake hazard and risk analysis for natural and induced seismicity: towards objective assessments in the face of uncertainty. *Bulletin of Earthquake Engineering*, 20(6): 2825–3069, Apr. 2022. doi: 10.1007/s10518-022-01357-4.

Bommer, J. J., Oates, S., Cepeda, J. M., Lindholm, C., Bird, J., Torres, R., Marroquín, G., and Rivas, J. Control of hazard due to seismicity induced by a hot fractured rock geothermal project. *Engineering Geology*, 83(4):287–306, Mar. 2006. doi: 10.1016/j.enggeo.2005.11.002.

Boore, D. M., Stewart, J. P., Seyhan, E., and Atkinson, G. M. NGA-West2 Equations for Predicting PGA, PGV, and 5% Damped PSA for Shallow Crustal Earthquakes. *Earthquake Spectra*, 30(3): 1057–1085, Aug. 2014. doi: 10.1193/070113eqs184m.

Browitt, C. UK Earthquake Monitoring 1989/90. *British Geological Survey Technical Report WL/SO/13*, page 36, 1991.

Butcher, A., Luckett, R., Verdon, J. P., Kendall, J.-M., Baptie, B., and Wookey, J. Local Magnitude Discrepancies for Near-Event Receivers: Implications for the U.K. Traffic-Light Scheme. *Bulletin of the Seismological Society of America*, 107(2):532–541, Jan. 2017. doi: 10.1785/0120160225.

Caprio, M., Tarigan, B., Worden, C. B., Wiemer, S., and Wald, D. J. Ground Motion to Intensity Conversion Equations (GMICEs): A Global Relationship and Evaluation of Regional Dependency. *Bulletin of the Seismological Society of America*, 105 (3):1476–1490, May 2015. doi: 10.1785/0120140286.

Clarke, H., Eisner, L., Styles, P., and Turner, P. Felt seismicity associated with shale gas hydraulic fracturing: The first documented example in Europe. *Geophysical Research Letters*, 41 (23):8308–8314, Dec. 2014. doi: 10.1002/2014gl062047.

Clarke, H., Verdon, J. P., Kettlety, T., Baird, A. F., and Kendall, J.-M. Real-Time Imaging, Forecasting, and Management of Human-Induced Seismicity at Preston New Road, Lancashire, England. *Seismological Research Letters*, July 2019. doi: 10.1785/0220190110.

Commissie-Meijdam. Eindadvies Handelingsperspectief voor Groningen Ad- viescommissie 'Omgaan met risico's van geïnduceerde aardbevingen', 2015.

Cremen, G. and Werner, M. J. A novel approach to assessing nuisance risk from seismicity induced by UK shale gas development, with implications for future policy design. *Natural Hazards and Earth System Sciences*, 20(10):2701–2719, Oct. 2020. doi: 10.5194/nhess-20-2701-2020.

Cremen, G., Werner, M. J., and Baptie, B. A New Procedure for Evaluating Ground-Motion Models, with Application to Hydraulic-Fracture-Induced Seismicity in the United Kingdom. *Bulletin of the Seismological Society of America*, 110(5):2380–2397, Mar. 2020. doi: 10.1785/0120190238.

Crowley, H. and Pinho, R. Report on the Fragility and Consequence Models for the Groningen Field (Version 7, 2020. https://nam-onderzoeksrapporten.data-app.nl/reports/download/groningen/en/9d8819b7-f0c5-4089-a036-71e755fda328. URL:.

Crowley, H., Polidoro, B., Pinho, R., and van Elk, J. Framework for Developing Fragility and Consequence Models for Local Personal Risk. *Earthquake Spectra*, 33(4):1325–1345, Nov. 2017. doi: 10.1193/083116eqs140m.

Cuadrilla Resources Ltd. Hydraulic Fracture Plan PNR 2, URL, 2019. https://consult.environment-agency.gov.uk/onshore-.

Cypser, D. A. and Davis, S. D. Induced seismicity and the potential for liability under U.S. law. *Tectonophysics*, 289(1-3):239–255, Apr. 1998. doi: 10.1016/s0040-1951(97)00318-1.

Eads, L., Miranda, E., and Lignos, D. G. Average spectral acceleration as an intensity measure for collapse risk assessment. *Earthquake Engineering & Structural Dynamics*, 44(12):2057–2073, Mar. 2015. doi: 10.1002/eqe.2575.

Edwards, B., Crowley, H., Pinho, R., and Bommer, J. J. Seismic Hazard and Risk Due to Induced Earthquakes at a Shale Gas Site. *Bulletin of the Seismological Society of America*, 111(2):875–897, Jan. 2021. doi: 10.1785/0120200234.

Esposito, S. and Iervolino, I. Spatial Correlation of Spectral Acceleration in European Data. *Bulletin of the Seismological Society of America*, 102(6):2781–2788, Dec. 2012. doi: 10.1785/0120120068.

Evensen, D., Varley, A., Whitmarsh, L., Devine-Wright, P., Dickie, J., Bartie, P., Napier, H., Mosca, I., Foad, C., and Ryder, S. Effect of linguistic framing and information provision on attitudes towards induced seismicity and seismicity regulation. *Scientific Reports*, 12(1), July 2022. doi: 10.1038/s41598-022-15448-4.

Foulger, G. R., Wilson, M. P., Gluyas, J. G., Julian, B. R., and Davies, R. J. Global review of human-induced earthquakes. *Earth-Science Reviews*, 178:438–514, Mar. 2018. doi: 10.1016/j.earscirev.2017.07.008.

Green, C., Styles, P., and Baptie, B. Preese Hall Shale Gas Fracturing Review and Recommendations for Induced Seismic Mitigation, Induced Seismicity. Mitigation report„ Department of Energy and Climate Change, London, 2012.

Heath, D. C., Wald, D. J., Worden, C. B., Thompson, E. M., and Smoczyk, G. M. A global hybrid Vs30 map with a topographic slope–based default and regional map insets. *Earthquake Spectra*, 36(3):1570–1584, June 2020. doi: 10.1177/8755293020911137.

Hicks, S. P., Verdon, J., Baptie, B., Luckett, R., Mildon, Z. K., and Gernon, T. A shallow earthquake swarm close to hydrocarbon activities: Discriminating between natural and induced causes for the 2018–2019 Surrey, United Kingdom, earthquake sequence. *Seismological Research Letters*, 90(6):2095–2110, Aug. 2019. doi: 10.1785/0220190125.

Hicks, S. P., Goes, S., Whittaker, A. C., and Stafford, P. J. Multivariate Statistical Appraisal of Regional Susceptibility to Induced Seismicity: Application to the Permian Basin, SW United States. *Journal of Geophysical Research: Solid Earth*, 126(12), Dec. 2021. doi: 10.1029/2021jb022768.

Jaiswal, K. and Wald, D. An Empirical Model for Global Earthquake Fatality Estimation. *Earthquake Spectra*, 26(4):1017–1037, Nov. 2010. doi: 10.1193/1.3480331.

Jaiswal, K., Wald, D., and Hearne, M. Estimating casualties for large earthquakes worldwide using an empirical approach. U.s geological survey open-file report, of 2009-1136„ 2009.

Kettlety, T., Verdon, J. P., Butcher, A., Hampson, M., and Craddock, L. High-resolution imaging of the ML 2.9 August 2019 earthquake in Lancashire, United Kingdom, induced by hydraulic fracturing during Preston New Road PNR-2 operations. *Seismological Research Letters*, 92(1):151–169, Oct. 2020. doi: 10.1785/0220200187.

Korswagen, P., Longo, M., Meulman, E., Licciardello, L., and Sousamli, M. *Damage Sensitivity of Groningen Masonry – Experimental and Computational Studies (Part 2*. NAM Report by Delft University of Technology, 2019.

Lei, X., Wang, Z., and Su, J. The December 2018 ML 5.7 and January 2019 ML 5.3 earthquakes in South Sichuan basin induced by shale gas hydraulic fracturing. *Seismological Research Letters*, 90(3):1099–1110, Apr. 2019. doi: 10.1785/0220190029.

Luckett, R., Ottemöller, L., Butcher, A., and Baptie, B. Extending local magnitude ML to short distances. *Geophysical Journal International*, 216(2):1145–1156, Nov. 2018. doi: 10.1093/gji/ggy484.

Majer, E., Nelson, J., Robertson-Tait, A., Savy, J., and Wong, I. Protocol for Addressing Induced Seismicity Associated with Enhanced Geothermal Systems. Technical report, Jan. 2012. doi: 10.2172/1219482.

Marzocchi, W., Iervolino, I., Giorgio, M., and Falcone, G. When Is the Probability of a Large Earthquake Too Small? *Seismological Research Letters*, 86(6):1674–1678, Sept. 2015. doi: 10.1785/0220150129.

Mignan, A., Broccardo, M., Wiemer, S., and Giardini, D. Induced seismicity closed-form traffic light system for actuarial decision-making during deep fluid injections. *Scientific Reports*, 7(1), Oct. 2017. doi: 10.1038/s41598-017-13585-9.

Monaghan, A. The Carboniferous shales of the Midland Valley of Scotland: geology and resource estimation. *British Geological Survey for Department of Energy and Climate Change*, page 105, 2014.

Mosca, I., Sargeant, S., Baptie, B., Musson, R. M. W., and Pharaoh, T. C. The 2020 national seismic hazard model for the United Kingdom. *Bulletin of Earthquake Engineering*, 20(2):633–675, Jan. 2022. doi: 10.1007/s10518-021-01281-z.

Musson, R. British earthquakes. *Proceedings of the Geologists' Association*, 118(4):305–337, Jan. 2007. doi: 10.1016/s0016-7878(07)80001-0.

Musson, R. M. W. A critical history of British earthquakes. *Annals of Geophysics*, 47(2-3), Dec. 2004. doi: 10.4401/ag-3325.

Nievas, C. I., Bommer, J. J., Crowley, H., and van Elk, J. Global occurrence and impact of small-to-medium magnitude earthquakes: a statistical analysis. *Bulletin of Earthquake Engineering*, 18(1):1–35, Sept. 2019. doi: 10.1007/s10518-019-00718-w.

Oil and Gas Authority. Consolidated Onshore Guidance, Version 2.2, North Sea Transition Authority Report, 2018. https://www.nstauthority.co.uk/media/4908/consolidated-onshore-guidance-compendium_vfinal12062018.pdf.

Pater, C. and Baisch, S. Geomechanical study of Bowland Shale seismicity. page 71, 2011.

Pawley, S., Schultz, R., Playter, T., Corlett, H., Shipman, T., Lyster, S., and Hauck, T. The Geological Susceptibility of Induced Earthquakes in the Duvernay Play. *Geophysical Research Letters*, 45 (4):1786–1793, Feb. 2018. doi: 10.1002/2017gl076100.

Redmayne, D. W. Mining induced seismicity in UK coalfields identified on the BGS National Seismograph Network. *Geological Society, London, Engineering Geology Special Publications*, 5(1): 405–413, Jan. 1988. doi: 10.1144/gsl.eng.1988.005.01.45.

Redmayne, D. W., Richards, J. A., and Wild, P. W. Mining-induced earthquakes monitored during pit closure in the Midlothian Coalfield. *Quarterly Journal of Engineering Geology*, 31(1): 21–36, Feb. 1998. doi: 10.1144/gsl.qjeg.1998.031.p1.03.

Rose, A., McKee, J., Urban, M., Bright, E., and Sims, K. LandScan 2018 High-Resolution Global Population Data Set (No. In *LandScan 2018 High-Resolution Global Population Da; 005854MLTPL00). Oak Ridge National Laboratory (ORNL*. Oak Ridge, TN, 2019. United States).

Roy, C., Nowacki, A., Zhang, X., Curtis, A., and Baptie, B. Accounting for Natural Uncertainty Within Monitoring Systems for Induced Seismicity Based on Earthquake Magnitudes. *Frontiers in Earth Science*, 9, May 2021. doi: 10.3389/feart.2021.634688.

Schultz, R., Atkinson, G., Eaton, D. W., Gu, Y. J., and Kao, H. Hydraulic fracturing volume is associated with induced earthquake productivity in the Duvernay play. *Science*, 359(6373): 304–308, Jan. 2018. doi: 10.1126/science.aao0159.

Schultz, R., Beroza, G., Ellsworth, W., and Baker, J. Risk-informed recommendations for managing hydraulic fracturing induced seismicity via traffic light protocols. *Bulletin of the Seismological Society of America*, 110(5):2411–2422, Apr. 2020a. doi: 10.1785/0120200016.

Schultz, R., Skoumal, R. J., Brudzinski, M. R., Eaton, D., Baptie, B., and Ellsworth, W. Hydraulic Fracturing-Induced Seismicity. *Reviews of Geophysics*, 58(3), July 2020b. doi: 10.1029/2019rg000695.

Schultz, R., Beroza, G. C., and Ellsworth, W. L. A risk-based approach for managing hydraulic fracturing-induced seismicity. *Science*, 372(6541):504–507, Apr. 2021a. doi: 10.1126/science.abg5451.

Schultz, R., Beroza, G. C., and Ellsworth, W. L. A Strategy for Choosing Red-Light Thresholds to Manage Hydraulic Fracturing Induced Seismicity in North America. *Journal of Geophysical Research: Solid Earth*, 126(12), Dec. 2021b. doi: 10.1029/2021jb022340.

Schultz, R., Quitoriano, V., Wald, D. J., and Beroza, G. C. Quantifying nuisance ground motion thresholds for induced earthquakes. *Earthquake Spectra*, 37(2):789–802, Jan. 2021c. doi: 10.1177/8755293020988025.

Schultz, R., Ellsworth, W. L., and Beroza, G. C. Statistical bounds on how induced seismicity stops. *Scientific Reports*, 12(1), Jan. 2022a. doi: 10.1038/s41598-022-05216-9.

Schultz, R., Muntendam-Bos, A., Zhou, W., Beroza, G. C., and Ellsworth, W. L. Induced seismicity red-light thresholds for enhanced geothermal prospects in the Netherlands. *Geothermics*, 106:102580, Dec. 2022b. doi: 10.1016/j.geothermics.2022.102580.

Smith, D. C. and Richards, J. M. Social License to Operate: Hydraulic Fracturing-Related Challenges Facing the Oil & Gas Industry. *SSRN Electronic Journal*, 2015. doi: 10.2139/ssrn.2591988.

Smith, N., Turner, P., and Williams, G. UK data and analysis for shale gas prospectivity. *Geological Society, London, Petroleum Geology Conference Series*, 7(1):1087–1098, Jan. 2010. doi: 10.1144/0071087.

SodM, Staatstoezicht op de Mijnen. Risico analyse aardgasbevingen Groningen (Risk assessment gas-earthquakes Groningen, in Dutch), 2014.

Thomas, M., Partridge, T., Harthorn, B. H., and Pidgeon, N. Deliberating the perceived risks, benefits, and societal implications of shale gas and oil extraction by hydraulic fracturing in the US and UK. *Nature Energy*, 2(5), Apr. 2017. doi: 10.1038/nenergy.2017.54.

UK Public General Acts. UK Infrastructure Act 2015, 2015. https://www.legislation.gov.uk/ukpga/2015/7/part/6/crossheading/other-provision-about-onshore-petroleum/enacted.

U.N.-P.D. United Nations Department of Economic and Social Affairs Population Division, 2022. https://population.un.org/wpp/. World Population Prospects 2022, Online Edition.

van der Voort, N. and Vanclay, F. Social impacts of earthquakes caused by gas extraction in the Province of Groningen, The Netherlands. *Environmental Impact Assessment Review*, 50: 1–15, Jan. 2015. doi: 10.1016/j.eiar.2014.08.008.

Verdon, J. P. and Bommer, J. J. Green, yellow, red, or out of the blue? An assessment of Traffic Light Schemes to mitigate the impact of hydraulic fracturing-induced seismicity. *Journal of Seismology*, 25(1):301–326, Oct. 2020. doi: 10.1007/s10950-020-09966-9.

Verdon, J. P. and Rodríguez-Pradilla, G. Assessing the variability in hydraulic fracturing-induced seismicity occurrence between North American shale plays. *Tectonophysics*, 859:229898, July 2023. doi: 10.1016/j.tecto.2023.229898.

Villani, M., Polidoro, B., McCully, R., Ader, T., Edwards, B., Rietbrock, A., Lubkowski, Z., Courtney, T. J., and Walsh, M. A Selection of GMPEs for the United Kingdom Based on Instrumental and Macroseismic Datasets. *Bulletin of the Seismological Society of America*, 109(4):1378–1400, July 2019. doi: 10.1785/0120180268.

Wald, D. J., Quitoriano, V., Worden, C. B., Hopper, M., and Dewey, J. W. USGS "Did You Feel It?" internet-based macroseismic intensity maps. *Annals of Geophysics*, 54(6), Jan. 2012. doi: 10.4401/ag-5354.

Westlake, S., John, C. H. D., and Cox, E. Perception spillover from fracking onto public perceptions of novel energy technologies. *Nature Energy*, 8(2):149–158, Jan. 2023. doi: 10.1038/s41560-022-01178-4.

Williams, L., Macnaghten, P., Davies, R., and Curtis, S. Framing 'fracking': Exploring public perceptions of hydraulic fracturing in the United Kingdom. *Public Understanding of Science*, 26(1): 89–104, Aug. 2016. doi: 10.1177/0963662515595159.

Wilson, M. P., Davies, R. J., Foulger, G. R., Julian, B. R., Styles, P., Gluyas, J. G., and Almond, S. Anthropogenic earthquakes in the UK: A national baseline prior to shale exploitation. *Marine and Petroleum Geology*, 68:1–17, Dec. 2015. doi: 10.1016/j.marpetgeo.2015.08.023.

doi:10.26443/seismica.v2i2.1082

Passive Assessment of Geophysical Instruments Performance using Electrical Network Frequency Analysis

M. R. Koymans * [1,2], **J. D. Assink** [1], **E. de Zeeuw-van Dalfsen** [1,3], **L. G. Evers** [1,2]

[1]Department of Seismology and Acoustics, Royal Netherlands Meteorological Institute, Utrechtseweg 297, De Bilt 3731 GA, Utrecht, the Netherlands, [2]Geoscience and Engineering, Delft University of Technology, Stevinweg 1, Delft 2628 CN, Zuid-Holland, the Netherlands, [3]Geoscience and Remote Sensing, Delft University of Technology, Stevinweg 1, Delft 2628 CN, Zuid-Holland, the Netherlands

Author contributions: *Conceptualization*: Mathijs Koymans. *Methodology*: Mathijs Koymans. *Software*: Mathijs Koymans. *Validation*: Mathijs Koymans, Jelle Assink, and Läslo Evers. *Writing - Original draft*: Mathijs Koymans. *Writing - Review & Editing*: Jelle Assink, Elske de Zeeuw-van Dalfsen, and Läslo Evers. *Supervision*: Elske de Zeeuw-van Dalfsen and Läslo Evers.

Abstract The electrical network frequency (ENF) of the alternating current operated on the power grid is a well-known source of noise in digital recordings. The noise is widespread and appears not just in close proximity to high-voltage power lines, but also in instruments simply connected to the mains powers grid. This omnipresent, anthropogenic signal is generally perceived as a nuisance in the processing of geophysical data. Research has therefore been mainly focused on its elimination from data, while its benefits have gone largely unexplored. It is shown that mHz fluctuations in the nominal ENF ($50/60\ \mathrm{Hz}$) induced by variations in power usage can be accurately extracted from geophysical data. This information represents a persistent time-calibration signal that is coherent between instruments over national scales. Cross-correlation of reliable reference ENF data published by electrical grid operators with estimated ENF data from geophysical recordings allows timing errors to be resolved at the $1\ \mathrm{s}$ level. Furthermore, it is shown that a polarization analysis of particle motion at the ENF can detect instrument orientation anomalies. While the source of the ENF signal in geophysical data appears instrument and site specific, its general utility in the detection of timing and orientation anomalies is presented.

Production Editor:
Gareth Funning
Handling Editor:
Catherine Rychert
Copy & Layout Editor:
Hannah F. Mark

Received:
July 6, 2023
Accepted:
November 6, 2023
Published:
December 12, 2023

1 Introduction

Sustaining reliable and continuous operation of instruments in the field is a key objective in the maintenance of geophysical monitoring infrastructures. This objective is particularly challenging for remote deployments, and equipment that cannot easily be accessed, e.g., for sensors buried at depth inside seismic boreholes. Active assessments that involve station maintenance visits are costly, time-consuming, and require perpetual planning and effort. Methods for passive quality assessment are often pursued due to their advantages in terms of scalability and reduced cost (McNamara and Boaz, 2006; Ahern et al., 2015; Ringler et al., 2015; Trani et al., 2017; Petersen et al., 2019; Pedersen et al., 2020; Koymans et al., 2021). Moreover, such passive techniques do not disturb the measurement setup itself and may be useful in, e.g., citizen science (Raspberry Shake, S.A., 2016) where the acquisition of high quality data can not be guaranteed. In the case where correction factors can be estimated, they can also be retroactively applied to an archived dataset. Data assessment is not exclusively useful to science, but also serves a purpose to detect malicious actors and data tampering that is critical in, e.g., the verification of the Comprehensive Nuclear-Test-Ban Treaty (Coyne et al., 2012).

Geophysical data may express characteristic spectral peaks that emerge from the electrical network frequency (ENF) of the alternating current (AC) operated on the electrical grid. This signal is sometimes referred to as *powerline* noise, but notably does not appear exclusively near high voltage power lines and is widespread. The signal is omnipresent in recordings from, e.g., seismometers (Bormann and Wielandt, 2013), gravimeters (Imanishi et al., 2022; Křen et al., 2021), microbarometers, and other digital instruments that are connected to or deployed near any type of electrical infrastructure or mains power supply. The ENF signal is usually perceived as a nuisance during the processing of geophysical data, and research has mainly been targeting its elimination (Butler and Russell, 1993; Xia and Miller, 2000; Levkov et al., 2005). For most purposes, the application of a narrow band-stop (notch) filter is sufficient to remove the signal. However, ringing artefacts, higher harmonics, or overlap with the bandwidth of interest sometimes makes the application of such filters impractical. For example, in seismoelectric acquisition and seismic exploration, advanced methods for the removal of coherent electrical noise are applied (Butler and Russell, 1993, 2003). While methods to eliminate the ENF signal from geophysical data are well known,

*Corresponding author: koymans@knmi.nl

the benefits of its presence are rarely explored. This study approaches the ENF from a different perspective, and demonstrates its utility as a signal in geophysics.

In this manuscript, two benefits of detecting the ENF in geophysical data are explored and used as passive quality assessment tools. First, the background information on the ENF is described (section 2), followed by an introduction of the data sets that are used (section 3.1). After that, the methodologies are described to **(i)** extract the ENF signal from spectrograms of geophysical data (section 3.2) and compute cross correlations (section 3.3), and **(ii)** complete a polarization analysis of the particle motion around the ENF (section 3.4). Results from cross correlations between spectrogram-estimated and reference ENF data are presented, demonstrating that timing errors with a resolution near the 1 s level can be resolved and verified (section 4.1). The accuracy of the recovered timing discrepancies are statistically quantified (section 4.2.1) and checked using teleseismic arrivals (section 4.2.2) that should be observed simultaneously on stations in close proximity, providing an alternative way of detecting relative time shifts. Results from the polarization analysis indicate that the method is capable of detecting gross sensor orientation anomalies (section 4.3). Finally, the source of the ENF signal in different geophysical instruments is discussed, and comments are provided on possible future avenues of research (section 5).

2 Background

2.1 Electrical Network Frequency

An abridged description of the electrical grid concerns power generators that supply electrical energy to consumers. Conceptually, generators are rotating turbines with magnetic cores that induce AC in coils following Faraday's law of electromagnetic induction. All generators on the grid collectively produce synchronous AC, with waveforms that are equal in amplitude, phase, and frequency. Because the electrical energy produced by the generators cannot be stored it must be immediately consumed, requiring a delicate balance between production and demand. At an instant when more energy is consumed than produced, the required excess power is drawn from the rotational inertia of the generators. This synchronously reduces the rotation speed of the generators on the grid, and subsequently lowers the effective ENF. Likewise, a sudden decrease in load causes the turbines to spin faster, leading to an increase of the ENF. Electrical grid operators balance the amount of electrical work done by the generators with the demand of consumers to keep the ENF stable at 50 Hz for continental Europe and 60 Hz for the United States. This balance is diligently maintained, and operational procedures are in place to limit deviations from the target ENF to within 10 to 50 mHz.

All electrical components – including geophysical instruments – are to some degree susceptible to the secondary effects of the AC operated on the electrical grid (fig. 1). Signals may be incurred from stray electromagnetic fields that are emitted from nearby current carrying wires and operating electronics. Common sources of the ENF signal being carried over in electric devices are through ground loops, and by direct electromagnetic induction of poorly shielded wires and circuitry. Magnetostriction in transformers (Gange, 2011) and full-bridge rectifiers (AC → DC) in power supplies may produce vibrations and audible sound at double the ENF. The well-known audible sound originating from the ENF is commonly referred to as *mains hum*. In broadband seismometers, a known coupling mechanism is through the suspension spring that responds to changing magnetic fields (Forbriger, 2007). Intense changing magnetic fields may even cause the housing of instruments to vibrate (Klun et al., 2019). At frequencies above the operated ENF, overtones at integer multiples of the ENF can sometimes be observed (Cohen et al., 2010; Schippkus et al., 2020).

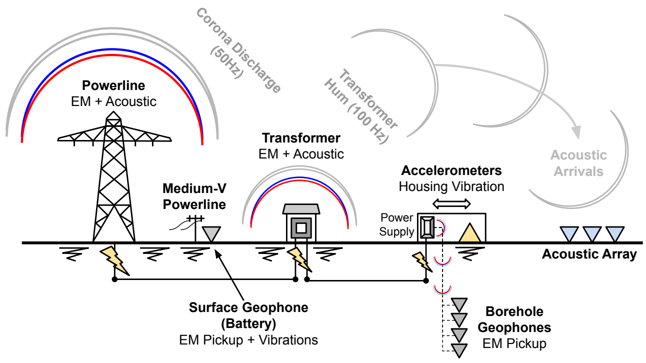

Figure 1 Overview of suspected sources of the ENF signal in geophysical data where the colors represent electromagnetic (red/blue), acoustic (grey), and seismic (black) coupling. The coupling mechanism varies between instruments and installation site. The signal may be coupled through physical vibrations, acoustic waves, or by direct magnetic induction.

While the ENF signal is typically of minor influence, equipment that integrates amplifiers may boost it to significant amplitudes. While the source of the ENF signal in high gain equipment is not always directly apparent from its surrounding, its persistence and omnipresence remains remarkable.

2.2 ENF Analysis

ENF analysis typically concerns the detection of mHz variations of the ENF in digital recordings as a function of time, of which an example is illustrated in fig. 2. These variations can be extracted from, e.g., audio (Cooper, 2008), optical (Garg et al., 2011), and geophysical data (Cohen et al., 2010). Because the AC is operated synchronously and uniformly on the electrical grid, digital recordings of the ENF represent a fingerprint that is coherent nationwide and, because of effectively random load fluctuations, represents a signal that is unique in time. The estimated variations in the ENF from digital recordings may thus be compared to an independent reliable reference measurement of the ENF that is provided by electrical grid operators. Such analysis of the ENF has been used to timestamp audio recordings (Garg et al., 2012) and confirm the authenticity of digital records. The successful use of ENF analysis as forensic evidence (Cooper, 2010) is a testament to the effectiveness and reliability of the technique.

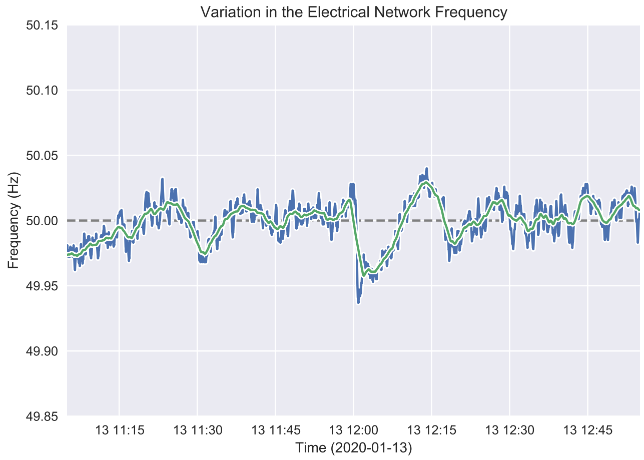

Figure 2 Example of minor mHz variations in the ENF during two minutes on Jan 13th, 2020 around the nominal European grid frequency of $50\,\mathrm{Hz}$ (grey dashed line). These data were not recorded by a geophysical instrument but illustrate reference ENF data that were downloaded from electrical grid operator TransnetBW. The raw data are plotted in blue, with a smoothed $150\,\mathrm{s}$ moving average illustrated in green.

3 Methodology

3.1 Instruments and Data Used

Various data types from different sensors are analysed in order to study the specific character of the ENF in these instruments. Data from the Netherlands Seismic and Acoustic Network (KNMI, 1993) and E-TEST temporary deployment (Shahar Shani-Kadmiel et al., 2020) (fig. 3 and table 1) are treated. The G-network of the Netherlands Seismic and Acoustic Network (NSAN) consists of nearly seventy $200\,\mathrm{m}$ deep boreholes in the Groningen province with geophones installed at $50\,\mathrm{m}$ depth intervals, and an accelerometer located at the surface. Data from the NSAN that belong to a low-frequency acoustic array installed at the Royal Netherlands Meteorological Institute in De Bilt (see supplementary information), and seismo-acoustic arrays at LOFAR sites in Drenthe are also analysed. The E-TEST temporary deployment consists of a dense array of battery-operated surface geophones located in the south of the province of Limburg without a main power supply.

3.2 Spectrogram Calculation and ENF Estimation

Independent ENF reference measurements at $1\,\mathrm{Hz}$ are universally accessible and downloaded from, e.g., the power-grid frequency database (Gorjão et al., 2020) and the website of TransnetBW GmbH. In this manuscript, ENF measurements from a German provider were used – data that are synchronous with the electrical grid operated in the Netherlands. The reference ENF data were smoothed using a centered moving average filter over $150\,\mathrm{s}$ (e.g., see fig. 2).

Geophysical data from the instruments summarised in table 1 were pre-processed using ObsPy (Beyreuther et al., 2010) (read and merged) and spectrograms were calculated using the SciPy *spectrogram* method (Virtanen et al., 2020) with a segment length of $150\,\mathrm{s}$, employing a $50\,\%$ overlap between consecutive segments. It was determined empirically that this segment length provided the most effective trade-off in resolution between time and frequency to resolve the ENF from the spectrograms. A linear trend was removed from each segment and the data were tapered using a cosine window with a shape parameter of 0.25. A Gaussian filter was applied in the frequency domain before the ENF was estimated from the spectrogram. This filter represents the mean and standard deviation of the yearly ENF signal ($\mathcal{N}_{50}(\mu,\,\sigma) = 50.000\,\mathrm{Hz},\,441 \times 10^{-4}\,\mathrm{Hz}$), and eliminates peaks in the spectrogram that are likely unrelated to the ENF. For each segment, the estimated ENF is represented by the frequency bin that associates with the maximum PSD within the 49.85 to $50.15\,\mathrm{Hz}$ band. An identical approach (with modified filter $\mathcal{N}_f$) was used for the extraction of overtones of the ENF in higher frequency bands (e.g., at $100\,\mathrm{Hz}$).

3.3 Cross-Correlation Analysis

The estimated variations in the ENF were interpolated to $1\,\mathrm{s}$ and cross-correlated with independent reference ENF data. A negative delay from the cross-correlation result implies that the reference signal leads the estimated ENF and is therefore behind *true* time. A statistical analysis of the accuracy and precision of the method was completed using an ensemble of cross correlations from instruments that are known to have zero time delay. The accuracy of the method and the recovered timing errors were further verified at a seismic array using teleseismic arrivals from an event near the Kermadec Islands, New Zealand (2021-03-04T19:28:33 UTC). Because the teleseismic arrivals are characterised by a near vertical incidence angle, the arrival times for proximal stations are expected to be similar, providing an alternative relative timing reference to compare against the obtained ENF analysis results.

3.4 ENF Polarization Analysis

Another independent aspect where the ENF signal can be leveraged is for surface accelerometers in the G-network that express a significant and strongly polarized susceptibility to the ENF. Accelerometer data were rotated towards a north-east orientation following the azimuth provided by the station metadata. The polarized ENF signal was isolated with a zero-phase band-pass filter between 49.85 to $50.15\,\mathrm{Hz}$. A principal component analysis (PCA) was applied to the three-dimensional particle motion data and eigenvalues (λ_1, λ_2, λ_3) were recovered, from which the degree of rectilinearity (Jurkevics, 1988) was calculated:

Sensor	Description	Network	Sampling Rate
SM6H	Borehole geophone	G-network (NL)	200
Kinematrics EpiSensor (ES-T)	Strong-motion accelerometer	G-network (NL)	200
SM-6/U-B 4.5Hz 375	Sensor B.V. Geophone	LOFAR Array (NL)	250
Hyperion Infrasound Sensor	Low-frequency sound microphone	De Bilt Array (NL)	500
SENSOR Nederland, PE-6/B, 3C	Battery operated geophone	E-TEST Deployment (3T)	500

Table 1 Descriptions and characteristics of geophysical instruments used for various aspects of ENF analysis that are treated in this manuscript and supplementary material. Instrument and response details are accessible from FDSN webservices (http://rdsa.knmi.nl and http://orfeus-eu.org).

$$1 - \left(\frac{\lambda_2 + \lambda_3}{2\lambda_1}\right) \tag{1}$$

The azimuth of the principal direction of motion (θ) was derived from the largest eigenvector $\mathbf{u}_1$, as given by its north and east components: $\theta = \arctan_2(\mathbf{u}_{1_\mathrm{N}}, \mathbf{u}_{1_\mathrm{E}})$. The goal of this method is to investigate whether the ENF can be used to verify the instrument orientation as specified in the station metadata.

4 Results

4.1 Timing Errors from ENF Analysis

An example ENF analysis for instrument EpiSensor accelerometer G180 is shown in fig. 4. The figure illustrates the reference variation in the ENF around $50\,\mathrm{Hz}$ (A), the raw seismometer spectrogram expressed in ground acceleration (B), the spectrogram with the Guassian filter applied (C), and that the ENF can be accurately recovered from the filtered spectrogram (D). fig. 5 panel A shows the measured and estimated ENF time series from fig. 4. The curves were vertically displaced from an average of $50\,\mathrm{Hz}$ to illustrate their similarity. The full cross-correlation of the measured and estimated ENF is illustrated in panel B and expresses a peak at a delay of $-1\,\mathrm{s}$ (C), meaning the instrument effectively runs behind *true* time. An identical analysis for an acoustic station is presented in the supplementary information because of additional complications that were encountered.

The presented example result in figs. 4 and 5 illustrates the method for a single instrument, but the approach has been successfully applied to all instruments in the NSAN network, including surface accelerometers, geophones, and microbarometers. The results indicate that the proposed method appears capable of detecting misfits between the estimated and reference ENF in geophysical data, potentially providing a stable nationwide timing calibration signal.

4.2 Validation of Timing Error Results

In the following sections, two methods are used to assess the precision and accuracy of the proposed method for the detection of timing anomalies.

4.2.1 Resolution of the Method

An estimate of the statistical significance of the recovered time lags is obtained through an ensemble of cross correlations between the measured and estimated ENF from all components of 71 surface accelerometers in the NSAN. These instruments are known to have accurate timestamps because they obtain timing through GPS and should thus express a zero-second delay from true time. fig. 6 shows an ensemble of 211 cross correlations with its average and $95\,\%$ confidence interval in blue. The peaks of all cross correlations and recovered time lags are also illustrated by grey markers. Accelerometers for which the ENF could not be resolved due to poor data quality or elevated noise have been removed from the ensemble. The majority of instruments express a lag of $-1\,\mathrm{s}$ between the estimated and measured ENF data, while the others express a $0\,\mathrm{s}$ time lag as expected. The confidence interval on the mean time lag from this ensemble illustrates the estimated accuracy and precision of the method at approximately $1\,\mathrm{s}$. Furthermore, the repeatability of the methodology between 211 data channels is a testament to its consistency. The minor stable deviation from the expected delay of zero may be caused by a non-precise or rounded off timestamp of the ENF data provided by the grid operator.

4.2.2 Verification Using Teleseismic Arrivals

The accuracy of the recovered timing errors was further verified using teleseismic arrivals at geophone ENV1 and nearby LOFAR arrays L106 and L208 of the M8.1 earthquake near the Kermadec Islands, New Zealand that occurred at 2021-03-04T19:28:33 UTC. The first two rows of fig. 7 show station ENV1 and L2082 at $24\,\mathrm{km}$ and $13\,\mathrm{km}$ distance from LOFAR array L106 (bottom 6 rows) respectively. The predicted seismic arrival times for the PKIKP phase of the event were calculated with TauPy (Beyreuther et al., 2010) using the IASP91 model (Kennett and Engdahl, 1991). The left column in fig. 7 shows that the recorded arrivals of the seismic phase of the original time-series are misaligned. The right panels show the same data shifted by the recovered delay from the ENF analysis (marked in the top-left corner of each panel). Geophone ENV1 and LOFAR station L2081 acquire timing through GPS and have near zero delay, while the L106 geophones express between -21 to $-7\,\mathrm{s}$ delays with the reference ENF. This effect is unsurprising as the instruments use the Network Time Protocol (NTP) instead of GPS and may experience clock drift over time without a stable internet connection. With the expected timing corrections applied, the alignment of the arrivals is vastly improved. The remaining misalignment may be a consequence of local geology and site-

Figure 3 Map of the Netherlands showing four groups and locations of geophysical instruments in the field (G-Network – geophones and surface accelerometers; E-TEST Deployment – battery operated geophone nodes; LOFAR – seismo-acoustic array; De Bilt – acoustic array). The acoustic instruments are treated in the supplementary material. Further details on the instruments are provided in Table 1.

response, and the inherent 1 s resolution limit of the technique. Furthermore, the timing misfits from the ENF analysis were calculated over 24 h while the timing error of the L106 array was observed to vary by multiple seconds in a day. At the time of the teleseismic arrival, the ENF delay appeared to be consistently 6 s behind the reference data for the entire NSAN network. This effect was corrected in fig. 7 using an average of many GPS

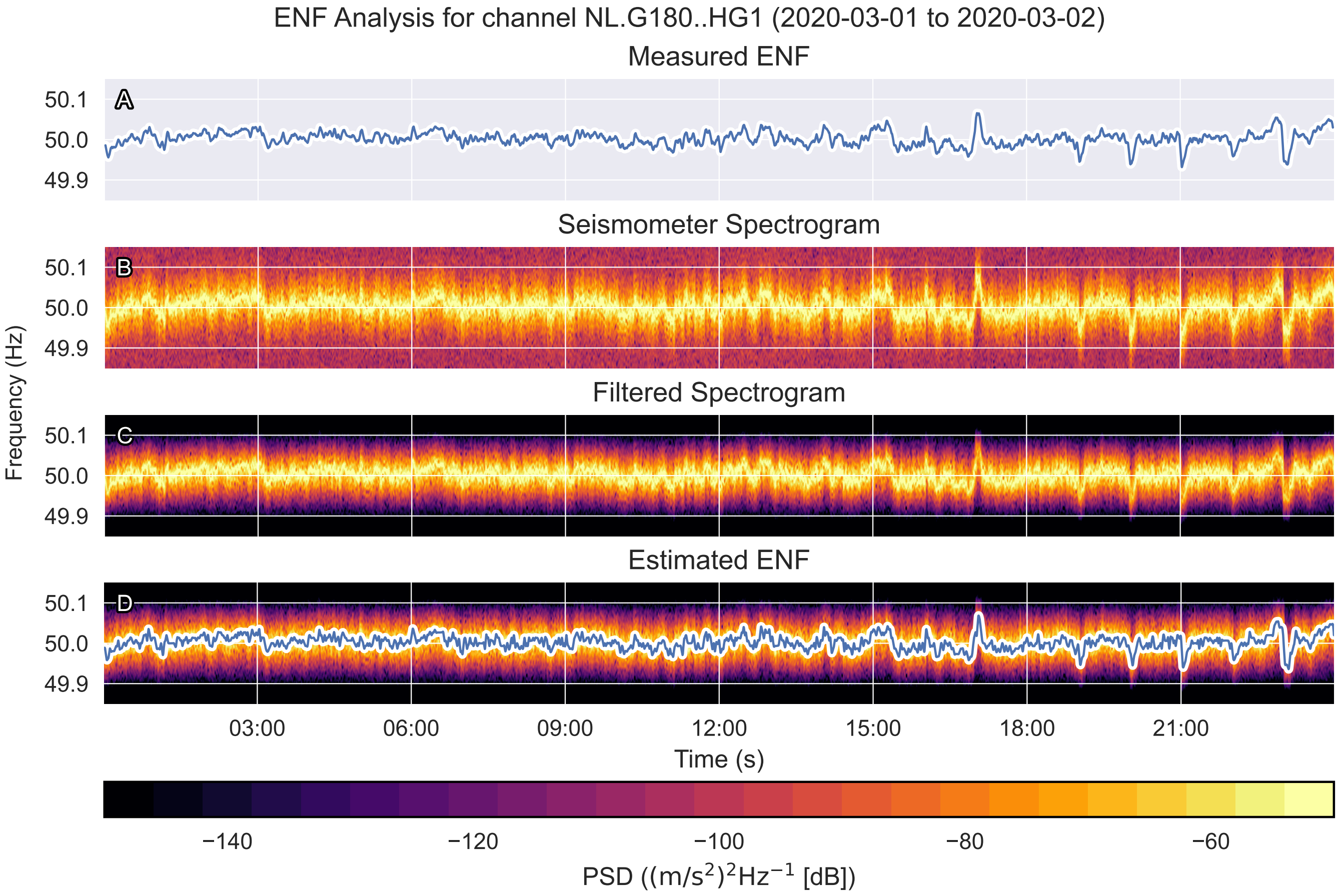

Figure 4 A) The reference ENF downloaded from the website of TransnetBW GmbH. B) Acceleration spectrogram of EpiSensor NL.G180..HG1 (Groningen, the Netherlands) between 2020-03-01 and 2020-03-02. C) The modified spectrogram using a simple Gaussian filter. D) The estimated ENF from the filtered spectrogram derived from the maximum PSD of each time segment.

locked stations.

4.3 Orientation Anomalies from ENF Analysis

A polarization analysis of the ENF signal was applied to three-component data from surface accelerometers in the G-network. A principal component analysis provides the dominant modes of variance of these data (i.e., the dominant direction of motion), of which an example is illustrated for surface accelerometer G450 (fig. 8). The three-component data are plotted together in three-dimensional space and the ground motion (represented by the position of a virtual particle) is projected onto three perpendicular two-dimensional slices. The results show that in the 49.85 to $50.15\,\mathrm{Hz}$ frequency band, the ground motion has a high probability of being on the colored elliptical path and not outside or inside of it, where the probability approaches zero.

Because the polarization was observed to be dominantly in the horizontal plane, the recovered azimuths from the polarization analysis (leftmost panel of fig. 8) were projected on geographic maps together with open electrical infrastructure data to identify potential directional sources of the ENF. It was however not possible to identify a regional source of the ENF signal such as medium and high voltage line and transformers. Instead, it was considered that for most instruments, local electronics inside the instrument's housing cabinet may be a more proximal and likely source of the signal. The cabinets that host both the accelerometers and electronics in the G-network is shaped like a rectangular box (ratio 1:3), with the internal setup organised in a similar fashion for all installations. Azimuths of the cabinet in the field (parallel with the elongated side) were estimated from technical drawings. The direction of polarized motion that is expressed by the accelerometer data appears to be consistent with the azimuth of the cabinet (fig. 9, left panel), confirming the source of the ENF is in fact local. The right panel of fig. 9 shows the misfit between the azimuth of particle motion and the cabinet orientation plotted against the degree of rectilinearity. Stations that express a lower degree of rectilinearity naturally have a larger variability on the direction of particle motion, resulting in a more probable angular misfit. The decreased degree of rectilinearity may be attributed to a diminished source of the ENF or instrument sensitivity issues, which can be considered another instrument health metric.

A clear outlier was identified as station G680 marked in that expresses a $87°$ near perpendicular angular misfit with a very strong rectilinearity (fig. 9). It was hypothesised that the instrument was rotated, or that the horizontal components were swapped during instrument installation. A field visit confirmed that surface ac-

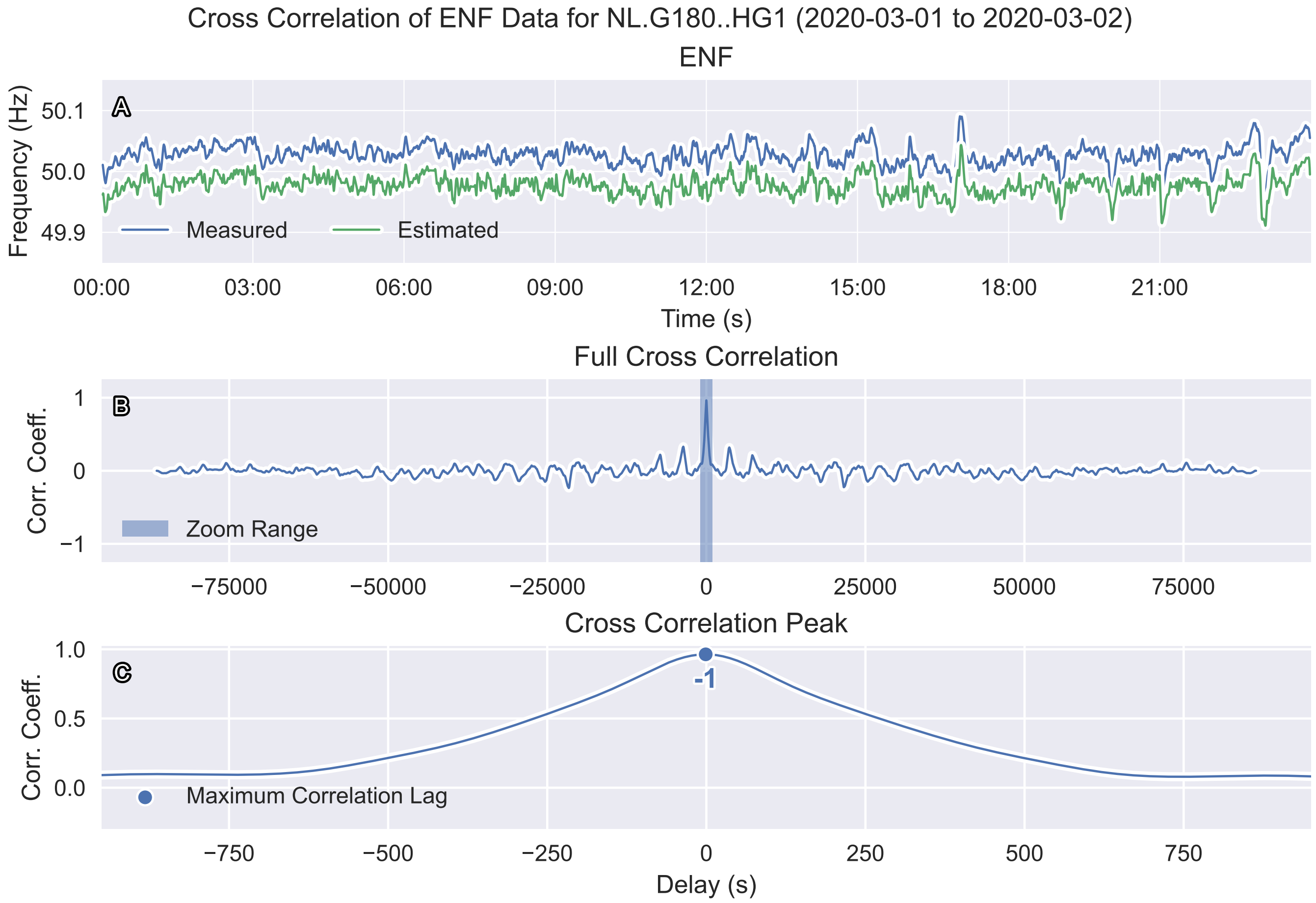

Figure 5 A) Comparison between the reference ENF (blue) provided by TransnetBW GmbH and the estimated ENF (green). Note that the data have been offset from the mean of $50\,\mathrm{Hz}$ for illustrative purposes to show their similarity. B) The full cross correlation between the estimated and reference ENF. C) Zoom in on the blue span around the correlation maximum ($\approx$ 0.96) with the recovered peak and time delay indicated ($-1\,\mathrm{s}$).

celerometer G680 was in fact rotated counter-clockwise by $90°$ and has been corrected since.

5 Discussion

The applied tracing algorithm (fig. 4D) to estimate the ENF from spectrograms using the maximum PSD per time bin is simple yet effective. The intensity of the ENF above ambient noise does not require the use of advanced track tracing algorithms (e.g., Lampert and O'Keefe, 2010). For the applications where the ENF needs to be eliminated from the data, subtraction algorithms (Butler and Russell, 1993, 2003) may benefit from using reference ENF data too. This is particularly true for extremely (ELF) and very low frequency (VLF) radio data between 300 to $30\,000\,\mathrm{Hz}$ (Cohen et al., 2010), since the affected bandwidth of the ENF fluctuations grows proportionally with higher overtones. With reference data, the ENF can be specifically targeted and generic bandstop filters can be avoided.

Cross correlations between estimated and reference ENF data provide a reliable, passive technique for the detection of timing anomalies in geophysical data. However, the limitations of the method are clear: the reliability of the timing corrections is contingent on the ability to accurately resolve the ENF signal from the data, which is not always easily achieved. The expected precision and accuracy of the technique illustrated in fig. 6 and reaches approximately $1\,\mathrm{s}$ for instruments that express a high susceptibility to the ENF. By increasing the sampling resolution of the reference ENF data, time discrepancies on the sub-second level may potentially be discovered. During the analysis of the teleseismic event (fig. 7) it was found that there was a consistent delay ($6\,\mathrm{s}$) with the reference ENF for the entire NSAN. This delay is not real considering most of the stations are GPS locked and show $0\,\mathrm{s}$ delays during other periods. It is expected that this effect may be introduced by poor timing quality of the reference ENF data itself, or potentially by another unknown cause that needs to be investigated further. A similar explanation concerning inaccurate timestamping of the reference ENF data may also explain the skew towards $-1\,\mathrm{s}$ in fig. 6. It should be noted that if the absolute timestamp of the reference data is inaccurate, relative timing differences between instruments using the ENF remain resolvable.

Results from the polarization analysis (figs. 8 and 9) shows that gross orientation anomalies can be successfully identified. Even if the source of the ENF signal is unknown, when the source remains stable through time (e.g., a non-mobile transformer or the installation cabinet), the rectilinearity of geophysical data at the ENF

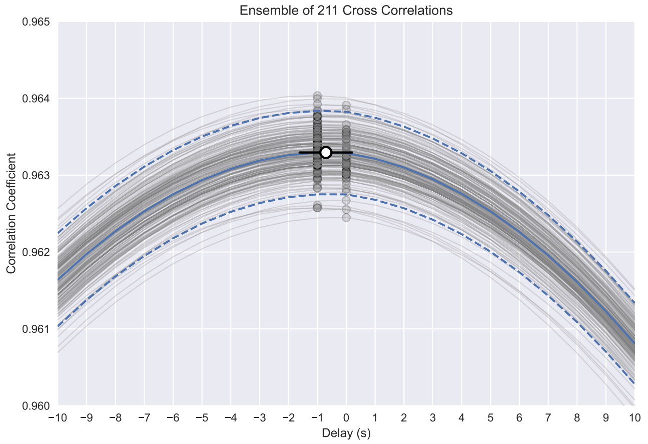

Figure 6 Average and $95\,\%$ confidence limits (blue curves) of an ensemble of 211 cross correlations with the measured ENF (grey curves) for all components of all Groningen surface accelerometer in the G-network on 2020-03-01. The accelerometer data have accurate timestamps and should resolve to a zero-time delay. The grey markers indicate the recovered peaks from the cross correlations and hence the respective delay times with the measured ENF. The black marker represents the mean time lag and $95\,\%$ confidence interval, illustrating the accuracy and precision of the method approaches $1\,\mathrm{s}$.

may thus provide a reasonable tool for the detection of temporal instrumental orientation anomalies. Furthermore, this method may provide a tool to more accurately determine three-dimensional orientations of geophones installed in seismic boreholes that needs to be investigated. Perhaps, even small orientation anomalies may be discovered that are on the order a few degrees.

5.1 Source of the ENF in Geophysical Data

The mechanisms through which the ENF signal is passed on to geophysical sensor networks remains enigmatic and appears to vary per instrument type and installation (fig. 1). In the following section, the expected sources in the different geophysical instruments are discussed. Because of the alternative suspected coupling mechanism, acoustic instruments are treated in the supplementary information.

5.1.1 G-network Accelerometers and Geophones

From the presented polarization analysis it is evident that the ENF signal is acquired locally in the G-network accelerometers. Despite this, in the operational NSAN, a sudden increase in the amplitude of the ENF has been observed to lead to false event detection in accelerometers deployed near high voltage power lines – suggesting that large-scale electrical infrastructure may under certain circumstances be a significant source of the ENF signal. Seismoacoustic coupling (e.g., Evers et al., 2007) from humming and corona discharge (Loeb, 1965) may provide a coupling mechanism up to $200\,\mathrm{m}$ away from high voltage power lines (Schippkus et al., 2020). The susceptibility of the G-network accelerometers to the ENF is strong and highly polarized. It is expected that the signal would be less dominant if it were induced along the wires between the sensor and digitizer where it is not amplified to such dominant amplitudes. Furthermore, accelerometers in the NSAN are connected with a two-wire differential setup, effectively limiting the influence of external magnetic fields on grounds loops specifically, but leaving the sensor itself susceptible to changing magnetic fields. The recorded power at the ENF in accelerometers with different gain settings and sensitivities appears similar across the G-network when the amplitude of the signal is expressed in physical ground motion units (acceleration, velocity, or displacement), suggesting that the ENF signal is not electromagnetic of nature. Alterations in the suspension spring or coils of the accelerometers (Forbriger, 2007) have been suggested as a likely source of the signal. The relationship between the cabinet orientation and the polarization azimuth of the accelerometer data indicates that physical vibration of the cabinet itself may be caused by the humming power supply that is mounted on its inside wall.

The geophones inside the seismic boreholes of the G-network share surface electronics with the aforementioned accelerometers. The geophones operate passively and have no direct power source but are connected to the power grid through a digitizer at the surface. The amplitude of the ENF in these data is orders of magnitude smaller compared to the accelerometers and show varying directions of polarization within a single borehole. The polarization is strong, yet orientations vary unpredictably over the $50\,\mathrm{m}$ depth levels inside the borehole, and because no decrease with depth inside the boreholes (from 50 to $200\,\mathrm{m}$) could be identified, it is suggested that the ENF signal is potentially established at the surface. For these instruments, it may be that unshielded signal cables connected to the datalogger allow for direct induction of stray magnetic fields from nearby electrical components. A more thorough assessment of the ENF signal in geophones inside the seismic boreholes is recommended.

5.1.2 E-TEST Battery Operated Geophones

Surface geophones from the E-TEST temporary deployment (Shahar Shani-Kadmiel et al., 2020) are fully battery operated and enclosed within a single unit. These instruments are of interest because they have no physical connection to the electrical grid. For these geophones, the ENF signal is only detectable and usable when the instruments are deployed near towns (fig. 10), visible overhead power lines, or sub-surface electrical infrastructure, as revealed by the presence of e.g., street lights. In the middle of a forest or field, the ENF signal could not be recovered from the data. It is still unknown whether the coupling is purely electromagnetic or through (coupled) waves as a result of the humming and vibration of the nearby electrical components.

5.2 Further Applications of ENF Analysis

In the previous sections, the benefits and versatile application of ENF analysis in the passive quality assessment

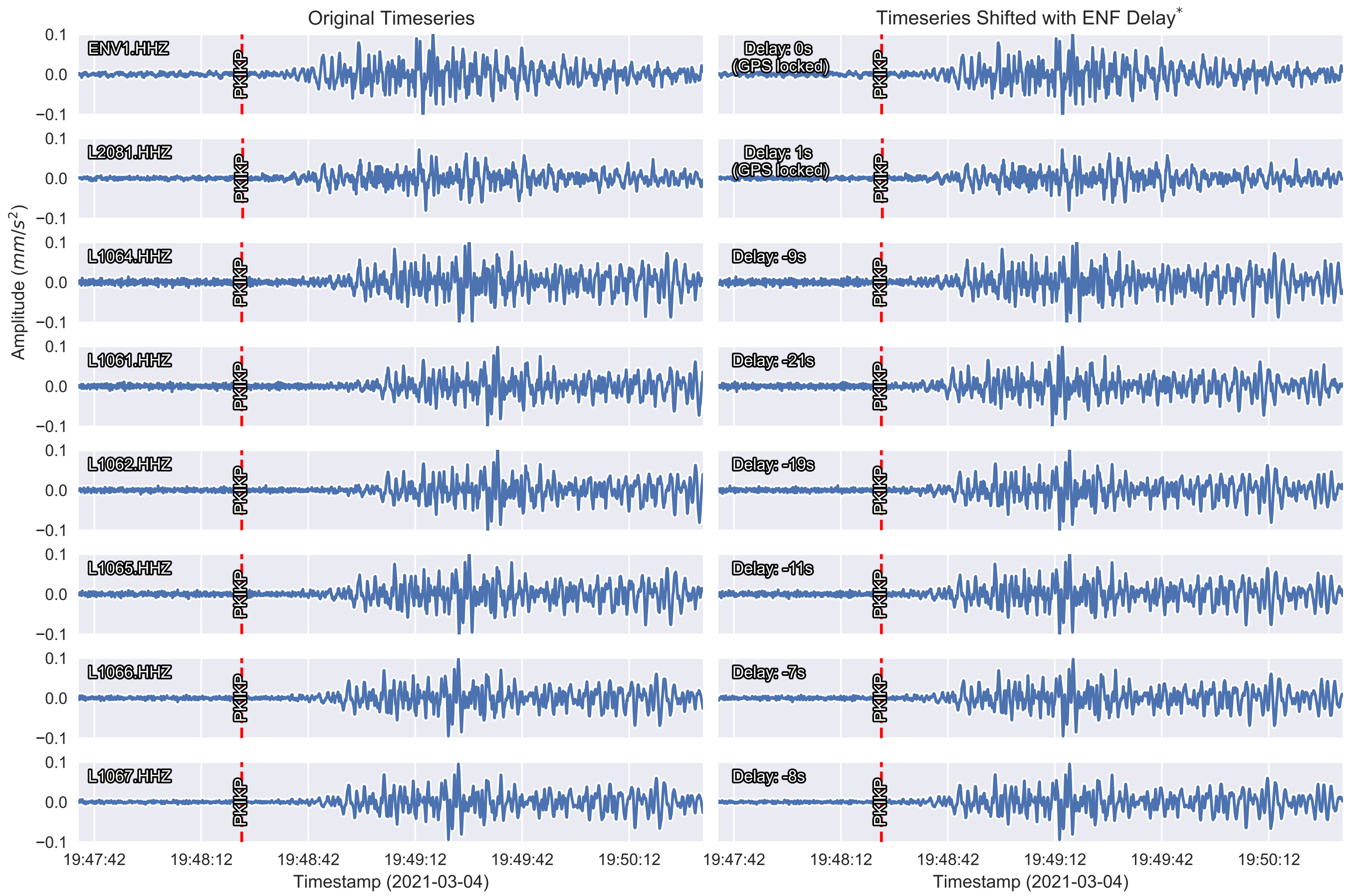

Figure 7 Comparison of GPS locked station with near zero delay (ENV1, L2081) with local array L106 (bottom 6 rows) recording a teleseismic arrival. The expected arrival times for PKIKP phase is illustrated. The right columns shows the same traces shifted by the recovered timing error from the ENF analysis. *Note: all delays were corrected for a consistent $-6\,\mathrm{s}$ offset across the entire network that appeared present on that day.

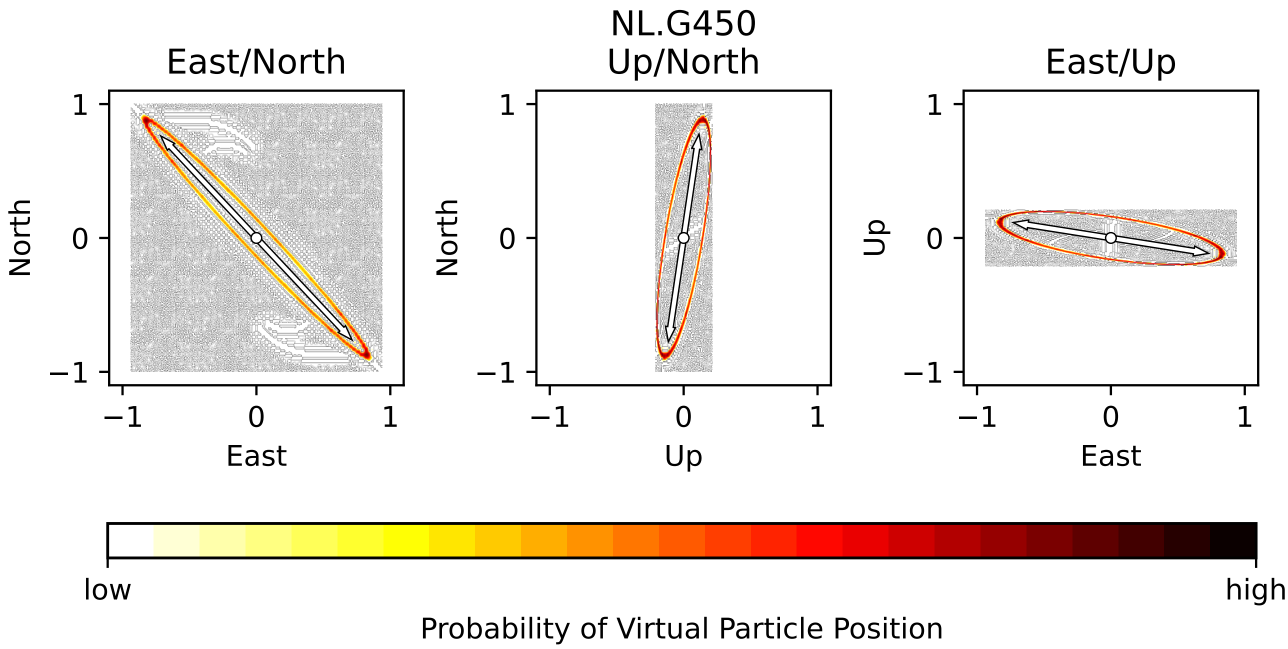

Figure 8 Strongly polarized motion at the ENF (bandpassed 49.85 to $50.15\,\mathrm{Hz}$) for surface accelerometer G450 (2020-03-01 – 2020-03-02). The three panels show 2-dimensional probabilistic histograms of the particle motion in East/North, Up/North, and East/Up directions, respectively. The white arrows with black outline represent the geographic orientation of the largest principal component ($\mathbf{u}_1$) that is equal to the direction of dominant particle motion. The leftmost panel can be interpreted as the geographical azimuth of dominant motion.

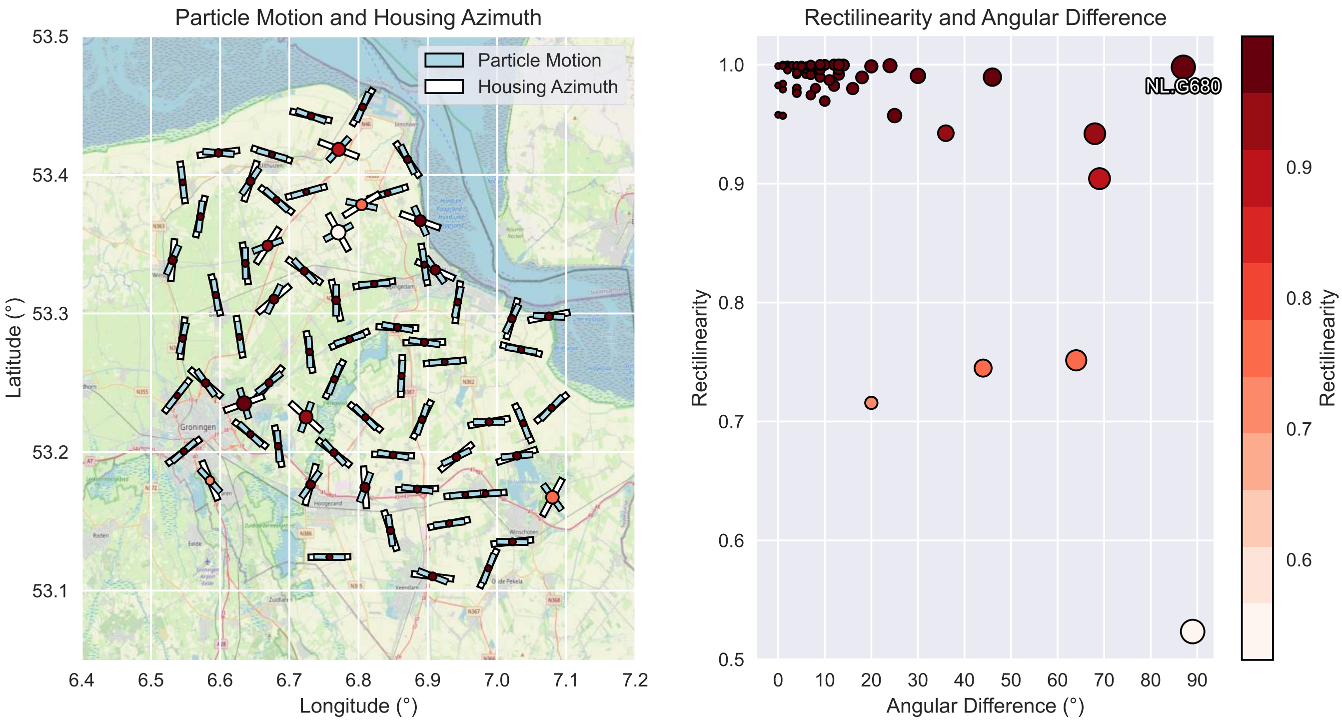

Figure 9 Left: comparison between azimuths of the principal direction of accelerometer particle motion (lightblue) and the orientation of the installation cabinet (white). **Right:** Angular misfit between the cabinet orientation and dominant particle motion against the degree of rectilinearity. Map data are provided by OpenStreetMap contributors (2017).

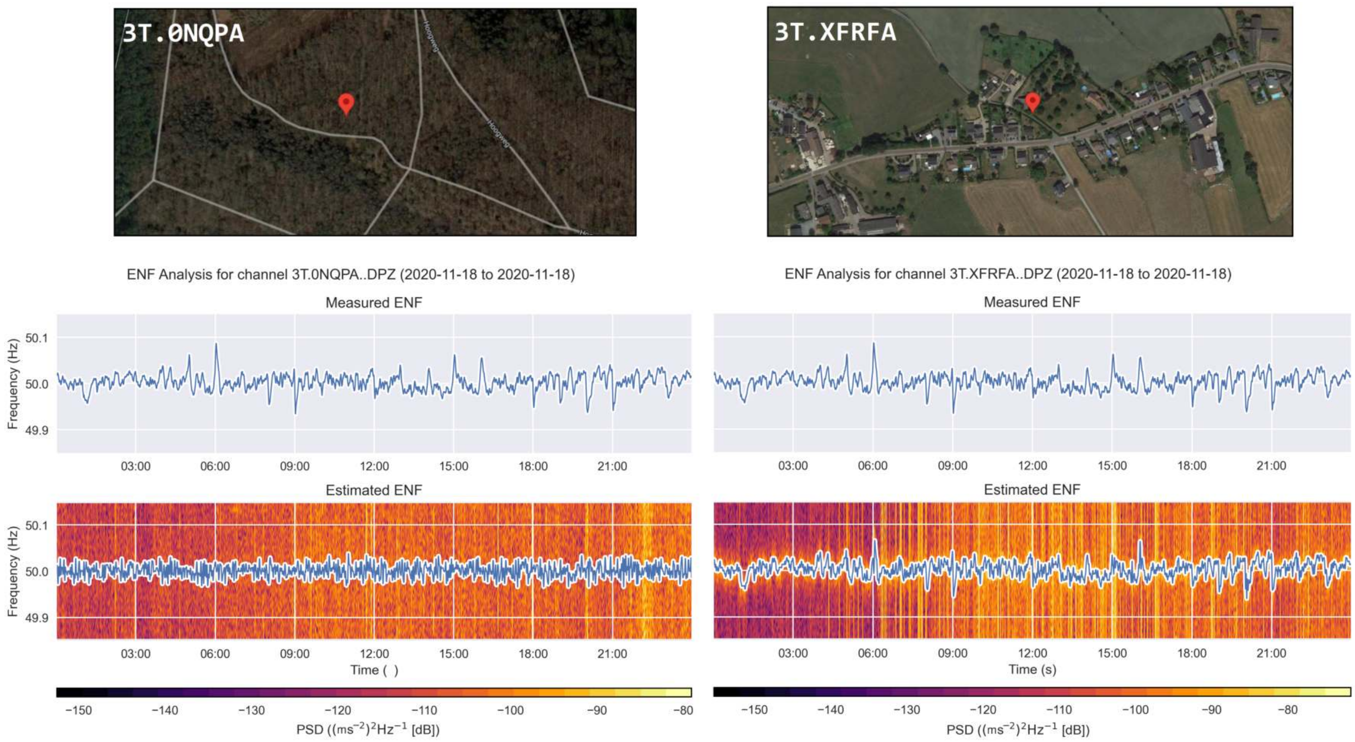

Figure 10 Columns showing two battery operated geophones in the 3T temporary deployment (Shahar Shani-Kadmiel et al., 2020). The left column shows geophone node 0NQPA remotely deployed in a forest and shows no trace of the ENF in its data. The right column represents data from geophone node XFRFA which is located near a town and electrical infrastructure. The ENF signal is clearly derived from anthropgenic activity in this area.

of geophysical data was demonstrated. Because the signal is persistent and omnipresent, some other foreseeable applications and possibilities for future consideration are discussed below.

Seismometers are considered to be linear time-invariant (LTI) systems. This description implies that an input of particular frequency should output a signal with equal frequency, albeit with modified amplitude and phase, as described by the instrument's transfer function. Because the input signal of the ENF is well-defined and predictable, its characteristics should be accurately reflected in the output signal. A number of LOFAR stations in the NSAN network show an anomalous consistent positive shift in the ENF of $0.01\,\mathrm{Hz}$. This feature may represent a deviation from a linear response, or that there exists a minor drift in the clock that may stretch sample spacing, providing the appearance of a higher frequency input signal. The latter hypothesis seems most likely considering the stations are known to use non-commercial dataloggers.

Additionally, the absolute (integrated) amount of power of the observed ENF in digital recordings varies significantly as a function of time. Many features are expressed in this variation, most of which do not yet have identified sources. The most coherent changes happen on timescales of minutes to days and occur simultaneously and proportionally between all stations in the network. Diurnal variation of the strength of the ENF signal appears to be to some degree coherent with measures of the consumer load. An in-depth investigation on these varying amplitude, including a better understanding of coupling mechanisms in geophysical instruments, may provide opportunities for other potential benefits of ENF analysis to be identified, such as the potential detection of sensitivity anomalies. Furthermore, the coherency of the varying ENF signal strength between stations may provide an alternative way to detect relative timing issues that needs to be investigated.

6 Conclusion

The application of ENF analysis to the passive quality assessment of geophysical data is a versatile technique that can be leveraged to identify timing issues at the $1\,\mathrm{s}$ level. It is also demonstrated that a polarization analysis of accelerometer data at the ENF enabled instrumentation orientation errors to be detected and resolved. ENF analysis may thus be considered for the passive detection of timing errors and sensor orientation anomalies, and in data where the provided timestamp may be tampered with, or generally unreliable, for example due to the lack of GPS connectivity. The mechanism through which the ENF is coupled to geophysical data appears to be instrument and installation specific and needs to be investigated further. Despite this, the proposed methods can potentially be adopted by geophysical monitoring institutes, and opens multiple avenues for further research.

Acknowledgements

We are grateful for our dear colleagues at the Seismology and Acoustics department at KNMI for their fruitful comments and assistance. Two anonymous reviewers are thanked for providing their input on the manuscript and suggestions to improve its clarity. We thank Carrick Talmadge for discussions on the detection of $100\,\mathrm{Hz}$ signals on low-frequency sound microphones. Henrietta Rákóczi is thanked for her input on the sections of the manuscript that were considered redundant and could be removed. L. Gorjão is thanked for an interesting discussion on power-grid dynamics and their effort in the creation and maintenance of the power-grid frequency database. This work was initially inspired by a science video created by Tom Scott on the electrical network frequency.

Data and code availability

Reference ENF data were downloaded from the power-grid frequency database (Gorjão et al., 2020) and the TransnetBW GmBH website that is accessible at https://www.transnetbw.com. Seismological waveform data were downloaded from the Netherlands Seismic Acoustic Network (KNMI, 1993) and the E-TEST deployment (Shahar Shani-Kadmiel et al., 2020). The ENF analysis script was written in Python 3.8.2 (Van Rossum and Drake, 2009), using SciPy (Virtanen et al., 2020) and NumPy (Harris et al., 2020). Figures were made with Matplotlib (Hunter, 2007), version 3.2.1 (Caswell et al., 2020) and a pre-release version of PyGMT (Uieda et al., 2021) using Generic Mapping Tools (GMT) version 6 (Wessel et al., 2019b,a). Electrical infrastructure data were downloaded from the Enexis homepage (https://www.enexis.nl/) and TenneT homepage (https://www.tennet.eu).

Competing interests

The authors declare no competing interests.

References

Ahern, T., Benson, R., Casey, R., Trabant, C., and Weertman, B. Improvements in Data Quality, Integration and Reliability: New Developments at the IRIS DMC. *Advances in Geosciences*, 40: 31–35, 2015. doi: 10.5194/adgeo-40-31-2015.

Beyreuther, M., Barsch, R., Krischer, L., Megies, T., Behr, Y., and Wassermann, J. ObsPy: A Python toolbox for seismology. *Seismological Research Letters*, 81(3):530–533, 2010. doi: 10.1785/gssrl.81.3.530.

Bormann, P. and Wielandt, E. Seismic signals and noise. In *New Manual of Seismological Observatory Practice 2 (NMSOP2)*, pages 1–62. Deutsches GeoForschungsZentrum GFZ, 2013. doi: 10.2312/GFZ.NMSOP-2_ch4.

Butler, K. E. and Russell, R. D. Subtraction of powerline harmonics from geophysical records. *Geophysics*, 58(6):898–903, 1993. doi: 10.1190/1.1443474.

Butler, K. E. and Russell, R. D. Cancellation of multiple harmonic noise series in geophysical records. *Geophysics*, 68(3): 1083–1090, 2003. doi: 10.1190/1.1581080.

Caswell, T. A., Droettboom, M., Lee, A., Hunter, J., Firing, E., Stansby, D., Klymak, J., Hoffmann, T., de Andrade, E. S., Varoquaux, N., Nielsen, J. H., Root, B., Elson, P., May, R., Dale, D., Lee, J.-J., Seppänen, J. K., McDougall, D., Straw, A., Hobson, P., Gohlke, C., Yu, T. S., Ma, E., Vincent, A. F., Silvester, S., Moad, C., Kniazev, N., Ivanov, P., Ernest, E., and Katins, J. matplotlib/matplotlib: REL: v3.2.1. doi: 10.5281/zenodo.3714460.

Cohen, M. B., Said, R., and Inan, U. Mitigation of 50–60 Hz power line interference in geophysical data. *Radio Science*, 45(06): 1–12, 2010. doi: 10.1029/2010RS004420.

Cooper, A. H. The electric network frequency (ENF) as an aid to authenticating forensic digital audio recordings – an automated approach. *Journal of the Audio Engineering Society*, 2008.

Cooper, A. J. An automated approach to the Electric Network Frequency (ENF) criterion - Theory and practice. *International Journal of Speech Language and the Law*, 16(2), 2010. doi: 10.1558/ijsll.v16i2.193.

Coyne, J., Bobrov, D., Bormann, P., Duran, E., Grenard, P., Haralabus, G., Kitov, I., and Starovoit, Y. CTBTO: Goals, networks, data analysis and data availability. In *New manual of seismological observatory practice 2 (NMSOP-2)*, pages 1–41. Deutsches GeoForschungsZentrum GFZ, 2012. doi: 10.2312/GFZ.NMSOP-2_ch15.

Evers, L. G., Ceranna, L., Haak, H. W., Pichon, A. L., and Whitaker, R. W. A seismoacoustic analysis of the gas-pipeline explosion near Ghislenghien in Belgium. *Bulletin of the Seismological Society of America*, 97(2):417–425, 2007. doi: 10.1785/0120060061.

Forbriger, T. Reducing magnetic field induced noise in broad-band seismic recordings. *Geophysical Journal International*, 169(1): 240–258, 2007. doi: 10.1111/j.1365-246X.2006.03295.x.

Gange, M. Low-frequency and tonal characteristics of Transformer noise. In *Proceedings of Acoustics*, 2011.

Garg, R., Varna, A. L., and Wu, M. "Seeing" ENF: Natural time stamp for digital video via optical sensing and signal processing. In *Proceedings of the 19th ACM International Conference on Multimedia*, MM '11, page 23–32. Association for Computing Machinery, 2011. doi: 10.1145/2072298.2072303.

Garg, R., Varna, A. L., and Wu, M. Modeling and analysis of electric network frequency signal for timestamp verification. In *2012 IEEE International Workshop on Information Forensics and Security (WIFS)*, pages 67–72. IEEE, 2012. doi: 10.1109/WIFS.2012.6412627.

Gorjão, L. R., Jumar, R., Maass, H., Hagenmeyer, V., Yalcin, G. C., Kruse, J., Timme, M., Beck, C., Witthaut, D., and Schäfer, B. Open database analysis of scaling and spatio-temporal properties of power grid frequencies. *Nature communications*, 11(1):1–11, 2020. doi: 10.1038/s41467-020-19732-7.

Harris, C. R., Millman, K. J., van der Walt, S. J., Gommers, R., Virtanen, P., Cournapeau, D., Wieser, E., Taylor, J., Berg, S., Smith, N. J., Kern, R., Picus, M., Hoyer, S., van Kerkwijk, M. H., Brett, M., Haldane, A., del Río, J. F., Wiebe, M., Peterson, P., Gérard-Marchant, P., Sheppard, K., Reddy, T., Weckesser, W., Abbasi, H., Gohlke, C., and Oliphant, T. E. Array programming with NumPy. *Nature*, 585(7825):357–362, 2020. doi: 10.1038/s41586-020-2649-2.

Hunter, J. D. Matplotlib: a 2D graphics environment. *Computing in Science & Engineering*, 9(3):90–95, 2007. doi: 10.1109/MCSE.2007.55.

Imanishi, Y., Nawa, K., Tamura, Y., and Ikeda, H. Effects of vertical nonlinearity on the superconducting gravimeter CT# 036 at Ishigakijima, Japan. *Earth, Planets and Space*, 74(1):1–15, 2022. doi: 10.1186/s40623-022-01609-2.

Jurkevics, A. Polarization analysis of three-component array data. *Bulletin of the seismological society of America*, 78(5):1725–1743, 1988. doi: 10.1785/BSSA0780051725.

Kennett, B. and Engdahl, E. Traveltimes for global earthquake location and phase identification. *Geophysical Journal International*, 105(2):429–465, 1991. doi: 10.1111/j.1365-246X.1991.tb06724.x.

Klun, M., Zupan, D., Lopatič, J., and Kryžanowski, A. On the Application of Laser Vibrometry to Perform Structural Health Monitoring in Non-Stationary Conditions of a Hydropower Dam. *Sensors*, 19(17):3811, 2019. doi: 10.3390/s19173811.

KNMI. Netherlands Seismic and Acoustic Network. Royal Netherlands Meteorological Institute (KNMI), Other/Seismic Network, 1993. doi: 10.21944/e970fd34-23b9-3411-b366-e4f72877d2c5.

Koymans, M., Domingo Ballesta, J., Ruigrok, E., Sleeman, R., Trani, L., and Evers, L. Performance assessment of geophysical instrumentation through the automated analysis of power spectral density estimates. *Earth and Space Science*, 8(9): e2021EA001675, 2021. doi: 10.1029/2021EA001675.

Křen, P., Pálinkáš, V., Val'ko, M., and Mašika, P. Improved measurement model for FG5/X gravimeters. *Measurement*, 171:108739, 2021. doi: 10.1016/j.measurement.2020.108739.

Lampert, T. A. and O'Keefe, S. E. A survey of spectrogram track detection algorithms. *Applied acoustics*, 71(2):87–100, 2010. doi: 10.1016/j.apacoust.2009.08.007.

Levkov, C., Mihov, G., Ivanov, R., Daskalov, I., Christov, I., and Dotsinsky, I. Removal of power-line interference from the ECG: a review of the subtraction procedure. *BioMedical Engineering OnLine*, 4(1):1–18, 2005. doi: 10.1186/1475-925X-4-50.

Loeb, L. B. *Electrical coronas, their basic physical mechanisms*. Univ of California Press, 1965.

McNamara, D. and Boaz, R. PQLX: A software tool to evaluate seismic station performance. In *AGU Fall Meeting Abstracts*, 2006.

OpenStreetMap contributors. Planet dump retrieved from https://planet.osm.org. https://www.openstreetmap.org, 2017.

Pedersen, H. A., Leroy, N., Zigone, D., Vallée, M., Ringler, A. T., and Wilson, D. C. Using Component Ratios to Detect Metadata and Instrument Problems of Seismic Stations: Examples from 18 Yr of GEOSCOPE Data. *Seismological Research Letters*, 91(1): 272–286, 2020. doi: 10.1785/0220190180.

Petersen, G. M., Cesca, S., and and, M. K. Automated Quality Control for Large Seismic Networks: Implementation and Application to the AlpArray Seismic Network. *Seismological Research Letters*, 90(3):1177–1190, 2019. doi: 10.1785/0220180342.

Raspberry Shake, S.A. Raspberry Shake, 2016. doi: 10.7914/SN/AM.

Ringler, A. T., Hagerty, M., Holland, J., Gonzales, A., Gee, L. S., Edwards, J., Wilson, D., and Baker, A. The data quality analyzer: A quality control program for seismic data. *Computers & Geosciences*, 76:96–111, 2015. doi: 10.1016/j.cageo.2014.12.006.

Schippkus, S., Garden, M., and Bokelmann, G. Characteristics of the Ambient Seismic Field on a Large-N Seismic Array in the Vienna Basin. *Seismological Research Letters*, 91(5):2803–2816, 2020. doi: 10.1785/0220200153.

Shahar Shani-Kadmiel, Frank Linde, Läslo Evers, and Bjorn Vink. Einstein Telescope Seismic Campaigns, 2020. doi: 10.7914/SN/3T_2020.

Trani, L., Koymans, M., Atkinson, M., Sleeman, R., and Filgueira, R. WFCatalog: A catalogue for seismological waveform data. *Computers & Geosciences*, 106:101–108, 2017. doi: 10.1016/j.cageo.2017.06.008.

Uieda, L., Tian, D., Leong, W., Toney, L., Schlitzer, W., Grund, M., Newton, D., Ziebarth, M., Jones, M., and Wessel, P. PyGMT: A Python interface for the Generic Mapping Tools. 2021. doi: 10.5281/zenodo.7772533.

Van Rossum, G. and Drake, F. L. *Python 3 Reference Manual*. CreateSpace, Scotts Valley, CA, 2009.

Virtanen, P., Gommers, R., Oliphant, T. E., Haberland, M., Reddy, T., Cournapeau, D., Burovski, E., Peterson, P., Weckesser, W., Bright, J., van der Walt, S. J., Brett, M., Wilson, J., Millman, K. J., Mayorov, N., Nelson, A. R. J., Jones, E., Kern, R., Larson, E., Carey, C. J., Polat, İ., Feng, Y., Moore, E. W., VanderPlas, J., Laxalde, D., Perktold, J., Cimrman, R., Henriksen, I., Quintero, E. A., Harris, C. R., Archibald, A. M., Ribeiro, A. H., Pedregosa, F., van Mulbregt, P., and SciPy 1.0 Contributors. SciPy 1.0: Fundamental Algorithms for Scientific Computing in Python. *Nature Methods*, 17:261–272, 2020. doi: 10.1038/s41592-019-0686-2.

Wessel, P., Luis, J., Uieda, L., Scharroo, R., Wobbe, F., Smith, W. H., and Tian, D. The Generic Mapping Tools version 6. *Geochemistry, Geophysics, Geosystems*, 20(11):5556–5564, 2019a. doi: 10.1029/2019GC008515.

Wessel, P., Luis, J. F., Uieda, L., Scharroo, R., Wobbe, F., Smith, W. H. F., and Tian, D. The Generic Mapping Tools version 6. doi: 10.5281/zenodo.3407866. Funded by US National Science Foundation grants OCE-1558403 and EAR-1829371.

Xia, J. and Miller, R. D. Design of a hum filter for suppressing powerline noise in seismic data. *Journal of Environmental & Engineering Geophysics*, 5(2):31–38, 2000. doi: 10.4133/JEEG5.2.31.

doi:10.26443/seismica.v2i2.1051

SEISMICA

Unraveling the Evolution of an Unusually Active Earthquake Sequence Near Sheldon, Nevada

D. T. Trugman *[1], **W. H. Savran** [1], **C. J. Ruhl** [1,2], **K. D. Smith** [1]

[1]Nevada Seismological Laboratory, University of Nevada, Reno, Reno NV, USA, [2]Verisk, Boston MA, USA

Author contributions: *Conceptualization*: D. Trugman, K. Smith, C. Ruhl. *Data Curation*: D. Trugman. *Formal Analysis*: D. Trugman, W. Savran. *Funding Acquisition*: D. Trugman, K. Smith, W. Savran. *Investigation*: D. Trugman, W. Savran, K. Smith, C. Ruhl. *Methodology*: D. Trugman, W. Savran. *Project Administration*: D. Trugman. *Resources*: D. Trugman, W. Savran. *Software*: D. Trugman, W. Savran. *Supervision*: D. Trugman. *Validation*: D. Trugman, W. Savran. *Visualization*: D. Trugman, W. Savran. *Writing – original draft*: D. Trugman, K. Smith. *Writing – review & editing*: D. Trugman, W. Savran, K. Smith, C. Ruhl.

Abstract One of most universal statistical properties of earthquakes is the tendency to cluster in space and time. Yet while clustering is pervasive, individual earthquake sequences can vary markedly in duration, spatial extent, and time evolution. In July 2014, a prolific earthquake sequence initiated within the Sheldon Wildlife Refuge in northwest Nevada, USA. The sequence produced 26 M4 earthquakes and several hundred M3s from 2014 through 2018, with no clear mainshock or obvious driving force. Here we combine a suite of seismological analysis techniques to better characterize this unusual earthquake sequence. High-precision relocations reveal a clear, east-dipping normal fault as the dominant structure that intersects with a secondary, subvertical cross fault. Seismicity occurs in bursts of activity along these two structures before migrating down-dip and eventually transitioning to shallower structures to the east. Inversion of nearly one hundred moment tensors constrain the overall normal faulting stress regime. Source spectral analysis suggests that the stress drops and rupture properties of these events are typical for tectonic earthquakes in the western US. While station coverage is sparse in this remote study region, the timely installation of a temporary seismometer allows us to detect nearly 70,000 earthquakes over a 40-month time period when the seismic activity is highest. Such immense productivity is difficult to reconcile with current understanding of crustal deformation in the region and may be facilitated by local hydrothermal processes and earthquake triggering at the transitional intersection of subparallel fault systems.

Production Editor:
Carmine Galasso
Handling Editor:
Andrea Llenos
Copy & Layout Editor:
Oliver Lamb

Received:
June 20, 2023
Accepted:
August 15, 2023
Published:
September 26, 2023

Non-technical summary It is sometimes said that earthquakes hunt in packs, and there is perhaps no clearer example of this phenomena than a recent earthquake sequence within the Sheldon Wildlife Refuge in the northwest corner of Nevada, USA. Over a three-year time period, we detected more nearly 70,000 earthquakes occurring over a spatial footprint of ~5km x 5km. This article uses advanced seismological techniques to examine the Sheldon sequence in great detail to better understand the factors driving it. Earthquakes are a regular facet of life in western Nevada and California, so an improved understanding of seismicity and earthquake processes can help mitigate risks posed to communities near active fault systems.

1 Introduction

A remarkable sequence of earthquakes occurred in the far northwest corner of Nevada within the Sheldon National Wildlife Refuge. The sequence began in July of 2014 and featured high seismicity rates through 2016, producing 262 earthquakes with local magnitude M_L 3 and greater, and 26 larger than M_L 4, with the largest event of M_L 4.73 (November 9, 2015, 13:55 UTC). Of these, ~100 well-constrained moment tensors were generated by the Nevada Seismological Laboratory (NSL), with the vast majority of solutions showing normal faulting in a WNW directed extension direction (T-axis) with a small oblique component. The spatiotemporal evolution of the sequence is complex, featuring several distinct periods of activity, each including several M4 events with no clear mainshock throughout. The objective of this article is to provide a comprehensive analysis of the Sheldon sequence informed by a diverse array of seismological techniques, including high-precision earthquake locations, detection of small earthquakes using machine learning algorithms, moment tensor inversions, and source spectral analysis. As we will demonstrate, the Sheldon sequence has unique characteristics but is representative of a broader pattern of highly productive earthquake sequences throughout the Walker Lane in recent years (Hatch-Ibarra et al., 2022; Ross et al., 2019; Ruhl et al., 2016a,b, 2021; Trugman et al., 2023; Trugman and Shearer, 2017b).

Earthquake locations for events early in the sequence are poor due to the sparse seismic station coverage in a remote region of northwest Nevada. Stations from partner networks in California (NC and BK), Oregon (UO), and Washington (UW) were incorporated into routine NSL processing and provided key coverage throughout the Sheldon sequence (Figure 1). Overall, 7966 earthquakes could be located. As activity rates and event

*Corresponding author: dtrugman@unr.edu

magnitudes increased, by November 18, 2014, the NSL had installed a 6-channel (broadband and strong motion) portable station, COLR, on private land at a distance of approximately 16 km from the central part of the sequence and with reliable cellular communications to Adel, Oregon (about 30 km to the northwest). Access to the Sheldon National Wildlife Reserve wilderness study area was restricted. Temporary station COLR provided high signal quality for body wave phase identification critical to developing high-precision event locations and machine learning detections for the remainder of the sequence. The site operated through February 6, 2018, contributing more than three years of continuous recordings.

Geologically, the Sheldon sequence occurred directly east of a series of 16.5 and 15.5 Ma, mid-Miocene silicic centers, the High Rock Caldera Complex (HRCC), and associated flood basalts (Coble and Mahood, 2016). These volcanics, along with McDermitt Caldera complex to the east, have been considered the initiation of the NE trending Snake River Plain-Yellowstone hot-spot system (Henry et al., 2017; Pierce and Morgan, 1992). Flood basalts aged 15 Ma and younger east of the HRCC (Coble and Mahood, 2016) cover the source area of the Sheldon sequence. Faulting within the basaltic tablelands is most likely much older and definitive extensive Quaternary faulting has not been identified.

Current Basin and Range extensional faulting is concentrated along the eastern Warner Range in Surprise Valley about 50 km west of the Sheldon sequence (Lerch et al., 2010, Figure 1). Slip rates for the Surprise Valley fault have been estimated to be 1 mm/yr and larger. Potential geothermal resources in Surprise Valley have resulted in several studies. The paleoseismic transect of northwest Nevada presented by Personius et al. (2017) did not establish significant post-15Ka extensional faulting comparable to Surprise Valley deformation near the Sheldon source area. It did, however, speculate on minor potential structures within Long Valley, a basin in northwest Nevada that borders Miocene tablelands and escarpments adjacent to the Sheldon sequence (Figure 1). There is nothing in the post Miocene geology that may represent deformation events associated with Sheldon sequence. However, the Long Valley feature within the basaltic volcanic terrain extends for approximately 150 km north-south and includes the 1968 Adel, Oregon earthquake sequence (described below).

The most notable recent earthquake activity in the vicinity of the Sheldon sequence in occurred at Adel, in southeast Oregon in 1968 (Schaff, 1976, Figure 1). The largest earthquake of the 1968 sequence was an M_L 5.1 on May 30 and caused structural damage in the community of Adel. The nascent NSL at the time deployed a local telemetered 4-station analog portable seismic array and was able to constrain a north striking left-lateral oblique short period focal mechanism for the mainshock with as many as 200 events recorded per day during the aftershock sequence. Nearly fifty years later, an equally notable sequence occurred less than 40 km to the southeast in the Sheldon Wildlife Refuge. This article is a report on what unfolded.

2 Data and Methods

In the following sections, we overview the data acquisition, processing, and analysis steps we used to characterize the Sheldon sequence. Derived datasets produced as part of this study, along with the velocity model used in the location analysis, are archived on Zenodo (see Data and code availability section).

2.1 Catalog and Waveform Data

For the purpose of earthquake monitoring in the state of Nevada, the NSL maintains an Antelope Datascope database of phase arrivals, associated events, and continuous waveforms from regional stations operated by the NSL and partner networks. All phase arrivals (at public stations) and earthquake origins determined by the NSL are also submitted to the US Geological Survey Comprehensive Catalog (ComCat) for public dissemination. For each reviewed and cataloged event in the Sheldon study region (Figure 1), we extract P and S arrival times from the database, as well as segments of waveform data (and metadata) encompassing these phases, from all recording stations within 250 km. Station coverage is generally sparse in this region, rendering focal mechanism determination through first motion polarity analysis unviable. Station COLR is the closest (~16 km) broadband sensor by a considerable distance (BK station MOD is ~56 km), so we also compile continuous data waveform from this station for its entire operating period (November 2014 to February 2018) for the purposes of small earthquake single-station detections. Moment tensor inversions may benefit from recordings at greater distances than are archived routinely by the NSL, and thus the waveform data and metadata used for that purpose is downloaded as a separate process (Beyreuther et al., 2010; Owens et al., 2004).

2.2 Earthquake Locations

We begin our analysis by working to refine the earthquake locations of reviewed events in the NSL database. Our two-step procedure involves both absolute location estimates based on analyst phase arrival picks and relative relocation refinements informed by waveform cross-correlation. In the first step, we estimate absolute locations by applying the NonLinLoc algorithm (Lomax et al., 2000, 2001) to the NSL phase arrival bulletin and a 1D velocity model. The NonLinLoc algorithm explicitly accounts for station elevations when computing travel time grids, but there can still be systematic station-specific misfits due to unmodeled subsurface velocity structure. To account for this, we first do an initial run of NonLinLoc to estimate the correction term for each station-phase combination, and then rerun the location algorithm after applying the correction term to the arrival time data to achieve the final solution.

We next refine the absolute locations obtained by NonLinLoc using GrowClust3D.jl (Trugman et al., 2022), a relative relocation technique that leverages precise differential travel times measured from waveform cross-correlation of pairs of events recorded at common stations. For these measurements, we focus on

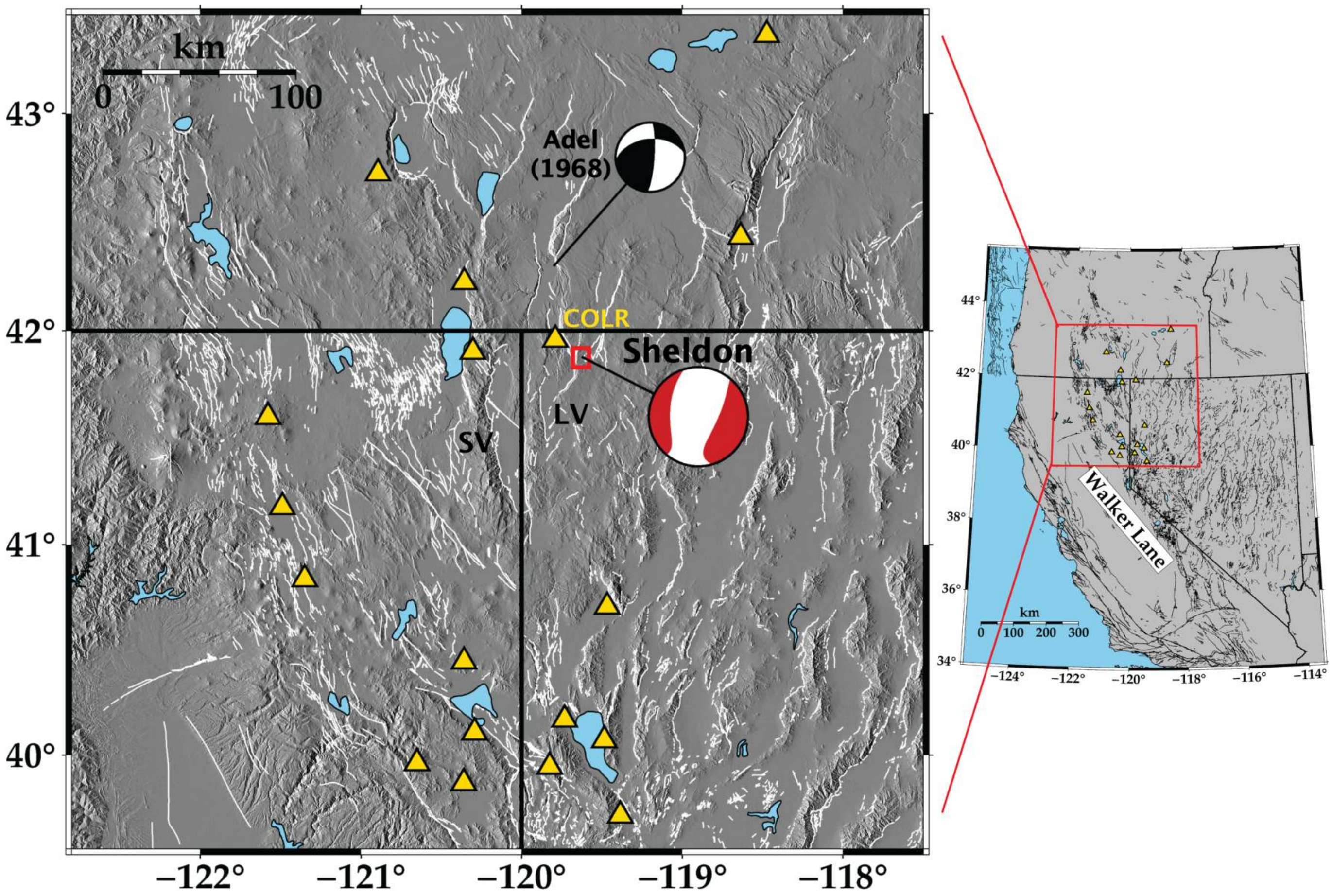

Figure 1 Overview map of the study region and its position within the western US (inset). Earthquakes concentrate within the Sheldon Wildlife Refuge, marked in red. Regional stations used in location analysis are marked as gold triangles. A normalized Kostrov (1974) summation of Sheldon moment tensors (red mechanism) demonstrates that normal faulting predominates during the sequence. The location of the 1968 Adel earthquake sequence, as well as the Surprise Valley (SV) and Long Valley (LV) fault zones are marked for reference.

a subset of events with M_L 1.0 and greater. We identify all pairs of nearby events within 5 km distance, and cross-correlate separately both P and S waveform windows at all stations recording both events. We bandpass filter the waveforms from 1-12 Hz and measure P and S differential times using 1.5 s and 2.5 s windows, respectively (Trugman et al., 2020); start times for time windows are determined at stations without listed phase arrivals through use of theoretical arrival times, which are later refined by cross-correlation (Trugman and Shearer, 2017a). Differential travel times are measured from the peaks of each cross-correlation function by applying a spline interpolation approach with subsample precision; measurements are discarded if the peak sidelobe is within 0.10 units of absolute amplitude of the peak value. The differential travel time database is then used as input to the GrowClust3D.jl software package, which uses a clustering algorithm to perform relative event relocations using the same station-specific travel time grids generated by NonLinLoc. For quality-control purposes, we use only differential times with cross-correlation value of 0.65 or greater and require at least 8 qualifying differential times to retain an event pair. With this workflow and quality control, we relocate 3811 of 6533 events with M_L 1.0 and greater. We use the events with refined positions as the basis for the structural interpretation of the sequence.

2.3 Moment Tensor Inversions

Because sparse azimuthal station coverage precludes reliable focal mechanism estimates, moment tensor inversions provide the most robust means of obtaining information about the style of faulting for earthquakes in the Sheldon sequence. To this end, we use MTINV (Ichinose et al., 1998), a time-domain inversion algorithm applied to long-period surface waves recorded at regional distances. Three-component waveforms are downloaded from all available stations with HH and BH channels within a search radius that depends on the earthquake size (generally 300 – 500 km) from regional data centers. Moment tensor inversions of this form are generally feasible for earthquakes of mid-magnitude 3 and greater; smaller earthquakes do not produce sufficient long-period energy. Because of the extreme productivity of the Sheldon sequence, we are able to complete more than 100 such inversions, and use a quality-controlled subset of 93 moment tensor solutions with variance reduction >40% for our seismotectonic analysis.

2.4 Earthquake Detections at Station COLR

The earthquakes listed in NSL and ComCat event databases are those that are well-recorded enough at regional distances to produce a viable location estimate. Because relatively few stations are located within 100 km of the Sheldon sequence, this database only includes events that are large enough to be clearly seen at these distances. If we instead focus on the problem of detection rather than location, it is possible to compile a much more complete listing of events and their approximate size through detailed analysis of the COLR station, which is the closest to the source region and whose broadband sensor can record small earthquakes with high fidelity. In this way we recover a detailed time history of the sequence at very small magnitudes, significantly below the network detection threshold for this station distribution geometry. The key assumption here is that nearly all of the arrivals observed at COLR that are not seen at more distant stations (and hence missing from the analyst arrival database) are in fact coming from the Sheldon sequence and not from another source. This is plausible, given the low background seismicity and extreme event rates near Sheldon during this deployment, and can be confirmed if the detections exhibit short S-minus-P times indicative of a local source.

We apply the open-source SeisBench package (Woollam et al., 2022) to detect P and S arrivals on continuous, three-component waveforms at station COLR from November 2014 through February 2016. We use the EQTransformer model architecture (Mousavi et al., 2020) trained on the Stanford Earthquake Dataset (Mousavi et al., 2019), saving all arrivals with detection probabilities >0.1. We remove duplicate arrivals and those with unusually low signal-to-noise, and group the remaining arrivals into events using a simple temporal clustering algorithms (typical S minus P times at this distance are <3 s and thus are simple to associate). For each detected event, we also measure the equivalent Wood-Anderson displacement A_{mm} (in millimeters) and use that to calculate a single-station local magnitude estimate consistent with the definition used for other NSL events:

$$M_L = \log_{10} A_{\mathrm{mm}} + A_0(R) \quad (1)$$

where $A_0(R)$ is a nonparametric distance-correction term (Richter, 1935). Each detected event thus comes with an origin time and magnitude estimate, assuming an approximate distance of 16 km from to station COLR. This is a reasonable approximation given the sequence's spatial footprint of ~5 km x 5 km, over which the distance correction to the magnitude scale varies by about 0.1 magnitude unit.

2.5 Source Spectral Analysis

Earthquake source spectra can provide useful insight into the rupture characteristics of individual earthquakes. Source spectral measurements are often interpreted in relation to a theoretical model in which the low-frequency asymptote Ω_0 of the displacement source spectra is proportional to seismic moment, and the corner frequency f_c that marks the transition to high-frequency spectral decay is inversely proportional to the characteristic source duration of the earthquake (Boatwright, 1980; Brune, 1970; Madariaga, 1976; Sato and Hirasawa, 1973). A key challenge in the analysis of source spectra is the need to correct for path and site effects to isolate the source contribution to the recorded spectrum (Abercrombie, 2021; Anderson and Hough, 1984; Hanks, 1982; Hough, 1996). This problem is particularly acute for the Sheldon sequence, where most of the stations used in the earthquake locations are at distances greater than 100 km, where the spectrum at moderate and high frequencies is severely attenuated.

Station COLR is a notable exception, with high-quality recordings of thousands of moderate and large events at a distance less than 20 km. There have been few normal faulting Walker Lane sequences, and none with this range of magnitudes, to begin to assess regional normal faulting source processes. For these reasons, we focus our analysis on the spectra recorded at COLR. Such single-station measurements should be treated with appropriate caution, as they inevitably neglect variations in spectral amplitude across the focal sphere that are caused by radiation pattern and directivity effects. Despite this concern, any assessment of the source spectral properties of these earthquakes has the potential to provide useful insight into the rupture characteristics of these earthquakes that complements well the other techniques used in this study.

The S-wave spectra of earthquakes recorded on the broadband seismometer at COLR generally exhibit good signal-to-noise (SNR) ratios for earthquakes of $\mathrm{M_L}$ 2.0 and greater within the 0.5-20.0 Hz frequency band. For each such earthquake, we estimate S-wave spectra from the vector summation of both horizontal components using the multitaper technique of Prieto et al. (2009). Time windows for the spectral estimates are magnitude-dependent and increase from 6.0 s at $\mathrm{M_L}$ 2.0 to 16.0 s at $\mathrm{M_L}$ 4.5. Note that these relatively long time windows may include some of the S-wave coda, which could suppress directivity effects (which we neglect in this work). Spectra are converted in the frequency domain into units of displacement and resampled with 75 logarithmically spaced data points from the 0.2 – 20 Hz. We exclude from analysis individual frequencies points with SNR <3 and discard all spectra in which 20% or greater of frequency points qualify as low SNR by this criterion.

We perform two types of analyses on this dataset of COLR spectra. First, for each event (regardless of size) we measure the spectral moment Ω_0 from the low-frequency asymptote and use this to estimate the seismic moment M_c of the earthquake, after correcting for distance (R), radiation pattern ($U_{\phi\varphi}$), and surface amplification effects (F):

$$M_0 = \frac{4\pi\rho c^3 R \Omega_0}{F U_{\phi\varphi}} \quad (2)$$

where ρ and c are the density and wavespeed (e.g., Aki and Richards, 2002).

This allows us to calibrate an $\mathrm{M_L}$ - $\mathrm{M_W}$ relation for this dataset that is useful in quantifying the total moment release of the sequence. Second, for a subset of 42 large events ($\mathrm{M_L}$ 3.5 and greater recorded by COLR), we identify nearby smaller events (M_L 2-3) as empirical Green's functions (EGFs) and form spectral ratios with the EGFs to correct for path and site effects (e.g., Hough, 1997). Candidate EGFs in this magnitude range are selected based on their spatial proximity (<3 km distance laterally and vertically) and cross-correlation with the larger target event. Here we select EGFs with correlation values greater than 0.75 in a frequency band 0.5 - 1.25 Hz, which is above the low-frequency noise band at COLR and below the corner frequency of ~ M_L 3.5 target events (Abercrombie, 2015; Abercrombie et al., 2017; Ruhl et al., 2017); we would not expect even high-quality EGFs to correlate with the targets above their corner frequency.

We input each such spectral ratio associated with a target event into a Bayesian inference algorithm in which the primary objective is to measure the target event corner frequency and its uncertainty (Trugman, 2022). For this work, we assume a Brune (1970) spectral model of the form:

$$S_i(f) = \frac{\Omega_0}{1 + (f/f_c)^2} \tag{3}$$

each event (EGF and target), which yields a spectral ratio model of the form:

$$R_{ij}(f) = \frac{\Omega_{0[i]}}{\Omega_{0[j]}} \frac{1 + (f/f_{c[j]})^2}{1 + (f/f_{c[i]})^2} \tag{4}$$

where the indices i and j denote target and EGF events respectively.

Bayesian inference is implemented through the PyMC software package (Salvatier et al., 2016), which uses the No U-Turns formulation of the Hamiltonian Monte Carlo algorithm (Hoffman and Gelman, 2011) to draw samples from the posterior distribution. The likelihood function that connects model parameters to observations is T-distributed, which helps to account for outlier data points common in spectral ratios (Trugman, 2022). Prior distributions for the moment ratio and target and EGF corner frequencies are weakly informative and magnitude-dependent (Trugman, 2022), scaling self-similarly with a median stress drop of 5.0 MPa. The results are not sensitive to the detailed parameterizations of the prior distributions, since each target event inversion is constrained by tens to hundreds of EGFs, and thus the data carries the dominant weight in the posterior parameter estimates (Trugman, 2022). We focus our analysis on the corner frequencies of the target events and not the EGFs, since the latter have large uncertainties as they are each constrained by a single spectral ratio. One advantage of this Bayesian framework is the inherent stability of the prior distributions imposed on EGF source parameters, which work to mitigate the potential for biasing mainshock source parameter estimates when EGF parameters are poorly constrained from lack of data (Shearer et al., 2019).

3 Results

3.1 Earthquake Locations and Sequence Time Evolution

As may be anticipated by the sparse station coverage, the initial absolute locations from NonLinLoc are highly scattered and uncertain, without any discernable structure (Figure 2a). These results are comparable to the locations from the ComCat database, which use the same phase arrival inputs but a slightly different velocity model suitable for statewide monitoring purposes. After applying GrowClust3D.jl however, the picture sharpens dramatically (Figure 2b). In map view, there is a dominant structure trending NNE and dipping to the east, and a secondary branch arcing NNW. These structures are presently unmapped, positioned several kilometers to the east of the Warner Valley fault, a west-dipping system listed in the USGS Quaternary Faults and Folds Database (USGS and CGS, 2006). The secondary NNW branch aligns particularly well with visible features of the surface topography. There is also another shallower cluster of seismicity to the east, closer to the mapped Guano Valley fault system.

The geometry of sequence is best seen in cross section (Figure 2c) or visualized in 3D (Movie S1). Here the eastward dip of the main fault is readily distinguished (dip angle ~67°), with the secondary NNW-trending cross structure at a steeper, subvertical angle. Earthquake locations for this sequence are best resolved from November 2014 through February 2018 when station COLR was operational, which captures the bulk of the sequence but misses the initial few months.

The spatiotemporal evolution during this time period is quite complex and again is best visualized in animated form (Movie S2). The seismicity exhibits no systematic migration or diffusion pattern, but instead features multiple waves of activity separated by times of near quiescence (Figure 3). The most notable such instance occurs in May 2015, where seismicity nearly shuts off before a second burst of events, including several M_W 4 earthquakes, occurs in July 2015. During the first year of the sequence, most earthquakes occur on either the primary, east-dipping fault or the steeply dipping secondary NNW striking cross-fault. The shallow cluster of events to the east of these structures initiates later in the sequence, starting in December 2015. There is also a general tendency for events occurring later in the sequence to occur deeper on the main structures than in the early part of the sequence, perhaps indicating a down-dip migration. Following this overall evolution of the sequence, the primary structures' activity rates decline and the sequence is essentially over.

3.2 Moment Tensor and Source Spectral Analysis

With its plethora of moderate magnitude events, the Sheldon sequence is particularly amenable to moment tensor inversions, and we analyze 93 quality-controlled solutions as part of this study. We display the results in map view (Figure 4a), color-coding each mechanism by the mean horizontal strain ϵ_M implied by the

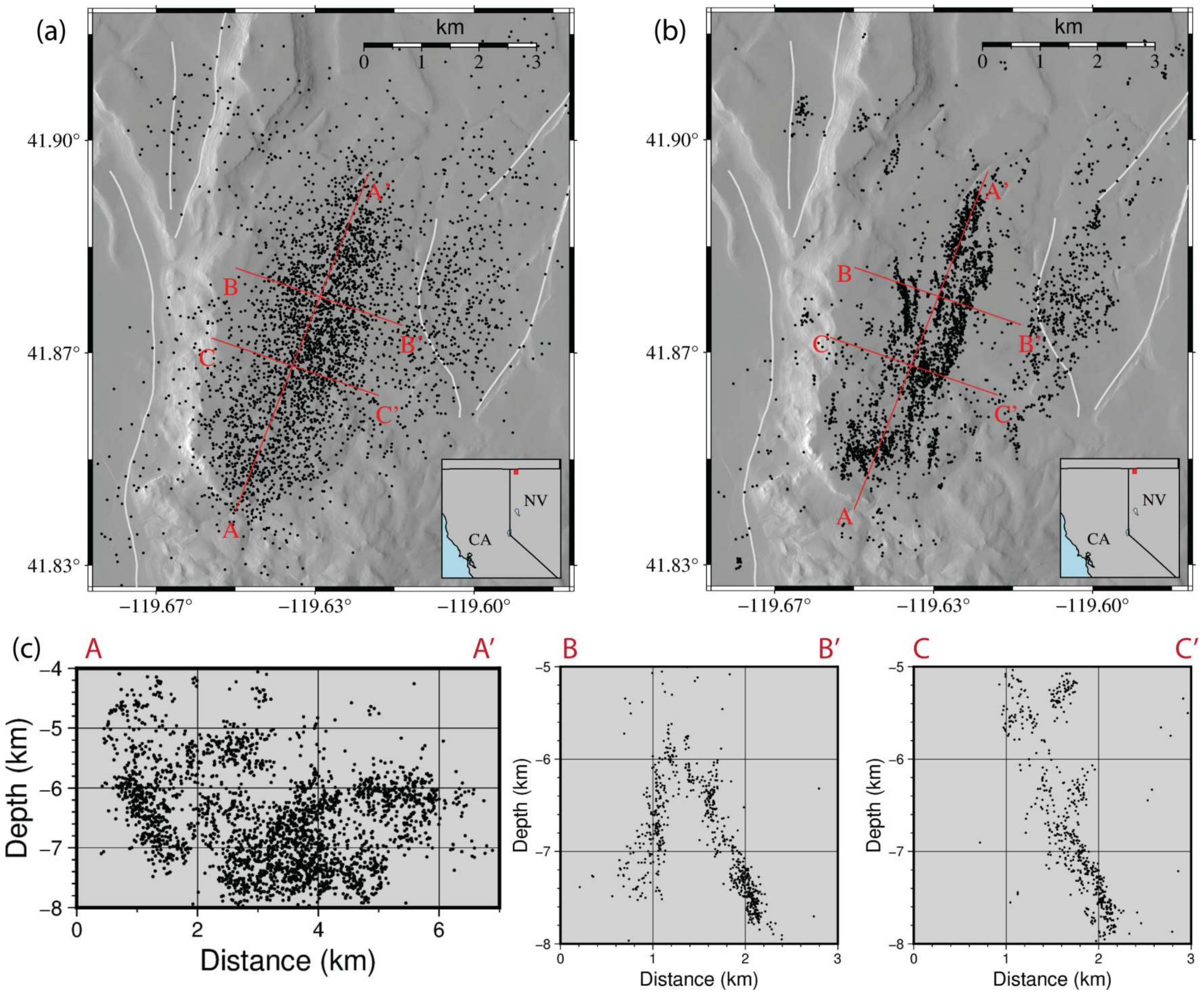

Figure 2 Relocation of the Sheldon sequence. (a) Initial epicentral locations in map view output by NonLinLoc, with faults from the USGS Quaternary faults database marked in white. (b) Refined locations of these events after applying GrowClust3D.jl. (c) Cross-sections of relocated seismicity, with AA', BB', and CC' defined in panel (b).

moment tensor components in geographic coordinates (e.g. Becker et al., 2018):

$$\epsilon_M = \frac{\epsilon_{EE} + \epsilon_{NN}}{2} \tag{5}$$

Here negative values indicate horizontal compression (thrust faulting), while positive values indicate extension (normal faulting). Most are normal faulting events, though several that align with the secondary cross-structure are strike-slip. The spatial density of high-quality moment tensor measurements also allows us to constrain the regional stress orientation under the assumption that on average, slip vectors are aligned with the shear direction resolved on individual fault planes (Angelier et al., 1982; Gephart and Forsyth, 1984; Michael, 1984, 1987). Here we adapt the iterative approach proposed by Vavryčuk (2014) that applies a Coulomb instability criterion to identify the active fault plane of each mechanism, which is a-priori ambiguous due to the symmetry of the seismic radiation pattern. We do not seek to resolve spatial or temporal variations in the stress field (Hardebeck and Michael, 2006), just its average value and uncertainty in our study region. We estimate the orientations of the three principal stresses (S_1, S_2, and S_3) and the shape ratio of principal stress magnitudes:

$$R = \frac{S_1 - S_2}{S_1 - S_3} \tag{6}$$

that best fits our dataset, with uncertainties obtained from bootstrap resampling. As expected, the stress orientations are consistent with an extensional regime (Personius et al., 2017) with a modest oblique component (Figure 4b): S_1 is subvertical (plunge of 71°) with azimuth of 18°, while S_2 is subhorizontal (plunge of 19°) with an azimuth of 194°.

Through our spectral ratio analysis, we obtain corner frequency measurements for 42 M_L3.5 and greater target events recorded by COLR (Figure 5). The primary outcome of this analysis are measurements of corner frequency which we can then translate to a stress drop value under the assumption of a circular source:

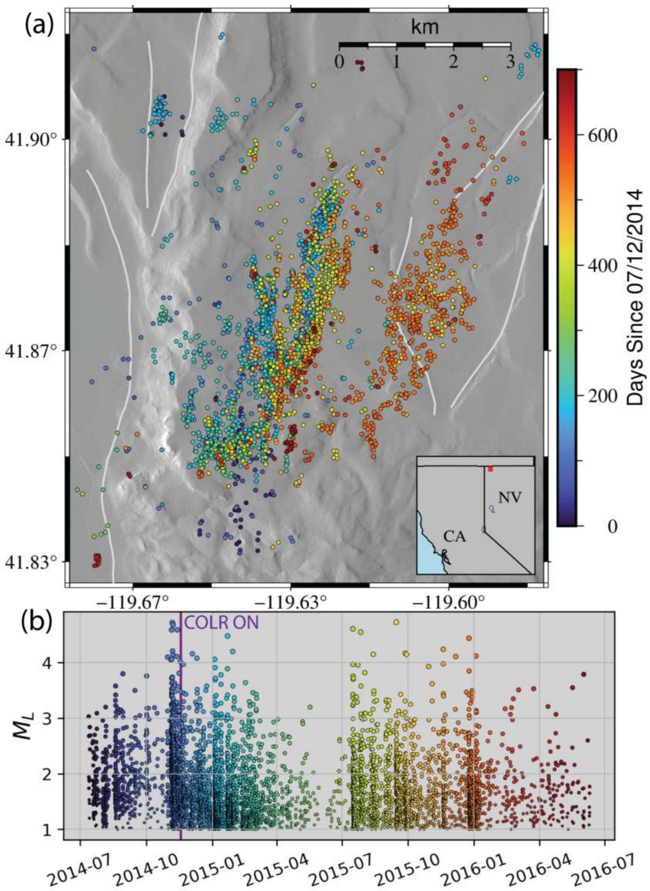

Figure 3 Time evolution of the Sheldon sequence during the most active period (2014-2016). (a) Relocated seismicity in map view, color-coded by occurrence time. (b) Local magnitude M_L versus time, with colorscale consistent to (a). The start date of COLR recordings is marked for reference.

$$\Delta\sigma = \frac{7}{16} M_0 \left(\frac{f_c}{k\beta} \right)^3 \tag{7}$$

In this relation, β is the shear wavespeed at the source (a value we obtain from the velocity model) and k is a numerical constant that depends on the spectral model; here we use 0.26, appropriate for S-wave spectra with rupture velocities of 0.8-0.9 β (Kaneko and Shearer, 2014). The distribution of stress drop values (~0.5 – 20 MPa) obtained from this analysis is typical for tectonic earthquakes in California and Nevada (Abercrombie, 2013; Hatch et al., 2018; Ruhl et al., 2017; Shearer et al., 2022; Trugman, 2022; Trugman et al., 2023; Trugman and Shearer, 2017a), suggesting there is nothing particularly unusual about the rupture properties of the Sheldon events. It is worth emphasizing again that these results should be treated with some caution as they are obtained from a single, albeit high-quality, station.

3.3 Event-detection and Frequency-Magnitude Statistics

The magnitudes reported by the NSL are local magnitudes M_L obtained from equivalent Wood-Anderson displacements and corrected for distance (Richter, 1935). These values provide a useful measure of earthquake size, especially for small events, but do not allow one to assess the total moment released by the sequence. Moment tensors are available for most (but not all) of the larger events and none of the smaller events, so there is a need to be able to approximate M_W in a consistent manner. To do this, we examine the moment measurements obtained through the spectral analysis at station COLR. The values are tightly correlated with independent measurements obtained in the moment tensor inversions (Figure 6a) and thus provide some confidence in their application.

Through least-squares regression analysis, we find a consistent scaling of the form:

$$M_W = 1.16 + 0.67 M_L \tag{8}$$

for smaller earthquakes (M_L <3.5), above which the scaling appears nearly unity (Figure 6b). This break in scaling is well understood in terms of a transition point of the corner frequency of the earthquake with respect to the dominant frequencies of a Wood-Anderson measurement (Hanks and Boore, 1984; Munafo et al., 2016; Uhrhammer et al., 1996). We can use this piecewise linear relation to estimate M_W for all events without moment tensors, and then compute the total moment released during the sequence. This equates to about M_W 5.6, with the greatest contributions coming from the bursts of seismicity starting in November 2014 and July 2015 (Figure 6c).

While they do not contribute much to this overall moment budget, very small earthquakes (M_L <1) can be detected on station COLR. After quality-control, our ma-

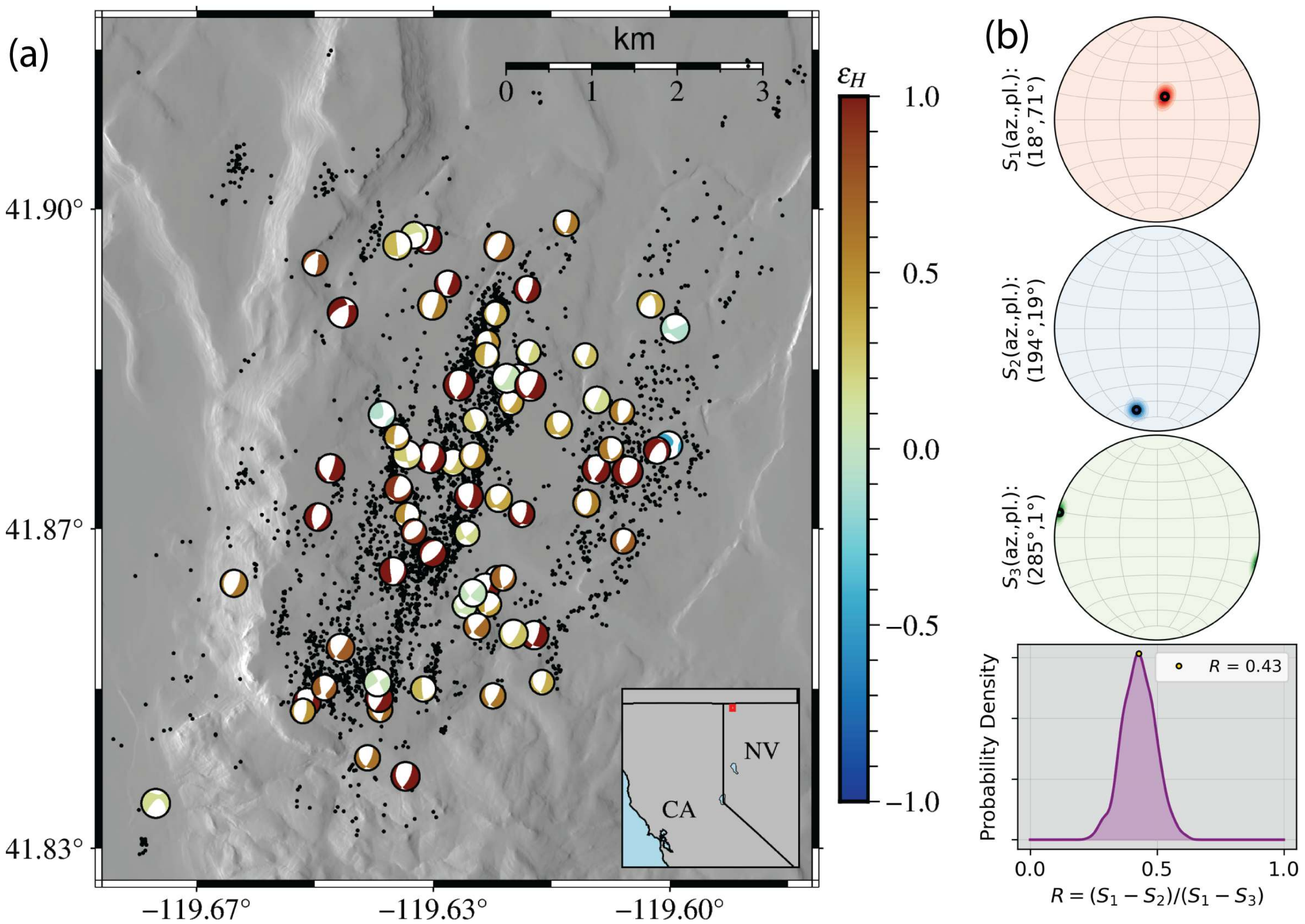

Figure 4 Moment tensor and stress field analysis. (a) Moment tensors of relocated events, color-coded by normalized horizontal strain, where red colors indicate extension and blue colors indicate compression. (b) Results from stress inversion analysis, showing orientations of principal stresses S_1, S_2, and S_3, as well as the shape ratio R defined in the text. Uncertainties come from 1000 bootstrap resamples of the input moment tensor dataset.

chine learning approach detects nearly 70,000 earthquakes during the time period in which the station is active, more than an order of magnitude greater than the number listed in the catalog during this time period. To confirm that these events are real and not false detections, we created a separate Antelope Datascope database to visualize the detected arrivals alongside existing analyst picks (Figure 7a). Manual scans of several active days confirm the quality of these detections, which identify nearly all of the analyst picks (Figure 7b; 97% have a machine learning arrival within 0.2s) along with more than 60,000 newly detected events. Short S-minus-P times for the detections confirm that these are local to the Sheldon area and not recordings of remote events. The time evolution of these detections (Figure 8a) is consistent with what is observed in the original monitoring catalog, including the bursts of seismicity interspersed with quiescent time periods noted above.

Through augmentation with our machine learning catalog, we are able to reduce the magnitude of completeness (for detected earthquakes) from 1.4 to 0.2 (Figure 7c). Using the “b-positive” estimator designed by van der Elst (2021) for robustness to potential changes in magnitude of completeness, we obtain a b-value for the detection-augmented catalog of 0.74 (95% confidence interval of 0.730-0.754 via bootstrap resampling). This value is fairly typical for a tectonic earthquake sequence, if slightly on the low side, indicating a relative prevalence of large magnitude events compared to a sequence with a canonical b-value of 1.0 (Gutenberg and Richter, 1944). Note however that this b-value measurement corresponds to the local magnitude scale M_L. If we instead use equation (8) to convert the local magnitudes of small events to approximate moment magnitude, the b-value measurement would increase accordingly to ~1.1.

We also explore temporal variations in b-value by applying the b-positive estimator to sliding 1000-event windows (Figure 8), with uncertainties again obtained through bootstrap resampling. The initial part of the sequence captured by station COLR is characterized by relatively low b-values, with temporal fluctuations associated with bursts of seismicity. During the main part of the sequence (2014 – 2016), b-values remain mostly within the 0.65-0.85 range to within the uncertainties. From late onward, the b-value steadily increased to ~0.95, as large magnitude events became less frequent.

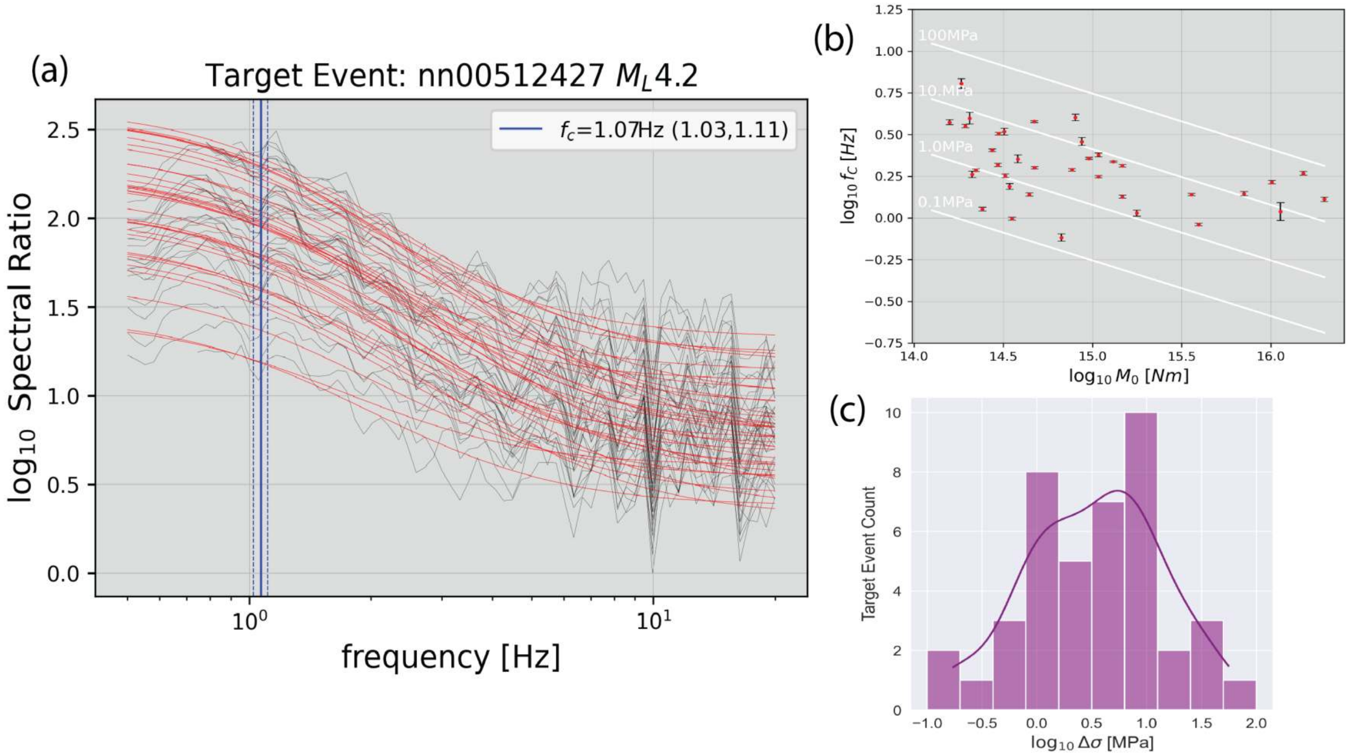

Figure 5 Spectral ratio and stress drop analysis. (a) S-wave spectral ratios for an example M_L 4.2 target event. Recorded spectral ratios with hundreds of EGFs are shown as black lines, and model fits are shown as red lines. The inferred target event corner frequency and uncertainty extracted from the posterior distribution are marked in blue. (b) Scaling of corner frequency with seismic moment for target earthquakes. (c) Distribution of target event stress drops.

4 Discussion

Our detailed analysis of the Sheldon earthquakes characterizes a highly productive sequence that initiated abruptly in the northwest corner of Nevada but does not provide any direct explanation for the physical forces that drive it. Seismicity in the Sheldon sequence is positioned at the intersection of the Warner Valley and Guano Valley fault systems listed in the Quaternary Faults and Folds Database (USGS and CGS, 2006), both of which have relatively low reported slip rates (<0.2 mm/yr). Most of the Sheldon earthquakes do not occur directly on either of these mapped faults, which dip mostly to the west and are geographically offset from the hypocentral positions. There likely exist other faults in between the Warner Valley and Guano Valley fault systems that are not in the USGS database that are either discernible in the local geomorphology or listed in older local geologic maps (Dohrenwend and Moring, 1991). Whether or not the Sheldon earthquakes lie on these liminal structures or ones that are completely invisible from their surface expression, the sequence is clearly positioned in the transitional zone of deformation between larger mapped systems.

The Sheldon sequence is by far the most prominent recent seismic activity in the northernmost Walker Lane (Figure 1), which is the tectonic province that marks the transition between strike-slip faulting in western California and extension in the Basin and Range (Busby, 2013; Faulds et al., 2005; Faulds and Henry, 2008; Hearn and Humphreys, 1998; Wesnousky, 2005). Sequences like Mogul (Anderson et al., 2009; Bell et al., 2012; Ruhl et al., 2016a, 2017), Nine Mile Ranch (Hatch-Ibarra et al., 2022), Ridgecrest (Barnhart et al., 2020; Ross et al., 2019; Trugman et al., 2020), Lone Pine (Hauksson et al., 2020), Monte Cristo (Kariche, 2022; Ruhl et al., 2021; Sethanant et al., 2023; Zheng et al., 2020), and Antelope Valley (Pollitz et al., 2022; Trugman et al., 2023; Wang et al., 2023) exhibit high seismicity rates and aftershock productivity along complex and sometimes incipient fault structures, many of which were not well-mapped in advance of the sequence. Throughout most of the Walker Lane, transtensional crustal deformation is accommodated by an intricate tapestry of strike-slip and normal faults. The diversity of these sequences reflects this transtension, with some earthquakes occurring dominantly on strike-slip structures (e.g., Mogul, Nine Mile Ranch, Monte Cristo) and others dominantly on normal faulting structures (e.g., Lone Pine and Antelope Valley). Strike-slip faulting is the primary mode of deformation on northern Walker Lane faults (Chupik et al., 2021; Faulds et al., 2005; Gold et al., 2014; Koehler, 2019), but the Sheldon sequence is far enough north (past the Mendocino triple junction, for example) that it may well be classified as outside of the Walker Lane altogether. The dominant structure in this region along the northern California-Nevada border is the Surprise Valley fault (Figure 1), a classic Basin and Range normal faulting range front, striking north and accommodating down-to-the-east slip in an east-west extensional environment generally consistent with deformation in the Sheldon sequence. East of the Surprise Valley fault and south-

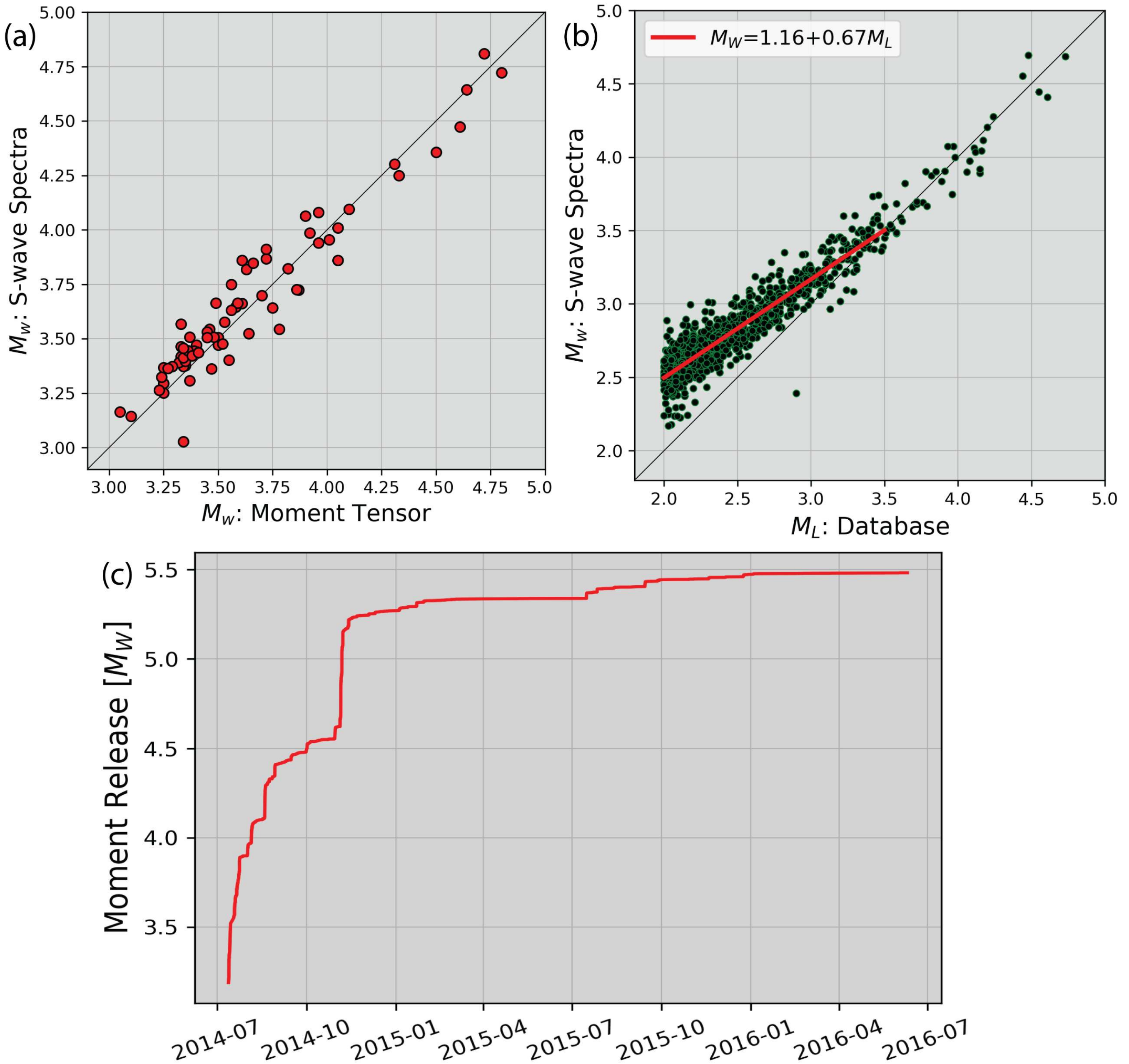

Figure 6 Calibration of moment magnitudes. (a) Comparison of M_W estimates from moment tensors versus those obtained from S-wave spectra at station COLR. (b) Piecewise linear scaling relation of M_W and M_L obtained from S-waves at COLR. (c) Cumulative moment release versus time during the sequence.

west of the Sheldon sequence, the Long Valley fault system (Figure 1) has produced earthquakes as large as M7.0 over the past 15 ka (Personius et al., 2017). The Sheldon sequence is subparallel to the complex network of faults confined within Long Valley and may fit within its broader deformation footprint.

The complex spatiotemporal evolution of the Sheldon sequence defies an easy description. Clearly, Sheldon is not a typical mainshock-aftershock sequence with a classic Omori (1894) decay in seismicity rate. The sequence is swarm-like in its persistent activity for several years duration (e.g., Hainzl, 2004; Hill, 1977; Mogi, 1963; Sykes, 1970), but its space-time progression shows no clear evidence of simple diffusion or migration patterns that could be readily linked to fluid injection or flow (e.g., Ross et al., 2020; Shapiro et al., 1997) or aseismic slip (e.g., Sadeghi Chorsi et al., 2022; Koper et al., 2018; Lohman and McGuire, 2007) as the dominant driving force. No geodetic transients can be clearly observed in InSAR or regional permanent and campaign GPS measurements (Blewitt et al., 2018), which is perhaps unsurprising given the depth of seismicity and cumulative moment release equivalent to a mid M_w 5 earthquake. The 2016-2019 Cahuilla swarm, another long-lived sequence in southern California (Cochran et al., 2023; Hauksson et al., 2019; Ross et al., 2020) provides a useful comparison to illustrate this point. While both sequences feature elevated seismicity rates over the course of several years, the Cahuilla swarm was characterized by a clear, radial migration pattern from a

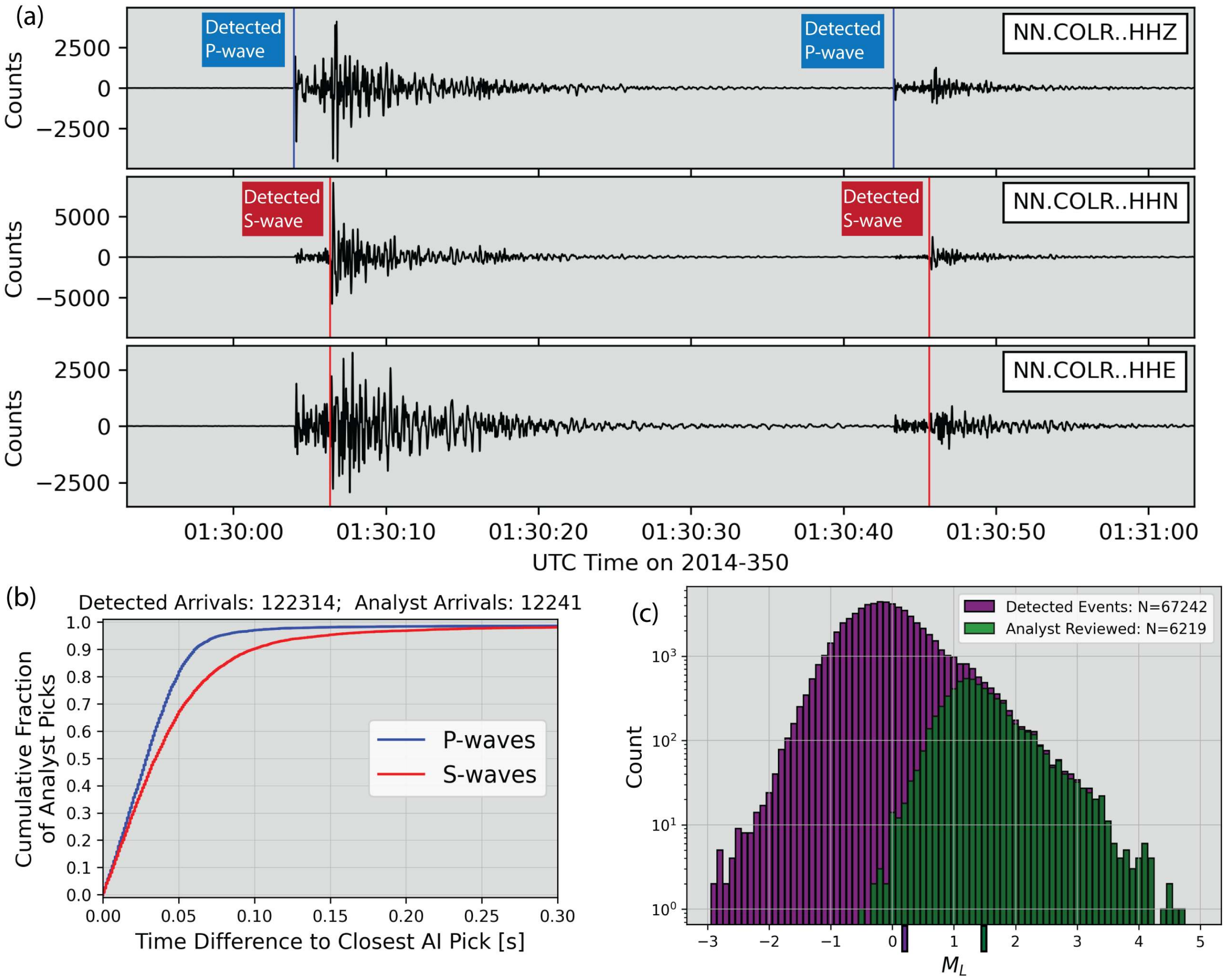

Figure 7 Earthquake detections at COLR. (a) Examples of two small events detected by the machine learning algorithm from continuous data at COLR. The event shown on the left is a M_L 2.0 event detected both by NSL analysts and the algorithm; their picks are overlapping (within 0.05s). The event shown on the right was too small for analysts to locate but was picked up by the algorithm. (b) Cumulative distribution of absolute time differences of analyst identified picks and the nearest machine learning pick. This figure shows, for example, that 95% and 90% of P-waves and S-waves (y-axis) have a machine learning phase arrival listed within 0.1s of the analyst pick (x-axis). (c) Comparison of magnitude distributions of detected events (purple) and cataloged events (green), with estimated magnitude of completeness for each catalog annotated on the x axis.

deep source point before triggering a M_L 4 mainshock and subsequent seismicity (Ross et al., 2020). The Sheldon sequence, in contrast, did not exhibit such beautiful simplicity, with dozens of M4 events repeatedly triggered in a somewhat chaotic fashion.

The Sheldon sequence features several distinct waves of intense seismicity, each with several bursts of activity associated with one or more M_L 4+ events, indicating the importance of earthquake triggering in sustaining, if not initiating, the sequence. In terms of spatial evolution, these phases include (i) an initiation of seismicity on the main NNE striking, E-dipping normal faulting structure, (ii) a subsequent illumination and complex migration patterns along an NNW trending, near-vertical cross fault, (iii) eventual migration down-dip to the east, and (iv) initiation of seismicity on shallower structures coincident with the Guano Valley faults. The overall productivity of the Sheldon sequence is truly immense, featuring 26 M_L 4+ and 262 M_L 3+ events. For comparison, the 2008 Mogul, NV sequence (mainshock M_w 4.9) produced two M_L 4+ events and 38 M_L 3+ events in total. Although several studies have associated earthquake swarm activity with relatively high b-values (e.g., Holtkamp and Brudzinski, 2011; von Seggern et al., 2008), relatively low b-values we observe here (0.65 – 0.85) are consistent with other swarms in extensional tectonic settings within the shallow continental crust (Ruhl et al., 2016a; Ibs-von Seht et al., 2008). The gradual increase in b-value observed over time may indicate a relaxation in differential stress as the sequence progresses and eventually dissipates (e.g., Scholz, 1968, 2015). This trend is also reminiscent of the 2014 Long Valley Caldera swarm, where Shelly et al. (2016) interpret the b-value evolution in terms of a transition in fluid confinement, with earthquakes initially localized to select larger faults (lower b-value) before

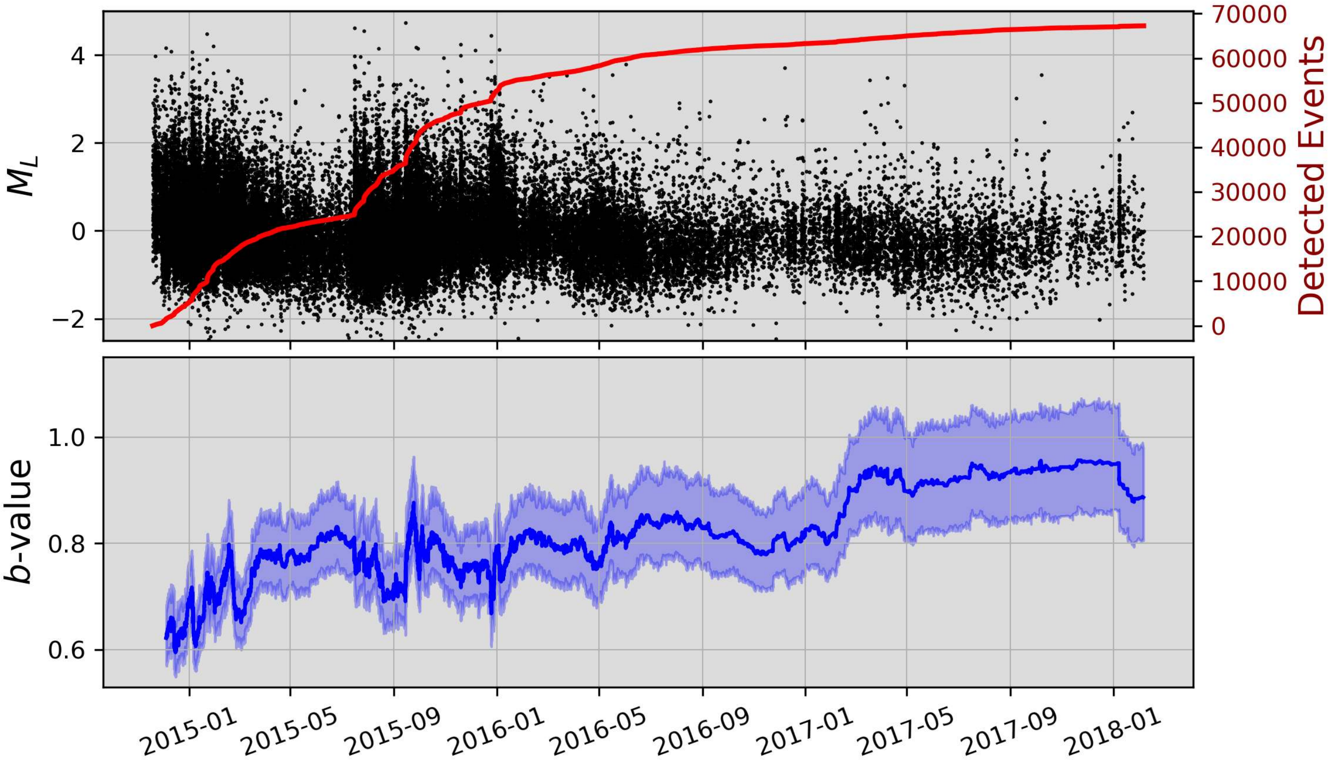

Figure 8 Magnitude distribution and cumulative event count of machine-learning detection (top) and b-value time evolution (bottom); uncertainties are obtained from bootstrap resampling each 1000-event window used to compute the b-value at a given timestamp.

eventually diffusing outward in three dimensions and sampling additional, smaller faults (higher b-value). In the Sheldon sequence, the b-value is lower during the most active part of the sequence, where seismicity is confined to the two primary structures, and increases significantly in 2017 as these structures deactivate.

While there is no obvious signature of the driving force for the Sheldon sequence, its position in a transitional zone of deformation within a volcanic geologic context provides a viable explanation. Earthquake swarms are commonly associated with hydrothermal activity throughout the western United States (Chen and Shearer, 2011; Hauksson et al., 2013, 2019; Li et al., 2021; Lohman and McGuire, 2007; Mesimeri et al., 2021; Ross et al., 2020; Ross and Cochran, 2021; Shelly and Hardebeck, 2019; Vidale and Shearer, 2006) and globally (Cox, 2016; Hainzl, 2002, 2004; Ibs-von Seht et al., 2008), and often occur at the intersection of active faults or within otherwise transitional deformation zones (Hill, 1977; Sibson, 1987). The Sheldon sequence fits this paradigm well, positioned between the Warner and Guano Valley faults in a weak crustal zone associated with volcanic terrains. Seismic activity within the Sheldon sequence appears to be most intense at the intersection of the east-dipping normal fault and north-northwest-striking cross-fault, somewhat reminiscent of fracture mesh structures (Sibson, 1996) observed in several other studies of earthquake swarms and hydrothermal systems in the western US (Ross et al., 2017; Shelly et al., 2023). The complex patterns of seismicity we observe could perhaps be explained by the interaction of fluid movement and earthquake-earthquake triggering, releasing elastic stresses built up progressively over time in this transitional deformation zone. While the remoteness of the Sheldon sequence makes it a challenging case study in providing the in-situ observations necessary to resolve the fine-scaled details of earthquake swarm dynamics, its occurrence is a useful reminder that such natural and violent swarm complexity can occur even in unexpected places in Nevada.

5 Conclusions

We characterize a highly active earthquake sequence beneath the Sheldon Wildlife Refuge in northwest Nevada using a broad set of seismological techniques. High-precision earthquake locations highlight a primary fault structure dipping to the east and a subvertical cross-fault striking north-northwest. Moment tensor and stress field analyses show results consistent with an overall normal faulting regime. The spatiotemporal progression of the sequence comprises repeated bursts of seismicity on these structures separated by quiescent periods. By leveraging machine learning algorithms, we detect nearly 70,000 events from 2014 – 2016. The physical factors driving the immense productivity of this sequence remain to be explained in full but are broadly consistent with models of earthquake swarms within transitional deformation zones and may combine both hydrothermal and earthquake triggering processes.

Acknowledgements

D. Trugman gratefully acknowledges support from NSF Awards EAR-2231705 and EAR-2121666. NSL earthquake monitoring, data product, and field efforts were funded by the USGS Cooperative Agreement Number G20AC00038. We thank current and former NSL operations team members, including W. Honjas, D. Slater, A. Main, E. Wicks, R. Hatch-Ibarra, E. Morton, J. Borrman, T. Rennie, and G. Plank for their support and contributions to the earthquake monitoring and data products used in this study, as well as R. Abercrombie, C. Henry, and S. Wesnousky for helpful discussions on seismicity, geology and tectonics in Nevada. We also thank Associate Editor A. Llenos and two reviewers for their constructive comments that improved the manuscript.

Data and code availability

We use phase arrival, event catalog, and waveform data products produced by the Nevada Seismological Laboratory (http://www.seismo.unr.edu/Earthquake) and publicly archived as part of USGS ComCat (https://earthquake.usgs.gov/earthquakes/search/) and delivered to the IRIS Data Management Center (https://ds.iris.edu/ds/). Quaternary faults and fold data were obtained from the USGS database (https://www.sciencebase.gov/catalog/item/589097b1e4b072a7ac0cae23), and surface topography downloaded from the USGS 3DEP program (https://apps.nationalmap.gov/downloader/). Waveform data were extracted using Antelope Software (https://brtt.com) and processed using ObsPy (Beyreuther et al., 2010). Additional analysis packages used, all publicly available, include NonLinLoc (Lomax et al., 2000, 2001), GrowClust3D.jl (Trugman et al., 2022), PyGMT (Wessel et al., 2019), and MTINV (Ichinose et al., 1998), mtspec (Krischer, 2016), and pymc (Salvatier et al., 2016). StressInversion.jl, a set of Julia software tools for stress inversions are publicly available on GitHub (https://github.com/dttrugman/StressInversion.jl). Regional waveforms for moment tensor inversion were downloaded using Standing Order for Data (Owens et al., 2004) and ObsPy (Beyreuther et al., 2010) programs. Supplementary Movies S1 and S2, along with the relocated catalog, velocity model, and moment tensor databases produced in this study are archived at Zenodo (https://doi.org/10.5281/zenodo.8030954). Full moment tensor solutions are also available on the Nevada Seismological Laboratory website (http://www.seismo.unr.edu/Earthquake).

Competing interests

The authors have no competing interests to declare.

References

Abercrombie, R. Comparison of direct and coda wave stress drop measurements for the Wells, Nevada, earthquake sequence. *Journal of Geophysical Research: Solid Earth*, 118(4):1458–1470, 2013. doi: 10.1029/2012JB009638.

Abercrombie, R. Investigating uncertainties in empirical Green's function analysis of earthquake source parameters. *Journal of Geophysical Research: Solid Earth*, 120(6):4263–4277, 2015. doi: 10.1002/2015JB011984.

Abercrombie, R. Resolution and uncertainties in estimates of earthquake stress drop and energy release. *Philosophical Transactions of the Royal Society A: Mathematical, Physical and Engineering Sciences*, 379(2196):20200131, 2021. doi: 10.1098/rsta.2020.0131.

Abercrombie, R., Bannister, S., Ristau, J., and Doser, D. Variability of earthquake stress drop in a subduction setting, the Hikurangi Margin, New Zealand. *Geophysical Journal International*, 208(1): 306–320, 2017. doi: 10.1093/gji/ggw393.

Aki, K. and Richards, P. *Quantitative seismology*. University Science Books, Sausalito, Calif, 2nd edition, 2002.

Anderson, J., Tibuleac, I., Anooshehpoor, A., Biasi, G., Smith, K., and Seggern, D. Exceptional Ground Motions Recorded during the 26 April 2008 Mw 5.0 Earthquake in Mogul, Nevada. *Bulletin of the Seismological Society of America*, 99(6):3475–3486, 2009. doi: 10.1785/0120080352.

Anderson, J. G. and Hough, S. A model for the shape of the fourier amplitude spectrum of acceleration at high frequencies. *Bulletin of the Seismological Society of America*, 74(5):1969–1993, 1984.

Angelier, J., Tarantola, A., Valette, B., and Manoussis, S. Inversion of field data in fault tectonics to obtain the regional stress — I. Single phase fault populations: a new method of computing the stress tensor. *Geophysical Journal International*, 69(3):607–621, 1982. doi: 10.1111/j.1365-246X.1982.tb02766.x.

Barnhart, W., Gold, R., and Hollingsworth, J. Localized fault-zone dilatancy and surface inelasticity of the 2019 Ridgecrest earthquakes. *Nature Geoscience*, 1–6, 2020. doi: 10.1038/s41561-020-0628-8.

Becker, T., Hashima, A., Freed, A., and Sato, H. Stress change before and after the 2011 M9 Tohoku-oki earthquake. *Earth and Planetary Science Letters*, 504:174–184, 2018. doi: 10.1016/j.epsl.2018.09.035.

Bell, J., Amelung, F., and Henry, C. InSAR analysis of the 2008 Reno-Mogul earthquake swarm: Evidence for westward migration of Walker Lane style dextral faulting. *Geophysical Research Letters*, 39(18), 2012. doi: 10.1029/2012GL052795.

Beyreuther, M., Barsch, R., Krischer, L., Megies, T., Behr, Y., and Wassermann, J. ObsPy: A Python Toolbox for Seismology. *Seismological Research Letters*, 81(3):530–533, 2010. doi: 10.1785/gssrl.81.3.530.

Blewitt, G., Hammond, W., and Kreemer, C. Harnessing the GPS Data Explosion for Interdisciplinary Science. *Eos*, 99, 2018. doi: 10.1029/2018EO104623.

Boatwright, J. A spectral theory for circular seismic sources; simple estimates of source dimension, dynamic stress drop, and radiated seismic energy. *Bulletin of the Seismological Society of America*, 70(1):1–27, 1980.

Brune, J. Tectonic stress and the spectra of seismic shear waves from earthquakes. *Journal of Geophysical Research*, 75(26): 4997–5009, 1970. doi: 10.1029/JB075i026p04997.

Busby, C. Birth of a plate boundary at ca. 12 Ma in the Ancestral Cascades arc, Walker Lane belt of California and Nevada. *Geosphere*, 9(5):1147–1160, 2013. doi: 10.1130/GES00928.1.

Chen, X. and Shearer, P. Comprehensive analysis of earthquake source spectra and swarms in the Salton Trough, California. *Journal of Geophysical Research*, 116(B9), 2011. doi: 10.1029/2011JB008263.

Chupik, C., Koehler, R., and Keen-Zebert, A. Complex Holocene

Fault Ruptures on the Warm Springs Valley Fault in the Northern Walker Lane, Nevada–Northern California. *Bulletin of the Seismological Society of America*, 112(1):575–596, 2021. doi: 10.1785/0120200271.

Coble, M. and Mahood, G. Geology of the High Rock caldera complex, northwest Nevada, and implications for intense rhyolitic volcanism associated with flood basalt magmatism and the initiation of the Snake River Plain–Yellowstone trend. *Geosphere*, 12(1):58–113, 2016. doi: 10.1130/GES01162.1.

Cochran, E., Page, M., Elst, N., Ross, Z., and Trugman, D. Fault Roughness at Seismogenic Depths and Links to Earthquake Behavior. *The Seismic Record*, 3(1):37–47, 2023. doi: 10.1785/0320220043.

Cox, S. Injection-Driven Swarm Seismicity and Permeability Enhancement: Implications for the Dynamics of Hydrothermal Ore Systems in High Fluid-Flux, Overpressured Faulting Regimes—An Invited Paper. *Economic Geology*, 111(3):559–587, 2016. doi: 10.2113/econgeo.111.3.559.

Dohrenwend, J. and Moring, B. Reconnaissance photogeologic map of young faults in the Vya 1°x2° quadrangle, Nevada-Oregon-California. *U.S. Geological Survey*, 1991. doi: 10.3133/mf2174.

Faulds, J. and Henry, C. Tectonic influences on the spatial and temporal evolution of the Walker Lane: An incipient transform fault along the evolving Pacific - North American plate boundary. *Arizona Geological Society Digest*, 22:437–470, 2008.

Faulds, J., Henry, C., and Hinz, N. Kinematics of the northern Walker Lane: An incipient transform fault along the Pacific–North American plate boundary. *Geology*, 33(6):505–508, 2005. doi: 10.1130/G21274.1.

Gephart, J. and Forsyth, D. An improved method for determining the regional stress tensor using earthquake focal mechanism data: Application to the San Fernando Earthquake Sequence. *Journal of Geophysical Research: Solid Earth*, 89(B11): 9305–9320, 1984. doi: 10.1029/JB089iB11p09305.

Gold, R., Briggs, R., Personius, S., Crone, A., Mahan, S., and Angster, S. Latest Quaternary paleoseismology and evidence of distributed dextral shear along the Mohawk Valley fault zone, northern Walker Lane, California. *Journal of Geophysical Research: Solid Earth*, 119(6):5014–5032, 2014. doi: 10.1002/2014JB010987.

Gutenberg, B. and Richter, C. Frequency of earthquakes in California. *Bulletin of the Seismological Society of America*, 34(4): 185–188, 1944.

Hainzl, S. Indications for a successively triggered rupture growth underlying the 2000 earthquake swarm in Vogtland/NW Bohemia. *Journal of Geophysical Research*, 107(B12), 2002. doi: 10.1029/2002JB001865.

Hainzl, S. Seismicity patterns of earthquake swarms due to fluid intrusion and stress triggering. *Geophysical Journal International*, 159(3):1090–1096, 2004. doi: 10.1111/j.1365-246X.2004.02463.x.

Hanks, T. f_{max}. *Bulletin of the Seismological Society of America*, 72 (6A):1867–1879, 1982.

Hanks, T. and Boore, D. Moment-magnitude relations in theory and practice. *Journal of Geophysical Research: Solid Earth*, 89 (B7):6229–6235, 1984. doi: 10.1029/JB089iB07p06229.

Hardebeck, J. and Michael, A. Damped regional-scale stress inversions: Methodology and examples for southern California and the Coalinga aftershock sequence. *Journal of Geophysical Research: Solid Earth*, 111(B11), 2006. doi: 10.1029/2005JB004144.

Hatch, R., Abercrombie, R., Ruhl, C., and Smith, K. Earthquake Interaction, Fault Structure, and Source Properties of a Small Sequence in 2017 near Truckee, California. *Bulletin of the Seismological Society of America*, 108(5A):2580–2593, 2018. doi: 10.1785/0120180089.

Hatch-Ibarra, R., Abercrombie, R., Ruhl, C., Smith, K., Hammond, W., and Pierce, I. The 2016 Nine Mile Ranch Earthquakes: Hazard and Tectonic Implications of Orthogonal Conjugate Faulting in the Walker Lane. *Bulletin of the Seismological Society of America*, 112(3):1727–1741, 2022. doi: 10.1785/0120210149.

Hauksson, E., Stock, J., Bilham, R., Boese, M., Chen, X., and Fielding, E. Report on the August 2012 Brawley Earthquake Swarm in Imperial Valley, Southern California. *Seismological Research Letters*, 84(2):177–189, 2013. doi: 10.1785/0220120169.

Hauksson, E., Ross, Z., and Cochran, E. Slow-Growing and Extended-Duration Seismicity Swarms: Reactivating Joints or Foliations in the Cahuilla Valley Pluton, Central Peninsular Ranges, Southern California. *Journal of Geophysical Research: Solid Earth*, 124(4):3933–3949, 2019. doi: 10.1029/2019JB017494.

Hauksson, E., Olson, B., Grant, A., Andrews, J., Chung, A., and Hough, S. The Normal-Faulting 2020 M_w 5.8 Lone Pine, Eastern California, Earthquake Sequence. *Seismological Research Letters*, 92(2A):679–698, 2020. doi: 10.1785/0220200324.

Hearn, E. and Humphreys, E. Kinematics of the southern Walker Lane Belt and motion of the Sierra Nevada block, California. *Journal of Geophysical Research: Solid Earth*, 103(B11): 27033–27049, 1998. doi: 10.1029/98JB01390.

Henry, C., Castor, S., Starkel, W., Ellis, B., Wolff, J., and Laravie, J. Geology and evolution of the McDermitt caldera, northern Nevada and southeastern Oregon, western USA. *Geosphere*, 13 (4):1066–1112, 2017. doi: 10.1130/GES01454.1.

Hill, D. A model for earthquake swarms. *Journal of Geophysical Research (1896-1977*, 82(8):1347–1352, 1977. doi: 10.1029/JB082i008p01347.

Hoffman, M. and Gelman, A. The No-U-Turn Sampler: Adaptively Setting Path Lengths in Hamiltonian Monte Carlo, 2011. ArXiv:1111.4246 [Cs, Stat].

Holtkamp, S. and Brudzinski, M. Earthquake swarms in circum-Pacific subduction zones. *Earth and Planetary Science Letters*, 305(1):215–225, 2011. doi: 10.1016/j.epsl.2011.03.004.

Hough, S. Observational constraints on earthquake source scaling: understanding the limits in resolution. *Tectonophysics*, 261(1): 83–95, 1996. doi: 10.1016/0040-1951(96)00058-3.

Hough, S. Empirical Green's function analysis: Taking the next step. *Journal of Geophysical Research: Solid Earth*, 102(B3): 5369–5384, 1997. doi: 10.1029/96JB03488.

Ibs-von Seht, M., Plenefisch, T., and Klinge, K. Earthquake swarms in continental rifts — A comparison of selected cases in America. *Africa and Europe. Tectonophysics*, 452(1):66–77, 2008. doi: 10.1016/j.tecto.2008.02.008.

Ichinose, G., Smith, K., and Anderson, J. Moment tensor solutions of the 1994 to 1996 Double Spring Flat, Nevada, earthquake sequence and implications for local tectonic models. *Bulletin of the Seismological Society of America*, 88(6):1363–1378, 1998.

Kaneko, Y. and Shearer, P. Seismic source spectra and estimated stress drop derived from cohesive-zone models of circular subshear rupture. *Geophysical Journal International*, 197(2): 1002–1015, 2014. doi: 10.1093/gji/ggu030.

Kariche, J. The 2020 Monte Cristo (Nevada) Earthquake Sequence: Stress Transfer in the Context of Conjugate Strike-Slip Faults. *Tectonics*, 41(3):2020 006506, 2022. doi: 10.1029/2020TC006506.

Koehler, R. Active faulting in the North Valleys region of

Reno, Nevada: A distributed zone within the northern Walker Lane. *Geomorphology*, 326:38–53, 2019. doi: 10.1016/j.geomorph.2018.09.015.

Koper, K., Pankow, K., Pechmann, J., Hale, J., Burlacu, R., and Yeck, W. Afterslip Enhanced Aftershock Activity During the 2017 Earthquake Sequence Near Sulphur Peak, Idaho. *Geophysical Research Letters*, 45(11):5352–5361, 2018. doi: 10.1029/2018GL078196.

Kostrov, V. Seismic moment and energy of earthquakes, and the seismic flow of rock, Izv. *Acad. Sci. USSR. Phys. Solid Earth*, 1: 23–44, 1974.

Krischer, L. *Mtspec Python Wrappers 0.3.2*. Zenodo, 2016. doi: 10.5281/zenodo.321789.

Lerch, D., Klemperer, S., Egger, A., Colgan, J., and Miller, E. The northwestern margin of the Basin-and-Range Province, part 1: Reflection profiling of the moderate-angle (30°) Surprise Valley Fault. *Tectonophysics*, 488(1–4):143–149, 2010. doi: 10.1016/j.tecto.2009.05.028.

Li, B., Smith, J., and Ross, Z. Basal nucleation and the prevalence of ascending swarms in Long Valley caldera. *Science Advances*, 7(35):8368, 2021. doi: 10.1126/sciadv.abi8368.

Lohman, R. and McGuire, J. Earthquake swarms driven by aseismic creep in the Salton Trough, California. *Journal of Geophysical Research*, 112(B4), 2007. doi: 10.1029/2006JB004596.

Lomax, A., Virieux, J., Volant, P., and Berge-Thierry, C. Probabilistic Earthquake Location in 3D and Layered Models. In Thurber, C. and Rabinowitz, N., editors, *Advances in Seismic Event Location*, page 101–134. Springer Netherlands, Dordrecht, 2000. doi: 10.1007/978-94-015-9536-0_5.

Lomax, A., Zollo, A., Capuano, P., and Virieux, J. Precise, absolute earthquake location under Somma–Vesuvius volcano using a new three-dimensional velocity model. *Geophysical Journal International*, 146(2):313–331, 2001. doi: 10.1046/j.0956-540x.2001.01444.x.

Madariaga, R. Dynamics of an expanding circular fault. *Bulletin of the Seismological Society of America*, 66(3):639–666, 1976.

Mesimeri, M., Pankow, K., Baker, B., and Hale, J. Episodic Earthquake Swarms in the Mineral Mountains, Utah Driven by the Roosevelt Hydrothermal System. *Journal of Geophysical Research: Solid Earth*, 126(6):2021 021659, 2021. doi: 10.1029/2021JB021659.

Michael, A. J. Determination of stress from slip data: Faults and folds. *Journal of Geophysical Research: Solid Earth*, 89(B13): 11517–11526, 1984. doi: 10.1029/JB089iB13p11517.

Michael, A. J. Use of focal mechanisms to determine stress: A control study. *Journal of Geophysical Research: Solid Earth*, 92(B1): 357–368, 1987. doi: 10.1029/JB092iB01p00357.

Mogi, K. Experimental study on the mechanism of the earthquake occurrences of volcanic origin. *Bulletin of Volcanology*, 26(1): 197–208, 1963. doi: 10.1007/BF02597286.

Mousavi, S., Sheng, Y., Zhu, W., and Beroza, G. STanford EArthquake Dataset (STEAD): A Global Data Set of Seismic Signals for AI. *IEEE Access*, 7:179464–179476, 2019. doi: 10.1109/ACCESS.2019.2947848.

Mousavi, S., Ellsworth, W., Zhu, W., Chuang, L., and Beroza, G. Earthquake transformer—an attentive deep-learning model for simultaneous earthquake detection and phase picking. *Nature Communications*, 11(1):3952, 2020. doi: 10.1038/s41467-020-17591-w.

Munafo, I., Malagnini, L., and Chiaraluce, L. On the Relationship between M_w and M_L for Small Earthquakes. *Bulletin of the Seismological Society of America*, 106(5):2402–2408, 2016. doi: 10.1785/0120160130.

Omori, F. Investigation of aftershocks. *Rep. Earthquake Inv. Comm*, 2:103–139, 1894.

Owens, T., Crotwell, H., Groves, C., and Oliver-Paul, P. SOD: Standing Order for Data. *Seismological Research Letters*, 75(4): 515–520, 2004. doi: 10.1785/gssrl.75.4.515-a.

Personius, S., Briggs, R., Maharrey, J., Angster, S., and Mahan, S. A paleoseismic transect across the northwestern Basin and Range Province, northwestern Nevada and northeastern California, USA. *Geosphere*, 13(3):782–810, 2017. doi: 10.1130/GES01380.1.

Pierce, K. and Morgan, L. Chapter 1: The track of the Yellowstone hot spot: Volcanism, faulting, and uplift. In Link, P., Kuntz, M., and Piatt, L., editors, *Regional Geology of Eastern Idaho and Western Wyoming*, volume 179, page 0. Geological Society of America, 1992. doi: 10.1130/MEM179-p1.

Pollitz, F., Wicks, C., and Hammond, W. Kinematic Slip Model of the 2021 M 6.0 Antelope Valley, California, Earthquake. *The Seismic Record*, 2(1):20–28, 2022. doi: 10.1785/0320210043.

Prieto, G., Parker, R., and Vernon III, F. A Fortran 90 library for multitaper spectrum analysis. *Computers & Geosciences*, 35(8): 1701–1710, 2009. doi: 10.1016/j.cageo.2008.06.007.

Richter, C. An instrumental earthquake magnitude scale. *Bulletin of the Seismological Society of America*, 25(1):1–32, 1935.

Ross, Z. and Cochran, E. Evidence for Latent Crustal Fluid Injection Transients in Southern California From Long-Duration Earthquake Swarms. *Geophysical Research Letters*, 48(12):2021 092465, 2021. doi: 10.1029/2021GL092465.

Ross, Z., Rollins, C., Cochran, E., Hauksson, E., Avouac, J.-P., and Ben-Zion, Y. Aftershocks driven by afterslip and fluid pressure sweeping through a fault-fracture mesh. *Geophysical Research Letters*, 44(16):2017 074634, 2017. doi: 10.1002/2017GL074634.

Ross, Z., Idini, B., Jia, Z., Stephenson, O., Zhong, M., and Wang, X. Hierarchical interlocked orthogonal faulting in the 2019 Ridgecrest earthquake sequence. *Science*, 366(6463):346–351, 2019. doi: 10.1126/science.aaz0109.

Ross, Z., Cochran, E., Trugman, D., and Smith, J. 3D fault architecture controls the dynamism of earthquake swarms. *Science*, 368(6497):1357–1361, 2020. doi: 10.1126/science.abb0779.

Ruhl, C., Abercrombie, R., Smith, K., and Zaliapin, I. Complex spatiotemporal evolution of the 2008 M_w 4.9 Mogul earthquake swarm (Reno, Nevada): Interplay of fluid and faulting. *Journal of Geophysical Research: Solid Earth*, 2016a. doi: 10.1002/2016JB013399.

Ruhl, C., Smith, K., Kent, G., and Seaman, T. Seismotectonic and Seismic Hazard Implications for the Reno-Tahoe Area of the Walker Lane in Nevada and California. *Applied Geology of California*, 2016b.

Ruhl, C., Abercrombie, R., and Smith, K. Spatiotemporal Variation of Stress Drop During the 2008 Mogul, Nevada, Earthquake Swarm. *Journal of Geophysical Research: Solid Earth*, 122(10): 2017 014601, 2017. doi: 10.1002/2017JB014601.

Ruhl, C., Morton, E., Bormann, J., Hatch-Ibarra, R., Ichinose, G., and Smith, K. Complex Fault Geometry of the 2020 M_{ww} 6.5 Monte Cristo Range, Nevada, Earthquake Sequence. *Seismological Research Letters*, 92(3):1876–1890, 2021. doi: 10.1785/0220200345.

Sadeghi Chorsi, T., Braunmiller, J., Deng, F., and Dixon, T. Afterslip From the 2020 M 6.5 Monte Cristo Range, Nevada Earthquake. *Geophysical Research Letters*, 49(17):2022 099952, 2022. doi: 10.1029/2022GL099952.

Salvatier, J., Wiecki, T., and Fonnesbeck, C. Probabilistic programming in Python using PyMC3. *PeerJ Computer Science*, 2:55, 2016. doi: 10.7717/peerj-cs.55.

Sato, T. and Hirasawa, T. Body Wave Spectra from Propagating

Shear Cracks. *Journal of Physics of the Earth*, 21(4):415–431, 1973. doi: 10.4294/jpe1952.21.415.

Schaff, S. The 1968 Adel, 1976. Retrieved from.

Scholz, C. The frequency-magnitude relation of microfracturing in rock and its relation to earthquakes. *Bulletin of the Seismological Society of America*, 58(1):399–415, 1968.

Scholz, C. H. On the stress dependence of the earthquake b value. *Geophysical Research Letters*, 42(5):1399–1402, 2015. doi: 10.1002/2014GL062863.

Sethanant, I., Nissen, E., Pousse-Beltran, L., Bergman, E., and Pierce, I. The 2020 M_w 6.5 Monte Cristo Range, Nevada, Earthquake: Anatomy of a Crossing-Fault Rupture through a Region of Highly Distributed Deformation. *Bulletin of the Seismological Society of America*, 113(3):948–975, 2023. doi: 10.1785/0120220166.

Shapiro, S., Huenges, E., and Borm, G. Estimating the crust permeability from fluid-injection-induced seismic emission at the KTB site. *Geophysical Journal International*, 131(2):15– 18, 1997. doi: 10.1111/j.1365-246X.1997.tb01215.x.

Shearer, P., Abercrombie, R., Trugman, D., and Wang, W. Comparing EGF Methods for Estimating Corner Frequency and Stress Drop From P Wave Spectra. *Journal of Geophysical Research: Solid Earth*, 124(4):3966–3986, 2019. doi: 10.1029/2018JB016957.

Shearer, P., Abercrombie, R., and Trugman, D. Improved Stress Drop Estimates for M 1.5 to 4 Earthquakes in Southern California From 1996 to 2019. *Journal of Geophysical Research: Solid Earth*, 127(7):2022 024243, 2022. doi: 10.1029/2022JB024243.

Shelly, D. and Hardebeck, J. Illuminating Faulting Complexity of the 2017 Yellowstone Maple Creek Earthquake Swarm. *Geophysical Research Letters*, 46(5):2544–2552, 2019. doi: 10.1029/2018GL081607.

Shelly, D., Ellsworth, W., and Hill, D. Fluid-faulting evolution in high definition: Connecting fault structure and frequency-magnitude variations during the 2014 Long Valley Caldera, California, earthquake swarm. *Journal of Geophysical Research: Solid Earth*, 121(3):1776–1795, 2016. doi: 10.1002/2015JB012719.

Shelly, D., Skoumal, R., and Hardebeck, J. Fracture-Mesh Faulting in the Swarm-Like 2020 Maacama Sequence Revealed by High-Precision Earthquake Detection, Location, and Focal Mechanisms. *Geophysical Research Letters*, 50(1):2022 101233, 2023. doi: 10.1029/2022GL101233.

Sibson, R. Earthquake rupturing as a mineralizing agent in hydrothermal systems. *Geology*, 15(8):701–704, 1987. doi: 10.1130/0091-7613(1987)15.

Sibson, R. Structural permeability of fluid-driven fault-fracture meshes. *Journal of Structural Geology*, 18(8):1031–1042, 1996. doi: 10.1016/0191-8141(96)00032-6.

Sykes, L. Earthquake swarms and sea-floor spreading. *Journal of Geophysical Research (1896-1977*, 75(32):6598–6611, 1970. doi: 10.1029/JB075i032p06598.

Trugman, D. Resolving Differences in the Rupture Properties of M5 Earthquakes in California Using Bayesian Source Spectral Analysis. *Journal of Geophysical Research: Solid Earth*, 127(4):2021 023526, 2022. doi: 10.1029/2021JB023526.

Trugman, D. and Shearer, P. Application of an improved spectral decomposition method to examine earthquake source scaling in southern California. *Journal of Geophysical Research: Solid Earth*, 122(4):2017 013971, 2017a. doi: 10.1002/2017JB013971.

Trugman, D. and Shearer, P. GrowClust: A Hierarchical Clustering Algorithm for Relative Earthquake Relocation, with Application to the Spanish Springs and Sheldon, Nevada, Earthquake Sequences. *Seismological Research Letters*, 88(2A):379–391, 2017b. doi: 10.1785/0220160188.

Trugman, D., Ross, Z., and Johnson, P. Imaging Stress and Faulting Complexity Through Earthquake Waveform Similarity. *Geophysical Research Letters*, 47(1):2019 085888, 2020. doi: 10.1029/2019GL085888.

Trugman, D., Chamberlain, C., Savvaidis, A., and Lomax, A. GrowClust3D.jl: A Julia Package for the Relative Relocation of Earthquake Hypocenters Using 3D Velocity Models. *Seismological Research Letters*, 94(1):443–456, 2022. doi: 10.1785/0220220193.

Trugman, D., Brune, J., Smith, K., Louie, J., and Kent, G. The Rocks That Did Not Fall: A Multidisciplinary Analysis of Near-Source Ground Motions From an Active Normal Fault. *AGU Advances*, 4(2):2023 000885, 2023. doi: 10.1029/2023AV000885.

Uhrhammer, R., Loper, S., and Romanowicz, B. Determination of local magnitude using BDSN broadband records. *Bulletin of the Seismological Society of America*, 86(5):1314–1330, 1996. doi: 10.1785/BSSA0860051314.

van der Elst, N. B-Positive: A Robust Estimator of Aftershock Magnitude Distribution in Transiently Incomplete Catalogs. *Journal of Geophysical Research: Solid Earth*, 126(2):2020 021027, 2021. doi: 10.1029/2020JB021027.

Vavryčuk, V. Iterative joint inversion for stress and fault orientations from focal mechanisms. *Geophysical Journal International*, 199(1):69–77, 2014. doi: 10.1093/gji/ggu224.

Vidale, J. and Shearer, P. A survey of 71 earthquake bursts across southern California: Exploring the role of pore fluid pressure fluctuations and aseismic slip as drivers. *Journal of Geophysical Research*, 111(B5), 2006. doi: 10.1029/2005JB004034.

von Seggern, D., Smith, K., and Preston, L. Seismic Spatial-Temporal Character and Effects of a Deep (25–30 km) Magma Intrusion below North Lake Tahoe, California–Nevada. *Bulletin of the Seismological Society of America*, 98(3):1508–1526, 2008. doi: 10.1785/0120060240.

Wang, K., Dreger, D., Burgmann, R., and Taira, T. Finite-Source Model of the. *Seismological Research Letters*, 94(3):1352–1366, 2023. doi: 10.1785/0220220262.

Wesnousky, S. Active faulting in the Walker Lane. *Tectonics*, 24(3), 2005. doi: 10.1029/2004TC001645.

Wessel, P., Luis, J., Uieda, L., Scharroo, R., Wobbe, F., Smith, W., and Tian, D. The Generic Mapping Tools Version 6. *Geochemistry, Geophysics, Geosystems*, 20(11):5556–5564, 2019. doi: 10.1029/2019GC008515.

Woollam, J., Münchmeyer, J., Tilmann, F., Rietbrock, A., Lange, D., and Bornstein, T. SeisBench—A Toolbox for Machine Learning in Seismology. *Seismological Research Letters*, 93(3):1695–1709, 2022. doi: 10.1785/0220210324.

Zheng, A., Chen, X., and Xu, W. Present-Day Deformation Mechanism of the Northeastern Mina Deflection Revealed by the 2020 M_w 6.5 Monte Cristo Range Earthquake. *Geophysical Research Letters*, 47(22):2020 090142, 2020. doi: 10.1029/2020GL090142.

doi:10.26443/seismica.v2i2.1033

SEISMICA

Seismic record of a long duration dispersive signal after the 15 January 2022 Hunga-Tonga eruption

J. Diaz *[1]

[1]Geosciences Barcelona (GEO3BCN), CSIC, Barcelona, Spain

Author contributions: *Conceptualization, Funding Acquisition, Investigation, Methodology, Validation, Visualization, Writing – original draft, Writing – review & editing*: J. Diaz.

Abstract Data acquired by broadband seismic stations distributed around the world are used to document the exceptionally long duration signal from the tsunami-associated gravity wave that followed the January 2022 Hunga-Tonga eruption. The first arrivals of this wave, with a frequency of around 2 mHz, are recorded at the time the tsunami arrives to each station, but the highest recorded frequencies, which reach 40 mHz, arrive 5 days later at some sites, following the prediction of a gravity wave originating at the Hunga-Tonga region and traveling in deep water. This dispersive signal is detected in most of the stations located in the Pacific Ocean basin and its coasts, but also in the Indian Ocean, Antarctica, and some stations in North America located hundreds of kilometers from the coastline. The signal is compared with the data gathered after earthquakes that have produced large tsunamis, showing that the seismic records from the Hunga-Tonga eruption are very different. Following the hypothesis pointed out by Omira et al 2023, we propose that the origin of this exceptional characteristic is due to the interaction between the tsunami and atmospheric waves that travel a little faster.

Production Editor:
Gareth Funning
Handling Editor:
Lise Retailleau
Copy & Layout Editor:
Hannah F. Mark

Signed reviewer(s):
Brad Lipovsky

Received:
June 28, 2023
Accepted:
October 26, 2023
Published:
November 29, 2023

1 Introduction

On January 15 2022, the Hunga-Tonga (H-T) volcano, located in the South Pacific Ocean, produced one of the most powerful volcanic events recorded to date, with an estimated TNT equivalent yield of 100-200 Mt (Vergoz et al., 2022) and a plume that reached 55 km high (Carr et al., 2022). This exceptional eruption generated a large seismic earthquake and powerful atmospheric waves, detected by multiple instruments throughout the world, from simple weather stations to satellites, infrasound detectors, microbarographs, tidal gauges, geodetic stations, and broad-band seismic stations. The effects of the violent eruption reached even the ionosphere, where they produced significant variations in the ionospheric total electron content (TEC) (e.g. Astafyeva et al., 2022). Probably the most outstanding feature after the H-T eruption was the atmospheric wave generated by the eruption, characterized by a sudden variation in pressure. The wave's passage was recorded during at least four laps of the planet. Various publications have shown that most of the energy injected into the atmosphere propagated as a Lamb wave (e.g. Amores et al., 2022). Atmospheric Lamb waves are characterized by their low-frequency range, typically below 10 mHz, their non-dispersive character, and their ability to travel long distances without significant attenuation. Analysis of the Lamb waves generated by the H-T eruption has shown that their propagation velocity is close to 310 ms^{-1} and that the pressure variations have been in the range of hundreds of Pascals (Matoza et al., 2022). Wright et al. (2022), based on the analysis of satellite images for several hours, also identified the propagation of gravity waves in the atmosphere, travelling with phase speeds between 240 and 270 ms^{-1} and showing frequency dispersion. As these authors pointed out, gravity waves that remain coherent and spread across the globe are unprecedented.

The H-T eruption generated an exceptional tsunami, recorded on a global scale, with a very long duration and unexpected wave heights in the far field (e.g. Omira et al., 2022). The onset of this tsunami was detected earlier than expected by tsunami propagation models, as the direct tsunami was preceded by a distinct, fast-travelling, moderate height tsunami that was clearly detected worldwide, arriving several hours before the main one (e.g. Carvajal et al., 2022; Zhou et al., 2023; Ho et al., 2023). This kind of feature, interpreted to result from the large pressure oscillation generated by the Lamb wave passing over the location, was first described by Harkrider and Press (1967) after the Krakatoa eruption and it is often called a meteotsunami (e.g. Denamiel et al., 2023). The main tsunami waves were observed on coastal tide gauges distributed throughout the world, although the largest values, with heights >3 m, were recorded off the coasts of California and Chile (Carvajal et al., 2022). The arrival time of these waves agrees well with the theoretical travel times of a free tsunami wave originating in the vicinity of the volcano at the time of the eruption and traveling at 198 ms^{-1}, the speed corresponding to the average depths of the Pacific waters. As shown by Ho et al. (2023), the differences in time and amplitude of both surges are af-

*Corresponding author: jdiaz@geo3bcn.csic.es

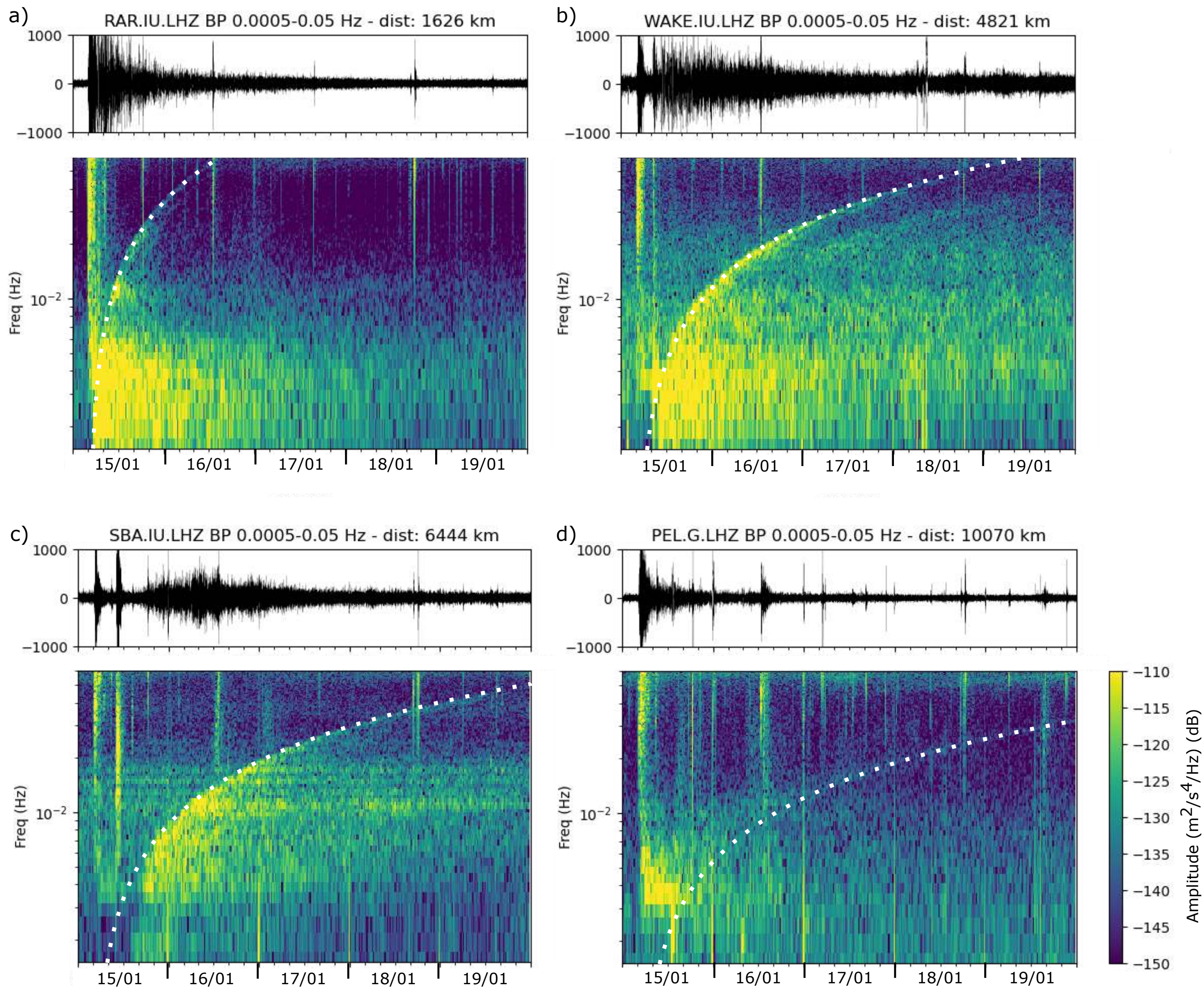

Figure 1 Examples of the long-duration dispersive arrivals detected at stations on the Pacific islands of Rarotonga (RAR) and Wake (WAKE), Antarctica (SBA), and Central Chile (PEL). Frequency is represented using a logarithmic scale. White dashed lines show the gravity dispersion curves.

fected by the bathymetry variations along their path. Zhou et al. (2023) noticed that the pressure disturbances produced by the Lamb wave (<200 Pa) are not sufficient to explain the relatively large amplitudes of the meteotsunami waves observed in some areas, particularly near the coast of Japan. They analyzed if this amplification could be related to the Proudman resonance, and concluded that it is better explained by nearshore amplification effects. However, Lynett et al. (2022) suggested that the air-pressure passing over the deep-water subduction zones in the Pacific triggered a Proudman resonance effect, with each major trench in the Pacific Basin generating a small tsunami. These multiple tsunamis could explain the persistent sea-level perturbations in the Pacific coasts.

The main phase of the eruptive process included four large explosions, observed in satellite data and generating seismic waves detected around the world. The main explosion, at 04:14 on January 15, 2022, was detected by global seismic networks, which assigned a magnitude of 5.8 to the event. This explosion resulted in the excitation of Earth normal modes, with the planet pulsing every 4.5 minutes for more than 4 hours (Diaz, 2022; Garza-Girón et al., 2023; Ringler et al., 2022). Broadband seismometers also recorded the successive passages of the Lamb waves, showing that the associated pressure variations were, even after traveling four times around the planet, strong enough to be detected in an instrument not specifically designed to detect them (Diaz, 2022).

In this contribution, seismic data recorded around the world are used to document another of the features that make post-eruption seismic records exceptional: the recording of surface gravity waves (SGW), in a frequency range between 5 and 50 mHz, which can be identified continuously in some places for time intervals up to five days. Although long-lived, dispersive SGW generated by cyclones have been reported in seismic data recorded on the Antactic ice shelves (e.g. Cathles et al., 2009), there are no previous examples to my knowledge of any signal being recorded continuously for such a long time interval all around the world. I show some representative examples of the signal, compare the seismic records with with hydroacoustic and deep-water pressure sensor data, analyze the differences between the seismic signal of the tsunami generated by the H-T eruption and the seismic records of large tsunamis, comment on the global distribution of the observations, and finally discuss the possible origins of this signal.

2 Seismic observations of tsunami-related dispersive signals

Data from low sampling channels from broadband seismic stations distributed all over the globe and integrated into the main worldwide large-scale seismic networks, including the Global Seismograph Network (Albuquerque Seismological Laboratory/USGS, 2014), IRIS/IDA seismic network (Scripps Institution of Oceanography, 1986), Geoscope (IPGP and EOST, 1982), and Geofon (GEOFON Data Centre, 1993), were retrieved, using the IRIS online services, to investigate the seismic record of the H-T tsunami. Data were merged into files of seven days of duration, from January 15 to 21, 2022, and transformed to the frequency-time domain using Obspy routines based on the classical FFT transform (Megies et al., 2011; Krischer et al., 2015). Spectrograms were calculated using a window length of 1800 s, with 80% overlap.

As stated above, I will focus on the long-duration dispersive signal that dominates the spectrograms in the 5-50 mHz band for time intervals ranging from one to five days. Fig. 1 shows the records of this signal at four representative stations located on Rarotonga and Wake Islands in the Pacific Ocean, Scott Base in Antarctica, and central Chile, covering distances between 1600 and 10000 km from H-T. The strong dispersive character of this feature, the wave onset propagation time, and the variable slope of the signal show that its origin is the main tsunami wave generated by the H-T eruption propagating across the ocean. To confirm this point, I have calculated the dispersion curves of a gravity wave assuming propagation in deep water. In this case,

$$v_p = \sqrt{\frac{g}{k}} = \frac{d}{t} \tag{1}$$

and

$$v_g = \frac{1}{2}\sqrt{\frac{g}{k}} \tag{2}$$

where g is gravity, k is the wavenumber, d is distance, t is propagation time, and v_g and v_p are group and phase velocities, respectively. Then,

$$k = \frac{g}{v_p^2} = \frac{g}{(2v_g)^2} = \frac{gt^2}{4d^2} \tag{3}$$

and, from the classical equation

$$\omega = \sqrt{gk} = 2\pi f \tag{4}$$

we can estimate frequency as a function of time for any given distance. White dashed lines in Fig. 1 show the resulting curves for each distance range, proving that this is the origin of the signal. The mismatches observed at the lower frequencies for distant sites can be explained by the deep water hypothesis, and do not affect to the interpretation of the signal. The identification of the first arrival of the dispersive curve is difficult since, on the one hand, the high energy Lamb wave, with frequencies below 5 mHz, arrives relatively close and, on the other hand, the excitation of the normal nodes on Earth generate a relatively large energy at 0.3 mHz for hours after the eruption (e.g. Diaz, 2022; Ringler et al., 2022).

The dispersive character of oceanic surface gravity waves (SGW) was first observed in the late 1950s by Munk and Snodgrass (1957), who analyzed the incoming swell at Guadalupe Island (Mexico) and showed that the wave trains had an increasing frequency. Broadband seismometers deployed on Antarctic ice shelves have provided multiple examples of days-long SGW generated by storms, as shown by Cathles et al. (2009), MacAyeal et al. (2006) or Lipovsky (2018). Recently, Hell et al. (2019) have proposed a method to use these data to verify the position of high wind speed areas over the Southern Ocean and Aster et al. (2021) have shown that the swell interaction with the Ross Ice shelf triggers small, near-front seismic signals.

SGW related to the Hunga-Tonga eruption have been observed by Le Bras et al. (2022) in the data recorded by four of the hydroacoustic sensors deployed in shallow waters by the International Monitoring System (IMS) network in the Pacific Ocean. In order to compare with the seismic records and confirm the common origin of the signals, I have recovered the data from the H11S1 instrument, located close to Wake Island, where seismic data is available. Additionally, I have recovered the data from the microbarometric sensor WAKE.IU.LDO, co-located with the seismic instrumentation. The spectrograms of the three sensors, shown at Fig. 2, have been calculated using the same parametrization in all the cases but are represented using adapted amplitude scales to better highlight the amplitude variations. As observed, the microbarograph (Fig. 2a) clearly records the passage of the Lamb waves traveling in opposite directions of the great arc (red and orange arrows) and no evidence of a tsunami-related signal is detected. The broad-band seismic data (Fig. 2b) is dominated in this frequency range by the tsunami-related dispersive wave. The arrival of the seismic waves, a few minutes after the H-T explosion, is observed at frequencies higher than 10 mHz. The first passage of the Lamb wave is detected as a low frequency signal preceding the arrival of the oceanic tsunami signal. For frequencies above 20 mHz, several teleseismic events can be identified, the most prominent corresponding to a M 6.1 earthquake with epicenter in Papua-Guinea on 16 January around 13:00.

The in-water hydroacoustic sensor (Fig. 2c) shows the dispersive gravity wave associated with the tsunami, visible between 8 and 50 mHz and clearly consistent with the seismic data. Le Bras et al. (2022) noted the presence of a secondary dispersive signal at this station, interpreted as an effect of the tsunami propagation though the Tonga-Kermadec trench. This signal is also clearly observed in the seismic data, which seems to provide the most complete record of the event at this location.

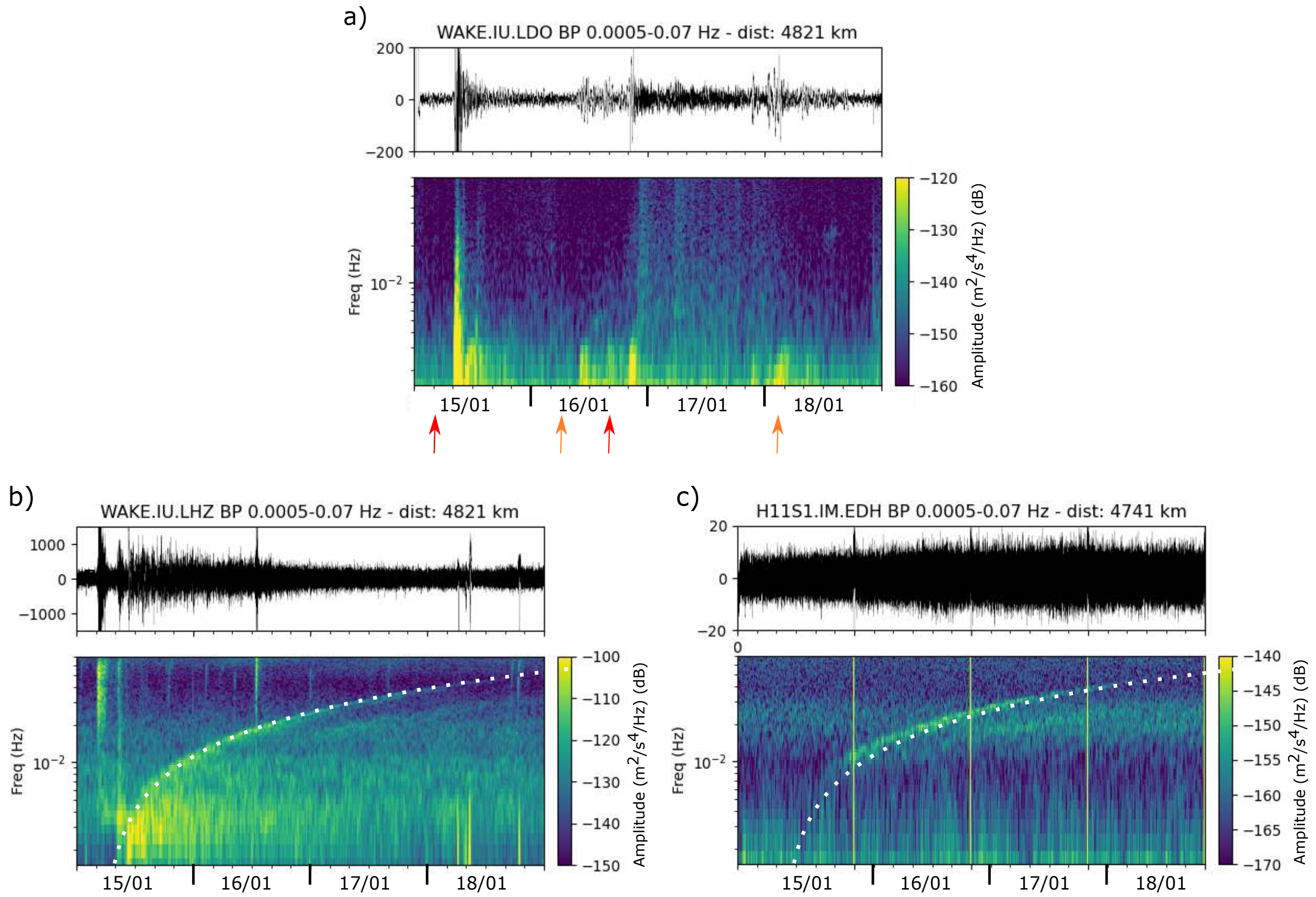

Figure 2 Waveforms and spectrograms for the microbarograph (a), broad-band station (b), and hydroacoustic sensor (c), located at Wake Island (North Pacific). The upper panels show the corresponding waveform, filtered between 0.5 and 70 mHz. The red and orange arrows in (a) show the arrival of Lamb waves. Dotted lines in (b) and (c) show the gravity wave arrival.

3 Uniqueness of the observation

The recording of tsunamis on near-shore seismic stations has been described previously (e.g., Yuan et al., 2005; Okal, 2007; Poplavskiy and Le Bras, 2013). However, the seismic recording of the oceanic gravity wave presented so far is limited to a few hours of duration following the tsunami arrival. There are not, to my knowledge, previous reports of dispersion curves related to oceanic gravity waves being recorded during several days by broad-band seismometers. To check the uniqueness of the event, I have recovered the seismic data recorded during the 5 days following the Chile 2010 M8.8, Tohoku 2011 M9.1, and Sumatra 2004 earthquakes, that resulted in three of the largest tsunamis recorded in the Pacific. Fig. 3 shows the spectrograms of the H-T event compared to those for these large earthquakes for stations located at Rarotonga (Cook Islands), Wake Island, and Eastern Island, all of them in the Pacific Ocean.

As noted, for large earthquakes the spectrograms in the 0.5-70 mHz range are dominated by arrival of the surface waves that circle the Earth every 3.5 hours, showing a decay on their frequency content. The amplitude of the waveform is two orders of magnitude larger for the earthquakes than for the H-T eruption, indicating that the seismic energy generated by H-T main eruptive episode was not exceptional. However, the long-lived dispersive oceanic gravity wave can only be identified for the H-T eruption, hence suggesting that this signal is not only related to the energy associated with the tsunami, but is probably boosted by a secondary mechanism.

4 Geographical distribution of the tsunami-related seismic signals

As commented above, I have retrieved the data for the vertical components of seismic stations of the global scale networks that distribute low sampling channels (LHZ, 1 sample per second). Data has been recovered for 134 locations covering Australia, Africa, the Americas, Europe, and a large number of islands in the Pacific and Indian oceans. The tsunami-associated gravity wave has been identified in 46 of these sites, 34% of the inspected sites, at distances ranging from 750 to 12500 km from H-T. Supplementary Figure S1 shows the waveforms and spectrograms of the stations with positive identifications of the signal, ordered accordingly to their distance.

As observed in Fig. 4, this feature has been identified for most of the stations located on islands in the Pacific basin and near the coasts surrounding this ocean

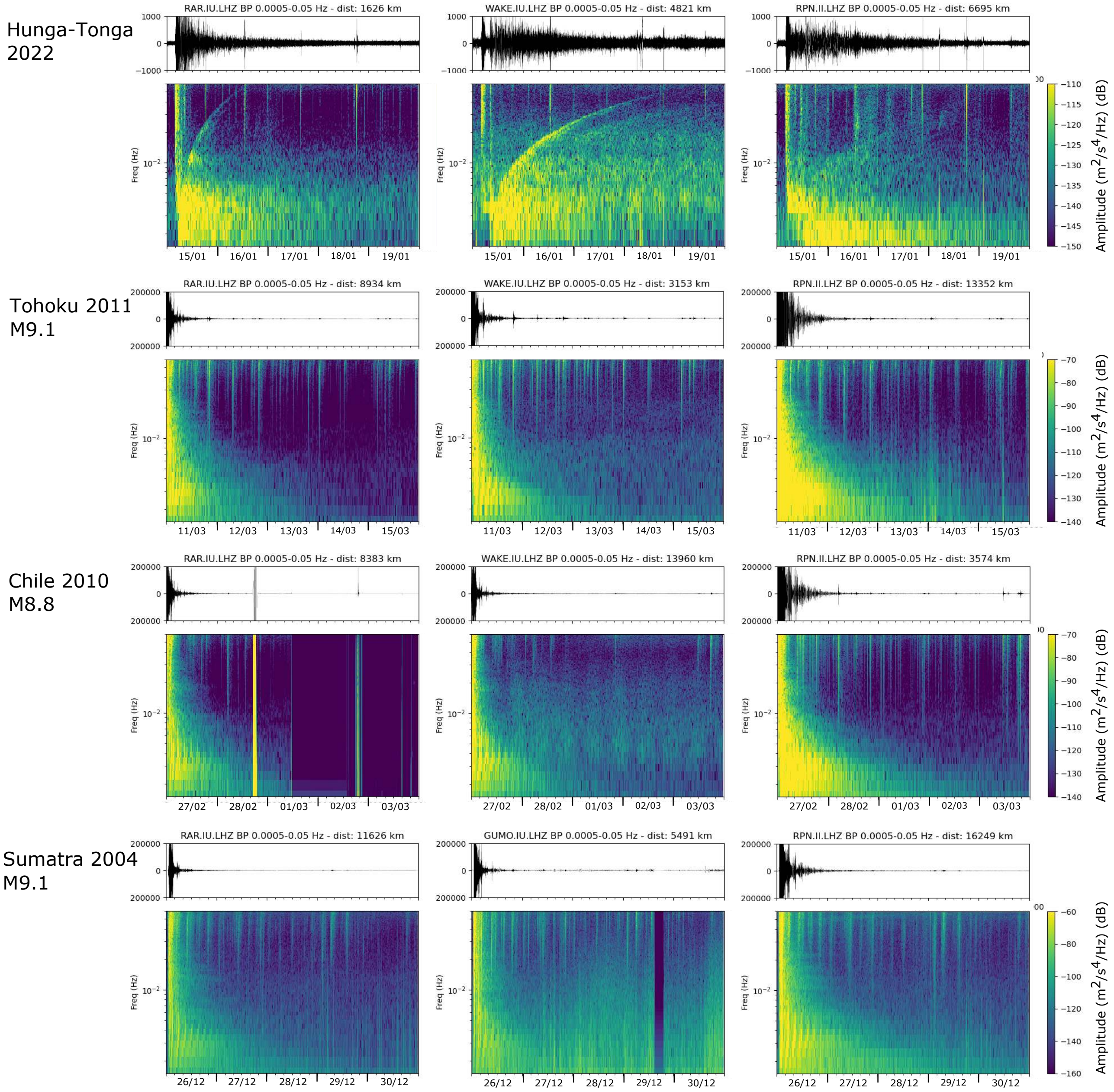

Figure 3 5-day long spectrograms after the H-T eruption at 3 sites in the Pacific Ocean, compared to records at the same sites after the Tohoku 2011 M9.1, Chile 2010 M8.8, and Sumatra 2004 M9.1 earthquakes. For the Sumatra event, WAKE records are not available and GUMO station is used instead.

(Japan, New Zealand, North, Central, and South America). Although some energy around 10 mHz is observed at times consistent with the gravity wave arrival, the two stations located on the Hawai'ian islands (KIP and POHA) show no evidence of the signal, suggesting that local conditions play a role in its detection. Fig. 5 shows the waveforms and the spectrograms at sites along a transect oriented approximately E-W across the SE Pacific Ocean (Rarotonga, Pitcairn and Eastern Islands), crossing the southern part of the Andes and reaching the Atlantic ocean at the South Georgia Islands. Although it is difficult to identify the tsunami-related signal in the filtered waveforms, the spectrograms clearly evidence the signal, which can be identified for several days at the most distant sites and is restricted to frequencies below 50 mHz. The figure also proves that the dispersive signal is not a local effect, but originates from the H-T eruption.

Many sites located along the Pacific coasts of North, Central, and South America detect the signal for intervals of two to four days after the first arrival, despite being located far from the coasts (Fig. 6a). It should be noted that the largest water heights reported by coastal tidal gauges correspond to sensors located in Chile and western North America (Carvajal et al., 2022). More surprisingly, stations located within the North American continent, in places like Tucson (Arizona), Albuquerque (New Mexico), and South Dakota show a low-energy dis-

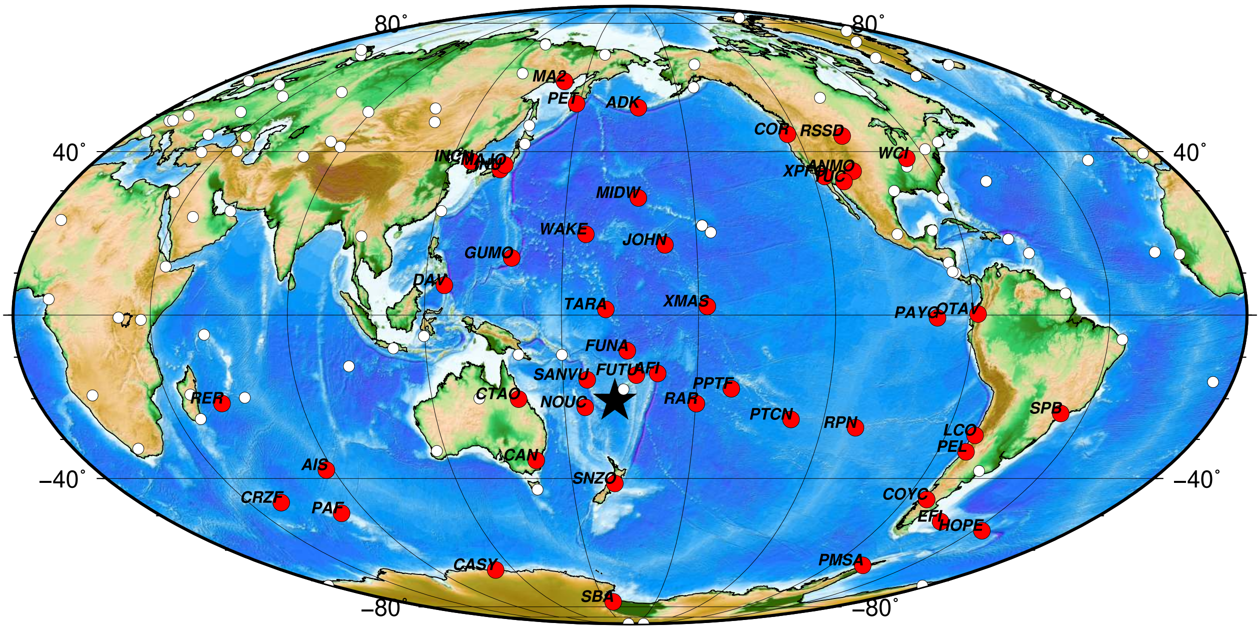

Figure 4 Map showing the locations where the tsunami-related dispersive signal has been identified (red dots). The black star shows the location of the H-T volcano and the white dots show the seismic stations where this signal has not been identified. Topography and bathymetry are from the ETOPO2 Gridded Globe Relief Data (National Geophysical Data Center, 2006).

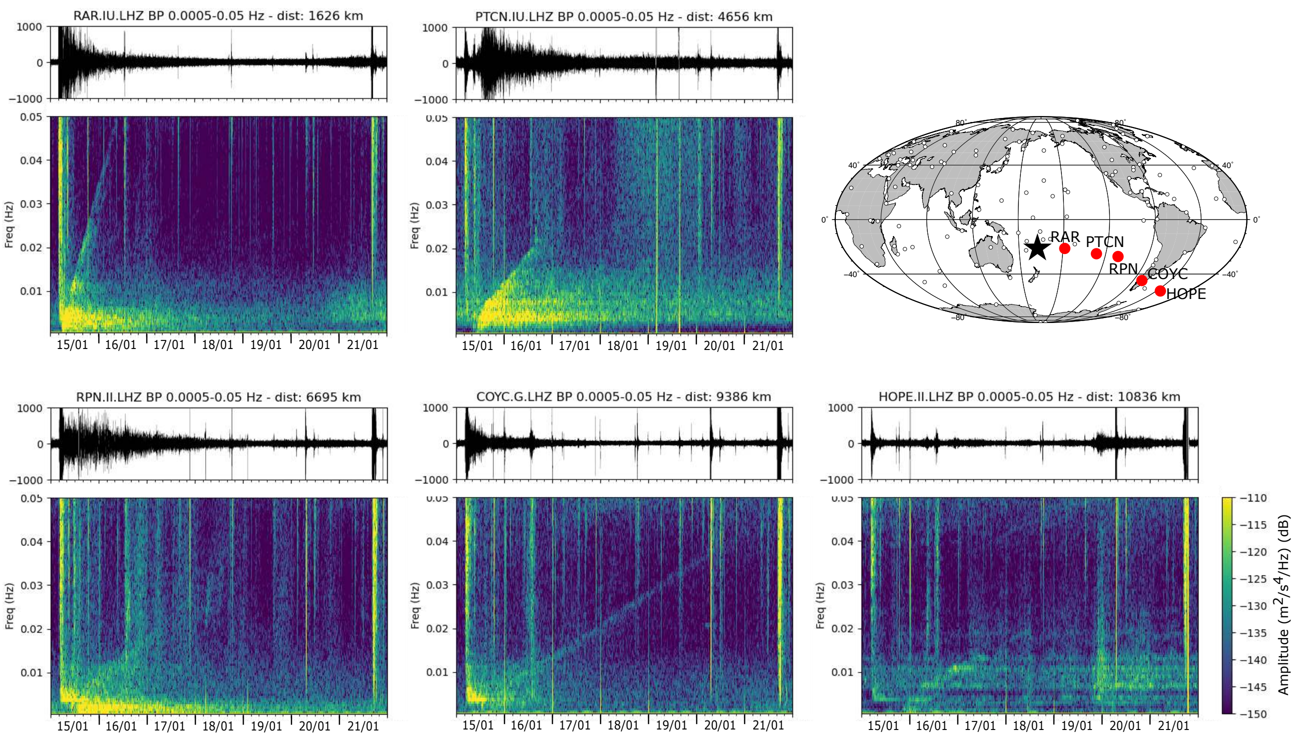

Figure 5 West-East transect across the south Pacific and Atlantic Ocean, showing gravity wave dispersion at distances ranging from 1600 to 10800 km.

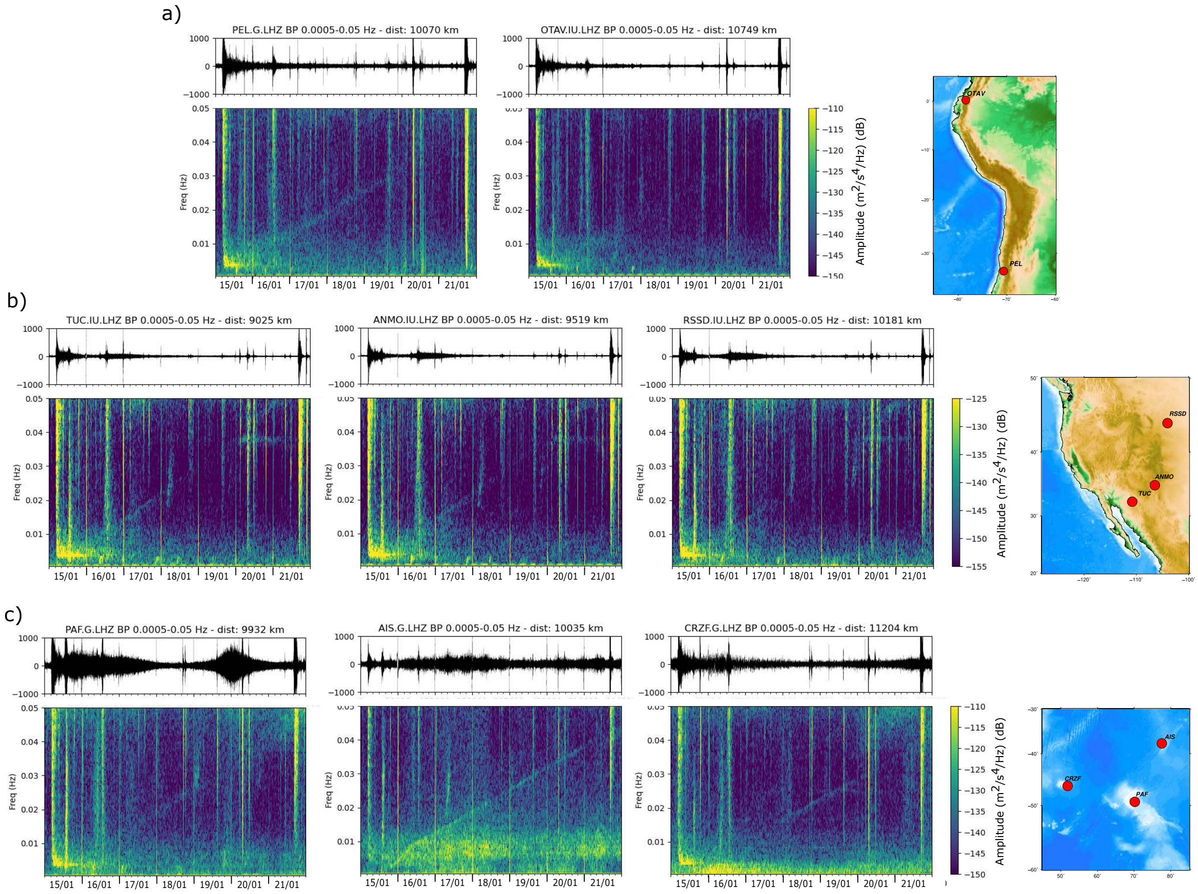

Figure 6 (a) Detection of the tsunami gravity wave at stations PEL and COYC, located in central and southern Chile. (b) Idem for stations located within the North America continent. (c) Idem for stations located in the Indian Ocean. The location of each station is shown in the inset maps

persive arrival for two to three days after the H-T eruption, consistent with the theoretical dispersion of the gravity wave generated by this eruption (Fig. 6b). Probably the most outstanding records of the tsunami-related gravity wave are obtained at the broad-band stations installed in small islands of the southern Indian Ocean, such as PAF in the Kerguelen Islands, CRZF in Ile de la Possesion, and AIS in Nouvelle Amsterdam Island, at distances around 10000 km from H-T. As observed in Fig. 6c, the AIS spectrogram shows the gravity wave arrivals during more than six days, disappearing only during January 21. This is the site where the dispersive signal can be identified for the longest time.

5 Discussion and Conclusions

Previous studies based on the analysis of sea level, atmospheric, and satellite data have documented the exceptional nature of the tsunami associated with the H-T eruption. Its salient features include high propagation speed, long duration, and unexpectedly large amplitudes measured in distant coastal areas, in particular in the Pacific coasts of North and South America (Carvajal et al., 2022). The tsunami records show two different arrivals, the first one coincident with the arrival of the Lamb wave and the second one starting with the arrival of the free tsunami wave. The arrival of the Lamb wave is marked by a clear onset in microbarographs, broadband seismic stations, and ocean-bottom pressure sensors, and coincides approximately with the onset times on the coastal tide gauges, which often show gradually increasing amplitudes over 2-4 hours. Near-surface hydroacoustic sensors in the IMS network do not detect the arrival of the precursory tsunami associated to the arrival of the Lamb wave (Le Bras et al., 2022), while deep-water pressure sensors record a clear pulse, doubling the amplitude of the atmospheric pressure signal (Matoza et al., 2022).

Omira et al. (2022) have proposed that these tsunami characteristics can be explained by a moving source generation mechanism that continuously pumps energy into the oceanic tsunami. The first water-height increase will correspond to the direct response of the ocean surface to the passage of the air-pressure disturbance, while the second arrival will correspond to the resonance between the ocean and the acoustic waves. According to their model, the interaction between acoustic and oceanic waves results in an air–water energy transfer that leads to an increase in the tsunami wave amplitude and explains the observed characteristics. The broad-band seismic records of these arrivals provide additional clues to their interpretation. As

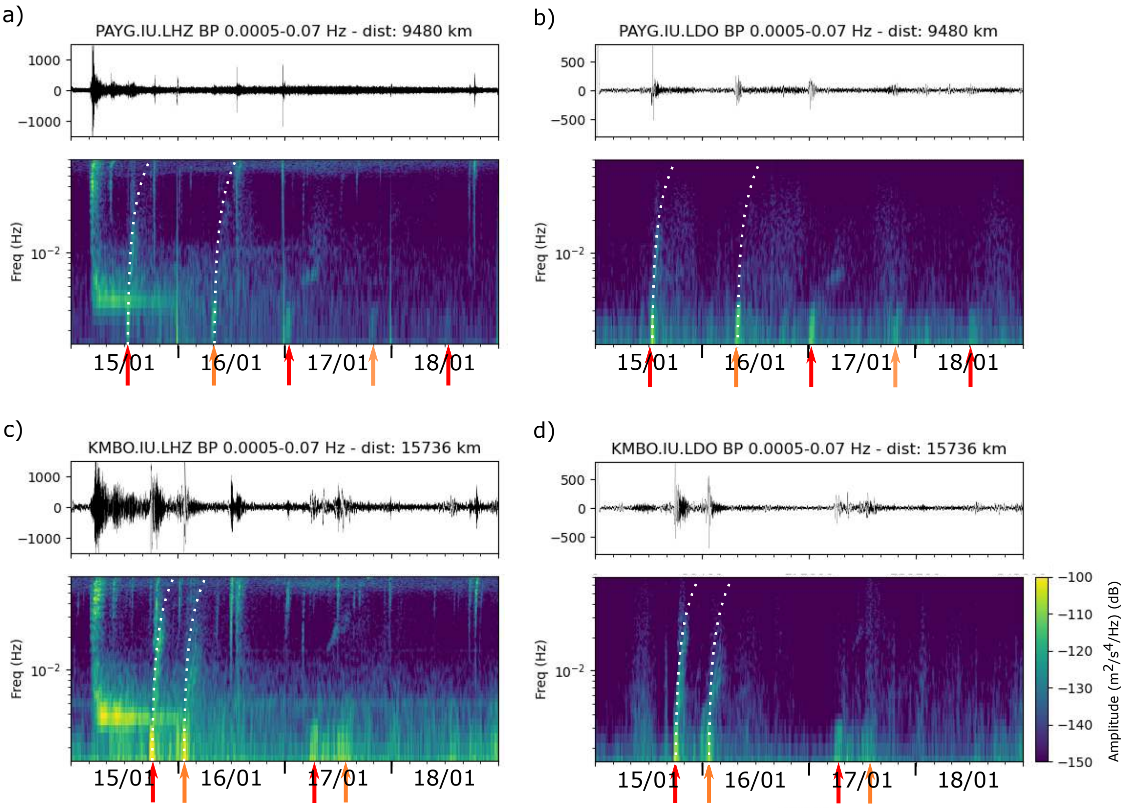

Figure 7 Seismic (a,c) and microbarometric (b,d) records at stations PAYG (a,b) and KMBO (c,d) located in the Galapagos Islands (Ecuador) and Nairobi (Kenya), respectively. Red and yellow arrows show the arrival of the successive passages of the Lamb waves following the two directions of the great arc. Dotted lines show the theoretical arrivals of a gravity wave generated at 200 km from the recording site.

shown in the previous sections, the tsunami-associated gravity wave has been seismically recorded for up to 5 days by a significant number of sites distributed within the islands and coasts of the Pacific and Indian Oceans, but also at some sites located hundreds of kilometres inland, particularly in North America. Oceanic gravity waves have been observed before using seismic instruments, mostly associated with the swell generated by distant storms. However, the global recording of long-lived dispersive waves after the H-T signal has to be considered as an exceptional feature, not observed during larger earthquake-generated tsunamis, such as the 2004 Sumatra or the 2011 Tohoku events. The most obvious difference between large earthquakes and the H-T eruption potentially affecting the tsunami generation is the highly energetic atmospheric Lamb wave generated by the H-T eruption. Therefore, it seems reasonable to relate the long duration dispersive signal observed in seismic data to a local interaction between the free oceanic tsunami and the arrival of the atmospheric pressure wave, consistently with the model presented by Omira et al. (2022). The large pressure variations detected in the ocean floor pressure sensors, but not in the shallow water hydroacoustic sensors, are also consistent with the proposed mechanism.

The inspection of seismic data at some of the stations, such as CMLA in the Azores Islands, SOK in Senegal, MBAR in Uganda, KMBO in Kenya, or PAYG in the Galapagos Islands, allows the identification of an additional dispersive signal immediately after the arrival of the Lamb wave that provides additional support for this interpretation (Fig. 7). This wave is also detected by the co-located microbarometric sensors (Fig. 7b and 7d), suggesting that it corresponds to an atmospheric perturbation. The pattern of this dispersive wave does not depend on the distance to H-T, as evidenced by the similar pattern observed at PAYG, located at a distance of 9500 km (Fig. 7a and 7b), and KMBO, at a distance of 15700 km (Fig. 7c and 7d). On the contrary, the arrival can be modeled by a local gravity wave, generated at distances of approximately 100-200 km from the recording site. This wave seems to be generated locally by the resonance effect proposed by Omira et al. (2022), hence evidencing the effects of the bidirectional interaction between the atmosphere and the oceans. It is important to note that this local wave can be identified for at least the first two passages of the Lamb wave, which once again highlights the high energy and low attenuation of this wave. However, developing a detailed physical model of the proposed interaction is needed before accepting or discarding this tentative hypothesis.

The seismic record, of more than four days duration, of a dispersive wave in the 0.5-50 mHz band in broadband stations distributed throughout the world is an unusual feature that clearly deserves attention. The origin of this wave is related to the tsunami generated by the H-T eruption and its properties are consistent with the hypothesis of a local resonance between the free tsunami and the acoustic waves, which has been proposed to explain the unusual characteristics of the tsunami. This is further supported by the observation, in seismic and microbarometric data, of locally generated gravity waves, interpreted as a nice example of oceanic, atmospheric, and solid Earth interaction. The seismic records presented here provide a new proof of the exceptional nature of the H-T eruption and are a further confirmation that broadband seismic records can contribute, beyond their usual use in seismology, to the analysis of other sources of vibration recorded in very different zones of the seismic spectrum.

Acknowledgements

I want to acknowledge all the teams involved in the design, installation, and maintenance of broadband seismic networks around the world, which provide the essential data to carry out this type of study. I also want to thank ORFEUS EIDA (http://www.orfeus-eu.org/data/eida/) and FDSN (https://www.fdsn.org/services/) data services for providing easy access to seismic data. The manuscript has been enriched by fruitful discussions with different colleagues, and in particular with Drs. M. Ruiz and M. Schimmel. The contructive reviews of Brad Lipovsky, and an anonymous reviewer, as well as the additional comments from the editor Lise Retailleau, have clearly improved the original manuscript. This work has benefited from the infrastructure of the GEO3BCN-CSIC LabSis laboratory (http://labsis.geo3bcn.csic.es).

6 Data and code availability

All the seismic data used in this contribution are publicly available using the ORFEUS EIDA (http://www.orfeus-eu.org/data/eida/) and FDSN (https://www.fdsn.org/services/) data services. The seismic networks used are: IU (Albuquerque Seismological Laboratory/USGS, 2014), II (Scripps Institution of Oceanography, 1986), G (IPGP and EOST, 1982), and GE (GEOFON Data Centre, 1993).

The instrument response has been removed from the data using the standard procedures included in the Obspy package. Spectra and spectrograms have been calculated using SAC (Goldstein et al., 2003) and Obspy (Krischer et al., 2015) routines using standard parametrizations.

7 Competing interests

The author declares no competing interests.

References

Albuquerque Seismological Laboratory/USGS. Global Seismograph Network – GSN-IRIS/USGS, 2014. doi: 10.7914/SN/IU.

Amores, A., Monserrat, S., Marcos, M., Argüeso, D., Villalonga, J., Jordà, G., and Gomis, D. Numerical Simulation of Atmospheric Lamb Waves Generated by the 2022 Hunga-Tonga Volcanic Eruption. *Geophysical Research Letters*, 49(6), Mar. 2022. doi: 10.1029/2022gl098240.

Astafyeva, E., Maletckii, B., Mikesell, T. D., Munaibari, E., Ravanelli, M., Coisson, P., Manta, F., and Rolland, L. The 15 January 2022 Hunga Tonga Eruption History as Inferred From Ionospheric Observations. *Geophysical Research Letters*, 49(10), May 2022. doi: 10.1029/2022gl098827.

Aster, R. C., Lipovsky, B. P., Cole, H. M., Bromirski, P. D., Gerstoft, P., Nyblade, A., Wiens, D. A., and Stephen, R. Swell-Triggered Seismicity at the Near-Front Damage Zone of the Ross Ice Shelf. *Seismological Research Letters*, 92(5):2768–2792, Apr. 2021. doi: 10.1785/0220200478.

Carr, J. L., Horváth, Á., Wu, D. L., and Friberg, M. D. Stereo Plume Height and Motion Retrievals for the Record-Setting Hunga Tonga-Hunga Ha'apai Eruption of 15 January 2022. *Geophysical Research Letters*, 49(9), Apr. 2022. doi: 10.1029/2022gl098131.

Carvajal, M., Sepúlveda, I., Gubler, A., and Garreaud, R. Worldwide Signature of the 2022 Tonga Volcanic Tsunami. *Geophysical Research Letters*, 49(6), Mar. 2022. doi: 10.1029/2022gl098153.

Cathles, L. M., Okal, E. A., and MacAyeal, D. R. Seismic observations of sea swell on the floating Ross Ice Shelf, Antarctica. *Journal of Geophysical Research: Earth Surface*, 114(F2), May 2009. doi: 10.1029/2007jf000934.

Denamiel, C., Vasylkevych, S., Žagar, N., Zemunik, P., and Vilibić, I. Destructive Potential of Planetary Meteotsunami Waves beyond the Hunga Tonga–Hunga Ha'apai Volcano Eruption. *Bulletin of the American Meteorological Society*, 104(1):E178–E191, Jan. 2023. doi: 10.1175/bams-d-22-0164.1.

Diaz, J. Atmosphere-solid earth coupling signals generated by the 15 January 2022 Hunga-Tonga eruption. *Communications Earth & Environment*, 3(1), Nov. 2022. doi: 10.1038/s43247-022-00616-1.

Garza-Girón, R., Lay, T., Pollitz, F., Kanamori, H., and Rivera, L. Solid Earth–atmosphere interaction forces during the 15 January 2022 Tonga eruption. *Science Advances*, 9(2), Jan. 2023. doi: 10.1126/sciadv.add4931.

GEOFON Data Centre. GEOFON Seismic Network, 1993. doi: 10.14470/TR560404.

Goldstein, P., Dodge, D., Firpo, M., and Minner, L. 85.5 SAC2000: Signal processing and analysis tools for seismologists and engineers. In *International Geophysics*, pages 1613–1614. Elsevier, 2003. doi: 10.1016/s0074-6142(03)80284-x.

Harkrider, D. and Press, F. The Krakatoa Air-Sea Waves: an Example of Pulse Propagation in Coupled Systems. *Geophysical Journal International*, 13(1-3):149–159, July 1967. doi: 10.1111/j.1365-246x.1967.tb02150.x.

Hell, M. C., Cornelle, B. D., Gille, S. T., Miller, A. J., and Bromirski, P. D. Identifying Ocean Swell Generation Events from Ross Ice Shelf Seismic Data. *Journal of Atmospheric and Oceanic Technology*, 36(11):2171–2189, Nov. 2019. doi: 10.1175/jtech-d-19-0093.1.

Ho, T.-C., Mori, N., and Yamada, M. Ocean gravity waves generated by the meteotsunami at the Japan Trench following the 2022 Tonga volcanic eruption. *Earth, Planets and Space*, 75(1), Feb. 2023. doi: 10.1186/s40623-023-01775-x.

IPGP and EOST. GEOSCOPE, French global network of broad band seismic stations, 1982. doi: 10.18715/GEOSCOPE.G.

Krischer, L., Megies, T., Barsch, R., Beyreuther, M., Lecocq, T., Caudron, C., and Wassermann, J. ObsPy: a bridge for seismology into the scientific Python ecosystem. *Computational Science & Discovery*, 8(1):014003, May 2015. doi: 10.1088/1749-4699/8/1/014003.

Le Bras, R. J., Zampolli, M., Metz, D., Haralabus, G., Bittner, P., Villarroel, M., Matsumoto, H., Graham, G., and Özel, N. M. The Hunga Tonga–Hunga Ha'apai Eruption of 15 January 2022: Observations on the International Monitoring System (IMS) Hydroacoustic Stations and Synergy with Seismic and Infrasound Sensors. *Seismological Research Letters*, 94(2A):578–588, Oct. 2022. doi: 10.1785/0220220240.

Lipovsky, B. P. Ice Shelf Rift Propagation and the Mechanics of Wave-Induced Fracture. *Journal of Geophysical Research: Oceans*, 123(6):4014–4033, June 2018. doi: 10.1029/2017jc013664.

Lynett, P., McCann, M., Zhou, Z., Renteria, W., Borrero, J., Greer, D., Fa'anunu, O., Bosserelle, C., Jaffe, B., Selle, S. L., Ritchie, A., Snyder, A., Nasr, B., Bott, J., Graehl, N., Synolakis, C., Ebrahimi, B., and Cinar, G. E. Diverse tsunamigenesis triggered by the Hunga Tonga-Hunga Ha'apai eruption. *Nature*, 609(7928):728–733, Aug. 2022. doi: 10.1038/s41586-022-05170-6.

MacAyeal, D. R., Okal, E. A., Aster, R. C., Bassis, J. N., Brunt, K. M., Cathles, L. M., Drucker, R., Fricker, H. A., Kim, Y.-J., Martin, S., Okal, M. H., Sergienko, O. V., Sponsler, M. P., and Thom, J. E. Transoceanic wave propagation links iceberg calving margins of Antarctica with storms in tropics and Northern Hemisphere. *Geophysical Research Letters*, 33(17), Sept. 2006. doi: 10.1029/2006gl027235.

Matoza, R. S., Fee, D., Assink, J. D., Iezzi, A. M., Green, D. N., Kim, K., Toney, L., Lecocq, T., Krishnamoorthy, S., Lalande, J.-M., Nishida, K., Gee, K. L., Haney, M. M., Ortiz, H. D., Brissaud, Q., Martire, L., Rolland, L., Vergados, P., Nippress, A., Park, J., Shani-Kadmiel, S., Witsil, A., Arrowsmith, S., Caudron, C., Watada, S., Perttu, A. B., Taisne, B., Mialle, P., Pichon, A. L., Vergoz, J., Hupe, P., Blom, P. S., Waxler, R., Angelis, S. D., Snively, J. B., Ringler, A. T., Anthony, R. E., Jolly, A. D., Kilgour, G., Averbuch, G., Ripepe, M., Ichihara, M., Arciniega-Ceballos, A., Astafyeva, E., Ceranna, L., Cevuard, S., Che, I.-Y., Negri, R. D., Ebeling, C. W., Evers, L. G., Franco-Marin, L. E., Gabrielson, T. B., Hafner, K., Harrison, R. G., Komjathy, A., Lacanna, G., Lyons, J., Macpherson, K. A., Marchetti, E., McKee, K. F., Mellors, R. J., Mendo-Pérez, G., Mikesell, T. D., Munaibari, E., Oyola-Merced, M., Park, I., Pilger, C., Ramos, C., Ruiz, M. C., Sabatini, R., Schwaiger, H. F., Tailpied, D., Talmadge, C., Vidot, J., Webster, J., and Wilson, D. C. Atmospheric waves and global seismoacoustic observations of the January 2022 Hunga eruption, Tonga. *Science*, 377(6601): 95–100, July 2022. doi: 10.1126/science.abo7063.

Megies, T., Beyreuther, M., Barsch, R., Krischer, L., and Wassermann, J. ObsPy - what can it do for data centers and observatories? *Annals of Geophysics*, 54, 2011. doi: 10.4401/ag-4838.

Munk, W. and Snodgrass, F. Measurements of southern swell at Guadalupe Island. *Deep Sea Research (1953)*, 4:272–286, Jan. 1957. doi: 10.1016/0146-6313(56)90061-2.

National Geophysical Data Center. 2-minute Gridded Global Relief Data (ETOPO2) v2, 2006.

Okal, E. A. Seismic Records of the 2004 Sumatra and Other Tsunamis: A Quantitative Study. In *Pageoph Topical Volumes*, pages 325–353. Birkhäuser Basel, 2007. doi: 10.1007/978-3-7643-8364-0_4.

Omira, R., Ramalho, R. S., Kim, J., González, P. J., Kadri, U., Miranda, J. M., Carrilho, F., and Baptista, M. A. Global Tonga tsunami explained by a fast-moving atmospheric source. *Nature*, 609(7928):734–740, June 2022. doi: 10.1038/s41586-022-04926-4.

Poplavskiy, A. S. and Le Bras, R. J. Recordings of Long-Period Fluctuations Associated with the Passage of Three Distinct Tsunamis at Broadband Seismometers Made at the International Monitoring System (IMS) Hydroacoustic T-station H06 (Socorro Island, Mexico). *Seismological Research Letters*, 84(4):567–578, July 2013. doi: 10.1785/0220120116.

Ringler, A. T., Anthony, R. E., Aster, R. C., Taira, T., Shiro, B. R., Wilson, D. C., Angelis, S. D., Ebeling, C., Haney, M., Matoza, R. S., and Ortiz, H. D. The global seismographic network reveals atmospherically coupled normal modes excited by the 2022 Hunga Tonga eruption. *Geophysical Journal International*, 232(3):2160–2174, July 2022. doi: 10.1093/gji/ggac284.

Scripps Institution of Oceanography. Global Seismograph Network – IRIS/IDA, 1986. doi: 10.7914/SN/II.

Vergoz, J., Hupe, P., Listowski, C., Pichon, A. L., Garcés, M., Marchetti, E., Labazuy, P., Ceranna, L., Pilger, C., Gaebler, P., Näsholm, S., Brissaud, Q., Poli, P., Shapiro, N., Negri, R. D., and Mialle, P. IMS observations of infrasound and acoustic-gravity waves produced by the January 2022 volcanic eruption of Hunga, Tonga: A global analysis. *Earth and Planetary Science Letters*, 591:117639, Aug. 2022. doi: 10.1016/j.epsl.2022.117639.

Wright, C. J., Hindley, N. P., Alexander, M. J., Barlow, M., Hoffmann, L., Mitchell, C. N., Prata, F., Bouillon, M., Carstens, J., Clerbaux, C., Osprey, S. M., Powell, N., Randall, C. E., and Yue, J. Surface-to-space atmospheric waves from Hunga Tonga–Hunga Ha'apai eruption. *Nature*, 609(7928):741–746, June 2022. doi: 10.1038/s41586-022-05012-5.

Yuan, X., Kind, R., and Pedersen, H. A. Seismic monitoring of the Indian Ocean tsunami. *Geophysical Research Letters*, 32(15), Aug. 2005. doi: 10.1029/2005gl023464.

Zhou, Y., Niu, X., Liu, H., Zhao, G., and Ye, X. Tsunami waves induced by the atmospheric pressure disturbance originating from the 2022 volcanic eruption in Tonga. *Applied Ocean Research*, 130: 103447, Jan. 2023. doi: 10.1016/j.apor.2022.103447.

doi:10.26443/seismica.v2i2.1030

SEISMICA

Optimal Network Design for Microseismic Monitoring in Urban Areas - A Case Study in Munich, Germany

Sabrina Keil * [1], **Joachim Wassermann** [1], **Tobias Megies** [1], **Toni Kraft** [2]

[1]Ludwig-Maximilians-Universität München, Germany, [2]Swiss Seismological Service, ETH-Zurich, Switzerland

Author contributions: *Software*: T. Megies, T. Kraft. *Formal Analysis*: S. Keil. *Writing - original draft*: S. Keil. *Writing - Review & Editing*: J. Wassermann, T. Megies, T. Kraft. *Visualization*: S. Keil. *Supervision*: J. Wassermann.

Abstract Well-designed monitoring networks are crucial for obtaining precise locations, magnitudes and source parameters, both for natural and induced microearthquakes. The performance of a seismic network depends on many factors, including network geometry, signal-to-noise ratio (SNR) at the seismic station, instrumentation and sampling rate. Therefore, designing a high-quality monitoring network in an urban environment is challenging due to the high level of anthropogenic noise and dense building infrastructure, which can impose geometrical limitations and elevated construction costs for sensor siting. To address these challenges, we apply a numerical optimization approach to design a microseismic surveillance network for induced earthquakes in the metropolitan area of Munich (Germany), where several geothermal plants exploit a deep hydrothermal reservoir. First of all, we develop a detailed noise model for the city of Munich, to capture the heterogeneous noise conditions. Then, we calculate the expected location precision for a randomly chosen network geometry from the body-wave amplitudes and travel times of a synthetic earthquake catalog considering the modeled local noise level at each network station. In the next step, to find the optimum network configuration, we use a simulated annealing approach in order to minimize the error ellipsoid volume of the linearized earthquake location problem. The results indicate that a surface station network cannot reach the required location precision (0.5 km in epicentre and 2 km in source depth) and detection capability (magnitude of completeness M_c = 1.0) due to the city's high seismic noise level. In order to reach this goal, borehole stations need to be added to increase the SNR of the microearthquake recordings, the accuracy of their body-wave arrival times and source parameters. The findings help to better quantify the seismic monitoring requirements for a safe operation of deep geothermal projects in urban areas.

Production Editor:
Gareth Funning
Handling Editor:
Yen Joe Tan
Copy & Layout Editor:
Théa Ragon

Signed reviewer(s):
Anthony Lomax

Received:
June 5, 2023
Accepted:
October 5, 2023
Published:
October 18, 2023

1 Introduction

The main purpose of seismic networks is to determine earthquake locations and magnitudes, which is important for earthquake characterization, hazard assessment and emergency response both for natural and induced seismicity (e.g., Havskov et al., 2012; Lomax et al., 2009). Specifically, induced seismicity caused by geothermal energy production is a growing concern, since the number of geothermal projects is raising in search of carbon-free heat and electricity generation (Hirschberg et al., 2014; Lund and Toth, 2021). In most cases the induced events have small magnitudes ($M_L <$ 2) and are not felt by the local population (Evans et al., 2012). However, examples like the Deep Heat Mining Project in Basel, Switzerland (Häring et al., 2008), and geothermal projects near Strasbourg, France (Schmittbuhl et al., 2021), where induced events with magnitudes $M_L > 3$ were recorded, highlight the importance of managing the induced seismicity risk. Consequently, a good monitoring network is a necessary component of the risk governance strategy to detect and locate small magnitude earthquakes, which enable the functioning of magnitude-based traffic light systems (Kraft et al., 2020). The precision of earthquake location depends on several factors, such as the distribution of seismic stations, detection of seismic waves and the accuracy of their observed and calculated arrival times (e.g., Bondár et al., 2004; Havskov et al., 2012). However, low-SNR recordings hamper the detection of small magnitude events and lead to high location uncertainties, which result in a poor performance of the monitoring network (e.g., Bormann and Wielandt, 2013). This is especially an issue in urban areas where often high seismic noise levels are encountered. Even though, well-designed monitoring networks are fundamental to allow the detection of weak seismic signals, seismic network planning is still mainly performed as a manual task based on simple design rules, which may fail in complex settings. Several different approaches have been proposed for the improvement of seismic networks including 1) the computation of the expected location errors and lowest detectable magnitude (Stabile et al., 2013; De Landro et al., 2020), 2) seismic network evaluation through simulation (e.g., D'Alessandro et al., 2011; Mahani et al., 2016), 3) correction of teleseismic travel times (e.g., Myers and Schultz, 2000), and 4) implementation of the D-criterion to identify an optimal seismic network configuration to decrease the location error (e.g., Steinberg

*Corresponding author: skeil@geophysik.uni-muenchen.de

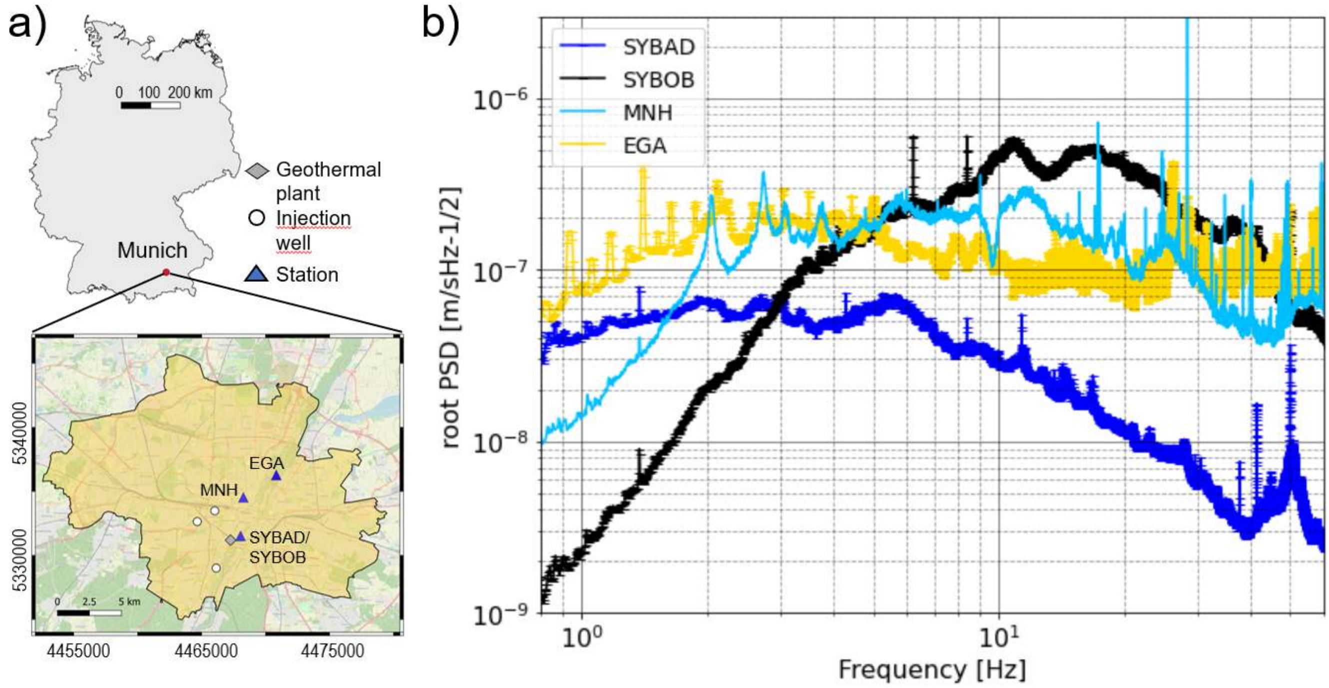

Figure 1 a) The upper map shows an overview of Germany with the location of Munich marked. The lower map shows an overview of the Munich city with the geothermal power plant at Schäftlarnstraße and its three injection wells. The locations of several seismic stations in Munich are marked. SYBAD corresponds to a 180m-deep borehole station and SYBOB is its overlying surface station. MNH is a permanent surface station and EGA was temporarily installed within a park area. At SYBOB a 4.5 Hz geophone is installed, at MNH a Mark L4-3D 1 Hz seismometer, at EGA a Trillium Compact 120s seismometer, and at SYBAD a Trillium Compact PH 20s seismometer. The coordinate system is Gauss-Krüger (GK4). b) Root Power spectral density (PSD) plots of data recorded at the seismic stations marked in a). The PSDs were computed from the vertical component for one day of data.

and Rabinowitz, 2003; Kijko, 1977). In the last case, the optimization problem can be solved using genetic algorithm techniques (e.g., Bartal et al., 2000), simulated annealing (e.g., Hardt and Scherbaum, 1994; Kraft et al., 2013), or Bayesian techniques (e.g., Coles and Curtis, 2011).

In this study we are applying the method of Kraft et al. (2013), which builds on the simulated annealing approach proposed by Hardt and Scherbaum (1994). This approach allows the optimization of seismic networks in complex settings, taking into account user-specified velocity models and heterogeneous noise conditions, as well as already existing monitoring stations. The program returns expected location uncertainties and detection thresholds of the resulting network.

We apply this method to the metropolitan area of Munich (Fig. 1 a), where currently 17 deep geothermal power plants operate (Agemar et al., 2014). This includes the geothermal project in Schäftlarnstraße (SLS), which is located in Munich's inner-city with a total of six deep wells (3 production, 3 re-injection) and a footprint of several square kilometers (Lentsch and Schweingruber, 2022). Since induced earthquakes were observed at surrounding geothermal power plants with magnitudes up to 2.4 (Megies and Wassermann, 2014; Seithel et al., 2019), the induced seismicity risk needs to be considered also at this recently realized project, which rises the requirement for a high quality monitoring network. The monitoring network for the geothermal power plants south of Munich was already optimized during the MAGS2 project (Megies and Wassermann, 2017), however, the inner-city project SLS had not been constructed at that time.

Since the number of geothermal projects in Germany is growing and consequently the risk of induced seismicity increases, Baisch et al. (2012) proposed a number of seismic monitoring recommendations for induced seismicity for the German Research College Physics of the Earth (FKPE). They recommend a monitoring network that is able to reliably detect and locate all earthquakes with magnitudes $M_L \geq 1$ with epicentral uncertainties of less than 500 m and vertical uncertainties of less than 2 km. These thresholds should be reached in an area of 5 km surrounding the target areas of the geothermal project. For the following quality assessment of the monitoring network in the Munich area, we are taking these recommendations into account.

First of all, we construct a detailed model of anthropogenic noise in the metropolitan region of Munich to capture its heterogeneous noise conditions. In the next step the quality of the existing monitoring network is evaluated according to the FKPE recommendations. Afterwards, a number of numerical network optimization runs are performed that test how the FKPE recommendations can be met by adding new surface and boreholes stations to the existing network.

2 Methodology

For the network optimization, we use a simulated annealing code initially developed by Hardt and Scherbaum (1994) that was substantially extended by Kraft et al. (2013) (hereafter referred to as NetOpt3D). Due to license issues, NetOpt3D was recently rewritten by Antuens et al. (2023) using open software libraries. For the current analysis, the python wrapper pyNetOpt3D (Megies et al., 2023) was built around the binaries of Antuens et al. (2023) to handle the input and output of the optimization code more easily. In the following, we briefly describe the concept of NetOpt3D and pyNetOpt3D.

NetOpt3D finds the D-optimal design by minimizing the volume of the error ellipsoid of the linearized earthquake location problem (D-criterion, e.g., Kijko, 1977) using a simulated annealing approach (Kirkpatrick et al., 1983). The simulated annealing parameters (e.g. starting temperature, minimum temperature, cooling schedule, maximum number of temperature steps, temperature reduction by step, and trials per step) were fine-tuned by trial and error in order to achieve a slow and smooth convergence of the solution to the global minimum. In order to solve the optimization problem the program computes traveltimes of seismic body waves using the finite difference ray tracer of Podvin and Lecomte (1991) and a user-defined velocity model. Furthermore, to evaluate the detectability of an event at the seismic stations body wave amplitudes are calculated based on earthquake source processes and wave propagation effects. Path effects are only treated in an approximate way by geometrical spreading, constant attenuation and free-surface amplification. The Brune model (Brune, 1970) is implemented as seismic source. The SNR is defined as the ratio of the synthetic body wave amplitude and the observed or estimated long-term root-mean-squared ground velocity at the station. We choose a SNR of 5 as the threshold for an earthquake to be observed at a certain station. In general a SNR ≥ 3 is considered being sufficient to reliably detect a seismic phase onset in a seismogram (e.g., Hardt and Scherbaum, 1994; Baisch et al., 2012). However, we chose a more conservative threshold as the estimated signal amplitude in our optimization approach corresponds to the maximum expected amplitude of the considered body wave at the recording station, which may be significantly larger than the amplitude of the phase onset (Kraft et al., 2013). We utilize the estimated SNR of a seismic phase at a station to calculate the expected uncertainty of the phase's onset time following the approach of Aki (1976) based on information theory (Shannon, 1948). According to Shannon (1948) a simple relation for the estimation of the information content of a signal exists:

$$WTlog_2 \frac{S^2 + N^2}{N^2} \tag{1}$$

where S^2 and N^2 represents the power of signal and noise, respectively, and T is the duration of the time series. The signal bandwidth W is approximated by max(fc, fmax). Here fc represents the Brune corner frequency of the event, and fmax corresponds to the high-frequency band limitation of the radiated field, as estimated from the attenuation model of Edwards et al. (2011) for Switzerland. More details about the NetOpt3D program, including the annealing schedule and the calculation of body wave traveltimes and amplitudes are given in Kraft et al. (2013).

In its current form, NetOpt3D is lacking usability and it is time consuming to set up new optimization problems. Input files (e.g. velocity models, synthetic earthquake catalogs) have to be set up manually in fixed legacy ASCII formats defined by the underlying C codes and a large number of helper programs (e.g. Linux shell scripts) are used for preparational steps and for analysis and visualization of results. Therefore, the consistent and easy-to-use Python Application Programming Interface (API) pyNetOpt3D was developed that internally uses NetOpt3D C codes but hides all unwieldy steps from the user. It enables the start of a complete optimization run with a single, short Python script using the newly developed API. All coordinate conversions from global geographic coordinates (WGS84) to local geodetic coordinates (e.g. UTM, Gauß-Krüger, Swiss Grid, ...) and vice versa are handled automatically. Functionalities to calculate convex hulls, buffers and equistant station grids are included. It also enhances reproducibility by providing (de)serialization of a full optimization run including all input data and results into a single file. Furthermore, pyNetOpt3D provides command line tools to quickly plot optimization results from a serialized file on disk.

In order for the NetOpt3D program to perform the optimization, a number of user-specified input data is required, which will be discussed in detail in the next sections.

3 Ambient Noise Analysis

The detectability of an event at a specific station depends on the amplitude of the earthquake signal and the noise level at the site. Therefore, an estimate of the background noise at the existing stations and the potential new network sites is required. First of all, we investigate the frequency content of the seismic noise by computing power spectral densities (PSD) at several stations located in the Munich city (Fig. 1). The surface station SYBOB[1] clearly shows higher PSD values for frequencies above 3 Hz compared to the underlying 180m-deep borehole station SYBAD. The highest power at SYBOB is observed between 10-20 Hz, while the PSD values at SYBAD decrease for frequencies above 6 Hz. The PSD values of the surface station MNH are high for frequencies larger than 2 Hz. Above 5 Hz the temporary installed station EGA displays PSD values lower than SYBOB and MNH, which can be explained by the installation within a park area. From these observations it can be inferred that the anthropogenic noise sources (e.g. trains, vehicles, construction work, industrial operation) influence the noise amplitudes at high frequencies (>1 Hz), which is consistent with findings of other

[1]Note that at SYBOB a 4.5 Hz geophone is installed, therefore the data should not be interpreted for frequencies much lower than 4.5 Hz.

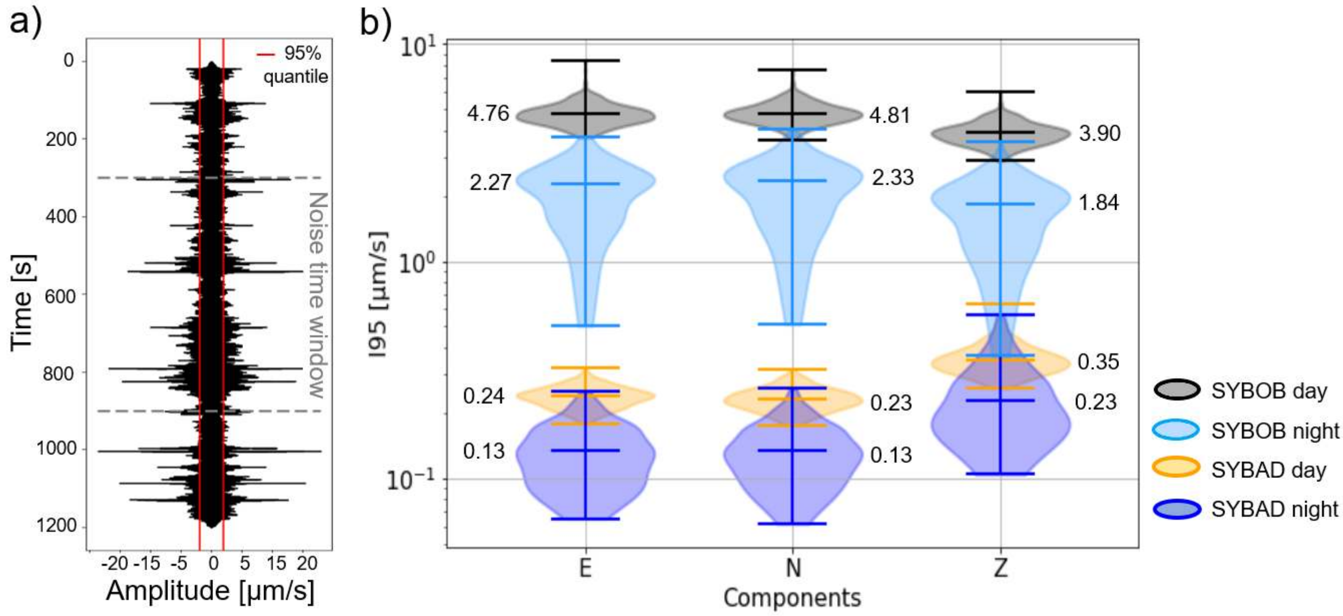

Figure 2 a) Seismic noise recorded at the surface station SYBOB in Munich in a frequency range of 1 - 20Hz. The 95% quantile of the data is shown by the red lines. The I95 value is computed from the 95% quantiles for 10 minute time windows. b) Violin plots of I95 values calculated at the surface station SYBOB and the underlying 180m-deep borehole station SYBAD for the east (E), north (N) and vertical (Z) component. The I95 values were calculated over 5 working days (Monday - Friday) in 10 minute time windows and were separated into daytime (6am - 10pm) and nighttime (10pm - 6am). The median values are marked in the plot.

authors (e.g., Asten and Henstridge, 1984; Groos and Ritter, 2009). In addition, the noise amplitudes at the seismic station can be reduced through installation in boreholes and more isolated areas, like parks and green spaces.

Another measure to evaluate the noise level at a site is the I95 value, which represent the 95^{th} percentiles of the ground velocity amplitude recordings (Fig. 2 a). We calculate the I95 values in a frequency range of 1-20 Hz, which contains the dominant amplitudes of the cultural noise and corresponds to the main frequency range of the induced events observed in the Munich area (Megies and Wassermann, 2017). To investigate the variation of anthropogenic noise, the I95 values are computed at the surface station SYBOB and the borehole station SYBAD for 10-minute time windows during the daytime and nighttime, respectively. The computed I95 values are summed in violin plots and the median is taken as a representative value for the noise amplitude at the site (Fig. 2 b). A clear variation between daytime and nighttime is visible. For the surface station SYBOB the median noise amplitudes are reduced by a factor of 2 during the night. In addition, the noise amplitudes at the surface station SYBOB are by a factor of 10 larger for the vertical component compared to the borehole station SYBAD. This value is close to a factor of 13 that is estimated using the simple assumption that the noise level in the borehole decreases by a factor of $\sqrt{depth[m]}$. Assuming the most inconvenient noise conditions for the detection of microseismic events, we take the median I95 value during the day as a measure for the noise amplitudes at the site. In order to implement the calculated noise values into the pyNetOpt3D program the I95 values have to be converted to root-mean-square (RMS) ground velocity values. Assuming that the noise distribution is Gaussian, the I95 values can be converted by $RMS = I95/2$ (Neuffer and Kremers, 2017).

To estimate the background noise at the potential new network sites, a noise map for the Munich area has to be developed. Kraft (2014, 2016) developed an ambient seismic noise model for Europe based on land-use data derived from satellite imagery by the European Commission project CORINE (Büttner et al., 2004) and open GIS data on infrastructure from the OpenStreetMap project. The model is available for Europe in a $250m \times 250m$ resolution and divides the surface into three classes that represent good, intermediate and bad ambient noise conditions. Kraft (2014, 2016) defined following RMS bounds for each noise class: Low: $RMS \leq 30nm/s$, Middle: $30nm/s < RMS \leq 120nm/s$, High: $RMS > 120nm/s$. Almost the entire Munich city is characterized by high ambient noise values (Fig. 3). By comparing the measured noise values at the stations with the values assigned in the noise map, we see that they are mainly underestimated in the model. Therefore, for optimizing the seismic monitoring network in the urban area of Munich a more detailed noise model is required in order to capture the small-scale heterogeneous noise conditions.

We develop such a noise model for the Munich city extending the approach of Kraft (2014, 2016). First of all, land-use data from the Bavarian surveying administration (see data availability) is used to categorize the area into different classes including industrial buildings, residential buildings, sports and recreation areas, vegetation or water bodies and based on that assign a minimum noise level (Table 1). In the second step, different types of roads are identified as noise sources and sub-

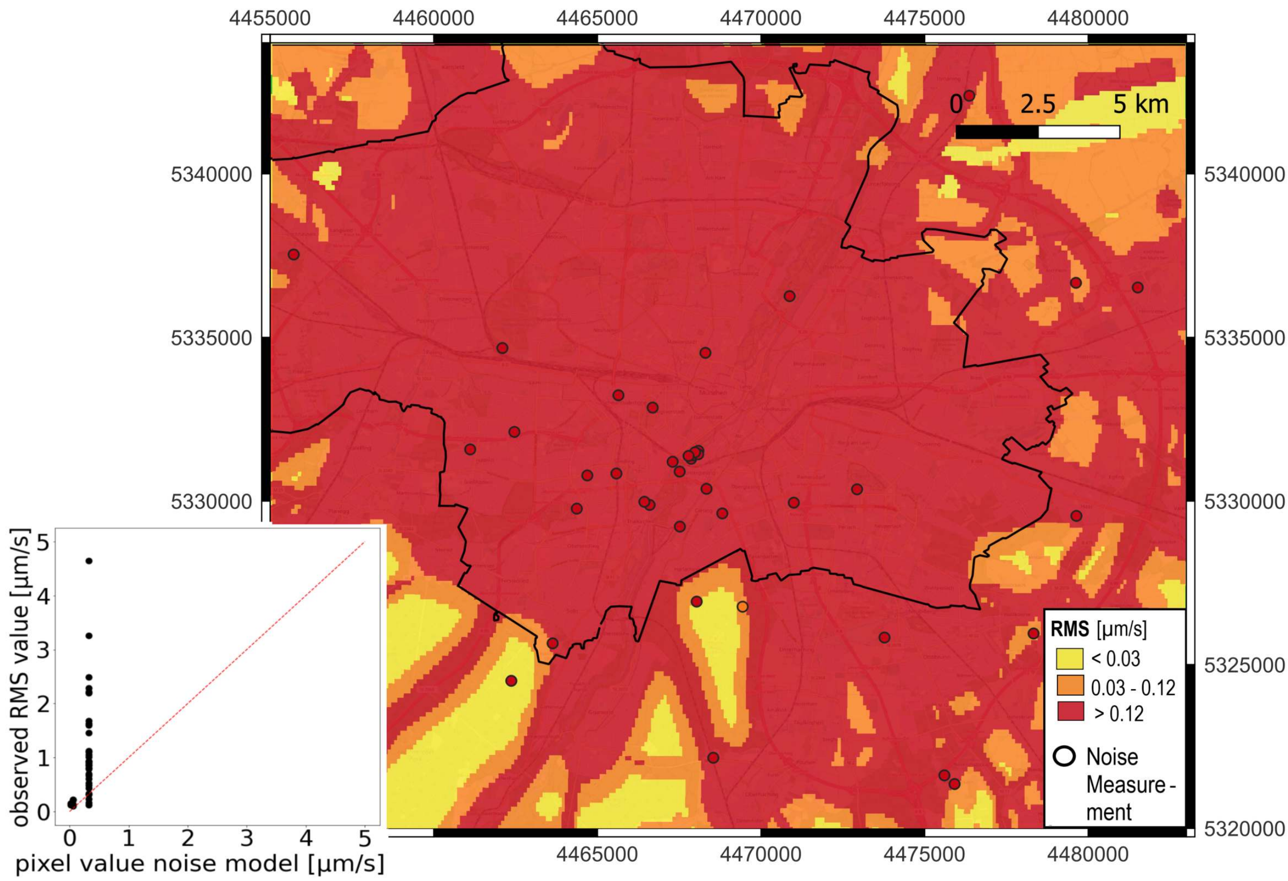

Figure 3 Noise map of Munich after Kraft (2014, 2016). The city boundary is outlined by the black line. The area is divided into three noise classes with low, intermediate and high noise values. The yellow areas are assigned a value of 0.015 µm/s, the orange areas 0.06 µm/s and the red areas a value of 0.325 µm/s. The small circles show noise measurements at permanent and temporary installed seismic stations. The coordinate system is Gauss-Krüger (GK4). In the lower left corner the observed RMS value at the seismic stations are plotted against the calculated pixel value in the noise model.

divided into different classes based on OpenStreetMap data (see data availability). Highways are assumed to have a higher noise contribution, compared to intercity roads, railways or residential streets. In order to account for noise propagation away from these sources, we implement noise-distance relations, that were derived from seismic measurements at distinct noise features (Riedl, 2017). Hereby, several seismometers were installed with increasing distance from the source to map the decreasing amplitude of the ambient vibrations. As last input traffic volume data from the city of Munich (see data availability) are implemented to adjust the noise level for busy roads. The overall noise value at one point is then calculated by adding the minimum noise level assigned from the land-use data and the noise contribution of the main sources scaled by the noise-distance relation. The resulting noise model of Munich's inner-city (Fig. 4) has a resolution of 5×5 m. To verify the calculated noise levels we compare them to the measured noise values at permanent and temporary installed stations. For sites with low noise level the calculated values are mostly close to the measured values. For sites with high noise level our model underestimates the RMS value, which is most likely due to noise sources and site effects that are not mapped into our model. As can be seen in Fig. 4, our noise model for

Table 1 Land use classes with assigned minimum I95 noise level after Riedl (2017).

Land use class	Noise value [μm/s]
Industrial usage	1.2
Housing	0.6
Sports/recreation	0.3
Vegetation, water	0.15

Munich is dominated by street traffic noise. In addition, the overall noise level in the city center is higher compared to the surroundings. Nevertheless, even within the city low noise areas are identified, which might be suitable for the installation of monitoring stations. We implement the high-resolution noise map of the Munich city into the larger-scale background noise map of Kraft (2014, 2016) for the surrounding areas.

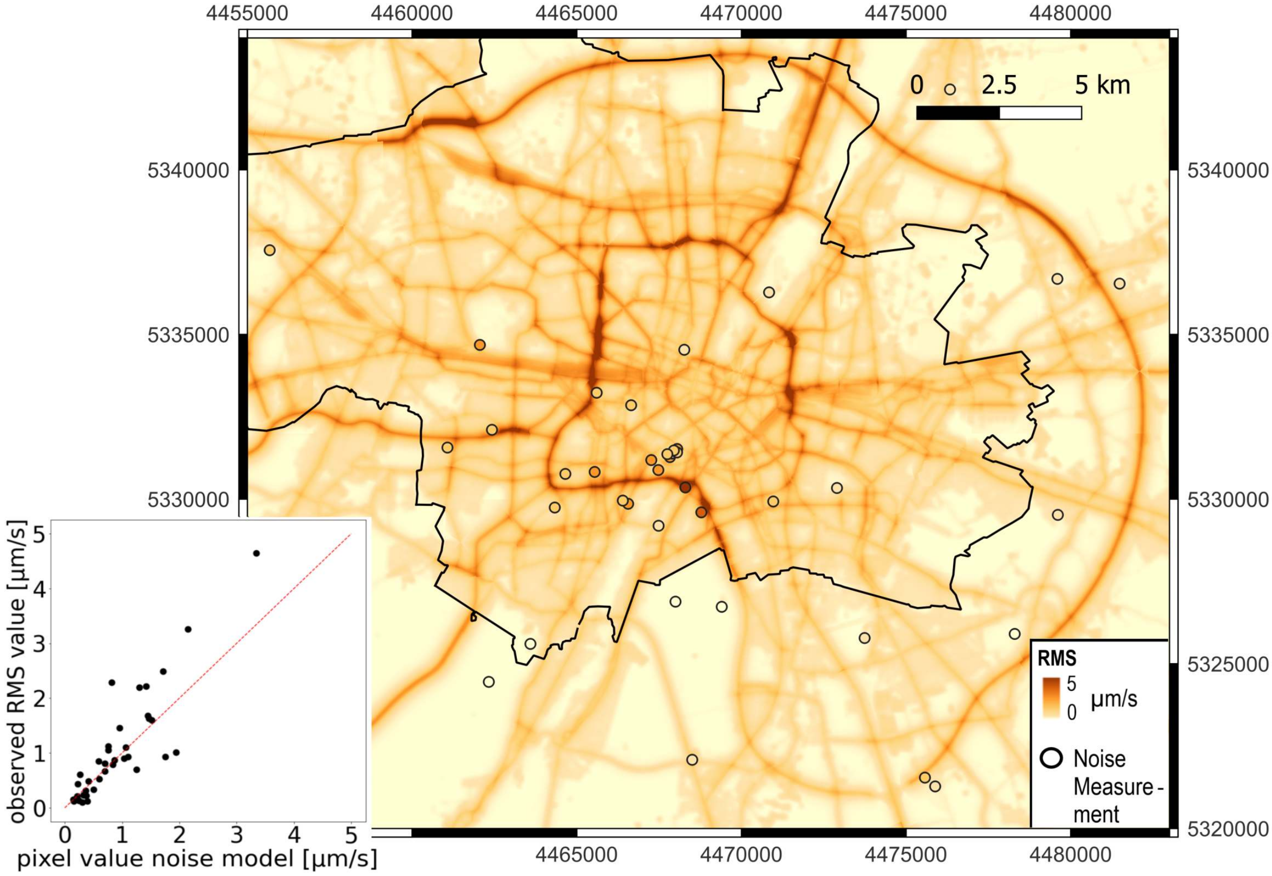

Figure 4 High-resolution noise map of Munich's inner-city. The city boundary is outlined by the black line. Colors represent the noise level, which is calculated as I95 values in a frequency range of 1-20 Hz and converted to RMS. Circles show locations of noise measurements from permanent and temporary installed seismic stations. The coordinate system is Gauss-Krüger (GK4). In the lower left corner the observed RMS value at the seismic stations are plotted against the calculated pixel value in the noise model.

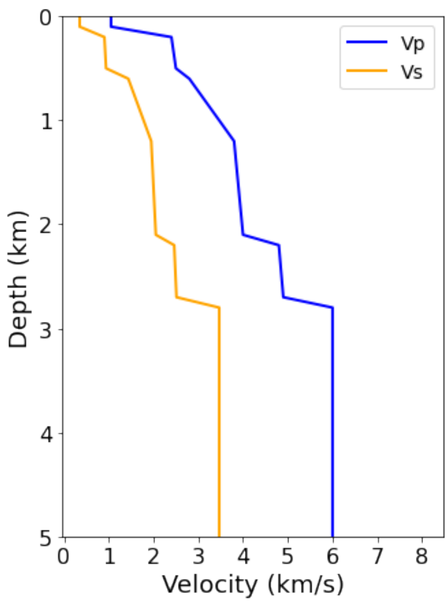

Figure 5 1D P- and S-wave velocity profiles (Vp, Vs) implemented into pyNetOpt3D for the calculation of body wave amplitudes and traveltimes.

4 Model Set-up

To calculate the signal-to-noise ratio at the potential station, we implement the high resolution noise model developed in section 3. As next step, in order to calculate body wave traveltimes, a velocity model has to be implemented. In the Munich area, information on the boundaries of the main geological units are available from a structural model developed by the Bavarian State Office for Environment (Bayerisches Landesamt für Umwelt, 2012). The P-wave velocities within the layers are based on a 3D seismic survey conducted in 2015/16 as part of the GRAME project (Hecht and Pletl, 2015), which covered 170 km^2 in the southern and western parts of Munich. The S-wave velocities are calculated from Vp/Vs ratios found by Wawerzinek et al. (2021) for the Munich area. The NetOpt3D program is able to implement 3D velocity models, however, in this study we only consider a 1D velocity profile (Fig. 5) since we assume that 3D effects only have a minor influence on the results.

Seismic waves attenuate while propagating and their amplitudes usually decrease with propagation distance. To account for seismic attenuation, we implement the attenuation model of Eulenfeld and Wegler (2016) for the geothermal project in Unterhaching south of Munich, since the ray geometry and geologic setting at this

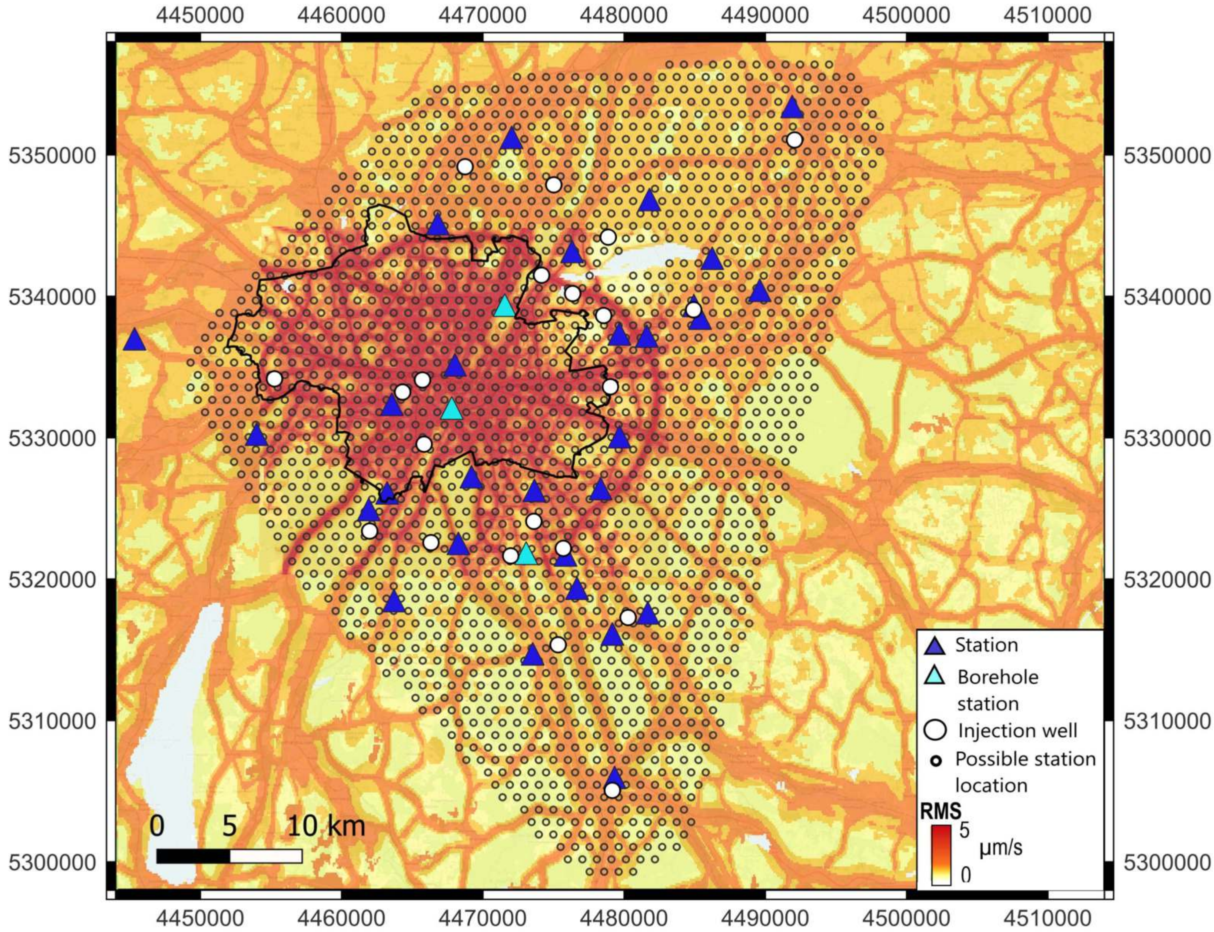

Figure 6 Set-up of the input data for the network optimization program. The Munich city boundary is outlined by the black line. Existing surface and borehole stations, as well as location of injection wells are plotted. The event locations are placed at the injection wells. The colors show the computed background noise level as RMS ground velocity. Small circles represent schematically the grid of possible station locations that can be selected during the optimization process. The coordinate system is Gauss-Krüger (GK4).

site is very similar to the one expected for other locations in the study area. They estimated a mean S-wave quality factor (Qs) of 100 averaged over the whole ray path, which is constant for frequencies lower than 8 Hz. Due to the lack of further information on the attenuation of P-waves, we set the P-wave quality factor (Qp) to 200, as literature suggests that Qp is approximately two times higher than Qs (e.g., Fowler, 1990).

For the network optimization a synthetic earthquake catalogue has to be generated. We place the events in the crystalline basement at 3 - 4 km depth underneath the re-injection wells of the geothermal power plants, as most of the recorded induced seismicity occurred close to these locations (Megies and Wassermann, 2014; Seithel et al., 2019). The focal mechanisms for the events were chosen to resemble those of the known induced earthquakes and the fault geometry in the study area, which generally corresponds to left-lateral strike-slip mechanisms with normal faulting component. We implement the events with M_W 1.3, which was converted from M_L 1.0 according to the relation found by Grünthal and Wahlström (2003) for earthquakes in central Europe.

As the optimization algorithm is able to take already existing stations into account, we implement the existing surface and borehole stations in the area with their observed noise levels.

As a last step, we have to define the geographical region for possible new station locations. We set the station perimeter with a maximum distance of 8 km to the earthquake epicenters, which corresponds to approximately twice the maximum hypocentral depth. Placing the stations at greater distance would not improve the network performance, as will be shown in section 5. The station perimeter was then filled by a grid of possible station locations with a spacing of 100 m, which is enough to cover the low-noise areas within the city. With decreasing station spacing the computational costs increase since a larger number of network configurations has to be tested. Locations where it would be impossible to install a station, e.g. in water bodies, were already excluded from this grid.

The final set-up of the input data, generated by pyNetOpt3D and used by the binaries of Antuens et al. (2023) for the optimization, is shown in Fig. 6.

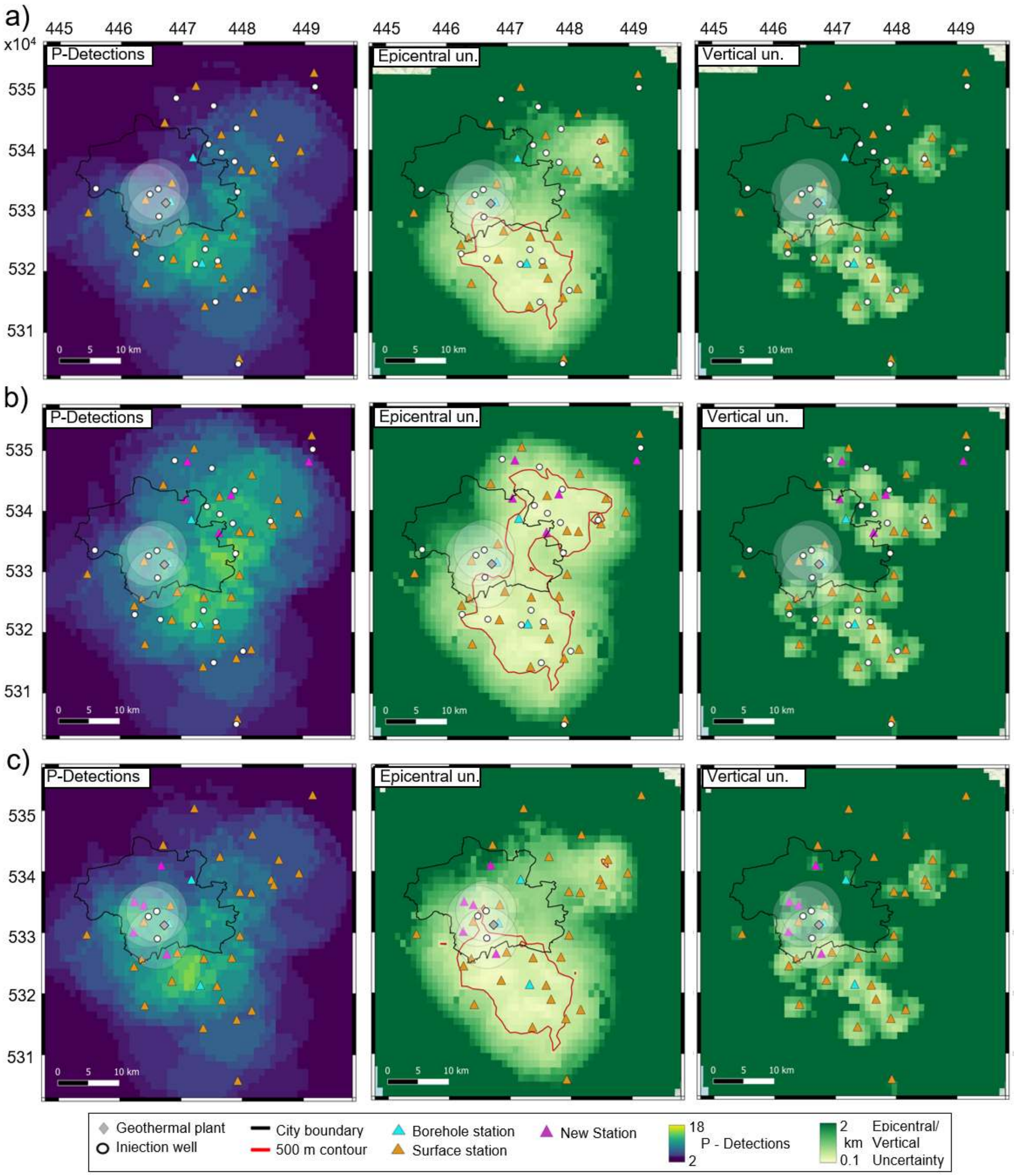

Figure 7 Evaluation of monitoring performance for a M_W 1.3 event at 3 km depth. The performance of the a) existing network, b) optimized network with 5 new stations under consideration of all re-injection wells in the region, c) optimized network with 5 new stations and focus on the three inner-city re-injection wells, is shown. The panels from left to right show the number of P-arrival detections (i.e., recordings with SNR ≥ 5), the epicentral uncertainty and the vertical uncertainty. The location of the inner-city geothermal power plant SLS is plotted. The shaded circles around the three SLS re-injection wells mark a radius of 5 km. The red outline in the epicentral uncertainty plots mark the 500 m contour line. The coordinate system is Gauss-Krüger (GK4).

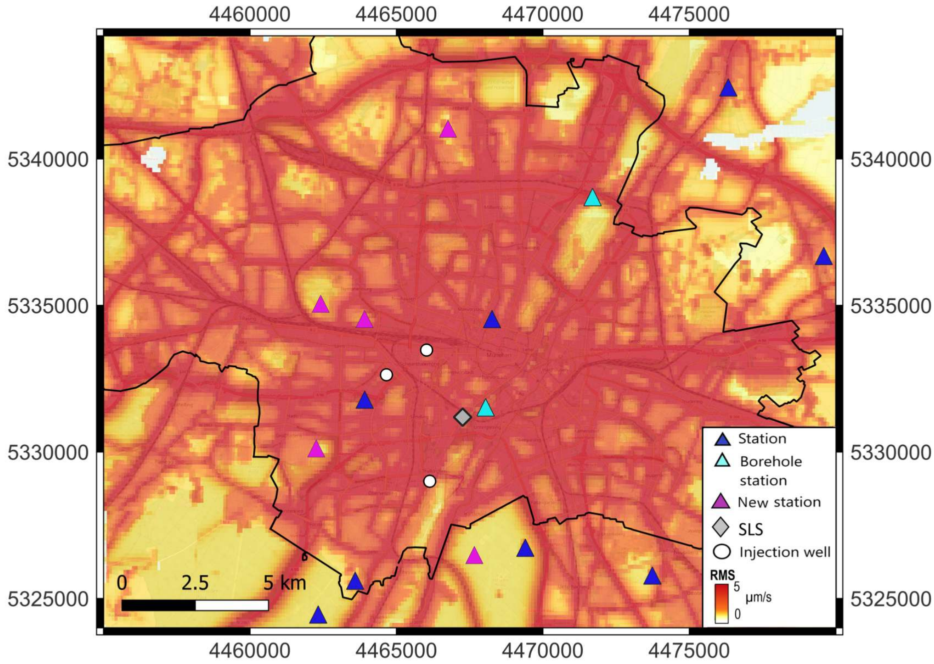

Figure 8 Zoom into the network optimization result for the scenario shown in Fig. 7(c). The pink triangles mark the 5 new surface stations placed by the algorithm. The colors show the computed background noise level as RMS ground velocity. The coordinate system is Gauss-Krüger (GK4).

5 Optimization results and discussion

First of all, the performance of the existing network with a focus on the area surrounding the recently installed SLS power plant is tested using the NetOpt3D program without optimization. The performance in case of a M_W 1.3 event at 3 km depth is tested, which corresponds to the minimum detectable M_W-converted magnitude recommended by the FKPE (Baisch et al., 2012), and is hereafter referred to as target event. The program returns expected location uncertainties and number of detections (i.e., recordings with SNR $\geq$ 5). The largest number of P-wave detections per event is reached for events occurring south of the city-center, while this number decreases significantly in the northeast and in the surrounding of SLS (Fig. 7 a). In the northernmost part of the 5 km radius surrounding SLS, the target events would be detected by even less than 3 stations. Since the source model is implemented based on scaling relations found for Switzerland, the location uncertainties have to be calibrated using recorded events at the geothermal plants in the southern part of the study area (Megies and Wassermann, 2014). To obtain comparable epicentral and vertical uncertainties, the computed values are divided by a factor of three. In this case, the threshold for the FKPE-recommended epicentral uncertainty of < 500 m is only reached south of the city-center, while in the vicinity of SLS epicentral uncertainties of more than 2 km are computed. The 2 km threshold for the vertical uncertainty is once more mostly reached south of the city-center. In general, the poor performance of the existing network in the SLS area can be explained by 1) a lack of monitoring stations in the northwest and a consequent azimuthal gap in this region and 2) the high noise levels in the inner-city, which cause low-SNR recordings resulting in poor onset-time precision and consequently higher location uncertainties.

Considering these observations, we next evaluate how to improve the seismic network by adding new stations. We perform an optimization run for the randomly chosen number of 5 new surface stations, implementing the input data as shown in Fig. 6. The NetOpt3D program performs the simulated annealing and returns the optimal locations for these 5 new stations (Fig. 7 b). All the new stations are placed in the north-northeast, which increases the number of P-wave detections and decreases the epicentral and vertical uncertainties in this area significantly. Nevertheless, in the vicinity of SLS the performance only slightly improved, since none of the stations was placed in the city center. The algorithm placed most of the stations in the north-northeast as the noise levels are lower compared to the city-center and the code tends to locate stations in the quietest sites only (Kraft et al., 2013). Furthermore, it resulted in the largest improvement of the network performance since the improved SNR at a quiet site overrules the lower SNR at a geometrically more optimal site (Kraft et al., 2013). In order to improve the network specifically in the city center, we perform a new optimization run with 5 new surface stations, but only considering the three SLS reinjection wells as event locations. Therefore, the grid of possible station locations only samples the city center. This time the algorithm places the 5 stations closer to SLS (Fig. 7 c). Accordingly, the number of P-wave detections increases in this region. In addition, the epicentral and vertical uncertainties decrease, however, it is not enough to reach the FKPE-recommended location accuracy. The reason are the relatively low SNR values, which results in a poor onset-time precision. Again,

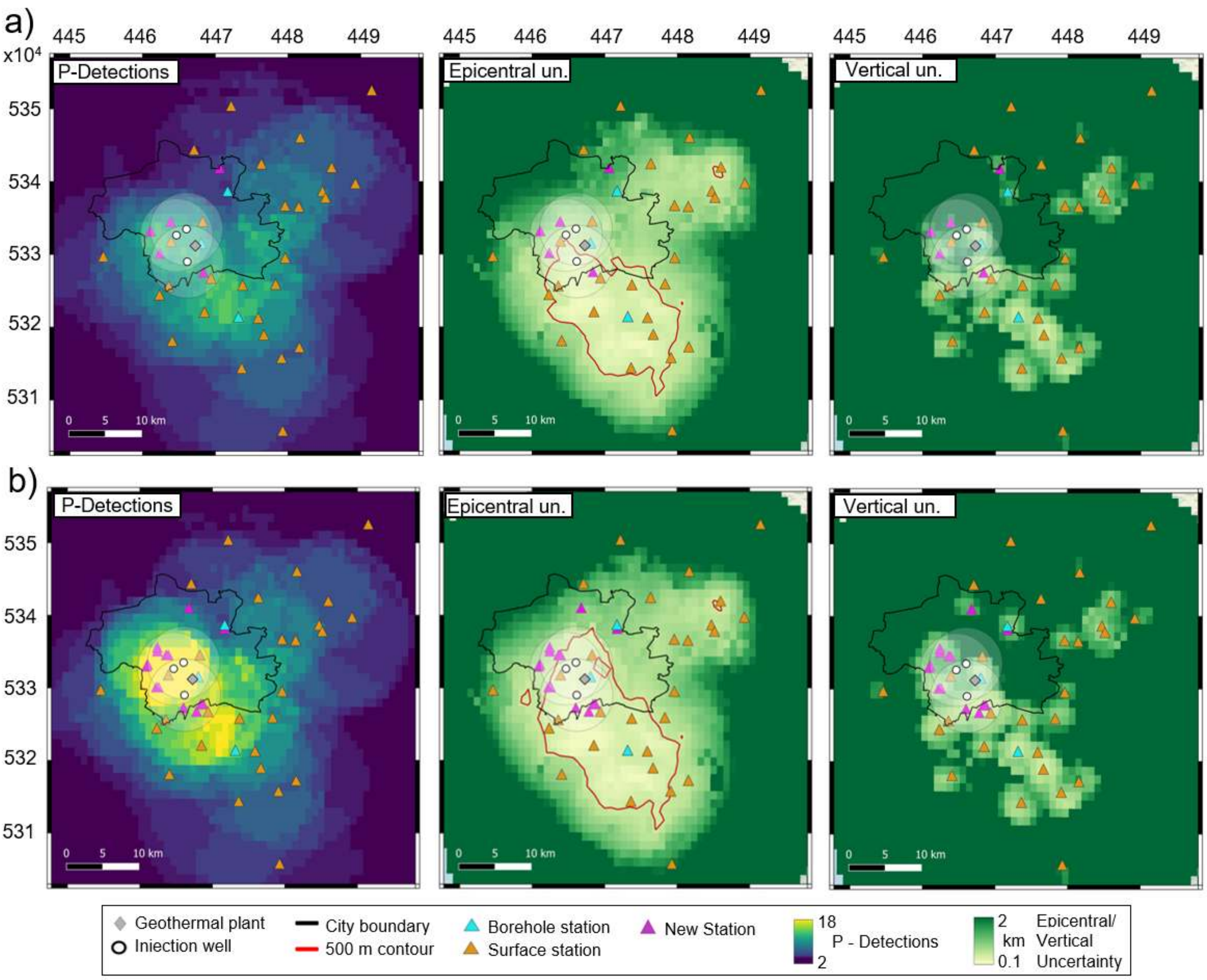

Figure 9 Evaluation of monitoring performance for a M_W 1.3 event at 3 km depth. The performance of the a) optimized network with 5 new stations considering a station perimeter of 12 km and focus on the three inner-city re-injection wells, b) optimized network with 15 new stations and focus on the three inner-city re-injection wells, is shown. The panels from left to right show the number of P-arrival detections (i.e., recordings with SNR $\geq$ 5), the epicentral uncertainty and the vertical uncertainty. The location of the inner-city geothermal power plant SLS is plotted. The shaded circles around the three SLS re-injection wells mark a radius of 5 km. The red outline in the epicentral uncertainty plots mark the 500 m contour line. The coordinate system is Gauss-Krüger (GK4).

the algorithm places the new stations in low noise areas (Fig. 8), which mainly correspond to park areas within the city. This highlights the importance of a high-resolution noise map.

To allow the algorithm to choose low-noise areas outside of the city, we increase the station perimeter from 8 km to 12 km. Nevertheless, the algorithm still places four of the new surface stations close to the SLS power plant and only one station closer to the edge of the city (Fig. 9 a). The resulting epicentral and vertical uncertainties are similar to the values in Fig. 7 c). Therefore, we have shown that considering a station perimeter of 8 km is enough, as placing stations at larger distance does not improve the monitoring performance significantly. This is most likely related to the decreasing amplitude of the ground motion away from the epicenter.

To see if a larger number of surface stations could reach the recommended location precision, the same optimization run is performed using 15 new stations (Fig. 9 b). The number of P-wave detections significantly increases. Nevertheless, even though the epicentral and vertical uncertainties improve it is not sufficient to reach the FKPE-recommended location precision in the vicinity of SLS. In fact, adding even more stations does not significantly improve the location precision any further.

In order to increase the SNR and allow a more accurate determination of the event location, borehole stations are considered in the next step of the optimization. In section 3 the 180m-deep borehole station SYBAD was compared to the overlying surface station SYBOB. We observed that for the vertical component the noise level in the borehole is a factor of 10 lower than at the surface. Therefore, to simulate the noise level for borehole stations in Munich we divide the noise model by a factor of 10 and input it into the NetOpt3D program. Then a net-

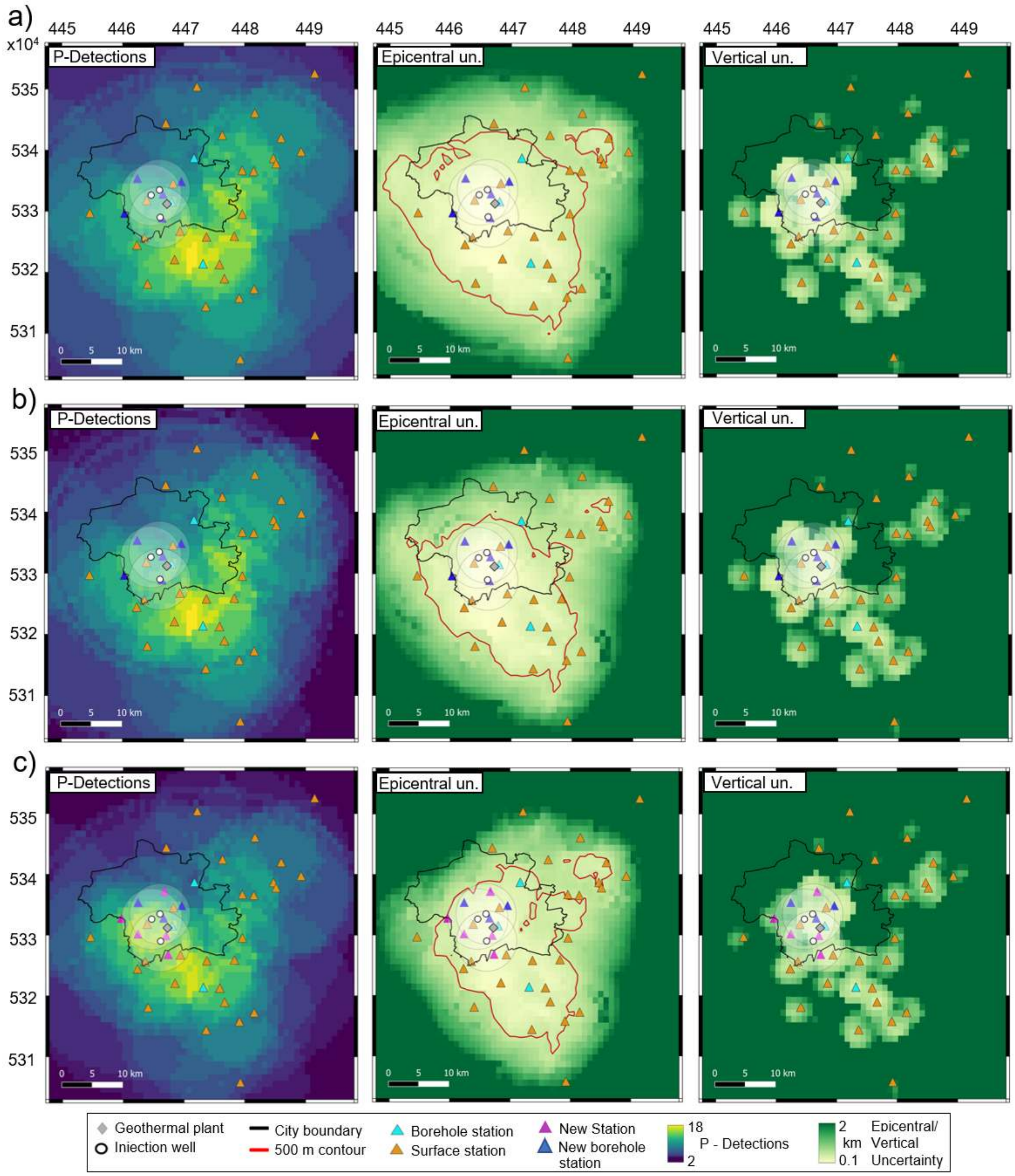

Figure 10 Evaluation of monitoring performance for a M_W 1.3 event at 3 km depth. The performance of the a) optimized network with 5 new 180m-deep borehole stations and focus on the three inner-city re-injection wells, b) optimized network with 5 new 36m-deep borehole stations and focus on the three inner-city re-injection wells, c) optimized network with 3 new 180m-deep borehole stations and 5 new surface stations and focus on the three inner-city re-injection wells. The panels from left to right show the number of P-arrival detections, the epicentral uncertainty and the vertical uncertainty. The location of the inner-city geothermal power plant SLS is plotted. The shaded circles around the three SLS re-injection wells mark a radius of 5 km. The red outline in the epicentral uncertainty plots mark the 500 m contour line. The coordinate system is Gauss-Krüger (GK4).

work optimization for borehole stations is performed. We find that at least 5 new borehole stations are sufficient to reach the recommended epicentral uncertainty of less than 500 m in the surroundings of the SLS reinjection wells (Fig. 10 a). Additionally, the vertical uncertainty threshold of < 2 km is reached almost within the entire 5 km radius, except for some outermost parts.

To estimate the minimum required borehole depth we stepwise decrease the borehole noise level factor for the background noise map. We find that a factor of 6 is sufficient to reach the recommended location accuracy (Fig. 10 b). Assuming the simple relation of noise decreasing with depth by a factor of $\sqrt{depth[m]}$ this would correspond to a borehole depth of 36 m.

Even though borehole stations significantly improve the quality of the monitoring network, their installation is not always feasible due to high costs and infrastructural limitations. Therefore, we test if less borehole stations in combination with additional surface stations could also reach the FKPE-recommended location precision. At first, the optimization is performed for 3 new borehole stations by scaling the noise map with a factor 10. This is followed by an optimization run with 5 new surface stations, while fixing the previously determined borehole stations. The recommended epicentral and vertical uncertainty thresholds are reached in this case (Fig. 10 c).

6 Conclusion

We performed a network optimization using the python wrapper pyNetOpt3D around the NetOpt3D program in order to improve the microseismic monitoring for a safe operation of deep geothermal plants in Munich's innercity. In the first step we constructed a noise model for the Munich area in order to capture the heterogeneous noise conditions. This high resolution noise model enabled the algorithm to find suitable station locations even within the city center. The results suggest that the current monitoring network is not suitable to locate M_L 1 earthquakes with a FKPE-recommended epicentral uncertainty of < 500 m and vertical uncertainty of < 2 km. We showed that adding solely surface stations to the inner-city network is not sufficient to reach the recommended thresholds. The addition of borehole stations significantly improved the quality of the monitoring network, which indicates that borehole installations may be indispensable in urban environments. However borehole installations are not always feasible and come with high costs. We were able to show that a combination of new borehole and new surface stations can be used to record and locate M_L 1 events in Munich with the recommended location precision. This study presents procedures and shows solutions for improving the microseismic monitoring within urban areas both for induced and natural seismicity. Nevertheless, we emphasise that proper seismic monitoring is only one component of a comprehensive risk governance strategy for induced seismicity.

Acknowledgements

This work was supported by the research project SEIGER (Project no. 03EE44003G), funded by the German Federal Ministry of Economic Affairs and Climate Action and managed by the research institute Jülich (PTJ). T. Megies was supported by the GEOBEST-CH project of the Swiss Seismological Service funded by the Swiss Energy Program of the Swiss Federal Office of Energy for the development of pyNetOpt3D. The authors thank the reviewer Anthony Lomax for the helpful comments, which improved the manuscript.

Data and code availability

The Geographical base data from the Bavarian administration for geographical surveying (Geobasisdaten Bayerische Vermessungsverwaltung 2017) was requested at https://www.ldbv.bayern.de/ (last request July 30, 2017). The OpenStreetMap data were downloaded from https://www.openstreetmap.org/export#map=11/48.0290/11.6331 (last request July 29, 2017). The traffic volume data from the city of Munich for 2019 were searched at https://stadt.muenchen.de/infos/verkehrsdaten.html (last accessed July 10, 2020). The pyNetOpt3D code and the binaries of NetOpt3D from Antuens et al. (2023) are available at Zenodo (https://doi.org/10.5281/zenodo.7638856).

Competing interests

The authors have no competing interests.

References

Agemar, T., Weber, J., and Schulz, R. Deep geothermal energy production in Germany. *Energies*, 7(7):4397–4416, 2014. doi: 10.3390/en7074397.

Aki, K. Signal to noise ratio in seismic measurements. *Volcanoes and Tectonos· phere, Tokai Univ. Press, Tokyo*, pages 187–192, 1976.

Antuens, V., Toledo, T., Kraft, T., Reyes, C., and Megies, T. Optimal Design and Ground Truth Performance Test for Deep Geothermal Seismic Monitoring Networks. (in preparation). 2023.

Asten, M. W. and Henstridge, J. Array estimators and the use of microseisms for reconnaissance of sedimentary basins. *Geophysics*, 49(11):1828–1837, 1984. doi: 10.1190/1.1441596.

Baisch, S., Fritschen, R., Groos, J., Kraft, T., Plenefisch, T., Plenkers, K., Ritter, J. R., and Wassermann, J. Empfehlungen zur Überwachung induzierter Seismizität-Positionspapier des FKPE. *DGG Mitteilungen*, (3):17–31, 2012.

Bartal, Y., Somer, Z., Leonard, G., Steinberg, D. M., and Horin, Y. B. Optimal seismic networks in Israel in the context of the Comprehensive Test Ban Treaty. *Bulletin of the seismological society of America*, 90(1):151–165, 2000. doi: 10.1785/0119980164.

Bayerisches Landesamt für Umwelt. Geothermische Charakterisierung von Karst-Kluft-Aquiferen im Großraum München. *Endbericht*, 2012.

Bondár, I., Myers, S. C., Engdahl, E. R., and Bergman, E. A. Epicentre accuracy based on seismic network criteria. *Geophysical Journal International*, 156(3):483–496, 2004. doi: 10.1111/j.1365-246X.2004.02070.x.

Bormann, P. and Wielandt, E. Seismic signals and noise. In *New manual of seismological observatory practice 2 (NMSOP2)*, pages 1–62. Deutsches GeoForschungsZentrum GFZ, 2013. doi: 10.2312/GFZ.NMSOP-2$_c h4$.

Brune, J. N. Tectonic stress and the spectra of seismic shear waves from earthquakes. *Journal of geophysical research*, 75 (26):4997–5009, 1970. doi: 10.1029/JB075i026p04997.

Büttner, G., Feranec, J., Jaffrain, G., Mari, L., Maucha, G., and Soukup, T. The CORINE land cover 2000 project. *EARSeL eProceedings*, 3(3):331–346, 2004.

Coles, D. and Curtis, A. Efficient nonlinear Bayesian survey design using DN optimization. *Geophysics*, 76(2):Q1–Q8, 2011. doi: 10.1190/1.3552645.

De Landro, G., Picozzi, M., Russo, G., Adinolfi, G. M., and Zollo, A. Seismic networks layout optimization for a high-resolution monitoring of induced micro-seismicity. *Journal of Seismology*, 24:953–966, 2020. doi: 10.1007/s10950-019-09880-9.

D'Alessandro, A., Luzio, D., D'Anna, G., and Mangano, G. Seismic network evaluation through simulation: An application to the Italian National Seismic Network. *Bulletin of the Seismological Society of America*, 101(3):1213–1232, 2011. doi: 10.1785/0120100066.

Edwards, B., Fäh, D., and Giardini, D. Attenuation of seismic shear wave energy in Switzerland. *Geophysical Journal International*, 185(2):967–984, 2011. doi: 10.1111/j.1365-246X.2011.04987.x.

Eulenfeld, T. and Wegler, U. Measurement of intrinsic and scattering attenuation of shear waves in two sedimentary basins and comparison to crystalline sites in Germany. *Geophysical Journal International*, 205(2):744–757, 2016. doi: 10.1093/gji/ggw035.

Evans, K. F., Zappone, A., Kraft, T., Deichmann, N., and Moia, F. A survey of the induced seismic responses to fluid injection in geothermal and CO2 reservoirs in Europe. *Geothermics*, 41: 30–54, 2012. doi: 10.1016/j.geothermics.2011.08.002.

Fowler, C. M. R. *The solid earth: an introduction to global geophysics*. Cambridge University Press, 1990.

Groos, J. and Ritter, J. Time Domain Classification and Quantification of Seismic Noise. In *Noise and diffuse wavefields: extended abstracts of the Neustadt workshop; Neustadt an der Weinstraße, Germany, 5-8 July 2009. Ed.: Ch. Sens-Schönfelder*, page 25, 2009. doi: 10.1111/j.1365-246X.2009.04343.x.

Grünthal, G. and Wahlström, R. An M w based earthquake catalogue for central, northern and northwestern Europe using a hierarchy of magnitude conversions. *Journal of seismology*, 7: 507–531, 2003. doi: 10.1023/B:JOSE.0000005715.87363.13.

Hardt, M. and Scherbaum, F. The design of optimum networks for aftershock recordings. *Geophysical Journal International*, 117 (3):716–726, 1994. doi: 10.1111/j.1365-246X.1994.tb02464.x.

Häring, M. O., Schanz, U., Ladner, F., and Dyer, B. C. Characterisation of the Basel 1 enhanced geothermal system. *Geothermics*, 37(5):469–495, 2008. doi: 10.1016/j.geothermics.2008.06.002.

Havskov, J., Ottemöller, L., Trnkoczy, A., and Bormann, P. Seismic networks. In *New Manual of Seismological Observatory Practice 2 (NMSOP-2)*, pages 1–65. Deutsches GeoForschungsZentrum GFZ, 2012. doi: 10.2312/GFZ.NMSOP-2$_c h8$.

Hecht, C. and Pletl, C. Das Verbundprojekt GRAME–Wegweiser für eine geothermische Wärmeversorgung urbaner Ballungsräume. *Geothermische Energie*, 82(2):02, 2015.

Hirschberg, S., Wiemer, S., and Burgherr, P. *Energy from the Earth: Deep Geothermal as a Resource for the Future?*, volume 62. vdf Hochschulverlag AG, 2014.

Kijko, A. An algorithm for the optimum distribution of a regional seismic network—I. *pure and applied geophysics*, 115(4): 999–1009, 1977. doi: 10.1007/BF00881222.

Kirkpatrick, S., Gelatt Jr, C. D., and Vecchi, M. P. Optimization by simulated annealing. *science*, 220(4598):671–680, 1983. doi: 10.1126/science.220.4598.671.

Kraft, T. A high-resolution ambient seismic noise model for Europe. *EGU General Assembly, EGU2014-2282*, 27, 2014.

Kraft, T. A high-resolution and calibrated model of man-made seismic noise for Europe. *Jahrestagung der Deutschen Geophysikalischen Gesellschaft*, pages S2–A, 2016.

Kraft, T., Mignan, A., and Giardini, D. Optimization of a large-scale microseismic monitoring network in northern Switzerland. *Geophysical Journal International*, 195(1):474–490, 2013. doi: 10.1093/gji/ggt225.

Kraft, T., Roth, P., and Wiemer, S. Good Practice Guide for Managing Induced Seismicity in Deep Geothermal Energy Projects in Switzerland: Version 2. 2020. doi: 10.3929/ethz-b-000453228.

Lentsch, D. and Schweingruber, M. First Multilateral Deep Geothermal Well in the South German Molasse Basin. *Eropean Geothermal Congress*, 2022.

Lomax, A., Michelini, A., Curtis, A., and Meyers, R. Earthquake location, direct, global-search methods. *Encyclopedia of complexity and systems science*, 5:2449–2473, 2009.

Lund, J. W. and Toth, A. N. Direct utilization of geothermal energy 2020 worldwide review. *Geothermics*, 90:101915, 2021. doi: 10.1016/j.geothermics.2020.101915.

Mahani, A. B., Kao, H., Walker, D., Johnson, J., and Salas, C. Performance evaluation of the regional seismograph network in northeast British Columbia, Canada, for monitoring of induced seismicity. *Seismological Research Letters*, 87(3):648–660, 2016. doi: 10.1785/0220150241.

Megies, T. and Wassermann, J. Microseismicity observed at a non-pressure-stimulated geothermal power plant. *Geothermics*, 52: 36–49, 2014. doi: 10.1016/j.geothermics.2014.01.002.

Megies, T. and Wassermann, J. Verbundprojekt MAGS2 - Vom Einzelsystem zur großräumigen Nutzung- EP2: Untersuchungen zur optimierten seismischen Überwachung hydrogeothermaler Systeme bei dichter räumlicher Lage der Bohrerlaubnisfelder am Beispiel der Situation im Süden Münchens. *Abschlussbericht*, 2017.

Megies, T., Kraft, T., and Reyes, C. pyNetOpt3D. *Zenodo*, https://-doi.org/10.5281/zenodo.7638856, 2023.

Myers, S. C. and Schultz, C. A. Improving sparse network seismic location with Bayesian kriging and teleseismically constrained calibration events. *Bulletin of the Seismological Society of America*, 90(1):199–211, 2000. doi: 10.1785/0119980171.

Neuffer, T. and Kremers, S. How wind turbines affect the performance of seismic monitoring stations and networks. *Geophysical Journal International*, 211(3):1319–1327, 2017. doi: 10.1093/gji/ggx370.

Podvin, P. and Lecomte, I. Finite difference computation of traveltimes in very contrasted velocity models: a massively parallel approach and its associated tools. *Geophysical Journal International*, 105(1):271–284, 1991. doi: 10.1111/j.1365-246X.1991.tb03461.x.

Riedl, C. A Seismic Noise Map for the Greater Munich Area. Master's thesis, LMU Munich, 2017.

Schmittbuhl, J., Lambotte, S., Lengliné, O., Grunberg, M., Jund, H., Vergne, J., Cornet, F., Doubre, C., and Masson, F. Induced and triggered seismicity below the city of Strasbourg, France from November 2019 to January 2021. *Comptes Rendus. Géoscience*, 353(S1):561–584, 2021. doi: 10.5802/crgeos.71.

Seithel, R., Gaucher, E., Mueller, B., Steiner, U., and Kohl, T. Probability of fault reactivation in the Bavarian Molasse Basin. *Geothermics*, 82:81–90, 2019. doi: 10.1016/j.geothermics.2019.06.004.

Shannon, C. E. A mathematical theory of communication. *The Bell system technical journal*, 27(3):379–423, 1948. doi: 10.1002/j.1538-7305.1948.tb01338.x.

Stabile, T., Iannaccone, G., Zollo, A., Lomax, A., Ferulano, M., Vetri, M., and Barzaghi, L. A comprehensive approach for evaluating network performance in surface and borehole seismic monitoring. *Geophysical Journal International*, 192(2):793–806, 2013. doi: 10.1093/gji/ggs049.

Steinberg, D. M. and Rabinowitz, N. Optimal seismic monitoring for event location with application to on site inspection of the comprehensive nuclear test ban treaty. *Metrika*, 58(1):31–57, 2003. doi: 10.1007/s001840200222.

Wawerzinek, B., Buness, H., von Hartmann, H., and Tanner, D. C. S-wave experiments for the exploration of a deep geothermal carbonate reservoir in the German Molasse Basin. *Geothermal Energy*, 9(1):1–21, 2021. doi: 10.1186/s40517-021-00189-w.

doi:10.26443/seismica.v2i2.1011

SEISMICA

Rayleigh-wave group velocities in Northwest Iran: SOLA Backus-Gilbert vs. Fast Marching tomographic methods

Saman Amiri * [1], **Alessia Maggi** [2], **Mohammad Tatar** [1], **Dimitri Zigone** [2], **Christophe Zaroli** [2]

[1]Department of Seismology, International Institute of Earthquake Engineering and Seismology, Tehran, Iran, [2]Institut Terre et Environnement de Strasbourg, UMR 7063, Université de Strasbourg, EOST/CNRS, 67084 Strasbourg cedex, France

Author contributions: *Conceptualization*: S. Amiri, A. Maggi. *Methodology*: C. Zaroli, D. Zigone. *Formal Analysis*: S. Amiri, A. Maggi. *Resources*: M. Tatar, S. Amiri. *Writing - original draft*: S. Amiri, A. Maggi, D. Zigone, C. Zaroli, M. Tatar. *Writing - Review & Editing*: S. Amiri, A. Maggi. *Supervision*: A. Maggi, M. Tatar. *Funding acquisition*: S. Amiri, A. Maggi, M. Tatar.

Abstract In this study, we focus on Northwest Iran and exploit a dataset of Rayleigh-wave group-velocity measurements obtained from ambient noise cross-correlations and earthquakes. We build group-velocity maps using the recently developed SOLA Backus-Gilbert linear tomographic scheme as well as the more traditional Fast-marching Surface-wave Tomography method. The SOLA approach produces robust, unbiased local averages of group velocities with detailed information on their local resolution and uncertainty; however, it does not as yet allow ray-path updates in the inversion process. The Fast-marching method, on the other hand, does allow ray-path updates, although it does not provide information on the resolution and uncertainties of the resulting models (at least not without great computational cost) and may suffer from bias due to model regularisation. The core of this work consists in comparing these two tomographic methods, in particular how they perform in the case of strong vs. weak seismic-velocity contrasts and good vs. poor data coverage. We demonstrate that the only case in which the Fast-marching inversion outperforms the SOLA inversion is for strong anomaly contrasts in regions with good path coverage; in all other configurations, the SOLA inversion produces more coherent anomalies with fewer artefacts.

Production Editor:
Gareth Funning
Handling Editor:
Suzan van der Lee
Copy & Layout Editor:
Théa Ragon

Received:
June 6, 2023
Accepted:
October 3, 2023
Published:
December 4, 2023

Non-technical summary Seismic tomography is an imaging technique that uses seismic waves generated by earthquakes and ambient seismic noise cross-correlations to create two- and three-dimensional images of Earth's interior. Tomographic images obtained in the past decades have greatly improved our understanding of the Earth's heterogeneous structure and dynamics. In this study, we focused on Northwest Iran, a region with complex structures, and tested two different tomographic methods to better understand how they perform in regions with different degrees of geological contrasts and data coverage.

1 Introduction

Northwest Iran is part of the Arabia-Eurasia collision, situated between the Caspian Sea, the southern Caucasus, eastern Anatolia, and the northern Zagros Mountains (Fig. 1a). This strongly deformed and seismically active region was formed from the closure of the Neotethys Ocean and the collision of the Arabian plate with the Central Iran block. It has been the subject of many imaging studies that aim to answer questions about its geological history and the processes that have shaped it. These studies have used body waves (Alinaghi et al., 2007; Bavali et al., 2016; Rezaeifar et al., 2016; Rezaeifar and Kissling, 2020), head waves (Hearn and Ni, 1994; Sandvol et al., 2001; Al-Lazki et al., 2003; Gök et al., 2003; Amini et al., 2012; Maheri-Peyrov et al., 2016; Lü and Chen, 2017), receiver functions (Paul et al., 2010), shear-wave splitting (Kaviani et al., 2009), coda attenuation (Rahimi et al., 2010a,b; Naghavi et al., 2012; Farrokhi et al., 2015; Forrokhi et al., 2016; Irandoust et al., 2016), and surface-waves both from earthquakes (Maggi and Priestley, 2005; Manaman et al., 2010; Rahimi et al., 2014; Mortezanejad et al., 2019; Zandi and Rahimi, 2020; Shakiba et al., 2020) and ambient seismic noise cross-correlations (Mottaghi et al., 2013; Movaghari and Doloei, 2019; Movaghari et al., 2021).

Among the authors of the surface-wave studies of the region, some (Maggi and Priestley, 2005; Manaman et al., 2010) implemented the Partitioned Waveform Inversion scheme of Nolet (1990) and van der Lee and Nolet (1997) that inverts surface-wave seismograms for 1D path-averaged shear-wave velocity profiles then applies a tomographic inversion based on the linear-damped-least squares LSQR algorithm of Paige and Saunders (1982) to produce 3D shear-wave velocity models. The others measured surface-wave dispersion then applied 2D tomographic methods to create group and/or phase velocity maps, using either the linear-inversion method of Ditmar and Yanovskaya (1987) and Yanovskaya and Ditmar (1990) (Rahimi et al., 2014; Mortezanejad et al., 2019; Zandi and Rahimi, 2020; Shakiba et al., 2020), or

*Corresponding author: samanaf@stu.iiees.ac.ir

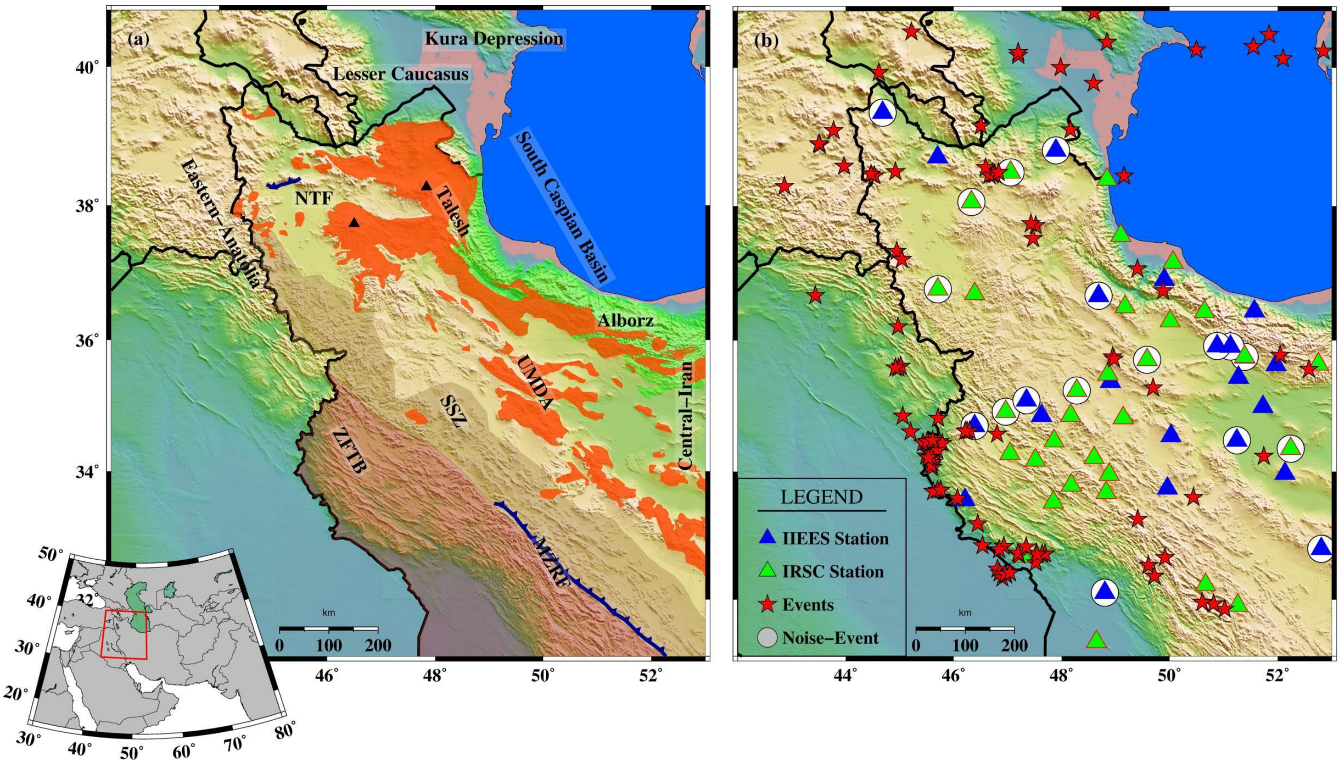

Figure 1 (a) The location map of the main seismotectonic units: the volcanic and intrusive rocks (brick red areas); the Zagros fold and thrust belt (ZFTB); the Sanandaj-Sirjan Zone (SSZ); the Urumieh-Dokhtar Magmatic Arc (UDMA), the Alborz and Talesh; the South Caspian Basin; and the Lesser Caucasus. Two major active faults are indicated with solid lines: the North Tabriz Fault (NTF) and the Main Zagros Reverse Fault (MZRF). The locations of the Sahand and Sabalan volcanoes are shown by black triangles. (b) Locations of the seismic stations and earthquakes used. Triangles indicate stations; red stars indicate earthquakes. Stations surrounded by circles were used for both earthquakes and ambient noise cross-correlations.

the Fast-marching Surface-wave Tomography method of Rawlinson and Sambridge (2005) (Mottaghi et al., 2013; Movaghari and Doloei, 2019; Movaghari et al., 2021). Of this latter group, some then inverted their dispersion maps at each point to obtain 3D shear-wave velocity models, using either a linearised least-squares inversion (Mottaghi et al., 2013; Movaghari and Doloei, 2019) or a non-linear inversion (Mortezanejad et al., 2019; Movaghari et al., 2021).

As is common when comparing the results of tomographic studies of a single region, the surface-wave studies mentioned earlier agree on the main structures of the region – they all show high velocities at shallow depth and short periods in the Sanandaj-Sirjan zone and low velocities in the Zagros fold and thrust belt – but differ in the details. For example, the group-velocities from Shakiba et al. (2020) are higher than those from Mortezanejad et al. (2019) and Zandi and Rahimi (2020), while the region south of Sahand volcano has slow group-velocities at short periods in Shakiba et al. (2020) and Mottaghi et al. (2013) and fast velocities in Mortezanejad et al. (2019), Zandi and Rahimi (2020), and Movaghari and Doloei (2019). There are multiple factors contributing to these discrepancies. We have previously discussed the diverse sources of surface-wave data (earthquakes or ambient noise) and variations in tomographic inversion methods. Additionally, we should consider disparities in uncertainty estimates for the measurements, differences in model parameterisation, and variations in the choice of trade-off parameters. In the absence of consistent resolution and uncertainty estimates of the tomographic models, meaningfully comparing them becomes difficult (e.g. Rawlinson et al., 2014). Of the studies cited above, only those using the linear-tomographic inversion method of Ditmar and Yanovskaya (1987) and Yanovskaya and Ditmar (1990) include spatial estimates of tomographic model resolution and uncertainties (Rahimi et al., 2014; Mortezanejad et al., 2019; Zandi and Rahimi, 2020; Shakiba et al., 2020), though not the full resolution-matrix with which to also quantify model bias. The other tomographic inversion methods used – the LSQR damped-least squares inversion method of Paige and Saunders (1982) for the studies using Partitioned waveform inversion and the subspace inversion method of Kennett et al. (1988) for those using Fast-marching seismic tomography – do not produce the full resolution-matrix either. For a good explanation of why producing the resolution matrix for such methods is computationally expensive, see Deal and Nolet (1996).

New seismic tomographic inversion methods are continuously being developed, including some that focus on the question of tomographic model resolution. One such method is called Subtractive Optimally Localised Averages (SOLA). This computationally efficient variant of the Backus–Gilbert linear-inversion paradigm (Backus and Gilbert, 1967, 1968) was introduced in helioseismology (Pijpers and Thompson, 1992, 1993) then adapted to seismic tomography (Zaroli, 2016; Zaroli et al., 2017; Zaroli, 2019; Latallerie et al., 2022). The

SOLA method not only produces full resolution and uncertainty information for tomographic models, it also constrains the models to be unbiased, and allows users direct control on the trade-off between resolution and uncertainty.

In this study, we apply the SOLA tomographic inversion of Zaroli (2016) to Northwest Iran to construct maps of Rayleigh-wave group-velocities, using a dataset of Rayleigh-wave dispersion measurements obtained both from earthquakes and from seismic noise cross-correlations. We compare the resulting tomographic images with those obtained using the same dataset and parameterisation but applying the Fast-marching surface-wave tomography method of Rawlinson and Sambridge (2005). We focus on how each method performs in cases of strong vs. weak seismic-velocity contrasts and good vs. poor data coverage.

2 Geological context

Northwest Iran forms part of the Arabia-Eurasia continental collision zone and is subject to a local transpressional tectonic regime with a high level of seismicity. The region is bounded in the North by the Lesser Caucasus thrust belt and the Kura depression, in the East by the Talesh mountains, the Alborz mountains, and the South Caspian Basin, in the South by the Zagros fold and thrust belt, and in the West by Eastern Anatolia. The crust and upper mantle structure of Northwest Iran has been strongly shaped by the convergence occurring on the southern edge of the Eurasian plate (e.g. Sengor, 1990).

The region contains two major active faults – the North Tabriz Fault and the Main Zagros Thrust Fault – and can be divided into a handful of tectonic units, as shown in Fig. 1a. The North Tabriz Fault (NTF in Fig. 1a) has a clear surface expression, is considered one of the most active faults in Northwest Iran, and has been implicated in catastrophic historical earthquakes (Moradi et al., 2011). The Main Zagros Reverse Fault (MZRF in Fig. 1a) forms the suture between the Arabian plate and Central Iran block, which occurred after the closure of the Neotethys Ocean (Talebian and Jackson, 2002).

To the southwest of this suture, the Zagros Fold and Thrust Belt (ZFTB in Fig. 1a) contains a 12-km thick sequence of sediments over an altered Precambrian basement (Stocklin, 1968), with several active reverse faults that accommodate surface folding (Jackson and Fitch, 1981). To the northeast of the Main Zagros Thrust Fault lies the Sanandaj-Sirjan zone (SSZ in Fig. 1a), a metamorphic region that extends northwestwards into Eastern Anatolia and becomes the East-West trending Bitlis metamorphic massif. To the northeast of the Sanandaj-Sirjan zone lies the Urmieh-Dokhtar magmatic Arc (UMDA in Fig. 1a), composed of intrusive magmatic rocks related to the Neotethys subduction and mostly emplaced during the Eocene (Alavi, 1994).

Further northeast, beyond the Alborz and Talesh mountains, lies the South Caspian Basin, a relatively aseismic rigid basement block that has affected the deformation history of the surrounding continental regions. The South Caspian Basin and the Kura depression to its west are thought to be a relic back-arc of the Tethyan Mesozoic subduction, or possibly a piece of unusually thick oceanic-like crust, trapped within a continental collision zone (Berberian, 1983; Mangino and Priestley, 1998; Brunet et al., 2003), similar to the Black Sea (Okay et al., 1994) and the eastern Mediterranean (de Voogd et al., 1992). Because of the South Caspian basin's low elevation and its southwest motion relative to central Iran, Talebian and Jackson (2002) and Allen et al. (2003) suggested that it underthrusts the Talesh and Alborz mountains on its western and southern margins. Accurate location of local seismicity along these margins by Aziz Zanjani et al. (2013) indicates that deep earthquakes beneath the Talesh mountain range only occur on its Caspian flank, implying that the underthrusting beneath the Talesh is not extensive.

Northwest Iran has experienced extensive volcanism throughout the Cenozoic and contains volcanic rocks that are Eocene to Quaternary in age. The Sahand and Sabalan volcanoes (Fig. 1a) are very large structures that dominate the Pliocene-Quaternary magmatic activity. The Eocene and Oligocene rocks of NW Iran are related to arc magmatism (e.g. Agard et al., 2011), while the late Miocene to Quaternary units are believed to have formed in a post-collisional setting and become progressively younger from West to East (Sengor and Kidd, 1979; Pang et al., 2013). The earliest post-collisional magmatism dated by Pang et al. (2013) occurred in the late Miocene (11 Ma) just east of Lake Urumieh, in the region of Sahand volcano, and was followed by eruptions in the late Miocene to Pliocene (6.5–4.2 Ma) and then farther east by eruptions at the Sabalan volcano in the Quaternary (<0.4 Ma).

3 Data Processing and Measurement

We measured Rayleigh-wave group velocity dispersion curves on both earthquake recordings and ambient seismic noise cross-correlations in Northwest Iran. We used 55 broad-band and mid-band stations (see Fig. 1b and Table S1): 32 operated by the Iranian Seismological Center (IRSC, affiliated with the Institute of Geophysics, University of Tehran) and 23 belonging to the International Institute of Earthquake Engineering and Seismology (IIEES, operated by the Iranian National Broadband Seismological Center).

3.1 Data processing

We collected vertical component seismograms (due to noisier signal and the misorientation issue in the horizontal components, documented for Iranian stations by Movaghari et al. (2021) with clear surface-waves at distances between 100 and 800 km from 103 $M>4.5$ earthquakes that occurred between 2012 and 2022. To equalise the sampling frequency and reduce computational time and storage, the data were decimated to 2 Hz. We detrended the signals, removed the instrument responses and filtered between 5 and 120 s period. We chose the lower limit of this filter to be able to make measurements at 10 s period to constrain the crustal structure without measuring too close the the fil-

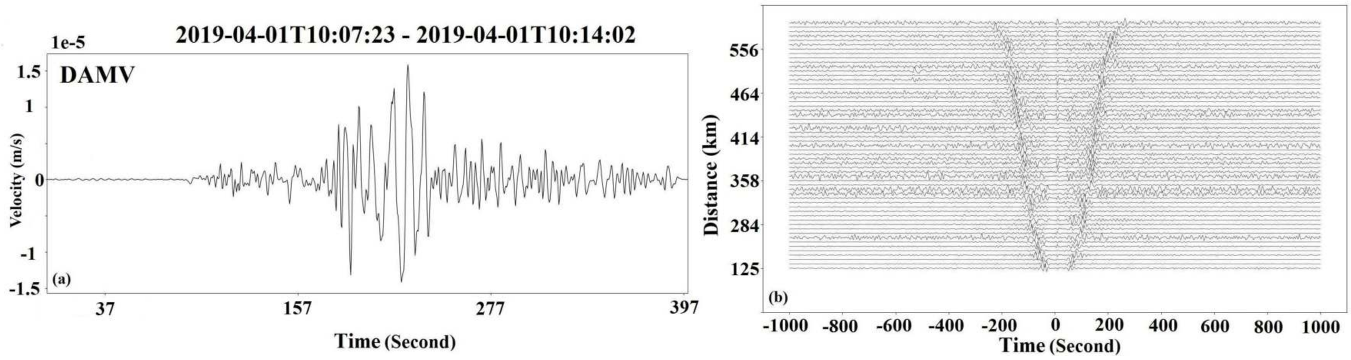

Figure 2 (a) Example of the vertical component of a seismogram (in velocity) used for dispersion measurements, filtered between 5 s and 120 s. Horizontal axes show time duration after origin time. The signal is detrended, decimated and station responses have been removed. Station names and times are shown. (b) Vertical two-sided noise correlation functions sorted by inter-station distance. The surface-wave move-out is between 2 and 4 km/s. Rayleigh-waves are observable at both positive (causal) and negative (acausal) lag times. Only the noise correlation functions with signal-to-noise ratios larger than 10 are plotted.

ter's edge; we chose its upper limit because of the inter-station distance (mean distance of 506 km) and the seismometer responses. We then visualised the waveforms and retained those with clear dispersed surface-waves. An example is shown in Fig. 2a.

We also collected continuous, vertical seismic records dating between January 2013 and December 2015 from 19 of the 55 available broad-band stations. Several of the broadband stations in the IRSC and IIEES networks were deployed after 2015 or at the end of 2014, so did not produce enough continuous data for our study. Moreover, some stations recorded part of the time as short-period stations and part of the time as broadband stations (instrument updates over the network). In some cases, we had insufficient coincident recording between two stations to cross-correlate and produce stable surface waves. We followed the procedures of Bensen et al. (2007), Lin et al. (2008), and Poli et al. (2012) to process continuous seismic noise data, and to extract Rayleigh-waves. We cut continuous data into one-day segments and decimated them to two samples per second. Then we removed the trend and instrument response from the daily segments and filtered them using a 5–120 s period band. We used a procedure similar to that of Zigone et al. (2015) to normalise the data and minimise the effects of transients and data irregularities: we cut the daily traces into 4-hour time windows then removed strong impulsive signals by discarding windows whose energy exceeded the daily average by over 30% and those with gaps over 10% of the total duration. We chose to remove signals based on 4-hour windows because there are often multiple aftershocks after larger impulsive earthquakes. We chose 30% for the daily average energy threshold by experimenting with a representative subset of our data: for larger values, some high amplitudes still remained in the signal and could perturb the correlations; for lower ones, windows without strong amplitudes started to be removed, reducing the overall amount of data available for correlation. We chose a 10% gap threshold to ensure that sufficient noise data was present in the selected windows before the computation of the correlation function. We then applied spectral-domain whitening between 5 and 120 s period and cut the processed data into one-hour windows to increase the speed of cross-correlation computation. Finally, we cross-correlated across all available station pairs and stacked the correlation functions over the fullest available time.

Fig. 2b shows the resulting stacked correlation functions sorted by inter-station distance. The amplitudes of the causal and a-causal parts are almost identical, indicating complete noise homogenisation over the three-year recording time. We averaged the two sides of each stacked correlation function to create one-sided symmetric correlation functions and evaluated their quality using the period-dependent signal-to-noise ratio: ratio of the peak amplitude of the narrow-band filtered surface-wave to the root-mean-square of the trailing noise. We defined the time window of the surface-wave signal by the arrival times at the maximum (4 km/s) and minimum (2 km/s) surface-wave velocities.

3.2 Dispersion Curve Measurements

We measured dispersion curves from seismograms and noise correlation functions in the same way. We excluded all paths with an epicentral or inter-station distance smaller than 100 km (approximately 3 wavelengths) to ensure a good sampling of the medium along the path and rejected noise correlation functions whose signal-to-noise ratios were lower than 5. We applied the automated multiple filter technique of Pedersen et al. (2003) to create the group-velocity dispersion diagrams, as shown in Figure 3. We selected the period range within which the maximum of the dispersion diagram corresponded to the fundamental mode Rayleigh-wave while rejecting all parts of the dispersion curves affected by scattered waves, multi-pathing effects, overtones, or persistent noise sources.

3.3 Data Uncertainties

Uncertainties are important in all tomographic inversions, but even more so for SOLA Backus-Gilbert inver-

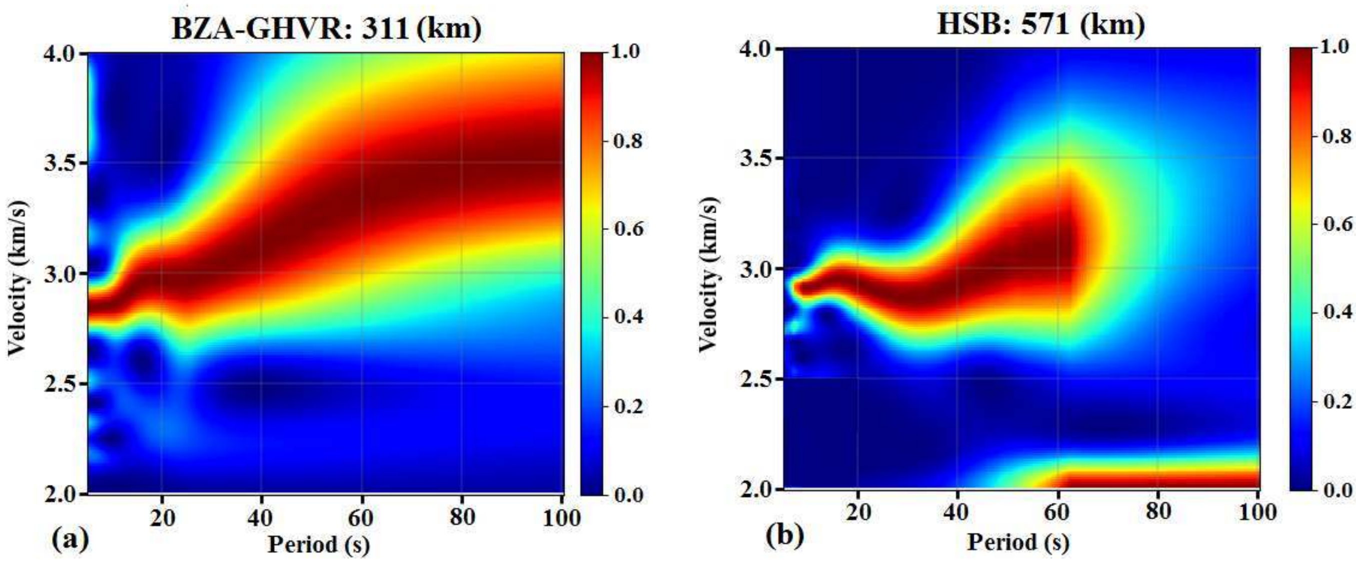

Figure 3 Examples of group-velocity dispersion diagrams for earthquakes and ambient seismic noise cross-correlations. Diagram (a) was measured from an earthquake waveform recorded at station HSB station at an epicentral distance of 571 km and related to the earthquake on 2020-04-29, 17:01:34; diagram (b) was measured from a noise correlation function for the station pair BZA-GHVR distant 311 km from each other. The color scale represents normalised energy. The maximum energy observed at different periods is indicated in red.

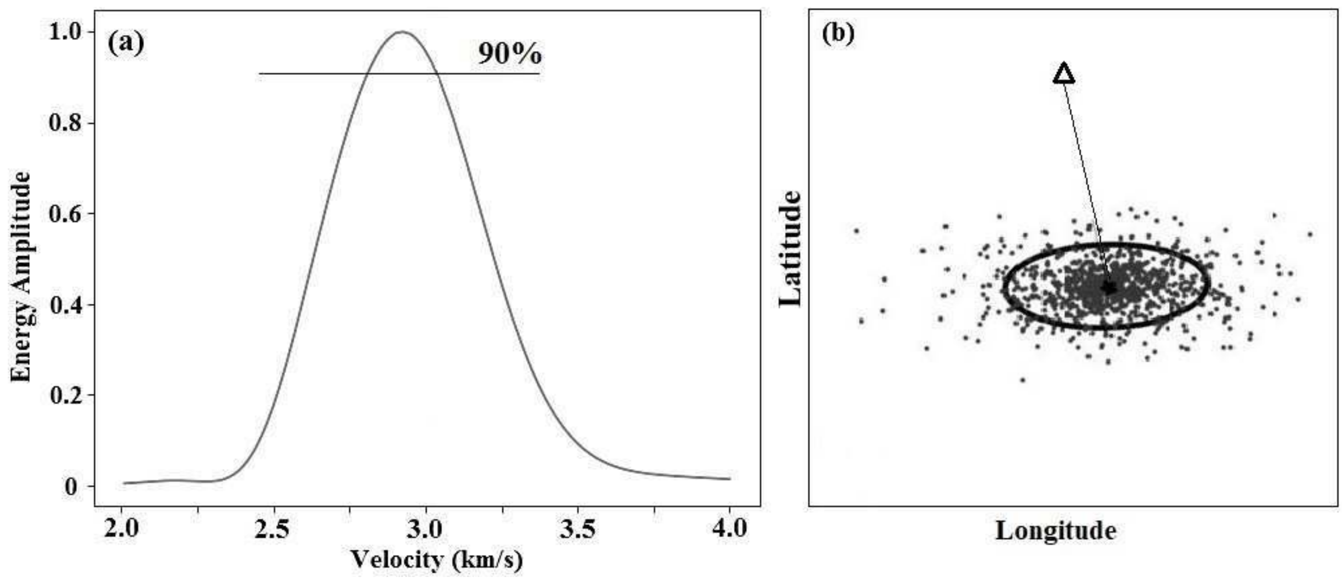

Figure 4 (a) From the dispersion diagrams in Fig. 3, we extract plots of energy versus velocity at a given period (in this example 50 s). We estimate the uncertainty of the velocity measurement from the range of velocities at which the seismic energy is at least 90% of that at the apex of the curve. (b) Schematic figure of the data error related to the location of the earthquake. The error ellipse is drawn around the exact location of the events and uniform points with Gaussian distribution surrounding it.

sions in which they trade-off directly with the model resolution. It is impossible to perform a meaningful SOLA Backus-Gilbert inversion without robust estimates of data uncertainties. We considered only the two largest sources of data uncertainties: those connected with measuring the maximum energy for each period on the group-velocity dispersion diagrams and those connected with the uncertainties in earthquake locations. For the ambient seismic noise cross-correlations measurements, only the first kind applies; for the earthquake measurements, both apply and are combined as independent errors.

To extract the group-velocity uncertainties from the dispersion diagrams, we used the strategy of Zigone et al. (2015) and Ouattara et al. (2019): we fit a Gaussian to the energy in the diagram at each period, picked the maximum of the fitted Gaussian as the group-velocity, and used the spread of the Gaussian at 90% of the max-

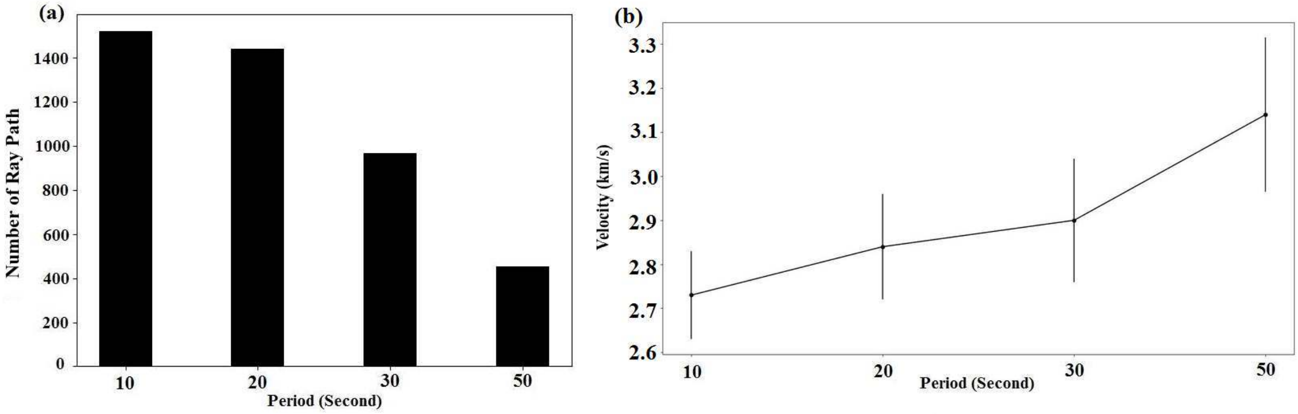

Figure 5 (a) The number of group-velocity measurements at periods of 10, 20, 30, and 50 s. (b) The average group-velocities at each period; the error bars show the average uncertainties of the measurements at each period.

imum to define the uncertainty (Fig. 4a). The uncertainty is half of the interval at 90% amplitude. Note that choosing the standard half-width of the fitted Gaussian would result in over-estimated uncertainties: Gaussian half-widths correctly estimate the uncertainty of a random variable with a normal distribution, but here we were trying to estimate the uncertainty of picking the maximum energy of an envelope.

To evaluate the contribution of the location uncertainties to the uncertainties in group-velocities, we used the latitude and longitude errors given by the International Institute of Earthquake Engineering and Seismology (IIEES) and Iran Seismological Center (IRSC) networks for each earthquake to plot an error ellipsoid around the hypocenter and drew points from the resulting 2D-Gaussian distribution (Fig. 4b). We used the distances from each of these points to the station to determine the distribution of the resulting group-velocity estimates; as this distribution was approximately Gaussian, we considered its σ value as the contribution of the location uncertainty to the group-velocity uncertainty.

We rejected group-velocity measurements with uncertainties larger than 0.35 km/s (approximately 10% of maximum observed velocity at 50s period). The resulting number of measurements per period and average group-velocities are shown in Fig. 5. Maps of the measured group velocities for each period are shown in Figure 6.

4 Tomographic Methods

We inverted the group-velocity measurements shown in Fig. 6 to produce maps of group velocities at periods of 10, 20, 30, and 50 s using two different tomographic methods: the Fast-marching surface-wave tomography method of Rawlinson and Sambridge (2005) and the SOLA Backus-Gilbert method of Zaroli (2016) and Zaroli et al. (2017). For detailed explanations of the two methods, we refer the reader to these publications. However, since the main objectives of this study are to compare the two methods using an identical dataset and explore their respective advantages and disadvantages, we present below an overview of how each method addresses the forward and inverse aspects of the tomographic problem.

4.1 Forward Problem

The forward problem is commonly expressed as the following path integral:

$$t_o = \int_{\text{path}} n(\mathbf{x})\, ds, \tag{1}$$

where t_o is the time taken by the seismic wave to travel along its path from source to receiver, $n(\mathbf{x})$ is the slowness (inverse of the velocity) of the seismic wave as a function of position, and s is a parametric variable that indicates the position along the path. Equation (1) is the integral form of the well-known eikonal equation that relates travel-times to the spatial distribution of slownesses. For group-velocity tomography, the equivalent formulation becomes

$$\frac{1}{U_o} = \frac{1}{L} \int_{\text{path}} \frac{ds}{U(\mathbf{x})}, \tag{2}$$

where U_o is the measured group-velocity, $U(\mathbf{x})$ is the group-velocity as a function of position, and L is the length of the path.

Equations (1) and (2) are linear in the integrands $n(\mathbf{x})$ and $1/U(\mathbf{x})$. If the position of the path is known in advance, then we can say that the whole tomographic forward problem is linear. However, seismic-wave paths have a non-linear relationship with the spatial distribution of seismic velocities. If the velocity anomalies are small, the ray path can be approximated by the great circle connecting the source and receiver. Otherwise, deviations from the great-circle path may be important and cannot be neglected.

Since the slowness distribution is unknown, tomographers assume a starting slowness model, then use an inverse method to update their model based on differences (residuals) between the measurements (in our case group-velocity measurements) and the predicted values. In the SOLA Backus-Gilbert tomographic inversion, only the slowness distribution is updated while the

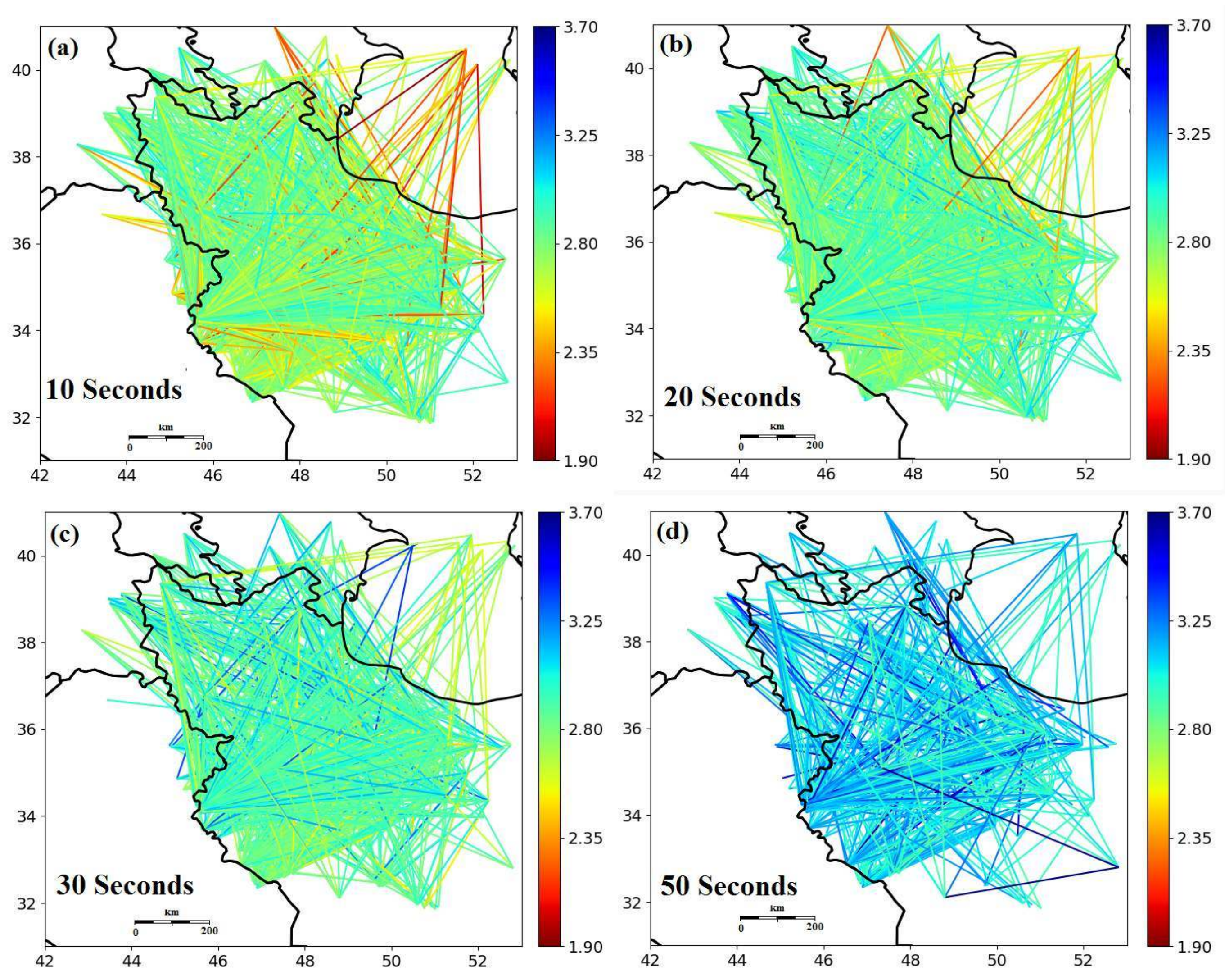

Figure 6 Path coverage of group-velocity measurements at periods of 10, 20, 30, and 50 s. Paths are colored by their respective group-velocity values.

ray path is fixed. In the Fast-marching tomographic inversion, the slowness distribution is updated first, then used to predict a new path that minimises the travel-time between source and receiver thanks to an eikonal solver (for more details on the workings of this specific eikonal solver, consult Rawlinson and Sambridge, 2005) and the process is repeated until the paths no longer move. As the path updates are a non-linear function of the slowness distributions, methods that perform such updates are termed non-linear-tomographic methods (amongst many examples, see Rawlinson and Spakman, 2016).

4.2 Inverse Problem

The inverse problem in seismic tomography consists in updating a starting slowness model m to minimise the residuals between the measurements and the corresponding predicted values. For simplicity, the following description assumes the slowness distribution is described by a set of values that represent slowness in a discrete set of geographical cells that span the region of interest. As the path is assumed to be known (albeit more or less accurately, as discussed above), we can write a discretised version of the integral expressions for the forward problem as the following matrix equation:

$$\mathbf{d} = \mathbf{G}\,\mathbf{m} + \mathbf{n}, \tag{3}$$

where $\mathbf{d}$ is a vector containing all measurements (in our case $1/U_i$ for the i'th path), $\mathbf{n}$ is a vector containing the noise on the measurements, $\mathbf{m}$ is a vector containing the slowness value in all cells (in our case $1/U_j$ for the j'th cell), and G is a matrix containing the length of each path in each cell (G_{ij} is the length of path i in cell j). An equivalent and more convenient formulation of the forward problem interprets $\mathbf{m}$ as corrections to the starting model and $\mathbf{d}$ as the residuals.

The point of inverse methods is to estimate the slowness (or the slowness perturbations) $\mathbf{m}$ as a function of the measurements (or measurement differences) $\mathbf{d}$. If the inverse method is linear, we can write the final slowness estimate as

$$\widetilde{\mathbf{m}} = \mathbf{G}^{-g}\,\mathbf{d}, \tag{4}$$

where $\mathbf{G}^{-g}$ is called the generalised inverse of $\mathbf{G}$ (Penrose, 1955). The process of estimating $\widetilde{\mathbf{m}}$ is complicated by many factors, including uncertainties in the measurements and uneven path coverage of the region lead-

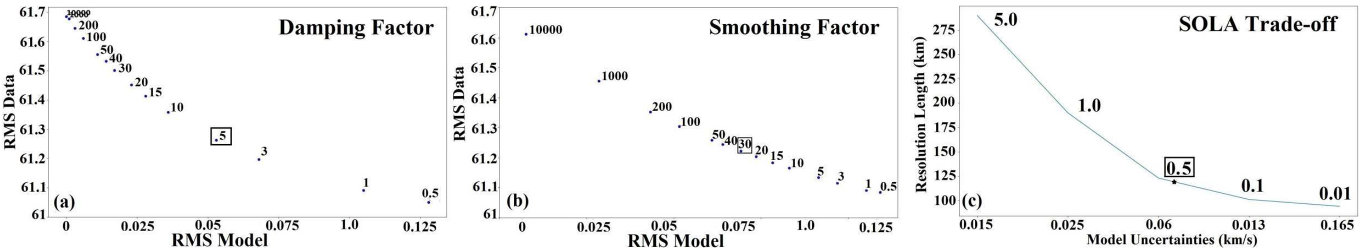

Figure 7 Trade-off curves (L-curves) for Fast-marching (a,b) and SOLA inversions (c). A trade-off between data residual and model variance for different values of the damping (a) and smoothing (b) parameters for the Fast-marching Surface-wave Tomography method. (c) A trade-off between average resolution and average uncertainty for the SOLA method for different values of the trade-off parameter η. The numbers in the boxes show the chosen trade-off value for the period of 10s.

ing to some cells being traversed by many independent paths and others by none at all. This led to the development of various inverse methods, each with its own advantages, disadvantages, and trade-offs. Some methods search for an appropriate slowness estimate $\widetilde{\mathbf{m}}$ by iteratively perturbing the prior slowness model without trying to construct the generalised inverse $\mathbf{G}^{-g}$, for example, the conjugate gradient method first proposed by Hestenes and Stiefel (1952) or the LSQR method developed by Paige and Saunders (1982); others try to estimate $\mathbf{G}^{-g}$ directly, for example the singular value decomposition method first proposed by Penrose (1955) and clarified by Lanczos (1961). If $\mathbf{G}^{-g}$ is estimated directly, we can combine equations (3) and (4) to obtain

$$\begin{aligned} \widetilde{\mathbf{m}} &= \mathbf{G}^{-g}(\mathbf{G}\,\mathbf{m} + \mathbf{n}) \\ &= \mathbf{R}\,\mathbf{m} + \mathbf{G}^{-g}\,\mathbf{n}, \end{aligned} \tag{5}$$

where $\mathbf{R} = \mathbf{G}^{-g}\,\mathbf{G}$ is called the resolution matrix. This shows that the slowness estimate is actually a weighted average of the true slowness perturbed by noise. For a single cell, for example the k'th cell, the estimated slowness is $\widetilde{m_k} = \sum_{j=1}^{M} R_{kj} m_j + \sum_{i=1}^{N} G_{k_i}^{-g} n_i$, where the k'th row of the resolution matrix $\mathbf{R}$ acts as an averaging operator called an averaging kernel by Backus and Gilbert (1968) and denoted $\mathbf{A}^{(k)}$.

Inverse methods can be split into two general categories, based on the trade-offs they use to stabilise the inversions. Most inverse methods trade fitting the measurements against prior beliefs about the slowness distribution (its smoothness, for example); we call such methods *data-fitting inversions* and they are often exemplified by, though not limited to, general least-squares inversions (e.g. Tarantola and Valette, 1982; Menke, 2015). Data fitting is the most intuitive inversion paradigm. The measurements force the model to update and where the measurements lack sensitivity or have large uncertainties, the model is not modified (e.g. Scales and Snieder, 1997). The Fast-marching surface-wave tomography method of Rawlinson and Sambridge (2005) fits into this paradigm and uses the subspace inversion method of Kennett et al. (1988) to minimise an objective function that includes the residuals, a damping factor that discourages changes in the starting model, and a smoothing factor that constrains the model smoothness.

Despite its intuitive appeal, data fitting is not the only inversion paradigm that exists. In the late 1960s, Backus and Gilbert introduced an inversion paradigm that constructed each row of the $\mathbf{G}^{-g}$ matrix independently by requiring an optimal resolution of the slowness distribution, and proved that the resulting distribution still fits the measurements (Backus and Gilbert, 1967, 1968). We call such methods *resolution-optimising inversions*, also known as *optimised local average* (OLA) methods. Although the Backus-Gilbert inversion paradigm can become numerically inefficient when the number of parameters and data is large and has been deemed difficult to apply to noisy data (Parker, 1994; Trampert, 1998; Nolet, 2008), it has been successfully applied to a few tomographic problems at scales ranging from local to global (e.g. Chou and Booker, 1979; Trampert and van Heijst, 2002; Bonadio et al., 2021). The comparatively small family of Backus-Gilbert inversion methods now contains a highly-efficient method first proposed in helioseismology (Pijpers and Thompson, 1993) then adapted to discrete and continuous tomographic inversions by Zaroli (2016), Zaroli et al. (2017), and Zaroli (2019): the SOLA (Subtractive Optimally Localised Average) Backus-Gilbert method. It estimates each row of $\mathbf{G}^{-g}$ by minimising an objective function that includes the difference between the averaging kernel $\mathbf{A}^{(k)}$ and a target kernel based on the path distribution, a trade-off factor called η that regulates the trade-off between resolution and uncertainties, and a condition that the sum of the values in the averaging kernel adds up to 1 (unimodular averaging kernels, the condition for obtaining unbiased model estimates).

4.3 Implementation Details

We used the Fast-marching Surface-wave Tomography (FMST) package developed by Rawlinson and Sambridge (2005) and the SOLA Backus-Gilbert code developed by Zaroli (2016) and Zaroli et al. (2017) and adapted to surface-wave tomography by Latallerie et al. (2022). We parameterised the slowness space in cells of 0.25° in latitude and longitude.

For the Fast-marching method we selected the values of the damping and smoothing factors of the subspace inversion by examining the trade-offs between data residual and model variance as shown in Fig. 7a,b (often called L-curves): the chosen values were 5 for the damping factor and 30 for the smoothing factor, each located near the elbow of its L-curve.

For the SOLA tomographic method we chose the tar-

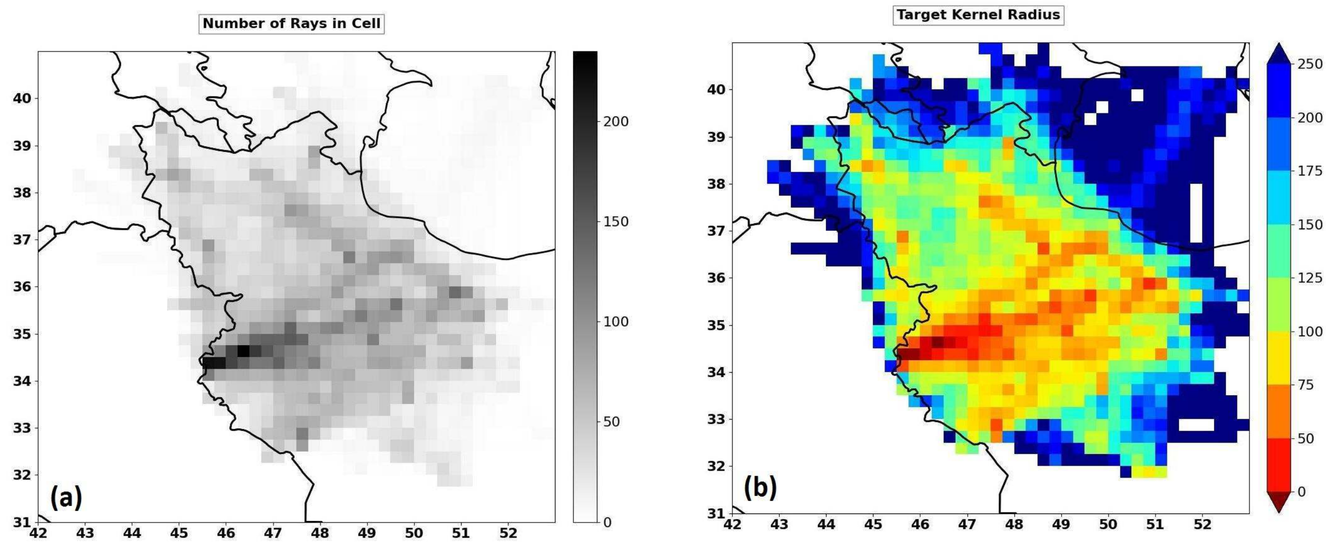

Figure 8 Path densities and SOLA target kernel radii at 10 s period. (a) The number of paths per 0.25° cell. (b) Radii of target kernels derived from the path densities using equation 6; cells containing no paths are masked in white.

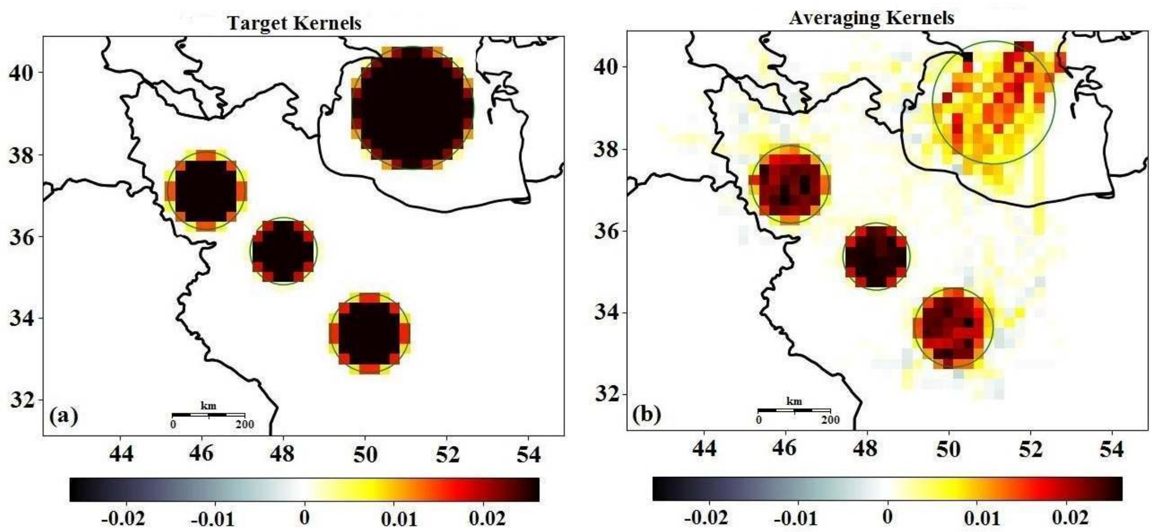

Figure 9 Target and averaging kernels for the SOLA inversion at 10 s period. (a) Circular target kernels at locations with different path densities. (b) Averaging kernels obtained after a SOLA inversion with $\eta = 0.4$.

get kernels for each cell to be circles whose radii depended on the logarithm of the path density (Zaroli et al., 2017; Latallerie et al., 2022):

$$r(\rho) = r_{\max} - (r_{\max} - r_{\min}) \left[\frac{\log(\rho - \rho_{\min})}{\log(\rho_{\max} - \rho_{\min})} \right], \quad (6)$$

where r is the target kernel radius, constrained to lie between $r_{\min}$ and $r_{\max}$, and ρ is the path density (sum of the columns of $\mathbf{G}$) whose minimum and maximum values are $\rho_{\min}$ and $\rho_{\max}$. We chose $r_{\min} = 50$ km and $r_{\max} = 250$ km, based on the dominant wavelengths and path lengths within the dataset. The path densities and target kernel radii are shown in Fig. 8. We selected the value of the trade-off parameter η between resolution and uncertainty of the SOLA inversion by examining the trade-offs between the average resolution length and the average model uncertainties as shown in Fig. 7c. Fig. **S3** of the Supplementary materials show tomographic models, uncertainty maps, and resolution lengths obtained using a range of η values.

Fig. 9 shows three target kernels and the corresponding averaging kernels produced by the SOLA inversion, projected onto the 0.25° grid. The size of the target kernels increases in regions of poor coverage and the shape of the averaging kernels shows potential smearing of information from outside the target kernel. As it would be unwieldy to plot averaging kernels for all points, in the following we summarise the size of the averaging kernel by a single number, the resolution length, which we take to be the mean of the semi-major and semi-minor axes of the ellipse that contains 68% of the averaging kernel (an approach roughly equivalent to that of Yanovskaya et al., 1998).

5 Results

Figure 10 shows Rayleigh-wave sensitivity kernels as a function of depth at various periods. Figures 11, 12, 13, and 14 show the group-velocity maps we obtained from our combined noise correlation and earthquake dataset using Fast-marching and SOLA tomographic approaches for periods of 10, 20, 30 and 50 s respectively. The figures also show the SOLA resolution lengths and uncertainties for each period.

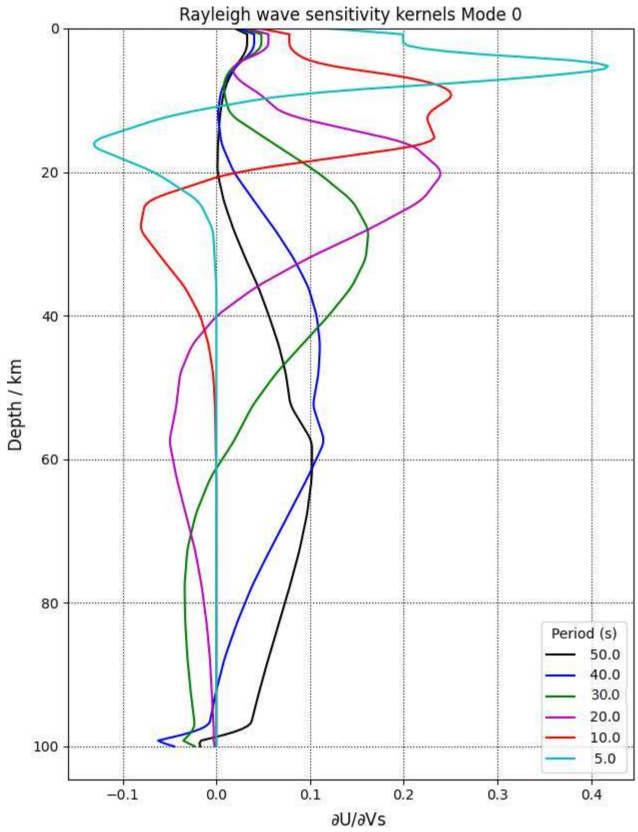

Figure 10 Sensitivity kernels of Rayleigh-wave group velocity at different periods.

5.1 Group velocities maps at 10 s period

At periods of 10 s, fundamental-mode Rayleigh-wave group velocities are expected to be primarily sensitive to the upper crust (Fig. 10). There is a strong correlation between the thick sedimentary basins of the upper crust and low short-period group velocities (e.g. Laske et al., 2013). Fig. 11 shows that the Fast-marching and SOLA maps share similar large-scale features though they differ in several details. Both maps contain high velocities along the Talesh mountains and the Sanandaj-Sirjan zone (SSZ in Fig. 11), sandwiched between low velocities in the South Caspian Basin and Kura Depression to the North and East and in Eastern Anatolia and the Zagros fault thrust belt (ZFTB in Fig. 11) to the South and West.

The slow velocities in the Caspian Sea basin and Kura Depression were observed in previous studies (e.g. Mortezanejad et al., 2019) and are related to thick, low-velocity sediments overlying lower crust thought to be oceanic in origin (Mangino and Priestley, 1998). The shape of these low-velocity anomalies seems to be more strongly smeared towards the southwest in the Fast-marching map than in the SOLA map.

The two maps also show a sharp velocity contrast along the boundary between the Sanadaj-Sirjan zone and the Zagros fault thrust belt. The fast group velocities of the Sandaj-Sirjan zone are related to its metamorphic Paleozoic-Cretaceous rocks, which show little to no surface sedimentation or volcanic activity. The low group velocities in the Zagros fold and thrust belt are related to weakening and fracturing on shallow and low-angle reverse faults because of intense deformation (Jackson and Fitch, 1981) and thick Meso-Cenozoic sediment cover (Mouthereau, 2011). The boundary between these two regions more clearly coincides with the main Zagros reverse fault (MZRF in Fig. 11) in the SOLA map than in the Fast-marching map. Both maps also show low velocities in the Urumieh-Dokhtar region (UMDA in Fig. 11) that in previous studies were attributed to volcanic and sedimentary rocks left by lava flows through pre-existing pyroclastic deposits (e.g. Mottaghi et al., 2013). The Fast-marching map shows a strong velocity contrast between this region and the Alborz mountains to the North, a contrast which is more attenuated in the SOLA map. In the lesser Caucasus, the SOLA map shows low group velocities north of the Sablan volcano that transition to high group velocities farther East, in the region of the Sabalan volcano; the low velocities are less pronounced in the Fast-marching map. The transition has been seen before and has been interpreted as a transition between warm magmatic rocks to colder ones (e.g. Zandi and Rahimi, 2020).

5.2 Group-velocities maps at 20 s period

At periods of 20 seconds, fundamental mode Rayleigh-wave group velocities are primarily sensitive to the average shear-wave velocity of the crust at depths up to 20-25 km (Fig. 10). Fig. 12 shows that the Fast-marching and SOLA maps have similar features to those at 10 s period, with fast velocities in the Sandaj-Sirjan zone flanked by lower velocities in the South Caspian Basin and the Zagros fault thrust belt. The strong low-velocities of the South Caspian and Kura basins visible in the Fast-marching map are elongated in the direction of the ray paths (Fig. 6), continuing to suggest these features may be both smeared and locally biased. The SOLA resolution lengths at 20 s period (Fig. 12c) are systematically larger than those at 10 s period (Fig. 11c), leading to SOLA maps that are smoother with less pronounced velocity contrasts.

5.3 Group-velocities maps at 30 s period

At periods of 30 seconds, fundamental mode Rayleigh-wave group velocities are expected to be primarily sensitive to the shear-wave velocity of the lower crust and uppermost mantle (Fig. 10). In continental regions, low group velocities at these periods indicate either a thick crust overlying a normal continental mantle lid or a normal crust overlying a weak lithospheric mantle, while high group velocities usually indicate a normal continental crust over a thick or oceanic-like mantle lid. Fig. 13 again shows similarities between the two maps, with stronger smearing in the South Caspian Basin region in the Fast-marching map. The low velocities in the Talesh region, visible in both images, may be related

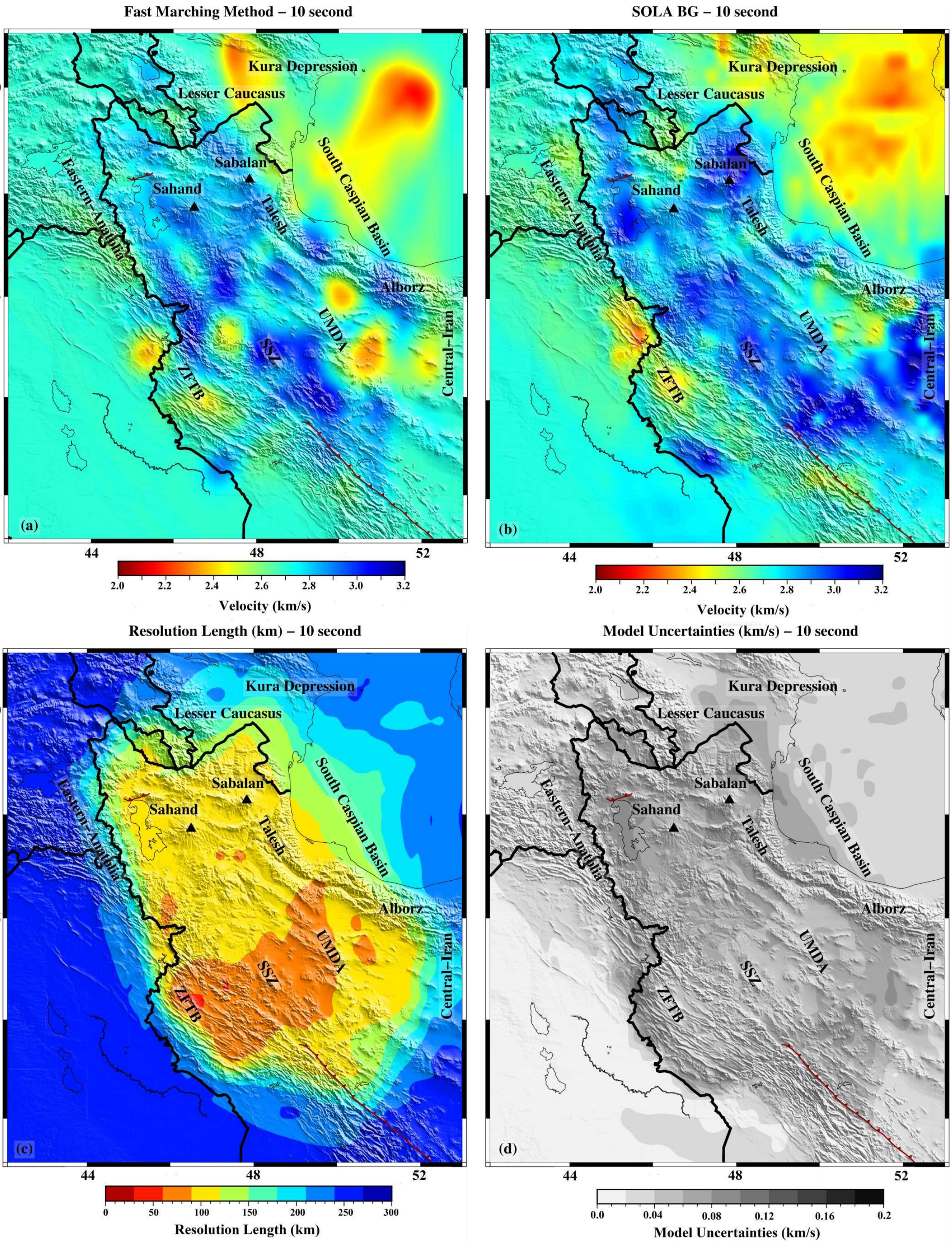

Figure 11 Tomographic results for group velocities at 10 s period. (a) Group velocity map obtained using Fast-marching tomography. (b) Group velocity map obtained using SOLA Backus-Gilbert tomography. (c) Resolution lengths and (d) model variances from the SOLA inversion.

to a thickening of the crust seen by Mortezanejad et al. (2013) and confirmed by receiver functions that show a Moho depth of 54 km compared to values of 46 km in the South Caspian Basin and 47 km in the rest of Northwest Iran (Mortezanejad et al., 2019). The high velocities in the Zagros fold and thrust belt, although visible in both models, are smaller than the SOLA resolution length. Previous studies of the region based on the Fast-marching method observed a similar high-velocity region under the belt that contrasts with slower velocities in the Sandaj-Sirjan zone. This correlates with crustal thickening from 38 km in the Zagros fold and thrust belt, to 54 km in the Sandaj-Sirjan zone, to 44 km in the Urumieh-Dokhtar region (Mortezanejad et al., 2019).

5.4 Group-velocities maps at 50 s period

At periods of 50 seconds, fundamental mode Rayleigh-wave group velocities are expected to be primarily sensitive to the shear-wave velocity of the uppermost man-

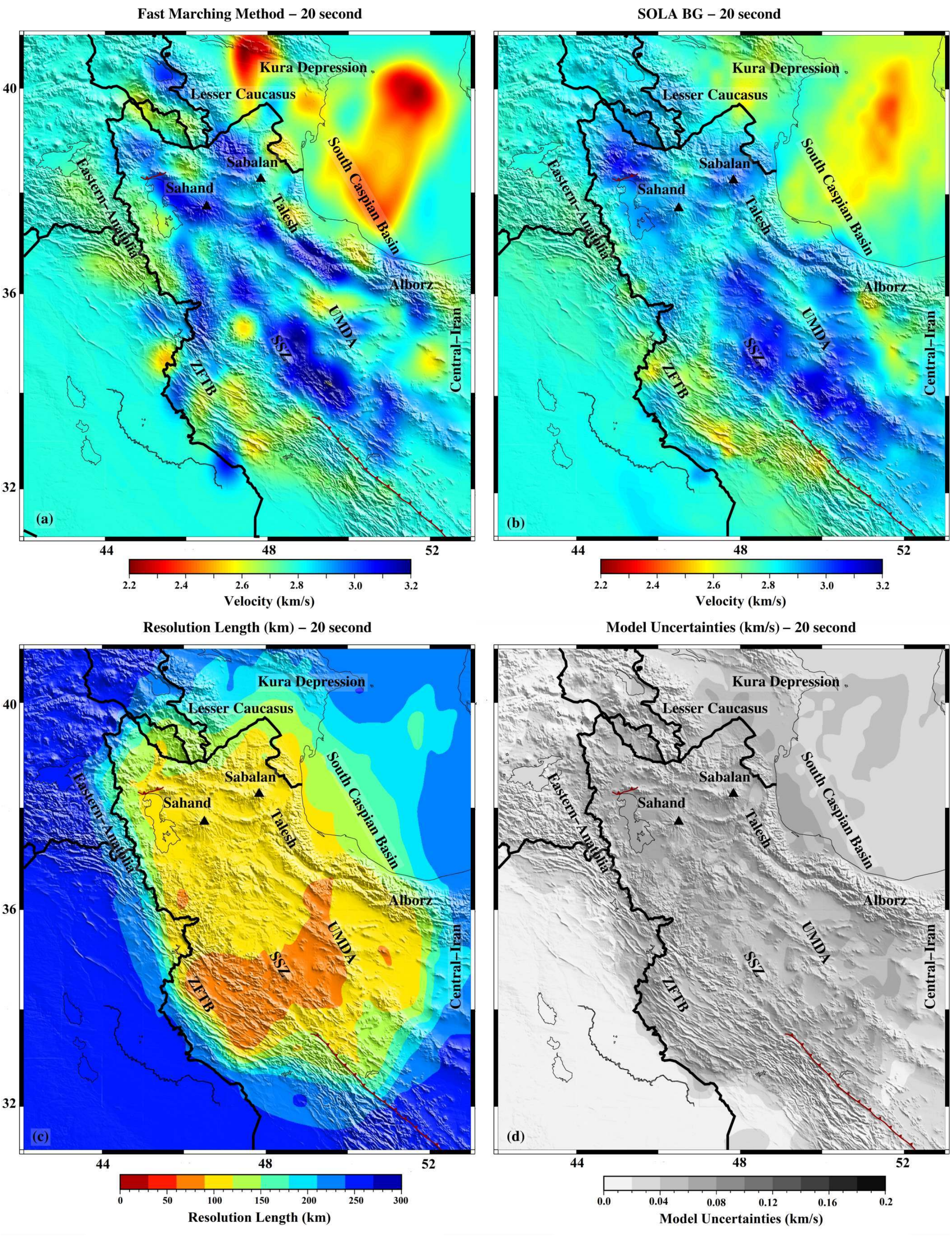

Figure 12 Tomographic results for group velocities at 20 s period. Panels as in Fig. 11.

tle (Fig. 10). Slow velocities at these periods are usually attributed to thin or absent lithosphere, while fast velocities are attributed to a stable continental mantle lid or to an oceanic lithosphere. Fig. 14 shows that Fast-marching and SOLA group-velocity maps both contain apparent short-wavelength structures, stronger and at smaller spatial scales in the Fast-marching map, that differ significantly between the maps. Disagreement between tomographic images is common when coverage is poor, as the priors imposed in the inversion act more strongly in the absence of data. The Fast-marching map contains three prominent features probably cased by smearing and/or local bias: the elongated slow velocities in the South Caspian Basin, the fast velocities that trend South-West from the Kura Basin, parallel to a group of paths with the same orientation seen in Fig. 6d; and the high velocity in Zagros fault and thrust belt (ZFTB). These artefacts are absent from the SOLA map. It is hard to reconcile the group-velocity maps in Fig. 14 with previous studies that find deeper lithosphere-asthenosphere boundaries beneath the Alborz and South Caspian Basin (Bavali et al., 2016), or a

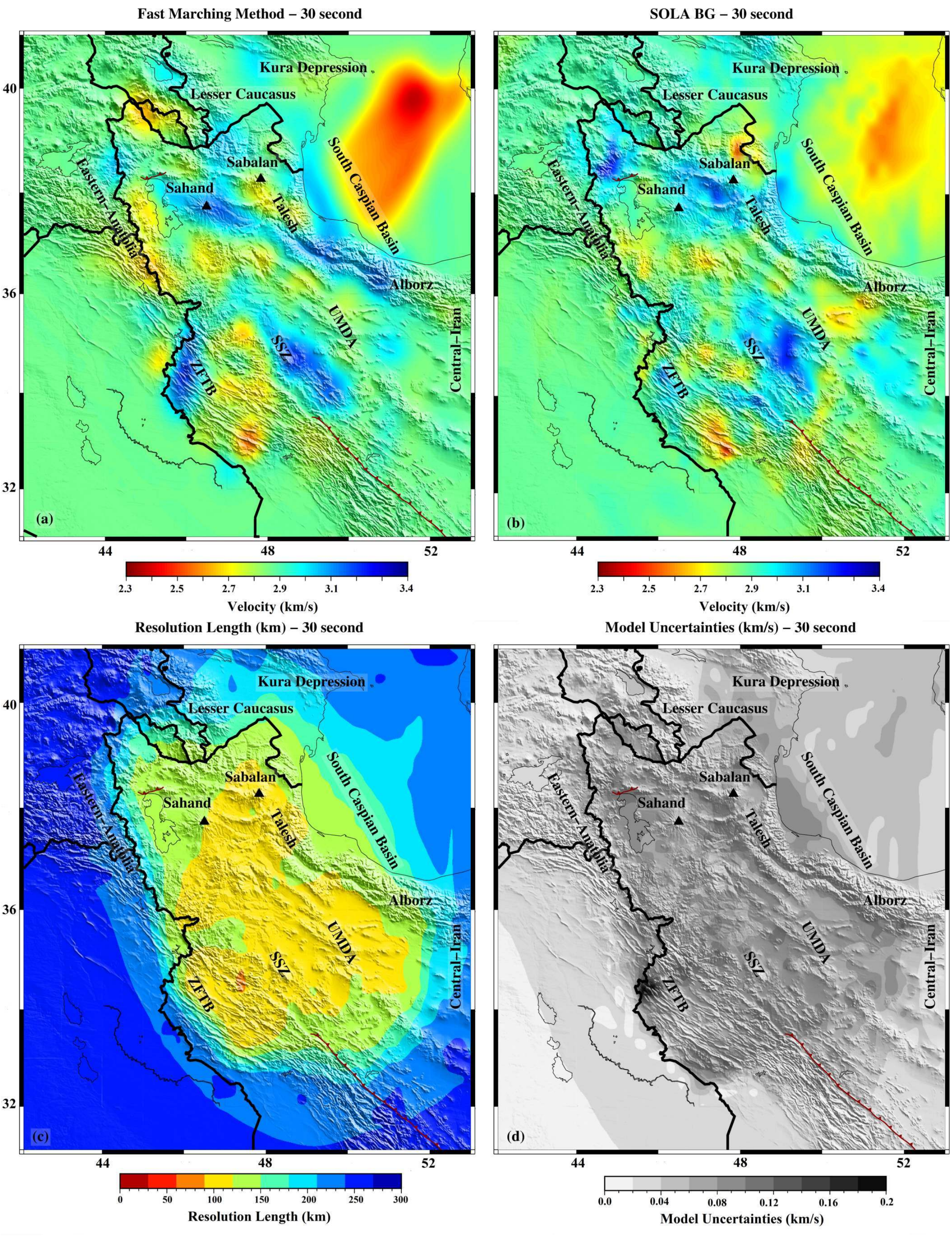

Figure 13 Tomographic results for group velocities at 30 s period. Panels as in Fig. 11.

thick high-velocity mantle lid under the Zagros and the South Caspian Sea (Mangino and Priestley, 1998), or that the lithosphere beneath the South Caspian Sea may underthrust the Talesh mountains (Mangino and Priestley, 1998; Bavali et al., 2016; Mortezanejad et al., 2019).

6 Discussion

We have constructed a dataset of fundamental mode group-velocity measurements from noise correlations and local/regional earthquakes in Northwest Iran and inverted them with two different techniques – Fast-marching and SOLA Backus-Gilbert – to obtain the group-velocity maps shown in Figs. 11 to 14. In the previous section, we attempted to compare the group-velocity maps produced by the two techniques to known geological features in the region seen by previous studies. Comparisons between tomographic images are notoriously difficult to make as their resolution and uncertainties differ. In our case, we know the resolution and uncertainties of the SOLA group-velocity map, but not those of the Fast-marching one. We have inferred

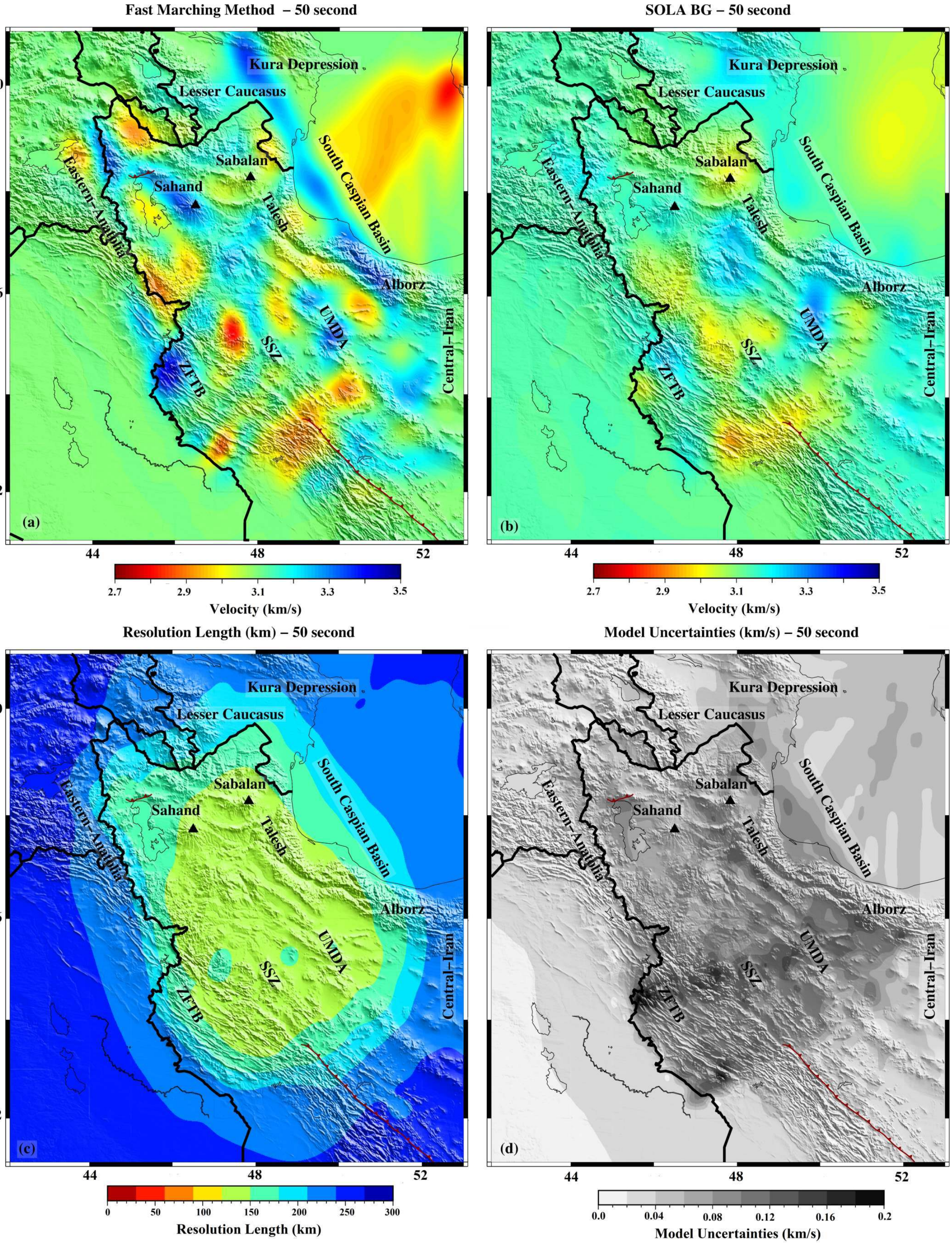

Figure 14 Tomographic results for group velocities at 50 s period. Panels as in Fig. 11.

several smearing artefacts and possible local bias in the Fast-marching maps by singling out regions with poor coverage where there is a convergence of paths, notably in the South Caspian Basin (g and h in Fig. 9) where the convergence is due to a few earthquakes on the Apscheron Sill that separates the northern and southern Caspian. Proving that these features are indeed artefacts requires careful construction of ad-hoc synthetic tests.

As the SOLA Backus-Gilbert tomographic inversion provides full-resolution and uncertainty information, we do not need to resort to such ad-hoc tests to identify robust features in the SOLA maps, but can follow a simple workflow proposed by Latallerie et al. (2022):

1. assume or construct a relevant reference model of seismic velocity to which we want to compare the tomographic images;
2. filter this reference model with the SOLA resolution to obtain the tomographic image that would be obtained if the Earth resembled the reference model;
3. subtract the filtered reference model from the

SOLA tomographic image to obtain an anomaly map;

4. divide the anomaly map by the SOLA uncertainties σ_m to obtain anomalies in "units" of σ_m;

5. mask regions where the anomalies are smaller than $\pm 1\sigma_m$ and/or $\pm 2\sigma_m$;

6. compare the sizes and shapes of the anomalies that remain with the resolution lengths and individual averaging kernels to spot unresolved regions and artefacts and identify significant anomalies for further analysis.

6.1 Anomaly analysis for SOLA group-velocity maps

Although the outcrop geology of Northwest Iran is well known (see section 2), transforming this geology into expected group-velocity maps at different periods requires making assumptions about the detailed shapes and seismic velocities of these geological bodies at depth. Although such an endeavor would be scientifically worthy, it falls outside of our team's expertise and would take this study outside of its seismological scope. Instead, we will take as our reference models uniform velocities equal to the average group-velocity measured at each period. Such uniform models remain uniform after filtering with the SOLA resolution because the averaging kernels (i.e. the rows of the resolution matrix) are constrained to be uni-modular (the sum of the averaging weights is equal to 1).

Figs 15 and 16 show the deviations of the SOLA tomographic maps from the uniform reference models in units of the model uncertainties, σ_m, with masks at $\pm 1\sigma_m$ (equivalent to a 68% confidence threshold) and $\pm 2\sigma_m$ (equivalent to a 95% confidence threshold) for regions traversed by at least 3 surface-wave paths. Simply identifying anomalies as exceeding $\pm\sigma_m$ or $\pm 2\sigma_m$ is not enough to declare them significant because even if the Earth were, in reality, identical to the reference model, we would still expect 32% of velocities to exceed $\pm\sigma_m$ and 5% of them to exceed $\pm 2\sigma_m$ because of how the measurement uncertainties propagate into model uncertainties. We could be justified in declaring anomalies to be significant only if more points than expected exceed the $\pm\sigma_m$ and $\pm 2\sigma_m$ thresholds, or if these points organised geographically in coherent regions and these anomalous regions could indeed be resolved by the tomography (anomalies larger than the resolving lengths) and showed no indication of smearing. This definition of significance is stricter than the one used in most tomographic studies and highlights the importance, when using SOLA, of correctly estimating the data uncertainties that feed into the estimates of σ_m.

At 10 s period (Fig. 15a,b), 42% of cells in the image exceed $\pm 1\sigma$ and 27% exceed $\pm 2\sigma$; the relevant resolution lengths and σ values are found in Fig. 11c,d. The large, slow anomaly in the Caspian basin is significant at both the 1 and 2-σ thresholds and its size (largest dimension ~ 100 km$\times 300$ km) is of a similar order as the resolution length (radius of 125-225 km). It shows some smearing in the NE-SW direction, following the dominant direction of the paths (Fig. 6); to verify this smearing hypothesis, we can examine the target and averaging kernels at the same location (Fig. 9), which indeed show evidence of low amplitude recovery and smearing along the same direction. We can conclude that the Caspian Basin is indeed significantly slower than the rest of the region, and is probably even slower than indicated in Fig. 11b. Without detailing the full analysis for each of the features visible in the 10 s period maps, we can be confident in the high velocities shown in the Sanandaj-Sirjan Zone and their contrast with the slower velocities of the Zagros Fold and Thrust Belt, at least in the ~ 100 km either side of the Iran-Irak border; the higher velocities under the Sabalan volcano also seem significant and well-resolved. However, many of the small scale features in the Talesh and Alborz mountains may be too small to be correctly resolved; should we be interested in resolving them in the future, we would need to improve the data coverage in this region.

At 20 s period (Fig. 15c,d), 38% of cells in the image exceed $\pm 1\sigma$ and 23% exceed $\pm 2\sigma$; the relevant resolution lengths and σ values are found in Fig. 12c,d. The Caspian Basin is again significantly slower than average, with the same smearing problem. The contrast between the high velocity Sanandaj-Sirjan Zone and the low-velocity Zagros Fold and Thrust Belt seems again both significant and well-resolved, as do the high velocities under the Sabalan volcano and in the northwesternmost corner of Iran, north of the North Tabriz Fault and the Urumia lake.

At 30 s period (Fig. 16e,f), 22% of cells in the image exceed $\pm 1\sigma$ and 13% exceed $\pm 2\sigma$; the relevant resolution lengths and σ values are found in Fig. 13c,d. The resolution lengths are systematically larger than for the 10 and 20 s maps (compare Fig. 13c with Figs. 11c and 12c) and there are few anomalies that seem well-resolved and significant at the 2σ level, with the exception of the high-velocity anomaly sandwiched between the Sanandaj-Sirjan Zone end the Urumieh-Dokhtar Magmatic Arc.

At 50 s period (Fig. 16g,h), 14% of cells in the image exceed $\pm 1\sigma$ and around 5% exceed $\pm 2\sigma$; the relevant resolution lengths and σ values are found in Fig. 14c,d. Here, we no longer have any well-resolved anomalies that are significant at the 2σ level, meaning that interpreting the group-velocity variations at this period (Fig. 14a,b) would probably be meaningless. Should we be interested in the deeper structure of this region, therefore, we would need to improve the data coverage and also reduce the uncertainties in the measurement of group-velocity dispersion at long periods.

6.2 Fast-marching vs SOLA

We have observed that having full-resolution and uncertainty information allows us to visualise robust anomalies and identify artefacts. We have also seen that the Fast-marching method – more precisely the subspace inversion method used by the Fast-marching tomographic implementation we used here (Rawlinson and Sambridge, 2005) – did not provide this information and so limited our capacity to compare rigorously its re-

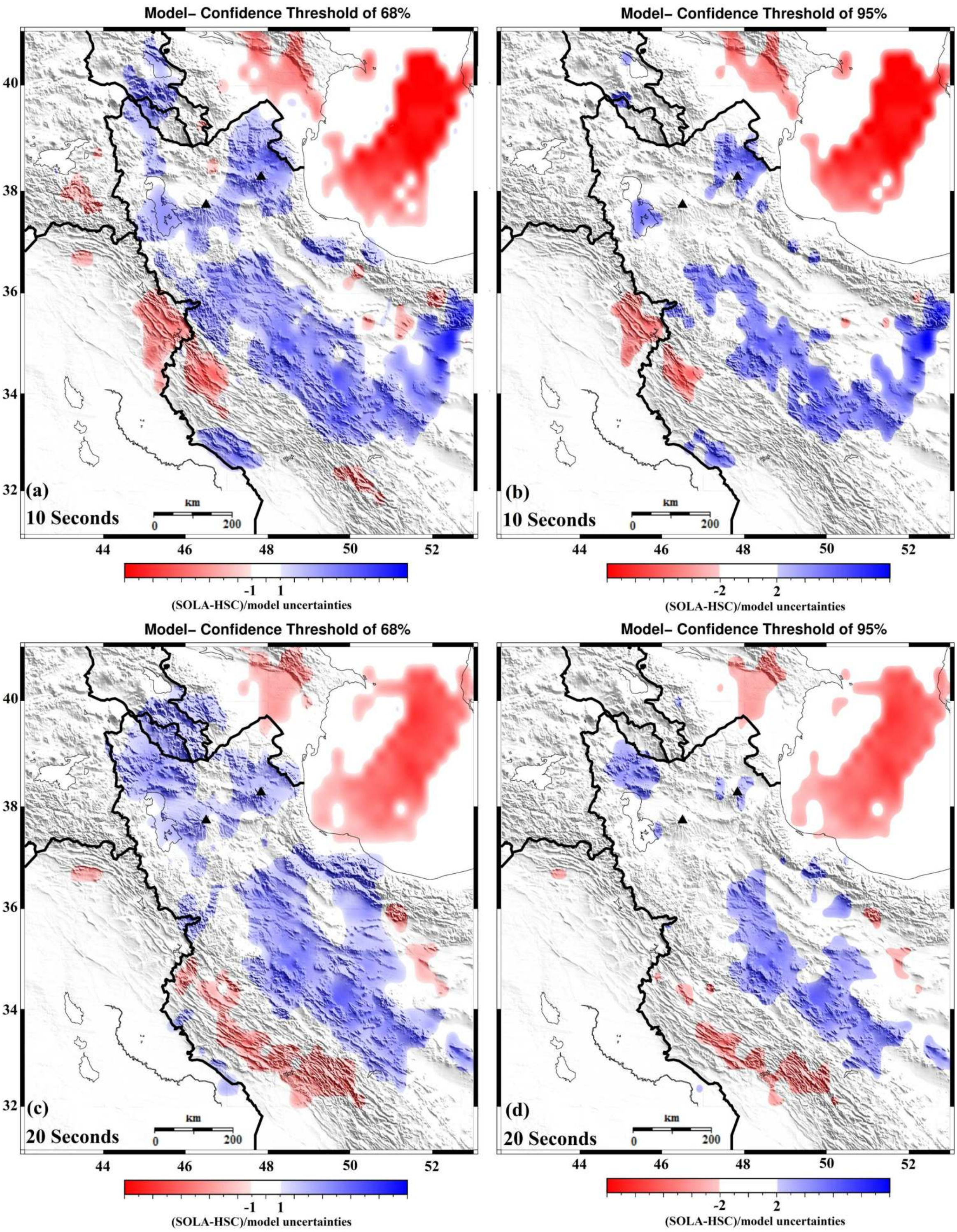

Figure 15 Group-velocity anomalies scaled by the SOLA uncertainties σ_m at periods of 10 and 20 s. (a), (c), are masked at $\pm 1\sigma_m$; (b), (d), are masked at $\pm 2\sigma_m$. We masked all cells with fewer than three rays passing through them.

sults with the SOLA results. Despite this, we do not believe that the current implementation of SOLA Backus-Gilbert tomography is necessarily the best method to use in all cases.

All tomography is data-driven: if the sensitivity of the data does not cover adequately the target region, tomographic studies that attempt to achieve resolutions finer than those compatible with the data coverage will produce images that are unreliable, while those that limit themselves to the resolution compatible with the data coverage will produce images that are uninformative, as this resolution is too poor to give meaningful information. On the other hand, we expect that where data coverage is sufficient and the forward tomographic problem ($\mathbf{G}$ in equation 3) identical at each iteration, then any well-implemented tomographic inversion should produce similar features. The relevance of these features could be analysed in detail if the inversion also provided resolution and uncertainty information at a reasonable computational cost.

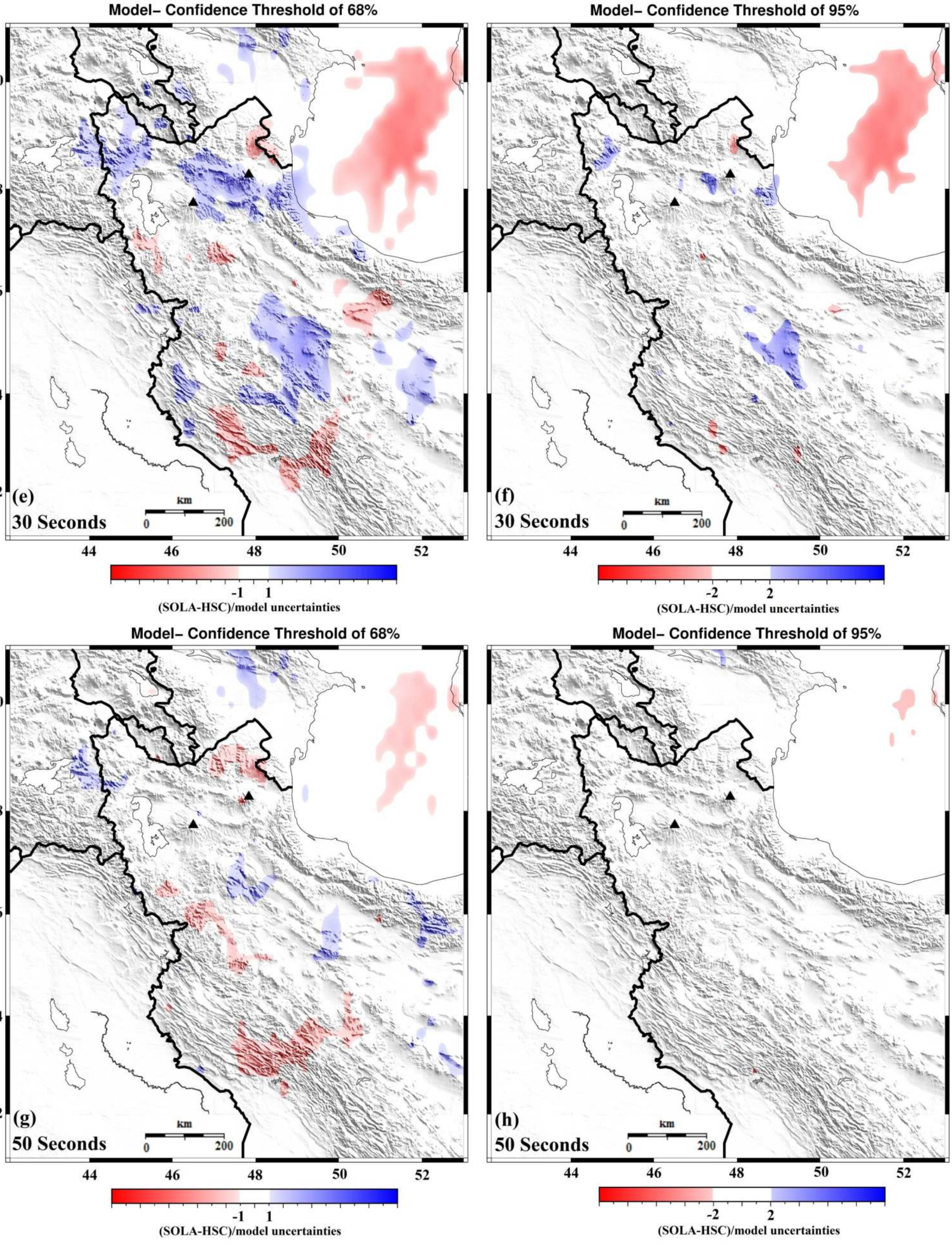

Figure 16 Group-velocity anomalies scaled by the SOLA uncertainties σ_m at periods of 30, and 50 s. (e) and (g) are masked at $\pm 1\sigma_m$; (f) and (h) are masked at $\pm 2\sigma_m$. We masked all cells with fewer than three rays passing through them.

Therefore, where data coverage is good, both data-fitting schemes and resolution-fitting tomographic inversion schemes should provide similar fits to the data and similar model resolutions and uncertainties. In such cases, it might be useful to choose the implementation of the forward problem (constructing $\mathbf{G}$ in equation 3) that is most adapted to the expected velocity or slowness variations of the region being studied. In particular, if we expect strong contrasts such as those created by geological units of different types, forward schemes that allow ray paths to adapt to the heterogeneous velocity or slowness distributions would be likely to allow the inversion to converge on tomographic models that are more similar to the true Earth compared to simpler forward schemes that predict straight ray paths and do not update them, such as the one implemented in the context of the SOLA Backus-Gilbert inversion we used here.

However, where data coverage is poor, we expect the implementation of the inverse problem to be a strong

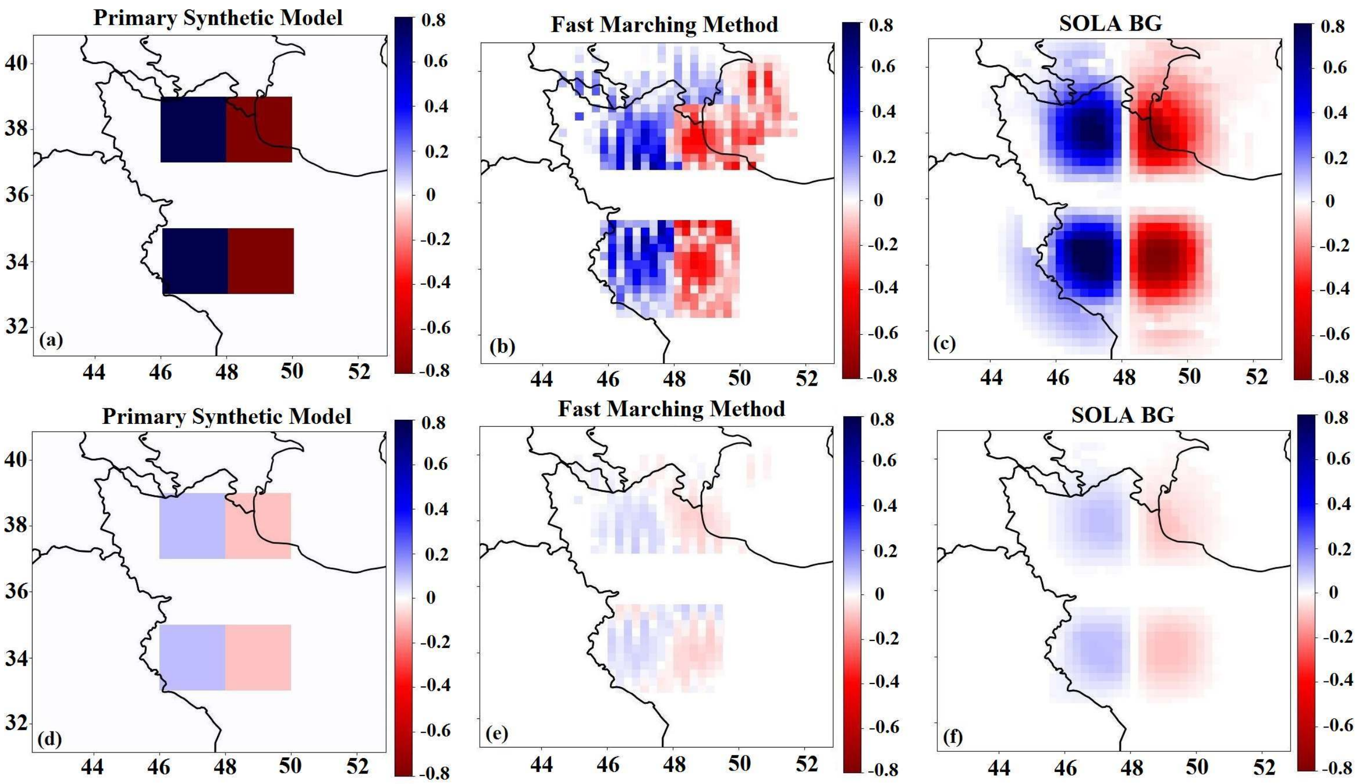

Figure 17 Synthetic tests for different regions. (a) and (d) are unfiltered synthetic model with sharp and weak anomaly contrasts, respectively. (b) and (e) are filtered models with Fast-marching method. (c) and (f) are filtered model with SOLA Backus-Gilbert. The ray-coverage used corresponds to the 20 s coverage from Fig. 6.

predictor of the quality of the final tomographic model. In particular, we expect that having the ability to influence the resolution, either indirectly through irregular parameterisation (Curtis and Sieder, 1997; Trampert, 1998; Bijwaard et al., 1998; Sambridge and Gudmundsson, 1998; Alinaghi et al., 2007) or directly using a Backus-Gilbert type inversion (Backus and Gilbert, 1968; Trampert and van Heijst, 2002; Zaroli, 2016; Bonadio et al., 2021; Latallerie et al., 2022) as we did here, would limit smearing and local bias artefacts. If full-resolution and uncertainty information are also available, then we could extract robust inferences from the tomographic models, know exactly how informative or uninformative they are, and spot artefacts.

If we apply this reasoning to the two tomographic methods we used in this study, we would expect Fast-marching to outperform (produce a more-interpretable seismic image with fewer smearing artefacts and/or better resolution of velocity contrasts) SOLA where velocity contrasts are strong and data coverage is good, for SOLA and Fast-marching to give equivalent results where velocity contrasts are weak and data coverage is good (in such cases the advantage may still go to SOLA because it constrains the resolution to neighboring areas and produces full-resolution and uncertainty information), and for SOLA to outperform Fast-marching where data coverage is poor, regardless of velocity contrasts. We tested this expectation with a series of synthetic tests based on the 20 s ray-coverage from Fig. 6: Fig. 17 shows strong and weak velocity contrasts in regions of poor ray-coverage (northern parts of Fig. 17a,d) and good ray-coverage (southern parts of Fig. 17a,d). The only case in which the Fast-marching inversion outperforms the SOLA inversion is indeed for the strong anomaly contrast in a good coverage region (southern part of Fig. 17b); in all other configurations, the SOLA inversion produces more coherent anomalies with fewer artefacts.

7 Conclusion

We have assembled a data-set of group-velocity measurements from ambient noise cross-correlations and earthquakes that cover Northwest Iran. Using this data-set, we have produced group-velocity maps using two tomographic techniques: the Fast-marching method of Rawlinson and Sambridge (2005) and the SOLA Backus-Gilbert approach of Zaroli (2016). We have compared them with each other and with known geological features in the region. Thanks to the resolution and uncertainty information provided by the SOLA inversion, we were able to single out robust features of the tomographic maps – for example the high velocities at short period (shallow depth) shown in the Sanandaj-Sirjan Zone and their contrast with the slower velocities of the Zagros Fold and Thrust Belt (Figs 15 and 16). We were also able to show that the SOLA method allows us to minimise artefacts caused by poor coverage and identify any ones that do remain.

Although the advantages of the SOLA Backus-Gilbert method for suppressing artefacts and allowing robust interpretation are clear and significant, the SOLA method as currently implemented (without path updating) may not produce the best tomographic images of regions with strong seismic-velocity contrasts and good data coverage. In such situations, the Fast-marching method may produce superior images albeit without the resolution and uncertainty information required for their robust interpretation. We suggest it could be advantageous to add path-updating capability to the SOLA Backus-Gilbert method, provided the uncertainties can be correctly estimated and the resolution correctly taken into account at each iteration.

Acknowledgements

The authors thank anonymous reviewers for their insightful comments that helped improve the manuscript, as well as the handling editor Suzan van der Lee. We would like to express our gratitude to Franck Latallerie who shared generously his experience in working with the SOLA Backus-Gilbert code. We wish to thank Ramin Movaghari (Southern University of Science and Technology, China) and Taghi Shirzad (Institute of Geophysics, Polish Academy of Sciences, Poland) for their useful comments and suggestions during the signal processing part of this work. Christophe Zaroli acknowledges the High-Performance Computing Center of the University of Strasbourg for supporting this work by providing scientific support and access to computing resources.

Data and code availability

All data used in this study are freely available. The continuous seismic data and raw earthquake data were provided by the Iranian Seismological Center (IRSC, http://irsc.ut.ac.ir/) and the International Institute of Earthquake Engineering and Seismology (IIEES, http://epp.iiees.ac.ir/datarequest/) to the corresponding author. The processed data and codes that support the findings of this study are available from the corresponding author (https://doi.org/10.5281/zenodo.8004726). The Fast-marching surface-wave tomography (FMST) package developed by Nick Rawlinson is available at http://iearth.edu.au/codes/FMST/ and we used http://rses.anu.edu.au/~nick/surftomo.html to obtain 2D Rayleigh-wave dispersion maps of the Iran plateau. The SOLA tomography code we use in this study consists in running the LSQR algorithm of Paige and Saunders (1982) with specific input matrix and vectors. These inputs can be constructed from the (study-dependent) sensitivity matrix and target kernels (denoted by G and T in this study) as detailed in the appendix A1 of Zaroli (2016). The LSQR code (Paige and Saunders, 1982) is freely downloadable on the web page of the Systems Optimisation Laboratory (Stanford University): https://web.stanford.edu/group/SOL/software/lsqr/. For those who prefer a pre-constructed software package for SOLA tomography, one is is available from Christophe Zaroli (c.zaroli@unistra.fr) upon e-mail request.

Competing interests

The authors have no competing interests.

References

Agard, P., Omrani, J., Jolivet, L., Whitechurch, H., Vrielynck, B., Spakman, W., Monie, P., Meyer, B., and Wortel, R. Zagros orogeny: a subduction-dominated process. *Geological Magazine*, 148(5-6):692–725, 2011. doi: 10.1017/S001675681100046X.

Al-Lazki, A., Seber, D., Sandvol, E., Turkelli, N., Randa, M., and Barazangi, ⊠ Tomographic Pn velocity and anisotropy structure beneath the Anatolian plateau (eastern Turkey) and the surrounding regions. *Geophysical Research Letters*, 24, 2003. doi: 10.1029/2003GL017391.

Alavi, M. Tectonics of the zagros orogenic belt of iran: new data and interpretations. *The International Journal of Integrated Solid Earth Sciences-Tectonophysics*, 229(3-4):211–238, 1994. doi: 10.1016/0040-1951(94)90030-2.

Alinaghi, A., Koulakov, I., and Thybo, H. Siemic tomographic imaging of P- and S-waves velocity perturbations in the upper mantle beneath Iran. *Geophysical Journal International*, 169: 1089–1102, 2007. doi: 10.1111/j.1365-246x.2007.03317.x.

Allen, M. B., Vincent, S., Alsop, G., Ismailzadeh, A., and Flecker, R. Late Cenozoic deformation in the South Caspian region: effects of a rigid basement block within a collision zone. *The International Journal of Integrated Solid Earth Sciences-Tectonophysics*, 366(3-4):223–239, 2003. doi: 10.1016/S0040-1951(03)00098-2.

Amini, S., Shomali, Z., Koyi, H., and Roberts, R. Tomographic upper-mantle velocity structure beneath the Iranian Plateau. *Tectonophysics*, 2012. doi: 10.1016/j.tecto.2012.06.009.

Aziz Zanjani, A., Ghods, A., Sobouti, F., Bergman, E., Mortezanejad, G., Priestley, K., Madanipour, S., and Rezaeian, M. Seismicity in the western coast of the South Caspian Basin and the Talesh Mountains. *Geophysical Journal International*, 195(2):799–814, 2013. doi: doi.org/10.1093/gji/ggt299.

Backus, G. E. and Gilbert, F. Numerical Applications of a Formalism for Geophysical Inverse Problems. *Geophysical Journal International*, 13(1-3):247–276, 1967. doi: 10.1111/j.1365-246X.1967.tb02159.x.

Backus, G. E. and Gilbert, F. The Resolving Power of Gross Earth Data. *Geophysical Journal International*, 16(2):169–205, 1968. doi: 10.1111/j.1365-246X.1968.tb00216.x.

Bavali, K., Motaghi, K., Sobouti, F., Ghods, A., Priestley, K., and Mortezanejad, G. Lithospheric structure beneath NW Iran using regional and teleseismic travel-time tomography. *Physics of the Earth and Planetary Interiors*, 253:97–107, 2016. doi: 10/1016/j.pepi.2016.02.006.

Bensen, G. D., Ritzwoller, M. H., Barmin, M. P., Levshin, A. L., Lin, F., Moschetti, M. P., Shapiro, N. M., and Yang, Y. Processing Seismic Ambient Noise Data to Obtain Reliable Broad-Band Surface Wave Dispersion Measurements. *Geophysical Journal International*, 169(3):1239–1260, 2007. doi: 10.1111/j.1365-246x.2007.03374.x.

Berberian, M. The Southern Caspian: A Compressional Depression Floored by a Trapped, Modified Oceanic Crust. *Canadian Journal of Earth Sciences*, 20:163–183, 1983. doi: 10.1139/e83-015.

Bijwaard, H., Spackman, W., and Engdahl, E. R. Closing the gap between regional and global travel time tomography. *Journal of Geophysical Research*, 103:30055–30078, 1998. doi: 10.1029/98jb02467.

Bonadio, R., Lebedev, S., Meier, T., Arroucau, P., Schaeffer, A. J., Licciardi, A., Agius, M. R., Horan, C., Collins, L., O'Reilly, B. M., Readman, P. W., and Group, I. A. W. Optimal resolution tomography with error tracking and the structure of the crust and upper mantle beneath Ireland and Britain. *Geophysical Journal International*, 226:2158–2188, 2021. doi: 10.1093/gji/ggab169.

Brunet, M.-F., Korotaev, M. V., Ershov, A. V., and Nikishin, A. M. The South Caspian basin : a review of its evolution from subsidence modelling. *Sedimentary Geology*, 156(1-4):119–148, 2003. doi: 10.1016/S0037-0738(02)00285-3.

Chou, C. W. and Booker, J. R. A Backus-Gilbert approach to inversion of travel-time data for three-dimensional velocity structure. *Geophysical Journal International*, 59:325–344, 1979. doi: 10.1111/j.1365-246x.1979.tb06770.x.

Curtis, A. and Sieder, R. Reconditioning inverse problems using the genetic algorithm and revised parameterization. *Geophysics*, 62: 1524–1532, 1997. doi: 10.1190/1.1444255.

de Voogd, B., Truffert, C., Chamot-Rooke, N., Huchon, P., Lallemant, S., and Le Pichon, X. Two-ship deep seismic soundings in the basins of the Eastern Mediterranean Sea. *Geophysical Journal International*, 109(3):536–552, 1992. doi: 10.1111/j.1365-246X.1992.tb00116.x.

Deal, M. and Nolet, G. Comment on "Estimation of resolution and covariance for large matrix inversions" by J. Zhang and G.A. McMechan. *Geophysical Journal International*, 127:245–250, 1996. doi: 10.1111/j.1365-246x.1996.tb01548.x.

Ditmar, P. and Yanovskaya, T. Generalization of Backus-Gilbert Method for estimation of lateral variations of surface wave velocities. *Physics of the Solid Earth, Izvestia Acad. Sci. USSR*, 23: 470–477, 1987.

Farrokhi, M., Hamzehloo, H., Rahimi, H., and Allamehzadeh, M. Estimation of Coda-Wave Attenuation in the Central and Eastern Alborz, Iran. *Bulletin of the Seismological Society of America*, 105: 1756–1767, 2015. doi: 10.1785/0120140149.

Forrokhi, M., Hamzehloo, H., Rahimi, H., and Zadeh, M. Separation of intrinsic and scattering attenuation in the crust of central and eastern Alborz region, Iran. *Physics of the Earth and Planetary Interiors*, 253:88–96, 2016. doi: 10.1016/j.pepi.2016.02.005.

Gök, R., Sandvol, E., Turkelli, N., Seber, D., and Barazangi, M. Sn attenuation in the Anatolian and Iranian plateau and surrounding regions. *Geophysical Research Letters*, 30, 2003. doi: 10.1029/2003gl018020.

Hearn, T. and Ni, J. Pn Velocities Beneath Continental Collision Zones: the Turkish-Iranian Plateau. *Geophysical Journal International*, 117:273–283, 1994. doi: 10.1111/j.1365-246x1994.tb03931.x.

Hestenes, M. R. and Stiefel, E. Methods of conjugate gradients for solving linear systems. *Journal of Research of the National Bureau of Standards*, 49:409–436, 1952.

Irandoust, M., Sobouti, F., and Rahimi, H. Lateral and depth variations of coda Q in the Zagros region of Iran. *Journal of Seismology*, 20:197–211, 2016. doi: 10.1007/s10950-015-9520-1.

Jackson, J. and Fitch, T. Basement faulting and the focal depths of the larger earthquakes in the Zagros mountains (Iran). *Geophysical Journal International*, 64(3):561–586, 1981. doi: 10.1111/j.1365-246X.1981.tb02685.x.

Kaviani, A., Hatzfeld, D., Paul, A., Tatar, M., and Priestley, K. Shear-wave splitting, lithospheric anisotropy, and mantle deformation beneath the Arabia-Eurasia collision zone in Iran. *Earth and Planetary Science Letters*, 286:371–378, 2009. doi: 10.1016/j.epsl.2009.07.003.

Kennett, B., Sambridge, M., and Williamson, P. R. Subspace methods for large inverse problems with multiple parameter classes. *Geophysical Journal International*, 94(2):237–247, 1988. doi: 10.1111/j.1365-246x.1988.tb05898.x.

Lanczos, C. *Linear differential operators*, chapter 3, pages 100–162. Society for Industrial and Applied Mathematics, 1961.

Laske, G., Masters, G., Ma, Z., and Pasyanos, M. E. Update on CRUST1. 0—A 1- degree global model of Earth's crust. *Geophysical Research Abstracts*, 15:2658, 2013. doi: 10.17611/DP/emccrust10.

Latallerie, F., Zaroli, C., Lambotte, S., and Maggi, A. Analysis of tomographic models using resolution and uncertainties: a surface wave example from the Pacific. *Geophysical Journal International*, 230(2):893–907, 2022. doi: 10.1093/gji/ggac095.

Lin, F.-C., Moschetti, M. P., and Ritzwoller, M. H. Surface Wave Tomography of the Western United States from Ambient Seismic Noise: Rayleigh and Love Wave Phase Velocity Maps. *Geophysical Journal International*, 173(1):281–298, 2008. doi: 10.1111/j.1365-246x.2008.03720.x.

Lü, Y. and Chen, L. Upper crustal P-wave velocity structure beneath two volcanic areas in northern Iran. *Science China Earth Sciences*, 60:786–795, 2017. doi: 10.1007/s11430-016-9005-7.

Maggi, A. and Priestley, K. Surface Waveform Tomography of Turkish-Iranian Plateau. *Geophysical Journal International*, 160 (3):1068–1080, 2005. doi: 10.1111/j.1365-246X.2005.02505.

Maheri-Peyrov, M., Ghods, A., Abbasi, M., Bergman, E., and Sobouti, F. ML shear wave velocity tomography for the Iranian Plateau. *Geophysical Journal International*, 205(1):179–191, 2016. doi: 10.1093/gji/ggv504.

Manaman, N., Shomali, H., and Koyi, H. New constraints on uppermantle S-velocity structure and crustal thickness of the Iranian plateau using partitioned waveform inversion. *Geophysical Journal International*, 184:247–267, 2010. doi: 10.1111/j.1365-246x.2010.04822.x.

Mangino, S. and Priestley, K. The crustal structure of the southern Caspian region. *Geophysical Journal International*, 133(3): 630–648, 1998. doi: 10.1046/j.1365-246X.1998.00520.x.

Menke, W. Review of the generalized least squares method. *Surveys in Geophysics*, 36:1–25, 2015. doi: 10.1007/s10712-014-9303-1.

Moradi, A., Hatzfeld, D., and Tatar, M. Microseismicity and seismotectonics of the North Tabriz fault (Iran). *The International Journal of Integrated Solid Earth Sciences-Tectonophysics*, 506(1-4): 22–30, 2011. doi: 10.1016/j.tecto.2011.04.008.

Mortezanejad, G., Aziz Zanjani, A., Ghods, A., and Sobouti, F. Insights into the crustal structure and the seismotectonics of the Talesh region using the local and teleseismic data. *Geosciences*, 88(2):38–47, 2013.

Mortezanejad, G., Rahimi, H., Romanelli, F., and Panza, G. Lateral variation of crust and upper mantle structures in NW Iran derived from surface wave analysis. *Journal of Seismology*, 23(1): 77–108, 2019. doi: 10.1007/s10950-018-9794-1.

Mottaghi, A., Rezapour, M., and Korn, M. Ambient noise surface wave tomography of the Iranian Plateau. *Geophysical Journal International*, 193(1):452–462, 2013. doi: 10.1093/gji/ggs134.

Mouthereau, F. Timing of uplift in the Zagros belt/Iranian plateau and accommodation of late Cenozoic Arabia–Eurasia convergence. *Geological Magazine*, 148(5):726–738, 2011. doi: 10.1017/s0016756811000306.

Movaghari, R. and Doloei, G. J. 3-D crustal structure of the Iran plateau using phase velocity ambient noise tomography. *Geophysical Journal International*, 220:1555–1568, 2019. doi: 10.1093/gji/ggz537.

Movaghari, R., Doloei, G., Yang, Y., Tatar, M., and Sadidkhouy, A. Crustal Radial Anisotropy of the Iranian Plateau Inferred from Ambient Noise Tomography. *Journal of Geophysical Research:*

Solid Earth, 126, 2021. doi: 10.1029/2020jb020236.

Naghavi, M., Shomali, Z., and Zare, M. Lg Coda Variations in North-Central Iran. *International Journal of Geophysics*, 2012. doi: 10.1155/2012/673506.

Nolet, G. Partitioned waveform inversion and two-dimensional structure under the network of autonomously recording seismographs. *Journal of Geophysical Research*, 95:8499–8512, 1990. doi: 10.1029/jb095ib06p08499.

Nolet, G. *A breviary of seismic tomography: imaging the interior of the Earth and sun*. Cambridge University Press, 2008.

Okay, A., Sengor, C., and Görur, N. Kinematic history of the opening of the Black Sea and its effect on the surrounding regions. *Geology*, 22(3):267–270, 1994. doi: 10.1130/0091-7613(1994)022<0267:KHOTOO>2.3.CO;2.

Ouattara, Y., Zigone, D., and Maggi, A. Rayleigh Wave Group Velocity Dispersion Tomography of West Africa Using Regional Earthquakes and Ambient Seismic Noise. *Journal of Seismology*, 23 (6):1201–1221, 2019. doi: 10.1007/s10950-019-09860-z.

Paige, C. and Saunders, M. LSQR: An Algorithm for Sparse Linear Equations and Sparse Least Squares. *ACM Transactions on Mathematical Software*, 8(1):43–71, 1982. doi: 10.1145/355984.355989.

Pang, K.-N., Chung, S.-L., Zarrinkoub, M. H., Khati, M. M., Mohammadi, S. S., Chiu, H.-Y., Chu, C.-H., Lee, H.-Y., and Lo, C.-H. Eocene–Oligocene post-collisional magmatism in the Lut-Sistan region, eastern Iran: Magma genesis and tectonic implications. *International Journal of Petrology, Mineralogy and Geochemistry-Lithos*, 180-181:234–251, 2013. doi: 10.1016/j.lithos.2013.05.009.

Parker, R. L. *Geophysical Inverse Theory*. Princeton University Press, 1994.

Paul, A., Hatzfeld, D., Kaviani, A., Tatar, M., and Péquegnat, C. Seismic imaging of the lithospheric structure of the Zagros mountain belt (Iran). *Geological Society, London, Special Publications*, 330(1):5–18, 2010. doi: 10.1144/SP330.

Pedersen, H. A., Mars, J. I., and Amblard, P. O. Improving Surface-Wave Group Velocity Measurements by Energy Reassignment. *GEOPHYSICS*, 68(2):677–684, 2003. doi: 10.1190/1.1567238.

Penrose, R. A generalized inverse for matrices. *Mathematical proceedings of the Cambridge Philosophical Society*, 51:406–413, 1955. doi: 10.1017/s0305004100030401.

Pijpers, F. and Thompson, M. J. Faster formulations of the optimally localized averages method for helioseismic inversions. *Astronomy and Astrophysics*, 262(1):33–36, 1992.

Pijpers, F. and Thompson, M. J. The SOLA method for helioseismic inversion. *Astronomy and Astrophysics*, 281(1):231–240, 1993.

Poli, P., Campillo, M., Pedersen, H., and Group, L. W. Body-Wave Imaging of Earth's Mantle Discontinuities from Ambient Seismic Noise. *Science*, 338(6110):1063–1065, 2012. doi: 10.1126/science.1228194.

Rahimi, H., Motaghi, K., Mukhopadhyay, S., and Hamzehloo, H. Estimation of coda and shear wave attenuation in the volcanic area in SE Sabalan Mountain, NW Iran. *Acta Geophysica*, 58: 244–268, 2010a. doi: 10.2478/s11600-009-0023-8.

Rahimi, H., Motaghi, K., Mukhopadhyay, S., and Hamzehloo, H. Variation of coda wave attenuation in the Alborz region and central Iran. *Geophysical Journal International*, 181:1643–1654, 2010b. doi: 10.1111/j.1365-246x.2010.04574.x.

Rahimi, H., Hamzehloo, H., Vaccari, F., and Panza, G. Shear-Wave Velocity Tomography of the Lithosphere-Asthenosphere System beneath the Iranian Plateau. *Bulletin of the Seismological Society of America*, 104:2782–2798, 2014. doi: 10.1785/0120130319.

Rawlinson, N. and Sambridge, M. The fast marching method: an effective tool for tomographic imaging and tracking multiple phases in complex layered media. *Exploration Geophysics*, 36 (4):341–351, 2005. doi: 10.1071/eg05341.

Rawlinson, N. and Spakman, W. On the use of sensitivity tests in seismic tomography. *Geophysical Journal International*, 205(2): 1221–1243, 2016. doi: 10.1093/gji/ggw084.

Rawlinson, N., Fichtner, A., Sambridge, M., and Young, M. Seismic tomography and the assessment of uncertainty. *Advances in Geophysics*, 55:1–76, 2014. doi: 10.1016/bs.agph.2014.08.001.

Rezaeifar, M. and Kissling, E. Regional 3-D lithosphere structure of the northern half of Iran by local earthquake tomography. *Geophysical Journal International*, 223:1956–1972, 2020. doi: 10.1093/gji/ggaa431.

Rezaeifar, M., Kissling, E., and Shomali, Hossein. Shahpasandzadeh, M. 3D crustal structure of the northwest Alborz region (Iran) from local earthquake tomography. *Swiss Journal of Geosciences*, 109(1):389–400, 2016. doi: 10.1007/s00015-016-0219-2.

Sambridge, M. and Gudmundsson, O. Tomographic systems of equations with irregular cells. *Journal of Geophysical Research: Solid Earth*, 103:773–781, 1998. doi: 10.1029/97JB02602.

Sandvol, E., Al-Damegh, K., Calvert, A., Seber, D., Barazangi, M., Homamad, R., Gök, R., et al. Tomographic Imaging of Lg and Sn Propagation in the Middle East. *Pure and Applied Geophysics*, 158:1121–1163, 2001. doi: 10.1007/PL00001218.

Scales, J. A. and Snieder, R. To Bayes or not to Bayes? *Geophysics*, 62:1045–1046, 1997. doi: 10.1190/1.6241045.1.

Sengor, A. A new model for the late Palaeozoic—Mesozoic tectonic evolution of Iran and implications for Oman. *Geol. Soc. Spec. Publ.*, 49(1):797–831, 1990. doi: 10.1144/GSL.SP.1992.049.01.49.

Sengor, A. and Kidd, W. Post-collisional tectonics of the Turkish-Iranian plateau and a comparison with Tibet. *Tectonophysics*, 55(3-4):361–376, 1979. doi: 10.1016/0040-1951(79)90184-7.

Shakiba, S., Amiri Fard, R., and Rahimi, H. 2D Local Earthquake Tomography of Rayleigh Waves in Northwest of Iran. In *Proceedings of the Iranian Geophysical Conference*, volume 19, pages 801–804. National Iranian Geophysical Society, 2020.

Stocklin, G. Structural history and tectonics of Iran: A review. *American Association of Petroleum Geologists Bulletin*, 52(7):1229–1258, 1968. doi: 10.1306/5D25C4A5-16C1-11D7-8645000102C1865D.

Talebian, M. and Jackson, J. Offset on the Main Recent Fault of NW Iran and implications for the late Cenozoic tectonics of the Arabia–Eurasia collision zone. *Geophysical Journal International*, 150(2):422–439, 2002. doi: 10.1046/j.1365-246X.2002.01711.x.

Tarantola, A. and Valette, B. Inverse Problems: Quest for information. *Journal of geophysics*, 50:159–170, 1982.

Trampert, J. Global seismic tomography: the inverse problem and beyond. *Inverse Problems*, 14:371–385, 1998. doi: 10.1088/0266-5611/14/3/002.

Trampert, J. and van Heijst, H. J. Global Azimuthal Anistotropy in the Transition Zone. *Science*, 296:1297–1299, 2002. doi: 10.1126/science.1070264.

van der Lee, S. and Nolet, G. Upper mantle S velocity structure of North America. *Journal of Geophysical Research: Solid Earth*, 102:22815–22838, 1997. doi: 10.1029/97JB01168.

Yanovskaya, T. and Ditmar, P. Smoothness criteria in surface wave tomography. *Geophysical Journal International*, 102:63–72, 1990. doi: 10.111/j.1365-246X.1990.tb00530.x.

Yanovskaya, T. B., Kizima, E., and Antonova, L. Structure of the crust in the Black Sea and adjoining regions from surface wave data. *Journal of Seismology*, 2:303–316, 1998. doi: 10.1023/A:1009716017960.

Zandi, H. and Rahimi, H. 2-D Surface Wave Tomography in the Northwest Part of the Iranian Plateau. *Journal of the Earth and Space Physics*, 45(4):133–142, 2020. doi: 10.22059/jesphys.2019.275722.1007087.

Zaroli, C. Global seismic tomography using Backus–Gilbert inversion. *Geophysical Journal International*, 207(2):876–888, 2016. doi: 10.1093/gji/ggw315.

Zaroli, C. Seismic tomography using parameter-free Backus–Gilbert inversion. *Geophysical Journal International*, 218(1): 619–630, 2019. doi: 10.1093/gji/ggz175.

Zaroli, C., Koelemeijer, P., and Lambotte, S. Toward Seeing the Earth's Interior Through Unbiased Tomographic Lenses. *Geophysical Research Letters*, 13(1173):11399–11408, 2017. doi: 10.1002/2017gl074996.

Zigone, D., Ben-Zion, Y., Campillo, M., and Roux, P. Seismic Tomography of the Southern California Plate Boundary Region from Noise-Based Rayleigh and Love Waves. *Pure and Applied Geophysics*, 172(5):1007–1032, 2015. doi: 10.1007/s00024-014-0872-1.

doi:10.26443/seismica.v2i2.978

SEISMICA

Characterizing High Rate GNSS Velocity Noise for Synthesizing a GNSS Strong Motion Learning Catalog

Timothy Dittmann * [1,2], **Jade Morton** [1], **Brendan Crowell** [3], **Diego Melgar** [4], **Jensen DeGrande** [3], **David Mencin** [2]

[1]Ann and H. J. Smead Aerospace Engineering Sciences Department, University of Colorado Boulder, Boulder, CO, USA, [2]EarthScope Consortium, USA, [3] Department of Earth and Space Sciences, University of Washington, Seattle, Washington, USA, [4]Department of Earth Sciences, University of Oregon, Eugene, U.S.A

Author contributions: *Conceptualization*: All. *Methodology*: DiegoM, TD. *Software*: TD, BC, DiegoM. *Validation*: TD, JD. *Formal Analysis*: TD, JM. *Writing - original draft*: TD, JM. *Writing - Review & Editing*: All authors. *Funding acquisition*: JM, DavidM.

Production Editor: Gareth Funning
Handling Editor: Mathilde Radiguet
Copy & Layout Editor: Hannah F. Mark

Received: May 9, 2023
Accepted: September 11, 2023
Published: October 5, 2023

Abstract Data-driven approaches to identify geophysical signals have proven beneficial in high dimensional environments where model-driven methods fall short. GNSS offers a source of unsaturated ground motion observations that are the data currency of ground motion forecasting and rapid seismic hazard assessment and alerting. However, these GNSS-sourced signals are superposed onto hardware-, location- and time-dependent noise signatures influenced by the Earth's atmosphere, low-cost or spaceborne oscillators, and complex radio frequency environments. Eschewing heuristic or physics based models for a data-driven approach in this context is a step forward in autonomous signal discrimination. However, the performance of a data-driven approach depends upon substantial representative samples with accurate classifications, and more complex algorithm architectures for deeper scientific insights compound this need. The existing catalogs of high-rate ($\geq$1Hz) GNSS ground motions are relatively limited. In this work, we model and evaluate the probabilistic noise of GNSS velocity measurements over a hemispheric network. We generate stochastic noise time series to augment transferred low-noise strong motion signals from within 70 kilometers of strong events ($\geq M_W$ 5.0) from an existing inertial catalog. We leverage known signal and noise information to assess feature extraction strategies and quantify augmentation benefits. We find a classifier model trained on this expanded pseudo-synthetic catalog improves generalization compared to a model trained solely on a real-GNSS velocity catalog, and offers a framework for future enhanced data driven approaches.

Non-technical summary Global Navigation Satellite System (GNSS) signals are a source of valuable earthquake ground motion data that is traditionally sourced from inertial-based instruments. Inertial-based instruments include a class of sensors that use Newton's first law to directly measure ground velocity or acceleration. Routine noise of GNSS is more complex than the inertial-based instruments, which in turn has limited the scope of adoption of GNSS in earthquake monitoring. Machine learning applied to the scientific domain has shown that it can separate signal from noise and offer deeper scientific insights, but our existing datasets are relatively limited. Implementing an effective machine learning model for any scientific objective depends on having a sufficiently large, accurately labeled dataset for training and validating the model. We present an expanded "psuedo-synthetic" catalog comprised of transferred real-world signals added to synthetic GNSS velocity noise generated from real world noise analysis. We demonstrate how training a model on our expanded synthetic dataset outperforms training on limited real data and can support more sophisticated learning objectives offering deeper understanding.

1 Introduction

Distributed observations of coseismic ground motions are the backbone of accurate ground motion models, finite fault modeling, and early warning. If available in real-time, GNSS-derived high rate time differenced carrier phase (TDCP) velocities (GRAAS and SOLOVIEV, 2004) applied to seismology (Colosimo et al., 2011) are an additional source of these intrinsic measurements (Parameswaran et al., 2023) that are traditionally sourced from dedicated inertial sensor networks. If available in near-real time or post processing, GNSS velocities can contribute to catalogs of ground motion measurements used for empirical regional and local ground motion models (Crowell et al., 2023). GNSS spatially complements or substitutes existing inertial ground motion observations (Crowell, 2021), especially valuable in sparse networks (Grapenthin et al., 2017). Furthermore, GNSS expands the dynamic range of inertial measurements, and contributes to magnitude estimation (Murray et al., 2023) when inertial sensors saturate (Melgar et al., 2013) during the largest, most destructive events.

However, ambient GNSS velocity noise remains well above the noise floor of inertial sensors, largely due to

*Corresponding author: stdi2687@colorado.edu

sources of uncertainty related to ranging of space-based weak radio frequency signals. Analysis of high rate positioning noise (Genrich and Bock, 2006), carrier phase noise (Wang et al., 2021), and TDCP velocities (Shu et al., 2018; Crowell et al., 2023) has shed valuable insight into the factors that influence the ambient noise floor of these GNSS velocities. To date, the GNSS velocity noise frequency spectrum has not been evaluated across sufficiently large temporal and spatial scales to statistically report on the ambient noise across a network. Ambient noise characterization methods developed in the seismic community offer a statistical approach to represent ambient noise frequency content for sensor network monitoring and calibration. The probabilistic spectrum of GNSS velocity noise illuminates the limit of seismic signal detection in GNSS.

Improved classification of seismic signals within GNSS noise will expand the range in which GNSS contributes material ground motion observations with minimal false alerting for denser in situ observations and early warning integrity. Methods for addressing this signal to noise (SNR) challenge exist: variations on a short term average over long term average (STA/LTA) detection adopted from inertial seismic sensors resolve static offsets (e.g. Allen and Ziv, 2011; Colombelli et al., 2013) but filter valuable dynamics encoded in the waveforms; threshold based detection methods (e.g. Crowell et al., 2009; Hodgkinson et al., 2020; Dittmann et al., 2022a) capture dynamics but struggle to balance sensitivity with false alerting, and must mitigate false alerts with external dependencies such as spatially correlating or temporally windowing from seismic triggers. Machine learning (ML) models combine a range of feature inputs to improve the decision confidence in separating seismic signal from noise (e.g. Meier et al., 2019; Dittmann et al., 2022b) in stand-alone mode. However, the generalization performance of any such classifier or deeper ML model will ultimately be limited by the model selection and optimization, the extent of the labeled catalog for training, and the quality of the labels.

Previous GNSS seismic catalogs illustrate how limited the observed long-tail, larger magnitude GNSS seismic events datasets are (Ruhl et al., 2018). For example, the EarthScope/UNAVCO continuous geodetic archive began archiving lower sampling rate GNSS observations in 1993 and 5Hz high rate data retrieval in 2006. Decreased hardware costs coupled with commercial and scientific demand only relatively recently allowed for global high-rate network expansion. Additional geodetic networks (e.g. INGV: Italy, GEONET: NZ) complement EarthScope's high rate catalog worthy of inclusion on the order of doubling, not the order(s) of magnitude needed for deeper learning to answer more sophisticated questions. One solution to this small data challenge is synthesizing waveforms using kinematic finite fault ruptures and Green's functions ("FakeQuakes," Melgar et al., 2016; Williamson et al., 2020). This model-driven approach is invaluable for the largest, most destructive events, where a data-driven strategy for these infrequent events is inherently insufficient. However, this method is not yet practical for generalizing across global rupture scenarios and great care must be taken to not bias results with *unknown unknowns* of fault models and ground motion propagation of future events. This is an area of active research.

An intermediate real-world-data driven alternative is to transfer samples from a separate source of our signals of interest (Hoffmann et al., 2019). Inertial sensors have existed at more locations for far longer than the first positioning satellite was launched. Event catalogs of zero-baseline inertial measurements offer low-noise ground motion velocities to be transferred as our truth waveforms of accurately labeled samples. The GNSS noise probabilistic power spectral density (PPSD) characterization offers the necessary information to superpose stochastic noise for training over a range of noise conditions. The final component to improved generalization are the learning training decisions, including model selection and feature engineering. With appropriately applied domain knowledge to increasingly larger data volumes, the revolution of transferable classification and regression model algorithm development is readily adaptable to earth science questions (Bergen et al., 2019; Kong et al., 2018).

To improve our understanding of GNSS velocity sensitivity relative to ambient noise, expand the quantity of available labeled training data, and improve detection classification performance in a highly variable noise environment, we characterized the GNSS velocity noise frequency spectrum from which we augmented transferred inertial velocity waveforms observed over 80 years with synthetic GNSS velocity time series. This manuscript presents a framework for expanding the available, accurately labeled GNSS velocity waveforms and evaluates the improved signal detection gained from learning on such a catalog. Finally, we present the expanded catalog to support evolving, deeper learned models to train on.

2 Materials and Methods

2.1 Lightweight GNSS Velocity Processing

A GNSS receiver generates precise relative phase estimations by tracking the signal carrier wave using a phase lock loop. To achieve absolute positioning using carrier phase measurements, a suite of measurement error source models must be estimated to account for thermal noise, satellite and receiver oscillators, multipath reflections, atmospheric and ionospheric effects from a 20,000 kilometer signal propagation path, and unknown carrier cycle integer offsets (Teunissen, 2020). These correction models incur costs, computationally, potentially monetarily, and in performance for resolving carrier phase ambiguities to estimate absolute position. In past and current implementations of using geodetic measurements for capturing earthquakes, absolute positions are differenced from an a priori position to extract relative topocentric motion, the signal of interest. TDCP or variometric processing (GRAAS and SOLOVIEV, 2004) differences these precise carrier phase measurements in consecutive epochs to remove temporally correlated error sources and consistent integer ambiguities. TDCP uses the precision of these measurements to its advantage, by foregoing absolute positioning in exchange for precise relative velocity measurements while still benefiting from multi-signal observability across a visible satellite constellation. In this context, TDCP advantageously does not require ambiguity resolution convergence, lacks complex error models which in turn minimizes measurement noise, and reduces computational requirements. These factors combined with the simplicity of the algorithmic inputs makes it ideal for seismic ground deformation applications (Colosimo et al., 2011; Benedetti et al., 2014; Hohensinn and Geiger, 2018; Grapenthin et al., 2018; Parameswaran et al., 2023) at higher rates and potentially on the network edge.

We use the SNIVEL processing method (Crowell, 2021) for estimating 5Hz GPS TDCP. This method uses the narrow lane GPS-only L1/L2 phase combination, the Klobuchar ionospheric correction, the Niell tropospheric correction, and broadcast satellite ephemeris. Observations are weighted as a function of satellite elevation angle with a seven degree elevation mask. While development accommodating precise orbits (Shu et al., 2020), multi-GNSS, cycle slip detection/mitigation (Fratarcangeli et al., 2018), and higher order noise source mitigation is ongoing and warranted, the current method is capable of capturing ground motions of nearfield M4.9 and larger sources at teleseismic distances (Crowell, 2021; Dittmann et al., 2022b).

2.2 Observed High Rate GNSS Velocity Noise Model and Synthetic Noise

Understanding GNSS noise is imperative to applying GNSS observations to answer complex geophysical questions. Such investigations range from low frequency estimation of secular plate velocities (Williams et al., 2004) to higher frequency (>1Hz) signals, including structural monitoring (SHEN et al., 2019; Hohensinn et al., 2020), space weather (Yang et al., 2017), and deformation monitoring (Geng et al., 2018; Avallone et al., 2011). Previous studies show that GNSS position noise is a combination of white and colored or power-law noise (Langbein and Bock, 2004). Starting from lowest frequencies, the "dam profile" of exponentially decaying noise with increased frequency is inferred to be a result of correlated signal path and processing contributions including multipath, ephemerides, clocks, and atmospheric effects. GNSS highest frequency position noise is attributed to receiver thermal noise and often presented as a white spectrum (Genrich and Bock, 2006). Receiver thermal noise is parameterized as a function of incoming signal strength and carrier phase tracking filter design, including filter bandwidth and sample integration time. These baseband signal tracking loop design choices balance dynamic stress response with thermal noise mitigation (Yang et al., 2017), and are reflected in this highest frequency noise profile (Moschas and Stiros, 2013; Häberling et al., 2015). As an aside, for these reasons a calibrated high frequency instrument response, similar to what has become the defacto standard in digital inertial instruments, has been proposed (Ebinuma and Kato, 2012). We note this as worthy of further investigation for future efforts integrating TDCP velocity noise into monitoring but have not yet observed an instrument bias with respect to capturing seismic strong motion signals in 5Hz velocities.

The EarthScope geodetic archive captures 5Hz data of stations recording concurrent with larger magnitude earthquakes. This includes at least 1 hour of "ambient" 5Hz data antecedent to the hour in which the event takes place. We process with SNIVEL all available 5Hz pre-event hour long windows for our ambient GNSS velocity dataset. This dataset consists of 1507 hours from 904 stations since 2007 distributed from the Caribbean to Alaska. We use this sample space to be representative of GNSS velocity distributions both spatially and temporally.

We evaluated the spectrum of GNSS TDCP noise over this sample set by adopting a seismic ambient noise characterization method of McNamara and Buland (2004) modified for GNSS displacements by Melgar et al. (2020). In this approach, further modified for 5Hz GNSS velocities, we calculated the power spectral density of 10 minute 5Hz single component velocity windows. We evaluated power spectral densities (PSD) at periods from 205s down to 0.4s in 512 bins. PSDs were smoothed in octave intervals and then stacked across 73 aligned frequency bins over all available PSD segments. The result is a probabilistic power spectral density (PPSD), or distribution of power spectral densities over the samples included. These PPSDs have been adopted for seismic network monitoring (Casey et al., 2018) and offer valuable insight for anticipated signal sensitivity. We combined horizontal topocentric components into a single PPSD and then estimated an independent vertical PPSD, given GNSS vertical noise is approximately 3-5 times larger.

We stored 19 distribution slices (every 5th percentile from 5% to 95%) of the real-world noise quantiles from which to generate synthetic stochastic noise time series (See the pre-event time window of Figure 2). We adopted the approach of Melgar et al. (2020) for GNSS position displacements, first proposed by Boore (1983) and further developed by Graves and Pitarka (2010). In this approach, we were able to maintain the frequency content of the noise at respective reference levels while randomizing the phase for generating unique time series. We accommodated amplitude loss in the domain transformations with linear scaling. For additional context of this strategy, Lin et al. (2021) demonstrated an ML application leveraging the Melgar et al. (2020) approach for generating displacement noise time series superposed on synthesized FakeQuake displacements to train a deep learning model estimating Chilean subduction zone moment magnitudes.

2.3 Strong Motion Observations and Augmentation

Our signals of interest are velocity waveforms from medium to larger earthquakes (>M5.0) which GNSS velocities are sensitive to (Dittmann et al., 2022a). The Next Generation Attenuation for Western United States 2.0 (NGAW2) project (Ancheta et al., 2014) is a database

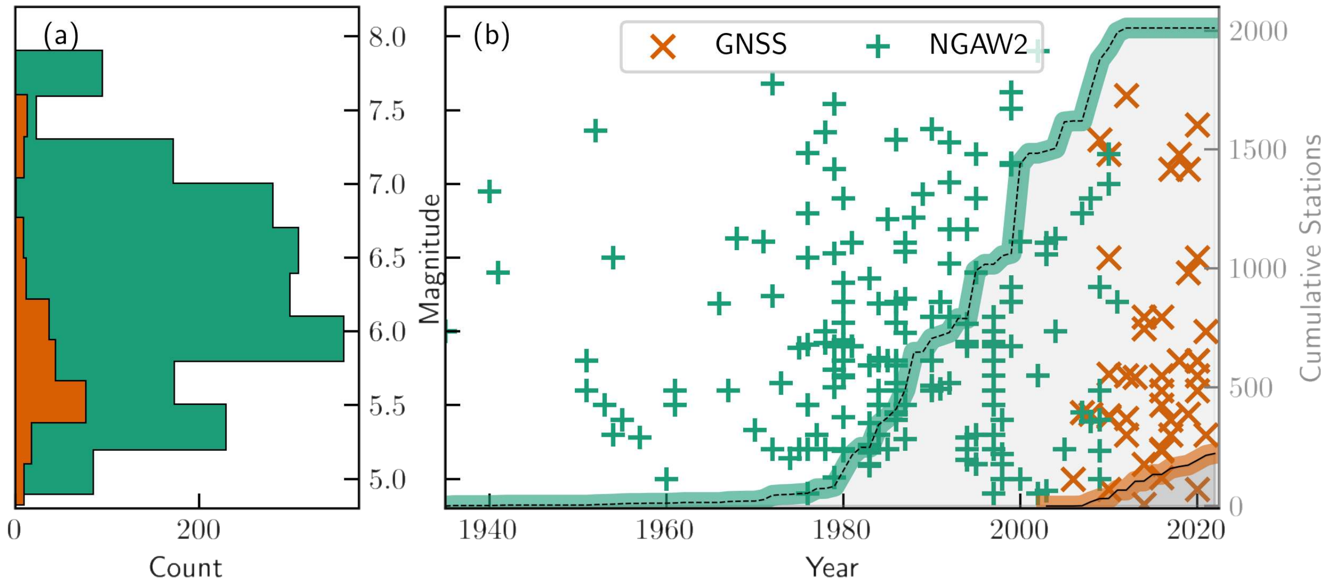

Figure 1 (a) A histogram comparing the EarthScope 5Hz GNSS catalog ("GNSS") with the NGA West-2 database ("NGAW2") for events observed by stations within 70 kilometers and sensitivity radii. The scatter plot in (b) shows the individual event magnitudes as a function of time, and the secondary axis line plot is the cumulative station count over time observing the events. In the cumulative line plot, the dashed line is the "NGAW2" and the solid line is "GNSS".

of global strong motion measurements and response spectral ordinates from "shallow crustal earthquakes in active tectonic regimes" spanning over 75 years including 21,339 three component records from 599 events ranging M3.0 to M7.9. Global seismic networks contribute strong motion accelerograms or broadband velocity measurements that are processed by the NGAW2 project into acceleration, velocity, and displacement waveforms. The processing consists of an acausal Butterworth filter to reduce high- and low-frequency noise and an instrument response correction; further information regarding processing is given by Ancheta et al. (2014). The records were visually inspected for corner frequency determination, quality, and completeness, making the catalog an ideal source of low-noise larger ground motion measurements. A primary application of such a catalog is for ground motion prediction research to inform earthquake engineering. We use the processed velocity waveforms as our noise-free signal. It is worth noting that the seismic community has coalesced around several extensive labeled datasets to benchmark and facilitate rapid growth of deep learning models for a variety of applications (Mousavi and Beroza, 2022). We considered the several existing curated seismic ML catalogs (Woollam et al., 2022), but found these predominantly emphasized weaker signals. This is logical given the signal-to-noise challenges from inertial measurements looking to ML for use in seismology, but provides insufficient amplitudes for detection in synthesized GNSS strong motion observations.

We focus our effort on the portion of the database containing nearfield ($\leq$70 km radius) observations of M5.0 to M7.9 within expected sensitivity radius of 1cm/s peak ground velocity given the scaling laws of Fang et al. (2020) for rapid hazard applications. Future work is extensible to the limits of detection above the noise floor (>1000km). We collected 2007 waveforms from 217 events (Figure 1). The processed velocity time series are offered at either 100 or 200 Hz sampling rate. We low pass filtered these waveforms with a filter corner frequency of 2.5Hz and then downsampled to 5Hz. We adopted a recursive short-term average over long-term average (STA/LTA) detection algorithm to label ground motion on each individual component. We found this is a sufficient automatic detector given its performance (Withers et al., 1998) in these relatively strong signals and factoring in the subsequent noise injected into our system. We used a 5 second short-term window and 10 second long-term window with a detection threshold ratio of 1.5. This metric was chosen through trial and error for its sensitivity for our larger strong motion signals of interest (Trnkoczy, 2012).

We exploited our "noise-free" signal waveforms and realistic stochastic noise generation by adopting data augmentation of transferred signals. Data augmentation is a form of regularization in which the size of a data catalog is artificially increased by creating augmented copies of our original waveforms (Zhu et al., 2020). Augmentation not only expands extents of a data catalog, valuable in relatively limited event datasets such as ours, but also improves generalization (Bishop, 1995). Successful augmentation trains a classifier to learn features or patterns in the presence of a larger range of authentic noise factors (Iwana and Uchida, 2021). In our application, we injected a synthetic noise time series derived from a single reference level of noise spectrum with unique phase values (Figure 2). We did this at seven noise reference levels on equivalent intervals from the 5th to 95th percentile to augment each strong motion waveform, a form of magnitude augmentation or jitter. We also buffered each augmented waveform with a random number of samples to misalign the samples in time

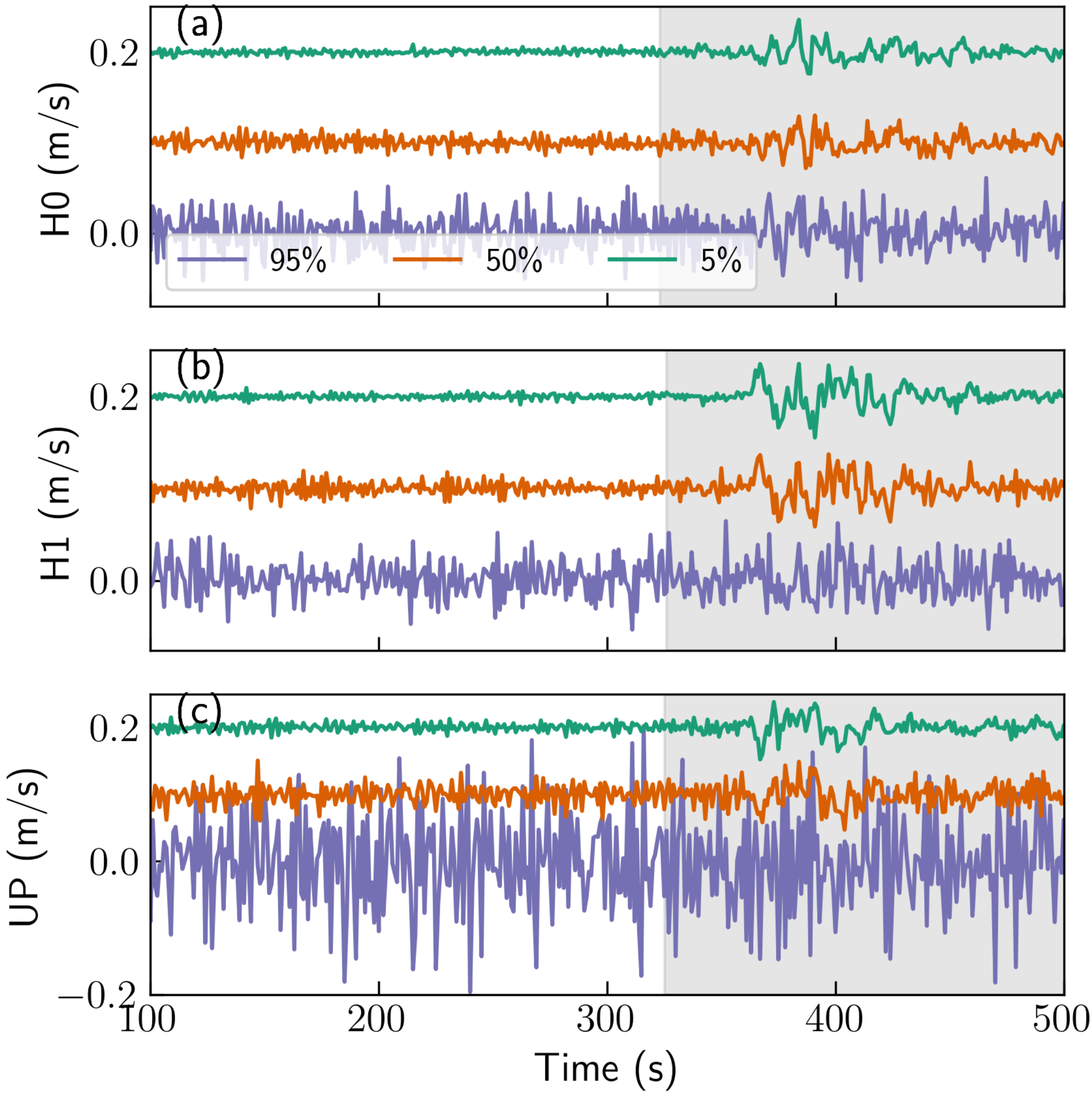

Figure 2 Example of three component waveforms from a single event NGAW2 waveform from Chi-Chi, Taiwan (2003, M6.2 50Km radius) with three levels of synthetic noise added (5%, 50%, and 95% quantiles). (a) and (b) are the horizontal components, H0 and H1 respectively. (c) is the vertical waveform and noise component.

relative to each waveform replica. This resulted in seven different pseudo-synthetic observational waveforms for each station-event pair. This approach minimized overfitting in our models by training on a range of noise for a given signal at different offsets in each feature window, and expanded our catalog seven-fold from 2,007 strong motion waveforms to 14,049 pseudo synthetic GNSS velocity waveforms (Figure 1).

Additionally, we included the ambient catalog used in creation of the PPSDs to ensure the classifier is both trained on and tested against real-world GNSS velocity noise. This strategy was particularly important for potential disturbances not captured by the ambient synthetic noise generation process, such as the most infrequent events that might get statistically removed from the stochastic power spectrum but could result in detrimental false alerts if their signature is not learned. For example, the lowest frequency offsets from processing artifacts are infrequent enough to barely impact the probabilistic spectrum, but if not these are not included in training they could present as a synchronized event. We validated the performance of training a classifier on this synthetic catalog against the previously labeled EarthScope 5Hz GNSS velocities (see *Data and code availability*). For description of this dataset, please refer to Dittmann et al. (2022b). This curated catalog of GNSS velocity waveforms was processed identically as the noise catalog of this work; but one fundamental difference is it is labeled through visual inspection instead of a known "truth" of our lowest noise inertial waveforms.

2.4 Model Selection, Feature Engineering and Training

First we validated the performance of a classifier trained on our strong motion waveforms relative to our previous GNSS velocity catalog approach. We used a random forest classifier (Breiman, 2001) for our detection model. Random forest is an ensemble method of decision trees. A decision tree is an algorithm that splits inputs along features to classify samples. A single decision tree can be biased by the initial features selected to seed the splitting; random forest overcomes this potential bias by running an ensemble of decision trees and having each cast a vote, where the majority eventually rules. We set up a binary classification that is demonstrated to have high accuracy and balance of sensitivity and false alerting in GNSS velocities. By keeping our model consistent with our previous work, we validated the newly formed catalog.

For validation comparison, we preserved our strategy from Dittmann et al. (2022b) of 30s overlapping windows. Future work will further optimize this sampling strategy with respect to sensitivity and real-time performance. From each window sample, we extracted a series of features to test their performance for our signal detection classification. In the time domain, we extract metrics akin to the traditional thresholding methods, including the four largest amplitudes, the median, and the median absolute deviation. In the frequency domain we included the entire PSD range over the 5Hz sampling of 30s windows, which includes periods from 1 second to 30 seconds. Variations on both of these time and frequency metrics were evaluated in our previous work, with the lower frequency (3s-15s period) horizontal PSD the most influential for the classifier model. However, while the overall performance over the entire catalog was a marked improvement from the current, variability in the false positive rate of the ambient dataset combined with missed detections of nearfield smaller magnitude events warrants further investigation.

Each sample consisted of one or a combination of these features for 30 second windows for all three components (Figure 3). STA/LTA labels were reduced to a single positive or negative outcome from 450 samples (150 samples per window x 3 components). Given our knowledge of signal relative to noise in this synthetic dataset, we also assigned a SNR metric for each sample, which was the peak single difference between signal power and noise power across all frequency bins. We employed a similar nested cross validation approach to our previous work for comparison and validation. Because the number of discrete events is still relatively small, we wished to minimize the potential bias from random validation and testing set selection.

In nested cross validation (Bishop and Nasrabadi, 2007), we ran 10 different testing scenarios, where each scenario keeps aside a different subset of one tenth of the events. Within each fold, we also ran an inner loop of 5 fold cross validation across a grid search of hyperparameters. This technique further minimized overfitting hyperparameters by cross validating across a range of sample subsets. Our hyperparameters included the depth of nodes, or the number of decision splits, the number of estimators or decision trees, class weighting, a strategy that can assist with imbalanced datasets such as ours, and finally a SNR training threshold. This last hyperparameter was uniquely available to this pseudo-synthetic dataset; we generated the noise added to the signal, and so with this information we can accurately quantify the relative detectability. Using this as a hyperparameter allowed us to optimize training sets to include the largest extent of low signal-to-noise samples that benefit the model, while avoiding degrading model performance with undetectable low SNR.

In cross validation, we optimized the model on F1 scores, a balance of precision and recall. F1 is the harmonic mean of precision and recall. Precision is equal to the number of true positives (TP) over the sum of TP and false positives (FP), and recall is the number of TP over the sum of TP and false negtives (FN). Dittmann et al. (see 2022b).

3 Results and Discussion

3.1 Noise Characteristics

In TDCP velocity noise, we observe a V-shaped noise spectral profile in the PPSD (Figure 4). Periods longer than 6s follow a power law profile, likely reflecting correlated errors such as multipath and atmospheric effects not completely removed in the time differencing. This result is aligned with Melgar et al. (2020), which identified 1Hz PPP displacement noise as a red noise with a dam profile down to their Nyquist frequency. They infer that multipath and troposphere are the primary sources of the PPP "random walk" correlated noise signature (5s-200s period), and anticipate a spectral flattening to white noise around their maximum resolvable frequency (0.5 Hz) (Melgar et al., 2020). 1Hz PPP PPSD had a corner around 3 seconds, while in TDCP the lower frequency power law corner is at 6 seconds period. Another notable difference with TDCP processing reflected in this profile is the absence of absolute atmospheric models. In TDCP, the single slant path phase differences with first order corrections remove all but higher order gradients. Unfiltered time-differenced velocities will not accumulate error from potentially biased corrections models, a challenge of PPP. Shu et al. (2020) noted that inclusion of precise satellite clocks and orbits can significantly reduce longer period drifts existing in displacements derived from GNSS variometric velocities that otherwise must be detrended.

At approximately 4-6s period the noise spectrum inflects and begins increasing at a mirrored power law exponential to the lower frequencies. In TDCP at higher rates (>1Hz), Crowell et al. (2023) observes in multiple sample rates from a single receiver that TDCP velocities have increased noise in the time domain, roughly a factor of 7 of standard deviation from 1 Hz to 10 Hz veloci-

	Number of Station-Event Waveforms	Number of Samples	Labeling Strategy
GNSS Event Catalog (<70km) (Dittmann et al., 2022b)	247	5,187	visual inspection
Ambient Noise Training	1,507	88,893	assumed event-free
Ambient Noise Testing	1,507	85,806	assumed event-free
NGAW2	2,007	60,330	zero-noise truth labels
NGAW2 with Augmentation	14,049	422,309	zero-noise truth labels

Table 1 Extent and strategy of catalogs used in this research of noise and M5+ events within expected detectability and 70km radius.

ties. In the frequency domain these velocities present as a reverse power law of increasing noise as frequency increases, flattening at a corner around 0.2s period (5Hz). We observe a similar spectral shape in our PPSDs. Furthermore, Shu et al. (2018) processed up to 50Hz and identified a spectral "knee" around 3.5Hz; the highest frequencies observed in our study terminated at this "knee". We infer this highest frequency (>1Hz) correlated noise to be predominantly influenced by receiver thermal noise, and likely receiver baseband design dependent (Moschas and Stiros, 2013). Crowell et al. (2023) also finds that the lowest noise power in the frequency domain exists in the 1-10s periods of the highest sample rate observations (20Hz in their study), notable given this intersects the spectral region of the seismic ground motion waveforms of interest. Given the spectrum at higher sampling rates, there is likely potential for improved screening of TDCP velocities for our signals of interest to reduce temporal aliasing (Hohensinn et al., 2020; Crowell et al., 2023).

A future PPSD product from continuous single station measurements would enable quantitative comparisons of the ambient noise levels from one station to another for monitoring and performance analysis. These noise levels, presented in a domain familiar scheme, are a meaningful proxy for the relative sensitivity to observe ground motions. Routine outliers can be observed and correlated to disturbances or events, a potentially valuable tool for network monitoring. In this study, without continuous 5Hz observations, it is not possible to assess time or spatially related variability outside the semi-arbitrary windows currently available.

3.2 Pseudo Synthetic Model Performance

We evaluated three different feature selection strategies by deploying three independent scenarios of random forest hyperparameter tuning and model fitting on identical training and testing splits. An advantage of our psuedo-synthetic approach is our knowledge at the individual waveform level about discrete true signals relative to artificial noise across our synthetic catalog. Our feature sets were time, frequency, and a combined time and frequency set "psd-t". Overall, we found the highest performance from the largest feature vector of all available features (Figure 5). We found the PSD-only performance similar to the "psd-t" combined feature vectors, which aligns with our feature importances from Dittmann et al. (2022b).

The overall F1 scores of Figure 5(a) indicate the optimal classifier will include both sets of information, but the PSD-only and time-only F1 scores suggest that the frequency domain information is most valuable for its stand alone performance relative to time only features. A benefit of our random forest model is readily extracted feature importance information (Figure 6). When our random forest model was presented with the time and frequency information, the trained model distributed feature importances across spatial components and features. The horizontal components (East-/North) contributed more than the vertical, consistent with previous findings aligned with increased vertical GNSS noise relative to signals (Figure 4, Genrich and Bock, 2006). Contrary to the stand alone performance of Figure 5(a), discrete time domain features have considerably more importance than the frequency domain features. However, the sum of all frequency features in Figure 6(b) is greater than the cumulative time domain features for each respective component.

Within the frequency domain, the most valuable features are in the 2-5s period range. This shape is distinct from our previous classifier Dittmann et al. (2022b), where the most valuable features were the lowest frequency power spectra (6-30s).

From a model explainability perspective, we interpret that this importance distribution reflects the strength of the ensemble decision tree algorithm to distribute its decisions across all features with encoded information to optimize performance. An equivalent algorithm would be difficult to implement and generalize using traditional thresholds or filtering of this combined information. From a domain interpretability perspective, the relative value of signal amplitudes and signal frequency content is comparable after factoring in the distribution of frequency importances across significantly more bins. A model trained on these combined features gets the best-of-all-worlds benefits that traditional approaches (e.g. STA/LTA, threshold) lack. Additionally,

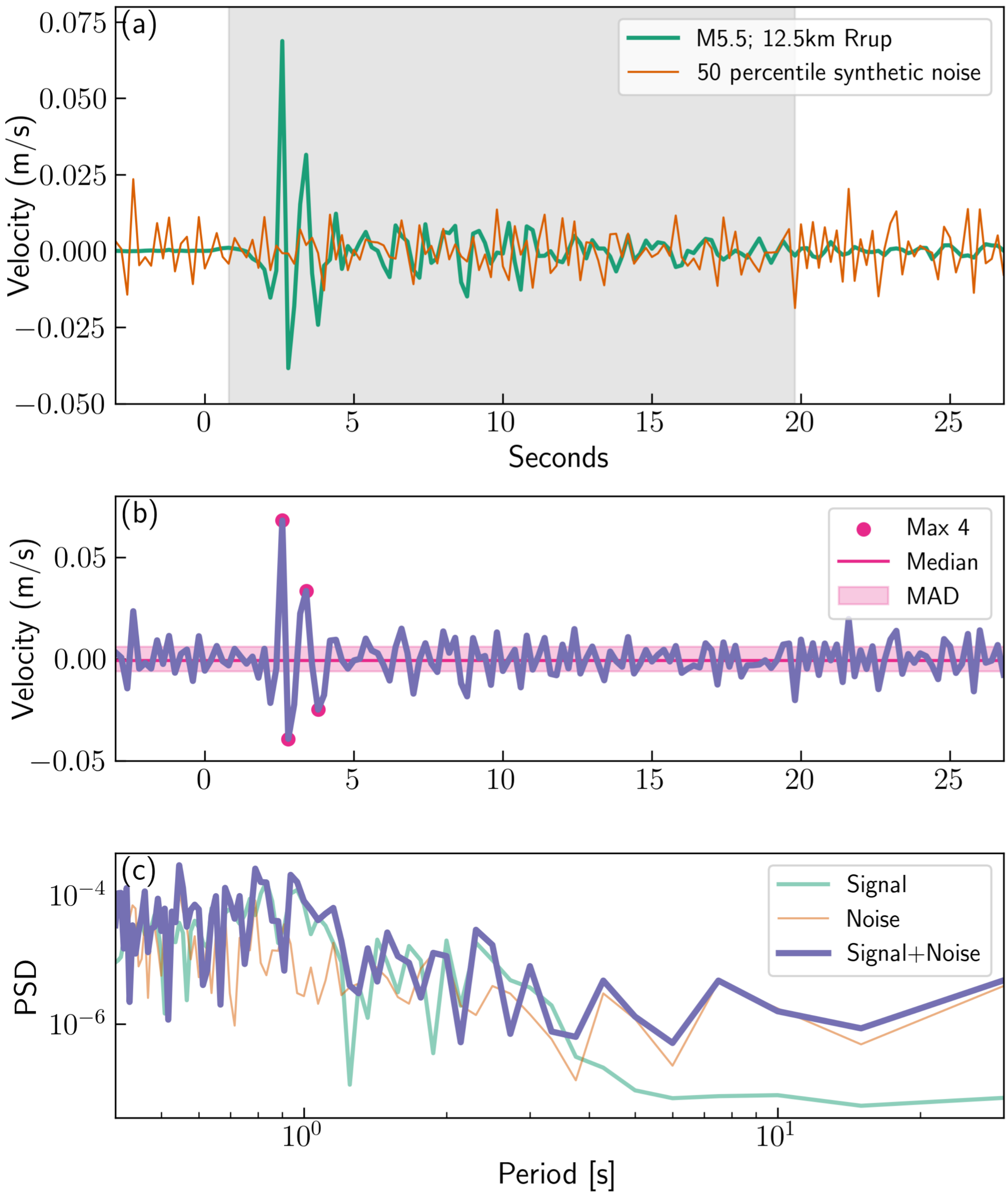

Figure 3 Demonstration of waveforms, noise and feature selection. The green timeseries in (a) is a downsampled NGAW2 waveform of a relatively weak signal for our application (a M5.5 at 12.5 km). The orange is a randomly generated noise time series using the 50th percentile noise spectrum. The gray shading is the region of detection triggered by the recursive STA/LTA. The sum of these time series (b) is then used as our observation. In the time domain (b) the features selected include the 4 largest amplitudes (solid magenta circles), the median, and the median absolute deviations, all indicated for this waveform in magenta. Finally, we also compute the power spectral density using a periodogram (in purple) and extract the power at each frequency bin. The original signal and noise periodograms are shown as well, for reference, though they are not included in the feature extraction.

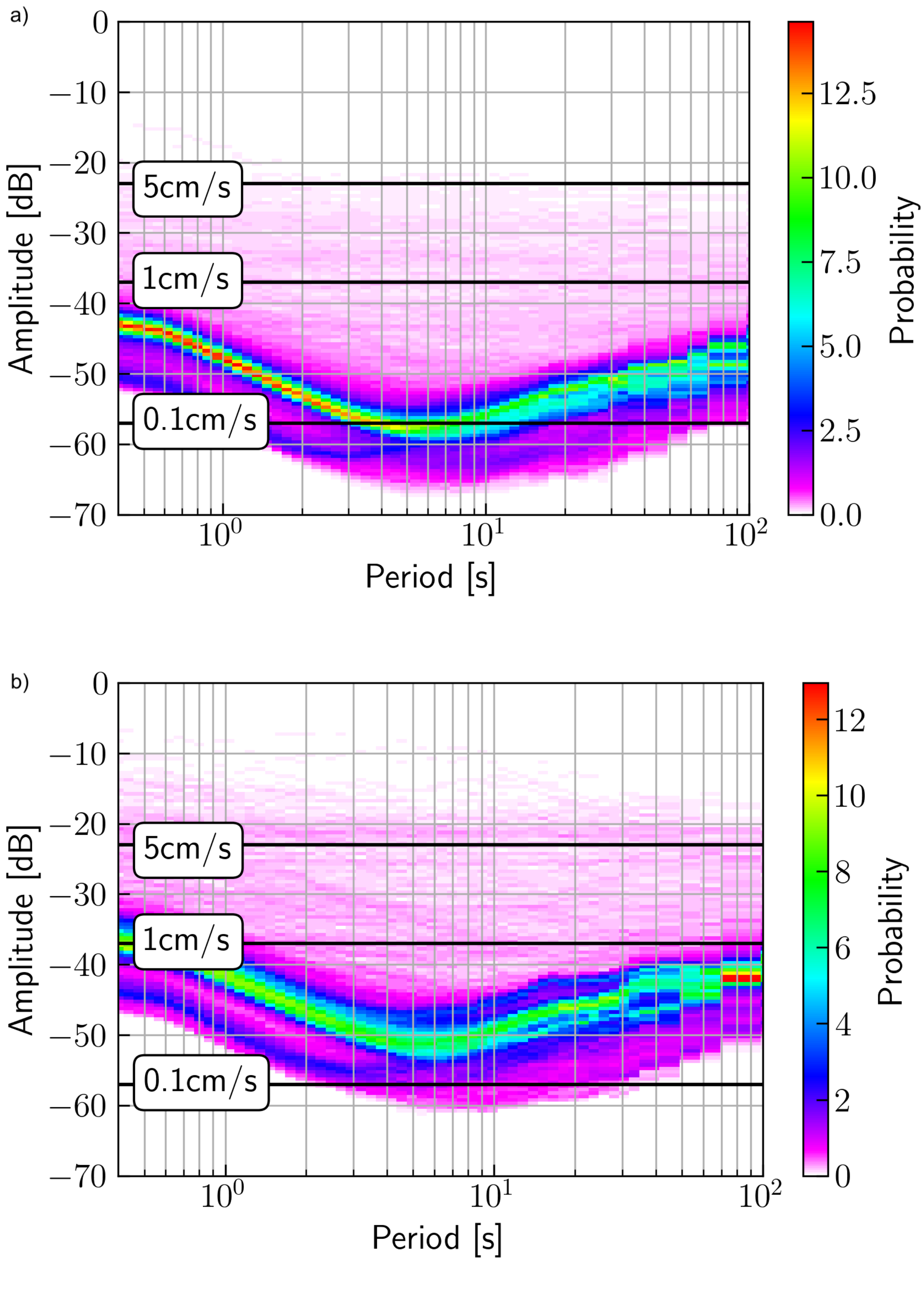

Figure 4 GNSS velocity PPSDs. Panel (a) is the combined horizontal components, panel (b) is the vertical component. Horizontal black lines are references for white noise timeseries of 3 respective standard deviations (5 cm/s, 1cm/s, 0.1cm/s).

the difference between the importances of this classifier and the previous classifier we infer is due to the nature of the labeling; these psuedo synthetic waveforms are labeled with low-noise "truth" models, so higher frequency, including more pulse-like signals, are more readily labeled. This is in contrast to the visual inspection, in which the human eye is inherently drawn to and presumably biased by longer period coherent signals. We will further evaluate in the validation section that training on augmented psuedo synthetic waveforms outperforms human-level classification performance.

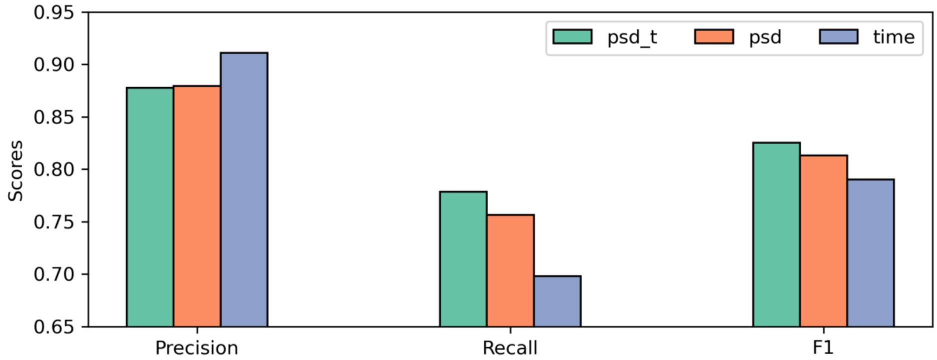

Figure 5 Testing feature extraction strategies across the NGAW2 synthetic dataset. Precision, recall, and F1 scores are presented as a function of feature extraction strategies across the entire catalog in 10 fold nested cross validation. "PSD" are the frequency domain features, "time" are the time domain features, and "psd-t" are the same time and frequency features concatenated into a single feature vector.

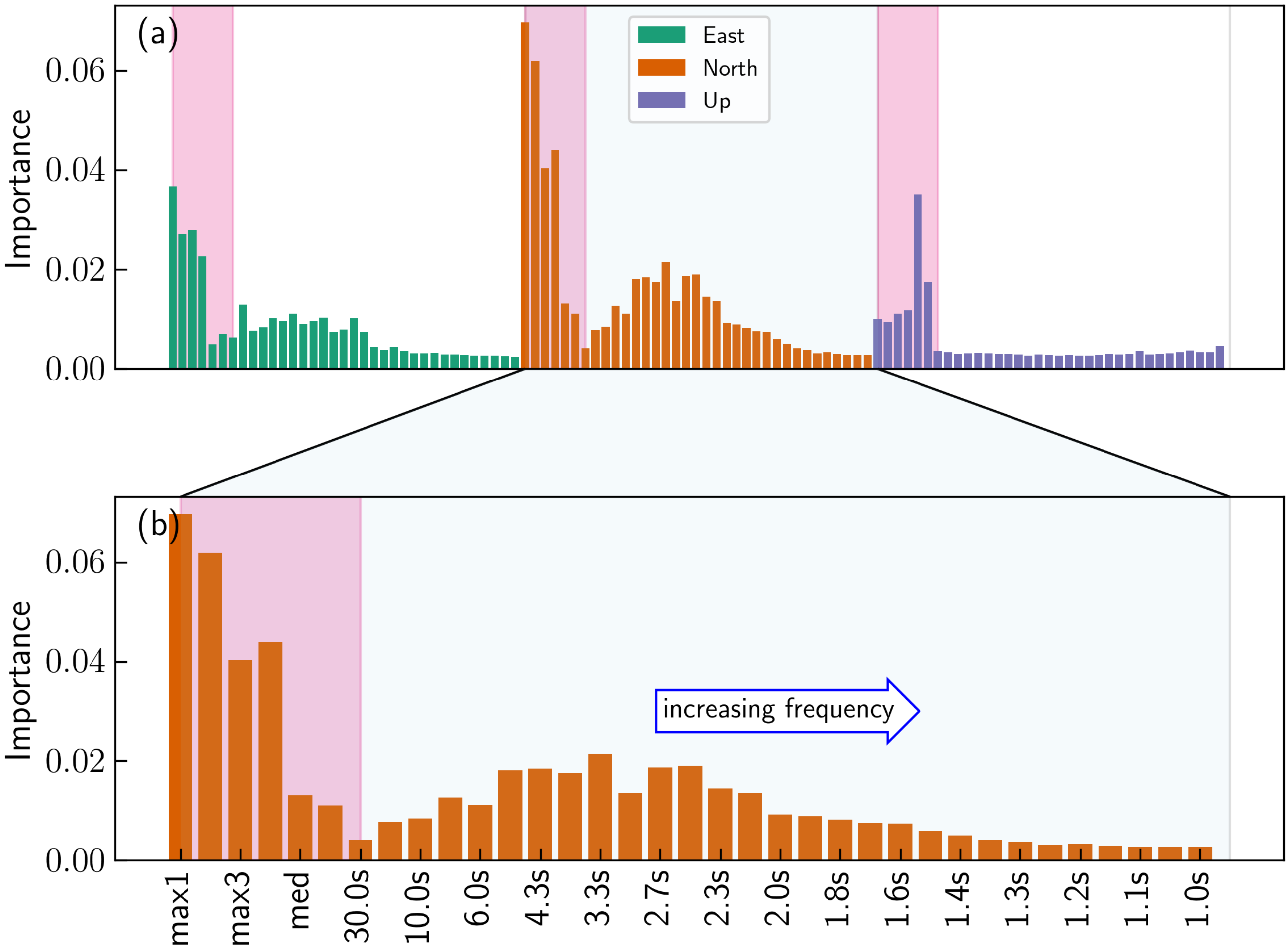

Figure 6 Feature importances for our random forest classification model cross validated and trained on the entire NGA West 2 synthetic GNSS dataset and the ambient noise dataset. Panel (a) shows the concatenated importances for all features across all components when a model is trained on all the features at once; the pink shading represents time domain features, the unshaded section are the frequency domain features. The second panel (b) is a close up of the North component features, with the same background shading schema. Every other feature is labeled for reference, max1 is largest amplitude, max2 is second largest, ..., 1.0s is the power in the 1s period bin of the PSD; for a single window example, see 3.

3.3 Quantifying Augmentation

Figure 1 and Table 1 make evident that transferred signals with data augmentation significantly expanded the GNSS velocity catalog with respect to the number of unique waveforms. Additionally, data augmentation is an opportunity to expand sample feature space by leveraging our knowledge of the signals relative to the noise to train high quality labels with elevated noise environments (Zhu et al., 2020). We quantified the performance impact of augmentation by comparing models trained with and without augmentation. We ran identical complete nested cross validation testing scenarios using two different training tactics. In the first, we allowed the model to train on all 7 replicas of each waveform. In the second, we only provided the lowest noise waveform in training. Panels (a-b) of Figure 7 are from the first training scenario with augmentation. We tested on all replicas of the testing set waveforms, but for visualization purposes the left panel (a) is the performance of the 20th percentile median noise waveforms, and the right panel (b) is the performance of the 80th percentile high noise waveforms. The 20th or 80th percentiles are chosen to represent the "high" and "low" noise levels. SNR metrics were derived from the known noise time series and known signal periodograms. With data augmentation, we observed decreasing SNR for the same catalog while testing against increased noise levels (from panel a to b or c to d), with an overall true positive rate from 90% to 84%. When we compared the 20% noise levels with and without data augmentation (panels a, c), we notice a similar drop in performance without augmentation. Finally, when we looked at the highest noise samples without augmentation, we see a dramatic decrease in performance despite testing on the identical waveforms with the same SNR, from 90% to 75%.

3.4 Validation with Observed High Rate GNSS Velocity Event Waveforms

Finally, to validate our synthesis of GNSS velocity waveforms against real-world GNSS velocities, we reran a nested cross validation experiment with the entire real-world GNSS velocity catalog of Dittmann et al. (2022b) as a reference to compare the synthetically generated model. Similar in testing design to the previous comparison of data augmentation, we evaluated the performance of two classification models against the same semi-random testing subsets in the nested cross validation loops and reported on the mean performance. In this testing split scenario, one model was fit on the remaining 'real' data using hyperparameters extracted from k-fold cross validation for each training set, while the other model was fit on the entire synthetic GNSS velocities catalog. All other feature engineering strategies were held consistent and both models were evaluated against the same 'real' testing sets. The synthetic GNSS trained model yielded better performance metrics, including increased precision, recall, and F1 (Figure 8). This performance can best be explained by the extent of training sets: the synthetic model was trained on 14,049 waveforms, where the "real" model was trained on ~200, depending on the nested cross validation run testing slice. The added extent and density of information in the transferred and augmented training data improved model generalization for unseen events.

Additionally, we ran an ambient test where we take the best fit model from each dataset and applied it to a yet unseen ambient noise dataset (for dataset description, see Table 1). We found the GNSS velocity trained model had a nearly identical false positive rate, where false positive rate is one minus the true negative rate (Figure 8). This further validates that our noise training and augmentation strategy was effective in improving performance in difficult noise conditions, as our performance improvement in the event catalog did not come at the expense of ambient performance.

From these improved classification results we infer that transferred, augmented "synthetic" waveforms are not only a valid substitute for high-rate GNSS measurements to partially overcome modern, smaller GNSS seismic datasets, but may outperform human-level classification performance. A future deployed classifier will be trained on the combination of data catalogs to achieve the best generalization performance for yet-to-occur events. This real-world versus pseudo-synthetic comparison and validation result also suggests that evolved transfer learning across measurement domains, including exploration of fine-tuning of more mature seismic deep ML models with GNSS velocities, could further advance GNSS seismology challenges.

4 Conclusions

We find the ambient GNSS velocity noise distribution's shape to be consistent with previous high-rate GNSS positioning noise analysis and spectral amplitudes, and find the noise distribution to be useful for signal sensitivity, synthetic noise generation, and future network monitoring. We find that frequency, time, and combined feature extraction strategies vary slightly under different SNR regions and that data augmentation boosts overall performance by training a model in higher noise settings.

Finally, we find that a model trained on these pseudo-synthetic waveforms, with the full suite of augmentation, outperforms the model trained on strictly GNSS velocity waveforms over the magnitudes (M_W 5.0-8.0) and hypocentral distances ($\leq$70 km) tested in this analysis. Augmentation improves detection around the noise-signal boundaries. The immediate benefit is an improved classification model from an expanded catalog that can be retrained on the combined pseudo-synthetic and real catalog for unseen events. Such a classifier will be embedded in enhanced network operations and hazard monitoring for automated, stand-alone event detection. The subsequent benefit is an expanded training catalog (Dittmann et al., 2023) and framework that supports deeper learning models that are "data hungry" (Mousavi and Beroza, 2022). This includes expanding functional learning outputs, such as denoising, regression for magnitude inversion, and forecasting. With respect to future training of the largest events using this catalog, we identify possible limitations of this approach for specific experimental hypotheses due to the potential for introducing magnitude saturation of inertial instruments into our model training, a phenomena we are explicitly avoiding by using GNSS as a source. Similarly, more sophisticated source-dependent learning (e.g. forecasting) will need to consider the distribu-

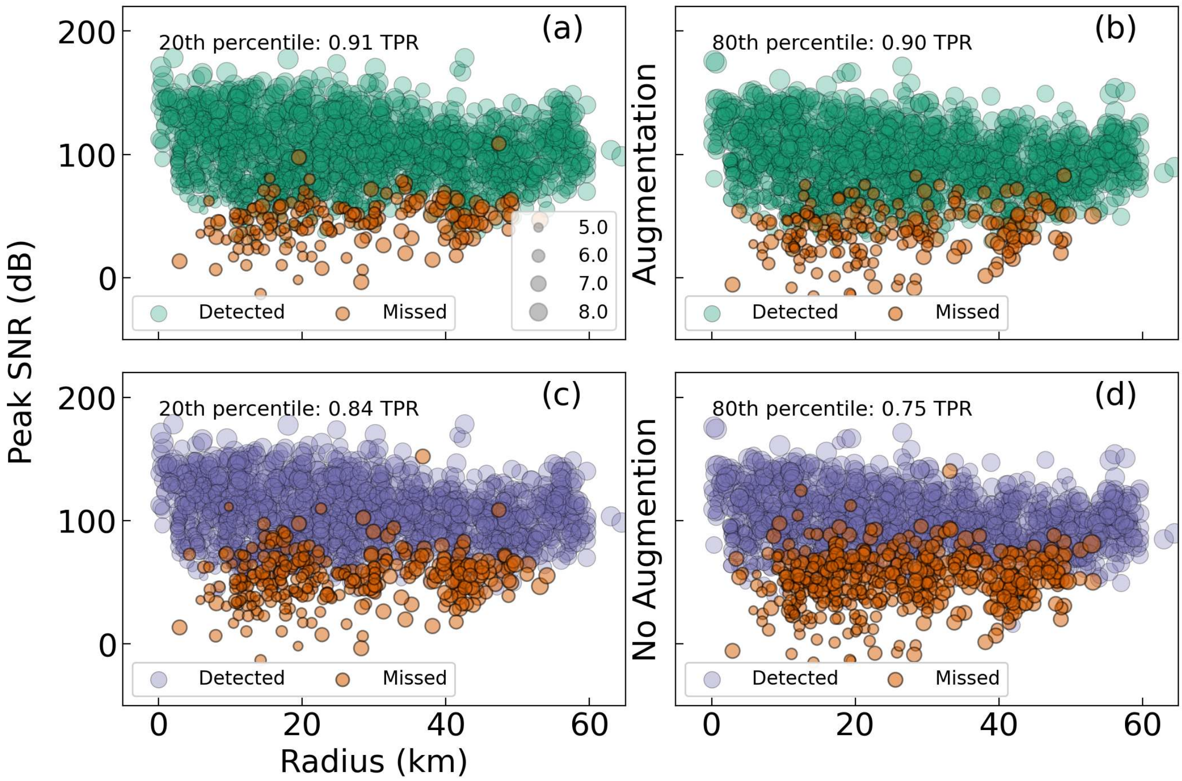

Figure 7 Comparing event detection with training on augmented noise samples across noise levels. Each panel includes the peak SNR of the waveform for each event as a function of radius from the event. This SNR metric is the peak of signal power to noise power for any frequency bin of periodograms calculated for all samples for all components for a given station-event waveform. The plot marker radius is determined by the event magnitude. The top panels (a-b) are testing the 20th noise model and 80th noise model of each station-event waveform using a classifier trained on all augmented samples. 20th and 80th are chosen to represent "low" and "high" noise. The markers are colored by a binary detected/not detected. The bottom panels (c-d) are testing the 20th/80th noise model waveforms with no data augmentation. This illustrates the value of augmentation for detection in noise, in addition to the approximate threshold of detection given our knowledge of signal and noise in this pseudo synthetic dataset. "TPR" - True Positive Rate.

tion of the NGAW2 source catalog used, specifically accounting for subduction events. Further investigations using this framework, perhaps paired with fully synthetic methods, is warranted. A loose ML integration of stand-alone inertial waveforms and this expanded GNSS-sourced waveforms enables fine-tuning (Yosinski et al., 2014) or transfer of existing inertial-based seismic detection ML models, such as Mousavi et al. (2020); Seydoux et al. (2020). Tighter amalgamation of stand-alone sensor sources benefiting from improved classification could include GNSS-sourced velocity waveforms directly in ground motion catalogs (Crowell et al., 2023) and operational monitoring systems. Such approaches would further blur distinctions between inertial and GNSS seismic signal sources, shifting from representations of different fields of earth sciences towards independent observational inputs with complimentary dynamic ranges and respective noise models.

Data and code availability

The inertial seismic records are available from the Pacific Earthquake Engineering Research Center (PEER) Next Generation Attenuation for Western United States 2.0 (https://ngawest2.berkeley.edu/, Ancheta et al., 2014).

The 5Hz GNSS data used for TDCP processing in the study are available from the Geodetic Facility for the Advancement of Geoscience (GAGE) Global Navigation Satellite Systems (GNSS) archives as maintained by EarthScope Inc. (previously UNAVCO, Inc). The data are available in RINEX (v.2.11) format at https://data.unavco.org/archive/gnss/highrate/5-Hz/rinex/. SNIVEL code used for TDCP velocity processing is developed openly at https://github.com/crowellbw/SNIVEL (Accessed December 2021) (Crowell, 2021). SNIVEL 5Hz velocity timeseries used in this study are preserved at (Dittmann, 2022). Labeled 5Hz GNSS velocity samples and pseudo synthetic samples are preserved at (Dittmann et al., 2023).

Version 1.0.1 of the scikit-learn software used for ran-

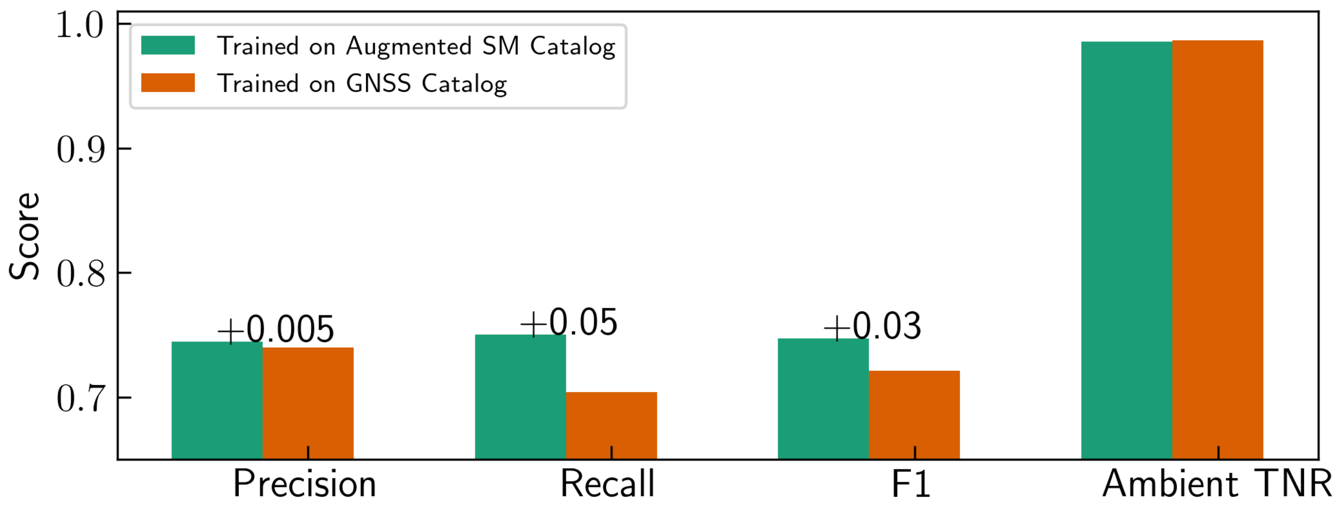

Figure 8 Testing performance of real GNSS velocity events as a function of training catalog used. These are the mean scores across the 10 testing folds of the nested cross validation. The purple results are from a model generated using cross validation of the remaining real gnss dataset; the green results are from the bulk model fit to the entire NGAW2 synthetic dataset. Each uses the "psd-t" feature extraction method (combined time and frequency features). The ambient true negative rate (TNR) is estimated using a separate dataset of unseen ambient data. TNR is (true negatives) / (true negatives + false positives), or equivalent to one minus the false positive rate. The annotated text is the difference between the two approaches.

dom forest classification is preserved at (Grisel et al., 2021) and developed openly at https://github.com/scikit-learn/scikit-learn (Pedregosa et al., 2011). Figures were made with Matplotlib version 3.5.1 (Caswell et al., 2021), available under the Matplotlib license at https://matplotlib.org/.

Version 1.2.1 of the obspy software used for seismic data handling and PPSD generation is preserved at (Team, 2020) and developed openly at https://github.com/obspy/obspy (Krischer et al., 2015). Software used to generate psuedo synthetic waveforms and train, test and validate models is available at https://github.com/timdittmann/psuedosynth_gnss_velocities

Acknowledgements

We would like to express gratitude for the reviews by editor Mathilde Radiguet and two anonymous reviewers that improved this manuscript.

This material is based on services provided by the GAGE Facility, operated by EarthScope Consortium, with support from the National Science Foundation, the National Aeronautics and Space Administration, and the U.S. Geological Survey under NSF Cooperative Agreement EAR-1724794.

High-rate processing and and ML for geoscience and hazards research is supported by NSF OAC-1835791.

Competing interests

The authors have no competing interests with this manuscript.

References

Allen, R. M. and Ziv, A. Application of real-time GPS to earthquake early warning. *Geophysical Research Letters*, 38(16), Aug. 2011. doi: 10.1029/2011gl047947.

Ancheta, T. D., Darragh, R. B., Stewart, J. P., Seyhan, E., Silva, W. J., Chiou, B. S.-J., Wooddell, K. E., Graves, R. W., Kottke, A. R., Boore, D. M., Kishida, T., and Donahue, J. L. NGA-West2 Database. *Earthquake Spectra*, 30(3):989–1005, Aug. 2014. doi: 10.1193/070913eqs197m.

Avallone, A., Marzario, M., Cirella, A., Piatanesi, A., Rovelli, A., Alessandro, C. D., D'Anastasio, E., D'Agostino, N., Giuliani, R., and Mattone, M. Very high rate (10 Hz) GPS seismology for moderate-magnitude earthquakes: The case of the Mw 6.3 L'Aquila (central Italy) event. *Journal of Geophysical Research*, 116(B2), Feb. 2011. doi: 10.1029/2010jb007834.

Benedetti, E., Branzanti, M., Biagi, L., Colosimo, G., Mazzoni, A., and Crespi, M. Global Navigation Satellite Systems Seismology for the 2012 Mw 6.1 Emilia Earthquake: Exploiting the VADASE Algorithm. *Seismological Research Letters*, 85(3):649–656, May 2014. doi: 10.1785/0220130094.

Bergen, K. J., Johnson, P. A., de Hoop, M. V., and Beroza, G. C. Machine learning for data-driven discovery in solid Earth geoscience. *Science*, 363(6433), Mar. 2019. doi: 10.1126/science.aau0323.

Bishop, C. M. Training with Noise is Equivalent to Tikhonov Regularization. *Neural Computation*, 7(1):108–116, Jan. 1995. doi: 10.1162/neco.1995.7.1.108.

Bishop, C. M. and Nasrabadi, N. M. Pattern Recognition and Machine Learning. *J. Electronic Imaging*, 16:049901, 2007.

Boore, D. M. Stochastic simulation of high-frequency ground motions based on seismological models of the radiated spectra. *Bulletin of the Seismological Society of America*, 1983. doi: https://doi.org/10.1785/BSSA07306A1865.

Breiman, L. Random Forests. *Machine Learning*, 45(1):5–32, 2001. doi: 10.1023/a:1010933404324.

Casey, R., Templeton, M. E., Sharer, G., Keyson, L., Weertman, B. R., and Ahern, T. Assuring the Quality of IRIS Data with MUSTANG.

Seismological Research Letters, 89(2A):630–639, Feb. 2018. doi: 10.1785/0220170191.

Caswell, T. A., Droettboom, M., Lee, A., de Andrade, E. S., Hoffmann, T., Hunter, J., Klymak, J., Firing, E., Stansby, D., Varoquaux, N., Nielsen, J. H., Root, B., May, R., Elson, P., Seppänen, J. K., Dale, D., Lee, J.-J., McDougall, D., Straw, A., Hobson, P., hannah, Gohlke, C., Vincent, A. F., Yu, T. S., Ma, E., Silvester, S., Moad, C., Kniazev, N., Ernest, E., and Ivanov, P. matplotlib/matplotlib: REL: v3.5.1, 2021. https://zenodo.org/record/5773480. doi: 10.5281/ZENODO.5773480.

Colombelli, S., Allen, R. M., and Zollo, A. Application of real-time GPS to earthquake early warning in subduction and strike-slip environments. *Journal of Geophysical Research: Solid Earth*, 118 (7):3448–3461, July 2013. doi: 10.1002/jgrb.50242.

Colosimo, G., Crespi, M., and Mazzoni, A. Real-time GPS seismology with a stand-alone receiver: A preliminary feasibility demonstration. *Journal of Geophysical Research: Solid Earth*, 116(B11), Nov. 2011. doi: 10.1029/2010jb007941.

Crowell, B., DeGrande, J., Dittmann, T., and Ghent, J. Validation of Peak Ground Velocities Recorded on Very-high rate GNSS Against NGA-West2 Ground Motion Models. *Seismica*, 2(1), Mar. 2023. doi: 10.26443/seismica.v2i1.239.

Crowell, B. W. Near-Field Strong Ground Motions from GPS-Derived Velocities for 2020 Intermountain Western United States Earthquakes. *Seismological Research Letters*, 92(2A): 840–848, Jan. 2021. doi: 10.1785/0220200325.

Crowell, B. W., Bock, Y., and Squibb, M. B. Demonstration of Earthquake Early Warning Using Total Displacement Waveforms from Real-time GPS Networks. *Seismological Research Letters*, 80(5): 772–782, Sept. 2009. doi: 10.1785/gssrl.80.5.772.

Dittmann, T. High Rate GNSS Velocities for Earthquake Strong Motion Signals, 2022. doi: 10.5281/ZENODO.6588601.

Dittmann, T., Hodgkinson, K., Morton, J., Mencin, D., and Mattioli, G. S. Comparing Sensitivities of Geodetic Processing Methods for Rapid Earthquake Magnitude Estimation. *Seismological Research Letters*, 93(3):1497–1509, Jan. 2022a. doi: 10.1785/0220210265.

Dittmann, T., Liu, Y., Morton, Y., and Mencin, D. Supervised Machine Learning of High Rate GNSS Velocities for Earthquake Strong Motion Signals. *Journal of Geophysical Research: Solid Earth*, 127(11), Oct. 2022b. doi: 10.1029/2022jb024854.

Dittmann, T., Morton, J., Crowell, B., Melgar, D., DeGrande, J., and Mencin, D. Real and Psuedosynthetic timeseries used in "Characterizing High Rate GNSS Velocity Noise for Synthesizing a GNSS Strong Motion Learning Catalog", 2023. https://zenodo.org/record/7909327. doi: 10.5281/ZENODO.7909327.

Ebinuma, T. and Kato, T. Dynamic characteristics of very-high-rate GPS observations for seismology. *Earth, Planets and Space*, 64 (5):369–377, May 2012. doi: 10.5047/eps.2011.11.005.

Fang, R., Zheng, J., Geng, J., Shu, Y., Shi, C., and Liu, J. Earthquake Magnitude Scaling Using Peak Ground Velocity Derived from High-Rate GNSS Observations. *Seismological Research Letters*, 92(1):227–237, Oct. 2020. doi: 10.1785/0220190347.

Fratarcangeli, F., Ravanelli, M., Mazzoni, A., Colosimo, G., Benedetti, E., Branzanti, M., Savastano, G., Verkhoglyadova, O., Komjathy, A., and Crespi, M. The variometric approach to real-time high-frequency geodesy. *Rendiconti Lincei. Scienze Fisiche e Naturali*, 29(S1):95–108, May 2018. doi: 10.1007/s12210-018-0708-5.

Geng, J., Pan, Y., Li, X., Guo, J., Liu, J., Chen, X., and Zhang, Y. Noise Characteristics of High-Rate Multi-GNSS for Subdaily Crustal Deformation Monitoring. *Journal of Geophysical Research: Solid Earth*, 123(2):1987–2002, Feb. 2018. doi: 10.1002/2018jb015527.

Genrich, J. F. and Bock, Y. Instantaneous geodetic positioning with 10-50 Hz GPS measurements: Noise characteristics and implications for monitoring networks. *Journal of Geophysical Research: Solid Earth*, 111(B3), Mar. 2006. doi: 10.1029/2005jb003617.

GRAAS, F. V. and SOLOVIEV, A. Precise Velocity Estimation Using a Stand-Alone GPS Receiver. *Navigation*, 51(4):283–292, Dec. 2004. doi: 10.1002/j.2161-4296.2004.tb00359.x.

Grapenthin, R., West, M., and Freymueller, J. The Utility of GNSS for Earthquake Early Warning in Regions with Sparse Seismic Networks. *Bulletin of the Seismological Society of America*, June 2017. doi: 10.1785/0120160317.

Grapenthin, R., West, M., Tape, C., Gardine, M., and Freymueller, J. Single-Frequency Instantaneous GNSS Velocities Resolve Dynamic Ground Motion of the 2016 Mw 7.1 Iniskin, Alaska, Earthquake. *Seismological Research Letters*, 89(3):1040–1048, Apr. 2018. doi: 10.1785/0220170235.

Graves, R. W. and Pitarka, A. Broadband Ground-Motion Simulation Using a Hybrid Approach. *Bulletin of the Seismological Society of America*, 100(5A):2095–2123, Sept. 2010. doi: 10.1785/0120100057.

Grisel, O., Mueller, A., Lars, Gramfort, A., Louppe, G., Prettenhofer, P., Blondel, M., Niculae, V., Nothman, J., Joly, A., Fan, T. J., Vanderplas, J., manoj kumar, Lemaitre, G., Qin, H., Hug, N., Estève, L., Varoquaux, N., Layton, R., Metzen, J. H., Jalali, A., (Venkat) Raghav, R., Schönberger, J., du Boisberranger, J., Yurchak, R., Li, W., la Tour, T. D., Woolam, C., Eren, K., and Eustache. scikit-learn/scikit-learn: scikit-learn 1.0.1, 2021. doi: 10.5281/ZENODO.5596244.

Hodgkinson, K. M., Mencin, D. J., Feaux, K., Sievers, C., and Mattioli, G. S. Evaluation of Earthquake Magnitude Estimation and Event Detection Thresholds for Real-Time GNSS Networks: Examples from Recent Events Captured by the Network of the Americas. *Seismological Research Letters*, 91(3):1628–1645, Mar. 2020. doi: 10.1785/0220190269.

Hoffmann, J., Bar-Sinai, Y., Lee, L. M., Andrejevic, J., Mishra, S., Rubinstein, S. M., and Rycroft, C. H. Machine learning in a data-limited regime: Augmenting experiments with synthetic data uncovers order in crumpled sheets. *Science Advances*, 5(4), Apr. 2019. doi: 10.1126/sciadv.aau6792.

Hohensinn, R. and Geiger, A. Stand-Alone GNSS Sensors as Velocity Seismometers: Real-Time Monitoring and Earthquake Detection. *Sensors*, 18(11):3712, Oct. 2018. doi: 10.3390/s18113712.

Hohensinn, R., Häberling, S., and Geiger, A. Dynamic displacements from high-rate GNSS: Error modeling and vibration detection. *Measurement*, 157:107655, June 2020. doi: 10.1016/j.measurement.2020.107655.

Häberling, S., Rothacher, M., Zhang, Y., Clinton, J. F., and Geiger, A. Assessment of high-rate GPS using a single-axis shake table. *Journal of Geodesy*, 89(7):697–709, Apr. 2015. doi: 10.1007/s00190-015-0808-2.

Iwana, B. K. and Uchida, S. An empirical survey of data augmentation for time series classification with neural networks. *PLOS ONE*, 16(7):e0254841, July 2021. doi: 10.1371/journal.pone.0254841.

Kong, Q., Trugman, D. T., Ross, Z. E., Bianco, M. J., Meade, B. J., and Gerstoft, P. Machine Learning in Seismology: Turning Data into Insights. *Seismological Research Letters*, 90(1):3–14, Nov. 2018. doi: 10.1785/0220180259.

Krischer, L., Megies, T., Barsch, R., Beyreuther, M., Lecocq, T., Caudron, C., and Wassermann, J. ObsPy: a bridge for seismology into the scientific Python ecosystem. *Computational Science & Discovery*, 8(1):014003, May 2015. doi: 10.1088/1749-4699/8/1/014003.

Langbein, J. and Bock, Y. High-rate real-time GPS network at

Parkfield: Utility for detecting fault slip and seismic displacements. *Geophysical Research Letters*, 31(15), 2004. doi: 10.1029/2003gl019408.

Lin, J.-T., Melgar, D., Thomas, A. M., and Searcy, J. Early Warning for Great Earthquakes From Characterization of Crustal Deformation Patterns With Deep Learning. *Journal of Geophysical Research: Solid Earth*, 126(10), Oct. 2021. doi: 10.1029/2021jb022703.

McNamara, D. E. and Buland, R. P. Ambient Noise Levels in the Continental United States. *Bulletin of the Seismological Society of America*, 94(4):1517–1527, Aug. 2004. doi: 10.1785/012003001.

Meier, M.-A., Ross, Z. E., Ramachandran, A., Balakrishna, A., Nair, S., Kundzicz, P., Li, Z., Andrews, J., Hauksson, E., and Yue, Y. Reliable Real-Time Seismic Signal/Noise Discrimination With Machine Learning. *Journal of Geophysical Research: Solid Earth*, 124(1):788–800, Jan. 2019. doi: 10.1029/2018jb016661.

Melgar, D., Bock, Y., Sanchez, D., and Crowell, B. W. On robust and reliable automated baseline corrections for strong motion seismology. *Journal of Geophysical Research: Solid Earth*, 118(3): 1177–1187, Mar. 2013. doi: 10.1002/jgrb.50135.

Melgar, D., LeVeque, R. J., Dreger, D. S., and Allen, R. M. Kinematic rupture scenarios and synthetic displacement data: An example application to the Cascadia subduction zone. *Journal of Geophysical Research: Solid Earth*, 121(9):6658–6674, Sept. 2016. doi: 10.1002/2016jb013314.

Melgar, D., Crowell, B. W., Melbourne, T. I., Szeliga, W., Santillan, M., and Scrivner, C. Noise Characteristics of Operational Real-Time High-Rate GNSS Positions in a Large Aperture Network. *Journal of Geophysical Research: Solid Earth*, 125(7), June 2020. doi: 10.1029/2019jb019197.

Moschas, F. and Stiros, S. Noise characteristics of high-frequency, short-duration GPS records from analysis of identical, collocated instruments. *Measurement*, 46(4):1488–1506, May 2013. doi: 10.1016/j.measurement.2012.12.015.

Mousavi, S. M. and Beroza, G. C. Deep-learning seismology. *Science*, 377(6607), Aug. 2022. doi: 10.1126/science.abm4470.

Mousavi, S. M., Ellsworth, W. L., Zhu, W., Chuang, L. Y., and Beroza, G. C. Earthquake transformer—an attentive deep-learning model for simultaneous earthquake detection and phase picking. *Nature Communications*, 11(1), Aug. 2020. doi: 10.1038/s41467-020-17591-w.

Murray, J. R., Crowell, B. W., Murray, M. H., Ulberg, C. W., McGuire, J. J., Aranha, M. A., and Hagerty, M. T. Incorporation of Real-Time Earthquake Magnitudes Estimated via Peak Ground Displacement Scaling in the ShakeAlert Earthquake Early Warning System. *Bulletin of the Seismological Society of America*, 113(3): 1286–1310, Feb. 2023. doi: 10.1785/0120220181.

Parameswaran, R. M., Grapenthin, R., West, M. E., and Fozkos, A. Interchangeable Use of GNSS and Seismic Data for Rapid Earthquake Characterization: 2021 Chignik, Alaska, Earthquake. *Seismological Research Letters*, Mar. 2023. doi: 10.1785/0220220357.

Pedregosa, F., Varoquaux, G., Gramfort, A., Michel, V., Thirion, B., Grisel, O., Blondel, M., Prettenhofer, P., Weiss, R., Dubourg, V., Vanderplas, J., Passos, A., Cournapeau, D., Brucher, M., Perrot, M., and Duchesnay, E. Scikit-Learn: Machine Learning in Python. *J. Mach. Learn. Res.*, 12(null):2825–2830, 2011.

Ruhl, C. J., Melgar, D., Geng, J., Goldberg, D. E., Crowell, B. W., Allen, R. M., Bock, Y., Barrientos, S., Riquelme, S., Baez, J. C., Cabral-Cano, E., Pérez-Campos, X., Hill, E. M., Protti, M., Ganas, A., Ruiz, M., Mothes, P., Jarrín, P., Nocquet, J., Avouac, J., and D'Anastasio, E. A Global Database of Strong-Motion Displacement GNSS Recordings and an Example Application to PGD Scaling. *Seismological Research Letters*, 90(1):271–279, Oct. 2018. doi: 10.1785/0220180177.

Seydoux, L., Balestriero, R., Poli, P., Hoop, M. d., Campillo, M., and Baraniuk, R. Clustering earthquake signals and background noises in continuous seismic data with unsupervised deep learning. *Nature Communications*, 11(1), Aug. 2020. doi: 10.1038/s41467-020-17841-x.

SHEN, N., CHEN, L., LIU, J., WANG, L., TAO, T., WU, D., and CHEN, R. A Review of Global Navigation Satellite System (GNSS)-based Dynamic Monitoring Technologies for Structural Health Monitoring. *Remote Sensing*, 11(9):1001, Apr. 2019. doi: 10.3390/rs11091001.

Shu, Y., Fang, R., Li, M., Shi, C., Li, M., and Liu, J. Very high-rate GPS for measuring dynamic seismic displacements without aliasing: performance evaluation of the variometric approach. *GPS Solutions*, 22(4), Sept. 2018. doi: 10.1007/s10291-018-0785-z.

Shu, Y., Fang, R., Liu, Y., Ding, D., Qiao, L., Li, G., and Liu, J. Precise coseismic displacements from the GPS variometric approach using different precise products: Application to the 2008 MW 7.9 Wenchuan earthquake. *Advances in Space Research*, 65(10): 2360–2371, May 2020. doi: 10.1016/j.asr.2020.02.013.

Team, T. O. D. ObsPy 1.2.1, 2020. doi: 10.5281/ZENODO.3706479.

Teunissen, P. J. GNSS Precise Point Positioning, Dec. 2020. doi: 10.1002/9781119458449.ch20.

Trnkoczy, A. Topic Understanding and parameter setting of STA/LTA trigger algorithm 1 Introduction. *New Manual of Seismological Observatory Practice 2 (NMSOP-2)*, 2012. doi: https://doi.org/0.2312/GFZ.NMSOP-2_IS_8.1.

Wang, Y., Breitsch, B., and Morton, Y. T. J. A State-Based Method to Simultaneously Reduce Cycle Slips and Noise in Coherent GNSS-R Phase Measurements From Open-Loop Tracking. *IEEE Transactions on Geoscience and Remote Sensing*, 59(10): 8873–8884, Oct. 2021. doi: 10.1109/tgrs.2020.3036031.

Williams, S. D. P., Bock, Y., Fang, P., Jamason, P., Nikolaidis, R. M., Prawirodirdjo, L., Miller, M., and Johnson, D. J. Error analysis of continuous GPS position time series. *Journal of Geophysical Research*, 109(B3), 2004. doi: 10.1029/2003jb002741.

Williamson, A. L., Melgar, D., Crowell, B. W., Arcas, D., Melbourne, T. I., Wei, Y., and Kwong, K. Toward Near-Field Tsunami Forecasting Along the Cascadia Subduction Zone Using Rapid GNSS Source Models. *Journal of Geophysical Research: Solid Earth*, 125(8), Aug. 2020. doi: 10.1029/2020jb019636.

Withers, M., Aster, R., Young, C., Beiriger, J., Harris, M., Moore, S., and Trujillo, J. A comparison of select trigger algorithms for automated global seismic phase and event detection. *Bulletin of the Seismological Society of America*, 88(1):95–106, Feb. 1998. doi: 10.1785/bssa0880010095.

Woollam, J., Münchmeyer, J., Tilmann, F., Rietbrock, A., Lange, D., Bornstein, T., Diehl, T., Giunchi, C., Haslinger, F., Jozinović, D., Michelini, A., Saul, J., and Soto, H. SeisBench—A Toolbox for Machine Learning in Seismology. *Seismological Research Letters*, 93(3):1695–1709, Mar. 2022. doi: 10.1785/0220210324.

Yang, R., Morton, Y., Ling, K.-V., and Poh, E.-K. Generalized GNSS Signal Carrier Tracking–Part II: Optimization and Implementation. *IEEE Transactions on Aerospace and Electronic Systems*, 53 (4):1798–1811, Aug. 2017. doi: 10.1109/taes.2017.2674198.

Yosinski, J., Clune, J., Bengio, Y., and Lipson, H. How transferable are features in deep neural networks? 2014. doi: 10.48550/ARXIV.1411.1792.

Zhu, W., Mousavi, S. M., and Beroza, G. C. Seismic signal augmentation to improve generalization of deep neural networks. In *Machine Learning in Geosciences*, pages 151–177. Elsevier, 2020. doi: 10.1016/bs.agph.2020.07.003.

doi:10.26443/seismica.v2i2.953

SEISMICA

The July–December 2022 earthquake sequence in the southeastern Fars Arc of Zagros mountains, Iran

Malte Metz * [1,2], **Behnam Maleki Asayesh** [1,2], **Mohammad Mohseni Aref** [2], **Mohammadreza Jamalreyhani** [3], **Pınar Büyükakpınar** [1,2], **Torsten Dahm** [1,2]

[1]GFZ German Research Centre for Geosciences, Potsdam, Germany, [2]Institute of Geosciences, University of Potsdam, Potsdam, Germany, [3]Institute of Geophysics, University of Tehran, Tehran, Iran

Author contributions: *Conceptualization*: Malte Metz, Behnam Maleki Asayesh, Mohammad Mohseni Aref, Mohammadreza Jamalreyhani. *Methodology*: Malte Metz. *Software*: Malte Metz. *Formal analysis*: Malte Metz, Pınar Büyükakpınar. *Data curation*: Mohammad Mohseni Aref, Mohammadreza Jamalreyhani, Pınar Büyükakpınar. *Writing - original draft*: Malte Metz, Behnam Maleki Asayesh, Mohammad Mohseni Aref, Mohammadreza Jamalreyhani. *Writing - review & editing*: Malte Metz, Behnam Maleki Asayesh, Mohammadreza Jamalreyhani, Pınar Büyükakpınar, Torsten Dahm. *Visualization*: Malte Metz, Behnam Maleki Asayesh, Pınar Büyükakpınar. *Supervision*: Pınar Büyükakpınar, Torsten Dahm.

Abstract Within two hours on 01 July 2022, three earthquakes of M_w 5.8–6.0 hit the SE Fars Arc, Iran. In the following months, the region, characterized by the collision of the Iranian and the Arabian plate, thrust faulting, and salt diapirism, was stroke by more than 120 aftershocks of mL 3.1–5.2, of which two of the largest events occurred within one minute on 23 July 2022 in spatial vicinity to each other. We analyzed both the large mainshocks and aftershocks using different techniques, such as the inversion of seismic and satellite deformation data in a joint process, and aftershock relocation. Our results indicate the activation of thrust faults within the lower sedimentary cover of the region along with high aftershock activity at significantly larger depths, supporting the model of a crustal strain decoupling during the collision in the Fars Arc. We resolved a magnitude difference of > 0.2 magnitude units between seismic and joint seismic and satellite deformation inversions probably caused by afterslip, thereby allowing to bridge between results from international agencies and earlier studies. We also find evidence for an event doublet and triplet activating the same or adjacent faults within the sedimentary cover and the basement.

Non-technical summary On 01 July 2022, three moderate earthquakes with magnitudes of 5.8–6.0 occurred in the Zagros mountain range in the Hormozghan province, SE Iran. Their close occurrence in space and time impedes the analysis of such events. Using seismic and satellite deformation data with well-proven and newly developed earthquake parameter estimation tools, we found evidence for south-dipping thrust events within the shallow sedimentary layer. The relocation of more than 120 aftershocks with local magnitudes 3.1–5.2 revealed a strong spatial concentration in larger depths of 10–$15\,\mathrm{km}$ beneath the mainshocks. This result is consistent with the scenario of shallow-depth mainshocks followed by separated, deeper aftershock sequences, as already observed at the western edge of the Hormuz Strait.

Production Editor:
Gareth Funning
Handling Editor:
Wenbin Xu
Copy & Layout Editor:
Abhineet Gupta

Signed reviewer(s):
Ezgi Karasozen
Wasja Bloch

Received:
May 2, 2023
Accepted:
August 31, 2023
Published:
October 18, 2023

Revised:
November 1, 2023

1 Introduction

The north-south convergence of $\sim$2–3 $\mathrm{cm\,yr^{-1}}$ between the Arabian and Eurasian plates has led to active faulting and folding, volcanic activities, mountainous terrain, and variable crustal thickness in the Iranian Plateau (IP) (e.g., Stoecklin, 1968; Vernant et al., 2004). This convergence gave rise to the $1800\,\mathrm{km}$ long and 200–$300\,\mathrm{km}$ wide Zagros continental collision zone in the southwestern part of the IP, which accommodates approximately one-third to one-half of the plate motion (e.g., Vernant et al., 2004; Masson et al., 2005). The Zagros mountain range, which is one of the seismically most active regions in the Alpine-Himalayan orogenic belt, is subdivided into three major tectonostratigraphic domains from SW to NE: (1) the Mesopotamia-Persian Gulf Foreland Basin, (2) the Zagros Fold-Thrust Belt (ZFTB), and (3) High Zagros Zone (HZZ). The Simply Folded Belt (SFB) or Zagros Foreland Folded Belt (ZFFB) as a subdomain of ZFTB, is the topographically lower-elevation part of the range where most of the active deformation in the Zagros is concentrated (e.g., Falcon, 1974; Hessami et al., 2001; Talebian and Jackson, 2004; Alavi, 2007; Oveisi et al., 2009). The SFB itself is laterally subdivided into four physiographic provinces from NW to SE, namely the Kirkuk Embayment, the Lurestan Arc, the Dezful Embayment, and the Fars Arc (FA, see Fig. 1a) (e.g., Stoecklin, 1968; Alavi, 2007; Nissen et al., 2011; Jamalreyhani et al., 2023). The collision zone in the foreland involves 10–$15\,\mathrm{km}$ thick sections of sedimentary rocks, including extended layers of evaporites

*Corresponding author: mmetz@gfz-potsdam.de

and salt decoupling the deformation in the sedimentary strata from the Arabian continental basement (e.g., Stoecklin, 1968; Jamalreyhani et al., 2023). This exceptional setting has resulted in one of the world's most productive oil and gas basins (Jamalreyhani et al., 2021).

Earthquake multiples and doublets are loosely defined as two (doublet) or more (multiple) triggered and sub-sequential mainshocks of comparable size rupturing the same or adjacent faults within a short time (e.g., Lay and Kanamori, 1980; Ammon et al., 2008). The occurrence of doublets is explained by heterogeneous stress on pre-existing faults with geometrical complexities (e.g., steps, bends) and stress transfers from the first to the second event of the doublet (e.g., Xu and Schwartz, 1993; Jia et al., 2020; Zhang et al., 2021; Taymaz et al., 2022; Astiz et al., 1988). Doublets have been observed in different tectonic settings, as (1) within subduction zones (Lay and Kanamori, 1980; Xu and Schwartz, 1993; Ammon et al., 2008; Lay, 2015; Ye et al., 2013, 2016; Jia et al., 2020), (2) in collision zones (e.g., Thapa et al., 2018), (3) strike-slip fault systems (e.g., Zhang et al., 2021; Sokos et al., 2015; Dal Zilio and Ampuero, 2023), or (4) on normal faults in sedimentary basins (e.g., Cesca et al., 2013).

The central IP and its bounding tectonic structure were hit by several doublets or multiple earthquakes during the last decade, like the NW Iranian 2012 Ahar-Varzagan and 2020 Qotur-Ravian doublets (Ansari, 2016; Ghods et al., 2015; Donner et al., 2015; Momeni and Tatar, 2018; Taymaz et al., 2022), or the December 2017 Hojedk triplet in SE Iran (e.g., Freund, 1970; Walker and Jackson, 2002; Savidge et al., 2019; Asayesh et al., 2020) (Fig. 1a). The occurrence of doublets in the ZFTB is associated with the complex thrust and fold belts in the Zagros mountains with a highly deformed and sliding sedimentary and evaporitic cover with massive syncline and anticline structures (Roustaei et al., 2010). More recently, the ZFTB hosted doublets in Southern Iran, the so-called 2021 Fin doublet (Fathian et al., 2022; Rezapour and Jamalreyhani, 2022), and the 2022 Charak events. These events drew the attention of scientists to the region to better understand the physical mechanism of earthquake doublets, which is crucial for hazard and risk assessment.

Our study area is located in the FA, which is the $\sim$700 km-long segment situated in the East of the SFB with a high-rate seismicity zone in Zagros (Fig. 1b) (e.g., Karasözen et al., 2019). The FA is bounded by the Kazerun Fault in the West and the Bandar Abbas syntaxis in the East and works as the transition zone to the Makran accretionary to the East (Edey et al., 2020) (Fig. 1b). The seismicity of the FA is dominated by shallow thrust events on steeply dipping (30°–60°) blind faults in the sedimentary cover or the underlying crystalline basement (e.g., Jahani et al., 2009; Nissen et al., 2011). Tatar et al. (2004) revealed $10\,\mathrm{mm\,yr^{-1}}$ present-day shortening trending NNE-SSW at the center of the FA. There, surface shortening is accommodated by several W-E to NW-SE trending, symmetric anticlines and synclines with amplitudes within the scale of kilometers and wavelengths of $\sim$10–20 km (e.g., Edey et al., 2020). The relationship between buried seismic faults and surface anticlines in the FA is still debated (Walker et al., 2005). Several surface diapirs, which indicate the presence of the Precambrian-Cambrian Hormuz salt layer between the basement and sedimentary cover, are also observed in the FA (Jahani et al., 2009). The occurrence of anthropogenic earthquakes has recently been reported in this collision zone (Jamalreyhani et al., 2021, and references therein).

On 14 November 2021, the Fin area in the FA was struck by an earthquake doublet (M_w 6.2 and M_w 6.3) (Nemati, 2022; Fathian et al., 2022; Rezapour and Jamalreyhani, 2022) co-located with an earlier sequence of earthquakes (M_w 4.9–5.7) on 25 March 2006 (Roustaei et al., 2010) (Figs. 1c, 2). Furthermore, our study area experienced many significant single events in 2021, including the 16 March NW Lenge earthquake (M_w 5.9), the 15 June Charak earthquake (M_w 5.5), the 21 June Mogham earthquake (M_w 5.2), and the second Charak earthquake on 25 June (M_w 5.6). Some other events, such as the 2005 Qeshm and the 2006 Fin earthquakes, ruptured the lower sedimentary cover and were accompanied by aftershocks in significantly greater depth (Nissen et al., 2010, 2011, 2014). This vertical separation of main- and aftershocks might be driven by the mainshock, causing stress changes within the deeper and harder Hormuz layer. As a result of the stress perturbation, the Hormuz salt may flow, leading to a breakup of intercalated, harder, non-evaporitic sediments and surrounding rocks (Nissen et al., 2014).

Within this tectonic frame, three earthquake sequences with event magnitudes of M_w 5.3–6.1 and a series of aftershocks stroke the Hormozgan Province. The sequences occurred on 01 July 2022 (three earthquakes of M_w 5.7–6.1), further sequence A, on 23 July 2022 (two earthquakes of M_w 5.3–5.6), further sequence B, and on 30 November 2022 (one earthquake of M_w 5.6), further sequence C (Figs. 1c and 2, Tab. 1). All sequences hit the same region SW from the Fin doublet, W from the 2005–2009 seismic sequence on the Island of Qeshm and close to the mapped Zagros Foredeep Fault (ZFF) and Mountain Front Fault (MFF). Different agencies reported the fault mechanisms for these earthquakes, which mainly indicate pure thrust faulting with ENE-WSW to ESE-WNW striking, and N-S oriented shortening. Reported locations scatter primarily along the eastern termination of the ZFF. The only exception is earthquake B2 located $\sim$25 km to the N along the MFF with a strong oblique component. Using satellite geodesy Yang et al. (2023) suggests that two south-dipping, ESE striking thrust faults were activated during the mainshocks A1 and A3 with dip angles of 65° and 33°, a peak slip of $\sim$1.1 m and $\sim$1.3 m, and a geodetic moment release equivalent to M_w 6.22 and M_w 6.23, respectively. Both, A2 and A3, and B1 and B2 occurred in quick succession with interevent times of 60–80 s.

Analysis of earthquake doublets or sequences is challenging, especially when interevent times are smaller than the travel time of surface waves to a station. Then, time windows and stations need to be selected carefully to avoid any overlay of seismic signals (e.g., Jia et al., 2022; Metz et al., 2022). The joint inversion of multiple sources using seismograms and near-field data,

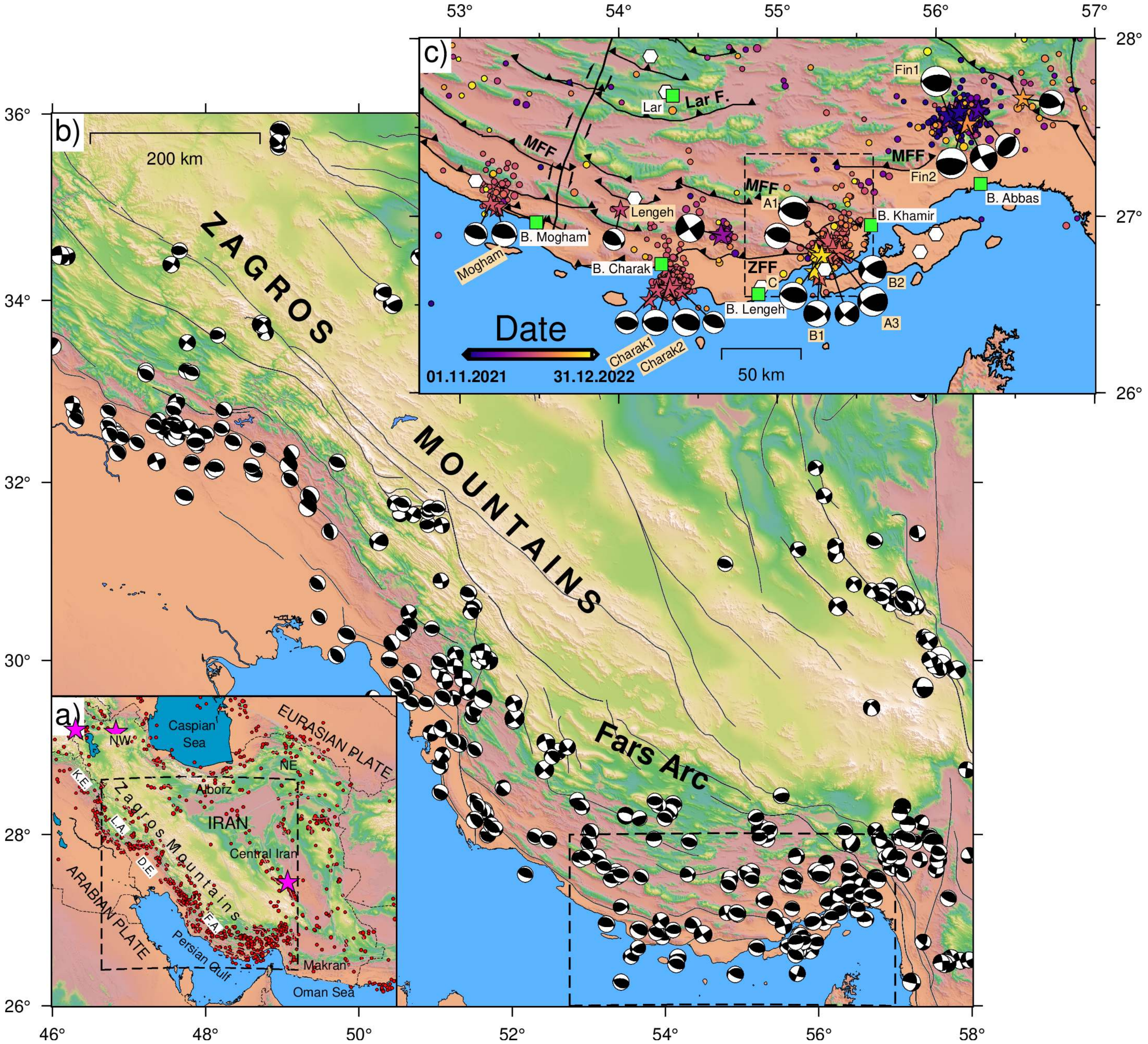

Figure 1 a) The Iranian plateau and its seismotectonic settings. Red circles are $\mathrm{M} > 5$ earthquakes from 1900 to 2022 from the USGS catalog. The magenta stars show the location of the 2012 Ahar-Varzagan doublet, the 2020 Qotur-Ravian doublet, and the 2017 Hojedk triplet. The Fars Arc (FA), Dezful embayment (DE), Lurestan Arc (LA), and the Kirkuk embayment (KE) from SE to NW are four tectonostratigraphic domains of the most active part of the Zagros (the Simply Folded Belt). b) SE part of the Zagros Mountains at the leading edge of the Arabia-Eurasia collision zone and focal mechanism of moderate and large events ($\mathrm{M}_w \geq 5$) from the gCMT catalog until October 2021. Black lines show major mapped active faults. c) A zoom-in of the Hormozghan area. The white hexagons show the historical events (Ambraseys and Melville, 2005) and colored circles demonstrate the seismicity from November 2021 until December 2022 from the Iranian Seismological Center (IRSC) catalog. Colored stars depict 33 events with $\mathrm{M} > 4.5$ during this period. For 20 of them, gCMT reported focal mechanisms (black beach balls). The dashed rectangle depicts the location of Fig. 2.

e.g., static displacements derived from InSAR (Steinberg et al., 2020, 2022), can help to constrain the geometry of and the dislocation on the activated faults within a sequence. Inversions of the rupture kinematics on a doublet fault network can resolve the onset and propagation of the ruptures (e.g., Metz et al., 2022). The back projection of the radiated high-frequency energy helps to unravel the rupture processes (e.g., Daout et al., 2020; Steinberg et al., 2022; Metz et al., 2022). Furthermore, the analysis of aftershocks might help to detect the faults activated during a sequence or doublet (e.g., Ammon et al., 2008; Ghods et al., 2015; Donner et al., 2015; He et al., 2018; Metz et al., 2022).

In this regard, we analyze the July–December 2022 earthquake sequence. We want to clarify if sequence A or B can be classified as an earthquake doublet (or triplet) according to the definition given in the introduction. In this context, we test a newly developed triplet inversion scheme using a combination of satellite deformation with seismic data covering epicentral distances

Table 1 Selected standard centroid moment tensor inversion results published by different agencies for 01 July 2022, 23 July 2022 and 30 November 2022 earthquakes. Centroid times are given.

ID	Agency	Time	Lat, Lon	Depth	M_w	Strike, Dip, Rake
Sequence A: 01 July 2022						
A1	gCMT	21:32:08	26.68°, 55.18°	12 km	6.1	113°, 52°, 110°
						282°, 42°, 66°
	GEOFON	21:32:08	26.89°, 55.23°	10 km	6.0	103°, 52°, 98°
						271°, 39°, 80°
	USGS	21:32:08	26.942°, 55.227°	10 km	6.0	95°, 51°, 83°
						286°, 39°, 98°
A2	GEOFON	23:24:13	26.85°, 55.29°	10 km	5.9	-, -, -
						-, -, -
	USGS	23:24:14	26.920°, 55.219°	10 km	5.7	96°, 47°, 100°
						262°, 47°, 80°
A3	gCMT	23:25:15	26.69°, 55.13°	12 km	6.1	121°, 45°, 138°
						245°, 62°, 54°
	GEOFON	23:25:15	26.82°, 55.33°	10 km	6.0	110°, 22°, 118°
						261°, 71°, 79°
	USGS	23:25:15	26.887°, 55.285°	10 km	6.0	94°, 34°, 96°
						267°, 56°, 86°
Sequence B: 23 July 2022						
B1	gCMT	16:07:56	26.65°, 55.52°	12 km	5.5	56°, 59°, 34°
						307°, 62°, 144°
	GEOFON	16:07:49	26.75°, 55.28°	10 km	5.3	82°, 33°, 108°
						240°, 59°, 79°
	USGS	16:07:48	26.880°, 55.210°	10 km	5.3	126°, 35°, 133°
						258°, 65°, 65°
B2	gCMT	16:09:08	26.73°, 55.22°	12 km	5.6	128°, 65°, 148°
						233°, 61°, 29°
	GEOFON	16:09:08	26.98°, 55.52°	10 km	5.5	120°, 48°, 140°
						240°, 61°, 50°
	USGS	16:09:07	27.002°, 55.366°	10 km	5.4	121°, 58°, 150°
						228°, 64°, 36°
Sequence C: 30 November 2022						
C1	gCMT	15:17:43	26.69°, 55.21°	12 km	5.6	107°, 54°, 101°
						270°, 40°, 77°
	GEOFON	15:17:43	26.83°, 55.29°	10 km	5.6	101°, 68°, 91°
						278°, 22°, 28°
	USGS	15:17:41	26.887°, 55.239°	5 km	5.6	94°, 65°, 86°
						285°, 26°, 99°

Agencies:
gCMT - Global CMT (Dziewoński et al., 1981; Ekström et al., 2012)
GEOFON - GEOFON program using data from the GEVN partner networks (Quinteros et al., 2021)
USGS - USGS National Earthquake Information Center, PDE

from local to teleseismic. We also aim at understanding the interaction of main- and aftershocks in the region using relocated aftershocks. The joint analysis of different data sets and main- and aftershocks shall provide deeper insights into source mechanisms and rupture kinematics of the mainshocks. Our work complements studies focusing on satellite deformation data (e.g., Yang et al., 2023) by resolving temporal aspects and rupture parameters and constraining the position of the activated fault system from aftershocks.

2 Materials and methods

We want to understand the characteristics of the July–November 2022, SE Iran, mainshocks (Tab. 1) from point and finite fault inversions using seismic and, if available, satellite deformation data. Complementing our analyses we relocate aftershocks to gain insights into the stress transfer and the activation of fault planes caused by the mainshocks. In the following, we introduce the pre-processing applied to the satellite deformation data. This dataset is used in the joint multiple source inversions. We also explain the settings of the single- and multiple-earthquake-inversion approaches for the point source and the finite fault models, which are used to study the mainshocks. Furthermore, the methodology for an independent measure of the focal depth based on teleseismic body wave phases is presented. Finally, a brief introduction of the aftershock relocation is given.

2.1 InSAR data pre-processing

Interferometric Synthetic Aperture Radar (InSAR) surface displacement measurements are crucial to constrain earthquake locations, particularly in finite fault inversions (e.g., Ide, 2007; Steinberg et al., 2020). For our multisource inversion approaches, we use interferograms recorded on Sentinel-1. The unwrapped and geocoded interferograms were obtained from an ascending orbit (track 130, 22 June 2022, to 04 July 2022) and a descending orbit (track 166, 25 June 2022, to 07 July 2022), each with a 12-day temporal baseline, via the COMET-LiCSAR web portal along with essential metadata and coherence data. The Generic Atmospheric Correction Online Service (GACOS) offers tropospheric delay products (Yu et al., 2017, 2018b,a), which aim at reducing tropospheric noise in interferograms. However, due to the negative impact of GACOS-based corrections on unwrapped interferograms, we opted to employ a linear method that leverages the correlation between phase and elevation for stratified tropospheric noise correction (Doin et al., 2015).

We processed InSAR time series for the tracks 130 (ascending) and 166 (descending) using the open-source Miami InSAR time-series software in Python (`MintPy`, Yunjun et al., 2022) and the Hybrid Pluggable Processing Pipeline (HyP3) service (Hogenson et al., 2016). HyP3 is a cloud-native infrastructure that offers a generic processing platform for SAR data, including interferometric processing. It streamlines the generation of interferograms, coherence maps, and unwrapped phase products by automating the necessary processing steps. The HyP3 service facilitated our processing of Sentinel-1 data, enabling consistent and efficient generation of interferometric products. The results demonstrated similar deformation patterns for both ascending and descending tracks, providing consistency and confidence in our findings.

Corrected displacement maps are post-processed using the software toolbox Kite (Isken et al., 2017) (Fig. 3). Post-processing includes an empirical variance-covariance estimation of the data error as an input for data weighting within the later inversion (Sudhaus and Jónsson, 2009) and irregular quadtree subsampling (Jónsson et al., 2002) (Fig. 7).

2.2 Bayesian moment tensor (MT) inversion of the mainshocks

We performed moment tensor (MT) point source inversions on both the individual mainshocks and also jointly on the whole sequence A using the Bayesian inversion software Grond (Heimann et al., 2018). Utilizing a particle swarm method combined with bootstrapping, Grond estimates non-linear uncertainties of all inversion parameters. We fit the MT components (full and deviatoric for the individual source inversions and double couple (DC) for the joint inversion), centroid loca-

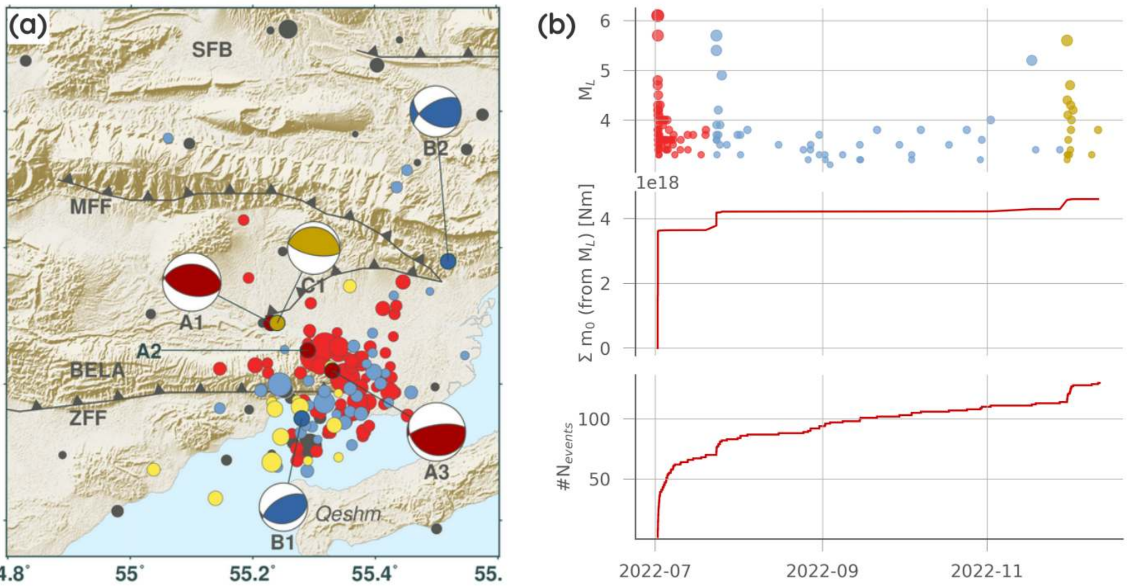

Figure 2 (a) Seismicity from IRSC in Southern Iran before 01 July 2022 (grey dots) and after (colored dots), including GEOFON MT solutions (or location for A2) for the mainshocks. Colors of the dots and MTs indicate the time after 1 July (red), after 22 July (blue), or after 30 November (yellow), respectively. (b) shows the temporal seismicity evolution (mL, cumulative moment, and the number of events) using the IRSC catalog with the same color coding as in (a). Major tectonic/seismic features highlighted/annotated in (a) are the Mountain Front Fault (MFF), the Zagros Foredeep Fault (ZFF), the Simply Folded Belt (SFB), and the Bandar-e-Lengeh anticline (BELA).

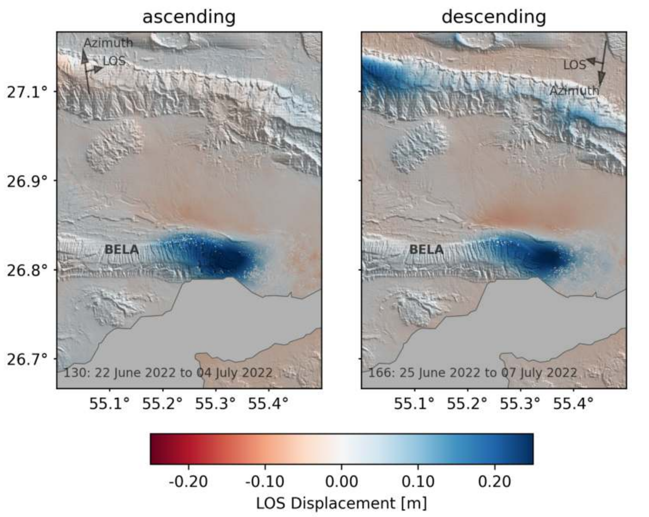

Figure 3 Ground deformation derived from satellite data from ascending (left) and descending tracks of Sentinel 1. Track ID and acquiring dates are shown in the bottom left. The line of sight (LOS) and satellite track (azimuth) directions are indicated by arrows. The displayed deformation is used as input for the joint inversions. BELA indicates the Bandar-e-Lengeh anticline.

tion, time, and duration based on waveform and static ground displacement fits.

Individual earthquake inversions used teleseismic and regional body wave signals, recorded at 18 teleseismic and seven regional stations with an epicentral distance of $\sim$230–10 000 km with carefully selected time windows to ensure less overlap between the signals emitted by subsequent earthquakes. Due to inaccessible regional data, all inversions for C1 used only the teleseismic dataset. Before inversion, data was visually inspected, and all noisy, incomplete, or corrupted signals were removed. All waveforms have been fitted as bandpass-filtered displacements (0.015–0.06 Hz for A1 and A3, 0.02–0.06 Hz for A2, B1, B2, and C1) in time domain on the vertical and transverse components. Lower frequency limits were chosen to suppress low-frequent noise. Relatively low upper-frequency limits diminish high-frequent site effects and reduce the effect of structural inhomogeneities not captured within our ground model on the data fit. Synthetic waveforms were generated based on Green's functions calculated with QSEIS (Wang, 1999) using the AK135 global and a regional velocity model (Karasözen et al., 2019; Jamalreyhani et al., 2021).

A joint inversion scheme described as the double DC or double single force source by Carrillo Ponce et al. (2021) was adapted and then used for the earthquakes of sequence A. The original approach allows for simultaneous source estimates via parameterizing the temporal and spatial distance between subevents with the focus on single, but complex earthquakes. It subsequently enables the use of seismic records characterized by overlapping signals of different subevents. Furthermore, ground displacements recorded by InSAR with their coarse temporal resolution can be fitted to the superposed synthetic ground displacements of all inverted subevents.

The mentioned double DC inversion scheme was enhanced for simultaneous inversions of three earthquakes as required for a complete assessment of sequence A. These inversions used seismic and satellite deformation data within separate and joint runs. Satellite deformation data was fitted to synthetic ground displacements calculated with PSGRN and PSCMP (Wang et al., 2003; Wang, 2005; Wang et al., 2006) using the regional velocity model by Karasözen et al. (2019); Jamalreyhani et al. (2021). An interpretation of the triple source inversion must be done with care as more free parameters within the inversion may also lead to overfitting or the fitting of noise signals. The double source setup could not be applied to sequence B due to high noise levels on the satellite deformation.

Throughout this paper, we will always refer to the mean model and the standard deviations derived from the inversions.

2.3 Bayesian inversion of the finite faults

Extended rupture characteristics have been estimated using the pseudo-dynamic rupture (PDR) (Metz, 2019; Dahm et al., 2021). This extended rupture model depends on a flexible boundary element method based on Okada (1992) to iteratively estimate the instantaneous dislocation on the fault from a prescribed stress drop behind a moving rupture front. The rupture front propagation is estimated using the 2D Eikonal equation and the rupture velocity linearly scaling with the shear wave velocity of the regional velocity model by Karasözen et al. (2019); Jamalreyhani et al. (2021). The further parametrization was chosen as in Metz et al. (2022) fitting 13 parameters per fault: the top edge location (lat, lon, depth), the rupture orientation (strike, dip), length and width of the rupture plane, the maximum shear slip, the rake, the relative origin coordinates, the origin time, and the scaling factor between the rupture and shear wave velocity.

The inversion settings are the same as for the MT inversions using individual and joint inversion approaches. Due to the lack of regional data for C1 and noisy satellite deformation records for sequence B, we performed PDR inversions only on the earthquakes of sequence A.

2.4 Focal depth estimation from teleseismic depth phases

We want to validate the depth estimates of our point source and finite fault inversions. Here, we apply a technique for an accurate focal depth computation based on the teleseismic delay between direct P phases and surface reflected, pP, phases using the abedeto tool (https://github.com/HerrMuellerluedenscheid/abedeto). Using the arrival time difference between the two phases (pP-P) recorded on several arrays at teleseismic distances (Fig. S18, Tab. S6 in supplementary material), we independently calculated the focal depth for the six greatest events as previously applied in the Zagros region (Jamalreyhani et al., 2021). The observed waveforms are stacked for each array to increase the signal-to-ratio. In order to create synthetic waveforms, first Green's functions are computed using a reflectivity approach (QSEIS; Wang, 1999) by taking into account the moment tensors calculated in this study. The Green's functions are based on local crustal velocity models at the source and array locations (CRUST2.0; Bassin et al., 2000), and a mantle model (AK135; Kennett et al., 1995).

2.5 Relocation of aftershocks

Earthquake relocation is vital to improve the spatial resolution of seismic sequences. We used the GrowClust3D.jl relocation method (Trugman and Shearer, 2017; Trugman et al., 2023), which implements a cluster-based relocation scheme based on relative time shifts between P- and S-wave arrivals of events with similar waveforms. The method requires a high waveform similarity among the different events and clustered initial locations.

Time shifts are converted into distance and azimuths using pre-calculated travel times based on a 1D velocity model; the required ray tracing was performed using the same regional ground model as for the inversions (Karasözen et al., 2019; Jamalreyhani et al., 2021). Due to limitations in waveform data access, we adopted the scheme to handle picked Pg, Pn, Sg, and Sn arrivals derived from the IRSC catalog. Required relative time shifts for two events were obtained by subtracting absolute arrival times for matching stations.

This approach allows getting a first-order relocation of the catalog with the limitations caused by the arrival time picks provided only to the tenth of a second and the lack of quality control parameters like the cross-correlation coefficient. In total, 120 aftershocks of all three sequences A, B, and C with mL larger than 3.0 from 01 July 2022 until 12 December 2022 were relocated (Fig. 2).

3 Results

In the following we will summarize our findings. We start with the pure seismic inversions of both point and finite source models. Thereafter, results from the joint satellite deformation and seismic data inversions are presented. We will also show results from the focal depth estimation. Finally, outcomes from the aftershock relocation are shown. Due to indications for dominant southward dipping thrusting (Yang et al., 2023) we will discuss our point source results emphasizing the south-dipping nodal planes.

The analysis of seismic data yields robust MT solutions for seven events with M_w larger than 5.3 from 01 July 2022 to 30 November 2022 (Figs. 4a,b, S1–S6, Tabs. 2, S1, S2). All indicate rupture on E-W striking planes ($88°$–$118°$) with one focal plane dipping with $37°$–$68°$ towards the South. Dips vary from shallow $37°$–$39°$ (A3, B1) to more than $60°$ (A1, B2, C1). While events A1, A2, and C1 show rather pure thrust (rake of $80°$–$100°$), events A3 (rake of $120°$) and especially B1 and B2 (rake of $132°$–$142°$) indicate oblique faulting. The magnitudes of the events range from 5.27 for event B1 to 6.01 for event A3 with the highest magnitudes observed for sequence A (M_w 5.73–6.01). All centroids of sequence A are located close to each other beneath or slightly to the North of the Bandar-e-Lengeh anticline (BELA) in depths of 6.8–$8.0\,\mathrm{km}$. B1 and B2 occurred in larger depths of 10.4–$11.5\,\mathrm{km}$, with B1 being co-located with sequence A and B2 shifted by $10\,\mathrm{km}$ towards the North. The later event C1 shows a strong location migration towards the West by $\approx 20\,\mathrm{km}$. Its centroid lays

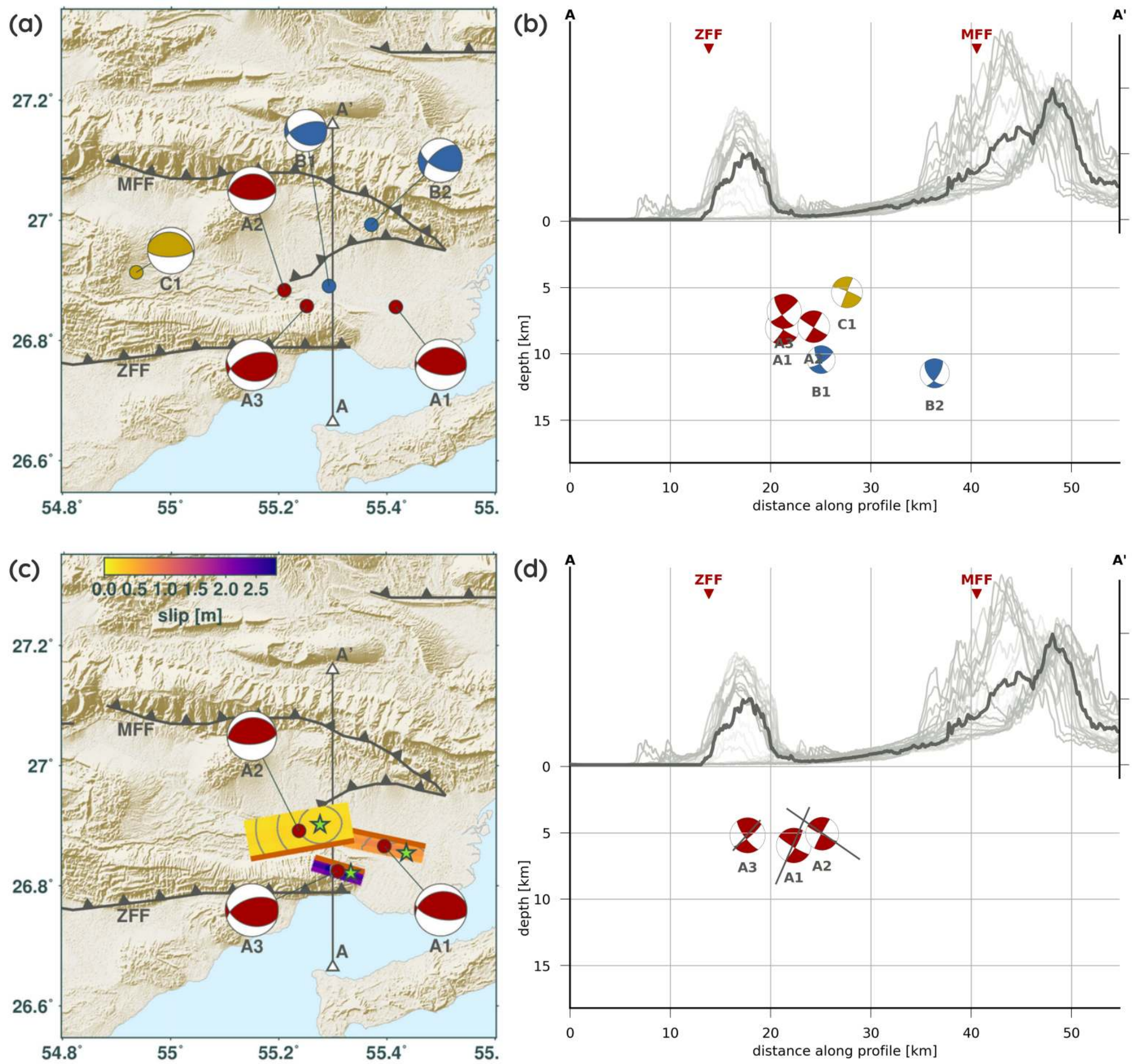

Figure 4 Results of seismic inversions with centroids from full MT inversions as map (a) and along the profile (b). PDR inversion results using seismic data are shown as map (c) and profile (d) with their centroids (dots), rupture plane locations, final slip, rupture origin (green star) and rupture propagation contour lines (every $2\,\mathrm{s}$, grey lines in (c)). Grey lines in (d) indicate the PDR rupture plane locations and orientations through their respective centroids. The topography in the profiles (b, d) is shown along the profile A–A' (dark grey) and along parallel lines extracted every $0.01°$ longitude from $55.15°$W to $55.45°$W (light grey). Increasing transparency scales with increasing distance to the profile A–A'.

beneath the BELA at a shallow depth of $5.4\,\mathrm{km}$.

Independent finite fault solutions obtained from seismic data for sequence A yield preferred orientations of the fault plane but with minimal misfit differences compared to the inversions for the auxiliary nodal plane (Figs. 4, S7–S9, Tabs. 2, S4). Preferred fault planes strike towards West ($260°$) and dip towards North by $28°$ for A2 or strike East ($102°$–$107°$) with a southward dip of $41°$–$61°$ for A1 and A3. Rakes of $85°$–$115°$ indicate pure thrust faulting with a slight oblique component for A3. Source plane extents range from $9.5 \pm 2.3\,\mathrm{km} \times 3.4 \pm 1.5\,\mathrm{km}$ in length and width for A3 up to $19.3 \pm 3.0\,\mathrm{km} \times 8.1 \pm 1.3\,\mathrm{km}$ for A2. Resolved top edge depths are similar through all events of sequence A ranging from $3.1 \pm 0.7\,\mathrm{km}$ for A1 to $4.1 \pm 0.6\,\mathrm{km}$ for A3 (Tab. S4). Significant uncertainties indicate a poor resolution of the rupture origin location and hence the rupture propagation. However, all events of sequence A yield prevailing westward motion along the respective fault planes. Centroids derived from the PDR are similar to the MT solutions in location, magnitude, and orientation. Inferred centroid depths are slightly smaller, with 5.2–$6.2\,\mathrm{km}$. Also, the magnitude estimate for event A2 deviates from the MT solutions with $\mathrm{M}_w\ 5.87$ compared to 5.73 ± 0.03.

Modeled waveforms show a high fit in amplitude and phase for both CMT and PDR inversions (Figs. 6 top row, S1–S9). PDR fits of the mean model of A1 indicate an overestimation of the amplitude at the displayed station GE.SANI. Fits for the later event A2 are characterized by a slight amplitude deficit of the modeled compared to the observed waveforms for both PDR and CMT solu-

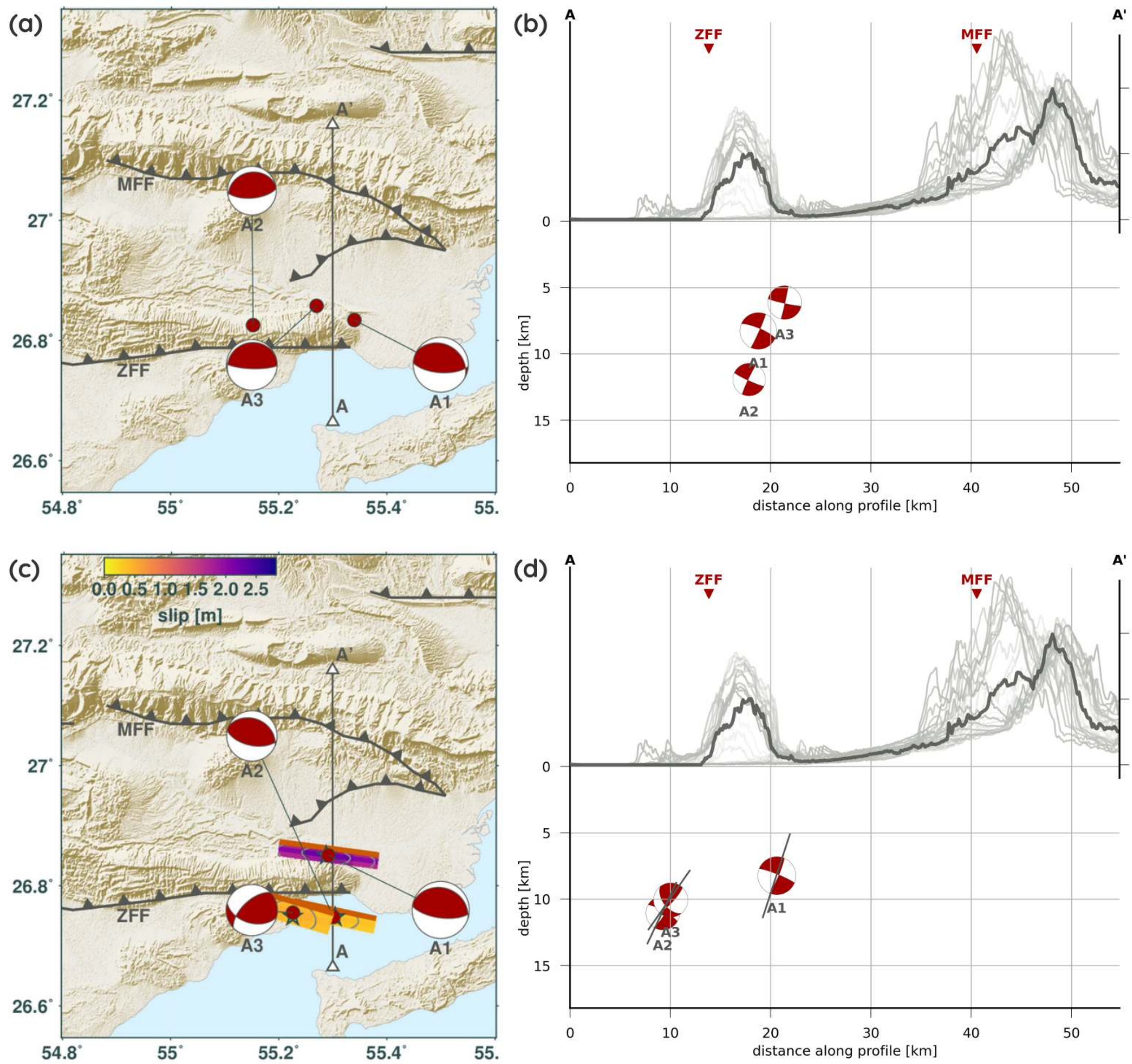

Figure 5 Results of joint seismic and satellite deformation data inversions with centroids from joint 3 DC inversion as map (a) and along the profile (b). Joint PDR inversion results using seismic and satellite deformation data are shown as map (c) and profile (d) with their centroids (dots), rupture plane locations, final slip, rupture origin (green star) and rupture propagation contour lines (every $2\,\mathrm{s}$, grey lines in (c)). Grey lines in (d) indicate the PDR rupture plane locations and orientations through their respective centroids. The topography in the profiles (b, d) is shown along the profile A–A' (dark grey) and along parallel lines extracted every $0.01°$ longitude from $55.15°$W to $55.45°$W (light grey). Increasing transparency scales with increasing distance to the profile A–A'.

tions.

For sequence A, joint inversions were carried out using seismic and satellite deformation data within a triple source inversion scheme. The triple source inversion accounts for the limited temporal resolution of satellite deformation data, which only measures the overlapping effect of the three sources. The triple DC point source inversion fits the seismic, and the satellite deformation data and yields results in agreement with our previous seismic inversions (Figs. 5a,b, 6, 7a,b, S10, Tabs. 2, S3). All mechanisms indicate thrust faulting along an E-W striking plane. The MT for A3 shows a significantly smaller oblique proportion and a much larger dip towards the South ($78°$) of one of its nodal planes compared to the similarly oriented plane of the pure seismic inversion ($39°$). The moment release indicates the highest magnitude for A1 with $\mathrm{M}_w\ 6.27$, which is about 0.3 magnitude units larger than the magnitude estimate for A1 from the pure seismic single source inversion. Synthetic waveforms (Figs. 6, S10) show significantly larger amplitudes compared to the observed and the synthetic traces from the pure seismic inversion (Fig. S1), suggesting that the satellite deformation data forces the seismic moment of A1 to have larger values. On the other hand, magnitude estimates for A2 and the corresponding waveform fits are similar to the observed traces. Finally, waveform amplitudes and the magnitude for A3 are underestimated when compared to the observed traces and the seismic modeling, respectively.

In general, the locations of the centroid double cou-

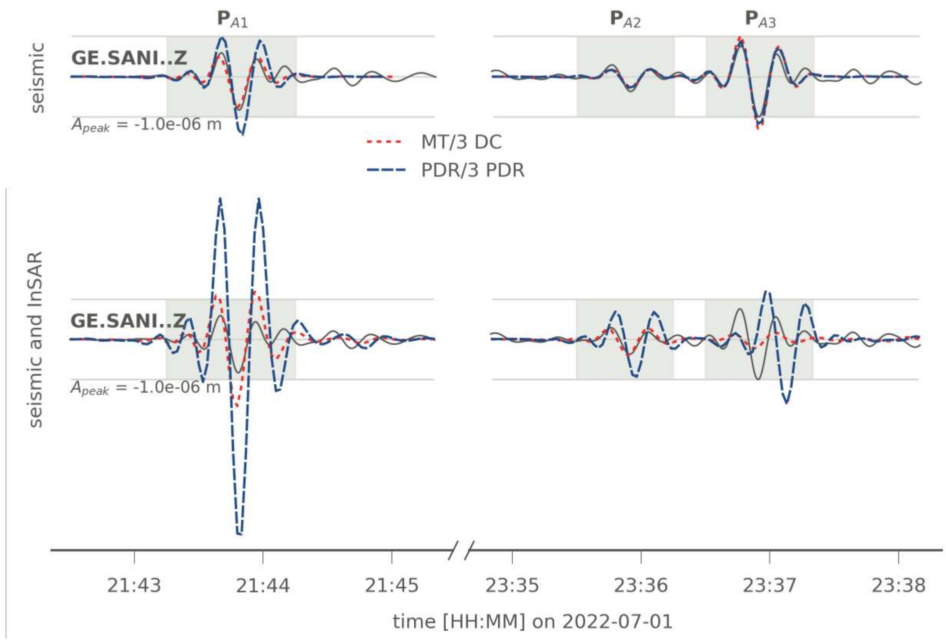

Figure 6 P-wave fits for sequence A (left A1, right A2 and A3) displayed on the vertical displacement records of station GE.SANI (distance $\approx 8215\,\mathrm{km}$, azimuth $\approx 119°$) for seismic (top row) and joint inversions (bottom row). Observed, restituted and filtered records are given in black, fitted traces in colored lines. Horizontal grey lines indicate the peak amplitude of the observed records with the value given as A_{peak}. Grey background with the top labels indicate the major P-wave signal of the different events.

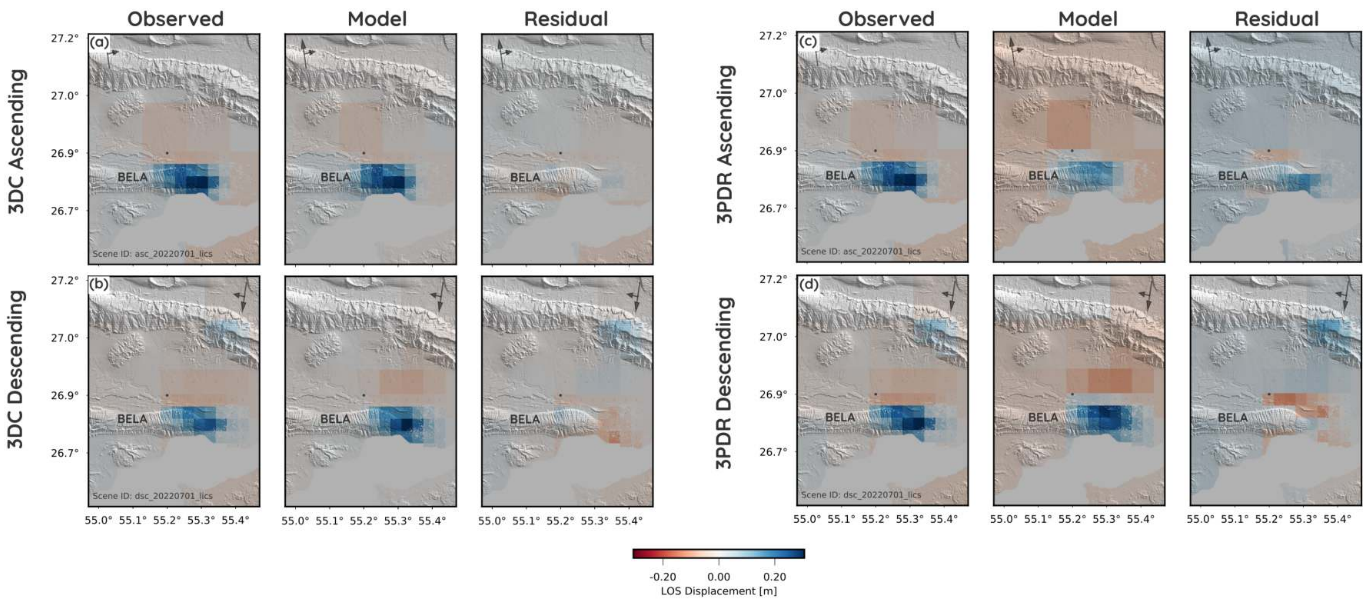

Figure 7 InSAR fits for joint 3DC (ascending - a, descending - b) and 3PDR (ascending - c, descending - d) inversions with quadtree subsampled observed data (1st column), the mean model fit (2nd column) and the corresponding residual (3rd column). BELA indicates the Bandar-e-Lengeh anticline.

ple MTs are resolved well with the largest errors for A2 (max. $5.1\,\mathrm{km}$ horizontal and 2.7 vertical error - Tab. S3). The depth of A2 ($11.9\,\mathrm{km}$) is significantly larger than estimated from seismic data ($7.9\,\mathrm{km}$).

The joint inversion of three PDR finite fault planes yields stable estimates, especially for A1, with more significant uncertainties for A2 and A3. All events are characterized as E-W striking thrust earthquakes with south dipping source planes (Figs. 5c,d, 6, 7, S11, Tabs. 2, S5). Fault orientations are mainly in agreement with results from the other inversion approaches. Contrary to the single PDR inversion, the joint inversion favors a south-dipping fault plane for A2. For A3, we obtain a large oblique component but with larger uncertainties (rake of $134° \pm 22°$) compared to point source and single finite fault inversions. The estimated seismic moment from the mean model centroid defines A1 as the largest event with M_w 6.42 and a maximum shear dislocation of $2.26 \pm 0.37\,\mathrm{m}$, while A2 and A3 released a moment equivalent to M_w 5.91 (slip of $0.39 \pm 0.20\,\mathrm{m}$) and

M_w 5.98 (slip of 0.50 ± 0.24 m). For A1 and A2, both magnitudes and maximum dislocations are overestimated compared to all other inversion approaches. The largest magnitude (> 0.4 magnitude units), and slip increase ($\sim$1.4 m), compared to the single point source or PDR seismic inversions, is observed for A1.

Waveform fits (Figs. 6, S11) indicate good phase retrieval, especially for A1 and A2. Slight phase shifts are observable for some records of A3. Similarly to the triple DC inversion, we obtain an amplitude overestimation for A1, but here even more prominent. In general, waveform amplitudes for A2 and A3 fit well.

Satellite deformation data shows a high correlation in the estimated deformation pattern with residuals of $\sim$10 cm. The ascending track fit is characterized by an underestimation of the maximum deformation measured at the BELA. In contrast, the descending track shows larger residuals along the NE boundary of the BELA (Fig. 7c,d). Both, centroid location and depth of A1 beneath the northern edge of the BELA are in good agreement with solutions from the other inversion approaches. Centroids of A2 and A3 are co-located south of the BELA beneath the Tangeh Khoran, indicating a shift of $\sim 10{\pm}8$–9 km towards the South compared to the other inversion results (Tab. S5). The respective depths are in the range of 10.1–11.1 km, up to 6 km larger than the results from our other inversion approaches.

Focal depths of the mainshocks estimated from P-wave phase arrival time differences are in the range of 7.0–11.0 km (Figs. S12–S17, Tabs. 2, S6). Smallest focal depths are obtained for C1 (7.0 km), and A1 and A2 (8.0 km). The origin depth for A3 is estimated with 10.0 km, while largest focal depths of 11.0 km are found for B1 and B2. The stacked waveform fits are rather good for the smaller events B1, B2, and C1. The larger events of sequence A generate more complex P-waves due to a longer rupture duration and, hence, source time functions. Therefore, stacked waveform fits are not as good as for the smaller events.

120 aftershocks of the IRSC catalog from 01 July 2022 to 12 December 2022 have been relocated with average vertical (depth) and horizontal location shifts and uncertainties of 0.41 ± 0.39 km and 0.67 ± 0.82 km, respectively (Figs. 8, S19, Tab. S7). The simultaneous optimization of the origin times yields an average shift of $0.1{\pm}0.1$ s. The majority of events are located in depths of 10–15 km scattering within a $\sim$10 km $\times$ 10 km wide area around 26.8° lat, 55.35° lon. They are characterized by minor location errors (Fig. S12). Larger errors in the relocation of up to 3 km horizontally and 2 km in depth are observed for the few events located towards the North and SW of the major aftershock area. The location of most aftershocks fits well with inversion results from both MT and PDR inversions, except the MT solution of C1. The westward location shift of C1 compared to sequences A and B (Fig. 4) is not reflected in the relocated aftershocks. We also do not resolve any scattering of aftershocks along preferred planes.

4 Discussion and interpretation

The analyzed earthquakes between 01 July 2022 and 12 December 2022 highlight the interaction of large, shallow thrust earthquakes in the sedimentary layer with smaller aftershocks in the upper basement or deeper sedimentary cover (Fig. 9), which is a peculiarity of the continent-continent collision in the Zagros Mountains (see e.g., Nissen et al., 2011, 2014). Using different inversion approaches, we can also resolve significant differences in the earthquake parameter estimates due to uncaptured tectonic processes or uncertainties in the used ground models. In the following, we will discuss our results related to regional tectonics, the effect of the incorporated satellite deformation data and its seismological implications, and the quality of the newly developed triple source inversion scheme.

4.1 Mainshock mechanisms and location

The earthquakes in Zagros generally have low to strong magnitudes up to M_w 7.3 and commonly occur on blind faults (Barnhart et al., 2013; Karasözen et al., 2019; Asayesh et al., 2022; Jamalreyhani et al., 2022; Nissen et al., 2019), often in depths of 8–14 km (e.g., Ni and Barazangi, 1986; Baker et al., 1993; Hessami et al., 2001; Talebian and Jackson, 2004; Jamalreyhani et al., 2021; Nissen et al., 2019). Ruptures often occur in the sedimentary layer, called a “competent group”, which spans from $\approx$4–8.5 km depth in the south eastern FA. The competent group is decoupled from the crystalline basement by the Hormuz Salt Formation at about 8–10 km (Nissen et al., 2011), a formation intercalated with stronger non-evaporitic layers. The centroids of the earthquakes A1, A3, and C1 locate in a depth of 5–8 km depth (Figs. 4, 5), which indicates an activation of faults in the lower competent group. This interpretation is supported by Roustaei et al. (2010); Nissen et al. (2010, 2011); Barnhart et al. (2013); Elliott et al. (2015) who found that most $\mathrm{M}_w > 5$ events occur in the shallow sedimentary layer between $\sim$5–10 km. Estimated focal depths for A1, A3, and C1 of 7.0–10.0 km are in line with results of our inversion and of the given studies (Tab. 2).

The later earthquake sequence B (and perhaps also A2) occurred at a larger depth of 10.5–11.5 km, shown by both centroid and focal depths, indicating a possible stress transfer from the shallow primary events A1 and A3 into depth with an activation of the deeper sedimentary Hormuz layer, interface between sediments and basement and/or faults within the crystalline basement. Both, stress transfer and the activation of significantly deeper strata are also evident from the aftershock depth range of 10–15 km below the Bandar-e-Lengeh anticline (BELA), which fits well with earlier estimates of aftershock depths, e.g., for the 2005 Qeshm or 2006 Fin earthquakes (e.g., Talebian and Jackson, 2004; Tatar et al., 2004; Nissen et al., 2011; Yaminifard et al., 2012). The scenario of a shallow mainshock followed by a separated, deeper aftershock sequence has been observed and described by Nissen et al. (2011); Yaminifard et al. (2012) for the 2005 Qeshm earthquake. The pattern may indicate that characteristic earthquakes in

Table 2 Centroid locations and orientations derived from MT and PDR inversions using both seismic and a joint seismic and InSAR dataset. The ensemble mean solution is given. Full set of resolved parameters including uncertainties are given in Tables S1–S5. Also, results from teleseismic focal depth estimation are given.

ID	Method	Time	Lat, Lon	Depth	M_w	max. Slip	Strike, Dip, Rake
Sequence A: 01 July 2022							
A1	MTs	21:32:08.7	26.856°, 55.417°	8.0 km	5.97	-	100°, 58°, 101°
							260°, 33°, 83°
	MTj	21:32:06.3	26.835°, 55.340°	8.3 km	6.27	-	94°, 66°, 79°
							299°, 26°, 113°
	PDRs	21:32:08.8	26.861°, 55.390°	6.2 km	5.96	0.82 m	102°, 61°, 102°
	PDRj	21:32:09.4	26.851°, 55.292°	8.2 km	6.42	2.26 m	98°, 67°, 87°
	TELE	-	-	8.0 km	-	-	-
A2	MTs	23:24:14.8	26.884°, 55.210°	7.9 km	5.73	-	93°, 59°, 95°
							264°, 32°, 83°
	MTj	23:24:15.7	26.826°, 55.153°	11.9 km	5.78	-	85°, 65°, 94°
							256°, 25°, 82°
	PDRs	23:24:14.6	26.896°, 55.234°	5.2 km	5.87	0.24 m	260°, 28°, 85°
	PDRj	23:24:11.6	26.748°, 55.301°	11.1 km	5.91	0.39 m	102°, 59°, 86°
	TELE	-	-	8.0 km	-	-	-
A3	MTs	23:25:14:3	26.858°, 55.252°	6.8 km	6.01	-	104°, 39°, 120°
							248°, 57°, 69°
	MTj	23:25:15.5	26.858°, 55.270°	6.1 km	5.93	-	92°, 78°, 95°
							251°, 13°, 69°
	PDRs	23:25:14.5	26.838°, 55.272°	5.6 km	5.98	2.83 m	107°, 41°, 115°
	PDRj	23:25:20.9	26.756°, 55.226°	10.1 km	5.98	0.50 m	106°, 48°, 134°
	TELE	-	-	10.0 km	-	-	-
Sequence B: 23 July 2022							
B1	MTs	16:07:47.6	26.891°, 55.293°	10.4 km	5.27	-	118°, 37°, 132°
							250°, 64°, 64°
	TELE	-	-	11.0 km	-	-	-
B2	MTs	16:09:07.8	26.993°, 55.372°	11.5 km	5.42	-	116°, 60°, 142°
							227°, 58°, 36°
	TELE	-	-	11.0 km	-	-	-
Sequence C: 30 November 2022							
C1	MTs	15:17:46.9	26.914°, 54.936°	5.4 km	5.63	-	88°, 68°, 83°
							286°, 23°, 107°
	TELE	-	-	7.0 km	-	-	-

Methods:

MTs - Full moment tensor inversion from seismic data.
MTj - Joint inversion of triple DC sources from seismic and InSAR data.
PDRs - PDR inversion from seismic data.
PDRj - Joint inversion of triple PDR sources from seismic and InSAR data.
TELE - Focal depth estimation from teleseismic depth phases.

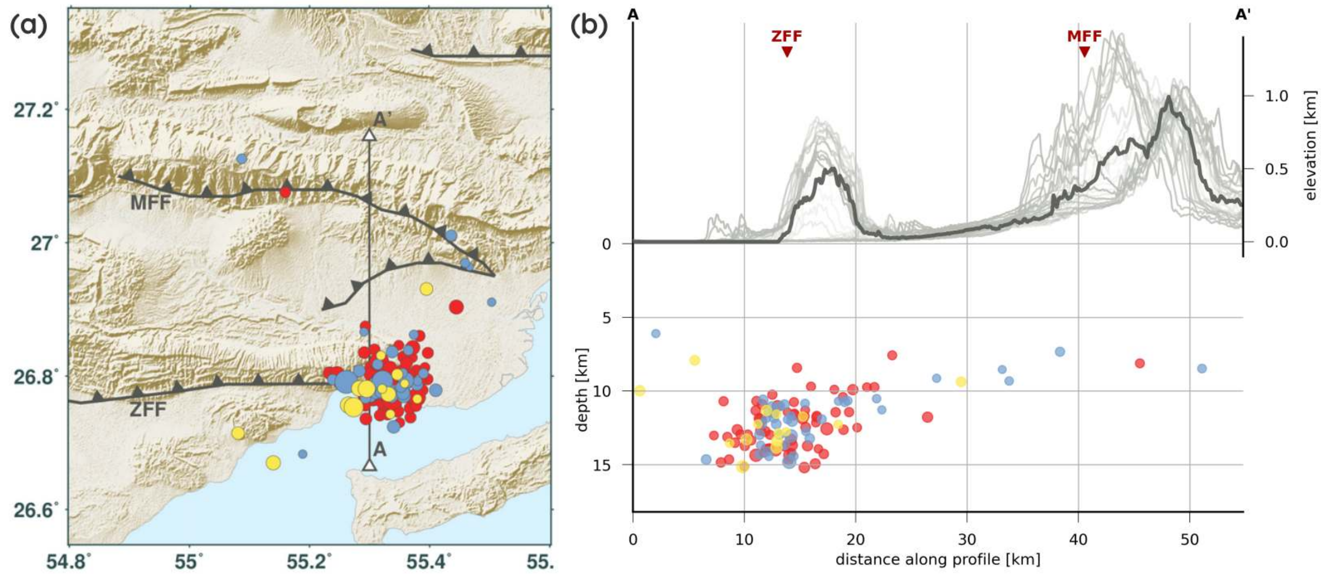

Figure 8 Map (a) and profile (b) of the IRSC catalog after relocation between 01 July 2022 and 12 December 2022. Mainshocks of sequences A, B and C are excluded. Colors indicate the time after sequence A (red), B (blue) or C (yellow). Points scale with reported local magnitude. The topography in the profile (b) is shown along the profile A–A' (dark grey) and along parallel lines extracted every $0.01°$ longitude from $55.15°$W to $55.45°$W (light grey). Increasing transparency scales with increasing distance to the profile A–A'.

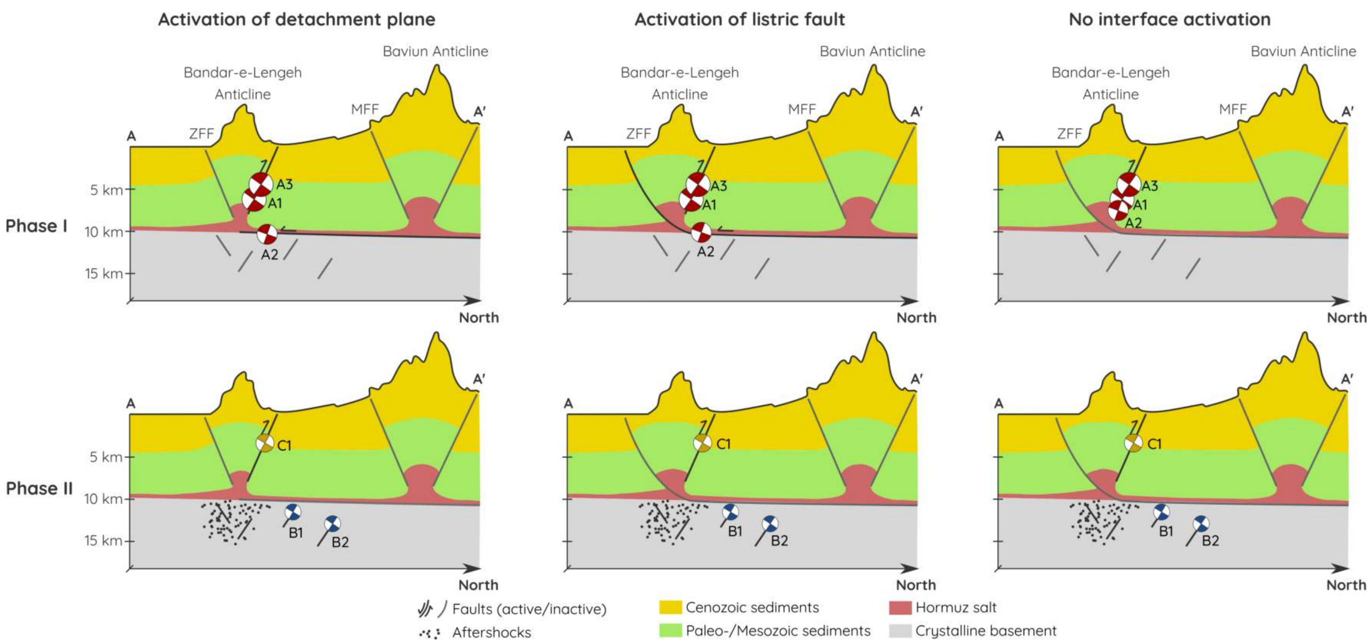

Figure 9 Interpretation of the tectonic processes during the July–December 2022 sequence. Phase I (top row) indicates the rupture processes on the 01 July 2022 while phase II (bottom row) resolves the later events. Moment tensors do not show correct rotations but shall illustrate general trends in location and mechanism. We show three interpretation possibilities using an activation of the detachment plane (left), a listric fault cutting through the sediments (center), or a rupture independent of the sediment to basement interface (right). North is indicated at each profile. The profiles are also referenced to the profile A–A' shown in Figs. 4, 5, and 8.

the competent group of the sedimentary cover are controlled by a combination of stress and forces from the horizontal collision and buoyant salt movements, while the crystalline basement of the crust is moving as a decoupled, rigid body beneath the ZFFB. Aftershocks can be induced in the basement if Coulomb stress changes occur. However, the crustal shortening in the basement is either accommodated by ductile deformation, or through crustal thickening as observed further to the north beneath the HZZ.

In addition to thrust faulting and shortening, transverse strike-slip faults play a role in the evolution of Zagros. For instance, Talebian and Jackson (2004) emphasized the importance of strike-slip faults in the basement of the southeastern-most Zagros, which has also been revealed by Yaminifard et al. (2012) studying aftershocks of the 2005 Qeshm Island event.

Sequence A is dominated by the two largest thrust events of $\mathrm{M}_w \sim 6.0$ (A1 and A3). Satellite deformation data (InSAR) show largest displacements on the BELA and minor deformation towards North (Figs. 3, 7). From the deformation pattern Yang et al. (2023) have derived two southward dipping rupture planes with dips of $33\text{–}65°$. Despite the steeply dipping planes, no surface ruptures were observed. This is, however, common for thrust events in Zagros mountains (e.g., Berberian, 1995; Regard et al., 2004; Yamini-Fard et al., 2007; Edey et al., 2020). From our joint seismic and InSAR inversion, we found a southward dipping plane of $48° \pm 13°$ (Triple PDR) or $78° \pm 2°$ (Triple DC) (Tabs. 2, S3) for the second large event of sequence A (A3). However, Yang et al. (2023) interpret A3 as a possible southward dipping but low angle, shallow splay fault of A1 with a dip of about $33°$.

The results of our single PDR seismic inversions yield similar dip angles as the triple PDR inversion between $41°$ and $48°$ on the southward dipping plane, supporting the results by USGS, gCMT, and GEOFON. Prevailing dips for thrust events are up to $60°$ (Jahani et al., 2009; Nissen et al., 2011). The steep dip estimate of $78°$ for A3 from the triple DC inversion is well above this range. It could be a result of our triple source inversion setup with many free parameters, allowing for overfitting of small amplitude satellite deformation data (Fig. 7). The poor waveform fits from the triple DC inversion for A3 compared to the single MT inversion support the interpretation of overfitting satellite deformation data at the expense of the waveform data fit (Figs. 6, S3, S10).

Event A2 is characterized by rather good waveform fits (Fig. 6) and comparable solutions through all applied techniques and inversion setups. However, the joint inversions yield a significantly larger centroid depth of $11.1\text{–}11.9\,\mathrm{km}$ vs. $5.2\text{–}7.9\,\mathrm{km}$. The larger depth would imply that A2 ruptured within the upper basement, lower sediments or along their interface. The low-angle northward dipping rupture plane, resolved from PDR inversions, fits well with the latter interpretation of a low-angle detachment earthquake along the interface (Nissen et al., 2011) (Fig. 9 left column). Resolved dips of more than $20°$ make this scenario unlikely.

Instead of a steeply northward dipping fault plane, the ZFF could also be of listrical shape propagating into the sediment-basement interface as indicated by Jahani et al. (2009) (Fig. 9 center column). Such fault shape could accommodate events with intermediate north dipping focal planes as observed.

A rupture of listric or ramp-flat faults within the basement, as suggested for the 2017 M_w 7.3 Sarpol-e Zahab earthquake (e.g., Fathian et al., 2021; Guo et al., 2022; Zhao et al., 2023) is unlikely in our case. A centroid depth at the top level of the basement and no observable spatial clustering of aftershocks along listric lineaments in the basement, prohibit such interpretation. We also obtain a origin depth of $8\,\mathrm{km}$ indicating a rupture within the lower sediments, and not within the basement. Further investigations of the fault geometry, e.g., by using teleseismic body waves (e.g., Braunmiller and Nábělek, 1996), are not easily applicable here due to the rather small magnitude, and hence, the small rupture plane extent of A2, and the complex rheology in the study area, which is not fully reflected in our ground models.

We favor the interpretation of Yang et al. (2023), assuming A2 as a foreshock to A3 on the thrust fault plane of A1 or A3 (Fig. 9 right column). The shallow centroid and focal point depths from seismic inversions and from P-wave phases arrival differences, and the similar focal plane orientations support their hypothesis. Coulomb failure stress changes caused by A1 or A2 on the fault plane of A3 calculated by Yang et al. (2023) also strengthen this interpretation.

Our finite fault inversions with slip estimates for the two largest events of $0.82 \pm 0.25\,\mathrm{m}$ (single PDR) or $2.26 \pm 0.37\,\mathrm{m}$ (triple PDR) for A1 and $2.82 \pm 0.88\,\mathrm{m}$ (single PDR) or $0.50 \pm 0.24\,\mathrm{m}$ (triple PDR) for A3 support findings on different recent earthquakes in the FA (e.g., for 2005 Qeshm, 2006 Fin, 2008 Qeshm or 2013 Khaki-Shonbe earthquakes) that coseismic slip is mainly accommodated within the competent group (Lohman and Barnhart, 2010; Elliott et al., 2015; Nissen et al., 2007, 2010; Roustaei et al., 2010; Jamalreyhani et al., 2021).

Slips are significantly larger than results from Yang et al. (2023), who estimate peak dislocations of up $\sim 1.25\,\mathrm{m}$. From seismic data, we also estimate different locations for the high slip patch of A1 compared to Yang et al. (2023). It is shifted further to the East with respect to their results. The joint finite fault inversion yields swapped locations of A1 and A3 compared to Yang et al. (2023). While they resolve A1 to the west of A3, we obtain the opposite results. This could be caused by the limited temporal resolution in the study of Yang et al. (2023) as based only on satellite deformation data.

Besides the slip, first-order estimates of the rupture kinematics are obtained from our finite fault inversions. Although shipping with larger uncertainties (Tab. S4), single PDR inversion solutions indicate dominant westward rupture propagation. This indicates that the earlier A1 ruptured into the region of A2 and A3 (Figs. 4, 5).

4.2 Vertical separation of aftershocks

Both, relocated aftershocks, and the larger earthquakes B1 and B2 are spatially concentrated around the eastern tip of the BELA and predominantly scatter in a depth of $10\text{–}15\,\mathrm{km}$, which implies aftershock activity is either in the upper crystalline basement (Talebian and Jackson, 2004; Tatar et al., 2004; Nissen et al., 2011) or deeper sediments (Jahani et al., 2009; Nissen et al., 2014). We also see a vertical separation of the aftershocks from the mainshock in the SFB, which fits well with observations by Nissen et al. (2010, 2011, 2014) for the 2005 Qeshm and 2006 Fin earthquakes. While mainshocks rupture the middle-lower sedimentary cover, aftershocks occur in the basement or the deeper sediments within the Hormuz formation. Hence our aftershock locations also indicate a relatively shallow top boundary of this aftershock region at $\approx 10\,\mathrm{km}$ depth compared to findings of Nissen et al. (2014).

The co-location of the mainshocks and aftershocks, despite C1, could highlight Coulomb stress changes, or dynamic stress transfer from the mainshocks into the deeper and harder Hormuz formation (Nissen et al., 2010, 2014). The salt may flow as a response to the stress changes causing aftershocks within the formation and its surroundings. The substantial location shift between C1 and its aftershocks could be due to location uncertainties and poor spatial resolution of our seismic inversion caused by the lack of regional seismic or ground deformation data.

Nevertheless, as derived from travel time picks without quality constraints, our relocations are only valid as a first-order approximation of the aftershock locations. As we used the same ground model for relocation as for the inversions, uncertainties and structural inconsistencies between the model and the actual underground structure might have also caused a bias within the relocation.

4.3 Implications from joint data and multi-source inversion

The newly implemented triple source inversion scheme has proven its usability for complex rupture inversions using multiple satellite deformation and seismic data. We resolved major features of deformation and seismic data, especially when using the triple DC source model. However, additional free parameters in the triple source inversion scheme have also affected the results, as increased centroid depths for A2 and partially A3, larger uncertainties and the large waveform fit residuals, especially for A3. Different weighting schemes for the relative misfit contribution of surface deformation data fits compared to waveform fits were employed to reduce the described effects but did not fully solve this issue. In this regard, our interpretations on the faults activated by A2 can not be validated from the triple source inversion results.

Comparing results from single source seismic and combined source joint seismic and satellite data inversions, we obtain a significant increase in the cumulative moment release with the latter inversion approach (Figs. 4, 5). Our seismic inversions for sequence A yield a cumulative moment release equivalent to M_w 6.24–6.26, similar to results from GEOFON (cumulative M_w 6.29) or USGS with a cumulative M_w 6.25. Meanwhile, our joint inversion approaches give a cumulative moment release equivalent to M_w 6.39–6.52. These values confirm results from Yang et al. (2023), who have obtained a cumulative moment release equivalent to M_w 6.43.

This 60–70 % increase in modeled moment release derived from the triple DC inversion could be caused by a significant afterslip resolved in the satellite deformation data with its broad temporal coverage but not reflected in the seismic data. Observations of afterslip within Zagros reveal a rather large relative contribution to the ground deformation (Zhao et al., 2023) and can yield significant overestimation of the magnitude in the range of 0.1 to > 0.2 magnitude units (Weston et al., 2012). This behavior might be caused by the complex tectonics of the Zagros, e.g., its salt diapirism (Yang et al., 2023).

Another reason for the magnitude differences could be our choice of the ground model. It is specific to the Zagros region (Karasözen et al., 2019; Jamalreyhani et al., 2021). Nevertheless, underground structure variations, as evident from, e.g., Nissen et al. (2011); Jahani et al. (2009); Jamalreyhani et al. (2021) along the Zagros, can not be fully resolved due to the lack of local tomographies. The choice of a rather low-frequency range for waveform fitting reduces such structural effects, though. Nevertheless, local studies, e.g., a tomography using the aftershocks of the sequence combined with seismic profiles, could enhance the knowledge and shed light on this issue.

The significant moment release overestimation by the triple PDR inversion with an increase of 145–165 % compared to the pure seismic inversions may also be influenced by our inversion setup with many free parameters as the larger uncertainties and misfits suggest (Figs. 7, 6, S11, Tabs. 2, S5).

We have resolved a sequence of three earthquakes close in time and space with similar focal mechanisms (sequence A). As likely rupturing the adjacent patches of the same faults or adjacent splay faults (Yang et al., 2023) sequence A can be characterized as an event triplet according to the definition of Lay and Kanamori (1980); Ammon et al. (2008). The sequence highlights a region of large tectonic complexity with overthrusting, opposed dipping splay faults, and the effect of the Hormuz salt formation limiting rupture propagation (Nissen et al., 2011; Jamalreyhani et al., 2023).

Sequence B might be a doublet with its short interevent time and similar mechanisms. We can not resolve if both ruptured on one common fault, though (Figs. 4a,b, 9). Here, a more detailed investigation of stress transfers could help to fully understand this part of the 2022 seismic unrest. Our observations of an event triplet and a possible doublet fit well with recent observations of two other doublets close to our study area (November 2021 Fin and June 2022 Charak - e.g., Nemati, 2022; Fathian et al., 2022; Rezapour and Jamalreyhani, 2022) highlighting the tectonic complexity of the south eastern FA.

5 Conclusions

The 2022 earthquake sequence in SE Iran has revealed a rather complex interaction of larger shallow thrust faults within the sedimentary cover with deeper, smaller events at the interface to and/or within the crystalline basement. The sequence was initialized by a triplet of thrust earthquakes on 01 July 2022. The two largest earthquakes of the triplet (both $\mathrm{M}_w \sim 6.0$) ruptured the lower sediments at depths of 4–9 km, likely occurring on a south-dipping splay fault to the Zagros Foredeep Fault beneath the Bandar-e-Lengeh anticline. The third, smaller, M_w 5.7–5.8 event occurred one minute before the second large event. This small earthquake either indicates an early activation of deeper strata or might also have been a foreshock co-located on the faults, which ruptured during the two mainshocks.

The event triplet caused high aftershock activity within the deeper sediments or upper crystalline basement characterized by depths of 10–15 km beneath the Bandar-e-Lengeh anticline with several larger thrust events. Hence, the 2022 seismic unrest is a new case of observable vertical separation of the main- and aftershocks in SE Iran, which may be caused by a complex stress state within the deeper sediments and the crystalline basement beneath.

Magnitude overestimations when utilizing satellite ground deformation data also indicate a significant afterslip activity due to salt diapirism.

The comprehensive analysis of main- and aftershocks using available seismic and ground deformation data has embedded the July–December 2022 sequence into the complex tectonics in the SE Fars Arc with a frequent occurrence of event doublets over the past year. The lack of regional and local seismic records and the rather uncertain ground models limited the accuracy of our results. This issue highlights the need for further detailed tectonic studies in the region and better data accessibility to properly understand the geophysical processes and their potential risk within the SE Fars Arc.

Conflict of competing interests

The authors declare that the research was conducted in the absence of any commercial or financial relationships that could be construed as a potential conflict of interest.

Contributions of the authors

MM, BMA, MMA, and MJ were involved in the general conceptualization of the study. MM developed and implemented the triple source inversion scheme and performed analysis of the main- and aftershocks. PB performed the focal depth estimation based on teleseismic body wave phases. BAM, MJ, and PB provided the IRSC seismic data and catalog. MMA performed preprocessing of the satellite deformation data and performed subsequent tests on satellite imagery.

MM wrote the original draft with major contributions of BAM and MJ within the introduction and discussion, and of PB within the methods section. MMA provided the methodological overview on satellite data preparation. Images within the draft were generated by MM, BAM, and PB (Fig. 1). MM, BAM, MJ, PB, and TD provided substantial feedback to the draft through their reviews.

TD, and PB have supervised and guided this study.

Acknowledgments

Malte Metz was supported by the BMBF project EWRICA (03G0891B). Behman Maleki Asayesh was funded by the DFG - Research Training Group "NatRiskChange" and Pınar Büyükakpınar is funded by project 407141557 of the Deutsche Forschungsgemeinschaft (DFG, German Research Foundation).

We would like to thank Simone Cesca, Sebastian Hainzl, Sebastian Heimann and Henriette Sudhaus for feedback and guidance on different parts of our study and continuous support. We are also grateful for the helpful comments of Daniel Trugman on the use of the GrowClust3D.jl algorithm.

Data and Resources

Our reference source mechanisms were derived from the GEOFON program of the GFZ German Research Centre for Geosciences using data from the GEVN partner networks, global CMT (e.g., Dziewoński et al., 1981; Ekström et al., 2012) and USGS.

The aftershock catalog, body wave travel time picks and regional waveforms were downloaded from the Iranian Seismological Center (IRSC) available at http://irsc.ut.ac.ir/.

Furthermore we used teleseismic waveform data from the following seismic networks: AK (Alaska Earthquake Center, Univ. of Alaska Fairbanks, 1987), DK (GEUS Geological Survey of Denmark and Greenland, 1976), G (Institut de physique du globe de Paris (IPGP) and École et Observatoire des Sciences de la Terre de Strasbourg (EOST), 1982), GE (GEOFON Data Centre, 1993), GT (Albuquerque Seismological Laboratory (ASL)/USGS, 1993), II (Scripps Institution of Oceanography, 1986), IC (Albuquerque Seismological Laboratory (ASL)/USGS, 1992), IN (India Meteorological Department, 2000), IU (Albuquerque Seismological Laboratory (ASL)/USGS, 1988), QZ (LTD Seismological Experience and Methodology Expedition of the Committee of Science of the Ministry of Education and Science of the Republic of Kazakhstan, 2003), RM (Regional Integrated Multi-Hazard Early Warning System (RIMES Thailand), 2008) and WM (San Fernando Royal Naval Observatory (ROA), Universidad Complutense De Madrid (UCM), Helmholtz-Zentrum Potsdam Deutsches GeoForschungsZentrum (GFZ), Universidade De Évora (UEVORA, Portugal) and Institute Scientifique Of Rabat (ISRABAT, Morocco), 1996).

Satellite deformation data was downloaded from LiCSAR. LiCSAR contains modified Copernicus Sentinel data 2022 analyzed by the Centre for the Observation and Modelling of Earthquakes, Volcanoes and Tectonics (COMET). LiCSAR uses JASMIN, the UK's collaborative data analysis environment (http://jasmin.ac.uk). LiCSAR products can be accessed through the COMET-LiCSAR-portal website at https://comet.nerc.ac.uk/COMET-LiCS-portal/.

Besides the mentioned software we used GMT5.4 for map plotting (Wessel et al., 2013) and their GSHHG dataset for shore lines (e.g., Wessel and Smith, 1996). Topographic data provided by SRTM (Becker et al., 2009) was used for our map and profile plots. Faults plotted were obtained from Hessami et al. (2003). For InSAR processing we used the the Hybrid Pluggable Processing Pipeline (HyP3) platform (Hogenson et al., 2016), while MintPy was utilized as a robust solution for InSAR time series analysis and unwrapping error correction (Yunjun et al., 2022). Furthermore kite was used for satellite deformation data pre-processing (Isken et al., 2017).

Our seismic and geodetic inversions used Grond (Heimann et al., 2018) and the Pyrocko software package (Heimann et al., 2017) with the implemented effective Greene's function handling algorithms (Heimann et al., 2019).

References

Alaska Earthquake Center, Univ. of Alaska Fairbanks. Alaska Regional Network, 1987. doi: 10.7914/SN/AK.

Alavi, M. Structures of the Zagros fold-thrust belt in Iran. *American Journal of science*, 307(9):1064–1095, 2007. doi: 0.2475/09.2007.02.

Albuquerque Seismological Laboratory (ASL)/USGS. Global Seismograph Network - IRIS/USGS, 1988. doi: 10.7914/SN/IU.

Albuquerque Seismological Laboratory (ASL)/USGS. New China Digital Seismograph Network, 1992. doi: 10.7914/SN/IC.

Albuquerque Seismological Laboratory (ASL)/USGS. Global Telemetered Seismograph Network (USAF/USGS), 1993. doi: 10.7914/SN/GT.

Ambraseys, N. and Melville, C. *A History of Persian Earthquakes*. Cambridge Earth Science Series. Cambridge University Press, 2005. https://books.google.de/books?id=1JkfKub5vakC.

Ammon, C. J., Kanamori, H., and Lay, T. A great earthquake doublet and seismic stress transfer cycle in the central Kuril islands. *Nature*, 451(7178):561–565, 2008. doi: 10.1038/nature06521.

Ansari, S. Co-seismic stress transfer and magnitude-frequency distribution due to the 2012 Varzaqan-Ahar earthquake doublets (Mw 6.5 and 6.4), NW Iran. *Journal of Asian Earth Sciences*, 132: 129–137, 2016. doi: 10.1016/j.jseaes.2016.10.006.

Asayesh, B. M., Zarei, S., and Zafarani, H. Effects of imparted Coulomb stress changes in the seismicity and cluster of the December 2017 Hojedk (SE Iran) triplet. *International Journal of Earth Sciences*, 109:2307–2323, 2020. doi: 10.1007/s00531-020-01901-0.

Asayesh, B. M., Zafarani, H., Hainzl, S., and Sharma, S. Effects of large aftershocks on spatial aftershock forecasts during the 2017–2019 western Iran sequence. *Geophysical Journal International*, 232(1):147–161, 2022. doi: 10.1093/gji/ggac333.

Astiz, L., Lay, T., and Kanamori, H. Large intermediate-depth earthquakes and the subduction process. *Physics of the Earth and Planetary Interiors*, 53(1-2):80–166, 1988. doi: 10.1016/0031-9201(88)90138-0.

Baker, C., Jackson, J., and Priestley, K. Earthquakes on the Kazerun Line in the Zagros Mountains of Iran: strike-slip faulting within a fold-and-thrust belt. *Geophysical Journal International*, 115(1):41–61, 1993. doi: 10.1111/j.1365-246X.1993.tb05587.x.

Barnhart, W. D., Lohman, R. B., and Mellors, R. J. Active accommodation of plate convergence in Southern Iran: Earthquake locations, triggered aseismic slip, and regional strain rates. *Journal of Geophysical Research: Solid Earth*, 118(10):5699–5711, 2013. doi: 10.1002/jgrb.50380.

Bassin, C., Laske, G., and Masters, G. The Current Limits of Resolution for Surface Wave Tomography in North America. *Eos Trans. AGU*, 81(F897), 2000. https://cir.nii.ac.jp/crid/1573105976172569088.

Becker, J. J., Sandwell, D. T., Smith, W. H. F., Braud, J., Binder, B., Depner, J., Fabre, D., Factor, J., Ingalls, S., H Kim, S-and Ladner, R., Marks, K., Nelson, S., Pharaoh, A., Trimmer, R., Von Rosenberg, J., Wallace, G., and Weatherall, P. Global Bathymetry and Elevation Data at 30 Arc Seconds Resolution: SRTM30_PLUS. *Marine Geodesy*, 32:355–371, 2009. doi: 10.1080/01490410903297766.

Berberian, M. Master "blind" thrust faults hidden under the Zagros folds: active basement tectonics and surface morphotectonics. *Tectonophysics*, 241(3-4):193–224, 1995. doi: 10.1016/0040-1951(94)00185-C.

Braunmiller, J. and Nábělek, J. Geometry of continental normal faults: Seismological constraints. *Journal of Geophysical Research: Solid Earth*, 101(2):3045–3052, 1996. doi: 10.1029/95jb02882.

Carrillo Ponce, A., Dahm, T., Cesca, S., Tilmann, F., Babeyko, A., and Heimann, S. Bayesian multiple rupture plane inversion to assess rupture complexity: application to the 2018 Mw 7.9 Alaska earthquake. In *EGU General Assembly Conference Abstracts*, EGU General Assembly Conference Abstracts, pages EGU21–1583, Apr. 2021. doi: 10.5194/egusphere-egu21-1583.

Cesca, S., Braun, T., Maccaferri, F., Passarelli, L., Rivalta, E., and Dahm, T. Source modelling of the M5–6 Emilia-Romagna, Italy, earthquakes (2012 May 20–29). *Geophysical Journal International*, 193(3):1658–1672, 03 2013. doi: 10.1093/gji/ggt069.

Dahm, T., Heimann, S., Metz, M., and Isken, M. P. A self-similar dynamic rupture model based on the simplified wave-rupture analogy. *Geophysical Journal International*, 225:1586–1604, 2021. doi: 10.1093/gji/ggab045.

Dal Zilio, L. and Ampuero, J. P. Earthquake doublet in Turkey and Syria. *Commun Earth Environ*, 4:73, 2023. doi: 10.1038/s43247-023-00747-z.

Daout, S., Steinberg, A., Isken, M. P., Heimann, S., and Sudhaus, H. Illuminating the spatio-temporal evolution of the 2008–2009 qaidam earthquake sequence with the joint use of insar time series and teleseismic data. *Remote Sensing*, 12(17):1–23, 2020. doi: 10.3390/rs12172850.

Doin, M.-P., Lasserre, C., Peltzer, G., Cavalie, O., and Doubre, C. Corrections of stratified tropospheric delays in SAR interferometry: Validation with global atmospheric models. *Remote Sensing of Environment*, 160:155–170, 2015. doi: 10.1016/j.jappgeo.2009.03.010.

Donner, S., Ghods, A., Krüger, F., Rößler, D., Landgraf, A., and Ballato, P. The Ahar-Varzeghan earthquake doublet (Mw 6.4 and 6.2) of 11 August 2012: Regional seismic moment tensors and a seismotectonic interpretation. *Bulletin of the Seismological Society of America*, 105(2):791–807, 2015. doi: 10.1785/0120140042.

Dziewoński, A. M., Chou, T.-A., and Woodhouse, J. H. Determination of earthquake source parameters from waveform data for studies of global and regional seismicity. *Journal of Geophysical Research*, 86(B4):2825–2852, 1981. doi: 10.1029/JB086iB04p02825.

Edey, A., Allen, M. B., and Nilfouroushan, F. Kinematic Variation Within the Fars Arc, Eastern Zagros, and the Development of Fold-and-Thrust Belt Curvature. *Tectonics*, 39, 2020. doi: 10.1029/2019TC005941.

Ekström, G., Nettles, M., and Dziewoński, A. M. The global CMT project 2004-2010: Centroid-moment tensors for 13,017 earthquakes. *Physics of the Earth and Planetary Interiors*, 200-201: 1–9, 2012. doi: 10.1016/j.pepi.2012.04.002.

Elliott, J., Bergman, E., Copley, A., Ghods, A., Nissen, E., Oveisi, B., Tatar, M., Walters, R., and Yamini-Fard, F. The 2013 Mw 6.2 Khaki-Shonbe (Iran) Earthquake: Insights into seismic and aseismic shortening of the Zagros sedimentary cover. *Earth and Space Science*, 2(11):435–471, 2015. doi: 10.1002/2015EA000098.

Falcon, N. L. Southern Iran: Zagros Mountains. *Geological Society, London, Special Publications*, 4(1):199–211, 1974. doi: 10.1144/GSL.SP.2005.004.01.11.

Fathian, A., Atzori, S., Nazari, H., Reicherter, K., Salvi, S., Svigkas, N., Tatar, M., Tolomei, C., and Yaminifard, F. Complex co- and postseismic faulting of the 2017–2018 seismic sequence in western Iran revealed by InSAR and seismic data. *Re-*

mote Sensing of Environment, 253(December), 2021. doi: 10.1016/j.rse.2020.112224.

Fathian, A., Atzori, S., Svigkas, N., Tolomei, C., Shugar, D. H., and Reicherter, K. Source Characteristics of the Fin Doublet Earthquake of 14 November 2021 (Mw 6.2 and Mw 6.3) Utilizing InSAR Data. In *IGARSS 2022 - 2022 IEEE International Geoscience and Remote Sensing Symposium*, pages 2119–2122, 2022. doi: 10.1109/IGARSS46834.2022.9883591.

Freund, R. Rotation of strike slip faults in Sistan, southeast Iran. *The Journal of Geology*, 78(2):188–200, 1970. doi: 10.1086/627500.

GEOFON Data Centre. GEOFON Seismic Network, 1993. doi: 10.14470/TR560404.

GEUS Geological Survey of Denmark and Greenland. Danish Seismological Network, 1976. https://www.fdsn.org/networks/detail/DK/.

Ghods, A., Shabanian, E., Bergman, E., Faridi, M., Donner, S., Mortezanejad, G., and Aziz-Zanjani, A. The Varzaghan-Ahar, Iran, Earthquake Doublet (Mw 6.4, 6.2): Implications for the geodynamics of northwest Iran. *Geophysical Journal International*, 203(1):522–540, 2015. doi: 10.1093/gji/ggv306.

Guo, Z., Motagh, M., Hu, J. C., Xu, G., Haghighi, M. H., Bahroudi, A., Fathian, A., and Li, S. Depth-Varying Friction on a Ramp-Flat Fault Illuminated by 3-Year InSAR Observations Following the 2017 Mw 7.3 Sarpol-e Zahab Earthquake. *Journal of Geophysical Research: Solid Earth*, 127(12), 2022. doi: 10.1029/2022JB025148.

He, P., Ding, K., and Xu, C. The 2016 Mw 6.7 Aketao earthquake in Muji range, northern Pamir: Rupture on a strike-slip fault constrained by Sentinel-1 radar interferometry and GPS. *International Journal of Applied Earth Observation and Geoinformation*, 73:99–106, 2018. doi: https://doi.org/10.1016/j.jag.2018.06.001.

Heimann, S., Kriegerowski, M., Isken, M., Cesca, S., Daout, S., Grigoli, F., Juretzek, C., Megies, T., Nooshiri, N., Steinberg, A., Sudhaus, H., Vasyura-Bathke, H., Willey, T., and Dahm, T. Pyrocko - An open-source seismology toolbox and library, 2017. doi: 10.5880/GFZ.2.1.2017.001.

Heimann, S., Isken, M., Kühn, D., Sudhaus, H., Steinberg, A., Vasyura-Bathke, H., Daout, S., Cesca, S., and Dahm, T. Grond - A probabilistic earthquake source inversion framework, 2018. doi: 10.5880/GFZ.2.1.2018.003.

Heimann, S., Vasyura-Bathke, H., Sudhaus, H., Paul Isken, M., Kriegerowski, M., Steinberg, A., and Dahm, T. A Python framework for efficient use of pre-computed Green's functions in seismological and other physical forward and inverse source problems. *Solid Earth*, 10(6):1921–1935, 2019. doi: 10.5194/se-10-1921-2019.

Hessami, K., Koyi, H. A., Talbot, C. J., Tabasi, H., and Shabanian, E. Progressive unconformities within an evolving foreland fold–thrust belt, Zagros Mountains. *Journal of the Geological Society*, 158(6):969–981, 2001. doi: 10.1144/0016-764901-007.

Hessami, K., Jamali, F., and Tabassi, H. Major active faults of Iran. *IIEES, Tehran*, 2003.

Hogenson, K., Kristenson, H., Kennedy, J., Johnston, A., Rine, J., Logan, T. A., Zhu, J., Williams, F., Herrmann, J., and Smale, J. Hybrid Pluggable Processing Pipeline (HyP3): A Cloud-Native Infrastructure for Generic Processing of SAR Data. In *In Proceedings of the 2016 AGU Fall Meeting, San Francisco, CA, USA, 12–16 December 2016*, 2016. https://ui.adsabs.harvard.edu/abs/2016AGUFMIN21B1740H.

Ide, S. Bayesian multiple rupture plane inversion to assess rupture complexity: application to the 2018 Mw 7.9 Alaska earthquake. In Kanamori, H., editor, *Slip inversion in Earthquake Seismology*, volume 4, pages 193–224. Elsevier, 2007. doi: 10.1016/B978-044452748-6/00068-7.

India Meteorological Department. National Seismic Network of India , 2000. https://www.fdsn.org/networks/detail/IN/.

Institut de physique du globe de Paris (IPGP) and École et Observatoire des Sciences de la Terre de Strasbourg (EOST). GEOSCOPE, French Global Network of broad band seismic stations, 1982. doi: 10.18715/GEOSCOPE.G.

Isken, M., Sudhaus, H., Heimann, S., Steinberg, A., Daout, S., and Vasyura-Bathke, H. Kite - Software for Rapid Earthquake Source Optimisation from InSAR Surface Displacement, 2017. doi: 10.5880/GFZ.2.1.2017.002.

Jahani, S., Callot, J. P., Letouzey, J., and De Lamotte, D. F. The eastern termination of the Zagros Fold-and-Thrust Belt, Iran: Structures, evolution, and relationships between salt plugs, folding, and faulting. *Tectonics*, 28(6), 2009. doi: 10.1029/2008TC002418.

Jamalreyhani, M., Pousse-Beltran, L., Büyükakpınar, P., Cesca, S., Nissen, E., Ghods, A., López-Comino, J. Á., Rezapour, M., and Najafi, M. The 2019–2020 Khalili (Iran) Earthquake Sequence—Anthropogenic Seismicity in the Zagros Simply Folded Belt? *Journal of Geophysical Research: Solid Earth*, 126(12):1–19, 2021. doi: 10.1029/2021JB022797.

Jamalreyhani, M., Rezapour, M., Cesca, S., Dahm, T., Heimann, S., Sudhaus, H., and Isken, M. P. Insight into the 2017–2019 Lurestan arc seismic sequence (Zagros, Iran); complex earthquake interaction in the basement and sediments. *Geophysical Journal International*, 230:114–130, 2022. doi: https://doi.org/10.1093/gji/ggac057.

Jamalreyhani, M., Pousse-Beltran, L., Hassanzadeh, M., Arabi, S. S., Bergman, E. A., Shamszadeh, A., Arvin, S., Fariborzi, N., and Songhori, A. Co-seismic slip of the 18 April 2021 Mw 5.9 Genaveh earthquake in the South Dezful Embayment of Zagros (Iran) and its aftershock sequence. *Seismica*, 2(1), 2023. doi: 10.26443/seismica.v2i1.246.

Jia, Z., Shen, Z., Zhan, Z., Li, C., Peng, Z., and Gurnis, M. The 2018 Fiji Mw 8.2 and 7.9 deep earthquakes: One doublet in two slabs. *Earth and Planetary Science Letters*, 531:115997, 2020. doi: https://doi.org/10.1016/j.epsl.2019.115997.

Jia, Z., Zhan, Z., and Kanamori, H. The 2021 South Sandwich Island Mw 8.2 earthquake: a slow event sandwiched between regular ruptures. *Geophys. Res. Lett.*, 49:1–8, 2022. doi: 10.1029/2021GL097104.

Jónsson, S., Zebker, H., Segall, P., and Amelung, F. Fault slip distribution of the 1999 Mw 7.1 Hector Mine, California, earthquake, estimated from satellite radar and GPS measurements. *Bulletin of the Seismological Society of America*, 92(4):1377–1389, 2002. doi: 10.1785/0120000922.

Karasözen, E., Nissen, E., Bergman, E. A., and Ghods, A. Seismotectonics of the Zagros (Iran) From Orogen-Wide, Calibrated Earthquake Relocations. *Journal of Geophysical Research: Solid Earth*, 124(8):9109–9129, 2019. doi: 10.1029/2019JB017336.

Kennett, B. L. N., Engdahl, E. R., and Buland, R. Constraints on seismic velocities in the Earth from traveltimes. *Geophysical Journal International*, 122(1):108–124, 1995. doi: 10.1111/j.1365-246X.1995.tb03540.x.

Lay, T. The surge of great earthquakes from 2004 to 2014. *Earth and Planetary Science Letters*, 409:133–146, 2015. doi: 10.1016/j.epsl.2014.10.047.

Lay, T. and Kanamori, H. Earthquake Doublets in the Solomon Islands. *Physics ofthe Earth and Planetary Interiors*, 21:283–304, 1980. doi: 10.1016/0031-9201(80)90134-X.

Lohman, R. B. and Barnhart, W. D. Evaluation of earthquake triggering during the 2005–2008 earthquake sequence on Qeshm Island, Iran. *Journal of Geophysical Research*, 115, 2010. doi: https://doi.org/10.1029/2010JB007710.

LTD Seismological Experience and Methodology Expedition of the Committee of Science of the Ministry of Education and Science of the Republic of Kazakhstan. Seismic network of the Seismological Experience and Methodology Expedition CS MES RK, 2003. doi: 10.7914/SN/QZ.

Masson, F., Chéry, J., Hatzfeld, D., Martinod, J., Vernant, P., Tavakoli, F., and Ghafory-Ashtiani, M. Seismic versus aseismic deformation in Iran inferred from earthquakes and geodetic data. *Geophysical Journal International*, 160(1):217–226, 2005. doi: 10.1111/j.1365-246X.2004.02465.x.

Metz, M. A quasi-dynamic and self-consistent rupture model to simulate earthquake ruptures. *Universität Potsdam*, 2019. doi: 10.25932/publishup-47310.

Metz, M., Vera, F., Carrillo Ponce, A., Cesca, S., Babeyko, A., Dahm, T., Saul, J., and Tilmann, F. Seismic and Tsunamigenic Characteristics of a Multimodal Rupture of Rapid and Slow Stages: The Example of the Complex 12 August 2021 South Sandwich Earthquake. *Journal of Geophysical Research: Solid Earth*, 127(11), 2022. doi: 10.1029/2022jb024646.

Momeni, S. and Tatar, M. Mainshocks/aftershocks study of the August 2012 earthquake doublet on Ahar-Varzaghan complex fault system (NW Iran). *Physics of the Earth and Planetary Interiors*, 283:67–81, 2018. doi: https://doi.org/10.1016/j.pepi.2018.08.001.

Nemati, M. The November 2021 Fin (SE Zagros , Iran) doublet earthquakes of reverse faults in a transpressional tectonic regime. Technical report, Shahid Bahonar University of Kerman, 2022. https://doi.org/10.21203/rs.3.rs-1314781/v1.

Ni, J. and Barazangi, M. Seismotectonics of the Zagros continental collision zone and a comparison with the Himalayas. *Journal of Geophysical Research: Solid Earth*, 91(B8):8205–8218, 1986. doi: 10.1029/JB091iB08p08205.

Nissen, E., Ghorashi, M., Jackson, J., Parsons, B., and Talebian, M. The 2005 Qeshm Island earthquake (Iran) - A link between buried reverse faulting and surface folding in the Zagros Simply Folded Belt? *Geophysical Journal International*, 171(1):326–338, 2007. doi: 10.1111/j.1365-246X.2007.03514.x.

Nissen, E., Yamini-Fard, F., Tatar, M., Gholamzadeh, A., Bergman, E., Elliott, J. R., Jackson, J. A., and Parsons, B. The vertical separation of mainshock rupture and microseismicity at Qeshm island in the Zagros fold-and-thrust belt, Iran. *Earth and Planetary Science Letters*, 296(3-4):181–194, 2010. doi: 10.1016/j.epsl.2010.04.049.

Nissen, E., Tatar, M., Jackson, J. A., and Allen, M. B. New views on earthquake faulting in the Zagros fold-and-thrust belt of Iran. *Geophysical Journal International*, 186(3):928–944, 2011. doi: 10.1111/j.1365-246X.2011.05119.x.

Nissen, E., Jackson, J., Jahani, S., and Tatar, M. Zagros "phantom earthquakes" reassessed - The interplay of seismicity and deep salt flow in the Simply Folded Belt? *Journal of Geophysical Research: Solid Earth*, 119(4):3561–3583, 2014. doi: 10.1002/2013JB010796.

Nissen, E., Ghods, A., Karasözen, E., Elliott, J. R., Barnhart, W. D., Bergman, E. A., Hayes, G. P., Jamal-Reyhani, M., Nemati, M., Tan, F., Abdulnaby, W., Benz, H. M., Shahvar, M. P., Talebian, M., and Chen, L. The 12 November 2017 M w 7.3 Ezgeleh-Sarpolzahab (Iran) Earthquake and Active Tectonics of the Lurestan Arc. *Journal of Geophysical Research: Solid Earth*, 124(2):2124–2152, 2019. doi: 10.1029/2018JB016221.

Okada, Y. Gravity and potential changes due to shear and tensile faults in a half-space. *Journal of Geophysical Research*, 82(2): 1018–1040, 1992. doi: 10.1029/92JB00178.

Oveisi, B., Lavé, J., Van Der Beek, P., Carcaillet, J., Benedetti, L., and Aubourg, C. Thick-and thin-skinned deformation rates in the central Zagros simple folded zone (Iran) indicated by displacement of geomorphic surfaces. *Geophysical Journal International*, 176(2):627–654, 2009. doi: 10.1111/j.1365-246X.2008.04002.x.

Quinteros, J., Strollo, A., Evans, P. L., Hanka, W., Heinloo, A., Hemmleb, S., Hillmann, L., Jaeckel, K., Kind, R., Saul, J., Zieke, T., and Tilmann, F. The GEOFON Program in 2020. *Seismological Research Letters*, 92(3):1610–1622, 02 2021. doi: 10.1785/0220200415.

Regard, V., Bellier, O., Thomas, J.-C., Abbassi, M., Mercier, J., Shabanian, E., Feghhi, K., and Soleymani, S. Accommodation of Arabia-Eurasia convergence in the Zagros-Makran transfer zone, SE Iran: A transition between collision and subduction through a young deforming system. *Tectonics*, 23(4), 2004. doi: 10.1029/2003TC001599.

Regional Integrated Multi-Hazard Early Warning System (RIMES Thailand). Regional Integrated Multi-Hazard Early Warning System, 2008. doi: 10.7914/SN/RM.

Rezapour, M. and Jamalreyhani, M. R. Source fault analyses from InSAR data and aftershocks for the Fin doublet earthquakes on 14 November 2021 in Hormozgan province, South Iran. *Earth and Space Physics*, 2022. doi: 10.22059/jesphys.2022.337959.1007399.

Roustaei, M., Nissen, E., Abbassi, M., Gholamzadeh, A., Ghorashi, M., Tatar, M., Yamini-Fard, F., Bergman, E., Jackson, J., and Parsons, B. The 2006 March 25 Fin earthquakes (Iran) - insights into the vertical extents of faulting in the Zagros Simply Folded Belt. *Geophysical Journal International*, 181(3):1275–1291, 2010. doi: 10.1111/j.1365-246X.2010.04601.x.

San Fernando Royal Naval Observatory (ROA), Universidad Complutense De Madrid (UCM), Helmholtz-Zentrum Potsdam Deutsches GeoForschungsZentrum (GFZ), Universidade De Évora (UEVORA, Portugal) and Institute Scientifique Of Rabat (ISRABAT, Morocco). The Western Mediterranean BB seismic Network, 1996. doi: 10.14470/JZ581150.

Savidge, E., Nissen, E., Nemati, M., Karasözen, E., Hollingsworth, J., Talebian, M., Bergman, E., Ghods, A., Ghorashi, M., Kosari, E., et al. The December 2017 Hojedk (Iran) earthquake triplet—sequential rupture of shallow reverse faults in a strike-slip restraining bend. *Geophysical Journal International*, 217(2): 909–925, 2019. doi: 10.1093/gji/ggz053.

Scripps Institution of Oceanography. Global Seismograph Network - IRIS/IDA, 1986. doi: 10.7914/SN/II.

Sokos, E., Kiratzi, A., Gallovič, F., Zahradník, J., Serpetsidaki, A., Plicka, V., Janský, J., Kostelecký, J., and Tselentis, G. A. Rupture process of the 2014 Cephalonia, Greece, earthquake doublet (Mw6) as inferred from regional and local seismic data. *Tectonophysics*, 656:131–141, 2015. doi: 10.1016/j.tecto.2015.06.013.

Steinberg, A., Sudhaus, H., Heimann, S., and Krüger, F. Sensitivity of InSAR and teleseismic observations to earthquake rupture segmentation. *Geophysical Journal International*, 223(2): 875–907, 2020. doi: 10.1093/gji/ggaa351.

Steinberg, A., Sudhaus, H., and Krüger, F. Using teleseismic backprojection and InSAR to obtain segmentation information for large earthquakes: a case study of the 2016 Mw 6.6 Muji earthquake. *Geophysical Journal International*, 2022. doi: 10.1093/gji/ggac392.

Stoecklin, J. Structural history and tectonics of Iran: a review. *AAPG bulletin*, 52(7):1229–1258, 1968. doi: 10.1306/5D25C4A5-16C1-11D7-8645000102C1865D.

Sudhaus, H. and Jónsson, S. Improved source modelling through combined use of InSAR and GPS under consideration of correlated data errors: Application to the June 2000 Kleifarvatn earthquake, Iceland. *Geophysical Journal International*, 176(2): 389–404, 2009. doi: 10.1111/j.1365-246X.2008.03989.x.

Talebian, M. and Jackson, J. A reappraisal of earthquake focal mechanisms and active shortening in the Zagros mountains of Iran. *Geophysical Journal International*, 156(3):506–526, 2004. doi: 10.1111/j.1365-246X.2004.02092.x.

Tatar, M., Hatzfeld, D., and Ghafory-Ashtiany, M. Tectonics of the Central Zagros (Iran) deduced from microearthquake seismicity. *Geophysical Journal International*, 156(2):255–266, 2004. doi: 10.1111/j.1365-246X.2003.02145.x.

Taymaz, T., Ganas, A., Berberian, M., Eken, T., Irmak, T. S., Kapetanidis, V., Yolsal-Çevikbilen, S., Erman, C., Keleş, D., Esmaeili, C., Tsironi, V., and Özkan, B. The 23 February 2020 Qotur-Ravian earthquake doublet at the Iranian-Turkish border: Seismological and InSAR evidence for escape tectonics. *Tectonophysics*, 838:229482, 2022. doi: 10.1016/j.tecto.2022.229482.

Thapa, D. R., Tao, X., Fan, F., and Tao, Z. Aftershock analysis of the 2015 Gorkha-Dolakha (Central Nepal) earthquake doublet. *Heliyon*, 4(7):e00678, 2018. doi: 10.1016/j.heliyon.2018.e00678.

Trugman, D. T. and Shearer, P. M. GrowClust: A Hierarchical clustering algorithm for relative earthquake relocation, with application to the Spanish Springs and Sheldon, Nevada, earthquake sequences. *Seismological Research Letters*, 88(2):379–391, 2017. doi: 10.1785/0220160188.

Trugman, D. T., Chamberlain, C. J., Savvaidis, A., and Lomax, A. GrowClust3D.jl: A Julia Package for the Relative Relocation of Earthquake Hypocenters Using 3D Velocity Models. *Seismological Research Letters*, 94(1):443–456, 2023. doi: 10.1785/0220220193.

Vernant, P., Nilforoushan, F., Hatzfeld, D., Abbassi, M., Vigny, C., Masson, F., Nankali, H., Martinod, J., Ashtiani, A., Bayer, R., et al. Present-day crustal deformation and plate kinematics in the Middle East constrained by GPS measurements in Iran and northern Oman. *Geophysical Journal International*, 157(1): 381–398, 2004. doi: 10.1111/j.1365-246X.2004.02222.x.

Walker, R. and Jackson, J. Offset and evolution of the Gowk fault, SE Iran: a major intra-continental strike-slip system. *Journal of structural Geology*, 24(11):1677–1698, 2002. doi: 10.1016/S0191-8141(01)00170-5.

Walker, R. T., Andalibi, M. J., Gheitanchi, M. R., Jackson, J. A., Karegar, S., and Priestley, K. Seismological and field observations from the 1990 November 6 Furg (Hormozgan) earthquake: A rare case of surface rupture in the Zagros mountains of Iran. *Geophysical Journal International*, 163(2):567–579, 2005. doi: 10.1111/j.1365-246X.2005.02731.x.

Wang, R. A simple orthonormalization method for stable and efficient computation of Green's functions. *Bulletin of the Seismological Society of America*, 89:733–741, 1999. doi: 10.1785/BSSA0890030733.

Wang, R. The dislocation theory: a consistent way for including the gravity effect in (visco)elastic plane-earth models. *Geophysical Journal International*, 161:191–196, 2005. doi: 10.1111/j.1365-246X.2005.02614.x.

Wang, R., Lorenzo-Martín, F., and Roth, F. Computation of deformation induced by earthquakes in a multi-layered elastic crust - FORTRAN programs EDGRN/EDCMP. *Computer and Geosciences*, 29:195–207, 2003. doi: 10.1016/S0098-3004(02)00111-5.

Wang, R., Lorenzo-Martín, F., and Roth, F. PSGRN/PSCMP - a new code for calculating co- and post-seismic deformation, geoid and gravity changes based on the viscoelastic-gravitational dislocation theory. *Computer and Geosciences*, 32:527–541, 2006. doi: 10.1016/j.cageo.2005.08.006.

Wessel, P. and Smith, W. H. F. A global, self-consistent, hierarchical, high-resolution shoreline database. *Journal of Geophysical Research*, 101:8741–8743, 1996. doi: 10.1029/96JB00104.

Wessel, P., Smith, W. H., Scharroo, R., Luis, J., and Wobbe, F. Generic mapping tools: Improved version released. *Eos*, 94(45): 409–410, 2013. doi: 10.1002/2013EO450001.

Weston, J., Ferreira, A. M., and Funning, G. J. Systematic comparisons of earthquake source models determined using InSAR and seismic data. *Tectonophysics*, 532-535:61–81, 2012. doi: 10.1016/j.tecto.2012.02.001.

Xu, Z. and Schwartz, S. Y. Large earthquake doublets and fault plane heterogeneity in the northern Solomon Islands subduction zone. *Pure and Applied Geophysics PAGEOPH*, 140(2): 365–390, 1993. doi: 10.1007/BF00879412.

Yamini-Fard, F., Hatzfeld, D., Farahbod, A., Paul, A., and Mokhtari, M. The diffuse transition between the Zagros continental collision and the Makran oceanic subduction (Iran): microearthquake seismicity and crustal structure. *Geophysical Journal International*, 170(1):182–194, 2007. doi: 10.1111/j.1365-246X.2006.03232.x.

Yaminifard, F., Tatar, M., Hessami, K., Gholamzadeh, A., and Bergman, E. Aftershock analysis of the 2005 November 27 (Mw 5.8) Qeshm Island earthquake (Zagros-Iran): Triggering of strike-slip faults at the basement. *Journal of Geodynamics*, 61: 138–147, 2012. doi: 10.1016/j.jog.2012.04.005.

Yang, Y.-h., Li, X., Hu, J.-c., Song, J., Zhao, J., and Yassaghi, A. The 2022 Hormozgan Doublet Earthquake : Two Blind Thrusts-Related Folding in Zagros Fold-And-Thrust Belt , Southeast Iran. *Geophysical Research Letters*, 50, 2023. doi: 10.1029/2022GL101902.

Ye, L., Lay, T., Kanamori, H., and Koper, K. D. Energy Release of the 2013 Mw 8.3 Sea of Okhotsk Earthquake and Deep Slab Stress Heterogeneity. *Science*, 341(September):1380–1384, 2013. doi: 10.1126/science.1242032.

Ye, L., Lay, T., Kanamori, H., Zhan, Z., and Duputel, Z. Diverse rupture processes in the 2015 Peru deep earthquake doublet. *Science Advances*, 2(6):1989–1990, 2016. doi: 10.1126/sciadv.1600581.

Yu, C., Penna, N. T., and Li, Z. Generation of real-time mode high-resolution water vapor fields from GPS observations. *Journal of Geophysical Research: Atmospheres*, 122:2008–2025, 2017. doi: 10.1002/2016JD025753.

Yu, C., Li, Z., and Penna, N. T. Interferometric synthetic aperture radar atmospheric correction using a GPS-based iterative tropospheric decomposition model. *Remote Sensing of Environment*, 204:109–121, 2018a. doi: 10.1016/j.rse.2017.10.038.

Yu, C., Li, Z., Penna, N. T., and Crippa, P. Generic Atmospheric Correction Model for Interferometric Synthetic Aperture Radar Observations. *Journal of Geophysical Research: Solid Earth*, 123: 9202–9222, 2018b. doi: 10.1029/2017JB015305.

Yunjun, Z., Fattahi, H., and Amelung, F. Small baseline InSAR time series analysis: Unwrapping error correction and noise reduction. *Remote Sens.*, 14(336), 2022. doi: 10.1016/j.cageo.2019.104331.

Zhang, X., Feng, W., Li, D., Yin, F., and Yi, L. Diverse rupture processes of the 2014 Kangding, China, earthquake doublet (MW 6.0 and 5.7) and driving mechanisms of aftershocks. *Tectonophysics*, 820:229118, 2021. doi: 10.1016/j.tecto.2021.229118.

Zhao, X., Xu, C., Wen, Y., He, K., and Yang, J. Early post-seismic deformation of the 2017 Mw 7.3 Darbandikhan, Iran/Iraq Earthquake on a flat-ramp-flat fault. *Tectonophysics*, 853:229809, 2023. doi: 10.1016/j.tecto.2023.229809.

doi:10.26443/seismica.v2i2.849

SEISMICA

Observation of a Synchronicity between Shallow and Deep Seismic Activities during the Foreshock Crisis Preceding the Iquique Megathrust Earthquake

Michel Bouchon *[1], **Stéphane Guillot** [1], **David Marsan** [1], **Anne Socquet** [1], **Jorge Jara** [2], **François Renard** [3]

[1]ISTerre, Université Grenoble Alpes, Université Savoie Mont Blanc, CNRS, IRD, Grenoble, France, [2]German Research Center for Geosciences (GFZ), Potsdam, Germany, [3]Njord Centre, Departments of Geosciences and Physics, University of Oslo, Oslo, Norway

Author contributions: *Conceptualization*: M. Bouchon. *Investigation*: M. Bouchon, D. Marsan, A. Socquet, J. Jara. *Validation*: S. Guillot, F. Renard. *Writing*: M. Bouchon, S. Guillot, D. Marsan, A. Socquet, J.Jara, F. Renard.

Abstract We analyze at a broad spatial scale the slab seismicity during one of the longest and best recorded foreshock sequences of a subduction earthquake to date: the M8.1 2014 Iquique earthquake in Chile. We observe the synchronisation of this sequence with seismic events occurring in the deep slab (depth ~100 km). We show that the probability that this synchronisation is obtained by chance is infinitesimal (<10^{-5}), indicating that it is the result of a physical process taking place in the subduction. A mechanically logical explanation for this synchronicity seems to be the presence of fluid connections between the intermediate-depth range of the slab and the shallow seismogenic zone where foreshocks occur. These connections could be in the form of transient fluid channels in which bursts of pressure pulses would propagate, or localized high permeability paths along the plate interface in which pore-pressure waves would travel. It suggests that, like for the 2011 Tohoku earthquake, the deep slab was involved in the nucleation process of the Iquique earthquake. These observations may seem surprising but they are in line with the short-lived pulse-like channelized water escape from the dehydration zone predicted by recent studies in slab mineralogy and geochemistry.

Non-technical summary In 2014 a large earthquake (M8.1) occurred in the North Chile subduction. This earthquake was preceded by an intense foreshock crisis which lasted for nine months. We analyze here this foreshock activity and we observe that it is synchronised with seismic activity occurring deep (~100 km) in the slab, far down-dip from the foreshock locations and below the future rupture zone of the earthquake. As this deep seismic activity is thought to be associated with the dehydration of slab minerals and the release of water, it suggests that rapid water ascent from the dehydration zone may have triggered the foreshocks. Other possible mechanisms for this synchronicity of foreshocks with activity deep in the slab are discussed.

Production Editor:
Gareth Funning
Handling Editor:
Christie Rowe
Copy & Layout Editor:
Kirsty Bayliss

Signed reviewer(s):
Pascal Audet and Cailey Condit

Received:
May 3, 2023
Accepted:
September 5, 2023
Published:
October 10, 2023

1 Introduction

Although it is still a controversial subject, an increasing number of observations support that broad spatial interactions occur in slabs. The rapidity and the scale of some of the interactions reported (Bouchon, 2016, 2022; Panet et al., 2018, 2022; Bedford, 2020; Bouih et al., 2022; Karabulut et al., 2022; Rousset et al., 2023) challenge our present understanding of slab dynamics and raise questions about the mechanism of communication across long (100km or more) distances. We analyze here, at a broad spatial scale, the long and well-recorded foreshock sequence which preceded the M8.1 2014 Iquique earthquake in the North Chile subduction. Signs of short-term and long-term correlations between shallow and deep seismic activities there have been previously reported (Bouchon, 2016; Jara et al., 2017). We present here more detailed observations expanded to the whole foreshock crisis which lasted for nine months. The earthquake broke the Nazca/South-American plate interface in a region which had been identified as a major seismic gap (Madariaga, 1998). Although its foreshock sequence has attracted considerable attention Ruiz (2014); Schurr (2014); Kato and Nakagawa (2014); Kato et al. (2016); Lay et al. (2014); Bedford et al. (2015); Meng et al. (2015); Duputel (2015), these investigations concerned activity in the the seismogenic zone, which in subducting plates is limited to ~50 km depth. Below, the plate boundary slips almost continuously due to ductile deformation at elevated temperature. Megathrust earthquakes break the seismogenic zone but are not thought to extend much deeper. Below ~60 km, another type of seismic event, however, occurs in the descending plate. These events, termed intermediate-depth earthquakes, take place not along the interface but inside the cold core of the slab. They are believed to be linked to the metamorphic dehydration of slab minerals.

*Corresponding author: michel.bouchon@univ-grenoble-alpes.fr

2 Synchronicity of Foreshocks with Activity Down-Dip in Slab

The pre-Iquique activity begins to be noticeable ~9 months before the mainshock (Kato et al., 2016; Socquet, 2017; Jara et al., 2017). The first phase of foreshock activity occurs in July-August 2013. It begins north of the epicenter and spreads southwards up to ~80 km from it in following weeks (Fig. 1). A quiescence period follows for a few months (September-December 2013, Aden-Antoniow et al., 2020). A second phase of foreshocks starts ~120 km south from the epicenter in January 2014, three months before the earthquake, and in the following weeks a broad slab segment is activated (Fig. 1). This activity intensifies on March 16, two weeks before the earthquake, when a M6.7 shock occurs. The evolution of this activity has been interpreted as migrating slow slip which is supported by GPS and tilt observations (Socquet, 2017; Boudin, 2021). The spatial extent of the foreshock zone, about 180 km, is intriguing as well as the rapidity with which seismicity spreads over a plate interface known to have been locked for decades (Madariaga, 1998; Chlieh, 2011; Metois et al., 2016).

We first study the relatively large (M > 4) events occurring in the subduction before the earthquake. We use for this the national catalog made by the Centro Seismologico Nacional of Chile (CSN, www.sismologia.cl, www.isc.ac.uk), whose completeness magnitude is around M4 (Jara et al., 2017). Whenever available (generally around and above magnitude 5), we use for these events the moment magnitudes published by the Global Centroid Moment Tensor (GCMT) Project (www.globalcmt.org, Ekström et al., 2012), which is the reference for large earthquakes worldwide.

In Fig. 2 we present the timing and magnitude of the shallow (depth<40 km) and deep (80 km<depth<125 km) earthquakes within increasing radial distance range (160 km, 170 km, and 200 km) from the future epicenter. The large depth separation differentiates shallow events (i.e. foreshocks) associated with the slip of the slab and intermediate-depth events associated with its internal deformation. The lower depth limit (125 km) has little effect as few events are deeper during the periods considered. Beyond this limit, events are far from stations and catalog resolution degrades. The first epicentral distance range considered is 160 km (Fig. 2a). At lower radii from the mainshock epicenter, the deep slab is not yet sampled because of the low dip of the slab. Within this distance range, the deep slab volume sampled lies directly down-dip from the epicentral zone. Fig. 2a shows that deep activity there is confined to the two foreshock crises and that one deep event shortly precedes (1 day) the intensification of the foreshock crisis which will lead to the earthquake two weeks later. Fig. 2b extends the exploration range to 170 km and focuses on the period preceding and including the first crisis. At this range where a larger volume of deep slab is sampled, a correlation emerges between deep and shallow activities. Fig. 2c extends the exploration range to 200 km and focuses on the period around the second crisis and on the largest shallow (M>4) and deep (M>4.5) events, the higher magnitude cut-off used for deep events reflecting the higher level of deep background activity present in this subduction. At this distance range a time correlation between the two activities emerges clearly. The wider exploration needed for a correlation to emerge during the second crisis seems consistent with the broader spatial extent of this crisis (Fig. 1).

In statistics the two time series displayed in Fig. 2, are termed temporal point processes. To estimate the probability that one temporal point process (A) is dependent on the other one (B), a distribution of interevent times is constructed by fixing the events from series (B) and measuring the time from each event in (A) to the closest event in (B). This method is described in (Galbraith et al., 2020). Probability is calculated by fixing the times of the deep events, drawing randomly the times of the shallow events, and comparing their mean interevent time with the one observed. In doing so we do not make any hypothesis on any of the properties of the two time series. We simply look if the interevent time observed is due to random chance or if it is an intrinsic property of the data. The application of the method to seismic sequences is straightforward and described in Bouchon (2022). In Fig. 2b (first crisis) the chance probability that shallow events (i.e. foreshocks) are as closely synchronized with the occurrence of deep events is $< 10^{-5}$ (more than 100,000 random draws of the 9 M>4 shallow events are required to reach an interevent time with the 7 deep events present as small as the one observed). A similarly small chance probability $< 10^{-5}$ that shallow events occurring during the second crisis (Fig. 2c) would be as closely synchronized with deep events located within 200 km of epicentral distance is obtained. The combined probability that shallow events would be as closely synchronized with deep events below during the two foreshock crises is thus infinitesimal. The smallness of the values may seem surprising but it likely reflects the burst-like characteristic of the seismicity: As shown in Fig. 3, a burst is not simply made up of one shallow and one deep event, but usually of a multiplicity of them interweaved together within a short time, a characteristic difficult to be reproduced by a random process.

Using the catalog of Sippl et al. (2018a) for North Chile, which decreases the magnitude of completeness to ~2.7, we can explore shallow and deep activities at lower magnitude. Because of the high level of deep background activity below magnitude 4 in the subduction and the long duration and broad spatial extent of the crisis, we focus on the period when the first foreshock activity is the most intense and on the subduction segment where this activity takes place (Fig. 3). To interpret this figure, one has to realize that deep activity is continuously present in this zone, regardless of the occurrence or not of foreshocks. Consequently, if some interaction occurs between deep and shallow activities it probably does not involve all the deep population. Furthermore each family of events has necessarily dynamics of its own and smaller events may be aftershocks of the larger ones. A notable feature of Fig. 3 is that shallow activity is usually accompanied by deep activity. Calculating, as in Fig. 2, the chance probability

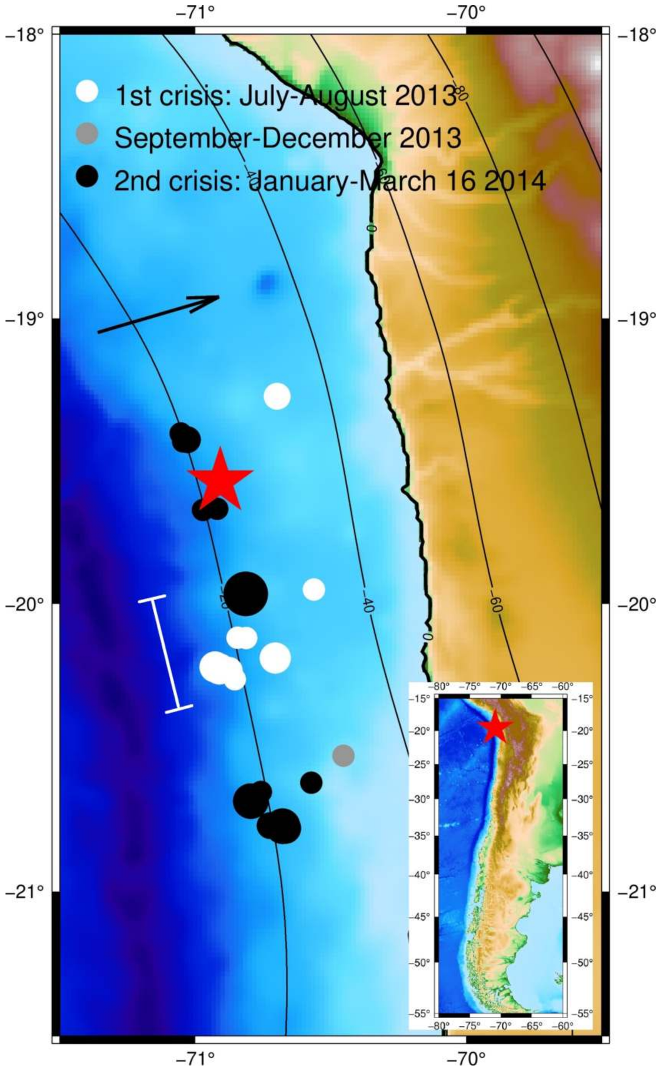

Figure 1 Location of the large (M>4) foreshocks showing their broad north-south spatial extent along the strike of the slab. All events with depth <40 km in the CSN catalog in the year preceding the earthquake up to the large M6.7 foreshock are shown. Most activity occurs in two crises. Circle size increases with magnitude. Star is the epicenter. Arrow indicates plate convergence direction (Vigny et al., 2009). Contour lines show slab interface depth (Hayes et al., 2012). Dark blue color marks the trench. White line shows the subduction segment considered in Fig. 3.

that the interevent time between the shallow (26 events) and the deep (22 events) occurrences is as small as the one observed yields a value $< 10^{-5}$.

An intriguing feature of Figs.2 and 3 is the burst-like occurrence of the events: The largest deep and shallow events occur in packets of short duration and, as can be seen in Fig. 3 (e.g. at -282, -266, -252 days etc), multiple deep and shallow events are often interweaved together within a burst. This complexity prevents the reading of a simplistic chronology between deep and shallow events.

3 Seismic Links indicative of Water Channels?

Fig. 4 shows where the M>4 shallow and deep events which make up the eight largest bursts (Fig. 2b-c) occur. It shows that during each burst, the deep events tend to occur nearly down-dip from the shallow events. This suggests a move along slab dip of the source of slip/deformation during each burst. The rapidity of this along dip move would be comparable to the migrating speed of tremors (Shelly et al., 2007; Ide, 2010; Ghosh, 2010; Gomberg, 2010; Peng and Gomberg, 2010; Beroza and Ide, 2011). The jumps of activity observed along subduction strike from one burst to the next are also tremor characteristics (Kao et al., 2007; Shelly et al., 2007; Ghosh, 2010).

Fig. 4 also displays the slab seismicity down to small magnitude during the entire 9-month long foreshock crisis. This seismicity map is made with the Sippl et al. (2018a) catalog. As we are interested in imaging possible seismic connections, it emphasizes clustered seismicity relative to isolated events. The spatial distribution of seismic events at depths of ~20-80 km, between the shallow and deep earthquake zones, is apparently aligned in lineaments parallel and oblique to the subduction interface dip direction. It supports the presence of seismic links connecting the shallow M>4 events to the deep slab. It also shows the tendency of these links to converge spatially towards the foreshock clusters and the epicenter. The paths these links define are

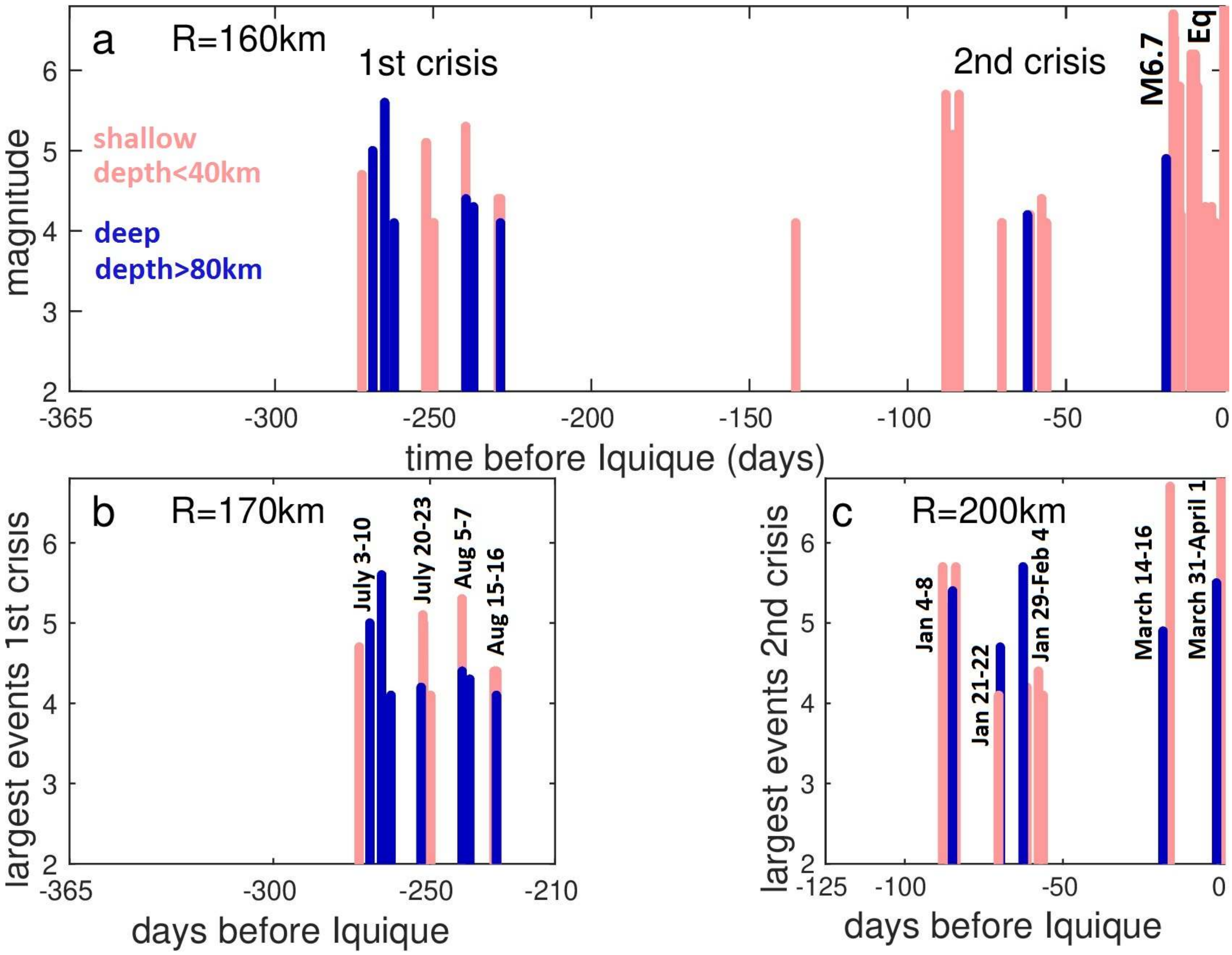

Figure 2 (a) Timings of all M>4 shallow and deep events located within 160 km from the epicenter in the year leading to the earthquake from the CSN catalog. The last event is the mainshock. (b) Increasing the epicentral distance to 170 km and focusing on the period before and during the first crisis. (c) Increasing the epicentral distance to 200 km and focusing on the largest shallow and deep events of the second crisis. Shallow events after the M6.7 foreshock are not shown because they are dominated by its own aftershocks. Periods of activity are indicated.

complex, sometimes multiple, but their long range continuity is notable.

Another illustration of seismic links between deep and shallow slab activities is presented in Fig. 5. This figure is made with the catalog of Aden-Antoniow et al. (2020) which uses a similar set of stations in North Chile as the Sippl et al. (2018a) catalog and has a comparable magnitude of completeness. It displays the seismicity pattern in August 2013 - the period when the first foreshock crisis is particularly intense. It shows the presence during this period of two seismic links connecting the future epicenter and the strongest foreshock cluster (M>5) to the locations of the largest intermediate-depth earthquakes (M>5) of this crisis.

4 Discussion

The presence of large volumes of water in subduction zones has long been documented (Raleigh and Paterson, 1965; Peacock, 1990; Green and Houston, 1995; Kirby et al., 1996; Hacker et al., 2003; Kawakatsu and Watada, 2007; Rondenay et al., 2008; Kawano et al., 2011; van Keken et al., 2011; John, 2012; Abers et al., 2013; Angiboust et al., 2014; Guillot et al., 2015; Plümper et al., 2017; Sippl et al., 2018b; Shapiro et al., 2018; Contreras-Reyes, 2021). The link between high-pressured fluids and seismic activity has itself long been recognized (Sibson, 1992; Miller et al., 1996).

The deep events in each burst occur in the depth range of 70 to 120 km where antigorite serpentine breaks down releasing the largest amount of water. Once released, water escape from the deep slab is thought to occur through transient channels (Miller et al., 2003; John, 2012; Angiboust et al., 2014; Plümper et al., 2017; Taetz et al., 2018).

The present observations are consistent with a mechanism involving the translation of pressure pulses in fluid-filled channels. The burst-like nature of the seismic activity would indicate that pressure propagation and fluid flow are very intermittent. This transient characteristic seems mechanically logical, with channels opening during overpressure passage and closing

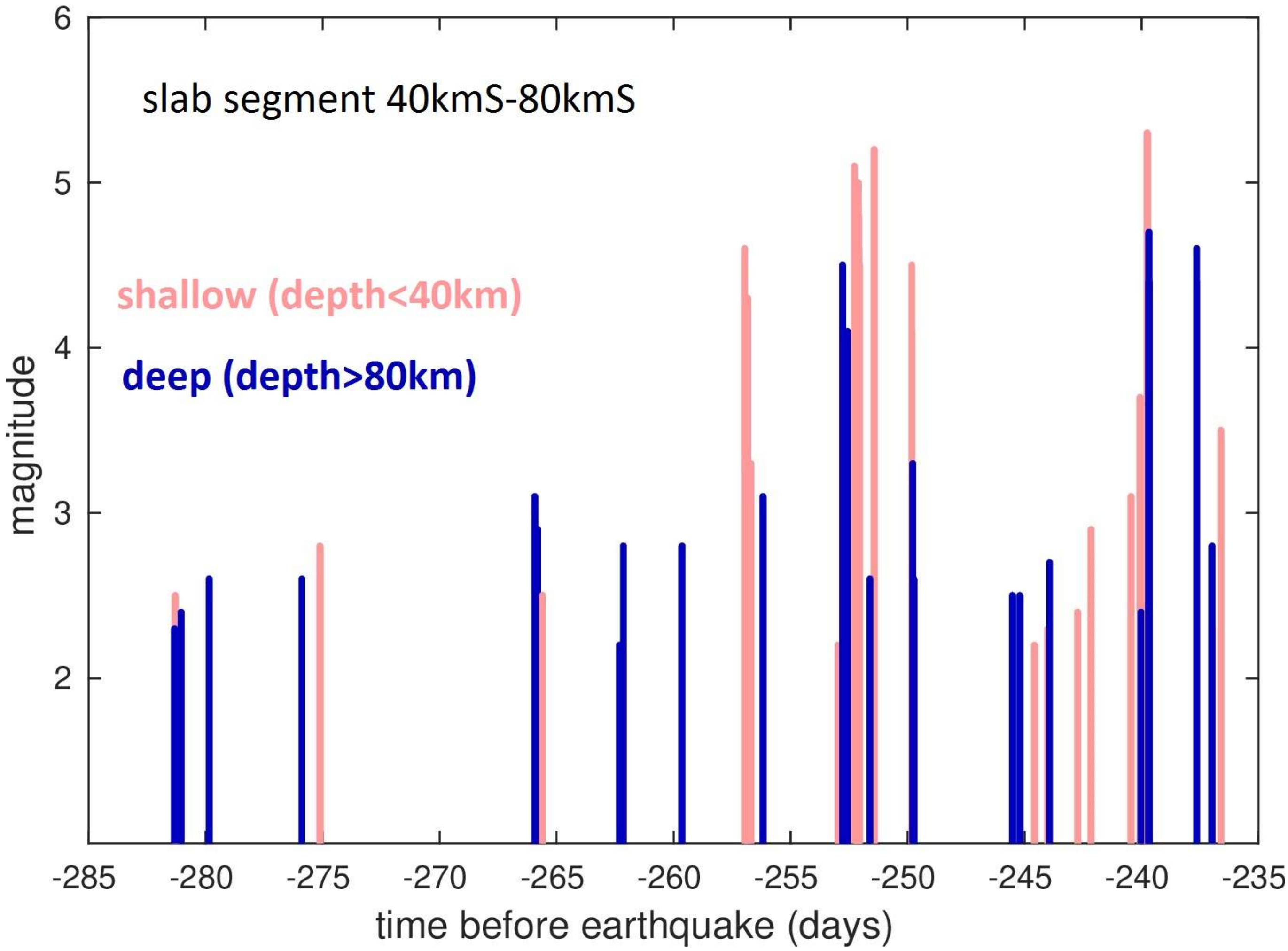

Figure 3 Timings of shallow and deep events in the subduction segment where the most intense activity of the first foreshock crisis takes place. This segment (white line in Fig. 1) extends from 40 km south to 80 km south of the epicenter and its limits are aligned with the plate convergence direction. All the shallow (depth<40 km) and deep (80 km<depth<125 km) events from Sippl et al. (2018a) catalog occurring on this segment during the period considered are presented. The segment and period investigated correspond to the occurrence of the second and third bursts in Fig. 2b. Slight differences in magnitude relative to Fig. 2 are catalog differences. What is notable is that shallow activity is closely synchronized with some deep activity.

as soon as fluid pressure locally in the channel drops below local confining pressure. The along-dip organization of the bursts denotes an along-dip orientation of the channels, which probably reflects the strong downslip corrugation of the Nazca slab interface (Soto, 2019). Such corrugations have been recently proposed to act as fluid conducts (Edwards, 2018). The occurrence of the events in packets of short duration, including both shallow and deep events, often interweaved together, suggests that they are associated with the updip and downdip propagation of pressure pulses. While surges of overpressured fluids in the seismogenic zone are probably producing the foreshocks, they are accompanied by decompression pulses propagating downdip.

Another clear characteristic of the seismic activity is its long remarkable extension along the strike of the subduction (Figs. 1, 4). This long extension of the activity does not evolve in a continuous fashion but occurs in jumps. For instance, after ~4 months of quiescence, the second crisis begins suddenly in early January ~150 km away from where the first crisis had started and 50 km beyond the zone where foreshocks had previously occurred. The activity was strong there for a few days, then completely disappeared and by the end of January, foreshock activity had jumped back to a zone close to where it initiated.

The major characteristics that are observed, the rapidity of the up-dip/down-dip interactions, the jumps of the activities along subduction strike, the broad width of the subduction zone involved are not characteristics unseen before. These same characteristics have long been reported for tremors (e.g. Shelly et al., 2007; Kao et al., 2007; Ide, 2010; Ghosh, 2010; Gomberg, 2010; Peng and Gomberg, 2010; Beroza and Ide, 2011). What is novel, here and before the Tohoku earthquake, are the very long range and the depth reach of these phenomena as well as the relatively large magnitude of the seismic events produced.

One may question the existence of physical fluid channels at the depths considered. Their presence in the dehydration zone itself, however, is observed in exhumed rocks originating from this zone and is now well

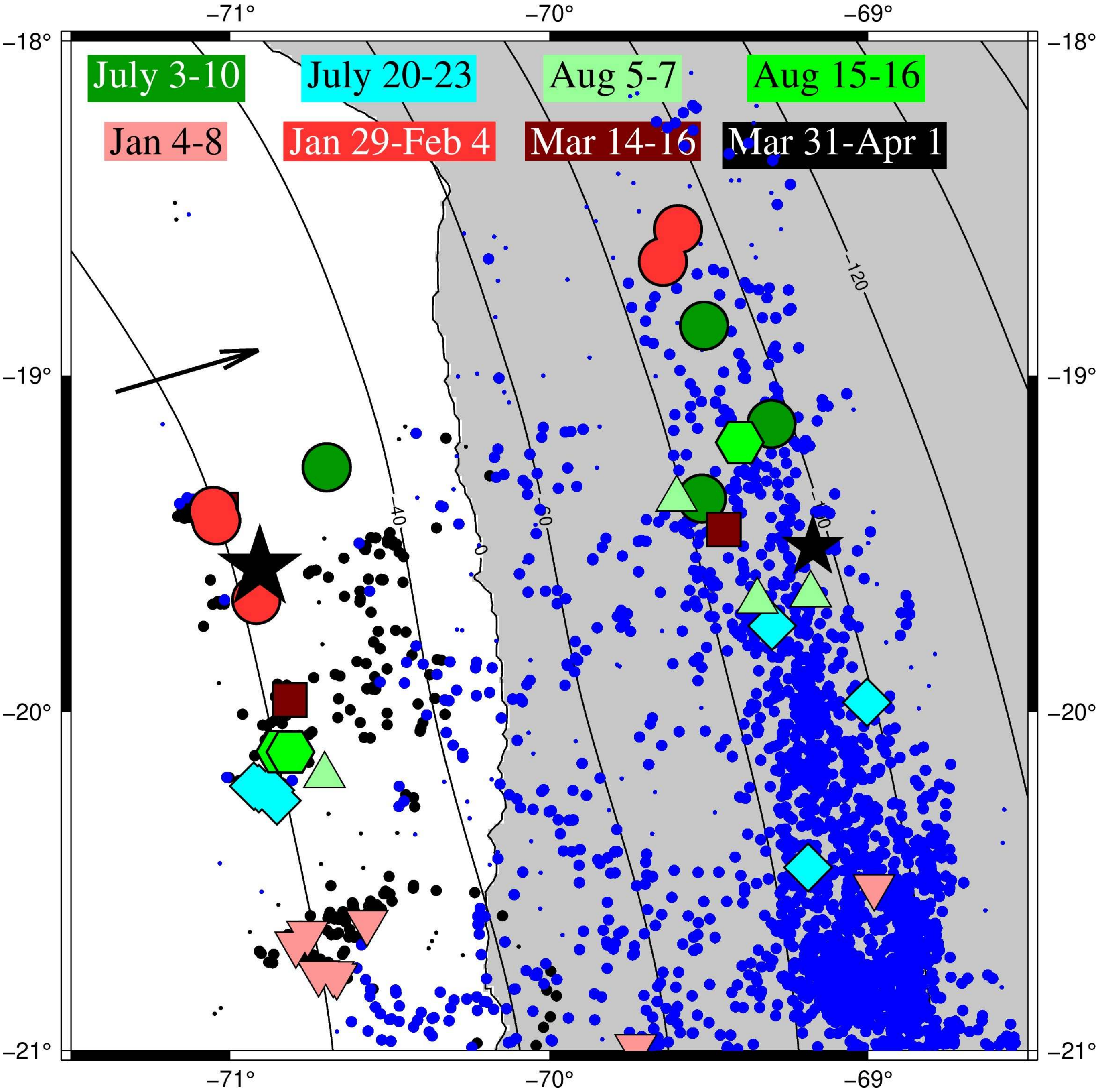

Figure 4 Location of M>4 shallow and deep events (large colored symbols) occurring during the eight largest foreshock bursts. Each color/symbol represents one burst (dates for each burst indicated at top of map). Last burst ends with the Iquique earthquake (large star). Shallow events are below sea, deep events below land. Shallow and deep events in each burst occur nearly along slab dip from each other. Superposed on the map is all the seismic activity during the entire crisis (July 2013 – March 2014) obtained from Sippl et al. (2018a) catalog (black dots: depth <40 km, blue dots: depth>40 km). The most spatially-clustered events (events with at least 3 neighbors within 10 km distance) are the larger dots.

documented (John, 2012; Angiboust et al., 2014; Plümper et al., 2017; Taetz et al., 2018) but direct observation on how these fluids migrate afterwards is lacking. Fig. 4 shows the presence of near continuous seismic paths connecting the foreshock zones to the locations of the largest intermediate depth events. The significance of these paths may at first be doubted on the ground that they are complex and multiple, but their convergence towards the foreshock and epicenter locations is clear and at least intriguing. The significance of the snapshot image of Fig. 5 might be also doubted because its statistical significance is difficult to assess, but it shows two clear seismic paths between the shallow and deep activities during one of the most active months of the foreshock crisis. The propagation of pore-pressure waves or porosity waves along or near the plate interface may be an alternative to the strong spatial localization of fluid flow of a channel model. Cruz-Atienza et al. (2018) have shown theoretically that tremor migration and speed can be explained by the propagation along the plate interface of non-linear pore-pressure waves under conditions that the interface is treated as a damage shear

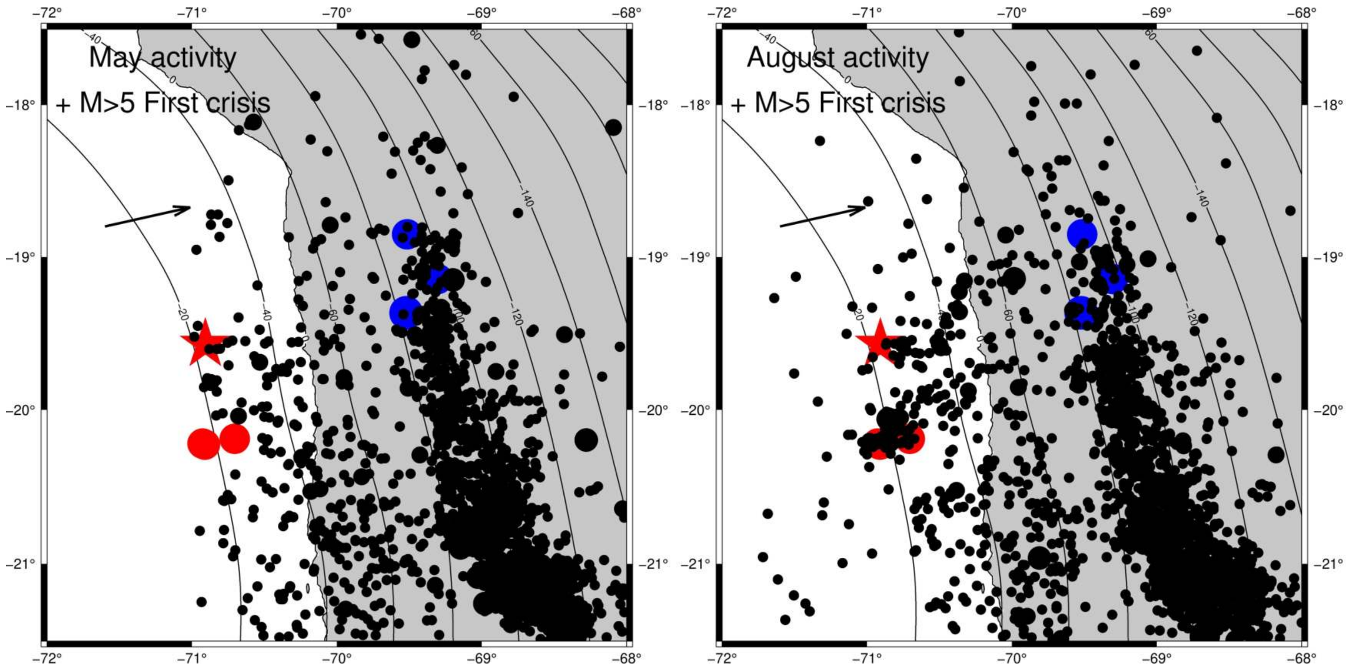

Figure 5 Seismic activity (black dots) in May (left) and August (right) 2013 from Aden-Antoniow et al. (2020) catalog. Only the events occurring near the slab interface and below are shown. Size of the dots increases with magnitude. Superposed on the maps are the locations of the largest (M>5) foreshocks (red dots) and intermediate-depth earthquakes (blue dots) during the first foreshock crisis (July-August 2013). Seismic paths, not present or recognizable in May, before the crisis begins, link in August the most intense intermediate-depth earthquake zone of this crisis (three blue dots) to the strongest foreshock cluster (two red dots) and to the future epicenter (red star).

zone with strong permeability anisotropy. The seismic paths observed here could then be following the zones of highest permeability/highest shear deformation at or near the plate interface.

If one accepts that fluid/pressure circulation is the motor of the slab seismic activity observed during the foreshock crisis, one intriguing question is why, in such a short time (a few months), overpressured pulses/fluids would ascend from different distant places spanning such a long segment of the subduction. One possible mechanism would be the existence of connections between the deep rock reservoirs where water from dehydration is thought to be stored, so that pressure changes in one would affect others. Another possible mechanism could be a rapid deformation or slip of the slab, too small or too deep to be detected geodetically, but of broad spatial extent, which could disturb the slab interface and the fluid present at depth. This probably would imply that the whole slab interface is nearing threshold stress so that effective stress limit is reached nearly simultaneously along strike for ~200 km. One may also wonder if the foreshock crisis could be driven by the updip pressures from slow slip events occurring at depth.

The present study is limited to the 9 months-long duration of the Iquique foreshock period, but it may be of interest that one of the largest intermediate-depth earthquake in instrumental time in Chile, the 2005 M7.8 Tarapaca earthquake, occurred 9 years before, precisely down-dip below the area which was to rupture during the Iquique earthquake (Jara, 2018; Ruiz and Madariaga, 2018). Although seismic instrumentation in North Chile at the time was too sparse to conduct the same study as the one done here, it is notable that this earthquake produced a long-term decrease in GPS eastward velocities in the region, interpreted as a decrease in plate coupling (Jara et al., 2017). This situation appears surprisingly comparable to the occurrence of the 2003 M7.1 intermediate-depth earthquake down-dip below the Tohoku epicentral zone 8 years earlier. Although the mechanisms by which slab dehydration, and its accompanying water release, induce intermediate-depth earthquakes are still debated (e.g. van Keken et al., 2012; Abers et al., 2013; Prieto, 2013; Poli and Prieto, 2014; Ferrand, 2017; Gasc et al., 2017; Cabrera et al., 2021), the association of the two seems now well established.

The interpretation of our observations seems supported by recent studies in subduction zone mineralogy and geochemistry which predict the short-lived pulse-like channelized water escape from the dehydration zone (John, 2012; Angiboust et al., 2014; Plümper et al., 2017; Taetz et al., 2018).

5 Conclusion

The present observations show the synchronisation of the foreshock activity which preceded the Iquique megathrust earthquake in Chile with seismic activity occurring below the foreshock locations in the intermediate-depth range of the slab. They also show the presence of near-continuous seismic links connecting the two activities. These characteristics are similar to the ones observed before the Tohoku earthquake, supporting that the same physical processes led to the two megathrust ruptures. The most logical interpretation of these observations in today's knowledge seems to be the rapid ascent of water from the slab dehydration zone.

Acknowledgements

We thank Christie Rowe for her extremely valuable comments and for her dedicated work in editing the manuscript. We also thank the two reviewers for their time and their numerous and helpful comments. We thank C. Sippl, B. Schurr, G. Asch, J. Kummerow, and F. Aden-Antoniow, C. Satriano, P. Bernard, N. Poiata, E. Aissaoui, J.P. Vilotte, W. Frank for making their catalogs publicly available. We thank the scientists, technicians and staff of the Centro Seismologico Nacional of Chile, the International Seismological Centre, and the Global Centroid Moment Tensor Project whose work made this study possible. This work benefited from discussions with C. Voisin, F. Brunet, M. Chlieh, M. Radiguet, P. Poli, E. Pathier, A. Walpersdorf.

Data and code availability

The data used in this study are open and available at: Sippl et al. (2018b), Aden-Antoniow et al. (2020), www.sismologia.cl, www.isc.ac.uk and www.globalcmt.org.

Competing interests

The authors declare that they have no competing interests.

References

Abers, G., Nakajima, J., Keken, P., Kita, S., and Hacker, B. Thermal-petrological controls on the location of earthquakes within subducting plates. *Earth Plan. Sc. Lett*, 369:178–187, 2013. doi: https://doi.org/10.1016/j.epsl.2013.03.022.

Aden-Antoniow, F., Satriano, C., Bernard, P., Poiata, N., Aissaoui, E., Vilotte, J., and Frank, W. Statistical analysis of the preparatory phase of the M8.1 Iquique earthquake, Chile. *J. Geophys. Res*, 2019JB019337, 2020. doi: https://doi.org/10.1029/2019JB019337.

Angiboust, S., Pettke, T., Hoog, J., Caron, B., and Oncken, O. Channelized fluid flow and eclogite-facies metasomatism along the subduction shear zone. *J. Petrol*, 55:883–916, 2014. doi: https://doi.org/10.1093/petrology/egu010.

Bedford, J. Months-long thousand-kilometre-scale wobbling before great subduction earthquakes. *Nature*, 580:628–635, 2020. doi: https://doi.org/10.1038/s41586-020-2212-1.

Bedford, J., Moreno, M., Schurr, B., Bartsch, M., and Oncken, O. Investigating the final seismic swarm before the Iquique-Pisagua 2014 Mw 8.1 by comparison of continuous GPS and seismic foreshock data. *Geophys. Res. Lett*, 42:3820–3828, 2015. doi: https://doi.org/10.1002/2015GL063953.

Beroza, G. and Ide, S. Slow earthquakes and nonvolcanic tremors. *Annu. Rev. Earth Planet. Sci*, 39:271–296, 2011. doi: https://doi.org/10.1146/annurev-earth-040809-152531.

Bouchon, M. Potential slab deformation and plunge prior to the Tohoku, Iquique and Maule earthquakes. *Nature Geosci*, 9: 380–383, 2016. doi: https://doi.org/10.1038/ngeo2701.

Bouchon, M. Observation of rapid long-range seismic bursts in the Japan Trench subduction leading to the nucleation of the Tohoku earthquake. *Earth Plan. Sc. Lett*, 594:117696, 2022. doi: https://doi.org/10.1016/j.epsl.2022.117696.

Boudin, F. Slow slip events precursory to the 2014 Iquique earthquake, revisited with long-base tilt and GPS records. *Geophys. J. Int*, 228:2092–2121, 2021. doi: https://doi.org/10.1093/gji/ggab425.

Bouih, M., Panet, I., Remy, D., Longuevergne, L., and Bonvalot, S. Deep mass redistribution prior to the 2010 Mw 8.8 Maule (Chile) Earthquake revealed by GRACE satellite gravity. *Earth Plan. Sc. Lett*, 584:117465, 2022. doi: https://doi.org/10.1016/j.epsl.2022.117465.

Cabrera, L., Ruiz, S., Poli, P., Contreras-Reyes, E., Osses, A., and Mancini, R. Northern Chile intermediate-depth earthquakes controlled by plate hydration. *Geophys. J. Int*, 226:78–90, 2021. doi: https://doi.org/10.1093/gji/ggaa565.

Chlieh, M. Interseismic coupling and seismic potential along the Central Andes subduction zone. *J. Geophys. Res*, 116(B12):1–21, 2011. doi: https://doi.org/10.1029/2010JB008166.

Contreras-Reyes, E. Subduction zone fluids and arc magmas conducted by lithospheric deformed regions beneath the central Andes. *Scientific Reports*, 11(23078), 2021. doi: https://doi.org/10.1038/s41598-021-02430-9.

Cruz-Atienza, V., Villafuerte, C., and Bhat, H. Rapid tremor migration and pore-pressure waves in subduction. *Nature Comm*, 2018. doi: 10.1038/s41467-018-05150-3.

Duputel, Z. The Iquique earthquake sequence of April 2014: Bayesian modeling accounting for prediction uncertainty. *Geophys. Res. Lett*, 42:7949–7957, 2015. doi: https://doi.org/10.1002/2015GL065402.

Edwards, J. Corrugated megathrust revealed offshore from Costa Rica. *Nature Geosci*, 11:197–202, 2018. doi: https://doi.org/10.1038/s41561-018-0061-4.

Ekström, G., Nettles, M., and Dziewonski, A. The global CMT project 2004-2010: Centroid-moment tensors for 13,017 earthquakes. *Phys.Earth Planet. Inter*, page 200–201, 2012. doi: 10.1016/j.pepi.2012.04.002.

Ferrand, T. Dehydration-driven stress transfer triggers intermediate-depth earthquakes. *Nature Comm*, 8:15247, 2017. doi: https://doi.org/10.1038/ncomms15247.

Galbraith, C., Smyth, P., and Stern, H. Quantifying the association between discrete event time series with applications to digital forensics. *J. Roy. Stat. Soc*, Series A:0964–1998 20 183000, 2020. doi: http://doi.org/10.1111/rssa.12549.

Gasc, J., Hilairet, N., Yu, T., Ferrand, T., Schubnel, A., and Y, W. Faulting of natural serpentine: Implications for intermediate-depth seismicity. *Earth Plan. Sc. Lett*, 474:138–147, 2017. doi: https://doi.org/10.1016/j.epsl.2017.06.016.

Ghosh, A. Rapid continuous streaking of tremor in Cascadia. *Geoch Geophys. Geosyst*, 11, Q12010, 2010. doi: https://doi.org/10.1029/2010GC003305.

Gomberg, J. Slow slip phenomena in Cascadia from 2007 and beyond: A review. *Geol. Soc. Am. Bull*, 122:963–978, 2010. doi: https://doi.org/10.1130/B30287.1.

Green, H. and Houston, H. The mechanics of deep earthquakes. *Ann. Rev. Earth Planet. Sci*, 23:169–213, 1995. doi: https://doi.org/10.1146/annurev.ea.23.050195.001125.

Guillot, S., Schwartz, S., Agard, P., Renard, B., and Prigent, C. Tectonic significance of serpentinites. *Tectonophysics*, page 1–19, 2015. doi: https://doi.org/10.1016/j.tecto.2015.01.020.

Hacker, B., Peacock, S., Abers, G., and Holloway, S. Subduction factory 2. Are intermediate-depth earthquakes in subducting slabs linked to metamorphic dehydration reactions? *J. Geophys. Res*, 108, 2003. doi: https://doi.org/10.1029/2001JB001129.

Hayes, G., Wald, D., and Johnson, R. Slab1.0: A three-dimensional model of global subduction zone geometries. *J. Geophys. Res*, 117, B01302, 2012. doi: https://doi.org/10.1029/2011JB008524.

Ide, S. Striations, duration, migration, and tidal response in deep tremor. *Nature*, 466:356–359, 2010. doi: https://doi.org/10.1038/nature09251.

Jara, J. Kinematic study of Iquique 2014 Mw8.1 earthquake; Understanding the segmentation of the seismogenic zone. *Earth Plan. Sc. Lett*, 503:131–143, 2018. doi: https://doi.org/10.1016/j.epsl.2018.09.025.

Jara, J., Soquet, A., Marsan, D., and Bouchon, M. Long-term interactions between intermediate depth and shallow seismicity in North Chile subduction Zone. *Geophys. Res. Lett*, 44, 2017. doi: https://doi.org/10.1002/2017GL075029.

John, T. Volcanic arcs fed by rapid pulsed fluid flow through subducting slabs. *Nature Geosci*, 5:489–492, 2012. doi: https://doi.org/10.1038/ngeo1482.

Kao, H., Shan, S., Rogers, G., and Dragert, H. Migration characteristics of seismic tremors in the northern Cascadia margin. *Geophys. Res. Lett*, 34, L03304, 2007. doi: https://doi.org/10.1029/2006GL028430.

Karabulut, H., Bouchon, M., and Schmittbuhl, J. Synchronization of small scale seismic clusters reveals large scale plate deformation. *Earth Planets Space*, 74(158), 2022. doi: https://doi.org/10.1186/s40623-022-01725-z.

Kato, A. and Nakagawa, S. Multiple slow-slip events during a foreshock sequence of the 2014 Iquique, Chile Mw 8.1 earthquake. *Geophys. Res. Lett*, 41:5420–5427, 2014. doi: https://doi.org/10.1002/2014GL061138.

Kato, A., Fukuda, J., Kumazawa, T., and Nakagawa, S. Accelerated nucleation of the 2014 Iquique, Chile Mw 8.2 earthquake. *Nature Sci. Rep*, 6:24792, 2016. doi: https://doi.org/10.1038/srep24792.

Kawakatsu, H. and Watada, S. Seismic Evidence for Deep-Water Transportation in the Mantle. *Science*, 316:1468–1471, 2007. doi: https://doi.org/10.1126/science.1140855.

Kawano, S., Katayama, I., and Okazaki, K. Permeability anisotropy of serpentine and fluid pathways in a subduction zone. *Geology*, 39:939–942, 2011. doi: https://doi.org/10.1130/G32173.1.

Kirby, S., Engdahl, R., and Denlinger, R. Intermediate-depth intraslab earthquakes and arc volcanism as physical expressions of crustal and uppermost mantle metamorphism in subducting slabs. *Subduction Top to Bottom, Am. Geophys. Un. Geophys. Monogr*, 96:195–214, 1996. doi: https://doi.org/10.1029/GM096p0195.

Lay, T., Yue, H., Brodsky, E., and An, C. The 1 April 2014 Iquique, Chile, Mw 8.1 earthquake rupture sequence. *Geophys. Res. Lett*, 41:3818–3825, 2014. doi: https://doi.org/10.1002/2014GL060238.

Madariaga, R. Sismicidad de Chile. *Fisica de la Tierra*, 10:221–258, 1998.

Meng, L., Huang, H., Bürgmann, R., Ampuero, J., and Strader, A. Dual megathrust behaviors of the 2014 Iquique earthquake sequence. *Earth Planet. Sci. Lett*, 411:177–187, 2015. doi: https://doi.org/10.1016/j.epsl.2014.11.041.

Metois, M., Vigny, C., and Socquet, A. Interseismic coupling, megathrust earthquakes and seismic swarms along the Chilean subduction zone (38°-18°S. *Pure Appl. Geophys*, 173:1431–1449, 2016. doi: https://doi.org/10.1007/s00024-016-1280-5.

Miller, S., Nur, A., and Olgaard, D. Earthquakes as a coupled shear stress-high pore pressure dynamical system. *Geophys. Res. Lett*, 23:197–200, 1996. doi: https://doi.org/10.1029/95GL03178.

Miller, S., Zee, W., Olgaard, D., and Connolly, J. A fluid-pressure feedback model of dehydration reactions: experiments, modelling, and application to subduction zones. *Tectonophysics*, 370:241–251, 2003. doi: https://doi.org/10.1016/S0040-1951(03)00189-6.

Panet, I., Bonvalot, S., Narteau, C., Remy, D., and Lemoine, J. Migrating pattern of deformation prior to the Tohoku-Oki earthquake revealed by GRACE data. *Nature Geosci*, 11, 2018. doi: https://doi.org/10.1038/s41561-018-0099-3.

Panet, I., Narteau, C., Lemoine, J., Bonvalot, S., and Remy, D. Detecting preseismic signals in GRACE gravity solutions : Application to the 2011 Mw 9.0 Tohoku earthquake. *J. Geophys. Res*, 127, 2022. doi: https://doi.org/10.1029/2022JB024542.

Peacock, S. Fluid processes in subduction zones. *Science*, 248:329–337, 1990. doi: https://doi.org/10.1126/science.248.4953.329.

Peng, Z. and Gomberg, J. An integrated perspective of the continuum between earthquakes and slow-slip phenomena. *Nature Geosci*, 3:599–607, 2010. doi: https://doi.org/10.1038/ngeo940.

Plümper, O., John, T., Podladchikov, Y., Vrijmoed, J., and Scambelluri, M. Fluid escape from subduction zones controlled by channel-forming reactive porosity. *Nature Geosci*, 10:150–155, 2017. doi: https://doi.org/10.1038/ngeo2865.

Poli, P. and Prieto, G. Global and along-strike variations of source duration and scaling for intermediate-depth and deep-focus earthquakes. *Geophys. Res. Lett*, 41:8315–8324, 2014. doi: https://doi.org/10.1002/2014GL061916.

Prieto, G. Seismic evidence for thermal runaway during intermediate-depth earthquake rupture. *Geophys. Res. Lett*, 40: 6064–6068, 2013. doi: https://doi.org/10.1002/2013GL058109.

Raleigh, C. and Paterson, M. Experimental deformation of serpentinite and its tectonic implications. *J. Geophys. Res*, 70:3965–3985, 1965. doi: https://doi.org/10.1029/JZ070i016p03965.

Rondenay, S., Abers, G., and P.E, K. Seismic imaging of subduction zone metamorphism. *Geology*, 36:275–278, 2008. doi: https://doi.org/10.1130/G24112A.1.

Rousset, B., Campillo, M., Shapiro, N., Walpersdorf, A., Titkov, N., and Chebrov, D. The 2013 slab-wide Kamchatka earthquake sequence. *Geophys. Res. Lett*, 50, 2023. doi: 10.1029/2022GL101856.

Ruiz, S. Intense foreshocks and a slow slip event preceded the 2014 Iquique Mw 8.1 earthquake. *Science*, 345:1165–1169, 2014. doi: https://doi.org/10.1126/science.1256074.

Ruiz, S. and Madariaga, R. Historical and recent large megathrust earthquakes in Chile. *Tectonophysics*, 733:37–56, 2018. doi: https://doi.org/10.1016/j.tecto.2018.01.015.

Schurr, B. Gradual unlocking of plate boundary controlled initiation of the 2014 Iquique earthquake. *Nature*, 512:299–302, 2014. doi: https://doi.org/10.1038/nature13681.

Shapiro, N., Campillo, M., Kaminski, E., Vilotte, J., and Jaupard, C. Low-frequency earthquakes and pore-pressure transients in subduction zones. *Geophys. Res. Lett*, 43:11083–11094, 2018. doi: https://doi.org/10.1029/2018GL079893.

Shelly, D., Beroza, G., and Ide, S. Complex evolution of transient slip derived from precise tremor locations in western Shikoku, Japan. *Geochem. Geophys. Geosyst*, 8, Q10014, 2007. doi: https://doi.org/10.1029/2007GC001640.

Sibson, R. Implications of fault-valve behavior for rupture nucleation and recurrence, Tectonophysics 18,1031–1042, 1992. doi: https://doi.org/10.1016/0040-1951(92)90065-E.

Sippl, C., Schurr, B., Asch, G., and Kummerow, J. *Catalogue of Earthquake Hypocenters for Northern Chile Compiled from IPOC* *(plus auxiliary) seismic stations*. GFZ Data Services, 2018a. doi: 10.5880/GFZ.4.1.2018.001.

Sippl, C., Schurr, B., Asch, G., and Kummerow, K. Seismicity structure of the northern Chile forearc from >100,000 double-difference relocated hypocenters. *J. Geophys. Res. Solid Earth*, 123:4063–4087, 2018b. doi: https://doi.org/10.1002/2017JB015384.

Socquet, A. An 8 month slow slip event triggers progressive nucleation of the 2014 Chile megathrust. *Geophys. Res. Lett*, 44, 2017. doi: https://doi.org/10.1002/2017GL073023.

Soto, H. Probing the Northern Chile Megathrust with Seismicity: The 2014 M8.1 Iquique Earthquake Sequence. *J. Geophys. Res*, 124:12935–12954, 2019. doi: https://doi.org/10.1029/2019JB017794.

Taetz, S., John, T., Bröcker, M., Spandler, C., and Stracke, A. Fast intraslab fluid-flow events linked to pulses of high pore fluid pressure at the subducted plate interface. *Earth Plan. Sc. Lett*, 482: 33–43, 2018. doi: https://doi.org/10.1016/j.epsl.2017.10.044.

van Keken, P., Hacker, B., Syracuse, E., and Abers, G. Subduction factory: Depth-dependent flux of H2O from subducting slabs worldwide. *J. Geophys. Res*, 116, B01401, 2011. doi: https://doi.org/10.1029/2010JB007922.

van Keken, P., Kita, S., and Nakajima, J. Thermal structure and intermediate-depth seismicity in the Tohoku-Hokkaido subduction zones. *Solid Earth*, 3:355–364, 2012. doi: https://doi.org/10.5194/se-3-355-2012.

Vigny, C., Rudloff, A., Ruegg, J., Madariaga, R., Campos, J., and Alvarez, M. Upper plate deformation measured by GPS in the Coquimbo gap. *Chile, Phys. Earth planet. Inter*, 175:86–95, 2009. doi: https://doi.org/10.1016/j.pepi.2008.02.013.

doi:10.26443/seismica.v2i2.691

SEISMICA

The rupture plane of the 16 February 2022 M_w 6.2 Guatemala, intermediate depth earthquake

R. Yani-Quiyuch * [1], **L. Asturias** [1], **D. Castro** [1]

[1]Instituto Nacional de Sismología, Vulcanología, Meteorología e Hidrología, INSIVUMEH, Guatemala.

Author contributions: *Conceptualization*: R. Yani-Quiyuch, L. Asturias. *Software*: L. Asturias, D. Castro. *Formal Analysis*: R. Yani-Quiyuch, L. Asturias, D. Castro. *Writing - original draft*: R. Yani-Quiyuch, L. Asturias.

Abstract On 16 February 2022, an intermediate depth intraplate earthquake of M_w 6.2 struck the Guatemalan subduction zone with its epicenter located to the southwest of the department of Escuintla, along the Pacific coast. Following the main event, over 275 aftershocks were recorded and subsequently relocated using the HypoDD algorithm. This analysis revealed a fault with an area of $\sim$350 km^2, significantly larger than what would typically be expected for an earthquake of this magnitude. The moment tensor at the centroid of the main earthquake, along with estimations of focal mechanisms for the largest aftershocks, enabled the identification of both normal earthquakes associated with the fault plane and inverse earthquakes linked to seismic activity in the upper part of the slab. Notably, the region where this seismic sequence occurred has experienced heightened seismic activity in recent years. We propose that the mainshock nucleated in the lower seismicity layer (LSL) of the region's double seismicity zone, subsequently triggering seismic activity on a pre-existing active fault, and also in the upper seismicity layer (USL). We estimate a separation of 12.2$\pm$5.0 km between these two seismicity layers.

Resumen Un sismo intraplaca de profundidad intermedia con M_w 6.2 ocurrió en la zona de subducción guatemalteca el 16 de febrero de 2022, con epicentro en el suroeste del departamento de Escuintla, en la costa del Pacífico. Se registraron más de 275 réplicas, las cuales fueron relocalizadas con el algoritmo HypoDD, pudiendo identificar una falla con un área de $\sim$350 km^2, la cual es considerablemente superior a la esperada para un sismo de esa magnitud. El tensor de momento en el centroide del sismo principal y la estimación de otros mecanismos focales de las réplicas más grandes, permitieron identificar sismos normales, relacionados al plano de falla y sismos inversos que fueron asociados a sismicidad en la zona superior del slab. La región de la secuencia ha presentado actividad sísmica alta en años recientes. Proponemos que el sismo principal nucleó en la capa inferior de sismicidad (CIS) de la zona doble de sismicidad de la región disparando actividad sísmica en una falla activa pre-existente y, además, en la capa superior de sismicidad (CSS). Estimamos una separación de 12.2$\pm$5.0 km entre estas dos capas de sismicidad.

Non-technical summary On 16 February 2022, a magnitude 6.2 earthquake struck with its epicenter located in the department of Escuintla, on the Pacific coast of Guatemala. The earthquake occurred at an approximate depth of 70 km, within the Cocos plate as it subducts beneath the Caribbean plate. While the earthquake caused alarm among the population, only minor damage to some buildings was reported. Recent advancements in the Red Sismológica Nacional (RSN) enabled the registration of a significant number of aftershocks. This data allowed the identification of the fault plane associated with the earthquake and the activation of additional seismicity in the upper region of the same plate. Notably, the identified fault area is twice the size typically expected for an earthquake of this magnitude. Given the region's recent seismic activity, we propose that this earthquake and its aftershocks occurred along a pre-existing seismic fault. The detailed understanding of this seismic source, provided for the first time through instrumental means, allows for a better characterization of the hazard and seismic risk in Guatemala related to subduction earthquakes.

Production Editor: Gareth Funning
Handling Editor: Marino Protti
Copy & Layout Editor: Oliver Lamb

Signed reviewer(s): Beatriz Cosenza-Muralles

Received: March 29, 2023
Accepted: October 3, 2023
Published: November 15, 2023

1 Introduction

On 16 February 2022, at 07:12 (UTC), a magnitude M_w 6.2 earthquake occurred in the subduction zone off the southern coast of Guatemala. The epicenter was situated in the department of Escuintla, near the department of Suchitepéquez (Figure 1). The seismic event had a depth of approximately 70 km and was felt by a significant portion of the country's population. According to the Instituto Nacional de Sismología, Vulcanología, Meteorología e Hidrología (INSIVUMEH) instrumental measurements, seismic intensities of VI on the Modified Mercalli Intensity scale (MMI) were recorded. Due to the hypocenter's location and its normal focal mechanism, it was classified as an intraslab earthquake (Güendel and Protti, 1998; Alvarez, 2009; Guzmán-Speziale and Zúñiga, 2016; Guzmán-Speziale and Molina, 2022).

*Corresponding author: royani@insivumeh.gob.gt

In recent years, the Red Sismológica Nacional (RSN) operated by INSIVUMEH (INSIVUMEH, 1976), has significantly expanded its number of seismic stations, equipped with velocity and acceleration sensors. Additionally, the Earthquake Early Warning in Central America (ATTAC) project, led by the Swiss Seismological Service (SED) at ETH Zurich in collaboration with Central American seismological agencies, has contributed further instrumentation provided by the Swiss Agency for Development and Cooperation (SDC). This network also includes stations donated by the Volcano Disaster Assistance Program (VDAP) of the US Geological Survey (USGS) for volcanic monitoring.

Moreover, INSIVUMEH benefits from real-time waveform data received from the Servicio Sismológico Nacional (SSN) of Mexico (SSN, 2022), the Ministerio de Ambiente y Recursos Naturales (MARN) of El Salvador (SNET, 2004), and the Comisión Permanente de Contingencias (COPECO) of Honduras (see Figure 1). These collaborative efforts have significantly improved hypocentral location accuracy and have opened up possibilities for conducting more detailed seismicity analyses in Guatemala and its surrounding regions.

In this paper, we utilize waveforms from a strengthened seismic network to conduct a detailed analysis of the earthquake that occurred on 16 February 2022, along with its subsequent sequence of aftershocks. By relocating the hypocenters, we successfully identified the rupture plane, which aligns with the moment tensor of the main earthquake and the normal focal mechanisms of certain aftershocks. Additionally, we discovered other earthquakes in the sequence, situated further away from the rupture plane, in the upper part of the slab, some of which exhibited an inverse focal mechanism. The analysis and interpretation procedure are described below.

2 The subducted Cocos Plate

Off the southern coast of Guatemala, the Cocos plate subducts under the Caribbean plate. This subduction zone gives rise to a significant number of earthquakes, which are monitored and recorded by the RSN. From southeastern Mexico to northwestern El Salvador (México-Guatemala-El Salvador Subduction Zone or MGESZ), the slab dip angle gradually changes from 20 to 60 degrees from the Middle America Trench to a depth of 280 km (Hayes et al., 2018), maintaining a relatively consistent overall shape (Hayes et al., 2018; Guzmán-Speziale and Zúñiga, 2016). The velocity of the Cocos plate with respect to the Central America forearc sliver to the northwest of MGESZ is 76.4 ± 2.5 mm/year, while to the southeast it is 75.0 ± 1.2 mm/year (Ellis et al., 2019) (Figure 1).

Historically, this subduction zone has been the source of several destructive earthquakes (e.g., Ambraseys and Adams, 1996; White et al., 2004; Ye et al., 2013; Ellis et al., 2018). Many of these events have been identified through both instrumental measurements and macroseismic observations, encompassing both interplate and intraplate regions (Ambraseys and Adams, 1996; White et al., 2004). Insights from centroid moment tensors (CMTs) reveal a mix of inverse (compression) and normal (extension) focal mechanisms throughout the entire subduction process (Güendel and Protti, 1998; Alvarez, 2009; Guzmán-Speziale and Zúñiga, 2016; Guzmán-Speziale and Molina, 2022).

To observe the spatial distribution of subduction earthquakes and their focal mechanisms with better precision within MGESZ, we used the ISC-GEM catalog (Storchak et al., 2013, 2015; Di Giacomo et al., 2018), where it could be noticed that along the Middle America Trench, where the bending of the Cocos Plate still occurs at the onset of subduction, focal mechanisms are predominantly normal. In the interplate region (down to depths of around 40 km), focal mechanisms are mostly inverse, while at greater depths, a combination of both types of focal mechanisms is more commonly observed (Figure 1). This pattern mirrors the behavior seen in other subduction zones worldwide that possess relatively straightforward geometries (Craig et al., 2022).

The trigger mechanism of intermediate depth earthquakes is still a matter of debate. Among the most widely accepted explanations are dehydration embrittlement and the reactivation of previously formed faults within the outer rise region, faults initially generated during the plate bending process and subsequently reactivated during subduction (e.g., Ranero et al., 2005; Brudzinski et al., 2007; Kiser et al., 2011; Marot et al., 2012; Cabrera et al., 2021).

As observed in other global regions, detailed studies of intermediate-depth earthquakes have unveiled a double seismicity zone (DSZ) within the MGESZ slab. This DSZ is characterized by a separation between the upper seismicity layer (USL) and the lower seismicity layer (LSL) (Brudzinski et al., 2007; Florez and Prieto, 2019). In proximity to the earthquake of 16 February 2022, Brudzinski et al. (2007) noted a separation of 8.0 ± 6.6 km betwen USL and LSL, whereas Florez and Prieto (2019) reported a separation of 11.3 ± 4.0 km. This relatively small separation, compared to other subduction zones, is attributed to the youthful age of the subducting plate (Brudzinski et al., 2007; Florez and Prieto, 2019), which is estimated to be approximately 24 million years old (Nishikawa and Ide, 2014).

Brudzinski et al. (2007) found that, in the subduction zones they examined (without specific information about MGESZ) normal focal mechanisms were present in the LSL. On the other hand, earthquakes ocurring at intermediate depths in the USL tend to exhibit inverse focal mechanisms (Craig et al., 2022; Chu and Beroza, 2022). Within the MGESZ, it has been estimated that normal earthquakes release more seismic moment than inverse earthquakes at these intermediate depths (Alvarez, 2009; Guzmán-Speziale and Zúñiga, 2016), this is consistent with other subduction zones in the world (Craig et al., 2022).

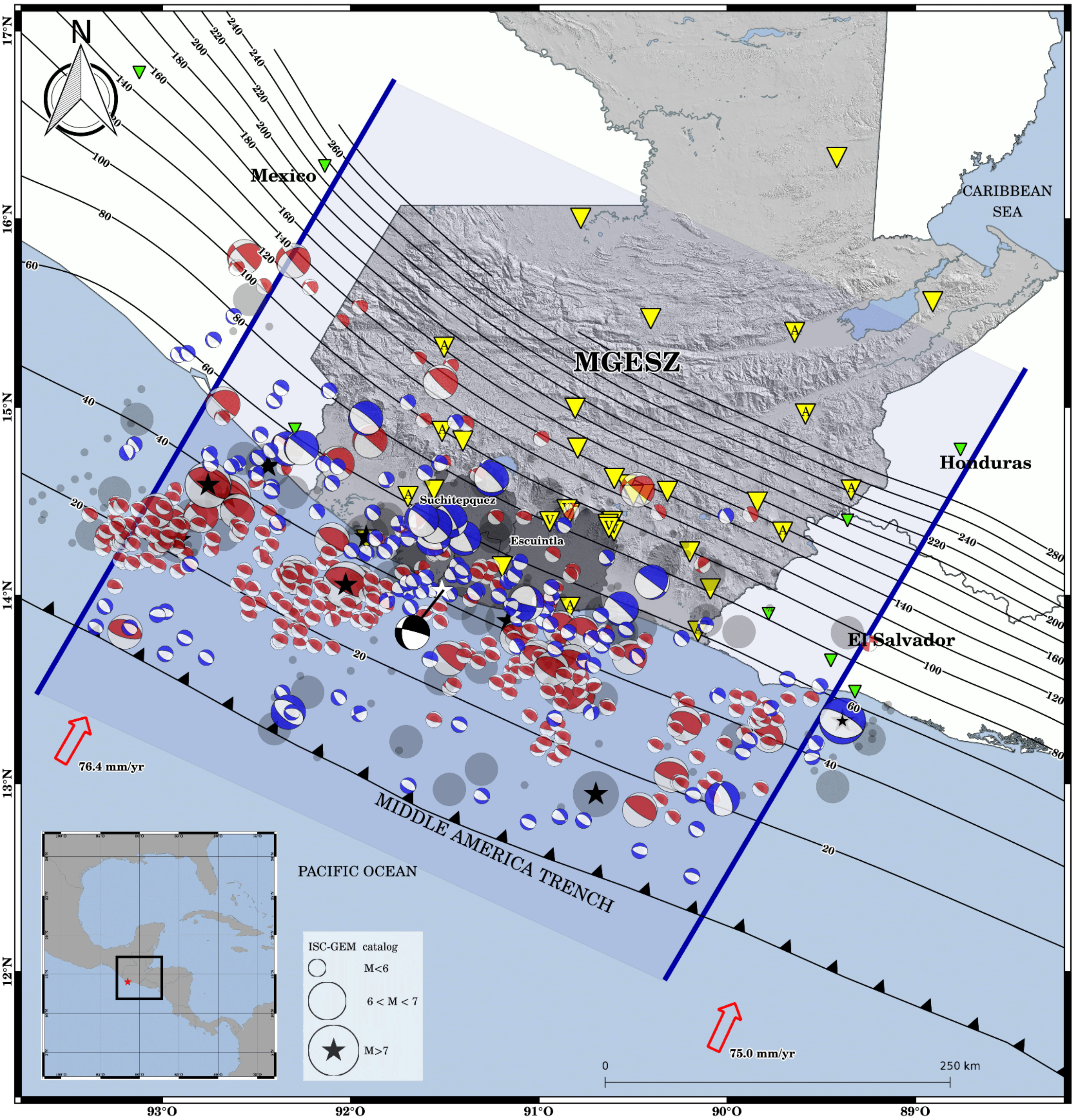

Figure 1 Subduction zone between the Cocos and Caribbean plates that includes the border with Mexico, Guatemala, and part of El Salvador (MGESZ). The iso-depth lines at the top of the slab (Hayes et al., 2018) indicate its relatively uniform shape. The preliminary epicenter of the 16 February 2022 earthquake is marked with a white star, and its focal mechanism is shown in black (this study). Red beachballs represent earthquakes with inverse focal mechanisms, while blue beachballs represent those with normal focal mechanisms, and gray circles represent earthquakes without a focal mechanism, according to the ISC-GEM catalog (Storchak et al., 2013, 2015; Di Giacomo et al., 2018), chosen for its higher accuracy in epicentral locations. Black stars denote subduction earthquakes with M_w>7. Inverted triangles represent seismic stations used for the seismic sequence analysis. The RSN (INSIVUMEH, 1976) is represented by yellow inverted triangles (with the letter A indicating the ATTAC project and the letter V indicating VDAP, see description in the text), while seismic stations from Mexico, El Salvador, and Honduras are represented by green inverted triangles. Red arrows indicate the convergence velocities of the Cocos plate relative to the Central America forearc sliver, according to Ellis et al. (2019).

3 Seismicity associated with the M_w 6.2 earthquake

During the initial 25 days, more than 275 aftershocks were recorded and located using the SeisAn software (Havskov and Ottemoller, 1999), with magnitudes ranging from 2.4 to 4.7. These aftershocks were dispersed throughout the vicinity of the mainshock, with their epicenters aligned in a NNE-SSW orientation. The main-

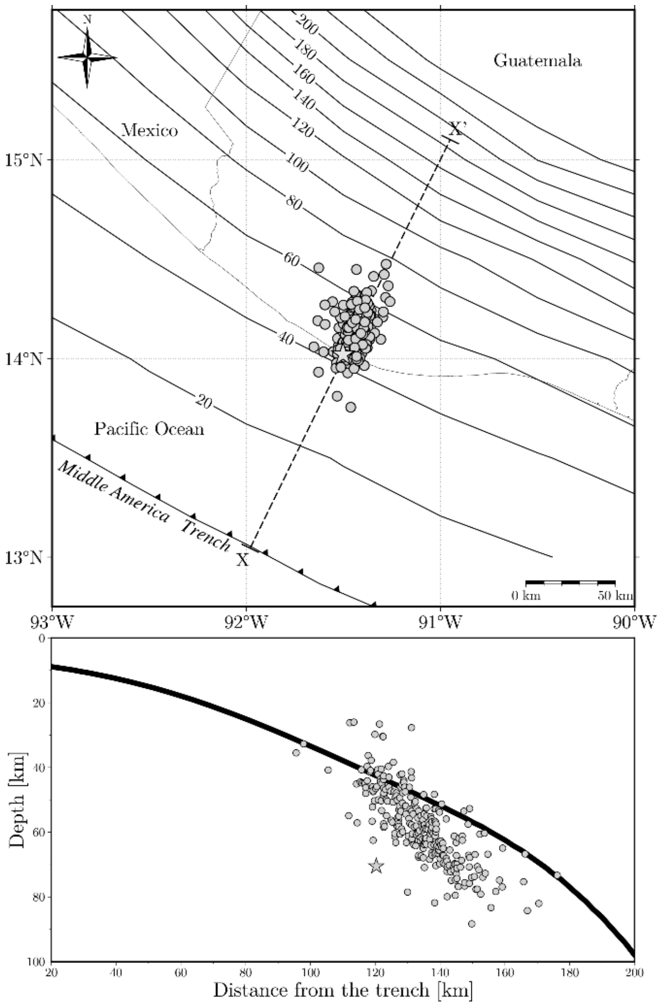

Figure 2 Geographic distribution and profile section (along X-X') of the preliminary main earthquake location (gray star) and the subsequent aftershocks sequence (gray dots). The slab model for the region is presented according to Hayes et al. (2018). The majority of earthquakes are situated at depths ranging from 40 to 80 km.

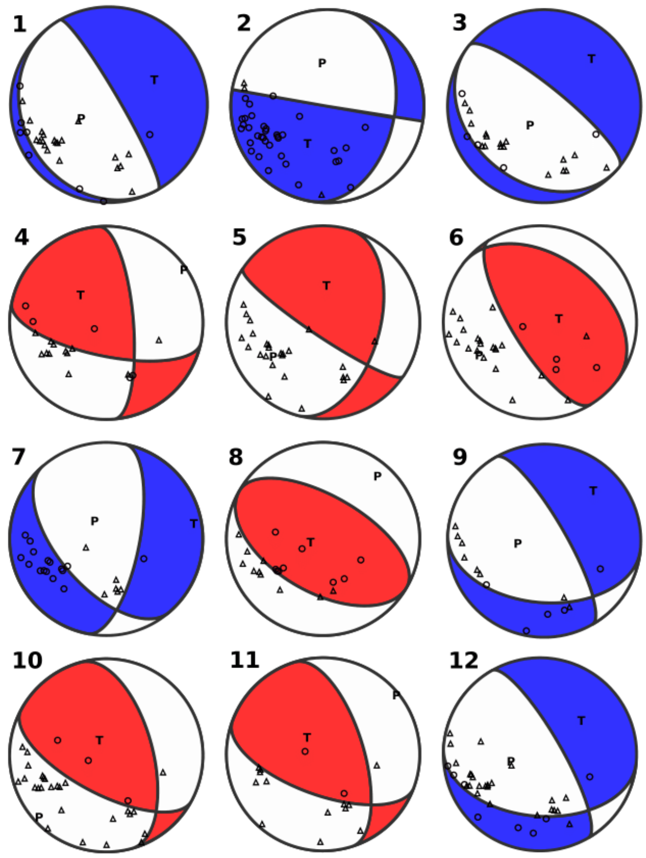

Figure 3 Focal mechanisms of the most significant aftershocks within the seismic sequence associated with the M_W 6.2 earthquake, determined using the first-arrival polarities method. Compression polarities are represented by circles, while dilation polarities are denoted by triangles. Events 1, 2, 3, 7, 9 and 12 exhibit larger components of normal focal mechanism, whereas events 4, 5, 6, 8, 10 and 11 display characteristics of inverse focal mechanism. P and T correspond to the pressure and tension axes, respectively.

shock's hypocenter was estimated to be at a depth of 70±7 km, surpassing the Slab2 model's approximate 50 km depth for that location (Hayes et al., 2018). Prior to the relocation process, the initial distribution of aftershock depths spanned from 40 to 80 km (Figure 2).

The CMT for the M_W 6.2 earthquake was derived using the W phase algorithm (Kanamori and Rivera, 2008; Hayes et al., 2018; Duputel et al., 2012). This solution incorporated data from the aforementioned seismic agencies as well as waveforms acquired through the Wilber 3 platform of the Incorporated Research Institutions for Seismology (Newman et al., 2013). The centroid depth was determinated to be 60.5 km (Figure 4). The outcomes of the inversion process are presented in Table 1, allowing for a comparison with the results from the Global Centroid-Moment-Tensor Project (Dziewonski et al., 1981; Ekström et al., 2012) and the Advanced National Seismic System (ANSS) of the USGS.

Additionally, 12 focal mechanisms were estimated for the largest magnitude aftershocks using the P-wave first-arrival polarity method. The focal mechanisms obtained showed dominant normal and inverse components (Figure 3). The SeisAn software (Havskov and Ottemoller, 1999) was utilized, employing the FOCMEC (Snoke, 2003) and FPFIT (Reasenberg and Oppenheimer, 1985) algorithms for this analysis.

3.1 Hypocentral relocation

We used the HypoDD v1.3 software in order to obtain a catalog of relocated seismic events (Waldhauser and Ellsworth, 2000; Waldhauser, 2001), which is a simultaneous relocation algorithm that minimizes the residual between observed and theoretical travel time differences (or double differences) for pairs of earthquakes recorded at each station while linking all observed event-station pairs (Waldhauser and Ellsworth, 2000). The Double-Differences technique takes advantage of the fact that if the hypocentral separation between two earthquakes is small compared to the event-station distance, then the ray paths between the source region and a common station are similar over almost the entire path (Fréchet, 1985; Got et al., 1994). In this case, the difference in travel times for two events observed at one station can be attributed to spatial shifting between the events with high precision. This approach

Agency	NP1	NP2	M_w	Centroid Depth (km)	Moment (N-m)
INSIVUMEH	182.6/ 34.0/ -14.9	285.1/ 81.7/ -123.1	6.24	60.5	2.85e+18
GCMT	189.2/ 49.2/ -10.6	286.2/ 82.0/ -138.7	6.20	63.5	2.41e+18
USGS	190.0/ 49.0/ -14.0	289.0/ 79.0/ -138.0	6.17	60.5	2.30e+18

Table 1 Comparison of the moment tensor's elements obtained in the present work with those of gCMT and USGS.

is especially useful in regions with a dense seismicity distribution (Waldhauser, 2001).

HypoDD calculates travel times in a layered velocity model for the current hypocenters at the station where the phase was recorded. Travel time differences are formed to link together all possible pairs of locations for which data is available. HypoDD solves for hypocentral separation after insuring that the network of vectors connecting each earthquake to its neighbors has no weak links that would lead to numerical instabilities.

For this, we built links from each event within a search radius of 8.0 km. We also required, at least, six links for each earthquake to form a neighborhood. With the network of phase pairs thus formed and using the local velocity model (INSIVUMEH, 1988), we obtained a relocated catalog with 234 events. Although the local velocity model is a 1D parallel layer model, HypoDD reduces the bias in locating individual events.

The results presented in Figure 4 show a significant clustering of earthquakes just beneath the upper part of the slab suggested by Hayes et al. (2018). This arrangement confines the depth of the majority of earthquakes to a range between roughly 50 and 65 km, with a handful of events reaching depths nearing 70 km, which includes the mainshock. Post-relocation, the mainshock was integrated into the sequence, although its depth was only slightly reduced to 69 km. As per the relocated catalog, the dimensions of the fault spanned ~16 km × 22 km, corresponding to an approximate area of 350 km^2.

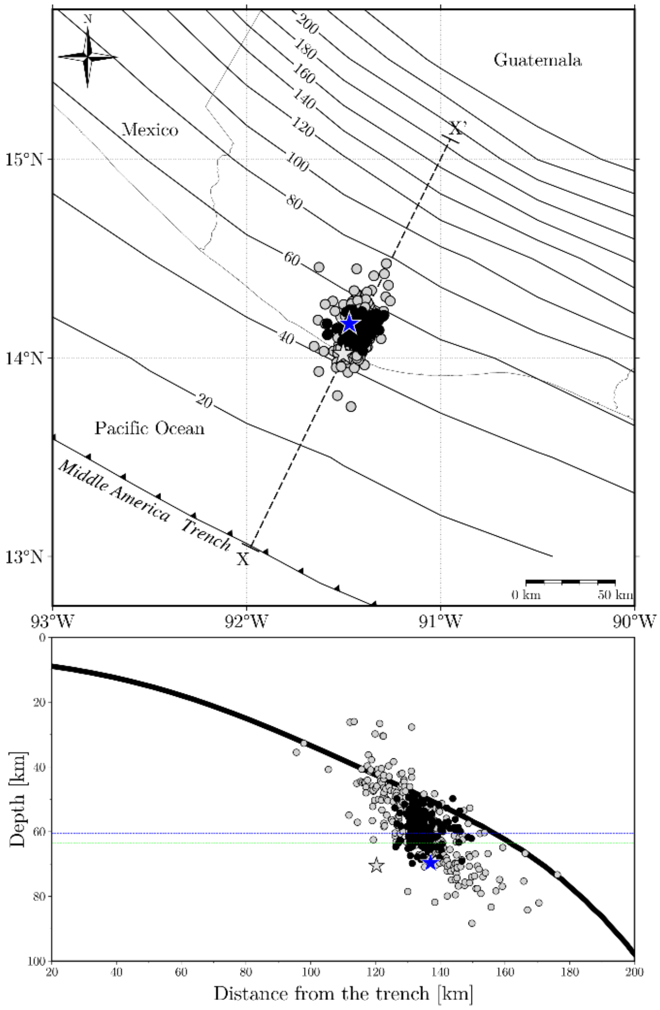

Figure 4 Comparison contrasting the initial positioning of the mainshock and the subsequent aftershock sequence (represented by the grey star and dots) with their subsequent relocation (indicated by the blue star and black dots), accomplished using the HypoDD technique (Waldhauser and Ellsworth, 2000; Waldhauser, 2001). The profile is along X-X' and the model of the top of the slab is according to Hayes et al. (2018). The horizontal dotted lines in the profile denoting the centroid depth reported by different agencies (blue line: INSIVUMEH, USGS; green line: gCMT. See Table 1).

3.2 Rupture plane and temporal evolution of seismicity

Based on the catalog of relocated earthquakes, the initial days showed concentrated seismic activity in a limited region with a subvertical orientation. As the seismic activity progressed, additional earthquakes were recorded both within this same area and further away, near the top of the slab, as depicted in Figure 5.

The estimated moment tensor analysis indicates that NP2 in Table 1 represents the primary rupture plane, where the majority of seismicity is distributed, as illustrated in Figure 6. Additionally, focal mechanisms with the highest normal component were found in the vicinity of this fault plane (blue beach balls in Figure 6), while focal mechanisms with the highest inverse components were observed in the upper region of the seismic activity (red beach balls in Figure 6).

3.3 Discussion and conclusions

The hypocenter's location at 69 km and the centroid's position at approximately 60 km (Figures 5 and 6) suggest that the rupture might have propagated from the LSL to the USL in the region of the estimated plane. Rupture planes for earthquakes between the LSL and the USL have been documented for some large-magnitude intermediate-depth earthquakes (Twardzik and Ji, 2015), identified through associated aftershocks: the 2014 M_w 7.9 earthquake in Rat Islands, Alaska (Twardzik and Ji, 2015), the 2005 M_w 7.7 earthquake in Tarapaca, Chile (Peyrat et al., 2006; Delouis and Legrand, 2007), the 1993 M_w 7.6 Kushiro-Oki earthquake in Japan (Ide and Takeo, 1996), and the 2017 M_w 8.2 earthquake in Tehuantepec, Mexico, where two parallel

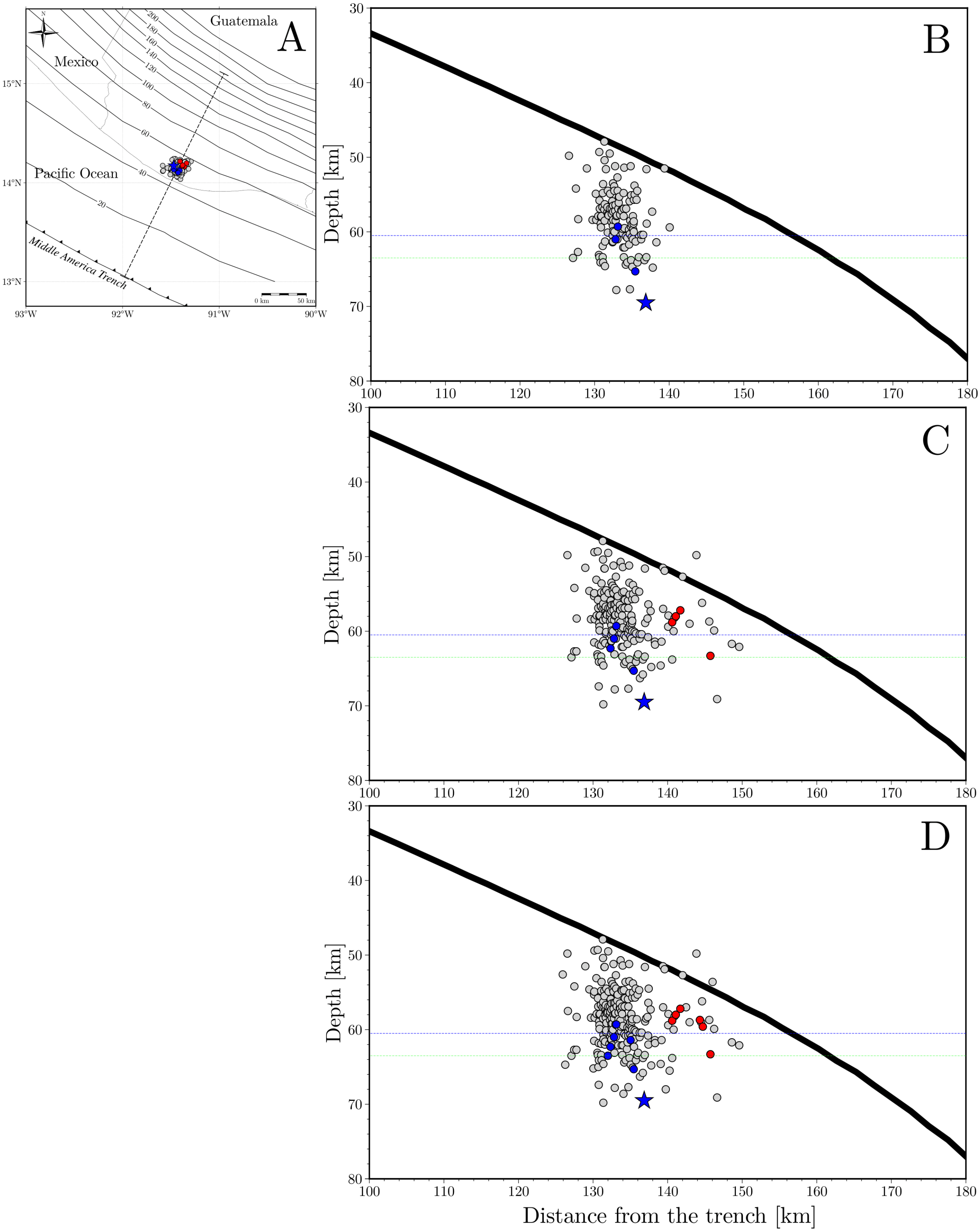

Figure 5 (A) Map of the relocated seismic sequence and profiles showing the temporal evolution of this seismicity in 5 days (B), 15 days (C) and 25 days (D). In the first interval (A), the earthquakes are distributed mainly in the region of the fault, while in the later intervals (B) and (C), hypocenters far from it can also be seen. The blue dots represent the earthquakes with normal focal mechanisms located in the main region of activity, while the red dots represent inverse focal mechanisms located near the upper region of the slab. The blue star represents the nucleation point and the horizontal dotted lines in the profile denoting the centroid depth reported by different agencies (blue line: INSIVUMEH, USGS; green line: gCMT. See Table 1).

faults were identified within the slab (SSN, 2017; Suárez et al., 2019). The dip angle of these earthquakes planes varies considerably.

In the Chilean subduction zone, moderate-magnitude earthquakes have been reported, and their rupture planes have been described through registered aftershocks. Marot et al. (2012) detailed the rupture plane of a M_w 5.7 earthquake that occurred in January 2003 in Central Chile, while Cabrera et al. (2021) identifies a fault plane for a M_w 6.3 earthquake in the northern region of the country that happened in October 2017.

As mentioned earlier, it is evident that most of the seismicity was generated in the region of the suggested plane, especially in the initial days of activity. However, later on, more dispersed seismicity is observed, with depths closer to the top of the slab, possibly in the USL (Figures 5 and 6). This scenario, where the seismicity generated by a normal earthquake triggers seismicity with inverse focal mechanisms, was also observed in the M_w 8.2 earthquake in Tehuantepec, Mexico (Ortega et al., 2019) and the M_w 5.7 earthquake in Central Chile (Marot et al., 2012). Chu and Beroza (2022) propose that intermediate-depth aftershocks are enabled by stress transfer and pore fluid redistribution in the proximity of the mainshock, which is enabled by dehydration. In our case, due to the proximity between the mainshock's fault plane and the USL, it is possible that such effects extend to that region, triggering seismic activity with a different rupture mechanism.

As shown in Figure 1, several intermediate-depth earthquakes with normal focal mechanisms have been documented in MGESZ (Storchak et al., 2013, 2015; Di Giacomo et al., 2018), similar to the M_w 6.2 earthquake analyzed in this study. However, this is the first instance where the fault plane has been identified through associated aftershocks, along with the triggering of seismicity outside the mainshock's rupture surface with a different focal mechanism.

Despite the fact that the sequence of earthquakes described was triggered by the M_w 6.2 earthquake, this zone had exhibited constant seismic activity (relative to the rest of the MGESZ region) before 16 February 2022, and continued in the subsequent months. Background seismicity in the area of the seismic sequence analyzed in this study can be seen in Figure 7, primarily with magnitudes less than four. Some earthquakes with magnitudes greater than five are notable. In mid-2021, a seismic swarm ocurred, although no earthquake of significant magnitude was recorded. This behavior is possibly linked to dehydration processes within the slab (Kiser et al., 2011; Chu and Beroza, 2022) in this region (e.g., Pasten-Araya et al., 2018) but the data is inconclusive, and this explanation falls outside the scope of this work.

Although the estimated area with the sequence of relocated aftershocks covers an area of $\sim$350 km^2, empirical relationships following Wells and Coppersmith (1994) suggest that the rupture area for a M_w 6.2 earthquake would extend to 170 km^2, about half of the area covered by the sequence. Furthermore, the estimate of 22 km fault length penetrating the slab aligns with the minimum value of 20 km reported by Ranero et al. (2003) through seismic reflection data for bending-related faulting in the incoming plate at the Middle America trench. Therefore, it is possible that the main event triggered seismicity on a pre-existing fault, generated on the outer rise (Ranero et al., 2005; Kiser et al., 2011; Marot et al., 2012), also triggering out-of-plane seismicity.

This seismicity outside the fault plane includes the inverse earthquakes of the Figures 5 and 6, possibly occurring in the USL. Assuming that the nucleation of the mainshock occurred in the LSL, we can estimate an average separation between the LSL and USL of 12.2$\pm$5.0 km (considering the estimated errors for preliminary hypocenter depth calculations and assigning a 10% error for values taken from Slab 2), consistent with previous estimates, particulary with Florez and Prieto (2019), confirming the trend of several double subduction zones with normal focal mechanisms in the LSL and inverse mechanisms in the USL (Craig et al., 2022; Chu and Beroza, 2022).

Acknowledgements

The support of the Swiss Agency for Development and Cooperation (SDC), the Swiss Seismological Service (SED) at ETH Zurich and the Volcano Disaster Assistance Program (VDAP) of the US Geological Survey (USGS), have been important for the expansion of the RSN and the improvement of the information generated by the INSIVUMEH. We want to express our sincere gratitude to Beatriz Cosenza, Marco Guzmán, and Xyoli Pérez for their valuable suggestions to the original manuscript of this work. Thanks to Gabriela Xol and Jorge Cárcamo for reviewing some of the data used.

Data and code availability

The HypoDD software (https://www.ldeo.columbia.edu/felixw/hypoDD.html) was used within the SeisAn software (http://seisan.info/). The preliminary and relocated catalogs, information about seismic stations, as well as the configuration and input files for the relocation can be found at: https://zenodo.org/doi/10.5281/zenodo.8433469.

For the inversion of W Phase, stations of the following seismic networks were also used: Caribbean Network (CU; doi: 10.7914/SN/CU), GEOFON (GE; doi: 10.14470/TR560404), Global Seismograph Network - IRIS/IDA (II; doi: 10.7914/SN/II), Mexican National Seismic Network (MX; doi: 10.21766/SSNMX/SN/MX), Nicaraguan Seismic Network (NU; doi: 10.7914/SN/NU), Servicio Nacional de Estudios Territoriales, El Salvador (SV; https://www.fdsn.org/networks/detail/SV/). We used the ISC-GEM Earthquake Catalogue (https://doi.org/10.31905/d808b825).

For the generation of maps we used QGIS V. 2.14.11 ESSEN (https://qgis.org/en/site/forusers/download.html) and GMT V. 6.4.0 (Wessel et al., 2019).

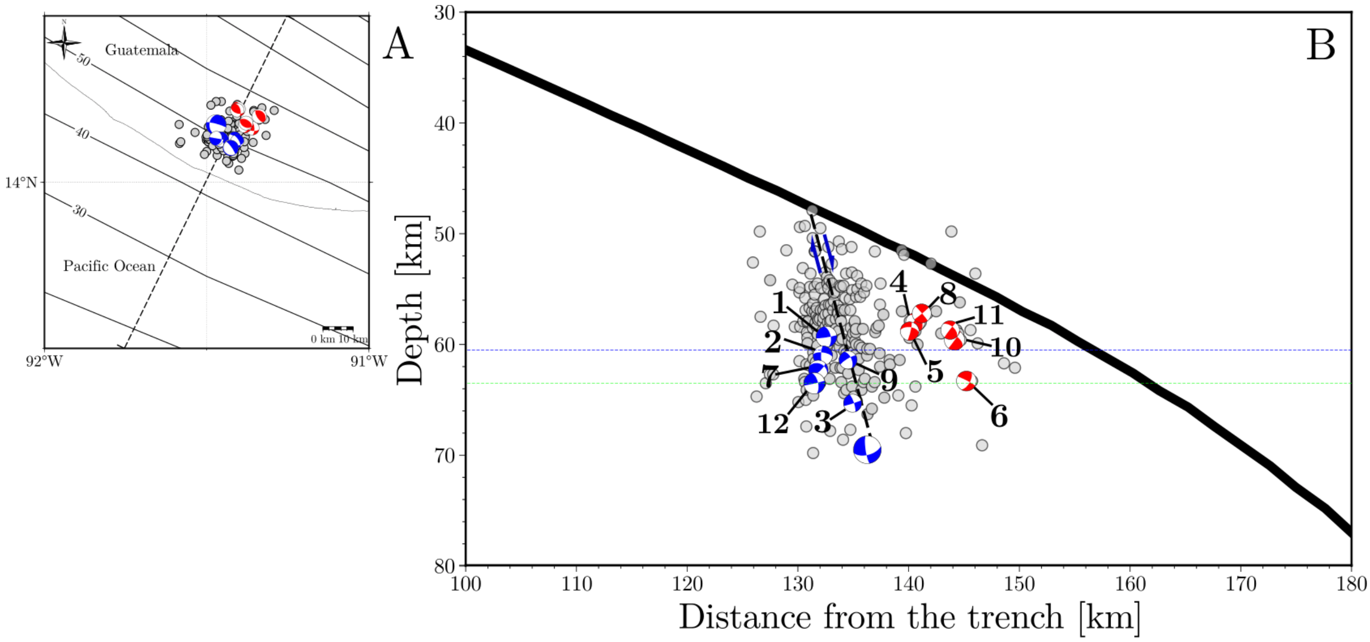

Figure 6 (A) Relocated seismic sequence (grey dots), blue beach balls are earthquakes with normal focal mechanisms located in the main region of activity, while red beach balls are inverse focal mechanisms located near the upper region of the slab as can be seen in profile (B). The numbering corresponds to Figure 3 and the focal mechanism of the M_w 6.2 earthquake is at the nucleation point. The dashed black line (approximately 22 km in length) in profile, shows the rupture plane with a dip angle as described for NP2 in Table 1 and the blue arrows represents normal fault movement. The horizontal dotted lines in the profile denoting the centroid depth reported by different agencies (blue line: INSIVUMEH, USGS; green line: gCMT. See Table 1).

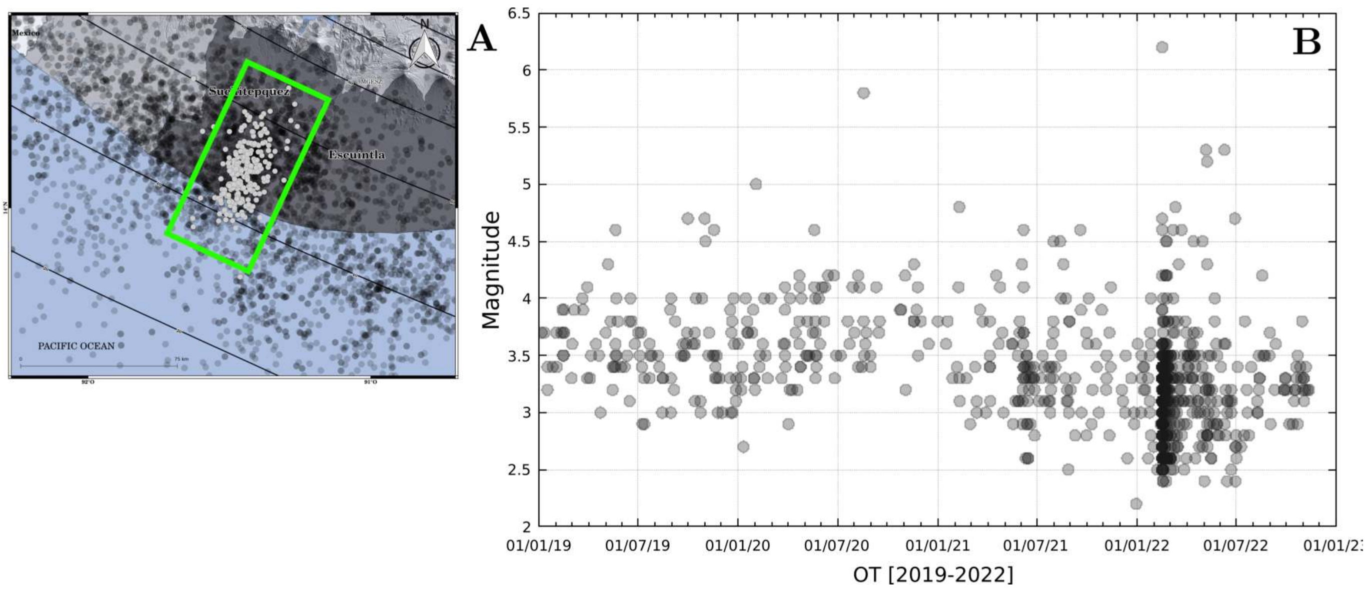

Figure 7 (A) Seismicity recorded by the RSN of INSIVUMEH from 2019 to 2022 on the southwest coast of Guatemala, the green square outlines the area where the sequence analyzed in this study occurred (before relocation). The temporal distribution of all seismic activity within that area is shown in (B). The horizontal axis displays the origin time (OT), and the magnitude is represented on the vertical axis. Earthquakes are depicted with transparent gray circles, where darker shades indicate a higher concentration of seismic events. Seismic activity has remained constant in the area, including some earthquakes with a magnitude greater than 5 and a seismic swarm in 2021. It is possible to observe an improvement in the RSN's ability to detect smaller magnitude earthquakes starting from 2021.

Competing interests

The authors have no competing interests.

References

Alvarez, J. Tectónica Activa y Geodinámica en el Norte de Centro América. *Universidad Compultense de Madrid*, Tésis Doctoral: 121–123, 2009.

Ambraseys, N. and Adams, R. Large-magnitude Central American earthquakes, 1898-1994. *Geophysical Journal International*, 127:665–692, Feb. 1996.

Brudzinski, M., Thurber, C., Hacker, B., and Engdahl, R. Global Prevalence of Double Benioff Zones. *Science*, 316:1472–1474, June 2007. doi: 10.1126/science.1139204.

Cabrera, L., Ruiz, S., Poli, P., Contreras-Reyes, E., Osses, A., and Mancini, R. Northern Chile Intermediate-Depth Earthquakes Controlled by Plate Hydration. *Geophysical Journal International*, 226:78–90, July 2021. doi: 10.1093/gji/ggaa565.

Chu, S. X. and Beroza, G. C. Aftershock productivity of intermediate-depth earthquakes in Japan. *Geophysical Journal International*, 230(1):448–463, 01 2022. doi: 10.1093/gji/ggac024.

Craig, J., Methley, P., and Sandiford, D. Imbalanced Moment Release Within Subducting Plates During Initial Bending and Unbending. *Journal of Geophysical Research: Solid Earth*, 127, Feb. 2022. doi: 10.1029/2021JB023658.

Delouis, B. and Legrand, D. Mw 7.8 Tarapaca intermediate depth earthquake of 13 June 2005 (northern Chile): Fault plane identification and slip distribution by waveform inversion. *Geophysical Research Letters*, 34, Jan. 2007. doi: 10.1029/2006GL028193.

Di Giacomo, D., Engdahl, E. R., and Storchak, D. A. The ISC-GEM Earthquake Catalogue (1904–2014): status after the Extension Project. *Earth System Science Data*, 10(4):1877–1899, 2018. doi: 10.5194/essd-10-1877-2018.

Duputel, Z., Rivera, L., Kanamori, H., and Hayes, G. W phase source inversion for moderate to large earthquakes (1990–2010). *Geophysical Journal International*, 189:1125–1147, May 2012. doi: 10.1111/j.1365-246X.2012.05419.x.

Dziewonski, A., Chou, T., and Woodhouse, J. Determination of earthquake source parameters from waveform data for studies of global and regional seismicity. *Journal of Geophyisical Research*, 86:2825–2852, Apr. 1981. doi: 10.1029/JB086iB04p02825.

Ekström, G., Nettles, M., and Dziewoński, A. The global CMT project 2004-2010: Centroid-moment tensors for 13,017 earthquakes. *Physics of the Earth and Planetary Interiors*, 200-201:1–9, June 2012. doi: 10.1016/j.pepi.2012.04.002.

Ellis, A., DeMets, C., McCaffrey, R., Briole, P., Cosenza, B., Flores, O., Graham, S., Guzmán-Speziale, M., Hernández, D., Kostoglodov, V., LaFemina, P., Lord, N., Lasserre, C., Lyon-Caen, H., Rodriguez, M., McCaffrey, R., Molina, E., Rivera, J., Rogers, R., and Staller, A. GPS constraints on deformation in northern Central America from 1999 to 2017, Part 1 – Time-dependent modelling of large regional earthquakes and their post-seismic effects. *Geophysical Journal International*, 214(214):2177–2194, June 2018. doi: doi: 10.1093/gji/ggy249.

Ellis, A., DeMets, C., McCaffrey, R., Briole, P., Cosenza, B., Flores, O., Guzmán-Speziale, M., Hernández, D., Kostoglodov, V., LaFemina, P., Lord, N., Lasserre, C., Lyon-Caen, H., Rodriguez, M., Molina, E., Rivera, J., Rogers, R., Staller, A., and Tikoff, B. GPS constraints on deformation in northern Central America from 1999 to 2017, Part 2: Block rotations and fault slip rates, fault locking and distributed deformation. *Geophysical Journal International*, 218:729–754, Apr. 2019. doi: 10.1093/gji/ggz173.

Florez, M. A. and Prieto, G. A. Controlling Factors of Seismicity and Geometry in Double Seismic Zones. *Geophysical Research Letters*, 46, 2019. doi: 10.1029/2018GL081168.

Fréchet, J. Sismogenèse et doublets sismiques. *Thèse d'Etat, Université Scientifique et Médicale de Grenoble*, 1985.

Got, J., Fréchet, J., and Klein, F. Deep fault plane geometry inferred from multiplet relative location beneath the south flank of Kilauea. *Journal of Geophysical Research*, 99(B8):15375–15386, Aug. 1994. doi: 10.1029/94JB00577.

Guzmán-Speziale, M. and Molina, E. Seismicity and seismically active faulting of Guatemala: A review. *Journal of South American Earth Sciences*, 115:103740, Feb. 2022. doi: 10.1016/j.jsames.2022.103740.

Guzmán-Speziale, M. and Zúñiga, R. Differences and similarities in the Cocos-North America and Cocos-Caribbean convergence, as revealed by seismic moment tensors. *Journal of South American Earth Sciences*, 71:296–308, 2016. doi: 10.1016/j.jsames.2015.10.002.

Güendel, F. and Protti, M. Sismicidad y Sismotectónica de América Central. *Física de la Tierra*, 10:19–51, 1998.

Havskov, J. and Ottemoller, L. SeisAn Earthquake Analysis Software. *Seismological Research Letters*, 70(5):532–534, Sept. 1999. doi: 10.1785/gssrl.70.5.532.

Hayes, G., Moore, G., Portner, D., Hearne, M., Flamme, H., Furtney, M., and Smoczyk, G. Slab2, a comprehensive subduction zone geometry model. *Science*, 362(6410):58–61, Oct. 2018. doi: 10.1126/science.aat4723.

Ide, S. and Takeo, M. The dynamic rupture process of the 1993 Kushiro-oki earthquake. *Journal of Geophysical Research*, 101 (B3):5661–5675, Mar. 1996. doi: 10.1029/95JB00959.

INSIVUMEH. Red Sismológica Nacional. *International Federation of Digital Seismograph Networks*, 1976. doi: 10.7914/SN/GI.

INSIVUMEH. Boletín Sismológico 1983. *Instituto Nacional de Sismología, Vulcanología, Meteorología e Hidrología*, 1988.

Kanamori, H. and Rivera, L. Source inversion of Wphase: speeding up seismic tsunami warning. *Geophysical Journal International*, 175:222–238, Oct. 2008. doi: 10.1111/j.1365-246X.2008.03887.x.

Kiser, E., Ishii, M., Langmuir, C. H., Shearer, P. M., and Hirose, H. Insights into the mechanism of intermediate-depth earthquakes from source properties as imaged by back projection of multiple seismic phases. *Journal of Geophysical Research: Solid Earth*, 116(B6), 2011. doi: https://doi.org/10.1029/2010JB007831.

Marot, M., Monfret, T., Pardo, M., Ranalli, G., and Nolet, G. An intermediate-depth tensional earthquake (M W 5.7) and its aftershocks within the Nazca slab, central Chile: A reactivated outer rise fault? *Earth and Planetary Science Letters*, 327-328: 9–16, Apr. 2012. doi: 10.1016/j.epsl.2012.02.003.

Newman, R., Clark, A., Trabant, C., Karstens, R., Hutko, A., Casey, R., and Ahern, T. Wilber 3: A Python-Django Web Application For Acquiring Large-scale Event-oriented Seismic Data. *Incorporated Research Institutions for Seismology*, Dec. 2013.

Nishikawa, T. and Ide, S. Earthquake size distribution in subduction zones linked to slab buoyancy. *Nature Geoscience*, 7: 904–908, Dec. 2014. doi: 10.1038/NGEO2279.

Ortega, R., Carciumaru, D., Quintanar, L., Huésca-Pérez, E., and Gutiérrez-Reyes, E. A Study of Ground Motion Excitation Based on the Earthquake of September 8, 2017: Evidence that Normal Faults Influence the Stress Parameter. *Pure and Applied Geophysics*, 176:1359––1377, Mar. 2019. doi: 10.1007/s00024-019-02150-2.

Pasten-Araya, F., Salazar, P., Ruiz, S., Rivera, E., Potin, B., Maksymowicz, A., Torres, E., Villarroel, J., Cruz, E., Valenzuela, J., Jaldín, D., González, G., Bloch, W., Wigger, P., and Shapiro, S. A. Fluids Along the Plate Interface Influencing the Frictional Regime of the Chilean Subduction Zone, Northern Chile. *Geophysical Research Letters*, 45(19):10,378–10,388, 2018. doi: https://doi.org/10.1029/2018GL079283.

Peyrat, S., Campos, J., de Chabalier, J., Perez, A., Bonvalot, S., Bouin, M., Legrand, D., Nercessian, A., Charade, O., Patau, G., Clévédé, E., Kausel, E., Bernard, P., and Vilotte, J. Tarapacá intermediate-depth earthquake (Mw 7.7, 2005, norther Chile): A slab-pull event with horizontal fault plane constrained from seismologic and geodetic observations. *Geophysical Research Letters*, 33, Nov. 2006. doi: 10.1029/2006GL027710.

Ranero, C. R., Phipps Morgan, J., McIntosh, K., and Reichert, C. Bending-related faulting and mantle serpentinization at the Middle America trench. *Nature*, 425:367–373, 2003. doi: 10.1038/nature01961.

Ranero, C. R., Villaseñor, A., Phipps Morgan, J., and Weinrebe, W. Relationship between bend-faulting at trenches and intermediate-depth seismicity. *Geochemistry, Geophysics and Geosystems*, 6(12), Dec. 2005. doi: 10.1029/2005GC000997.

Reasenberg, P. and Oppenheimer, D. Fpfit, fpplot, and fppage: Fortran computer programs for calculating and displaying earthquake fault plane solutions. *Technical report, USGS*, 1985.

SNET. Servicio Nacional de Estudios Territoriales (SNET), El Salvador. 2004.

Snoke, A. FOCMEC: FOCal MEChanism Determinations. *Virgina Tech*, Jan. 2003.

SSN. Sismo de Tehuantepec (2017-09-07 23:49 Mw 8.2). *Servicio Sismológic Nacional, UNAM, Reporte Especial*, Nov. 2017.

SSN. Servicio Sismológico Nacional, Instituto de Geofísica, Universidad Nacional Autónoma de México, México. 2022. doi: https://doi.org/10.21766/SSNMX/SN/MX.

Storchak, D., Di Giacomo, D., Engdahl, E., Harris, J., Bondár, I., Lee, W., Bormann, P., and Villaseñor, A. The ISC-GEM Global Instrumental Earthquake Catalogue (1900–2009): Introduction. *Physics of the Earth and Planetary Interiors*, 239:48–63, 2015. doi: https://doi.org/10.1016/j.pepi.2014.06.009.

Storchak, D. A., Di Giacomo, D., Bondár, I., Engdahl, E. R., Harris, J., Lee, W. H. K., Villaseñor, A., and Bormann, P. Public Release of the ISC–GEM Global Instrumental Earthquake Catalogue (1900–2009). *Seismological Research Letters*, 84(5): 810–815, 09 2013. doi: 10.1785/0220130034.

Suárez, G., Santoyo, M. A., Hjorleifsdottir, V., Iglesias, A., Villafuerte, C., and Cruz-Atienza, V. M. Large scale lithospheric detachment of the downgoing Cocos plate: The 8 September 2017 earthquake (Mw 8.2). *Earth and Planetary Science Letters*, 509:9–14, 2019. doi: https://doi.org/10.1016/j.epsl.2018.12.018.

Twardzik, C. and Ji, C. The Mw 7.9 2014 intraplate intermediate-depth Rat Islands earthquake and its relation to regional tectonics. *Earth and Planetary Science Letters*, 431:26–35, Dec. 2015. doi: 10.1016/j.epsl.2015.08.033.

Waldhauser, F. hypoDD – A Program to Compute Double-Difference Hypocenter Locations. *Open File Report USGS*, 2001.

Waldhauser, F. and Ellsworth, W. A Double-Difference Earthquake Location Algorithm: Method and Application to the Northern Hayward Fault, California. *Bulletin of the Seismological Society of America*, 90(6):1353–1368, Dec. 2000. doi: 10.1785/0120000006.

Wells, D. and Coppersmith, K. New Empirical Relationships among Magnitude, Rupture Length, Rupture Width, Rupture Area, and Surface Displacement. *Bulletin of the Seismological Society of America*, 84(4):974–1002, Aug. 1994. doi: 10.1785/BSSA0840040974.

Wessel, P., Luis, J. F., Uieda, L., Scharroo, R., Wobbe, F., Smith, W. H. F., and Tian, D. The Generic Mapping Tools Version 6. *Geochemistry, Geophysics, Geosystems*, 20(11):5556–5564, 2019. doi: https://doi.org/10.1029/2019GC008515.

White, R., Ligorría, J., and Cifuentes, I. Seismic history of the Middle America subduction zone along El Salvador, Guatemala, and Chiapas, Mexico: 1526–2000. *Geological Society of America*, Special Paper 375:379–396, 2004. doi: 10.1130/0-8137-2375-2.379.

Ye, L., Lay, T., and Kanamori, H. Large earthquake rupture process variations on the Middle America megathrust. *Earth and Planetary Science Letters*, 381:147–155, 2013. doi: 10.1016/j.epsl.2013.08.042.

doi:10.26443/seismica.v2i2.527
SEISMICA

Geocoding Applications for Social Science to Improve Earthquake Early Warning

Danielle F. Sumy *[1]

[1]EarthScope Consortium, Inc., Washington, DC, USA

Author contributions: *Conceptualization*: D. F. Sumy. *Formal Analysis*: D. F. Sumy. *Investigation*: D. F. Sumy. *Methodology*: D. F. Sumy. *Project Administration*: D. F. Sumy. *Visualization*: D. F. Sumy. *Writing – original draft*: D. F. Sumy. *Writing – review & editing*: D. F. Sumy.

Abstract Geocoding is a spatial analysis method that uses address information (e.g., street address, intersection, census tract, zip code, etc.) to determine geographical coordinates (latitude and longitude). In recent decades, geocoding has gone beyond its primary use for census and demographic information to novel applications in disaster risk reduction, even to earthquake early warning. Here I demonstrate the utility of geocoding techniques as applied to two case studies that: 1) rely on survey response data to understand the efficacy of tests conducted on ShakeAlert®, the earthquake early warning system for the West Coast of the United States; and 2) use crowd-sourced video footage that shows how people behave during earthquakes. Geocoding these data can improve our overall technical understanding of alerting systems, demonstrate whether individuals take protective actions such as 'Drop, Cover, and Hold On' in response to an alert, and spotlight individuals or communities that the system is reaching or unintentionally missing. The combination of these social science datasets with geocoding information deepens our knowledge of these fundamentally human-centered systems, including the potential to improve the distribution of alerts for people and individuals with access and functional needs.

Production Editor:
Gareth Funning
Handling Editor:
Carmine Galasso
Copy & Layout Editor:
Théa Ragon

Received:
March 23, 2023
Accepted:
July 23, 2023
Published:
September 25, 2023

Non-technical summary As of May 2021, the ShakeAlert earthquake early warning (EEW) system sends public alerts via cellphones and triggers automatic actions for infrastructure (e.g., shutting off gas valves, slowing down trains to prevent derailment, etc.) in the states of California, Oregon, and Washington, United States. The societal benefits of EEW are expanding worldwide and the efficacy of these systems will be tested by how well received and understood alerts are by various publics and whether individuals and groups will take protective actions. In this study, I demonstrate the importance of geospatial techniques, such as geocoding, as applied to two case studies that: 1) rely on surveys to understand the spatial efficacy of alerting in Oakland, California, and 2) use video footage to understand what protective actions people take during an earthquake. Geocoding, a method employed to determine a geographic location, provides information on where alerts are received, what people experienced at that location during an earthquake, and how their experiences may have influenced their behavior. Geocoding and other geospatial techniques may be of use to emergency responders, structural engineers, and physical and social science researchers who seek to improve earthquake early warning systems and how people interact with the technology to inform their decision making.

1 Introduction

Geocoding is the process of using a street address, intersection, census tract, zip code, or some other type of location information and determining its geographical coordinates (latitude and longitude). Pioneered in the late 1960s for use in the census, New Haven, Connecticut was the first city in the world with a geocodable street network database (e.g., Smith and White, 1971). Over the decades, scholars have used geocoding techniques to examine the effect that physical proximity has had on the careers of women writers in Victorian-era London, England (Bourrier et al., 2021), to help with the recovery in New Orleans post-Hurricane Katrina in 2005 (Gardere et al., 2020), and in disease surveillance for public health purposes (Lin, 2022; Shaheen et al., 2021; Cohen et al., 2022), to name only a few applications.

In addition, geolocation through location-based services (LBS) has become very popular for use in various mobile phone applications (or apps) since the early 2000s (e.g., Huang, 2022). LBS have greatly increased our ability to understand individual and community demographics and the ways in which they travel and move about the world. There are many humanitarian applications to the use of LBS, such as tracking the location of individuals with dementia (Abbas and Michael, 2022), helping students around campus during the COVID-19 pandemic to avoid transmission 'hotspots' (Elalami et al., 2022), and with alerting capabilities for impending weather, flooding, and other natural hazards (e.g., Bopp and Douvinet, 2020).

Geolocation also extends to earthquake early warning (EEW) alerting capabilities. The U.S. Geological Survey

*Corresponding author: danielle.sumy@gmail.com

(USGS) operates and maintains the ShakeAlert® EEW system (e.g., Given et al., 2018), which is now operational in California, Oregon, and Washington. The idea for an EEW system in the United States has been around since the late 1980s after the 1989 M6.9 Loma Prieta, California earthquake (for a timeline, see McBride et al., 2022b), and gained traction in the United States in 2006 (U.S. Geological Survey, 2019). Although early warning systems are human-centered (e.g., Kelman and Glantz, 2014; Sumy et al., 2021), the ideas and conceptualization around EEW largely came from seismologists and the physical science community. For the United States, this changed almost a decade later in 2015 with the development of the Joint Committee for Communication, Education, Outreach, and Technical Engagement (JCCEO&TE, de Groot et al., 2022).

Earthquake early warning (EEW) alerts are sent out based on magnitude and intensity thresholds. Geolocation is vital in determining seismic intensity, or the severity of earthquake shaking, as intensity varies by location on relatively small spatial scales (on the order of tens to hundreds of meters) due to microzonation (e.g., Kumar Shukla, 2022; Rastogi et al., 2023; Pilz et al., 2015). Seismic intensity impacts what an individual feels during earthquake shaking, whether they receive an earthquake early warning alert (or not), and whether a person takes a protective action (or not). The magnitude and intensity thresholds for EEW vary from country to country; for example, the West Coast of the United States (California, Oregon, and Washington) receives alerts at lower intensities (Bostrom et al., 2022; U.S. Geological Survey, 2021) compared to Japan (Nakayachi et al., 2019) and New Zealand (Becker et al., 2020).

As EEW expands worldwide, the earthquake science community is collecting a wealth of social science data and information about those who received an EEW alert, what people experienced during earthquake shaking (seismic intensity), people's behavior and whether they take protective action during an earthquake, such as 'Drop, Cover, and Hold On' (e.g., McBride et al., 2022b). In this study, I demonstrate the range and utility of geocoding social science data for the purposes of informing and improving EEW. I first discuss the Google Maps Geocoding Application Programming Interface (API) methodology for geocoding, chosen here because the software is open-access and free to use. I then demonstrate the applications of geocoding to two case studies using: 1) survey data collected in Oakland, California, United States (McBride et al., 2023), and 2) video data from the 2018 M7.1 Anchorage, Alaska, United States earthquake (McBride et al., 2022b). I conducted the geocoding in the two case studies described here. I then consider limitations and ethical considerations around the methods used and how to address privacy and protection of these data. Finally, I discuss applications of geocoding and other location-based techniques to evaluate the distribution and effectiveness of alerts, which will inform future improvements to earthquake early warning (and earthquake science broadly) worldwide.

2 Methods: Google Maps Geocoding Application Programming Interface (API)

The Google Maps Geocoding Application Programming Interface (API) is freely and openly available, does not require proprietary software that may be cost prohibitive, is accessible over the Internet, and can be enabled within several clients, such as JavaScript and Python, without the need for large amounts of scale up time. A call to the Google Maps Geocoding API does require an API key, which may require a small fee depending on how frequently the Geocoding API is used.

Geocoding works best when starting with an accurate street address (e.g., Yang et al., 2004; Kilic and Gülgen, 2020), either provided by the individual directly or through the identification of a landmark from which a street address can be obtained. From a street address, I use the Google Maps Geocoding API to obtain geographic coordinates (latitude and longitude) for mapping purposes. The output from the Google Maps Geocoding API is in JavaScript Object Notation (JSON) format and is easily readable by a range of different computing languages.

As an example, I examine the street address for the headquarters of the EarthScope Consortium: '1200 New York Avenue NW Suite 400 Washington DC 20005-3929' (Figure 1). The address for the EarthScope Consortium headquarters has nine 'address components': the suite number or subpremise (400), the street number (1200), the route or street (New York Avenue Northwest), the neighborhood (Northwest Washington), the locality (Washington), the administrative area (District of Columbia), country (United States), postal code (20005), and postal code suffix (3929). The 'long name' has all parts spelled out, while the 'short name' contains abbreviations; for example, the US ('short name') for the United States ('long name'). The readable address is provided in the 'formatted address' output (1200 New York Ave NW #400). I conduct a quality check on the data by comparing the 'address components' (input) with the 'formatted address' (output).

The geographic coordinates (latitude and longitude) are provided in the 'geometry' section of the JSON output (Figure 1). The 'location' is the geocoded location of the EarthScope Consortium headquarters, with latitude ('lat') and longitude ('lng') coordinates. There are four 'location types' that the Google Maps Geocoding API uses: rooftop, range interpolated, geometric center, and approximate. The 'rooftop' output is the most precise, while the 'approximate' output is the least precise. I will discuss these outputs in context with the case studies and examples in the following sections.

Lastly, the 'viewport' output provides a level of uncertainty on the location. I use the Euclidean distance formula between the 'location' output with the 'northeast' and 'southwest' viewport bounds, respectively, and take a mean (average) of these two outputs to obtain a level of uncertainty on the geolocation. In this example, the distance between the 'location' and the 'northeast' and 'southwest' viewports are 1.6 m and 1.8 m, respectively, with a mean of 1.7 m (5 feet). The view-

Address Components

1) Subpremise or Suite Number
2) Street Number
3) Street or Route
4) Neighborhood
5) Locality or City
6) Administrative Area (State and/or County)
7) Country
8) Postal Code
9) Postal Code Suffix

Formatted Address

Geometry

Geographic Coordinates

Location Type

Viewport Bounds (Proxy for Uncertainty


```
{
   results : [
      {
         address_components : [
            {
               long_name : 400
               short_name : 400
               types : [ subpremise ]
            }
            {
               long_name : 1200
               short_name : 1200
               types : [ street_number ]
            }
            {
               long_name : New York Avenue Northwest
               short_name : New York Ave NW
               types : [ route ]
            }
            {
               long_name : Northwest Washington
               short_name : Northwest Washington
               types : [ neighborhood
            }
            {
               long_name : Washington
               short_name : Washington
               types : [ locality
            }
            {
               long_name : District of Columbia
               short_name : DC
               types : [ administrative_area_level_1
            }
            {
               long_name : United States
               short_name : US
               types : [ country
            }
            {
               long_name : 20005
               short_name : 20005
               types : [ postal_code ]
            }
            {
               long_name : 3929
               short_name : 3929
               types : [ postal_code_suffix ]
            }
         ]
         formatted_address : 1200 New York Ave NW #400
         geometry : {
            location : {
               lat : 38.90020730000001
               lng : -77.02841359999999
            }
            location_type : ROOFTOP
            viewport : {
               northeast : {
                  lat : 38.9014802802915
                  lng : -77.02708596970848
               }
               southwest : {
                  lat : 38.8987823197085
                  lng : -77.02978393029149
               }
            }
         }
```


Figure 1 The Google Maps Geocoding API JSON output for the EarthScope Consortium headquarters in Washington DC. The nine 'address components' (input) are individually labeled. The 'formatted address' (output) provides a quality control check on the input parameters. The geocoded output in the 'geometry' section contains the geographic coordinates (latitude and longitude), and location type and viewport bounds, which together provide a proxy for geographic uncertainty.

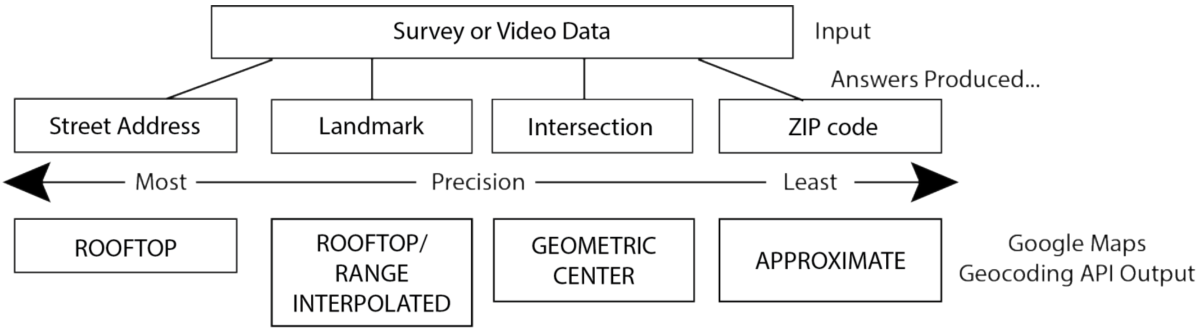

Figure 2 Flowchart showing the survey or video data inputs, the types of answers produced based on the information provided, the precision of these types of information, and the location type output from the Google Maps Geocoding Application Programming Interface (API).

port bounds provide a level of location uncertainty that is smaller than the footprint of the building itself; thus, these considerations should be taken as a proxy or level of uncertainty, rather than a robust location uncertainty. Additional context on location uncertainty will be provided within the case study sections below. For more thorough and complete information on the Google Maps Geocoding API, the reader is referred to the Developers page (https://developers.google.com/maps/documentation/geocoding).

3 Case Study 1: Survey Data for Geolocation

Most online survey providers have built-in tools to obtain an internet protocol (IP) address without any input from the survey responder (e.g., Sumy et al., 2020). However, geocoding IP addresses may be unreliable and output inaccurate geographic locations (e.g., Poese et al., 2011; Callejo et al., 2022), with potential uncertainties on the order of kilometers (e.g., Ma et al., 2023). Due to the potentially large location uncertainties, survey designers can directly ask questions about an individual's location, with approval by an Institutional Review Board or other research ethics committee (e.g., Grady, 2015). The respondent can then 'opt-in' to providing details about their location to a specificity that they feel comfortable with, whether it be a postal address, landmark, or some other geographic identifier.

For earthquake early warning, people receive alerts within a certain spatial area based on earthquake magnitude and intensity thresholds. This spatial area is known as an alerting geofence. Extending the work of McBride et al. (2023), I seek to use survey data to examine the data latencies at the top ten locations with the most survey responses inside the alerting geofence to determine: 1) who received an alert and with what data latencies; and 2) who did not receive an alert (and should have) or who received alerts at very long data latencies (>120 s).

McBride et al. (2023) conducted two tests of the ShakeAlert system in coordination with the Federal Emergency Management Agency's (FEMA) Integrated Public Alerting & Warning System (IPAWS) Wireless Emergency Alert (WEA) in Oakland and San Diego County, California, respectively, before the system went live for public alerting for California in October 2019. The two survey questions asked about location were: 1) What was your physical location [during the test]? You can choose to report your Zone Improvement Plan (ZIP) code, physical address, or suburb, and 2) If you do not know your exact location, can you provide the closest identifiable landmark? These two questions allowed McBride et al. (2023) to gather broad information around location in a way that respected the survey respondent's privacy (see Acknowledgements for ethical approval information). However, upon examination, I found that these questions also produced widely different information ranging from a postal address (precise information that can be easily geocoded), to a landmark or building that required some initial identification and preprocessing of the information, or a ZIP code (broad information that was difficult to narrow down, and therefore often discarded; Figure 2).

The test of the ShakeAlert system in Oakland, California provides an excellent example of the types of location responses received by survey. The USGS coordinated with the California Governor's Office of Emergency Services (CalOES), the Federal Communications Commission (FCC), and local emergency management partners to conduct a test of the ShakeAlert system in Oakland, California on 27 March 2019 at 11 AM local time. The test took place in downtown Oakland during a weekday a year before the COVID-19 pandemic, so many respondents were at their offices and workplaces in public or commercially zoned locations. This alleviates a privacy concern about revealing too much information about an individual's personal or residential property in this study.

The Oakland, California test covered a spatial area of 2.24 km^2 in downtown Oakland centered around Broadway. The survey gathered a total of 1,013 responses in an area with 40,000 people, reaching 2.5% of the population within the alerting geofence (McBride et al., 2023). Initial data cleaning to remove inaccurate results left 828 responses to analyze. Here I discuss the manual inspection of the raw survey data to find the best postal addresses (and most easily geocoded location information) from a variety of different responses, starting with the landmark information (Figure 2), a practice not de-

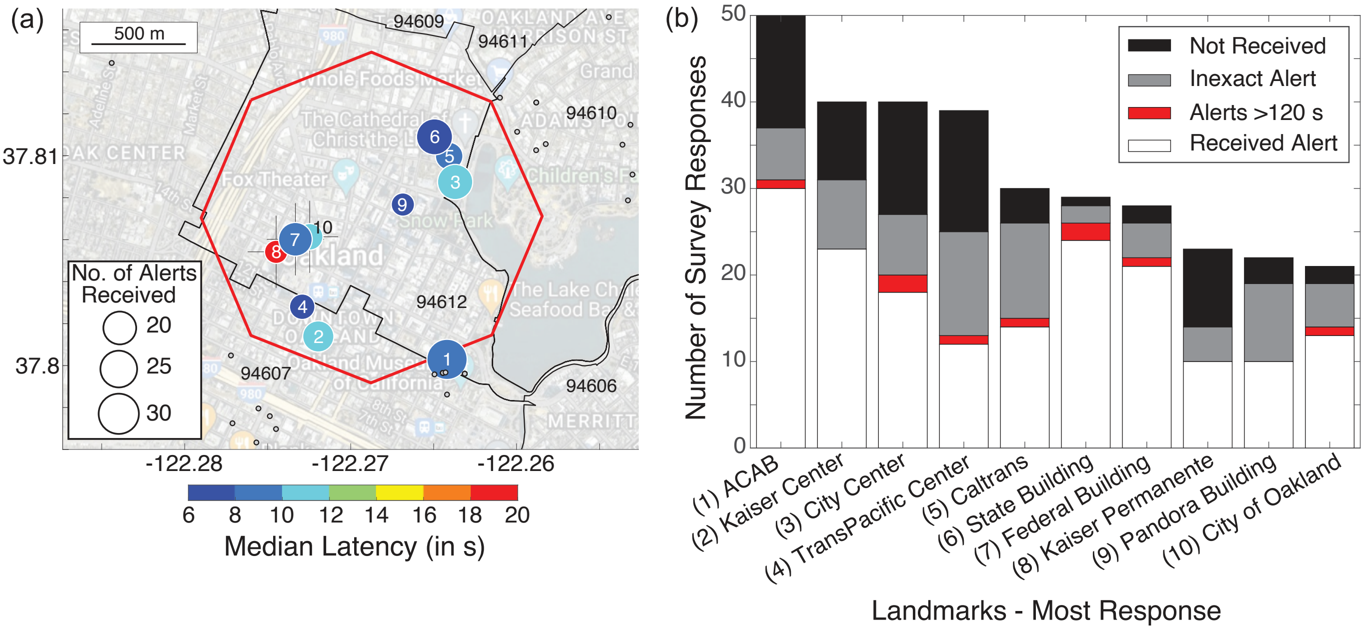

Figure 3 (a) Map of the alerting geofence (red polygon) and the ten locations with the largest survey response. The symbols are color-coded by their median data latency (e.g., when the alert arrived at a particular location) and sized by the number of survey responses that reported receiving an alert. Alerts that arrived at >120 s at that location are removed and not considered in the median calculation. The numbers at each location refer to the landmarks identified in the x-axis of Figure 3b. There are locations that received alerts that are located outside of the geofence and are denoted with a black circle. (b) The number of survey responses by location. We examine the number of received alerts (white), with alerts that arrived >120 s (red), inexact timing of alerts (grey), and did not receive (black). The Alameda County Administration Building (ACAB) received the most alerts and is located on the perimeter of the alerting geofence.

scribed in McBride et al. (2023). For Oakland, California, landmark information included the 'Caltrans Building' or the 'Alameda County Administration Building' (ACAB). Other types of landmarks included intersections, such as 'Near Wells Fargo on 12th and Broadway' or 'Oak Street and 13th'. More difficult types of landmarks to assess were responses, such as 'Main Library' which we interpreted to mean 'Main Oakland Public Library'. Because of the small spatial area (2.24 km^2), even landmarks such as 'Starbucks' were accurately identified. The most commonly incorrect part of the postal address for the Oakland test was the ZIP code, which may reflect the difference between their home and office addresses and their corresponding ZIP codes. This is also recognized as a common error within the U.S. Geological Survey's 'Did You Feel It?' (DYFI?) community intensity survey (Wald et al., 2011).

Once I had street addresses, either from the survey respondent themselves or from the use of Google Maps (maps.google.com) to translate a landmark or intersection to a street address, I found a geographic location through the Google Maps Geocoding API. The location type output of the Google Maps Geocoding API (Figure 1), the description of these location types, and the survey data from the Oakland test of the ShakeAlert EEW system that most likely resulted in the location type are documented in Table 1. There are four main location type outputs: rooftop, range interpolated, geometric center, and approximate, in order from most precise (rooftop) to least (approximate, Figure 2 and Table 1). The approximate location type stems from ZIP code information only and has uncertainty on the order of kilometers. The median uncertainty for the approximate locations was 1.5 km, which I adopt as the maximum uncertainty threshold for the other location types. The other location types have median uncertainty on the order of 200 m or less. I reiterate that the viewport information (Figure 1) is a proxy for uncertainty and does not reflect the actual uncertainty in these locations. I geocoded a total of 823 survey responses (Table 1). Of these, 64 locations (8% of the total) resulted in 'approximate' location types and two were above the median uncertainty threshold of 1.5 km; all were discarded.

Here, I used the remaining 757 geocoded locations combined with the data latency information collected via surveys during the Oakland test of the ShakeAlert EEW system to examine the alert receipt and median alert latency at the top ten locations with survey responses (Figure 3), which extends the work of McBride et al. (2023). The map (Figure 3a) shows the alerting polygon and the distribution of locations, which are primarily confined to government offices or other large office buildings. The largest number of survey responses received at any one location (location #1: ACAB; Figure 3a) was fifty (50), regardless of whether an alert was received or not (Figure 3b). In context with the research questions identified above, I find that at the top ten locations with the most survey response, 1) the median latency of the alerts ranged from 6-19 s (Figure 3a), and 2) alerts were largely received, yet some alerts took a very long time (>120 s) or were not received at all (Figure 3b).

4 Case Study 2: Video Data for Geolocation

Now I consider a second case study for geolocation with the use of video data, which demonstrates the utility of geolocation. While the previous method with survey data was forward approaching (e.g., can ask the survey respondent about their location), this method with video data is backward (or forensic) approaching (e.g., using metadata provided via social media or identifying landmarks within the video itself, without contacting the individual). Video data from household surveillance cameras are increasingly used to check in on children and pets (e.g., Ur et al., 2014; Bernd et al., 2022), provide insurance claim information (e.g., Wong et al., 2009; Ahmad et al., 2019), and protect from theft (e.g., Pandya et al., 2018). As a society, we also are increasingly publicly surveilled waiting at a stoplight by state and local departments of transportation (e.g., Zhang et al., 2022), in a grocery store to better understand retail behavior and prevent theft (e.g., Alikhani and Renzetti, 2022), and even in school classrooms for safety-related and distance learning purposes (e.g., Johnson et al., 2018; King and Bracy, 2019; Fisher et al., 2020).

An increasing ubiquity of smartphone cameras combined with social media platforms (YouTube, TikTok, Facebook, and Twitter, as examples) provide public spaces for content related to earthquake experiences (e.g., Earle et al., 2010; Crooks et al., 2013; Stefanidis et al., 2013). After a potentially damaging earthquake, the Earthquake Engineering Research Institute (EERI) deploys a Virtual Earthquake Reconnaissance Team (VERT, 2023, EERI Learning) to collect online videos and imagery (McBride et al., 2022a). These ephemeral data must be identified and downloaded within a short time span. For instance, the social media platforms WhatsApp and Instagram allow users to post 'stories' that are only available for 24 hours after the original post. In addition, videos may sometimes be deleted or removed from a site due to its sensitive content (e.g., the terrifying nature of earthquake shaking, building collapse, etc.). Traditional news media sources may also help as they typically piece together several videos with location information for 'B-roll' that can be individually examined for protective action behavior.

Video data must be collected quickly and efficiently through a variety of approaches. Teams already in place and ready to virtually deploy, such as through EERI VERT, gather video information over a span of one week or more after the event (e.g., McBride et al., 2022b). The use of keywords and hashtags help to identify earthquake footage, and dates and location information help to rule out unrelated videos (e.g., Crooks et al., 2013; McBride et al., 2022a). At times, a video is tagged by the original poster (OP) or reposter and/or news reporter as coming from the event or a certain geolocation nearby the event. Social media comments on the post or newsreel help to determine whether this geographic information is correct. Often people will comment asking for location information, and if the OP responds, this helps provide a landmark or other identifying information to determine a geolocation. At other times, location information can be gleaned by examining the film frame-by-frame for identifying features. Information is more easily obtained from videos collected at a public location, such as a restaurant, public park, or school or work environment. These landmarks are translated into a street address for use in the Google Maps Geocoding API (Figure 2), and often result in a 'rooftop' location type (Table 1).

However, unlike the survey data, I cannot directly ask for location related information. People may also post videos from their personal (home) address or a private location. In this instance, if someone comments for more location information on social media, the OP typically provides a nearby landmark, neighborhood, and/or intersection that provides inexact location information. These data often result in the 'geometric center' or 'range interpolated' output from the Google Maps Geocoding API (Figure 2). However, the OP may post the video to social media under their own name. Depending on the location of the natural hazard event, the area that the hazard impacted, and the uniqueness of a person's name, a street address can be determined through online, open-access resources such as White Pages (www.whitepages.com) or through Voter Records (www.voterrecords.com). More common names in the United States, such as Smith or Johnson, are more difficult to determine. We also may obtain an inaccurate result if a person moved or switched jobs, yet updates

Table 1 Google Maps Geocoding API output for the Oakland test of the ShakeAlert system

Google Maps Geocoding API Location Type	Description	Survey Data Type	For Oakland Test (McBride et al., 2023) Median Uncertainty (km)	For Oakland Test (McBride et al., 2023) N (N_{total} = 823)
ROOFTOP	Street address precision	Street Address/Landmark	0.079	739
RANGE INTERPOLATED	Interpolated between two precise points	Landmark	0.191	7
GEOMETRIC CENTER	Geometric center of a street or polygon	Intersection	0.191	13
APPROXIMATE	Approximate location	Zip Code	1.50	64

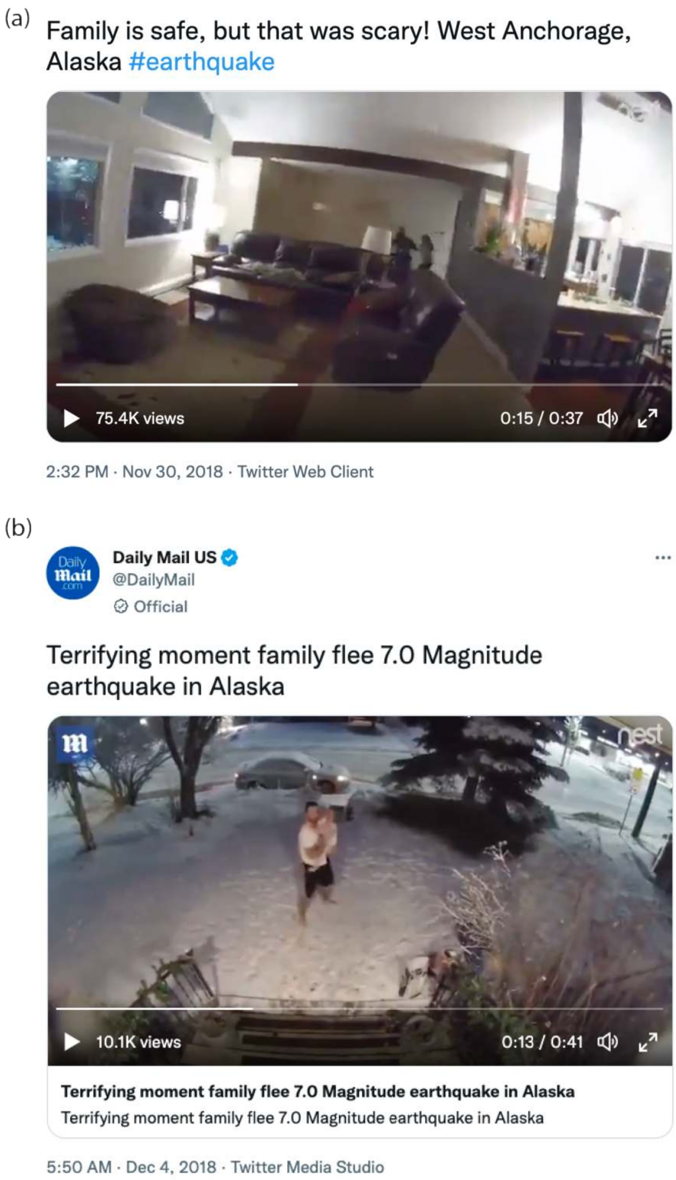

Figure 4 Videos posted to Twitter from home security cameras. (a) Two adults flee their home during earthquake shaking. The hashtag #earthquake, information about which earthquake in the post, and the timing of the posting all help to determine that this was the 30 November 2018 Anchorage, Alaska, United States earthquake. This information was posted to a personal account which helped with geolocation. (b) The Daily Mail US obtained video footage from an adult who evacuated a house with a child. Note that the adult is barefoot and lightly clothed outside in the snow where exposure to the weather presents a concern. The family highlighted in this video provided a news conference about their experience using their names, which allowed for geolocation. Personal information on both Twitter posts is redacted here due to privacy concerns.

were not made to their social media accounts or other open-access directories. Considerations for privacy are paramount and we are unable to geocode videos with insufficient metadata or lack of other open-access information. Additional information about privacy concerns is discussed in the Limitations and Considerations section.

The 30 November 2018 M7.1 Anchorage, Alaska, United States earthquake (U.S. Geological Survey, 2023) provides an example of how we can use video data to obtain location information.

The 2018 Anchorage earthquake was a deep event (46.7 km or 29 mi deep) and people experienced a maximum Modified Mercalli Intensity (MMI; Stover and Coffman, 1993) VIII (severe shaking and moderate to heavy damage). According to the USGS Prompt Assessment of Global Earthquakes for Response (PAGER), the estimated economic losses were significant, requiring a regional or national response (U.S. Geological Survey, 2023). Fortunately, due to the depth of the earthquake and lessons learned during the 1964 M9.2 Alaska earthquake, there were no earthquake shaking related fatalities (Alaska Earthquake Center, 2018).

As an example, a YouTube video collected by the Anchorage (Alaska) School District shows a classroom of high school students taking the recommended protective action in the United States ('Drop, Cover, and Hold On') within three seconds (Anchorage School District YouTube Channel, 2018). This video demonstrates the importance of earthquake drills, as the students did not hesitate to take the recommended protective measures (Adams et al., 2022). In Figure 4, we provide snapshots of two videos posted to Twitter from personal locations that demonstrate individuals fleeing their homes during earthquake shaking. The earthquake occurred in late November with snow on the ground, thus people who chose to flee risked exposure to the elements (Figure 4).

McBride et al. (2022a) found a total of 124 videos for the Anchorage earthquake from social media (Twitter and YouTube) and news media sources. Videos from the news media typically included multiple video segments, which brought the total up to 145 videos. Geolocating videos also helps to compare the video data gathered at a particular location and remove any duplicates. I geolocated a total of 80 videos (55%) using the procedures outlined above (Figure 5). The output from the Google Maps Geocoding API had a 'rooftop' location type for all but three of the locations, with a median uncertainty of 80 m.

For the 2018 Anchorage earthquake, I determine the level of shaking (seismic intensity) that people experienced based on the USGS ShakeMap (U.S. Geological Survey, 2021). The ShakeMap reports the MMI along with other seismic information, such as peak ground acceleration (PGA) and peak ground velocity (PGV) at certain frequencies (Wald et al., 2006; Worden et al., 2010). The nominal grid spacing for the 2018 Anchorage earthquake is on the order of 0.167° (1.85 km) in both latitude and longitude. I determine the closest grid node by calculating the Euclidean distance between each of the geolocated videos with the USGS ShakeMap information to determine the MMI that people felt during this earthquake. The median distance between the geolocated videos and the closest MMI grid node is on the order of 688 m.

I find that the people who uploaded videos experienced MMI 4.7-7.6 with a median MMI 7.1 (Figure 5). The minimum MMI 4.7 was a video uploaded to YouTube from Seward, Alaska, 140 km away from the

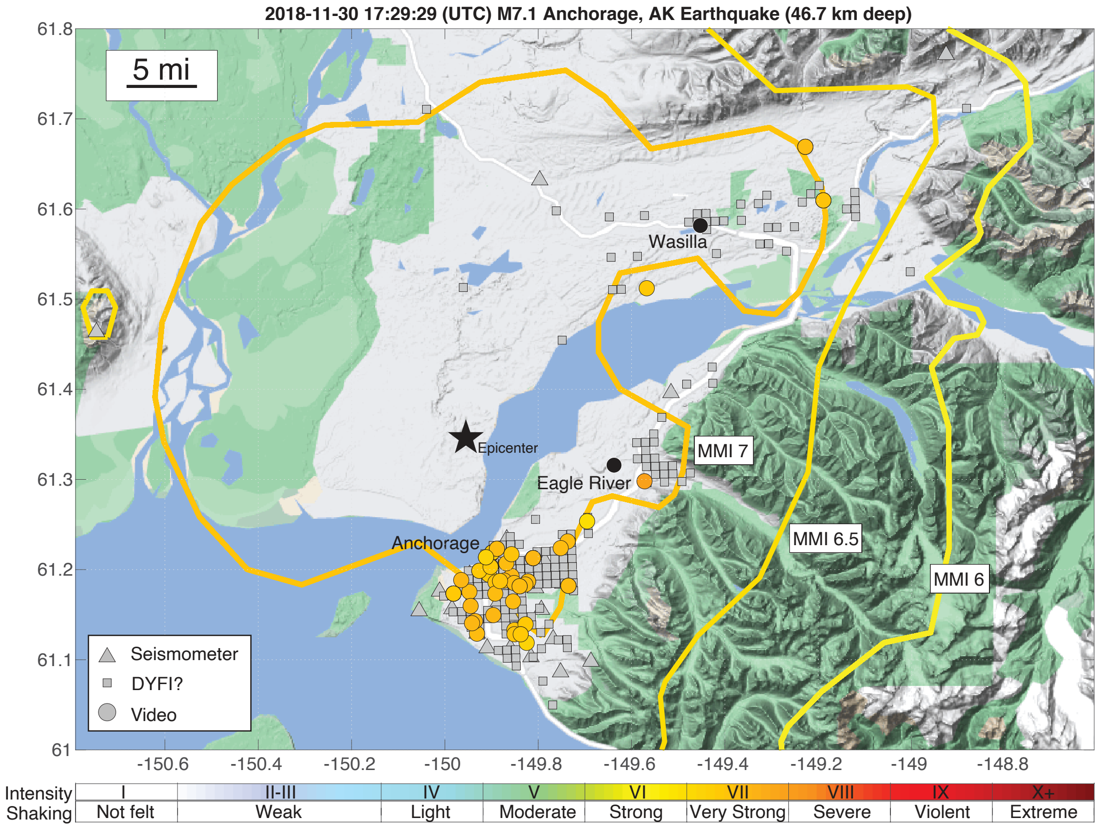

Figure 5 Intensities from the 2018 Anchorage, Alaska, United States earthquake. The locations of the video footage (circles) in the Anchorage, Eagle River, and Wasilla areas are color-coded by Modified Mercalli Intensity (MMI). The instrumental (grey triangles) and 'Did You Feel It?' (grey squares) intensity information are shown in the background to provide context as to how this video information may help. MMI 6, 6.5, and 7 contours are shown and labeled.

earthquake epicenter. Even with this video removed, the median MMI 7.1 remains. Most of the videos are clustered within Anchorage and neighboring areas such as Eagle River and Wasilla (Figure 5). Additional videos were collected from rural areas of Alaska that experienced light to moderate levels of shaking. For this case study, I use the ShakeMap to determine the seismic intensity of the geocoded videos (color coded circles in Figure 5). However, the videos also may provide a source of information about what people experienced during the event that could help determine the seismic intensity, especially in areas where instrument coverage is sparse and/or people are unaware of the DYFI survey.

5 Discussion: Applications to Earthquake Early Warning

There are several benefits of determining the geographic location of social science data through geospatial analyses, such as geocoding. First, geocoding helps to reduce both the survey and video datasets. For instance, I want to concatenate survey responses that originate from the same location to better understand EEW alert latencies such as in case study 1, which can be done once the geocoding is completed. With the videos, I can sort them by geolocation and compare the videos to verify the authenticity of the video and make sure that I do not double count. This is particularly helpful for large datasets and instances where the news media uses different cuts of a video or splices/jumps the video to save time. Sorting by locations helps an analyst look through the videos more carefully and determine duplicates that may not have been caught in the initial processing.

Second, the geocoding of social science data allows researchers to determine whether earthquake early warning alerts are reaching areas within the alerting geofence. The data latencies in alert receipt, and whether an alert was even received or not, can then be examined by location. In EEW, there is a seismic intensity threshold at which people want to be alerted that varies from country to country (e.g., Nakayachi et al., 2019; Becker et al., 2020; Bostrom et al., 2022). Further, if an alert is deemed appropriate for a given spatial area, alerts need to stay within that area and not 'leak' outside of the alerting zone. If not, alerting areas that do not feel shaking or only feel light shaking could potentially give rise to the 'cry wolf' effect (e.g., LeClerc and Joslyn, 2015).

Through geocoding techniques, McBride et al. (2023) find that the alerts mostly stay within the geofence during a test of the ShakeAlert system in Oakland, California. However, geocoding demonstrates that data latencies within the alerting geofence are on the order of 10s and that even individuals at the same location within the alerting geofence might not all receive an alert, as demonstrated by the new analysis of the top ten locations that received alerts as presented in Figure 3. These findings give rise to concerns over the long latencies in alert delivery and in the variation between cellphones that receive an alert (e.g., cellphone carriers, wireless data transmission networks, and cell phone types). In a technical test of the system, McBride et al. (2023) found that there did not appear to be any technological privilege associated with different cell phone types; further examination outside of the lab and placed into practice is still needed.

Third, geocoding social science data allows for an understanding of what people experienced during an earthquake. Geocoding allows us to correlate a particular location with its seismic intensity, as demonstrated through the video reconnaissance footage. An understanding of seismic intensity, which is location dependent, provides information about an individual's choice of protective action (if any). From surveys collected in Japan and New Zealand, people tend to use the time afforded by earthquake early warning to mentally prepare themselves for shaking and do not take a protective action (Nakayachi et al., 2019; Becker et al., 2020). Survey respondents reported that they mentally prepare themselves over taking a physical protective action because they still expect low shaking intensities that would not warrant protection, even when they receive an alert. Mental preparation was also found from video footage collected after an alert was sent during the 2021 M6.2 Petrolia, California, United States earthquake (Baldwin, 2022). Geolocation allows researchers to place the video footage in context with seismic intensity and allows for a better understanding of what people experienced during an earthquake and whether this impacts their choice of protective action.

Conversely, the geolocation of social science data may provide additional information about what happened during an earthquake (e.g., books falling off shelves, light fixtures shaking, etc.), which aids in determination of seismic intensity and whether alerts were received by those who should have. Instrumental intensity is collected by seismometers from around the world, which can readily detect moderately sized earthquakes (M5+) at large epicentral distances (e.g., Ekström et al., 2012). However, in remote areas, areas without dense seismometer coverage, and/or for small earthquakes (M<3), collecting instrumentally recorded information may be challenging. The geolocation of surveys has already proven useful for seismologists to better understand seismic intensity through the USGS 'Did You Feel It?' survey (Wald et al., 2011; Quitoriano and Wald, 2020; Goltz et al., 2022), where location and now even EEW alerting information can be asked directly. A potential next step for 'Did You Feel It?' would be to upload videos that could corroborate survey response information, such as objectively viewing how long shaking lasted instead of relying on survey responses alone.

The videos also capture the duration of earthquake shaking and what people experienced during an earthquake, which may affect how a person or group chooses how to respond to an earthquake, early warnings, and in the aftermath of an event (e.g., Jon et al., 2016; Vinnell et al., 2022). Conversely, these social science data may also be relevant to physical science in helping to constrain a duration magnitude (e.g., Lee et al., 1972; Eaton, 1992; Hirshorn et al., 1987), with the realization that one would have to correct for 'building response' (instead of instrument response) which is affected by the amplitude, duration, and frequency of earthquake shaking. This may prove too difficult to use for magnitude in practice, as each building would have its own response to correct for, yet these videos may be able to help in regions where seismic networks are sparse and more data is needed. Both magnitude and intensity are required parameters in estimating earthquake alerting accuracy and calibrating alerting thresholds.

In addition, earthquake early warning is simply one mechanism to help individuals and communities prepare for earthquakes, know what protective actions to take during an earthquake, and how to respond in the aftermath of an event. These survey and video data also could help structural and civil engineers, emergency responders, and even insurance companies accurately account for damage that occurred during earthquakes (e.g., Coburn and Spence, 2002). VERTs collect videos to understand human behavior during earthquakes and to assess the level of damage within a particular region for structural health monitoring purposes (e.g., McBride et al., 2022a). The combination of video reconnaissance with geolocation can also help emergency responders by showing where damaged areas are after an earthquake event and therefore prioritizing where emergency services are needed most (e.g., Shan et al., 2012; Li et al., 2022). Videos could also demonstrate to insurance companies unbiased information about the damage sustained during an earthquake, to better document how the earthquake impacted a particular building and/or adjust insurance rates. Broadly, geocoding can assist in better understanding the relationship between seismic intensity and earthquake damage, which can be used to calibrate risk informed earthquake early warning alerting thresholds.

6 Limitations and Considerations

The user response information obtained via surveys or videos may be biased. Surveys can be biased because only those willing to fill out the survey and contribute respond (otherwise known as self-selection or a convenience sample), so they often do not include a representative sample of a particular population (e.g., Sackett, 1979; Salkind, 2010; Sumy et al., 2020; McBride et al., 2023; Goltz et al., 2020). For earthquakes or other potentially traumatic experiences, survey information may be biased depending on their own perceptions, such as people often thinking that earthquake shaking lasts longer than they experienced or other exaggerated reports (e.g., Fraser et al., 2016; Bossu et al., 2017).

While videos may present an opportunity for more objective information, the videos can be cut, cropped, or otherwise filtered or changed in some way that could also provide biased information. Also, those who stop to take videos versus those who have security cameras operating in the background have likely altered their behavior in some way, such that they are not taking an appropriate protective action (e.g., Martin-Jones, 2022). These considerations likely bias the data.

In addition, tradeoffs exist between the information that survey respondents provide and the geolocation uncertainty. For example, although landmarks are straightforward to geocode from survey responses, they may be overemphasized because a landmark is easily identifiable and may garner a disproportionate number of mentions in the survey responses. In the case study on Oakland, California, this is unlikely to be the case due to self-selection bias as the surveys went to primarily local and state government office 'landmarks' (Figure 3). While a landmark can be easily geocoded, there is uncertainty of whether a person was at this location or not. The bias towards landmark information may need to be considered in future applications of the geocoding methodology.

The collection of survey and video data around a potentially traumatic earthquake experience and narrative must be considered with care, for both the human subject and the researcher. For instance, the USGS DYFI? survey is subject to the Privacy Act of 1974 and the Paperwork Reduction Act of 1995, respectively. Location information can only be asked by generic questions (e.g., ZIP code, landmark, partial address, etc.), and a street address cannot be asked for directly or specifically requested (Goltz et al., 2020). This limits our ability to geocode all addresses and adds to the uncertainty in our location information. Ethical considerations around privacy limit the ability to reach out to a survey respondent, even if their contact information is provided, and care must be taken to keep their responses confidential and anonymous when working collaboratively due to cybersecurity concerns (e.g., Natural Hazards Center, 2021). For the survey collected in Oakland, California, the geolocations were for mostly commercially zoned and public places since the test of the ShakeAlert system took place in downtown Oakland on a weekday before COVID-19, which alleviated a privacy concern. I note that human subjects research approval is only required with the surveys and not when we download publicly available video information.

In addition, it is important to not directly contact the individuals who responded to a survey or uploaded a video to protect their privacy, as further inquiry may cause emotional upset or harm. In turn, researchers' interactions with the video data must be limited because viewing someone's experience during a natural hazard event can also be traumatic (e.g., Kiyimba and O'Reilly, 2016). Secondary trauma, when another individual sees or listens to the traumatic experience of another person, also can take an emotional toll on the part of the researcher. Reducing or limiting the amount of daily interaction with the video data and/or turning the sound off can lessen the impact of secondary trauma on the researcher (McBride et al., 2022a).

For geocoding purposes, accurate data entry can significantly improve the ability to geolocate the data (e.g., Yang et al., 2004; Kilic and Gülgen, 2020). As researchers, we need to consider how important the accuracy and precision of the geocoded result needs to be (e.g., Roongpiboonsopit and Karimi, 2010), which will vary based on the research questions and context. For understanding EEW alert receipt and seismic intensity, I would want the most accurate and precise information possible, with an uncertainty on the order of meters. As determined through other studies, the street addresses with 'rooftop' location type output from the Google Maps Geocoding API typically produces a geolocation within the footprint of the building, produces better results within the United States compared to internationally, and is the best among web-based solutions, with errors on the order of tens of meters (e.g., Chow et al., 2016; Kilic and Gülgen, 2020).

Additional sources of uncertainty include the online, freely available, personal records used. These records (like voting records) can sometimes be out of date, and there is very little control or understanding of the uncertainty of this information in this study. For instance, someone could have moved locally or have a relatively common last name that makes it sometimes difficult to determine whether the information is correct. In particularly transient areas or for socially vulnerable individuals, online records such as the White Pages may be incorrect or out of date (e.g., Dempsey, 2022). As an example, I looked my own name up in online records and found that my listed address is incorrect. The limitations and considerations around the data and the geocoding methodology limit our ability to extend this work to a plethora of physical science applications, yet these limitations may be overcome in the future.

7 Conclusions and Future Directions

Here I demonstrate the usefulness of geocoding social science data to improve the ShakeAlert earthquake early warning system in the United States. The novelty here is not in the geocoding method itself, but rather in its application to survey and video data used to better understand the functionality and inform potential improvements to EEW. Geocoding social science data allows researchers to: 1) determine whether earthquake early warning alerts stay within the alerting geofence, so as to not cause undue panic or stress to those who may only experience light shaking; 2) determine when an alert is received at a particular location and whether there is a range of data latencies at a particular location to suggest improvements to the system, such as demonstrated in the case study for Oakland, California; and 3) correlate the survey or video location with seismic intensity to corroborate what a person experienced during an earthquake to more accurately calibrate earthquake early warning alerting thresholds, such as demonstrated with the 2018 M7.1 Anchorage, Alaska earthquake. The approaches described here are very manually intensive, requiring a team of researchers to manually collect and analyze data, which can take months or more. A future direction includes incorporating machine learning and artificial intelligence techniques to simplify the data gathering, geolocation analysis, and understanding of human behavior (e.g., Chachra et al., 2022; Ofli et al., 2022).

In addition, geolocation has underexplored and underutilized seismological applications for earthquakes that occur in relatively remote and rural areas, structural and civil engineering applications for structural health monitoring, and emergency response and management to provide resources to areas who need them the most, to name a few (e.g., Kankanamge et al., 2019). The geocoding of online and thumbnail questionnaires, such as DYFI? (Wald et al., 2011; Quitoriano and Wald, 2020), the European-Mediterranean Seismological Center's LastQuake app (Bossu et al., 2015, 2018), and the University of California-Berkeley's MyShake app (Chachra et al., 2022; Kong et al., 2023), contributes to the situational awareness in emergency response after an earthquake. Thus, the future of geocoding for the benefit of EEW lies with calibrating these felt reports with who received an alert (or not) to determine appropriate EEW intensity thresholds for a particular area and how people responded during the event (e.g., Goltz et al., 2022), and adjust the thresholds if necessary.

Additionally, cell phone applications and their location-based services improve situational awareness and emergency response efforts. However, we need to look beyond those who are using EEW apps to those who are not (e.g., Bopp and Douvinet, 2022). Through geocoding, we may find potentially vulnerable sociodemographic groups who we need be thoughtful about how to best reach through alerting strategies. Targeted public education and outreach campaigns around earthquake early warning to these communities, potentially through drills in formal education environments (Adams et al., 2022) or at museums and other free-choice learning environments (Sumy et al., 2022b), may provide a potential solution. As earthquake early warning is expanding in use worldwide (Allen and Stogaitis, 2022; McBride et al., 2022a), a focus on communities who might not have the socioeconomic ability or technological privilege to use apps or receive alerts (e.g., due to the poor coverage of wireless communication networks), have language barriers that prevent their understanding of alert messages, and/or other access and functional needs will help drive education and outreach around earthquakes and early warning in a way that can increase societies' resilience and disaster preparedness (e.g., Sumy et al., 2022a).

Acknowledgements

I would like to thank Drs. Sara K. McBride and Dare Baldwin for their encouragement to write this manuscript. I thank Handling Editor Carmine Galasso, Rob Casey, Andrea Llenos, and two anonymous reviewers for their input which significantly improved the manuscript. ShakeAlert is a registered trademark of the U.S. Geological Survey (USGS) and is used with permission. Consistent with requirements of the Federal Paperwork Reduction Act, the information-collection activities for the survey described in this study were approved by the Office of Management and Budget [2019, OMB 1090-0011].

Data and code availability

Data used in this study are protected due to privacy and cybersecurity concerns, as discussed in the manuscript. I made the maps in Figures 3 and 5 with the `plot_google_maps` functionality in Matlab; however, maps could be made with any mapping software of choice.

Competing interests

The author declares that she has no competing interests.

References

Abbas, R. and Michael, K. Co-Designing Location-Based Services for Individuals Living With Dementia: An Overview of Present and Future Modes of Operation. *IEEE Technology and Society Magazine*, 41(2):42–46, 2022. doi: 10.1109/MTS.2022.3173353.

Adams, R. M., Tobin, J., Peek, L., Breeden, J., McBride, S., and R, G. The generational gap: Children, adults, and protective actions in response to earthquakes. *Australas. J. Disaster Trauma Stud*, 26:2, 2022.

Ahmad, M., Abdullahi, A., Muhammad, A., Saleh, Y., and Usman, U. The Various Types of sensors used in the Security Alarm system. *International Journal of New Computer Architectures and their Applications*, 9(2):50–59, 2019. doi: 10.17781/P002618.

Alaska Earthquake Center. Anchorage M7.1: What We Know So Far, 2018. https://earthquake.alaska.edu/anchorage-m71-what-we-know-so-far. Last consulted 24 February 2023.

Alikhani, M. and Renzetti, B. You're on Camera: Data Collection in Food Retailing Markets. *Yale Law & Policy Review*, 2022. doi: 10.2139/ssrn.4192775.

Allen, R. and Stogaitis, M. Global growth of earthquake early warning. *Science*, 375(6582):717–718, 2022. doi: 10.1126/science.abl5435.

Anchorage School District YouTube Channel. Earthquake Classroom Video, 2018. https://www.youtube.com/watch?v=NJZqREPc9k0. Last consulted 24 January 2023.

Baldwin, D. ShakeAlert earthquake warnings can give people time to protect themselves – but so far, few have actually done so, The Conversation, 2022. https://theconversation.com/shakealert-earthquake-warnings-can-give-people-time-to-protect-themselves-but-so-far-few-have-actually-done-so-174685. Last consulted 8 November 2022.

Becker, J., Potter, S., Vinnell, L., Nakayachi, K., McBride, S., and Johnston, D. Earthquake early warning in Aotearoa New Zealand: A survey of public perspectives to guide warning system development. Humanities and Social Sciences, 2020. doi: 10.1057/s41599-020-00613-9.

Bernd, J., Abu-Salma, R., and Frik, A. Privacy: The Perspectives of Nannies on Smart Home Surveillance. In *FOCI@ USENIX Security Symposium*, 2022.

Bopp, E. and Douvinet, J. Spatial performance of location-based alerts in France. *Int. J. Disaster Risk Reduct*, 50:101909, 2020. doi: 10.1016/j.ijdrr.2020.101909.

Bopp, E. and Douvinet, J. Alerting people prioritising territories over technologies. A design framework for local decision makers in France. Applied Geography, 146, 102769, 2022. doi: 10.1016/j.apgeog.2022.102769.

Bossu, R., Steed, R., Mazet-Roux, G., Roussel, F., and Etivant, C. The key role of eyewitnesses in rapid impact assessment of global earthquakes. In *Earthquakes and their Impact on Society, S. D'Amico (Editor)*. Springer Natural Hazards, Springer, 2015. doi: 10.1007/978-3-319-21753-6_25.

Bossu, R., Landès, M., Roussel, F., Steed, R., Mazet-Roux, G., Martin, S., and Hough, S. Thumbnail-based questionnaires for the rapid and efficient collection of macroseismic data from global earthquakes. *Seismological Research Letters*, 88(1):72–81, 2017. doi: 10.1785/0220160120.

Bossu, R., Roussel, F., Fallou, L., Landès, M., Steed, R., Mazet-Roux, G., Dupont, A., Frobert, L., and Petersen, L. LastQuake: From rapid information to global seismic risk reduction. *Int. J. Disaster Risk Reduct.*, 28:32–42, 2018. doi: 10.1016/j.ijdrr.2018.02.024.

Bostrom, A., McBride, S., Becker, J., Goltz, J., Groot, R.-M., Peek, L., Terbush, B., and Dixon, M. Great expectations for earthquake early warnings on the United States West Coast. *Int. J. Disaster Risk Reduct.*, 82, 2022. doi: 10.1016/j.ijdrr.2022.103296.

Bourrier, K., Anderson, H., Jarmula, S., Lapins, D., Macaulay, K., Peller, P., Reiche, I., Brosz, J., and Jacobson, D. Mapping Victorian Homes and Haunts: A Methodological Introduction. *J. Victorian Culture*, 26(2):300–309, 2021. doi: 10.1093/jvcult/vcab003.

Callejo, P., Gramaglia, M., Cuevas, R., and Cuevas, A. A deep dive into the accuracy of IP Geolocation Databases and its impact on online advertising. *IEEE Transactions on Mobile Computing*, 2022. doi: 10.1109/TMC.2022.3166785.

Chachra, G., Kong, Q., Huang, J., Korlakunta, S., Grannen, J., Robson, A., and Allen, R. Detecting damaged buildings using real-time crowdsourced images and transfer learning. Scientific, 2022. doi: 10.1038/s41598-022-12965-0.

Chow, T., Dede-Bamfo, N., and Dahal, K. Geographic disparity of positional errors and matching rate of residential addresses among geocoding solutions. *Annals of GIS*, 22(1):29–42, 2016. doi: 10.1080/19475683.2015.1085437.

Coburn, A. and Spence, R. *Earthquake Protection*. John Wiley & Sons Ltd, Chichester, 2nd edition, 2002. doi: 10.1002/0470855185.

Cohen, S. E., Stookey, J., Anderson, N., Morris, D., Singzon, T., Dann, M., Burk, K., and Chen, C. Using Geocoding to Identify COVID-19 Outbreaks in Congregate Residential Settings: San Francisco's Outbreak Response in Single-Room Occupancy Hotels. *Public Health Reports*, 0(0), 2022. doi: 10.1177/00333549221128301.

Crooks, A., Croitoru, A., Stefanidis, A., and Radzikowski, J. #Earthquake: Twitter as a distributed sensor system. *Transactions in GIS*, 17(1):124–147, 2013. doi: 10.1111/j.1467-9671.2012.01359.x.

de Groot, R., Sumy, D., McBride, S., Jenkins, M., Lotto, G., Vinci, M., and Olds, S. ShakeAlert: A people-focused earthquake early warning system. In *Proc. of the 12th National Conf. on Earthquake Engineering*, 2022.

Dempsey, M. Reimaging take-up in challenging times: determining the predictive value of publicly available socio-demographic data for social assistance programs. *Honors Theses*, 2022.

Earle, P., Guy, M., Buckmaster, R., Ostrum, C., Horvath, S., and Vaughan, A. OMG earthquake! Can Twitter improve earthquake response? *Seismol. Res. Lett*, 81(2):246–251, 2010. doi: 10.1785/gssrl.81.2.246.

Eaton, J. Determination of amplitude and duration magnitudes and site residuals from short-period seismographs in Northern California. *Bull. Seismol. Soc. Amer*, 82(2):533–579, 1992. doi: 10.1785/BSSA0820020533.

Ekström, G., Nettles, M., and Dziewoński, A. The global CMT project 2004–2010: Centroid-moment tensors for 13,017 earthquakes. *Phys. Earth Planet. Inter*, 200:1–9, 2012. doi: 10.1016/j.pepi.2012.04.002.

Elalami, M., Elshafei, I., and Abdelkader, H. Location-Based Services Using Web-GIS By An Android Platform To Improve Students' Navigation During Covid-19. *J. Theor. Appl. Inf. Technol*, 100(10):3441–3456, 2022.

Fisher, D., Frey, N., and Hattie, J. *The distance learning playbook, grades K-12: Teaching for engagement and impact in any setting*. Corwin Press, 2020.

Fraser, S., Doyle, E., Wright, K., Potter, S., McClure, J., Johnston, D., Leonard, G., Coomer, M., Becker, J., and Johal, S. Tsunami response behaviour during and following two local-source earthquakes in Wellington. *New Zealand, Int. J. Disaster Risk Reduct*, 2016. doi: 10.1016/j.ijdrr.2016.02.008.

Gardere, L., Plyer, A., and Ross, D. How Data Became Part of New Orleans' DNA during the Katrina Recovery. *New England Journal of Public Policy*, 32(1), 2020.

Given, D., Allen, R., Baltay, A., Bodin, P., Cochran, E., Creager, K., Groot, R., Gee, L., Hauksson, E., Heaton, T., Hellweg, M., Murray, J., Thomas, V., Toomey, D., and Yelin, T. Revised technical implementation plan for the ShakeAlert system—An earthquake early warning system for the West Coast of the United States: U.S. *Geological Survey Open-File Report*, page 42, 2018. doi: 10.3133/ofr20181155.

Goltz, D. J., Park, H., Nakano, G., and Yamori, K. Earthquake ground motion and human behavior: Using DYFI data to assess behavioral response to earthquakes. *Earthquake Spectra*, 36(3): 1231–1253, 2020. doi: 10.1177/8755293019899958.

Goltz, J., D.J., W., SK, M., R, G., JK, B., and A, B. Development of a companion questionnaire for "Did You Feel It?": Assessing response in earthquakes where an earthquake early warning may have been received. *Earthquake Spectra*, 0(0), 2022. doi: 10.1177/87552930221116133.

Grady, C. Institutional review boards. *Purpose and*, 148(5): 1148–1155, 2015. doi: 10.1378/chest.15-0706.

Hirshorn, B., Lindh, A., and Allen, R. Real time signal duration magnitudes from low-gain short period seismometers, U.S. *Geol. Surv. Open-File Rep*, page 87–630, 1987.

Huang, H. Location Based Services. In Kresse, W. and Danko, D., editors, *Springer Handbook of Geographic Information*. Springer Handbooks. Springer, Cham, 2022. doi: 10.1007/978-3-030-53125-6_22.

Johnson, S., Bottiani, J., Waasdorp, T., and Bradshaw, C. Surveillance or safekeeping? How school security officer and camera presence influence students' perceptions of safety, equity, and support. *J. Adolesc. Health*, 63(6):732–738, 2018. doi: 10.1016/j.jadohealth.2018.06.008.

Jon, I., Lindell, M., Prater, C., Huang, S., Wu, H., Johnston, D., and Lambie, E. Behavioral response in the immediate aftermath of shaking: Earthquakes in Christchurch and Wellington, New Zealand, and Hitachi. *Japan. International Journal of Environmental Research and Public*, 13(11):1137, 2016. doi: 10.3390/ijerph13111137.

Kankanamge, N., Yigitcanlar, T., Goonetilleke, A., and Kamruzzaman, M. Can volunteer crowdsourcing reduce disaster risk? A systematic review of the literature. *Int. JReduct, Disaster Risk*, 2019. doi: 10.1016/j.ijdrr.2019.101097.

Kelman, I. and Glantz, M. Early warning systems defined. Reducing disaster: Early warning systems for climate change. page 89–108, 2014. doi: 10.1007/978-94-017-8598-3_5.

Kilic, B. and Gülgen, F. Accuracy and similarity aspects in online geocoding services: A comparative evaluation for Google and Bing maps. *Int. J. Eng. and Geosci*, 5(2):109–119, 2020. doi: 10.26833/ijeg.629381.

King, S. and Bracy, N. School security in the post-Columbine era: Trends, consequences, and future directions. *J. Contemp. Crim. Justice*, 35(3):274–295, 2019. doi: 10.1177/1043986219840188.

Kiyimba, N. and O'Reilly, M. The risk of secondary traumatic stress in the qualitative transcription process: a research note. *Qual. Res*, 16(4):468–476, 2016. doi: 10.1177/1468794115577013.

Kong, Q., Allen, R. M., Allen, S., Bair, T., Meja, A., Patel, S., Strauss, J., and Thompson, S. Crowdsourcing Felt Reports Using the MyShake Smartphone App. *Seismological Research Letters*, July 2023. doi: 10.1785/0220230027.

Kumar Shukla, A. Site Response Studies Application in Seismic Hazard Microzonation and Ground Characterization. In *Theory and Practice in Earthquake Engineering and Technology*, page 55–97. Springer Nature Singapore, Singapore, 2022.

LeClerc, J. and Joslyn, S. The cry wolf effect and weather-related decision making. *Risk Analysis*, 35(3):385–395, 2015. doi: 10.1111/risa.12336.

Lee, W., Bennet, R., and Meagher, K. A method of estimating magnitude of local earthquakes from signal duration. *U.S. Geol. Surv. Open-File Rept*, 1972.

Li, H., Chen, X., Chen, H., Wang, B., Li, W., Liu, S., Peng, L., Qi, Z., He, Z., and Zhao, X. Simulation of smartphone-based public participation in earthquake structural response emergency monitoring using a virtual experiment and AI. *Buildings*, 12(4):492, 2022. doi: 10.3390/buildings12040492.

Lin, G. GIS in Building Public Health Infrastructure. In *New Thinking in GIScience*, page 367–373. Springer Nature Singapore, Singapore, 2022.

Ma, Z., Hu, X., Zhang, S., Li, N., Liu, F., Zhou, Q., Wang, H., Hu, G., and Dong, Q. SubvectorS_Geo: A Neural-Network-Based IPv6 Geolocation Algorithm. *Appl. Sci*, 13(2):754, 2023. doi: 10.3390/app13020754.

Martin-Jones, E. Social media posts reveal human responses to deadly Tongan eruption. *Eos*, 103, 2022. doi: 10.1029/2022EO220553.

McBride, S., Bellizzi, J., Gin, S., Henry, G., Sumy, D., Baldwin, D., and Fischer, E. 2018 M7.1 Anchorage and 2021 M7.2 Nippes, Haiti earthquake case studies for Virtual Earthquake Reconnaissance Team (VERT) activation protocols, policies, and procedures to gather CCTV and earthquake response videos. In *Proceedings of the 12th National Conference on Earthquake Engineering*, 2022a.

McBride, S., Smith, H., Morgoch, M., Sumy, D., Jenkins, M., Peek, L., Bostrom, A., Baldwin, D., Reddy, E., Groot, R., Becker, J., Johnston, D., and Wood, M. Evidence-based guidelines for protective actions and earthquake early warning systems. *Geophysics*, 87 (1):77– 102, 2022b. doi: 10.1190/geo2021-0222.1.

McBride, S., Sumy, D., Llenos, A., Parker, G., McGuire, J., Saunders, J., Meier, M.-A., Schuback, P., Given, D., and Groot, R. Latency and geofence testing of wireless emergency alerts intended for the ShakeAlert® earthquake early warning system for the West Coast of the United States of America. *Saf. Sci*, 157:105898, 2023. doi: 10.1016/j.ssci.2022.105898.

Nakayachi, K., Becker, J., Potter, S., and Dixon, M. Residents' reactions to earthquake early warnings in Japan. Risk Analysis, 39(8, 2019. doi: 10.1111/risa.13306.

Natural Hazards Center. New CONVERGE Training Module: Broader Ethical Considerations for Hazards and Disaster Researchers, 2021. https://hazards.colorado.edu/news/center-news/new-converge-training-module-broader-ethical-considerations-forhazards-and-disaster-researchers. Last consulted 27 February 2023.

Ofli, F., Qazi, U., Imran, M., Roch, J., Pennington, C., Banks, V., and Bossu, R. A real-time system for detecting landslide reports on social media using artificial intelligence. In *Web Engineering: 22nd International Conference, ICWE 2022*, page 49–65, Bari, Italy, 2022. Springer International Publishing. doi: 10.1007/978-3-031-09917-5_4.

Pandya, S., Ghayvat, H., Kotecha, K., Awais, M., Akbarzadeh, S., Gope, P., Mukhopadhyay, S., and Chen, W. Smart home anti-theft system: a novel approach for near real-time monitoring and smart home security for wellness protocol. *Appl. Syst. Innov*, 1(4):42, 2018. doi: 10.3390/asi1040042.

Pilz, M., Abakanov, T., Abdrakhmatov, K., Bindi, D., Boxberger, T., Moldobekov, B., Orunbaev, S., Silacheva, N., Ullah, S., S., Y., P., and Parolai, S. An overview on the seismic microzonation and site effect studies in Central Asia. *Ann. Geophys*, 58(1), 2015. doi: 10.4401/ag-6662.

Poese, I., Uhlig, S., Kaafar, M., Donnet, B., and Gueye, B. IP geolocation databases: Unreliable? Comput. *Commun. Rev*, 41(2): 53–56, 2011. doi: 10.1145/1971162.1971171.

Quitoriano, V. and Wald, D. USGS "Did You Feel It?"—Science and Lessons From 20 Years of Citizen Science-Based Macroseismology, Front. *Earth Sci*, 8(120), 2020. doi: 10.3389/feart.2020.00120.

Rastogi, B., Mohan, K., Sairam, B., Singh, A., and Pancholi, V. Geotechnical, Geological and Geophysical Investigations for Seismic Microzonation and Site-Specific Earthquake Hazard Analysis in Gujarat. In Sitharam, T., Jakka, R., and Kolathayar, S., editors, *Advances in Earthquake Geotechnics. Springer Tracts in Civil Engineering*. Springer, Singapore, 2023. doi: 10.1007/978-981-19-3330-1_4.

Roongpiboonsopit, D. and Karimi, H. Quality Assessment of Online Street and Rooftop Geocoding Services, Cartogr. *Geogr. Inf. Sci*, 37(4):301–318, 2010. doi: 10.1559/152304010793454318.

Sackett, D. Bias in analytic research. *J. Chron. Dis*, 32(1/2):51–63, 1979.

Salkind, N. *Encyclopedia of Research Design*. SAGE Publications, Inc., Thousand Oaks, California, 2010. doi: 10.4135/9781412961288.

Shaheen, A., Ciesco, E., Johnson, K., Kuhnen, G., Paolini, C., and Gartner, G. Interactive, on-line visualization tools to measure and drive equity in COVID-19 vaccine administrations. *J. Am. Med. Inf. Assoc*, 28(11):2451–2455, 2021. doi: 10.1093/jamia/ocab180.

Shan, W., Feng, J., Chang, J., Yang, F., and Li, Z. Collecting earthquake disaster area information using smart phone. *International Conference on System Science and Engineering*, page 310–314, 2012. doi: 10.1109/ICSSE.2012.6257197.

Smith, C. and White, Jr., M. Geocoding techniques developed by the census use study. In *International Workshop on Managing Requirements Knowledge, Las Vegas*. Nevada, 1971. doi: 10.1109/AFIPS.1971.97.

Stefanidis, A., Crooks, A., and Radzikowski, J. Harvesting ambient geospatial information from social media feeds. *GeoJournal*, 78: 319–338, 2013. doi: 10.1007/s10708-011-9438-2.

Sumy, D., Welti, R., and Hubenthal, M. Applications and evaluation of the IRIS earthquake browser: A web-based tool that enables multidimensional earthquake visualization. *Seismol. Res. Lett*, 91(5):2922–2935, 2020. doi: 10.1785/0220190386.

Sumy, D., McBride, S., Hillebrandt-Andrade, C., Kohler, M., Orcutt, J., Kodaira, S., Moran, K., McNamara, D., Hori, T., Vanacore, E., Pirenne, B., and Collins, J. Long-term ocean observing for international capacity development around tsunami early warning, 2021. doi: 10.5670/oceanog.2021.supplement.02-27. A Supplement to Oceanography.

Sumy, D., Jenkins, M., Crayne, J., Olds, S., Anderson, M., Johnson, J., Magura, B., Pridmore, C., and Groot, R. Education Initiatives to Support Earthquake Early Warning: A Retrospective and a Roadmap. Seismol. *Res. Letts*, 93(6):3498–3513, 2022a.

doi: 10.1785/0220220159.

Sumy, D., Jenkins, M., McBride, S., and Groot, R.-M. Typology development of earthquake displays in free-choice learning environments, to inform earthquake early warning education in the United States. *Int. J Disaster Risk Reduct*, 73, 2022b. doi: 10.1016/j.ijdrr.2022.102802.

Ur, B., Jung, J., and Schechter, S. Intruders versus intrusiveness: teens' and parents' perspectives on home-entryway surveillance. In *Proceedings of the 2014 ACM International Joint Conference on Pervasive and Ubiquitous Computing*, page 129–139, 2014. doi: 10.1145/2632048.2632107.

U.S. Geological Survey. Safeguarding the Nation: From the Destructive Loma Prieta earthquake to an Earthquake Early Warning System, 2019. https://www.usgs.gov/news/featured-story/usgs-shakealert-earthquake-early-warning-system. Last consulted 26 March 2023.

U.S. Geological Survey. Alert Thresholds for ShakeAlert, 2021. https://www.usgs.gov/media/images/alert-thresholds-shakealert. Last consulted 22 March 2023.

U.S. Geological Survey. M7.1 – 1 km SE of Point MacKenzie, 2023. https://earthquake.usgs.gov/earthquakes/eventpage/ak20419010/pager. Last consulted 24 February 2023.

VERT. Virtual Earthquake Reconnaissance Team, EERI Learning from Earthquakes, 2023. https://www.learningfromearthquakes.org/activities/vert. Last consulted 22 March 2023.

Vinnell, L., Inch, P., Johnston, D., and N, H. Behavioral responses to earthquake shaking: Video footage analysis of the 2016 Kaikōura earthquake in Wellington. *Aotearoa New Zealand. Earthquake Spectra*, 38(3):1636–1660, 2022. doi: 10.1177/87552930221086303.

Wald, D., Worden, C., Quitoriano, V., and Pankow, K. ShakeMap Manual, Technical Manual, Users Guide, and Software Guide, 2006. http://pubs.usgs.gov/tm/2005/12A01/pdf/508TM12-A1.pdf. Last consulted 23 March 2023.

Wald, D., Quitoriano, V., Worden, B., Hopper, M., and Dewey, J. USGS ''Did You Feel It?'' Internet-based macroseismic intensity maps. *Ann. Geophys*, 54:688–707, 2011. doi: 10.4401/ag-5354.

Wong, W., Liew, J., Loo, C., and Wong, W. Omnidirectional surveillance system for digital home security. In *2009 International Conference on Signal Acquisition and Processing*, page 8–12, 2009. doi: 10.1109/ICSAP.2009.13.

Worden, C., Wald, D., Allen, T., Lin, K., Garcia, D., and Cua, G. A Revised Ground-Motion and Intensity Interpolation Scheme for ShakeMap. *Bull. Seismol. Soc. Amer*, 100(6):3083–3096, 2010. doi: 10.1785/0120100101.

Yang, D., Bilaver, L., Hayes, O., and Goerge, R. Improving geocoding practices: evaluation of geocoding tools. *J. Med. Syst*, 28(4): 361–370, 2004. doi: 10.1023/b:joms.0000032851.76239.e3.

Zhang, X., Feng, Y., Angeloudis, P., and Demiris, Y. Monocular visual traffic surveillance: a review. *IEEE Transactions on Intelligent Transportation Systems*, 23:14148–14165, 2022. doi: 10.1109/TITS.2022.3147770.

doi:10.26443/seismica.v2i2.499

SEISMICA

Continuous isolated noise sources induce repeating waves in the coda of ambient noise correlations

S. Schippkus * [1], **M. Safarkhani** [1], **C. Hadziioannou** [1]

[1]Institute of Geophysics, Centre for Earth System Research and Sustainability (CEN), Universität Hamburg, Hamburg, Germany

Author contributions: *Conceptualization*: SS, MS, CH. *Methodology*: SS. *Software*: SS. *Data curation*: MS. *Formal Analysis*: SS. *Investigation*: SS, MS. *Resources*: SS, CH. *Writing - original draft*: SS. *Writing - Review & Editing*: SS. *Visualization*: SS. *Supervision*: CH. *Funding acquisition*: SS,CH.

Abstract Continuous excitation of isolated noise sources leads to repeating wave arrivals in cross correlations of ambient seismic noise, including throughout their coda. These waves propagate from the isolated sources. We observe this effect on correlation wavefields computed from two years of field data recorded at the Gräfenberg array in Germany and two master stations in Europe. Beamforming the correlation functions in the secondary microseism frequency band reveals repeating waves incoming from distinct directions to the West, which correspond to well-known dominant microseism source locations in the Northeastern Atlantic Ocean. These emerge in addition to the expected anti-causal and causal correlation wavefield contributions by boundary sources, which are converging onto and diverging from the master station, respectively. Numerical simulations reproduce this observation. We first model a source repeatedly exciting a wavelet, which helps illustrate the fundamental mechanism behind repeated wave generation. Second, we model continuously acting secondary microseism sources and find good agreement with our observations. Our observations and modelling have potentially significant implications for the understanding of correlation wavefields and monitoring of relative velocity changes in particular. Velocity monitoring commonly assumes that only multiply scattered waves, originating from the master station, are present in the coda of the correlation wavefield. We show that repeating waves propagating from isolated noise sources may dominate instead, including the very late coda. Our results imply that in the presence of continuously acting noise sources, which we show is the case for ordinary recordings of ocean microseisms, velocity monitoring assuming scattered waves may be adversely affected with regard to measurement technique, spatial resolution, as well as temporal resolution. We further demonstrate that the very late coda of correlation functions contains useful signal, contrary to the common sentiment that it is dominated by instrument noise.

Production Editor:
Garreth Funning
Handling Editor:
Lise Retailleau
Copy & Layout Editor:
Ethan Williams

Signed reviewer(s):
Joshua Russell

Received:
17 March 2023
Accepted:
12 September 2023
Published:
9 October 2023

Non-technical summary Seismic waves are generated by all kinds of sources, including earthquakes, ocean waves, and machinery. Some sources produce a consistently present background level of seismic energy, so-called ambient seismic noise. It is well-established that, under the condition of evenly distributed noise sources, cross-correlation of ambient seismic noise, which was recorded on two separate seismic stations, yields a new wavefield that propagates directly from one station to the other. We call this new wavefield the correlation wavefield. Here, we show that in the presence of an additional isolated noise source that excites seismic waves continuously, for example ocean waves induced by storm systems over the Northeastern Atlantic, a new contribution to the correlation wavefield emerges: repeating waves propagating from the isolated noise source. These repeating waves can be more coherent across several stations than the expected correlation wavefield contribution, which propagates from one station to the other. We observe such repeating waves propagating from isolated noise sources on correlation wavefields computed from two years of seismic recordings of the Gräfenberg seismic array in Germany and two master stations in Europe. We reproduce our observations with numerical simulations of the sources and resulting correlation wavefields. Our findings have potentially significant implications for seismic monitoring based on relative velocity changes, which is used to monitor geological faults, volcanoes, groundwater, and other processes in the Earth. Velocity monitoring commonly relies on the assumption that the correlation wavefield contains only the contribution that propagates from one station to the other, which we show is not necessarily correct. This can lead to misinterpretation of measured velocity variations.

1 Introduction

Seismic interferometry of the ambient seismic field gives rise to new correlation wavefields that relate to the Green's function under the condition of uniformly distributed noise sources (Wapenaar et al., 2005; Gouédard et al., 2008). These correlation wavefields are now routinely used for imaging (e.g., Schippkus et al., 2018; Lu et al., 2018) and monitoring (e.g., Wegler and Sens-Schönfelder, 2007; Hadziioannou et al., 2009; Sheng et al., 2023) of Earth's structure. In the presence of an isolated noise source, a second contribution to this wavefield is introduced, sometimes referred to as spurious arrival (Snieder et al., 2006; Zeng and Ni, 2010; Retailleau et al., 2017; Schippkus et al., 2022). This cor-

*Corresponding author: sven.schippkus@uni-hamburg.de

relation wavefield contribution can lead to biased measurements of seismic wave speed due to interference of direct waves from the master station and the isolated noise source (Schippkus et al., 2022).

Monitoring applications, on the other hand, rely on estimating relative velocity changes by repeatedly computing correlation wavefields throughout time and measuring changes in the arrival time of their coda (Wegler and Sens-Schönfelder, 2007; Sens-Schönfelder and Larose, 2010). Current strategies often rely on the assumption that the coda of a given correlation wavefield is comprised of multiply scattered waves, originating from the master station, which also dictates its spatial sensitivity (Planès et al., 2014; Margerin et al., 2016; van Dinther et al., 2021). If the spatial sensitivity of the coda is known, seismic velocity changes can be located (Obermann et al., 2014; Mao et al., 2022). Some progress has been made in accounting for the impact of changes in sources on the correlation wavefield, particularly in the context of monitoring at frequencies above 1 Hz, e.g., by carefully selecting time windows in which the same sources are active and produce similar correlation wavefields (Yates et al., 2022; Sheng et al., 2023).

In this study we demonstrate that isolated noise sources may impact correlation wavefields to a degree previously not considered. Continuously acting isolated noise sources, such as ocean microseisms, produce repeating waves throughout the entire correlation function that propagate from the isolated source location. These waves coincide with and are more coherent than multiply scattered waves originating from the master station. This may have significant impact on the understanding of measured velocity changes. In the following, we show observations of these repeating waves on field data correlation functions in the ocean microseism frequency band using stations throughout Europe, illustrate the mechanism behind repeated direct-wave generation in correlation functions, and finally reproduce our field data observations by modelling continuously acting isolated noise sources, i.e., secondary ocean microseisms.

2 Beamforming the correlation wavefield

We compute correlation wavefields from two years of continuous vertical component seismograms, recorded in 2019 and 2020 at the Gräfenberg array in Germany and two master stations, IV.BRMO in Italy (Fig. 1a) and PL.OJC in Poland (Fig. 2a). IV.BRMO was chosen randomly and PL.OJC was chosen to showcase a different backazimuth and slightly larger distance to the Gräfenberg array. We apply a standard processing workflow: remove instrument response, cut two years of data into two-hour long segments overlapping by 50%, apply spectral whitening (Bensen et al., 2007), cross-correlate each segment, and stack all segments linearly. No further processing, e.g., earthquake removal or other segment selection, has been applied, because whitening in each segment already normalises the energy potentially introduced by earthquakes and we find no evidence for earthquakes-related bias in the resulting correlation wavefields.

To estimate from which directions the correlation wavefield arrives at the Gräfenberg array, we beamform the correlation functions (Fig. 1). We beamform in 200 s windows, overlapping by 75%, in the secondary microseism frequency band (0.1 to 0.3 Hz), and assuming plane-wave propagation (Rost and Thomas, 2002). We present a sample correlation function to give orientation in lapse time (Fig. 1b, top panel), and compute Pearson correlation coefficients of all correlation functions with the best-fitting beam for each window to estimate how well the beam explains the data within a window (Fig. 1b, second panel). Similarity is highest for the expected anti-causal arrival, which also emerges more clearly in the correlation function than the causal arrival, due to the commonly observed strong noise sources in the Northeastern Atlantic (e.g., Friedrich et al., 1998; Chevrot et al., 2007; Juretzek and Hadziioannou, 2016). Throughout the coda, similarity remains nearly constant with a correlation coefficient ~ 0.4. We detect several dominant directions of arrival (Fig. 1b, third panel). First, the anti-causal arrival of the correlation wavefield converging onto the master station at negative lapse time (dashed orange line) and the causal arrival diverging from the master station at positive lapse time (dotted orange line), i.e., the correlation wavefield contribution that usually arises in seismic interferometry (Wapenaar et al., 2005). Second, distinct directions throughout the correlation functions pointing towards West (Fig. 1b, third panel), which we project onto the map view (Fig. 1a).

A second master station in Poland (PL.OJC) illustrates how the converging (anti-causal) and diverging (causal) parts of the correlation wavefield depend on the geometry of array stations to master station and point roughly towards the great-circle between the two (Soergel et al., 2022), whereas the dominant directions towards West appear to be independent of the master station (Fig. 2). A North-Northeast direction, however, still emerges in the beamforming results as most coherent, which coincides approximately with the great circle direction for the converging part of the correlation wavefield for master station IV.BRMO (Fig. 1). Similarly, the converging direction for master station PL.OJC coincides with the dominant directions towards West (Fig. 2). This hints at the impact the geometry of master station and array stations has on the detection and identification potential of these other directions. We propose the dominant directions detected by beamforming and pointing towards West represent repeating direct waves emerging at isolated noise source locations in the Northeastern Atlantic Ocean. The North-Northeasterly direction observed in the coda in both examples similarly represents waves arriving from isolated source locations off the coast of Norway, which were previously observed as dominant on continuous seismograms (e.g., Juretzek and Hadziioannou, 2016). We call these direct waves, because they propagate directly from the isolated source to the seismic stations. These are not to be confused with the direct waves propagating between the stations, i.e., the expected anti-causal and causal arrivals.

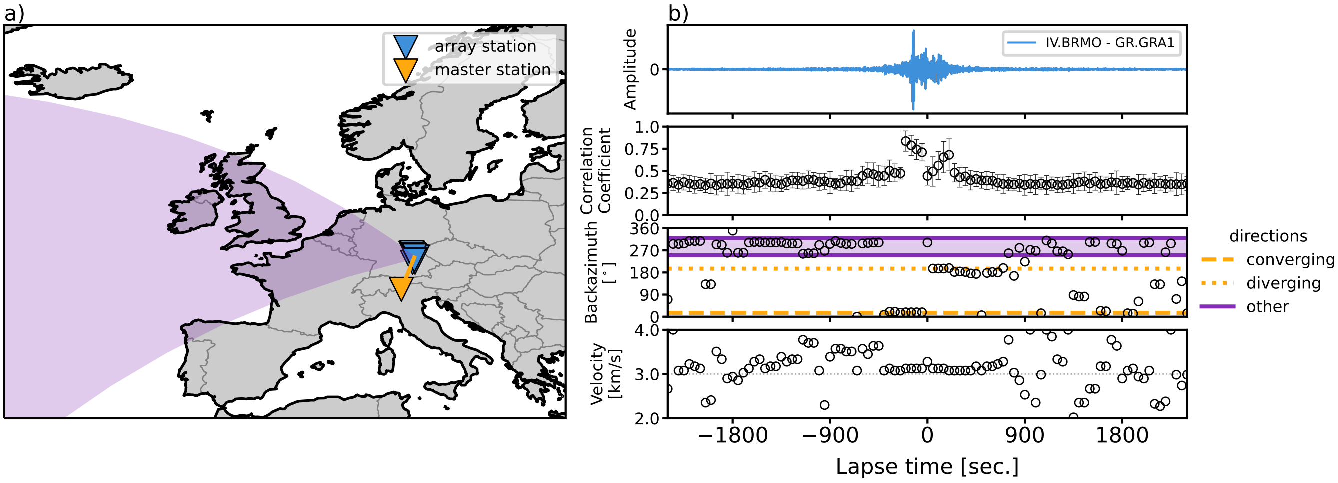

Figure 1 Beamforming the correlation wavefield between the Gräfenberg array in Germany (blue triangle) and master station IV.BRMO, Italy (yellow triangle), in the secondary microseism frequency band (0.1 to 0.3 Hz). a) Overview map with master station and array stations. The orange line and purple area correspond to the dominant directions detected by beamforming. b) Beamforming results: sample cross-correlation between the master station and one array station (top), mean Pearson correlation-coefficient of correlation functions with best-fitting beams in each window (second panel), detected direction of arrival (third panel), and estimated phase velocity (bottom). Detected directions correspond to the correlation wavefield converging onto and diverging from the master station (orange lines), and a range of directions pointing towards the Atlantic Ocean (purple area).

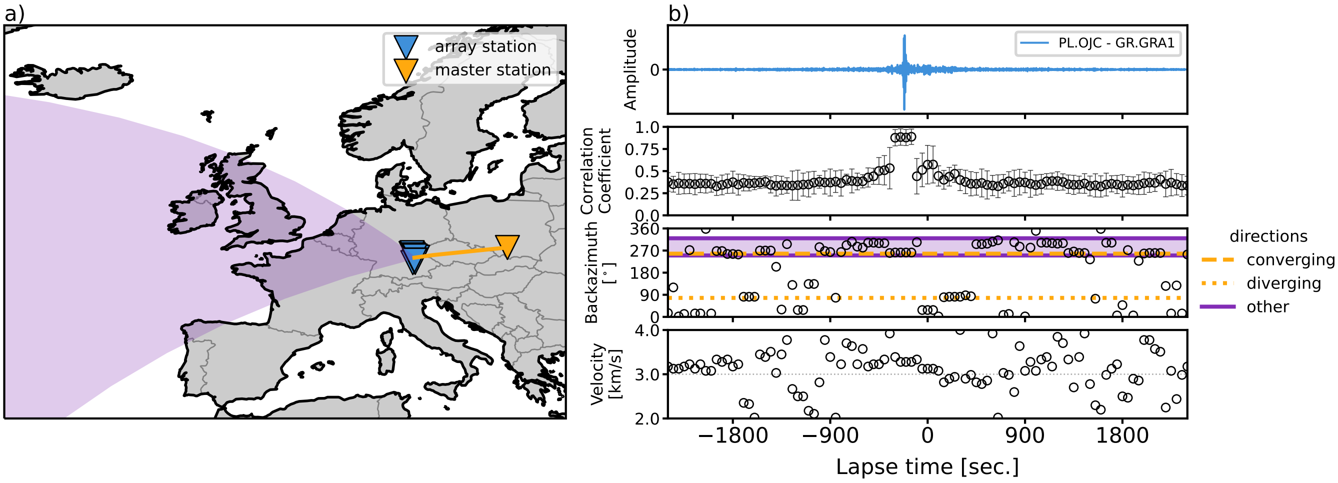

Figure 2 Same as Figure 1, but for master station PL.OJC, Poland. The directions detected by beamforming corresponding to the diverging and converging part of the correlation wavefield change with master station as expected (orange lines), whereas the range of directions towards the Northern Atlantic remains constant (purple area). Note that the converging part of the correlation wavefield points towards West, similar to one of the dominant directions detected pointing towards the Atlantic Ocean for master station IV.BRMO (Fig. 1).

3 A repeating impulsive isolated noise source

To substantiate our hypothesis and explain the observations above, we start from the concept of an isolated noise source (Schippkus et al., 2022). Consider a wavefield that is excited by sources on a boundary S and an isolated noise source at $\mathbf{r}_N$, recorded on a station at location $\mathbf{r}$

$$u(\mathbf{r}) = \oint_S N_B(\mathbf{r}')G(\mathbf{r},\mathbf{r}')d\mathbf{r}' + N_I G(\mathbf{r},\mathbf{r}_N)\ , \quad (1)$$

with G the Green's function and N_B and N_I the source spectra of boundary sources and the isolated source, respectively. This section is formulated in the frequency domain. The cross-correlation of this wavefield at location $\mathbf{r}$ with the wavefield recorded on a master station at $\mathbf{r}_M$ is given by (eq. 6 of Schippkus et al., 2022)

$$\begin{aligned}\langle u(\mathbf{r})u^*(\mathbf{r}_M)\rangle = \frac{\rho c |N_B|^2}{2}\left(G(\mathbf{r},\mathbf{r}_M) + G^*(\mathbf{r},\mathbf{r}_M)\right) \\ + |N_I|^2 G(\mathbf{r},\mathbf{r}_N)G^*(\mathbf{r}_M,\mathbf{r}_N)\ ,\end{aligned} \quad (2)$$

with ρ the mass density of the medium and c the propagation velocity. The first term describes the contribution of uncorrelated sources on the boundary S surrounding the stations, which usually arises in seismic interferometry (as in Wapenaar et al., 2005), and the second term describes the contribution of the isolated noise source. The relation of these terms has been investigated by Schippkus et al. (2022), who demonstrate how the direct arrivals of these two wavefield contributions interfere for certain station geometries, leading to biased surface wave dispersion measurements. In their modelling, the authors assumed the source term of the isolated source N_I to be a wavelet, excited once.

Here, we expand upon this idea by considering the isolated noise source to be excited multiple times in a correlated manner. For illustration purposes, we express its source term as $N_I = W_I E_I$, with a wavelet W_I and excitation pattern E_I. The contribution of the isolated noise source to the correlation wavefield is hence

$$|W_I|^2 |E_I|^2 G(\mathbf{r}, \mathbf{r}_N) G^*(\mathbf{r}_M, \mathbf{r}_N) \; . \tag{3}$$

A simple example of an isolated noise source exciting a Ricker wavelet, repeating 5 times with a 20 s interval, illustrates how such a source manifests in correlation functions (Fig. 3). For such a source, the excitation pattern is a time series with 1 at every interval of 20 s (5 times), and 0 elsewhere. The auto-correlation of the wavelet $|W_I|^2$ (Fig. 3a), auto-correlation of the excitation pattern $|E_I|^2$ (Fig. 3b), and cross-correlation of the Green's functions $G(\mathbf{r}, \mathbf{r}_N)G^*(\mathbf{r}_M, \mathbf{r}_N)$ for surface waves in a homogeneous, isotropic, acoustic medium and an arbitrary geometry (Fig. 3c) are convolved to result in a repeating wavelet with the same 20 s interval, present in the correlation wavefield (Fig. 3d). These repeating wavelets represent direct waves emitted from the isolated source location.

A sketch of the correlation wavefield in the presence of a repeating impulsive isolated noise source helps illustrate its evolution with lapse time (Fig. 4). The wavefield is comprised of the two contributions by boundary sources (first term of eq. 2, yellow in Fig. 4) and the isolated noise source (eq. 3, purple in Fig. 4). The boundary source contribution converges onto the master station at negative lapse times (the anti-causal part), and diverges from the station at positive lapse times (the causal part, Fig. 4a-g). This is the expected contribution that usually arises in seismic interferometry. The repeating isolated noise source induces waves that emerge earlier and with lower amplitude than the main arrival (Fig. 4a) and eventually reach the array station (Fig. 4b). The main arrival (highest amplitude, indicated by line thickness) of the isolated noise source emerges at $\tau = -|\mathbf{r}_M - \mathbf{r}_N|/c$ and touches the boundary source contribution along the line connecting the isolated source and master station (Fig. 4c-f, as in Schippkus et al., 2022). At lapse time $\tau = 0$, both the wavefield contribution by boundary sources and the main arrival of the isolated noise source reach the master station (Fig. 4e). At causal lapse times, the last repeating waves from the isolated noise source reach the array station (Fig. 4f) before the boundary source contribution diverging from the master station arrives at the at array station (Fig. 4g). The exact timing of each arrival depends on the geometry of isolated source, master station, and array stations, as well as the excitation pattern.

Note that the repeating direct waves from the isolated noise source are asymmetrical in lapse time (Figs. 3, 4), because there is no part of the correlation wavefield converging onto the isolated noise source (Schippkus et al., 2022). How strongly these repeating direct waves manifest depends on how highly correlated the isolated source is with itself throughout time. The example presented here constitutes the most extreme case, i.e., identical wavelet and exactly regular excitation pattern. Even under these conditions, amplitudes decay linearly with time due to the finite length of the excitation pattern (Fig. 3b). In this example, the amplitude of the excitation pattern auto-correlation decreases by $1/5$ of the maximum amplitude with each interval away from 0 s, because the source is excited 5 times. Slight variations in amplitude, shape of the wavelet, or excitation timing lead to reduced correlation, and thus repeating direct waves with reduced amplitude or different shape. If there was no correlation, the repeating waves would disappear. The main arrival would remain.

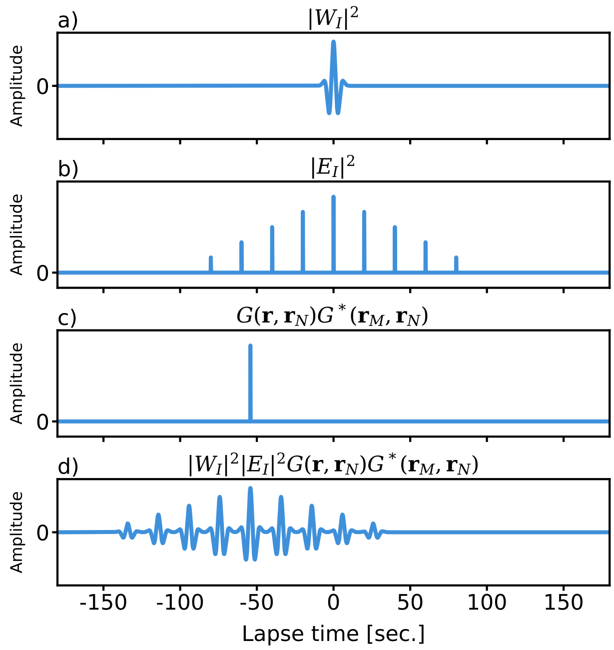

Figure 3 A repeating isolated noise source produces repeating direct waves in correlation functions, depicted in time domain. a) Auto-correlation of the wavelet $|W_I|^2$. b) Auto-correlation of the excitation pattern $|E_I|^2$ with a regular 20 s interval, excited 5 times. Note that amplitudes decay by $1/5$ every interval away from 0 s lapse time. c) Cross-correlation of the Green's functions between the isolated noise source and both station locations for an arbitrary geometry. d) Second term of the correlation wavefield (eq. 3, the convolution of a-c), where each arriving wavelet represents a direct wave emitted from the isolated noise source at $\mathbf{r}_N$.

To confirm the repeating wavelets in the correlation functions indeed represent repeating direct waves emitted from the isolated noise source, we model a master station in Italy (same location as IV.BRMO), array stations in Southern Germany (same locations as the Gräfenberg array), 1000 boundary sources surrounding the stations in a small-circle with 1000 km distance to them, as well as a repeating isolated noise source Southwest of Iceland (Fig. 5a). All sources excite Ricker

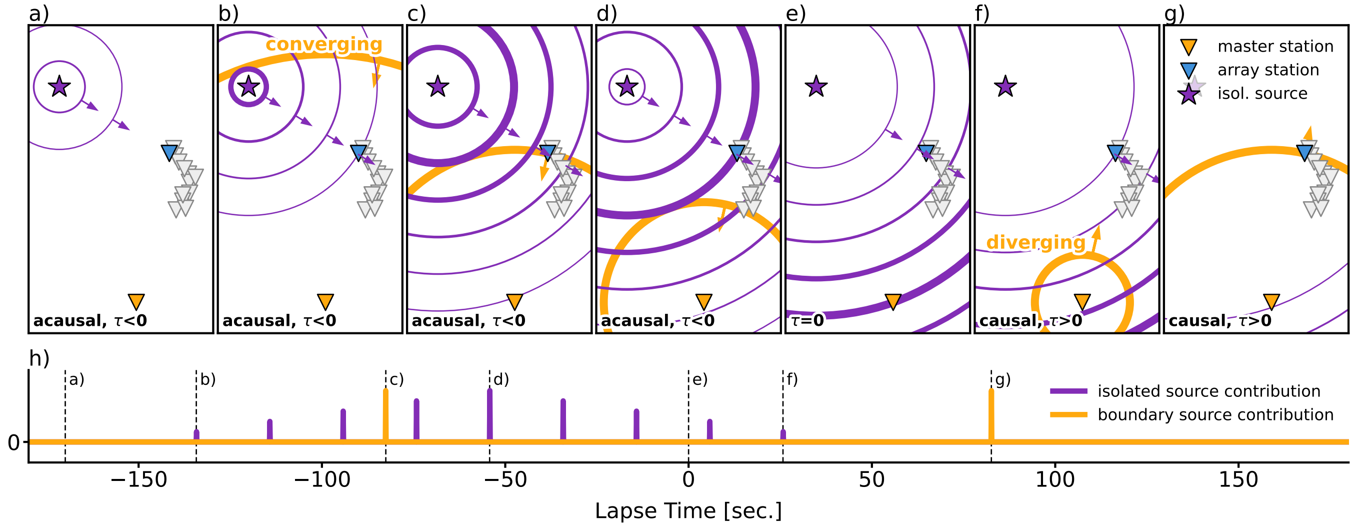

Figure 4 Schematic illustration of the correlation wavefield in the presence of a repeating impulsive source (5 excitations, 20 s interval, same as in Figure 3). We remove the wavelet for improved clarity. a-g) Snapshots of the correlation wavefield at different lapse times, indicated by dashed lines in h). The contributions of the isolated source (purple lines) and boundary sources surrounding the master and array stations (yellow line) propagate through the medium. Line thickness indicates amplitude. h) Correlation function between the array station and the master station, color-coded by isolated source and boundary source contribution (purple and yellow, respectively). Dashed vertical lines mark the lapse time snapshots displayed in a-g. The anti-causal part of the correlation function contains repeating waves propagating from the isolated source and the boundary source contribution converging onto the master station (a-d). At lapse time $\tau = 0$, both the main arrival of the isolated source contribution and the boundary source contribution reach the master station (e). At causal lapse time, the last arrivals of the isolated source reach the array station (f) and finally the diverging contribution of the boundary sources (g).

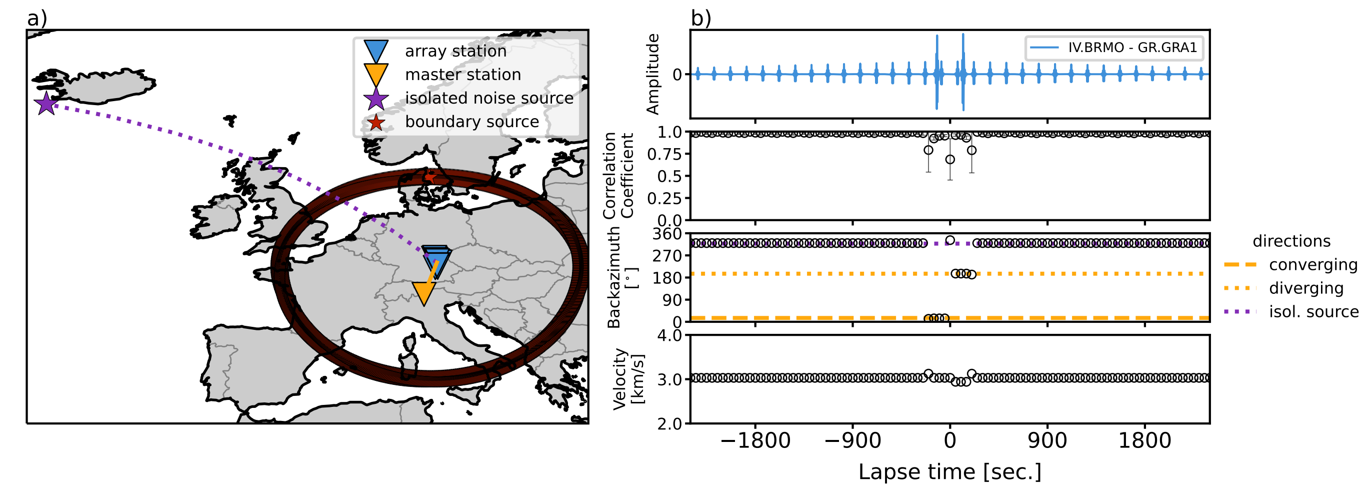

Figure 5 Beamforming synthetic cross-correlation functions detects repeating direct waves from the regularly repeating isolated noise source. a) Overview map: master station (orange triangle), array stations (blue triangle), boundary sources in a small circle surronding the stations (red stars) and the isolated noise source Southwest of Iceland (purple star). b) Beamforming results: sample cross-correlation between master station and one array station, mean correlation-coefficients between windowed correlation functions and beams, detected direction of arrival, and estimated phase velocity. The boundary source contribution to the correlation wavefield converging onto and diverging from the master station (orange lines, first term in eq. 2) is detected as well as repeating direct waves from the isolated noise source (purple line, second term in eq. 2).

wavelets, and only the isolated noise source repeats it 50 times with a 150 s interval (similar to Figs. 3, 4). We compute synthetic surface wave seismograms by assuming a homogeneous, isotropic, acoustic half-space with a medium velocity $v = 3$ km/s for simplicity (i.e., Green's functions are of the form $e^{-i\omega x/v}$), and compute cross correlations of those waveforms. During the calculations, we treat boundary sources and the isolated noise source separately in accordance with equation (2). The maximum amplitude of the isolated noise source contribution is scaled to $1/4$ of the boundary source contribution to distinguish them easily (Fig. 5b, top panel). The correlation wavefield contains both wavefield contributions. Beamforming the cross-correlation functions between the master station and all array stations detects three directions of arrival (Fig. 5b, third panel): the first term of the correlation wavefield converging onto the master station at negative lapse time (dashed orange line) and diverging from the master station at positive lapse time (dotted orange line), and repeating direct waves from the isolated source (purple dotted line) throughout the correlation function. The estimated phase velocity of ~ 3 km/s is the medium velocity (Fig. 5b, bottom panel). Note that the correlation functions match exactly with the beam (correlation coefficent of 1) only for time windows that do not contain both contributions simultaneously (Fig. 5b, second panel).

This example illustrates the principle behind repeating direct waves emerging in correlation functions. However, we observed this effect on field data of secondary ocean microseisms (Figs. 1, 2), which are better described as continuously acting sources, which we introduce in the following.

4 Continuously acting isolated noise sources

To describe the suspected isolated noise source (Figs. 1, 2) as a continuously acting microseism source, we rely on the parametrization employed by Gualtieri et al. (2020) (eq. 3 therein). The surface pressure P at colatitude θ and longitude ϕ excited by the secondary microseism mechanism is described as a superposition of many harmonics

$$P(t,\theta,\phi) = \sum_{i=1}^{H} A(f_i,\theta,\phi)\cos(2\pi f_i t + \Phi_i), \quad (4)$$

with H the number of harmonics, A the amplitude of the harmonic frequency f_i, and $\Phi_i \in [0, 2\pi)$ its phase, sampled uniformly random. The amplitude A relates to the power spectral density of ocean gravity waves and incorporates local site effects, and is described in more detail by Gualtieri et al. (2020). For our considerations, we neglect the amplitude term ($A = 1$), because we investigate a fairly narrow frequency band and the exact amplitude of each harmonic is irrelevant for explaining the effect observed in this study. In the following, we use $P(\theta, \phi)$ (the spectrum of $P(t, \theta, \phi)$) with harmonics from 0.1 to 0.3 Hz directly as the source term N_I (Fig. 6a). Its auto-correlation (Fig. 6b), convolved with the same Green's function cross-correlation as above (Fig. 3c) contains one clear main arrival and weak, repeating direct waves (Fig. 6c). These repeating waves excited by a microseism source have much lower amplitude and inconsistent shape compared to a repeating impulsive isolated noise source (Fig. 3) due to decreased correlation of the source term with itself throughout time.

We repeat the numerical simulation above (Fig. 5) with $P(\theta, \phi)$ as the source term for both boundary and isolated noise sources (Fig. 7). Both contributions to

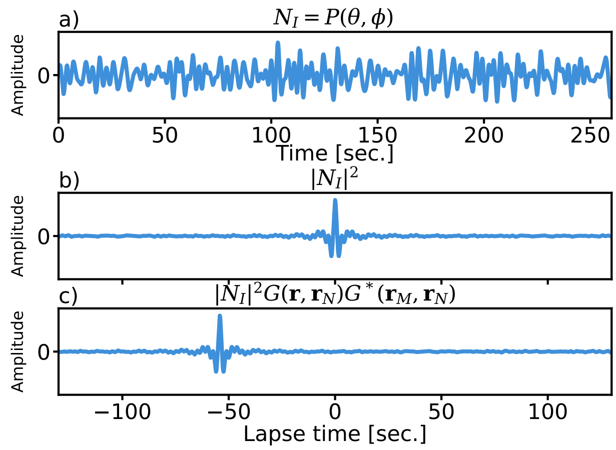

Figure 6 Contribution to the correlation wavefield by a continuously acting isolated noise source. a) Source term for a secondary microseism source, if all harmonics between 0.1 and 0.3 Hz are excited with a uniformly random phase $\Phi_i \in [0, 2\pi)$ and equal amplitude $A = 1$ (eq. 4). b) Auto-correlation of the source term $|N_I|^2$. c) Convolution of $|N_I|^2$ with the same Green's function cross-correlation as in Figure 3c, i.e., the second term of the correlation wavefield (eq. 2), with a main arrival and low-amplitude, repeating direct waves throughout the coda.

the correlation wavefield are scaled to have similar amplitudes. A secondary microseism source produces repeating direct waves in correlation wavefields (Fig. 7b), similar to the regularly repeating source (Fig. 5). Near the main arrival of the isolated source (at ~ -100 s, after the anti-causal arrival due to boundary sources) and throughout the coda, repeating direct waves from the isolated noise source location are detected as most coherent. Distinct main arrivals (the "spurious" arrival) have been observed for localised microseism sources before (Zeng and Ni, 2010; Retailleau et al., 2017). These main arrivals must arrive in-between the anti-causal and causal arrivals of the boundary source contribution (Schippkus et al., 2022). In this study, we do not observe a particularly clear main arrival on field data (Figs. 1, 2). Still, the coda of the field data correlation wavefields appears to be dominated by repeating waves from isolated noise sources. Correlation coefficients of the synthetic correlation functions with the beams for each window reach ~ 1 for the main causal arrival, and ~ 0.75 for the anti-causal arrival due to interference with the isolated source arrival (Fig. 7b). Throughout the coda, correlation coefficients do not exceed 0.75 significantly, because continuously acting boundary sources also induce a repeating contribution in the correlation wavefield. In other words, the best beam does not represent the correlation functions entirely, even under the ideal conditions considered here, i.e., no heterogeneous structure, no dispersion, and no scattering.

To account for the fact we do not observe a distinct main arrival due to an isolated noise source in our field data correlations and to approximate a more realistic scenario by considering an extended source region, we place a cluster of 50 isolated noise sources Southwest of Iceland, each with a random realisation

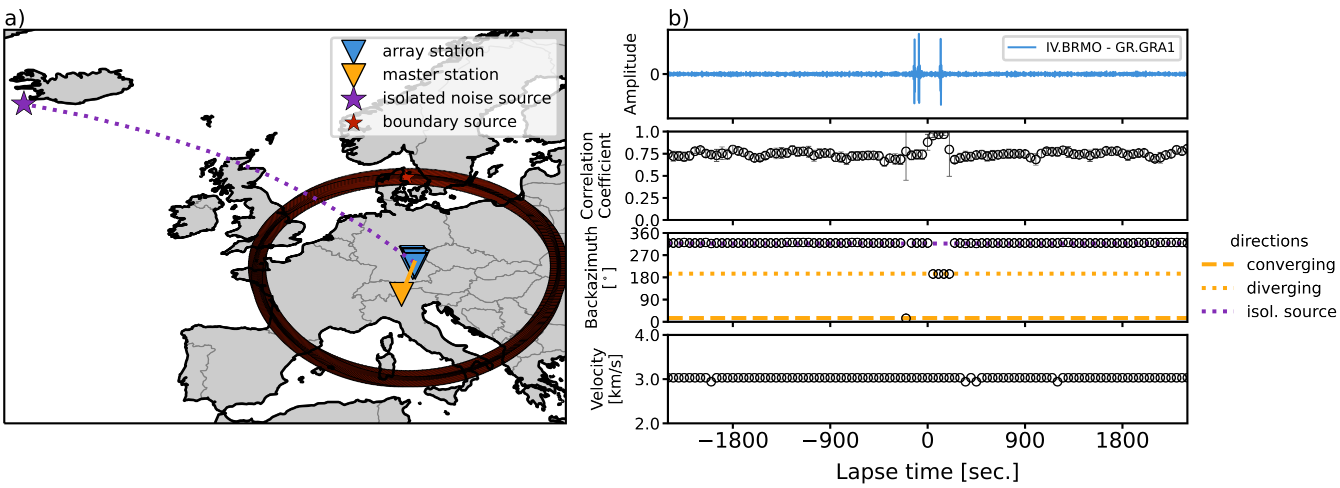

Figure 7 Same as Figure 5 but for secondary microseism source terms for both boundary and isolated sources. Both contributions to the correlation wavefield are scaled to have similar amplitudes. Distinct main arrival (the "spurious" arrival) of the isolated noise source at ~ -100 s lapse time. For this arrival and throughout the coda, direct waves from the isolated source are detected as most coherent.

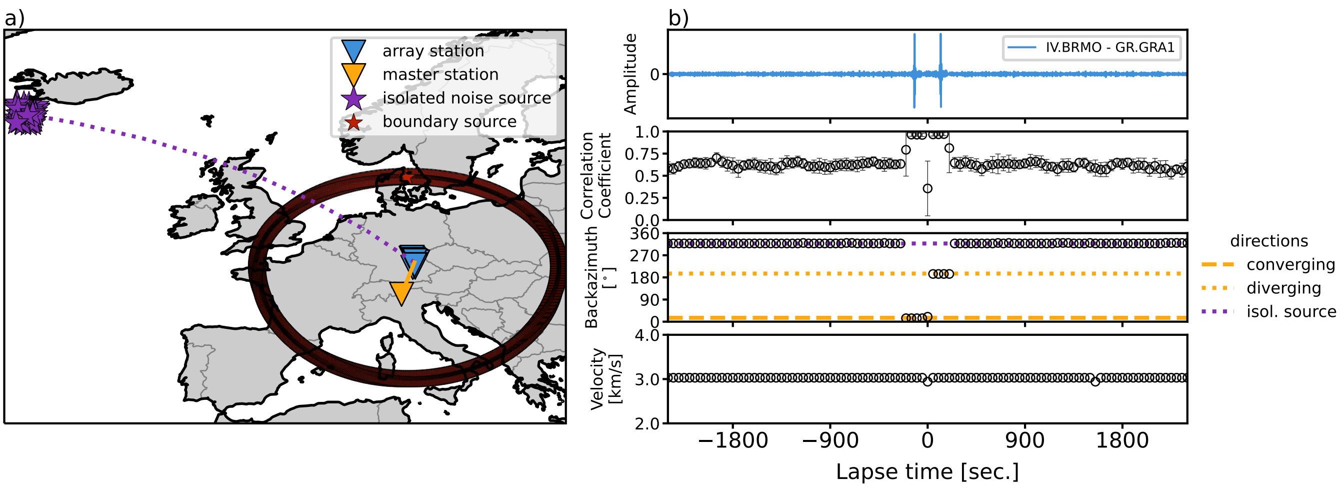

Figure 8 Same as Figure 7 but for a cluster of isolated sources. Amplitudes of the summed isolated noise source contribution is scaled to 1/10 of the boundary source contribution. No distinct spurious arrival but coda still dominated by repeating direct waves from the isolated noise source cluster.

of the source term $P(\theta, \phi)$ and repeat the computations (Fig. 8). The wavefield contributions of those isolated noise sources, where each isolated source produces an additional term in equation (2), interfere to mask the main arrival (Fig. 8b). The amplitudes of the summed isolated noise source cluster contribution is scaled to $1/10$ of the boundary source contribution. Beamforming correlation functions again detects the converging and diverging part of the boundary source contribution, as well as the isolated noise source cluster as dominant throughout the coda (Fig. 8b). Correlation coefficients with the beams stabilise at ~ 0.65 in the coda, and are lower than for the case of a single source (Fig. 7b).

Finally, we place a second cluster of 50 isolated noise sources Northwest of the Iberian Peninsula (Fig. 9a) to account for the observation that within the range of directions toward the Northern Atlantic, two distinct directions appear to dominate (Figs. 1, 2). Both clusters of isolated noise sources are treated separately and their combined amplitudes are again scaled to $1/10$ of the boundary source contribution. Beamforming detects either one of the clusters as dominant, seemingly randomly throughout lapse time (Fig. 9b). Mean correlation coefficients with the beams are ~ 0.55 throughout the coda. This numerical simulation produces beamforming results closely resembling the measurements on field data correlation functions (Figs. 1, 2) and confirms that clusters of isolated noise sources produce repeating direct waves.

5 Discussion

In this study, we observe repeating direct waves propagating from isolated noise sources in the coda of correlation functions. We reproduce the observations by numerical modelling of continuously acting isolated sources.

The most significant question our analysis raises is: are repeating direct waves from isolated noise sources

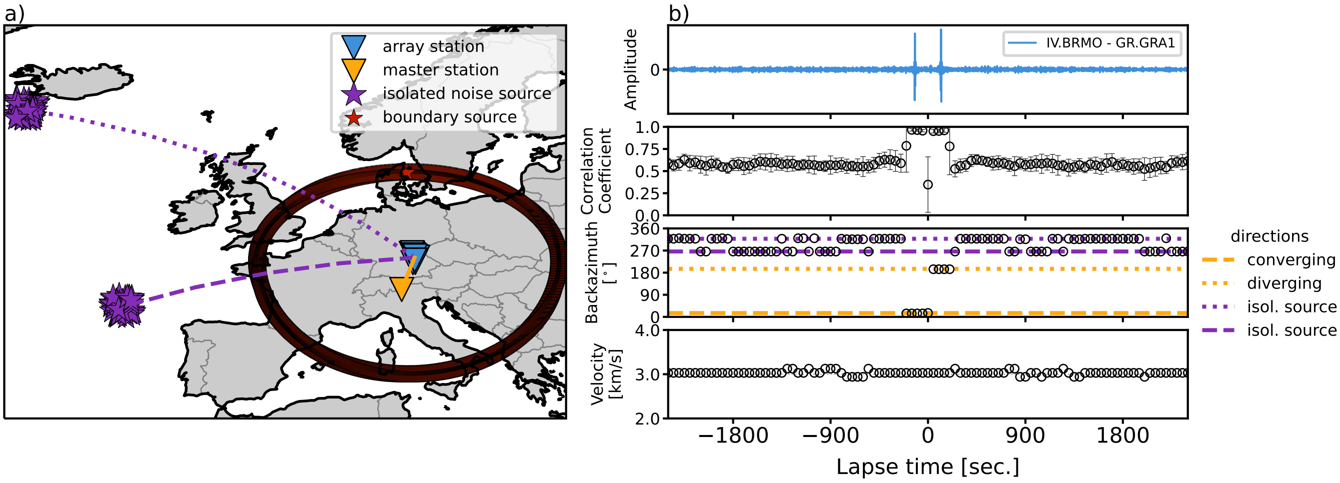

Figure 9 Same as Figure 8 but for two clusters of isolated noise sources. The additional cluster is placed Northwest of the Iberian Peninsula. The backazimuth to that cluster is indicated by a purple dashed line (a & b, third panel). Amplitudes of the isolated noise source contribution is scaled to $1/10$ of the boundary source contribution. No distinct spurious arrival. Beamforming detects either of the two clusters at a given lapse time in the coda as dominant.

more dominant than multiply scattered waves, originating from the master station, also for individual correlation functions? If they were, our observations would have far-reaching implications. Beamforming, however, only shows that the contribution by isolated noise sources is more coherent across an array of stations (Figs. 1, 2). It is not surprising that multiply scattered waves can be incoherent across an array. To address this aspect, we compute correlation coefficients of all correlation functions with the beam in each beamforming window. These reach 0.75 to 0.9 (never 1) for the expected stronger, coherent anti-causal arrival on field data correlations (Figs. 1, 2), which indicates that not all factors are accounted for during beamforming, namely heterogeneous structure, scattering, elastic wave propagation, and additional isolated sources. Still, these correlation coefficients provide a benchmark of what can be expected for the most coherent part of the correlation wavefield. In our numerical simulations, correlation coefficients are ~ 1 for the main arrivals without the interference of distinct spurious arrivals (Figs. 5, 7, 8, 9). Throughout the coda, we observe that correlation coefficients remain nearly constant for both the field data examples (~ 0.4, Figs. 1, 2) and the numerical simulations, decreasing with increasing complexity of the original wavefield from one isolated noise source (~ 0.75, Fig. 7), to a cluster of sources (~ 0.65, Fig. 8), to two clusters (~ 0.55, Fig. 9). Without taking into account the additional factors mentioned above (scattering, heterogeneous structure, or elastic waves), we reproduce a match between the modelled correlation functions and beams, comparable to the field data results. It is therefore reasonable to assume that the coda is not dominated by scattered waves, at least for absolute lapse times larger than a few hundred seconds.

At lapse times close to the direct arrivals from the master station (up to a few hundred seconds), correlation coefficients are higher than for the later coda and a transition to the stable regime observed in the later coda appears to manifest (Figs. 1, 2). In the early coda, scattered waves are likely dominant and thus also coherent in the correlation wavefield, although question arise about the degree of scattering. However, first tests on whether scattered waves are more coherent when the master station is much closer have shown no noticable difference in the beamforming results. The distinction between early coda and late coda arises, because amplitudes of the two correlation wavefield contributions decay for different reasons. Multiply scattered waves orginating from the master station decay due to attenuation during wave propagation, whereas repeating direct waves from isolated noise sources decay only due to correlation of the source term with itself through time (Figs. 3,6). As demonstrated above, even under ideal circumstances, amplitudes of repeating direct waves in correlation functions decay due to the finite length of the source and signal considered (Fig. 3).

In the later coda (absolute lapse times larger than a few hundred seconds), the commonly held assumption that the coda of a correlation wavefield is comprised dominantly, or even exclusively, of multiply scattered waves appears to be false. The beams pointing towards isolated noise sources represent a significant fraction of the correlation wavefield coda (Figs. 1, 2). Instead of spatially sampling the medium in a statistical manner (Margerin et al., 2016), the late coda, and thus measured velocity changes, may be dominantly sensitive to the path from the isolated noise source to the array station. Here, it is important to be clear about the nature of the coda and measurement principle. In the standard coda wave interferometry model, coda waves originate from the master station, are multiply scattered, and eventually reach the other receiver. A measured velocity change is then sensitive to this entire path. Because there is no clear way to know where exactly the wave has been and thus where the change has happened, recently developed coda wave sensitivity kernels are statistical descriptions of where the wave might have been, depending on the scattering properties of the medium (Margerin et al., 2016). However, if one would repeat the beamforming measurement described above, e.g., daily, to estimate the velocity of seismic waves in the coda, a potential velocity variation of those waves over time would have happened within the array, assuming constant sources. The standard coda wave interferometry measurement, in contrast, is performed on single correlation functions. If the measurement is performed in some part of the coda where repeating waves by isolated sources dominate, velocity variations may then be sensitive to the entire propagation path from isolated source to receiver, similar to the case where the coda is dominated by scattered waves and the sensitivity is along the path from master station to receiver. The difference here lies in the origin of the correlation wavefield contribution probed during the measurement and the ability to constrain the velocity change spatially. The main hypothesis in this paper is that the repeating waves we observe in beamforming originate from the isolated source, not the master station (Fig. 4).

A similar effect occurs in the presence of a strong nearby scatterer (van Dinther et al., 2021). As the multiply scattered part of the correlation wavefield reaches the strong scatterer, spatial sensitivity focuses along the path between stations and scatterer. In other words, the scatterer "emits" a direct wave, induced by the master station, that is recorded in the coda of the correlation function. This principle is similar to our considerations here, with the major difference that, in the modelling of van Dinther et al. (2021), the direct wave propagating from the scatterer originates from the master station. For isolated noise sources, direct waves originate from the source. The master station has no impact on the isolated source contribution to the correlation wavefield, as long as it coherently records the same isolated noise sources as the array stations, as the two field data examples suggest (Figs. 1, 2). We have no reason to suspect a strong scatterer to the West of the Gräfenberg array that could explain our measurements. Instead, our measurements are consistent with repeating direct waves from isolated noise sources, and reproduced by modelling without considering any scatterers. This means that different station pairs do not lead to different spatial sensitivity when recording such repeating direct waves. In some contexts, this may be advantageous by allowing repeated measurement of a repeating or continuous isolated source by considering multiple master stations. In the context of seismic monitoring of relative velocity variations, the impact of such sources has to be carefully considered.

The presence of repeating direct waves in the very late coda (30 minutes and more) furthermore challenges the common assumption that the very late coda of correlation wavefields is dominated by instrument noise and contains no useful signal. The very late coda is commonly used as a noise window for the estimation of signal-to-noise ratios of correlation functions, also for coda windows. We show that the very late coda does instead contain useful information, because repeating direct waves from isolated noise sources are still detected by beamforming (Figs. 1, 2). This also suggests amplitudes decay only slowly due to low correlation of the isolated source with itself over time (compared to Fig. 3), at least for the correlation wavefields investigated here, which were stacked over two years.

The early coda of correlation wavefields likely contains a significant contribution of scattered waves, as well as direct repeating waves from isolated noise sources. This suggests great care should be taken in measuring velocity variations and attributing them spatially also for the early coda. Common strategies to measure velocity variations, e.g., the stretching method (Lobkis and Weaver, 2003), assume that absolute timing delays increase with lapse time, because the seismic waves spent more time in the changed medium. For the contribution by repeating direct waves, stretching should not occur since absolute time delays are likely constant throughout the coda, as long as the isolated source does not change. A strategy that involves estimating the degree of stretching throughout the coda may give insight into the dominant regime (scattered waves vs. repeating waves) and whether the measurement approach is applicable. A different strategy to discriminate the correlation wavefield contributions may be to include measurements of wavefield gradients, which allow to separate the seismic wavefield using only single stations (Sollberger et al., 2023).

Further questions arise about the temporal sensitivity of measured velocity variations. When considering scattered waves in the coda, velocity variation measurements are usually attributed to the entire time window used for correlation, e.g, a single measurement that represents an entire day. Repeating direct waves from isolated noise sources should in principle allow to improve temporal resolution, because arrivals at different lapse times likely have different temporal sensitivity in raw signal time domain, i.e., at what points in time the raw signal was recorded. However, it is not immediately obvious what time exactly a specific repeated arrival is sensitive to. This is a target for future studies.

Pre-processing of seismic records before cross-correlation plays an important role when investigating cross correlations of ambient seismic noise. We apply spectral whitening, a commonly adopted pre-processing strategy (Bensen et al., 2007). Spectral whitening is the normalisation of the amplitude spectrum before cross-correlation, often with a water level or smoothed spectrum to avoid introducing artefacts. Whitening is often successful in suppressing the impact of near-monochromatic signals, e.g., in the context of the 26 s microseism in the Gulf of Guinea (Bensen et al., 2007; Bruland and Hadziioannou, 2023) or wind turbine noise (Schippkus et al., 2022). On the other hand, whitening will also emphasise signals with relatively low amplitude in the original data. To confirm that our interpretation of the results above is not significantly biased by the processing strategy, we repeat the measurements for master station IV.BRMO (Fig. 1) with temporal normalisation, both whitening and temporal normalisation, and neither pre-processing (Fig. 10). Temporal normalisation (running window average) is performed in a 5 s moving window. As long as any processing to stabilise the correlation functions is applied (Fig. 10a-c), the fundamental observation of repeating direct waves remains. Slight differ-

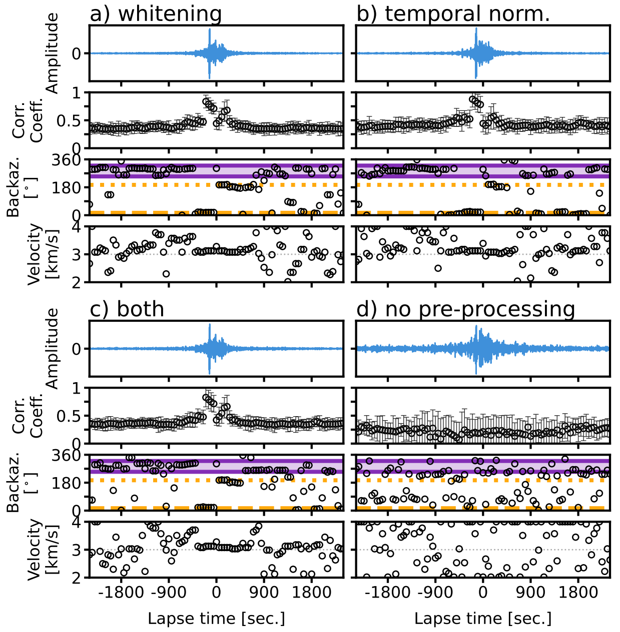

Figure 10 Impact of pre-processing scheme on the detection of repeating direct waves for master station IV.BRMO. a) Same as Figure 1b. b) Sample correlation function and beamforming result, if only temporal normalisation is applied. c) Results when both whitening and temporal normalisation are applied. d) Results when neither pre-processing is applied.

ences emerge in the correlation functions themselves, and also which direction and velocity are detected at a given lapse time. Temporal normalisation is commonly applied in studies that measure relative velocity variations, often in its most extreme version one-bit normalisation. Here we demonstrate that common pre-processing schemes produce correlation functions with repeating direct waves. Without any processing, however, results become unstable and beamforming neither detects stable directions of arrival nor gives consistent phase velocity estimates (Fig. 10d). Correlation functions are more stable after such pre-processing, as is commonly observed, because these approaches (in addition to addressing some data glitches) reduce the impact of certain isolated noise sources on the recorded wavefield, in particular from transient high-amplitude sources (e.g., earthquakes) and continuous near-monochromatic sources (e.g., machinery). The sources that remain as dominant, after this pre-processing is applied, are continuously acting broadband sources (e.g., ocean microseisms) as is confirmed by beamforming (Figs. 1 & 2).

The temporal stability of ocean microseism sources that we impose in our modelling has been observed on field data correlations before. Zeng and Ni (2010) computed and stacked correlations over one year that show clear spurious energy due to a localized microseism source in Japan. Similarly, Retailleau et al. (2017) found localized microseism sources off the coasts of Iceland and Ireland, also in correlations stacked over one year. It may be unintuitive that ocean microseisms, often assumed to be a largely random process, would show any coherence at all. These previous and our results are clear indications that indeed the secondary microseism mechanism generates coherent sources that are somewhat stable over time. We are, however, not aware of a microseism source model that incorporates all these factors satisfactorily. Instead, we follow the current standard formulation, i.e., each frequency is excited with random but constant phase (Gualtieri et al., 2020). Investigations on how varying temporal source stability and stacking influence the beamforming detections or measured velocity changes will likely be part of future work.

It may also be surprising that the highly idealised Earth model employed in our simulations, i.e., Green's functions in an acoustic homogeneous half-space, is sufficient to reproduce our observations on field data to first order. We do not take any elastic wave propagation effects such as scattering into account. This suggests that these effects certainly present in real Earth structure and thus field data may play a less important role than often thought, at least for the specific case investigated here: the nature of the coda of ambient noise correlations.

Machinery- or traffic-based monitoring of velocity variations is likely similarly affected by the findings in this study. Rotating machinery, such as generators in wind turbines (Friedrich et al., 2018; Schippkus et al., 2020; Nagel et al., 2021), likely have source terms that are significantly correlated throughout time due to their mechanism, with higher correlation than ocean microseisms. These sources could produce repeating direct waves with high amplitude. Traffic, e.g., trains repeatedly passing the same spot, resembles repeatedly acting noise sources (as in Fig. 3), although with more complex wavelets and longer intervals. In case of traffic at a regular interval, e.g., trains on a schedule, the late coda of the correlation wavefield could allow to extract their signature reliably. Recently, approaches that identify and select appropriate time windows to use for cross-correlation and subsequent velocity monitoring have emerged (e.g., Yates et al., 2022; Sheng et al., 2023). These approaches are motivated by the realisation that correlation wavefields can be highly complex and depend significantly on the presence of isolated noise sources, similar to this study. Still, our findings also have impact on these strategies. In time windows where an isolated noise source is known to be particularly active, repeating direct waves may still emerge and coincide with the coda of that source, depending on the source signature and length of time window considered for cross-correlation. Further investigations on this aspect may help improve the accuracy of detected velocity changes in time and space.

6 Conclusion

Continuously acting isolated noise sources generate repeating direct waves that may dominate the coda of correlation wavefields, as observed on field data correlations (Figs. 1, 2) and reproduced by numerical simulations (Figs. 3-9). In the simulations, we start from the established concept of an isolated noise source (Schippkus et al., 2022) that repeatedly excites a wavelet to illustrate the fundamental principle of how repeated direct waves emerge in correlation functions (Figs. 3, 5). To better reproduce the measurements on field data correlations, we model an isolated secondary microseism source, starting with one source (Fig. 7), which shows a distinct main arrival of that source (the "spurious arrival") that is not always observed clearly on field data correlations. With a cluster of isolated noise sources, mimicking an extended source region, this main arrival disappears due to interference between the sources (Fig. 8). Finally, we model two clusters to show that either may be detected at a given lapse time (Fig. 9), reliably reproducing the observations on our field data correlation wavefields (Figs. 1, 2). Throughout our modelling, we keep the numerical setup as simple as possible to emphasise the impact of only the isolated noise sources, i.e., we exclude any influence due to heterogeneous Earth structure, any elastic wave propagation effects such as multiple wave types or conversion between them, and importantly do not include any scattering.

Our results suggest that the coda of correlation wavefields should not be assumed to be mainly comprised of scattered waves, which originated from the master station. Instead, repeating direct waves from isolated noise sources may dominate. There is likely a transition in dominating regime from scattered waves (in the early coda) to repeating direct waves (in the late coda). This occurs, because amplitudes of scattered waves decay due to attenuation, whereas repeating direct waves decay slower only due to the auto-correlation of the source term throughout time. This has implications for ambient noise correlation based monitoring applications, commonly assuming multiply scattered waves, and raises questions about the validity of such measurements, in particular about the spatial sensitivity.

This study also opens up new opportunities for future research. In the presence of a continuously acting isolated noise source, the very late coda of correlation wavefields retains the source signature and is not dominated by instrument noise. This in principle allows to extract seismic waves repeatedly propagating along the same path, undisturbed by other contributions, which may be an attractive target for monitoring applications. The spatial distribution of isolated noise sources, however, severely limits the spatial sensitivity of the very late correlation wavefield coda.

Data Availability and Resources

This manuscript is fully reproducible. All computed correlation functions and code necessary to produce all figures are hosted on Github and Zenodo (Schippkus, 2023). Seismograms used in this study to compute correlation functions are provided by the network operators of the German Regional Seismic Network (GR, Federal Institute for Geosciences and Natural Resources, 1976), Polish Seismological Network (PL, Polish Academy of Sciences (PAN) Polskiej Akademii Nauk, 1990), and Italian National Seismic Network (IV, Istituto Nazionale di Geofisica e Vulcanologia (INGV), 2005). We rely on open-source software for our computations and visualisations (Hunter, 2007; Met Office, 2010; Krischer et al., 2015; Harris et al., 2020; Virtanen et al., 2020). Color sequences are designed to be accessible (Petroff, 2021).

Acknowledgements

The authors thank Joshua Russell and one anonymous reviewer for their insightful comments that helped improve the manuscript, as well as the handling editor Lise Retailleau. The authors acknowledge funding provided by the Emmy Noether program (HA7019/1-1) of the German Research Foundation (DFG). The authors acknowledge funding provided by the European Union's Horizon 2020 research and innovation programme under the Marie Skłodowska-Curie grant agreement No. 955515 (SPIN ITN).

References

Bensen, G. D., Ritzwoller, M. H., Barmin, M. P., Levshin, A. L., Lin, F., Moschetti, M. P., Shapiro, N. M., and Yang, Y. Processing Seismic Ambient Noise Data to Obtain Reliable Broad-Band Surface Wave Dispersion Measurements. *Geophysical Journal International*, 169(3):1239–1260, June 2007. doi: 10.1111/j.1365-246X.2007.03374.x.

Bruland, C. and Hadziioannou, C. Gliding Tremors Associated with the 26 Second Microseism in the Gulf of Guinea. *Communications Earth & Environment*, 4(1):1–9, May 2023. doi: 10.1038/s43247-023-00837-y.

Chevrot, S., Sylvander, M., Benahmed, S., Ponsolles, C., Lefèvre, J. M., and Paradis, D. Source Locations of Secondary Microseisms in Western Europe: Evidence for Both Coastal and Pelagic Sources. *Journal of Geophysical Research: Solid Earth*, 112(B11), Nov. 2007. doi: 10.1029/2007JB005059.

Federal Institute for Geosciences and Natural Resources. German Regional Seismic Network (GRSN), 1976.

Friedrich, A., Krüger, F., Klinge, K., and 1998. Ocean-Generated Microseismic Noise Located with the Gräfenberg Array. *Journal of Seismology*, 2:47–64, 1998. doi: 10.1023/A:1009788904007.

Friedrich, T., Zieger, T., Forbriger, T., and Ritter, J. R. R. Locating Wind Farms by Seismic Interferometry and Migration. *Journal of Seismology*, 22(6):1469–1483, Nov. 2018. doi: 10.1007/s10950-018-9779-0.

Gouédard, P., Stehly, L., Brenguier, F., Campillo, M., Colin de Verdière, Y., Larose, E., Margerin, L., Roux, P., Sánchez-Sesma, F. J., Shapiro, N. M., and Weaver, R. L. Cross-Correlation of Random Fields: Mathematical Approach and Applications. *Geophysical Prospecting*, 56(3):375–393, 2008. doi: 10.1111/j.1365-2478.2007.00684.x.

Gualtieri, L., Bachmann, E., Simons, F. J., and Tromp, J. The Origin of Secondary Microseism Love Waves. *Proceedings of the National Academy of Sciences of the United States of America*, 117 (47):29504–29511, Nov. 2020. doi: 10.1073/pnas.2013806117.

Hadziioannou, C., Larose, E., Coutant, O., Roux, P., and Campillo, M. Stability of Monitoring Weak Changes in Multiply Scattering Media with Ambient Noise Correlation: Laboratory Experiments. *The Journal of the Acoustical Society of America*, 125(6): 3688–3695, June 2009. doi: 10.1121/1.3125345.

Harris, C. R., Millman, K. J., van der Walt, S. J., Gommers, R., Virtanen, P., Cournapeau, D., Wieser, E., Taylor, J., Berg, S., Smith, N. J., Kern, R., Picus, M., Hoyer, S., van Kerkwijk, M. H., Brett, M., Haldane, A., del Río, J. F., Wiebe, M., Peterson, P., Gérard-Marchant, P., Sheppard, K., Reddy, T., Weckesser, W., Abbasi, H., Gohlke, C., and Oliphant, T. E. Array Programming with NumPy. *Nature*, 585(7825):357–362, Sept. 2020. doi: 10.1038/s41586-020-2649-2.

Hunter, J. D. Matplotlib: A 2D Graphics Environment. *Computing in Science & Engineering*, 9(3):90–95, 2007. doi: 10.1109/MCSE.2007.55.

Istituto Nazionale di Geofisica e Vulcanologia (INGV). Rete Sismica Nazionale (RSN), 2005.

Juretzek, C. and Hadziioannou, C. Where Do Ocean Microseisms Come from? A Study of Love-to-Rayleigh Wave Ratios. *Journal of Geophysical Research: Solid Earth*, 121(9):6741–6756, Sept. 2016. doi: 10.1002/2016JB013017.

Krischer, L., Megies, T., Barsch, R., Beyreuther, M., Lecocq, T., Caudron, C., and Wassermann, J. ObsPy: A Bridge for Seismology into the Scientific Python Ecosystem. *Computational Science & Discovery*, 8(014003), Jan. 2015. doi: 10.1088/1749-4699/8/1/014003.

Lobkis, O. I. and Weaver, R. L. Coda-Wave Interferometry in Finite Solids: Recovery of P -to- S Conversion Rates in an Elastodynamic Billiard. *Physical Review Letters*, 90(25):254302, June 2003. doi: 10.1103/PhysRevLett.90.254302.

Lu, Y., Stehly, L., Paul, A., and the AlpArray Working Group. High-Resolution Surface Wave Tomography of the European Crust and Uppermost Mantle from Ambient Seismic Noise. *Geophysical Journal International*, 214(2):1136–1150, May 2018. doi: 10.1093/gji/ggy188.

Mao, S., Lecointre, A., van der Hilst, R. D., and Campillo, M. Space-Time Monitoring of Groundwater Fluctuations with Passive Seismic Interferometry. *Nature Communications*, 13(1): 4643, Aug. 2022. doi: 10.1038/s41467-022-32194-3.

Margerin, L., Planès, T., Mayor, J., and Calvet, M. Sensitivity Kernels for Coda-Wave Interferometry and Scattering Tomography: Theory and Numerical Evaluation in Two-Dimensional Anisotropically Scattering Media. *Geophysical Journal International*, 204(1):650–666, Jan. 2016. doi: 10.1093/gji/ggv470.

Met Office. *Cartopy: A Cartographic Python Library with a Matplotlib Interface*. Exeter, Devon, 2010.

Nagel, S., Zieger, T., Luhmann, B., Knödel, P., Ritter, J., and Ummenhofer, T. Ground Motions Induced by Wind Turbines. *Civil Engineering Design*, 3(3):73–86, 2021. doi: 10.1002/cend.202100015.

Obermann, A., Froment, B., Campillo, M., Larose, E., Planès, T., Valette, B., Chen, J. H., and Liu, Q. Y. Seismic Noise Correlations to Image Structural and Mechanical Changes Associated with the Mw 7.9 2008 Wenchuan Earthquake. *Journal of Geophysical Research: Solid Earth*, 119(4):3155–3168, Apr. 2014. doi: 10.1002/2013JB010932.

Petroff, M. A. Accessible Color Sequences for Data Visualization. July 2021. doi: 10.48550/arXiv.2107.02270.

Planès, T., Larose, E., Margerin, L., Rossetto, V., and Sens-Schönfelder, C. Decorrelation and Phase-Shift of Coda Waves Induced by Local Changes: Multiple Scattering Approach and Numerical Validation. *Waves in Random and Complex Media*, 24 (2):99–125, Apr. 2014. doi: 10.1080/17455030.2014.880821.

Polish Academy of Sciences (PAN) Polskiej Akademii Nauk. Polish Seismological Network, 1990.

Retailleau, L., Boué, P., Stehly, L., and Campillo, M. Locating Microseism Sources Using Spurious Arrivals in Intercontinental Noise Correlations. *Journal of Geophysical Research: Solid Earth*, 122 (10):8107–8120, 2017. doi: 10.1002/2017JB014593.

Rost, S. and Thomas, C. Array Seismology: Methods and Applications. *Reviews of Geophysics*, 40(3):2–1–2–27, 2002. doi: 10.1029/2000RG000100.

Schippkus, S. Schipp/Repeating_direct_waves. Sept. 2023. doi: 10.5281/zenodo.7643286.

Schippkus, S., Zigone, D., Bokelmann, G. H. R., and the AlpArray Working Group. Ambient-Noise Tomography of the Wider Vienna Basin Region. *Geophysical Journal International*, 215(1): 102–117, June 2018. doi: 10.1093/gji/ggy259.

Schippkus, S., Garden, M., and Bokelmann, G. Characteristics of the Ambient Seismic Field on a Large-N Seismic Array in the Vienna Basin. *Seismological Research Letters*, 91(5):2803–2816, July 2020. doi: 10.1785/0220200153.

Schippkus, S., Snieder, R., and Hadziioannou, C. Seismic Interferometry in the Presence of an Isolated Noise Source. *Seismica*, 1 (1), Dec. 2022. doi: 10.26443/seismica.v1i1.195.

Sens-Schönfelder, C. and Larose, E. Lunar Noise Correlation, Imaging and Monitoring. *Earthquake Science*, 23(5):519–530, Oct. 2010. doi: 10.1007/s11589-010-0750-6.

Sheng, Y., Mordret, A., Brenguier, F., Boué, P., Vernon, F., Takeda, T., Aoki, Y., Taira, T., and Ben-Zion, Y. Seeking Repeating Anthropogenic Seismic Sources: Implications for Seismic Velocity Monitoring at Fault Zones. *Journal of Geophysical Research: Solid Earth*, 128(1), Jan. 2023. doi: 10.1029/2022JB024725.

Snieder, R., Wapenaar, K., and Larner, K. Spurious Multiples in Seismic Interferometry of Primaries. *GEOPHYSICS*, 71(4): SI111–SI124, July 2006. doi: 10.1190/1.2211507.

Soergel, D., Pedersen, H. A., Bodin, T., Paul, A., Stehly, L., AlpArray Working Group, Hetényi, G., Abreu, R., Allegretti, I., Apoloner, M.-T., Aubert, C., Bes De Berc, M., Bokelmann, G., Brunel, D., Capello, M., Cărman, M., Cavaliere, A., Chèze, J., Chiarabba, C., Clinton, J., Cougoulat, G., Crawford, W., Cristiano, L., Czifra, T., D'Alema, E., Danesi, S., Daniel, R., Dasović, I., Deschamps, A., Dessa, J.-X., Doubre, C., and Egdorf, S. Bayesian Analysis of Azimuthal Anisotropy in the Alpine Lithosphere from Beamforming of Ambient Noise Cross-Correlations. *Geophysical Journal International*, 232(1):429–450, Sept. 2022. doi: 10.1093/gji/ggac349.

Sollberger, D., Bradley, N., Edme, P., and Robertsson, J. O. A. Efficient Wave Type Fingerprinting and Filtering by Six-Component Polarization Analysis. *Geophysical Journal International*, 234(1): 25–39, Feb. 2023. doi: 10.1093/gji/ggad071.

van Dinther, C., Margerin, L., and Campillo, M. Implications of Laterally Varying Scattering Properties for Subsurface Monitoring With Coda Wave Sensitivity Kernels: Application to Volcanic and Fault Zone Setting. *Journal of Geophysical Research: Solid Earth*, 126(12), Dec. 2021. doi: 10.1029/2021JB022554.

Virtanen, P., Gommers, R., Oliphant, T. E., Haberland, M., Reddy, T., Cournapeau, D., Burovski, E., Peterson, P., Weckesser, W., Bright, J., van der Walt, S. J., Brett, M., Wilson, J., Millman, K. J., Mayorov, N., Nelson, A. R. J., Jones, E., Kern, R., Larson, E., Carey, C. J., Polat, İ., Feng, Y., Moore, E. W., VanderPlas, J., Laxalde, D., Perktold, J., Cimrman, R., Henriksen, I., Quintero, E. A., Harris, C. R., Archibald, A. M., Ribeiro, A. H., Pedregosa, F., van Mulbregt, P., and SciPy 1.0 Contributors. SciPy 1.0: Fundamental Algorithms for Scientific Computing in Python. *Nature Methods*, 17:261–272, 2020. doi: 10.1038/s41592-019-0686-2.

Wapenaar, K., Fokkema, J., and Snieder, R. Retrieving the Green's Function in an Open System by Cross Correlation: A Comparison of Approaches (L). *The Journal of the Acoustical Society of America*, 118(5):2783–2786, Nov. 2005. doi: 10.1121/1.2046847.

Wegler, U. and Sens-Schönfelder, C. Fault Zone Monitoring with Passive Image Interferometry. *Geophysical Journal International*, 168(3):1029–1033, Mar. 2007. doi: 10.1111/j.1365-246X.2006.03284.x.

Yates, A., Caudron, C., Lesage, P., Mordret, A., Lecocq, T., and Soubestre, J. Assessing Similarity in Continuous Seismic Cross-Correlation Functions Using Hierarchical Clustering: Application to Ruapehu and Piton de La Fournaise Volcanoes. *Geophysical Journal International*, 233(1):472–489, Nov. 2022. doi: 10.1093/gji/ggac469.

Zeng, X. and Ni, S. A Persistent Localized Microseismic Source near the Kyushu Island, Japan. *Geophysical Research Letters*, 37(24), 2010. doi: 10.1029/2010GL045774.

doi:10.26443/seismica.v2i2.498

SEISMICA

Inferring rock strength and fault activation from high-resolution *in situ* V_p/V_s estimates surrounding induced earthquake clusters

M.P. Roth * [1], **A. Verdecchia** [1], **R.M. Harrington** [1], **Y. Liu** [2]

[1]Institute of Geology, Mineralogy and Geophysics, Ruhr University Bochum, Bochum, Germany, [2]Department of Earth and Planetary Sciences, McGill University, Montréal, Québec, Canada

Author contributions: *Conceptualization* M.P. Roth, A. Verdecchia. *Software* M.P. Roth. *Formal Analysis* M.P. Roth, A. Verdecchia. *Writing - original draft* M.P. Roth, A. Verdecchia. *Writing - Review & Editing* R.M. Harrington, Y. Liu. *Visualization* M.P. Roth, A. Verdecchia. *Funding acquisition* R.M. Harrington, Y. Liu.

Production Editor: Gareth Funning
Handling Editor: Atalay Ayele Wondem
Copy & Layout Editor: Anant Hariharan

Received: March 16th, 2023
Accepted: September 13th, 2023
Published: November 15th, 2023

Abstract Fluid injection/extraction activity related to hydraulic fracturing can induce earthquakes. Common mechanisms attributed to induced earthquakes include elevated pore pressure, poroelastic stress change, and fault loading through aseismic slip. However, their relative influence is still an open question. Estimating subsurface rock properties, such as pore pressure distribution, crack density, and fracture geometry can help quantify the causal relationship between fluid-rock interaction and fault activation. Inferring rock properties by means of indirect measurement may be a viable strategy to help identify weak structures susceptible to failure in regions where increased seismicity correlates with industrial activity, such as the Western Canada Sedimentary Basin. Here we present *in situ* estimates of V_p/V_s for 34 induced earthquake clusters in the Kiskatinaw area in northeast British Columbia. We estimate significant changes of up to $\pm$4.5% for nine clusters generally associated with areas of high injection volume. Predominantly small spatiotemporal V_p/V_s variations suggest pore pressure increase plays a secondary role in initiating earthquakes. In contrast, computational rock mechanical models that invoke a decreasing fracture aspect ratio and increasing fluid content in a fluid-saturated porous medium that are consistent with the treatment pressure history better explain the observations.

Non-technical summary The number of hydraulic-fracturing-induced earthquakes in Western Canada has risen significantly in the last two decades. Common mechanisms used to explain induced earthquakes include pore-pressure changes, stress changes in the rocks into which fluids are injected/extracted, and loading from slowly creeping faults near injection sites. One way to help identify causes of human-induced earthquakes is to measure changes in rock properties near injection wells, such as pressure increases, crack density, and crack shape. Here, we estimate such properties and their spatiotemporal changes by proxy using earthquake-wave velocity ratios. In combination with rock-mechanical models, we interpret mechanisms for changes in fault strength that can lead to earthquakes. Our results show predominantly small spatiotemporal variations in a total of 34 induced earthquake clusters that are inconsistent with the broad pore-pressure changes that are commonly used to explain induced earthquakes. We perform rock-mechanical modeling that provides a more consistent explanation for changes in rock properties. Our models suggest that the increasing fluid volume and increasingly narrow cracks in rocks near hydraulic fracturing treatment wells can alter rock strength in ways that are both consistent with rates and observed properties of earthquakes.

1 Introduction

Industrial subsurface operations that inject or extract fluid can activate fault slip that leads to felt seismicity. The triggering mechanisms most commonly invoked to explain induced fault activation include pore-pressure increases, poroelastic stress changes, and/or fault loading due to aseismic slip (e.g., Igonin et al., 2021; Schultz et al., 2020; Eyre et al., 2019). The relative importance of such mechanisms (and their relevant length scales) is still an open question that may be better answered with reliable estimates of subsurface rock mechanical properties, such as crack density and fluid-pressure distribution. For example, accelerated fluid diffusion driven by pore-pressure gradients resulting from sudden changes in porosity and permeability usually occur over relatively small length scales (Yu et al., 2019; Goebel and Brodsky, 2018). In contrast, elastic stress changes can surpass pressure perturbations at larger distances (e.g., Goebel et al., 2017; Keranen and Weingarten, 2018) where fluid flow plays a secondary role. Similarly, aseismic slip, i.e., creep along a stable fault segment, can outpace the pore pressure diffusion front and initiate rupture at an unstable fault segment (Bhattacharya and Viesca, 2019).

Sites where fluid injection correlates with induced earthquakes present unique opportunities to study fault

*Corresponding author: marco.roth@rub.de

activation processes under the influence of fluid-rock interaction. For example, high-volume, low-pressure wastewater disposal targeting a shallow reservoir at ∼1.3 km in southern Kansas induces earthquakes in basement layers at depths of 2-6 km. Some work suggests the combination of pore-pressure increase along permeable, basement-rooted faults and earthquake-earthquake interaction driven by coseismic static stress changes to be the leading mechanism for fault (re)activation (Cochran et al., 2018; Peterie et al., 2018; Verdecchia et al., 2021). In Oklahoma, Goebel et al. (2017) observed that pore-pressure increases and poroelastic stress changes played dominant roles in inducing earthquakes both proximal and distal to wells, respectively. In contrast, injection at hydraulic fracturing (HF) sites employs low fluid volume and high pressure relative to wastewater disposal in order to enhance hydraulic diffusivity in low-permeability reservoirs. Despite lower relative injection volume, the major oil and gas-bearing formations in the Western Canada Sedimentary Basin (WCSB) in northeast British Columbia and western Alberta commonly experience small (M<3) to occasionally moderate-sized (M∼4.5) injection-induced earthquakes (Atkinson et al., 2016). For example, the Kiskatinaw area (covering part of the Montney Formation) is one of the largest unconventional shale gas plays within the WCSB. Here, HF stimulation of the target formation at ∼2 km depth has induced several M 4+ earthquakes, including a M_w 4.6 on 17 August 2015 near Fort St. John (Babaie Mahani et al., 2017; Wang et al., 2020, 2021), a M_w 4.2 (M_L 4.5) on 30 November 2018 in the Kiskatinaw area (Babaie Mahani et al., 2019; Peña Castro et al., 2020), and a M_L 4.2 on 12 November 2022 near Fort St. John (Natural Resources Canada, 2023). The large distances over which comparatively small fluid-injection volumes induced M > 4 earthquakes on short time scales are puzzling. The low permeability of stimulated rock units implies that elevated pore pressure brought on by fluid diffusion is not the main stress-perturbation mechanism to activate faults. Recent modeling and observational work suggests that aseismic slip may also play a role in inducing some of the M 4+ events in the region (Guglielmi et al., 2015; Eyre et al., 2019; Yu et al., 2021). One fundamental step to identifying plausible mechanisms that are most consistent with observations of earthquake occurrence is through detailed studies of rock properties.

Lithology and rock physical properties can help delineate where pore pressure may be elevated, where fluid diffusivity properties may vary, and where rock strength may favor aseismic vs. seismic slip conditions. Specifically, lithology, crack density, fluid content, and/or fluid pressure, can induce measurable changes in rock properties, such as the compressional and shear wave velocities, V_p and V_s. Imaging the compressional-to-shear-wave velocity ratio, V_p/V_s, is therefore a meaningful tool for analyzing and interpreting fluid-related rock properties. In particular, several authors used V_p/V_s to infer changes in Poisson's ratio to detect the presence of fluid-filled cracks and quantify their properties (e.g., Zhao et al., 1996; Chevrot and van der Hilst, 2000; Takei, 2002). Other examples connect fluids in a rock volume to the weakness of the rock material. For instance, Yu et al. (2020) see a correlation between seismic attenuation and static stress drop for earthquakes at variable distances from the injection well. The authors conclude that higher seismic attenuation and a lower static stress-drop values proximal to injection sites result from higher fracture density and/or elevated pore pressure in the rock matrix (Worthington and Hudson, 2000) due to hydraulic stimulation. Similarly, Pimienta et al. (2018) observe anomalous V_p/V_s in subduction zones, which they interpret to result from zones of intense fracturing with high permeability ($> 10^{-16}$ m^2) and pore pressure.

In this study, we use seismological observations of HF-induced earthquakes to estimate the *in situ* V_p/V_s and use it as a proxy measurement of lithological properties and their relation to fluid injection. The term *in situ* in this context describes the localized damaged rock volume in which closely related earthquake pairs occur that are used to resolve V_p/V_s based on P- and S-arrival-time-differences within the pairs. The method was developed by Lin and Shearer (2007) and has been applied in various settings to document the spatiotemporal variation of V_p/V_s ratios within earthquake clusters, including sites with natural (Liu et al., 2023; Mesimeri et al., 2022; Lin and Shearer, 2021; Hsu et al., 2020) and induced seismicity (Lin, 2020). This work specifically aims to quantify the relative importance of rock damage and fluid pressure related to induced seismicity. To do so, we use continuous seismic records of 49 HF induced earthquake clusters in the Kiskatinaw area, British Columbia, Canada, between July 2017 and December 2020 to estimate *in situ* V_p/V_s ratios. We employ a method that compares differential travel times of co-located earthquakes to recover the V_p/V_s ratio of the source rock volume. We then compare our *in situ* estimates to grid values of a 3D velocity model for the complete time period in the study area. We show significant spatiotemporal variations of the *in situ* V_p/V_s ratio with respect to the underlying background model and discuss the reasons why the predominantly small spatiotemporal variations of V_p/V_s ratio do not point to a broad fluid-pressure increase. Namely, the lack of a broad change implies that pore-pressure increase is unlikely the leading triggering mechanism. Further, we compute the V_p/V_s ratio of an effective medium with varying crack aspect ratio and fluid volume content to infer the potential implications of fracture growth on rock strength. We show that the fracture/fluid evolution can explain the observed changes in V_p/V_s ratio and suggest an inverse correlation between seismicity rates and rock strength. The relative importance of aseismic vs. poroelastic triggering remains an open question due to a lack of direct evidence of aseismic slip.

2 Earthquake clusters and background velocity model

We use 8,731 earthquakes associated with HF operations in the Kiskatinaw area in the time period from 12 July 2017 to 31 December 2020 (updated from Roth et al.,

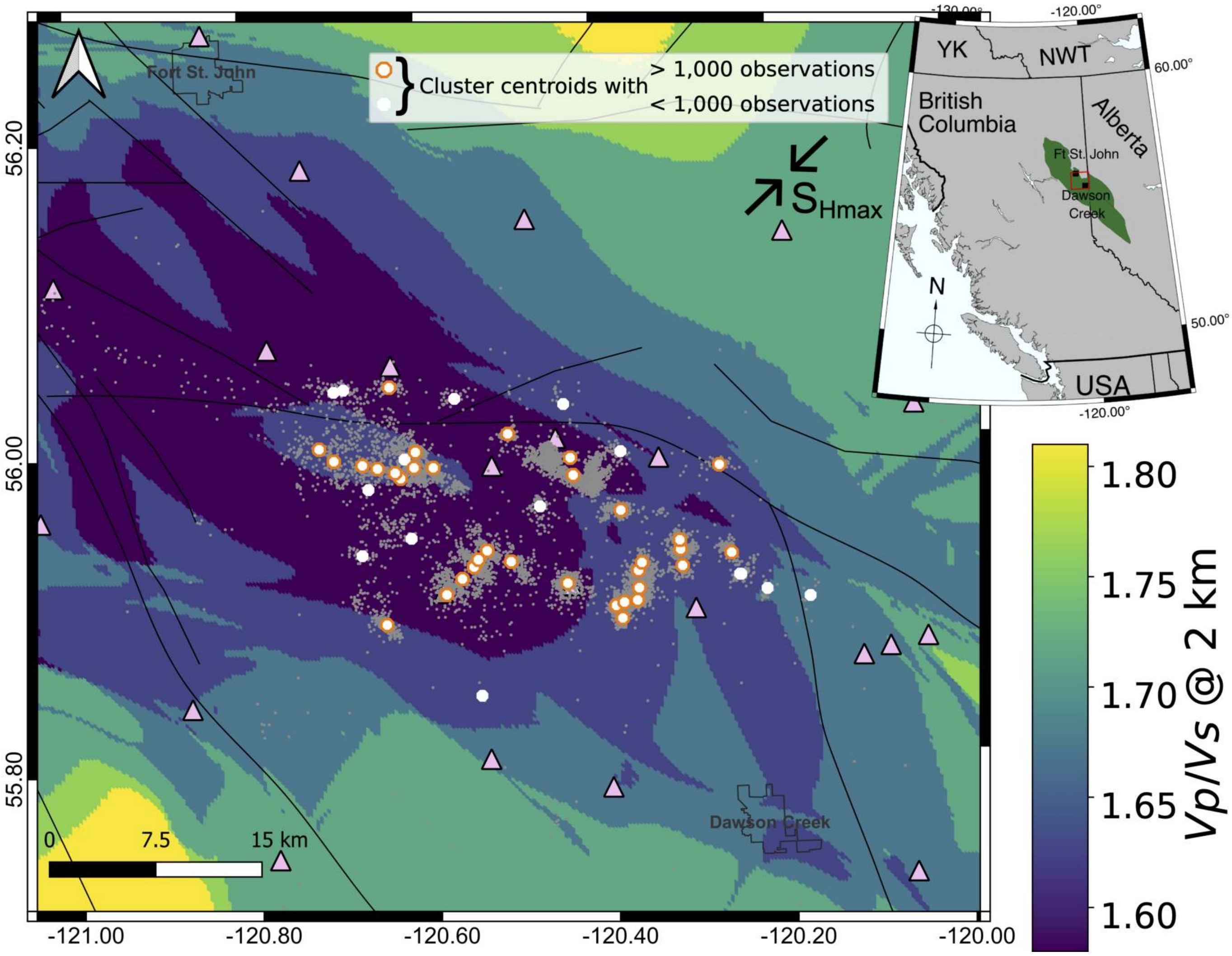

Figure 1 Overview of the Kiskatinaw area between Fort St. John (NW) and Dawson Creek (SE). Grey dots show 8,731 individual earthquake epicenters between 12 July 2017 to 31 December 2020. White dots show centroids of 49 spatiotemporally related earthquake clusters. Triangles denote seismic stations from networks XL, 1E, and PQ. Colorbar shows the starting model of V_p/V_s ratios at 2 km depth with mapped fault traces in black lines (Berger et al., 2009; Davies et al., 2018; Norgard, 1997). Estimates of regional S_{Hmax} are from Bell and Grasby (2012). Map inset shows the geographical extension of the Montney Formation (in green) and the Kiskatinaw area (red box). See Figure S1 for a detailed map of HF well locations and additional station information.

2020, Figure 1). The initial catalog results from an automated short-term average/long-term average (STA/LTA) trigger with analyst-reviewed phase arrivals. We refer to Roth et al. (2020) for details of the earthquake catalog development. The analysis here uses 25 broadband surface stations operated by McGill University, the Ruhr University Bochum, and Natural Resources Canada.

We define earthquake clusters in the group of 8,731 earthquakes analogous to Roth et al. (2020). First, we identify 32 time windows with at least four events on consecutive days. Second, we perform a waveform-similarity-based clustering approach within the time windows to identify spatial clustering. The two steps lead to classification of 49 event families, where each family is related to fluid injection in at least one HF well. Results from Roth et al. (2022) suggest that the clustered seismicity is related to the (re)activation of multiple optimally-oriented parallel left-lateral and strike-slip faults that are near the horizontal well trajectories of the respective HF wells. Unclustered seismicity exists as well, and is likely characterized by reverse-faulting mechanisms on deeper, isolated, and re-activated normal faults that were formed during the genesis of the Fort St. John graben system. The clustered events analysed here are therefore assumed to be associated with strike-slip faulting.

The method we use to estimate *in situ* V_p/V_s (described below) requires clustered seismicity. We describe changes of V_p/V_s using a reference 3D-velocity model calculated by Nanometrics Inc. The reference model is based on more than 100 compressional and 40 shear sonic logs, guided by 6 horizon top surfaces (Nanometrics Inc., 2020). The reference velocity model results from an optimization using a Particle Swarm Optimization method in an effort to obtain a smooth 3D model with an objective function weighted by phase residuals and event depth accuracy. It consists of estimates for V_p and V_s from which we calculate the V_p/V_s

ratios by element-wise division. As no error was reported for individual grid points, we apply a Gaussian error propagation with the assumption of 1.5% error per grid point (Supporting Information S1) and estimate an error of 2.12%, which is necessary for the high-resolution interpretation of the results. We note that the assumed uncertainty of 2.12% solely reflects the model error. The 140 sonic logs used to build the publicly available Nanometrics regional model do not enable resolving the velocity structure in high resolution or the geological structural complexity in the region.

3 Localized V_p/V_s estimation

The temporal and spatial proximity of individual earthquake clusters near wellbores (Figures 1, S1) allows focusing on the small rock volume affected by individual HF stimulation treatments. We adopt a method that compares the differential travel time differences of multiple inter-cluster earthquakes to recover the V_p/V_s ratio of the rock volume surrounding each cluster. We apply the method of Lin and Shearer (2007) that makes use of stationwise differential travel times between co-located event pairs with coincident ray paths, and removes the need to consider event origin times.

The method works by first considering that the differential S-wave travel time δt_s^i of an event pair is linearly related to the differential P-wave travel time δt_p^i per common station i by

$$\delta t_s^i = \left(\frac{V_p}{V_s}\right) \delta t_p^i + \delta t_0 \left(1 - \frac{V_p}{V_s}\right), \tag{1}$$

with δt_0 being the difference in origin times of the respective events. As the (4D-)origin information contains the sum of all errors, such as picking error, velocity-model uncertainty, and spatial errors, a cluster-wide, high-resolution method requires eliminating the absolute reference to temporal origin time information. To do so, Lin and Shearer (2007) establish a normalized version of Equation 1 by first calculating the mean values of the differential S- and P-times over all stations and then subtracting the normalized equation from Equation 1. The resulting equation relates the demeaned differential S-travel time ($\hat{\delta t}_s^i$) linearly to the P-travel times ($\hat{\delta t}_p^i$), by the coefficient V_p/V_s:

$$\hat{\delta t}_s^i = \left(\frac{V_p}{V_s}\right) \hat{\delta t}_p^i. \tag{2}$$

The V_p/V_s ratio as fitted in Equation 2 can be treated as a constant for each earthquake cluster, as long as the source-station distances are large compared to the hypocentral offsets among events in each cluster.

In addition, the P- and S-ray paths are assumed to have the same takeoff angles. As a final check on the suitability of the common ray-path assumption to the data set considered here, we compare the theoretical takeoff angles of direct P- and S-waves using TauP (Crotwell et al., 1999). We consider two sets of takeoff angles: (1) P- and S-angles for an individual event and (2) angles measured at hypothetical source-station distances of <5 km and >50 km for inter-event distances of 100 m. The hypothetical source-station distances reflect the observed range of source-station distances in our study area (Figure S2). We calculate arrivals using the IASP91 velocity model (Kennett and Engdahl, 1991). While P- and S-wave takeoff angles for shallow events (<2 km depth) at source-station distances of 5 to 50 km are approximately equal, the calculations show minor differences in takeoff angles on the order of $0.4°$ at source-station distances up to 5 km and inter-event distances of 100 m.

Liu et al. (2023) point out the importance of quality control criteria, which can have a major impact on the final V_p/V_s estimates. Our quality control procedure contains the following steps. We start with predefined event clusters based on waveform similarity detailed in Roth et al. (2020). We first identify time windows of consecutive days with a minimum of four events per day, and perform waveform-similarity clustering in each time window based on individual cross-correlation coefficients. Clusters are based on overall minimum correlation coefficients ranging from threshold values $\geq$ 0.6 up to 0.875. Next, we inspect the individual events in the defined clusters to remove potentially imprecise phase picks, i.e. erroneous phase arrivals, which result in perturbations to travel time curves. We do so by removing individual picks that deviate by more than 0.8 s or 2.5 s from predicted P- and S-wave arrival times based on constant velocities of 5.1 km/s and 2.9 km/s (comparable to the slope of the travel time curves in Figure S2), respectively. We note that the generally higher S-phase energy results in a more frequent cross-correlation correction of S-picks compared to P-phases, which have a lower signal-to-noise ratio. We then apply a cross-correlation-based picking correction to ensure that time-difference estimates come from exactly the same (relative) phase. We then further limit the calculation to stations with cross-correlation coefficients $>$ 0.8 for a given event pair to ensure the quality of the differential travel-time estimates, as even small deviations of the travel times from a linear travel time curve can lead to strong outliers (up to $\pm$0.15 s; Figure S2).

In the last steps of the quality-control procedure, we apply a hybrid L_1-L_2 fitting method (Huber, 1973, Figure S3) to automatically remove differential travel-time outliers that potentially bias numerical fitting. Initial analysis showed ambiguous V_p/V_s-ratio fits in the first analysis step for data sets with $<$ 300 observations (i.e., $\hat{\delta t}_s^i$ and $\hat{\delta t}_p^i$ observations per station among all event pairs). We therefore remove clusters with fewer than 300 observations to ensure robust fitting. The subsequent analysis step also initially showed uncertainties related to the number of observations. For example, clusters with $<$ 1,000 observations led to the lowest and highest estimates for V_p/V_s (Figure S4a) and the largest errors (Figure S4b). As a result, the relative difference between *in situ* estimates and the background model was initially largest for clusters with $<$ 1,000 observations (Figure S4c), suggesting a threshold of 1000 is required for robust observations. We therefore focus on clusters with $>$ 1,000 observations to eliminate any clear correlation between estimated V_p/V_s and the standard deviation of the fit (Figure S4d). Finally, we perform a least-squares minimization linear curve fitting with the remaining dataset with a fixed y-intercept of 0 and a range for the slope varying between 0.8 and 5 for conservative and flexible fitting limits. Figure 2 shows a representative example of the linear regression in $\hat{\delta t}_s$ vs. $\hat{\delta t}_p$ differential body wave travel time differences.

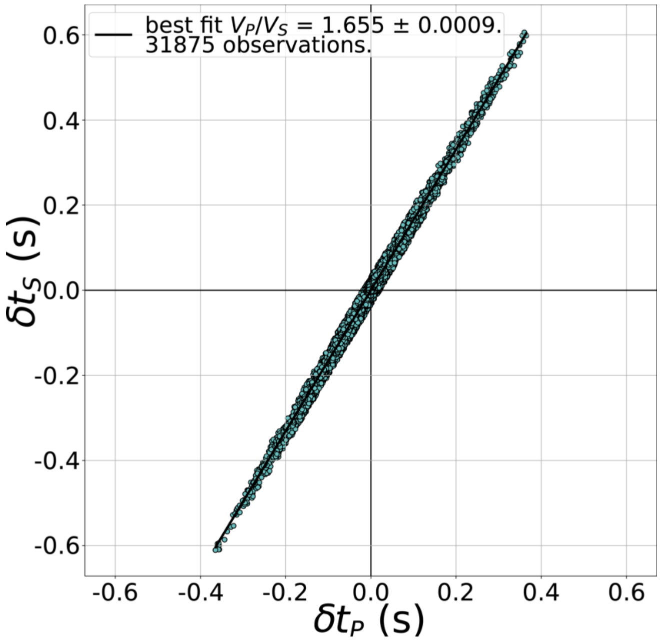

Figure 2 Representative example of a V_p/V_s ratio regression (black line) for one earthquake cluster. Each circle denotes the demeaned δt_s vs. δt_p differential travel time difference of one event pair recorded at a common station. The slope of the best-fit line returns the V_p/V_s estimate of the rock volume hosting the cluster as indicated in Equation 2.

4 V_p/V_s ratios of earthquake clusters

We estimate V_p/V_s ranging between 1.562 $\pm$ 0.0070 and 1.692 $\pm$ 0.0019 for a total of 34 clusters. The relative deviation of the *in situ* estimates with respect to the 3D background model varies between $\pm$4.5%. The two sections that follow first present the broad variation of V_p/V_s with respect to its spatiotemporal evolution and injected fluid volume (Figure 3) and then examine the evolution in more detail at an individual wellhead.

4.1 Broad spatiotemporal variations

Figure 3a shows the spatial variation of V_p/V_s changes normalized to the background value together with spatial variation of the injection volume (greyscale hexagons). Green and purple shaded dots show clusters with estimated increases and decreases of V_p/V_s relative to the background model, respectively. Figure 3b shows the relative variation of V_p/V_s along the NW-SE profile shown by the red dashed line in (a), as well as the time evolution in panel Figure 3(c) of the clusters. The dark, thicker vs. light, thinner green and purple shaded lines differentiate between significant and insignificant changes in V_p/V_s, respectively. (In other words, significance refers to a greater or less than 2.12% change from background and the linear regression, respectively; See Supporting Information S1 for further details). Out of the 34 clusters that pass the quality control criteria, 9 experience a significant V_p/V_s change, where 7 experience an increase, and 2 a decrease. The grey-shaded hexagons summarize the total injected fluid volume per HF wellhead within each hexagon in the time period from March 2013 to December 2020. We note that the injection history is reported from 2013 onward and the earthquake catalog starts in 2017. Figure 3a highlights four hexagons with injected fluid volume $>$ 1,000,000 m^3 that contain several cluster centroids (outlined in orange). It is noteworthy that all the highlighted areas experience a relative increase in V_p/V_s.

Figure 3 also shows 9 clusters with a relative V_p/V_s ratio change ranging between -1% and 1%, which we interpret as minor changes, despite their relative lower significance. We observe a moderate increase in V_p/V_s following fluid injection for 19 out of 34 clusters, and a moderate relative decrease for the remaining 6 clusters. The spatial distribution of estimates reveals a V_p/V_s ratio decrease that is concentrated primarily in the southeast part of the study area (Figure 3a-b).

The temporal evolution shown in Figure 3c suggests that the V_p/V_s ratio decreased relative to the starting model prior to ~May 2018 and was followed by a subsequent increase. However, we note that both the injection database and earthquake catalog do not cover the complete HF history of the study area. In addition, we do not see any change in V_p/V_s prior to and following the COVID-19 pandemic operational shutdown (Salvage and Eaton, 2021). As an independent check, we also use ambient seismic noise monitoring over the catalog time period to estimate background changes in the medium velocity (Lecocq et al., 2014). Figure S5 shows a change in $\delta v/v$ on the order of ± 0.05 % without clear temporal anomalies, consistent with an absence of significant V_p/V_s changes relative to the background model over time.

4.2 Variations at an individual wellhead

Earthquakes in the dataset generally follow a temporal migration in the direction of hydraulic fracturing stimulation (e.g. Roth et al., 2020). Seismicity typically begins in clusters near the end of a horizontal well (toe) and progressively migrates toward the vertical bending point (heel) of the horizontal well as stimulation proceeds. We examine the spatial migration pattern in further detail for a seismically active well with $>$ 100,000 observations (i.e., $\hat{\delta t}_s^i$ and $\hat{\delta t}_p^i$ estimates among all event pairs and stations) that occur between 12 March 2020 and 29 March 2020. We begin by first examining the two groups of wells with trajectories to the northwest and southeast of the wellhead, respectively. Figure 4 shows seven horizontal wells targeting the same shale layer at a depth of roughly 2.2 km. The high-resolution double-difference earthquake relocations show distinct clusters of seismicity centered around the three horizontal wells with southeastward trajectories (cyan box) and four horizontal wells with northwest trajectories (maroon box). Both clusters follow the timing of the stage

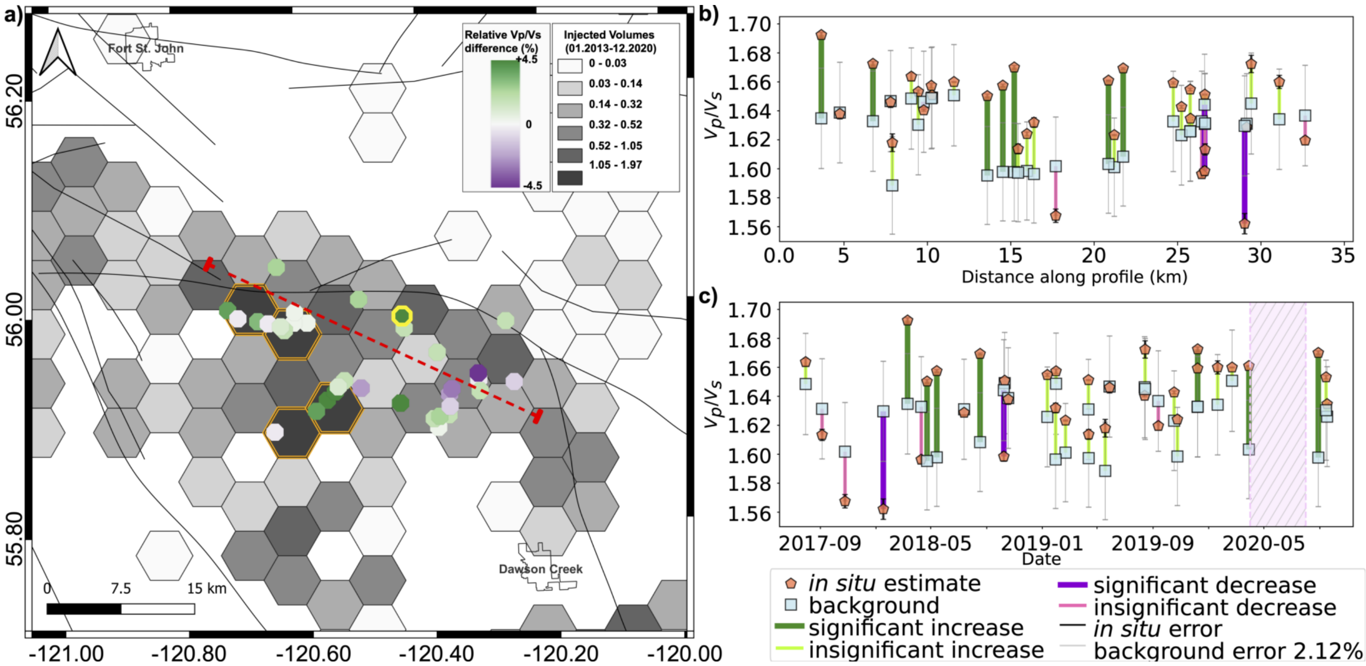

Figure 3 a) *In situ* V_p/V_s estimates per earthquake cluster relative to the reference model as in Figure 1. Green and purple show relative increases and decreases in V_p/V_s ratio relative to the background model, respectively. Greyscale shading is proportional to the total injection volume per HF wellhead within each hexagon from March 2013 to December 2020. The red line shows a profile along all clusters. The example cluster highlighted in yellow is further detailed in Figure 4. b) V_p/V_s estimates along the profile in a) from northwest (0 km) to southeast (37.07 km). Orange pentagons are *in situ* V_p/V_s estimates relative to the change in background value indicated by the light blue boxes. Green and purple shaded lines connecting the boxes highlight relative increases and decreases of V_p/V_s, respectively. Thick, dark lines describe significant changes that are larger than estimated errors and thin, light lines indicate changes that are within estimated errors. Black error bars are for the *in situ* V_p/V_s estimates, while grey error bars show the estimated 2.12% background model error (Section S1). c) Similar to b) but showing the temporal evolution during the catalog time period. The hatched, pink area shows the period of seismic quiescence due to suspension of HF operations (Salvage and Eaton, 2021) between April and August 2020.

stimulation. The southeast cluster exhibits a linear pattern that likely represents an activated structure that is several kilometers long. The northwest cluster (maroon box) contains multiple shorter, parallel lineations and a total of ~300 events.

We examine the northwest cluster (maroon box) in further detail by splitting the seismicity cluster into two subsets (Figure 4, red and blue tilted boxes). The choice of two subsets arises from a natural division between well-proximal ($<$ 200 m from a hydraulic-fracturing stage; Figure 4 (blue box)) and well-distal ($>$ 200 m; red box) events seen in the distribution of epicenters (Figure S7). There are 173 events in the 'proximal' subset (blue diagonal box), and 127 events in the 'distal' subset (red diagonal box). The individual V_p/V_s ratio regression fits for the two subsets are 1.648 ± 0.0009 (proximal) and 1.635 ± 0.0011 (distal).

We further examine the temporal variation within the northwestern seismicity cluster (Figure 4, larger maroon box). As the seismicity migration direction largely follows the direction of HF-stage stimulation and broadly follows the same timing, we divide the cluster into smaller subsets with similar timing. For example, Figure 5a-d shows the chronological division of 300 events in the northwestern cluster in Figure 4 (maroon box) into four equally sized groups of 67 to 68 events in non-overlapping windows. We note that applying quality control criteria removes certain event pairs and hence reduces the number of grouped events from the original 300 to 269. The temporal progression of estimated V_p/V_s values (Figure 5e) shows a slight initial decrease from the starting value of 1.653 (Figure 5a-b), followed by a steep decrease to a minimum of 1.590 (Figure 5c, corresponding to a total decrease of ~3.8%, comparable to the regional observed maximum of ± 4.5%). The V_p/V_s then rebounds to a comparable value of 1.631. The seemingly small absolute changes in V_p/V_s in the range of 0.06 are already significant with respect to reported values between 1.98 and 1.42 (Gregory, 1976), which were estimated for different types of consolidated sedimentary rocks with porosities ranging from 4.45% to 41.1%, water-air-saturation ratios ranging from 0% to 100%, and confining pressures ranging from 0 MPa to ~69 MPa. Figure S8 shows a consistent trend and similar V_p/V_s variation when testing variable event group sizes that range from three to six groups with 90 to 44 events per group, respectively. There are three additional clusters in the entire data set with $>$ 100,000 observations (Table S1, Figure S9), which include the southeast cluster in Figure 4 (cyan box). They exhibit similar temporal evolution with a minimum V_p/V_s in the intermediate HF stages.

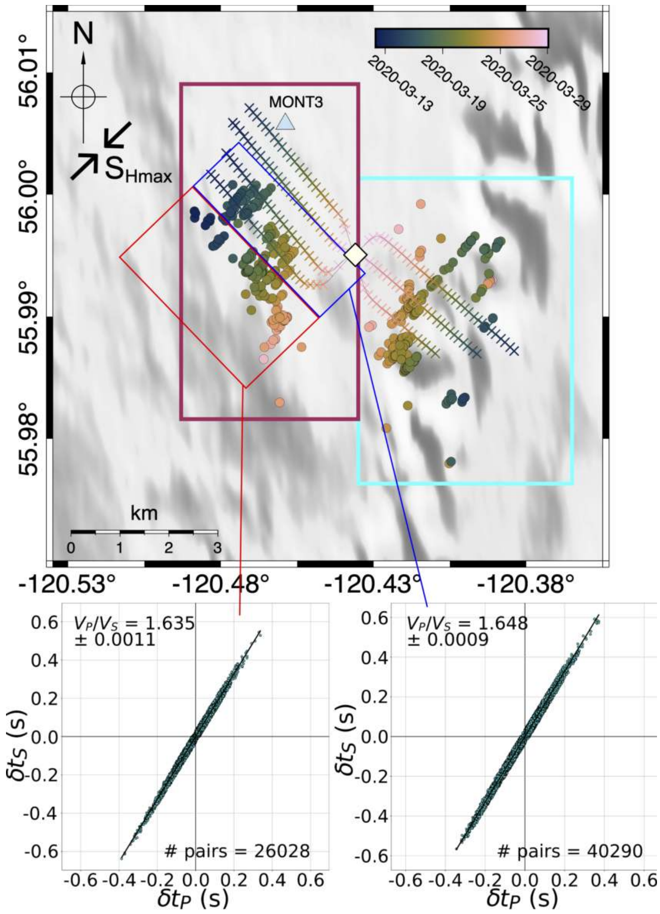

Figure 4 One example cluster from Figure 3a (outlined in yellow). High-resolution earthquake relocations show two distinct earthquake clusters near seven diametrically opposed well trajectories (lines) extending from a single wellhead (white diamond). Hatched lines on the well trajectories are individual HF injection stage locations with timing indicated by the colorbar. Earthquake epicenters (colored dots) have origin times marked by the same colorbar. The cyan and maroon boxes separate the southeastern and northwestern clusters, respectively. Blue and red boxes show subsets of the northwestern cluster described as HF-stage proximal (distance < 200 m) and distal (> 200 m), respectively (see text). The respective V_p/V_s ratio regression plots the two subsets shown below the map with each corresponding box color. Figure S6 shows the respective distribution of hypocentral depths.

5 Fracture evolution

In order to interpret the V_p/V_s estimates in the context of rock properties and fluid injection, we develop physical rock mechanics models to investigate the consistency with injection history. Specifically, we vary sets of material properties and elastic constants (e.g., bulk and shear modulus) in an effective medium to test their effects on the seismic wave velocities (related to an effective density) and the V_p/V_s ratio. An effective rock volume consists of a rock matrix and fluid-filled voids and cavities such as fractures and pores. Multiple physical properties, such as fluid fraction, elastic modulus of each medium component, and/or fracture geometry, control the elastic moduli of the effective porous medium. As the seismic body-wave velocities depend on the effective elastic moduli and rock densities, so will the V_p/V_s ratio. Hence, the increase or decrease of V_p/V_s will directly depend on fluid content and pore geometry (e.g., Takei, 2002; Brantut and David, 2019).

To explore the observed *in situ* V_p/V_s changes and their dependence on the rock matrix and resultant fluid content, we use a model with randomly oriented spheroidal, fully water-saturated pores. We model fluid content with porosity Φ and pore shape with the aspect ratio α, where $0 < \alpha \leq 1$. An aspect ratio of $\alpha = 1$ describes a sphere, where increasingly smaller values describe thin ellipsoids. We apply self-consistent estimates for bulk and shear moduli, K and μ, respectively, from Berryman (1980) to estimate V_p/V_s for an effective medium with aspect ratios ranging between $10^{-3} \leq \alpha \leq 1$ and fluid content ranging from $0 \leq \Phi \leq 0.2$. We use six iterations to numerically solve the self-consistent estimates (Figure S10). The model does not violate the (arithmetic) upper Voigt (Voigt, 1910) and lower Reuss boundaries (Reuss, 1929) and fulfills the Hashin-Shtrikman bounds (Hashin and Shtrikman, 1963) for isotropic, linear and elastic media for the most common geometries. We model the shale layers of the Montney Basin using $K = 35$ GPa and $\mu = 25$ GPa, which is in general agreement with global observations of shale reservoirs (Omovie and Castagna, 2020). We use $K = 2.2$ GPa and $\mu = 0$ GPa for the pore fluid and explore the model space of changes in V_p/V_s as a function of porosity and crack aspect ratio (see Figure S11).

We then combine the impact of both the aspect ratio and the fluid fraction (porosity) on the bulk and shear moduli (shown in Figure S11) into individually evolving trends to estimate the effective V_p/V_s based on the two moduli (Figure 6a). We allow the trends to vary in both aspect ratio and porosity in order to explore consistency scenarios with injection history and determine how the two free parameters might influence V_p/V_s evolution (Figure 6). The range of porosity/aspect ratio pairs can lead to highly varying V_p/V_s estimates. For illustration purposes, Figure 6a only displays values between 1.65 and 2.1 that cover the initial V_p/V_s values observed by Gregory (1976). Specifically, we explore four possible trajectories: (1) a large decrease in aspect ratio and a small increase in fluid content (Figure 6 orange lines, with $\log(\alpha)_{init} = -0.1$, $\log(\alpha)_{final} = -2.25$ and $\Phi_{init} = 0.01$, $\Phi_{final} = 0.02$), (2) a moderate decrease in aspect ratio and moderate increase in fluid content (Figure 6 beige lines, with $\log(\alpha)_{init} = -0.1$, $\log(\alpha)_{final} = -1.75$ and $\Phi_{init} = 0.01$, $\Phi_{final} = 0.05$), and (3) a small decrease in aspect ratio and large increase of fluid content (Figure 6 copper-colored lines, with $\log(\alpha)_{init} = -0.1$, $\log(\alpha)_{final} = -1.25$ and $\Phi_{init} = 0.01$, $\Phi_{final} = 0.15$), and (4) a segmented trajectory with an initial increase in fluid fraction and subsequent decrease in aspect ratio (Figure 6 red lines, with $\log(\alpha)_{init} = -0.1$, $\log(\alpha)_{final} = -1.15$ and $\Phi_{init} = 0.01$, $\Phi_{final} = 0.105$). Although the detailed geological well reports do not provide insights into the aspect ratio, the porosity of the Montney Formation is documented to be between 1% and 3%, where local differences of up to 5%+ can occur (BC-ER, 2023).

Figure 6a shows that V_p/V_s decreases slowly with de-

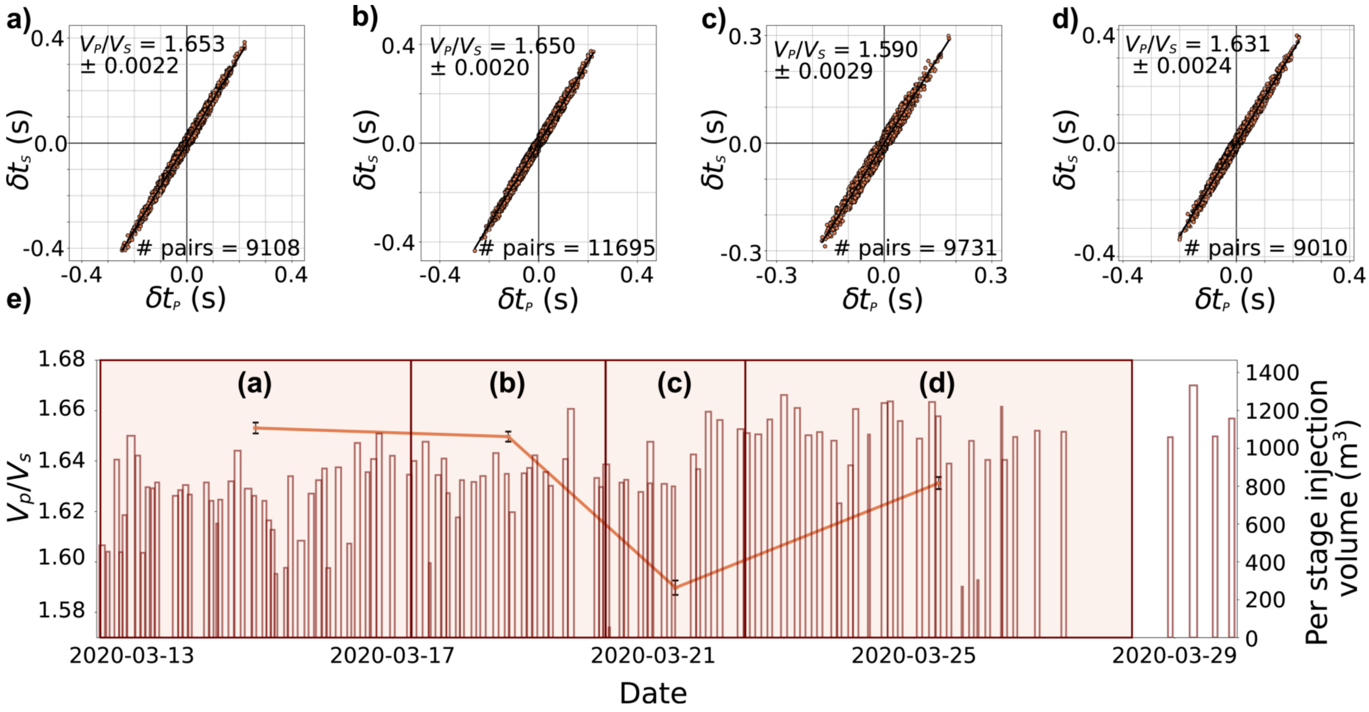

Figure 5 Temporal evolution of V_p/V_s ratios of the northwestern event cluster in Figure 4 (maroon box). a)-d) show equally-sized temporal groups of 67-68 events per group. e) shows the temporal V_p/V_s progression (orange line) along with the injected fluid volume per stage (red bars). Bright orange shading highlights the time period in which each successive temporal subset of earthquakes was active.

creasing aspect ratio and increasing porosity (fluid content) when aspect ratios are above values of α greater than $\sim$ 0.03-0.1 ($\log \alpha > -1.5$). The most significant V_p/V_s changes are exhibited at lower aspect ratios ($\alpha <\sim 0.03$-0.1), where V_p/V_s increases rapidly with decreasing aspect ratio and moderately increases with porosity. It is logical to assume that during HF-stimulation, fluid content first increases before fracture growth is promoted. Once significant fracture growth initiates, the fracture aspect ratio decreases as crack geometry becomes thin and elongated. The interplay and relative timing of the porosity increase and aspect ratio changes during HF-stimulation likely correspond to scenario #4, where a significant increase in fluid volume and porosity occurs first, followed by a rapid decrease in aspect ratio. The trajectory #4 in 6 (maroon line) would therefore correspond to an initial drop of V_p/V_s in the early to intermediate HF stages, followed by subsequent increases in V_p/V_s towards the end of HF stimulation. Scenario #4 is also most consistent with the data (blue line). We note that Figure 6 is not intended to precisely model the fluid-fracture evolution, but rather as a consistency check. It shows that in the scenario which most likely emulates porosity and aspect ratios during HF-stimulation, both effects of (i) decreasing fracture aspect ratios and (ii) increases in fluid fraction can lead to an initial decrease followed by an increase in V_p/V_s. In reality, the relative amplitudes of V_p/V_s decrease and increase, hence the overall change before and after a HF treatment, will depend on the exact fluid-rock mechanical property trajectory. Therefore, it is possible to observe bulk V_p/V_s decreases following fluid injection activity. It is important to note that the rock physical model shown in Figure 6 accounts for two-phase porous media with approximated estimates of elastic moduli and only one pore geometry. Nevertheless, the two-phase model is still able to capture the same spatial-temporal trend in observations.

6 Discussion

The following sections first describe how pore pressure variation can explain the role of fluids in the observed V_p/V_s changes and then discuss the implications of V_p/V_s changes in the context of injection history for earthquake triggering mechanisms. We will then compare our results to effective-medium models and rock physics analysis as a consistency check on our interpretations.

6.1 The impact of fluids on V_p/V_s

Lin (2020) applies the *in situ* V_p/V_s estimate methodology (Lin and Shearer, 2007) to induced seismicity. To the best of our knowledge, this study is the first to apply the method to a HF-induced seismicity setting. Although both settings involve fluid-injection, we see remarkable differences in the study sites. Our results point to neither systematic operationally-related increases nor decreases of V_p/V_s. On the contrary, Gritto and Jarpe (2014) found a positive correlation between increasing V_p/V_s and total injected water volume at the Geysers geothermal field. They conclude that V_p/V_s estimates can be interpreted to predict fluid saturation changes around injection wells. They found that long-term fluid injection led to an observed V_p/V_s increase of $\sim$ 6%. Lin (2020) observes a decrease in V_p/V_s accompanying the extraction of water at the Salton Sea geothermal field and subsequent increases in V_p/V_s as the reservoir replenishes. The long-term net fluid production at the Salton Sea geothermal field led to a decrease of up to ~7%, which is consistent with the above interpretations (Lin, 2020). By comparison, the V_p/V_s changes associated with short-term HF operation observed here are within -4% and 4.5%. However, at geothermal power plants, the driving mechanism for changes in V_p and V_s would be pore pressure variation, fluid diffusion, and/or fluid saturation. Assuming a saturated medium at seismogenic depths, an increase in fluid volume would cause a relative increase in V_p and decrease in V_s (e.g. Han and Batzle, 2004), leading to an absolute increase in V_p/V_s. For example, Winkler and Nur (1982) showed in laboratory measurements that the V_p/V_s ratio of fully saturated rock samples is higher compared to V_p/V_s ratios of partially (~90%) saturated or dry samples.

Another well-known mechanism to increase V_p/V_s is tensile fracture opening. Brantut and David (2019) describe that in a fully fluid-saturated setting, a fracture opening is equivalent to the reduction of confining pressure. Experimental data confirm an increase of V_p/V_s with decreasing confining pressure that occurs as the pore pressure inside fluid-filled cracks increases (Christensen, 1984). The scenario is in agreement with observations of Dawson et al. (1999) and McNutt (2005), who interpreted seismic tomographic images of high V_p/V_s zones at the Kilauea Caldera, Hawaii, to be either highly fractured material or the accumulation of partial melt. Similar to HF operations in this study, fracturing below the volcano might result from volumetric changes (tensile opening) while melt ascends (Schmid et al., 2022). Seismic events resulting from tensile fracture opening as a direct result of HF operations are most likely associated with microseismicity (M_w < 0; Eaton et al., 2014; Bohnhoff et al., 2009) aligned perpendicular to the direction of the minimum horizontal regional stress. The detailed relocations and fault plane solutions (where available) of seismicity in our study area suggest that the earthquakes with typical magnitudes of M_L > 0 occur primarily on (likely) reactivated, optimally-oriented strike-slip faults (Roth et al., 2020, 2022). Neither fluid saturation nor changes in confining pressure and/or fracture model fully describe the observed V_p/V_s ratio changes in the observations presented here.

Our results do not represent trends that have been observed from geothermal systems and/or fracture opening scenarios. Hence, we have to invoke more complex mechanisms and models that explain how HF operations can affect V_p/V_s. For example, Gosselin et al. (2020) and Wang et al. (2022) interpret V_p/V_s changes at the northern Cascadia and Hikurangi margins, respectively, with phases of fluid-pressure increase and dissipation caused by fault-valve behavior. HF treatments in Kiskatinaw in a fully fluid-saturated rock initiate tensile fracture growth near the stages that correspond to decreasing fracture aspect ratios and increasing fluid content. We explore various physical models of fluid-saturated rocks to infer how fracture growth affects rock strength. One fundamental assumption is that HF treatments (re)activate faults and modify the existing fractures (in addition to creating new ones). Figures 6a and S10 show our theoretical estimates of V_p/V_s for an effective fluid-saturated porous two-phase medium (a rock matrix and pore fluid) leading to variable V_p/V_s values when allowing the aspect ratio and fluid-saturated porosity to vary.

Figure S11 shows a relatively rapid decrease in shear modulus with increasing fluid content when aspect ratios are small. The shear modulus decrease leads to a decreased shear wave velocity V_s, (which is dependent on the shear modulus and effective porosity), and a corresponding slower decrease in V_p. Hence, V_p/V_s could potentially exceed the suggested limits by Gregory (1976) for small aspect ratios and high fluid content. Figure S12 illustrates the impact of small aspect ratios, where large aspect ratios ($0.1 \leq \alpha \leq 1$; i.e. spheroid to penny-shaped fractures) lead first to a decrease V_p/V_s with increasing fluid content. Conversely, small aspect ratios ($0.001 < \alpha < 0.03$) lead to rapid increase in V_p/V_s.

One limiting factor of our work is in the reference velocity model. While Nanometrics Inc. (2020) utilized all available data at the time to develop the velocity model, it is likely a small fraction of a more comprehensive dataset required to resolve the geological complexity of the study area. Due to the existing resolution limit of the reference velocity model, we can not rule out that larger changes in V_p/V_s (and hence velocity changes) are due to reference model uncertainties rather than only due to realistic changes in the earthquake cluster areas.

6.2 Earthquake triggering mechanisms

The *in situ* V_p/V_s estimates in this study result from seismological observations. As such, the results presented here are implicitly limited in space and time to the rock volume affected by fault (re)activation, as well as the starting 3D velocity model (Figure 1). To avoid over-interpretation of V_p/V_s changes, we consider estimates outside of the assumed 2.12% error in the reference 3D velocity model (Section S1) in addition to the standard deviation inferred from the linear regression (Figure 2) to be significant. With respect to the aforementioned error and uncertainty estimates, 25 out of 34 V_p/V_s estimates do not deviate significantly from the underlying background model, and therefore do not imply any significant V_p/V_s variation resulting from fluid injection. Nine out of 34 V_p/V_s estimates show significant increases or decreases relative to background values. The areas within the hexagons in Figure 3 with high cumulative injection volume (outlined in orange) would experience large anticipated increases in pore pressure, similar to increases observed at geothermal sites (Gritto and Jarpe, 2014). Large pore pressure increases that result as a consequence of fluid injection would cause a reduction of effective stresses, and would be consistent with earthquake triggering in a classical Mohr-Coloumb-failure framework. On the other hand, we also observe significant V_p/V_s decreases in areas with large amounts of injected fluid (southeast end of the profile in Figure 3), suggesting that additional factors to pore pressure increase may have an important

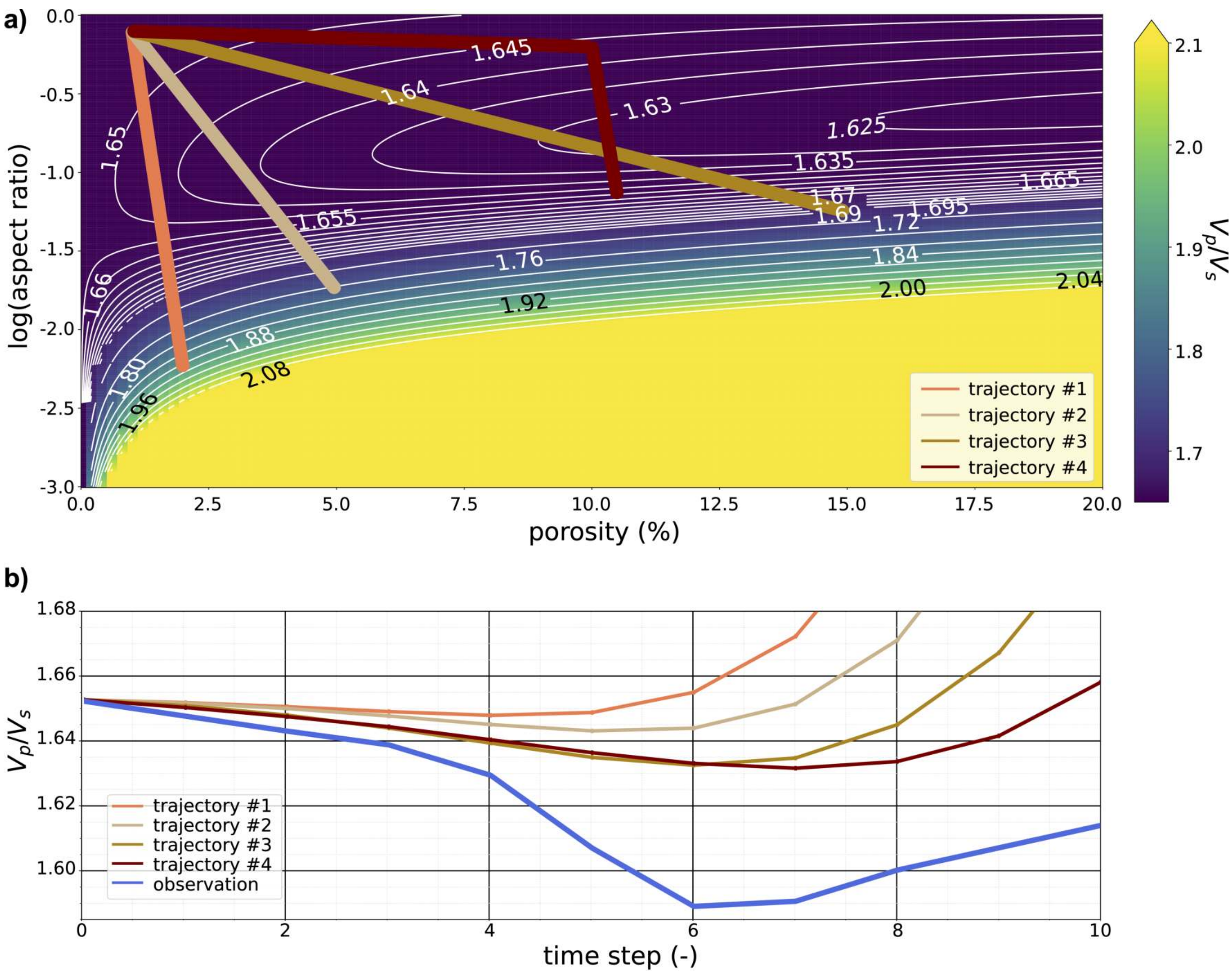

Figure 6 a) Theoretical V_p/V_s ratio (colorbar) as a function of crack aspect ratio and fraction of fluids in the effective medium (porosity). The four trajectories show scenarios of possible fracture and fluid evolution with V_p/V_s computed according to the self-consistent estimates in Berryman (1980). b) Conceptual V_p/V_s ratio per fracture evolution in a), as a function of HF operation time. The line colors of the four scenarios correspond to the colors in (a), and the blue curve shows the estimated mean *in situ* V_p/V_s with interpolated time progression as from Figures 5 and S8.

role in activating faults here. In other words, the lack of large-scale V_p/V_s increase expected from fluid injection and corresponding pore pressure increase suggests broad significant fluid-pressure increases are not sufficient to explain the induced seismicity in Kiskatinaw, at least on their own.

Poroelastic stress changes and fault loading from aseismic slip can (re)activate faults and general zones of weakness over a large range of distances compared to pore pressure changes (e.g., Deng et al., 2016; Bhattacharya and Viesca, 2019). In addition, tensile fracture opening adjacent to HF stages in the target formation can result in static elastic stress transfer that can trigger seismicity in close proximity (Kettlety et al., 2020). The rock volume that hosts seismicity need not experience significant V_p/V_s changes. Other studies have observed direct or indirect evidence of slow and aseismic slip in western Canada (e.g., Eyre et al., 2022; Yu et al., 2021). However, the observations in this study do not indicate any correlation of the earthquake clusters to aseismic slip. Therefore, we are unable to definitively capture the relative importance between poroelastic and aseismic slip triggering in the study area based on V_p/V_s changes inferred from seismological observations alone. Nevertheless, the results presented here suggest rock properties play an equally important role in fault activation as pore pressure changes.

7 Conclusion

We present *in situ* estimates of V_p/V_s ratios based on spatiotemporally correlated clusters of HF-induced earthquakes in the Kiskatinaw area in the Montney Formation, British Columbia, between July 2017 and December 2020. Out of the 49 clusters analyzed, 34 contain $> 1{,}000$ body wave differential travel-time observations that enable robust fitting with no clear correlation between estimated V_p/V_s and the standard deviation of the fit. Among the 34 clusters, 9 indicate significant changes of up to $\pm$ 4.5%, beyond the error range of 2.12% of the starting velocity model. The spatiotemporal heterogeneity in V_p/V_s suggests broad pore-pressure increases are not singularly sufficient to explain the induced earthquakes. Considering the V_p/V_s variations in the context of rock physical models and injection history suggests that rock physical properties may have an equally influential role in triggering. The absence of clear evidence for aseismic slip leaves the question open regarding the relative importance of aseismic slip vs. poroelastic triggering.

Exploring various compositions of fluid-saturated porous media shows the evolution of fracture growth and changing fluid content can explain the observed changes in V_p/V_s ratios. It also suggests that seismicity rates may inversely correlate with changing rock strength conditions. The observed V_p/V_s ratios first decrease with increasing fluid content, followed by increases at intermediate HF stages, presumably coincident with fracture growth, i.e., when aspect ratio decreases. The model's consistency with the observations demonstrates the utility of effective media in interpreting the role of rock properties in controlling fault activation, in concert with seismic observations.

Acknowledgements

This project is partially funded by the Deutsche Forschungsgemeinschaft (DFG, German Research Foundation)—Project Number 428868223, Ruhr University Bochum (RUB) New Faculty startup funds, and Natural Sciences and Engineering Research Council of Canada (NSERC) Strategic Partnership Grant for Projects 494141-2016. The authors would like to acknowledge H. Kao from Natural Resources Canada (NRCan), G. Langston, J. Onwuemeka, B. Wang, and C. Esteve (at McGill University, and NRCan during the time of this study), for help in seismic station deployment and maintenance. The authors would also like to thank S. Venables, M. Gaucher, and British Columbia Energy Regulator staff for providing well data, the 3D reference velocity model, and logistical support, and K. D. Fischer from RUB Seismological Observatory for help in data acquisition. We want to thank E. Korkolis (RUB) for discussions on rock mechanical work approaches and feedback for the manuscript. We thank Editor Atalay Ayele Wondem and two anonymous reviewers for their constructive comments that helped to improve the quality of this manuscript.

Data and code availability

Waveform data used in this study are archived at IRIS under network codes XL, 1E, and PQ (e.g., https://ds.iris.edu/gmap/XL). Well data are provided by British Columbia Energy Regulator (BC-ER; https://www.bc-er.ca/data-reports/data-centre/, last accessed August 2022). The seismicity catalog used in this study was maintained using SeisComP3 (Weber et al., 2007) and can be accessed via https://doi.org/10.5281/zenodo.5152857. Figures were made using Matplotlib v3.3.2 (Hunter, 2007), and maps were made with GIS v3.22.3 (QGIS Development Team, 2022) and Generic Mapping Tools v6.1.1 (Wessel et al., 2019). Topographic information comes from Jarvis et al. (2008). The reference 3D velocity model was provided by Nanometrics Inc. and BC-ER (Nanometrics Inc., 2020). We used the ObsPy toolbox v1.2.2 for seismological data processing Beyreuther et al. (2010). We use color maps from Crameri (2021).

Competing interests

The authors declare that they have no conflict of interest.

References

Atkinson, G. M., Eaton, D. W., Ghofrani, H., Walker, D., Cheadle, B., Schultz, R., Shcherbakov, R., Tiampo, K., Gu, J., Harrington, R. M., Liu, Y., van der Baan, M., and Kao, H. Hydraulic Fracturing and Seismicity in the Western Canada Sedimentary Basin. *Seismological Research Letters*, 87(3):631–647, 2016. doi: 10.1785/0220150263.

Babaie Mahani, A., Schultz, R., Kao, H., Walker, D., Johnson, J., and Salas, C. Fluid injection and seismic activity in the northern Montney play, British Columbia, Canada, with special reference to the 17 August 2015 Mw 4.6 induced earthquake. *Bulletin of the Seismological Society of America*, 107(2):542–552, 2017. doi: 10.1785/0120160175.

Babaie Mahani, A., Kao, H., Atkinson, G. M., Assatourians, K., Addo, K., and Liu, Y. Ground-Motion Characteristics of the 30 November 2018 Injection-Induced Earthquake Sequence in Northeast British Columbia, Canada. *Seismological Research Letters*, 90 (4):1457–1467, 2019. doi: 10.1785/0220190040.

BC-ER. Well Lookup and Reports, 2023. Data retrieved from BC-ER Data Centre, https://www.bc-er.ca/data-reports/data-centre/.

Bell, J. and Grasby, S. The stress regime of the Western Canadian Sedimentary Basin. *Geofluids*, 12(2):150–165, 2012. doi: 10.1111/j.1468-8123.2011.00349.x.

Berger, Z., Boast, M., and Mushayandebvu, M. The contribution of integrated HRAM studies to exploration and exploitation of unconventional plays in North America. *Canadian Society of Petroleum Geologists, Reservoir*, 36:40–45, 2009.

Berryman, J. G. Long-wavelength propagation in composite elastic media II. Ellipsoidal inclusions. *The Journal of the Acoustical Society of America*, 68(6):1820–1831, 1980. doi: 10.1121/1.385172.

Beyreuther, M., Barsch, R., Krischer, L., Megies, T., Behr, Y., and Wassermann, J. ObsPy: A Python Toolbox for Seismology. *Seismological Research Letters*, 81(3):530–533, 2010. doi: 10.1785/gssrl.81.3.530.

Bhattacharya, P. and Viesca, R. C. Fluid-induced aseismic fault slip outpaces pore-fluid migration. *Science*, 364(6439):464–468, 2019. doi: 10.1126/science.aaw7354.

Bohnhoff, M., Dresen, G., Ellsworth, W. L., and Ito, H. Passive Seismic Monitoring of Natural and Induced Earthquakes: Case Studies, Future Directions and Socio-Economic Relevance. In *New Frontiers in Integrated Solid Earth Sciences*, pages 261–285. Springer Netherlands, 2009. doi: 10.1007/978-90-481-2737-5_7.

Brantut, N. and David, E. C. Influence of fluids on V_p/V_s ratio: increase or decrease? *Geophysical Journal International*, 216(3): 2037–2043, 2019. doi: 10.1093/gji/ggy518.

Chevrot, S. and van der Hilst, R. D. The Poisson ratio of the Australian crust: geological and geophysical implications. *Earth and Planetary Science Letters*, 183(1-2):121–132, 2000. doi: 10.1016/s0012-821x(00)00264-8.

Christensen, N. I. Pore pressure and oceanic crustal seismic structure. *Geophysical Journal International*, 79(2):411–423, 1984. doi: 10.1111/j.1365-246x.1984.tb02232.x.

Cochran, E. S., Ross, Z. E., Harrington, R. M., Dougherty, S. L., and Rubinstein, J. L. Induced Earthquake Families Reveal Distinctive Evolutionary Patterns Near Disposal Wells. *Journal of Geophysical Research: Solid Earth*, 123(9):8045–8055, 2018. doi: 10.1029/2018jb016270.

Crameri, F. Scientific colour maps. *Zenodo*, 7.0.1, 2021. doi: 10.5281/zenodo.1243862.

Crotwell, H. P., Owens, T. J., and Ritsema, J. The TauP Toolkit: Flexible Seismic Travel-time and Ray-path Utilities. *Seismological Research Letters*, 70(2):154–160, 1999. doi: 10.1785/gssrl.70.2.154.

Davies, G. R., Watson, N., Moslow, T. F., and MacEachern, J. A. Regional subdivisions, sequences, correlations and facies relationships of the Lower Triassic Montney Formation, west-central Alberta to northeastern British Columbia, Canada — with emphasis on role of paleostructure. *Bulletin of Canadian Petroleum Geology*, 66(1):23–92, 2018.

Dawson, P. B., Chouet, B. A., Okubo, P. G., Villaseñor, A., and Benz, H. M. Three-dimensional velocity structure of the Kilauea Caldera, Hawaii. *Geophysical Research Letters*, 26(18): 2805–2808, 1999. doi: 10.1029/1999gl005379.

Deng, K., Liu, Y., and Harrington, R. M. Poroelastic stress triggering of the December 2013 Crooked Lake, Alberta, induced seismicity sequence. *Geophysical Research Letters*, 43(16):8482–8491, 2016. doi: 10.1002/2016gl070421.

Eaton, D. W., van der Baan, M., Birkelo, B., and Tary, J.-B. Scaling relations and spectral characteristics of tensile microseisms: evidence for opening/closing cracks during hydraulic fracturing. *Geophysical Journal International*, 196(3):1844–1857, 2014. doi: 10.1093/gji/ggt498.

Eyre, T. S., Eaton, D. W., Garagash, D. I., Zecevic, M., Venieri, M., Weir, R., and Lawton, D. C. The role of aseismic slip in hydraulic fracturing–induced seismicity. *Science Advances*, 5(8): eaav7172, 2019. doi: 10.1126/sciadv.aav7172.

Eyre, T. S., Samsonov, S., Feng, W., Kao, H., and Eaton, D. W. InSAR data reveal that the largest hydraulic fracturing-induced earthquake in Canada, to date, is a slow-slip event. *Scientific Reports*, 12(1), 2022. doi: 10.1038/s41598-022-06129-3.

Goebel, T., Weingarten, M., Chen, X., Haffener, J., and Brodsky, E. The 2016 Mw5.1 Fairview, Oklahoma earthquakes: Evidence for long-range poroelastic triggering at $>$40 km from fluid disposal wells. *Earth and Planetary Science Letters*, 472:50–61, 2017. doi: 10.1016/j.epsl.2017.05.011.

Goebel, T. H. W. and Brodsky, E. E. The spatial footprint of injection wells in a global compilation of induced earthquake sequences. *Science*, 361(6405):899–904, 2018. doi: 10.1126/science.aat5449.

Gosselin, J. M., Audet, P., Estève, C., McLellan, M., Mosher, S. G., and Schaeffer, A. J. Seismic evidence for megathrust fault-valve behavior during episodic tremor and slip. *Science Advances*, 6 (4), 2020. doi: 10.1126/sciadv.aay5174.

Gregory, A. R. Fluid saturation effects on dynamic elastic properties of sedimentary rocks. *GEOPHYSICS*, 41(5):895–921, 1976. doi: 10.1190/1.1440671.

Gritto, R. and Jarpe, S. P. Temporal variations of V_p/V_s-ratio at The Geysers geothermal field, USA. *Geothermics*, 52:112–119, 2014. doi: 10.1016/j.geothermics.2014.01.012.

Guglielmi, Y., Cappa, F., Avouac, J.-P., Henry, P., and Elsworth, D. Seismicity triggered by fluid injection–induced aseismic slip. *Science*, 348(6240):1224–1226, 2015. doi: 10.1126/science.aab0476.

Han, D. and Batzle, M. L. Gassmann's equation and fluid-saturation effects on seismic velocities. *GEOPHYSICS*, 69(2):398–405, mar 2004. doi: 10.1190/1.1707059.

Hashin, Z. and Shtrikman, S. A variational approach to the theory of the elastic behaviour of multiphase materials. *Journal of the Mechanics and Physics of Solids*, 11(2):127–140, 1963. doi: 10.1016/0022-5096(63)90060-7.

Hsu, Y.-F., Huang, H.-H., Huang, M.-H., Tsai, V. C., Chuang, R. Y., Feng, K.-F., and Lin, S.-H. Evidence for Fluid Migration During the 2016 Meinong, Taiwan, Aftershock Sequence. *Journal of Geophysical Research: Solid Earth*, 125(9), 2020. doi: 10.1029/2020jb019994.

Huber, P. J. Robust Regression: Asymptotics, Conjectures and Monte Carlo. *The Annals of Statistics*, 1(5):799–821, 1973.

Hunter, J. D. Matplotlib: A 2D graphics environment. *Computing in Science & Engineering*, 9(3):90–95, 2007. doi: 10.1109/MCSE.2007.55.

Igonin, N., Verdon, J. P., Kendall, J.-M., and Eaton, D. W. Large-Scale Fracture Systems Are Permeable Pathways for Fault Activation During Hydraulic Fracturing. *Journal of Geophysical Research: Solid Earth*, 126(3), 2021. doi: 10.1029/2020jb020311.

Jarvis, A., Reuter, H., Nelson, A., and Guevara, E. Hole-Filled Seamless SRTM Data V4: International Centre for Tropical Agriculture (CIAT). http://srtm.csi.cgiar.org, 2008.

Kennett, B. L. N. and Engdahl, E. R. Traveltimes for global earthquake location and phase identification. *Geophysical Journal International*, 105(2):429–465, may 1991. doi: 10.1111/j.1365-246x.1991.tb06724.x.

Keranen, K. M. and Weingarten, M. Induced Seismicity. *Annual Review of Earth and Planetary Sciences*, 46(1):149–174, 2018. doi: 10.1146/annurev-earth-082517-010054.

Kettlety, T., Verdon, J. P., Werner, M. J., and Kendall, J. M. Stress Transfer From Opening Hydraulic Fractures Controls the Distribution of Induced Seismicity. *Journal of Geophysical Research: Solid Earth*, 125(1), 2020. doi: 10.1029/2019jb018794.

Lecocq, T., Caudron, C., and Brenguier, F. MSNoise, a Python Package for Monitoring Seismic Velocity Changes Using Ambient Seismic Noise. *Seismological Research Letters*, 85(3):715–726, 2014. doi: 10.1785/0220130073.

Lin, G. Spatiotemporal variations of in situ V_p/V_s ratio within the Salton Sea Geothermal Field, southern California. *Geothermics*, 84:101740, 2020. doi: 10.1016/j.geothermics.2019.101740.

Lin, G. and Shearer, P. M. Estimating Local V_p/V_s Ratios within Similar Earthquake Clusters. *Bulletin of the Seismological Society of America*, 97(2):379–388, 2007. doi: 10.1785/0120060115.

Lin, G. and Shearer, P. M. Spatiotemporal Variations of Focal Mechanism and In Situ V_p/V_s Ratio During the 2018 Kīlauea Eruption. *Geophysical Research Letters*, 48(18), 2021. doi: 10.1029/2021gl094636.

Liu, T., Gong, J., Fan, W., and Lin, G. *In-situ* V_p/V_s ratio reveals fault-zone material variation at the westernmost Gofar transform fault, East Pacific Rise. *Journal of Geophysical Research: Solid Earth*, 128(3), 2023. doi: 10.1029/2022jb025310.

McNutt, S. R. Volcanic Seismology. *Annual Review of Earth and Planetary Sciences*, 33(1):461–491, 2005. doi: 10.1146/annurev.earth.33.092203.122459.

Mesimeri, M., Ganas, A., and Pankow, K. L. Multisegment ruptures and V_p/V_s variations during the 2020–2021 seismic crisis in western Corinth Gulf, Greece. *Geophysical Journal International*, 230(1):334–348, 2022. doi: 10.1093/gji/ggac081.

Nanometrics Inc. BCER Kiskatinaw Seismic Monitoring and Mitigation Area Velocity Model developed by Nanometrics Inc. https://www.bc-er.ca/data-reports/data-centre/, May 2020.

Natural Resources Canada. Earthquakes Canada, GSC, Earthquake Search (On-line Bulletin). https://earthquakescanada.nrcan.gc.ca/stndon/NEDB-BNDS/bulletin-en.php, 2023. https://earthquakescanada.nrcan.gc.ca/stndon/NEDB-BNDS/bulletin-en.php. (Date accessed: 2023-02-09).

Norgard, G. T. Structural inversion of the Middle Triassic Halfway Formation, Monias Field, northeast British Columbia. *Bulletin of Canadian Petroleum Geology*, 45(4):614–623, 1997. doi: 10.35767/gscpgbull.45.4.614.

Omovie, S. J. and Castagna, J. P. Relationships between Dynamic Elastic Moduli in Shale Reservoirs. *Energies*, 13(22):6001, 2020. doi: 10.3390/en13226001.

Peña Castro, A. F., Roth, M. P., Verdecchia, A., Onwuemeka, J., Liu, Y., Harrington, R. M., Zhang, Y., and Kao, H. Stress Chatter via Fluid Flow and Fault Slip in a Hydraulic Fracturing-Induced Earthquake Sequence in the Montney Formation, British Columbia. *Geophysical Research Letters*, 47(14), 2020. doi: 10.1029/2020gl087254.

Peterie, S. L., Miller, R. D., Intfen, J. W., and Gonzales, J. B. Earthquakes in Kansas Induced by Extremely Far-Field Pressure Diffusion. *Geophysical Research Letters*, 45(3):1395–1401, 2018. doi: https://doi.org/10.1002/2017GL076334.

Pimienta, L., Schubnel, A., Violay, M., Fortin, J., Guéguen, Y., and Lyon-Caen, H. Anomalous V_p/V_s Ratios at Seismic Frequencies Might Evidence Highly Damaged Rocks in Subduction Zones. *Geophysical Research Letters*, 45(22):12,210–12,217, 2018. doi: 10.1029/2018gl080132.

QGIS Development Team. *QGIS Geographic Information System 3.22.3*. QGIS Association, 2022. https://www.qgis.org. https://www.qgis.org.

Reuss, A. Calculation of the flow limits of mixed crystals on the basis of the plasticity of monocrystals. *Z. Angew. Math. Mech*, 9: 49–58, 1929.

Roth, M. P., Verdecchia, A., Harrington, R. M., and Liu, Y. High-Resolution Imaging of Hydraulic-Fracturing-Induced Earthquake Clusters in the Dawson-Septimus Area, Northeast British Columbia, Canada. *Seismological Research Letters*, 91(5): 2744–2756, 2020. doi: 10.1785/0220200086.

Roth, M. P., Kemna, K. B., Harrington, R. M., and Liu, Y. Source Properties of Hydraulic-Fracturing-Induced Earthquakes in the Kiskatinaw Area, British Columbia, Canada. *Journal of Geophysical Research: Solid Earth*, 127(3), 2022. doi: 10.1029/2021jb022750.

Salvage, R. O. and Eaton, D. W. Unprecedented quiescence in resource development area allows detection of long-lived latent seismicity. *Solid Earth*, 12(3):765–783, 2021. doi: 10.5194/se-12-765-2021.

Schmid, F., Petersen, G., Hooft, E., Paulatto, M., Chrapkiewicz, K., Hensch, M., and Dahm, T. Heralds of Future Volcanism: Swarms of Microseismicity Beneath the Submarine Kolumbo Volcano Indicate Opening of Near-Vertical Fractures Exploited by Ascending Melts. *Geochemistry, Geophysics, Geosystems*, 23(7), 2022. doi: 10.1029/2022gc010420.

Schultz, R., Skoumal, R. J., Brudzinski, M. R., Eaton, D., Baptie, B., and Ellsworth, W. Hydraulic Fracturing-Induced Seismicity. *Reviews of Geophysics*, 58(3), 2020. doi: 10.1029/2019rg000695.

Takei, Y. Effect of pore geometry on V_p/V_s: From equilibrium geometry to crack. *Journal of Geophysical Research*, 107(B2), 2002. doi: 10.1029/2001jb000522.

Verdecchia, A., Cochran, E. S., and Harrington, R. M. Fluid-Earthquake and Earthquake-Earthquake Interactions in Southern Kansas, USA. *Journal of Geophysical Research: Solid Earth*, 126(3):e2020JB020384, 2021. doi: https://doi.org/10.1029/2020JB020384.

Voigt, W. *Lehrbuch der Kristallphysik:(mit Ausschluss der Kristalloptik)*, volume 34. BG Teubner, 1910.

Wang, B., Harrington, R. M., Liu, Y., Kao, H., and Yu, H. A Study on the Largest Hydraulic-Fracturing-Induced Earthquake in Canada: Observations and Static Stress-Drop Estimation. *Bulletin of the Seismological Society of America*, 110(5):2283–2294, 2020. doi: 10.1785/0120190261.

Wang, B., Verdecchia, A., Kao, H., Harrington, R. M., Liu, Y., and Yu, H. A Study on the Largest Hydraulic Fracturing Induced Earthquake in Canada: Numerical Modeling and Triggering Mechanism. *Bulletin of the Seismological Society of America*, 2021. doi: 10.1785/0120200251.

Wang, W., Savage, M. K., Yates, A., Zal, H. J., Webb, S., Boulton, C., Warren-Smith, E., Madley, M., Stern, T., Fry, B., Mochizuki, K., and Wallace, L. Temporal velocity variations in the northern Hikurangi margin and the relation to slow slip. *Earth and Planetary Science Letters*, 584:117443, 2022. doi: 10.1016/j.epsl.2022.117443.

Weber, B., Becker, J., Hanka, W., Heinloo, A., Hoffmann, M., Kraft, T., Pahlke, D., Reinhardt, J., Saul, J., and Thoms, H. SeisComP3 - Automatic and Interactive Real Time Data Processing. In *Geophysical Research Abstracts*, 2007.

Wessel, P., Luis, J. F., Uieda, L., Scharroo, R., Wobbe, F., Smith, W. H. F., and Tian, D. The Generic Mapping Tools Version 6. *Geochemistry, Geophysics, Geosystems*, 20(11):5556–5564, 2019. doi: 10.1029/2019gc008515.

Winkler, K. W. and Nur, A. Seismic attenuation: Effects of pore fluids and frictional-sliding. *GEOPHYSICS*, 47(1):1–15, 1982. doi: 10.1190/1.1441276.

Worthington, M. H. and Hudson, J. A. Fault properties from seismic Q. *Geophysical Journal International*, 143(3):937–944, 2000. doi: 10.1046/j.1365-246x.2000.00315.x.

Yu, H., Harrington, R. M., Liu, Y., and Wang, B. Induced Seismicity Driven by Fluid Diffusion Revealed by a Near-Field Hydraulic Stimulation Monitoring Array in the Montney Basin, British Columbia. *Journal of Geophysical Research: Solid Earth*, 124, 2019. doi: 10.1029/2018JB017039.

Yu, H., Harrington, R. M., Kao, H., Liu, Y., Abercrombie, R. E., and Wang, B. Well Proximity Governing Stress Drop Variation and Seismic Attenuation Associated With Hydraulic Fracturing Induced Earthquakes. *Journal of Geophysical Research: Solid Earth*, 125(9), 2020. doi: 10.1029/2020jb020103.

Yu, H., Harrington, R. M., Kao, H., Liu, Y., and Wang, B. Fluid-injection-induced earthquakes characterized by hybrid-frequency waveforms manifest the transition from aseismic to seismic slip. *Nature Communications*, 12(1), 2021. doi: 10.1038/s41467-021-26961-x.

Zhao, D., Kanamori, H., Negishi, H., and Wiens, D. Tomography of the Source Area of the 1995 Kobe Earthquake: Evidence for Fluids at the Hypocenter? *Science*, 274(5294):1891–1894, 1996. doi: 10.1126/science.274.5294.1891.

doi:10.26443/seismica.v2i2.402

SEISMICA

Homogenizing instrumental earthquake catalogs – a case study around the Dead Sea Transform Fault Zone

Iason Grigoratos * [1], **Valerio Poggi** [2], **Laurentiu Danciu** [1], **Ricardo Monteiro** [3]

[1]Swiss Seismological Service (SED) at ETH Zurich, Switzerland, [2]National Institute of Oceanography and Applied Geophysics – OGS, Italy, [3]University School of Advanced Studies IUSS Pavia, Italy

Author contributions: *Conceptualization*: I.G., V.P.. *Data Curation*: I.G.. *Formal Analysis*: I.G., V.P.. *Funding Acquisition*: I.G., R.M.. *Investigation*: I.G., V.P., L.D.. *Methodology*: I.G., V.P.. *Project Administration*: R.M.. *Resources*: R.M.. *Software*: I. ., V.P.. *Supervision*: L.D.. *Validation*: V.P., L.D.. *Visualization*: I.G.. *Writing – original draft*: I.G.. *Writing – review & editing*: I.G., V.P., L.D., R.M..

Abstract The creation of a homogenized earthquake catalog is a fundamental step in seismic hazard analysis. The homogenization procedure, however, is complex and requires a good understanding of the heterogeneities among the available bulletins. Common events within the bulletins have to be identified and assigned with the most suitable origin time and location solution, while all the events have to be harmonized into a single magnitude scale. This process entails several decision variables that are usually defined using qualitative measures or expert opinion, without a clear exploration of the associated uncertainties. To address this issue, we present an automated and data-driven workflow that defines spatio-temporal margins within which duplicate events fall and converts the various reported magnitudes into a common scale. Special attention has been paid to the fitted functional form and the validity range of the derived magnitude conversion relations. The proposed methodology has been successfully applied to a wide region around the Dead Sea Transform Fault Zone (27N-36N, 31E-39E), with input data from various sources such as the International Seismological Centre and the Geophysical Institute of Israel. The produced public catalog contains more than 5500 events, between 1900 and 2017, with moment magnitude Mw above 3. The MATLAB/Python scripts used in this study are also available.

Non-technical summary Earthquake catalogs are a fundamental input into seismic hazard and risk assessment studies. Unfortunately, data about the location and size of an earthquake can be reported from different sources in inconsistent ways. To address this issue, we developed statistical methods that can automatically combine and standardize earthquake data from different sources. In the end, our workflow produces unified earthquake catalogs, free of duplicated entries, with all event sizes being reported in a single magnitude scale. We applied our framework to a large area around the Dead Sea Transform Fault Zone (27N-36N, 31E-39E), using data from various sources such as the International Seismological Centre and the Geophysical Institute of Israel. The resulting public catalog contains more than 5500 events, between 1900 and 2017, with magnitude above 3. The MATLAB/Python scripts used in this study are also available.

Production Editor:
Gareth Funning
Handling Editor:
Andrea Llenos
Copy & Layout Editor:
Hannah F. Mark

Signed reviewer(s):
Domenico Di Giacomo,
Annemarie
Christophersen

Received:
February 27, 2023
Accepted:
October 12, 2023
Published:
November 7, 2023

1 Introduction

An earthquake catalog is a parametric list of events with each entry providing an earthquake's epicenter, origin time, and magnitude size; and sometimes additional data such as depth, associated uncertainties, and focal mechanism information (Woessner et al., 2010). In an instrumental catalog these properties have been computed by analyzing seismic recordings, either analog or digital. In many cases they form the principal datasets from which seismologists interpret the earthquake process and build forecasting statistical models (e.g. Sesetyan et al., 2018). Earthquake catalogs that span many decades are usually inherently heterogeneous. From the early days of (pre-)instrumental seismology, in the beginning of the twentieth century, seismological networks have undergone many changes that are reflected in the databases in use today. These changes can be gradual, such as improvements in location and magnitude estimation over time, as networks gradually increase in size and advances in instrumentation enhance the signal-to-noise ratio in the seismological record. They can also be rapid, such as a systematic change in operating, recording and processing procedures (Husen and Hardebeck, 2010).

Even without network changes, however, discrepancies should be expected due to the sensitivity of the models used to derive parametric information from seismic records. Such procedures employ (i) signal processing techniques, (ii) phase picking algorithms, (iii) subsurface velocity models, (iv) calibration of the instruments, and (v) calibration of the attenuation model used to reconcile observations at different distances (Gomberg et al., 1990; Douglas, 1967). Steps (i)-(iv) affect both origin time and location (epicenter and hypocenter) (Waldhauser and Ellsworth, 2000; Kagan, 2003), while (v) is often coupled to the earthquake's magni-

*Corresponding author: iason.grigoratos@sed.ethz.ch

tude, presenting a formidable inversion problem (Tormann et al., 2010). As a result, refinements over time either in the models or in the technology used can lead to significant differences in the output. Large discrepancy is observed also due to the fact that the models and techniques used in steps (i)-(v) are network-specific and often are not standardized (Bormann and Saul, 2008).

Heterogeneity among earthquake catalogs leads to significant data contamination and misinterpretations of the results in a number of analyses, such as seismicity rate evaluation and hazard assessment (Musson, 2012). These problems are more evident when the analysis needs to include data from periods with durations on the order of century and in regions where the coverage from the seismic network is sparse. Our case study region, the Dead Sea Transform Fault Zone (DSTFZ), lacked local seismic networks for a long time (until 1983), although it comprises one of the most rapidly deforming non-subduction region worldwide (Garfunkel et al., 1981). This is why the scope of the present study is to present a framework for merging and homogenizing multiple instrumental earthquake catalogs. We developed automated data-driven methods to minimize the need for expert opinion, which is inherently subjective. Specifically, using as sole input the available parametric catalogs (§3), the procedure can generate models to convert the various reported magnitudes into a common scale (§4) and to define the spatio-temporal margins within which duplicate events fall (§5). The application of these models leads to a unified instrumental earthquake catalog containing only unique events with standardized parametric information (§6). Similar efforts with variations in the methodology have been done in the past for Italy (Rovida et al., 2020), Lebanon (Brax et al., 2019), Ecuador (Beauval et al., 2013), the Middle East (Zare et al., 2014), South Asia (Nath et al., 2016), Europe (Gruenthal and Wahlstroem, 2012) and for global large magnitude events (Storchak et al., 2015), to name a few. Compared to such past efforts, some of the key improvements presented here relate to data-driven workflows in order to group similar magnitude types to address data-scarcity, define saturation levels for various functional forms, and select time-dependent spatio-temporal windows for the removal of duplicated entries by utilizing metadata of the International Seismological Centre (ISC). Our investigated area (27N-36N and 31E-39E) is meant to match the boundaries of the latest regional historical catalog (Figure 1, Grigoratos et al., 2020). The two catalogs combined can serve as valuable input to probabilistic seismic hazard assessment (PSHA) studies in the region. The latter can be paired with existing exposure (e.g. Grigoratos et al., 2018) and vulnerability models (e.g. Grigoratos et al., 2016; Rodriquez et al., 2018; Cerchiello et al., 2018; Meo et al., 2018) that are available for some parts of the DSTFZ.

2 Seismotectonic setting

The DSTFZ is the main expression of the movement of the European, Arabic and African plates. It consists of a sequence of left-lateral transform faults (Figure 1) connecting the spreading oceanic ridge of the Red Sea in the south with the compressional deformation zones of the Arabia-Eurasia collision zone in the north (Garfunkel et al., 1981). Although the large majority of earthquakes occur at a depth range between 10 and 20 km, the total seismogenic thickness beneath the midpoint of the DSTFZ is about 28 km (Aldersons and Ben-Avraham, 2014). Global Positioning System (GPS) measurements indicate significant crustal motion with slip rates of about 4–5 mm$\cdot$yr^{-1} for the whole DSTFZ, perhaps somewhat larger in the northern parts and smaller further south (Marco and Klinger, 2014; Ambraseys, 2009).

In recent times, there is an apparent quiescence of the DSTFZ; excluding the large earthquake of November 22 1995 (M_s 7.1) in the Gulf of Aqaba, only one mainshock of M_s 6.0 or larger has occurred during the past century, on July 11 1927 (Ambraseys, 2001). The frequency of large earthquakes in the last 2000-3000 years, however, is quite different (Grigoratos et al., 2020), with the majority of historical earthquakes rupturing fault segments above the 31st parallel north (Figure 1).

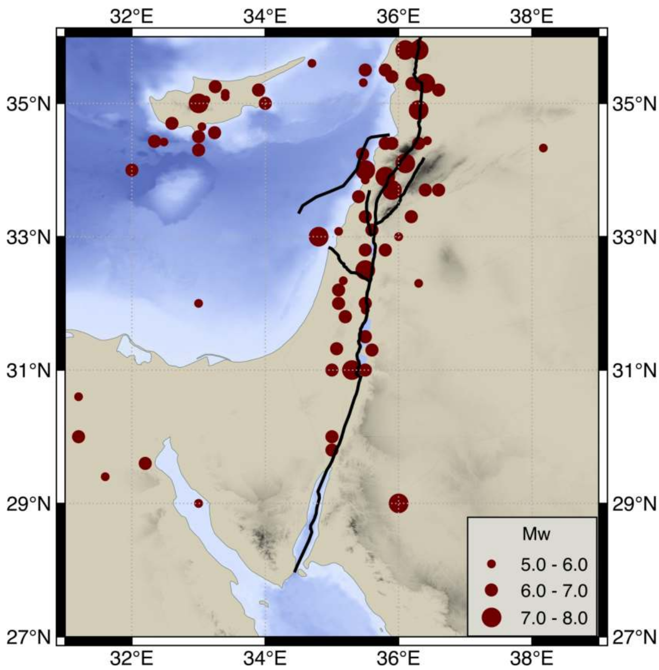

Figure 1 Historical earthquakes with M_w≥5 between 31BC and 1900, inside our investigated zone (Grigoratos et al., 2020). The black lines indicate main faults along the DSTFZ.

3 Input datasets

Our goal was to present a unified catalog containing unique events with M_w≥3. To arrive at that point after magnitude homogenization, we initially used a cut-off scale-independent magnitude of 2. The catalogs and bulletins we used as input sources are described below and are summarized in Table 1.

The International Seismological Centre (ISC) was established in 1964 as the successor to the International Seismological Summary. It collects and standardizes raw and parametric seismic data from about 130 networks worldwide (ISC, 2023). With the exception of Africa, Central Asia, and SE Asia, the reporting instru-

Source	Time period	Magnitude ≥	Events	Magnitude Scale
ISC Bulletin	1918 – Jan. 2018	2	34167	varied
ISC-GEM	1900 – 2013	5.5	25	M_w
EMSC	Oct. 2004 – Jan. 2018	2	2998	$M_L/M_d/m_b/M_w$
GII	1903 – Jan. 2018	2	10709	$M_d/m_b/M_w$
EMME	1900 – 2006	4	837	M_w
EMEC	1900 – 2006	4	763	M_w
IRIS	1968 – Jul. 2016	2	18321	Varied

Table 1 Sources of parametric earthquake data (within our spatial boundaries).

mental agencies in most parts of the world are contributing members to ISC (Willemann and Storchak, 2001). ISC re-analyzes all events above magnitude 3.5 and often assigns new epicenters (Bondar and Storchak, 2011) and/or magnitudes (Di Giacomo and Storchak, 2015), using all the available raw data (Storchak et al., 2017). The ISC Bulletin was a fundamental source of data for this study.

The ISC-GEM catalog (Storchak et al., 2015) is a major step forward compared to previously available sources of information. Version 4 of the catalog includes around 27,000 global earthquake epicenters and hypocenters between 1900 and 2013, recomputed using the original arrival time data and the same technique and velocity model throughout. Where possible, earthquake magnitudes are expressed using the M_w scale based on seismic moment; proxy M_w values are estimated for the other cases based on the newly developed empirical relationships with M_S and m_b (Di Giacomo et al., 2015). Uncertainties around the parametric information are estimated using uniform techniques (Storchak et al., 2015). The cut-off magnitude thresholds (M_s) for Version 4 were: 7.5 after 1900, 6.25 after 1918, 5.5 after 1920 (newer versions have lower thresholds).

The European-Mediterranean Seismological Centre (EMSC) collects real time parametric data (source parameters and phase pickings) since 1998 from about 70 seismological networks in more than 50 Euro-Mediterranean countries (Godey et al., 2009). We herein refer to this bulletin as CSEM, following the naming scheme of the ISC Bulletin (http://www.isc.ac.uk/iscbulletin/agencies/). The online bulletin provides events only after mid-2004. Epicentral relocations are performed for all events (Godey et al., 2006). When amplitude/period information is available (provided by 50% of the contributing networks), original body wave and local magnitudes are computed by EMSC (Godey et al., 2013); otherwise, the reported magnitude values are taken from the contributing networks. We should note that the exact source of the magnitude estimates is not cited in the online bulletin. Since 2006, EMSC is integrated in the ISC Bulletin.

The Geophysical Institute of Israel (GII, formerly IPRG) processes the seismic data collected by the Israel Seismic Network (operating since 1983), which contains about 20 stations in and around Israel. The geographic region, which is covered by this bulletin is within the geographic boundaries 27N-36N and 32E-38E (Feldman). We used GII's relocations as the preferred parametric information for the events that were reported in the study of Wetzler and Kurzon (2016). We were unable to find original catalogs from other regional networks.

Within the framework of the "Earthquake Model of the Middle East Region" (EMME) project (Danciu et al., 2017; Sesetyan et al., 2018), Zare et al. (2014) published a catalog up to year 2006 for the Middle East, compiling parametric information provided by past studies and bulletins (mainly ISC). It provides origin time, epicentral coordinates and magnitudes, homogenized in M_w. For several events, the source of the original magnitude estimate remains unclear, due to limitations in the original national data.

The European-Mediterranean earthquake catalogue (EMEC; Gruenthal and Wahlstroem, 2012) is an extension of the CEntral, Northern and northwestern European earthquake Catalogue (CENEC) (Grünthal et al., 2009) covering Europe and the Mediterranean Sea until 2006. Like EMME, it compiled parametric information provided by past studies and bulletins. For the eastern Mediterranean and the Levant area, the vast majority of the events originate from Papaioannou (2001) and Abdallah et al. (2004).

The Incorporated Research Institutions for Seismology (IRIS) has an online bulletin that collects (without further review) parametric data from the ISC Bulletin and the National Earthquake Information Center (NEIC) (Trabant et al., 2012). The IRIS Earthquake Browser (IEB) is the main expression of this bulletin, but does not provide the source of each entry and the magnitude scale of each magnitude value. Therefore, we did not make use of IEB. Instead, we used another tool of IRIS called SeismiQuery which does not present such drawbacks. Unfortunately, SeismiQuery was shut down in January 2017.

In principle, using the ISC Bulletin as the only source of instrumental seismicity should be sufficient, since the other available sources are either incorporated in, or based on ISC. However, for reasons that might have to do with the reviewing procedure, some events published in the bulletin of a local agency are not reported by the ISC Bulletin, even though the local agency in question is a contributing member. The opposite scenario is also possible, i.e. the ISC Bulletin lists an event solution citing a local contributing agency which does not report the same event in its own bulletin. The same is true for other international bulletins such as EMSC or IRIS: even though they share most of their contributing agencies with the ISC Bulletin, in some cases their reported events do not match. As a result, for specific cases including our case study region, one has to consider several international bulletins and local agencies, even if they are closely related to the ISC Bulletin. Furthermore, regional networks with localized velocity models can provide better estimates for the epicenter and depth of an event.

The ISC Bulletin and GII are the only sources still reporting more than one magnitude solution per event, thus enabling the correlation between different magnitude scales, and agencies (only ISC). The ISC Bulletin is also the only source providing numerically quantified uncertainty on the time, magnitude and location solutions.

4 Magnitude homogenization

4.1 Magnitude scales and their limitations

Numerous different magnitude scales have been proposed through time (Kanamori, 1983; Lay and Wallace, 1995), each based on a different analyzed property of the recorded earthquake signal and with a different applicability. Defining the most suitable magnitude scale for all purposes is generally not possible, as it depends on the practical needs, and it may vary considerably between different regions and seismic networks. Often a single network reports multiple magnitude scales for different event sizes and occasionally for the same event; the latter case enables empirical correlations between scales to be established. Although the different magnitude scales were defined so that they would behave overall similarly within certain magnitude ranges (Gutenberg and Richter, 1956), there can still be considerable variation between estimates of a single event. This heterogeneity may produce artifacts in the magnitude-frequency statistics of the unified catalog (Tormann et al., 2010).

The most commonly used class of magnitude scales, following Richter's original formulation for the local magnitude scale (Richter, 1935), is based on the logarithm of the amplitude of the recorded seismic waves (Deichmann, 2006). The local magnitude (M_L) is arbitrarily defined based on the maximum observed amplitude on a Wood-Anderson seismometer, with a period of 0.8s, recorded at 100 km from the earthquake. In practice, however, the recording distance is never exactly 100 km and region-dependent corrections must be made to account for amplitude changes with distance due to anelastic attenuation and geometrical spreading. Station corrections are also needed, to account for site effects. Further corrections must be made for recordings from instruments other than the standard Wood-Anderson, which is practically not used anymore. Because of these constraints, M_L is most suitable for earthquakes at moderate distances (Luckett et al., 2018), with magnitudes between 3 and 5 (Hanks and Boore, 1984).

Other scales are based on the log of the amplitude of a particular phase. The most common are the body wave magnitude, m_B (Gutenberg, 1945a), based on body waves with periods of 1-10s, and the surface wave magnitude, M_S (Gutenberg, 1945b), based on 20s surface waves (Gutenberg and Richter, 1956). These magnitude scales are used mostly for teleseismic (global) earthquakes. M_S strictly measured around 20s is not appropriate for magnitudes greater than 7 or 8 (Di Giacomo et al., 2015; Bormann et al., 2009) because the amplitude of 20s period waves does not increase as the rupture length increases beyond 60 km (Kanamori, 1978). However, broadband M_S suffers less from saturation and deviates from M_w only for tsunami earthquakes (Kanamori, 1972) and ~M9 earthquakes (Di Giacomo and Storchak, 2022). The m_B magnitude was progressively replaced by many observatories of the "western world" with the 1s period body wave magnitude m_b (Bormann and Saul, 2008). Although m_b worked well for the purpose of monitoring nuclear tests, its qualities as far as the moderate-to-large earthquakes are concerned were inferior to those of the original m_B (Storchak et al., 2015). The short-period m_b usually presents extensive scatter (Di Giacomo et al., 2015) and performs best with distant small-to-moderate earthquakes, with magnitudes between 4 and 6 (Gasperini et al., 2013).

One scale of magnitude that is independent of amplitude is the coda duration magnitude, which is based solely on the duration of the seismic signal. Common notations found in the literature include M_d, $M_{D,}$ M_C. Coda duration magnitude is intended for locally-recorded events, where the various reflected and refracted phases are not well separated and instead form a prolonged coda following the initial phase arrivals. The amplitude of the coda diminishes as the reflected and refracted phases attenuate; the larger the initial waves, the longer the duration of the observable coda. It is thus sensitive to the signal-to-noise ratio (Del Pezzo et al., 2003). Although this magnitude scale requires no amplitude calibration, it does require empirical calibration of event durations, as well as corrections for distance and event depth. Most agencies have calibrated these parameters so that their product matches the observed values of M_L (Eaton, 1992). As a result, often M_d and M_L values are heavily correlated. One potential artifact is that coda duration magnitudes may be biased towards larger magnitudes during aftershock sequences or other times of intense seismicity, as additional earthquakes may occur within the coda of the first event and lengthen it.

The moment magnitude scale, M_w (Hanks and Kanamori, 1979), is based on the log of the seismic moment (M_0) which can be directly derived by fitting a double couple moment tensor solution to the recorded earthquake waveforms (Dziewonski et al., 1981), rather than from just the single amplitude of a particular phase at a particular frequency. Alternatively, for well-recorded earthquakes, the moment can be estimated from a finite source model of the earthquake. Because of that, M_w lacks saturation effects, which makes it the most suitable scale for many practical applications. The moment magnitude is the standard practice when it comes to seismic hazard assessment studies, i.e. both the activity rates and the ground motion models (Danciu et al., 2016) should be defined in terms of M_w. Unfortunately, M_w has been routinely calculated for large earthquakes worldwide only since the beginning of the

Global Centroid Moment Tensor (GCMT) catalog in 1976 (Dziewonski et al., 1981). Therefore, all smaller or older earthquakes have to be converted to M_w empirically based on conversion relations from other magnitude scales. The magnitude scale that correlates best with M_w within the crucial magnitude range for seismic hazard assessment, i.e. 4<M<7, is M_s (Kanamori, 1983). That said, solutions in M_s are extremely rare in our study region (available for only 1% of the events). The most popular scales are M_L (74%) and M_d (42%), which are very sensitive to agency-specific calibrations, and to a lesser extent m_b (8%).

4.2 Methodology

4.2.1 Regression methods and magnitude uncertainty

To derive appropriate relations between two magnitude types, say GII M_d and GCMT M_w, one should first identify which events are available in both types, plot the reported values (in pairs) and derive a best-fit curve using regression analysis. Once defined, one can then use this conversion relation to transform any other M_d estimate of GII to a proxy M_w, assumed equivalent to the standardized estimates of GCMT, in this case.

We should note that in the literature, the terms "magnitude scale" and "magnitude type" are often used interchangeably. We, however, herein define the latter term as the property of the magnitude that describes both its scale and the agency that originally computed it.

In the past, the fitting of the magnitude pairs was usually carried out using standard least squares regression (SR), often without explicit note (e.g. Papazachos et al., 1997; Scordilis, 2006; Yadav et al., 2009). In this approach, the vertical offsets to the best-fit curve are minimized, with the independent variable (in our example GII M_d) being assumed error-free. The latter does not hold for magnitude estimates that are prone to both random and systematic errors, limiting the applicability of SR for magnitude conversions (Stromeyer et al., 2004; Gasperini et al., 2015). According to Castellaro et al. (2006), the application of SR may induce bias of around 30% when later deriving the b-value of the Gutenberg-Richter distribution (Gutenberg and Richter, 1956). Hence, they note that observed variations in b-values may be to some extent an artifact of improper catalog data processing (Musson, 2012; Shelly et al., 2021).

Orthogonal regression (OR) has been proposed as a more appropriate technique to deal with least-squares problems in which dependent (y) and independent variables (x) are both considered to have some finite error. In its general form, it minimizes the weighted orthogonal distance to the best-fit curve (Madansky, 1959; Pujol, 2016). The weighted scheme is dictated by the error variance ratio (η) between the two variables. For η equal to unity, Castellaro and Bormann (2007) introduced the term Particular Orthogonal least-squares Regression (POR), which we adopted. POR minimizes the offsets perpendicular to the best-fit curve, eliminating any weighting scheme ($\eta = 1$). Thus, the resulting relations, contrary to the ones based on SR, can be inverted. As an alternative to OR, Stromeyer et al. (2004) and Krystek and Anton (2008) proposed the chi-square maximum likelihood regression (CSQ) and weighted total least squares (WLS), respectively. Lolli and Gasperini (2012) showed that, under the common assumption that only the variance ratio η is known or assumed, all three methods are substantially equivalent.

We should note that, in general, the error in M_w is generally smaller than the error in the older scales (Gasperini et al., 2015), meaning that, when converting any scale to M_w, η is smaller than 1. This implies the following:

- setting η equal to 1 is certainly an approximation, but probably not a rough one, since Di Giacomo et al. (2015) did not observe improvements when they tried weighting schemes and quantile regression;
- OR is in most cases more suitable than SR for conversion to M_w, since Castellaro and Bormann (2007) demonstrated that SR provides better estimates compared to OR only when $\eta^{0.5} > 1.8$.

The effect that the regression algorithm can have on the fitted curve is illustrated in Figure S1 of the supplementary material. Overall, in recent years, POR has been the de facto regression method used in magnitude conversion studies globally (e.g. Di Giacomo et al., 2015; Weatherill et al., 2016; Bormann et al., 2009; Nath et al., 2016; Shahvar et al., 2013) and that is also another reason why we adopted it.

Finally, the accuracy of older magnitude measurements tends to be lower; given that larger errors lead to a positive shift in the a-value that is proportional to the square of magnitude errors (Tinti and Mulargia, 1985), the seismic activity for older time intervals may spuriously appear to exceed more recent activity by a significant margin. This effect may be, at least partly, responsible for the often-claimed discrepancy between earthquake rates in recent and old catalogs.

4.2.2 Combining magnitude types to address data scarcity

Direct moment magnitude estimates are available for a limited number of events, resulting in a shortage of data when deriving some conversion equations, especially at smaller magnitudes. To address this issue, seismologists often perform regressions conditional only to the magnitude scale, ignoring the sensitivity to the reporting agency. However, the calibration needed for most magnitude scales depends on the instrument, soil profile and processing techniques. Hence, the solution might vary between agencies, even if the scale is common (e.g. Figure 5d). Regional scale is also an important factor, since regression using local and global data can lead to different fits (Figure S2).

In order to achieve a balanced trade-off, we developed the following procedure. For each magnitude type (agency-scale) that has less than 200 of its data points available in M_w or a magnitude range than spans less than 3 magnitude units, we check how it correlates with any other magnitude type that shares the same magnitude scale; if the common events were more than 20 and the root-mean-square orthogonal error (RMSOE) with respect to the one-to-one diagonal (green dotted line in Figure 4a) is smaller than 0.25, then the two magnitude types were grouped together, i.e. their values were considered equivalent when performing POR (Figure 2). We termed this metric $RMSOE_{y=x}$. We chose $RMSOE_{y=x} < 0.25$ as threshold because:

- it is smaller than the average RMSOE of the later derived relations (Table 2), meaning that the decision to group does not deteriorate the data scatter;
- it is equal to the largest $RMSOE_{y=x}$ among the most common sources of original direct M_w values (Figure S3).

For the purposes of this procedure, two magnitude scales were considered as potentially equivalent when their first two letters were identical (e.g. M_S, M_{S7}). Exceptions to that rule were the scales M_L, M_d, M_D, and M_C, which were also considered grouping candidates, since the formulation of coda duration magnitudes is usually calibrated using local magnitude values (Eaton, 1992). Solutions of unknown magnitude scale (M) were checked against all scales.

Given the overall scarcity of original M_w values, we had to merge different sources, following common practices followed in magnitude-homogenization efforts. Therefore, all available moment magnitude solutions were assumed equivalent to the "true" M_w, with the exception of MED-RCMT (Med-Net Regional Centroid Moment Tensor; Pondrelli et al., 2011), which showed 50% more scattering than any other source, with a clear tendency to overestimate magnitudes below 5 (Figure S3a). The other sources of original M_w estimates were consistently trending close to the diagonal, when plotted against each other (Figure S3b-f).

4.2.3 Indicator for goodness of fit

Traditionally seismologists employ either expert opinion or the dependent variable's correlation coefficient (R_x^2) to quantify the goodness of fit or to rank the available conversion equations. The closer R_x^2 is to 1, the better the fit. This approach is valid, however, only when the regression is standard least-squares (SR). For orthogonal distance regression, R_x^2 is not strictly applicable because the independent variable is not error-free (Gasperini et al., 2015). Since we are using OR, we had to find an alternative data-driven indicator for the goodness of fit. It should perform consistently well for all sample sizes, functional forms, magnitude scales and magnitude ranges. Following Bormann et al. (2007), we selected the root of the mean squared orthogonal errors (RMSOE). The smaller the RMSOE, the better. Given the wide range of magnitude pairs and the varying functional forms (§4.2.4) considered, we corrected for sample size and complexity of the functional form:

$$\mathrm{RMSOE}_{adj} = \frac{\mathrm{RMSOE} \cdot (\mathbf{n} - 1)}{\mathbf{n} - \mathbf{p} - 1} \tag{1}$$

where n is the sample size and p the number of free parameters. The applied correction is not novel, since it is identical to the one commonly used for R_x^2.

4.2.4 Functional forms

The simplest and thus most frequently used functional form to fit and apply is the linear case (e.g. Papazachos et al., 1997). However, older magnitude scales saturate at larger magnitudes due to their limited frequency bandwidth. They also often underestimate magnitudes below about 3, due to a disproportionate amount of high-frequency attenuation along the path (Hanks and Boore, 1984; Deichmann, 2006). The functional form of the fitted curve should be able to capture both tendencies. To that end, seismologists have employed bilinear models (e.g. Scordilis, 2006), quadratic polynomials (e.g. Grünthal et al., 2009, their eq. 3), exponential models (e.g. Di Giacomo et al., 2015) or even more complex forms (e.g. Grünthal et al., 2009, their eq. 6). Adding free parameters (c_i) increases both the adaptability of the functional form and the data points needed to constrain the fit. We experimented with all the above formulations, plus cubic polynomials and power-law models, and concluded that the most likely candidates for our dataset were:

- two-parameter linear model, $y = c_1 * x + c_2$;
- three-parameter exponential model, $y = e^{(c3 + c4*x)} + c_5$;
- three-parameter power-law model, $y = c_6 * x^{c7} + c_8$.

A bi-linear model was not selected, because it introduces a discontinuity point in the relations where the uncertainty is hard to map (Di Giacomo et al., 2015). The standard linear model cannot capture saturation or inverse-saturation effects, and thus it usually performs well only when the magnitude range of the data points is between 4 and 6. The other two models are more flexible, since they are able to capture both linear and non-linear trends. They can present, however, unreasonably curved shapes when extrapolated outside the magnitude range used for their calibration. That is why we imposed $c_3 > -6$, $c_6 > 0$ and $c_7 < 3$. For similar reasons, we did not allow c_1 to be smaller than 0.5 or larger than 1.8. Furthermore, if the maximum magnitude of the independent variable was smaller than 5, we imposed the linear fit as the preferred one. All three functional forms were fitted to each magnitude type. The one leading to the smallest $RMSOE_{adj}$ (Equation 1), given the aforementioned constraints on the free parameters, was the preferred one (Figure 2).

4.2.5 Magnitude range and saturation effects

Due to issues already discussed in section 4.1, we had to discard magnitude values outside the frequency range of the older magnitude scales, i.e. M_s<3, M_s>8, m_b or M_L or M_d>6.0, before performing POR (Figure 2). No considerations were made regarding m_B since our input sources lack estimates for this scale. We also discarded data points where the difference between the two variables was larger than 1.5 as outliers (Figure 5d).

M_L and M_d calculations can either overestimate Luckett et al. (2018) or underestimate (Deichmann, 2006) the true size of events with M_w smaller than about 3, depending on the agency-specific calibration. To avoid having to visually examine each case, we relied again on $RMSOE_{adj}$ (Equation 1). If an abrupt nonlinearity is observed at the low end of the magnitude range, the goodness of fit would deteriorate (increased $RMSOE_{adj}$), since the selected functional forms are not capable of capturing a double asymptotic trend. This would indicate that this magnitude type does not perform consistently at low magnitudes, since it is calibrated for a limited frequency range. To check for this, we performed each regression two times (Figure 2); once applying no lower bound cut-off (Figure S4a) and once discarding all data points whose independent variable (x axis) was smaller than a threshold value M_t (Figure S4b). The value of M_t was chosen based on the frequency sampling behind each magnitude scale and was 4 for M_s and 3 for m_b or M_L or M_d. Whichever case led to the smallest $RMSOE_{adj}$ was preferred for the conversion of events of magnitude larger than M_t.

Finally, the validity range of the derived conversion equations is defined by the 1^{st} and 99^{th} percentile of the independent variable, after the application of all the above filters (Table 2). A schematic summary of the fitting procedure described in sections 4.2.1 - 4.2.5 is shown in Figure 2.

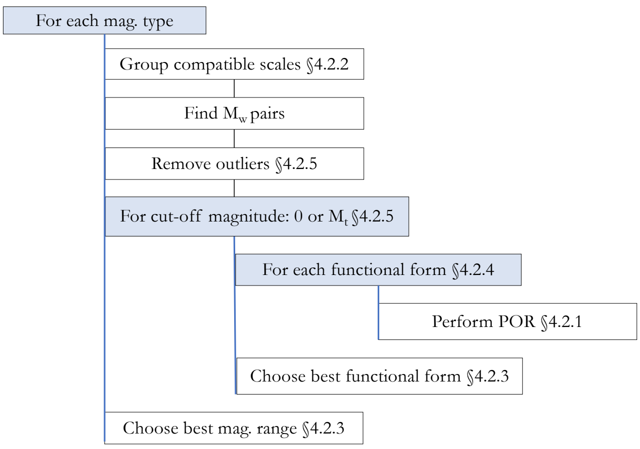

Figure 2 Flowchart of the fitting procedure used in the derivation of the conversion relations.

4.2.6 Application of conversion relations

The application procedure for the conversion relations is illustrated in Figure 3. If at least one available magnitude type is M_w, we select this value as the homogenized magnitude. If multiple M_w are available for one event we prioritize in descending order: CSEM, GII/IPRG, Cyprus Geological Survey (NIC), Harvard University, US Geological Survey (NEIC) and GCMT (Figure S3). This hierarchy can be modified by the user on a case-by-case basis. Alternatively, the M_w reporting agencies can be ranked based on increasing $RMOSE_{y=x}$ against the rest.

If an event is not available in M_w, we select the magnitude type available for this event, whose conversion relation has the lowest $RMSOE_{adj}$ (Equation 1), respecting possible validity range constraints. If no relation is applicable, we repeat this step overlooking the validity range, and the relation with the lowest $RMSOE_{adj}$ is extrapolated to match the size of the event. If the latter is below the validity range, we ignore any potential abrupt nonlinearity at low magnitudes and apply the corresponding conversion relation derived without any lower bound cut-off. If none of the magnitude solutions has a conversion relation, then the median of the available magnitudes (regardless of scale) is used as proxy M_w. For the homogenized events, we report the total uncertainty around the M_w estimate as $\sigma = \sqrt{\sigma_y^2 + \sigma_{\text{meas}}^2}$, where σ_y is the root of the mean squared (vertical) errors of the conversion relation (with M_w plotted on the y axis) and σ_{meas} is the measurement uncertainty accompanying the original magnitude scale. The latter was provided only in the ISC data. Since POR minimizes the perpendicular offsets and not the vertical ones, it leads to larger σ_y compared to a SR with M_w as the dependent variable.

4.3 Results

4.3.1 Combining magnitude types of compatible magnitude scales

The grouping procedure worked well, leading to magnitude types of the same agency and of similar scale, e.g. JSO M_L and JSO M_{Lv}, being identified as equivalent. The acronyms used for each agency follow ISC's naming scheme (http://www.isc.ac.uk/iscbulletin/agencies/). Overall, M_L and M_d estimates coming from the same agency were frequently grouped, since their calibration is interconnected (see §4.1). The procedure increased the sample size of the fitted data points and expanded the validity range of the derived equations (e.g. Figure 5d; S5a), without affecting their scatter. With the grouping procedure enabled, the average number of events behind each conversion increased by 40%, while the mean $RMSOE_{adj}$ among all the derived conversion relations remained unchanged.

$RMSOE_{y=x}$ performed well as an unsupervised indicator, even in challenging situations. In Figure 4a, the m_b estimates of ISC and NEIC are close to the diagonal with reasonable scatter, resulting in $RMSOE_{y=x} < 0.25$. On the other hand, in Figure 4b, $RMSOE_{y=x}$ is significantly larger than the threshold we set, since even though IPRG M_L and JSO M_L are centered around the diagonal, they present extensive scatter, with differences up to 2 magnitude units. In both cases, blindly fitting a single-parameter linear curve (solid black line in Figure 4) would have misinformed us that the fit was equally good.

4.3.2 Regression trends

The frequency-band limitations of each magnitude scale (§4.1) were verified during our analysis. A lot of the derived conversion relations display saturation effects above M_w 5 (e.g. Figure 5d; S5cd) and below M_w 3

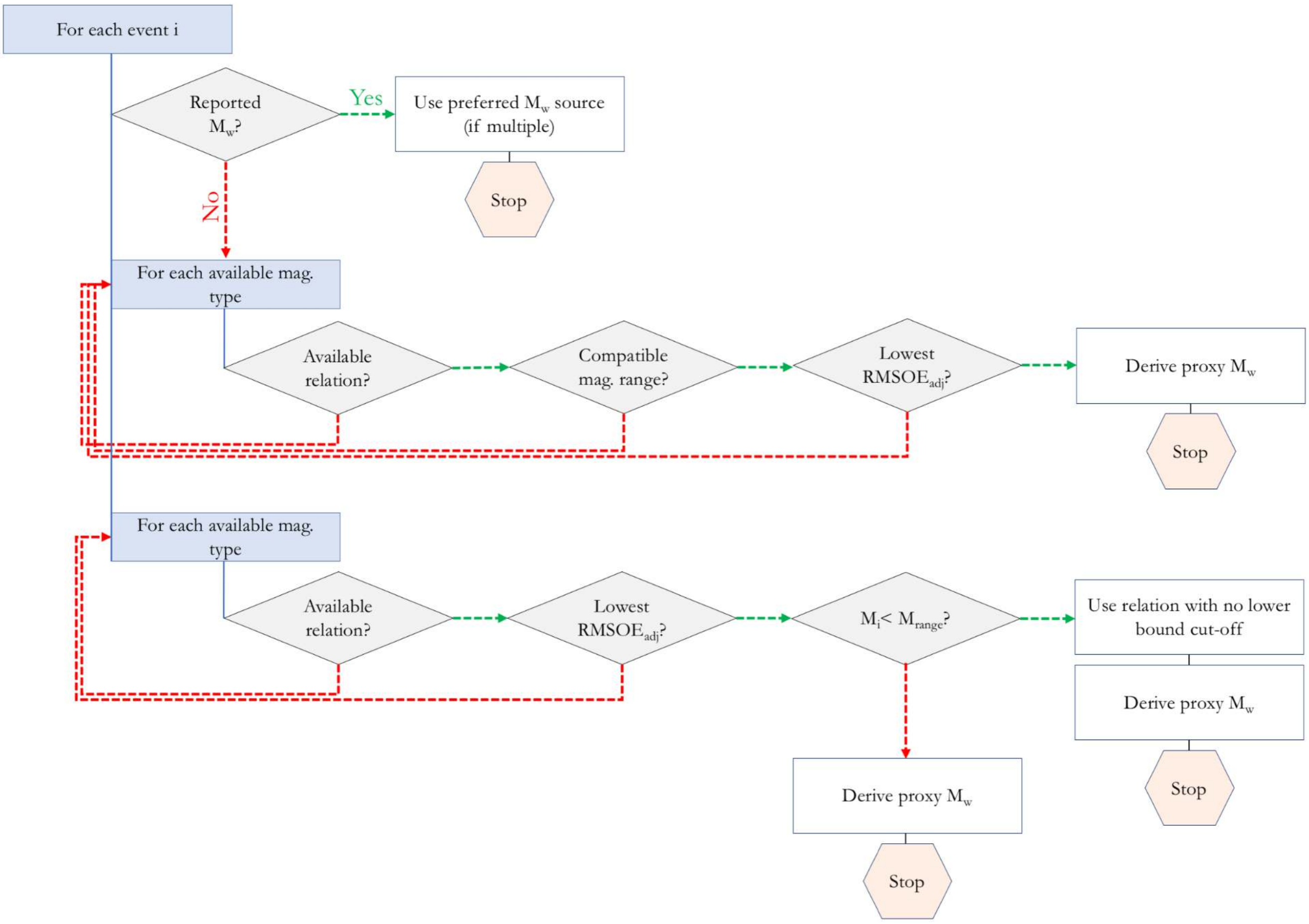

Figure 3 Flowchart describing the application of the derived conversion relations. M_{range} is the validity range of the conversion relation and M_i is the magnitude value of the event in the reported magnitude scale.

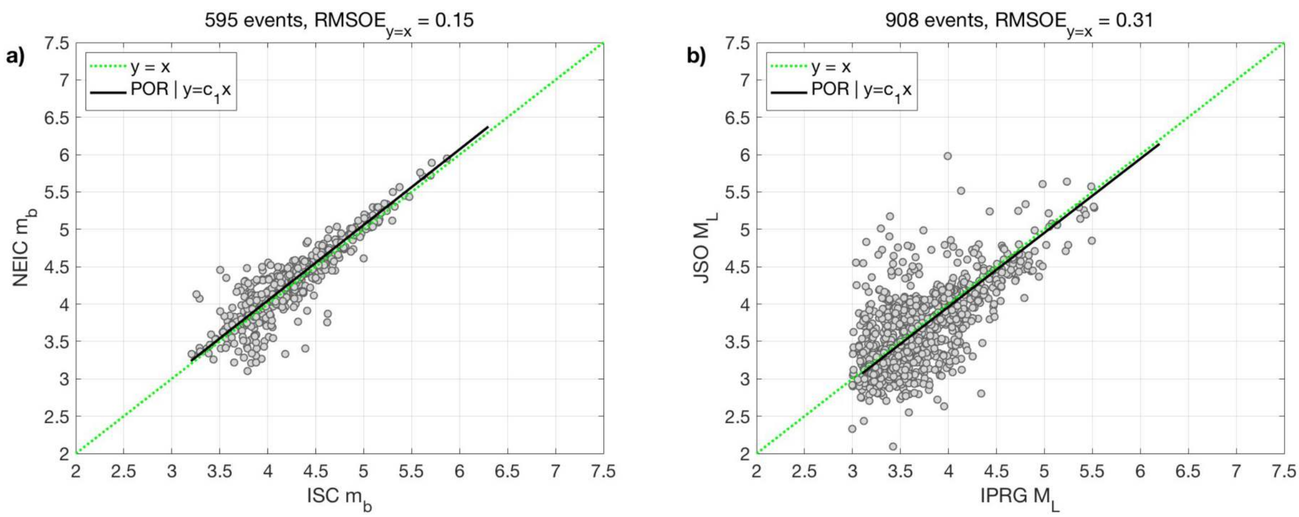

Figure 4 Correlating magnitude estimates from different agencies.

(e.g. Figure S5b). Had we not tested for the lower bound cut-off at M 3, most of the fitted functional forms would have been nonlinear (Figure 5ac; S4). For large sample sizes, our two nonlinear fits present similar shapes that differ a lot from the linear curve if extrapolated outside the fitted magnitude range (Figure 5cd). We did not come across magnitude types that underestimate larger magnitudes while overestimating smaller ones. Datasets containing such a trend could benefit from third-degree polynomial fitting.

The conversion relations that were most frequently used when homogenizing the original magnitude estimates in the various catalogs (Figure 5; S5) present reasonable scatter around the diagonal, except for JSO M_L which does not correlate well with M_w (Figure S5d). Even though the ISC Bulletin includes dozens of magni-

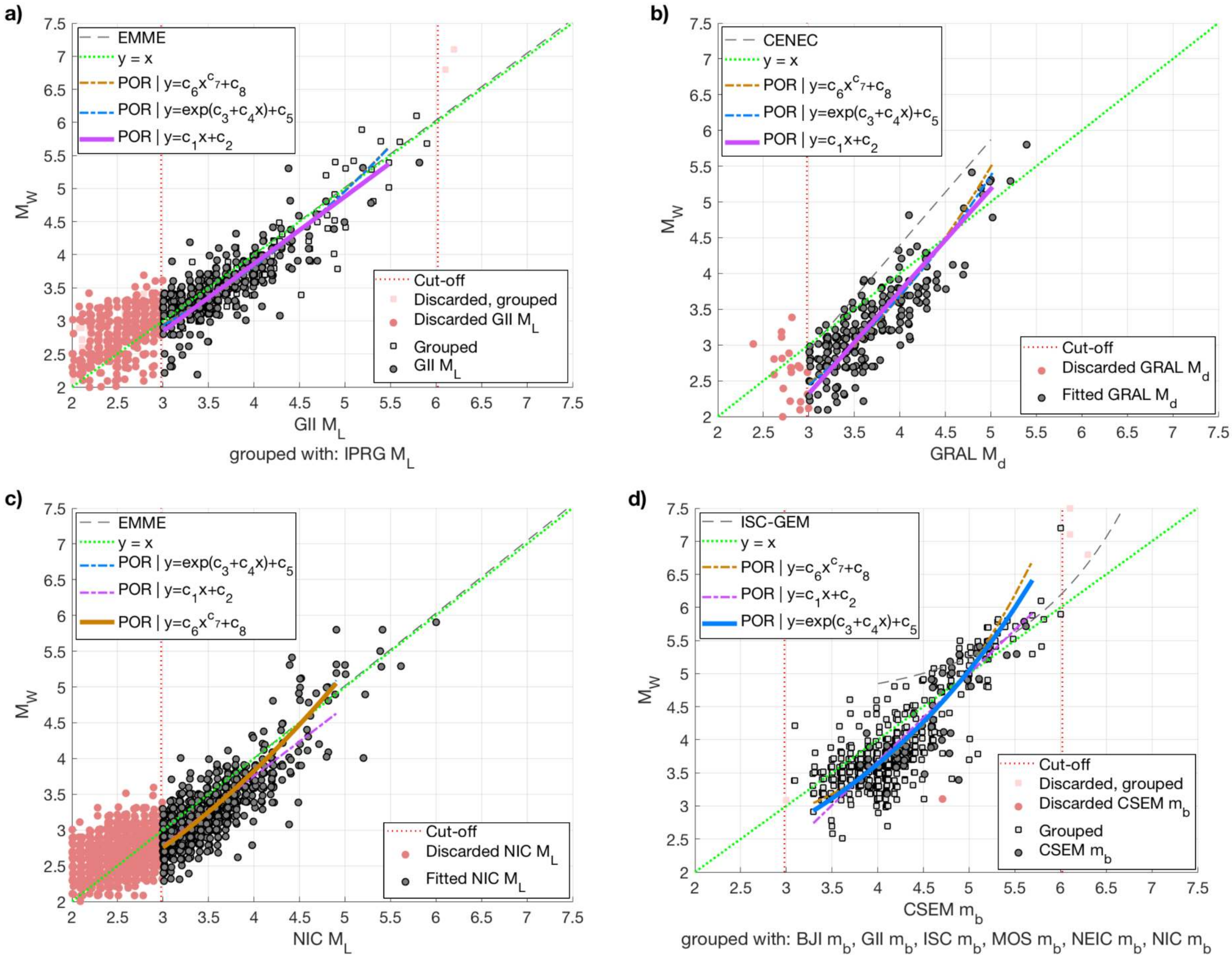

Figure 5 Derived conversion relations for four of the most common magnitude types. The functional form with the lowest $RMSOE_{adj}$ is plotted as a solid curve.

tude types, only 10 were needed to homogenize almost every event (Table 2).

4.3.3 Comparison with other already homogenized catalogs

Regarding the proxy M_w values already present in our input catalogs, ISC-GEM used OR (Di Giacomo et al., 2015) and EMME probably used SR (since they are reporting R_x^2 values). Within our case study region, the vast majority of EMEC's events originate from Papaioannou (2001) and Abdallah et al. (2004). Papaioannou (2001) reports moment magnitudes, which are converted mostly using the equations of Papazachos et al. (1997), who used SR. As a result, Papaioannou (2001)'s proxy M_w values do not agree well with the corresponding M_w values from Moment Tensor Solutions (Gruenthal and Wahlstroem, 2012). Abdallah et al. (2004) report M_L, for which CENEC derived a conversion equation to convert to M_w, employing CSQ. With all of that in mind, the significant scatter in the proxy M_w values developed in this study, when compared mainly to EMME's and EMEC's (Figure 6) should be expected.

5 Merging multiple catalogs

The first step towards building a unified catalog is to identify which seismic events are included in more than one catalog, i.e. duplicates. Usually, each input catalog has its own scheme for assigning a unique identifier (ID) to each event, thus making the identification of common events non-trivial and the use of a "duplicate finding" algorithm a necessity. This generally takes the form of a window-searching algorithm by which multiple representations of the same event are identified due to their proximity in space, time, and, occasionally, magnitude. The configuration of these windows (margins) and the quality of the information provided by the catalog will greatly influence the possibility of misassigning duplicates (Weatherill et al., 2016). One of the most common pitfalls are inaccuracies in the earthquake's origin time. For example, EMEC (Gruenthal and Wahlstroem, 2012) systematically provides origin times down to minutes (and not seconds). The electronic versions of the catalogs fill in empty entries of missing time information (e.g. second) with zeros. Finally, a bulletin might report local time and not Coordinated Universal Time (UTC) or use a non-standard geographical coordinate system.

Magnitude type	Relation	Validity range	RMSOE	σ_y (RMSE)	Data-points	Region
GII M_L	y=1.02x-0.21	$3.0 \le x \le 5.5$	0.21	0.30	478	Israel
GII M_d	y=0.99x-0.12	$3.0 \le x \le 5.5$	0.19	0.27	213	Israel
IPRG m_b	$y=0.14x^{2.17}+0.64$	$4.0 \le x \le 5.8$	0.17	0.34	288	Israel
CSEM M_L	$y=0.22x^{1.76}+1.22$	$3.0 \le x \le 5.1$	0.18	0.27	1151	Euro-Med.
CSEM m_b	$y=e^{-0.53x+0.40}+0.75$	$3.3 \le x \le 5.8$	0.25	0.41	467	Euro-Med.
GRAL M_d	y=1.43x-1.98	$3.0 \le x \le 5.1$	0.21	0.37	232	Lebanon
NIC M_L	$y=0.16x^{1.99}+1.37$	$3.0 \le x \le 4.9$	0.18	0.26	1125	Cyprus
SNSN M_L	$y=e^{0.49x+0.23}-0.16$	$2.1 \le x \le 5.2$	0.24	0.31	143	Saudi Arabia
RYD M_d	$y=e^{0.29x+0.29}-0.53$	$3.0 \le x \le 5.3$	0.19	0.30	587	Saudi Arabia
JSO M_L	y=1.30x-1.92	$3.1 \le x \le 5.9$	0.37	0.61	94	Jordan

Table 2 Derived conversion relations for the ten most common magnitude types.

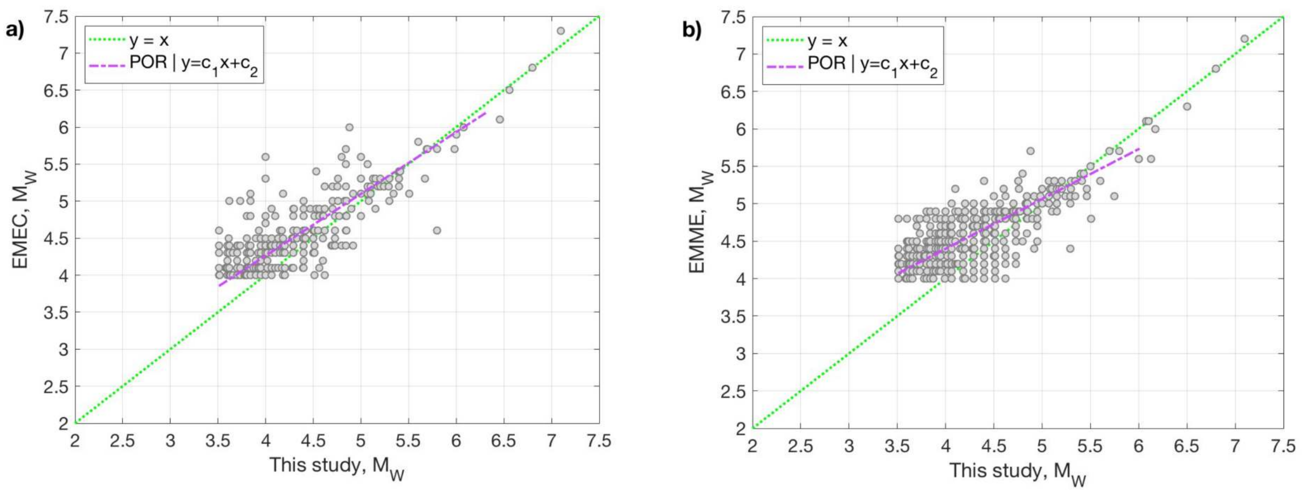

Figure 6 Comparison of proxy M_w values computed by this study, with the ones derived by either EMEC (a) and EMME (b).

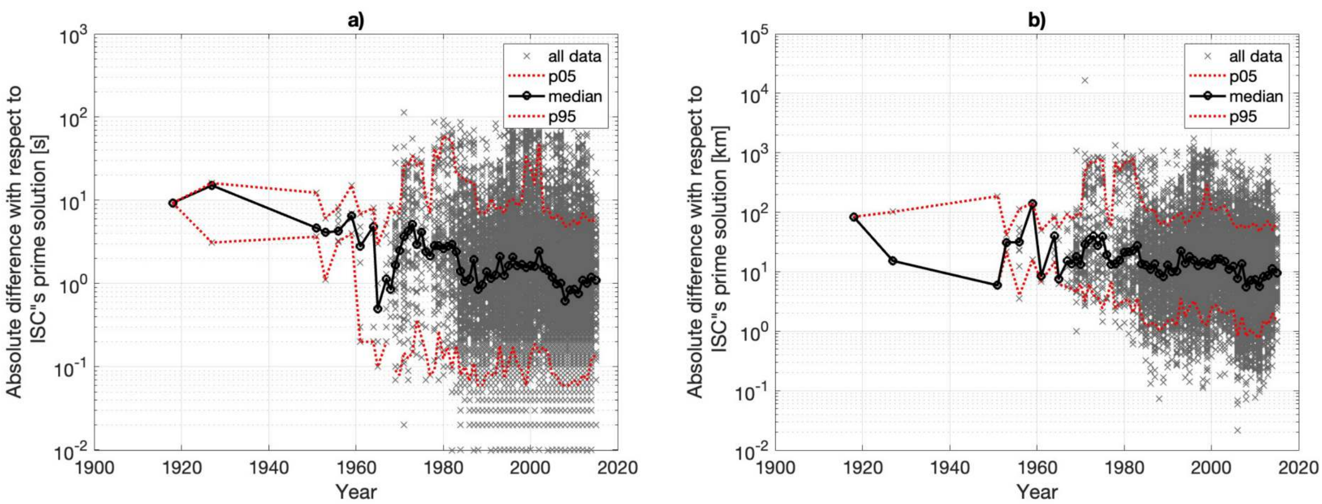

Figure 7 Temporal trend of the absolute differences among ISC's contributing agencies with respect to ISC's prime solution in terms of (a) origin time and (b) location. Red lines indicate the 5 to 95 percentile range; the black line indicates the median (50^{th} percentile).

To ensure best practice, the compiler should adopt margins that are larger than the uncertainty of the methods and models used by the agencies (Schweitzer, 2006). That said, an algorithm with overestimated margins might mistakenly flag clustered events (fore/aftershocks) as duplicates. To address this trade-off, researchers often define margins that are bulletin-specific or variable with time (e.g. Wang et al., 2009). For the analog era, when the data were sparser, it is likely that wider time/space windows are needed. Some studies even resort to manual inspection for the few larger magnitude events that have a greater impact on the hazard estimates (e.g. Beauval et al., 2013).

Most modern unified catalogs either do not clearly state their criteria for identifying the duplicate events or choose arbitrary values based more on expert opinion than data-driven analysis. The chosen margins for instrumental catalogs vary significantly, on the order of 10-120 seconds and of 30-100 km (e.g. Wang et al., 2009; Faeh et al., 2011; Beauval et al., 2013; Poggi et al., 2017), while the magnitude is rarely used as a deciding factor.

5.1 Relevance of the magnitude scale when merging catalogs

The order in which the compiler will do the merging and the magnitude homogenization is not always fixed. If the compiler chooses to discard the magnitude as a criterion for the identification of duplicates and has great confidence in the selected margins for origin time and location, then one could first merge all catalogs into one, storing all magnitude solutions for each unique event, and then perform the magnitude homogenization. This way, the compiler ends up with more magnitude solutions per event, hence more potential magnitude pairs to derive the conversion relations. We, however, preferred to do the opposite: first homogenize all sources in M_w (using the magnitude solutions of ISC and GII), and then merge all datasets utilizing the event's size to constrain the duplicate finding algorithm. One reason to do that is that when one relies on earthquake solutions alone (no stations data), it is often impossible to distinguish a fore/aftershock from a duplicate, even if the margins are ideally selected. Our main concern was not to contaminate the derivation of the magnitude conversion relations with any artifacts that the merging process might introduce. For example, events of the same earthquake sequence can be misidentified as duplicates, mixing up incompatible solutions as magnitude pairs for the regression.

5.2 Methodology

We aimed at deriving both margins (i.e. origin time and location difference) based on the trends we observe in the actual data used in this study, minimizing the need for expert opinion. To do that, multiple solutions for the same event are needed in order to calculate the discrepancy in the data. The ISC Bulletin reports for each event available parametric solutions from all contributing agencies, as well as a "prime" set, which according to ISC describes best the reviewed event. This rich database enables the statistical analysis of the discrepancy in the solutions, either between agency-pairs or in comparison to ISC's proposed "prime" solution. We did the latter, assuming that ISC's origin solutions were the most accurate, since they are derived using the richest available dataset. Although this is a valid assumption in terms of epicenter and origin time, local velocity models from regional networks often lead to more accurate depth estimates. We did not use the depth as a criterion for duplicate finding, however.

For our case study region (and for most of the world), ISC's IASPEI Seismic Format (Storchak, 2006) files are sufficient to deduct data-driven margins for all of the input catalogs and bulletins. GII and EMSC are contributing agencies to ISC, while ISC-GEM, IRIS, EMME and EMEC are compiled using mainly ISC data in the first place. Hence, using only the ISC Bulletin, we were able to derive margins that are suitable for all our input catalogs.

The performed statistics do not have to be complex. Once the distribution of differences is established, the compiler can pre-define a percentile-based value to be used as the margin for duplicate-finding. If the differences in time, space, and (optionally) magnitude solutions between two events fall within these data-driven margins, then a duplicate is flagged. We chose to use the 95th percentile as threshold for the definition of the margins in the duplicate-finding algorithm. The chosen percentile was large enough to ensure that the margins cover the modeling uncertainty in the computed solutions, yet small enough to discard unreasonably large outliers that are often observed possibly due to logging errors or miscalculations.

When two events in different catalogs are identified as duplicates, one should decide which parametric information describe the event best. A hierarchy must be defined in advance to dictate this process. Regarding the origin time and location, this hierarchy is usually pre-defined by the compiler based on the following considerations:

- ISC-GEM has re-assigned origin times, epicenters and hypocenters to moderate-to-large magnitude events after 1900, following clearly documented up-to-date methods (Di Giacomo et al., 2015). Hence, ISC-GEM was considered as the most reliable source of parametric information.
- ISC collects and reviews the most comprehensive dataset of both raw and parametric seismic data for each event. As a result, the solutions they recommend or originally compute are highly credible. EMSC does a similar job having, however, fewer contributing agencies.
- Local agencies close to the epicenter are more likely to have a detailed velocity model for the region and higher network density, when compared to global agencies.
- The level of accuracy in date and time is also an important factor. For example, EMEC provides origin times down to minutes (and not seconds), while GII reports seconds with consistency only after 1983.
- Compilations providing unclear documentation regarding their merging procedure and original sources should not be favored.
- The regression methods used in the magnitude homogenization process (§4.2.1) should be taken into account when ranking magnitude estimates.
- Bulletins reporting more than one magnitude solution provide greater flexibility in selecting the most suitable conversion equation (§4.2.6).

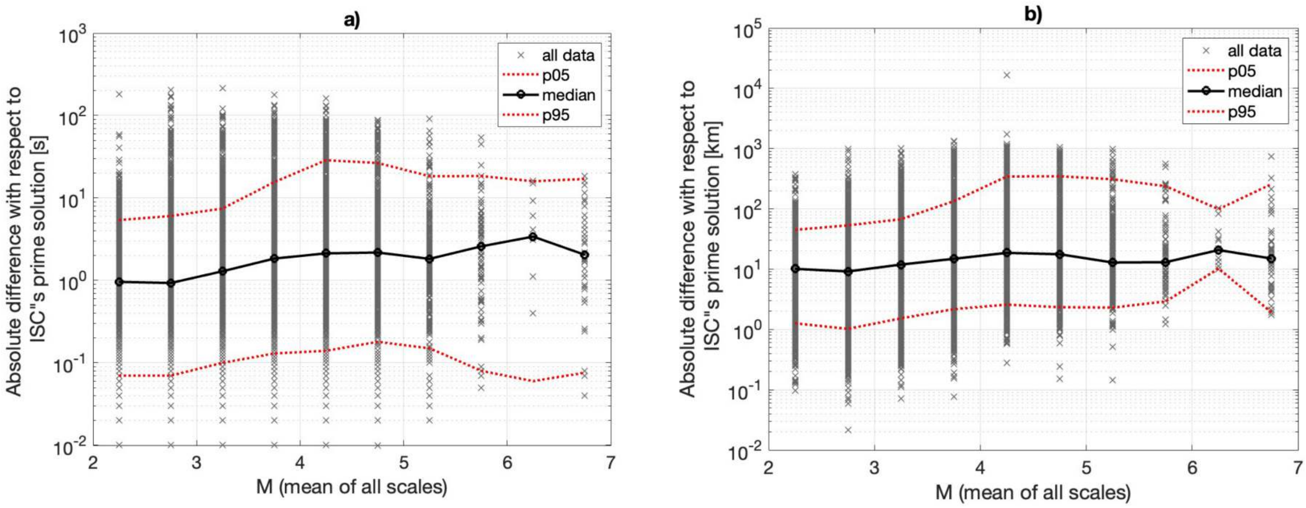

Figure 8 Trend of absolute differences among ISC's contributing agencies with respect to ISC's prime solution with magnitude; (a) origin time and (b) location. Red lines indicate the 5 to 95 percentile range; the black line indicates the median (50th percentile).

Our preferred hierarchy regarding the proxy M_w was: ISC-GEM; ISC; IRIS; GII; EMSC; EMEC; EMME (§4.3.3), prioritizing our conversion relations over EMME's and EMEC's, and acknowledging the flexibility that the multiple magnitude solutions in the ISC Bulletin provide. Regarding the time and location solutions, our preferred hierarchy (Figure S3) was: ISC-GEM; ISC; EMSC; GII; IRIS; EMME; EMEC, prioritizing the reviewed relocations of ISC, GII and EMSC. The merging process is sequential, i.e. we are always looking for duplicates between two catalogs only. The margins are tested against the difference of the catalog that is being merged with the preferred solution among all the catalogs that have already been unified.

5.3 Results

5.3.1 Variability in origin time and location solutions within ISC

The vast majority of absolute differences in origin time among ISC's contributing agencies with respect to ISC's prime solution are less than 10s, with 9.5s being 95th percentile (Table S1). That said, outliers of more than two minutes also exist, perhaps due to a zero value being added when a measurement of seconds is not available. As far as location is concerned, the vast majority of the differences is less than 100 km, with 85 km being the 95th percentile (Table S1). Observed differences, in the order of 500-1000 km, were attributed to input errors (typos).

Figure 7 demonstrates that the median annual differences in origin time and location are decreasing with time, probably due to increasing number of stations and improved velocity models (Bondar et al., 2015). That said, after 1985, namely when most nearby national networks were set up, the differences appear to be relatively stable with time.

Figure 8 shows that the differences in origin time and location are increasing with magnitude, with a 2-fold increase between magnitudes below 3 and magnitudes above 4. Moderate-to-large events are usually also covered by more distant networks with large-scale velocity models and looser azimuthal coverage. That could explain these observations. One would also expect decreasing uncertainty in the location with decreasing rupture size (Kagan, 2003).

Figure 9 shows that the deviation from ISC's prime solutions is largely agency-dependent. Interestingly, national agencies nearby (e.g. JSO) do not perform consistently better than teleseismic ones (e.g. NEIC), as one would expect (Bondar et al., 2004). Nevertheless, when looking at the origin time differences of the most important agencies for the case study area, the 90th percentile is usually less than 5s and always less than 10s, in agreement with previous studies (e.g. Bondar et al., 2004, 2015). On the other hand, the variability in the epicentral location is higher than expected (Bondar et al., 2015), with the 90th percentile being rarely below 30 km.

5.3.2 Parametric windows for duplicate identification

We utilized the absolute differences among agencies with respect to ISC's prime solution as a data-driven proxy for the definition of parametric windows during the duplicate identification. We defined the margins for location and origin time as the 95th percentile of the aforementioned deviation. We used the values of the second and third column of Table S1 as margins for the instrumental events after 1964, i.e. 10s and 85 km (Table 3). Special attention was paid to specific limitations in the input catalogs. In particular, EMEC does not report seconds for any event, while GII reports seconds only after 1983. Therefore, this margin should be adjusted to 2 minutes and these catalogs should be the last ones merged. For the events before 1964 there is not enough data to do any sort of statistical analysis (Figure 7) and thus expert opinion cannot be avoided. We used 30 minutes and 100 km as margins for that time-period (Poggi et al., 2017).

Additional levels of complexity could be added. One

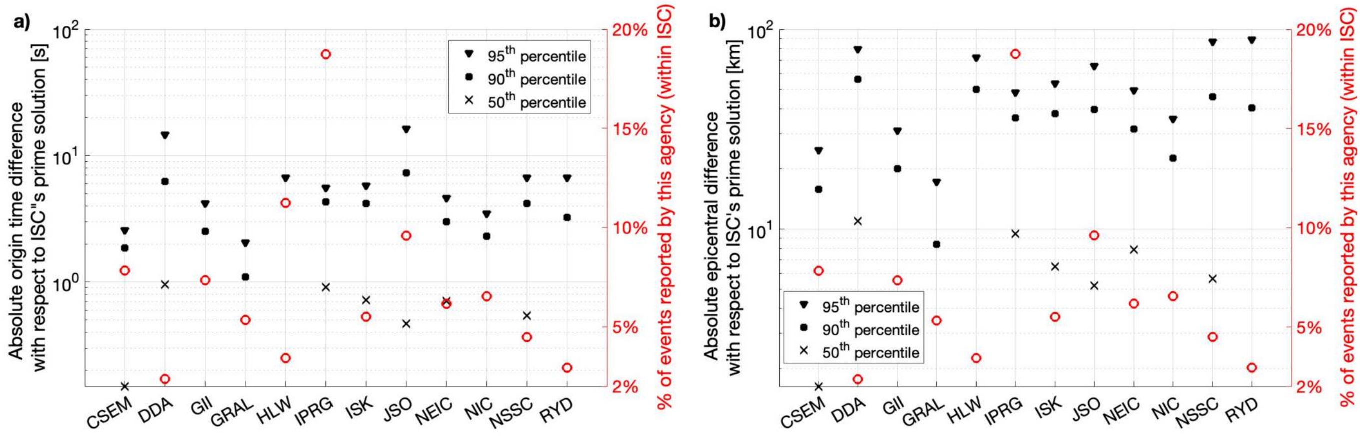

Figure 9 Agency-specific statistics on deviation from ISC's prime solution: (a) origin time; (b) epicenter.

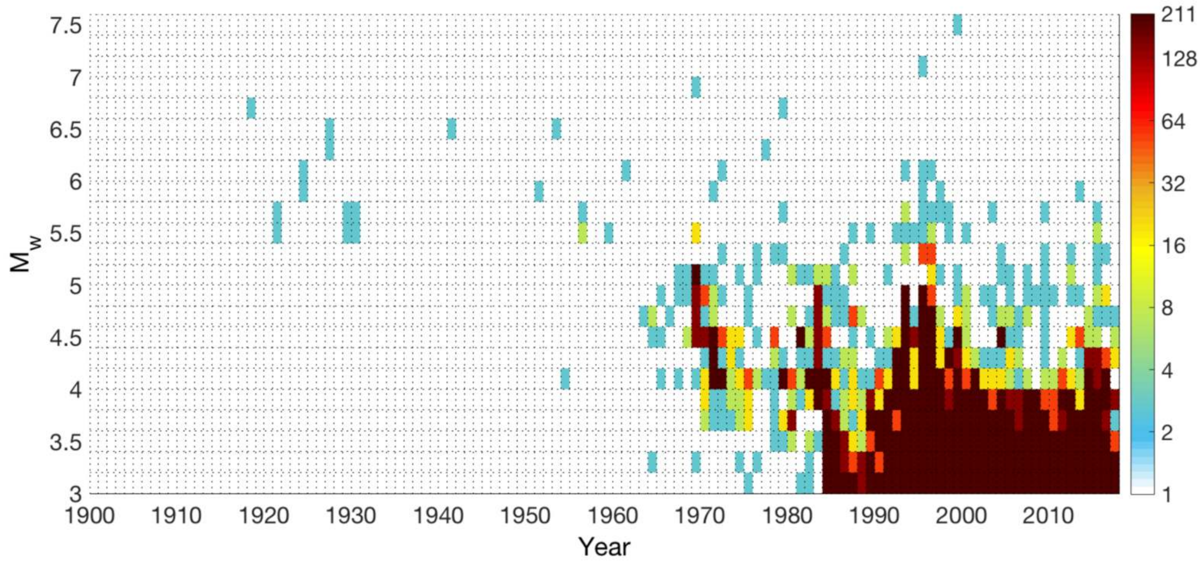

Figure 10 Density of earthquake magnitudes with time for the homogenized catalog.

could make the margins magnitude-dependent, to capture the trends shown in Figure 8 or use tighter post-1964 and post-1983 margins when merging the ISC Bulletin with CSEM and their product with GII respectively (Table S1).

6 Catalog overview

The unified catalog contains 25000 time-stamped hypocenters between 1900 and 2017, of which more than 5500 events have moment magnitude M_w larger than 3. It is available in electronic format online (Grigoratos et al., 2023). We also report the preferred original sources for the origin and magnitude solutions, the measurement uncertainty behind the original magnitude estimate, and the total magnitude uncertainty after conversion. Moment tensor solutions were available for only a quarter of the events, while the rest had magnitude solutions that needed conversion to M_w. The average conversion uncertainty (σ_y) was 0.3 and none of the events required extrapolation of the derived conversion relations. For only 3% of the events, none of their magnitude solutions could be associated with a conversion relation and thus the median of their original magnitudes is reported.

Most of the events in our catalog are post-1983 (Figure 10), coinciding with the development of the first local networks along the DSTFZ, by Israel and Jordan. The foundation of ISC in 1964 had already expanded the magnitude range of the cataloguing below magnitude 5.5, while also improving the reliability of the location solutions. That said, about 7% of the events in the unified catalog were not reported by the ISC Bulletin (Table S2).

One third of the events in our catalog, including the 1995 M_w 7.2 rupture, are found in the Gulf of Aqaba (Figure 11), in contrast to the low seismic activity reported there in the previous millennium (Figure 1) (Grigoratos et al., 2020). On the other hand, the many large historical earthquakes in the segments north of the Dead Sea lake have not been followed by similar levels of activity in recent decades. Finally, the cluster of post-1985 seismicity east of the DSTFZ, in south Jordan (Latitude ~30; Figure 11), is most likely related to potash mines (Rodgers et al., 2003). Groundwater extraction is also linked to a few clusters in and around Lake Kinneret

	Margin		
Time period	Origin-time	Epicenter	M_w
1900-1963	30 minutes	100 km	1 unit*
1964-2018	10 seconds**	85 km	1 unit*

*2 units when merging EMEC or EMME (see Figure 1)

**2 minutes when merging EMEC or pre-1983 GII events

Table 3 Margins used in the duplicate finding algorithm.

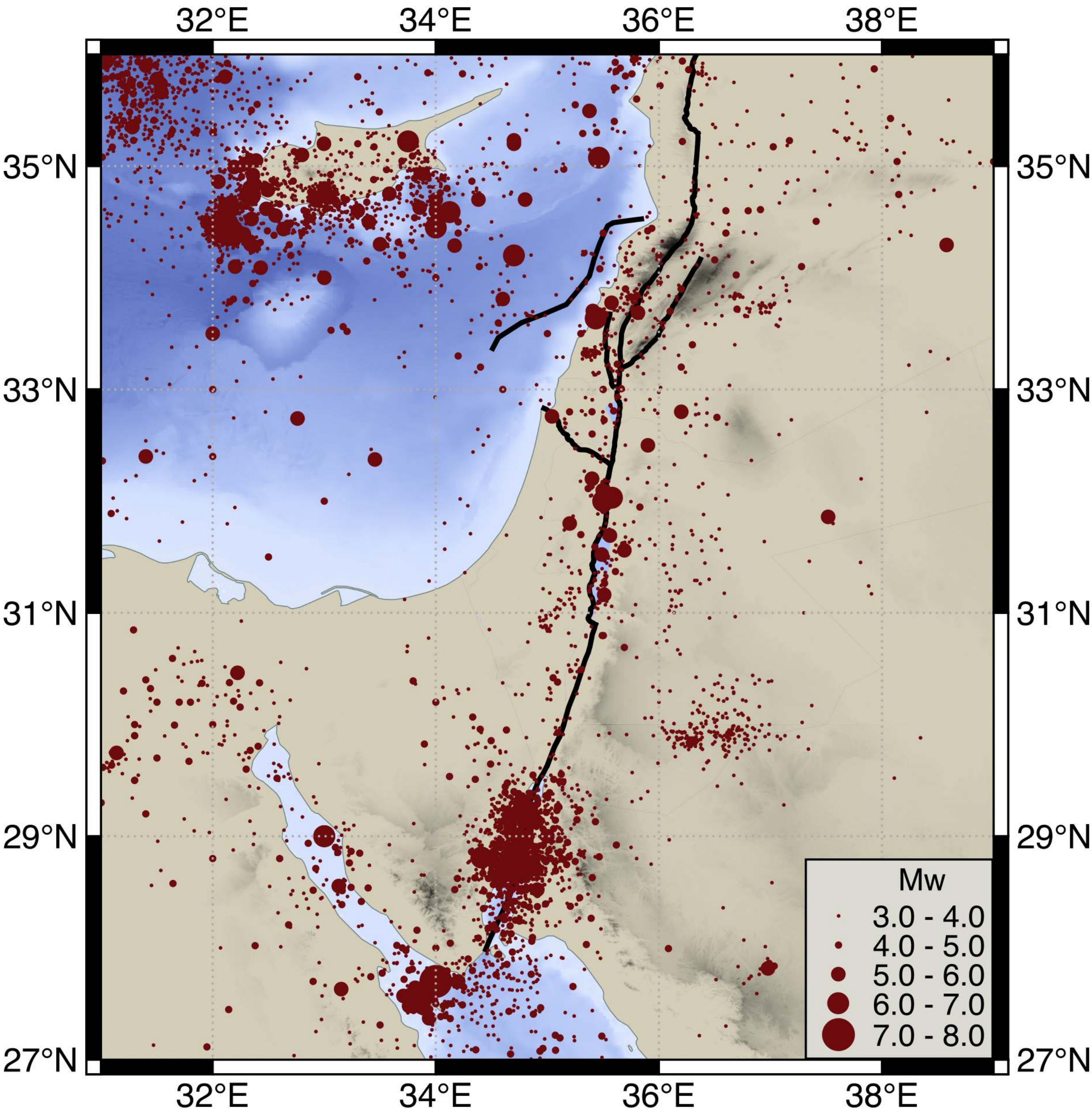

Figure 11 Homogenized catalog of earthquakes with $M_w \geq 3$ between 1900 and 2017. The black lines indicate main faults along the DSTFZ (Grigoratos et al., 2020).

(Sea of Galilee; Shalev et al., 2023). Although we cannot exclude other instances of anthropogenic seismicity, we are not aware of other established cases.

We should specify that the catalog has not been declustered and the spatio-temporal variation of the magnitude of completeness of the catalog has not been assessed. The target magnitude of M_w 3 was chosen simply because it was viewed as a low enough value to aid future derivations of the regional b-values.

7 Conclusions

The creation of a homogenized earthquake catalog is an error-prone procedure that requires a good understanding of the heterogeneities among the available bulletins. Common events within the bulletins have to be identified and assigned with the most suitable origin time and location solution, while all the events have to be harmonized into a single magnitude scale. This process requires several decision variables that are usually defined using qualitative measures or expert opinion, without a clear exploration of the associated uncertainties. To address this issue in a more quantitative way, we developed a framework, which can utilize multiple databases, such as the ISC Bulletin, to explore the relations between earthquake solutions from different seismic networks and agencies, in order to produce a unified parametric earthquake catalog. The proposed data-driven approach defines spatio-temporal margins within which duplicate events fall and converts the various reported magnitudes into a common scale. Given the density and geographical coverage of ISC's database, we believe that the proposed methodology can be applied to a number of regions worldwide.

To that end, the MATLAB and Python scripts used in this workflow have been made publicly available. We applied them to the Dead Sea Transform Fault Zone and derived a list of more than 5500 instrumental events with M_w larger than 3. One third of the events in our catalog, including the 1995 M_w 7.2 rupture, are found in the Gulf of Aqaba, in contrast to the low seismic activity reported there in the previous millennium (Grigoratos et al., 2020). On the other hand, the many large historical earthquakes in the segments north of the Dead Sea lake have not been followed by similar levels of activity in the last century.

As far as the magnitude homogenization is concerned, the frequency dependence of the older magnitude scales was evident during our analysis. Most of the derived conversion relations underestimate events with M_w either below 3 or above 6. We introduced the root of the mean squared orthogonal errors (RMSOE), corrected for sample size and number of free parameters, as a metric to determine the magnitude range of the regression, the fitted functional form, and which of the available magnitude solutions is to be converted to M_w. In cases where the data points for the regression were limited, we further employed RMSOE to determine whether magnitude estimates of similar scale could be grouped together without alteration of their underlying correlation with M_w. With the exception of JSO M_L, all key magnitude types in the catalogs correlated reasonably well with M_w, given their frequency-band limitations. The average conversion uncertainty (σ_y) in our unified catalog was 0.3 magnitude units, which assuming a (mostly underreported) measurement uncertainty of 0.2, results in an overall uncertainty of about 0.36 behind each proxy M_w.

Having homogenized the magnitude of the events, we then used a window-searching algorithm to identify multiple representations of the same event in the various catalogs, based on their proximity in space and time. We defined these two margins analyzing the discrepancies in the solutions provided by ISC's contributing members. The differences in origin time and location are agency-dependent, and are generally decreasing with time and decreasing magnitude. In the last 50 years, the solutions rarely deviate more than 10s or 85 km from ISC's reviewed solution.

Acknowledgments

The first author acknowledges the funding he received in the past from the Doctoral Program of the University School of Advanced Studies IUSS Pavia (Italy). We would like to thank the Editor Andrea Llenos, Domenico Di Giacomo and Annemarie Christophersen for constructive comments that led to improvements in the article.

Data and code availability

The produced homogenized earthquake catalog is available online (Grigoratos et al., 2023). The MATLAB scripts we developed for the derivation of the magnitude conversion relations are available on Zenodo (Grigoratos, 2023). The Python code-base for the duplicate-removal process can be found at https://github.com/klunk386/CatalogueTool-Lite/tree/master/OQCatk. Derived conversion relations not provided in Table 2 can become available upon reasonable request. The following input datasets are also available online: ISC Bulletin http://www.isc.ac.uk/iscbulletin/search/, ISC-GEM http://www.isc.ac.uk/iscgem/index.php, EMSC https://www.emsc-csem.org/Earthquake/?filter=yes, IRIS http://service.iris.edu/fdsnws/event/1/, EMEC http://emec.gfz-potsdam.de/, GII https://eq.gsi.gov.il/en/earthquake/searchEQS.php. We used v4 of ISC-GEM and all other datasets were last accessed in February 2018. The acronyms used for each agency follow ISC's naming scheme (http://www.isc.ac.uk/iscbulletin/agencies/).

Competing Interests

The authors have no relevant financial or non-financial interests to disclose.

References

Abdallah, A., Feldman, L., and Shapira, A. The Unified Earthquake Catalogue of the region, 2004. Geophysical Institute of Israel (http://earthquake.co.il/heb/hazards/docs/Catalog-rprt.pdf).

Aldersons, F. and Ben-Avraham, Z. The Seismogenic Thickness in the Dead Sea Area. In *Modern Approaches in Solid Earth Sciences*, pages 53–89. Springer Netherlands, 2014. doi: 10.1007/978-94-017-8872-4_3.

Ambraseys, N. *Earthquakes in the Mediterranean and Middle East: a multidisciplinary study of seismicity up to 1900*. Cambridge University Press, Oct. 2009. doi: 10.1017/cbo9781139195430.

Ambraseys, N. N. Reassessment of earthquakes, 1900-1999, in the Eastern Mediterranean and the Middle East. *Geophysical Journal International*, 145(2):471–485, May 2001. doi: 10.1046/j.0956-540x.2001.01396.x.

Beauval, C., Yepes, H., Palacios, P., Segovia, M., Alvarado, A., Font, Y., Aguilar, J., Troncoso, L., and Vaca, S. An Earthquake Catalog for Seismic Hazard Assessment in Ecuador. *Bulletin of the Seismological Society of America*, 103(2A):773–786, Mar. 2013. doi: 10.1785/0120120270.

Bondar, I. and Storchak, D. Improved location procedures at the International Seismological Centre. *Geophysical Journal International*, 186(3):1220–1244, July 2011. doi: 10.1111/j.1365-246x.2011.05107.x.

Bondar, I., Myers, S., Engdahl, E., and Bergman, E. Epicentre accuracy based on seismic network criteria. *Geophysical Journal International*, 156(3):483–496, Mar. 2004. doi: 10.1111/j.1365-246x.2004.02070.x.

Bondar, I., Engdahl, E., Villasenor, A., Harris, J., and Storchak, D. ISC-GEM: Global instrumental earthquake catalogue (1900-2009), II. Location and seismicity patterns. *Physics of the Earth and Planetary Interiors*, 239, 2015. doi: 10.1016/j.pepi.2014.06.002.

Bormann, P. and Saul, J. The new IASPEI standard broadband magnitude mB. *Seismological Research Letters*, 79(5):698–705, Sept. 2008. doi: 10.1785/gssrl.79.5.698.

Bormann, P., Liu, R., Ren, X., Gutdeutsch, R., Kaiser, D., and Castellaro, S. Chinese National Network Magnitudes, Their Relation to neic Magnitudes, and Recommendations for New iaspei Magnitude Standards. *Bulletin of the Seismological Society of America*, 97(1B):114–127, 02 2007. doi: 10.1785/0120060078.

Bormann, P., Liu, R., Xu, Z., Ren, K., Zhang, L., and Wendt, S. First application of the new IASPEI teleseismic magnitude standards to data of the China National Seismographic Network. *Bulletin of the Seismological Society of America*, 99(3):1868–1891, June 2009. doi: 10.1785/0120080010.

Brax, M., Albini, P., Beauval, C., Jomaa, R., and Sursock, A. An Earthquake Catalog for the Lebanese Region. *Seismological Research Letters*, 90(6):2236–2249, Sept. 2019. doi: 10.1785/0220180292.

Castellaro, S. and Bormann, P. Performance of Different Regression Procedures on the Magnitude Conversion Problem. *Bulletin of the Seismological Society of America*, 97(4):1167–1175, Aug. 2007. doi: 10.1785/0120060102.

Castellaro, S., Mulargia, F., and Kagan, Y. Y. Regression problems for magnitudes. *Geophysical Journal International*, 165(3):913–930, June 2006. doi: 10.1111/j.1365-246x.2006.02955.x.

Cerchiello, V., Ceresa, P., Monteiro, R., and Komendantova, N. Assessment of social vulnerability to seismic hazard in Nablus, Palestine. *International Journal of Disaster Risk Reduction*, 28: 491–506, June 2018. doi: 10.1016/j.ijdrr.2017.12.012.

Danciu, L., Kale, O., and Akkar, S. The 2014 Earthquake Model of the Middle East: ground motion model and uncertainties. *Bulletin of Earthquake Engineering*, 16(8):3497–3533, Aug. 2016. doi: 10.1007/s10518-016-9989-1.

Danciu, L., Şeşetyan, K., Demircioglu, M., Gülen, L., Zare, M., Basili, R., Elias, A., Adamia, S., Tsereteli, N., Yalçın, H., Utkucu, M., Khan, M. A., Sayab, M., Hessami, K., Rovida, A. N., Stucchi, M., Burg, J.-P., Karakhanian, A., Babayan, H., Avanesyan, M., Mammadli, T., Al-Qaryouti, M., Kalafat, D., Varazanashvili, O., Erdik, M., and Giardini, D. The 2014 Earthquake Model of the Middle East: seismogenic sources. *Bulletin of Earthquake Engineering*, 16(8): 3465–3496, Feb. 2017. doi: 10.1007/s10518-017-0096-8.

Deichmann, N. Local Magnitude, a Moment Revisited. *Bulletin of the Seismological Society of America*, 96(4A):1267–1277, Aug. 2006. doi: 10.1785/0120050115.

Del Pezzo, E., Bianco, F., and Saccorotti, G. Duration Magnitude Uncertainty due to Seismic Noise: Inferences on the Temporal Pattern of G-R b-value at Mt. Vesuvius, Italy. *Bulletin of the Seismological Society of America*, 93(4):1847–1853, Aug. 2003. doi: 10.1785/0120020222.

Di Giacomo, D. and Storchak, D. A. A scheme to set preferred magnitudes in the ISC Bulletin. *Journal of Seismology*, 20(2): 555–567, Dec. 2015. doi: 10.1007/s10950-015-9543-7.

Di Giacomo, D. and Storchak, D. A. One hundred plus years of recomputed surface wave magnitude of shallow global earthquakes. *Earth System Science Data*, 14(2):393–409, Feb. 2022. doi: 10.5194/essd-14-393-2022.

Di Giacomo, D., Bondar, I., Storchak, D., Engdahl, E., Bormann, P., and Harris, J. ISC-GEM: Global Instrumental Earthquake Catalogue (1900–2009), III. Re-computed MS and mb, proxy MW, final magnitude composition and completeness assessment. *Physics of the Earth and Planetary Interiors*, 239:33–47, 2015. doi: 10.1016/j.pepi.2014.06.005.

Douglas, A. Joint Epicentre Determination. *Nature*, 215(5096): 47–48, July 1967. doi: 10.1038/215047a0.

Dziewonski, A. M., Chou, T.-A., and Woodhouse, J. H. Determination of earthquake source parameters from waveform data for studies of global and regional seismicity. *Journal of Geophysical Research: Solid Earth*, 86(B4):2825–2852, Apr. 1981. doi: 10.1029/jb086ib04p02825.

Eaton, J. Determination of amplitude and duration magnitudes and site residuals from short-period seismographs in Northern California. *Bulletin of the Seismological Society of America*, 82 (2):533–579, 1992.

Faeh, D., Giardini, D., Kaestli, P., Deichmann, N., Gisler, M., Schwarz-Zanetti, G., and Bethmann, F. ECOS-09 earthquake catalogue of Switzerland release 2011 report and database. In *Public catalogue, 17.4.2011, Swiss Seismological Service ETH*. Zurich, RISK, 2011.

Feldman. Earthquakes in and around Israel in 2012.

Garfunkel, Z., Zak, I., and Freund, R. Active faulting in the Dead Sea rift. *Tectonophysics*, 80(1-4):1–26, Dec. 1981. doi: 10.1016/0040-1951(81)90139-6.

Gasperini, P., Lolli, B., and Vannucci, G. Body-Wave Magnitude mb Is a Good Proxy of Moment Magnitude Mw for Small Earthquakes (mb<4.5-5.0). *Seismological Research Letters*, 84(6): 932–937, Oct. 2013. doi: 10.1785/0220130105.

Gasperini, P., Lolli, B., and Castellaro, S. Comparative Analysis of Regression Methods Used for Seismic Magnitude Conversions. *Bulletin of the Seismological Society of America*, 105(3): 1787–1791, Apr. 2015. doi: 10.1785/0120150018.

Godey, S., Bossu, R., Guilbert, J., and Mazet-Roux, G. The Euro-Mediterranean Bulletin: A Comprehensive Seismological Bulletin at Regional Scale. *Seismological Research Letters*, 77(4): 460–474, July 2006. doi: 10.1785/gssrl.77.4.460.

Godey, S., Mazet-Roux, G., Bossu, R., Merrer, S., and Guilbert, J. Ten years of seismicity in the euro-mediterranean region: panorama of the EMSC bulletin 1998-2007. In *Geophysical Research Abstracts*, volume 11. 2009.

Godey, S., Bossu, R., and Guilbert, J. Improving the Mediterranean seismicity picture thanks to international collaborations. *Physics and Chemistry of the Earth, Parts A/B/C*, 63:3–11, Jan. 2013. doi: 10.1016/j.pce.2013.04.012.

Gomberg, J. S., Shedlock, K. M., and Roecker, S. W. The effect of S-wave arrival times on the accuracy of hypocenter estimation. *Bulletin of the Seismological Society of America*, 80(6A): 1605–1628, Dec. 1990. doi: 10.1785/bssa08006a1605.

Grigoratos, I. Matlab code to derive conversion relations between earthquake magnitudes, 2023. https://zenodo.org/records/8412186. doi: 10.115/magn_conv_grigoratos.

Grigoratos, I., Dabeek, J., Faravelli, M., Meo, A. D., Cerchiello, V., Borzi, B., Monteiro, R., and Ceresa, P. Development of a fragility and exposure model for Palestine–application to the city of Nablus. *Procedia Engineering*, 161:2023–2029, 2016. doi: 10.1016/j.proeng.2016.08.797.

Grigoratos, I., Monteiro, R., Ceresa, P., Meo, A. D., Faravelli, M., and Borzi, B. Crowdsourcing Exposure Data for Seismic Vulnerability Assessment in Developing Countries. *Journal of Earthquake Engineering*, 25(5):835–852, Nov. 2018. doi: 10.1080/13632469.2018.1537901.

Grigoratos, I., Poggi, V., Danciu, L., and Rojo, G. An updated parametric catalog of historical earthquakes around the Dead Sea Transform Fault Zone. *Journal of Seismology*, 24(4):803–832, Feb. 2020. doi: 10.1007/s10950-020-09904-9.

Grigoratos, I., Poggi, V., and Danciu, L. A homogenized instrumental earthquake catalog around the Dead Sea Transform Fault Zone. *ISC Seismological Dataset Repository*, 2023. doi: 10.31905/UQUUGRGH.

Gruenthal, G. and Wahlstroem, R. The European-Mediterranean earthquake catalogue (EMEC) for the last millennium. *Journal of seismology*, 16(3):535–570, 2012. doi: 10.1007/s10950-012-9302-y.

Grünthal, G., Wahlström, R., and Stromeyer, D. The unified catalogue of earthquakes in central, northern, and northwestern Europe (CENEC)—updated and expanded to the last millennium. *Journal of Seismology*, 13(4):517–541, Jan. 2009. doi: 10.1007/s10950-008-9144-9.

Gutenberg, B. Amplitudes of P, PP, and S and magnitude of shallow earthquakes∗. *Bulletin of the Seismological Society of America*, 35(2):57–69, Apr. 1945a. doi: 10.1785/bssa0350020057.

Gutenberg, B. Amplitudes of surface waves and magnitudes of shallow earthquakes. *Bulletin of the Seismological Society of America*, 35(1):3–12, Jan. 1945b. doi: 10.1785/bssa0350010003.

Gutenberg, B. and Richter, C. F. Earthquake magnitude, intensity, energy, and acceleration: (Second paper). *Bulletin of the Seismological Society of America*, 46(2):105–145, Apr. 1956. doi: 10.1785/bssa0460020105.

Hanks, T. C. and Boore, D. M. Moment-magnitude relations in theory and practice. *Journal of Geophysical Research: Solid Earth*, 89(B7):6229–6235, July 1984. doi: 10.1029/jb089ib07p06229.

Hanks, T. C. and Kanamori, H. A moment magnitude scale. *Journal of Geophysical Research: Solid Earth*, 84(B5):2348–2350, May 1979. doi: 10.1029/jb084ib05p02348.

Husen, S. and Hardebeck, J. Earthquake location accuracy, Community Online Resource for Statistical Seismicity Analysis, 2010. doi: 10.5078/corssa-55815573.

ISC. ISC Bulletin, 2023. doi: 10.31905/d808b830.

Kagan, Y. Y. Accuracy of modern global earthquake catalogs. *Physics of the Earth and Planetary Interiors*, 135(2-3):173–209, Feb. 2003. doi: 10.1016/s0031-9201(02)00214-5.

Kanamori, H. Mechanism of tsunami earthquakes. *Physics of the Earth and Planetary Interiors*, 6(5):346–359, 1972. doi: 10.1016/0031-9201(72)90058-1.

Kanamori, H. Quantification of earthquakes. *Nature*, 271, 1978. doi: 10.1038/271411a0.

Kanamori, H. Magnitude scale and quantification of earthquakes. *Tectonophysics*, 93(3-4):185–199, Apr. 1983. doi: 10.1016/0040-1951(83)90273-1.

Krystek, M. and Anton, M. A weighted total least-squares algorithm for fitting a straight line. *Measurement Science and Technology*, 19(7):079801, June 2008. doi: 10.1088/0957-0233/19/7/079801.

Lay, T. and Wallace, T. Modern Global Seismology. *International Geophysics Series*, 58, 1995.

Lolli, B. and Gasperini, P. A comparison among general orthogonal regression methods applied to earthquake magnitude conversions. *Geophysical Journal International*, 190(2):1135–1151, June 2012. doi: 10.1111/j.1365-246x.2012.05530.x.

Luckett, R., Ottemöller, L., Butcher, A., and Baptie, B. Extending local magnitude ML to short distances. *Geophysical Journal International*, 216(2):1145–1156, Nov. 2018. doi: 10.1093/gji/ggy484.

Madansky, A. The Fitting of Straight Lines when Both Variables are Subject to Error. *Journal of the American Statistical Association*, 54(285):173–205, Mar. 1959. doi: 10.1080/01621459.1959.10501505.

Marco, S. and Klinger, Y. Review of On-Fault Palaeoseismic Studies Along the Dead Sea Fault. In *Modern Approaches in Solid Earth Sciences*, pages 183–205. Springer Netherlands, 2014. doi: 10.1007/978-94-017-8872-4_7.

Meo, A. D., Borzi, B., Faravelli, M., Pagano, M., Ceresa, P., Monteiro, R., and Al-Dabbeek, J. Seismic Vulnerability Assessment of the Urban Building Environment in Nablus, Palestine. *International Journal of Architectural Heritage*, 12(7-8):1196–1215, Aug. 2018. doi: 10.1080/15583058.2018.1503364.

Musson, R. M. W. The Effect of Magnitude Uncertainty on Earthquake Activity Rates. *Bulletin of the Seismological Society of America*, 102(6):2771–2775, Dec. 2012. doi: 10.1785/0120110224.

Nath, S. K., Mandal, S., Adhikari, M. D., and Maiti, S. K. A unified earthquake catalogue for South Asia covering the period 1900–2014. *Natural Hazards*, 85(3):1787–1810, Nov. 2016. doi: 10.1007/s11069-016-2665-6.

Papaioannou, C. A model for the shallow and intermediate depth seismic sources in the eastern Mediterranean region. *Bollettino di Geofisica Teorica ed Applicata*, 42(1):57–73, 2001.

Papazachos, B. C., Kiratzi, A. A., and Karacostas, B. G. Toward a homogeneous moment-magnitude determination for earthquakes in Greece and the surrounding area. *Bulletin of the Seismological Society of America*, 87(2):474–483, Apr. 1997. doi: 10.1785/bssa0870020474.

Poggi, V., Durrheim, R., Tuluka, G. M., Weatherill, G., Gee, R., Pagani, M., Nyblade, A., and Delvaux, D. Assessing seismic hazard of the East African Rift: a pilot study from GEM and Africa Array. *Bulletin of Earthquake Engineering*, 15(11):4499–4529, May 2017. doi: 10.1007/s10518-017-0152-4.

Pondrelli, S., Salimbeni, S., Morelli, A., Ekström, G., Postpischl, L., Vannucci, G., and Boschi, E. European–Mediterranean regional centroid moment tensor catalog: solutions for 2005–2008. *Physics of the Earth and Planetary Interiors*, 185(3-4):74–81, Apr. 2011. doi: 10.1016/j.pepi.2011.01.007.

Pujol, J. Regression between earthquake magnitudes having errors with known variances. *Journal of Seismology*, 20(3):1041–1056, June 2016. doi: 10.1007/s10950-016-9580-x.

Richter, C. F. An instrumental earthquake magnitude scale. *Bulletin of the Seismological Society of America*, 25(1):1–32, Jan. 1935. doi: 10.1785/bssa0250010001.

Rodgers, A., Harris, D., Ruppert, S., Lewis, J. P., O'Boyle, J., Pasyanos, M., Abdallah, A. Q. F., Al-Yazjeen, T., and Al-Gazo, A. A Broadband Seismic Deployment in Jordan. *Seismological Research Letters*, 74(4):374–381, July 2003. doi: 10.1785/gssrl.74.4.374.

Rodriquez, C., Monteiro, R., and Ceresa, P. Assessing Seismic Social Vulnerability in Urban Centers—the Case-Study of Nablus, Palestine. *International Journal of Architectural Heritage*, 12(7-8):1216–1230, Aug. 2018. doi: 10.1080/15583058.2018.1503369.

Rovida, A., Locati, M., Camassi, R., Lolli, B., and Gasperini, P. The Italian earthquake catalogue CPTI15. *Bulletin of Earthquake Engineering*, 18(7):2953–2984, Mar. 2020. doi: 10.1007/s10518-020-00818-y.

Schweitzer, J. How can the ISC location procedures be improved? *Physics of the Earth and Planetary Interiors*, 158(1):19–26, Sept. 2006. doi: 10.1016/j.pepi.2006.03.017.

Scordilis, E. M. Empirical global relations converting Ms and mb to moment magnitude. *Journal of Seismology*, 10(2):225–236, Apr. 2006. doi: 10.1007/s10950-006-9012-4.

Sesetyan, K., Danciu, L., Tuemsa, M., Giardini, D., Erdik, M., Akkar, S., and Arakelyan, A. The 2014 seismic hazard model of the Middle East: overview and results. *Bulletin of Earthquake Engineering*, 16(8):3535–3566, 2018. doi: 10.1007/s10518-018-0346-4.

Shahvar, M. P., Zare, M., and Castellaro, S. A Unified Seismic Catalog for the Iranian Plateau (1900-2011). *Seismological Research Letters*, 84(2):233–249, Mar. 2013. doi: 10.1785/0220120144.

Shalev, E., Wetzler, N., Shatanawi, A., Rödiger, T., Kurzon, I., Lyakhovsky, V., Salameh, E., and Siebert, C. Induced Seismicity by Groundwater Extraction at the Dead Sea Fault, Jordan. *Journal of Geophysical Research: Solid Earth*, 128(1), Jan. 2023. doi: 10.1029/2022jb025044.

Shelly, D. R., Mayeda, K., Barno, J., Whidden, K. M., Moschetti, M. P., Llenos, A. L., Rubinstein, J. L., Yeck, W. L., Earle, P. S., Gök, R., and Walter, W. R. A Big Problem for Small Earthquakes: Benchmarking Routine Magnitudes and Conversion Relationships with Coda Envelope-Derived Mw in Southern Kansas and Northern Oklahoma. *Bulletin of the Seismological Society of America*, 112(1):210–225, Aug. 2021. doi: 10.1785/0120210115.

Storchak, D., Giacomo, D. D., Engdahl, E., Harris, J., Bondár, I., Lee, W., Bormann, P., and Villaseñor, A. The ISC-GEM Global Instrumental Earthquake Catalogue (1900–2009): Introduction. *Physics of the Earth and Planetary Interiors*, 239:48–63, Feb. 2015. doi: 10.1016/j.pepi.2014.06.009.

Storchak, D. A. Results of locating the IASPEI GT(0-5) reference events using the standard ISC procedures. *Physics of the Earth and Planetary Interiors*, 158(1):4–13, Sept. 2006. doi: 10.1016/j.pepi.2006.03.003.

Storchak, D. A., Harris, J., Brown, L., Lieser, K., Shumba, B., Verney, R., Giacomo, D. D., and Korger, E. I. M. Rebuild of the Bulletin of the International Seismological Centre (ISC), part 1: 1964–1979. *Geoscience Letters*, 4(1), Dec. 2017. doi: 10.1186/s40562-017-0098-z.

Stromeyer, D., Grünthal, G., and Wahlström, R. Chi-square regression for seismic strength parameter relations, and their uncertainties, with applications to an Mw based earthquake catalogue for central, northern and northwestern Europe. *Journal of Seismology*, 8(1):143–153, Jan. 2004. doi: 10.1023/b:jose.0000009503.80673.51.

Tinti, S. and Mulargia, F. Effects of magnitude uncertainties on estimating the parameters in the Gutenberg-Richter frequency-magnitude law. *Bulletin of the Seismological Society of America*, 75(6):1681–1697, Dec. 1985. doi: 10.1785/bssa0750061681.

Tormann, T., Wiemer, S., and Hauksson, E. Changes of Reporting Rates in the Southern California Earthquake Catalog, Introduced by a New Definition of ML. *Bulletin of the Seismological Society of America*, 100(4):1733–1742, July 2010. doi: 10.1785/0120090124.

Trabant, C., Hutko, A. R., Bahavar, M., Karstens, R., Ahern, T., and Aster, R. Data Products at the IRIS DMC: Stepping Stones for Research and Other Applications. *Seismological Research Letters*, 83(5):846–854, Sept. 2012. doi: 10.1785/0220120032.

Waldhauser, F. and Ellsworth, W. A Double-Difference Earthquake Location Algorithm: Method and Application to the Northern Hayward Fault, California. *Bulletin of the Seismological Society of America*, 90(6):1353–1368, Dec. 2000. doi: 10.1785/0120000006.

Wang, Q., Jackson, D. D., and Kagan, Y. Y. California Earthquakes, 1800-2007: A Unified Catalog with Moment Magnitudes, Uncertainties, and Focal Mechanisms. *Seismological Research Letters*, 80(3):446–457, May 2009. doi: 10.1785/gssrl.80.3.446.

Weatherill, G., Pagani, M., and Garcia, J. Exploring earthquake databases for the creation of magnitude-homogeneous catalogues: tools for application on a regional and global scale. *Geophysical Journal International*, 206(3):1652–1676, June 2016. doi: 10.1093/gji/ggw232.

Wetzler, N. and Kurzon, I. The Earthquake Activity of Israel: Revisiting 30 Years of Local and Regional Seismic Records along the Dead Sea Transform. *Seismological Research Letters*, 87(1): 47–58, Jan. 2016. doi: 10.1785/0220150157.

Willemann, R. J. and Storchak, D. A. Data Collection at the International Seismological Centre. *Seismological Research Letters*, 72 (4):440–453, July 2001. doi: 10.1785/gssrl.72.4.440.

Woessner, J., Hardebeck, J., and Haukkson, E. What is an instrumental seismicity catalog. *Community Online Resource for Statistical Seismicity Analysis*, 10, 2010.

Yadav, R. B. S., Bormann, P., Rastogi, B. K., Das, M. C., and Chopra, S. A Homogeneous and Complete Earthquake Catalog for Northeast India and the Adjoining Region. *Seismological Research Letters*, 80(4):609–627, July 2009. doi: 10.1785/gssrl.80.4.609.

Zare, M., Amini, H., Yazdi, P., Sesetyan, K., Demircioglu, M. B., Kalafat, D., Erdik, M., Giardini, D., Khan, M. A., and Tsereteli, N. Recent developments of the Middle East catalog. *Journal of Seismology*, 18(4):749–772, June 2014. doi: 10.1007/s10950-014-9444-1.

INVITED
doi:10.26443/seismica.v2i2.389

SEISMICA

Local station correlation: large-N arrays and DAS

Brian L.N. Kennett * [1], **Chengxin Jiang** [1], **Krystyna T. Smolinski** [2]

[1]Research School of Earth Sciences, Australian National University, Canberra, Australia, [2]Institute of Geophysics, ETH Zürich, Switzerland

Author contributions: *Conceptualization*: B.L.N. Kennett. *Formal Analysis*: B.L.N. Kennett, C. Jiang, K.T. Smolinski. *Writing - original draft*: B.L.N. Kennett, C. Jiang, K.T. Smolinski. *Writing - Review & Editing*: B.L.N. Kennett, C. Jiang, K.T. Smolinski.

Abstract The use of cross-correlation between seismic stations has had widespread applications particularly in the exploitation of ambient seismic noise. We here show how the effects of a non-ideal noise distribution can be understood by looking directly at correlation properties and show how the behaviour can be readily visualised for both seismometer and DAS configurations, taking into account directivity effects. For sources lying in a relatively narrow cone around the extension of the inter-station path, the dispersion properties of the correlation relate directly to the zone between the stations. We illustrate the successful use of correlation analysis for both a large-N array perpendicular to a major highway and a DAS cable along a busy road. When considering cross-correlations, the co-array consisting of the ensemble of inter-station vectors provides an effective means of assessing the behaviour of array layouts, supplementing the standard plane-wave array response. When combined with knowledge of the suitable correlation zones for noise sources, the co-array concept provides a useful way to design array configurations for both seismometer arrays and DAS.

Production Editor:
Gareth Funning
Handling Editor:
Catherine Rychert
Copy & Layout Editor:
Abhineet Gupta

Received:
February 22, 2022
Accepted:
July 13, 2023
Published:
September 18, 2023

Non-technical summary The long-term average of the cross-correlation of the seismograms recorded at two different points, with a broad distribution of sources of seismic energy, provides an approximation to the response, with a source at one of the points recorded at the other. With a non-ideal distribution of arriving seismic energy, useful results can be obtained by paying close attention to the properties of the correlated wavefield. In particular, it is possible to extract surface wave dispersion as a function of frequency for the path between the two recording points. This is demonstrated here with examples for both an $\sim$100-station array close to a highway in Australia and the use of distributed acoustic sensing (DAS) from a fibre optic cable along a busy street in Switzerland. Suitable designs for the configuration of a suite of seismic stations or a DAS cable to be used in correlation studies need to take into account the zones of useful sources and the directional properties of the correlation.

1 Introduction

The use of inter-station correlations to extract a surface wave component from the ambient noise field has been widely applied and successful results achieved even when the conditions do not meet theoretical expectations (see, e.g., Nakata et al., 2019). In the ideal conditions of a uniform distribution of uncorrelated noise sources, the cross-correlation of seismic records between two stations is closely related to the Green's function for the path between them. A number of different derivations have been made with different assumptions such as a diffuse wavefield (Lobkis and Weaver, 2001), energy equipartitioned among surface wave modes (Weaver, 2010), or with sources on a boundary surrounding the two stations (Wapenaar, 2004; Wapenaar and Fokkema, 2006). A summary of this theoretical background is provided by Fichtner and Tsai (2019).

Here we approach the situation by looking directly at the cross-correlation of seismic records between two stations and examining how far the result can approach an approximation to the Green's function with a non-ideal noise distribution. Our objective is to explore how best to exploit available noise sources when using high-density observations.

For large-N arrays the distribution of stations is, in principle, under user control. Although, use of large scale deployments is often made in the context of exploration or production (Chmiel et al., 2019), or seismicity monitoring (Dougherty et al., 2019) where the typical pattern is a regular rectangular grid. Where likely noise sources are well-characterised in advance, the array design can be adapted to their configuration and exploit their correlation properties.

However, with Distributed Acoustic Sensing (DAS) the array of sensor points is confined to the line of the fibre-optic cable and there are strong directivity effects. When a cable is specifically deployed for an experiment, the array's configuration can be optimised with knowledge of likely noise sources, but often 'dark-fibre' is used exploiting existing telecommunication channels, and then the orientation of the cable can be important. Nevertheless, useful results can be achieved in circumstances that may appear unpropitious, such as a DAS cable running along a major highway (Yang et al., 2022).

We show how the properties of local correlation can

*Corresponding author: brian.kennett@anu.edu.au

be understood directly from the interaction of the influence of distributed sources, by analysing the nature of the cross-correlation between the seismograms at two separated stations. We then illustrate the application of such local station correlations to a large-N nodal experiment in southeastern Australia adjacent to a major highway and a wind farm, and to a DAS recording in an urban environment in Bern, Switzerland.

2 Inter-station correlations from distributed sources

We provide an outline of the theoretical development for inter-station correlation based on Chapter 6 of Kennett and Fichtner (2020), using a local coordinate system rather than spherical coordinates. We consider a situation with structure that depends solely on depth and represent the seismograms at each location in terms of a synthesis in frequency-slowness space. For simplicity we concentrate on a single frequency ω and consider the vertical component from an isotropic source with source spectrum $M(\omega)$. Then for a station at a distance X from a source we can represent the resulting seismogram in the frequency domain as an integral over slowness p of the response of the local stratified medium $G_z(p,\omega)$ multiplied by a horizontal phase term:

$$u_z(X,\omega) = \left[\frac{\omega}{X}\right]^{1/2} M(\omega) \int_0^{p_0} \mathrm{d}p\, p^{1/2} G_z(p,\omega) \exp[\mathrm{i}\omega p X]. \tag{1}$$

Here we have assumed that we can use the high frequency asymptotic form for the horizontal phase dependence. For the same source recorded at stations 1 and 2 at distances X_1, X_2, the cross-correlation $\mathcal{U}^{12}(\omega)$ is represented by a multiplication in the frequency domain and

$$\mathcal{U}^{12}(\omega) = u_z(X_1,\omega) u_z(X_2,\omega)^*. \tag{2}$$

A natural consequence of this relation is that the cross-correlation involves the difference in the phase of the contributions from the two stations, and it is this property that allows the emergence of path related effects in the presence of many sources. Using equation 1, the cross-correlation can be written as

$$\begin{aligned}\mathcal{U}^{12}(\omega) = {} & \frac{\omega}{(X_1X_2)^{1/2}} |M(\omega)|^2 \\ & \int_0^{p_0} \mathrm{d}p\, p^{1/2} G_z(p,\omega) \exp[\mathrm{i}\omega p X_1] \\ & \int_0^{p_0} \mathrm{d}q\, q^{1/2} G_z^*(q,\omega) \exp[-\mathrm{i}\omega q X_2].\end{aligned} \tag{3}$$

We now introduce the distance between the two stations $X_{12} = |X_1 - X_2| - \delta X_{12}$ and recast the second slowness integration in terms of the difference in slowness $\zeta = p - q$. Then

$$\begin{aligned}\mathcal{U}^{12}(\omega) = {} & \frac{\omega}{(X_1X_2)^{1/2}} |M(\omega)|^2 \\ & \int_0^{p_0} \mathrm{d}p\, p^{1/2} \exp\left[\mathrm{i}\omega p(X_{12} + \delta X_{12})\right] \\ & \int_{-p_0}^{p_0} \mathrm{d}\zeta \Big[(p-\zeta)^{1/2} G_z(p,\omega) \\ & \qquad G_z^*(p-\zeta,\omega) \exp\left[\mathrm{i}\omega\zeta X_2\right]\Big].\end{aligned} \tag{4}$$

In this form for the cross-correlation between the two stations from a single source we are able to identify a phase component relating directly to propagation between the stations $\exp[\mathrm{i}\omega p X_{12}]$, which is modulated by a further slowness integral.

Simplification occurs when we have contributions from a distribution of sources, because only the coherent part corresponding to the direct propagation path survives, and the the remainder is eliminated by destructive interference. A broad distribution of sources is needed to achieve the suppression. The application of a stationary phase treatment to the integral over differential slowness, as in Snieder (2004), extracts the neighbourhood of $\zeta = 0$. In consequence, the slowness of the arrivals that contribute to the net cross-correlation is the same at both stations and equation 4 reduces to a single integral over slowness. Full suppression of slowness contamination requires a good distribution of sources relative to the inter-station path (Halliday and Curtis, 2008). But, when the wavefield is dominated by fundamental mode surface waves, well separated in slowness from the other contributions, the requirements are less stringent.

The first integral in equation 4 includes a term $\exp[\mathrm{i}\omega p \delta X_{12}]$ that depends on δX_{12}, the extent that the inter-station distance X_{12} deviates from the difference between the distances from each source to the two stations $|X_1 - X_2|$. This oscillatory term is again suppressed by destructive interference leaving just contributions where $\delta X_{12} \sim 0$, so that the paths from the effective sources to the two stations are approximately aligned with the inter-station path. Two such zones are present stretching out from the two stations along the continuation of the inter-station path.

The summed cross-correlation over many sources reduces to a form representing a virtual source-receiver pair at the two stations with contributions from propagation in each direction

$$\begin{aligned}\langle \mathcal{U}^{12}(\omega) \rangle = {} & \frac{\omega}{F(X)} |M(\omega)|^2 \int_0^{p_0} \mathrm{d}p \Big[p^{1/2} G_z(p,\omega) \\ & G_z^*(p,\omega) \Big(\exp[\mathrm{i}\omega p X_{12}] \\ & \qquad + \exp[-\mathrm{i}\omega p X_{12}]\Big)\Big].\end{aligned} \tag{5}$$

Equation 5 has a similar form to the time derivative of the Green's function between the two stations, but the combination $G_z(p,\omega)G_z^*(p,\omega)$ replaces $G_z(p,\omega)$. The geometrical spreading term $F(X)$ will not have a simple relation to the path, but will tend to be dominated by source contributions from near the two stations, and hence $F(X) \sim X_{12}$.

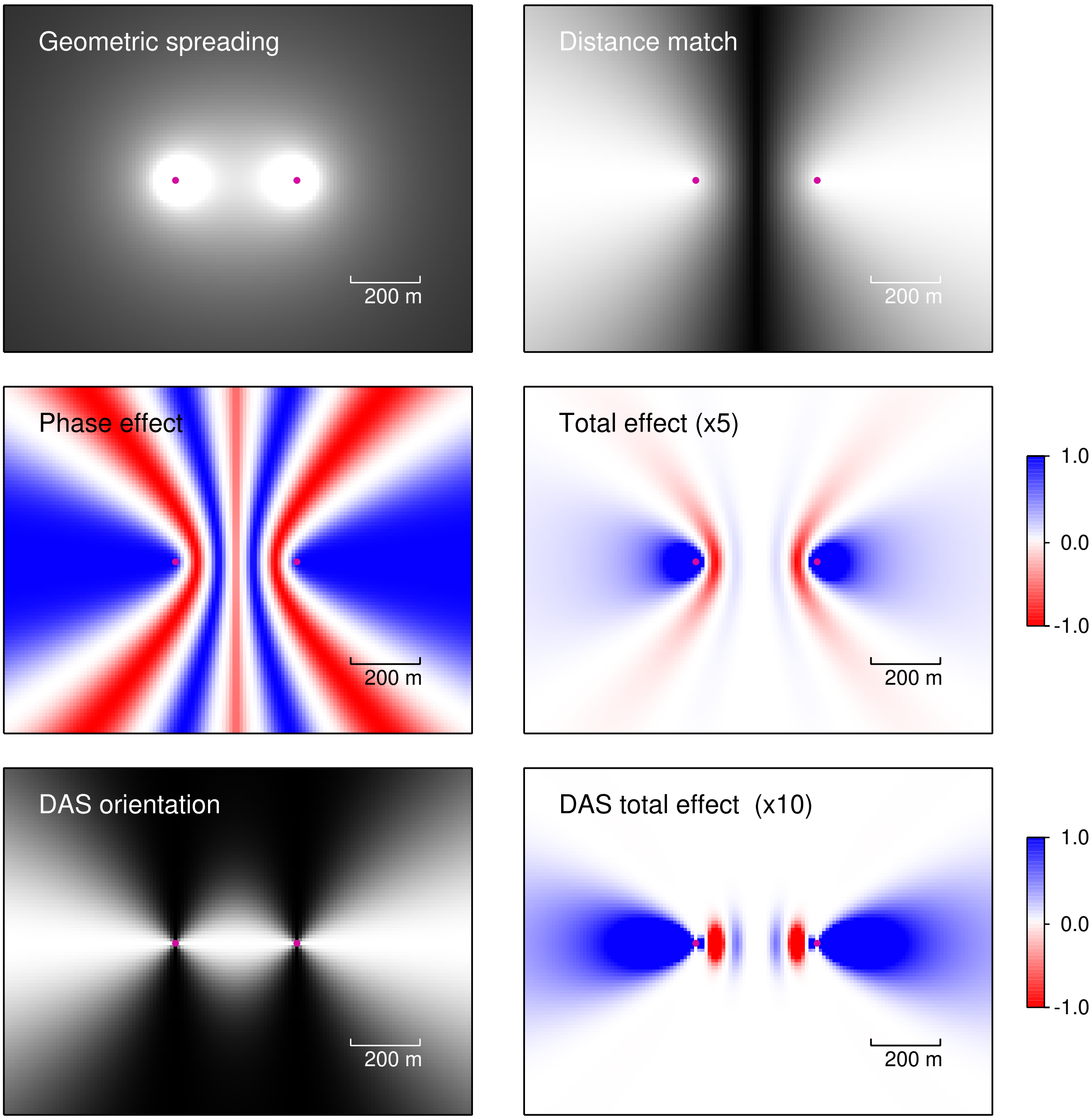

Figure 1 Correlation simulation for $2\,\mathrm{Hz}$ waves with phase speed $500\,\mathrm{m/s}$ at stations $350\,\mathrm{m}$ apart. The positions of stations are shown by purple dots in each panel. (a) Geometric spreading effects from a source to the two stations. (b) The ratio of the difference between the distance from each source to the two stations and the inter-station path length. (c) Phase contributions to the cross-correlation. (d) Total effect for two seismometers of the terms in (a), (b) and (c) – amplified by 5. (e) Orientation effects for DAS cable with orientation along the inter-station path. (f) Net effect for two DAS sensors of the terms (a), (b), (c) and (e) – amplified by 10.

Surface wave contributions come from the poles of the integrand in equation 5. Their position in slowness, which controls dispersion, is unchanged from the Green's function but the pole is now second order (rather than first order for the Green's function) and so the amplitude factor is modified (Kennett and Fichtner, 2020). Typically the dominant contribution comes from the fundamental mode and so, provided there are sources with a broad range of azimuths to the inter-station path to contribute to the net cross-correlation, the contribution from between the stations is emphasised and the dispersion for the fundamental mode can readily be extracted.

We can examine the way that the cross-correlation field is built up by looking at the various contributions at a single frequency (Figure 1). We show two stations separated by $350\,\mathrm{m}$ in a simulation of local conditions.

The effect of a source drops off quite rapidly with distance. So, if we consider the net geometrical spreading effects to the two stations, those sources close to the two stations dominate even when we make an improved approximation to the spreading function than the asymptotic form used in the theory above (Figure 1a). We have noted that the constructive interference condition emphasises those source locations for which the difference between the distance from the source to the two stations is close to the inter-station distance. In Figure 1(b) we represent this effect by plotting the ratio of the difference in distance to the path length $|X_1 - X_2|/X_{12}$, from zero (black) to unity (white).

With the specification of frequency ω and slowness p_f we can display the phase effects through the function $\cos[\omega p_f(|X_1 - X_2| - X_{12})]$ as in Figure 1(c). We here use a frequency of $2\,\mathrm{Hz}$ and phase speed of $500\,\mathrm{m/s}$ (slowness $= 0.002\,\mathrm{s/m}$), typical of situations at local arrays. As would be expected, the zones approximately in line with the stations show slow variation in phase, but as the inclination to the path increases, variation is rapid and increasingly so at higher frequencies. It is the superposition of these rapidly varying phases that leads to destructive interference and the concentration of the cross-correlation on the inter-station path.

When all the contributions to the correlation are combined for a pair of seismometer stations, the total effect is as in Figure 1(d). The distance-match term has been applied here as a multiplier to the product of the geometric spreading and the phase variation. The dominant component comes from beyond the stations, but some contamination is possible from sources lying between the stations.

When considering the correlation of stations in a DAS array, additional factors have to be taken into consideration, because the strain-rate along the cable assigned to a reference point is averaged over a gauge length g around the point. For a Rayleigh wave, with slowness p arriving with an inclination ψ relative to the cable, the gauge-length effect is (e.g., Kennett, 2022)

$$\langle \dot{\epsilon}_d(\omega) \rangle = \frac{2\omega}{g} u \, \cos\psi \sin\left(\tfrac{1}{2}\omega g p \cos\psi\right). \qquad (6)$$

For a typical gauge length of $10\,\mathrm{m}$ and a phase speed of $500\,\mathrm{m/s}$, for frequencies less than $10\,\mathrm{Hz}$ the sine function does not impose much distortion.

The most common local ambient noise is Rayleigh waves from anthropogenic activities such as traffic, and Love waves are less frequently encountered since they have a less favourable orientation effect. Because strain is a tensorial quantity, the effect of inclination depends on 2ψ and to a good approximation for Rayleigh waves along a cable with uniform orientation

$$\langle \dot{\epsilon}_d(\omega) \rangle \sim \omega^2 u_r p \cos^2\psi. \qquad (7)$$

In consequence there is a strong dependence on the position of any source. The effect of the orientation factor $\cos^2\psi$ for Rayleigh waves, is displayed in Figure 1(e) and has a strong suppression effect for sources broadside to either of the stations. This factor modulates the response for the seismometer to give a total contribution shown in Figure 1(f) where there is a strong emphasis on sources nearly in-line with the cable.

It is interesting to note that the application of the distance-match mask produces a net effect that has a strong resemblance to the source kernels derived by Sager et al. (2017). In a similar way we can simulate the structural kernel. Figure 2(a) displays the phase factor $\cos[\omega p_f(X_1 + X_2 - X_{12})]$ representing the difference between the phase accumulated in passage from the source to the two stations compared with that for the inter-station path. When the pattern in Figure 2(a) is modulated by the geometric spreading effect from Figure 1(a), the result displayed in Figure 2(b) emphasises the zone in the immediate vicinity of the inter-station path (cf. Sager et al., 2017). It is thus possible to achieve an effective visualisation of the effects of local correlation with a simple implementation that can be adapted to the configuration of a distributed array, or DAS cable.

3 Illustrations of inter-station correlations

In Figure 1 we see significant differences between the net effect of sources for the seismometer and DAS configurations. For the correlation of a pair of seismometers, the dominant contribution lies in a cone behind the stations with a significant width of potential useful zone. Contributions will be muted by the effect of geometrical spreading, but if sufficient noise sources are present over time, stacking will readily enhance the correlation functions. For correlations of channels along a DAS cable the strong orientation effects limit the zone of most effective sources. In this case, noise sources travelling beside the cable can be exploited to create stacked correlation functions.

We here illustrate the exploitation of the correlation properties of traffic dominated noise fields in two different configurations associated with independent experiments.

The first case is a nodal experiment adjacent to a major highway in southeastern Australia, where the array stretches perpendicular to the highway on a dry lake bed. The dispersion of Rayleigh waves across the nodes allows the delineation of the thickening sediments. The second case shows how a DAS cable running along a street in Bern, Switzerland can be used to extract correlation functions that provide insight into the nature of the noise field with secondary sources linked to road conditions and also to characterise the near-surface structure from Rayleigh wave dispersion.

3.1 Large-N array - Lake George experiment near Canberra, Australia

The Lake George nodal array was a short-term seismic experiment conducted on a then dry lake bed located $\sim 35\,\mathrm{km}$ northeast of the Australian capital city, Canberra (Figure 3). This experiment was conceived and led by Meghan Miller from the Australian National University. The nodal array included 97 three-component SmartSolo sensors recording continuously with $250\,\mathrm{Hz}$ sampling rate, and was operated between December 2020 and January 2021 with an average inter-station spacing of 30–$40\,\mathrm{m}$. The array configuration is mainly composed of five lines right next to and perpendicular to the Federal Highway connecting Canberra to Sydney, thus recording dramatic amounts of traffic noise. Apart from the five lines, this array also included three nodes as a separated group about $500\,\mathrm{m}$ away from the nearest stations in the west to increase the array aperture. To the southeast, the array lies about $15\,\mathrm{km}$ away from the capital wind farm, with a series

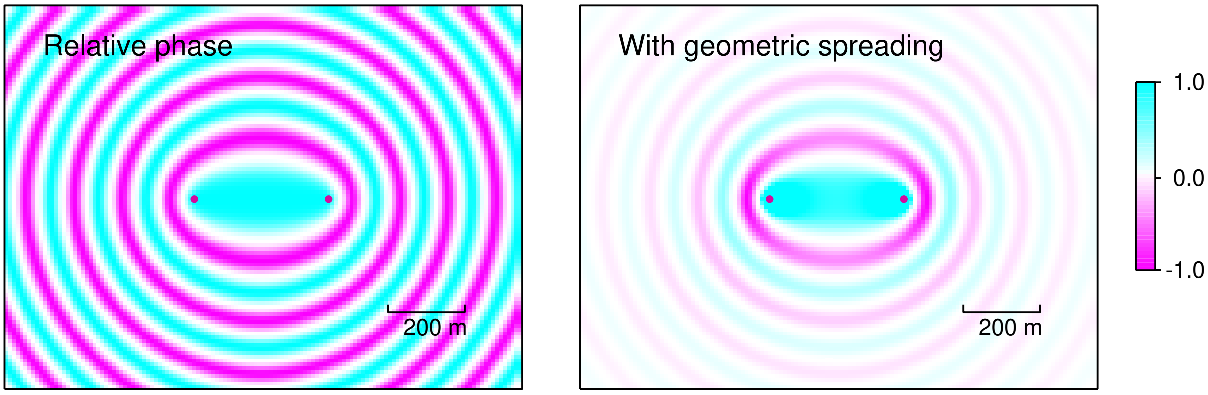

Figure 2 (a) Relative phase between the contributions from propagation from a source to the two stations and the inter-station path. (b) Net effect of modulating the phase term by geometrical spreading. The configuration is the same as in Figure 1.

of windmills operating continuously during the deployment time.

Cross-correlations across the array

To process the traffic noise data, we take advantage of the open-source Python package NoisePy (Jiang and Denolle, 2020), which is a high-performance tool designed specifically for large-N ambient noise seismology. In NoisePy, the main noise data processing procedures generally follow the conventional workflow of Bensen et al. (2007) and are briefly described below.

First, continuous noise data are down-sampled to $60\,\mathrm{Hz}$ sampling rate, before they are cut into 4-hour long traces. Each trace is further divided into 15-min segments with a 75% overlap between adjacent segments to increase the signal-to-noise ratio of the stacked cross-correlation functions at a later stage. Any 15-min segments with maximum amplitudes over 10 times the standard deviation of the amplitude within each 4-hour window are removed to reduce contamination from large transient signals (such as earthquakes). Second, the mean and trend of the remaining time series are removed before a taper and a 4-pole 2-pass Butterworth filter with corners at 0.05–$28\,\mathrm{Hz}$ are applied. To further reduce the effects of large transient signals, each time-series is normalized by the corresponding smoothed version produced using a moving average over a window length of 500 samples. The cross-correlation is then calculated in the frequency domain and a moving average with a window length of 20 samples is used to smooth the source and receiver spectra. Finally, the cross-correlations of the small-time windows are linearly stacked for each station-pair, generating about 4650 stacked cross-correlation functions across the array.

Since the above procedures are applied to all three components of each station, each station pair has nine components of cross-correlation functions in the R-T-Z system, i.e., RR, RT, RZ, TR, TT, TZ, ZR, ZT, and ZZ (with the first letter denoting the component of the source station and the second letter the receiver station), forming a complete correlation tensor.

We focus on the frequency band of 1–$10\,\mathrm{Hz}$ to take advantage of the dominant signals from traffic noise. Figure 4(a) displays the filtered vertical-vertical (ZZ) cross-correlation functions for the station pair LG015–LG049 stacked over every 4-hour time window throughout the deployment time. Strong asymmetric features can be observed with the negative lag displaying generally higher frequency energy than those in the positive lag. This is due to the dominant origin of traffic noise from the west. Though strong coherency exists in the correlations through time, some variations can also be observed, possibly due to the changing traffic conditions on the highway. To quantify the similarities, we compute the correlation coefficients of each trace relative to the final stacked (i.e., mean) cross-correlation function (Figure 4b). When the traffic is active, the resulting correlations are almost the same as the final stack with the associated correlation coefficients mostly larger than 0.9. During quiet times, particularly the Christmas and New Year holidays, the 4-hour cross-correlation functions are significantly different from the average with correlation coefficients as low as 0.5. A comparable analysis for a pair of stations on opposite sides of the highway (LG069–LG094) is shown in Figure S3 of the Supplementary Material. The temporal pattern is in phase with that in Figure 4, indicating the greater importance of traffic conditions than station location.

To further demonstrate the time dependence of the cross-correlation functions, we stack the cross-correlations using different time periods and matrices and summarize the resulting waveforms in Figure 5. As can be seen from the figure, the stack over the 4-hour time window with busy traffic conditions (between 11 am and 3 pm each day) is almost the same as the final stack as well as the stack using waveforms of high correlation coefficients relative to the final stack; while it is distinct from the stack using a same length of 4-hour time window but crossing midnight (between 11 pm and 3 am). Such behaviour shows little frequency dependence within the 1–$10\,\mathrm{Hz}$ band investigated here (see Supplementary Material Section S1.2). This further indicates that the coherent contributions from the traffic noise dominate the final stacked cross-correlation.

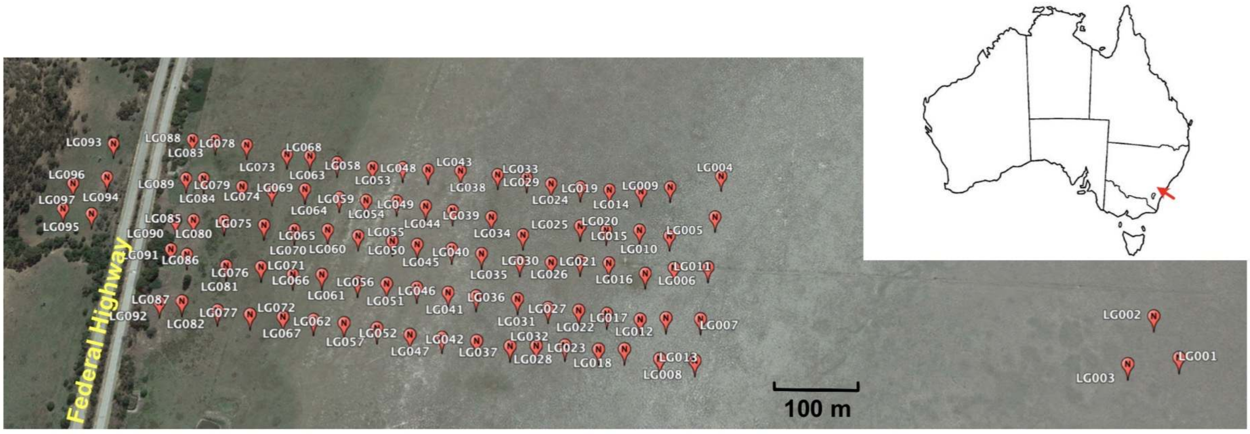

Figure 3 The station distribution of the Lake George Seismic array in Australia. The inset shows the geographic location of the array (red arrow) with respect to the Australian continent.

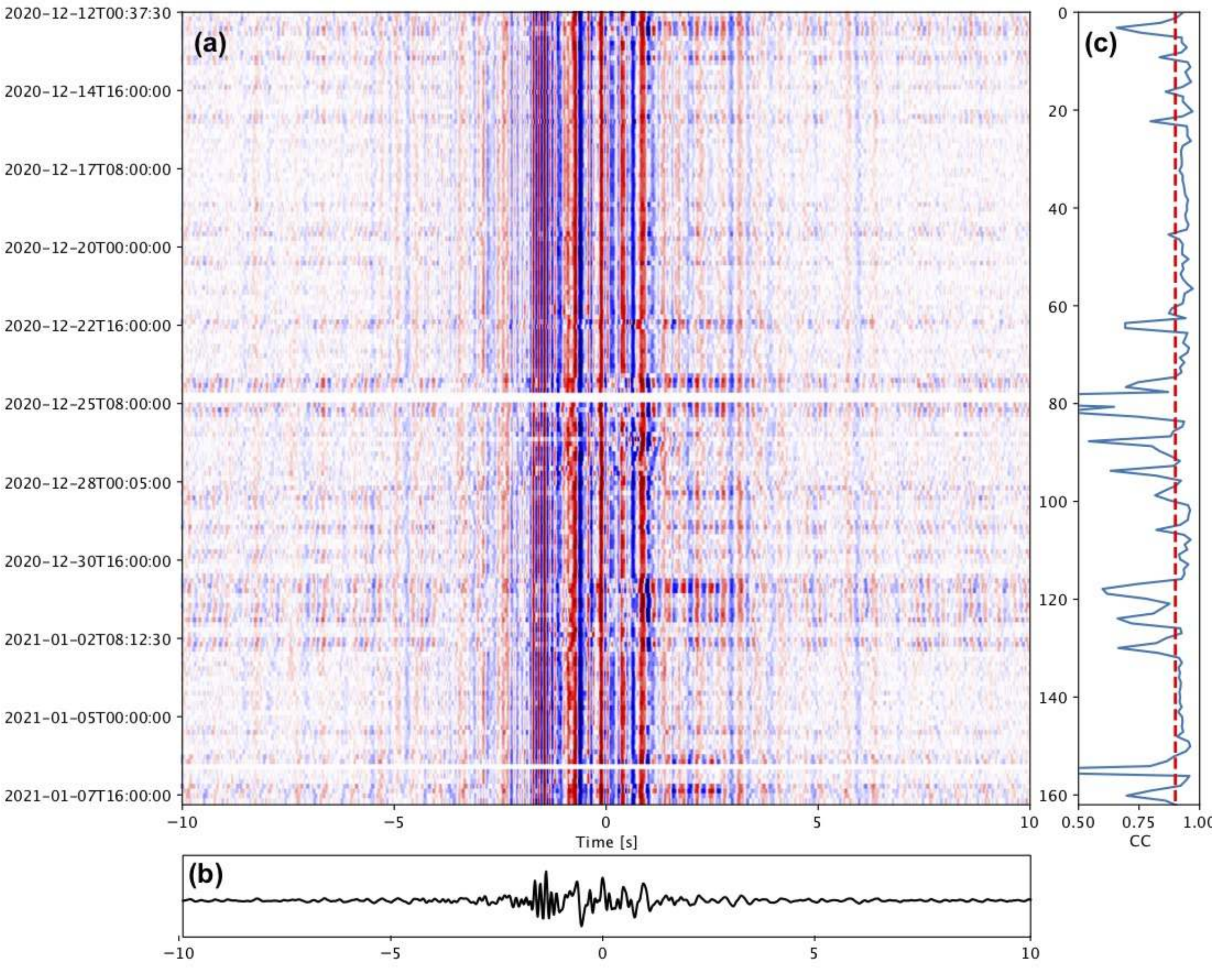

Figure 4 (a) The 4-hour stacked cross-correlation functions over the entire deployment time for the station pair of LG015 and LG049 plotted in matrix form. (b) The final stacked cross-correlation for the station pair by taking the mean of the 2D matrix in (a). (c) The correlation coefficients (CC) of each trace relative to the mean. The red dashed line denotes the correlation coefficient of 0.9.

Enhancing Rayleigh wave signals

Due to the complex waveforms of the cross-correlation functions, we enhance the Rayleigh wave signals assuming retrograde elliptical particle motion by manipulating the cross-component of the correlation tensor. This is achieved by following equation 3 of Nayak and Thurber (2020). We refer to the resulting correlation function as the *M0* component. The general idea behind this process is to correct the different initial phases of the fundamental-mode Rayleigh wave (assumed to

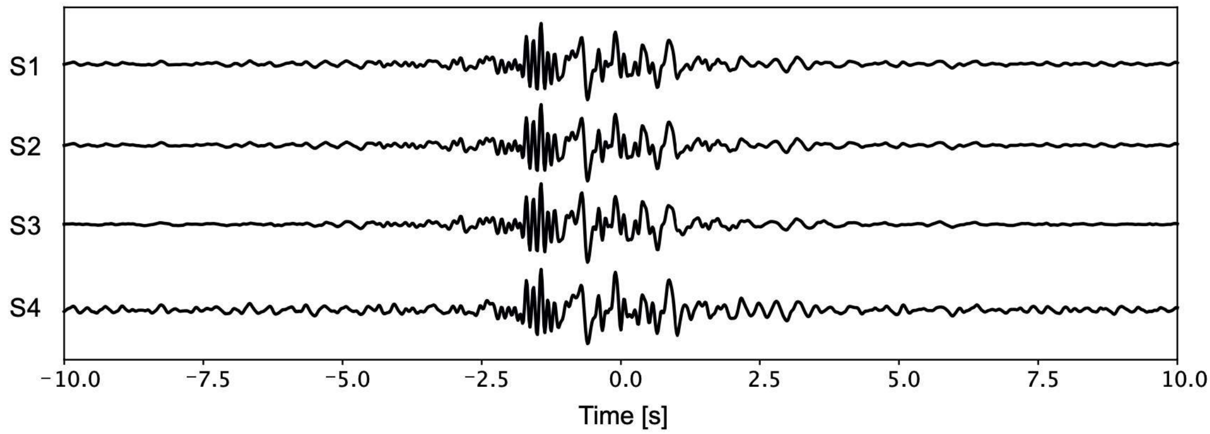

Figure 5 Comparison of stacked cross-correlation functions using different time periods and matrix. S1 is the stack of all cross-correlation functions (same as the black line in Figure 4a). S2 is the stack of all cross-correlation functions with a correlation coefficient large than 0.7 relative to S1. S3 is the stack of correlation functions over the time window 11 am–3 pm. S4 is the stack of correlation functions over the time window 11 pm–3 am each day.

have retrograde motion) on different cross-components and stack them to boost the signal. A similar approach has also been applied in van Wijk et al. (2011), Takagi et al. (2014), and Gribler and Mikesell (2019). We also performed an equivalent procedure to enhance the prograde motion using the cross-component of the correlation tensor but found generally weak coherent energy. This suggests surface wave energy is dominated by retrograde motion in the correlation functions from the traffic noise.

Dispersion extraction

To extract the dispersion information, we apply slant-stacking in the $c-\omega$ domain to the *M0* correlation functions,

$$F(c,\omega) = \frac{1}{N}\left|\sum_{r=1}^{N} e^{i\phi_r} e^{i\omega|\mathbf{x}_r-\mathbf{x}_s|/c(\omega)}\right|, \tag{8}$$

where ϕ_r denotes the phase of the cross-correlation function between source station s and receiver station r at an angular frequency ω, c is the phase velocity, $\mathbf{x}$ is the station location, and $|\mathbf{x}_r - \mathbf{x}_s|$ is the distance between the station-pair r and s. F is the sum of the phase-shifted cross-correlation functions over a total of N receiver stations in the neighbouring region of each station source ($\mathbf{x}_s$). In spite of its simplicity, this method has been demonstrated to be effective for extracting short period dispersion data ($< 5\,\mathrm{s}$) from dense arrays to characterize sedimentary structures (e.g., Nayak and Thurber, 2020; Jiang and Denolle, 2022).

We adopt a two-step approach to construct a phase diagram for a single site via the slant-stacking method represented by equation 8. Firstly, we define a receiver bin with a radius of $150\,\mathrm{m}$ around each station and pair each station within the receiver bin with a virtual source station that is at least $300\,\mathrm{m}$ away from the bin center to respect the plane-wave assumption underlying equation 8. The slant-stacking using these cross-correlations generate one phase diagram for this receiver bin. Secondly, we linearly stack the phase diagrams from all virtual sources satisfying the above distance criteria to form the final image for that receiver bin. Figure 6(a) shows one example of the final phase diagram for the receiver bin centered around LG015, and clear, coherent and relatively simple dispersion energy can be observed over the 0.1–$0.4\,\mathrm{s}$ period range. We then extract the dispersion data by tracking the maximum envelope of the stacked data and quantify the uncertainty using the band of 90% of the maximum energy at each period. We conduct the above procedure for each receiver bin, and the 30–$40\,\mathrm{m}$ inter-station spacing allows us to extract high-quality dispersion data at 0.1–$0.4\,\mathrm{s}$ period range across most of the array (except the western edge with sparse stations as well as a topographic change). Figure 6(b) shows the period dependent phase velocity variations across the five lines of the array with the major feature of the increasing period range for low velocities when moving to the east. This reflects the gradual thickening of a slow and weak regolith layer in the region from west to east, as the stations move out onto the dry lake bed.

3.2 DAS correlation along Bern Street, Switzerland

This DAS deployment was a pilot experiment conducted in Bern, Switzerland in November 2019 by a group from ETH Zürich, under the direction of Andreas Fichtner. The experiment ran for 2 weeks, and utilised 'dark' telecommunication fibre – currently unused fibres within telecommunication fibre cables (access provided by the SWITCH foundation). The fibre optic cables are believed to be housed in a plastic conduit, buried at a depth of $\sim 0.7\,\mathrm{m}$ beneath the surface of the road. During construction, this conduit was covered with sand before the road surface was laid on top, and is likely to have been cemented in places (for example, near manholes).

The DAS layout consisted of $\sim 3\,\mathrm{km}$ of cable in a T-configuration, with the signal reflected at the far end, resulting in signal measured over $\sim 6\,\mathrm{km}$ of fibre, with repeating sections. Data were collected using a Silixa

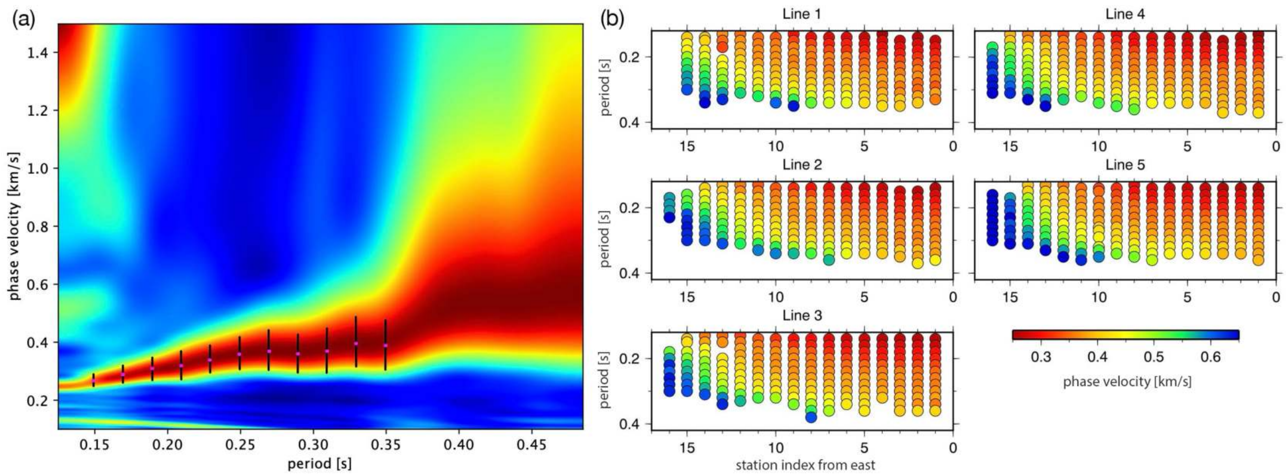

Figure 6 (a) The final dispersion diagram for the receiver bin centered around the station LG015. The pink circles show the extracted phase velocities at each period with the error bars representing the associated uncertainties. (b) The variations of extracted dispersion across the five lines of the array with line 1 representing the northernmost and line 5 the southernmost. The horizontal axes represent the index of the corresponding receiver bin (not necessarily same to the station location) from the east.

iDAS Version 2.4 interrogator, with a $200\,\mathrm{Hz}$ sampling rate, $2\,\mathrm{m}$ channel spacing and a $10\,\mathrm{m}$ fixed gauge length.

For the production of cross-correlations in this study, we chose to use the $\sim 1\,\mathrm{km}$ section of fibre running along Länggassstrasse (Figure 7), to allow us to assume that we are only seeing Rayleigh surface waves, without components of Love waves. The road was treated as a separate top and bottom section, to avoid any complications arising due to the slight bend in the road. The southern section lies on glacial gravels, whilst at the northern end of the street there is a transition to moraine material (Ketterhals et al., 2000).

The anthropogenic noise sources in this experiment are primarily cars and buses travelling along the road, parallel to the fibre (as illustrated in Supplementary Material S2.1). The main train station for the city is also situated at the end of the fibre, resulting in more diffuse train noise (as the trains do not pass directly on top of the fibre).

For much of the length of the Bern street, the road is bordered by substantial concrete basements. Such barriers in the near surface tend to channel surface waves along the road conduit. At the northern end of the road near point **a** the situation is more open, and there are fewer concrete structures below ground close to the road. The road also has regular manholes marking access points to the subsurface and these structures also act as scatterers to produce a more complex wavefield.

Computation of cross-correlations

Mean and linear trends were first removed from the raw data. We then computed cross-correlations, using 1-hour windows of night-time data (spanning 11 pm – 5 am, local time), as we found that this time period contained fewer noise sources directly on top of the fibre, therefore the noise field was more diffuse and homogeneous. We also applied spectral whitening, to suppress the most dominant peaks in the frequency spectrum (Bensen et al., 2007).

Cross-correlations were computed for $100\,\mathrm{m}$ sections of the fibre - the northernmost channel along the straight section of the fibre was used as a virtual source, and a 1-hour window of data was cross-correlated with the same hour for all other channels within this $100\,\mathrm{m}$ section (at distances of $2\,\mathrm{m}$, $4\,\mathrm{m}$, etc.). All defined night-time hours were then stacked (6 hours per night for 12 days, totalling 72 1-hour windows), from which we kept the central 4 seconds of each stack to reduce the final data volume. This process was then repeated for each channel along the fibre, using each channel as a virtual source and producing a cross-correlation record section covering $100\,\mathrm{m}$. We were limited to just $100\,\mathrm{m}$ distance due to the presence of significant secondary sources along the fibre, resulting in non-ideal cross-correlations, with many additional signals present (see Supplementary Material S2.2).

An example of a cross-correlation section using channel **a** as the virtual source is displayed in Figure 8, showing the complex nature of the observed signals, largely due to the presence of secondary sources.

F-k filtering was applied to all the cross-correlation record sections, in order to remove signals propagating in the opposite direction to the desired signal, and this largely eliminates the extraneous effects.

Production of dispersion curves

In order to produce dispersion curves from our cross-correlation record sections, we apply the MASW (Multi-channel Analysis of Surface Waves) method outlined in Park et al. (1998, 1999). MASW has already been successfully applied to DAS data; for example in Lancelle et al. (2021). This method is almost identical to the slant-stack described in section 3.1, however, following Park et al. (1999), there is a normalisation of each spectra with its own absolute value, to ensure equal weighting of each trace. Additionally, we use a phase-weighted stack to help the dispersion curve to converge more quickly (e.g. Cheng et al., 2021). Examples of the resulting dispersion

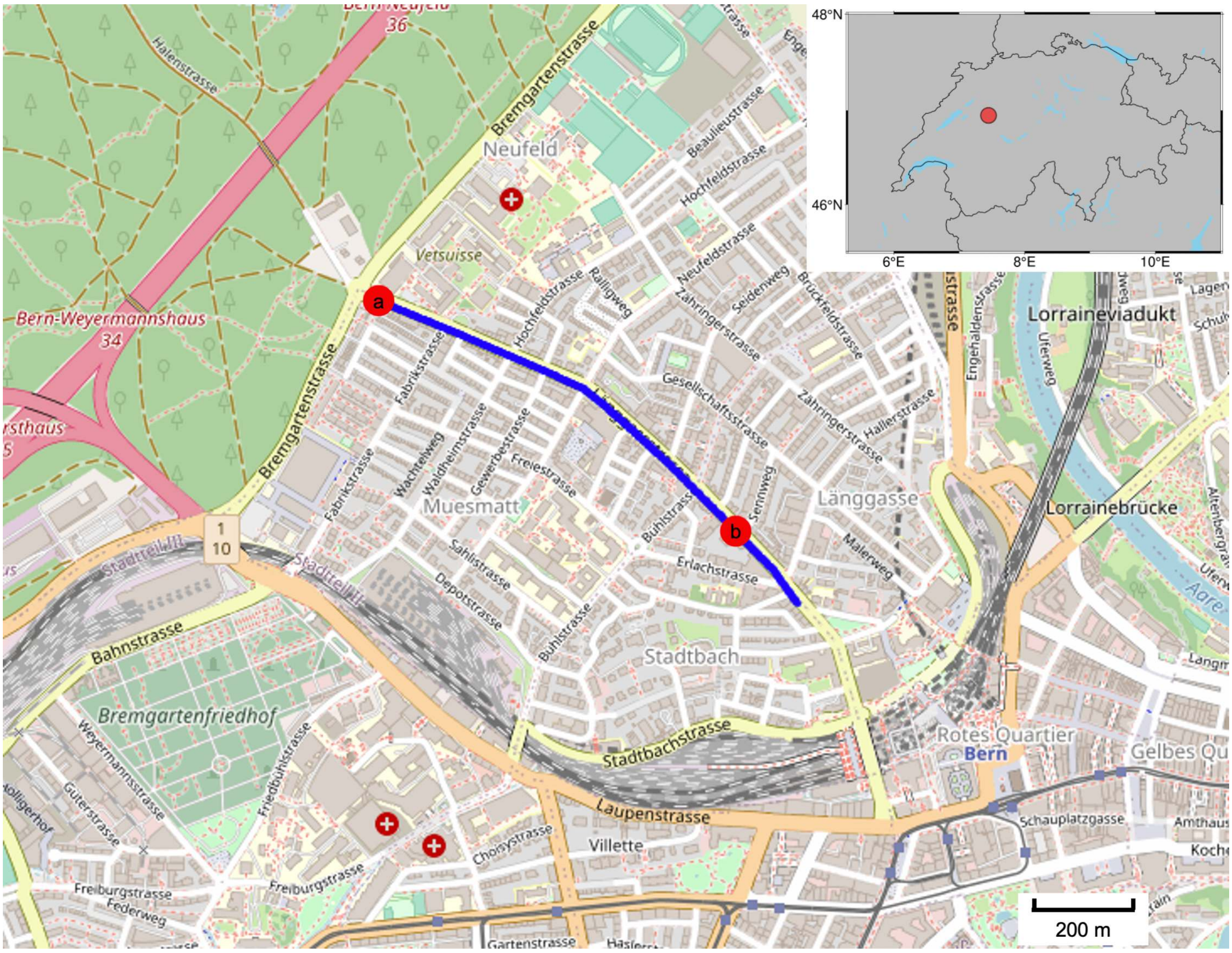

Figure 7 Map showing the fibre section used to produce cross-correlations (blue). The red circles **a** and **b** denote the positions of a reference northern and southern channel along the DAS line. Note the proximity of the Bern main train station to the southern end of the fibre. The inset map shows the location of Bern (red circle) within Switzerland.

curves are shown in Figure 9.

In spite of the complex nature of the data and the short inter-channel distances over which the cross-correlations are computed, we are still able to produce reasonable dispersion curves, particularly for frequencies between 10 and 21 Hz. The subsurface phase velocity along the DAS array is expected to be low for higher frequencies, as the street is built upon unconsolidated sediments; particularly late glacial retreat gravels and alluvial sands (Ketterhals et al., 2000). While the dispersion curves show some variability and local oscillations, this is not unexpected given the complex geological and anthropogenic structure along the street (concrete infrastructure built on top of soft sediments, with bedrock beneath).

The dispersion behaviour for the southern segment (Figure 9b) is more coherent. This portion of the road has consistent geology and a similar building style with basements directly lining the street. At the northern end there is more variation in surface geology and some buildings lie further away from the road. The net result is a lower-quality of dispersion estimate (Figure 9a). The higher phase velocities seen for lower frequencies ($<$ 10 Hz) correspond to the presence of bedrock at depths of $\sim$40 m.

In Bern, Switzerland, the road is bounded by deep concrete structures and multiple access points along the road that act as secondary sources and need to be treated with careful processing. These structures lie just in the zone most strongly sampled by surface waves. There is a major contrast with a similar experiment in Athens, Greece where only minimal processing was needed, with good coherent signal for hundreds of metres. The built environment in Athens does not have such consistent deep structures and so there are fewer impediments for surface wave propagation.

4 Discussion

For situations where noise sources are well characterised, such as traffic noise, it is frequently possible to adapt experimental layouts to make good use of the source and its directionality. Where space allows it can be feasible to lay out lines of recorders just beside a highway, mimicking the way that active source seismology is conducted using seismic vibrators to generate strong seismic energy along the road. Several seismic experiments have demonstrated the feasibility of such array-source configurations to generate reasonable dispersion results. For example, Zhang et al. (2020) con-

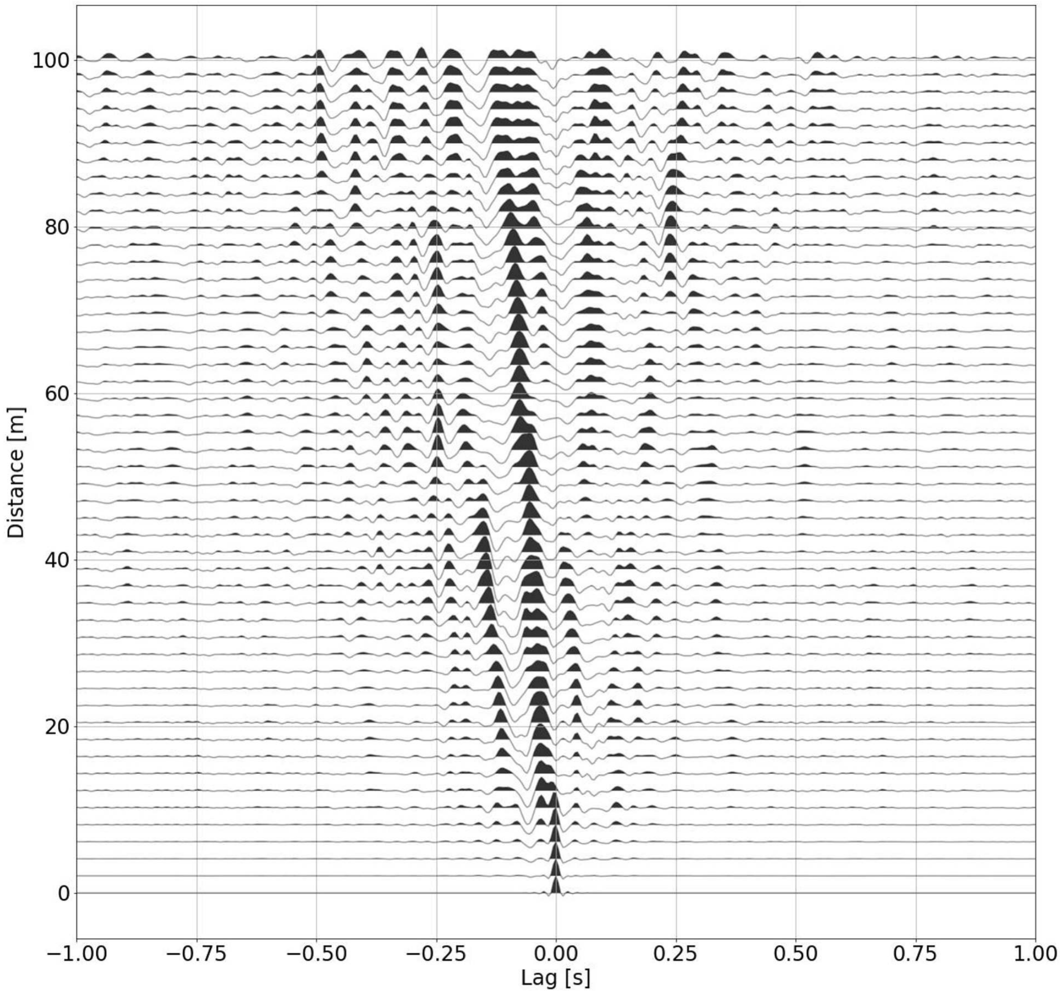

Figure 8 An example of a $100\,\mathrm{m}$ cross-correlation record section, produced using channel **a** as the virtual source, and cross-correlating with each of the other channels within a distance of $100\,\mathrm{m}$ to the south.

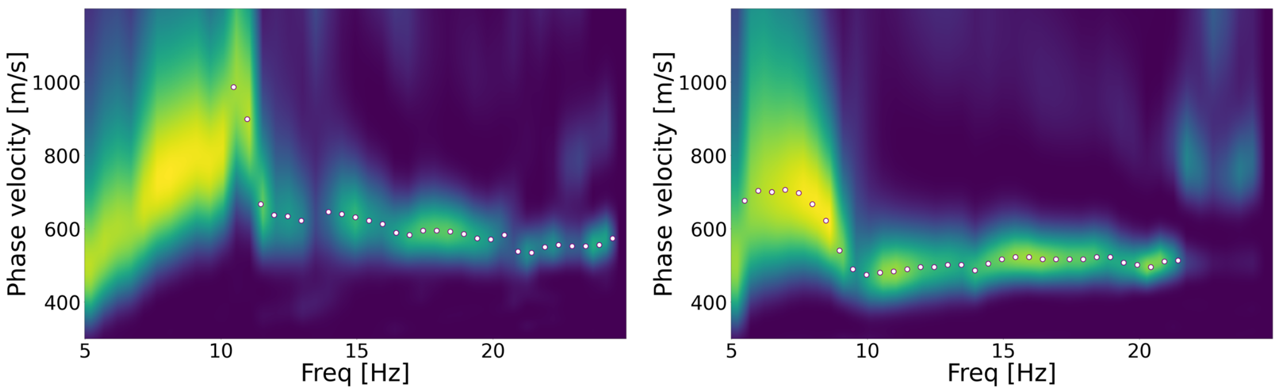

Figure 9 A comparison between the dispersion curves produced at channel **a** at the northern end of the fibre (a) and channel **b** at the southern end of the fibre (b). We observe a significant decrease in the quality of dispersion curves towards the northern end of the fibre. The circles indicate picked phase velocities with frequency, in increments of $0.5\,\mathrm{Hz}$, where the dispersion curves were deemed to be reliable.

duct a seismic survey of 352 geophones along a country road in the North China Plain and managed to extract dispersion curves up to 18–$20\,\mathrm{Hz}$ range using 80 minutes long segments of continuous traffic noise. The resulting dispersion has also been benchmarked with that from active source survey. Quiros et al. (2016) deployed about 100 geophones along a railway within the Rio Grande rift, New Mexico, and used about 120 hours of continuous train noise to extract Rayleigh wave dispersion data up to $12\,\mathrm{Hz}$. They also managed to reveal clear, direct and reflected P-wave signals. However, the proximity of the seismic arrays to a highway or a railway means such environments can have a modified structure. As we have seen for the Lake George experiment, an alternative is to work with an array perpendicular to the road, so that only a small portion of the highway acts as a persistent source as traffic passes through the zone. By getting away from the immediate vicinity of the road the siting is improved and extraneous noise reduced. However, we note that such configurations sometimes could be limited by space and environmental concerns.

Many DAS cables are laid under roads or just beside them, as in the Bern Street, and then the traffic noise can be exploited directly with signals aligning with the axis of the cable as detected by the modification of laser scattering in the DAS system. However, a cable laid parallel to the road but at some distance from the road itself largely picks up broadside signals and the axial component is weak (Dou et al., 2017). In these circumstances, a perpendicular DAS cable can be used with the effective source being the passage of vehicles through a rather narrow part of the road, thanks to the DAS inclination factors. Dou et al. (2017) have demonstrated that such a perpendicular cable can be used for time lapse analysis. Often the layout of DAS cables, as in dark fibre, is determined by the most convenient geometries for telecommunication purposes and so the orientation may not be ideal for seismic applications. It may be possible to compensate to some extent with directional corrections, but it is probably preferable to choose portions of the DAS cable for analysis that have the best orientation (e.g., Fang et al., 2022).

When the source of noise is not known or there are many different forms of noise, such as traffic noise from many directions, there are a different set of challenges. Conventional analysis of array behaviour is based on the response to a plane wave with a specified slowness. For a set of N sensors at positions $\mathbf{x}_j$ relative to a reference site at a suitable origin, the linear array sum for frequency ω as a function of slowness $\mathbf{s}$ takes the form

$$\mathcal{S}(\mathbf{s},\omega) = \sum_{j=1}^{N} w_j e^{\mathrm{i}\omega[\mathbf{s}.\mathbf{x}_j]}, \tag{9}$$

where the terms w_j allow for signal weighting by sensor. The array response $\mathcal{S}(\mathbf{s},\omega)$ is a scaled version of the Fourier transform with respect to the wavenumber of a set of weighted delta-functions placed at the array positions. The same functional form is derived irrespective of the slowness of an incoming wave $\mathbf{p}$, with the pattern shifted to be centred on $\mathbf{p}$ and characterised by the differential slowness $\Delta\mathbf{s} = \mathbf{p} - \mathbf{s}$. The function $\mathcal{S}(\Delta\mathbf{s},\omega)$ can be characterised by calculating the response for a vertically incident wave for which $s_1 = s_2 = 0$. Good array designs display a strong central lobe in the array response, with weak secondary peaks well removed from the origin.

For DAS systems, the strain-rate response is modulated by the slowness p and the directional factors at each segment of the cable depend on the specific incoming wave. As demonstrated by Näsholm et al. (2022) and Kennett (2022), the result is that the actual response is distorted from the ideal expressed by equation 9 with bias toward larger slowness. Nevertheless the array response (equation 9) remains a useful comparator.

For each array configuration specified by the set of points $\{\mathbf{x_j}\}$, there is an associated "co-array" (Haubrich, 1968) comprising the vectors

$$\mathbf{X}_{ij} = \mathbf{x}_i - \mathbf{x}_j, \quad i,j = 1,2,\ldots,N. \tag{10}$$

In the context of inter-station correlation, the pattern of the co-array specifies the sampling achievable. For optimum performance when using correlations, we desire both a reasonable array response function and thorough sampling by the co-array vectors.

Maranò et al. (2014) have presented an optimisation scheme for the design of small arrays with an objective function based on the character of the array response. For the co-array, it is not obvious what would be the most suitable criterion for any optimisation. Haubrich (1968) used a space-filling approach based on direct search for a small number of sensors, but this is not easy to generalise. Here we use the visual properties of the co-array as a guide to its behaviour.

We consider arrays with around 36 elements, sufficiently large to show complex character but small enough that the nature of the response can be readily appreciated. We first look at designs that can be readily implemented with a suite of seismometers, and then transfer attention to the case for DAS where the 'sensors' are required to be directly connected.

Co-Array for large-N array deployments

In Figure 10 we compare the behaviour of three designs using 36 elements and uniform weighting. The first is based on a rectangular 6×6 configuration, to which mild dithering has been applied to provide some distortion of the regularity. Such configurations are often used for large-N array deployments. The second uses a random configuration that ends up with rather variable spacing of stations. The third uses a 6-arm spiral array (Kennett et al., 2015). Despite the effort to reduce the regularity of the near-rectangular array, very strong side-lobes appear in the slowness response and the co-array shows concentrations of vectors. The side lobes of the array function are not too close to the main lobe so that suitable windowing can be found, but the co-array behaviour is restrictive. In contrast, a random array achieves a good co-array pattern and side-lobes of the array-function are much suppressed. It is unlikely that such a pattern would be chosen for field implementation, but it demonstrates the merits of breaking regularity. The array designs of Haubrich (1968) based on co-array properties also show a mixture of concentration and sparseness. The third array with spiral arms achieves a good compromise in array behaviour. The local side lobes are suppressed near the main lobe and there is a good azimuthal and distance coverage in the co-array. Such arrays also have the merit that their properties are resilient to distortions introduced in layout and even missing stations (Kennett et al., 2015), whilst achieving good areal coverage.

From Figure 10 we can see that it is desirable to minimise regularity in the layout of a large-N array where

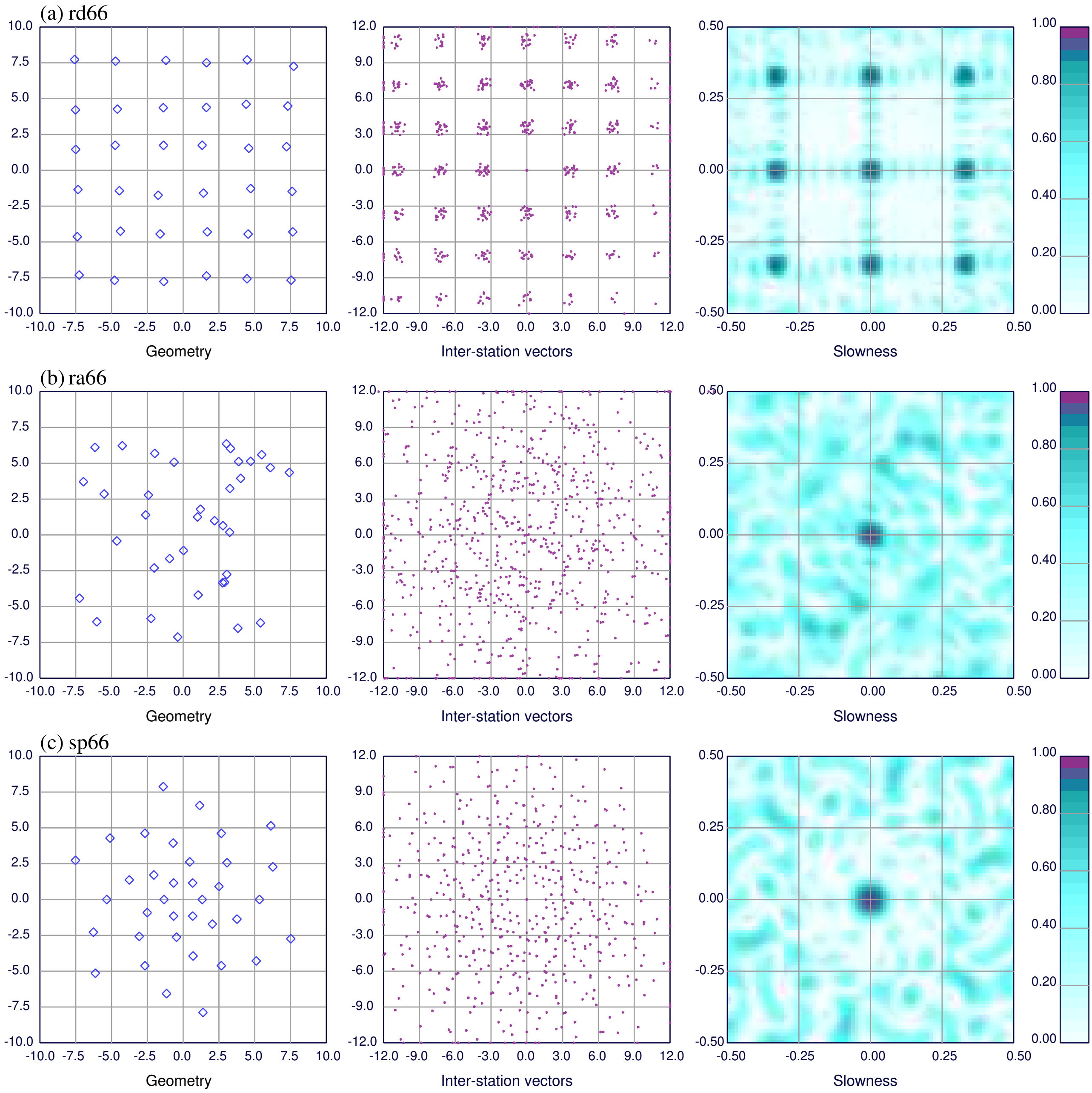

Figure 10 36 element array responses showing the geometrical layout, the co-array behaviour and the array function in slowness space for a $1\ \mathrm{Hz}$ signal. (a) Rectangular array with mild dithering; (b) a 36-element random array with similar aperture; (c) a 6-arm spiral array.

the primary aim is the exploitation of inter-station correlations, and there is no dominant noise source. A set of patches exploiting simple spiral-arm layouts can achieve comparable areal coverage and improved array behaviour without too great experimental complexity.

Co-Array with orientation factors for DAS

When we turn to the design of DAS configurations with a broad range of noise sources, we are faced with the topological necessity that all sensor locations can be connected by a single cable. To allow direct comparison with the arrays in Figure 10 we have scaled DAS designs up to comparable size and selected only about 36 elements on each cable.

The regular co-array is very helpful for assessing the potential of an array of seismometers for cross-correlation analysis, but when we consider an application to DAS arrays we also need to bear in mind the influence of cable orientation relative to the path between the stations (cf. Martin et al., 2021).

At the two stations being correlated with angles ψ_1, ψ_2 between the local cable configuration and the path between the stations, the scaling factor for Rayleigh waves due to the relative orientation is

$$R = \cos^2\psi_1 \cos^2\psi_2, \quad 0 \le R \le 1; \tag{11}$$

and the equivalent factor for Love waves is

$$L = \sin\psi_1 \cos\psi_2 \sin\psi_2 \cos\psi_2, \quad -\tfrac{1}{2} \le L \le \tfrac{1}{2}. \tag{12}$$

For each vector in the co-array we can associate these orientation factors and so assess the effectiveness of the

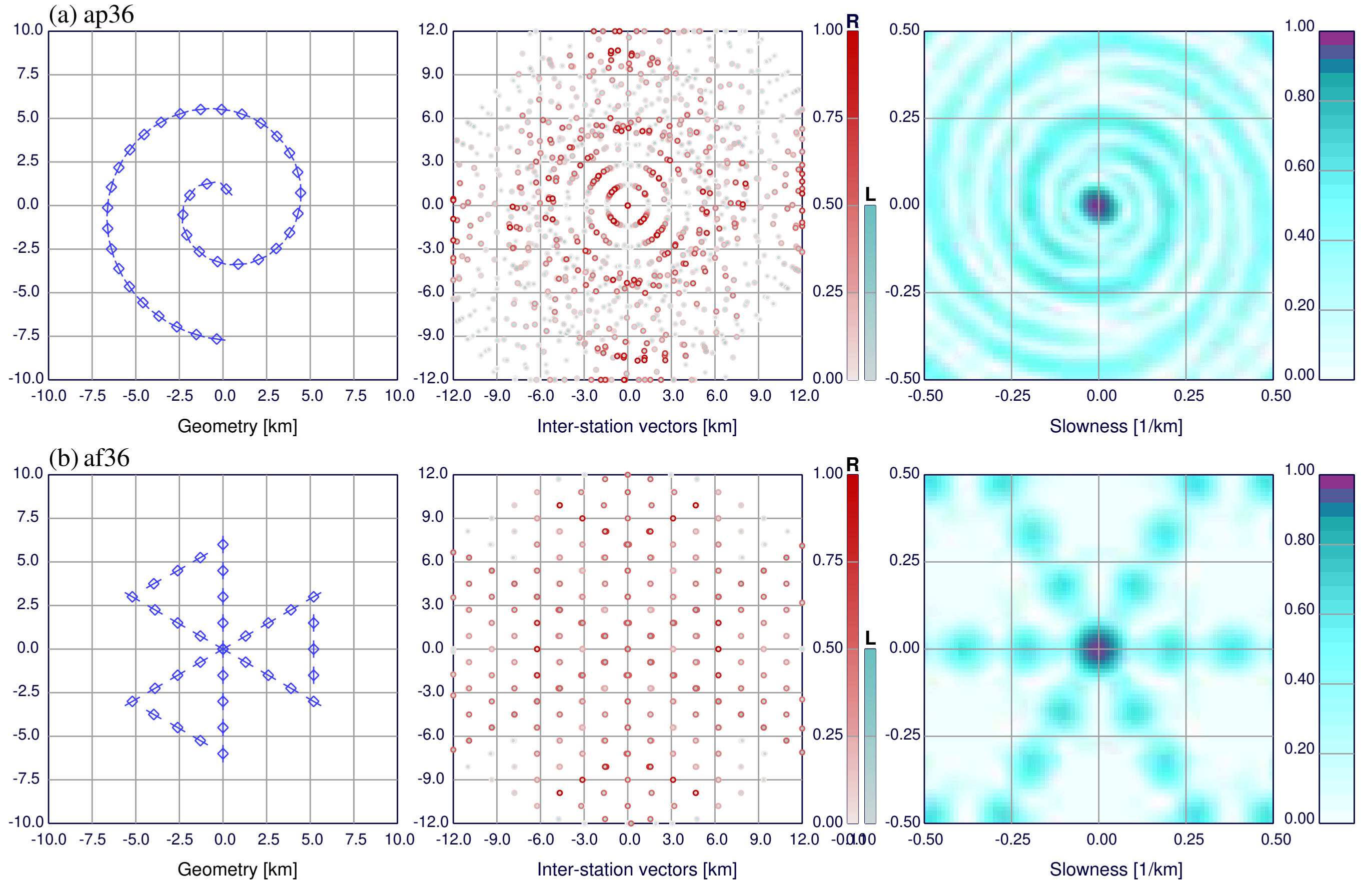

Figure 11 DAS array responses showing the geometrical layout with the cable orientation at each sample point marked, the co-array behaviour with orientation factors and the array function in slowness space for a 1 Hz signal. The arrays are scaled to match those in Figure 10. (a) Archimedean spiral with 36 elements; (b) 36-element fan using a continuous cable. The amplitudes of R and L orientation factors for Rayleigh and Love waves from equations 11 and 12 are plotted for each vector in the co-array, with the L factor superimposed on the centre of the larger R symbol. Stronger colours indicate the expectation of good cross-correlation results for the wave type.

array design for the analysis of ambient Rayleigh waves and incidentally examine where there may be the possibility of picking up sensitivity to Love waves. In the DAS co-array plots we display both the R and L factors for each vector. The R factors are shown in red and the inner, half-size, L factors in cyan. The intensity of the colour indicates the level of potential recovery – very weak factors are faded towards white. Thus distinctly visible co-array vectors indicate the combinations of inter-station separation and orientations for which good correlation results can be expected.

In Figure 11 we show two possible DAS configurations with reasonable properties for both slowness response and co-array properties. The first is the Archimedean spiral considered by both Näsholm et al. (2022) and Kennett (2022). Even where the cable does not complete a full loop, the geometry of the co-array including the orientation factors gives good azimuthal coverage for Rayleigh waves – though there is some clumping in distance.

The second design, a fan array with 36-elements, is aimed to exploit the roughly 60° span around the vector between 'sensors' that will make an effective contribution to the correlation. With 6 such cable segments, and their external coupling, surprisingly good properties are achieved. As might be expected, the strongest Rayleigh factors are associated with direct propagation along the arms of the fan, but reasonable sensitivity for Rayleigh waves is achieved across a wide range of directions. For such an array configuration, some mild irregularity in layout could also be beneficial by spreading the range of azimuths. A similar 'umbrella' design for a DAS layout has been suggested by van den Ende and Ampuero (2021), but they do not provide any analysis of its performance.

In general, we see that the Rayleigh wave response for the arrays dominates that for Love waves, even when the DAS cable has a significant curvature. For both DAS designs, the L factors remain quite small for most station pairs (Figure 11), so that Love wave contamination of Rayleigh wave results will only become an issue if the local ambient noise has much stronger Love wave content. It is possible to weight array contributions to enhance Love waves and suppress Rayleigh contributions (e.g. Kennett, 2022), and such schemes are likely to be needed to extract and identify Love waves.

With a DAS cable it is possible to use a much larger number of recording positions than illustrated in Figure 11, so that the discrete spots will spread into diffuse patches. It is also possible to select the portions of a DAS cable to be used for correlation, so that poorly oriented segments or linking loops can be excluded.

Future DAS interrogators may prove capable of handling multiple cables simultaneously, and then a wider range of designs will become feasible. Already, some experiments use two separate interrogators that allows more complex geometrical configurations to be exploited if a common time base is available.

5 Conclusions

For both large-N array and DAS experiments it is possible to extract the correct dispersion behaviour for Rayleigh waves from cross-correlated records even though the amplitude factors differ from the true Green's function between the stations. With careful processing to remove extraneous signals, e.g., reflections from lateral structures, well-defined modal dispersion can be achieved for the fundamental mode at higher frequencies. The lower frequency limit depends on the maximum spacing between stations in an array deployment and on the maximum span with coherent behaviour along a straight segment of cable for DAS work. The high frequency end for DAS arises from the influence of gauge length averaging to produce the local strain-rate signal (e.g., Näsholm et al., 2022). In principle, the unaliased wavefield attainable with DAS allows the extraction of multiple modes, but this depends on the nature of the excitation. For surface sources such as traffic, low surface wavespeeds and a strong vertical gradient in wavespeed provides favourable conditions for higher mode excitation.

When working with traffic as a source of noise, good results can be achieved provided that a significant component of the noise sources lies inline with recorder pairs. For large-N arrays, the requirements of placing recorders very close to the traffic can be a limitation for deployment parallel to the road. Fortunately a perpendicular arrangement works just as well, though again local circumstances may affect the ease of deployment. For DAS, dark fibre is commonly within a conduit under or just at the side of roads, so recorder pairs are naturally in a suitable arrangement. Where cable is to be laid specifically, a line perpendicular to a road may well prove easier to install.

For situations with a broad distribution of noise sources it is desirable to use deployment configurations that provide a wide range of measurable azimuths. The use of rectangular grids for large-N array deployment does not meet this objective at all, even when deployment is non ideal. Alternative space-filling designs can provide better azimuthal control. For DAS, even though the recording points have to lie along a continuous cable, we have been able to show that it is possible to achieve effective azimuthal coverage with simple configurations.

Acknowledgements

CJ acknowledges the support from an Australian Research Council Discovery Early Career Researcher Award (DE220100907). The Lake George experiment was initiated by Meghan Miller and Brad Pillans helped with access issues. CJ also thanks Brad Pillans, Meghan Miller, Robert Pickle, Voon Hui Lai and Kimberley Berends for their invaluable fieldwork assistance at Lake George.

KTS was supported by the European Union Horizon 2020 research and innovation program under Grant Agreement 821115; *Real-Time Earthquake Risk Reduction for a Resilient Europe* (RISE), as well as Eidgenossische Technische Hochschule (ETH) Zürich. Andreas Fichtner, Daniel Bowden, Patrick Paitz and Pascal Edme helped with the Bern experiment and thanks also to Felix Kugler from the Switch Foundation who provided access to the cable.

Data and code availability

The codes used in the project are available at Zenodo (doi:10.5281/zenodo.7734919), organised by the displays of local correlation and array response, surface wave analysis for the large-N array, and analysis for the DAS results.

The data for the Lake George seismic nodal array will be available from AusPass (https://auspass.edu.au): Australian Passive Seismic Server – network 1G – at the end of 2023 (doi:10.7914/t2z3-2m87; https://www.fdsn.org/networks/detail/1G_2020).

For the Bern experiment, the cross-correlations used in this paper are available at Zenodo (doi:10.5281/zenodo.7734919) together with the associated code.

References

Bensen, G. D., Ritzwoller, M. H., Barmin, M. P., Levshin, A. L., Lin, F., Moschetti, M. P., Shapiro, N. M., and Yang, Y. Processing seismic ambient noise data to obtain reliable broad-band surface wave dispersion measurements. *Geophysical Journal International*, 169(3):1239–1260, 06 2007. doi: 10.1111/j.1365-246X.2007.03374.x.

Cheng, F., Xia, J., Zhang, K., Zhou, C., and Ajo-Franklin, J. B. Phase-weighted slant stacking for surface wave dispersion measurement. *Geophysical Journal International*, 226(1):256–269, 03 2021. doi: 10.1093/gji/ggab101.

Chmiel, M., Mordret, A., Boué, P., Brenguier, F., Lecocq, T., Courbis, R., Hollis, D., Campman, X., Romijn, R., and Van der Veen, W. Ambient noise multimode Rayleigh and Love wave tomography to determine the shear velocity structure above the Groningen gas field. *Geophysical Journal International*, 218(3):1781–1795, 05 2019. doi: 10.1093/gji/ggz237.

Dou, S., Lindsey, N., Wagner, A. M., Daley, T. M., Freifeld, B., Robertson, M., Peterson, J., Ulrich, C., Martin, E. R., and Ajo-Franklin, J. B. Distributed Acoustic Sensing for Seismic Monitoring of The Near Surface: A Traffic-Noise Interferometry Case Study. *Scientific Reports*, 7(1):11620, 2017. doi: 10.1038/s41598-017-11986-4.

Dougherty, S. L., Cochran, E. S., and Harrington, R. M. The LArge-n Seismic Survey in Oklahoma (LASSO) Experiment. *Seismological Research Letters*, 90(5):2051–2057, 08 2019. doi: 10.1785/0220190094.

Fang, J., Yang, Y., Shen, Z., Biondi, E., Wang, X., Williams, E. F., Becker, M. W., Eslamian, D., and Zhan, Z. Directional Sensitivity of DAS and Its Effect on Rayleigh-Wave Tomography: A Case

Study in Oxnard, California. *Seismological Research Letters*, 94 (2A):887–897, 11 2022. doi: 10.1785/0220220235.

Fichtner, A. and Tsai, V. Theoretical Foundations of Noise Interferometry. In *Seismic Ambient Noise*, pages 109–143. Cambridge University Press, 2019. doi: 10.1017/9781108264808.006.

Gribler, G. and Mikesell, T. D. Methods to isolate retrograde and prograde Rayleigh-wave signals. *Geophysical Journal International*, 219(2):975–994, 07 2019. doi: 10.1093/gji/ggz341.

Halliday, D. and Curtis, A. Seismic interferometry, surface waves and source distribution. *Geophysical Journal International*, 175 (3):1067–1087, 12 2008. doi: 10.1111/j.1365-246X.2008.03918.x.

Haubrich, R. A. Array design. *Bulletin of the Seismological Society of America*, 58(3):977–991, 06 1968. doi: 10.1785/BSSA0580030977.

Jiang, C. and Denolle, M. A. NoisePy: A New High-Performance Python Tool for Ambient-Noise Seismology. *Seismological Research Letters*, 91(3):1853–1866, 04 2020. doi: 10.1785/0220190364.

Jiang, C. and Denolle, M. A. Pronounced Seismic Anisotropy in Kanto Sedimentary Basin: A Case Study of Using Dense Arrays, Ambient Noise Seismology, and Multi-Modal Surface-Wave Imaging. *Journal of Geophysical Research: Solid Earth*, 127(8):e2022JB024613, 2022. doi: https://doi.org/10.1029/2022JB024613.

Kennett, B. L. N. The seismic wavefield as seen by distributed acoustic sensing arrays: local, regional and teleseismic sources. *Proceedings of the Royal Society A: Mathematical, Physical and Engineering Sciences*, 478(2258):20210812, 2022. doi: 10.1098/rspa.2021.0812.

Kennett, B. L. N. and Fichtner, A. *Exploiting Seismic Waveforms: Correlation, Heterogeneity and Inversion*. Cambridge University Press, 2020. doi: 10.1017/9781108903035.

Kennett, B. L. N., Stipčević, J., and Gorbatov, A. Spiral-Arm Seismic Arrays. *Bulletin of the Seismological Society of America*, 105(4): 2109–2116, 07 2015. doi: 10.1785/0120140354.

Ketterhals, P., Haefeli, C., and Staeger, D. Blatt 1166 Bern. Geologisches Atlas der Schweiz 1:25000, Karte 100, 2000. https://www.swisstopo.admin.ch/en/geodata/geology/maps/ga25/raster.html.

Lancelle, C. E., Baldwin, J. A., Lord, N., Fratta, D., Chalari, A., and Wang, H. F. Using Distributed Acoustic Sensing (DAS) for Multichannel Analysis of Surface Waves (MASW). In *Distributed Acoustic Sensing in Geophysics*, chapter 16, pages 213–228. American Geophysical Union (AGU), 2021. doi: 10.1002/9781119521808.ch16.

Lobkis, O. I. and Weaver, R. L. On the emergence of the Green's function in the correlations of a diffuse field. *The Journal of the Acoustical Society of America*, 110(6):3011–3017, 2001. doi: 10.1121/1.1417528.

Maranò, S., Fäh, D., and Lu, Y. M. Sensor placement for the analysis of seismic surface waves: sources of error, design criterion and array design algorithms. *Geophysical Journal International*, 197 (3):1566–1581, 04 2014. doi: 10.1093/gji/ggt489.

Martin, E. R., Lindsey, N. J., Ajo-Franklin, J. B., and Biondi, B. L. *Introduction to Interferometry of Fiber-Optic Strain Measurements*, chapter 9, pages 111–129. American Geophysical Union (AGU), 2021. doi: 10.1002/9781119521808.ch9.

Nakata, N., Gualtieri, L., and Fichtner, A., editors. *Seismic Ambient Noise*. Cambridge University Press, 2019. doi: 10.1017/9781108264808.

Näsholm, S. P., Iranpour, K., Wuestefeld, A., Dando, B. D. E., Baird, A. F., and Oye, V. Array Signal Processing on Distributed Acoustic Sensing Data: Directivity Effects in Slowness Space. *Journal of Geophysical Research: Solid Earth*, 127(2):e2021JB023587, 2022. doi: 10.1029/2021JB023587.

Nayak, A. and Thurber, C. H. Using multicomponent ambient seismic noise cross-correlations to identify higher mode Rayleigh waves and improve dispersion measurements. *Geophysical Journal International*, 222(3):1590–1605, 06 2020. doi: 10.1093/gji/ggaa270.

Park, C. B., Miller, R. D., and Xia, J. Imaging dispersion curves of surface waves on multi-channel record. In *SEG Technical Program Expanded Abstracts 1998*, pages 1377–1380. Society of Exploration Geophysicists, 1998. doi: 10.1190/1.1820161.

Park, C. B., Miller, R. D., and Xia, J. Multichannel analysis of surface waves. *Geophysics*, 64(3):800–808, 1999. doi: 10.1190/1.1444590.

Quiros, D. A., Brown, L. D., and Kim, D. Seismic interferometry of railroad induced ground motions: body and surface wave imaging. *Geophysical Journal International*, 205(1):301–313, 02 2016. doi: 10.1093/gji/ggw033.

Sager, K., Ermert, L., Boehm, C., and Fichtner, A. Towards full waveform ambient noise inversion. *Geophysical Journal International*, 212(1):566–590, 10 2017. doi: 10.1093/gji/ggx429.

Snieder, R. Extracting the Green's function from the correlation of coda waves: A derivation based on stationary phase. *Phys. Rev. E*, 69:046610, Apr 2004. doi: 10.1103/PhysRevE.69.046610.

Takagi, R., Nakahara, H., Kono, T., and Okada, T. Separating body and Rayleigh waves with cross terms of the cross-correlation tensor of ambient noise. *Journal of Geophysical Research: Solid Earth*, 119(3):2005–2018, 2014. doi: 10.1002/2013JB010824.

van den Ende, M. P. A. and Ampuero, J.-P. Evaluating seismic beamforming capabilities of distributed acoustic sensing arrays. *Solid Earth*, 12(4):915–934, 2021. doi: 10.5194/se-12-915-2021.

van Wijk, K., Mikesell, T. D., Schulte-Pelkum, V., and Stachnik, J. Estimating the Rayleigh-wave impulse response between seismic stations with the cross terms of the Green tensor. *Geophysical Research Letters*, 38(16), 2011. doi: 10.1029/2011GL047442.

Wapenaar, K. Retrieving the Elastodynamic Green's Function of an Arbitrary Inhomogeneous Medium by Cross Correlation. *Phys. Rev. Lett.*, 93:254301, Dec 2004. doi: 10.1103/PhysRevLett.93.254301.

Wapenaar, K. and Fokkema, J. Green's function representations for seismic interferometry. *Geophysics*, 71(4):SI33–SI46, 2006. doi: 10.1190/1.2213955.

Weaver, R. L. Equipartition and retrieval of Green's function. *Earthquake Science*, 23(5):397–402, 2010. doi: 10.1007/s11589-010-0738-2.

Yang, Y., Atterholt, J. W., Shen, Z., Muir, J. B., Williams, E. F., and Zhan, Z. Sub-Kilometer Correlation Between Near-Surface Structure and Ground Motion Measured With Distributed Acoustic Sensing. *Geophysical Research Letters*, 49(1): e2021GL096503, 2022. doi: 10.1029/2021GL096503.

Zhang, K., Li, H., Wang, X., and Wang, K. Retrieval of shallow S-wave profiles from seismic reflection surveying and traffic-induced noise. *Geophysics*, 85(6):EN105–EN117, 2020. doi: 10.1190/geo2019-0845.1.

doi:10.26443/seismica.v2i2.388

SEISMICA

Bayesian eikonal tomography using Gaussian processes

Jack B. Muir * [1]

[1]Department of Earth Sciences, University of Oxford, now at Fleet Space Technologies

Author contributions: *Conceptualization*: Jack Muir. *Software*: Jack Muir. *Formal Analysis*: Jack Muir. *Visualization*: Jack Muir. *Writing — Original draft*: Jack Muir.

Abstract Eikonal tomography has become a popular methodology for deriving phase velocity maps from surface wave phase delay measurements. Its high efficiency makes it popular for handling datasets deriving from large-N arrays, in particular in the ambient-noise tomography setting. However, the results of eikonal tomography are crucially dependent on the way in which phase delay measurements are predicted from data, a point which has not been thoroughly investigated. In this work, I provide a rigorous formulation for eikonal tomography using Gaussian processes (GPs) to smooth observed phase delay measurements, including uncertainties. GPs allow the posterior phase delay gradient to be analytically derived. From the phase delay gradient, an excellent approximate solution for phase velocities can be obtained using the saddlepoint method. The result is a full Bayesian posterior distribution for phase velocities of surface waves, incorporating the nonlinear wavefront bending inherent in eikonal tomography, with no sampling required. On studying these posterior distributions, the outcomes of these analyses imply that the uncertainties reported for eikonal tomography are often underestimated.

Non-technical summary Eikonal tomography is an imaging method that uses slight variations between seismic waves trapped at the surface of the Earth to infer information about the properties beneath the surface. To be able to perform the best possible eikonal tomography, we need to be able to predict in between measurements of these variations at different seismic recording stations as best we can. Furthermore, end-users of seismic tomography require information about the uncertainty of the images. In this paper, I perform this prediction using Gaussian processes (GPs), a method with particularly nice mathematical properties. The GP prediction results in robust uncertainty measurements for our imaging problem without many of the computational difficulties associated with other uncertainty quantification methods.

Production Editor:
Gareth Funning
Handling Editor:
Suzan van der Lee
Copy & Layout Editor:
Kirsty Bayliss

Received:
February 20, 2023
Accepted:
November 6, 2023
Published:
December 22, 2023

1 Introduction

Surface wave tomography is a cornerstone imaging technique for the investigation of the crust and upper mantle. However, due to the significant non-planarity of scattered surface waves, interpretation of surface wave data is not straightforward (e.g., Wielandt, 1993). Despite this issue, the increasing proliferation of dense seismic arrays, combined with the advent of ambient-noise correlation methods, has motivated intense study into surface wave tomographic techniques. To ameliorate the great cost of nonlinear ray tracing for large inverse problems, a large part of this study has focused on methods that derive surface wave properties from only local information contained in the wavefield. Beginning with a wavefield perturbation approach (e.g., Friederich et al., 1994; Friederich and Wielandt, 1995; Pollitz, 2008), theoretical efforts in local surface wave inversion have since concentrated on direct measurement of wavefield derivatives (e.g Lin et al., 2009; Lin and Ritzwoller, 2011; de Ridder and Biondi, 2015; de Ridder and Maddison, 2018). Likely owing to its simplicity, the most popular extant method is eikonal tomography (Lin et al., 2009), which relies on the determination of the wavefield phase gradient across an entire local or regional array. For a single surface wave mode propagating with phase velocity C_p, frequency ω, phase delay T and amplitude A, the Helmholtz equation implies that (Tromp and Dahlen, 1993)

$$\frac{1}{C_p^2} = |\nabla T|^2 - \frac{\nabla^2 A}{\omega^2 A}. \tag{1}$$

*Corresponding author: jack.muir@fleet.space

Simplifying this relationship under the assumption that the frequency of the wave is large compared to perturbations in the wave amplitude gives us the eikonal equation:

$$C_p = \frac{1}{|\nabla T|}. \tag{2}$$

Eikonal tomography uses Equation 2 to directly infer local phase velocity from local phase gradient. A distinction compared to local gradiometry is that calculation of the phase gradient is performed simultaneously for all desired locations by fitting a delay curve across an array, rather than by local analysis of sub-arrays (Langston, 2007a, e.g.,). The assumption that the wavefront is smooth relative to frequency is strong, but the difficulty associated with measuring wavefront curvature accurately has ensured that eikonal tomography remains a central technique in array analysis. Application of eikonal tomography in practice has typically resulted in images comparable to other tomographic methods and Helmholtz tomography (which uses Equation 1 directly), especially when results are averaged azimuthally (Bodin and Maupin, 2008; Lin et al., 2009; Lehujeur and Chevrot, 2020). While the typical use case of eikonal tomography is surface-wave phase-velocity inversion (a 2D problem), other potential use cases of eikonal tomography could include 1D linear inversions along DAS arrays (e.g. Yang et al., 2022) or 3D inversions of first arrivals within mine arrays (e.g. Mandic et al., 2018), so interpolation schemes that work well in arbitrary dimensions are useful for eikonal tomography workflows.

In this work, I employ Gaussian process theory (Rasmussen and Williams, 2006) to derive semi-analytic closed-form approximations for the posterior distribution of eikonal-equation-based phase-velocity measurements using the saddlepoint method (Butler, 2007). In this case, semi-analytic means that the posterior approximations have a single parameter that must be solved using constrained minimization techniques — no Monte Carlo methods need be used. As a result, the approximate posterior can be calculated very quickly. As an intermediate result, I derive fully analytic posteriors for the gradient of phase delay. The delay gradient posteriors can be sampled using standard multivariate normal random number generators, which provides an efficient way to compute arbitrary statistics of the GP posterior when the semi-analytic approximations are difficult to obtain.

2 Eikonal tomography from derivatives of Gaussian processes

The least well-defined problem in eikonal tomography is how to go from point measurements of phase delay to the phase delay gradient map (Lin et al., 2009). It is in this process that the practitioner has the greatest control over the resulting phase velocity map; intuitively, we can immediately see that over-smoothing the map will result in a measurement of C_p that is too large; conversely, maps that are too rough will result in too small C_p. Past studies have typically employed splines (either in tension (e.g., Lin et al., 2009; Lin and Ritzwoller, 2011) or smoothing (Chevrot and Lehujeur, 2022)) to perform prediction. The spline framework is a robust general interpolation or smoothing method, however in its basic formulation it gives a single maximum-likelihood estimate of the prediction, with no associated uncertainty information. As I later show in the paper, phase velocities derived by eikonal tomography are biased due to the presence of uncertainty, so it is important to understand the scale of uncertainties when creating eikonal tomography maps.

This study aims to place the problem of estimating an optimal phase gradient map on a robust Bayesian footing, where all assumptions are explicit, adjustable, and optimizable in the face of the data. In this study, the problem of predicting phase delay measurements is posed as a Gaussian process (GP) regression (often referred to as Kriging in geostatistical literature) — we will see that this framework meets the desiderata for estimating phase gradients. GPs are a particular framework for defining distributions over function spaces (Rasmussen and Williams, 2006). GPs have the property that any finite collection of points sampled from them will have a multivariate Gaussian distribution. A GP is defined by a mean function $m(x)$ and covariance function $k(x, x')$, which generate the mean and covariance matrix of a finite collection of points drawn from the GP. Concretely, for any collection of points $(x_1, x_2, ...x_n)$ and associated function values $(d_1, d_2, ...d_n)$, the GP model assumes that

$$\begin{bmatrix} d_1 \\ d_2 \\ \vdots \\ d_n \end{bmatrix} \sim N\left(\begin{bmatrix} m(x_1) \\ m(x_2) \\ \vdots \\ m(x_n) \end{bmatrix}, \begin{bmatrix} k(x_1,x_1) & k(x_1,x_2) & \dots & k(x_1,x_n) \\ k(x_2,x_1) & k(x_2,x_2) & \dots & k(x_2,x_n) \\ \vdots & \vdots & \ddots & \vdots \\ k(x_n,x_1) & k(x_n,x_2) & \dots & k(x_n,x_n) \end{bmatrix}, \right) \tag{3}$$

where $N(\mu, \Sigma)$ is a multivariate Gaussian with mean vector μ and covariance matrix Σ. In the context of regression, this leads to a powerful result — if we assume a GP prior for an unknown function, and we then observe data with a Gaussian likelihood, the posterior distribution for the unknown function will also be a GP. Thus, GPs fully generalize finite linear regression and Gaussian inverse problems to the function space setting (Valentine and Sambridge, 2020a,b). As differentiation is a linear operation, derivatives of GPs are again also GPs. We will use these properties to derive closed-form posterior distributions for the derivatives of observed data under a GP prior. While the motivating example is eikonal tomography, these techniques are applicable to regression problems generally. Derivatives of GPs have long been used in the dynamical control community (e.g. Solak et al., 2002; Rasmussen, 2003). Closer in spirit to seismology, GP derivatives have also been applied to the identification of geodetic transients (Hines and Hetland, 2018). The presentation described here is generalized from McHutchon (2014).

In this manuscript, bold font refers to collections of observed data and capitals to matrices. Boldfont capitals are therefore collections of n data in m coordinates and will have dimensions $n \times m$. Coordinates (i.e., x) may be vector quantities but will not be boldfont. To begin, assume that there are measurements $(\boldsymbol{X}, \boldsymbol{d})$ of the observed phase delay $\boldsymbol{d}$ at points $\boldsymbol{X}$. Assume that the data $\boldsymbol{d}$ are noisy; for the purposes of exposition this is taken to be identically distributed Gaussian noise η with the distribution $N(0, \sigma)$, but arbitrary multivariate Gaussian noise distributions with data covariance C_D are also easily handled by GP theory. This implies that there is an unknown true phase delay field $T(x)$ with

$$\boldsymbol{d} = T(\boldsymbol{X}) + \eta. \tag{4}$$

The objective of eikonal tomography is to know the field $T(x)$ so that we can differentiate it and get C_p. I assume that

$$T(x) = T_0(x) + r(x) \tag{5}$$

where r is a zero-mean GP and $T_0(x)$ is a reference phase delay field, for example for a laterally homogeneous medium. Therefore, $T(x)$ is a GP with mean $T_0(x)$.

$$T(x) \sim GP(T_0(x), k(x, x')), \tag{6}$$

where $k(x, x')$ is the assumed covariance function. It should be noted that r is a distribution over functions; it incorporates uncertainty due to errors in the observed data and the effect of heterogeneities on the travel time function. r in effect models the residuals between the reference model T_0 and the observed data. For the examples in this work, I will use a squared-exponential kernel with independent length scales in each dimension for the covariance function:

$$k(x, x') = a^2 \exp\left(-\sum_{i=1}^{m} \frac{(x_i - x_i')^2}{2l_i^2}\right). \tag{7}$$

This covariance function promotes very smooth fields with characteristic amplitude a (it is infinitely differentiable), and provides a degree of flexibility that improves regression performance in the face of inhomogeneous data observation and complex travel time fields due to the independent length scales l_i. This covariance function allows the observed data points to “talk” to one another and build a smooth underlying interpolation field that captures variations in travel time due to structural heterogeneity. The hyperparameters $a, l_1, ...$ etc. are optimized by minimizing the negative log marginal likelihood of the GP model given the observed data — this is further discussed in Section 2.2.

I also assume that $T_0(x) = s_0|x|$ for a fixed reference slowness s_0. Let $K_{\boldsymbol{X}\boldsymbol{X}'}$ be the matrix of evaluating k with rows given by $\boldsymbol{X}$ and columns by $\boldsymbol{X}'$. The fundamental idea of GP regression is that, given this problem setup, then the observed data $\boldsymbol{d}$ and the predicted data $T(\boldsymbol{X}')$ has the joint multivariate Gaussian distribution

$$\begin{bmatrix} \boldsymbol{d} \\ T(\boldsymbol{X}') \end{bmatrix} \sim N\left(\begin{bmatrix} T_0(\boldsymbol{X}) \\ T_0(\boldsymbol{X}') \end{bmatrix}, \begin{bmatrix} K_{\boldsymbol{X}\boldsymbol{X}} + \sigma^2 I & K_{\boldsymbol{X}\boldsymbol{X}'} \\ K_{\boldsymbol{X}'\boldsymbol{X}} & K_{\boldsymbol{X}'\boldsymbol{X}'} \end{bmatrix}.\right) \tag{8}$$

By conditioning $T(\boldsymbol{X}')$ on the observed data $\boldsymbol{d}$ (i.e. finding the distribution of $T(\boldsymbol{X}')$ given fixed $\boldsymbol{d}$) we have (Rasmussen and Williams, 2006)

$$T(\boldsymbol{X}')|\boldsymbol{d} \sim N(T_0(\boldsymbol{X}') + K_{\boldsymbol{X}'\boldsymbol{X}}(K_{\boldsymbol{X}\boldsymbol{X}} + \sigma^2 I)^{-1}(\boldsymbol{d} - T_0(\boldsymbol{X})), K_{\boldsymbol{X}'\boldsymbol{X}'} - K_{\boldsymbol{X}'\boldsymbol{X}}(K_{\boldsymbol{X}\boldsymbol{X}} + \sigma^2 I)^{-1}K_{\boldsymbol{X}\boldsymbol{X}'}). \tag{9}$$

Note that data error models with Gaussian covariance just require replacing $\sigma^2 I$ with C_D.

Figure 1 shows an example application of GP regression for obtaining $T(x)|\boldsymbol{d}$, with comparison to the approach based on regression using splines (e.g., Lin et al., 2009; Lin and Ritzwoller, 2011) — in this case, using smoothing splines (e.g., Chevrot and Lehujeur, 2022). This example emulates a typical local surface wave application, using 100 data points uniformly distributed within the inversion region with 0.2 s added Gaussian noise. The squared slowness is obtained using the method of manufactured solutions from the eikonal equation to avoid any errors in the simulated data, and the synthetic phase delay field is strongly perturbed away from the reference model to highlight differences between the GP and spline based methods. The GP mean and standard deviation are given analytically, and show substantial differences with the smoothing spline fit — here, the spline smoothing parameter is automatically set by the FitPack routine (Dierckx, 1993). In comparison to the GP, the spline performs less well, especially in areas of data gaps. Figure 2 compares the GP reconstruction with the true values of the phase delay map. The GP mean closely fits the true values, although the level of uncertainty becomes quite substantial near the edges of the domain.

I can now calculate expectation values (the mean of the probability distribution) for the derivatives; note that from now on I implicitly condition on $\boldsymbol{d}$ but will not write it out for ease of notation, unless it seems particularly germane to do so. Since differentiation is a linear operation, and linear operations acting on normal distributions result in normal distributions, the components of ∇T must also be normally distributed, and are completely specified by

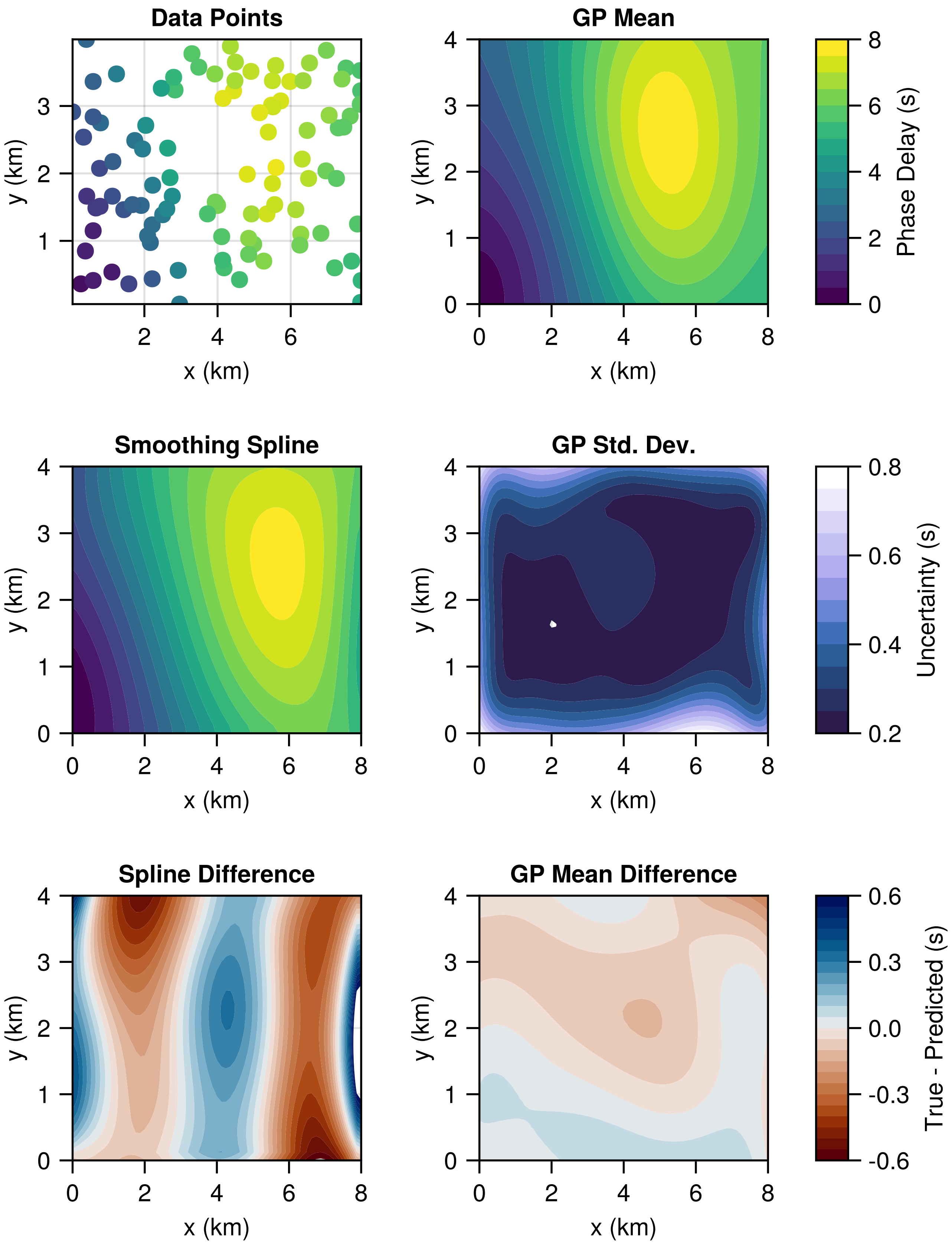

Figure 1 Comparison of the GP posterior (showing mean and point-wise standard deviation) of the estimated phase delay with a smoothing-spline based solution for an example phase delay data set with 100 randomly distributed points and 0.2 s Gaussian noise. The data is generated using the method of manufactured solutions, assuming a seismic source at $(0, 0)$. There are notable differences in the estimated phase delay, especially where there are gaps in the data coverage. The difference plots show the difference between the true phase delay field and the spline solution or the GP mean respectively. The colouring of the difference plots is arranged according to the usual seismic convention of blue being a fast and red being slow; in this case blue means that the predicted arrival is fast compared to the truth and vice versa.

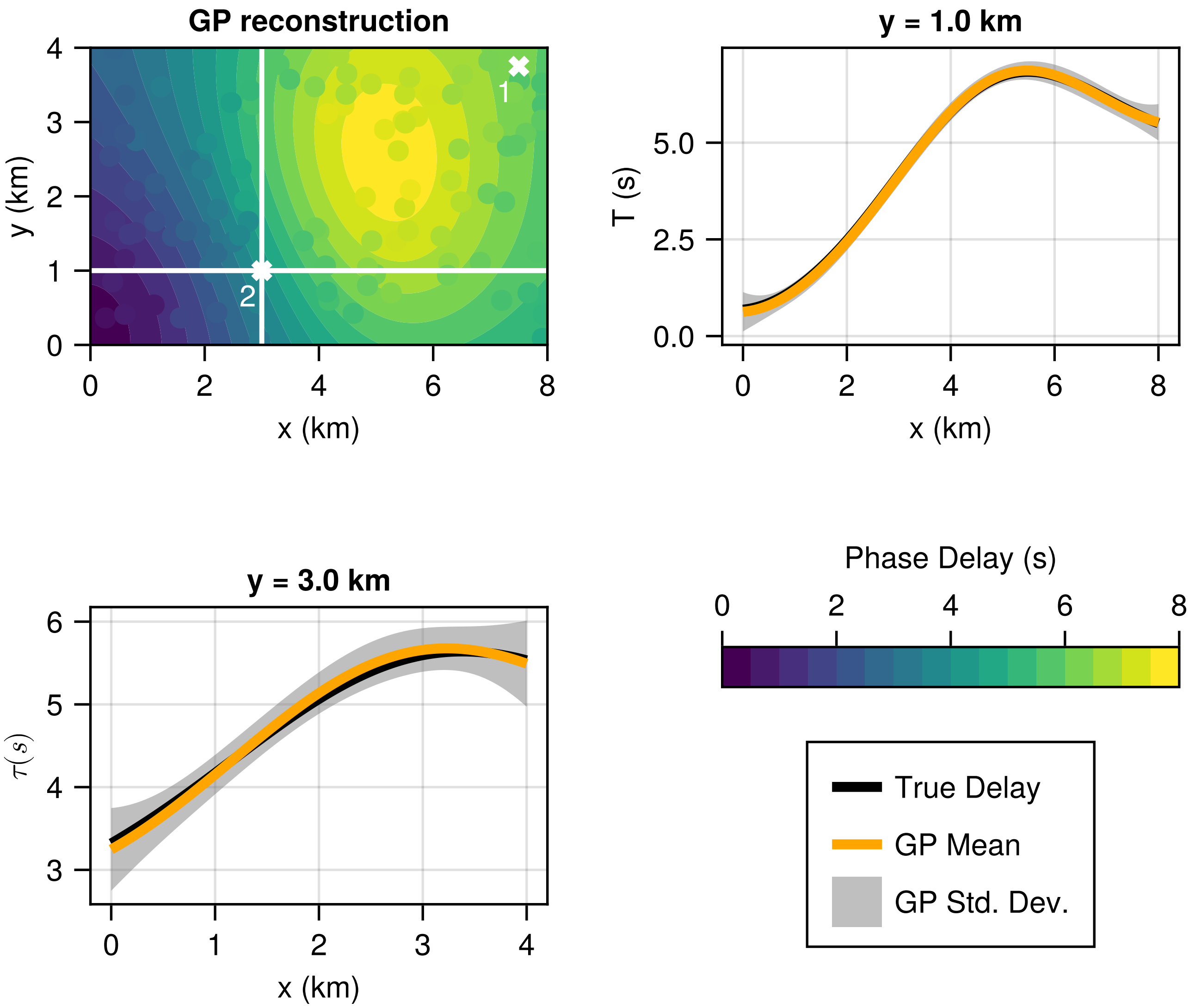

Figure 2 Cross-sections through the GP reconstruction of Figure 1, showing the true phase delay (black), GP mean (orange) and standard deviation (grey). The GP reconstruction is overlaid with the noisy observed delay values. The GP posterior closely follows the true phase delay curve, with substantially higher uncertainty near the edges of the domain, even before extrapolation. The test points used later in Figure 3 are shown by white crosses.

their mean and covariance. The collection of means for component i are immediately given by recognizing that as the expectation operator is also linear, it commutes with the derivative operator:

$$\begin{aligned}\mathbb{E}\left[\frac{\partial T(\boldsymbol{X}')}{\partial x_i'}\right] &= \frac{\partial \mathbb{E}\left[T(\boldsymbol{X}')\right]}{\partial x_i'} \\ &= \frac{\partial T_0(\boldsymbol{X}')}{\partial x_i'} + \frac{\partial K_{\boldsymbol{X}'\boldsymbol{X}}}{\partial x_i'}(K_{\boldsymbol{X}\boldsymbol{X}} + \sigma^2 I)^{-1}(\boldsymbol{d} - T_0(\boldsymbol{X})).\end{aligned} \tag{10}$$

Note that the mean value of the derivatives are calculated independently for each dimension; however as we will see they do have covariance between output points and between dimensions. For the covariance, consider $n \times n$ blocks of the covariance matrix of size $nd \times nd$ where d is the dimension and n is the number of output points. Note that I choose to order the hierarchy of the covariance matrix first by derivative coordinate, and second by data point index, as it makes the notation more convenient. As the covariance is bilinear,

$$\text{Cov}\left(\frac{\partial T(\boldsymbol{X}')}{\partial x_i'}, \frac{\partial T(\boldsymbol{X}'')}{\partial x_j''}\right) = \frac{\partial^2 \text{Cov}(T(\boldsymbol{X}'), T(\boldsymbol{X}''))}{\partial x_i' \partial x_j''} \tag{11}$$

where I introduce the dummy variable x'' to represent the second argument in the covariance ($\boldsymbol{X}' = \boldsymbol{X}''$, but we want to formally differentiate in respect to the second slot only when using x''). Continuing on,

$$\begin{aligned}\frac{\partial^2 \text{Cov}(T(\boldsymbol{X}'), T(\boldsymbol{X}''))}{\partial x_i' \partial x_j''} &= \frac{\partial^2 \left(K_{\boldsymbol{X}'\boldsymbol{X}''} - K_{\boldsymbol{X}'\boldsymbol{X}}(K_{\boldsymbol{X}\boldsymbol{X}} + \sigma^2 I)^{-1} K_{\boldsymbol{X}\boldsymbol{X}''}\right)}{\partial x_i' \partial x_j''} \\ &= \frac{\partial^2 K_{\boldsymbol{X}'\boldsymbol{X}''}}{\partial x_i' \partial x_j''} - \frac{\partial K_{\boldsymbol{X}'\boldsymbol{X}}}{\partial x_i'}(K_{\boldsymbol{X}\boldsymbol{X}} + \sigma^2 I)^{-1}\frac{\partial K_{\boldsymbol{X}\boldsymbol{X}''}}{\partial x_j''}.\end{aligned} \tag{12}$$

So that I can compress the notation somewhat, let us define $\hat{K}_{\boldsymbol{X}\boldsymbol{X}} = K_{\boldsymbol{X}\boldsymbol{X}} + \sigma^2 I$ and $\Delta \boldsymbol{d} = \boldsymbol{d} - T_0(\boldsymbol{X})$. For the 2D case (noting that other dimensions immediately generalize), the conditional posterior is a multivariate Gaussian with mean given by Equation 10 and covariance given by Equation 12:

$$\begin{aligned}\nabla T(\boldsymbol{X}')|\boldsymbol{d} &= \begin{bmatrix}\frac{\partial T(\boldsymbol{X}')}{\partial x'} \\ \frac{\partial T(\boldsymbol{X}')}{\partial y'}\end{bmatrix}|\boldsymbol{d} \\ &\sim N\left(\begin{bmatrix}\frac{\partial T_0(\boldsymbol{X}')}{\partial x'} + \frac{\partial K_{\boldsymbol{X}'\boldsymbol{X}}}{\partial x'}\hat{K}^{-1}_{\boldsymbol{X}\boldsymbol{X}}\Delta\boldsymbol{d} \\ \frac{\partial T_0(\boldsymbol{X}')}{\partial y'} + \frac{\partial K_{\boldsymbol{X}'\boldsymbol{X}}}{\partial y'}\hat{K}^{-1}_{\boldsymbol{X}\boldsymbol{X}}\Delta\boldsymbol{d}\end{bmatrix}, \begin{bmatrix}\frac{\partial^2 K_{\boldsymbol{X}'\boldsymbol{X}''}}{\partial x'\partial x''} - \frac{\partial K_{\boldsymbol{X}'\boldsymbol{X}}}{\partial x'}\hat{K}^{-1}_{\boldsymbol{X}\boldsymbol{X}}\frac{\partial K_{\boldsymbol{X}\boldsymbol{X}''}}{\partial x''} & \frac{\partial^2 K_{\boldsymbol{X}'\boldsymbol{X}''}}{\partial x'\partial y''} - \frac{\partial K_{\boldsymbol{X}'\boldsymbol{X}}}{\partial x'}\hat{K}^{-1}_{\boldsymbol{X}\boldsymbol{X}}\frac{\partial K_{\boldsymbol{X}\boldsymbol{X}''}}{\partial y''} \\ \frac{\partial^2 K_{\boldsymbol{X}'\boldsymbol{X}''}}{\partial y'\partial x''} - \frac{\partial K_{\boldsymbol{X}'\boldsymbol{X}}}{\partial y'}\hat{K}^{-1}_{\boldsymbol{X}\boldsymbol{X}}\frac{\partial K_{\boldsymbol{X}\boldsymbol{X}''}}{\partial x''} & \frac{\partial^2 K_{\boldsymbol{X}'\boldsymbol{X}''}}{\partial y'\partial y''} - \frac{\partial K_{\boldsymbol{X}'\boldsymbol{X}}}{\partial y'}\hat{K}^{-1}_{\boldsymbol{X}\boldsymbol{X}}\frac{\partial K_{\boldsymbol{X}\boldsymbol{X}''}}{\partial y''}\end{bmatrix}\right),\end{aligned} \tag{13}$$

which is an exact distribution for the derivatives evaluated at $\boldsymbol{X}'$. Figure 3 shows the mean and covariance structure for the derivatives at two test points calculated using the above theory, compared to the true derivative of the phase delay, and finite-difference estimates computed using random draws of the GP estimate of the phase delay (i.e., Monte-Carlo finite-difference derivatives). Both the analytic and Monte-Carlo results closely agree with each other and with the true values for the derivatives. In Figure 4, I use the multivariate normal posterior for the derivatives to generate samples of the posterior for the squared slowness and compare it against the predictions from the smoothing spline. The GP posterior is in this case more accurate than the spline result, and also delivers uncertainty information.

Unfortunately, it turns out that this is as far as it is possible to go with exact distributions, as the velocity is a nonlinear function of the gradients in eikonal tomography. Thankfully, however, there is well-developed theory for approximating quadratic forms of normal random variables, and as $\frac{1}{C_p^2} = (\nabla T)^2$, which is a quadratic form of a normal random variable, it may be possible to try for a good approximation to the velocity. Before deriving one, however, there are two important issues to investigate — setting hyperparameters, and closed forms for the expectation value of velocity.

2.1 A realistic example — Rayleigh wave phase velocities near Ridgecrest, CA

Having investigated some of the features of the GP interpolation method for eikonal tomography using a synthetic with large amplitude perturbations, I now perform the same investigation for a realistic problem setup. I simulated phase velocity data, beginning with the V_P and V_S model of White et al. (2021) for the region immediately surrounding the fault traces of the Ridgecrest, CA July 2019 earthquake sequence. I converted White's model to UTM zone 11 coordinates within the area between 324–587 km easting, 3820–4094 km northing, and used the Nafe-Drake empirical relationship to obtain ρ from V_P (Brocher, 2005), and then the fundamental-mode Rayleigh-wave phase velocity at 30 s period was calculated for each point using surfdisp96 (Herrmann, 2013). The travel time field was calculated from the southwest corner of the domain (324 km easting, 3820 km northing; UTM zone 11) using the factored-eikonal fast-marching method (Treister and Haber, 2016). I interpolated the travel time field to the 154 station locations used in

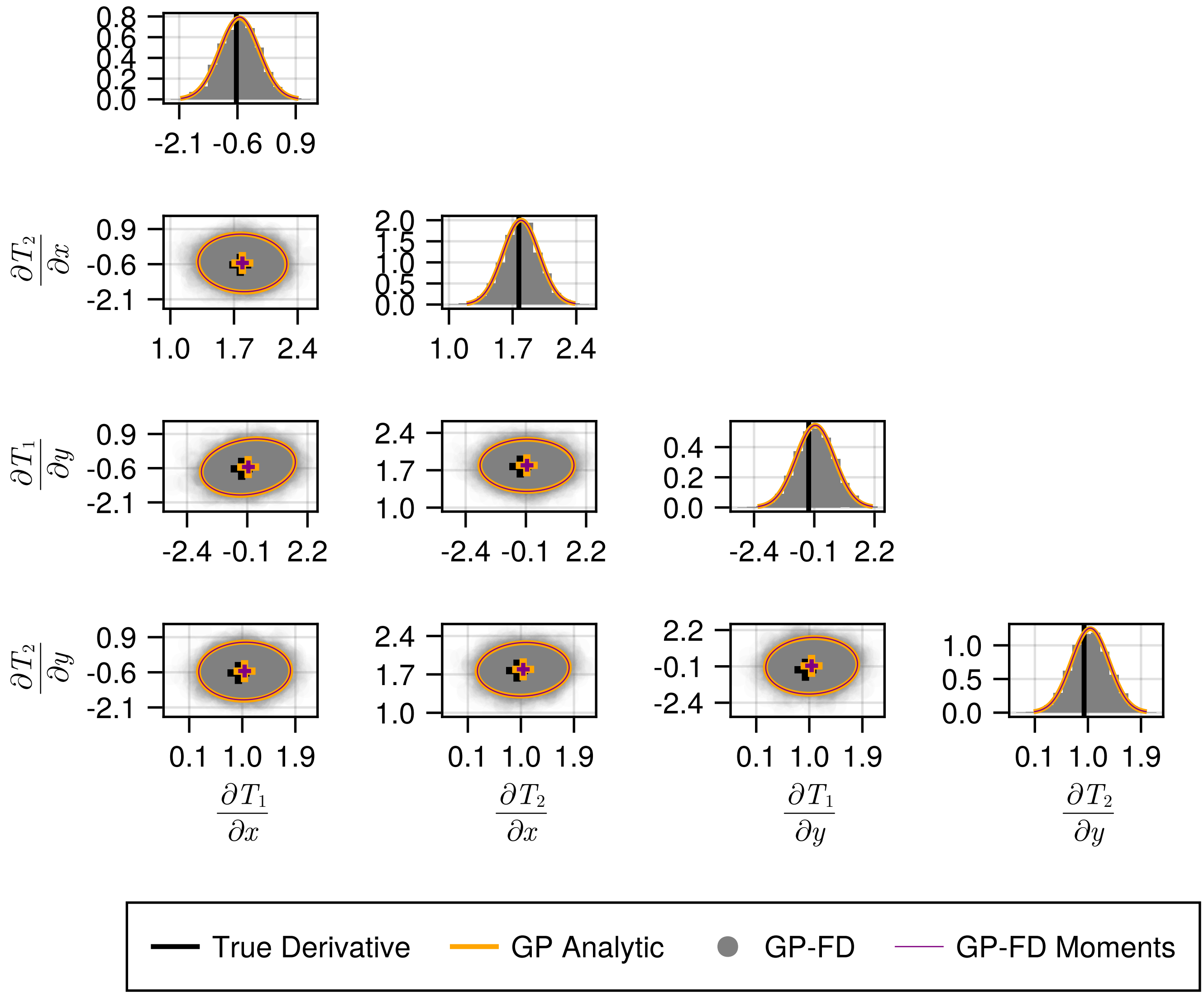

Figure 3 Corner plot showing the covariance of derivatives at two test points, and their individual histograms. The test points are T_1 at (7.5,3.75) (a near-edge point), and T_2 at (3.0, 1.0) (a more centered point). Black crosses and lines show the true value of the derivatives. Orange lines show the analytical GP based solutions derived in this paper, with ellipses drawn at the 95% credible level and crosses showing the mean. Grey circles and histograms show finite-difference (FD) based derivatives using Monte-Carlo samples of the GP posterior for phase delay, and red crosses and ellipses show the mean and estimated covariance at 95% confidence from the FD draws. For the 1D histograms, the y-axis represents the value of the PDF.

the generation of the White et al. (2021) model within the simulation domain box. Finally, I added Gaussian random noise with 0.1 s standard deviation to the simulated travel times to create the dataset.

The salient points of difference between this experiment and the previous ones are: firstly, the strength of the velocity perturbations is much smaller, resulting in smaller travel time effects; secondly, the distribution of stations is highly non-uniform resulting in variable spatial resolution; and thirdly, the travel time is calculated using a numerical method, and so may contain minor errors (although these will be mitigated by using the high-accuracy algorithm of Treister and Haber (2016)). Figures 5, 6 and 7 are the equivalents of Figures 1, 2 and 4, respectively. Even in this substantially different setting, the GP based interpolation performs better than the spline. In particular, the spline based method appears to have trouble with the edges of the domain when the density of stations is highly non-uniform, resulting in artifacts near the southwest corner in the derived phase velocity field, whereas the GP based method does not suffer from these issues.

2.2 Finding good values for GP hyperparameters

The hyperparameters of the GP may be optimized by maximizing the log marginal likelihood of observations, where the marginalization is performed over the unknown function values $T(\boldsymbol{X})$ (Rasmussen and Williams (2006)). This gives the type-II maximum likelihood estimate; the hyperparameters have a point-estimate, whereas the function

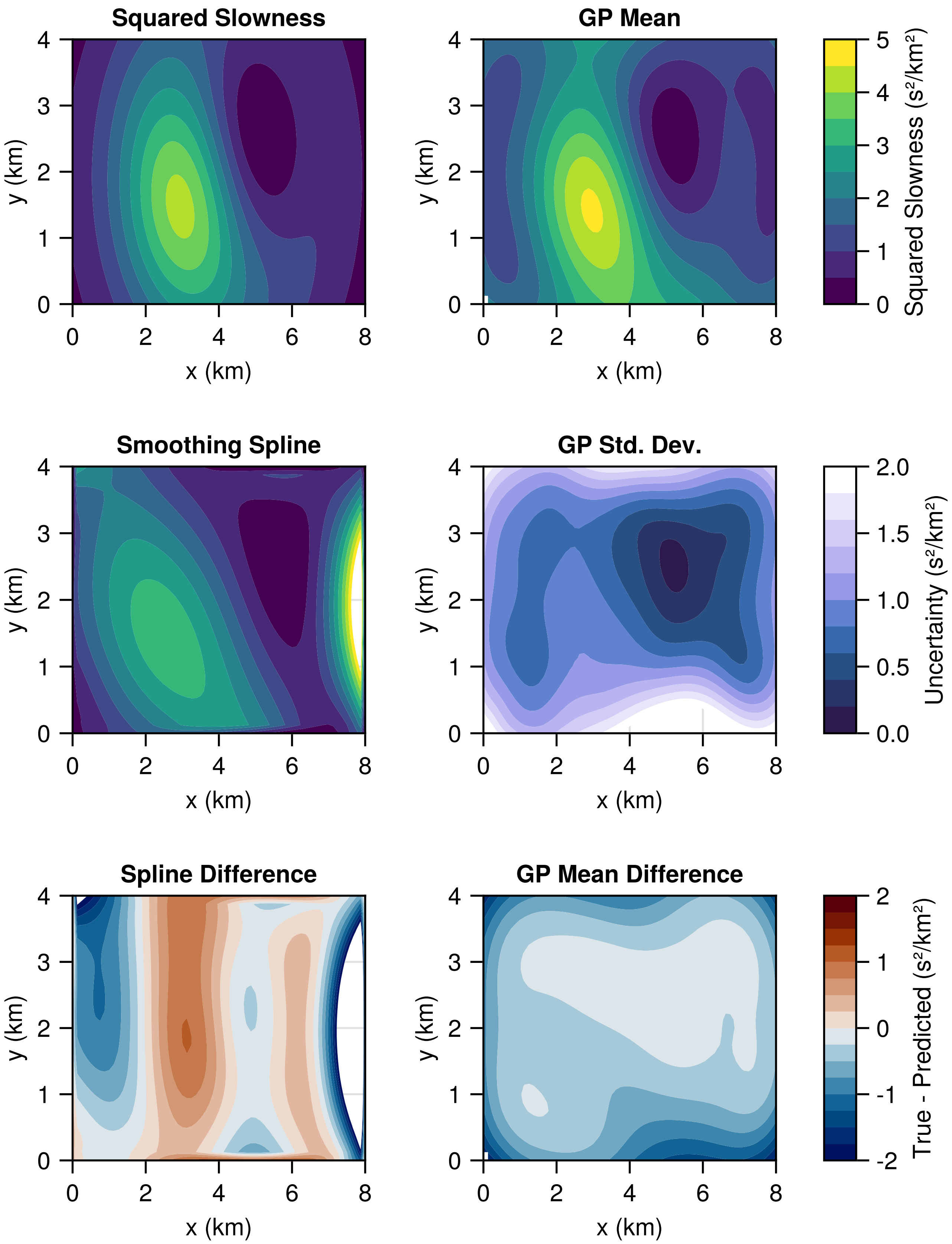

Figure 4 Comparison of the true squared slowness against results calculated using a squared-exponential Gaussian process with tuned hyperparameters. The GP mean and standard deviation are calculated by drawing 100,000 predicted travel time gradients. The spline squared slowness has been calculated using 5^{th} order centred finite differences. The GP result has a mean closer to the truth, and additionally adds uncertainty information, when compared to the smoothing spline. The colouring of the difference plots is arranged according to the usual seismic convention of blue being fast and red being slow; in this case blue means that the predicted slowness is smaller compared to the truth and vice versa; note that this induces a colour flip compared to Figure 1.

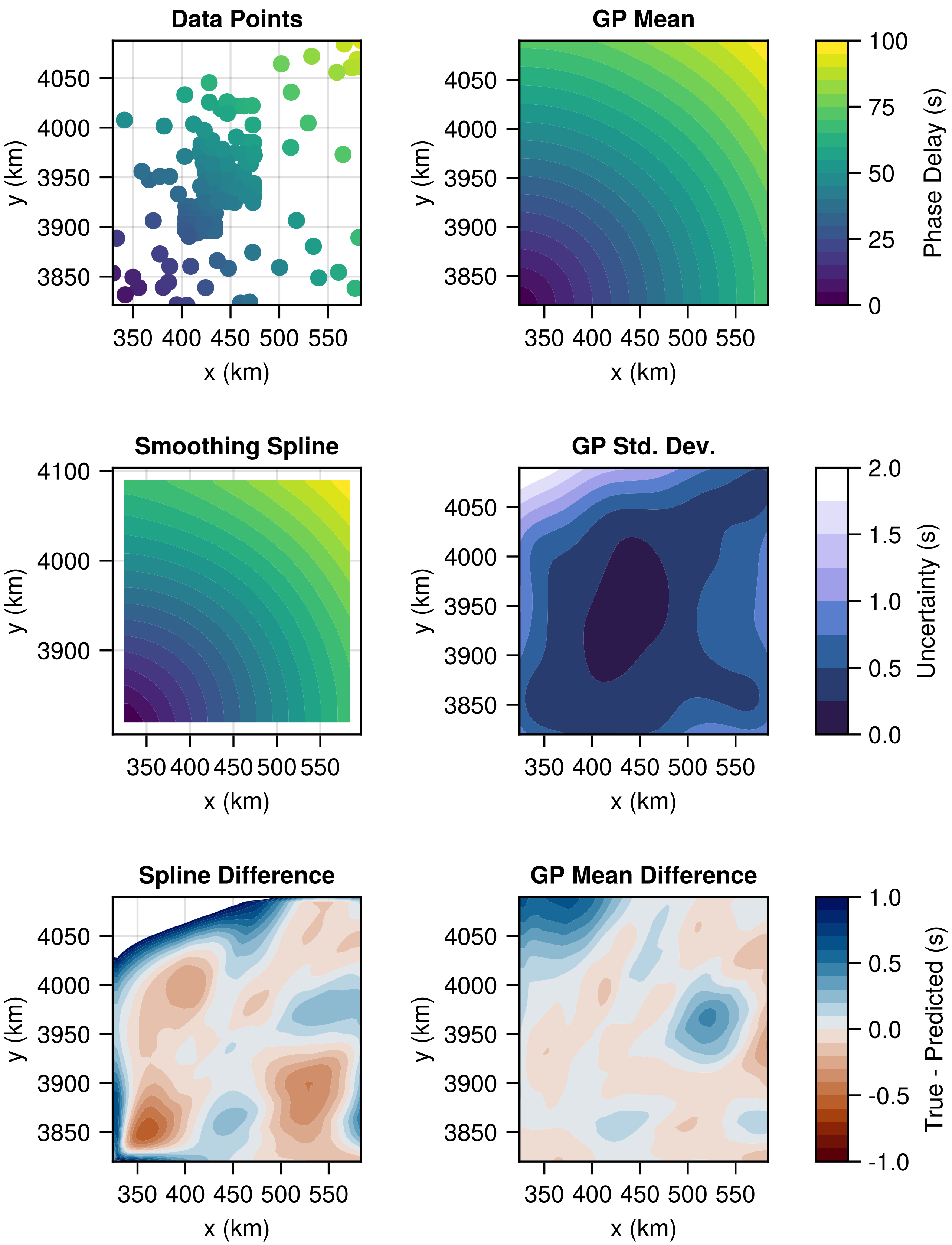

Figure 5 Comparison of the GP posterior (showing mean and point-wise standard deviation) of the phase delay with a smoothing-spline based solution for the example phase delay dataset derived from the model of White et al. (2021), with 154 station locations and 0.1 s added Gaussian noise. There are notable differences in the estimated phase delay, especially where there are gaps in the data coverage. The colouring of the difference plots is arranged according to the usual seismic convention of blue being a fast and red being slow; in this case blue means that the predicted arrival is fast compared to the truth and vice versa.

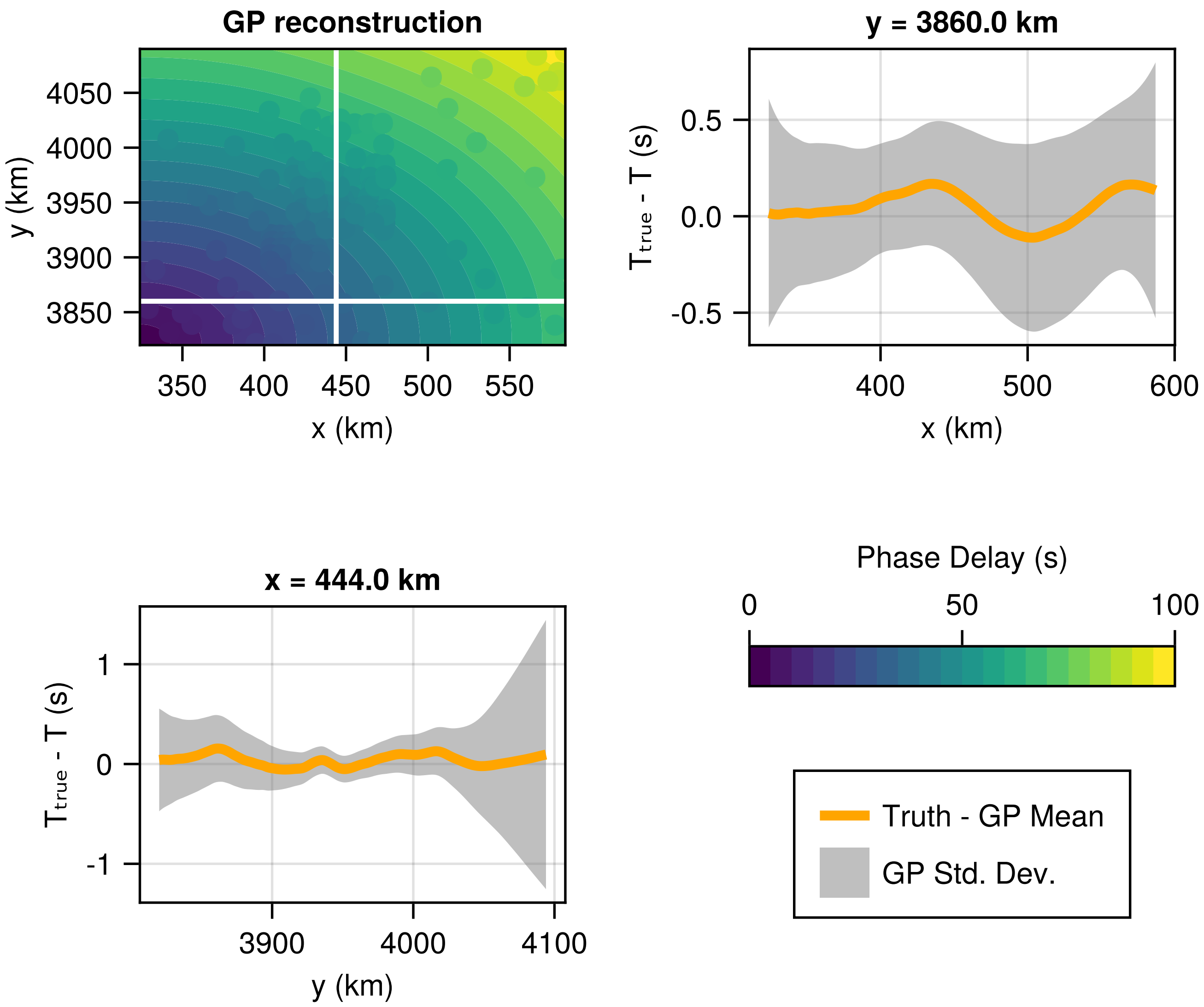

Figure 6 Cross-sections through the GP reconstruction of Figure 5, showing the residual between the true travel time field and the GP mean (orange) and standard deviation (grey). The GP reconstruction is overlaid with the noisy observed delay values.

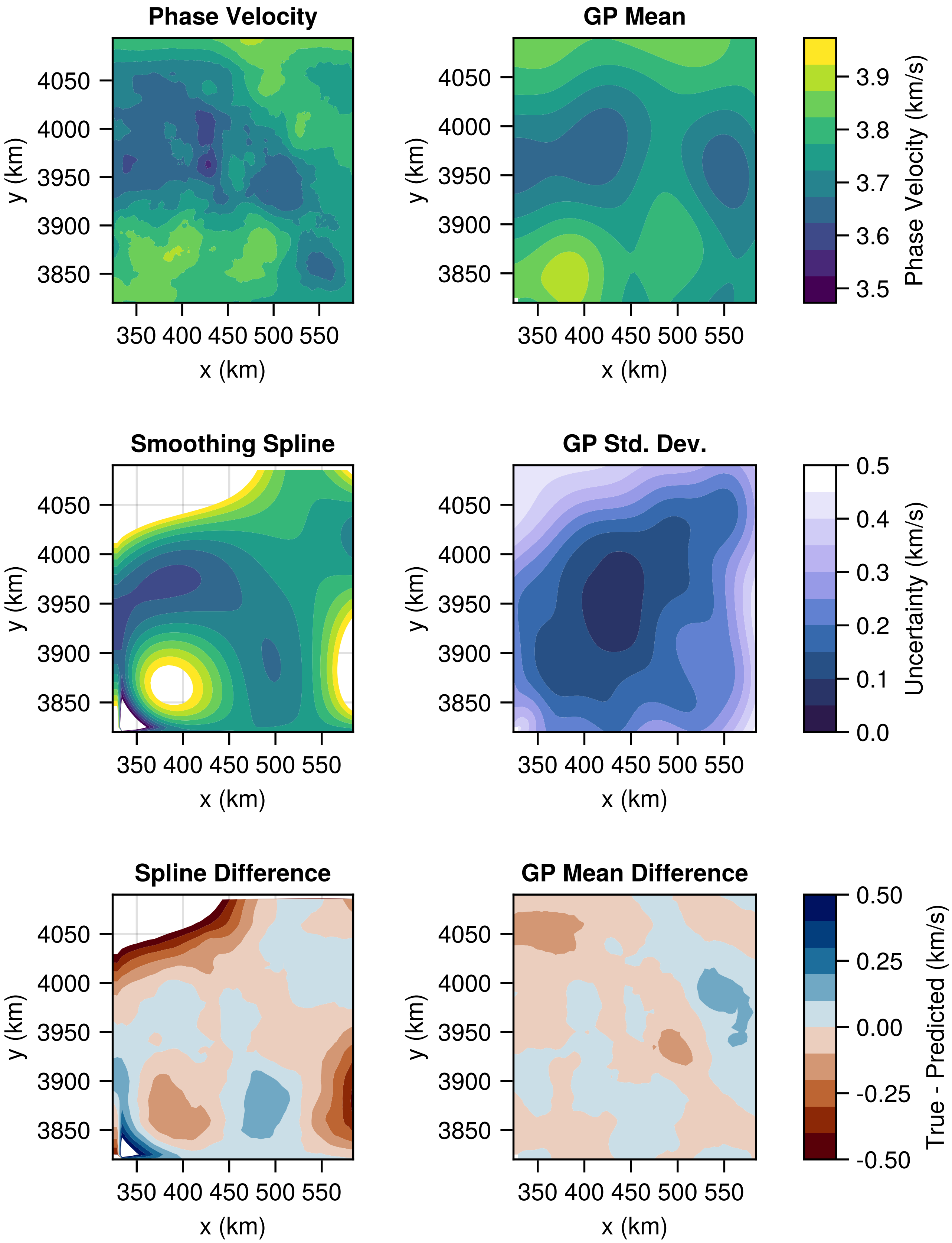

Figure 7 Comparison of the true phase velocity against results calculated using a squared-exponential Gaussian process with tuned hyperparameters for the Ridgecrest, CA velocity model of White et al. (2021). The GP mean and standard deviation are calculated by drawing 100,000 predicted travel time gradients. The spline phase velocity has been calculated using 5^{th} order centred finite differences. The GP result has a mean closer to the truth, and additionally adds uncertainty information, when compared to the smoothing spline.

values have a full posterior distribution given that point-estimate. The log marginal likelihood for GP regression is given by

$$\log p(\boldsymbol{d}|\theta, \boldsymbol{X}) = -\frac{1}{2}\Delta\boldsymbol{d}^T \hat{K}^{-1}_{\boldsymbol{XX}}(\theta)\Delta\boldsymbol{d} - \frac{1}{2}|\hat{K}_{\boldsymbol{XX}}(\theta)| - \frac{n}{2}\log(2\pi), \tag{14}$$

where the covariance matrix $\hat{K}_{\boldsymbol{XX}}(\theta)$ is treated as a function of the hyperparameters θ, and n is the number of data. Intuitively, the log marginal likelihood parsimoniously balances data misfit (the first term) with the level of uncertainty (the second term). For a 2D squared-exponential kernel with independent length scales, independent Gaussian data noise, and a laterally homogeneous medium as a reference model, the hyperparameters are $\theta = (a, l_1, l_2, \sigma, s_0)$.

2.3 A special exact case for eikonal tomography: The expectation value of squared slowness given normally distributed derivatives

Consider without loss of generality a 2D case. The squared slowness is given by $1/C_p^2 = \left(\frac{\partial T}{\partial x}\right)^2 + \left(\frac{\partial T}{\partial y}\right)^2 = T_x^2 + T_y^2$. Assume the phase gradient is given by a multivariate Gaussian random variable

$$\begin{aligned}\nabla T &= \begin{bmatrix} T_x \\ T_y \end{bmatrix} \\ &\sim N\left(\begin{bmatrix} \mu_x \\ \mu_y \end{bmatrix}, \begin{bmatrix} \sigma_x^2 & \nu_{xy} \\ \nu_{xy} & \sigma_y^2 \end{bmatrix}\right) \\ &= N(\mu, \Sigma)\end{aligned} \tag{15}$$

that describes the joint distribution of the two derivatives T_x, T_y, and let S^2 be the random variable describing the distribution of slowness squared. This is, for example, the distribution that arises for the derivatives of a single point conditioned on observations under GP regression as described above. Then $\mathbb{E}[S^2] = \mathbb{E}[\nabla T^T \nabla T]$. Note that $Cov[\nabla T, \nabla T] = \mathbb{E}[\nabla T \nabla T^T] - \mathbb{E}[\nabla T]\mathbb{E}[\nabla T]^T$. As the slowness squared is a scalar, I can take the trace to proceed as follows, following Kendrick (2002):

$$\begin{aligned}\mathbb{E}[S^2] &= \mathbb{E}[\nabla T^T \nabla T] \\ &= \mathbb{E}[tr(\nabla T^T \nabla T)] \\ &= tr(\mathbb{E}[\nabla T^T \nabla T]) \\ &= tr(\mathbb{E}[\nabla T]\mathbb{E}[\nabla T]^T + Cov[\nabla T, \nabla T]) \\ &= tr(\mu\mu^T + \Sigma) \\ &= \mu_x^2 + \mu_y^2 + \sigma_x^2 + \sigma_y^2 \\ &> \mu_x^2 + \mu_y^2 = (\mathbb{E}[T_x])^2 + (\mathbb{E}[T_y])^2\end{aligned} \tag{16}$$

It is instructive to note that the expectation value of squared slowness is strictly greater than the sum-of-squares of the mean derivatives, so that velocities are "biased" lower after accounting for errors. Note that this is true for any calculation that assumes the derivatives have a Gaussian distribution, not just the Gaussian process framework analysed here. This assumption is implicit in any interpolation scheme that is linear in the observed data, if the data has Gaussian uncertainty.

3 Approximation of the posterior using the saddlepoint method

The analytic results obtained for the derivative ∇T have already given us a great deal. Any expectation value that depends on these derivatives (in particular, moments of the phase velocity) can be calculated using the Monte-Carlo method — i.e., by drawing many random samples of ∇T and then calculating the desired statistics on this random sample. Because it is possible to draw directly from the posterior of ∇T given Equation 13, every sample can be used and is independent (unlike in Markov-Chain Monte-Carlo). As such, these expectation values will usually converge quickly. However, there are cases where it is still useful to have approximations of the posterior that can be even more quickly calculated; for instance if the eikonal tomography derived phase velocities are being used in a joint inverse problem, or if accurate statistics for extreme values need to be calculated. A frequently used simple approximation would be to use Laplace's method directly on the posterior distribution for $||\nabla T||^2$ or C_p. The approximate posterior using this technique is the best fitting Gaussian distribution. However, looking at Figure 8, it is clear that neither distribution is close to Gaussian, and may not in fact have a clear mode to fit.

Instead of approximating the posterior directly, I instead use the saddlepoint approximation. The saddlepoint approximation for the distribution of random variables was originally proposed by Daniels (1954), with Butler (2007) giving a thorough account of the basic method. Very roughly, the idea is to examine the cumulant generating function (CGF) for a scalar random variable U

$$\begin{aligned}K(s) &= \log \mathbb{E}[\exp(sU)] \\ &= \log \int_{\mathcal{U}} e^{su} f(u) du,\end{aligned} \tag{17}$$

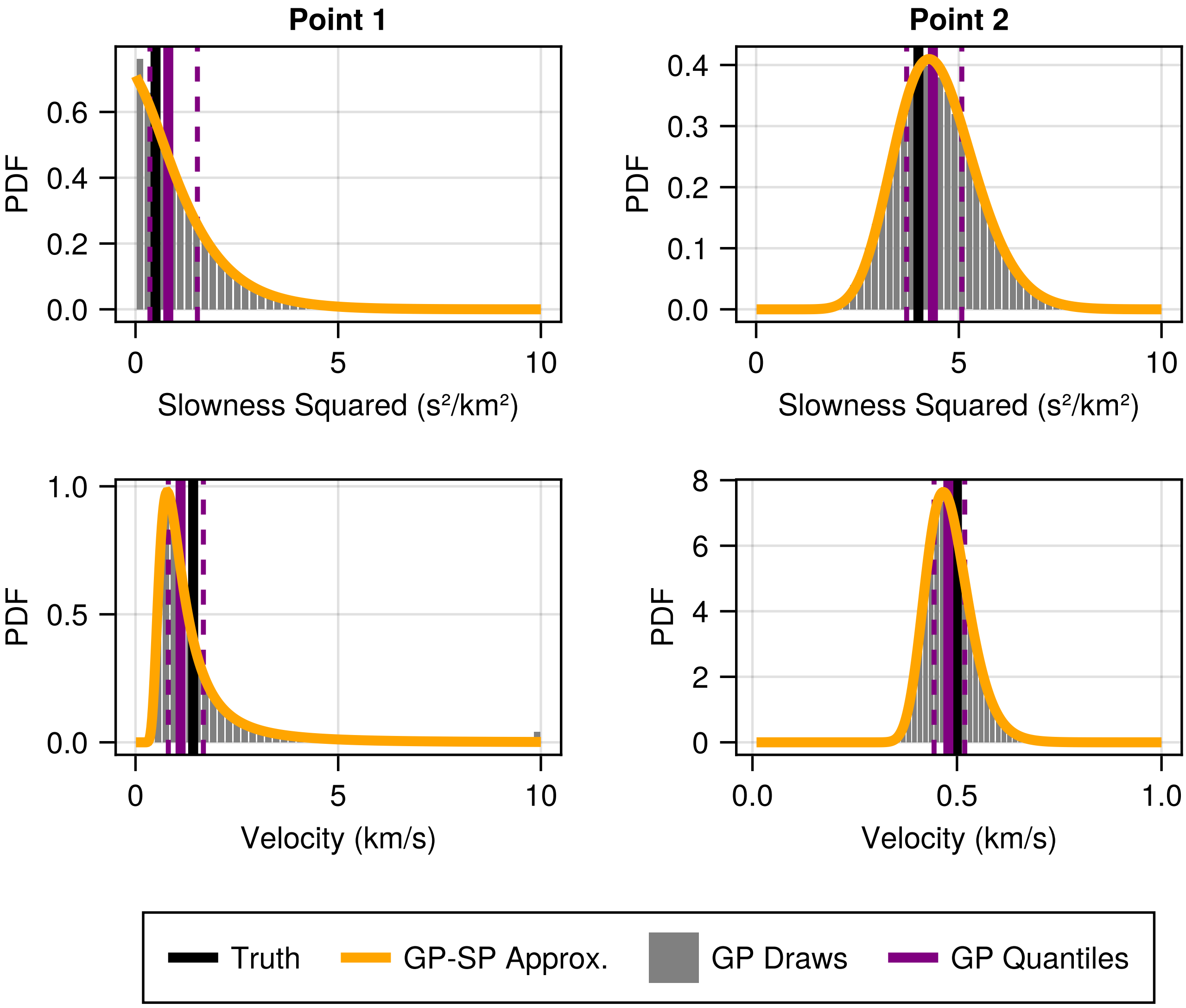

Figure 8 Comparison of the empirical CDF and PDF (grey) for the squared slowness and phase velocity for the near-edge point 1 (7.5,3.75) and more centered point 2 (3.0, 1.0) with the saddlepoint (SP) approximation (orange). For the PDF, the true value is also shown in black and the median, 25^{th} and 75^{th} percentiles of the empirical PDF are shown in purple. The empirical distributions are truncated between 0.01 and 10 for plotting purposes, other than for the velocity of Point 2 which is truncated between 0.01 and 1 due to minimal probability mass above 1.

where $f(u)$ is the probability distribution of U and $\mathcal{U}$ is its domain of support. u could be, for example, the slowness squared or the phase velocity at a particular point, while s is a scalar auxiliary variable with units that are the inverse of those of u. Note that $K(s)$ is different from the various K covariance matrices (we have maintained use of K in both cases as they are by far the most common symbols used in the literature for both cases). The existence of the CGF requires that there is some interval $a < 0 < b$ such that the above integral converges. Daniels (1954) showed that the CGF could be used to derive a highly accurate approximation of the PDF (see Butler, 2007, for more information),

$$\hat{f}(u) = \sqrt{\frac{1}{2\pi K''(\hat{s})}}\exp(K(\hat{s}) - \hat{s}u), \tag{18}$$

where $\hat{s}$ is the solution of $K'(s) = u$. $\hat{s}$ is a saddlepoint of the integrand in Equation 17, hence the name "saddlepoint approximation". If the application requires it, $\hat{f}(u)$ then typically has to be normalized to integrate to unity so that it is a true probability distribution, giving us

$$\bar{f}(u) = \frac{\hat{f}(u)}{\int_{\mathcal{U}} \hat{f}(u)du}. \tag{19}$$

If the application only requires the PDF up to proportionality (as is often the case), then the above normalization is not required, and the saddlepoint approximation requires no integration whatsoever. Butler (2007) shows that this optimization problem is well posed and gives a unique real solution for $\hat{f}$, if s is constrained to be inside the interval that contains 0 for which $K(s)$ converges. Serendipitously, this low order method often provides extremely good approximations to the PDF, as the CGF K contains the full information about the distribution of X. For sums of random variables (such as $||\nabla T||^2$), it is almost always easier to construct the CGF K analytically rather than the PDF f, as $K_{U+V}(s) = K_U(s) + K_V(s)$, whereas $f_{U+V}(x) = f_U(x) * f_V(x)$ where U and V are arbitrary random variables and $*$ is the convolution operator. Therefore, when using the saddlepoint approximation to obtain the PDF, multiple potentially slowly converging convolution integrals are converted into a simple root-finding problem with a unique solution. Let us now apply this concept to deriving the PDFs of $||\nabla T||^2$ and C_p from our closed form posteriors for phase delay derivatives ∇T. To do this, my goal is to write the distribution of $||\nabla T||^2$ in a form for which I can determine the CGF $K_{||\nabla T||^2}$, and then use the saddlepoint approximation to obtain the posterior PDF $\hat{f}_{||\nabla T||^2}$, from which I can also obtain the posterior PDF $\hat{f}_{C_p}$ using a change-of-variables formula.

For simplicity, I approximate the posterior for a single point x' given data $(\mathbf{X}, \mathbf{d})$. I have shown that $\nabla T(x')|\boldsymbol{d} \sim N(\mu, \Sigma)$ for a d dimensional mean vector μ and a $d \times d$ covariance matrix Σ. Therefore we can write $\nabla T(x')|\boldsymbol{d}$ in non-centered form using a coordinate transform,

$$\nabla T(x')|\boldsymbol{d} = Q\Lambda^{1/2}h + \mu, \tag{20}$$

where $Q\Lambda Q^T = \Sigma$ is an eigenvalue decomposition of Σ and h is a d-dimensional standard normal variable $h \sim N(0, I)$. Q contains the normalized eigenvectors as its columns and Λ is a diagonal matrix of corresponding eigenvalues. Assuming that the phase delay measurements are taken in different locations, all of the terms in Λ are positive as then Σ, as a non-degenerate covariance matrix, is positive definite. I can then write

$$\begin{aligned} ||\nabla T(x')||^2 &= (Q\Lambda^{\frac{1}{2}}h + \mu)^T(Q\Lambda^{\frac{1}{2}}h + \mu) \\ &= (Qh + \bar{\mu})^T\Lambda(Qh + \bar{\mu}) \\ &= (h + Q^T\bar{\mu})^T Q^T\Lambda Q(h + Q^T\bar{\mu}) \end{aligned} \tag{21}$$

where $\bar{\mu} = \Lambda^{-\frac{1}{2}}\mu$. The eigenvalues collected in Λ are labelled λ_i, with corresponding components of $\bar{\mu}$ labelled $\bar{\mu}_i$. The quadratic form in Equation 21 can be written as a sum over non-central chi-squared distributions (Imhof, 1961; Butler and Paolella, 2008). The degree of freedom of each non-central chi-squared corresponds to the multiplicity of the eigenvalues of Σ, which will for our purposes always be distinct, giving

$$||\nabla T(x')||^2 = \sum_{i=1}^{m} \lambda_i \chi^2(1, \bar{\mu}_i^2). \tag{22}$$

Because of the summation property of the CGF, the CGF of $||\nabla T(x')||^2$ is then (Butler and Paolella, 2008)

$$K_{||\nabla T(x')||^2}(s) = \sum_{i=1}^{m}\left[-\frac{1}{2}\log(1 - 2s\lambda_i) + \frac{s\lambda_i\bar{\mu}_i^2}{1 - 2s\lambda_i}\right], \tag{23}$$

and the derivatives are given by

$$K^{(j)}_{||\nabla T(x')||^2}(s) = 2^{j-1}(j-1)!\sum_{i=1}^{m}\lambda_i^j(1 - 2s\lambda_i)^{-j}\left(1 + \frac{j\bar{\mu}_i^2}{1 - 2s\lambda_i}\right). \tag{24}$$

The domain of convergence in which the root of $K'(s) = u$ is sought is the largest open interval containing zero for which $K_{||\nabla T(x')||^2}(s)$ is defined, which from looking at Equation 23 is $s \in (-\infty, \frac{1}{2\lambda_{max}})$, where λ_{max} is the largest eigenvalue of Σ. Applying the saddlepoint approximation given the above K gives us the saddlepoint distribution $\hat{f}_{||\nabla T(x')||^2}(u)$ for the squared slowness, which can be normalized to give

$$\bar{f}_{||\nabla T(x')||^2}(u) = \frac{\hat{f}_{||\nabla T(x')||^2}(u)}{\int_0^\infty \hat{f}_{||\nabla T(x')||^2}(u)}. \tag{25}$$

The transformation between squared slowness $||\nabla T||^2$ and phase velocity C_p is given by $C_p = g(||\nabla T||^2)$ with $g(u) = \frac{1}{\sqrt{u}}$, which is a monotone decreasing function. The appropriate Jacobian transformation rule to obtain the approximate PDF of phase velocity is then (Kadane, 2011)

$$\begin{aligned} \bar{f}_{C_p(x')}(u) &= -\bar{f}_{||\nabla T(x')||^2}(g^{-1}(u))\frac{dg^{-1}}{du}(u) \\ &= \frac{2\bar{f}_{||\nabla T(x')||^2}\left(\frac{1}{u^2}\right)}{u^3}. \end{aligned} \tag{26}$$

The approximate distributions $\bar{f}_{||\nabla T(x')||^2}(u)$ and $\bar{f}_{C_p(x')}(u)$ are plotted against a histogram of 1,000,000 draws of the squared slowness and phase velocity using the analytic derivatives in Figure 8, showing that the saddlepoint approximations are a close fit. Higher order saddlepoint approximation terms and approximations for the cumulative distribution function (CDF) are collected in Butler (2007).

The saddlepoint method can be further applied to the joint distribution function for phase velocity or squared slowness at two different points to derive the approximate spatial covariance (Al-Naffouri et al., 2016). Because the underlying posterior distributions for the derivatives is given by a GP, the covariance completely describes the spatial behaviour of the velocity distribution, and so the ability to calculate the distribution for any two arbitrary points is sufficient to fully characterize the posterior. However, the resulting root-finding problem will be in two variables rather than one and is substantially more complicated than the forms derived here, so they are left for future work.

4 Discussion

4.1 Implications for sample statistics

Most eikonal tomography applications report per-station per-frequency error statistics by computing the standard error in the mean phase velocity over multiple sources; this averaging process is the second essential step in robust eikonal tomographic results (Lin et al., 2009). Studies typically appeal to the central limit theorem to justify the use of the sample standard error formula and sample mean for quantifying the data distribution. The reported standard errors are then used to weight data in further inversions — a typical use case is to perform 1D Bayesian inversion beneath each station using the mean values and the reported error. Previous methods do not optimally smooth the phase delay regression that underlies eikonal tomography, potentially producing biased results, and do not produce uncertainty estimates for each source. However, uncertainties reported in studies using these methods are often extremely low, amounting to a few percent of the estimated phase velocity.

In our GP framework, Monte Carlo sampling can be used to directly estimate the distribution for sample statistics such as the mean over multiple sources, and hence compute the full PDFs for these averaged quantities. As a motivation, observe that both the empirical distribution for phase velocity and its saddlepoint approximation is heavy tailed for point 1 in Figure 8. This is a point relatively close to the edge, which can result in a distribution that is far from Gaussian. Taking point 1, I draw 4^n samples of velocity from the GP posterior for $n = 0 \ldots 6$, calculate the sample mean and median for the batch of 4^n, and then repeat 100,000 times to find the distribution in the sample statistics. Figure 9 shows the results. The sample mean converges only slowly to a normal distribution, and is still broad even with 16 samples. In comparison, the sample median is well-behaved and converges quickly as the sample size increases. For both sample statistics, the distribution for small numbers of samples is unsurprisingly quite similar to the underlying velocity distribution, and is consequently heavy tailed — this should be taking under consideration for applications such as fitting azimuthal anisotropy profiles to eikonal tomography results, where many azimuth bins near the edges of arrays will often have few contributing sources. Assuming that the standard error formula describes the uncertainty in the measurements is likely an underestimate in that case.

4.2 Future work

In this study, I present the simplest possible implementation of a GP framework for eikonal tomography with analytic derivatives of phase delay. The flexibility of GP modelling offers several opportunities for future improvements that should result in more robust inversions. The first of these is that multi-frequency eikonal inversion is naturally handled by GP modelling by assuming a space-frequency covariance function. The most simple model would use a separable function $k((x, f), (x', f')) = k_x(x, x')k_f(f, f')$. A smooth frequency covariance $k_f(f, f')$ would reduce

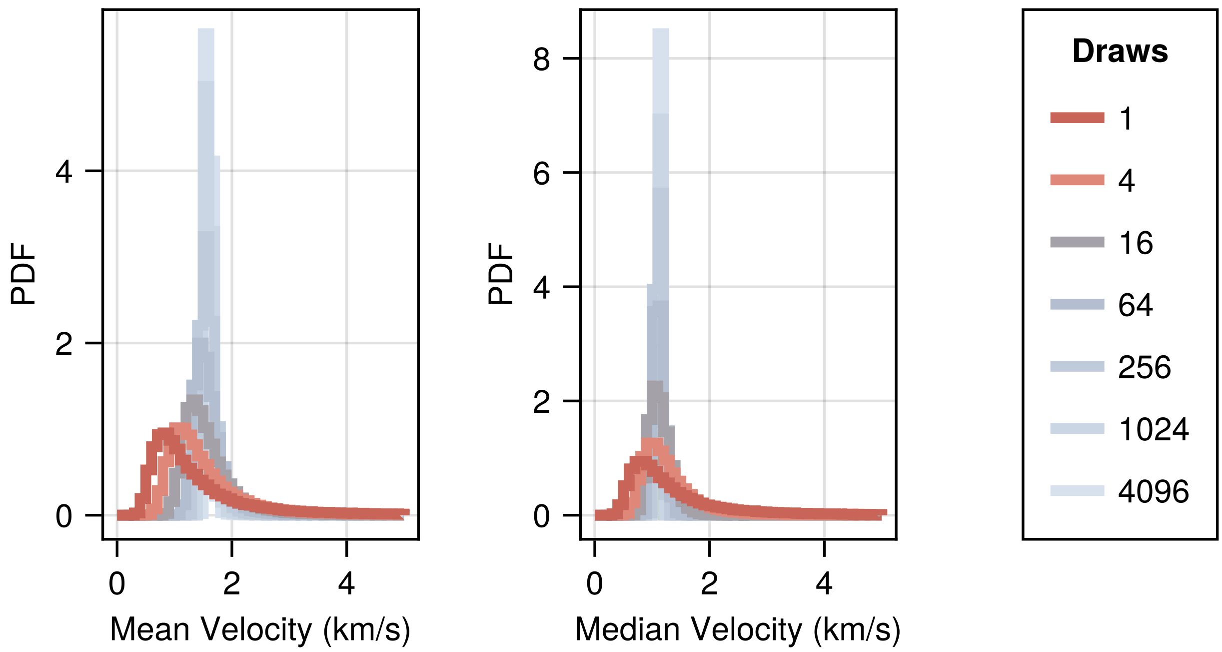

Figure 9 Comparison of the distribution of sample means and sample medians for the phase velocity at (7.5,3.75). The mean or median is calculated by drawing 4^n samples for $n = 0 \ldots 6$. This process is repeated 100,000 times to obtain the distributions of sample means and medians. Compared to the sample median, the sample mean converges to a normal distribution slowly.

the impact of missing data in particular frequency bins, which can be an issue due to spectral holes in surface wave trains.

Secondly, the squared-exponential kernel used in this study could be further improved to better represent the behaviour of true seismic wavefields; for instance, the problem could be recast in radial coordinates with a radial-azimuthal kernel as studied in Padonou and Roustant (2015). Due to the natural cylindrical symmetry of wave propagation, this may allow us to reduce the uncertainty in the eikonal tomography results. In particular, this kernel choice would be appropriate in use cases such as ambient-noise tomography where the seismic source is inside the array, resulting in highly non-planar wavefronts.

A third option would be to use the GP framework for smoothing the underlying full wavefield records before processing them for phase delay measurements or for other gradient based techniques such as wavefield gradiometry (e.g., Langston, 2007a,b; de Ridder and Biondi, 2015; de Ridder and Maddison, 2018) or full Helmholtz tomography (Lin and Ritzwoller, 2011). These applications would potentially require extending the GP derivative theory to higher order, but again noting that derivatives are linear, the resulting distributions for higher order spatial terms will also be GPs. The GP framework is especially well suited towards the inclusion of strain measurements in joint wavefield reconstruction (e.g., Muir and Zhan, 2021) as the appropriate covariance kernels can be calculated using the results in Equation 13 — an enticing prospect considering the proliferation of distributed acoustic sensing (DAS) strain sensors (Zhan, 2020). GP based techniques have also been used in geodesy to investigate transient strain rates (e.g., Hines and Hetland, 2018), and the saddlepoint approximation techniques investigated here could offer a way to more accurate quantification of strain invariants arising from geodetic analysis.

Finally, as the number of phase delay measurements increases across stations and frequency bins, the size of the data covariance matrix $\hat{K}$ increases. For n measurements, the cost of inverting this matrix scales like $O(n^3)$, so very large collections of measurements pose a challenge for GP based inversion. Due to the popularity of GPs in machine learning research, there are a wide range of sparse GP approximations that produce almost identical results and still result in analytic derivatives once the sparsity structure is determined (e.g., Titsias, 2009; Lindgren et al., 2011; Wilson and Nickisch, 2015). Employing these methods would allow efficient upscaling of the methodology presented here to multi-frequency inversion of USArray-scale datasets.

4.3 Conclusions

This study derives an analytic posterior distribution for phase delay derivatives, and then derives approximate posteriors for phase velocity using the saddlepoint approximation applied to the eikonal equation. The result is a fully

Bayesian eikonal tomography that requires no MCMC sampling to characterize the posterior. As such, computations are easily implemented and highly efficient. Using the GP framework as a basis, I investigated two important effects that impact the interpretation of eikonal tomography results, namely the effect of the inclusion of data uncertainty on the expectation value of velocity and the behaviour of sample statistics, both of which suggest that the uncertainty in eikonal tomography results is greater than previously assessed. The GP framework presents a fully interpretable way forward to improve eikonal tomography in the future, with many opportunities for future work due to the flexible and robust nature of GP modelling.

Data and code availability

The Pluto notebook and data (White et al., 2021) used to generate the results may be found on Zenodo (Muir, 2023). To run the Pluto notebook, users must first install Julia (Bezanson et al., 2017), then use the inbuilt package manager to install Pluto (enter the REPL, hit `]` to enter package management mode, then `install Pluto`, and `backspace` to re-enter REPL mode). Typing `using Pluto; Pluto.run()` will bring up the Pluto notebook environment from where the notebook can be opened by navigating to it through the filesystem. This will automatically run the notebook, including installing all version-controlled modules required.

Acknowledgements

I acknowledge the support of the European Commission via Marie Skłodowska-Curie Actions Individual Fellowship award number 101027079. I also acknowledge Professor Ron Butler of Southern Methodist University for forwarding the technical report supporting Butler and Paolella (2008), and Professor Victor Tsai of Brown University for providing a pre-submission internal review that was very helpful, as well as the helpful comments of Suzan van der Lee and two anonymous reviewers.

References

Al-Naffouri, T. Y., Moinuddin, M., Ajeeb, N., Hassibi, B., and Moustakas, A. L. On the Distribution of Indefinite Quadratic Forms in Gaussian Random Variables. *IEEE Transactions on Communications*, 64(1):153–165, Jan. 2016. doi: 10.1109/TCOMM.2015.2496592.

Bezanson, J., Edelman, A., Karpinski, S., and Shah, V. B. Julia: A Fresh Approach to Numerical Computing. *SIAM Review*, 59(1):65–98, Jan. 2017. doi: 10.1137/141000671.

Bodin, T. and Maupin, V. Resolution Potential of Surface Wave Phase Velocity Measurements at Small Arrays. *Geophysical Journal International*, 172(2):698–706, Feb. 2008. doi: 10.1111/j.1365-246X.2007.03668.x.

Brocher, T. A. Empirical Relations between Elastic Wavespeeds and Density in the Earth's Crust. *Bulletin of the Seismological Society of America*, 95(6):2081–2092, Dec. 2005. doi: 10.1785/0120050077.

Butler, R. W. *Saddlepoint Approximations with Applications*. Cambridge Series in Statistical and Probabilistic Mathematics. Cambridge University Press, Cambridge, 2007. doi: 10.1017/CBO9780511619083.

Butler, R. W. and Paolella, M. S. Uniform Saddlepoint Approximations for Ratios of Quadratic Forms. *Bernoulli*, 14(1):140–154, Feb. 2008. doi: 10.3150/07-BEJ6169.

Chevrot, S. and Lehujeur, M. Eikonal Surface Wave Tomography with Smoothing Splines—Application to Southern California. *Geophysical Journal International*, 229(3):1927–1941, June 2022. doi: 10.1093/gji/ggac034.

Daniels, H. E. Saddlepoint Approximations in Statistics. *The Annals of Mathematical Statistics*, 25(4):631–650, 1954.

de Ridder, S. A. L. and Biondi, B. L. Near-surface Scholte Wave Velocities at Ekofisk from Short Noise Recordings by Seismic Noise Gradiometry. *Geophysical Research Letters*, 42(17):7031–7038, Sept. 2015. doi: 10.1002/2015GL065027.

de Ridder, S. A. L. and Maddison, J. R. Full Wave Field Inversion of Ambient Seismic Noise. *Geophysical Journal International*, Aug. 2018. doi: 10.1093/gji/ggy328.

Dierckx, P. *Curve and surface fitting with splines*. Oxford University Press, 1993. doi: https://doi.org/10.1093/oso/9780198534419.001.0001.

Friederich, W. and Wielandt, E. Interpretation of Seismic Surface Waves in Regional Networks: Joint Estimation of Wavefield Geometry and Local Phase Velocity. Method and Numerical Tests. *Geophysical Journal International*, 120(3):731–744, 1995. doi: 10.1111/j.1365-246X.1995.tb01849.x.

Friederich, W., Wielandt, E., and Stange, S. Non-Plane Geometries of Seismic Surface Wavefields and Their Implications For Regional Surface-Wave Tomography. *Geophysical Journal International*, 119(3):931–948, 1994. doi: 10.1111/j.1365-246X.1994.tb04026.x.

Herrmann, R. B. Computer Programs in Seismology: An Evolving Tool for Instruction and Research. *Seismological Research Letters*, 84(6): 1081–1088, Nov. 2013. doi: 10.1785/0220110096.

Hines, T. T. and Hetland, E. A. Revealing Transient Strain in Geodetic Data with Gaussian Process Regression. *Geophysical Journal International*, 212(3):2116–2130, Mar. 2018. doi: 10.1093/gji/ggx525.

Imhof, J. P. Computing the Distribution of Quadratic Forms in Normal Variables. *Biometrika*, 48(3/4):419–426, 1961. doi: 10.2307/2332763.

Kadane, J. B. *Principles of Uncertainty*. Chapman and Hall/CRC, 2011.

Kendrick, D. *Stochastic Control for Economic Models*. University of Texas, Austin, 2 edition, 2002.

Langston, C. A. Spatial Gradient Analysis for Linear Seismic Arrays. *Bulletin of the Seismological Society of America*, 97(1):265–280, Feb. 2007a. doi: 10.1785/0120060100.

Langston, C. A. Wave Gradiometry in Two Dimensions. *Bulletin of the Seismological Society of America*, 97(2):401–416, Apr. 2007b. doi: 10.1785/0120060138.

Lehujeur, M. and Chevrot, S. On the Validity of the Eikonal Equation for Surface-Wave Phase-Velocity Tomography. *Geophysical Journal International*, 223(2):908–914, Nov. 2020. doi: 10.1093/gji/ggaa352.

Lin, F.-C. and Ritzwoller, M. H. Helmholtz Surface Wave Tomography for Isotropic and Azimuthally Anisotropic Structure: Helmholtz Surface Wave Tomography. *Geophysical Journal International*, 186(3):1104–1120, Sept. 2011. doi: 10.1111/j.1365-246X.2011.05070.x.

Lin, F.-C., Ritzwoller, M. H., and Snieder, R. Eikonal Tomography: Surface Wave Tomography by Phase Front Tracking across a Regional Broad-Band Seismic Array. *Geophysical Journal International*, 177(3):1091–1110, June 2009. doi: 10.1111/j.1365-246X.2009.04105.x.

Lindgren, F., Rue, H., and Lindström, J. An Explicit Link between Gaussian Fields and Gaussian Markov Random Fields: The Stochastic Partial Differential Equation Approach: Link between Gaussian Fields and Gaussian Markov Random Fields. *Journal of the Royal Statistical Society: Series B (Statistical Methodology)*, 73(4):423–498, Sept. 2011. doi: 10.1111/j.1467-9868.2011.00777.x.

Mandic, V., Tsai, V. C., Pavlis, G. L., Prestegard, T., Bowden, D. C., Meyers, P., and Caton, R. A 3D Broadband Seismometer Array Experiment at the Homestake Mine. *Seismological Research Letters*, 89(6):2420–2429, Aug. 2018. doi: 10.1785/0220170228.

McHutchon, A. *Nonlinear Modelling and Control Using Gaussian Processes*. PhD thesis, Cambridge, 2014.

Muir, J. GP-Eikonal. 2023. doi: 10.5281/zenodo.10036494.

Muir, J. B. and Zhan, Z. Wavefield-Based Evaluation of DAS Instrument Response and Array Design. *Geophysical Journal International*, 229 (1):21–34, Dec. 2021. doi: 10.1093/gji/ggab439.

Padonou, E. and Roustant, O. Polar Gaussian Processes for Predicting on Circular Domains. page 24, 2015. https://hal.science/hal-01119942v2/document.

Pollitz, F. F. Observations and Interpretation of Fundamental Mode Rayleigh Wavefields Recorded by the Transportable Array (USArray). *Journal of Geophysical Research: Solid Earth*, 113(B10), 2008. doi: 10.1029/2007JB005556.

Rasmussen, C. E. Gaussian Processes to Speed up Hybrid Monte Carlo for Expensive Bayesian Integrals. *Bayesian Statistics*, 7:651–659, 2003. doi: 10.1093/oso/9780198526155.003.0045.

Rasmussen, C. E. and Williams, C. K. I. *Gaussian Processes for Machine Learning*. Adaptive Computation and Machine Learning. MIT Press, Cambridge, Mass, 2006. doi: 10.7551/mitpress/3206.001.0001.

Solak, E., Murray-smith, R., Leithead, W., Leith, D., and Rasmussen, C. Derivative Observations in Gaussian Process Models of Dynamic Systems. In *Advances in Neural Information Processing Systems*, volume 15. MIT Press, 2002. https://dl.acm.org/doi/abs/10.5555/2968618.2968750.

Titsias, M. Variational Learning of Inducing Variables in Sparse Gaussian Processes. In *Proceedings of the Twelth International Conference on Artificial Intelligence and Statistics*, pages 567–574. PMLR, Apr. 2009. https://proceedings.mlr.press/v5/titsias09a.html.

Treister, E. and Haber, E. A Fast Marching Algorithm for the Factored Eikonal Equation. *Journal of Computational Physics*, 324:210–225, 2016. doi: 10.1016/j.jcp.2016.08.012.

Tromp, J. and Dahlen, F. A. Variational Principles for Surface Wave Propagation on a Laterally Heterogeneous Earth - III. Potential Representation. *Geophysical Journal International*, 112:195–209, 1993. doi: 10.1111/j.1365-246X.1993.tb01449.x.

Valentine, A. P. and Sambridge, M. Gaussian Process Models—II. Lessons for Discrete Inversion. *Geophysical Journal International*, 220(3): 1648–1656, Mar. 2020a. doi: 10.1093/gji/ggz521.

Valentine, A. P. and Sambridge, M. Gaussian Process Models—I. A Framework for Probabilistic Continuous Inverse Theory. *Geophysical Journal International*, 220(3):1632–1647, Mar. 2020b. doi: 10.1093/gji/ggz520.

White, M. C. A., Fang, H., Catchings, R. D., Goldman, M. R., Steidl, J. H., and Ben-Zion, Y. Detailed Traveltime Tomography and Seismic Catalogue around the 2019 Mw 7.1 Ridgecrest, California, Earthquake Using Dense Rapid-Response Seismic Data. *Geophysical Journal International*, 227(1):204–227, June 2021. doi: 10.1093/gji/ggab224.

Wielandt, E. Propagation and Structural Interpretation of Non-Plane Waves. *Geophysical Journal International*, 113(1):45–53, Apr. 1993. doi: 10.1111/j.1365-246X.1993.tb02527.x.

Wilson, A. G. and Nickisch, H. Kernel Interpolation for Scalable Structured Gaussian Processes (KISS-GP). *Proceedings of the 32 nd International Conference on Machine Learning*, pages 1775–1784, 2015. doi: 10.48550/arXiv.1503.01057.

Yang, Y., Atterholt, J. W., Shen, Z., Muir, J. B., Williams, E. F., and Zhan, Z. Sub-Kilometer Correlation Between Near-Surface Structure and Ground Motion Measured With Distributed Acoustic Sensing. *Geophysical Research Letters*, 49:e2021GL096503, 2022. doi: 10.1029/2021GL096503.

Zhan, Z. Distributed Acoustic Sensing Turns Fiber-Optic Cables into Sensitive Seismic Antennas. *Seismological Research Letters*, 91(1):1–15, Jan. 2020. doi: 10.1785/0220190112.

doi:10.26443/seismica.v2i2.385

SEISMICA

False positives are common in single-station template matching

Jack B. Muir * [1], **Benjamin Fernando** [2], **Elizabeth Barrett**[3]

[1]Department of Earth Sciences, University of Oxford, Oxford, United Kingdom, [2]Department of Physics, University of Oxford, Oxford, United Kingdom, [3]Jet Propulsion Laboratory, National Aeronautics and Space Administration, United States of America

Author contributions: *Conceptualization*: J. B. Muir, B. Fernando. *Investigation*: J. B. Muir. *Writing - Original Draft*: J. B. Muir, B. Fernando, E. Barrett. *Writing - Review & Editing*: J. B. Muir, B. Fernando, E. Barrett. *Visualization*: J. B. Muir.

Abstract Template matching has become a cornerstone technique of observational seismology. By taking known events, and scanning them against a continuous record, new events smaller than the signal-to-noise ratio can be found, substantially improving the magnitude of completeness of earthquake catalogues. Template matching is normally used in an array setting, however as we move into the era of planetary seismology, we are likely to apply template matching for very small arrays or even single stations. Given the high impact of planetary seismology studies on our understanding of the structure and dynamics of non-Earth bodies, it is important to assess the reliability of template matching in the small-n setting. Towards this goal, we estimate a lower bound on the rate of false positives for single-station template matching by examining the behaviour of correlations of filtered white noise (given that the unfiltered data before processing is totally uncorrelated). We find that, for typical processing regimes and match thresholds, false positives are likely quite common. We must therefore be exceptionally careful when considering the output of template matching in the small-n setting.

Production Editor:
Garreth Funning
Handling Editor:
Yen Joe Tan
Copy & Layout Editor:
Ethan Williams

Received:
17 February 2023
Accepted:
25 July 2023
Published:
11 August 2023

Non-technical summary Many signals of interest to seismologists are so small that they cannot be easily seen on seismograms. In order to identify these signals, seismologists have developed the technique of template matching, which takes a large signal and runs it over a seismogram. If the template signal matches the seismogram under a certain mathematical definition, then we consider it to be a match, and we add that part of the seismogram to the catalogue of signals. Normally, seismologists cross-check this process using multiple seismograms recorded at different instruments, but this is not necessarily possible on other planets where it is too expensive to deploy many seismometers. Without this cross-checking, it is possible that many of the "matches" are in fact false positives. We performed a statistical experiment to show that these false positives are in fact likely to be quite common, which means that we must be careful when handling template matching with single seismometers.

1 Introduction

One of the most important goals in observational seismology is to observe the smallest interesting signals possible. As codified in the Gutenberg-Richter law, the number of seismic events decreases exponentially with magnitude. This implies that the overwhelming majority of events create seismic signals smaller than can be observed above the noise that contaminates seismic observations. Access to these small events gives us great insight into tectonic processes across timescales, including the geometry of buried faults, fault heterogeneity, earthquake statistics etc.

Correlation based methods have proven to be one of the most successful ways of extracting small signals from the noise. This class of methods relies on the fact that interesting seismic signals typically have different structure to both instrumental noise and ambient ground motions produced by environmental processes. Furthermore, within the elastic regime ground motions are linear, so events with different magnitudes will still look similar (albeit with different amplitudes) if they occur at approximately the same location and are filtered appropriately. The cross-correlation class of methods scans the seismic record with templates—snippets of known high-amplitude signals that will match lower amplitude signals buried in the noise. Correlation based techniques using previously observed or calculated templates are therefore also known in the literature as template matching or matched filter analyses. These methods have been prominent in geophysics for many decades, especially in exploration settings, as comprehensive early reviews will attest (Anstey, 1964).

In observational and monitoring settings, the collation of suitable template catalogues had to wait until the proliferation of broadband digital seismograms, but the technique is now ubiquitous across distance ranges and period bands (e.g., Shearer, 1994; Gibbons and Ringdal, 2006; Bobrov et al., 2014). Template matching has been used extensively for the purposes of identifying repeating earthquakes, and also more generally for con-

*Corresponding author: jack.muir@earth.ox.ac.uk

structing catalogues where earthquakes are required to merely be similar, rather than exact matches. It is the latter case (which typically has relaxed assumptions on the required level of waveform matching) that we are concerned with in this study. While advanced matching algorithms have been proposed to mitigate various failure mechanisms (e.g. Gao and Kao, 2020; Kurihara et al., 2021), we here focus on the most basic form of template matching based on the normalized cross-correlation coefficient of a single window, which is heavily used in contemporary studies.

Template matching is extremely computationally intensive, although the calculations are simple. The advent of general-purpose graphical processing units (GPGPUs) has thus benefited template matching analyses immensely, and allowed large continuous waveform databases to be scanned efficiently with many templates, resulting in a huge increase in the number of catalogued events, albeit with potential concerns regarding the overall rate of false detections (e.g., Beaucé et al., 2017; Ross et al., 2019).

Template matching studies are potentially especially useful in planetary seismology contexts, which suffer from the constraints of temporary single-station deployments where extracting all possible events from the limited data available is particularly advantageous. In the Martian context, which has been the prime recent focus of planetary seismology, the InSight single-station Mars seismometer demonstrated that a larger-than-terrestrial fraction of the seismicity comes about from events which are very similar to each other. These include events of geological (thermal/tectonic) origin (Dahmen et al., 2021; Sun and Tkalčić, 2022) which are identified through matching, and those of impact origin which display very similar infrasonic chirps (Garcia et al., 2022); similar techniques have recently been re-applied to Apollo data to isolate diurnal variations in crustal properties (Tanimoto et al., 2008) and identify new deep moonquakes (Sun et al., 2019). Given the paucity of data in planetary settings, all successful detections of seismic sources are incredibly useful, and are likely to be influential in our understanding of the planetary target.

An interesting additional application of template matching in a planetary seismology context would be in the search for signals which are expected and which would have predictable waveforms, but are likely to be at or near the noise floor. Such signals are exceedingly rare, but can include cases such as expected impact events (Fernando et al., 2022). Although not currently used by any planetary seismology missions, the potential for automated triggering (e.g., to switch into high-sampling mode) upon detection of seismic precursor phases exists. Similarly, the current procedure of downlinking low-resolution data from spacecraft to Earth, uplinking requests for specific data segments back to the spacecraft, and downlinking these back to Earth may be made substantially more efficient through on-board event detection and selection. On-board detection of seismic signals is therefore a potentially impactful future planetary seismology capability albeit with significant challenges including sampling rates, timing concerns, template generation, processing capabilities, data storage, and downlink planning. Some of these challenges persist for any implementation of on-board detection; however, false positives would exacerbate the issues with processing, data storage, and downlink planning at a minimum. Every proposed event detection would require on-board processing to first detect and then additional processing to bound the timeframe of the event and transfer the highest available rate data for all relevant instrumentation into a downlink/storage buffer. The availability of on-board data storage, especially for downlink, could be challenging to provide when detection rates are high, depending on the overall design and downlink buffer sizes for detected events. Downlink priorities and rates would need to be carefully managed to make sure that all the data can be returned before any downlink buffers overflow and data is lost. False positive detections may not be fully preventable in the on-board single-station setting, but steps should be taken to minimize these instances, particularly if on-board detection is a capability as there are fewer resources on a spacecraft to accommodate the added burden. In all cases, then, these capabilities would require robust template matching via cross-correlation for single stations, and a minimal rate of false positives. In return, savings may be made in the power and communications budgets. Whilst current limitations of power, on-board processing capacity, and the identification of appropriate templates mean that these techniques have not been used to date, they are likely to become more advantageous as more sophisticated geophysical networks are deployed off-world.

In light of these opportunities for advancing both the instrumental methodology, and interpretation, of planetary seismology, it is of vital importance to thoroughly understand the failure modes of template matching so that we have confidence in proposed detections. In this short manuscript, we investigate a basic issue in template matching—the rate of false positives. It is immediately apparent that any finite length template correlated against an infinitely long target signal will eventually result in a match that is arbitrarily good—the question is, under realistic data processing conditions, does this happen sufficiently quickly as to pose an issue for the interpretation of template matches?

2 Template Matching Definitions

The normalized cross-correlation between two signals of equal length $\mathbf{X} = [x_1, x_2, \ldots, x_n]^T$ and $\mathbf{Y} = [y_1, y_2, \ldots, y_n]^T$ is defined to be

$$CC(\mathbf{X}, \mathbf{Y}) = \frac{\langle \mathbf{X} - \hat{\mathbf{X}}, \mathbf{Y} - \hat{\mathbf{Y}} \rangle}{\sqrt{\langle \mathbf{X} - \hat{\mathbf{X}}, \mathbf{X} - \hat{\mathbf{X}} \rangle \langle \mathbf{Y} - \hat{\mathbf{Y}}, \mathbf{Y} - \hat{\mathbf{Y}} \rangle}}, \quad (1)$$

where

$$\langle \mathbf{X}, \mathbf{Y} \rangle = \sum_{i=1}^{n} x_i y_i, \quad (2)$$

and

$$\hat{\mathbf{X}} = \frac{1}{n} \sum_{i=1}^{n} x_i. \quad (3)$$

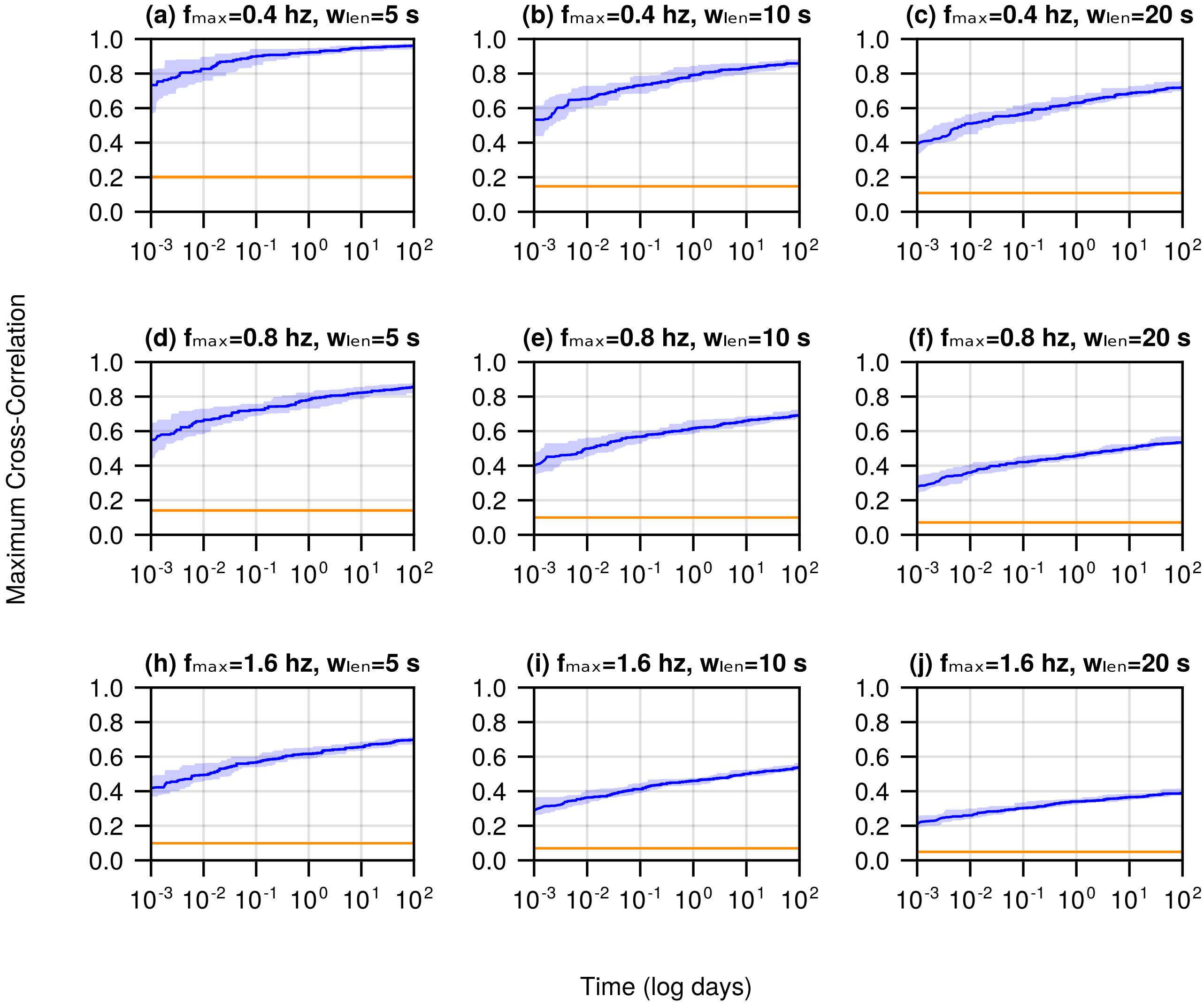

Figure 1 Maximum [-1,1] normalized cross-correlations between three-component random noise segments. Blue lines show the maximum cross-correlation up to some time, with the $\pm 1\sigma$ shown in light blue. Orange lines show the Median Absolute Deviation (MAD) over 100 days, with the $\pm 1\sigma$ shown in light orange (not visible due to narrow uncertainty over this interval).

This definition produces a value in [-1,1], where 1 is perfectly correlated and -1 is perfectly anticorrelated, independent of the relative amplitude of the signals or any static offsets. The normalized three-component cross-correlation between two three-component signals $\mathbf{X} = (\mathbf{X}_1, \mathbf{X}_2, \mathbf{X}_3)$ and $\mathbf{Y} = (\mathbf{Y}_1, \mathbf{Y}_2, \mathbf{Y}_3)$ is then defined to be the average

$$CC_3(\mathbf{X}, \mathbf{Y}) = \frac{CC(\mathbf{X}_1, \mathbf{Y}_1) + CC(\mathbf{X}_2, \mathbf{Y}_2) + CC(\mathbf{X}_3, \mathbf{Y}_3)}{3}. \tag{4}$$

To calculate the cross-correlation time series when $\mathbf{X}$ and $\mathbf{Y}$ are not the same length, we scan the cross-correlation function along the longer signal. Specifically, assume $\mathbf{X}$ is the shorter signal, and that it has M samples, while $\mathbf{Y}$ has N samples. Denoting $\mathbf{Y}^i = [y_i, y_{i+1}, \ldots, y_{i+M-1}]^T$, then $CC(\mathbf{X}, \mathbf{Y}) = \left[CC(\mathbf{X}, \mathbf{Y}^1), CC(\mathbf{X}, \mathbf{Y}^2), \ldots, CC(\mathbf{X}, \mathbf{Y}^{N-M+1})\right]^T$, and similarly for CC_3 for 3 component signals. The Median Absolute Deviation (MAD) of a signal $\mathbf{X}$ is defined to be

$$MAD(\mathbf{X}) = median(|\mathbf{X} - median(\mathbf{X})|). \tag{5}$$

Template-matches are typically defined by a threshold that is some multiple of the MAD of the cross-correlation signal, that is, $\mathbf{X}$ is a match to a segment of $\mathbf{Y}$ at starting index i if

$$CC_{(3)}(\mathbf{X}, \mathbf{Y}^i) \geq cMAD(CC_{(3)}(\mathbf{X}, \mathbf{Y})), \tag{6}$$

for some constant c, where $c \sim 7$ is a typical choice for 3-component seismograms (e.g., Sun and Tkalčić, 2022).

Simulation Results and Discussion

We investigated the base rate of expected false-positives for three-component, single-station template matching. We considered pairs of signals $\mathbf{X}$ and $\mathbf{Y}$ that are

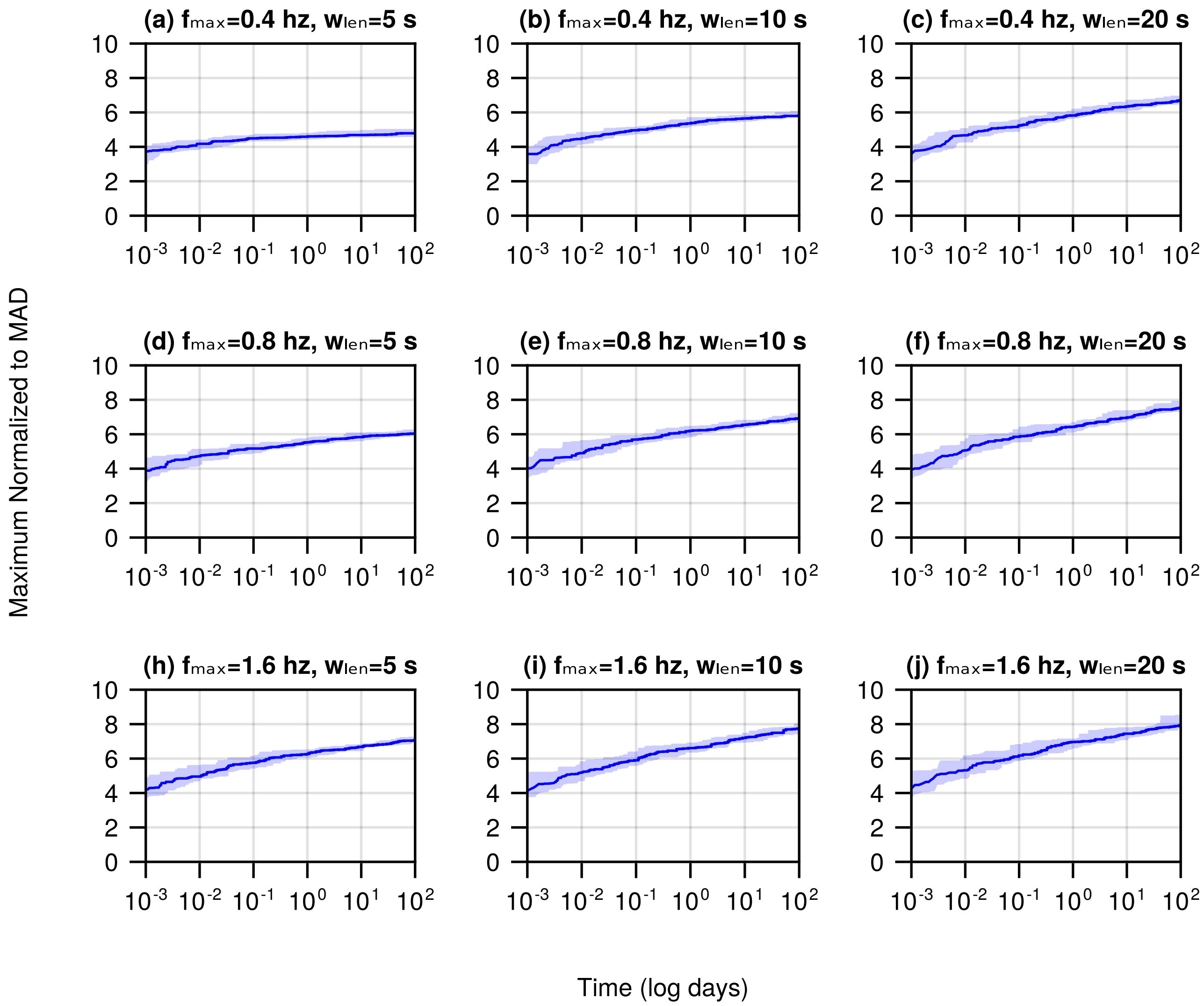

Figure 2 Maximum cross-correlation between three-component random noise segments, normalized by the Median Absolute Deviation (MAD) over 100 days. Blue lines show the maximum MAD normalized cross-correlation up to some time, with the $\pm 1\sigma$ shown in light blue.

completely white-noise, that is, the underlying signals before processing are totally uncorrelated. The rate of production of false positives for initially white noise signals (after data processing) will therefore give a lower bound on the true rate of false positives for general signals (given the same processing). Due to the timescale invariance of white noise, it would be possible to perform this analysis in non-dimensional units, however we have chosen to present results in physical units to aid intuition. We considered a typical setup for teleseismic planetary applications, with signals recorded at 20 Hz, bandpass filtered with lower corner frequency 0.1 Hz and upper corner frequencies of $f_{max} = 0.4$, 0.8, and 1.6 Hz, using a 4 pole zero-phase Butterworth filter. The shorter signal $\mathbf{X}$ has a variable window length of $w_{len} =$ 5, 10, or 20 s, while the longer signal $\mathbf{Y}$ is 100 (Earth) days long. When initially generating signals, we added 40 s of padding to either end (4 times the lower bandpass period) to avoid filter edge effects, before cutting to the required lengths. For each of the 9 combinations of upper corner frequency and window length, we generated 32 pairs of three-component filtered white noise signals $\mathbf{X}$ and $\mathbf{Y}$. We then calculated the MADs and running maximums of the cross correlation signals $CC_3(\mathbf{X}, \mathbf{Y})$. By calculating the results for 32 random pairs, we can also calculate the standard deviation of the resulting estimates. As the underlying raw data is white noise, the results for different parameter regimes can be immediately obtained by scaling frequency f and time t with a common factor α so that $f' = \alpha f$, $t' = t/\alpha$; for example, the results of the f_{max} = 1.6 Hz, w_{len} = 20 s case over a 100 day run are equivalent to a 1-16 Hz, 2 s window over 10 days, recorded at 200 Hz.

Figure 1 shows the running maximum cross-correlations and MADs for the 9 combinations of filter and window length. Figure 2 shows the cross-correlations normalized by MAD. Combinations with narrow filter bands and short window lengths, which are seen in the top left corner of the figures (e.g. subfigures (a), (b), (d)), unsurprisingly result in large maximum cross-correlations relatively quickly. However, they also result in relatively high MAD (i.e., there are relatively many periods with high cross-correlation, due to the quasi-sinusoidal nature of the signals over a short time window). As a result, the MAD normalized cross-correlations saturate quickly for these combinations. Conversely, combinations with longer windows and wider passbands, found in the bottom right of the figures (e.g. subfigures (f), (i), (j)) have overall lower maximum cross-correlations, but also lower MADs and so the MAD normalized cross-correlations continue to grow even after 100 days. In particular, in the worst case (f_{max} = 1.6 Hz, w_{len} = 20 s), the maximum MAD normalized cross-correlation exceeds 7 after one day, and 8 after 100 days—or on average about 15 false positives at an MAD ratio of 8 for the 1480 days the Insight mission was active on Mars. As seen in Figure 1, the estimates of the MAD of the cross correlations is very stable by the end of the 100-day correlation period for all cases. This allows us to estimate the maximum possible multiplier of MAD achievable for the different filter/window configurations, which is shown in Table 1.

This experiment considers random pairs of three-component signal $\mathbf{X}$ and $\mathbf{Y}$. A more typical experiment is to hold the longer signal $\mathbf{Y}$ fixed (we only record one seismogram), and to scan multiple templates across it. For the filtered white noise case, because the data that are processed to give $\mathbf{X}$ and $\mathbf{Y}$ are uncorrelated, the effect of multiple templates is simple to calculate. If the average time between cross-correlations exceeding the MAD threshold of c is T_c for a single template (i.e., matches occur at a rate of $1/T_c$), then for N templates the average time between matches is T_c/N (i.e., a rate of N/T_c). For example, taking the lower-right case of Figure 2, scanning 100 white noise templates would result in a false positive match with MAD normalized cross-correlation exceeding $c = 8$ approximately once a day.

Modern workflows for template matching in observational seismology normally further consider the averaged cross correlation across an array, up to and including arrays with extremely large numbers of instruments such as Distributed Acoustic Sensors (DAS) (e.g., Gibbons and Ringdal, 2006; Li and Zhan, 2018). Array deployments implicitly create a "barcode" of relative arrival time patterns for each potential source location that must be generally be satisfied for a signal to count as a match. As such, array deployments are much more resilient to false positives in general. This is not to say that false positives are not an issue; in particular, for arrays with narrow apertures relative to the content of waveform frequency, coherent noise sources can correlate well. Likewise, templates containing common noise phenomenon (such as passing cars, or electronic 'glitch' noise as with InSight on Mars (Kim et al., 2021)) may match waveform segments that do not contain any interesting seismic signals but do contain a similar noise signal. These effects should be considered as additive to the basic analysis of random noise false-positives investigated here, and are almost certainly more important for larger arrays. The key takeaway of this paper is to emphasize that for single station, that are the current state-of-the-art for planetary applications (as well as some circumstances on Earth), *the baseline rate of false-positive detection is significant under realistic processing choices.*

		w_{len} (s)		
		5	10	20
f_{max} (Hz)	0.4	5	7	9
	0.8	7	10	14
	1.6	10	14	20

Table 1 Estimated maximum multiple of MAD to the nearest unit for each configuration of filter corner frequency f_{max} and window length w_{len}.

3 Conclusions

In this work, we investigated the rate of false-positive detection of template matching for snippets of filtered white noise scanned across filtered white noise records. We used realistic processing for 3-component traces for pre-processing, and found that the rate of false-positive detection is significant. Because the unprocessed white noise data used to generate the templates and long-run signals is on average totally uncorrelated by definition, these results act as a lower bound on the rate of false positives for realistic signals using the same processing. Real seismic signals will contain features that may induce "spurious" correlations (in the sense that they are not related to seismic activity), and the relationship between the spectra of real seismic noise and pre-processing filter choices will also have implications for the rate of false positives in excess of the baseline considered here.

Acknowledgements

J.B. Muir acknowledges the support of the European Commission via Marie Skłodowska-Curie Actions Individual Fellowship award number 101027079. The authors acknowledge the useful comments of two anonymous reviewers, which have improved the manuscript considerably.

Data and code availability

The Pluto notebook and associated data files used to generate the results in this manuscript may be found on Zenodo (Muir et al., 2023).

Competing interests

The authors declare no competing interests.

References

Anstey, N. A. Correlation Techniques –a Review*. *Geophysical Prospecting*, 12(4):355–382, 1964. doi: 10.1111/j.1365-2478.1964.tb01911.x.

Beaucé, E., Frank, W. B., and Romanenko, A. Fast Matched Filter (FMF): An Efficient Seismic Matched-Filter Search for Both CPU and GPU Architectures. *Seismological Research Letters*, 89(1): 165–172, Dec. 2017. doi: 10.1785/0220170181.

Bobrov, D., Kitov, I., and Zerbo, L. Perspectives of Cross-Correlation in Seismic Monitoring at the International Data Centre. *Pure and Applied Geophysics*, 171(3):439–468, 2014. doi: 10.1007/s00024-012-0626-x.

Dahmen, N. L., Clinton, J. F., Ceylan, S., van Driel, M., Giardini, D., Khan, A., Stähler, S. C., Böse, M., Charalambous, C., Horleston, A., et al. Super High Frequency Events: A New Class of Events Recorded by the InSight Seismometers on Mars. *Journal of Geophysical Research: Planets*, 126(2):e2020JE006599, 2021. doi: 10.1029/2020JE006599.

Fernando, B., Wójcicka, N., Maguire, R., Stähler, S. C., Stott, A. E., Ceylan, S., Charalambous, C., Clinton, J., Collins, G. S., Dahmen, N., et al. Seismic Constraints from a Mars Impact Experiment Using InSight and Perseverance. *Nature Astronomy*, 6(1):59–64, 2022. doi: 10.1038/s41550-021-01502-0.

Gao, D. and Kao, H. Optimization of the Match-Filtering Method for Robust Repeating Earthquake Detection: The Multisegment Cross-Correlation Approach. *Journal of Geophysical Research: Solid Earth*, 125(7):e2020JB019714, 2020. doi: 10.1029/2020JB019714.

Garcia, R. F., Daubar, I. J., Beucler, É., Posiolova, L. V., Collins, G. S., Lognonné, P., Rolland, L., Xu, Z., Wójcicka, N., Spiga, A., et al. Newly Formed Craters on Mars Located Using Seismic and Acoustic Wave Data from InSight. *Nature Geoscience*, 15(10): 774–780, 2022. doi: 10.1038/s41561-022-01014-0.

Gibbons, S. J. and Ringdal, F. The Detection of Low Magnitude Seismic Events Using Array-Based Waveform Correlation. *Geophysical Journal International*, 165(1):149–166, Apr. 2006. doi: 10.1111/j.1365-246X.2006.02865.x.

Kim, D., Davis, P., Lekić, V., Maguire, R., Compaire, N., Schimmel, M., Stutzmann, E., C. E. Irving, J., Lognonné, P., Scholz, J.-R., Clinton, J., Zenhäusern, G., Dahmen, N., Deng, S., Levander, A., Panning, M. P., Garcia, R. F., Giardini, D., Hurst, K., Knapmeyer-Endrun, B., Nimmo, F., Pike, W. T., Pou, L., Schmerr, N., Stähler, S. C., Tauzin, B., Widmer-Schnidrig, R., and Banerdt, W. B. Potential Pitfalls in the Analysis and Structural Interpretation of Seismic Data from the Mars InSight Mission. *Bulletin of the Seismological Society of America*, 111(6):2982–3002, Oct. 2021. doi: 10.1785/0120210123.

Kurihara, R., Kato, A., Kurata, S., and Nagao, H. Detection of Low-Frequency Earthquakes by the Matched Filter Technique Using the Product of Mutual Information and Correlation Coefficient. *Earth, Planets and Space*, 73(1):225, Dec. 2021. doi: 10.1186/s40623-021-01534-w.

Li, Z. and Zhan, Z. Pushing the Limit of Earthquake Detection with Distributed Acoustic Sensing and Template Matching: A Case Study at the Brady Geothermal Field. *Geophysical Journal International*, 215(3):1583–1593, Dec. 2018. doi: 10.1093/gji/ggy359.

Muir, J. B., Fernando, B., and Barrett, E. Notebook & Data for ”False Positives Are Common in Single-Station Template Matching”, July 2023. doi: 10.5281/zenodo.8181443.

Ross, Z. E., Trugman, D. T., Hauksson, E., and Shearer, P. M. Searching for Hidden Earthquakes in Southern California. *Science*, 364 (6442):767–771, May 2019. doi: 10.1126/science.aaw6888.

Shearer, P. M. Global Seismic Event Detection Using a Matched Filter on Long-Period Seismograms. *Journal of Geophysical Research: Solid Earth*, 99(B7):13713–13725, 1994. doi: 10.1029/94JB00498.

Sun, W. and Tkalčić, H. Repetitive Marsquakes in Martian Upper Mantle. *Nature Communications*, 13(1):1695, Mar. 2022. doi: 10.1038/s41467-022-29329-x.

Sun, W., Zhao, L., Wei, Y., and Fu, L.-Y. Detection of Seismic Events on Mars: A Lunar Perspective. *Earth and Planetary Physics*, 3(4): 290–297, 2019. doi: 10.26464/epp2019030.

Tanimoto, T., Eitzel, M., and Yano, T. The Noise Cross-Correlation Approach for Apollo 17 LSPE Data: Diurnal Change in Seismic Parameters in Shallow Lunar Crust. *Journal of Geophysical Research: Planets*, 113(E8), 2008. doi: 10.1029/2007JE003016.

doi:10.26443/seismica.v2i2.384

SEISMICA

Assessing Earthquake Rates and *b*-value given Spatiotemporal Variation in Catalog Completeness: Application to Atlantic Canada

Alexandre P. Plourde * [1]

[1]Geological Survey of Canada (Atlantic), Natural Resources Canada, Dartmouth, Nova Scotia, Canada

Abstract Spatiotemporal variations in the magnitude of completeness M_c make it challenging to confidently assess seismic hazard or even to simply compare earthquake rates between regions. In this study, we introduce new techniques to correct for heterogeneous M_c in a treatment of the eastern and Atlantic Canada earthquake catalog (1985–2023). We first introduce new methodology to predict $M_c(x, t)$ based on the distribution of seismometers. Second, we introduce a modified maximum-likelihood estimator (MLE) for b (the b-value) that accounts for spatiotemporal M_c variation, allowing the inclusion of more earthquakes. Third, we compute the ratio of detected/predicted $M>1$ earthquakes as a function of M_c and apply it to create a calibrated $M>1$ event-rate map. The resulting map has advantages over a moment-rate map, which is effectively sensitive only to the very largest earthquakes in the dataset. The new MLE results in a modestly more precise b when applied to the Charlevoix Seismic Zone, and a substantial increase in precision when applied to the full Atlantic Canada region. It may prove useful in future hazard assessments, particularly of regions with highly heterogeneous M_c and relatively sparse catalogs.

Non-technical summary Earthquake hazard assessments, and earthquake science in general, can be complicated by the uneven distribution of the seismometers used to detect earthquakes. This study examines the earthquake catalog from eastern and Atlantic Canada (from 1985 to 2023) and introduces new methods to deal with the uneven seismometer distribution. We first analyze what magnitude of earthquake we are able to detect as a function of location and time. Second, we introduce a new way to estimate the "b-value", which describes the ratio of the number of large earthquakes to small earthquakes. We apply the new method to the full map region and, separately, to the earthquake-dense Charlevoix Seismic Zone in Quebec. Finally, we produce an earthquake map that is calibrated for the historical distribution of seismometers. These methods may be useful in future earthquake hazard assessments, particularly for regions with highly-uneven seismometer coverage and low to moderate earthquake rates.

Production Editor:
Gareth Funning
Handling Editor:
Andrea Llenos
Copy & Layout Editor:
Kirsty Bayliss

Signed reviewer(s):
Maria Mesimeri

Received:
February 02, 2023
Accepted:
July 07, 2023
Published:
September 13, 2023

1 Introduction

The rate of earthquake occurrence in a given region is generally reported as either an event rate, a moment rate, or, most formally, with a Gutenberg-Richter (GR) model (Ishimoto and Iida, 1939; Gutenberg and Richter, 1944). An event rate is the simplest way to communicate earthquake density, it is the number of earthquakes per unit time, generally considering only those above some threshold magnitude. A moment rate sums the seismic moment of all earthquakes in the region, and is effectively only sensitive to the largest earthquakes in the region. GR models express the number of earthquakes as a function of magnitude $N(M)$ through a log-linear relation $\log_{10} N(M) = a - bM$, where the constant a describes the overall abundance of earthquakes and b (the b-value) describes the relative abundance of small earthquakes to large ones, and typically $b \approx 1$. This is a central equation to probabilistic seismic hazard assessments, and reliable estimates of a and b are therefore critical to seismic hazard analysis.

The magnitude-frequency distribution (MFD) in actual earthquake catalogs always deviates from the strict log-linear model. They are often characterized by a double-truncated GR model, which has an upper magnitude limit $M_{\max}$ based on the maximum fault size in the region, as well as a magnitude of completeness M_c, below which there will be fewer earthquakes detected than predicted because of our limited ability to detect them. M_c can be affected by noise conditions as well as geological factors that affect seismic attenuation, but it primarily depends on the distribution of seismometers in the region. High M_c increases uncertainty in hazard assessments and complicates even event-rate estimates. Knowledge of background rates of naturally-occurring earthquakes is critical to the responsible management of any activity that can pose risk of induced seismicity, such as hydraulic fracturing and wastewater injection in the oil and gas industry, as well as geological carbon storage (Schultz et al., 2020; Cheng et al., 2023).

This paper introduces new methodologies to calculate b and compare event rates across regions that account for spatiotemporal M_c variations. It will focus on

*Corresponding author: ap.plourde@dal.ca

eastern and Atlantic Canada, which generally has low to moderate levels of seismicity and seismometer coverage, but does contain several prominent onshore and offshore seismic zones.

2 Data and regional seismicity

This study examines the Canadian National Earthquake Database (CNED, see section "Data and code availability") from 1985–2023. We selected this timespan for two reasons: i) 1985 is the first year for which the catalog is publicly available, and ii) it is challenging to determine what seismometers were operational and used in routine earthquake detection at any given time before approximately the mid-1990s. Seismometer locations and operating dates were downloaded from the IRIS database, and supplemented with an annual publication on the network that ended in the late 1980s (Munro et al., 1988). Note that these sources indicate when stations became active, but not periods of time they were nonoperational. A map of epicenters and a magnitude-time plot are shown in Figure 1, and Figure 2a shows the location of all stations that may have contributed to the catalog.

The catalog contains 13612 earthquakes, with a variety of magnitude types. We follow the procedure of Halchuk et al. (2015) to convert all magnitudes to M_W; the method is partly based on the m_N–M_W relation computed by Bent (2011), but does not follow it directly. We note that the linear scaling suggested by Bent (2011) would directly affect b estimates; more details on the treatment of magnitudes is found in Appendix 1. The magnitude-time plot (Figure 1b) shows a drastic change around 1995, when the seismograph network and detection routines underwent several major changes (Bent, 2011). It also has notably few events in the range of approximately $0 < M_W < 1$ (the range is higher pre-1995 than post-1995), whereas there are lobes of relatively abundant events both above and below. The lower-magnitude lobe consists mainly of onshore events reported with only a local magnitude M_L, for which the conversion to M_W may be more dubious. Proper scaling of onshore M_L to M_W may warrant future investigation, but for this study we opt to simply ignore $M_W < 0$ for subsequent analyses, removing the vast majority of these onshore M_L events.

Following the approach taken in Canadian Seismic Hazard models (Kolaj et al., 2020), we do not attempt to decluster the earthquake catalog. Declustering is often performed as part of probabilistic seismic hazard analysis to remove foreshocks and aftershocks, such that the remaining earthquakes can be considered a Poisson process in time (Gerstenberger et al., 2020). However, declustering techniques require arbitrary thresholds to define what constitutes a foreshock or aftershock, and can cause unintended bias of b and hazard level estimates (Gerstenberger et al., 2020; Mizrahi et al., 2021). We also assume, given the vast geographic scale and generally low event rates and high M_c of this dataset, that temporal variation of M_c due to short-term aftershock incompleteness (Stallone and Falcone, 2021; van der Elst, 2021) is not a significant issue.

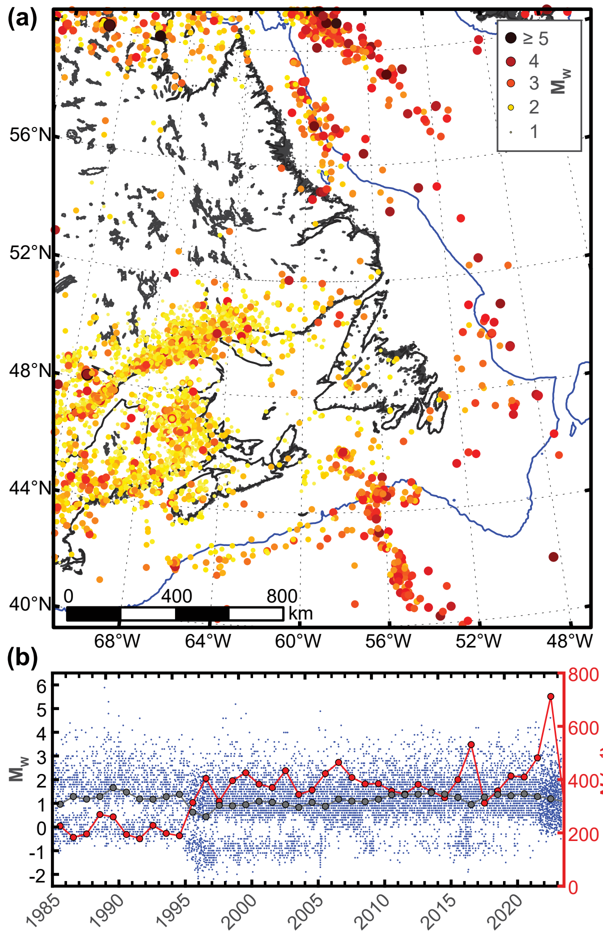

Figure 1 (a) Map of $M_W \geq 1$ earthquakes, with dots coloured and sized by magnitude. A 600 m bathymetric contour, corresponding roughly to the continental shelf edge, is plotted in blue. (b) Scatter plot of earthquake magnitudes in time (blue dots). The grey markers and line mark the mean magnitude by year. The red markers and line indicate the total number of earthquakes per year, corresponding to the second y-axis on the right side.

Map boundaries were chosen in order to include the Charlevoix Seismic Zone (CSZ, Lamontagne et al., 2003a; Yu et al., 2016) and Lower St. Lawrence Seismic Zone (LSZ, Lamontagne et al., 2003b; Plourde and Nedimović, 2021) in the west, as well as the less-studied seismic zones at the Laurentian slope and fan in the south (Adams and Basham, 1989; Bent, 1995), and in the the Labrador Sea to the north (Bent and Hasegawa, 1992; Bent and Voss, 2022). These areas are labeled in the earthquake density map in Figure 2b. The map includes all M_W>1 earthquakes and is significantly affected by spatial M_c variations. The CSZ and LSZ stand out as the most earthquake-dense regions on the map, with another prominent area in northern New Brunswick around the epicenter of the 1982 Miramichi M 5.7 event (Wetmiller et al., 1984).

Different trends emerge if we map moment-density of the same earthquake catalog (Figure 2c). The CSZ and LSZ are still prominent, but they have much more similar moment-rates to the offshore seismic zones than in the event-rate map. Spatial M_c variation biases moment-rates much less than event-rates, but the trade-off is that moment-rate is controlled almost entirely by the largest, infrequent events, so it is more highly affected by the limited catalog duration. The highest mapped moment-rate results from the largest event in the catalog, the M_W 6.3 Ungava Bay earthquake of December 1989 (Bent, 1994), which falls in the northwestern corner of the map. The anomaly just east of it is a M_W 5.7 that occurred in March 1989. Another prominent anomaly lies just north of the CSZ, and results from the second-largest earthquake in the dataset, the 1988 Saguenay M_W 5.9 (Haddon, 1995).

3 Earthquake density mapping in Atlantic Canada

We assume that the MFD in Atlantic Canada follows a GR model allowing us to predict the distribution of undetected small earthquakes based on the distribution of larger earthquakes. This requires i) knowledge of M_c as a function of both space and time, i.e. $M_c(x, t)$, ii) a method for estimating b given spatiotemporal variations in M_c, and iii) a function to predict the ratio of undetected to detected earthquakes for a given $M_c(x, t)$. New methodologies to address these three issues are presented in the following subsections, along with results from their application to Atlantic Canada.

3.1 Estimating $M_c(x, t)$

In practice, it is challenging to estimate $M_c(x, t)$ precisely. M_c is typically estimated from GR plots either by visual inspection or using any number of algorithms (several popular ones are reviewed by Woessner and Wiemer, 2005), but that requires many earthquakes (typically hundreds or more). We resolve this by using a predictive $M_c(x, t)$ model based on the distribution of seismometers (Mignan et al., 2011), which uses the distance to the n^{th} closest seismometer $d_n = d_n(x, t)$. Mignan et al. (2011) produces empirical power-law models of the form $M_c^{\text{pred}} = c_1 d_n^{c_2} + c_3$, where c_i are constants, based on a dense earthquake catalog from Taiwan. They produce models for distance to the 3$^{\text{rd}}$-, 4$^{\text{th}}$-, and 5$^{\text{th}}$-nearest seismometer, each with similarly close fits. Here we form a similar model for our dataset, but to partially reduce the effect of temporarily nonoperational stations we define a (admittedly arbitrary) weighted station distance metric as a weighted sum of the distances to the 4$^{\text{th}}$–6$^{\text{th}}$ nearest stations:

$$d(x, t) = 0.70 d_4 + 0.25 d_5 + 0.05 d_6. \tag{1}$$

We evaluate $d(x, t)$ for each earthquake in the dataset using the distribution of seismometers that were active when it occurred.

Earthquake density in our Atlantic Canada catalog is orders of magnitude lower than the Taiwan catalog used by Mignan et al. (2011)—it has about one tenth the number of earthquakes in a region 20 times larger. As such, there are few areas with enough earthquakes in a small radius (e.g. 50 km) to reliably estimate a, b, or M_c. We therefore need an alternative way to fit the power-law model, and take the following approach. We first compute $d(x, t)$, as defined above, for each earthquake given its origin time and epicentre. We then sort the earthquakes by their $d(x, t)$ and bin into groups of 300 with 50% overlap, resulting in 78 groups with maximum $d(x, t)$, or $d_{\max}$, of 21 to 1310 km. For each group of 300 earthquakes, we apply the method of Ogata and Katsura (1993) to estimate M_c. The method assumes the number detected earthquakes of a given magnitude $N(M)$ depends on the actual number $N_0(M)$ and a "thinning" function q:

$$N(M) = q(M|\sigma, \mu) N_0(M). \tag{2}$$

The thinning function is assumed to be a cumulative normal distribution function:

$$q(M|\sigma, \mu) = \frac{1}{\sigma\sqrt{2\mu}} \int_{-\infty}^{M} \exp\left(-\frac{(M-\mu)^2}{2\sigma^2}\right) dM, \tag{3}$$

where μ is the magnitude at which 50% are detected and σ describes the width of the thinning function; a low σ indicates a steep falloff in detection below M_c, whereas a high σ indicates a more gradual falloff. We use the nonlinear optimization toolbox of MATLAB® to find the set of b, σ, and μ that maximizes the log-likelihood function defined by Ogata and Katsura (1993) (see their Equation 8 or Si and Jiang, 2019 for details). $M_c(d_{\max})$ is then taken to be $\mu + 2.4\sigma$, i.e. the magnitude where we expect 99% of earthquakes are detected. We provide the optimizer limits on b, selecting $0.85 \leq b \leq 1.05$, as we found the output b to vary dramatically otherwise. Also, given that we threshold our catalog at $M_W \geq 0$, we set 0 as the lower integral bound in Eq. 3, rather than $-\infty$.

Results for three example distance bins with $d_{\max}$ = 23, 192, and 684 km are shown in Figure 3a–c, and the overall results shown in Figure 3d. Note that we attempted to estimate uncertainties of each M_c by repeating the Ogata and Katsura (1993) method in 200 bootstrap iterations (and these are shown in Figure 3). However, we find that systematic trends in the $M_c(d)$ data are more relevant to model fits rather than "noise" that is characterized by the bootstrap confidence intervals, so we opt not to use these uncertainties in the model-fitting process. The thinning width $\sigma(d)$ generally covaries with $M_c(d)$, although it has a prominent peak at d<100 km, where there is little range between M_c and the cutoff magnitude of M_W 0, so σ is less well constrained; this results in an overall σ–M_c correlation coefficient of 0.60.

The resulting $M_c(d)$ is poorly fit by a power law due to a bend to unexpectedly low M_c in the d range of ~100–500 km, and we therefore omit that distance range to compute the power-law model shown in Figure 3d (red curve). We compute an alternative, non-analytical $M_c(d)$ function as a best-fit smooth, continually increasing model (hereafter smooth-increasing, shown by the black dashed line in Figure 3d). The curve minimized an L1 data misfit $||M_c^{\text{pred}}(d) - M_c^{\text{meas}}(d)||_1$, plus a second-derivative smoothing term which was weighted subjectively by trial-and-error. Note that M_c^{pred} is the $M_c(d)$ predicted by the smooth-increasing model and M_c^{meas} is the input $M_c(d)$ as estimated with the Ogata and Katsura (1993) method. This model has

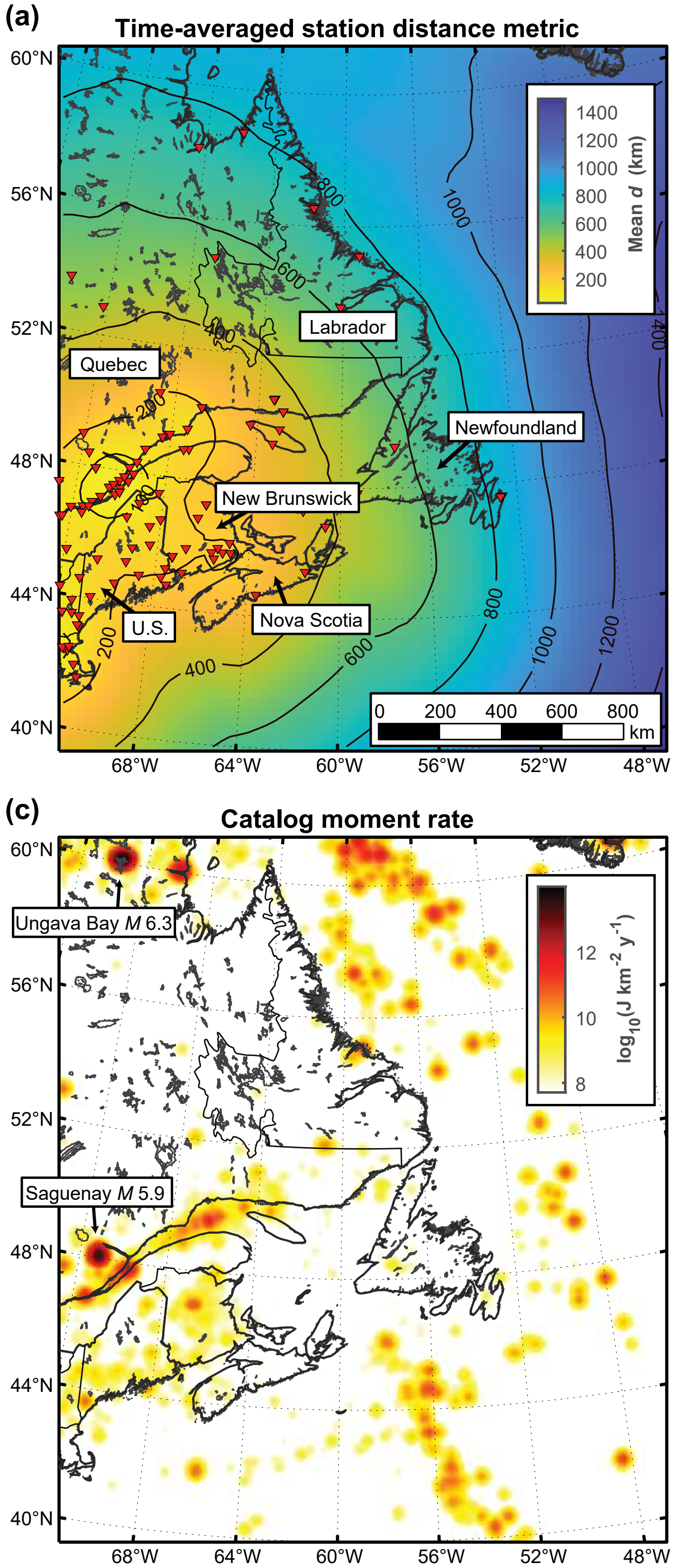

Figure 2 (a) Time-averaged weighted station-distance metric d over the study period of 1985–2023. Contours indicate distance in kilometres. Red triangles indicate locations of seismometers active for $\geq$3 years of the study period. Canadian provinces/regions and the United States (U.S.) are labeled. (b) Uncorrected yearly $M>1$ earthquake density (N km^{-2} y^{-1}) from the CNED catalog. (c) Moment density (J km^{-2} y^{-1}) for the same catalog. (d) The main result of this study (Section 3): Predicted yearly earthquake density based on the CNED catalog and the magnitude-of-completeness analysis of this study. All maps were first computed on a coarse grid ($\sim$15 km spacing), then converted to a finer grid and smoothed with a 2D Gaussian filter.

far greater freedom than the power-law, and as a result fits the data much more closely. For the remaining sections we use the smooth-increasing $M_c(d)$ model. However, we repeat the analyses using the power-law model and plot the results in Supplemental Figures S1–S4, which demonstrate that the choice has little impact on our overall conclusions.

3.2 Estimating b given spatiotemporal M_c variations

The standard and most-accepted way to estimate b is the Aki-Utsu maximum-likelihood estimator (MLE) (Utsu, 1965; Aki, 1965):

$$b = \frac{\log_{10}(e)}{\langle M \rangle - M_c}, \tag{4}$$

where $\langle M \rangle$ is the mean magnitude of the catalog, including only earthquakes with $M \geq M_c$. There have been several techniques introduced to allow time-varying M_c in the MLE (e.g. Weichert, 1980; Kijko and Smit, 2012; van der Elst, 2021). Taroni (2021) presented a convenient modification of the MLE that does not require the evaluation of b for subcatalogs. Ignoring two minor corrections, their MLE can be written:

$$b = \frac{\log_{10}(e)}{\langle M - M_{cE} \rangle}, \tag{5}$$

where M_{cE} is $M_c(t)$ evaluated for each earthquake. In this study, we further generalize their method by allowing spatial variation of M_c in addition to temporal variation, i.e. we consider $M_{cE} = M_c(x,t)$, evaluated using $d(x,t)$ for each earthquake. Derivation of Equation 5 is shown in Appendix 2, beginning from the magnitude probability density function of Aki (1965) and including an extension to incorporate a maximum magnitude (Page, 1968). The notion of considering the completeness level for each earthquake is not only useful in applying the MLE, but more generally we can examine the MFD using the relative magnitude $M^* = M - M_{cE}$.

Figure 4 displays regular M_W and M^* GR plots for both the CSZ and the full Atlantic Canada region, as defined by the map area in Figures 1 and 2. In both cases, M^*-derived b are lower than the M_W-derived estimate, but not significantly so according to the 95% confidence limits from bootstrapping. Confidence limits are highly dependent on the number of events included, and thus the M_c chosen. We therefore plot b vs. M_c (or b^* vs. M_c^*) for each GR plot (Figure 4c,d,g,h). These plots demonstrate that b^* is more stable over M_c^* than their equivalent M_W-derived estimates. Note that here we are ignoring potential variations of b to get average results over broad areas and times, despite observing varying b in the previous section.

3.3 Correcting density maps for undetected earthquakes

Here we apply our new MLE (Eq. 5) in order to estimate $r = r(M_c)$, defined as the ratio (total $M_W \geq 1$ earthquakes)/(recorded $M_W \geq 1$ earthquakes) expected for a given $M_c(x,t)$. If the thinning parameter σ was consistent in space and time, we could estimate the function $r(M_c)$ using only the MFD in Figure 4d. However, because we noted in Section 3.1 that σ is not constant, we expect more accurate results if we estimate $r(M_c)$ from multiple MFDs, formed using narrower ranges of M_c (or, equivalently, narrower ranges of d). We therefore consider the following procedure for a series of M_c spanning 1.0 to 5.2, using increments of 0.1:

1. Select all earthquakes with $M_{cE} \leq$ max(M_c, 2) to form the M^* MFD.
2. Estimate b using the MLE described in Eq. 5 and Appendix 2.
3. Fit a thinning function $q(M^*|\sigma,\mu)$ on the MFD, with b constrained to the MLE value.
4. Compute the ratio $r(M_c)$ as:

$$r(M_c) = \frac{\int_{1-M_c}^{M^*_{\max}} 10^{-bM^*} dM^*}{\int_{1-M_c}^{M^*_{\max}} q(M^*) 10^{-bM^*} dM^*}, \tag{6}$$

where the integral limits define the range between $M_W = 1$ and the maximum magnitude in the MFD.

The resulting $r(M_c)$ function is shown in Figure 5; note that it approaches a log-linear relationship with slope of ~1, which is expected as $b \approx 1.0$ in Figure 4f,h. As an alternative model that does not depend on fitting a thinning function, we can simply extrapolate the GR model fit in step 2 to predict the total number events $N_{\text{pred}} = N(M^* \geq 0)10^{-b(M_c-1)}$ and divide by $N_{\text{obs}} = N(M^* \geq 1 - M_c)$, which is equivalent to $N(M_W \geq 1)$. This ratio is plotted as the green curve in Figure 5 and produces similar results.

We opt not to fit a best-fit curve and instead directly interpolate the $r(M_c)$ results to compute $r_E = r(M_{cE})$ for each earthquake. The ratios r_E represent the predicted number of $M_W \geq 1$ earthquakes each (recorded) earthquake represents, and can be used to make the calibrated event-rate map shown in Figure 2d. This is in practice very similar to how the scalar moment of each earthquake is used to make the moment-rate map. Note that we cannot simply multiply the grid-cell values from Figure 2b by a ratio like $r(M_c)$ because M_c varies in time, as well as space. Finally, the resulting map shows that offshore seismic zones have comparable earthquake densities to the CSZ and LSZ, and it is much smoother than the moment-rate map because it is not dominated by the infrequent, largest earthquakes.

4 Discussion and Conclusions

Although we opted to use the smooth-increasing $M_c(d)$ model rather than the power-law fit (which was highly sensitive to the particular data range included), we are not suggesting that a power-law is inappropriate for the region. The Mignan et al. (2011) $M_c(d)$ power-law fitting results show significant scatter for individual M_c estimates, but they converge to a best-fit model because they have sufficient data to average M_c from many MFDs

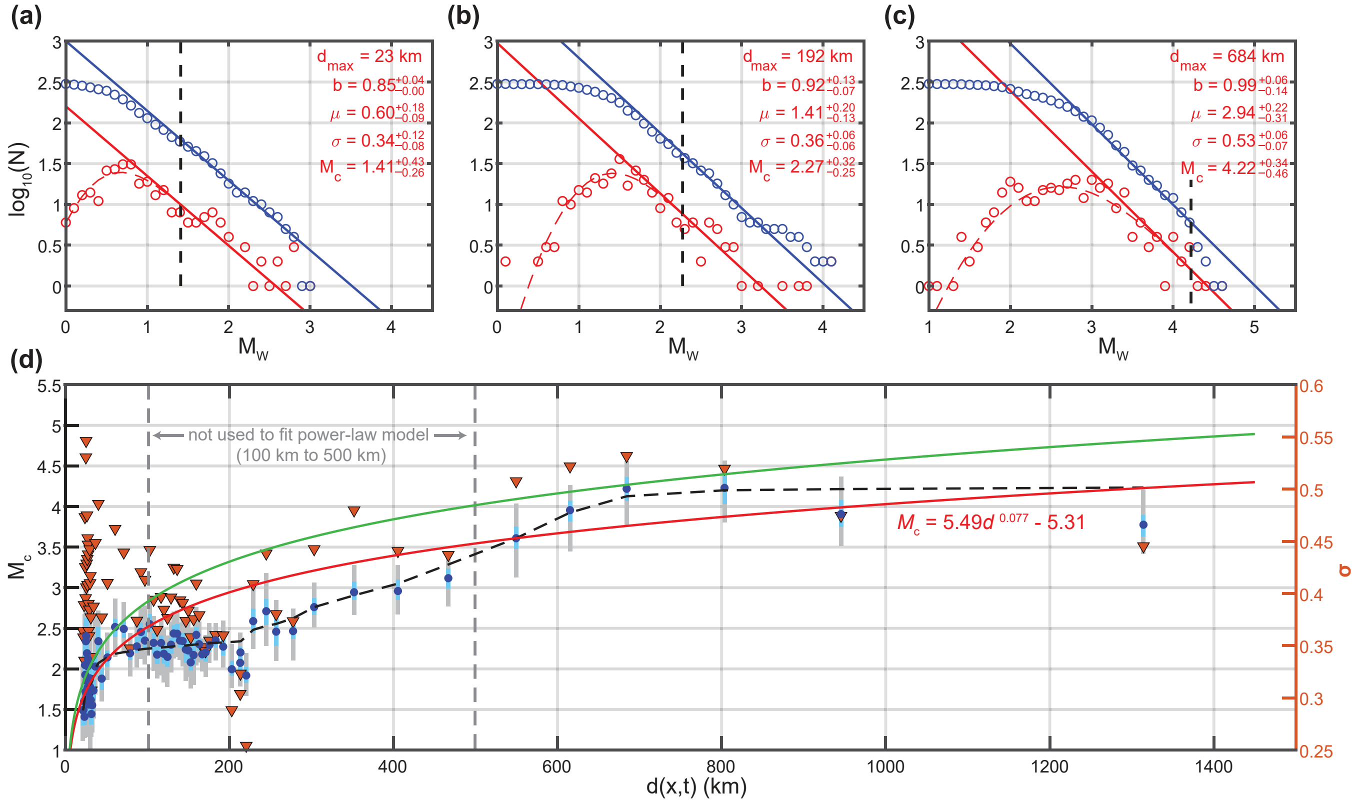

Figure 3 (a-c) The MFD and resulting Ogata and Katsura (1993) model fit for three distance bins of 300 earthquakes. 95% confidence intervals from bootstrapping are reported for each model parameter. (d) Overall $M_c(d)$ results (blue dots) with a power-law fit (red curve) and a best-fit smooth, increasing model (black dashed curve). Cyan and grey error bars indicate the 50% and 95% confidence intervals from bootstrapping, respectively. The green curve indicates the (4th-nearest station) model of Mignan et al. (2011), $M_c = 5.96d_4^{0.0803} - 5.80$. Orange triangles indicate the corresponding σ for each distance bin, as indicated on the right-hand side y-axis.

per distance bin. It is therefore unsurprising our $M_c(d)$ data show substantial scatter, but this does not fully explain why our $M_c(d)$ seems to have systematic deviations for a power-law, and remains constant over a range of $\sim 50 < d < 200$ km. It could be that the true $M_c(d)$ follows a power-law more closely and that our $M_c(d)$ estimates for this distance range are underestimated due to non–log-linear effects in their MFDs, although we have no hypothesis to suggest why this should be the case over an extensive range of $d(x,t)$. We demonstrate with Supplemental Figures S1–S4 that this issue does not substantially affect our following results or conclusions, but nevertheless this topic may warrant further investigation in future studies. The assessment of $M_c(x,t)$ more generally is discussed further near the end of this section.

Upon visual inspection, the GR plot produced by Equation 5 for the CSZ is quite similar to the raw M_W plot (Figure 4a,b), but the b vs. M_c plots show a modest improvement in the stability of b when using M^* (Figure 4c,d). M^* provides a much more dramatic improvement for the full Atlantic Canada catalog, as it produces much smaller confidence intervals on b, more stable b vs. M_c, and a lower thinning width σ (Figure 4e–h). The lower σ (0.39 for M^* vs. 0.65 for M_W) suggests a more angular MFD, rather than the gradual curvature that is caused by spatiotemporal heterogeneity in M_c (Mignan, 2012). The full Atlantic Canada catalog is an extreme case, where M_c varies greatly in both space and time, and there may be interesting b variation within the sample. Nevertheless, these observations suggest that M^*-derived b are more reliable than traditional estimates and that future studies, even those in areas where earthquakes and seismometers are more abundant, should consider spatiotemporal M_c variation when estimating b.

The predicted event-rate map (Figure 2d), as well as the associated methodology introduced here, are a robust way to compare earthquake rates between regions with different levels of seismometer coverage. It may be preferable to moment rate maps because it is sensitive to all earthquakes, instead of (effectively) only very large ones. With regard to the regulation of geological fluid-injection activities and induced-earthquake risk, the method is no replacement for local seismic monitoring efforts, but it may provide the best-available baseline earthquake rate estimates. Due to variable b and non–log-linear effects in MFDs, event rates will not always correlate perfectly with hazard. We also note that, for the purposes of hazard assessment, any map of recorded earthquakes is only useful to the extent that previous earthquakes locations can help predict the sites of future large earthquakes; our analysis does nothing to account for the possibility that areas of elevated intraplate seismicity today are extended aftershock sequences (Basham and Adams, 1983; Toda and

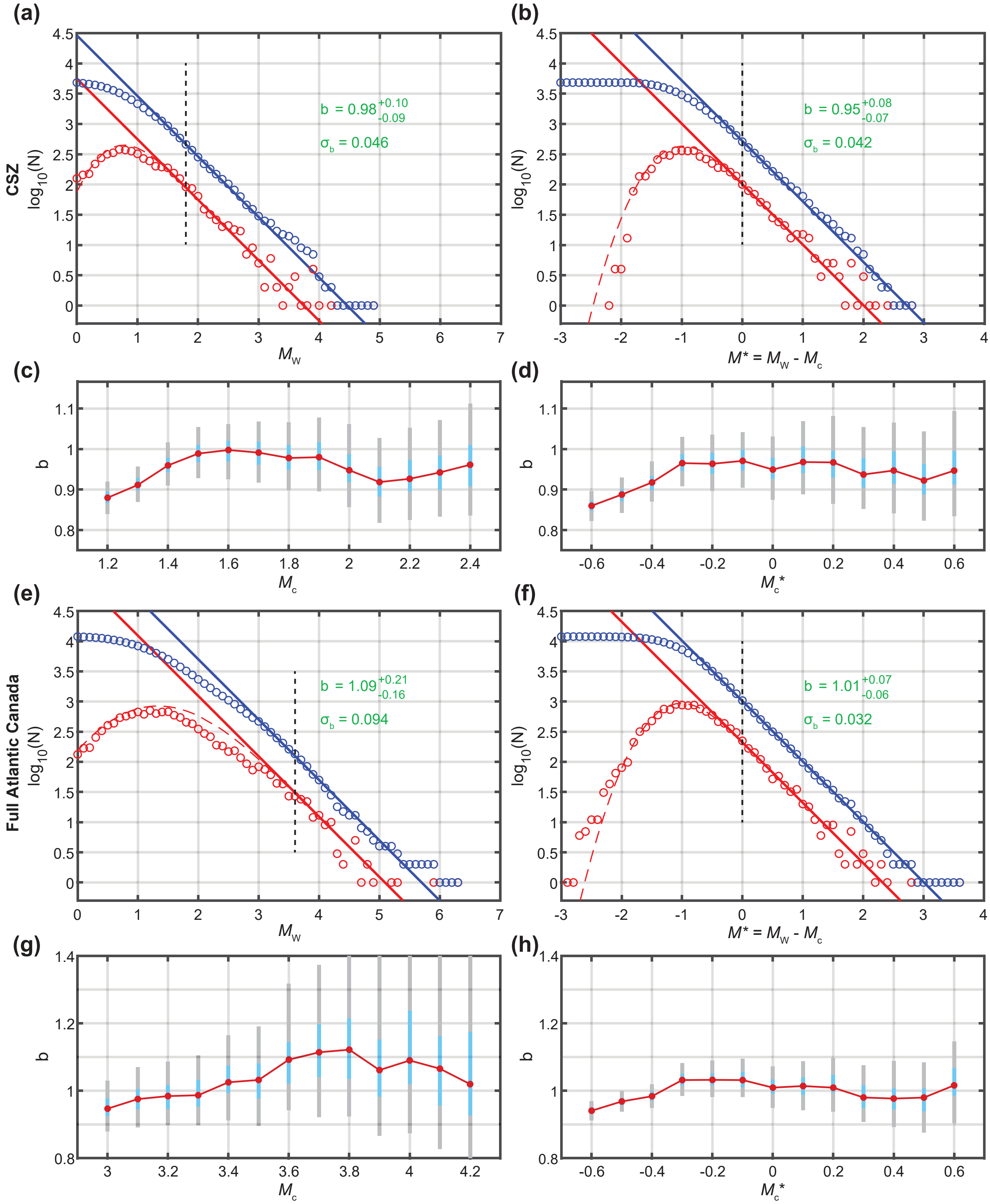

Figure 4 (a) Standard GR plot for the CSZ. Red and blue markers show the non-cumulative and cumulative MFDs, respectively. MLE-derived b is printed with 95% confidence intervals from 500 bootstrap iterations, as well as the standard error σ_b, which depends directly on the number of events with $M \geq M_c$ (N): $\sigma_b = b/\sqrt{N}$. The M_c used is shown with the dashed black line. (b) CSZ GR plot using M^* to account for variable $M_c(x,t)$. (c) b vs. M_c for the CSZ, using raw M_W, cyan and grey error bars show the 50% and 95% intervals from 500 bootstrap iterations. (d) b vs. M_c^* for the CSZ, using M^*, (e–h) like a–d except for the full map region of Figure 1. The Ogata and Katsura (1993) model fits in panels a, b, e, and f, were computed with b and M_c fixed to be consistent with the MLE fit and resulted in thinning widths σ of 0.39, 0.39, 0.65, and 0.39, respectively.

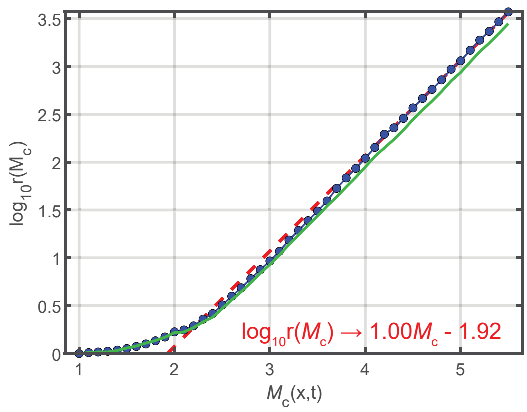

Figure 5 The predicted ratio of total/detected $M_W \geq 1$ earthquakes r, as a function of M_c, computed using Equation 6 for $1.0 \leq M_c \geq 5.2$ using increments of 0.1. The ratio approaches the log-linear relationship $\log_{10} r = 1.00 M_c - 1.92$ (computed using least-squares over the range $3.9 \geq M_c \leq 5.2$). The green curve is an alternative $r(M_c)$ model computed by extrapolating the GR model (without the thinning function), as described in the text.

Stein, 2018).

Finally, we must acknowledge some of the limitations of our $M_c(x,t)$ analysis. In addition to uncertainty in station metadata and the "noise" caused by periods where a seismometer was nonoperational that we have not accounted for, treating all seismometers equally is also a severe limitation. Noise levels, and signal-to-noise ratio, vary between seismometers for many reasons; geology at the site, instrument type, and proximity to anthropogenic or ocean-wave noise sources all being important factors. Instrumentation quality and noise levels also generally improve throughout the study period. Although we do not expect it to be a major factor in this dataset, short-term aftershock incompleteness (Stallone and Falcone, 2021) can also cause M_c variation in time. Schorlemmer and Woessner (2008) use a full phase pick catalog to empirically determine the likelihood of an earthquake being picked at a particular seismometer as a function of magnitude and distance; then, taking these functions at all seismometers, they equate $M_c(x,t)$ to a threshold probability of the earthquake being detected at four or more seismometers. Mahani et al. (2016) measure ambient noise levels at each seismometer and compare them with theoretical earthquake amplitudes in order to spatially map M_c. We expect that incorporating either system in place of, or in combination with, our simplified d–M_c relation would further improve the predicted event rate and b estimates.

Acknowledgements

This work was funded by NRCan (Contribution Number 20220415). We would like to thank Nicholas Ackerley for his thorough internal review, as well as John Adams and Allison Bent for their guidance early on, which were critical to creating the methodology and forming the datasets necessary for this study. We further thank Maria Mesimeri and an anonymous reviewer for their constructive comments.

Data and code availability

The earthquake catalog analyzed in this study comes from the Canadian National Earthquake Database (CNED), and was accessed at https://earthquakescanada.nrcan.gc.ca/stndon/NEDB-BNDS/bulletin-en.php in April 2022. Digital seismometer operating dates were taken from the Incorporated Research Institutions for Seismology (IRIS) database, and were accessed using the Python ObsPy package in June 2022.

Competing interests

The authors declare that they have no competing interests.

References

Adams, J. and Basham, P. The seismicity and seismotectonics of Canada east of the cordillera. *Geoscience Canada*, 16(1):3–16, 1989.

Aki, K. Maximum likelihood estimate of b in the formula log N = a-bM and its confidence limits. *Bull. Earthq. Res. Inst., Tokyo Univ.*, 43:237–239, 1965.

Basham, P. and Adams, J. Earthquakes on the continental margin of eastern Canada: Need future large events be confined to the locations of large historical events. *U.S. Geological Survey Open File Report*, 83-843:456–467, 1983.

Bent, A. L. The 1989 (MS 6.3) Ungava, Quebec, earthquake: a complex intraplate event. *Bulletin of the Seismological Society of America*, 84(4):1075–1088, 1994. doi: 10.1785/BSSA0840041075.

Bent, A. L. A complex double-couple source mechanism for the Ms 7.2 1929 Grand Banks earthquake. *Bulletin of the Seismological Society of America*, 85(4):1003–1020, 1995. doi: 10.1785/BSSA0850041003.

Bent, A. L. Moment magnitude (Mw) conversion relations for use in hazard assessment in eastern Canada. *Seismological Research Letters*, 82(6):984–990, 2011. doi: 10.1785/gssrl.82.6.984.

Bent, A. L. and Hasegawa, H. S. Earthquakes along the Northwestern Boundary of the Labrador Sea. *Seismological Research Letters*, 63(4):587–602, 1992. doi: 10.1785/gssrl.63.4.587.

Bent, A. L. and Voss, P. Seismicity in the Labrador-Baffin Seaway and surrounding onshore regions. In Dafoe, L. T. e. and Bingham-Koslowski, N. e., editors, *Geological synthesis of Baffin Island (Nunavut) and the Labrador-Baffin Seaway*, volume Bulletin 608, pages 379–387. Geological Survey of Canada, 2022. doi: 10.4095/321857.

Cheng, Y., Liu, W., Xu, T., Zhang, Y., Zhang, X., Xing, Y., Feng, B., and Xia, Y. Seismicity induced by geological CO_2 storage: A review. *Earth-Science Reviews*, 239:104369, 2023. doi: 10.1016/j.earscirev.2023.104369.

Gerstenberger, M. C., Marzocchi, W., Allen, T., Pagani, M., Adams, J., Danciu, L., Field, E. H., Fujiwara, H., Luco, N., Ma, K.-F., Meletti, C., and Petersen, M. D. Probabilistic seismic hazard analysis at regional and national scales: State of the art and future challenges. *Reviews of Geophysics*, 58(2):e2019RG000653, 2020. doi: 10.1029/2019RG000653.

Gutenberg, B. and Richter, C. F. Frequency of earthquakes in California. *Bulletin of the Seismological Society of America*, 34(4): 185–188, 1944. doi: 10.1785/BSSA0340040185.

Haddon, R. A. W. Modeling of source rupture characteristics for the Saguenay earthquake of November 1988. *Bulletin of the Seismological Society of America*, 85(2):525–551, 1995. doi: 10.1785/BSSA0850020525.

Halchuk, S., Allen, T. I., Rogers, G. C., and Adams, J. Seismic Hazard Earthquake Epicentre File (SHEEF2010) used in the Fifth Generation Seismic Hazard Maps of Canada. *Geological Survey of Canada, Open File*, 7724, 2015. doi: 10.4095/296908.

Ishimoto, M. and Iida, K. Observations of earthquakes registered with the microseismograph constructed recently. *Bulletin of the Earthquake Research Institute*, 17:443–478, 1939.

Kijko, A. and Smit, A. Extension of the Aki-Utsu b-Value Estimator for Incomplete Catalogs. *Bulletin of the Seismological Society of America*, 102(3):1283–1287, 2012. doi: 10.1785/0120110226.

Kolaj, M., Adams, J., and Halchuk, S. Seismic hazard in southeastern Canada: uncertainty and controls on seismic hazard in a region of low-to-moderate seismicity. In *17th World Conference on Earthquake Engineering*, 2020.

Lamontagne, M., Beauchemin, M., and Toutin, T. Earthquakes in the Charlevoix seismic zone, Quebec. *International Journal on Hydropower & Dams*, 10(2):98–99, 2003a.

Lamontagne, M., Keating, P., and Perreault, S. Seismotectonic characteristics of the Lower St. Lawrence Seismic Zone, Quebec: insights from geology, magnetics, gravity, and seismics. *Canadian Journal of Earth Sciences*, 40(2):317–336, 2003b. doi: 10.1139/e02-104.

Mahani, A. B., Kao, H., Walker, D., Johnson, J., and Salas, C. Performance evaluation of the regional seismograph network in northeast British Columbia, Canada, for monitoring of induced seismicity. *Seismological Research Letters*, 87(3):648–660, 2016. doi: 10.1785/0220150241.

Mignan, A. Functional shape of the earthquake frequency-magnitude distribution and completeness magnitude. *Journal of Geophysical Research: Solid Earth*, 117(B8):B009347, 2012. doi: 10.1029/2012JB009347.

Mignan, A., Werner, M. J., Wiemer, S., Chen, C.-C., and Wu, Y.-M. Bayesian estimation of the spatially varying completeness magnitude of earthquake catalogs. *Bulletin of the Seismological Society of America*, 101(3):1371–1385, 2011. doi: 10.1785/0120100223.

Mizrahi, L., Nandan, S., and Wiemer, S. The effect of declustering on the size distribution of mainshocks. *Seismological Research Letters*, 92(4):2333–2342, 2021. doi: 10.1785/0220200231.

Munro, P. S., Halliday, R. J., Shannon, W. E., and Shieman, D. R. J. Canadian Seismograph Operations — 1986. *Geological Survey of Canada*, Paper 88-16, 1988. doi: 10.4095/130933.

Ogata, Y. and Katsura, K. Analysis of temporal and spatial heterogeneity of magnitude frequency distribution inferred from earthquake catalogues. *Geophysical Journal International*, 113 (3):727–738, 1993. doi: 10.1111/j.1365-246X.1993.tb04663.x.

Ogata, Y. and Yamashina, K. Unbiased estimate for b-value of magnitude frequency. *Journal of Physics of the Earth*, 34(2):187–194, 1986. doi: 10.4294/jpe1952.34.187.

Page, R. Aftershocks and microaftershocks of the great Alaska earthquake of 1964. *Bulletin of the Seismological Society of America*, 58(3):1131–1168, 1968. doi: 10.1785/BSSA0580031131.

Plourde, A. P. and Nedimović, M. R. Earthquake depths, focal mechanisms, and stress in the Lower St. Lawrence Seismic Zone. *Seismological Research Letters*, 92(4):2562–2572, 2021. doi: 10.1785/0220200429.

Schorlemmer, D. and Woessner, J. Probability of detecting an earthquake. *Bulletin of the Seismological Society of America*, 98 (5):2103–2117, 2008. doi: 10.1785/0120070105.

Schultz, R., Skoumal, R. J., Brudzinski, M. R., Eaton, D., Baptie, B., and Ellsworth, W. Hydraulic fracturing-induced seismicity. *Reviews of Geophysics*, 58(3):e2019RG000695, 2020. doi: https://doi.org/10.1029/2019RG000695.

Si, Z. and Jiang, C. Research on parameter calculation for the Ogata-Katsura 1993 model in terms of the frequency-magnitude distribution based on a data-driven approach. *Seismological Research Letters*, 90(3):1318–1329, 2019. doi: 10.1785/0220180372.

Stallone, A. and Falcone, G. Missing earthquake data reconstruction in the space-time-magnitude domain. *Earth and Space Science*, 8(8):e2020EA001481, 2021. doi: 10.1029/2020EA001481.

Taroni, M. Back to the future: old methods for new estimation and test of the Gutenberg-Richter b-value for catalogues with variable completeness. *Geophysical Journal International*, 224(1): 337–339, 2021. doi: 10.1093/gji/ggaa464.

Toda, S. and Stein, R. S. Why aftershock duration matters for probabilistic seismic hazard assessment. *Bulletin of the Seismological Society of America*, 108(3A):1414–1426, 2018. doi: 10.1785/0120170270.

Utsu, T. A method for determining the value of 'b' in a formula log n = a-bM showing the magnitude-frequency relation for earthquakes. *Geophys. Bull. Hokkaido Univ.*, 13:99–103, 1965.

Utsu, T. A statistical significance test of the difference in b-value between two earthquake groups. *Journal of Physics of the Earth*, 14(2):37–40, 1966. doi: 10.4294/jpe1952.14.37.

van der Elst, N. J. B-Positive: A robust estimator of aftershock magnitude distribution in transiently incomplete catalogs. *Journal of Geophysical Research: Solid Earth*, 126(2):e2020JB021027, 2021. doi: 10.1029/2020JB021027.

Weichert, D. H. Estimation of the earthquake recurrence parameters for unequal observation periods for different magnitudes. *Bulletin of the Seismological Society of America*, 70(4): 1337–1346, 1980. doi: 10.1785/BSSA0700041337.

Wetmiller, R. J., Adams, J., Anglin, F. M., Hasegawa, H. S., and Stevens, A. E. Aftershock sequences of the 1982 Miramichi, New Brunswick, earthquakes. *Bulletin of the Seismological Society of America*, 74(2):621–653, 1984. doi: 10.1785/BSSA0740020621.

Woessner, J. and Wiemer, S. Assessing the quality of earthquake catalogues: Estimating the magnitude of completeness and its uncertainty. *Bulletin of the Seismological Society of America*, 95 (2):684–698, 2005. doi: 10.1785/0120040007.

Yu, H., Liu, Y., Harrington, R. M., and Lamontagne, M. Seismicity along St. Lawrence paleorift faults overprinted by a meteorite impact structure in Charlevoix, Québec, eastern Canada. *Bulletin of the Seismological Society of America*, 106(6):2663–2673, 2016. doi: 10.1785/0120160036.

Appendices

Appendix 1: Converting to $\mathrm{M_W}$

The most commonly used type of magnitude used in eastern Canada is the Nuttli magnitude m_N; it is reported for 82% of the earthquakes in our catalog. Bent (2011) analyzed the relation between m_N and M_W in eastern Canada and estimated conversion formulas of $M_W = 0.99m_N - 0.36 \pm 0.16$ for pre-1995 earthquakes and $M_W = 0.93m_N - 0.22 \pm 0.19$ for 1995–present.

Halchuk et al. (2015) reference this study and opt to use simplified relations of $M_W = m_N - 0.4$ for pre-1995 and $M_W = m_N - 0.5$ for 1995–present. They also treat local magnitude M_L as equivalent to m_N, and all other magnitudes (which form <0.02% of our catalog) as equivalent to M_W. In this work, we follow the procedure of Halchuk et al. (2015). However, as we have not seen this explicitly discussed elsewhere, we will point out here that linear conversions directly affect the estimated b. If, for example, we consider $M_W \propto 0.93 m_N$, we should expect b_W and b_N (estimates of b derived from the M_W and m_N catalogs, respectively), to differ according to the proportionality $b_N \propto 0.93 b_W$ (although we cannot verify that the proportionality is statistically significant). The Bent (2011) formula therefore suggests that our analysis (for which data is mostly from 1995–present) underestimates b_W. Note that this does not suggest a bias in seismic hazard analyses since m_N and other local magnitudes are more closely related to local amplitudes than M_W.

Appendix 2: Modification of maximum-likelihood estimator

In this section we justify Equation 5 beginning from the (unnormalized) probability density function for earthquake magnitude in a Gutenberg-Richter distribution (Aki, 1965):

$$f(M|M_c,\beta) = \beta e^{-\beta(M-M_c)} \tag{A1}$$

where $\beta = \ln(10)b$. We begin with similar reasoning as Kijko and Smit (2012), who consider the total likelihood to be a product of likelihoods from N subcatalogs with distinct M_c, but in our case we effectively consider each earthquake its own subcatalog, such that N is the total number of earthquakes. The total likelihood (ignoring a normalization constant) can be expressed as:

$$\begin{aligned} L(\beta) &= \prod_i^N f(M_i|M_{c,i},\beta) \\ &= \prod_i^N \beta \exp\left(-\beta(M_i - M_{c,i})\right) \\ &= \beta^N \exp\left(-\beta \sum_i^N (M_i - M_{c,i})\right). \end{aligned} \tag{A2}$$

We can then closely follow the original MLE derivation and differentiate to find the maximum:

$$\begin{aligned} \frac{\partial L(\beta)}{\partial \beta} &= 0 \\ &= \left(N\beta^{N-1} - \beta^N \sum_i^N M_i \right. \\ &\quad \left. - M_{c,i}\right) \exp\left(-\beta \sum_i^N (M_i - M_{c,i})\right). \end{aligned} \tag{A3}$$

After eliminating the remaining exponential term (as it cannot be zero) we can rearrange to find:

$$\begin{aligned} \beta &= \frac{1}{\frac{1}{N}\sum_i^N M_i - M_{c,i}} \\ &= \frac{1}{\langle M - M_c \rangle}, \end{aligned} \tag{A4}$$

which is equivalent to Equation 5. As a minor correction, this result should also be multiplied by $(N-1)/N$ to achieve an unbiased results (Ogata and Yamashina, 1986), resulting in the estimator:

$$b = \frac{\frac{N-1}{N}\log_{10}(e)}{\langle M - M_{cE} \rangle}. \tag{A5}$$

This is equivalent to Eq. 6 of Taroni (2021), except we omit the correction for binned magnitudes (adding $\Delta M/2$ to the denominator; Utsu, 1966) which is unnecessary because $M^* = M - M_{cE}$ is effectively unbinned. In practice, we also incorporate an upper magnitude limit in the MLE, which is important when the maximum magnitude is less than $M_c + 2$ (Page, 1968). To do this, we effectively replace M with M^* and set $M_c^* = 0$, then follow the MLE of Page (1968), which becomes:

$$\frac{1}{\beta} = \langle M^* \rangle - \frac{M^*_{\max}\exp(-\beta M^*_{\max})}{1 - \exp(-\beta M^*_{\max})}. \tag{A6}$$

We solve this formula using a line search, and then apply the $(N-1)/N$ correction to b for our final estimate.

doi:10.26443/seismica.v2i2.285

SEISMICA

Recent seismicity on the Kerguelen Islands

O. Lengliné * [1], **J. Rimpôt** [1], **A. Maggi** [1], **D. Zigone** [1]

[1]Université de Strasbourg/CNRS, Institut Terre et Environnement de Strasbourg, *UMR7063*, 67084 Strasbourg Cedex, France

Author contributions: *Conceptualization*: D. Z., A. M.. *Methodology*: A.M, J. R., O. L.. *Validation*: O.L, J. R., A. M., D. Z. *Writing - original draft*: O.L, J. R., A. M., D. Z.

Production Editor: Gareth Funning
Handling Editor: Atalay A. Wondem
Copy & Layout Editor: Jack B. Muir

Received: December 8, 2022
Accepted: August 23, 2023
Published: October 30, 2023

Abstract The Kerguelen Archipelago, one of the largest oceanic archipelagos in the world, was built by an active hotspot interacting with a ridge between 110 and 40 million years ago; since then, the ridge has migrated over 1000 km away and the archipelago's volcanic activity has been steadily decreasing. Despite the lack of recent active tectonics and the quiescent volcanism of the Kerguelen Islands, there have been several observations of seismic events of unknown origin in its vicinity. The only seismic instrument within 1000 km of the archipelago was installed on Kerguelen's main island in the 1980s. In this study we apply an AI-assisted P- and S- arrival detection algorithm to the continuous waveforms recorded by this seismometer over the past 20 years. We reveal that the Kerguelen main island hosts abundant seismicity. This seismicity exhibits swarm-like characteristics in several clustered locations while at other places the earthquakes appear more steady over time. We locate most events near the largest ice cap of the main island. We propose that the origin of the earthquakes can be linked to residual volcanic, magmatic, or hydrothermal activity at depth, all of which can be favored by flexural stress caused by the documented fast retreat of the ice cap. This seismicity may also indicate that the Kerguelen hotspot shows signs of unrest.

Non-technical summary The seismicity around the Kerguelen Islands (Indian Ocean) remains poorly known. This is mainly due to the low density of seismological stations in the area around the island. In this study we analyze the continuous seismological signal, recorded by the only seismological station that is in operation on the island. Using an artificial intelligence algorithm we identify numerous earthquakes that we locate on the main island of Kerguelen or in its immediate vicinity. This abundant seismic activity is present during the whole duration of the study (20 years) and thus suggests a remnant magmatic activity on the island possibly favored by the melting ice cap.

1 Introduction

The Kerguelen Archipelago, located in the oceanic domain of the Antarctic plate (Indian Ocean ; 49°S, 69°E; see Figure 1), represents the northernmost, sub-aerial part of the Kerguelen plateau and is the third largest oceanic archipelago after Iceland and Hawaii (Giret, 1990). It has a unique geological history: first a strong ridge-hotspot interaction built the Kerguelen oceanic plateau (110-90Ma), then a change in spreading rate of the Southeast Indian Ridge caused the Kerguelen and Broken-Ridge Plateaus to rift apart ($\sim$ 45Ma), building the northern plateau (e.g. Coffin et al., 2002). Today, the Kerguelen Islands are located over 1000 km away from the closest tectonic plate boundary, the southeast Indian Ridge (Figure 1). They have experienced slowly decaying volcanic activity from 40 Ma to the present, with the last eruptions occurring a few thousand years ago (Gagnevin et al., 2003).

Despite the distance of the Kerguelen Islands from active tectonic plate boundaries and their quiescent volcanism, there have been several observations of seismic events in their vicinity. The largest recorded earthquake occurred in 1973 (Okal, 1981, 1983; Wiens and Stein, 1984; Adams and Zhang, 1984; Bergman et al., 1984): it had a primarily normal faulting mechanism, was located quite far from the Kerguelen Islands themselves, and was attributed to thermal and bending stresses associated with an asthenospheric channel (Okal, 1983; Bergman et al., 1984). Since the 1980s, there have been no further studies of the seismicity of the Kerguelen region in the international literature. The International Seismological Commission (ISC) catalog shows a handful of earthquakes with locations close to Kerguelen (Table 1), all recorded since the French global seismic network Geoscope (Institut de physique du globe de Paris (IPGP) and École et Observatoire des Sciences de la Terre de Strasbourg (EOST), 1982) installed broad-band seismic stations on Kerguelen (in 1983), Crozet (in 1986), Amsterdam (in 1994), and Petrel Island in east Antarctica (in 1986). Each of these stations, including the one installed at Port aux Français (PAF) on Kerguelen, records local earthquakes of magnitude lower than 4.0 that remain undetected by the others, or by any other station world-wide. The recent seismicity visible on the island includes some episodes of elevated activity in 2014 and 2017. In particular, a M4.7 earthquake on 6 October 2017 produced surface deformation that was captured by InSAR (Raphael Grandin, personal communication).

The origin of the seismicity of the northern Kergue-

*Corresponding author: lengline@unistra.fr

len plateau remains largely unknown. The seismicity of the Antarctic plate is generally low and spots of elevated activity might indicate the presence of a specific underlying tectonic structure (Reading, 2007). For example, in Antarctica, denser station coverage has unveiled intraplate tectonic earthquakes linked to a rift zone (Lough et al., 2018). However, no such tectonic feature is visible on the Kerguelen Islands. Seismicity can also occur in diffuse plate-boundary zones, as seen elsewhere in the Antarctic plate (for example the 1998 M_w8 Balleny islands earthquake Antonioli et al. (2002)). However, there is no evidence that a zone like this exists in the Kerguelen region. Most of the Antarctic intraplate activity is confined to coastal regions of the continent and seems to be caused by crustal uplift due to glacial unloading (Reading, 2006). A similar uplifting mechanism operates in Fennoscandia and has been linked to the occurrence of earthquakes (Steffen and Wu, 2011). However, the Kerguelen Archipelago is distant nearly 2000 km from the Antarctic continent, and the surrounding southern Indian Ocean has a very low seismicity. It is unlikely, therefore, that the Kerguelen seismicity is linked with the glacial unloading of Antarctica (Reading, 2007).

Another hypothesis involves remnant volcanic hotspot activity. Volcanic activity linked to the Kerguelen hotspot took place mainly between 122 Ma and 90 Ma (Jiang et al., 2020). As the Kerguelen Islands drifted southwards and progressively disconnected from the hotspot, the erupted volume decreased (Jiang et al., 2020). Recent volcanic activity has been documented within the Kerguelen Plateau, in particular on Heard and McDonald Islands, about 400 km from the Kerguelen Islands (Stephenson et al., 2005). The last major eruptive event on the Kerguelen Islands occurred 26±3 thousand years ago (Gagnevin et al., 2003), but some volcanic activity still seems to continue. An airborne thermal survey of the eastern part of the main island (Grande Terre) found evidence of fumaroles and hot water springs located near the limits of the island's ice cap, suggesting a deep heat reservoir (Ballestracci and Nougier, 1984). It seems possible, therefore, that some of the recorded earthquakes could be related to a circulation of hydro-thermal fluid or magma at depth.

Before being able to address the question of why earthquakes occur on the Kerguelen Islands, we need a more detailed picture of this seismicity and of its evolution. To obtain this, we analysed all available continuous waveform data recorded by the seismometer installed at Port aux Français (PAF), detected several thousand local and near-regional earthquakes, and located them using single-station methods. We describe our findings in this paper.

2 Data and Methods

Given the remoteness of the Kerguelen main island, most of its local earthquakes are recorded by a single seismic station: PAF (Port aux Français, Geoscope global seismological network), which is equipped with a Streckheisen STS-1 seismometer. The station started operating in 1983 and has produced continuous, 20 sample-per-second data streams since 1999. For this study, we used the three-component waveforms recorded at PAF between 7 January 1999 and 31 December 2021 (over 20 years of continuous data). The station stopped working completely between 2013/03/11 and 2013/09/16, during which time the original STS-1 electronics were upgraded to their Metrozet E300 successors. The East component STS-1 sensor malfunctioned during several months in 2017. Fortunately, a short period Mark-L4C sensor installed a few meters from the STS-1 instruments was operating during the 2017 malfunction, so we substituted waveforms from the L4C instrument in our analysis for that time period.

To identify earthquakes and automatically pick P and S-wave arrival times, we cut the continuous three-component data-streams into 24-hour windows and processed them using the EQTransformer algorithm of Mousavi et al. (2020). This algorithm relies on a deep neural-network architecture both for earthquake identification and phase picking and has been trained on a worldwide database of local to regional waveforms. We kept the detection level threshold probability and the P and S picking probabilities at their default values, i.e. 0.3, 0.1, and 0.1. The EQTransformer algorithm identified 6826 P-wave picks and 6864 S-wave picks in our data-set. As we were only interested in seismicity local to Kerguelen and required both a P and an S pick to locate the earthquakes, we retained only those events whose S pick followed its P-wave pick by less than 20s; this led to the identification of 6591 events.

We estimated the locations of these events from our single-station three-component data by combining epicentral (source-station) distances obtained from S-P travel-time differences with back-azimuths obtained from the direction of horizontal polarization of the P-wave arrival. We estimated the epicentral distances by matching the observed S-P travel-time differences with those computed in a 1D velocity model. Past geophysical campaigns in the region had found that the crust in the central region of the main island is thicker than normal oceanic crust (16-20 km) and that the crust-mantle boundary exhibits a 2-3 km thick transition zone (Recq et al., 1990, 1994; Charvis et al., 1995). This depth of the Moho is compatible with the value of 24 km inferred from receiver function analysis at PAF (Kumar et al., 2007). We adopted the 1D P-wave velocity model of the area proposed by Gregoire et al. (2001) based on a compilation of seismic measurements (Table 2). As we have no information regarding the V_P/V_S ratio below the main island, we decided to use the location of the 2017, M4.7 of October 6th as a reference. We performed various locations changing the V_P/V_S ratio and each time computing the distance between our location of this M4.7 event and the location of its associated surface rupture. The minimum distance of 9.5 km between the two locations is obtained for a V_P/V_S ratio of 1.85 and we retained this value for our analysis.

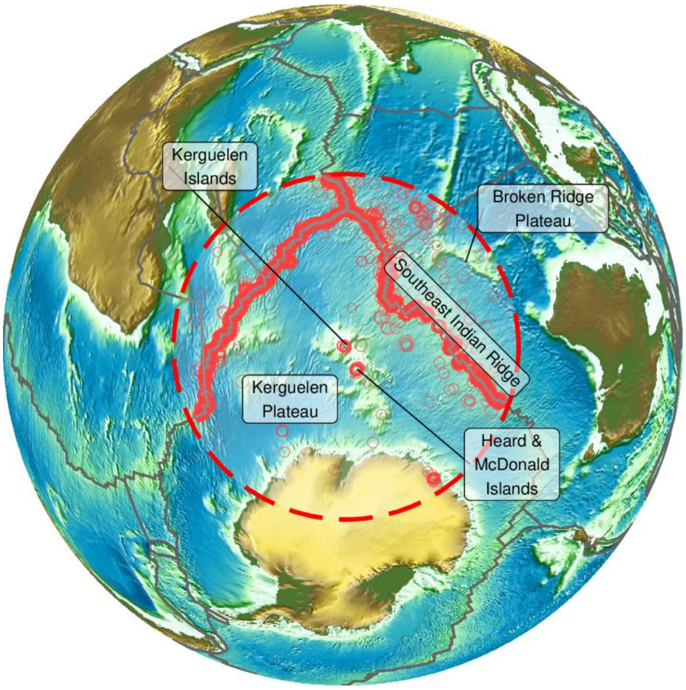

Figure 1 Regional map with the locations of the Kerguelen Islands and relevant bathymetric/topographic features. Tectonic plate boundaries are displayed as thick gray lines DeMets et al. (2010). All earthquakes within the NEIC, USGS catalog within a 30 degrees radius from the main Kerguelen island are shown as red circles.

Date	Time	Latitude (°S)	Longitude (°E)	Depth (km)	Magnitude	Source
1973-03-20	18:13:25	57.82	83.59	33	5.2	ISC
1973-05-03	23:11:06	46.14	73.22	18	5.9 (Mw)	ISC
1974-09-21		46.15	53.63	33	-	ISC
1980-04-24	23:44:41	48.78	69.24	10	4.6	ISC
1980-04-25	01:54:21	48.72	69.17	10	4.7	ISC
1980-04-25	15:50:06	48.56	69.47	10	4.9	ISC
1981-04-06		57.99	82.50	0	4.7	ISC
2007-07-28	15:32:50	49.16	68.92	4	5.3	ISC
2014-03-12	17:54:03	49.30	69.62	19	4.5	NEIC
2014-03-12	18:15:11	49.32	69.55	20	4.9	NEIC
2014-03-15	14:00:13	49.17	69.51	10	4.3	NEIC
2014-03-15	14:20:59	49.35	69.45	10	4.6	NEIC
2014-03-15	14:57:01	49.22	69.57	16	4.7	NEIC
2014-03-15	15:42:47	49.40	69.58	10	4.3	NEIC
2014-03-15	15:48:08	48.97	69.69	10	4.4	NEIC
2014-03-21	04:39:24	49.66	69.73	10	4.7	NEIC
2015-06-10	03:12:29	49.33	69.75	10	4.7	NEIC
2017-10-06	18:43:44	49.22	68.949	14	4.7	NEIC
2017-10-15	22:21:31	49.104	68.991	15	4.6	NEIC

Table 1 Seismicity of the northern Kerguelen plateau available from global catalogs. Earthquakes from 1973 to 1981 were discussed by Adams and Zhang (1984); the two earthquakes in 1973 were also discussed by Okal (1981). Magnitude are mb (body-wave magnitudes) unless otherwise indicated.

Depth (km)	V_P (km/s)
0.0	3.8
1.0	4.8
10.0	7.0
18.0	7.5
20.0	8.0

Table 2 P-wave velocity model used for locating earthquakes, derived from (Gregoire et al., 2001).

We computed S-P travel-time differences as a function of distance for the P-wave velocity model in Table 2 and this V_P/V_S ratio using the code from Heimann et al. (2017). We allowed the earthquake depths to range from 1 to 20 km depth, then averaged the S-P travel-time distances over the entire depth range. We inferred the epicentral distances by matching these average values as a function of distance to the recorded S-P travel-time differences.

We estimated the back-azimuths using the method proposed by Roberts et al. (1989): we applied a high-pass filter above 2 Hz, isolated the P-wave pulses within a 1 s window starting 0.15 s before the P-wave picks, then computed the back-azimuths, ϕ, as

$$\phi = \arctan\left(\frac{-\langle y_e y_z \rangle}{-\langle y_n y_z \rangle}\right), \tag{1}$$

where y_e, y_z, and y_n are respectively the east, vertical and north component of the P-wave pulse. We also computed the uncertainty on the value of ϕ using equation (11) of Roberts et al. (1989). We found a mean azimuthal uncertainty in our locations of about 9°. A further source of location uncertainty, touching both distance and azimuth estimates, can arise from the use of an incorrect or over-simplified seismic velocity model (we used a 1D velocity model but the wave-speed under this volcanic island archipelago is likely to vary in 3D).

We kept only those events for which the joint probability of the P and S phase picks was higher than 0.1 and whose azimuth uncertainty was below 40°. This led to a final selection of 4507 events. For each earthquake, we estimated a local magnitude following the original Richter approach (Richter, 1935). This magnitude estimate, computed at a single site, is subject to large uncertainties, and should be interpreted as a relative magnitude among the recorded events of each cluster rather than an absolute magnitude.

3 Results

We located numerous signals originating very close to the seismic station, in the direction of the permanent scientific base-camp. Due to their location, we supposed them to be anthropogenic, and we discarded all signals located at epicentral distances less than 5 km. This left us with 3158 non-anthropogenic events.

The locations of these earthquakes, shown in Figure 2, indicate that they are not evenly distributed around the main island but form diffuse clumps and streaks at different distances from the Port aux Français station. To investigate the temporal distribution of earthquakes in each seismically active region, we grouped earthquakes into clusters based on their spatial distribution. We grouped events with similar locations first visually, then using a simple clustering algorithm. For the clustering step, we used the density-based spatial clustering DBSCAN (Ester et al., 1996). We used a 2 dimensional metric for clustering events based on the S-P time and azimuth (See Text S1). The algorithm identified 4 clusters comprising at least 90 earthquakes each, shown in colour in Figure 2. The clusters span 4 bands of epicentral distances that thicken as a function of distance from the Port aux Français station. We show in Figure 3 the magnitude of the earthquakes in each cluster as a function of their occurrence times.

The farthest cluster from the station, clusters 1, is located on the west of the island and contain 1404 events. It is the more populous cluster and is located 10 to 20 km north-north-west of the Cook ice cap. The earthquakes in this cluster occurred almost continuously over the past 20 years, with periods of increased activity in 2007 and 2017. Cluster 2 (east of the ice cap) contains 459 earthquakes, most of which occurred during a seismic sequence in March 2014. The two remaining clusters, clusters 3 and 4, are located southwest of Port aux Français, at distances of 20 and 40 km. The timing of earthquakes in these two clusters indicates that cluster 3 (the closer one) first appeared in 2007, and has since been activated in several short bursts. Cluster 4 (the farther one) was active at the end of 2011 and has since become nearly quiescent.

Also shown as purple circles on Figure 2 are 1007 events that do not belong to the 4 main identified clusters and are distributed evenly over the entire region; these may be mislocated because of low signal-to-noise ratio around the P-wave arrival time or may represent true diffuse seismicity.

4 Discussion

We have produced the first catalog of seismicity of the Kerguelen Islands covering a period of over 20 years (1999-2021). We have found clusters of events on either side of the Cook ice cap in the west of the island and others in the south-east of the island. All clusters lie on concentric circles around the seismic station PAF; these circles have narrow widths for the clusters close to the station and larger widths for those farther from the station. Such distributions are expected from the uncertainties inherent in single-station location methods.

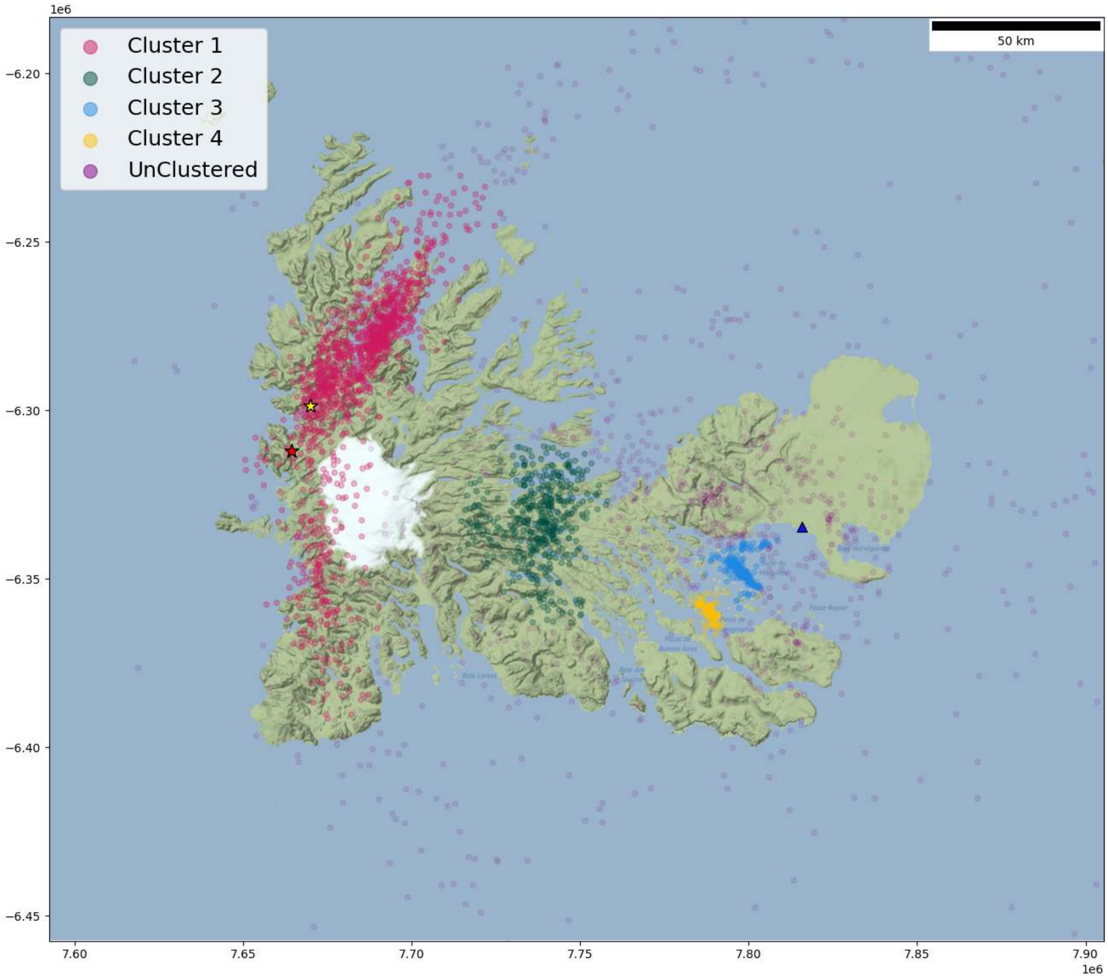

Figure 2 Map of all earthquakes located in this study (circles). Colored circles indicate earthquakes that belong to identified clusters (red: cluster 1, green: cluster 2, blue: cluster 3, yellow: cluster 4); purple circles indicate earthquakes do not belong to a cluster. The yellow star indicates our location of a M4.7 earthquake on October 6th, 2017; the same earthquake produced surface deformation visible from InSar and was located at the position of the red star (Raphael Grandin, personal communication). The blue triangle marks the location of the seismic station used in this study (PAF, Port aux Français). The white area shows the contour of the Cook ice cap.

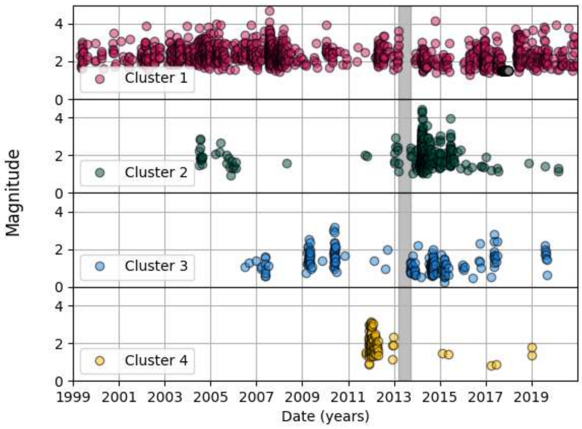

Figure 3 Magnitude of earthquakes as a function of time in each cluster. The color of each circle refers to its cluster. Gray circles indicate events that occurred during the time period in 2017 in which the broadband seismometer at PAF (Port aux Français) stopped functioning (no magnitude are available for these events and all magnitudes were fixed to 1.5). The gray background indicates time period when no instrument was recording.

Inferring the causal mechanism of earthquake clusters is notoriously difficult in regions of little to no tectonic deformation such as the Kerguelen main island. Some clusters are dominated by a single larger event at their onset (e.g. cluster 2) and exhibit a number of smaller events that decay over time in both size and frequency; these behave like mainshock-aftershock sequences whose amplitude and frequency follow Omori's law (Omori, 1895; Utsu et al., 1995), but give no indication of the causal mechanism for the mainshock itself. Other clusters lack a large event and exhibit an increased rate of earthquakes over a short time (e.g. clusters 3 and 4); these behave more like seismic swarms (Zhang and Shearer, 2016). Such swarms may be driven by fluids and are often encountered in volcanic environments or in other regions of the crust where pressurized fluids are present (e.g. De Barros et al., 2019; Duputel et al., 2019), however we lack, at present, geophysical evidence indicating that fluids are present at depth at the locations of these clusters. Another way to investigate if sub-surface mass (fluid) movements caused a particular seismic swarm is to identify signs of migration of the seismicity (Chen et al., 2012), however the uncertainties of our single-station locations are too large for us to perform this investigation. Deployment of a seismic network on the main island will help to constrain the depth and focal mechanisms of these earthquakes and will provide better location accuracy.

Among the possible explanations for the long-lived and nearly continuous seismicity in northwestern Kerguelen (cluster 1), we wish to draw attention to the elastic rebound caused by rapid melting of the Cook ice cap. The glacial wastage that has occurred over the last 60 years on Kerguelen is one of the fastest on Earth (Favier et al., 2016). After a stable period between the 1800s

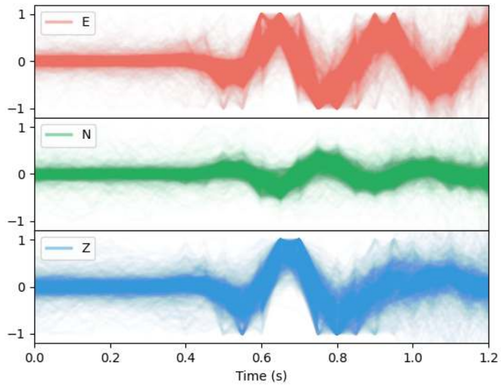

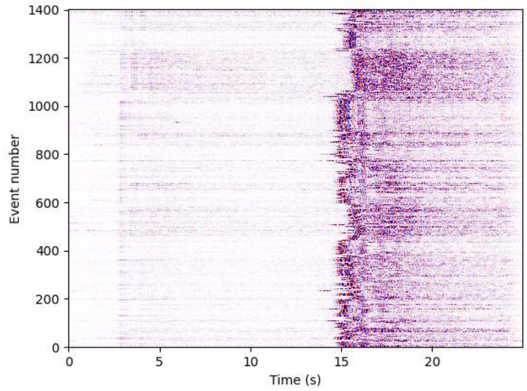

Figure 4 Top: Superposition of seismograms of all events located in cluster 1. The seismograms are windowed around the P-wave arrival on the three components (E: East, N: North and Z: vertical). Bottom: Waveforms recorded on the East component for all seismograms of cluster 1. Events are ordered chronologically and amplitude are normalized for each event. All seismograms have been aligned on the P-wave arrival. We observe that the P-wave pulses are coherent for all events of the cluster and that the S-P time is nearly identical as well.

and the 1960s (Frenot et al., 1993), the Cook ice cap retreated rapidly, losing 20% of its surface area in 40 years (Berthier et al., 2009). During this time, the ice retreat accelerated from 1.9 km^2/year between 1963 and 1991 to 3.6 km^2/year between 1991 and 2003, equivalent to a thinning rate of 1.4-1.7 m/year which is still measured today (Favier et al., 2016). Such rapid ice wastage abruptly reduces the vertical stresses previously imposed by the weight of the ice and causes immediate elastic rebound of the lithosphere, associated with flexural stress, crustal uplift, faulting, and seismicity (e.g. Stein et al., 1989; Stewart et al., 2000). Ice wasting can decrease the pressure on shallow magma reservoirs and increase melting within them, as seems to be occurring in regions of Iceland's rift zone that are subject to glacial unloading (Sigmundsson et al., 2010). Ice retreat also influences stress conditions in shallow magma chambers and hence modifies their failure conditions and promotes dike intrusions (underground mass transfers) that can trigger seismic swarms (Albino et al., 2010).

Although it is unknown if the Kerguelen main island has a shallow magma reservoir that could be influenced in this way by melting of the Cook ice cap, recent observations of crustal deformation indicate ongoing uplift over the western part of the archipelago, possibly linked to elastic rebound (Raphael Grandin, personal communication). We propose that the ice-wasting scenario may explain part if not all of the recent seismicity that surrounds the Cook ice cap, by a combination of flexural stresses, melt generation, and mass transfers at shallow depth.

5 Conclusion

Our analysis of the seismicity of the Kerguelen Islands with a single seismic station, over more than 20 years, revealed that the islands host significant seismic activity. This activity is temporally heterogeneous: in some regions it exhibits swarm-like behavior ; in others, such as the main active zone northwest of the Cook ice cap, it appears continuous over the full time extent of our study. As the Kerguelen Islands are located far from any plate boundary, we tentatively explain their persistent recent seismicity by the combination of flexural stress and the promotion of a magmatic activity, both caused by the unloading resulting from the ice wastage of the Cook ice cap over the recent years. Documenting the depth of these earthquakes, their focal mechanisms and the sign of possible migration would help to refine our understanding of this activity but would require the installation of temporary network close to the active regions.

Acknowledgments

The authors thank Frichnel W. Mamfoumbi for her manual picking work which started this study. The authors also thank Armelle Bernard, Jean-Yves Thoré, and Maxime Bès De Berc who, through their dedication to maintain PAF station, make it possible to coherently analyze seismological data spanning several decades. We also thank A. Reading and an anonymous reviewer for their numerous suggestions. The GEOSCOPE PAF station in Kerguelen Island is managed with support from the French Polar Institute (IPEV) under Program Number 133 "Global Seismological Observatory (SISMOLOGIE/OBS)".

Data and code availability

All data from the GEOSCOPE PAF station are available through FDSN webservices on RESIF data center https://seismology.resif.fr/networks/#/G/PAF. All of the data recovery and some processing have been done using the Obspy python package (Krischer et al., 2015). Some figures have been created with the GMT software (Wessel et al., 2013). The catalog of located earthquakes is available on Zenodo (Lengliné et al., 2023).

Competing interests

The authors have no competing interests.

References

Adams, R. and Zhang, B. A further earthquake on the Kerguelen Plateau. *Geophysical Journal International*, 79(2):697–703, 1984. doi: 10.1111/j.1365-246X.1984.tb02248.x.

Albino, F., Pinel, V., and Sigmundsson, F. Influence of surface load variations on eruption likelihood: application to two Icelandic subglacial volcanoes, Grímsvötn and Katla. *Geophysical journal international*, 181(3):1510–1524, 2010. doi: 10.1111/j.1365-246X.2010.04603.x.

Antonioli, A., Cocco, M., Das, S., and Henry, C. Dynamic stress triggering during the great 25 March 1998 Antarctic Plate earthquake. *Bulletin of the Seismological Society of America*, 92(3): 896–903, 2002. doi: 10.1785/0120010164.

Ballestracci, R. and Nougier, J. Detection by infrared thermography and modelling of an icecapped geothermal system in Kerguelen archipelago. *Journal of volcanology and geothermal research*, 20(1-2):85–99, 1984. doi: 10.1016/0377-0273(84)90067-2.

Bergman, E. A., Nábělek, J. L., and Solomon, S. C. An extensive region of off-ridge normal-faulting earthquakes in the southern Indian Ocean. *Journal of Geophysical Research: Solid Earth*, 89 (B4):2425–2443, 1984. doi: 10.1029/JB089iB04p02425.

Berthier, E., Le Bris, R., Mabileau, L., Testut, L., and Rémy, F. Ice wastage on the Kerguelen Islands (49 S, 69 E) between 1963 and 2006. *Journal of Geophysical Research: Earth Surface*, 114(F3), 2009. doi: 10.1029/2008JF001192.

Charvis, P., Recq, M., Operto, S., and Brefort, D. Deep structure of the northern Kerguelen Plateau and hotspot-related activity. *Geophysical Journal International*, 122(3):899–924, 1995. doi: 10.1111/j.1365-246X.1995.tb06845.x.

Chen, X., Shearer, P., and Abercrombie, R. Spatial migration of earthquakes within seismic clusters in Southern California: Evidence for fluid diffusion. *Journal of Geophysical Research: Solid Earth*, 117(B4), 2012. doi: 10.1029/2011JB008973.

Coffin, M. F., Pringle, M., Duncan, R., Gladczenko, T., Storey, M., Müller, R., and Gahagan, L. Kerguelen hotspot magma output since 130 Ma. *Journal of petrology*, 43(7):1121–1137, 2002. doi: 10.1093/petrology/43.7.1121.

De Barros, L., Baques, M., Godano, M., Helmstetter, A., Deschamps, A., Larroque, C., and Courboulex, F. Fluid-induced swarms and coseismic stress transfer: A dual process highlighted in the aftershock sequence of the 7 April 2014 earthquake (Ml 4.8, Ubaye, France). *Journal of Geophysical Research: Solid Earth*, 124(4): 3918–3932, 2019. doi: 10.1029/2018JB017226.

DeMets, C., Gordon, R. G., and Argus, D. F. Geologically current plate motions. *Geophysical journal international*, 181(1):1–80, 2010. doi: 10.1111/j.1365-246X.2009.04491.x.

Duputel, Z., Lengliné, O., and Ferrazzini, V. Constraining spatiotemporal characteristics of magma migration at Piton de la Fournaise volcano from pre-eruptive seismicity. *Geophysical Research Letters*, 46(1):119–127, 2019. doi: 10.1029/2018GL080895.

Ester, M., Kriegel, H.-P., Sander, J., Xu, X., et al. A density-based algorithm for discovering clusters in large spatial databases with noise. In *kdd*, volume 96, pages 226–231, 1996.

Favier, V., Verfaillie, D., Berthier, E., Menegoz, M., Jomelli, V., Kay, J., Ducret, L., Malbéteau, Y., Brunstein, D., Gallée, H., et al. Atmospheric drying as the main driver of dramatic glacier wastage in the southern Indian Ocean. *Scientific Reports*, 6(1):1–12, 2016. doi: 10.1038/srep32396.

Frenot, Y., Gloaguen, J., Picot, G., Bougère, J., and Benjamin, D. Azorella selago Hook. used to estimate glacier fluctuations and climatic history in the Kerguelen Islands over the last two centuries. *Oecologia*, 95(1):140–144, 1993. doi: 10.1007/BF00649517.

Gagnevin, D., Ethien, R., Bonin, B., Moine, B., Féraud, G., Gerbe, M.-C., Cottin, J.-Y., Michon, G., Tourpin, S., Mamias, G., et al. Open-system processes in the genesis of silica-oversaturated alkaline rocks of the Rallier-du-Baty Peninsula, Kerguelen Archipelago (Indian Ocean). *Journal of volcanology and geothermal research*, 123(3-4):267–300, 2003. doi: 10.1016/S0377-0273(02)00509-7.

Giret, A. Typology, evolution, and origin of the Kerguelen plutonic series, Indian Ocean: a review. *Geological Journal*, 25(3-4): 239–247, 1990. doi: 10.1002/gj.3350250307.

Gregoire, M., Jackson, I., O'Reilly, S., and Cottin, J. The lithospheric mantle beneath the Kerguelen Islands (Indian Ocean): petrological and petrophysical characteristics of mantle mafic rock types and correlation with seismic profiles. *Contributions to Mineralogy and Petrology*, 142(2):244–259, 2001. doi: 10.1007/s004100100289.

Heimann, S., Kriegerowski, M., Isken, M., Cesca, S., Daout, S., Grigoli, F., Juretzek, C., Megies, T., Nooshiri, N., Steinberg, A., et al. Pyrocko-An open-source seismology toolbox and library. 2017. doi: 10.5880/GFZ.2.1.2017.001.

Institut de physique du globe de Paris (IPGP) and École et Observatoire des Sciences de la Terre de Strasbourg (EOST). GEOSCOPE, French Global Network of broad band seismic stations. 1982. doi: 10.18715/GEOSCOPE.G.

Jiang, Q., Jourdan, F., Olierook, H. K., Merle, R. E., and Whittaker, J. M. Longest continuously erupting large igneous province driven by plume-ridge interaction. *Geology*, 49(2):206–210, 10 2020. doi: 10.1130/G47850.1.

Krischer, L., Megies, T., Barsch, R., Beyreuther, M., Lecocq, T., Caudron, C., and Wassermann, J. ObsPy: A bridge for seismology into the scientific Python ecosystem. *Computational Science & Discovery*, 8(1):014003, 2015. doi: 10.1088/1749-4699/8/1/014003.

Kumar, P., Yuan, X., Kumar, M. R., Kind, R., Li, X., and Chadha, R. The rapid drift of the Indian tectonic plate. *Nature*, 449(7164): 894–897, 2007. doi: 10.1038/nature06214.

Lengliné, O., Rimpôt, J., Maggi, A., and Zigone, D. Catalog of Seismicity for the Kerguelen Islands (1999-2020), Sept. 2023. doi: 10.5281/zenodo.8328841.

Lough, A. C., Wiens, D. A., and Nyblade, A. Reactivation of ancient Antarctic rift zones by intraplate seismicity. *Nature Geoscience*, 11(7):515–519, 2018. doi: 10.1038/s41561-018-0140-6.

Mousavi, S. M., Ellsworth, W. L., Zhu, W., Chuang, L. Y., and Beroza, G. C. Earthquake transformer—an attentive deep-learning model for simultaneous earthquake detection and phase picking. *Nature communications*, 11(1):1–12, 2020. doi: 10.1038/s41467-020-17591-w.

Okal, E. A. Intraplate seismicity of Antarctica and tectonic implications. *Earth and planetary science letters*, 52(2):397–409, 1981. doi: 10.1016/0012-821X(81)90192-8.

Okal, E. A. Oceanic intraplate seismicity. *Annual Review of Earth and Planetary Sciences*, 11(1):195–214, 1983. doi: 10.1146/annurev.ea.11.050183.001211.

Omori, F. On the After-shocks of Earthquakes. *The journal of the College of Science, Imperial University, Japan*, 7:111–200, 1895.

Reading, A. M. On seismic strain-release within the Antarctic Plate. In *Antarctica*, pages 351–355. Springer, 2006. doi: 10.1007/3-540-32934-X_43.

Reading, A. M. The seismicity of the Antarctic plate. In *Continental Intraplate Earthquakes: Science, Hazard, and Policy Issues*. Geological Society of America, 01 2007. doi: 10.1130/2007.2425(18).

Recq, M., Brefort, D., Malod, J., and Veinante, J.-L. The Kerguelen Isles (southern Indian Ocean): new results on deep structure from refraction profiles. *Tectonophysics*, 182(3-4):227–248, 1990. doi: 10.1016/0040-1951(90)90165-5.

Recq, M., Roy, I. L., Charvis, P., Goslin, J., and Brefort, D. Structure profonde du mont Ross d'après la réfraction sismique (îles Kerguelen, océan Indien austral). *Canadian Journal of Earth Sciences*, 31(12):1806–1821, 1994. doi: 10.1139/e94-161.

Richter, C. F. An instrumental earthquake magnitude scale. *Bulletin of the Seismological Society of America*, 25(1):2–32, January 1935. doi: 10.1785/BSSA0250010001.

Roberts, R., Christoffersson, A., and Cassidy, F. Real-time event detection, phase identification and source location estimation using single station three-component seismic data. *Geophysical Journal International*, 97(3):471–480, 1989. doi: 10.1111/j.1365-246X.1989.tb00517.x.

Sigmundsson, F., Pinel, V., Lund, B., Albino, F., Pagli, C., Geirsson, H., and Sturkell, E. Climate effects on volcanism: influence on magmatic systems of loading and unloading from ice mass variations, with examples from Iceland. *Philosophical Transactions of the Royal Society A: Mathematical, Physical and Engineering Sciences*, 368(1919):2519–2534, 2010. doi: 10.1098/rsta.2010.0042.

Steffen, H. and Wu, P. Glacial isostatic adjustment in Fennoscandia—a review of data and modeling. *Journal of geodynamics*, 52 (3-4):169–204, 2011. doi: 10.1016/j.jog.2011.03.002.

Stein, S., Cloetingh, S., Sleep, N. H., and Wortel, R. Passive margin earthquakes, stresses and rheology. In *Earthquakes at North-Atlantic passive margins: Neotectonics and postglacial rebound*, pages 231–259. Springer, 1989. doi: 10.1007/978-94-009-2311-9_14.

Stephenson, J., Budd, G., Manning, J., and Hansbro, P. Major eruption-induced changes to the McDonald Islands, southern Indian Ocean. *Antarctic Science*, 17(2):259–266, 2005. doi: 10.1017/S095410200500266X.

Stewart, I. S., Sauber, J., and Rose, J. Glacio-seismotectonics: ice sheets, crustal deformation and seismicity. *Quaternary Science Reviews*, 19(14):1367–1389, 2000. doi: https://doi.org/10.1016/S0277-3791(00)00094-9.

Utsu, T., Ogata, Y., et al. The centenary of the Omori formula for a decay law of aftershock activity. *Journal of Physics of the Earth*, 43(1):1–33, 1995. doi: 10.4294/jpe1952.43.1.

Wessel, P., Smith, W. H., Scharroo, R., Luis, J., and Wobbe, F. Generic mapping tools: improved version released. *Eos, Transactions American Geophysical Union*, 94(45):409–410, 2013. doi: 10.1029/98EO00426.

Wiens, D. A. and Stein, S. Intraplate seismicity and stresses in young oceanic lithosphere. *Journal of Geophysical Research: Solid Earth*, 89(B13):11442–11464, 1984. doi: 10.1029/JB089iB13p11442.

Zhang, Q. and Shearer, P. M. A new method to identify earthquake swarms applied to seismicity near the San Jacinto Fault, California. *Geophysical Journal International*, 205(2):995–1005, 2016. doi: 10.1093/gji/ggw073.

doi:10.26443/seismica.v2i2.272

SEISMICA

Seismic Architecture of the Lithosphere-Asthenosphere System in the Western United States from a Joint Inversion of Body- and Surface-wave Observations: Distribution of Partial Melt in the Upper Mantle

J. S. Byrnes * [1], **J. B. Gaherty** [1,2], **E. Hopper** [2]

[1]School of Earth and Sustainability, Northern Arizona University, Flagstaff, AZ, USA, [2]Lamont-Doherty Earth Observatory, Columbia University New York, NY, USA

Author contributions: *Conceptualization*: E. Hopper, J. S. Byrnes, J. B. Gaherty. *Methodology*: E. Hopper, J. S. Byrnes, J. B. Gaherty. *Formal Analysis*: J. S. Byrnes, J. B. Gaherty, E. Hopper. *Writing - original draft*: J. S. Byrnes, J. B. Gaherty, E. Hopper.

Abstract Quantitative evaluation of the physical state of the upper mantle, including mapping temperature variations and the possible distribution of partial melt, requires accurately characterizing absolute seismic velocities near seismic discontinuities. We present a joint inversion for absolute but discontinuous models of shear-wave velocity (Vs) using 4 types of data: Rayleigh wave phase velocities, P-to-s receiver functions, S-to-p receiver functions, and Pn velocities. Application to the western United States clarifies where upper mantle discontinuities are lithosphere-asthenosphere boundaries (LAB) or mid-lithospheric discontinuities (MLD). Values of Vs below 4 km/s are observed below the LAB over much of the Basin and Range and below the edges of the Colorado Plateau; the current generation of experimentally based models for shear-wave velocity in the mantle cannot explain such low Vs without invoking the presence of melt. Large gradients of Vs below the LAB also require a gradient in melt-fraction. Nearly all volcanism of Pleistocene or younger age occurred where we infer the presence of melt below the LAB. Only the ultrapotassic Leucite Hills in the Wyoming Craton lie above an MLD. Here, the seismic constraints allow for the melting of phlogopite below the MLD.

Production Editor:
Gareth Funning
Handling Editor:
Catherine Rychert
Copy & Layout Editor:
Hannah F. Mark

Received:
November 8, 2022
Accepted:
July 24, 2023
Published:
August 29, 2023

Non-technical summary Constraints from seismology on the structure of the lithosphere-asthenosphere system often come from one of two types of observations, surface wave tomography or receiver function analysis. Surface wave tomography gives smooth models of absolute velocities, while receiver functions give relative constraints on velocities across abrupt boundaries. This study develops a joint inversion of the two types of constraints for structure in the upper mantle. With jointly constrained velocity models for the Western United States, we infer that shear-wave velocities are too low to be explained without invoking the presence of melt below the lithosphere-asthenosphere boundary beneath much of the area surrounding the Colorado Plateau. The distribution of melt in the asthenosphere agrees well with the distribution of young volcanism in the study area, with the most significant outlier being a volcanic field with anomalous compositions.

1 Introduction

The state of Earth's asthenosphere exerts a fundamental control on the tectonic and magmatic evolution of the crust and lithosphere. The asthenosphere is a rheologically weak layer beneath the lithospheric plates, with ambient temperatures near or above the solidus for silicate melting in a peridotite mantle. The low viscosities facilitate a wide range of advection processes that deliver heat and stress to the overriding plate, and the production, accumulation, and subsequent removal of partial melt drives volcanic and plutonic processes at plate-boundary and intraplate settings. In detail, the rheology of the asthenosphere likely depends strongly on the presence and distribution of melt, which is inferred to weaken mantle rocks at both geological and seismic time scales as it accumulates on interstitial grain boundaries (e.g. Hammond and Humphreys, 2000; Takei, 2002; Holtzman, 2016; Chantel et al., 2016; Takei and Holtzman, 2009). However, due to tradeoffs and uncertainty between the effects of melt, temperature, volatile content, and grain size on the seismic and other geophysical properties of the mantle, detailed quantification of the distribution of partial melt in Earth's mantle remains elusive.

Over the past decade, significant progress has been made in estimating the state of the asthenosphere beneath the diverse tectonic physiography of the western United States (Fig 1). This progress has been enabled by the deployment of EarthScope's USArray, which blanketed the continental US with seismic observations of sufficient density to resolve crustal and upper-mantle structure on length scales as small as 100 km, comparable to length scales of major tectonic features and boundaries, including mountain belts and vol-

*Corresponding author: joseph.byrnes@nau.edu

canic fields. This allows for accurate quantification of seismic characteristics at depths that can be directly compared to surface observations derived from geology and geochemistry (e.g. Plank and Forsyth, 2016; Porter and Reid, 2021). In particular, two imaging approaches have emerged that provide distinct but complementary constraints on crustal and upper-most mantle structure. Array-based surface-wave phase velocities provide excellent constraints on three-dimensional variations in absolute velocities in the upper mantle (e.g. Lin and Ritzwoller, 2011; Jin and Gaherty, 2015; Ekström, 2017), key for quantifying melt in the asthenosphere and its impact on overlying lithospheric structure. However, surface waves lack the ability to constrain abrupt velocity changes laterally or with depth, and surface-wave images contain strong trade-offs between reducing the model misfit and geologically reasonable but ad hoc constraints such as model smoothness and model length. Common-conversion-point (CCP) images of S-to-p converted phases (receiver functions) provide critical data on abrupt changes in velocity with depth (e.g. Kawakatsu et al., 2009; Rychert et al., 2007; Levander and Miller, 2012; Lekić and Fischer, 2014; Hansen et al., 2015; Liu and Shearer, 2021), including quantifying the change in physical characteristics across major boundaries within the lithosphere-asthenosphere system in two dimensions. These observations lack sensitivity to absolute velocity, however, making it difficult to quantitatively interpret them in the context of temperature, melt content, or other state variables. For example, S-to-p images of the upper mantle often produce sharp negative velocity gradients (NVGs) within the upper mantle (a negative gradient is defined as a decrease in seismic velocity with increasing depth). NVGs are often interpreted as the lithosphere-asthenosphere boundary (LAB) (e.g. Kawakatsu et al., 2009; Rychert et al., 2005, 2007; Kumar et al., 2012; Levander and Miller, 2012; Lekić and Fischer, 2014), but in some cases NVGs clearly fall within the lithosphere and are interpreted as a mid-lithospheric discontinuity (MLD) (e.g. Abt et al., 2010; Ford et al., 2010, 2016; Fischer et al., 2010) of widely debated origin (Hansen et al., 2015; Selway et al., 2015; Saha et al., 2021; Karato et al., 2015; Helffrich et al., 2011). Distinguishing between these interpretations requires additional information to constrain temperature, such as absolute velocities.

The joint inversion of surface waves and receiver functions merges the best attributes of each technique: constraints on absolute velocities from surface waves with rapid transitions in velocity with depth resolved by receiver functions. Thus, much more confident interpretations of the resulting structures are possible: accurate absolute velocities both above and below an NVG enable a more explicit interpretation than is possible from each observation independently. Joint inversions of surface wave and receiver function data are now quite common. Primarily, these efforts consist of joint inversion of P-to-s converted wave data to better constrain crustal thickness (e.g. Chai et al., 2015; Delph et al., 2015; Schmandt et al., 2015; Shen and Ritzwoller, 2016; Delph et al., 2018). More recently, inversions incorporating S-to-p conversions have improved quantitative velocity estimates across upper mantle discontinuities such as the LAB (e.g. Bodin et al., 2016; Eilon et al., 2018). These localized inversions model the full receiver function at individual stations, and a benefit of these inversions is their lack of imposed constraints; however, this can lead to complex velocity models that vary considerably between stations and can be difficult to explain geologically.

In this paper we present an alternative joint inversion of surface wave and receiver function data that takes advantage of our geological intuition. We think of the upper 400 km of the earth as a layered structure, with a crust overlying a strong high-velocity lithosphere, which in turn overlies a lower-velocity asthenosphere. Previous studies of receiver functions provide spatially coherent sets of data that define the layering, specifically the depth to (or more accurately, the travel time to) and magnitude of abrupt velocity changes, including the Moho and (in many regions) the lithosphere-asthenosphere boundary. Surface-wave dispersion constrains the absolute shear velocities within this layered framework. The resulting 3-D layered velocity model provides new constraints on the absolute velocity at the top of the asthenosphere, enabling unique quantitative estimates of partial melting in the upper mantle.

2 Tectonic Background

To first order, the continental United States can be divided into a tectonically stable (cratonic) eastern half, and a western half characterized by active and/or recent tectonic deformation. The crust and upper mantle in the active western US has long been observed to be seismically distinct from the stable east, with lower seismic velocity and high seismic attenuation in the upper mantle suggesting higher temperatures and the presence of partial melting (e.g. Grand and Helmberger, 1984; Humphreys and Dueker, 1994; Pakiser, 1963; Solomon, 1972), which also correlate with higher elevations and heat flow relative to the eastern continent. The western half can be further subdivided into provinces that feature distinct magmatic and tectonic activity. USArray and similar regional broadband deployments enable a detailed characterization of the subsurface on small regional scales. Fig 1 highlights the major provinces and geologic features that we focus on here.

The eastern edge of our study region captures the western portion of stable North America (SNA), which primarily consists of Archean and Proterozoic basement overlain by Phanerozoic sedimentation (Whitmeyer and Karlstrom, 2007). Upper-mantle seismic wavespeeds in the area are high (e.g. Schmandt and Humphreys, 2010; Shen and Ritzwoller, 2016; Porter et al., 2016), and NVGs are usually interpreted as an MLD (e.g. Hopper and Fischer, 2018). Abutting the stable platform to the west are high-standing mountain ranges and moderately deformed plateaus that were uplifted during the widespread Laramide orogeny from the late Mesozoic to the early Cenozoic, including the modern Rocky Mountains, the Archean-cored Wyoming province, and the Proterozoic-cored Colorado Plateau (CP). Subsequent to Laramide uplift, the Wyoming Craton returned to relative quiescence (Humphreys et al., 2015), and the subsurface is characterized by moderately thick, high-velocity lithosphere (Shen and Ritzwoller, 2016; Porter et al., 2019; Xie et al., 2018). In contrast, from the mid-Cenozoic onwards, volcanism and modest extension have encroached from the Basin and Range towards the center of the CP (Roy et al., 2009; Crow et al., 2011), creating a plateau "transition zone" along the western and southern borders with the Basin and Range that is characterized in the subsurface as highly thinned lithosphere underlain by anomalous hot asthenosphere (Schmandt and Humphreys, 2010; Levander et al., 2011; Shen and Ritzwoller, 2016; Porter et al., 2019; Golos and Fischer, 2022). These features are absent from the eastern side of the CP and the southern Rocky Mountains. Localized volcanic centers in the region can be highly voluminous (e.g. Marysvale volcanic center), and persist to recent times.

Further west and south lies the modern Basin and Range province (BR), interpreted to be a former high-standing orogenic plateau that underwent significant, wide-spread extensional collapse during the middle-to-late Cenozoic. Prior to extension, the region experienced a sweep of volcanic activity that is expressed primarily as widely distributed ignimbrite-producing calderas (Best et al., 2016). Today, the region is characterized by anomalous thin crust (e.g. Gilbert, 2012) and lithosphere (e.g. Lekić and Fischer, 2014; Hansen et al., 2015; Hopper and Fischer, 2018; Kumar et al., 2012; Levander and Miller, 2012) underlain by hot asthenosphere (Humphreys and Dueker, 1994; Plank and Forsyth, 2016; Porter and Reid, 2021). Volcanism in the region is highly distributed throughout the province, and persists to recent times. North of the BR, the Snake River Plain (SRP) stretches from the Yellowstone Hotspot to the High Lava Plains of central Oregon, and is characterized by voluminous surface volcanism that initiated at approximately 15 Ma and continues to the present. Seismic characterization of the subsurface suggests that the entire SRP is underlain by hot asthenosphere (e.g. Schmandt and Humphreys, 2010; Shen and Ritzwoller, 2016; Porter and Reid, 2021).

We limit this presentation to the region shown in Fig 1, which captures a rich diversity of tectonic environments while also avoiding subducting slabs and other plate-boundary complexity to the west and north (for example, see Schmandt and Humphreys, 2011) that may not be well described by the three-layer parameterization that we describe below.

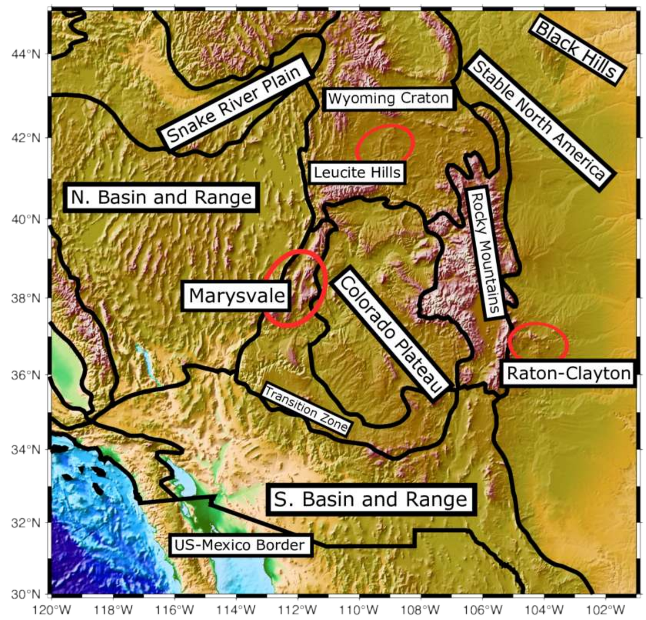

Figure 1 Major geologic, tectonic, and volcanic features in the study area. Black lines are, here and in subsequent figures, the physiographic provinces of Fenneman and Johnson (1946), with modifications described in the text. Red circles approximately demarcate select volcanic fields that are discussed in the text. White labels are names used for features in the main text.

3 Datasets

We construct profiles of seismic velocity from depths of 0 to 400 km by combining four published datasets with complementary sensitivity to structure. Each dataset is derived from seismic data recorded by the EarthScope USArray, including the Transportable Array (nominal background station spacing of 70 km) plus more densely spaced Flex Arrays and other regional data sets. In each case described below, we refer the reader to the relevant citations for the specific data utilized and methodological details.

3.1 Surface-wave phase velocities

We use the phase velocities of Rayleigh waves in three non-overlapping period bands from three studies. From 8 to 15 s, we use phase velocities from Ekström (2017). These phase velocities were estimated from ambient seismic noise using Aki's formula (Ekström et al., 2009; Ekström, 2014, 2017). From 20 to 100 s, we use the phase velocities of Jin and Gaherty (2015) derived from the cross-correlation of Rayleigh waves from teleseismic events, with Helmholtz tomography applied for correcting focusing effects (Lin and Ritzwoller, 2011). From 20 to 40 s, these data agree well with the ambient-noise results of Ekström (2017). We extend our phase velocity dataset over 120-180 s with the results of Babikoff and Dalton (2019), who used the cross-correlation methodology of Jin and Gaherty (2015). Maps of phase velocity at periods of 10, 60, and 120 s across our study area are shown in Fig 2, with periods chosen to show one map from each of our three sources. Uncertainties vary by period and are estimated in the referenced studies, varying from 0.025 to 0.097 km/s at 10 and 180 s, respectively.

3.2 P-to-s conversions from the Moho

Conversions of teleseismic P-to-s phases provide constraints on both the depth to and the contrast in seismic velocity across the Moho. While most P-to-s studies of the crust focus on constraining intracrustal properties, including Moho depth and Vp/Vs ratio (e.g., Gilbert, 2012), the study of Shen and Ritzwoller (2016) constrain both depth and contrast across the Moho by fitting the

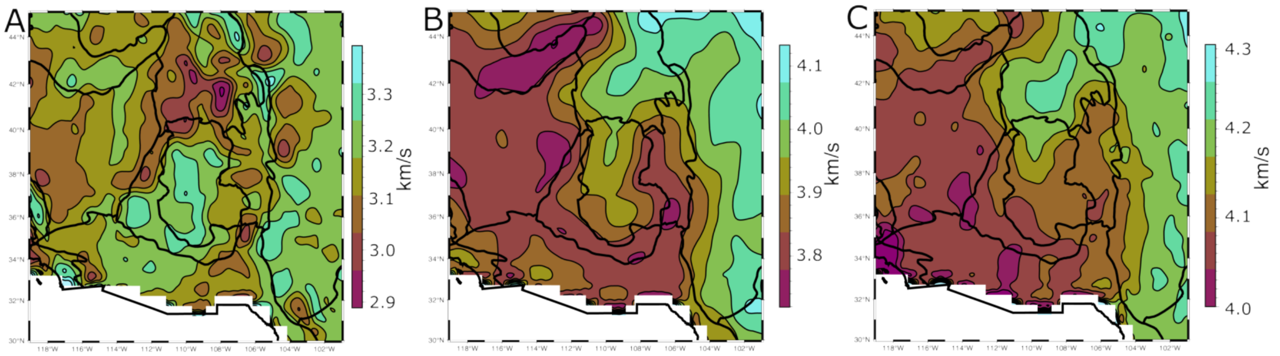

Figure 2 Phase velocities of Rayleigh waves at 10, 60, and 120 s in panels A, B, and C, respectively.

waveforms of the P-to-s receiver functions as part of a joint inversion along with the phase velocity, group velocity, and ellipticity of Rayleigh waves. Two constraints are extracted from the model of Shen and Ritzwoller (2016): first, a time to the Moho by calculating the travel time of a vertically propagating S wave from the surface to the Moho through the model, accounting for variations in the Vp/Vs ratios in the crust from Schmandt et al. (2015); and second, the contrast in velocity across the Moho from the difference in velocity directly above and below the discontinuity. Uncertainties for both quantities are directly calculated from errors given on Vs at each depth and are divided by a factor of 4 to convert from a standard deviation to a standard error (see section 4.2 of Shen and Ritzwoller (2016) for a discussion). We then apply a Gaussian filter with a width of 0.25° to both datasets to approximate the smoothness of the 20-32 s phase velocities, and the resulting datasets are shown in Fig 3a,b.

3.3 S-to-p conversions from an NVG

Travel times to and the velocity contrast (including uncertainties) across the NVG are provided by Hopper and Fischer (2018). A spatially varying Vp/Vs ratio in the crust from Schmandt et al. (2015) is used to convert from the observed S minus P times to S times for a vertically propagating wave, to match the type of constraint on the Moho described above. Converted-phase amplitudes are converted to a change in velocity over a specified width of the NVG (Supplementary section S1, and see Hopper and Fischer (2018) for details). The widths of the NVG are not directly observed in the original S-to-p receiver functions, but are imprecisely inferred from waveform modeling. We explore modifications to the width during the subsequent inversions and so consider the widths a different type of constraint than other data. Finally, we apply a Gaussian filter with a half-width of 0.5° to approximate the smoothness of the 50-100 s phase velocities to both datasets. The magnitude of the velocity contrast across the NVG ranges from 4-15% across the study area. Filtered travel times and velocity contrasts are shown in Fig 3c,d, respectively.

3.4 Pn velocities

The final dataset we use is the velocity of Pn phases taken from Buehler and Shearer (2017). Pn travels along the underside of the Moho, and we use the observed Pn velocity to derive a direct constraint on shear velocity just below the Moho. This requires an assumed Vp/Vs ratio for the shallow mantle, as well as an adjustment to account for anisotropic structure, as Pn phases are primarily sensitive to the P-wave velocity in the horizontal plane, Vph, while Rayleigh waves and phase conversions are primarily sensitive to the S-wave velocity in the vertical plane, Vsv. We assume a mean Vp/Vs ratio of 1.76 and correct for radial anisotropy assuming a $(Vsh/Vsv)^2$ of 1.04 (Clouzet et al., 2018) with the scaling relationships of Montagner and Anderson (1989). The estimated shear velocities for the upper-most mantle (immediately beneath the Moho) are shown in Fig 4. We assign a large uncertainty of 0.1 km/s to this constraint, which results in a weaker constraint on our final models than the other three datasets. This uncertainty is based on observed variations of sub-Moho Vp/Vs in the uppermost mantle for portions of the western United States (Buehler and Shearer, 2014), as well as the significant uncertainty in radial anisotropy at the relatively short (tectonic) scales represented here.

4 Joint Inversion Methodology

4.1 Inversion approach

Our philosophy in this inversion is to capitalize on the geological intuition that, to first order, the shallow velocity structure of the Earth can be described by three layers coinciding with the crust, lithospheric mantle, and asthenospheric mantle (with ambiguity in the terminology in the case of an MLD). Receiver function studies constrain the boundaries between these layers (Ps and Sp for the Moho and NVG, respectively) and phase velocities of surface waves provide constraints on the absolute velocities within the layers. Using a linearized least-squares approach, we invert these data for a set of one-dimensional shear velocity models at each point within a geographic grid with 0.25° spacing in both latitude and longitude. Within each layer, the shear velocity is constrained to behave smoothly. The thickness of the Moho and NVG are assumed a priori; the Moho jump is assumed to occur over 1 km, while the breadth of the NVG is taken from Hopper and Fischer (2018) and ranges from 10-50 km (Figure S1). Alternative choices for the width of the NVG are discussed below. By com-

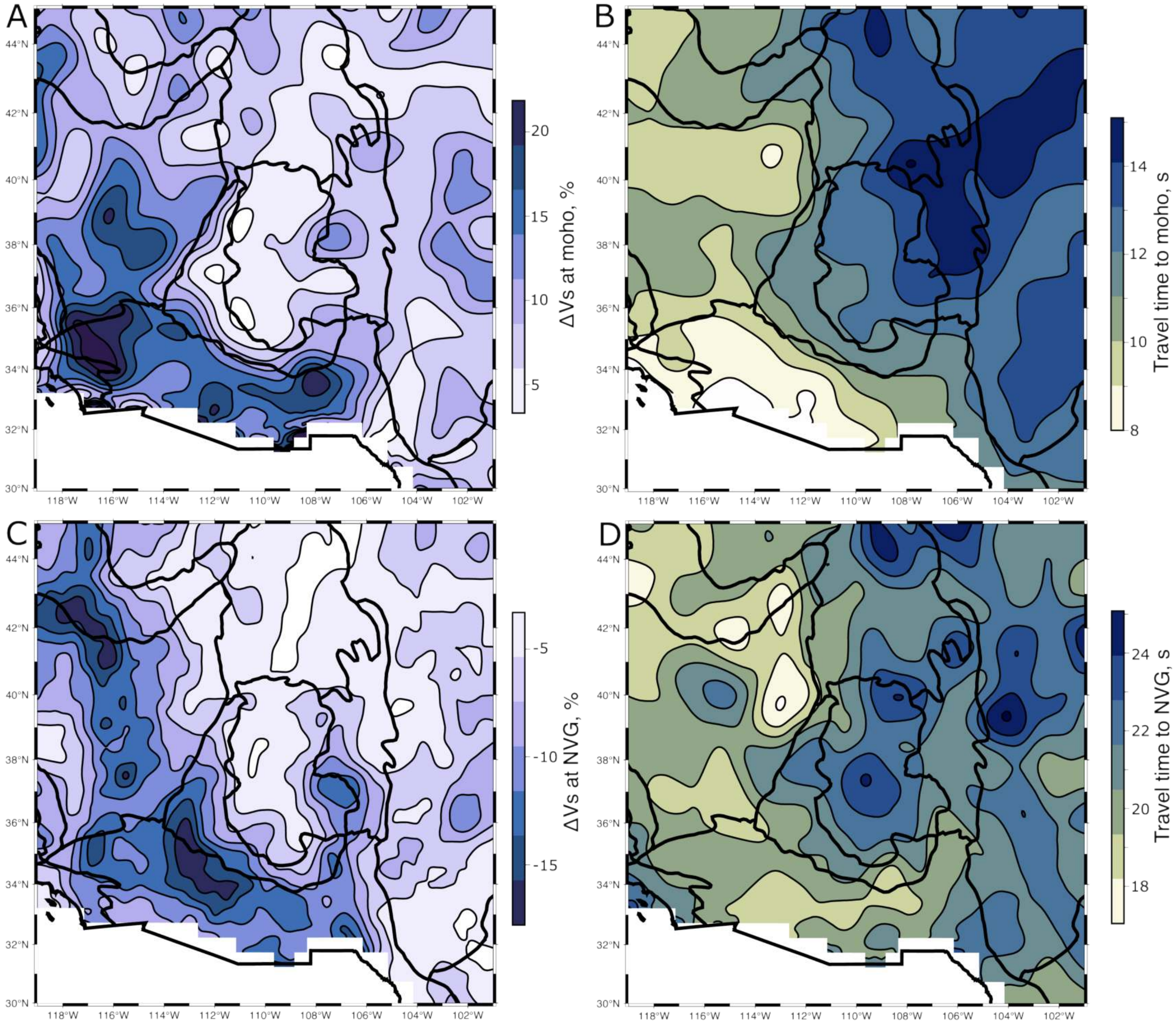

Figure 3 Constraints from converted phases. Panels on the top row are data describing the Moho and on the bottom row are data describing the NVG. The left-hand column shows contrasts in velocity with increasing depth in percentage relative to the shallower layer, and the right-hand column shows the travel time expressed as the travel time of a vertically propagating S wave from the mid-point of the discontinuity to the surface. The contrast in Vs across the NVG (panel C) depends on the breadth of the NVG (see Supplementary Section S1)

bining these one-dimensional profiles, we construct a three-dimensional, layered shear-velocity model for the region.

4.2 Model Parameterization

We define the model to be solved for (Fig 5) as

$$\boldsymbol{p} = [\boldsymbol{s}, \boldsymbol{t}] \tag{1}$$

where s is a vector of vertically polarized shear wave velocities (Vsv) defined at fixed depths, and t is a vector of the thicknesses of layers above discontinuities in the model, in this application corresponding to the crust and the mantle layer above the NVG (Fig 5). These abrupt boundaries are not explicit discontinuities in velocity (the Moho has a width of 1 km, and the NVG has variable width), but to simplify the terminology we call them “discontinuities” in the following discussion. The model is constructed such that the top and bottom of each discontinuity corresponds explicitly to an element of s. In the layers above and below the discontinuities, an integer number of elements in s is chosen so that the spacing between elements is greater than 6 km or so that there are at least 5 elements. The number of elements in s in a given layer may update when the elements of t change. Linear gradients in Vsv are assumed between each point in s. The shear-velocity models presented here utilize 67-72 parameters at each location: the two values of t and 65-70 values of s as a function of depth z. We initialize the inversion using a starting model constructed with velocities above a depth 150 km taken from Shen and Ritzwoller (2016), and velocities from 150-410 km depth taken from PREM (Dziewonski and Anderson, 1981). In all cases investigated, both with

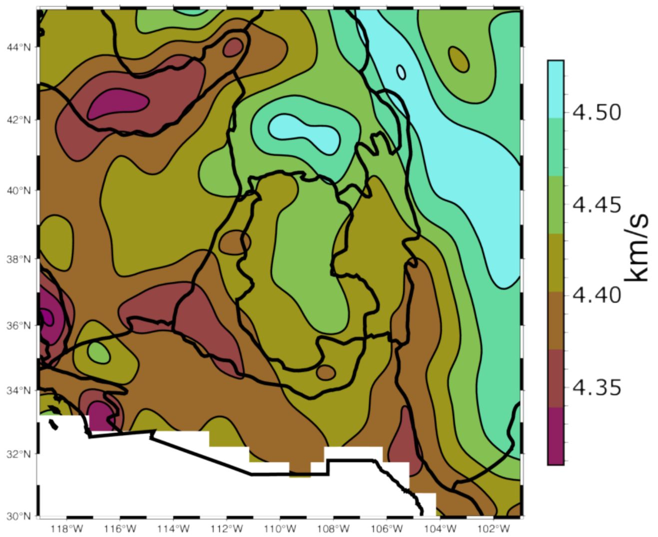

Figure 4 Shear-wave velocity at the top of the mantle as estimated from Pn tomography. See text for details.

synthetic and real data, the final model was found to be essentially independent of the starting model.

The Gauss-Newton method is used to find a model of this form that adequately fits each dataset under regularization. Partial derivatives between the observations and model parameters are found with MINEOS and directly from the geometry of the model (boxed equations in Fig 5, for the surface and body wave observations, respectively. MINEOS is executed on a constant grid (purple in Fig 5), and the inverse model must be related to this intermediate structure. Details are given in the Appendix.

4.3 Uncertainties on parameters from the recovery of synthetic models

We assess the resolving power of the data and inversion by attempting to recover known velocity models. We first invert two velocity profiles to evaluate the relative importance of the different observations used in this study for accurately characterizing key components of the lithosphere-asthenosphere system. For these two tests, noise is not added to the synthetic data, and the thickness of the Moho and NVG are 1 and 10 km, respectively. The first model (black line in Fig 6a) features a nearly linear gradient above the Moho, a moderate negative gradient with some curvature below the Moho, and a large NVG. The second model (black line in Fig 6b) features stronger curvature in the crust with a steep slope above the Moho, a steep negative slope below the Moho, and a lower minimum Vs below the NVG. When these two models are inverted with only the surface wave and P-to-s constraints (yellow models in Fig 6), the crust is reasonably well reconstructed, but the layered structure in the mantle is not accurately recovered. At the depth where the minimum Vs is reached in the input models, Vs is overestimated by 0.2 and 0.4 km/s, and the steepness of the gradient in Vs is underestimated both above and below the NVG. Adding constraints from S-to-p converted phases leads to an excellent recovery of the first model at all depths, and the inclusions of the head-wave velocities does not noticeably affect the outcome. For the second model, however, the head waves are necessary to properly estimate the gradient below the Moho, which leads to an improvement in recovery both above and below the NVG. Crustal structure - and not mantle structure - appears to be the primary control on whether the slope below the Moho can be recovered without the head waves (Supplementary Section S2). We conclude that all four datasets are necessary to accurately describe the upper mantle, with the head-waves supplying the least information.

To further evaluate the modeling approach and to quantify uncertainties for key model characteristics, we generate 500 random velocity models (Supplementary Section S3), add noise to synthetic data predicted for each model (see Section 2 for the uncertainties on each dataset), invert, and compare the resulting model with the input model. We seek to quantify the recovery of several key parameters of the layered models: the depths to a Moho and an NVG; the shear-velocity contrast across the Moho and NVG; the shear-wave velocity immediately above and below the Moho, and immediately above and below the NVG; and the slope of the shear-wave velocity within 10-km above the Moho, between the Moho and the NVG, and within 50-km below the NVG. We attempted to recover the second derivative of shear velocity within the layers but conclude that the data lacks a strong intrinsic constraint on the curvature of the velocities in any of the three layers (Fig 6). Table 1 quantifies our ability to accurately recover these key parameters, in the form of the standard deviation of the difference between the input and recovered parameters in this test. Since we have not utilized data with direct constraints on shallow crustal structure, we do not interpret values in the upper half of the crust.

Parameter, units	Standard deviation
Depth to Moho, km	2.5
ΔVs at Moho, %	1.6
Depth to NVG, km	2.2
ΔVs at NVG, %	0.84
Vs, above the Moho, km/s	0.10
Vs, below the Moho, km/s	0.11
Vs, above the NVG, km/s	0.1
Vs, below the NVG, km/s	0.08
∂Vs/∂z, <10 km above the Moho, (km/s)/km	1.1×10^{-3}
∂Vs/∂z, between the Moho and NVG, (km/s)/km	6.2×10^{-3}
∂Vs/∂z, <50 below the NVG, (km/s)/km	2.8×10^{-3}

Table 1 Errors on specific features, based on the inversions of many synthetic models

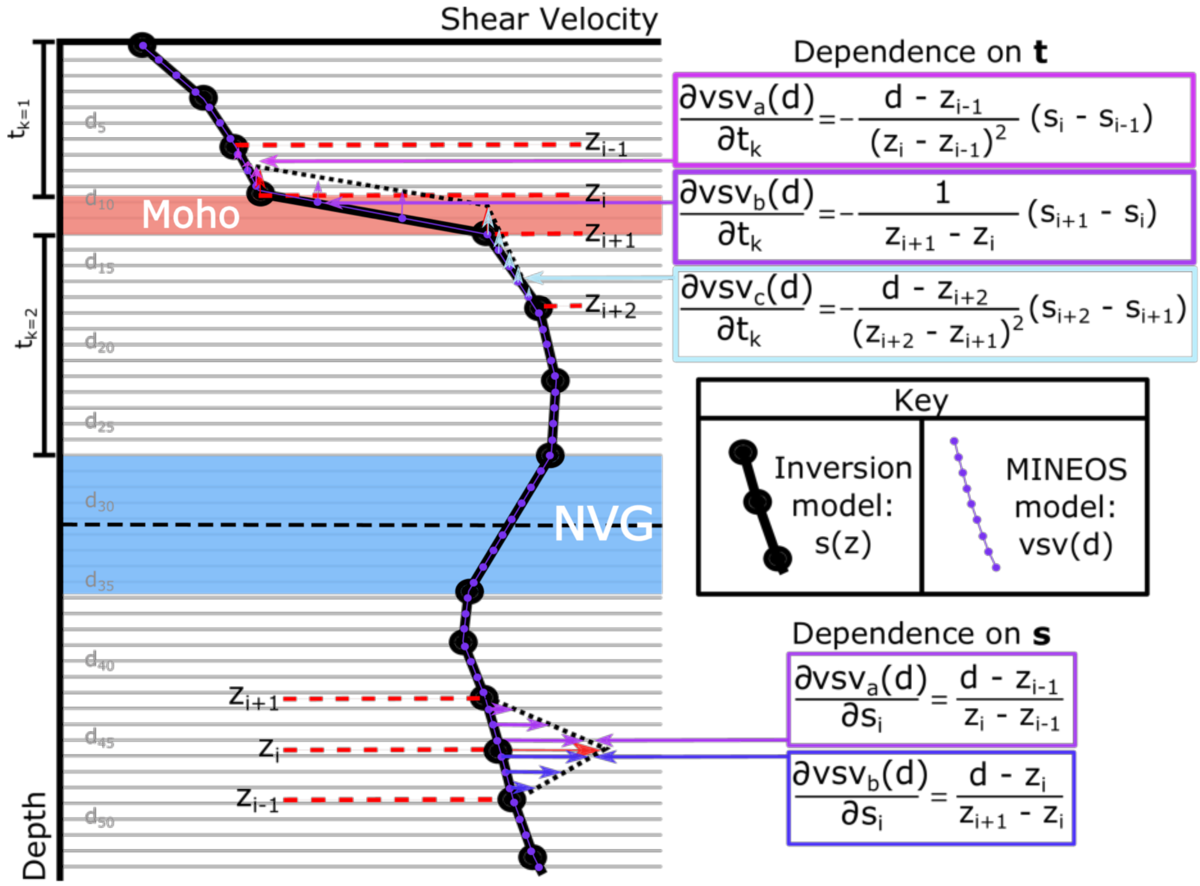

Figure 5 Cartoon showing the parameterization of the models and the relationship between the inversion model (parameterized as shear velocity values, s, at depths, z) and the MINEOS model (parameterized as shear velocity values, Vsv, at depths, d). The depth points in the inversion model are fixed except for the depth of the top of the boundary layers (Moho and NVG), which are parameterized as the thicknesses of the layer above the boundary layers, t. Equations relating features of the inversion model and the intermediate MINEOS model are shown (see the Appendix for details).

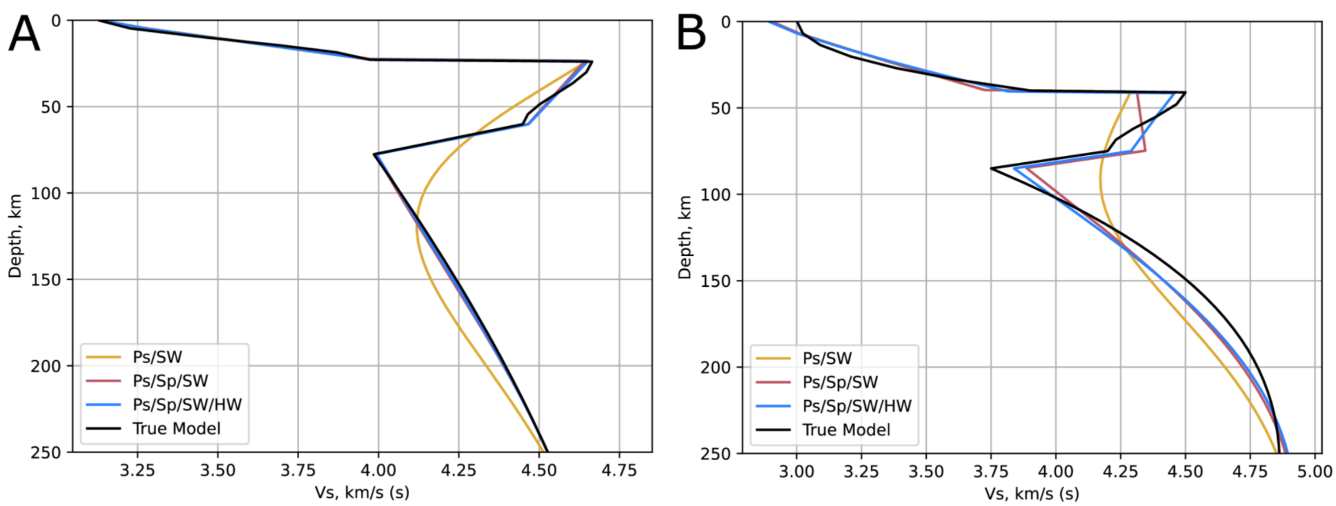

Figure 6 Results of inversions of synthetic datasets. In both panels, black lines are the models used to generate the synthetic dataset, and models in color are inversions of the datasets described in the legend. Ps is P-to-s conversions from the Moho, SW is surface wave phase velocities, Sp is S-to-p conversions from the NVG, and HW is the velocity at the top of the mantle constrained by head waves.

5 Results

5.1 Preferred inversion of the data

We invert the suite of observations from Section 2 for 3D models of shear velocity over the study region by applying the 1D parameterization in Section 3 on a 0.5 by 0.5 degrees spatial grid. The resulting models satisfy the discrete observations within estimated uncertainty (Fig 7). Misfits of the model predictions to each dataset expressed as the mean squared error, $\overline{\chi}^2$, are very low, exceeding the nominal target value of one (where one means that on average the data is fit to the error) only for the phase velocities at 25 s and the velocity contrast from Ps conversions. These higher misfits likely indicate tension between the two observations as to the contrast at the Moho, but are acceptable. Given this uncertainty, we demonstrate the acceptability of our Moho structure by comparing predicted receiver functions between our model and the model of Shen and Ritzwoller (2016) in Supplementary Section S5.

Fig 8 displays the depths of the two discontinuities across the region. The depth to the Moho varies from over 50 km at locations within stable North America to less than 35 km in much of the BR province. The Moho is shallower in the southern than northern BR, and the Colorado Plateau typically features transitional values between 35 and 50 km, with thinner crust beneath the transition zone along its southern and western margin. Overall, the Moho depths and their variation are generally consistent with previous studies from the region, with RMS difference of 2.3 km compared to Schmandt et al. (2015) and 3.8 km relative to Gilbert (2012). Both are comparable to our uncertainty in Moho depth (2.5 km), with the greater difference compared to Gilbert (2012) likely caused by Gilbert (2012) migrating Ps conversions to depth with a fixed model, while both our study and Schmandt et al. (2015) are joint inversions of data from receiver functions and surface wave phase velocities.

Depths to the NVG are typically greater beneath SNA (average of 90 km) than in the BR (average of 75 km), but the depths also feature shorter-wavelength variations that are likely associated with smaller-scale tectonic processes. Within the Basin and Range, the depths to the NVG are highly variable, especially in the north, with a swath of shallower depths in the south (Liu and Shearer, 2021). Relatively shallow depths extend from the BR through the Rio Grande Rift and into the southern Rocky Mountains. Somewhat greater NVG depths characterize the Colorado Plateau, Wyoming craton, and northern Rockies, but again with significant short-wavelength variations. Beneath the CP, a local maximum in the depth of the NVG occurs beneath the center of the plateau embedded among shallower NVGs to the west, south and east. Beneath the transition zone of the Colorado Plateau, depths are more similar to those beneath the BR than the center of the Plateau.

Fig 9 displays the regional variations in shear velocities and associated vertical velocity gradients directly above and below these layer boundaries. Lower crustal gradients are averaged over 10 km above the top of the Moho, and gradients below the Moho are averaged from the base of the Moho and the top of the NVG. Fig 10 shows cross-sections through our study area with shear-wave velocities specified every 1 km in depth. Velocities within the lower crust (Fig 9a) show a similar long-wavelength pattern to that seen in the depths to the Moho, but with more pronounced short-wavelength variations. Lower-crustal velocities are highest in SNA in the east and are lowest across a broad swath of the Basin and Range province. Velocities are 0.2-0.4 km/s faster in the northern-most BR than to the south, but this division occurs at approximately 39°N (Fig 9a) and so is not coincident with the decrease in crustal thickness that occurs 36°N (Fig 8a). The slowest lower-crust velocities in the BR surround the western, southern, and eastern rim of the Colorado Plateau, with a contrast in velocity from the BR to the interior plateau ranging from 0.3 to 0.5 km/s with only minor variations in velocity within the plateau itself. Low-velocity anomalies in the lower crust are typically associated with weak gradients in shear-wave velocity above the Moho, for example along the southern and western edges of the Colorado Plateau and at an anomaly beneath the San Juan Mountains at 38°N/108°W (Hansen et al., 2013). The gradient in the lower crust anticorrelates with the velocity in the lower crust over much of the BR and CP. However, the correlation is imperfect as maxima in the gradient correspond with intermediate shear velocities in the northern BR and the high crustal velocities in SNA are typically associated with intermediate or weak gradients.

The velocities between the Moho and the NVG (Fig 9b,e) are less variable than the other two layers, and less obviously correlated with surface tectonics. Shear velocities are high beneath the Great Plains and Wyoming craton, intermediate beneath the CP and much of the BR, and low only in localized anomalies such as beneath Yellowstone and the western transition zone of the CP. The vertical velocity gradient in the mantle lithosphere is generally positive over much of the region, with negative gradients localized to the Snake River Plain, the Marysvale volcanic fields (as also seen in the profiles in Figs 10,11), and the Rio Grande Rift. Local maxima in negative velocity gradients below the Moho in the same three locations were reported by both Shen and Ritzwoller (2016) (their Fig. 17) and Buehler and Shearer (2017) (their Fig. 7c,d). The negative gradients extend over a more extensive region in Shen and Ritzwoller (2016) than in this study or in Buehler and Shearer (2017), and we do not reproduce the local maximum in positive gradients in the BR in Buehler and Shearer (2017). The gradient in this depth range is the most poorly constrained feature of the model space (Table 1). The strongly negative gradients correspond to regions with slow surface-wave velocities (Fig 2b) and often with moderately large Moho contrasts. In a few locations, this results in a sub-Moho velocity gradient of similar magnitude to the imposed NVG associated with the Sp contrast. Forward modeling of Sp receiver functions confirms that these high-gradient models do satisfy Sp travel times within uncertainty, despite contradicting the intuition that the NVG should have the highest gradient in Vs with depth (Supplementary Section S6). Buehler and Shearer (2014) also directly observed Sn across a portion of our study region, and to first order our sub-Moho Vs variations are in agreement, noting the low Vs below the Moho beneath a wide swath of the Western Colorado Plateau in particular.

Velocities below the NVG exhibit pronounced patterns at both short and long wavelengths and excellent correlation with the tectonic provinces observed on the surface (Figs 9c,11). Velocities are high (Vs > 4.4 km/s) beneath most of SNA and the Wyoming Craton, with relatively low velocity anomalies of approximately 4.3

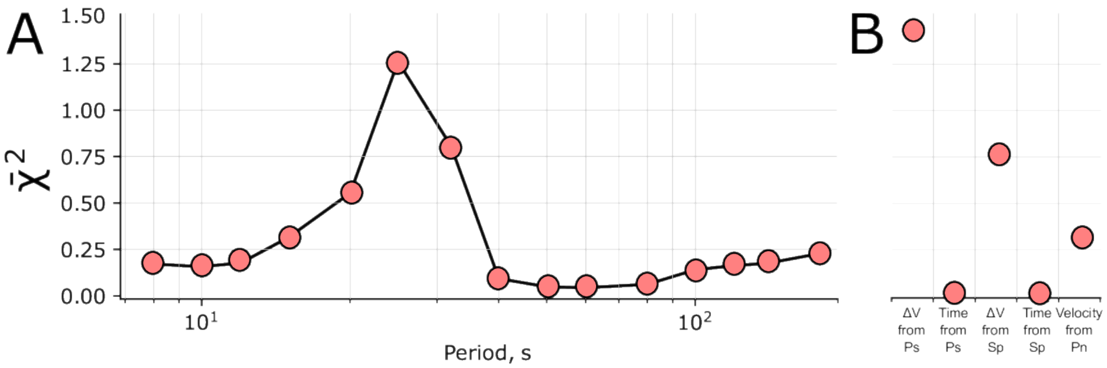

Figure 7 Fit to the surface (A) and body (B) wave datasets expressed as the mean squared error, $\overline{\chi}^2$, for our preferred dataset and inverse approach. The datasets are described in Section 2.

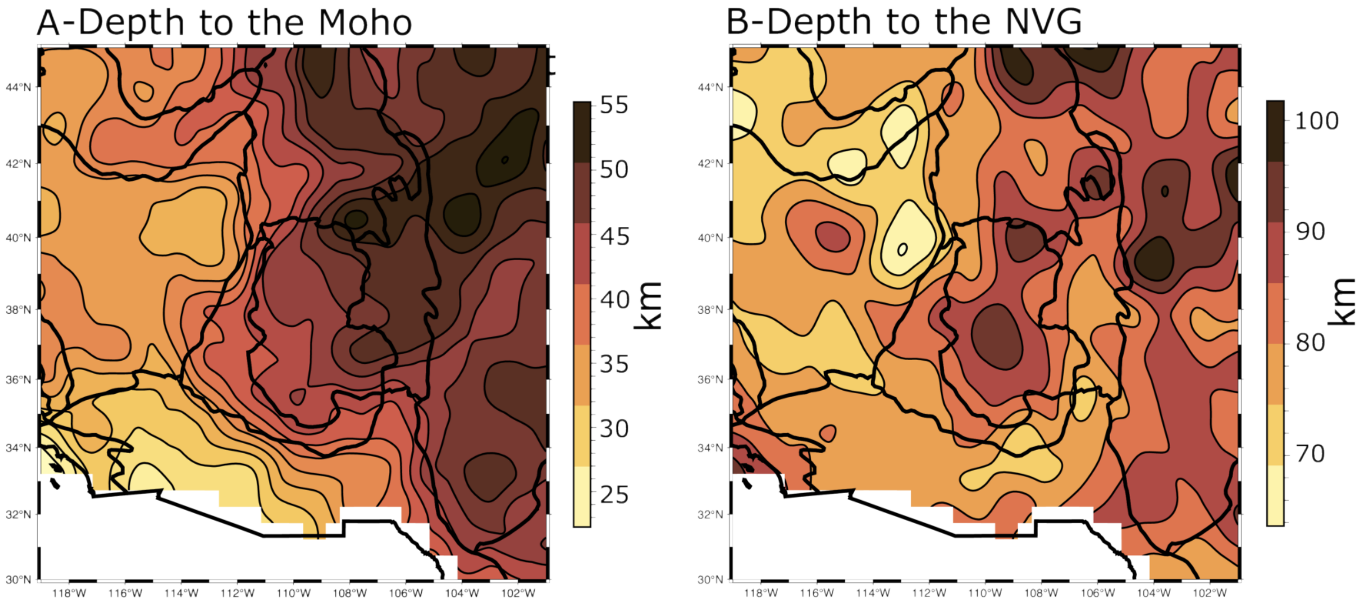

Figure 8 Depth to boundary layers. Darker colors indicate greater depths to the Moho and NVG (panels A and B, respectively). Depths are defined as the mid-point of the gradient.

km/s only occurring beneath the Black Hills and from 35°N to 39°N along 104°W. Velocities are lower beneath the interior of the Colorado Plateau but are never < 4.2 km/s (Fig 10b,c,Fig 11b). Velocities beneath the transition zone of the Colorado Plateau are typically <4 km/s, and such low velocities span the entire BR province. Remarkably low Vs <3.9 km/s is observed in patches along the eastern, southern, and western rim of Colorado Plateau (Fig 9c,Fig 10b,c), extending from the transition zone into the plateau interior. This encroachment of BR-like structure inboard of the surface expression of the CP rim is observed at similar depths in a variety of geophysical imaging studies (e.g. Porter et al., 2019; Schmandt and Humphreys, 2010; Shen and Ritzwoller, 2016; Wannamaker et al., 2008; van Wijk et al., 2010; Xie et al., 2018), and distinguishes the boundary of the CP in the mantle from that in the crust, where the CP/BR transition correlates more closely with the surface expression of the plateau rim. Similarly, very slow Vs anomalies occur beneath the Snake River Plain but are not strongly associated with the modern Yellowstone hotspot (Fig 10a).

The spatial variations in shear velocity below the NVGs agree well with previous surface-wave tomography models of western North America, except that the absolute velocities just below the NVG are typically much lower due to the explicit inclusion of constraints from Sp conversions. At the depth of the base of the NVG in our model, the mean difference between our results for Vs and the Vs reported by Shen and Ritzwoller (2016), Porter et al. (2016), and Xie et al. (2018) are 0.17, 0.24, and 0.2 km/s, respectively, with peak differences of 0.45, 0.5, and 0.45 km/s. That the differences are a large fraction of the total range in Vs emphasizes the importance of the Sp constraint.

The vertical shear-velocity gradient within 50 km below the NVG (Fig 9f) has a tectonic affinity that is similar to the absolute velocities just below the NVG (Fig 9c). The correlation coefficient between these model characteristics is high (0.89), and nowhere in the study area do these two quantities deviate from this correlation outside of twice the standard error. This behavior differs from the crust and the shallow mantle layer, where correlations between absolute velocity and the gradient

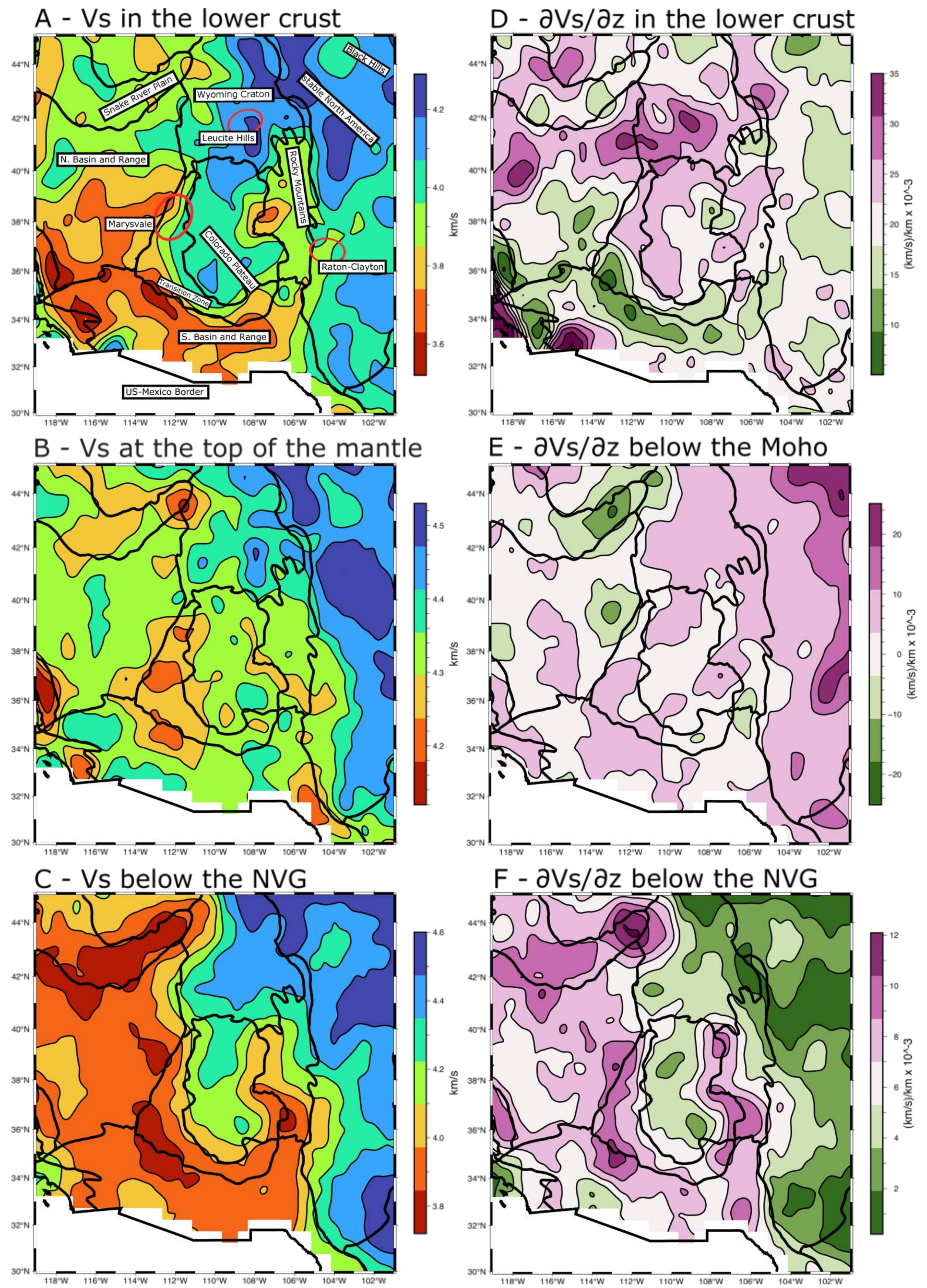

Figure 9 Shear wave velocities and gradients with depth in three layers. A) Shear wave velocity above the Moho (shown in Fig 8a); $\pm$10% variation from a mean of 3.90 km/s. B) Average shear wave velocity between the base of the Moho and the top of the NVG (shown in Fig 7b); $\pm$4.5% variation from a mean of 4.38 km/s C) Shear wave velocity below the NVG; $\pm$12% variation from a mean of 4.28 km./s. D) Average gradient in Vs over 10 km above the Moho. E) Average gradient in shear-wave velocity between the base of the Moho and the top of the NVG. F) Average shear-wave velocity gradient in a 50 km deep interval below the NVG. Tectonic and magmatic features labeled in Fig 1 are included on panel A. See Supplemental Section S4 for demeaned maps of velocity.

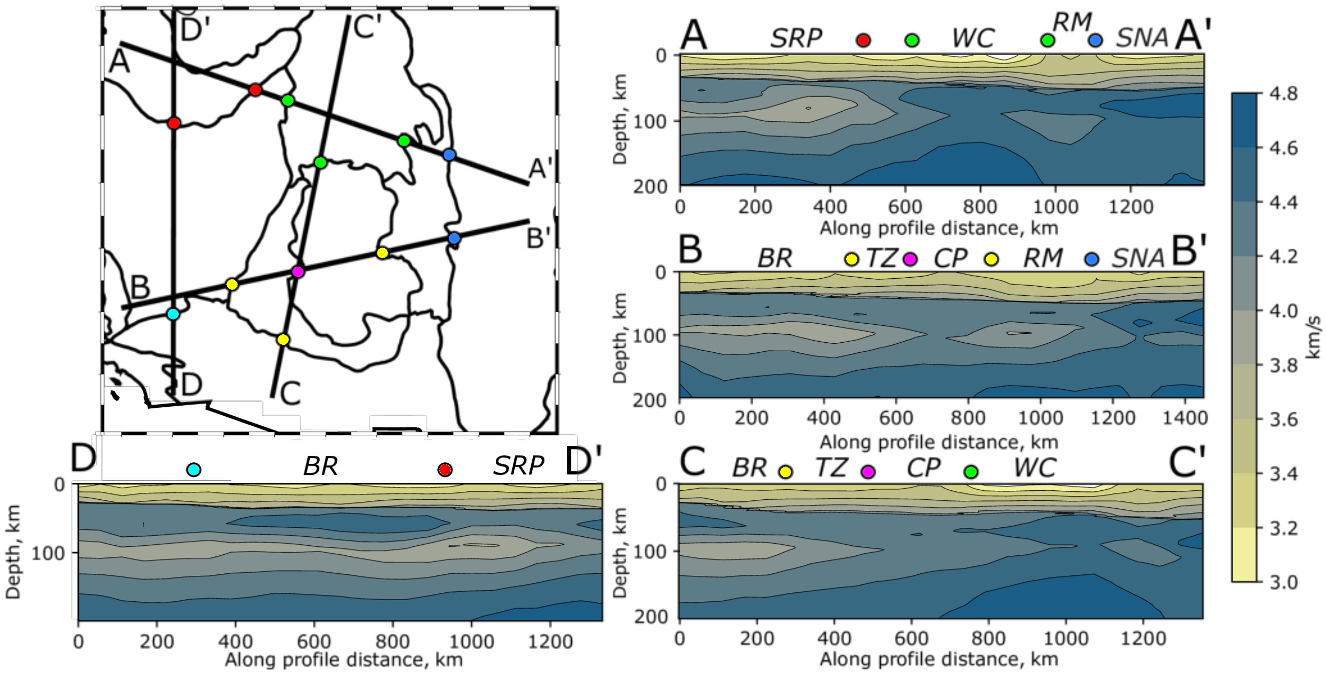

Figure 10 Cross sections through the preferred velocity model. The locations of the cross-sections are shown in the top-left panel, and velocities are contoured in 0.2 km/s intervals. Depth and distances are not to scale, and colored circles mark the boundaries of tectonic provinces defined in Fig 1 for reference. Abbreviations are BR: Basin and Range, SRP: Snake River Plain, WC: Wyoming Craton, CP: Colorado Plateau, TZ: Transition Zone of the Colorado Plateau, RM: Rocky Mountains, and SNA: Stable North America.

are not always strong. The strong correlation between sub-NVG shear-wave velocity and the associated gradient could hypothetically be an artifact of our inversion procedure – the model is damped to the Vs in PREM at 400 km depth (4.75 km/s), and so overly damping the second derivative could force a correlation between absolute velocity and the average gradient. However, the set of randomized synthetic models discussed in Section 3.5 have no correlation between sub-NVG velocity and associated vertical gradient, and the inversion of the synthetic datasets produced models with a negligible correlation coefficient (0.05) between these model characteristics (see Supplementary Section S3). We conclude that the strong correlation in the inversion of the real dataset between velocity and the gradient of velocity is robust.

5.2 Impact of Modeling Choices

The inclusion of an NVG that explains Sp conversions is the primary difference between our study and previous shear-velocity models of the upper mantle in the western US (e.g. Shen and Ritzwoller, 2016; Porter et al., 2016; Xie et al., 2018). The inclusion of the NVG lowers Vs in the mantle just below the discontinuity, compared to models that vary smoothly with depth (Fig 6). We quantify this effect by performing the inversion without an NVG and associated Sp data in the modeling and find the difference between this new model and the preferred inversion at the depth of the base of the NVG (Fig 12a). Omitting the Sp constraints results in significantly higher velocities compared to the preferred model at all locations (Fig 12a), with the largest differences (up to 0.4 km/s) falling within the BR. The mean effect of the Sp constraint is 0.16 km/s, which is nearly identical to the mean difference between our preferred model and Shen and Ritzwoller (2016). The spatial variation in these differences correlates strongly with the magnitude of the Sp-derived velocity contrast (Fig 3c), demonstrating the strong impact of these observations on the model. However, the difference is less well correlated with the modeled velocity beneath the NVG (Fig 9c), suggesting that the surface-wave phase velocities (Fig 2b) also play a significant role in constraining the minimum velocities reached beneath the NVG.

The incorporation of head-wave velocities (Fig 4) represents a second difference compared to prior models, and we test the impact of this choice by comparing the preferred inversion to one omitting these observations (Fig 12b). The use of the head-wave constraint systematically increases velocities just below the Moho over a wide swath of the study region. As suggested by Fig 6b, Pn constraints are accommodated by producing models with negative vertical gradients in the mantle lithosphere; the average velocity across this upper-lithosphere layer is primarily controlled by the surface-wave data and remains largely unchanged between the preferred model and the model lacking Pn constraints. The difference between the models is not strongly correlated with the Pn constraints (Fig 4), and is largest where the crust is thick below the Rockies and over much of the Colorado Plateau. The effect is more muted over much of the Basin and Range and SNA. These differences likely reflect the correction that the head-wave constraint makes to the synthetic test in Fig 6b (see Supplemental Section S2 for further discussion).

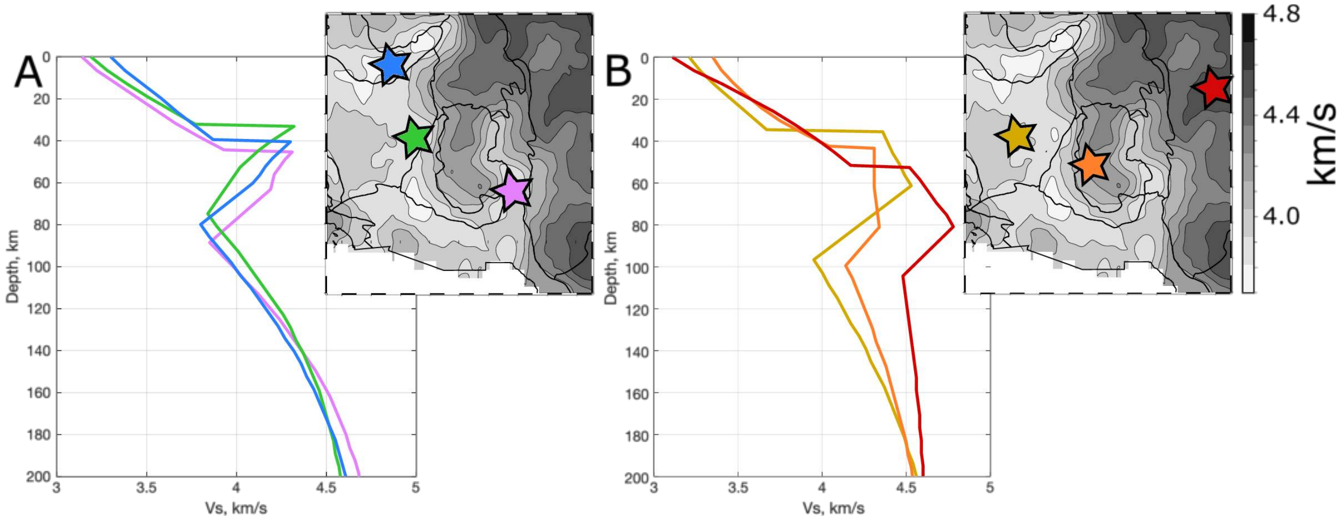

Figure 11 Profiles in Vs with depth at major volcanic sites with low shear wave velocities (panel A) and at representative sites in select tectonic provinces (panel B). Insets are velocity below the NVG in grayscale (cf Fig. 9c)

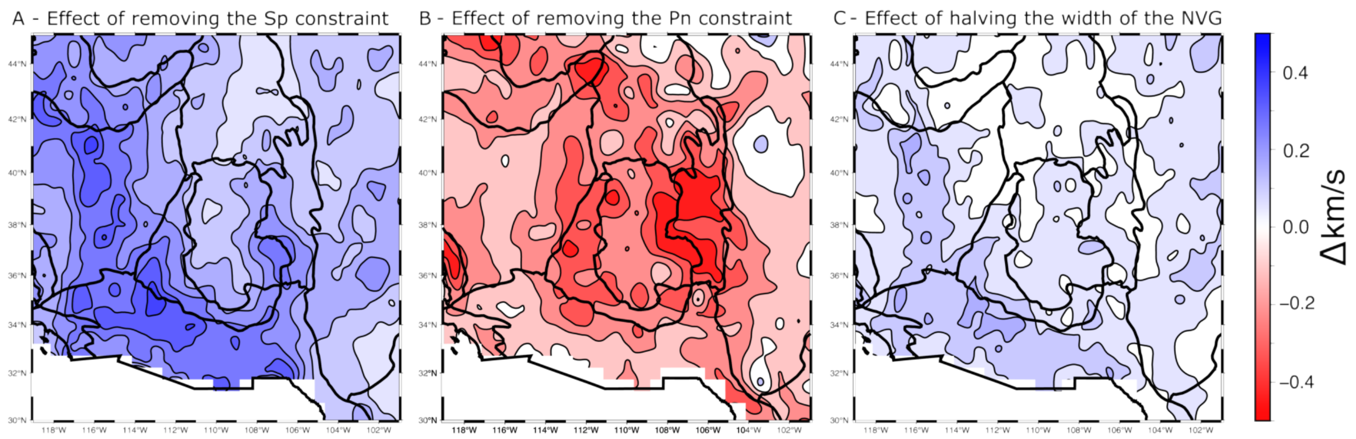

Figure 12 Changes in velocity relative to the preferred inversion when different approaches are taken. Positive indicates a higher velocity relative to the preferred inversion. A) Change in velocity at the depth of the base of the NVG in the preferred inversion when the Sp constraint is removed. B) Change at the base of the Moho when the constraint on the upper mantle inferred from Pn velocities is removed. C) Change in velocity at the base of the NVG where the width of the NVG is halved.

Finally, we make an important choice in the construction of the preferred inversion by assuming spatially variable widths of the NVG that are constrained by modeling Sp waveforms in Hopper and Fischer (2018). The widths of the discontinuities are only loosely constrained, ranging from 10 to 50 km (Supplementary Figure S1), and the implied velocity contrasts depend on the width, becoming larger as the width of the boundary increases (Rychert et al., 2007). We test the effect of this choice by inverting for an alternative set of models that utilize NVG widths that are half of the value of the widths estimated by Hopper and Fischer (2018). The widths are bounded at a minimum of 10 km. The difference at the base of the NVG between a model using the half widths and our preferred inversion are shown in Fig 12c. The primary effect is to increase velocities by up to 0.3 km/s in several localized areas, with marginal difference in many locations. On a regional scale, the effect is greatest in the central Basin and Range and to the south-west of the rim of the Colorado Plateau, where the velocities in the preferred model are systematically slower by 0.1-0.2 km/s compared to a model with a sharper NVG. Some of the most pronounced anomalies, such as beneath the Snake River Plain and the Marysvale volcanic fields, are unaffected by the change in the width, and may be driven more strongly by the constraints from surface waves than from receiver functions.

6 Discussion

The relationship between the NVG and the lithosphere-asthenosphere system is not always straightforward. A common inference is that the NVG is the lithosphere-asthenosphere boundary. Under this interpretation, the high velocity layer on the shallow side of the NVG is the lithosphere, which is cooler and possibly compositionally distinct from the underlying asthenosphere; in contrast to the lithosphere, the asthenosphere is hotter and may have additional reduction in velocities due to hydration or the presence of melt (e.g. Fischer et al., 2010; Kind et al., 2012; Rychert et al., 2005, and many others). This interpretive framework fails to explain NVGs in locations where the extension of high velocities to sufficiently great depths is inconsistent with warm asthenosphere below the discontinuity. When the NVG is thus within the lithosphere, the term "Mid-lithospheric Discontinuity" is commonly used and the cause must be different (Abt et al., 2010; Ford et al., 2010). A change in the hydration of the upper mantle offers a universal mechanism for both LABs and MLDs (Olugboji et al., 2013; Karato et al., 2015), but competing possibilities include the metasomatism of the lithosphere (Hansen et al., 2015; Selway et al., 2015; Saha et al., 2021) or anisotropy (Wirth and Long, 2014; Ford et al., 2016). In some cases, the NVG may even lie within the convecting asthenosphere (Byrnes et al., 2015). A key difficulty when interpreting the NVG is that only the depth and contrast in velocity are typically known. In many places including in the Western United States, precisely where discontinuities transition from an LAB to an MLD is uncertain (Abt et al., 2010; Lekić and Fischer, 2014; Hansen et al., 2015). The absolute velocity models presented in this study reduce the ambiguity in the interpretation of the NVG.

We use our preferred model for the region to evaluate the physical state of the lithosphere-asthenosphere system across the western US. The refined constraints on absolute shear velocity and associated gradients above and below the NVG are compared to those predicted for experimentally based solid-state models of an olivine-dominated upper mantle. We find that the lithosphere-asthenosphere system falls into one of three states: (1) regions where velocities below the NVG are too low to be explained by plausible solid-state models, requiring the presence of partial melt in the asthenosphere; (2) regions where melt is not required in the asthenosphere, but associated temperature estimates suggest that the NVG represents a lithosphere-asthenosphere boundary; and (3) regions where temperature estimates below the NVG imply that the NVG is within the thermal boundary layer, and thus an MLD.

To make predictions for the shear-wave velocity in a melt-free upper mantle, we use models based on two experimental deformation studies, as implemented in the Very Broadband Rheology (VBR) Calculator (Havlin et al., 2021). The first study, Jackson and Faul (2010), hereafter JF10, measured the shear modulus and dissipation in fine-grained, nominally melt-free olivine samples and provided a model for the velocity and attenuation of a shear-wave at seismic frequencies that depends on the temperature and grain-size of the upper mantle. The second study, Yamauchi and Takei (2016), hereafter YT16, proposed a model for the velocity and attenuation of shear-waves in the upper mantle that additionally depends on the melting temperature of the upper mantle. The measurements were made on an organic material that scales to upper mantle conditions when experimental frequencies are normalized by the Maxwell frequency (McCarthy et al., 2011). A "pre-melting" reduction in viscosity occurred in their experiments that causes YT16 to predict lower shear-wave velocities than JF10 at the same temperatures and grain-sizes where the temperature is near the solidus. We assume the asthenosphere is at the solidus when using YT16, which will be the case if the asthenosphere in the Western United States features typical concentrations of either water or CO2 (Yamauchi and Takei, 2020). Havlin et al. (2021) provide a detailed comparison of JF10 and YT16 and their implementation in the VBR - in the terminology of the VBR, JF10 is eburgers_psp with the bg_peak fit, and YT16 is xfit_premelt.

6.1 Distribution of Partial Melt in the Asthenosphere

We evaluate whether the shear-wave velocities above and below the NVG are consistent with a melt-free or melt-bearing upper mantle. The presence of melt below an NVG can often explain contrasts in velocity too great to be explained by other means. Our results provide two pieces of information typically not available for testing this hypothesis: the absolute value of the shear-wave velocities at the NVG and the gradient in shear-wave velocity below the discontinuity.

To use the VBR to test the hypothesis that the mantle is melt-free, we first calculate shear-wave velocities for a range of potential temperatures and grain-sizes with both JF10 and YT16. Bayes's theorem is used to infer the probability that the observations can be explained by the predictions (see Havlin et al., 2021, for details), both of which are for a sub-solidus mantle. The $a\ priori$ distribution of potential temperatures is Gaussian with a mean and standard deviation of 1400 and 75°C. These values encompass the range of potential temperatures inferred for the western United States at several sites of volcanism in previous studies within two standard deviations (i.e. Plank and Forsyth, 2016; Porter and Reid, 2021), neglecting higher temperatures that are possible at the Yellowstone hotspot. An adiabatic effect of 0.5 °C/km converts from potential temperature to temperature. The prior distribution for grain-sizes is log-normal with a mean of 5 mm and a (unitless) standard deviation of 0.75. This is chosen to encompass plausible estimates of grain-sizes in the asthenosphere (Ave Lallemant et al., 1980; Karato and Wu, 1993; Behn et al., 2009), with a grain-size of 1 mm occurring at the approximate 95% lower bound of the prior, and a grain size of 1 cm occurring at the 95% upper bound. The calculations utilize a period of 100 s (appropriate for the asthenosphere), and an uncertainty of 0.08 km/s on Vs below the NVG (Table 1). We present the calculations without a correction for radial anisotropy even though our model only constrains Vsv because current evidence suggests that $(Vsh/Vsv)^2$ is small. A $(Vsh/Vsv)^2$ of 1.04 (Clouzet et al., 2018) would correct a Vsv of 4.0 km/s to 4.02 km/s, which is within the observational uncertainty.

The hypothesis that the upper mantle can be explained by JF10 and YT16 is rejected at 95% confidence across much of the study area (Fig 13a). JF10 and YT16 can both explain the observations without invoking the presence of melt down to shear-wave velocities of approximately 4.0 km/s, with slight deviations due to variations in the depth of the NVG (Fig 8b). The two models do not, in general, predict precisely the same Vs under the same conditions and the close agreement of the 95% limit for the two models occurs because they reach similar minimum Vs values at high-temperatures and small grain-sizes. Velocities below nearly the entire Basin and Range province, the Rio Grande Rift, and the CP transition zone cannot be explained by either model, and therefore likely require retained asthenospheric melt. The center and northern portions of the Colorado Plateau, the bulk of the Rocky Mountains, and SNA to the east all feature Vs consistent with a melt-free upper mantle. The melt-free hypothesis is rejected with greater confidence for more pronounced low velocities anomalies, with probabilities becoming as low of 10^{-5} and 10^{-3} for JF10 and YT16, respectively. Nearly all volcanism of age Pleistocene or younger in the NAVDAT database (Glazner, 2004; Walker et al., 2004) lies where the melt-free hypothesis has been rejected (green circles in Fig 13a). The Leucite Hills (LH) in Wyoming is the only volcanic field to clearly lie outside of the confidence interval for both JF10 and YT16; the Raton-Clayton volcanic field (RCV) near 37°N, 104°W coincides with a slight divergence of the two models and lies near but outside of the confidence interval for YT16 and partly outside for JF10.

Within the region where a solid-state asthenosphere can be confidently rejected, we can utilize the shear velocity estimates to hypothesize variations in retained melt fraction. To do so, we find the difference in shear-wave velocity between the observations (Fig 9c) and the 95% confidence interval for YT16, and use the model of Hammond and Humphreys (2000) (1% melt = 8% Vs reduction) to convert residual velocities to a melt fraction. We find that melt fractions below 1% across the entire study area are sufficient to explain the shear-wave velocities below the NVG (Fig 13b). Such melt fractions are in accord with the amount of melt that can plausibly be retained in the upper mantle without being rapidly extracted (Faul, 1997, 2001). In detail, the effect of melt fraction on shear-wave velocity is uncertain (e.g. Holtzman, 2016; Chantel et al., 2016), due primarily to a strong dependence of velocity on the poorly known aspect ratio of melt inclusions. At higher aspect ratios than assumed in Hammond and Humphreys (2000) (e.g. Garapić et al., 2013), smaller melt fractions can explain our observations (Takei, 2002). The relative distribution of retained melt is robust if the geometry of the melt inclusions are constant across the study area, although variations in the inclusion aspect ratio are possible (Holtzman and Kendall, 2010).

The estimates of shear-velocity gradient below the NVG (Fig 13c) provide an additional test on the necessity of the presence of retained melt in the asthenosphere, and a possible constraint on melt distribution. We consider two hypotheses for the large positive slopes in Vs below the NVG: an increase in the grain-size of the upper mantle with increasing depth (Faul and Jackson, 2005), or a decrease in the melt fraction with increasing depth. For the former, we generated a suite of velocity profiles for increasing grain-sizes using both JF10 and YT16. Assuming a nominal asthenosphere temperature of 1400°C, we search over gradients in grain sizes of 0 to 333 mm/km (Faul and Jackson, 2005) and a mean grain size within the gradient zones of 1 mm to 1 cm. Models with grain sizes that go below 1 mm are not considered. Grain-size increases fail to produce the range of slopes in Vs observed in our models, with both JF10 and YT16 spanning only one-fourth to one-half of the range of slopes observed in the study area (polygons in Fig 13c; see Supplemental Section S7 for the individual calculations). Note that these polygons do not account for variations in temperature, and so the range of predicted Vs is more limited than found in the Bayesian test in Fig 13a. In contrast, assuming a reference model with a velocity of 4.25 km/s and a gradient of

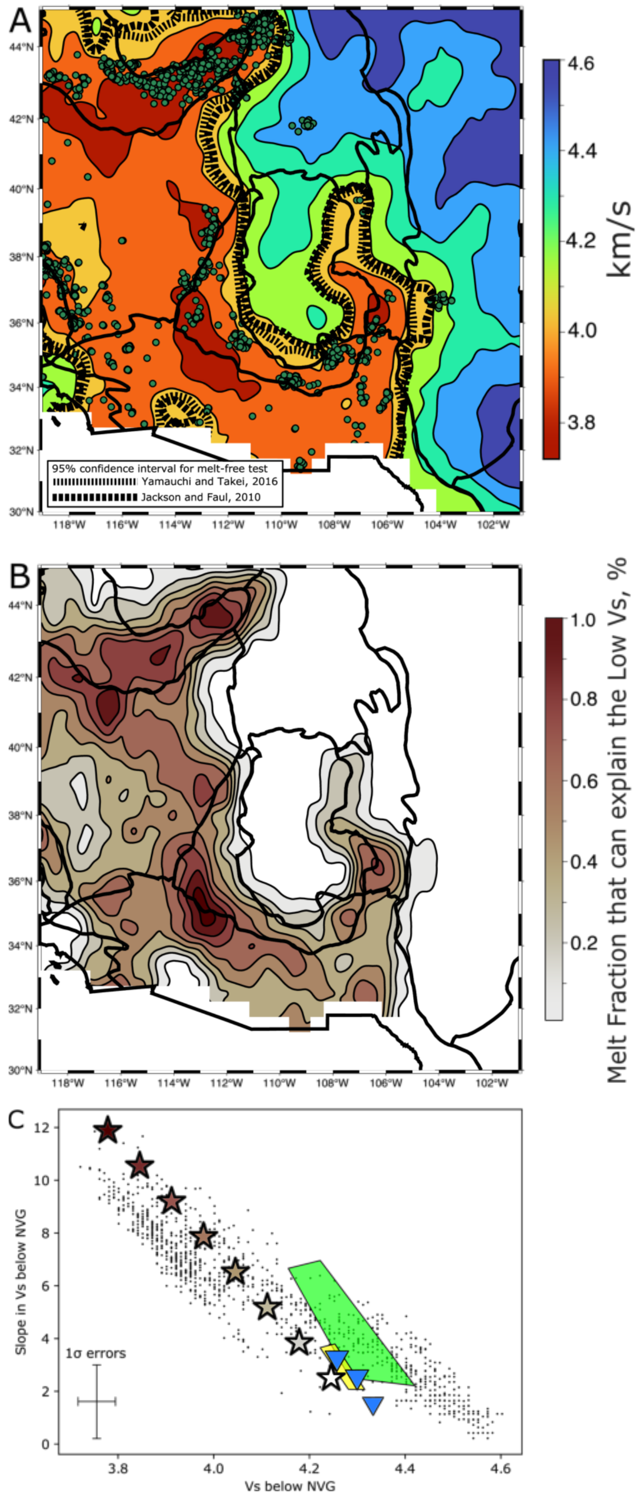

Figure 13 Caption on next page.

Figure 13 Tests of the hypothesis that the upper mantle is melt-free. A) Shear-wave velocity below the NVG is contoured and identical to Fig 9c, 95% confidence limits from the hypothesis tests are shown in dashed lines, and sites of Pleistocene or younger volcanism are marked by green circles. B) Hypothetical in-situ melt-fractions that can explain the gap between the observed velocity below the NVG and the 95% confidence limit for the YT16 hypothesis test. C) Observed shear-wave velocities and gradients in shear-wave velocities below the NVG are marked by black dots, estimates of error along both axes from Table 1 are marked in the bottom left, the range of predictions for JF10 and YT16 when gradients in grain-size are explored are shown by yellow and green polygons, and colored stars show the effect of melt-fractions from 0 to 1.5% on a hypothetical reference model (see text for details). Blue triangles show the velocities and slopes from previous studies: from upper-left to bottom right, these values are from Tan and Helmberger (2007) from 163 to 303 km depth, from Gaherty et al. (1996) from 166 to 415 km depth, and Stixrude and Lithgow-Bertelloni (2005) from 70 to 120 km depth for 10-million-year oceanic lithosphere.

2.2 (km/s)/km x 10^{-3} (Gaherty et al., 1996; Stixrude and Lithgow-Bertelloni, 2005; Tan and Helmberger, 2007), including melt fractions just below the NVG from 0 to 1.5% that linearly taper to 0% over 50 km depth can explain the full range of Vs and the vertical gradient in Vs to within error (Fig 13c). This distribution is qualitatively consistent with melt production in the 120-150 km depth range in a hydrated (Katz et al., 2003) and/or carbonated (Dasgupta et al., 2013) asthenosphere, accompanied by an upward migration and systematic accumulation of melt between the initiation depth and the base of the thermally controlled lithosphere. The latter is consistent with the accumulation depth of mafic melts from the region (Plank and Forsyth, 2016; Porter and Reid, 2021). In detail, the intrinsic sensitivity of the surface-wave constraint limits our ability to precisely define the depth extent of the melt-bearing zone (Supplemental Section S8).

The inferred distribution of partial melt is broadly in agreement with previous estimates of melt distribution in the region. Porter and Reid (2021) combine a smooth seismic-derived thermal model for the North America upper mantle with an assumed set of peridotite solidi to map out regions of likely partial melting in the asthenosphere. They find peaks in likely melting along the southwest and northwest margins of the Colorado Plateau transition zone and beneath the Snake River Plain that closely correspond to peaks in melt content shown here (Fig 13b). Our melt distribution is spatially more extensive, wrapping around the Colorado Plateau with significant melting beneath the northern Rio Grande Rift and southern Rockies; this difference most likely reflects the lower velocities that can be achieved in our discontinuous model compared to smooth surface-wave models. Debayle et al. (2020) combine shear-velocity and attenuation models with experimental constraints (YT16) to estimate melt content on a global scale. While they cannot resolve the regional variations evaluated here, they infer asthenosphere melt contents beneath the western US very similar to those found here (up to 0.7% over the entire region), as high as any other region in their model.

The melt distribution (Fig 13b) is not highly correlated with lithospheric thickness variations (Fig 8b); in particular, the shallowest depths to the NVG do not generally correlate with peaks melt content that might suggest the ponding of melt at the base of the lithosphere, as likely occurs in oceanic environments (Mehouachi and Singh, 2018; Sparks and Parmentier, 1991). Instead, melt is concentrated either along strong gradients in lithospheric thickness (e.g the CP transition zone), or in the broader Snake River Plain region. This suggests that thermal variations in the asthenosphere associated with small-scale and/or edge-driven convection (Schmandt and Humphreys, 2010; van Wijk et al., 2010; Ballmer et al., 2015) control melt accumulation, rather than topography on the base of the lithosphere (Golos and Fischer, 2022).

Our quantification of melt distribution omits the possibility that hydration (or other volatile-induced weakening) provides a plausible interpretation of shear velocities too low to be explained by solid-state mechanisms (e.g. Karato and Jung, 1998; Karato et al., 2015; Olugboji et al., 2013; Ma et al., 2020). Hydration is typically invoked to explain modest reductions in shear velocities, with minimum velocities in the range of 4.0-4.2 km/s, often in conjunction with additional constraints such as boundary sharpness (e.g. Gaherty et al., 1996; Mark et al., 2021) or shear attenuation (Ma et al., 2020). Our interpreted melt distribution displays shear velocities <4.0 km/s, which almost certainly requires a contribution of melt, and the hydration hypothesis does not provide an explanation for the large slopes in Vs below the NVG. Hydration or other volatiles may be important in explaining the NVG at more moderate asthenosphere velocities.

6.2 Interpreting the NVG – LAB, MLD, or something else?

The dominant mechanism controlling the state of the lithosphere-asthenosphere system (including the distribution of melt) is temperature. While the temperature associated with the LAB is depth dependent and not uniquely defined, most studies place the base of the lithospheric thermal boundary layer in the range of 1350-1450°C (Priestley and McKenzie, 2006; Fishwick, 2010; Priestley and McKenzie, 2013; Porter and Reid, 2021), with higher temperatures clearly corresponding to convecting asthenosphere (e.g. Sarafian et al., 2017). We utilize the VBR to estimate temperature both above and below the NVG (Fig 14), with a goal of evaluating where the discontinuity represents the LAB and where it more like represents an MLD. In both cases, two estimates are made by fixing the grain size to 1 and 5 mm, and searching for the best-fitting temperature returned by JF10 with the VBR (Havlin et al., 2021). When estimating temperature below the NVG, we mask regions where we inferred retained melt in the previous sec-

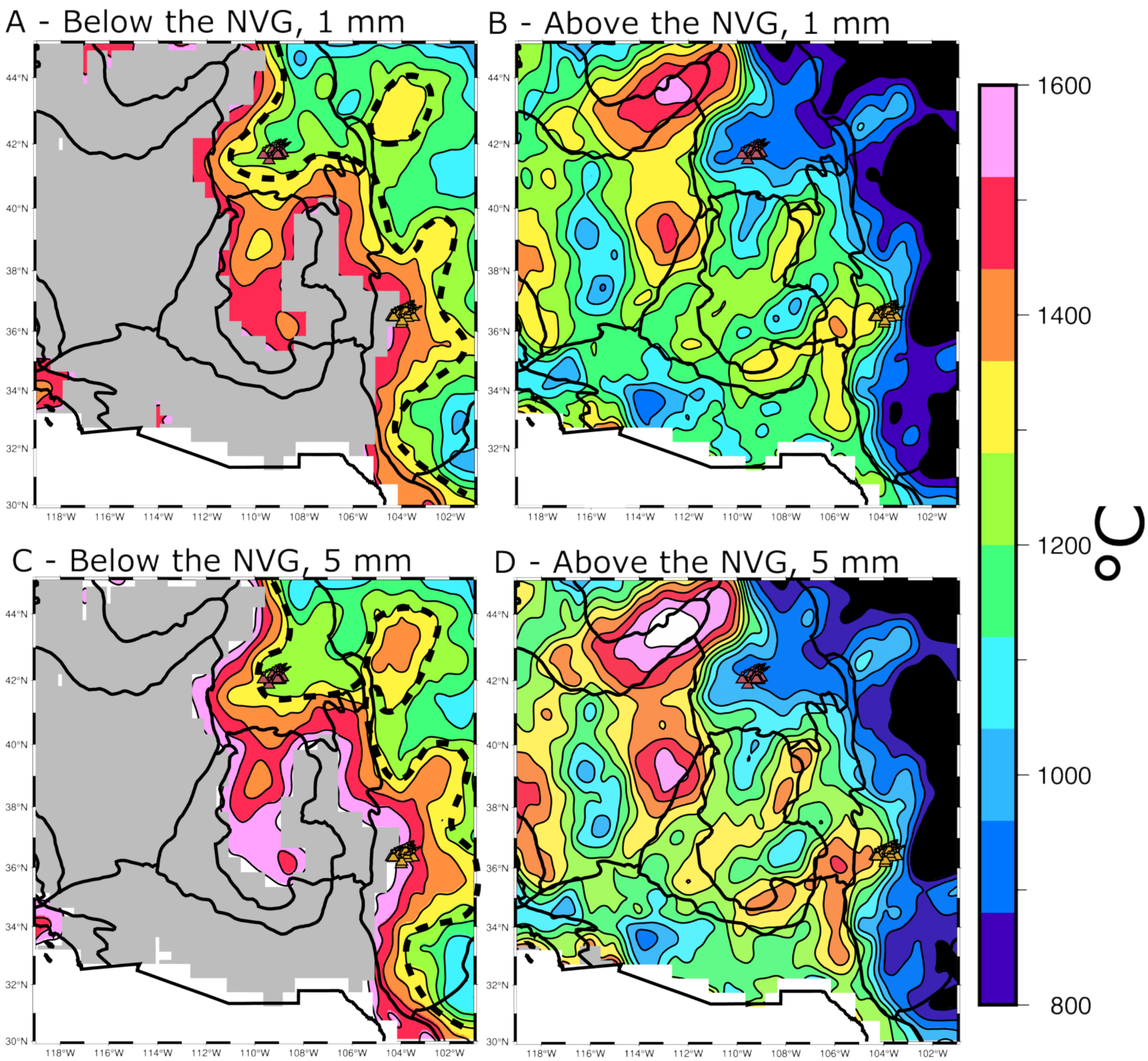

Figure 14 Estimate of the temperature in the mantle at fixed grain sizes. Estimates are for below and above the NVG in the left- and right-hand columns, respectively, and at grain sizes of 1 mm and 5 mm in the top and bottom rows, respectively. The dashed-line in the right-hand column approximately marks the boundary between the LAB and MLD. The Leucite Hills (LH) and Raton-Clayon volcanic (RCV) fields are shown in purple and yellow in all panels.

tion (Fig 14a,c); inferred temperatures in these regions (>1500°C) are well over expected solidus temperatures (e.g. Sarafian et al., 2017), and masking them allows for a clearer evaluation of likely temperatures where melt is not required. The results show that the uncertainty in grain size introduces approximately ±50°C of uncertainty into the estimates, with higher temperatures inferred at larger grain sizes. The two volcanic fields above regions where melting in the asthenosphere was not inferred (the Leucite Hills and Raton-Clayton) are individually marked.

The "LAB" interpretation likely applies across more of the study area than where we inferred melt in the previous section. The boundary between the LAB and MLD is marked in 14a,c approximately follows the 1300°C contour but should be interpreted as a semi-quantitative estimate. Below the Colorado Plateau, sub-NVG temperatures are within the range for asthenosphere, and the estimated temperature exceeds the volatile-free and water-bearing solidus (1490 and 1447°C, respectively, at a depth of 95 km) at both grain sizes tested (Hirschmann, 2000; Katz et al., 2003). High temperatures extend beneath much of the Rocky Mountains and across the borders of the Wyoming Craton and SNA, with a relatively broad region of higher temperatures near the RCV. The mantle below the Black Hills is likely an LAB regardless of the grain size. The Bayesian test in Section 5.1 does not exclude the possibility that there is melt beneath the NVG in these high-temperature regions. However, even if melt is not present, the discontinuity can be plausibly interpreted as an LAB in these regions by inferring temperatures typical of the asthenosphere below an inferred thermal boundary layer.

In the regions where we inferred melt below the NVG (masked in Fig 14a,c), the temperatures above the discontinuity (Fig 14b,d) are typically sub-adiabatic (that is, below a 1350°C adiabat). This conforms well to the hypothesis of a lithosphere-asthenosphere boundary, in that the NVG can be ascribed to the base of a thermal boundary layer with melt in the deeper asthenosphere. Thus, we confidently identify most regions that are masked in Fig 14a,c as LABs. In detail, a few locations within this zone (Snake River Plain, Marysvale volcanic field, Rio Grande Rift) have inferred temperatures above the NVG that are higher than expected for the lithosphere. This is similar to other temperature estimates for the region (Porter et al., 2019; Porter and Reid, 2021), and suggests that the distinction between lithosphere and asthenosphere in these regions is arbitrary. We speculate that the NVG in these locations could reflect an increase in the mobility of basaltic melt as depth decreases (Sakamaki et al., 2013), so that melt ponds within the asthenosphere at the depth where the NVG is observed. Such regions must have thinner lithosphere than marked by the NVG as we consider such high-temperature regions to be asthenosphere by definition.

In SNA on the eastern edge of our study area, our estimates of temperature below the NVG are clearly lower than a plausible potential temperature for the convecting asthenosphere by up to hundreds of degrees in some locations. Low temperatures extend beneath the Wyoming Craton as far south as 41°N and includes the region of the Leucite Hills (Fig 14a,c). Broadly, regions with shear-wave velocities exceeding 4.4 km/s below the discontinuity can be confidently ascribed to an MLD, with confidence increasing with increasing velocity. Whenever this condition is met, temperatures above and below the NVG are estimated to be below 1000°C (Fig 14b,d), with much of the great plains region characterized by temperatures at the MLD that are typical of cratons (<800°C). These temperature estimates provide important constraints on the plausible mechanisms producing the MLD, including crystallized metasomatic products (Hansen et al., 2015; Selway et al., 2015; Saha et al., 2021), and/or changes in intracrystalline deformation processes (Karato et al., 2015). We explore the implications of these constraints for the Leucite Hills region in the next section.

6.3 Relationship between NVGs and recent intraplate volcanism

Nearly all intraplate volcanism of Pleistocene or younger age occurred within the region where we inferred melt must be present beneath the NVG. Broadly, the volcanism in the western United States is sourced by asthenospheric melts at ambient to elevated temperatures, with compositions ranging from primitive to evolved (Fig 15a,b). Compositions are from NAVDAT (Glazner, 2004; Walker et al., 2004) with data from Mirnejad and Bell (2006) for the Leucite Hills included. Relating the petrology of each of these eruptions to the upper mantle structure inferred here is beyond the scope of this study, but to first order an LAB at ~70 km depth above a melt-bearing asthenosphere is consistent with petrologically inferred depths of magma generation (Golos and Fischer, 2022; Plank and Forsyth, 2016; Porter and Reid, 2021). Of the two volcanic fields that fall outside of the region where the Bayesian test in Section 5.1 required the presence of melt, the RCV is characterized by temperatures below the NVG (~1450°C) that are near a peridotite solidus and exhibits compositions (yellow dots in Fig 15a,b) that fall along the bimodal trend for the rest of the volcanism (black dots in Fig 15a,b). Thus, some unique mechanism for explaining volcanism at the RCV is not required.

The Leucite Hills, in contrast, are both seismically and petrologically unique. First, the LH lie above an MLD, with temperature conditions well below the peridotite solidus. Second, looking at the LH petrologically, samples from the LH do not fall along the bimodal trend observed in the western United States because of a strong enrichment in potassium at a given SiO_2 (Fig 15a), and low Na_2O/K_2O and Al_2O_3/TiO_2 ratios (Fig 15b). Both of these observations appear consistent with metasomatism of the low-temperature lithosphere. Ultrapotassic compositions (Foley et al., 1987) are often explained either by the melting of recycled oceanic crust and possible reaction with surrounding peridotite (Dasgupta et al., 2007; Mallik and Dasgupta, 2013), or metasomatized veins within the lithosphere (Foley, 1992; Pilet, 2015). We do not consider the melting of recycled oceanic crust because the temperatures beneath the LH (Fig 14) are too low and recycled oceanic crust cannot explain the unique trace element profile in the LH (Fig 15b) (see Pilet, 2015, for a discussion). As discussed in the previous section, MLDs in general can also be explained by metamosomatic compositions in the lower lithosphere (e.g. Selway et al., 2015). How the lithosphere becomes metasomatized is not perfectly understood and beyond the scope of this study.

Metasomatic enrichment of the lithosphere both lowers the solidus and seismic velocity of the mantle, and so provides an explanation for the unique volcanism at the LH and the presence of an MLD. Both seismic and petrologic studies have suggested amphibole (Pilet, 2015; Pilet et al., 2008; Saha et al., 2021; Selway et al., 2015) and phlogopite (Hansen et al., 2015) as the active metasomatic phase that explains MLDs. Several lines of evidence support phlogopite for the location in question. The depth of the MLD beneath the Wyoming Craton (~85 km) is very close to the maximum depth of stability for amphibole (Frost, 2006; Hansen et al., 2015) and the temperature below the boundary (1250°C) is below the amphibole solidus (Pilet et al., 2008) and is thus unlikely to produce the LH melts. In contrast, phlogopite stability extends below the observed MLD (Frost, 2006), and the solidus at this depth (<1175°C; Thibault et al., 1992) implies that melt can be produced at the seismically inferred temperature. The composition of the magmas erupted at the LH also do not overlap with the experimentally measured composition of

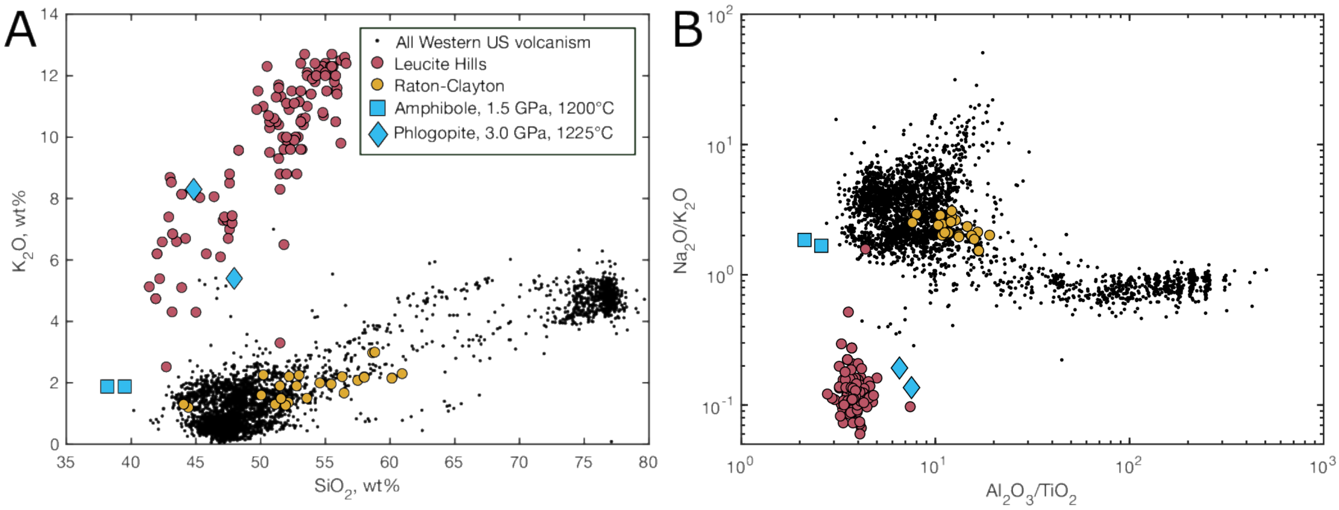

Figure 15 Testing causes of the discontinuity beneath volcanic sites. Major (A) and trace (B) element compositions for all volcanism shown in Fig 13a (age Pleistocene or younger) are shown by black dots. The Raton-Clayton and Leucite Hills fields are separately marked in yellow and magenta, respectively. The composition of melt from amphibole and phlogopite are marked by blue symbols (see Pilet et al., 2008, for details of each experiment).

amphibole melts (Pilet et al., 2008) and are better fit by the composition produced by the melting of phlogopite (Thibault et al., 1992) in both major (Fig 15a) and trace element spaces (Fig 15a,b). The velocity contrast across the MLD in this region may be caused directly by the low velocity of phlogopite (2.47 km/s, which is for a temperature and pressure of 1175°C and 3 GPa; Hacker and Abers, 2004), but other factors such as a melt phase could contribute as well.

7 Conclusions

The inclusion of an NVG into the parameterization of seismic velocity profiles allows for the construction of models for shear-wave velocity across the Western United States that can simultaneously explain observations of Rayleigh wave phase velocities from short to long periods, P-to-s conversions from the Moho, S-to-p conversions from an NVG in the upper mantle, and Pn velocities. The resulting models allow for several advances in our understanding in the physical state of the upper mantle in this region:

1) The shear-wave velocity below the NVG is too low to be explained by the current generation of experimentally based predictions for shear-wave velocity in the upper mantle without invoking the presence of partial melt.

2) The shear-wave velocity below the NVG is strongly correlated with the slope of the velocity profile. As above, the large slopes cannot be explained without invoking the presence of melt in the upper mantle. Linearly tapering melt fractions from a maximum below the NVG to zero percent at 50 km deeper depth can explain both observations.

3) At nearly all locations where we infer the presence of melt in the upper mantle, the NVG can be interpreted as an LAB due to sufficiently high velocities above the discontinuity, and asthenospheric velocities below the discontinuity.

4) Beneath the Wyoming Craton and much of stable North America, Vs and associated temperature estimates below the NVG are too high to represent the asthenosphere and an MLD is inferred instead.

5) The presence of phlogopite in the upper mantle beneath the Leucite Hills can explain the presence of an MLD.

The inversion algorithm presented here provides a flexible and efficient platform for jointly inverting discontinuity constraints from scattered-wave imaging with velocity constraints from surface-wave phase velocities, at a variety of spatial and depth scales. The structures are best resolved when the discontinuity constraints include both depth and velocity-contrast information, and we encourage scattered-wave imaging analyses to document not only timing information but amplitude as well.

8 Appendix - Joint Inversion methodology

8.1 Inverse approach

We define the model to be solved for as

$$\boldsymbol{p} = [\boldsymbol{s}, \boldsymbol{t}] \tag{2}$$

where $\boldsymbol{s}$ is a vector of vertically polarized shear wave velocities (Vsv) defined at fixed depths, and $\boldsymbol{t}$ is a vector of depths to abrupt boundaries within the model, in this application corresponding to the tops of the Moho and the NVG. To solve for a model of this parameterization, we follow the framework of Russell et al. (2019) and Menke (2012), iterating over a linearized least-squares inversion to minimize the misfit between our predicted and observed values, $\boldsymbol{\delta o}$, by making changes to the model parameters, $\boldsymbol{p}$. Given a matrix of the partial derivatives of our observed values with respect to our model parameters, $\boldsymbol{G}$, we have the following equation in matrix form:

$$\boldsymbol{G}(\boldsymbol{p}-\boldsymbol{p_o})=\boldsymbol{\delta o} \quad (3)$$

which can be rearranged to

$$\boldsymbol{Gp}=\boldsymbol{\delta o}+\boldsymbol{Gp_o} \quad (4)$$

As we are now multiplying G by the model, $\boldsymbol{p}$, rather than the model perturbation, we add linear constraint equations that are applied directly to the model. Following Menke (2012),

$$\boldsymbol{Fp}=\boldsymbol{f} \quad (5)$$

$$\boldsymbol{F}=\begin{bmatrix}\boldsymbol{W_e}^{\frac{1}{2}}\boldsymbol{G}\\ \boldsymbol{W_d}^{\frac{1}{2}}\boldsymbol{H}\end{bmatrix} \quad (6)$$

$$\boldsymbol{f}=\begin{bmatrix}\boldsymbol{W_e}^{\frac{1}{2}}(\boldsymbol{\delta o}+\boldsymbol{Gp_o})\\ \boldsymbol{W_d}^{\frac{1}{2}}\boldsymbol{H}\end{bmatrix} \quad (7)$$

where $\boldsymbol{W_e}$ is a diagonal matrix of the uncertainties in the observations, i.e. $\frac{1}{\sigma^2}$, and $\boldsymbol{W_d}$ is a diagonal matrix with the damping parameters for the constraint equations. The dampening constraints minimize the second derivative of the model, expressed by the matrix $\boldsymbol{H}$, within each geologically defined layer (i.e. within the crust, above the NVG, and below the NVG). Smoothing constraints are not applied across the boundary layers so that the dampening is considered separately for each geological layer. The weight given to dampening parameters is placed along the diagonal of the matrix $\boldsymbol{W_d}$, with a value of 1, 2, and 4 used for the three layers, respectively, for all inversions of both real and synthetic data shown in this study. Once $\boldsymbol{F}$ is known, the Gauss-Newton least squares solution is

$$\boldsymbol{p}=(\boldsymbol{F}^T\boldsymbol{F})^{-1}\boldsymbol{F}^T\boldsymbol{f} \quad (8)$$

and all that remains to be defined is the forward problem that predicts observations for a given model along with their partial derivatives.

8.2 The forward problem

We calculate phase velocities and associated partial-derivative kernels using the spherical-earth normal-mode solver MINEOS (Masters et al., 2011). We construct an input model for MINEOS by linearly interpolating velocities at depth (radius) intervals of 2 km between each node defined in $\boldsymbol{s}$ from the surface to 410 km depth. Below 410 km, we extend the model to the center of the Earth with PREM. The MINEOS model is parameterized to allow for radial anisotropy, incorporating independently defined values for P and S velocities in the vertical and horizontal directions, an anisotropic shape factor η, density, and shear and bulk attenuation. Because our Rayleigh-wave and Ps and Sp datasets have little sensitivity to the horizontal velocities, only the vertically polarized S-wave velocity (Vsv) is independently varied in the inversion. We constrain $Vsh = Vsv$, $Vph = Vpv$, and η is set to 1. P-wave velocities are scaled to the S-wave velocities using a Vp/Vs ratio of 1.76; the Vp/Vs ratios from Schmandt et al. (2015) were already accounted for when calculating travel times to the Moho (Section 3.2), and tests including these values in the forward problem instead did not change the results. Phase velocities are corrected for physical dispersion based on a PREM Q model with a reference frequency of 35 mHz (Kanamori and Anderson, 1977; Dziewonski and Anderson, 1981). Forward calculations of receiver function travel times, the contrasts in Vsv, and head wave velocities are direct given a velocity model. The velocity contrast is defined as the percentage change in shear velocity across the boundary layer relative to the velocity in the upper layer.

8.2.1 Dependence of phase velocities on the model

The sensitivity kernels for phase velocity at each period with respect to elastic parameters (P and S velocities) as a function of depth are straightforward to calculate using a normal mode formalism. Here we provide the mapping between mode-based partial derivative kernels for a smooth, finely sampled model space, and partial derivatives for our parameterization of relatively coarsely sampled values of velocity separated by abrupt discontinuities in velocity of a finite thickness ($[\boldsymbol{s},\boldsymbol{t}]$). These partials are connected by the chain rule,

$$\frac{\partial\, c}{\partial\, p}=\frac{\partial\, c}{\partial\, vsv}\,\frac{\partial\, vsv}{\partial\, p} \quad (9)$$

where c is the phase velocity, p is an element of the parameterized inversion model $[\boldsymbol{s},\boldsymbol{t}]$, and vsv is an element of vertically polarized shear velocity in the MINEOS model. The first term on the right side of Equation 9, $\frac{\partial c}{\partial vsv}$, is thus the existing partial with respect to the finely sampled MINEOS model, and the left side is the kernel that we seek. The final term, $\frac{\partial vsv}{\partial p}$, describes the perturbation to a MINEOS model parameter given a change in the inversion model, and we analytically define these here. We use the Vsv structure to demonstrate the relationship between $\boldsymbol{dvsv}$ and $\boldsymbol{dp}$, but similar relationships can be expressed for other scaled and/or free parameters (e.g. Vpv, Vsh) utilized in the inversion. We first describe the dependence of elements in vsv for the velocities in $\boldsymbol{s}$ before giving the dependence for the thicknesses, $\boldsymbol{t}$. The process is described graphically Fig 5.

The depth vector, $\boldsymbol{z}$, that gives the depth for each element in $\boldsymbol{s}$ is coarser and does not necessarily intersect with the regularly spaced MINEOS depth vector, $\boldsymbol{d}$, and so velocities must be linearly interpolated between elements of $\boldsymbol{s}$. Any change to any value in $\boldsymbol{s}$ at depth $\boldsymbol{z_i}$, $\boldsymbol{s_i}\equiv\boldsymbol{s}(\boldsymbol{z_i})$, will have non-zero impacts on vsv only where $z_{i-1}<\boldsymbol{d}<z_{i+1}$, with two analytical forms for locations above and below the depth of the perturbation.

For any vsv points between z_{i-1} and z_i, called vsv_a in Fig 5 under "Dependence on s",

$$vsv(d)=s_{i-1}+\frac{d-z_{i-1}}{z_i-z_{i-1}}(s_i-s_{i-1}) \quad (10)$$

$$\frac{\partial\, vsv(d)}{\partial s_i}=\frac{d-z_{i-1}}{z_i-z_{i-1}} \qquad for\ z_{i-1}\leq\boldsymbol{d}\leq z_i \quad (11)$$

Similarly for any vsv points between z_i and z_{i+1}, called vsv_b in Fig 5 under "Dependence on s",

$$vsv(d) = s_i + \frac{d - z_i}{z_{i+1} - z_i}(s_{i+1} - s_i) \tag{12}$$

$$\frac{\partial\, vsv(d)}{\partial s_i} = 1 - \frac{d - z_i}{z_{i+1} - z_i} \quad for\ z_i \le \boldsymbol{d} \le z_{i+1} \tag{13}$$

The remainder of the inversion model, $\boldsymbol{p}$, are parameters controlling the depth to the top of each discontinuity. Because we define the coarse model $s(z)$ to have a node corresponding to the top of each discontinuity, changes in the depth of a discontinuity directly correspond to changes in the thickness of the layer immediately above the discontinuity, which we define as the parameter t_k, where k corresponds to the discontinuity in question. If z_i is the depth to the top of the k^{th} boundary layer, $t_k = z_i - z_{i-1}$. The width of the boundary layers, $\boldsymbol{w}$, are fixed for any given inversion, but it is convenient to track these widths as $w_k = z_{i+1} - z_i$. The change in t_k is balanced by a change in thickness of equal magnitude but opposite sign in the layer below the base of the discontinuity, i.e. $z_{i+2} - z_{i+1}$. As such, any change to any value in $\boldsymbol{t}$, t_k, will thus have non-zero impacts on vsv and $\boldsymbol{z}$ only where $z_{i-1} < \boldsymbol{d} < z_{i+2}$. Using the above definitions for t_k and w_k, we define three expressions for the sensitivity of vsv to t_k above, within, and below the discontinuity, respectively.

For any vsv points between z_{i-1} and z_i (i.e. above the discontinuity), called vsv_a in Fig 5 under "Dependence on t",

$$vsv(d) = s_{i-1} + \frac{d - z_{i-1}}{z_i - z_{i-1}}(s_i - s_{i-1}) \tag{14}$$

$$vsv(d) = s_{i-1} + \frac{d - z_{i-1}}{t_k}(s_i - s_{i-1}) \tag{15}$$

$$\frac{\partial\, vsv(d)}{\partial t_k} = -\frac{d - z_{i-1}}{t_k^2}(s_i - s_{i-1}) \quad for\ z_{i-1} \le \boldsymbol{d} \le z_i \tag{16}$$

For any vsv points within the discontinuity between z_i and z_{i+1}, called vsv_b in Fig 5 under "Dependence on t",

$$vsv(d) = s_i + \frac{d - z_i}{z_{i+1} - z_i}(s_{i+1} - s_i) \tag{17}$$

$$vsv(d) = s_i + \frac{d - (t_k + z_{i-1})}{(z_{i-1} + t_k + w_k) - (t_k + z_{i-1})}(s_{i+1} - s_i) \tag{18}$$

$$\frac{\partial\, vsv(d)}{\partial t_k} = -\frac{(s_{i+1} - s_i)}{w_k} \quad for\ z_i \le \boldsymbol{d} \le z_{i+1} \tag{19}$$

For vsv points below the discontinuity between z_{i+1} and z_{i+2}, called vsv_c in 5 under "Dependence on t",

$$vsv(d) = s_{i+1} + \frac{d - z_{i+1}}{z_{i+2} - z_{i+1}}(s_{i+2} - s_{i+1}) \tag{20}$$

$$vsv(d) = s_{i+1} + \frac{d - (z_{i-1} + t_k + w_k)}{z_{i+2} - (z_{i-1} + t_k + w_k)}(s_{i+2} - s_{i+1}) \tag{21}$$

$$\frac{\partial\, vsv(d)}{\partial t_k} = \frac{d - z_{i+2}}{(z_{i+2} - z_{i+1})^2}(s_{i+2} - s_{i+1}) \quad for\ z_{i+1} \le \boldsymbol{d} \le z_{i+2} \tag{22}$$

8.2.2 Dependence of receiver function observations on the model

We have two kinds of observations from receiver functions: velocity contrasts across the boundary layers and travel times to the boundary layers. In the following discussion, we notate the k^{th} boundary layer as extending from z_i to z_{i+1} in depth, with velocity s_i at the top and s_{i+1} at the base.

Velocity contrast for the k^{th} boundary layer, dV_k, is only a function of the velocity above and below the boundary layer

$$dV_k = \frac{s_{i+1}}{s_i} - 1 \tag{23}$$

$$\frac{\partial dV_k}{\partial s_i} = -\frac{s_{i+1}}{s_i^2} \tag{24}$$

$$\frac{\partial dV_k}{\partial s_{i+1}} = \frac{1}{s_i} \tag{25}$$

Travel time is a function of all $\boldsymbol{s}$ and $\boldsymbol{t}$ defined at $\boldsymbol{z} \le z_{i+1}$, assuming that the converted wave energy originates on average in the center of the boundary layer.

$$tt_k = 2\left(\frac{z_1 - z_o}{s_1 + s_o} + \cdots + \frac{z_i - z_{i-1}}{s_i + s_{i-1}} + \frac{z_{i+1} - z_i}{s_{i+1} + 3s_i}\right) \tag{26}$$

For any $\boldsymbol{s}$ points shallower than z_i,

$$\frac{\partial tt_k}{\partial s_j} = -2\frac{z_j - z_{j-1}}{(s_j + s_{j-1})^2} - 2\frac{z_{j+1} - z_j}{(s_{j+1} + s_j)^2} \tag{27}$$

For others that will affect the calculated travel time,

$$\frac{\partial tt_k}{\partial s_i} = -2\frac{z_i - z_{i-1}}{(s_i + s_{i-1})^2} - 6\frac{z_{i+1} - z_i}{(s_{i+1} + 3s_i)^2} \tag{28}$$

$$\frac{\partial tt_k}{\partial s_{i+1}} = -2\frac{z_{i+1} - z_i}{(s_{i+1} + 3s_i)^2} \tag{29}$$

For any $\boldsymbol{t}$ shallower than z_i, where s_{h-1} is the velocity at the top of the layer and s_h is the velocity at the base of the layer of thickness t_j,

$$\frac{\partial tt_k}{\partial t_j} = \frac{2}{s_h + s_{h-1}} \tag{30}$$

8.2.3 Dependence of head wave observations on the model

The velocity of the Pn phase constraints the model below the Moho. The partial derivative of the predicted head wave velocity, HW_v, with the shear velocity below the moho, vsv_M, is given by

$$\frac{\partial HW_v}{\partial vsv_M} = 1 \tag{31}$$

Acknowledgements

Funding for this study was provided by the NSF through EAR 1853296 and EAR 2045264 and by Northern Arizona University. Comments from two anonymous reviewers and editor Catherine Rychert greatly improved this manuscript. The model of Shen and Ritzwoller (2016), Buehler and Shearer (2017), and Schmandt et al. (2015) were accessed thorough the IRIS EMC (IRIS-DMC, 2011). Seismic data used in the referenced studies were provided by EarthScope USArray facility, the GSN, PASSCAL, and the SCSN. We thank Chris Havlin for assistance with the VBR.

Data and code availability

Data from this study can be found from the relevant citations provided in Section 2; no new seismic observations were performed for this study. The joing inversion and results of the preferred inversions are available at Byrnes et al. (2023).

Competing interests

The authors have no competing interests.

References

Abt, D. L., Fischer, K. M., French, S. W., Ford, H. A., Yuan, H., and Romanowicz, B. North American lithospheric discontinuity structure imaged by Ps and Sp receiver functions. *Journal of Geophysical Research: Solid Earth*, 115(B9), 2010. doi: 10.1029/2009JB006914.

Ave Lallemant, H. G., Mercier, J.-C. C., Carter, N. L., and Ross, J. V. Rheology of the upper mantle: Inferences from peridotite xenoliths. *Tectonophysics*, 70(1):85–113, Dec. 1980. doi: 10.1016/0040-1951(80)90022-0.

Babikoff, J. C. and Dalton, C. A. Long-Period Rayleigh Wave Phase Velocity Tomography Using USArray. *Geochemistry, Geophysics, Geosystems*, 20(4):1990–2006, 2019. doi: 10.1029/2018GC008073.

Ballmer, M. D., Conrad, C. P., Smith, E. I., and Johnsen, R. Intraplate volcanism at the edges of the Colorado Plateau sustained by a combination of triggered edge-driven convection and shear-driven upwelling. *Geochemistry, Geophysics, Geosystems*, 16(2):366–379, 2015. doi: 10.1002/2014GC005641.

Behn, M. D., Hirth, G., and Elsenbeck II, J. R. Implications of grain size evolution on the seismic structure of the oceanic upper mantle. *Earth and Planetary Science Letters*, 282(1-4):178–189, May 2009. doi: 10.1016/j.epsl.2009.03.014.

Best, M. G., Christiansen, E. H., de Silva, S., and Lipman, P. W. Slab-rollback ignimbrite flareups in the southern Great Basin and other Cenozoic American arcs: A distinct style of arc volcanism. *Geosphere*, 12(4):1097–1135, Aug. 2016. doi: 10.1130/GES01285.1.

Bodin, T., Leiva, J., Romanowicz, B., Maupin, V., and Yuan, H. Imaging anisotropic layering with Bayesian inversion of multiple data types. *Geophys. J. Int.*, 206(1):605–629, July 2016. doi: 10.1093/gji/ggw124.

Buehler, J. S. and Shearer, P. M. Anisotropy and *Vp* / *Vs* in the uppermost mantle beneath the western United States from joint analysis of *Pn* and *Sn* phases. *J. Geophys. Res. Solid Earth*, 119 (2):1200–1219, Feb. 2014. doi: 10.1002/2013JB010559.

Buehler, J. S. and Shearer, P. M. Uppermost mantle seismic velocity structure beneath USArray. *Journal of Geophysical Research: Solid Earth*, 122(1):436–448, 2017. doi: 10.1002/2016JB013265.

Byrnes, J., Gaherty, J., and Hopper, E. Seismic Architecture of the Lithosphere- Asthenosphere System in the Western United States from a Joint Inversion of Body- and Surface-wave Observations: Distribution of Partial Melt in the Upper Mantle, Sept. 2023. https://doi.org/10.5281/zenodo.8237272. doi: 10.5281/zenodo.8237272.

Byrnes, J. S., Hooft, E. E. E., Toomey, D. R., Villagómez, D. R., Geist, D. J., and Solomon, S. C. An upper mantle seismic discontinuity beneath the Galápagos Archipelago and its implications for studies of the lithosphere-asthenosphere boundary. *Geochemistry, Geophysics, Geosystems*, 16(4):1070–1088, 2015. doi: 10.1002/2014GC005694.

Chai, C., Ammon, C. J., Maceira, M., and Herrmann, R. B. Inverting interpolated receiver functions with surface wave dispersion and gravity: Application to the western U.S. and adjacent Canada and Mexico. *Geophysical Research Letters*, 42(11):4359–4366, 2015. doi: 10.1002/2015GL063733.

Chantel, J., Manthilake, G., Andrault, D., Novella, D., Yu, T., and Wang, Y. Experimental evidence supports mantle partial melting in the asthenosphere. *Science Advances*, 2(5):e1600246, May 2016. doi: 10.1126/sciadv.1600246.

Clouzet, P., Masson, Y., and Romanowicz, B. Box Tomography: first application to the imaging of upper-mantle shear velocity and radial anisotropy structure beneath the North American continent. *Geophysical Journal International*, 213(3):1849–1875, June 2018. doi: 10.1093/gji/ggy078.

Crow, R., Karlstrom, K., Asmerom, Y., Schmandt, B., Polyak, V., and DuFrane, S. A. Shrinking of the Colorado Plateau via lithospheric mantle erosion: Evidence from Nd and Sr isotopes and geochronology of Neogene basalts. *Geology*, 39(1):27–30, Jan. 2011. doi: 10.1130/G31611.1.

Dasgupta, R., Hirschmann, M. M., and Smith, N. D. Partial Melting Experiments of Peridotite + CO2 at 3 GPa and Genesis of Alkalic Ocean Island Basalts. *Journal of Petrology*, 48(11):2093–2124, Nov. 2007. doi: 10.1093/petrology/egm053.

Dasgupta, R., Mallik, A., Tsuno, K., Withers, A. C., Hirth, G., and Hirschmann, M. M. Carbon-dioxide-rich silicate melt in the Earth's upper mantle. *Nature*, 493(7431):211–215, Jan. 2013. doi: 10.1038/nature11731.

Debayle, E., Bodin, T., Durand, S., and Ricard, Y. Seismic evidence for partial melt below tectonic plates. *Nature*, 586(7830):555–559, Oct. 2020. doi: 10.1038/s41586-020-2809-4.

Delph, J. R., Zandt, G., and Beck, S. L. A new approach to obtaining a 3D shear wave velocity model of the crust and upper mantle: An application to eastern Turkey. *Tectonophysics*, 665:92–100, Dec. 2015. doi: 10.1016/j.tecto.2015.09.031.

Delph, J. R., Levander, A., and Niu, F. Fluid Controls on the Heterogeneous Seismic Characteristics of the Cascadia Margin. *Geophysical Research Letters*, 45(20):11,021–11,029, 2018. doi: 10.1029/2018GL079518.

Dziewonski, A. M. and Anderson, D. L. Preliminary reference Earth model. *Physics of the Earth and Planetary Interiors*, 25(4):297–356, June 1981. doi: 10.1016/0031-9201(81)90046-7.

Eilon, Z., Fischer, K. M., and Dalton, C. A. An adaptive Bayesian inversion for upper-mantle structure using surface waves and scattered body waves. *Geophysical Journal International*, 214 (1):232–253, July 2018. doi: 10.1093/gji/ggy137.

Ekström, G. Love and Rayleigh phase-velocity maps, 5–40 s, of the western and central USA from USArray data. *Earth and Planetary Science Letters*, 402:42–49, Sept. 2014. doi: 10.1016/j.epsl.2013.11.022.

Ekström, G. Short-period surface-wave phase velocities across the conterminous United States. *Physics of the Earth and Planetary Interiors*, 270:168–175, Sept. 2017. doi: 10.1016/j.pepi.2017.07.010.

Ekström, G., Abers, G. A., and Webb, S. C. Determination of surface-wave phase velocities across USArray from noise and Aki's spectral formulation. *Geophysical Research Letters*, 36(18), 2009. doi: 10.1029/2009GL039131.

Faul, U. H. Permeability of partially molten upper mantle rocks from experiments and percolation theory. *Journal of Geophysical Research: Solid Earth*, 102(B5):10299–10311, 1997. doi: 10.1029/96JB03460.

Faul, U. H. Melt retention and segregation beneath mid-ocean ridges. *Nature*, 410(6831):920–923, Apr. 2001. doi: 10.1038/35073556.

Faul, U. H. and Jackson, I. The seismological signature of temperature and grain size variations in the upper mantle. *Earth and Planetary Science Letters*, 234(1):119–134, May 2005. doi: 10.1016/j.epsl.2005.02.008.

Fenneman, N. M. and Johnson, D. W. Reston, VA: US Geological Survey, Physiographic Committee Special Map. *Physiographic divisions of the conterminous U.S.*, Sept. 1946.

Fischer, K. M., Ford, H. A., Abt, D. L., and Rychert, C. A. The Lithosphere-Asthenosphere Boundary. *Annual Review of Earth and Planetary Sciences*, 38(1):551–575, 2010. doi: 10.1146/annurev-earth-040809-152438.

Fishwick, S. Surface wave tomography: Imaging of the lithosphere–asthenosphere boundary beneath central and southern Africa? *Lithos*, 120(1):63–73, Nov. 2010. doi: 10.1016/j.lithos.2010.05.011.

Foley, S. Vein-plus-wall-rock melting mechanisms in the lithosphere and the origin of potassic alkaline magmas. *Lithos*, 28 (3):435–453, Nov. 1992. doi: 10.1016/0024-4937(92)90018-T.

Foley, S. F., Venturelli, G., Green, D. H., and Toscani, L. The ultrapotassic rocks: Characteristics, classification, and constraints for petrogenetic models. *Earth-Science Reviews*, 24(2):81–134, Apr. 1987. doi: 10.1016/0012-8252(87)90001-8.

Ford, H. A., Fischer, K. M., Abt, D. L., Rychert, C. A., and Elkins-Tanton, L. T. The lithosphere–asthenosphere boundary and cratonic lithospheric layering beneath Australia from Sp wave imaging. *Earth and Planetary Science Letters*, 300(3):299–310, Dec. 2010. doi: 10.1016/j.epsl.2010.10.007.

Ford, H. A., Long, M. D., and Wirth, E. A. Midlithospheric discontinuities and complex anisotropic layering in the mantle lithosphere beneath the Wyoming and Superior Provinces. *Journal of Geophysical Research: Solid Earth*, 121(9):6675–6697, 2016. doi: 10.1002/2016JB012978.

Frost, D. J. The Stability of Hydrous Mantle Phases. *Reviews in Mineralogy and Geochemistry*, 62(1):243–271, Jan. 2006. doi: 10.2138/rmg.2006.62.11.

Gaherty, J. B., Jordan, T. H., and Gee, L. S. Seismic structure of the upper mantle in a central Pacific corridor. *J. Geophys. Res.*, 101 (B10):22291–22309, Oct. 1996. doi: 10.1029/96JB01882.

Garapić, G., Faul, U. H., and Brisson, E. High-resolution imaging of the melt distribution in partially molten upper mantle rocks: evidence for wetted two-grain boundaries. *Geochem. Geophys. Geosyst.*, 14(3):556–566, Mar. 2013. doi: 10.1029/2012GC004547.

Gilbert, H. Crustal structure and signatures of recent tectonism as influenced by ancient terranes in the western United States. *Geosphere*, 8(1):141–157, Feb. 2012. doi: 10.1130/GES00720.1.

Glazner, A. F. Animation of space-time trends in Cenozoic magmatism of western North America. *Geological Society of America Abstracts With Programs*, 36(4):10, Sept. 2004.

Golos, E. M. and Fischer, K. M. New Insights Into Lithospheric Structure and Melting Beneath the Colorado Plateau. *Geochemistry, Geophysics, Geosystems*, 23(3):e2021GC010252, 2022. doi: 10.1029/2021GC010252.

Grand, S. P. and Helmberger, D. V. Upper mantle shear structure of North America. *Geophysical Journal International*, 76(2):399–438, Feb. 1984. doi: 10.1111/j.1365-246X.1984.tb05053.x.

Hacker, B. R. and Abers, G. A. Subduction Factory 3: An Excel worksheet and macro for calculating the densities, seismic wave speeds, and H2O contents of minerals and rocks at pressure and temperature. *Geochemistry, Geophysics, Geosystems*, 5(1), 2004. doi: 10.1029/2003GC000614.

Hammond, W. C. and Humphreys, E. D. Upper mantle seismic wave velocity: Effects of realistic partial melt geometries. *Journal of Geophysical Research: Solid Earth*, 105(B5):10975–10986, 2000. doi: 10.1029/2000JB900041.

Hansen, S. M., Dueker, K. G., Stachnik, J. C., Aster, R. C., and Karlstrom, K. E. A rootless rockies—Support and lithospheric structure of the Colorado Rocky Mountains inferred from CREST and TA seismic data. *Geochemistry, Geophysics, Geosystems*, 14(8), 2013. doi: https://doi.org/10.1002/ggge.20143.

Hansen, S. M., Dueker, K., and Schmandt, B. Thermal classification of lithospheric discontinuities beneath USArray. *Earth and Planetary Science Letters*, 431:36–47, Dec. 2015. doi: 10.1016/j.epsl.2015.09.009.

Havlin, C., Holtzman, B. K., and Hopper, E. Inference of thermodynamic state in the asthenosphere from anelastic properties, with applications to North American upper mantle. *Physics of the Earth and Planetary Interiors*, 314:106639, May 2021. doi: 10.1016/j.pepi.2020.106639.

Helffrich, G., Kendall, J.-M., Hammond, J. O. S., and Carroll, M. R. Sulfide melts and long-term low seismic wavespeeds in lithospheric and asthenospheric mantle. *Geophys. Res. Lett.*, 38(11), June 2011. doi: 10.1029/2011GL047126.

Hirschmann, M. M. Mantle solidus: Experimental constraints and the effects of peridotite composition. *Geochemistry, Geophysics, Geosystems*, 1(10), 2000. doi: 10.1029/2000GC000070.

Holtzman, B. K. Questions on the existence, persistence, and mechanical effects of a very small melt fraction in the asthenosphere. *Geochemistry, Geophysics, Geosystems*, 17(2):470–484, 2016. doi: 10.1002/2015GC006102.

Holtzman, B. K. and Kendall, J.-M. Organized melt, seismic anisotropy, and plate boundary lubrication. *Geochem. Geophys. Geosyst.*, 11(12), Dec. 2010. doi: 10.1029/2010GC003296.

Hopper, E. and Fischer, K. M. The Changing Face of the Lithosphere-Asthenosphere Boundary: Imaging Continental Scale Patterns in Upper Mantle Structure Across the Contiguous U.S. With Sp Converted Waves. *Geochemistry, Geophysics, Geosystems*, 19(8):2593–2614, 2018. doi: 10.1029/2018GC007476.

Humphreys, E. D. and Dueker, K. G. Physical state of the western U.S. upper mantle. *J. Geophys. Res.*, 99(B5):9635–9650, May 1994. doi: 10.1029/93JB02640.

Humphreys, E. D., Schmandt, B., Bezada, M. J., and Perry-Houts, J. Recent craton growth by slab stacking beneath Wyoming. *Earth and Planetary Science Letters*, 429:170–180, Nov. 2015. doi: 10.1016/j.epsl.2015.07.066.

IRIS-DMC. Data Services Products: EMC, A repository of Earth models. 2011. doi: https://doi.org/10.17611/DP/EMC.1.

Jackson, I. and Faul, U. H. Grainsize-sensitive viscoelastic relaxation in olivine: Towards a robust laboratory-based model for seismological application. *Physics of the Earth and Planetary Interiors*, 183(1):151–163, Nov. 2010. doi: 10.1016/j.pepi.2010.09.005.

Jin, G. and Gaherty, J. B. Surface wave phase-velocity tomography based on multichannel cross-correlation. *Geophysical Journal International*, 201(3):1383–1398, June 2015. doi: 10.1093/gji/ggv079.

Kanamori, H. and Anderson, D. L. Importance of physical dispersion in surface wave and free oscillation problems: Review. *Reviews of Geophysics*, 15(1):105–112, 1977. doi: 10.1029/RG015i001p00105.

Karato, S.-i. and Jung, H. Water, partial melting and the origin of the seismic low velocity and high attenuation zone in the upper mantle. *Earth and Planetary Science Letters*, 157(3):193–207, Apr. 1998. doi: 10.1016/S0012-821X(98)00034-X.

Karato, S.-i. and Wu, P. Rheology of the Upper Mantle: A Synthesis. *Science*, 260(5109):771–778, May 1993. doi: 10.1126/science.260.5109.771.

Karato, S.-i., Olugboji, T., and Park, J. Mechanisms and geologic significance of the mid-lithosphere discontinuity in the continents. *Nature Geosci*, 8(7):509–514, July 2015. doi: 10.1038/ngeo2462.

Katz, R. F., Spiegelman, M., and Langmuir, C. H. A new parameterization of hydrous mantle melting. *Geochemistry, Geophysics, Geosystems*, 4(9), 2003. doi: 10.1029/2002GC000433.

Kawakatsu, H., Kumar, P., Takei, Y., Shinohara, M., Kanazawa, T., Araki, E., and Suyehiro, K. Seismic Evidence for Sharp Lithosphere-Asthenosphere Boundaries of Oceanic Plates. *Science*, 324(5926):499–502, Apr. 2009. doi: 10.1126/science.1169499.

Kind, R., Yuan, X., and Kumar, P. Seismic receiver functions and the lithosphere–asthenosphere boundary. *Tectonophysics*, 536-537:25–43, Apr. 2012. doi: 10.1016/j.tecto.2012.03.005.

Kumar, P., Kind, R., Yuan, X., and Mechie, J. USArray Receiver Function Images of the Lithosphere-Asthenosphere Boundary. *Seismological Research Letters*, 83(3):486–491, May 2012. doi: 10.1785/gssrl.83.3.486.

Lekić, V. and Fischer, K. M. Contrasting lithospheric signatures across the western United States revealed by Sp receiver functions. *Earth and Planetary Science Letters*, 402:90–98, Sept. 2014. doi: 10.1016/j.epsl.2013.11.026.

Levander, A. and Miller, M. S. Evolutionary aspects of lithosphere discontinuity structure in the western U.S. *Geochem. Geophys. Geosyst.*, 13(7), July 2012. doi: 10.1029/2012GC004056.

Levander, A., Schmandt, B., Miller, M. S., Liu, K., Karlstrom, K. E., Crow, R. S., Lee, C.-T. A., and Humphreys, E. D. Continuing Colorado plateau uplift by delamination-style convective lithospheric downwelling. *Nature*, 472(7344):461–465, Apr. 2011. doi: 10.1038/nature10001.

Lin, F.-C. and Ritzwoller, M. H. Helmholtz surface wave tomography for isotropic and azimuthally anisotropic structure. *Geophysical Journal International*, 186(3):1104–1120, Sept. 2011. doi: 10.1111/j.1365-246X.2011.05070.x.

Liu, T. and Shearer, P. M. Complicated Lithospheric Structure Beneath the Contiguous US Revealed by Teleseismic S-Reflections. *Journal of Geophysical Research: Solid Earth*, 125(5):e2020JB021624, 2021. doi: https://doi.org/10.1029/2020JB021624.

Ma, Z., Dalton, C. A., Russell, J. B., Gaherty, J. B., Hirth, G., and Forsyth, D. W. Shear attenuation and anelastic mechanisms in the central Pacific upper mantle. *Earth and Planetary Science Letters*, 536:116148, Apr. 2020. doi: 10.1016/j.epsl.2020.116148.

Mallik, A. and Dasgupta, R. Reactive Infiltration of MORB-Eclogite-Derived Carbonated Silicate Melt into Fertile Peridotite at 3 GPa and Genesis of Alkalic Magmas. *Journal of Petrology*, 54(11): 2267–2300, Nov. 2013. doi: 10.1093/petrology/egt047.

Mark, H. F., Collins, J. A., Lizarralde, D., Hirth, G., Gaherty, J. B., Evans, R. L., and Behn, M. D. Constraints on the Depth, Thickness, and Strength of the G Discontinuity in the Central Pacific From S Receiver Functions. *Journal of Geophysical Research: Solid Earth*, 126(4):e2019JB019256, 2021. doi: 10.1029/2019JB019256.

Masters, G., Woodhouse, J. H., and Freeman, G. Mineos v1.0.2. Computational infrastructure for geodynamics. 2011. doi: http://geoweb.cse.ucdavis.edu/cig/software/mineos/.

McCarthy, C., Takei, Y., and Hiraga, T. Experimental study of attenuation and dispersion over a broad frequency range: 2. The universal scaling of polycrystalline materials. *Journal of Geophysical Research: Solid Earth*, 116(B9), 2011. doi: 10.1029/2011JB008384.

Mehouachi, F. and Singh, S. C. Water-rich sublithospheric melt channel in the equatorial Atlantic Ocean. *Nature Geosci*, 11(1): 65–69, Jan. 2018. doi: 10.1038/s41561-017-0034-z.

Menke, W. *Geophysical Data Analysis: Discrete Inverse Theory: MATLAB Edition*. Academic Press, July 2012.

Mirnejad, H. and Bell, K. Origin and Source Evolution of the Leucite Hills Lamproites: Evidence from Sr-Nd-Pb-O Isotopic Compositions. *Journal of Petrology*, 47(12):2463–2489, Sept. 2006. doi: 10.1093/petrology/egl051.

Montagner, J.-P. and Anderson, D. L. Petrological constraints on seismic anisotropy. *Physics of the Earth and Planetary Interiors*, 54(1-2):82–105, Apr. 1989. doi: 10.1016/0031-9201(89)90189-1.

Olugboji, T. M., Karato, S., and Park, J. Structures of the oceanic lithosphere-asthenosphere boundary: Mineral-physics modeling and seismological signatures. *Geochem. Geophys. Geosyst.*, 14(4):880–901, Apr. 2013. doi: 10.1002/ggge.20086.

Pakiser, L. C. Structure of the crust and upper mantle in the western United States. *Journal of Geophysical Research (1896-1977)*, 68(20):5747–5756, 1963. doi: 10.1029/JZ068i020p05747.

Pilet, S. Generation of low-silica alkaline lavas: Petrological constraints, models, and thermal implications. *The Interdisciplinary Earth: A Volume in Honor of Don L. Anderson: Geological Society of America Special Paper 514 and American Geophysical Union Special Publication*, Oct. 2015. doi: 10.1130/2015.2514(17).

Pilet, S., Baker, M. B., and Stolper, E. M. Metasomatized Lithosphere and the Origin of Alkaline Lavas. *Science*, 320(5878):916–919, May 2008. doi: 10.1126/science.1156563.

Plank, T. and Forsyth, D. W. Thermal structure and melting conditions in the mantle beneath the Basin and Range province from seismology and petrology. *Geochemistry, Geophysics, Geosystems*, 17(4):1312–1338, 2016. doi: 10.1002/2015GC006205.

Porter, R. and Reid, M. Mapping the Thermal Lithosphere and Melting Across the Continental US. *Geophysical Research Letters*, 48 (7):e2020GL092197, 2021. doi: 10.1029/2020GL092197.

Porter, R., Liu, Y., and Holt, W. E. Lithospheric records of orogeny within the continental U.S. *Geophysical Research Letters*, 43(1):

144–153, 2016. doi: 10.1002/2015GL066950.

Porter, R. C., van der Lee, S., and Whitmeyer, S. J. Synthesizing EarthScope data to constrain the thermal evolution of the continental U.S. lithosphere. *Geosphere*, 15(6):1722–1737, Nov. 2019. doi: 10.1130/GES02000.1.

Priestley, K. and McKenzie, D. The thermal structure of the lithosphere from shear wave velocities. *Earth and Planetary Science Letters*, 244(1):285–301, Apr. 2006. doi: 10.1016/j.epsl.2006.01.008.

Priestley, K. and McKenzie, D. The relationship between shear wave velocity, temperature, attenuation and viscosity in the shallow part of the mantle. *Earth and Planetary Science Letters*, 381:78–91, Nov. 2013. doi: 10.1016/j.epsl.2013.08.022.

Roy, M., Jordan, T. H., and Pederson, J. Colorado Plateau magmatism and uplift by warming of heterogeneous lithosphere. *Nature*, 459(7249):978–982, June 2009. doi: 10.1038/nature08052.

Russell, J. B., Gaherty, J. B., Lin, P.-Y. P., Lizarralde, D., Collins, J. A., Hirth, G., and Evans, R. L. High-Resolution Constraints on Pacific Upper Mantle Petrofabric Inferred From Surface-Wave Anisotropy. *Journal of Geophysical Research: Solid Earth*, 124(1): 631–657, 2019. doi: 10.1029/2018JB016598.

Rychert, C. A., Fischer, K. M., and Rondenay, S. A sharp lithosphere–asthenosphere boundary imaged beneath eastern North America. *Nature*, 436(7050):542–545, July 2005. doi: 10.1038/nature03904.

Rychert, C. A., Rondenay, S., and Fischer, K. M. P-to-S and S-to-P imaging of a sharp lithosphere-asthenosphere boundary beneath eastern North America. *Journal of Geophysical Research: Solid Earth*, 112(B8), 2007. doi: 10.1029/2006JB004619.

Saha, S., Peng, Y., Dasgupta, R., Mookherjee, M., and Fischer, K. M. Assessing the presence of volatile-bearing mineral phases in the cratonic mantle as a possible cause of mid-lithospheric discontinuities. *Earth and Planetary Science Letters*, 553:116602, Jan. 2021. doi: 10.1016/j.epsl.2020.116602.

Sakamaki, T., Suzuki, A., Ohtani, E., Terasaki, H., Urakawa, S., Katayama, Y., Funakoshi, K.-i., Wang, Y., Hernlund, J. W., and Ballmer, M. D. Ponded melt at the boundary between the lithosphere and asthenosphere. *Nature Geosci*, 6(12):1041–1044, Dec. 2013. doi: 10.1038/ngeo1982.

Sarafian, E., Gaetani, G. A., Hauri, E. H., and Sarafian, A. R. Experimental constraints on the damp peridotite solidus and oceanic mantle potential temperature. *Science*, 355(6328):942–945, Mar. 2017. doi: 10.1126/science.aaj2165.

Schmandt, B. and Humphreys, E. Complex subduction and small-scale convection revealed by body-wave tomography of the western United States upper mantle. *Earth and Planetary Science Letters*, 297(3):435–445, Sept. 2010. doi: 10.1016/j.epsl.2010.06.047.

Schmandt, B. and Humphreys, E. Seismically imaged relict slab from the 55 Ma Siletzia accretion to the northwest United States. *Geology*, 39(2):175–178, Feb. 2011. doi: 10.1130/G31558.1.

Schmandt, B., Lin, F.-C., and Karlstrom, K. E. Distinct crustal isostasy trends east and west of the Rocky Mountain Front. *Geophysical Research Letters*, 42(23):10,290–10,298, 2015. doi: 10.1002/2015GL066593.

Selway, K., Ford, H., and Kelemen, P. The seismic mid-lithosphere discontinuity. *Earth and Planetary Science Letters*, 414:45–57, Mar. 2015. doi: 10.1016/j.epsl.2014.12.029.

Shen, W. and Ritzwoller, M. H. Crustal and uppermost mantle structure beneath the United States. *Journal of Geophysical Research: Solid Earth*, 121(6):4306–4342, 2016. doi: 10.1002/2016JB012887.

Solomon, S. C. Seismic-wave attenuation and partial melting in the upper mantle of North America. *J. Geophys. Res.*, 77(8): 1483–1502, Mar. 1972. doi: 10.1029/JB077i008p01483.

Sparks, D. W. and Parmentier, E. M. Melt extraction from the mantle beneath spreading centers. *Earth and Planetary Science Letters*, 105(4):368–377, Aug. 1991. doi: 10.1016/0012-821X(91)90178-K.

Stixrude, L. and Lithgow-Bertelloni, C. Mineralogy and elasticity of the oceanic upper mantle: Origin of the low-velocity zone. *Journal of Geophysical Research: Solid Earth*, 110(B3), 2005. doi: 10.1029/2004JB002965.

Takei, Y. Effect of pore geometry on VP/VS: From equilibrium geometry to crack. *Journal of Geophysical Research: Solid Earth*, 107(B2):ECV 6–1–ECV 6–12, 2002. doi: 10.1029/2001JB000522.

Takei, Y. and Holtzman, B. K. Viscous constitutive relations of solid-liquid composites in terms of grain boundary contiguity: 1. Grain boundary diffusion control model. *Journal of Geophysical Research: Solid Earth*, 114(B6), 2009. doi: 10.1029/2008JB005850.

Tan, Y. and Helmberger, D. V. Trans-Pacific upper mantle shear velocity structure. *Journal of Geophysical Research: Solid Earth*, 112(B8), 2007. doi: 10.1029/2006JB004853.

Thibault, Y., Edgar, A. D., and Lloyd, F. E. Experimental investigation of melts from a carbonated phlogopite lherzolite: Implications for metasomatism in the continental lithospheric mantle. *American Mineralogist*, 77(7-8):784–794, Aug. 1992.

van Wijk, J., Baldridge, W., van Hunen, J., Goes, S., Aster, R., Coblentz, D., Grand, S., and Ni, J. Small-scale convection at the edge of the Colorado Plateau: Implications for topography, magmatism, and evolution of Proterozoic lithosphere. *Geology*, 38(7):611–614, July 2010. doi: 10.1130/G31031.1.

Walker, J. D., Bowers, T. D., Glazner, A. F., Famer, G. L., , and Carlson, R. Creation of a North American volcanic and plutonic rock database (NAVDAT). *Geological Society of America Abstracts With Programs*, 4(4):9, Sept. 2004.

Wannamaker, P. E., Hasterok, D. P., Johnston, J. M., Stodt, J. A., Hall, D. B., Sodergren, T. L., Pellerin, L., Maris, V., Doerner, W. M., Groenewold, K. A., and Unsworth, M. J. Lithospheric dismemberment and magmatic processes of the Great Basin–Colorado Plateau transition, Utah, implied from magnetotellurics. *Geochemistry, Geophysics, Geosystems*, 9(5), 2008. doi: 10.1029/2007GC001886.

Whitmeyer, S. J. and Karlstrom, K. E. Tectonic model for the Proterozoic growth of North America. *Geosphere*, 3(4):220–259, Aug. 2007. doi: 10.1130/GES00055.1.

Wirth, E. A. and Long, M. D. A contrast in anisotropy across mid-lithospheric discontinuities beneath the central United States—A relic of craton formation. *Geology*, 42(10):851–854, Oct. 2014. doi: 10.1130/G35804.1.

Xie, J., Chu, R., and Yang, Y. 3-D Upper-Mantle Shear Velocity Model Beneath the Contiguous United States Based on Broadband Surface Wave from Ambient Seismic Noise. *Pure and Applied Geophysics*, 175, May 2018. doi: 10.1007/s00024-018-1881-2.

Yamauchi, H. and Takei, Y. Polycrystal anelasticity at near-solidus temperatures. *Journal of Geophysical Research: Solid Earth*, 121 (11):7790–7820, 2016. doi: 10.1002/2016JB013316.

Yamauchi, H. and Takei, Y. Application of a Premelting Model to the Lithosphere-Asthenosphere Boundary. *Geochemistry, Geophysics, Geosystems*, 21(11):e2020GC009338, 2020. doi: 10.1029/2020GC009338.

doi:10.26443/seismica.v2i2.247

SEISMICA

Spatiotemporal evaluation of Rayleigh surface waves estimated from roadside dark fiber DAS array and traffic noise

Rafał Czarny * [1], **Tieyuan Zhu** [1], **Junzhu Shen** [1]

[1]Department of Geosciences, The Pennsylvania State University, University Park, United States

Author contributions: *Conceptualization*: R. Czarny. *Data Curation*: R. Czarny, T. Zhu. *Formal Analysis*: R. Czarny. *Funding Acquisition*: T. Zhu. *Investigation*: R. Czarny, T. Zhu. *Methodology*: R. Czarny. *Project Administration*: R. Czarny, T. Zhu. *Resources*: T. Zhu. *Software*: R. Czarny, J. Shen. *Supervision*: T. Zhu. *Validation*: R. Czarny. *Visualization*: R. Czarny. *Writing – original draft*: R. Czarny, T. Zhu. *Writing – review & editing*: R. Czarny, T. Zhu, J. Shen.

Abstract Seismic imaging and monitoring of the near-surface structure are crucial for the sustainable development of urban areas. However, standard seismic surveys based on cabled or autonomous geophone arrays are expensive and hard to adapt to noisy metropolitan environments. Distributed acoustic sensing (DAS) with pre-existing telecom fiber optic cables, together with seismic ambient noise interferometry, have the potential to fulfill this gap. However, a detailed noise wavefield characterization is needed before retrieving coherent waves from chaotic noise sources. We analyze local seismic ambient noise by tracking five-month changes in signal-to-noise ratio (SNR) of Rayleigh surface wave estimated from traffic noise recorded by DAS along the straight university campus busy road. We apply the seismic interferometry method to the 800 m long part of the Penn State Fiber-Optic For Environment Sensing (FORESEE) array. We evaluate the 160 virtual shot gathers (VSGs) by determining the SNR using the slant-stack technique. We observe strong SNR variations in time and space. We notice higher SNR for virtual source points close to road obstacles. The spatial noise distribution confirms that noise energy focuses mainly on bumps and utility holes. We also see the destructive impact of precipitation, pedestrian traffic, and traffic along main intersections on VSGs. A similar processing workflow can be applied to various straight roadside fiber optic arrays in metropolitan areas.

Production Editor:
Gareth Funning
Handling Editor:
Nicola P. Agostinetti
Copy & Layout Editor:
Jack B. Muir

Received:
May 15th, 2023
Accepted:
July 6th, 2023
Published:
August 14th, 2023

1 Introduction

To develop and reinforce urban infrastructure for smart cities, the number of fiber optic cable installations rapidly increases. Recent studies show that these networks can be used not only for communication and transferring data but also for monitoring and imaging the near-surface structure using DAS (Li et al., 2022). For rapidly growing urban population densities, shallow subsurface characterization of physical and mechanical properties regarding groundwater resources management, infrastructure safety, road inspection, or geohazards monitoring is crucial for sustainable development. DAS can turn the fiber optic cable into a sensor array sensitive to ground vibrations (Lindsey and Martin, 2021). Consequently, the fiber optic line can work like a geophone spread in seismic methods. This technology can operate in tough conditions like extreme temperature or power supply limitations and record vibrations within 17 octaves (Paitz et al., 2021). Therefore, it has been used simultaneously in global seismology (Nayak and Ajo-Franklin, 2021) and at a laboratory scale (Titov et al., 2022). Furthermore, it requires only a single power point source to record vibration from tens of km of fiber lines with meter-scale sampling resolution. Hence, it is less expensive and easier to maintain than a standalone geophone array, especially with the city's pre-existing dark fiber optic cables.

Ambient seismic noise, which is dominated by surface waves (Nakata et al., 2019), gives the ability to analyze elastic properties of the subsurface cost-effectively. Seismic interferometry is one of those methods which allows extracting useful information from randomly distributed sources (Wapenaar et al., 2010). This method mimics a standard seismic survey by focusing the chaotic seismic wavefield into the virtual source (VS) and then exciting it toward receivers. The main drawback of seismic interferometry application in a metropolitan area is the complex nature of the noise therein. In such conditions, the dominant noise source can be localized out of the stationary-phase region (out of line crossing virtual source-receiver pair) and produce apparent surface wave velocity. This azimuthal-dependent source distribution can be analyzed using a large-N geophone array (Nakata et al., 2015), or dense DAS array (Zeng et al., 2017; van den Ende and Ampuero, 2021). Unfortunately, many dark fibers are limited to straight-line profiles deployed close to the main roads in the city and sense only the vibrations in the direction of fiber optic cable. For such limitations, spatial noise distribution analysis of the high-frequency range noise, which can change the behavior every couple of meters, is complicated. The most common practice for such an environment is to increase the illumination time to retrieve reliable surface waves (Spica et al., 2020;

*Corresponding author: rkc5556@psu.edu

Yang et al., 2022), or use well-recognized strong local seismic sources, e.g., trains (?), cars (Dou et al., 2017; Song et al., 2021) or quarry blasts (Fang et al., 2020). When the noise source is more complex, one can use coda wave interferometry and scattering waves which are less sensitive to noise inhomogeneity (?). In a recent paper, Song et al. (2022) present the promising three-station interferometry technique, which can increase the coherence of noise correlation functions. However, estimating a stable high-frequency surface wave from ambient noise in the city remains challenging, and understanding what influences local Green's function is mandatory.

In this paper, we investigate high-frequency ambient noise behavior in time and space by analyzing the signal-to-noise ratio (SNR) of Rayleigh surface waves estimated from traffic noise recorded by the Penn State Fiber-Optic For Environment Sensing (FORESEE) array in State College, Pennsylvania. We utilize an 800 m straight profile of telecom fiber along Pollock Rd, one of the busiest university campus roads where thousands of students pass by every day during the semester. First, we characterize the ambient seismic noise through the city. Then we analyze 160 virtual shots gathers (VSGs) from the beginning of May to the end of September 2019. We recognize the main factors determining the SNR of Rayleigh surface waves along the road. We also characterize noise source distribution in space using back projection technique. Our method can be used for other sites with straight-line geometry.

2 Data characterization

2.1 The DAS Array

The Penn State FORESEE DAS array consists of 4.2 km of dark fiber that crosses the Pennsylvania State University campus (Fig. 1a). The recording started in April 2019 and finished in October 2021 with three different frequency samplings: 250 Hz, 500 Hz, and 1000 Hz (Fig. 1b). The depth of the telecom fiber optic cable varies with an average of 1 m (personal communication). The interrogator Silixa iDAS2 as sensing the 2137 channels every 2 m with a 10 m gauge length. More details about the array and observations can be found in Zhu et al. (2021). We analyze the 800 m straight segment along Pollock Rd (Fig. 1c).

2.2 Seismic ambient noise

Figure 2 presents the power spectrum density (PSD) changes over two weeks of May 2019 for 2137 channels. The PSD is averaged within four different frequency ranges: 0.5–4 Hz, 4–10 Hz, 10–20 Hz, and 20–50 Hz. For each range, the higher amplitudes start around 8 AM and end around 8 PM. The strongest noise comes from the main streets of University Dr, Curtin Rd, and Pollock Rd (Fig. 1a). However, Curtin Rd shows the highest values, especially between channels 808 and 1120, where the cable is set up close to the road shoulder. The higher PSD values in all frequency ranges for channels near the road suggest that the anthropogenic noise sources originate in traffic. During the weekends, we observe a slight PSD decrease, mainly in the lower frequency range (0.5–4 Hz), probably due to reduced heavy vehicle traffic these days. A similar pattern of anthropogenic noise emerging during the day and decaying at night (Shen and Zhu, 2021) was observed in other cities (e.g., Díaz et al., 2017).

We also observe the weather condition imprint on PSD. The wind and rain during the storm on May 4 changed the PSD in all frequency ranges. The wind amplifies PSD but only for the first 500 channels and when the wind gusts exceed 15 m/s (Fig. 2b). The first 500 channels are in the open space area near campus football pitches, where the wind can much more easily induce ground vibration than in built-up areas. During heavy rain, the PSD values increase for a few channels close to the storm sewers (Fig. 2c). The increase starts a few minutes after the beginning of the rain and vanishes a couple of minutes after the rain. It is likely the acoustic effect of fluid flowing through the drainage system (Shen and Zhu, 2023, submitted).

3 Rayleigh surface wave evaluation

3.1 Rayleigh surface wave estimation

Figure 2 shows that most of the seismic noise concentrates along the roads and is caused by traffic. Around 75 % of FORESEE DAS channels are installed beneath the sidewalks and near the road shoulders (Fig. 1). For such geometry, where the noise source propagates inline, the Rayleigh surface wave is amplified (e.g., Spica et al., 2020). However, in some heavy traffic intersections, Love surface waves can also be sensed by the DAS fiber array (Martin et al., 2018). To monitor and image the first few meters of the subsurface with the ambient noise interferometry along the straight road, we need to understand better what influences the SNR of the estimated Rayleigh surface wave in time and space. To do so, we focus on the 400 channels along Pollock Rd (from channel 1460 to 1860) (Fig. 1c). It is the longest straight part of the array within the built-up campus area. Our processing workflow is similar to what was introduced in seismology (Bensen et al., 2007) (Fig. 3).

We only modify the preprocessing step by running the same workflow for each 1-minute continuous recording input file twice for negative and positive wavenumbers. Czarny and Zhu (2022) used a similar approach for 1D S-wave velocity model estimation along Pollock Rd. This procedure gives us more information about the spatial distribution of the noise source described later. We also constrain the wavefield between phase velocity 100 m/s and 5500 m/s in the f-k domain to reduce the influence of the noise sources out of the stationary-phase region. Then, we process both wavefields separately. We detrend the data, decimate to 100 Hz sampling frequency, band-pass between 1 and 45 Hz, and flatten the spectrum using spectral whitening. Eventually, we generate VSGs with a step of 5 channels for a new VS point. It gives us 160 virtual source points (80 for each wavenumber). Following these steps, we process data from May to September 2019. To reduce

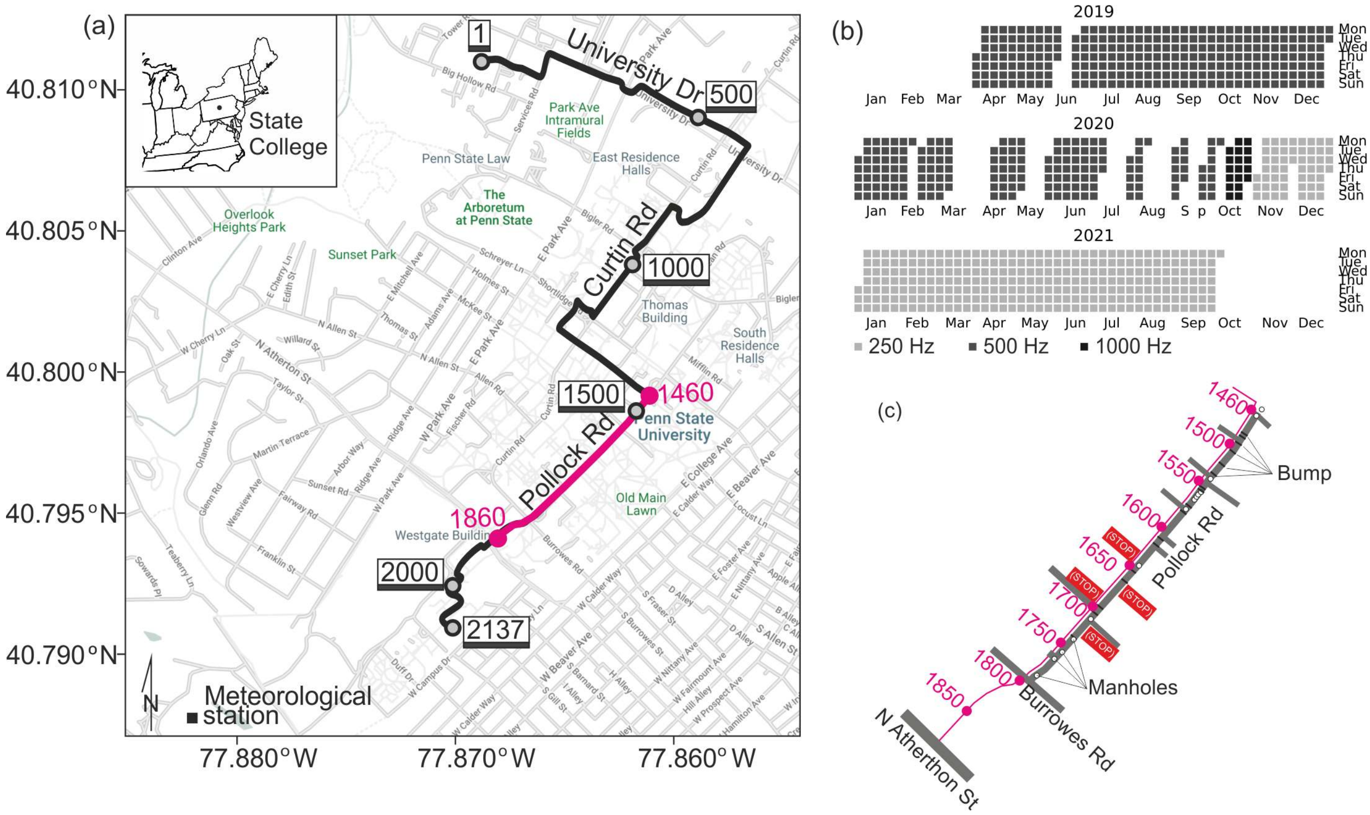

Figure 1 (a) Dark fiber DAS array layout. (b) The scope of FORESEE project recordings. (c) A part of the array (from channel 1460 to channel 1860) and the main road infrastructure we use in the study.

computation time, we take only daytime (from 8 AM to 8 PM) when the heaviest traffic occurs.

3.2 Signal-to-noise ratio

VSGs stacked over one month (Fig. 3) show that the main energy of the Rayleigh surface wave travels as a fundamental mode with an average velocity for higher frequencies (10-35 Hz) around 1120 m/s. To evaluate the SNR of the estimated Rayleigh surface wave in time and space, we use the slant-stack method (Vidal et al., 2014) and transform VSGs obtained for every 1-minute data to the slowness representation using the formula:

$$C(f,p) = \left\| \sum_{j=1}^{N} e^{i2\pi f x_j p} A\left(f, x_j\right) \right\|_{\max} \tag{1}$$

where $C(f,p)$ is the maximum value searching from the summation over different phase shifts in the frequency domain; $A\left(f, x_j\right)$ is a Fourier transform of the VSG where each j receiver has x_j offset from the VS point; p and f denote slowness and frequency, respectively. We use 100 channels around each VS. In figure 4, we present the slant-stacking summation for 3 different VSGs for the same VS point with different SNR of the estimated Rayleigh surface wave. To make analysis easier, we change slowness to phase velocity. We use the wave between 1 and 45 Hz. To assess SNR, we determine the ratio between maximum energy focused on the fundamental mode (900–1500 m/s) and the other velocities. We similarly process all VS points for positive and negative wavenumbers.

4 Results and Discussion

4.1 Temporal SNR changes

Figure 5 presents the distribution of SNRs along Pollock Rd in a daily time frame from the beginning of May to the end of September 2019, except June. Figures 5d and 5e represent VSGs for negative wavenumber (we call it negative wavefield - propagates from higher to lower channels) and VSGs for positive wavenumber (we call it positive wavefield - propagates from lower to higher channels), respectively. To better understand temporal SNR variations, we add temperature (Fig. 5b) and the precipitation (Fig. 5c) from the local meteorological station (Fig. 1a) and depth to water level (Fig. 5c) from the USGS observatory well located 4 km from our array.

Both wavefields generally show a similar pattern, but the negative one reveals higher SNR values overall. This difference is visible in Figure 5f, which represents the SNR averaged for all VS points. For all days except May 12 and 13, we notice intense illumination by the ambient noise coming from the west. It is probably seismic noise due to heavy car traffic along the 4-lane N Atherton St. that crosses the FORESEE array around channel 1880 (Fig. 1c). In Figure 5g, as a result of subtracting the SNR for negative from the SNR for positive wavefields, we can also observe how this western noise source amplifies the wavefield in almost all VS points.

SNR distribution over five months shows some long- and short-term changes. For long-term changes, we can distinguish three periods: from May 1 to May 16, May 16 to August 23, and August 23 to the end of September. During the first and last periods, the SNR decreases.

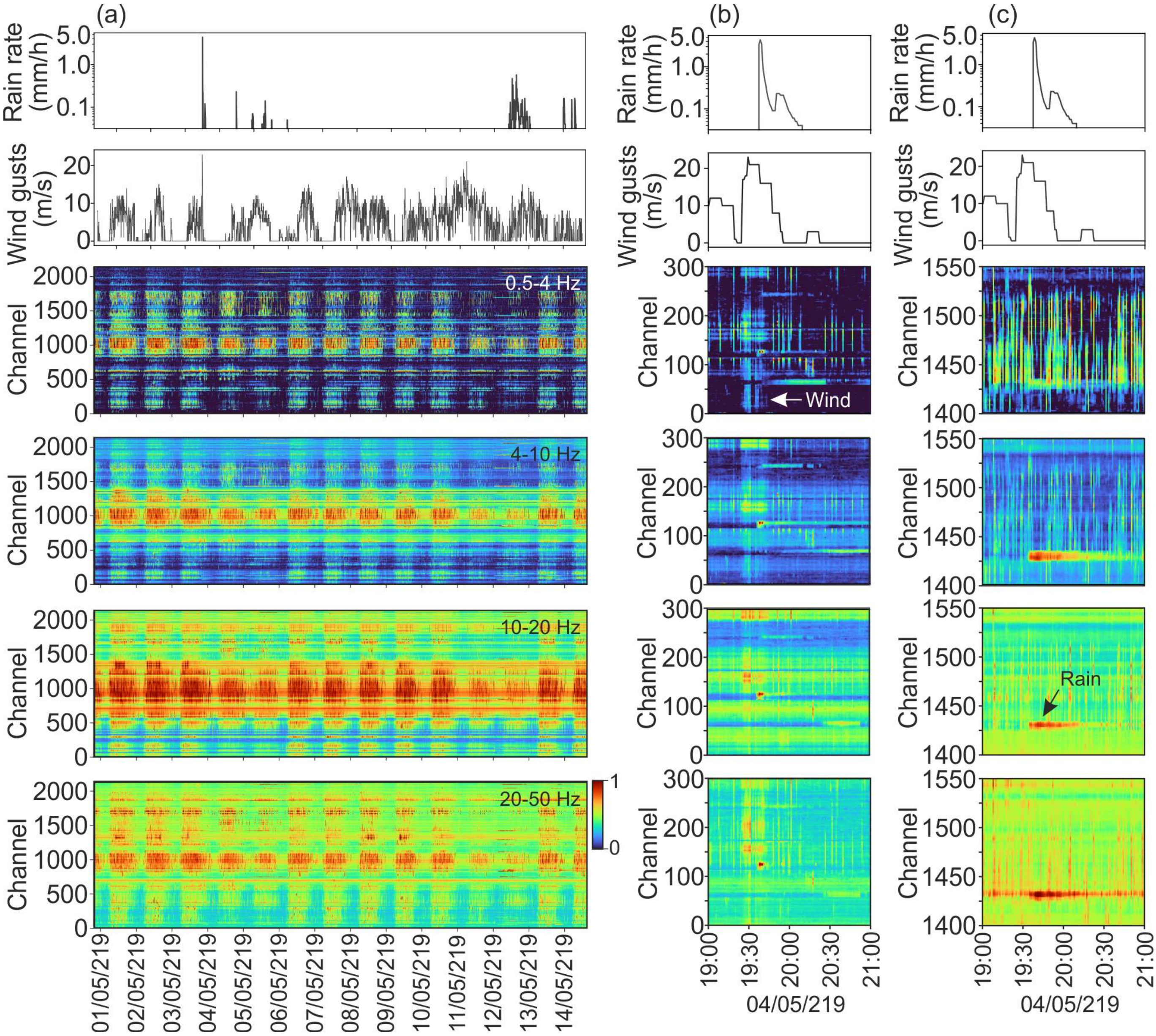

Figure 2 (a) PSD averaged in 4 frequency ranges: 0.5-4 Hz, 4-10 Hz, 10-20 Hz, and 20-50 Hz. Higher PSD values are noticed for fiber optic cable installed near the main campus roads. (b) Amplitude increase due to wind gusts for the first 500 channels located in an open-space area. (c) Amplitude increase due to water flowing through the drainage system close to the fiber optic cable conduit.

We link this drop with students' activity on the University campus during the spring and fall semesters. Pollock Rd is the main campus path for walking and riding bikes. The local high-frequency noise from pedestrians and cyclists can contaminate coherent surface wave phases from distant sources. Moreover, telecom fiber in many places is installed directly below the pavement and close to the surface, which amplifies this effect.

Short-term SNR changes are connected with weather conditions and urban activity. The SNR increases on almost all weekends, particularly during the summer break. Generally, at the weekend, the university is visited by fewer people. This pattern disturbs May 5 (Fig 5f, labeled as A), when the commencement ceremonies occurred. The beginning of the fall semester is also a time with more pedestrians at the university, even during the weekends. That is why we do not see an increase in SNR at weekends from August 23 to the mid of September.

The PSD shows that wind does not generate strong ground vibration in the build-up area (Fig. 2). However, precipitation and temperature impact the SNR. For example, between May 12 and 14, a long-hour lasting moderate precipitation occurred and changed the depth to the water level of about 50 cm in next following days (Fig. 5a). It was the highest precipitation during all five months of our analysis. As a result, the SNR significantly decreases. Interestingly, in next following two days, we observe higher average SNR for the positive wavefield (Fig. 5e, labeled as B) than the negative one. We posit that the ambient noise from N Atherton St. is attenuated more due to higher water content in the shallow surface.

In addition, in Figure 6, we present the maximum amplitudes of the Rayleigh surface wave in the range of 1-

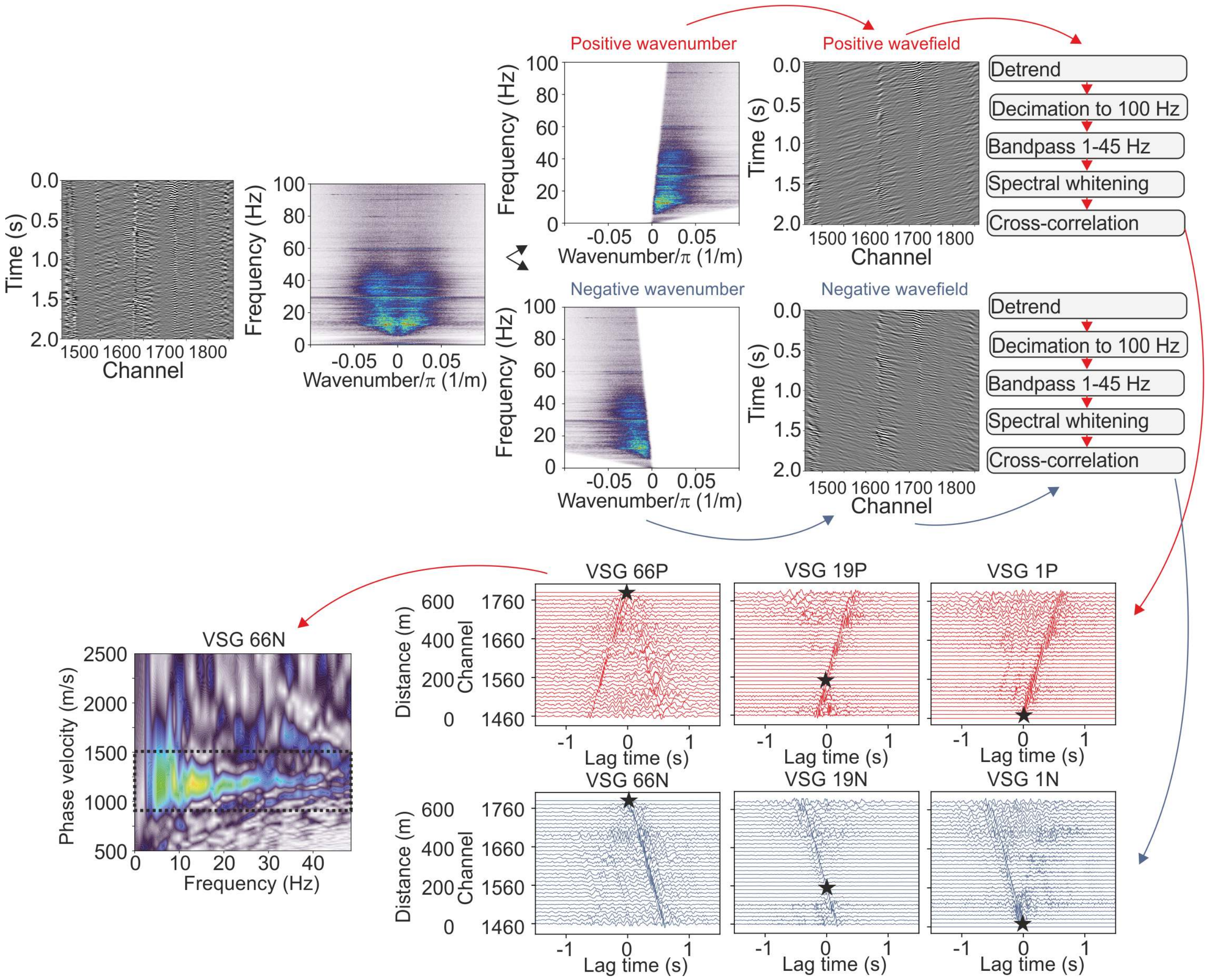

Figure 3 The processing flowchart of Rayleigh surface wave estimation from seismic ambient noise regarding the wavefield direction. The examples of VSGs obtained by linear stacking of the one-month data show consistency in Rayleigh surface wave velocity of the main energy. The fundamental model propagates between 1000-1500 m/s in the higher frequency range.

45 Hz between May 12 and May 16. These surface waves are generated by cars passing through the same bump around channel 1540. For each day, we select 8 waveforms (from 8 cars) with similar strain rate values in a source (channel below the bump). Due to the high contamination of other seismic noise to the selected wavefield, we examine only the near field around the bump. Indeed, the surface wave attenuates the most on May 12 (Fig. 6f). The attenuation can be visible on pure waveforms in Figures 6g and 6h. The amplitudes decay much faster on May 12 (wet day) than on May 16 (dry day) for comparable source energy.

We do not see such strong attenuation on May 13 and May 14 for nearfield, but only SNR drop from farfield (west noise from N Atherton St.). We hypothesize that the water did not evaporate but slowly percolated to the topsoil layer and then infiltrated into the deeper layers. It happened because of the lower temperature those days. The shallow subsurface, up to tens of meters around the campus, contains fractured dolomite above the limestone layer with karst features in this region (Drake and Harmon, 1973). The top 2 to 4 m is built with clay. Water can easily migrate through the well-developed subsurface drainage within such prone sinkhole hazards carbonate strata. However, testing this hypothesis is beyond this study's scope. It is worth noting that when a few short storms occurred at the end of May, rapidly changing the water table, the SNR (Fig. 5e, labeled as (C)) remained high when the temperature is around 20 °C in this period.

4.2 Spatial SNR changes

One-component data recorded along the straight dark fiber DAS array is challenging to characterize the noise origin in space. However, we identify the primary seismic noise sources in the investigation area using the back projection technique (e.g., Li et al., 2020; Rabade et al., 2022; Song et al., 2022). This method illuminates the most likely distribution of noise source energy in space by migrating the amplitude from the time domain VSG to the grid in space using the averaged velocity of the investigated seismic wave. First, the difference between the distance of the VS point to the grid point and

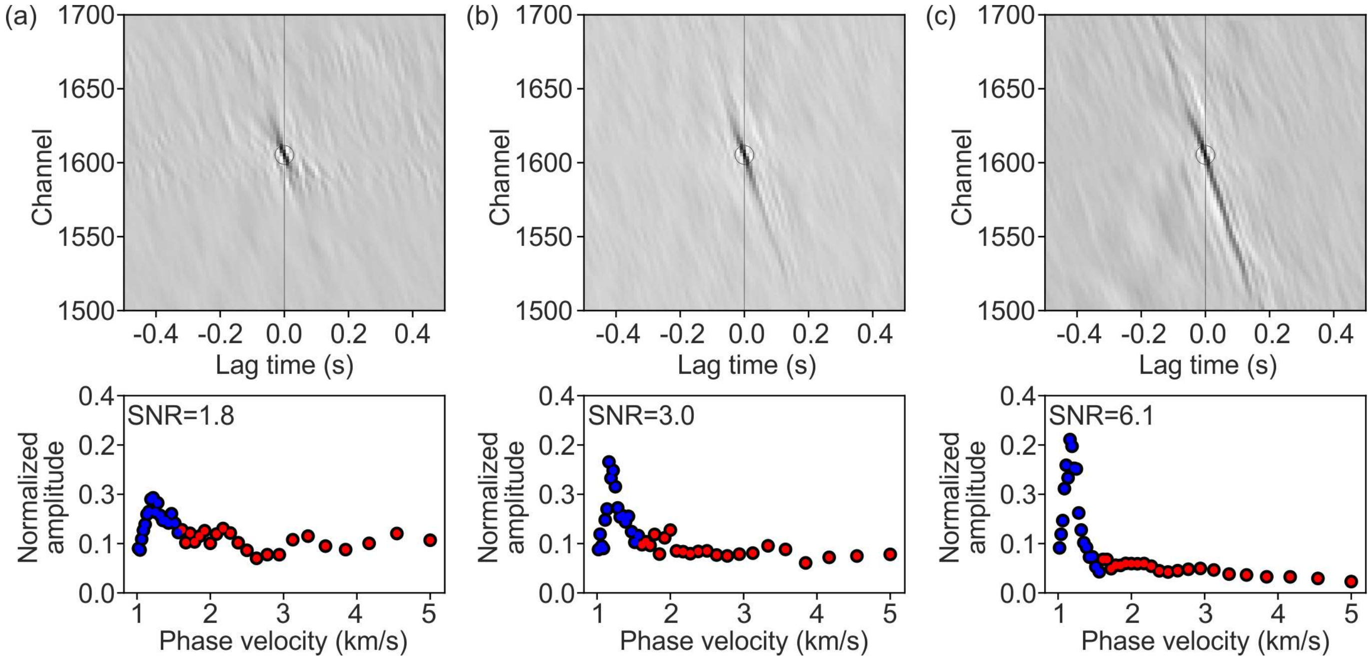

Figure 4 The slant-stack analysis examples for the same VS point but three different minutes with three different SNR of Rayleigh surface wave: 1.8, 3.0, and 6.1.

the distance of VS point to the receiver is computed. Then, for this difference, the wave is focused on the grid point using the averaged velocity. The wave energy is the root-mean-square of amplitudes in the time window with the length of the wave duration. We use the 40 ms window as an optimum parameter for our array. This window corresponds to the duration of the fundamental mode Rayleigh wave on VSGs. As an averaged velocity, we set 1100 m/s based on the dispersion spectrum generated along Pollock Rd (Fig. 3) and the velocity model in Czarny and Zhu (2022). We operate on the VSGs stacked over one month July 2019, when the SNR is the highest. We do not apply f-k filtering to analyze all effects around the fiber. We set the 600×1000 m grid and the limit frequency band to 10–45 Hz. We constrain our analysis to 200 m around VS. We evaluate VSG every 10 meters (VS point locations as in the case of temporal studies).

Figure 7 shows 12 selected VS points for noise source spatial distribution analysis. The results for all 80 VS points are presented in supplementary materials. Generally, each VS point gives unique spatial noise distribution. However, for most examples, the noise source is connected with car traffic through Pollock Rd. Starting from VSG in point (1), the dominant noise source comes from the east side of Pollock Rd. The noise source may originate in the utility hole (A). At point (2), the major energy shifts to the west toward higher channels. The energy still accumulates inline and is probably connected with the right edge of the wide 20 meters long bump (B). This noise source also dominates the VSG at point (3). However, the SNR rapidly decreases when the car passes between two edges of this bump (Fig 7b). One can also see these shadow zones with lower SNR in Figures 5c and 5d. For point (4), located at the top of the bump, the other noise sources on the west start appearing (C, D). At point (5), we notice the energy which can have an origin in two intersections that lead to local parking (C). However, the most energy probably travels from few utility holes (D) and two bumps (E). The high contribution of obstacle (D) in noise generation in the area is visible on VSG around 200 m (points (5) and (6)). It is worth noting that between bump (B) and the first STOP sign (around 400 m), cars drive smoothly at the highest speed along Pollock Rd. That is probably why the SNRs in this region are high. At point (8), we still observe some energy from bumps (E) and some inline noise from the west where manhole (F) is localized. This maintenance hole is in the center of the road, and almost every car hits it when driving. The SNRs for the next following VSGs decrease and reach a minimum of around 600 m.

We have several STOP signs from 400 m to the intersection with Burrowes Rd, so cars drive slower in this segment. Therefore, some off-axis sources, like traffic along Fraser Rd (G), the road to local parking (G), or more distant Burrowes Rd (H), can disturb the retrieving surface wave. We cannot exclude the impact of local lateral structural changes in dolomite bedrock or another noise source from nearby facilities. Finally, at points (11) and (12), the noise energy focuses on Burrowes Rd and N Atherton St, respectively.

5 Conclusions

We characterized high-frequency seismic ambient noise in the urban area in the city of State College using a straight roadside dark fiber DAS array and the seismic interferometry method. By analyzing the SNR estimated for VS points for every 10 m along the fiber optic cable, we identified the origin of the seismic ambient noise sources in the area and showed its spatial distribution. We also explained the factors that impact the Rayleigh surface wave estimation

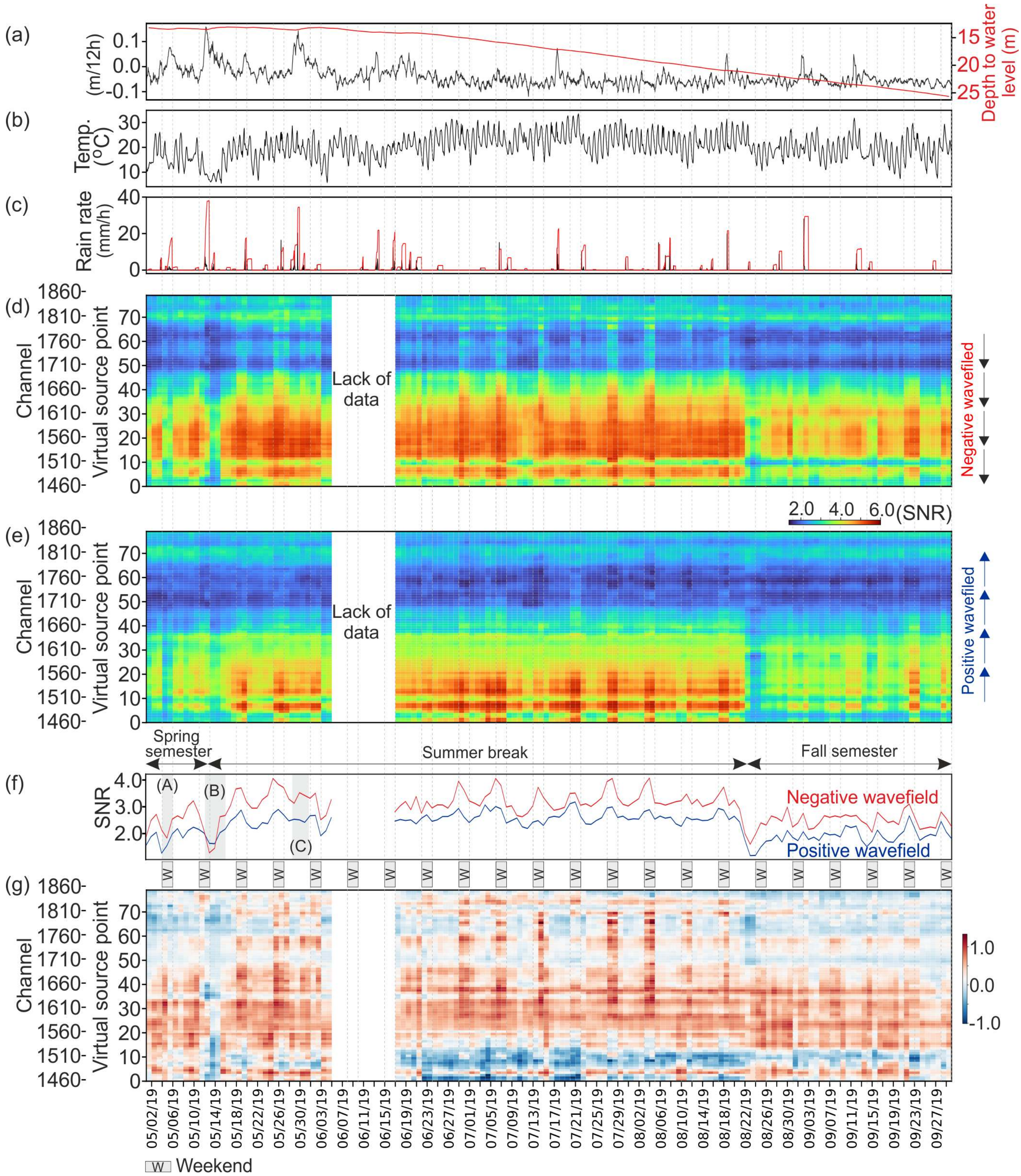

Figure 5 (a) Depth to water level from the nearest observation well; (b) Temperature and (c) rain rate from the local meteorological station (Fig. 1); SNR of the estimated Rayleigh surface wave for (d) negative and (e) positive wavefields. (f) SNR averaged for all VS points. (g) The difference between (d) and (e).

from ambient noise interferometry. We observed a significant SNR drop due to rain and pedestrian traffic. The high-quality data we get for virtual source points close to bumps and maintenance holes, particularly in region where cars are driving at higher speeds. The presented processing scheme can be applied to different sites, especially for the city's linear fiber optic array geometry. Our results can be helpful in ambient noise interferometry applications for higher frequency surface wave estimation in the city using DAS.

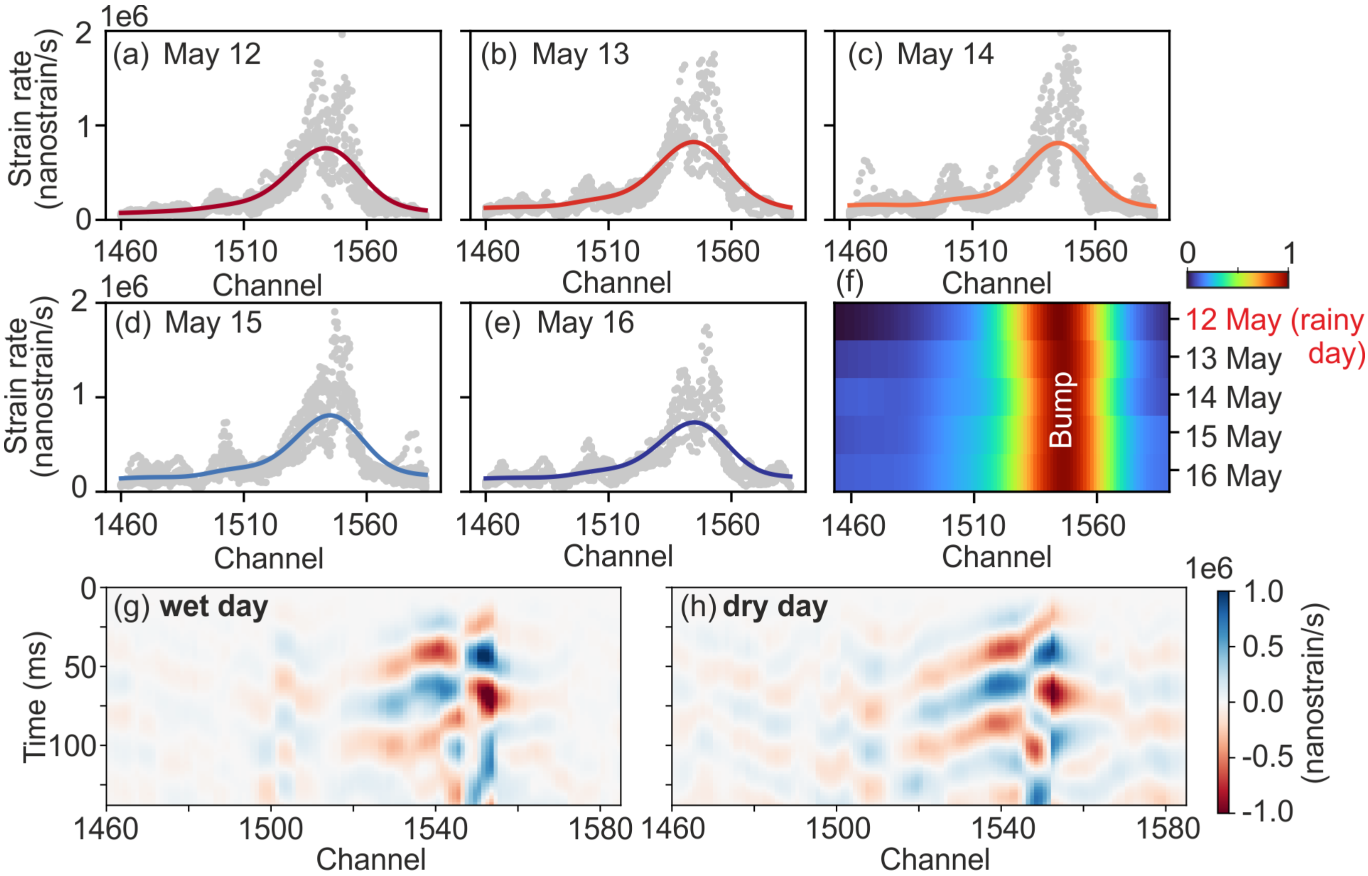

Figure 6 (a-e) Rayleigh surface wave amplitude distributions around the selected bump at channel 1560 for different days of May. (f) Comparison of the results from (a) to (f). Raw waveforms for similar source energy (comparable car hits) on wet (g) and dry (h) days. The higher attenuation is visible on a wet day.

Acknowledgements

The Penn State FORESEE array was supported by Penn State Institute of Environment and Energy seed grant and Institute of Natural Gas Research. We acknowledge the financial support from the Department of Energy (DOE) grant DE-FE0032058 and the National Science Foundation under Grants CMMI-2034363 and RISE-2228314.

Data and code availability

FORESEE data is available via PubDAS Globus https://app.globus.org/filemanager?origin_id=706e304c-5def-11ec-9b5cf9dfb1abb183&originpath=%2F Spica et al. (2022). The processing codes one can find at https://github.com/ravczarny/foresee_data_proc.git.

Competing interests

The authors have no competing interests.

References

Ajo-Franklin, J. B., Dou, S., Lindsey, N. J., Monga, I., Tracy, C., Robertson, M., Rodriguez Tribaldos, V., Ulrich, C., Freifeld, B., Daley, T., and Li, X. Distributed Acoustic Sensing Using Dark Fiber for Near-Surface Characterization and Broadband Seismic Event Detection. *Scientific Reports*, 9(1):1328, Feb. 2019. doi: 10.1038/s41598-018-36675-8.

Bensen, G., Ritzwoller, M., Barmin, M., Levshin, A., Lin, F., Moschetti, M., Shapiro, N., and Yang, Y. Processing seismic ambient noise data to obtain reliable broad-band surface wave dispersion measurements. *Geophysical Journal International*, 169: 1239–1260, 2007. doi: 10.1111/j.1365-246X.2007.03374.x.

Czarny, R. and Zhu, T. Estimating Rayleigh surface wave from ambient noise recorded by Distributed Acoustic Sensing (DAS) dark fiber array in the city. *SEG Technical Program Expanded Abstracts*, page 2133–2137, 2022. doi: 10.1190/image2022-3750564.1.

Dou, S., Lindsey, N., Wagner, A., Daley, T., Freifeld, B., Robertson, M., Peterson, J., Ulrich, C., Martin, E., and Ajo-Franklin, J. Distributed Acoustic Sensing for Seismic Monitoring of the Near Surface: A Traffic-Noise Interferometry Case Study. *Scientific Reports*, 7(1):1–12, 2017. doi: 10.1038/s41598-017-11986-4.

Drake, J. and Harmon, R. Hydrochemical environments of carbonate terrains. *Water resources research*, 9(4):949–957, 1973.

Díaz, J., Ruiz, M., Sánchez-Pastor, P., and Romero, P. Urban Seismology: On the origin of earth vibrations within a city. *Scientific Reports*, 7(1):1–11, 2017. doi: 10.1038/s41598-017-15499-y.

Fang, G., Li, Y., Zhao, Y., and Martin, E. Urban Near-Surface Seismic Monitoring Using Distributed Acoustic Sensing. *Geophysical Research Letters*, 47(6):1–9, 2020. doi: 10.1029/2019GL086115.

Li, L., Tan, J., Schwarz, B., Staněk, F., Poiata, N., Shi, P., and Gajewski, D. Recent advances and challenges of waveform-based seismic location methods at multiple scales. *Reviews of Geophysics*, 58(1), 2020. doi: 10.1029/2019rg00066.

Li, Y., Karrenbach, M., and Ajo-Franklin, J. *Distributed acoustic sensing in geophysics: Methods and applications (268*. John Wiley and Sons, 2022.

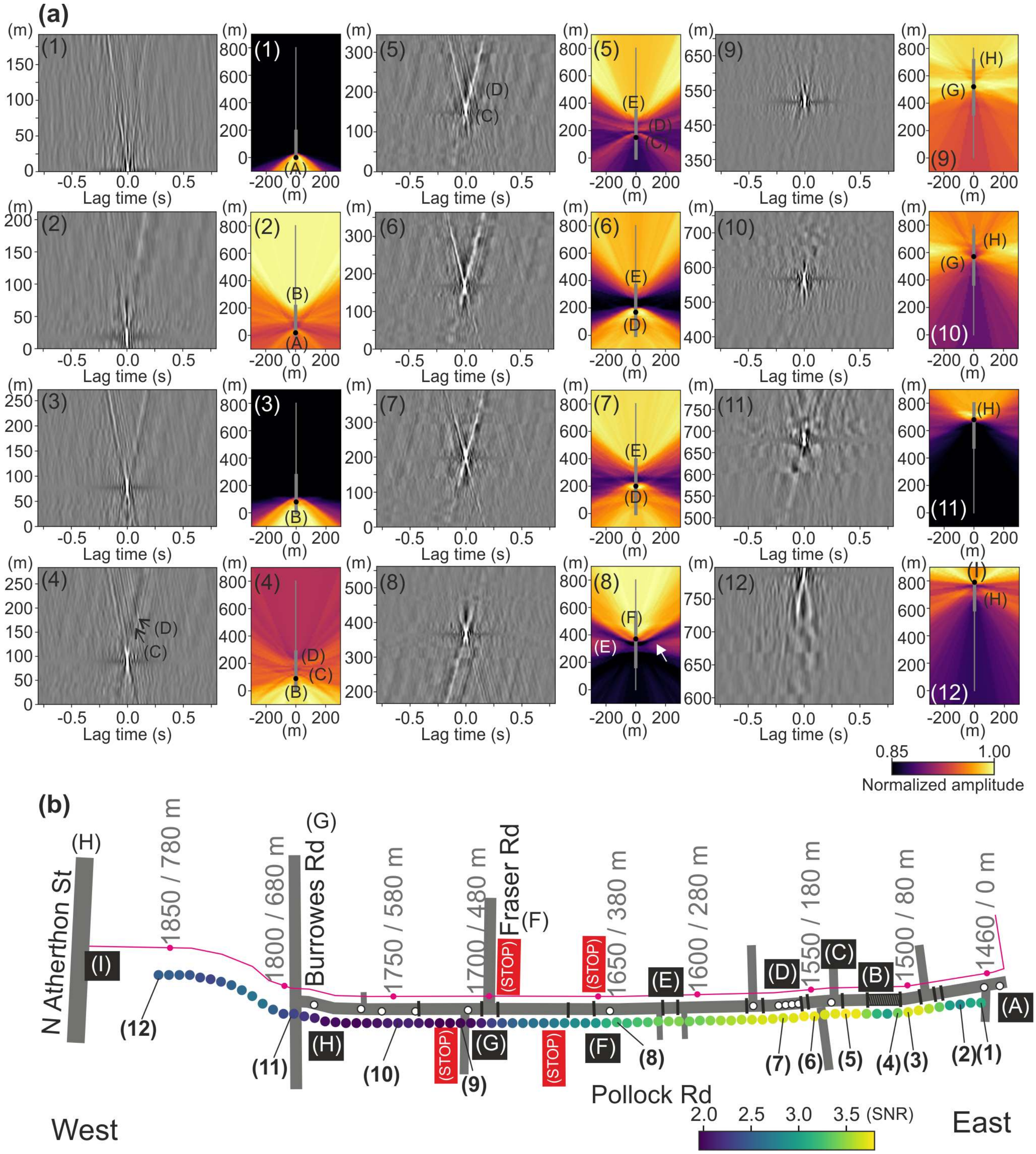

Figure 7 (a) Spatial distribution on noise source around the fiber optic cable for 12 selected VSGs. Thin and thick gray lines indicate an 800 m DAS array (channels 1460–1860) and the profile for which the spatial distribution of noise is determined, respectively. (b) Pollock Rd with road infrastructure (A-I). SNR is averaged from five months for positive and negative wavefields (Fig. 5d and 5e).

Lindsey, N. and Martin, E. Fiber-Optic Seismology. *Annual Review of Earth and Planetary Sciences*, 49(1):1–35, 2021. doi: 10.1146/annurev-earth-072420-065213.

Martin, E., Lindsey, N., and Biondi, B. Introduction to Interferometry of Fiber Optic Strain Measurements. *EarthArXiv*, 2:1–33, 2018. doi: 10.31223/osf.io/s2tjd.

Nakata, N., Chang, J., Lawrence, J., and Boué, P. Body wave extraction and tomography at Long Beach, California, with ambient-noise interferometry. *Journal of Geophysical Research: Solid Earth*, 120(2):1159–1173, 2015. doi: 10.1002/2015JB011870.

Nakata, N., Gualtieri, L., and Fichtner, A. *Seismic ambient noise*. Cambridge University Press, 2019.

Nayak, A. and Ajo-Franklin, J. Distributed Acoustic Sensing Using Dark Fiber for Array Detection of Regional Earthquakes. *Seismological Research Letters*, 92(4):2441–2452, 2021. doi: 10.1785/0220200416.

Paitz, P., Edme, P., Gräff, D., Walter, F., Doetsch, J., Chalari, A., and Fichtner, A. Empirical investigations of the instrument response for distributed acoustic sensing (DAS) across 17 octaves. *Bulletin of the Seismological Society of America*, 111(1):1–10, 2021. doi: 10.1785/0120200185.

Rabade, S., Wu, S., Lin, F., and Chambers, D. Isolating and Tracking Noise Sources across an Active Longwall Mine Using Seismic Interferometry. *Bulletin of the Seismological Society of America*, 112(5):2396–2407, 2022. doi: 10.1785/0120220031.

Shen, J. and Zhu, T. Seismic noises by telecommunication fiber optics reveal the impact of COVID-19 measures on human activities. *The Seismic Record*, 1(1):46–55, 2021. doi: 10.1785/0320210008.

Shen, J. and Zhu, T. DAS with telecommunication fiber-optic cable in urban areas can record storm-induced seismic noise, 2023. GJI, submitted.

Song, Z., Zeng, X., Xie, J., Bao, F., and Zhang, G. Sensing Shallow Structure and Traffic Noise with Fiber-optic Internet Cables in an Urban Area. *Surveys in Geophysics*, 42(6):1401–1423, 2021. doi: 10.1007/s10712-021-09678-w.

Song, Z., Zeng, X., Chi, B., Bao, F., and Osotuyi, A. Using the three-station interferometry method to improve urban DAS ambient noise tomography. *Frontiers in Earth Science*, 10, 2022. doi: 10.3389/feart.2022.952410.

Spica, Z., Perton, M., Martin, E., Beroza, G., and Biondi, B. Urban Seismic Site Characterization by Fiber-Optic Seismology. *Journal of Geophysical Research: Solid Earth*, 125(3):1–14, 2020. doi: 10.1029/2019JB018656.

Spica, Z., J., A.-F., C., B. G., B., B., F., C., B., G., B., L., E., M., J., S., C., T., L., V., H., W., A., W., H., X., and T, Z. PubDAS: a PUBlic Distributed Acoustic Sensing1datasets repository for geosciences. *EarthArXiv*, 2022. doi: 10.31223/X5D07S.

Titov, A., Fan, Y., Kutun, K., and Jin, G. Distributed Acoustic Sensing (DAS) Response of Rising Taylor Bubbles in Slug Flow. *Sensors*, 22(3), 2022. doi: 10.3390/s22031266.

Tribaldos, V. and Ajo-Franklin, J. Aquifer Monitoring Using Ambient Seismic Noise Recorded with Distributed Acoustic Sensing (DAS) Deployed on Dark Fiber. *Journal of Geophysical Research: Solid Earth*, page 1–20, 2021. doi: 10.1029/2020jb021004.

van den Ende, M. and Ampuero, J. Evaluating seismic beamforming capabilities of distributed acoustic sensing arrays. *Solid Earth*, 12(4):915–934, 2021. doi: 10.5194/se-12-915-2021.

Vidal, C., Draganov, D., Neut, J., Drijkoningen, G., and Wapenaar, K. Retrieval of reflections from ambient noise using illumination diagnosis. *Geophysical Journal International*, 198(3):1572–1584, 2014. doi: 10.1093/gji/ggu164.

Wapenaar, K., Draganov, D., and Snieder, R. Tutorial on seismic interferometry: Part 1 - Basic principles and applications. *Geophysics*, 75:75 195–75 209, 2010. doi: 10.1190/1.3457445.

Yang, Y., Atterholt, J., Shen, Z., Muir, J., Williams, E., and Zhan, Z. Sub-Kilometer Correlation Between Near-Surface Structure and Ground Motion Measured With Distributed Acoustic Sensing. *Geophysical Research Letters*, 49(1), 2022. doi: 10.1029/2021GL096503.

Zeng, X., Lancelle, C., Thurber, C., Fratta, D., Wang, H., Lord, N., Chalari, A., and Clarke, A. Properties of noise cross-correlation functions obtained from a distributed acoustic sensing array at Garner Valley, California. *Bulletin of the Seismological Society of America*, 107(2):603–610, 2017. doi: 10.1785/0120160168.

Zhu, T., Shen, J., and Martin, E. Sensing Earth and environment dynamics by telecommunication fiber-optic sensors: An urban experiment in Pennsylvania, USA. *Solid Earth*, 12(1):219–235, 2021. doi: 10.5194/se-12-219-2021.

REPORT
doi:10.26443/seismica.v2i2.1160

Potential Volcanic Origin of the 2023 Short-period Tsunami in the Izu Islands, Japan

A. Mizutani *[1,2], **D. Melgar** [2]

[1]Faculty of Science, Hokkaido University, Sapporo, Japan, [2]Department of Earth Sciences, University of Oregon, Eugene, U.S.A

Author contributions: *Conceptualization*: A. Mizutani. *Data Curation*: A. Mizutani. *Formal Analysis*: A. Mizutani. *Funding Acquisition*: A. Mizutani. *Investigation*: A. Mizutani. *Methodology*: A. Mizutani. *Project Administration*: A. Mizutani, D. Melgar. *Resources*: D. Melgar. *Software*: A. Mizutani. *Supervision*: D. Melgar. *Validation*: A. Mizutani. *Visualization*: A. Mizutani. *Writing – original draft*: A. Mizutani. *Writing – review & editing*: A. Mizutani, D. Melgar.

Abstract On October 8, 2023, at 21:40 UTC (6:40 on October 9 local time), a tsunami warning was issued for the Izu Islands and southwest Japan. This tsunami was initially considered to be associated with the M_w 4.7 earthquake at 20:25 UTC (5:25 JST). However, we know events of this magnitude are far too small to generate observed tsunamis from coseismic deformation alone. In this study, we analyzed the ocean-bottom pressure records of DONET and S-net, real-time cabled observation networks on the Pacific coast of Japan. We find that the dominant period of this tsunami was relatively short, 250 sec, and that the largest tsunami occurred at 21:13 (6:13 JST) near Sofu-gan volcano. In addition, T waves, or the ocean-acoustic waves, were clearly observed by DONET – we posit these correspond to a vigorous swarm-like seismic event at the same region of the tsunami source. We formally invert for the tsunami source and find that several tsunami sources with an interval of about 4 min are necessary to reproduce the observed records. These most likely correspond to volcanic eruptions.

概要 2023 年 10 月 9 日 (JST) に鳥島近海において発生した津波について、日本列島太平洋沖に展開されている DONET および S-net の水圧計記録を解析した。その結果、(1) 約 250 秒の短周期成分が卓越した津波だったこと、(2) 最大波は 6 時 13 分 (JST) に発生したことが明らかとなった。また最大波について津波インバージョンを用いて波源推定を行ったところ、孀婦岩西側の領域に波源が求まった。また、6 時 13 分から 4 分間隔で計 3 回の津波の発生を仮定したモデルが、単一の津波生成を仮定したモデルに比べて観測記録をよく説明した。

Production Editor:
Kiran Kumar Thingbaijam
Handling Editor:
Ryo Okuwaki
Copy & Layout Editor:
Théa Ragon

Signed reviewer(s):
Ryo Okuwaki

Received:
November 28, 2023
Accepted:
December 21, 2023
Published:
December 26, 2023

1. Introduction

On October 8, 2023, at 21:40 UTC (6:40 on October 9 in Japan Standard Time; JST), the Japan Meteorological Agency (JMA) issued a tsunami warning for the Izu Islands, and for the Pacific coast of Japan from Chiba Prefecture to Kagoshima Prefecture (Figure 1a). The warning was issued after observing anomalous increases in water levels at the tide gauge at the Izu Islands. The largest tsunami was observed at Hachijo-jima Island (60 cm) and 10-40 cm tsunamis were observed over southwest Japan (Japan Meteorological Agency, 2023). This tsunami was at first thought to be caused by an earthquake 75 mins before the warning, at 20:25 UTC (5:25 JST), whose moment magnitude (M_w) was 4.7 as estimated by the United States Geological Survey (USGS). Events of this magnitude typically have coseismic deformation < 1 cm, which is far too small to cause hazardous tsunamis. This suggests that the tsunami might not have been associated with the earthquake and was possibly caused by a non-seismic source.

Today real-time ocean-bottom observation networks, called DONET and S-net, have been deployed on the Pacific coast of Japan and their ocean-bottom pressure (OBP) records have been used for tsunami analyses (e.g., Aoi et al., 2020, Figures 1a and S1). Because of their dense and widespread deployment, we can easily detect small tsunami signals and identify their origin by computing the theoretical tsunami travel times from candidate sources to stations. In this paper, we first detect the tsunami signal from these OBP records, identify their potential origin from travel times and then formally estimate a tsunami source model of this event.

2. Data

We downloaded the 10 Hz sampled OBP records of DONET and S-net from the website of the National Research Institute for Earth Science and Disaster Resilience (NIED; https://www.seafloor.bosai.go.jp/). The time window used in this study was 4 hours between 20:00 and 24:00 UTC (from 5:00 to 9:00 JST). DONET and S-net have sub-networks named DONET1 and DONET2, and S1, S2, S3, S4, S5, and S6, respectively; each consisting of 22 to 29 sensors. For DONET1 and DONET2 there was little characteristic difference in the records of this event, so we will refer to them collectively as DONET in this paper. For preprocessing, we fitted the cubic functions to raw OBP data and removed the long-period components such as the ocean tide and the DC or static com-

*Corresponding author: mizutaniayumumail@gmail.com

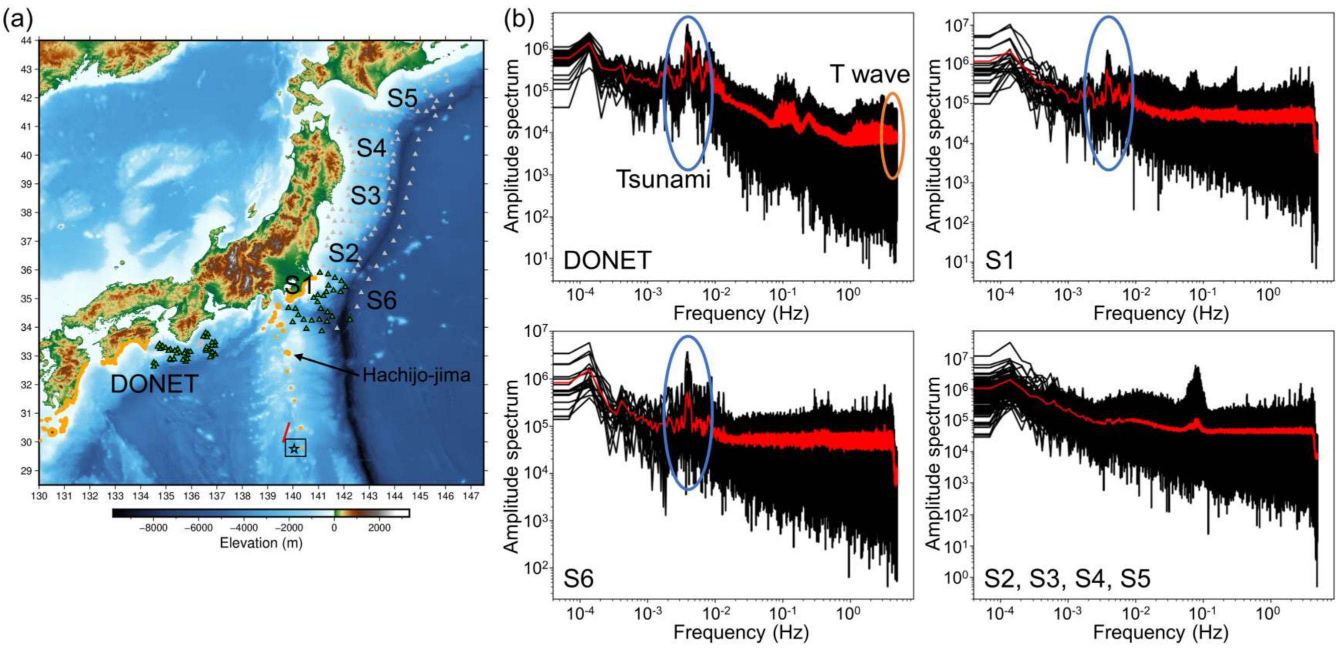

Figure 1 (a) Station distribution of DONET and S-net. The green triangles are the stations used for the tsunami source modeling; the grays are existing sites not used in the modeling. The orange lines show the area where the tsunami warning was issued by the JMA. The cyan star represents the source for the travel time calculation, i.e., the average location of the swarm-like seismic event. The black rectangle is the area of Figure 3. The red line represents the location of the pumice raft observed by the Japan Coast Guard on October 20. The elevation data comes from ETOPO1. (b) Amplitude spectrum of DONET and S-net OBP records. The black lines are the spectrum of each station, and the red ones are their average.

ponent due to the station depth.

3. Tsunami Detection

To establish whether individual records show evidence of the tsunami, first we investigated them in the frequency domain. Figure 1b shows the amplitude spectrum of DONET, S1, S6, and the other subnetworks calculated using the Fast Fourier Transform with the Tukey window. The stations in DONET, S1, and S6 clearly observed a signal with a dominant period of ~250 sec (~0.004 Hz), which is much less clear in the other S-net stations. In subnetwork S6, only southern stations observed such tsunamis (Figure S2). That is most likely because of the refraction at the Japan Trench and the Izu-Bonin Trench which acts as a waveguide and focuses energy towards southwest Japan (e.g., Heidarzadeh and Satake, 2014). In addition, only DONET stations observed the high-frequency signal (>2 Hz). Though there is also a small peak at around 10 sec (0.1 Hz), we do not treat it in this study because this frequency range is known to be associated with the sea ground acceleration (Kubota et al., 2020; Mizutani et al., 2020; Nosov et al., 2018).

To establish the detection of the above signals in the time domain, we calculated theoretical tsunami and acoustic wave travel times from the source to the stations. The M_w 4.7 earthquake occurred at 20:25 UTC as one of the events of a longer-lived swarm-like event; in fact, 14 earthquakes were detected by the USGS from 19:53 to 21:26 UTC. We therefore initially set the potential source locations for travel time calculation to the average of these earthquake locations (140.04°E, 29.76°N; Figure 1a).

We used the Fast Marching Method (FMM) to calculate the theoretical travel times (Sethian, 1999). The phase speed maps for the FMM were calculated with the 0.02° gridded bathymetry based on the ETOPO1 (Amante and Eakins, 2009) for the tsunami, and as the constant value of 1500 m/s for the T wave. Since the dispersive effect cannot be ignored for the tsunami with the dominant period of 250 sec, the tsunami phase speed map was calculated accounting for the dispersion using the method of Sandanbata et al. (2017).

Figure 2a shows the tsunami waveforms at DONET stations, which were time-shifted by the theoretical travel time from (140.04°E, 29.76°N). Here, we set the origin of lapse time to 20:25 UTC (5:25 JST), that is, if the tsunami waves had been generated at that source location at 20:25 UTC, they would align at $t = 0$. Any delay forward or backward in time indicates either that the origin time or the source location is incorrect. To focus on the tsunami and high-frequency signals, we applied the band-pass filters of 100–1000 sec and 1–4 Hz to the OBP records (Figures 2a and 2c).

In the tsunami records (Figure 2a), we can see clear coherent signals. The largest tsunami is observed approximately 2900 sec after the origin time and continues for 1500 sec (the period between two vertical red lines; Figure 2b). Since we shifted the OBP records with the tsunami travel time, it indicates that the largest tsunami occurred not at 20:25 UTC (5:25 JST) but most likely ~48 mins later at 21:13 UTC (6:13 JST). At that time, another earthquake with M_b 5 according to the USGS earthquake catalog (black dashed line in Figure 2 and Table S1). It is also possible that the time shift is due to the source location being wrong, however if that were the case

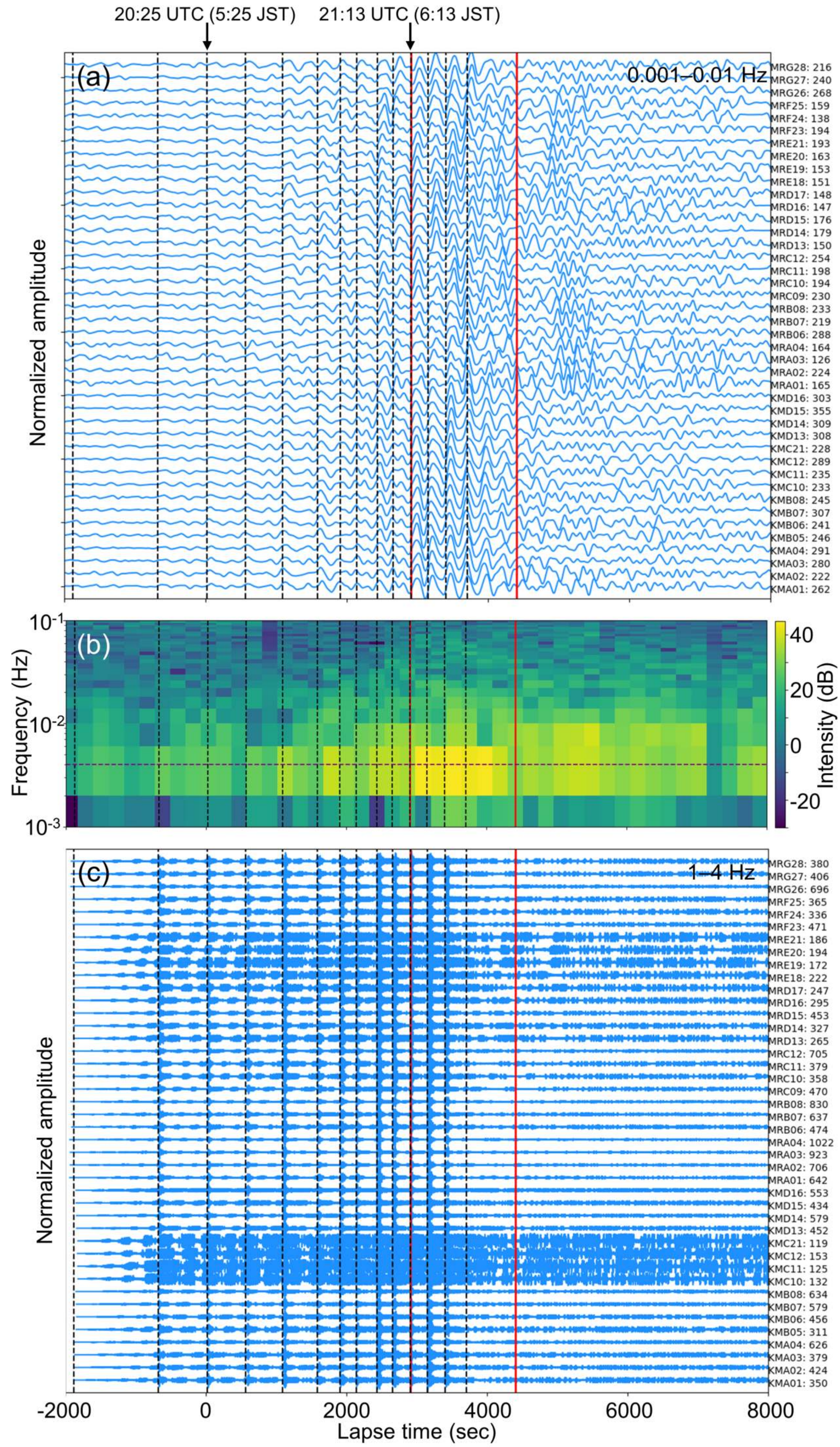

Figure 2 (a) Time-shifted OBP records of DONET with the theoretical travel time of tsunami and the band-pass filter of 100 – 1000 sec. Each record is normalized to the maximum amplitude, which is described with the station name on the right (unit is Pa). The black dashed lines are the origin time of the earthquakes detected by the USGS. The red vertical lines represent the time window used in the tsunami waveform inversion. (b) Spectrogram at station KMA01. The horizontal axis and the vertical lines are the same as (a). The horizontal purple line represents the frequency of 0.004 Hz. (c) Same as (a) except that the T wave, that is, the time-shifted records with the T wave travel time and the band-pass filter of 1 – 4 Hz.

the waveforms would not be coherent and would show a "move out" or distance-dependent time shift which is not seen in the record section. In other words, the tsunami was associated somehow with the swarm-like event in the Izu Islands, but its main wave was generated at 21:13 UTC (6:13 JST).

In the high-frequency OBP records (Figure 2c), we can find several waves corresponding to the earthquakes in the USGS catalog (black dashed lines). Since we shifted these records with the travel time of the ocean acoustic wave, these can be considered as the T wave. The signal to noise ratio at stations KMC10, KMC11, KMC12, KMC21, MRD17, MRE18, MER19, MER20, and MRE21 were worse than the others. This is because the deployment depth of these stations is deeper than 2500 m, which is deeper than the SOFAR channel, which typically exists at around 1200 m, where the T wave is trapped. Because there are the Izu Islands between the source and S-net, the T wave was observed only at DONET (Fig 1).

4. Tsunami Source Estimation

Having established that the tsunami likely originates from the area around an active swarm, in this section, we estimate the tsunami source model (the initial sea-surface disturbance) by tsunami waveform inversion. From the result in Section 3, we assumed that the tsunami occurred at 21:13 UTC, and set the target area to cover the swarm-like seismic event: from 139.81°E to 140.37°E in the east-west direction; and from 29.56°N to 29.96°N in the north-south direction. We estimated the sea surface displacement with the following equation:

$$\begin{bmatrix} d \\ 0 \end{bmatrix} = \begin{bmatrix} G \\ \alpha S \end{bmatrix} m$$

where d, G, S and m are the data vector, kernel matrix (Green's functions), spatial smoothing matrix, and model vector, respectively. We solved this equation by the singular value decomposition. The weight parameter α and threshold of the singular value are determined based on the trade-off curve of the variance reduction (VR) and model variance. In this study, the variance reduction is defined as:

$$VR = \left(1 - \frac{\sum_i \int \left[u_i^{OBS}(t) - u_i^{SYN}(t)\right]^2 dt}{\sum_i \int \left[u_i^{OBS}(t)\right]^2 dt}\right) \times 100[\%]$$

where $u_i^{OBS}(t)$ and $u_i^{SYN}(t)$ are the observed and synthetic waveforms at station i. For calculating the kernel matrix or Green's functions, we used JAGURS (Baba et al., 2015; Saito et al., 2010), the open-source tsunami calculation code, and made synthetic tsunami records considering the dispersive effect. For the bathymetry data, the same as in the travel time estimation was used. Potential sources were represented as the 2D Gaussian function with an amplitude of 1 m, a width (i.e., variance) of 4 km, and set on a regular grid each 0.04° in latitude and longitude. We used the records of DONET, and S1 and S6 subnetworks of S-net, which are shown as green triangles in Figure 1a. The records were preprocessed and applied the band-pass filter of 100–1000 sec as same as in the previous section. The time window for the inversion analysis was 1500 sec from the theoretical travel time, represented as red vertical lines in Figure 2.

Sandanbata et al. (2023) estimated the tsunami source time function using the records of DONET1 and suggested that several tsunamigenic events, some of which occurred at the same time as the T wave events, can explain the observed record. Since two additional earthquakes with T waves were observed after 21:13 UTC, at 21:17 and 21:21 UTC, we conducted a multiple time window inversion (Hossen et al., 2015; Satake et al., 2013) to consider these events by which we allow tsunami sources at these three different times to contribute to the inversion. In other words, three kinds of Green's functions, the second and third ones were shifted in time of 4 min and 8 min from the first one, were involved in the kernel matrix. Note that each synthetic tsunami was assumed to occur instantaneously.

Figure 3 shows the tsunami source model. We chose the model with the smoothing parameter of 0.1 and the threshold of the singular value of 0.2 as the best model, whose VR was 64.1% (Figure S3). At all the time steps, the large uplift (>0.2 m) was located to the northeast of the swarm-like event. The uplift at 21:17 UTC was slightly smaller than the others. In addition, at 21:21 UTC, there was a subsidence of 0.27 m in the east of the target area.

5. Discussion

To investigate the uncertainty of our tsunami source model, we employed a bootstrap approach with 100 sample inversions (Chernick, 2007). We randomly selected OBP stations for each inversion process and calculated the average and standard deviation of the results. The estimated standard deviation is less than 0.06 m (Figure S4), sufficiently small compared to the source amplitude. In addition, the inversion result with other smoothing and damping parameters was confirmed (Figure S5). In all the cases, the large uplift (>0.2 m) on the northeast of the earthquake swarm is stably estimated. On the other hand, the subsidence peak on the east of the uplift is varied with parameter selection. We therefore conclude that the main source of this tsunami event is the uplift on the northeast of the seismic swarm.

In the previous section, we conducted the multiple time window inversion based on the observed T wave signals. To confirm the effectiveness of using the multiple time window, we conducted the same inversion except for the single tsunami source at 21:13 UTC (Figure S6). As a result, although we obtained the same pattern as in Figure 3a, the VR became worse (43.0%). In other words, the multiple tsunami source is more appropriate than the single source for this tsunami event. At 21:26 or after the three tsunamigenic events considered so far, another earthquake without T wave (M_b 4.5) was detected by the USGS (Fig 2c and Table S1). We conducted the multiple time window inversion including this event

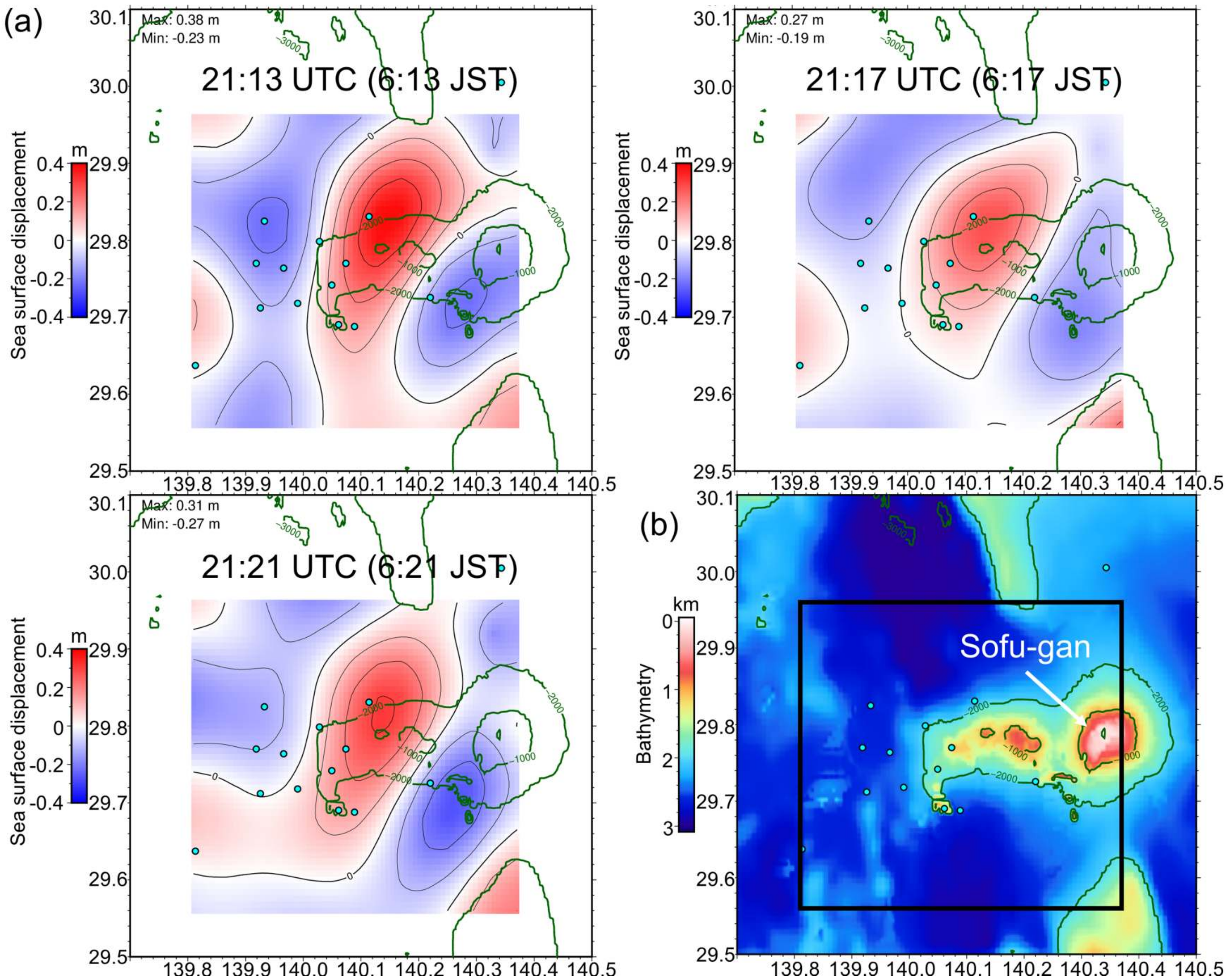

Figure 3 (a) Tsunami source models at 21:13, 21:17, and 21:21 UTC with the contours at each 0.1 m. The cyan circles represent the epicenter distribution of the earthquakes detected by the USGS. The green contours are the bathymetry at each 1000 m. (b) Bathymetry map at the area of (a). The black rectangle is the target area of the tsunami inversion analysis.

(i.e., four tsunami sources; Figure S7), but the VR increased little (65.9%; the improvement is 1.8%). We therefore conclude that the earthquake at 21:26 did not contribute to the observed tsunami, i.e., three seismic events with T wave are the main source of this tsunami.

Figure S8 compares the observed records with the synthetic ones calculated from the inversion results. Even when considering the multiple tsunami sources, the synthetic records have a smaller amplitude than the observed ones. This may be because we considered the tsunami events only after 21:13, i.e., our model cannot explain the later phase of tsunamis that occurred before 21:13.

It is interesting that the time interval of T wave generation (4 min) agrees with the dominant period of the tsunami (250 sec). Although more investigations are necessary, the occurrence interval of the earthquakes might enhance the 250-sec period tsunami (Sandanbata et al., 2023).

As discussed above, the tsunami was generated on the northeast of the swarm-like event of the earthquake. Immediately due east of the swarm, there is an active volcano named Sofu-gan (Figure 3b; Geological Survey of Japan, 2013). The uplifts at all time steps of the estimated tsunami source are adjacent to the western bulge of the Sofu-gan volcano. Based on this result, we speculate that the tsunami and seismic swarm were caused by the intermittent volcanic eruptions, whose vent opened on the western bulge of the Sofu-gan volcano and generated the sea surface uplift; and the eruption ended at 21:21 UTC. It is consistent with that the earthquakes that generated T waves stopped at 21:21 UTC (Figure 2c). In addition, although the exact details of the source are unknown, on October 20, 11 days after this event, a pumice raft with a length of 80 km was observed northwest of the Sofu-gan volcano by the Japan Coast Guard (Japan Coast Gard, 2023). The last recorded eruption of the Sofu-gan volcano was in 1975 (Geological Survey of Japan, 2013). The tsunami and swarm-like seismic event analyzed in this paper may be possibly associated with the new eruption.

6. Conclusions

Based on the OBP records of DONET and S-net, we revealed that the tsunami on October 8 (October 9 JST) was a short-period tsunami with a dominant period of 250 sec. The origin time of the largest tsunami was 21:13 UTC (6:13 JST). We also estimated the tsunami source model. It suggested that multiple tsunami sources are necessary to reproduce the observed records. This paper focused only on the largest tsunami that occurred at 21:13 UTC. In Figure 2a, however, there are other coherent signals outside of the time window for the source estimation. Constructing the source model based on the whole tsunami records will help to understand the details of this event.

Acknowledgements

The records of OBP gauges used in this study were provided by the NIED. This work benefitted from access to the University of Oregon high performance computing cluster, Talapas. We appreciate the editor, Ryo Okuwaki, and an anonymous reviewer for their constructive comments. This work was partially supported by JSPS KAKENHI grant number 22J10212.

Data and code availability

The OBP records of DONET (National Research Institute for Earth Science and Disaster Resilience (NIED), 2019b) and S-net (National Research Institute for Earth Science and Disaster Resilience (NIED), 2019a) can be downloaded from the NIED website (https://www.seafloor.bosai.go.jp/, in Japanese) with data request and permission. The USGS earthquake catalog can be accessed from the USGS website (https://earthquake.usgs.gov/earthquakes/search/). The JAGURS code calculating synthetic tsunamis is freely available from GitHub (https://github.com/jagurs-admin/jagurs). Some figures were made by the Generic Mapping Tools (GMT; Wessel et al., 2019). To plot the tsunami warning area, the data from the ROIS-DS Center for Open Data in the Humanities (https://geoshape.ex.nii.ac.jp/jma/resource/AreaTsunami/) was used.

Competing interests

The authors have no competing interests.

References

Amante, C. and Eakins, B. *ETOPO1 Global Relief Model converted to PanMap layer format*. PANGAEA, 2009. doi: 10.1594/PANGAEA.769615.

Aoi, S., Asano, Y., Kunugi, T., Kimura, T., Uehira, K., Takahashi, N., Ueda, H., Shiomi, K., Matsumoto, T., and Fujiwara, H. MOWLAS: NIED observation network for earthquake, tsunami and volcano. *Earth, Planets and Space*, 72(1), Sept. 2020. doi: 10.1186/s40623-020-01250-x.

Baba, T., Takahashi, N., Kaneda, Y., Ando, K., Matsuoka, D., and Kato, T. Parallel Implementation of Dispersive Tsunami Wave Modeling with a Nesting Algorithm for the 2011 Tohoku Tsunami. *Pure and Applied Geophysics*, 172(12):3455 – 3472, Feb. 2015. doi: 10.1007/s00024-015-1049-2.

Chernick, M. R. *Bootstrap Methods: A Guide for Practitioners and Researchers*. Wiley, Apr. 2007. doi: 10.1002/9780470192573.

Geological Survey of Japan. *Sofugan, Volcano of Japan*. 2013. https://gbank.gsj.jp/volcano/Quat_Vol/volcano_data/G19.html.

Heidarzadeh, M. and Satake, K. The El Salvador and Philippines Tsunamis of August 2012: Insights from Sea Level Data Analysis and Numerical Modeling. *Pure and Applied Geophysics*, 171(12):3437 – 3455, Feb. 2014. doi: 10.1007/s00024-014-0790-2.

Hossen, M. J., Cummins, P. R., Dettmer, J., and Baba, T. Tsunami waveform inversion for sea surface displacement following the 2011 Tohoku earthquake: Importance of dispersion and source kinematics. *Journal of Geophysical Research: Solid Earth*, 120(9):6452 – 6473, Sept. 2015. doi: 10.1002/2015jb011942.

Japan Coast Gard. Press release about suspended solids in the sea around Torishima Island, 2023. https://www.kaiho.mlit.go.jp/info/kouhou/r5/k231020_1/k231020_1.pdf. Observed on October 20.

Japan Meteorological Agency. Press release about the earthquake near Tori-shima Island at 05:25 on October 9, 2023. 2023. https://www.jma.go.jp/jma/press/2310/09b/kaisetsu202310091100.pdf.

Kubota, T., Saito, T., Chikasada, N. Y., and Suzuki, W. Ultrabroadband Seismic and Tsunami Wave Observation of High-Sampling Ocean-Bottom Pressure Gauge Covering Periods From Seconds to Hours. *Earth and Space Science*, 7(10), Sept. 2020. doi: 10.1029/2020ea001197.

Mizutani, A., Yomogida, K., and Tanioka, Y. Early Tsunami Detection With Near-Fault Ocean-Bottom Pressure Gauge Records Based on the Comparison With Seismic Data. *Journal of Geophysical Research: Oceans*, 125(9), Aug. 2020. doi: 10.1029/2020jc016275.

National Research Institute for Earth Science and Disaster Resilience (NIED). *NIED S-net*. 2019a. doi: 10.17598/nied.0007.

National Research Institute for Earth Science and Disaster Resilience (NIED). *NIED DONET*. 2019b. doi: 10.17598/nied.0008.

Nosov, M., Karpov, V., Kolesov, S., Sementsov, K., Matsumoto, H., and Kaneda, Y. Relationship between pressure variations at the ocean bottom and the acceleration of its motion during a submarine earthquake. *Earth, Planets and Space*, 70(1), June 2018. doi: 10.1186/s40623-018-0874-9.

Saito, T., Satake, K., and Furumura, T. Tsunami waveform inversion including dispersive waves: the 2004 earthquake off Kii Peninsula, Japan. *Journal of Geophysical Research: Solid Earth*, 115(B6), June 2010. doi: 10.1029/2009jb006884.

Sandanbata, O., Watada, S., Satake, K., Fukao, Y., Sugioka, H., Ito, A., and Shiobara, H. Ray Tracing for Dispersive Tsunamis and Source Amplitude Estimation Based on Green's Law: Application to the 2015 Volcanic Tsunami Earthquake Near Torishima, South of Japan. *Pure and Applied Geophysics*, 175(4):1371 – 1385, Dec. 2017. doi: 10.1007/s00024-017-1746-0.

Sandanbata, O., Satake, K., Takemura, S., Watada, S., and Maeda, T. Enigmatic tsunami waves amplified by repetitive source events in the southwest of Torishima Island, Japan. *Not peer-reviewed preprint, ESS Open Archive*, Oct. 2023. doi: 10.22541/essoar.169878726.62136311/v1.

Satake, K., Fujii, Y., Harada, T., and Namegaya, Y. Time and Space Distribution of Coseismic Slip of the 2011 Tohoku Earthquake as Inferred from Tsunami Waveform Data. *Bulletin of the Seismological Society of America*, 103(2B):1473 – 1492, May 2013. doi: 10.1785/0120120122.

Sethian, J. *Level Set Methods and Fast Marching Methods*. Cambridge University Press, 2nd edition, 1999.

Wessel, P., Luis, J. F., Uieda, L., Scharroo, R., Wobbe, F., Smith, W. H. F., and Tian, D. The Generic Mapping Tools Version 6.

Geochemistry, Geophysics, Geosystems, 20(11):5556 – 5564, Nov. 2019. doi: 10.1029/2019gc008515.

doi:10.26443/seismica.v2i2.1091

SEISMICA

Editorial workflow of a community-led, all-volunteer scientific journal: lessons from the launch of *Seismica*

Hannah F. Mark *[1], **Théa Ragon** [2], **Gareth Funning** [3], **Stephen P. Hicks** [4], **Christie Rowe** [5], **Samantha Teplitzky** [6], **Jaime Convers** [7], **Ezgi Karasözen** [8], **R. Daniel Corona-Fernandez** [9], **Åke Fagereng** [10]

[1]Department of Geology and Geophysics, Woods Hole Oceanographic Institution, Woods Hole, MA, USA, [2]Division of Geological and Planetary Sciences, Caltech, Pasadena, CA, USA, [3]Department of Earth & Planetary Sciences, University of California Riverside, Riverside, CA, USA, [4]Department of Earth Sciences, University College London, United Kingdom, [5]Earth & Planetary Sciences Department, McGill University, Montréal, QC, Canada, [6]University of California Berkeley Library, Berkeley, USA, [7]Instituto de Astronomia, Geofísica e Ciências Atmosféricas, Universidade de Sao Paulo, Brazil, [8]Alaska Earthquake Center, University of Alaska, Fairbanks, Alaksa, USA, [9]Instituto de Geofísica, Universidad Nacional Autónoma de México, [10]School of Earth and Environmental Sciences, Cardiff University, Wales, United Kingdom

Author contributions: *Conceptualization*: H. F. Mark, T. Ragon, G. Funning. *Writing - original draft*: H. F. Mark, T. Ragon, G. Funning. *Writing - Review & Editing*: C. D. Rowe, S. Teplitzky, S. P. Hicks, E. Karasözen, J. Convers, Å. Fagereng. *Visualization*: H. F. Mark, J. Convers, E. Karasözen, D. Corona-Fernandez. *Translation*: E. Karasözen, Å. Fagereng, D. Corona-Fernandez.

Abstract *Seismica* is a community-led, volunteer-run, diamond open-access journal for seismology and earthquake science, and *Seismica*'s mission and core values align with the principles of Open Science. This article describes the editorial workflow that *Seismica* uses to go from a submitted manuscript to a published article. In keeping with Open Science principles, the main goals of sharing this workflow description are to increase transparency around academic publishing, and to enable others to use elements of *Seismica*'s workflow for journals of a similar size and ethos. We highlight aspects of *Seismica*'s workflow that differ from practices at journals with paid staff members, and also discuss some of the challenges encountered, solutions developed, and lessons learned while this workflow was developed and deployed over *Seismica*'s first year of operations.

Resumen (Spanish) Seismica es una revista de sismología y ciencias de la Tierra de acceso abierto tipo Diamante, dirigida por la comunidad y por voluntarios. La misión y los valores fundamentales de Seismica están en consonancia con los principios de la Ciencia Abierta. Este artículo describe el flujo de trabajo editorial que se usa en Seismica, para pasar de un manuscrito enviado a un artículo publicado. De acuerdo con los principios de la Ciencia Abierta, los principales objetivos de compartir esta descripción del flujo de trabajo son: aumentar la transparencia en torno a la publicación académica, y permitir a otros utilizar estos elementos para revistas de un tamaño y ética similares. Destacamos los aspectos del flujo de trabajo de Seismica, que difieren con las prácticas de revistas con personal pagado, y también discutimos algunos de los retos encontrados, las soluciones desarrolladas y las lecciones aprendidas durante el desarrollo y despliegue de este flujo de trabajo en el primer año de operaciones de Seismica.

Özet (Turkish) Seismica, topluluk liderliğinde, gönüllüler tarafından yürütülen, sismoloji ve deprem bilimi için kurulmuş bir elmas açık erişim dergisidir. Seismica'nın misyonu ve temel değerleri Açık Bilim ilkeleriyle uyumludur. Bu makale, Seismica'nın, makale gönderiminden yayınlanmasına uzanan editoryal iş akışını açıklamaktadır. Bu iş akışını paylaşmanın ana hedefleri, Açık Bilim ilkelerine uygun olarak, akademik yayıncılık konusunda şeffaflığı arttırmak ve benzer büyüklük ve amaca sahip dergilerin Seismica'nın iş akış unsurlarını kullanabilmesini sağlamaktır. Bu makalede, Seismica'nın iş akışının, ücretli personeli olan dergilerdeki uygulamalardan farklı yönlerini vurguluyor ve ayrıca Seismica'nın ilk faaliyet yılı boyunca bu iş akışını geliştirip uygularken karşılaşılan bazı zorlukları, geliştirilen çözümleri ve öğrenilen dersleri tartışıyoruz.

Production Editor: Carmine Galasso
Handling Editor: Carmine Galasso
Copy & Layout Editor: Anant Hariharan

Signed reviewer(s): Jamie Farquharson, Mohamed Gouiza

Translated by: Martijn van den Ende

Received: July 17, 2023
Accepted: September 23, 2023
Published: October 4, 2023

*Corresponding author: hmark@whoi.edu

Sammendrag (Norwegian) Seismica er et fellesskapsledet, frivillig-drevet tidsskrift for seismologi og jordskjelvvitenskap med diamant åpen tilgang. Seismica's formål og kjerneverdier følger prinsipper for åpen vitenskap. Denne artikkelen beskriver den redaksjonelle arbeidsflyten Seismica bruker til å gå fra innsendt manuskript til publisert artikkel. Hovedmålene med å dele denne arbeidsflytbeskrivelsen er, I henhold til prinsipper for åpen vitenskap, og øke åpenheten rundt vitenskapelig publisering og hjelpe tidsskrifter med lignende størrelse og etos til å bruke deler av Seismica's arbeidsflyt. Vi fremhever elementer av Seismica's arbeidsflyt som skiller seg fra vanlig praksis hos tidsskrifter med betalte ansatte, og diskuterer våre erfaringer, utfordringer vi har møtt, og løsninger vi har funnet under utvikling og implementering av denne arbeidsflyten i Seismica's første driftsår.

Samenvatting (Dutch) Seismica is een "Diamond Open Access" wetenschappelijk tijdschrift voor seismologie en aardbevingswetenschappen dat wordt geleid door vrijwilligers uit de gemeenschap. Seismica's missie en kernwaarden zijn direct in overeenstemming met de principes van Open Science. Dit artikel beschrijft onze redactionele workflow, vanaf het inzenden van een artikel tot de uiteindelijke publicatie. In lijn met de principes van Open Science delen wij deze workflowbeschrijving met het doel om de transparantie rond het academische publicatieproces te vergroten en anderen in staat te stellen om bepaalde elementen van deze workflow te gebruiken voor tijdschriften van vergelijkbare omvang en ethos. We benadrukken aspecten van Seismica's workflow die verschillen van de praktijken bij tijdschriften die niet door vrijwilligers worden geleid, en we bespreken ook een aantal uitdagingen, oplossingen en lessen die zijn geleerd tijdens de ontwikkeling en implementatie van de workflow gedurende het eerste jaar van Seismica's activiteiten.

1 Introduction

What goes on behind the scenes at academic journals typically remains closed to authors and readers. The purpose of this article is to help open up the "black box" of journal editing and operations (Baruch et al., 2008) in order to increase transparency, promote trust in academic publishing, and support the establishment and growth of new journals. Journals established and led by researchers with little or no connection to traditional publishers can benefit from having access to in-depth information on editorial processes beyond what individual researchers may know from personal experience with academic publishing; we hope that sharing this information will enable researchers across disciplines to better understand and optimize editorial workflows over time through further sharing and collaboration.

The standard process of publishing an academic paper has multiple steps. It starts with authors preparing and submitting a manuscript to a journal, continues with journal editors shepherding the manuscript through peer review, and if the article is accepted, concludes with the journal publishing and distributing the paper. Prior to launching the Diamond Open-Access journal (DOAJ) *Seismica*, we, members of the founding Editorial Board, knew this process primarily from experience as authors, reviewers, and editors for other journals. However, within that broad framework from manuscript submission through peer review to publication, a community-led, all-volunteer journal such as *Seismica* necessarily does some things differently than a professionally staffed journal. To launch and build *Seismica*, we adapted existing frameworks and open-source tools, and developed additional tools and workflows during the first year of journal operation to meet both anticipated and unexpected operational and editorial needs.

This editorial describes how we at *Seismica* have designed and implemented a paper handling workflow and highlights how a community-led, all-volunteer journal operates in ways both similar to, and distinct from, professionally staffed journals. Here "professionally staffed" refers to journals that have paid full-time editors and/or paid staff who handle aspects of author and reviewer communications, copy-editing, article layout, and media promotion. We hope to assist future community-led journals by sharing the processes and tools developed by *Seismica* before the journal launched and refined through *Seismica*'s first year of operations, and by discussing how these processes and tools may continue to evolve with the journal.

This editorial does not cover the philosophical and scientific aspects of journal building (see, e.g., Rowe et al., 2022; Ndungu, 2021; Graf et al., 2007; Thomas et al., 2023; Farquharson and Wadsworth, 2018; Fernández-Blanco et al., 2023) although the core values of a journal, its disciplinary focus, and its organizational structure will influence practical aspects of paper handling. Rather, we focus on the practical workflow steps and tools we have developed to handle papers at *Seismica*, and will describe the technical infrastructure that supports our workflow. *Seismica* uses the Open Journal System (OJS) for paper handling (version 3.2.1.1, Public Knowledge Project, 2023); we will not cover OJS setup or configuration here, but will describe the in-house technical tools that we developed to facilitate paper handling that are complementary to those provided by OJS. *Seismica*'s OJS installation is hosted and maintained by the McGill University Library as part of the in-kind support provided by the McGill Library to the journal (Rowe et al., 2022).

2 Submission to acceptance

Seismica processes submitted articles following the standard framework for academic publishing (Mabe, 2009) (Figure 1). Submissions are assessed against the journal's scope, checked for adherence to minimum manuscript formatting requirements, assigned to a handling editor (HE), and sent out for anonymous (or double-anonymous, at the authors' request) peer review. One or more rounds of reviewer reports and a subsequent HE judgment informs a decision on whether to accept the article for publication. Accepted manuscripts are formatted according to *Seismica*'s requirements and then forwarded to production.

2.1 Article submission

Submitted manuscripts are first assigned to a production editor who performs initial checks to ensure that the manuscript is within journal scope. For the majority of articles, this production editor will be one of *Seismica*'s executive editors. Articles submitted as Fast Reports go to the Fast Reports editorial team, and articles submitted to special issues may go to associated guest editors. If an article is within scope, the production editor will also check to ensure the submission adheres to minimum formatting requirements. Submitted articles must be in PDF format with a minimum font size of 12 pt, double line spacing, and line numbers. Formatting requirements for submission are intentionally minimal, and this is a policy choice intended to reduce the burden on authors in line with *Seismica*'s core value of inclusivity (Clotworthy et al., 2023; Kozlov, 2023). We provide *Seismica*-specific document templates for several different word processing programs for authors' convenience[1], but authors are not required to use them at the submission stage.

Required sections for submitted articles include an English-language abstract (maximum 200 words), a list of author contributions using the Contributor Roles Taxonomy (CRediT, Brand et al., 2015), a complete reference list with digital object identifiers (DOI) included where available, and a Data and Code Availability statement (Callaghan, 2014). *Seismica* encourages authors to include a non-technical summary and up to two additional translations of the abstract into languages other than English to make their work accessible to broader communities.

Seismica publishes standard research articles and several types of reports, as well as occasional editorials and reviewed opinion pieces. Articles submitted in one category might be better suited to another, particularly as report-type articles are less common and may be unfamiliar to authors. Editors may discuss changing the article type with authors if they believe a submission belongs in a different category.

2.1.1 Author contributions and identifiers

While developing journal policies for *Seismica*, we identified transparency as a key guiding value, including transparency in terms of authorship (Rowe et al., 2022). To this end we require an Author Contributions statement in each manuscript specifying the role(s) played by each author, using the 14 potential roles defined by the CRediT taxonomy (Brand et al., 2015). In the operations of *Seismica* to date, the Author Contributions statement is a common omission from initial submitted manuscripts; in such cases, we require modification of the manuscript before a HE is assigned and the review process can be initiated.

To assist with indexing of author contributions, we request that each author includes their Open Researcher and Contributor ID (ORCID, https://orcid.org/) in the text of their submission, and supplying an ORCID is mandatory for the lead author. Author ORCIDs are hyperlinked in published article PDFs. Additionally, we use the OJS ORCID plugin to link to author ORCIDs on article webpages, provided authors authenticate and link their ORCID accounts to *Seismica*. *Seismica*'s host, McGill University Library, is a member of ORCID, so *Seismica* is also able to add publication metadata to authors' ORCID profiles using the ORCID member API.

2.1.2 Facilitating Open Science through sharing of data and codes

Open Science is an ethos promoting free and open access to scientific data, tools for scientific inquiry, scholarly communications and educational materials (e.g., UNESCO, 2021). As such, the mission of a DOAJ like *Seismica* has significant overlap with the principles of Open Science. As we designed and built *Seismica*, we recognized that we had an opportunity to build Open Science principles into the journal from the outset. We created a senior editorial position, the Executive Editor for Open Science, to facilitate implementation of Open Science practices and track developments in the field, and we codified requirements for sharing of data and the codes necessary to analyze and/or model results into our editorial policies (Rowe et al., 2022).

One of the ways that authors submitting to *Seismica* signal compliance with these policies is through the inclusion of a 'Data and Code Availability' statement at the end of their manuscript; if no data or codes are involved in the study, we ask for the inclusion of an affirmative statement to that effect. Data citation requirements and practices are not consistent across seismology and earthquake science, but formal citations of data factor into operational and funding decisions for future data collection and curation, so it is in our community's best interests to consistently cite data in our work (Staats et al., 2023). If data were obtained from a public domain archive, such as the Federation of Digital Seismograph Networks (FDSN, https://www.fdsn.org/), we ask that the archive be named and appropriately cited in the statement. If the data are not available in a public domain archive, we ask that they be uploaded to a DOI-citable public domain archive such as Zenodo[2] or figshare[3]. Similarly, if codes used for a study are not published in a stable and long-term citable form, we require that a

[1] https://seismica.library.mcgill.ca/templates/

[2] https://zenodo.org

[3] https://figshare.com

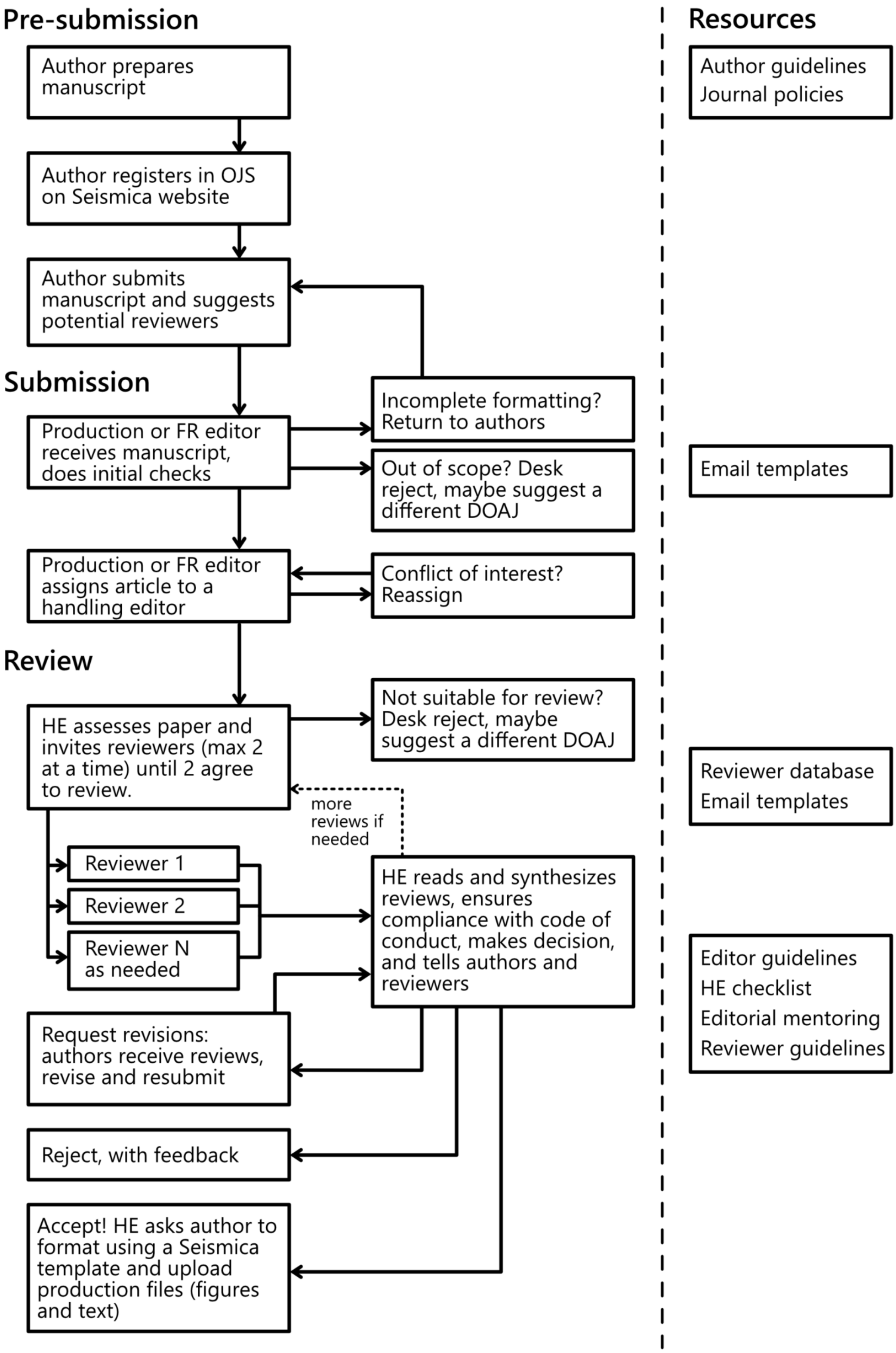

Figure 1 Paper handling flowchart from article submission through peer review. HE: handling editor; FR: Fast Reports; OJS: Open Journal System; DOAJ: Diamond Open Access Journal.

full snapshot of the code and scripts used in the study be uploaded to a DOI-citable archive to facilitate reproduction of the authors' original workflow and replication of their results. While reviewers may not always be able to verify that software works as reported (for example, when codes require high-performance computing resources), data and codes associated with software or data report manuscripts are subject to scrutiny as part of the review process. As with Author Contributions statements, Data and Code Availability statements have been frequently omitted from initial submissions to *Seismica*, adding delays to the handling of those submissions.

Seismica does not provide archiving services for data or code in-house. Instead, we encourage authors to share data and codes on widely-used platforms such as figshare and Zenodo. If Zenodo is selected, we ask authors to upload their data to the *Seismica* Zenodo Community[4] in an effort to organize *Seismica* contributions in a central location. These and several other options for archiving are listed in *Seismica*'s Author Guidelines, and authors are invited to contact *Seismica* editors prior to submission for advice and consultation.

2.2 Peer-review process

Submissions that are within scope and compliant with minimum formatting requirements are assigned by the production editor to a HE with relevant expertise. The HE assesses the manuscript and decides whether it meets our scientific criteria for being sent for review.

HEs draw on author suggestions, personal knowledge, and a tagged reviewer database[5] to find potential peer reviewers. The reviewer database was built by *Seismica*'s Tech Team, as OJS's native functionality for tagging and filtering registered users by expertise did not fully meet our needs. OJS allows users registering as reviewers to self-assign expertise tags, but does not limit those tags to any pre-defined list, so users could self-assign a wide variety of tags with similar meanings: for example, 'seismic imaging' and 'tomography'. This presents a difficulty to HEs, who would need to come up with creative and expansive search terms to filter users by these tags. In contrast, *Seismica*'s reviewer database has a simple interface where potential reviewers can register by signing in with their ORCID and can then self-assign tags for their areas of expertise from a predefined list. HEs have access to filter registered reviewers by field. Personal information is not collected in the reviewer database to ensure compliance with the European Union's General Data Protection Regulation (GDPR, European Commission, 2016).

Seismica's HEs have started with varying levels of experience with managing the editorial process. Resources for HEs include extensive guidelines on philosophical and practical aspects of the editorial process, task checklists, email templates for communicating with authors and reviewers, and access to editorial mentors on the *Seismica* board (Mark et al., 2023). The editorial mentors are members of the HE team with prior experience in journal editing, and they are available to guide those who are new to managing the review process from the editorial side.

We also provide guidelines for reviewers that describe both the general process of peer review and the specifics of reviewing for *Seismica* (Mark et al., 2023). The guidelines list potential questions to consider when reviewing a paper, outline the timeline for peer review at *Seismica*, and discuss ethical aspects of peer review, including confidentiality, conflicts of interest, and signing reviews. *Seismica* publishes reviewer reports alongside accepted articles, and reviewers are informed of this policy when they are asked to review.

Upon receipt of reviews, HEs can choose to accept, decline, or more commonly, request further revisions. A revised manuscript may or may not be subject to a further round of review. Generally, the HE will decide whether a manuscript will be subject to another review round after reading the revised version. Authors are not given a strict due date for revisions. While it is generally in authors' best interests to return revisions as soon as possible, we do not want to put pressure on authors to rush through the revising process.

At *Seismica*, we have intentionally assembled and curated a team of HEs whose expertise spans the journal's scope. At the time of writing, *Seismica*'s Editorial Board includes 28 HEs, some of whom are also executive editors or members of operational teams. Sharing the workload among this group helps ensure both that individual volunteers are not overburdened, and that each submission is highly likely to be handled by a subject matter expert, so that confident executive decisions can be made on submissions and unnecessary rounds of review can be avoided.

2.3 Accepted manuscripts

If a manuscript is accepted, HEs inform authors that at this stage they are required to format their work using one of *Seismica*'s document templates[6] if they have not yet done so. Required files for production include an editable article file (docx, odt, or TeX) in a *Seismica* template, individual high-resolution figure files, and supplementary materials (if applicable). As noted previously, not requiring template-formatted manuscripts at the time of submission may save authors some effort in the event that a manuscript is declined, but accepting arbitrarily formatted articles for production would impose an unsustainable burden on volunteer copy/layout editors. HEs are also encouraged to proofread accepted articles during the review process to expedite article production and reduce the workload of the copy/layout editors. Once accepted manuscript files are uploaded in the required format, they are forwarded to production.

2.4 Appeals

Seismica has a transparent process for authors who want to appeal an editorial decision or dispute a review, in alignment with *Seismica*'s core values. A clearly described process for handling complaints and appeals is also a core practice of the Committee on Publication Ethics (COPE, https://publicationethics.org). Appeals first go to *Seismica*'s standing appeals team, which is comprised of one executive editor, one early-career HE, and one other HE. An alternative HE is recruited on a case-by-case basis if an appeals team member has

[4] https://zenodo.org/communities/seismica-journal/
[5] https://seismica.eu.pythonanywhere.com/
[6] https://seismica.library.mcgill.ca/templates/

already been handling the manuscript or has another conflict of interest. This internal appeal board will render a decision to either uphold the original decision, or make a new decision in light of information provided in the appeal. Their decision should not be a re-review of the manuscript, but rather an assessment of the complaint made in the appeal, that acknowledges any mistakes that may have been made in the editorial process.

The appeal board's decision is communicated to the author making the appeal, and the original HE. If appropriate, one or more original reviewer(s) may also be notified. If any procedures need to be reviewed in light of issues highlighted in the appeal, then that will be raised with the *Seismica* board. The author can challenge the appeal board's decision, in which case the question will be passed up to a multi-journal appeals committee. The committee is composed of representatives from the journals *Geomorphica*, *Sedimentologika*, *Seismica*, and *Tektonika* (as of July 2023), and will assess the merit of any appeals with respect to the journals' policies and scientific community standards. The decision of the multi-journal appeals committee is considered final.

3 Article production and promotion

After an article is accepted, three main tasks remain: (1) finalize the text of the article through copy-editing, (2) generate final files of the completed article for publication, and (3) promote the published paper to readers (Figure 2). Most journals delegate copy-editing and layout tasks to paid professionals separate from editorial staff (e.g., Mabe, 2009), and article promotion will often be a paid service offered by press or media offices. In contrast, *Seismica*'s HEs oversee the production process in collaboration with copy and layout editors from *Seismica*'s Standards and Copy-editing (S&CE) team and members of the Media & Branding (M&B) team, who are all also researchers with expertise in *Seismica*'s core disciplines. The production process at *Seismica*, just like editorial work and reviewing, is undertaken by volunteers from the scientific community. We aim to provide high-quality article production services while remaining respectful of the time and effort of volunteers.

The final products of the editorial workflow are a PDF article, a machine-readable web-page displaying the same article, PDFs of peer-review reports and supplementary materials, coordinated social media posts, and an optional press release.

3.1 Production to publication

Once an article has been accepted for publication, HEs assign the manuscript to the chairs of the S&CE and M&B teams. In turn, the chairs then assign an S&CE team member as copy/layout editor for the manuscript, and one or more M&B team members to coordinate media and promotion. Manuscript assignment to copy-/layout editors is based on expected work hours needed for the manuscript, experience, previous workload, and availability; and copy/layout editors may decline to handle a manuscript. M&B team members are on stand-by until proofs are validated, unless the article is a Fast Report, in which case M&B will start corresponding with the author immediately. The promotion workflow is detailed in Section 3.3.

The copy/layout editors read and typeset each accepted article with the procedures and tools detailed in Section 3.2. They exchange typeset PDF proofs of the accepted manuscript with the authors as many times as necessary to arrive at a version that meets with the authors' approval. Currently, authors are not asked to check or approve the machine-readable web-page version of the article, mainly because the OJS system does not allow it. There are no strict time constraints for authors to check proofs – authors are typically motivated to get articles published quickly, but flexibility allows people to take extra time if they need it and will hopefully lead to fewer missed typographical errors. Similarly, there are no strict deadlines for copy-/layout editors to produce and update proofs, although the S&CE team does expedite making proofs for fast reports. Standard copy-editing is intended to catch spelling and grammar mistakes. S&CE also offers copy-editing beyond proofreading, including writing style recommendations, to authors who are interested. This is inspired by *Volcanica*'s copy-editing philosophy (Farquharson and Wadsworth, 2018).

HEs step back into the process when the authors approve the article proofs. The HE sets a target publication date that is communicated to both the copy/layout editor and the M&B team members. Target publication dates default to 7 working days after proofs are approved by authors, or 3 days for fast reports. The HE, copy/layout editor, or M&B team members may delay the target publication date if they anticipate needing more time due to either operational or personal reasons. The HE then communicates the target date to the corresponding author, and the M&B team corresponds with authors to solicit images and text for publicity posts (see Section 3.3).

HEs communicate article metadata to the copy/layout editors, including the volume and issue of the article, dates of article submission and acceptance, and the names of all volunteers involved in each article. In the published version of each article, we credit the production editor; the HE; the copy/layout editor; translators for multiple-language abstracts, if any; and non-anonymous reviewers. Authors of accepted articles are also encouraged to acknowledge reviewers in their Acknowledgments section, including both anonymous reviewers and those who choose to sign their comments. Other volunteers, such as members of the M&B team, are acknowledged in the cover of each issue when the issue is finalized.

Copy/layout editors produce final article versions (see Section 3.2) and upload them in OJS, along with any supplements to the article and a plain-text list of references for proper indexing by Crossref (a DOI registration agency and indexing organization, Hendricks et al., 2020). Reviewer reports are compiled by the HE and uploaded by either the HE or the copy/layout editor. The HE is responsible for double-checking the article metadata in OJS and the final versions of the article. Finally,

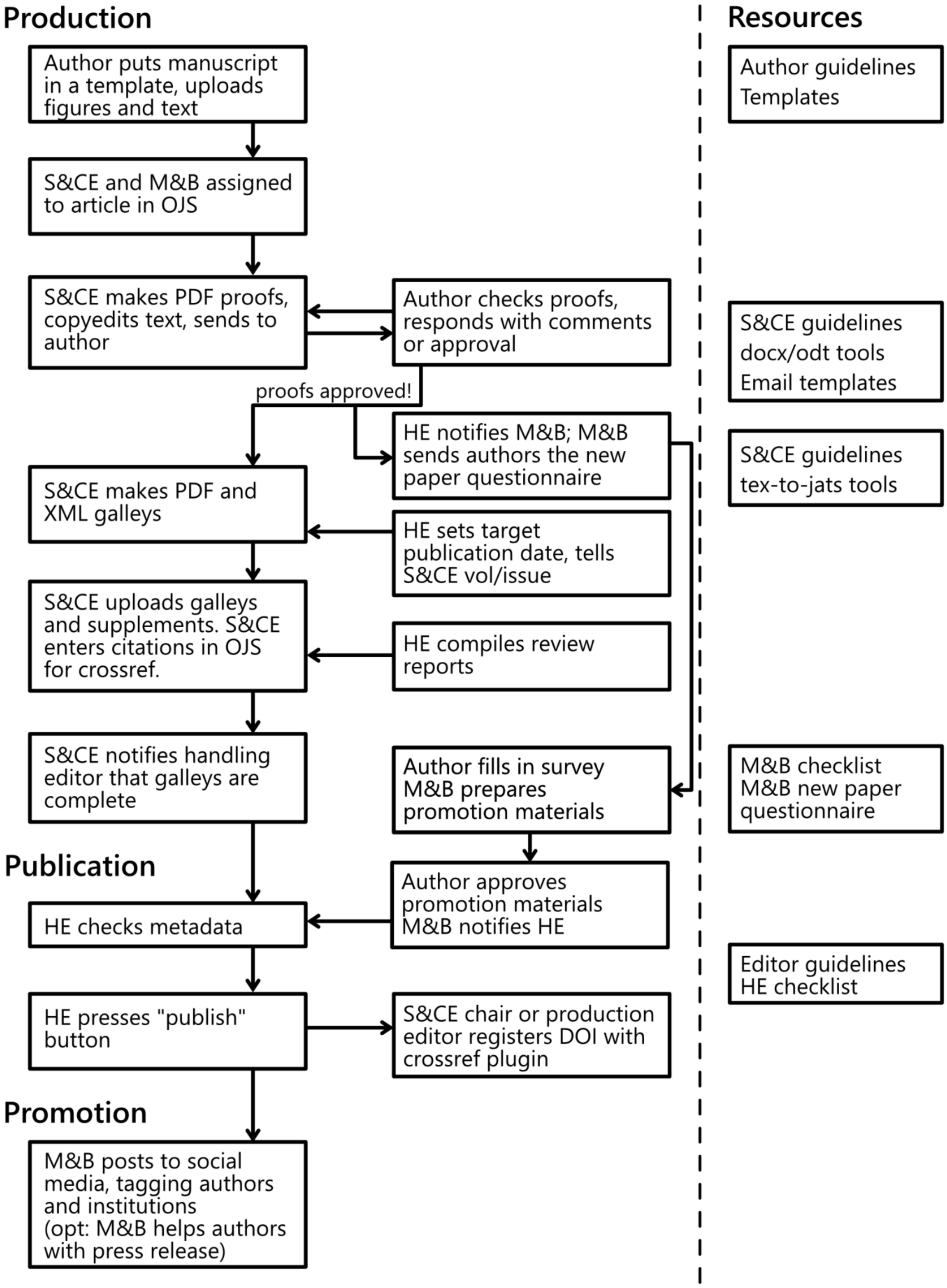

Figure 2 Paper handling flowchart from article production through publication. HE: handling editor; S&CE: Standards and Copy-Editing team; M&B: Media and Branding team.

the HE presses the ”publish” button once all the files are in place, and an S&CE chair or the production editor registers the article DOI with Crossref. DOI registration via Crossref is provided by the McGill Library as in-kind support, at no cost to *Seismica*.

3.2 Workflow and software tools for formatting and layout

Seismica’s articles are published in two formats: PDF and Journal Article Tag Suite (JATS), which is a eXtensible Markup Language (XML) format specifically designed for describing scientific literature. We chose to offer a JATS version of the final article because it is machine-readable (unlike the PDF format) and therefore enhances indexing by search engines. Also, JATS is required for indexing services on third-party online repositories such as PubMed (e.g., Huh, 2016).

Articles are typeset for PDF publication in LuaTeX (Hagen, 2005), and then converted to JATS. The accepted version of an article will thus go through three main stages of modification and formatting prior to publication: (1) generating a typeset PDF proof from a template-formatted manuscript; (2) copy-editing iterations until the PDF proofs are approved by the author(s); and (3) converting the TeX file used to make the PDF into JATS.

The technical problem of converting article files from one format to another while preserving the metadata is unfortunately fairly complex (e.g. for a docx or odt file to JATS, Gebhard and Rosenblum, 2016). Many proprietary and some free solutions exist for the conversions we are interested in, but open-source codes that can be modified and tailored to our needs, or free software packages that guarantee data protection, are rare. We therefore rely on a set of open-source and homebrewed codes, including *Pandoc* (a Haskell library for converting from one markup format to another, MacFarlane, 2006) and custom Python and shell scripts, to automate as much of the process as possible. Below, we describe in detail our TeX templates and our conversion workflows and tools to go from docx/odt to TeX and from TeX to JATS.

3.2.1 *Seismica* Templates

Seismica's TeX template for publication is designed to be user-friendly, flexible, and aligned with the journal's brand identity (Rowe et al., 2022). Importantly, TeX is free and open-source, unlike some other commonly used tools for generating publication-quality PDFs like Adobe InDesign. The first version of the template was based on the *Volcanica* template (Volcanica, 2023), which was converted to a TeX class for flexibility. Macros for article metadata help copy/layout editors to easily include and format key information such as article submission, acceptance, and publication dates; article DOIs; volume and issue numbers; and editor names. The template is designed primarily for a 2-column format for ease of reading (Doumont, 2009) but also includes a 1-column option for articles with many long equations. *Seismica*'s brand identity is expressed through the use of a color palette, a set of fonts, and journal banner in the first page header (Rowe et al., 2022). There is also a TeX submission template which uses a 1-column format, double line spacing, and line numbers, and it has an option for producing a preprint-ready PDF[7]. We continue to update the *Seismica* TeX templates regularly, based on user suggestions and on our needs.

Templates for article submission are also available in docx and odt formats. The docx and odt templates make use of document styles and section ordering for metadata, with the goal of generating documents that retain some amount of structure when converted to generic TeX using *Pandoc*. The template documents contain instructions prompting authors to fill in metadata and use the appropriate styles for section headings.

We note that TeX PDFs and JATS versions are not fully compliant with Universal Accessibility standards. We are encouraged that the LaTeX Project is actively working on implementing accessibility features (Mittelbach and Rowley, 2020), and we will incorporate these improvements as they become available. On the other hand, XML files can be structured and tagged, and we are working towards using these features to produce accessible galleys.

3.2.2 Conversion tools

From docx/odt to TeX Submissions received in *Seismica*'s docx and odt templates have to be converted to TeX for copy-editing and layout. The primary goal of the docx/odt-to-TeX conversion process is to link in-text citations to bibliographic entries automatically, as replacing parenthetical citations with reference tags manually would otherwise be the most time-consuming and error-prone part of article production. Importantly, while *Pandoc* is able to convert the bulk of a docx or odt file to TeX syntax, citation linking is not a *Pandoc* functionality. We therefore use *Pandoc* to convert docx and odt manuscript files to generic TeX and then post-process the *Pandoc* output into the *Seismica* template using Python, relying on document structure cues to identify section headings, figure captions, tables, equations, and other document elements. Plain-text reference lists are converted to bibtex entries using *anystyle* (a machine learning-based citation parser, Fenton et al., 2023), and in-text citations are found and pattern-matched to references in the bibtex file using Python. The success of this process depends strongly on authors using the docx and odt templates in a predictable way. Copy/layout editors will correct some small errors in template usage as needed, but authors who submit article files for production that are clearly not in a *Seismica* template are asked to reformat their work before article production can proceed. Even in perfectly formatted documents, there are some elements that cannot be parsed automatically and must be manually corrected by copy/layout editors. The tools for converting docx and odt manuscript files to TeX are available for others to use or adapt (Mark et al., 2023).

From TeX to JATS A second set of scripts are used by the copy/layout editors to convert the final TeX version of the article to JATS. While *Pandoc* is able to convert basic TeX syntax to JATS, it will not parse article metadata, cross-references, complex hyperlinks, or locally defined commands. We designed scripts that rely on the expected JATS document structure to include article metadata and correct the output of *Pandoc* for, among other things, mathematical formulas, cross-references, figure file extensions, and author CRediTs. The process presents similar challenges to those that arise in converting docx or odt to TeX.

The OJS system relies on a plugin embedding the eLife Lens open-source JATS viewer to display the con-

[7] https://www.overleaf.com/latex/templates/seismica/bvnbjbkycdjb and https://seismica.library.mcgill.ca/templates/

tents of JATS files on webpages, and this plugin has known issues with displaying code and some forms of metadata. We therefore do not offer a final JATS version for articles with large amounts of code quoted in the text where a significant portion of the article cannot be displayed with the OJS reader. The scripts for running the TeX to JATS conversion are available for others to use or adapt (Mark et al., 2023).

3.3 Media and promotion

Once the authors have approved the article proof, the HE contacts the M&B team and adds them to the OJS workflow. M&B then contacts the author with a questionnaire to solicit information for article publicity materials aimed at a general scientific audience. This information typically includes an image (and/or video) representative of their work, and a short text describing the work with minimal jargon. This material helps the M&B team optimize the announcement for a wider audience and to stay within certain social media character limits. Once the M&B team receives the responses from the authors, they prepare posts for *Seismica*'s social media accounts by adjusting the text and imagery for different platforms (Figure 3). The final version (mock-up graphics and text) is sent back to the authors for approval.

M&B announces the publication of each new paper on *Seismica*'s social media accounts. At the time of writing, *Seismica* has social media channels on Twitter, Facebook, Instagram, and Mastodon. M&B also suggests that authors contact their home institutions in case they want to publish a press release for articles that are anticipated to have high impacts outside of the scientific community (e.g., USC, 2023), and the M&B team is available to help with structuring the press release and providing any additional information that the host institution might need. M&B works with the HE to promptly announce the manuscript after publication, but we do not attempt to exactly synchronize M&B's posts with the publication of an article through OJS as team members are often working in different time zones.

At *Seismica*'s present size, it is still feasible for M&B to work with the authors of every article on promotional posts. The purpose is to make science more accessible and inclusive by communicating the value of the research to broader audiences worldwide. Helping authors share and promote their work is part of how *Seismica* is building a brand and, hopefully, growing an audience of both readers and potential future authors and volunteers.

4 Using the workflow and measuring workload

4.1 Who reads the guidelines?

The processes and guidelines developed for *Seismica* theoretically provide support to journal volunteers tasked with a wide variety of different jobs, but having support structures in place does not guarantee that they will be used. While the S&CE and M&B team tools and guidelines are consistently used, it is less clear whether HEs use *Seismica*'s tools and guidelines or rely primarily on their expectations and/or previous experiences in scientific publishing.

We surveyed *Seismica*'s HEs about their awareness and use of several resources, specifically template text for email communications, a flowchart of the editorial workflow, written editor guidelines, and editorial mentoring. The response rate was approximately 38%. The survey results generally indicate that these resources are actively used by HEs. All of the survey respondents were aware of the email template text and the editor guidelines, and most were aware of the flowchart and the availability of editorial mentoring. HEs who reported using the resources gave strongly positive feedback on them. Editorial mentoring had the least reported use among respondents, with almost all saying they had not needed to consult editorial mentors. We also asked respondents where they looked for answers when they had questions about editorial tasks, and the two most-selected options were the *Seismica* resources previously listed, and the *Seismica* Slack group. We acknowledge that there may be some selection bias in the survey results, in the sense that HEs who are strongly engaged with the Editorial Board are more likely both to know about available resources and to take the time to fill out a survey.

4.2 How much time and effort do we put into *Seismica*?

Tracking the workload of Editorial Board members and balancing assignments accordingly has proved challenging. Anecdotally, time commitments vary widely between different people, articles, and editorial tasks. Through handling the first two issues' worth of papers we have learned that there is not necessarily a standard amount of time required for any stage of paper handling. We strive to be flexible and have some redundancy of skills on the board, so that people can cover for each other if an article ends up requiring more time than one person has to spare.

The HE survey included an open-ended question asking respondents to describe how much time they spent on each article they have handled. Responses ranged from 3-20 hours, with several around 8-10. Respondents who described how that time was allocated generally included time for reading the paper, finding reviewers, reading reviews/making decisions, and handling communications with authors. The S&CE team has found that the time required for copy-editing and layout varies widely between papers, with copy-editing time depending primarily on the length of the paper. Processing for articles received in the docx or odt templates requires at least 2 additional hours to convert the manuscript to TeX, and the conversion may take much longer if the template has not been used correctly. Additional time is required to convert TeX files to JATS XML, and to upload files and add metadata in OJS. For the M&B team, manuscript promotion and other tasks like content creation and messaging, social media communications and meetings, and conference planning, takes

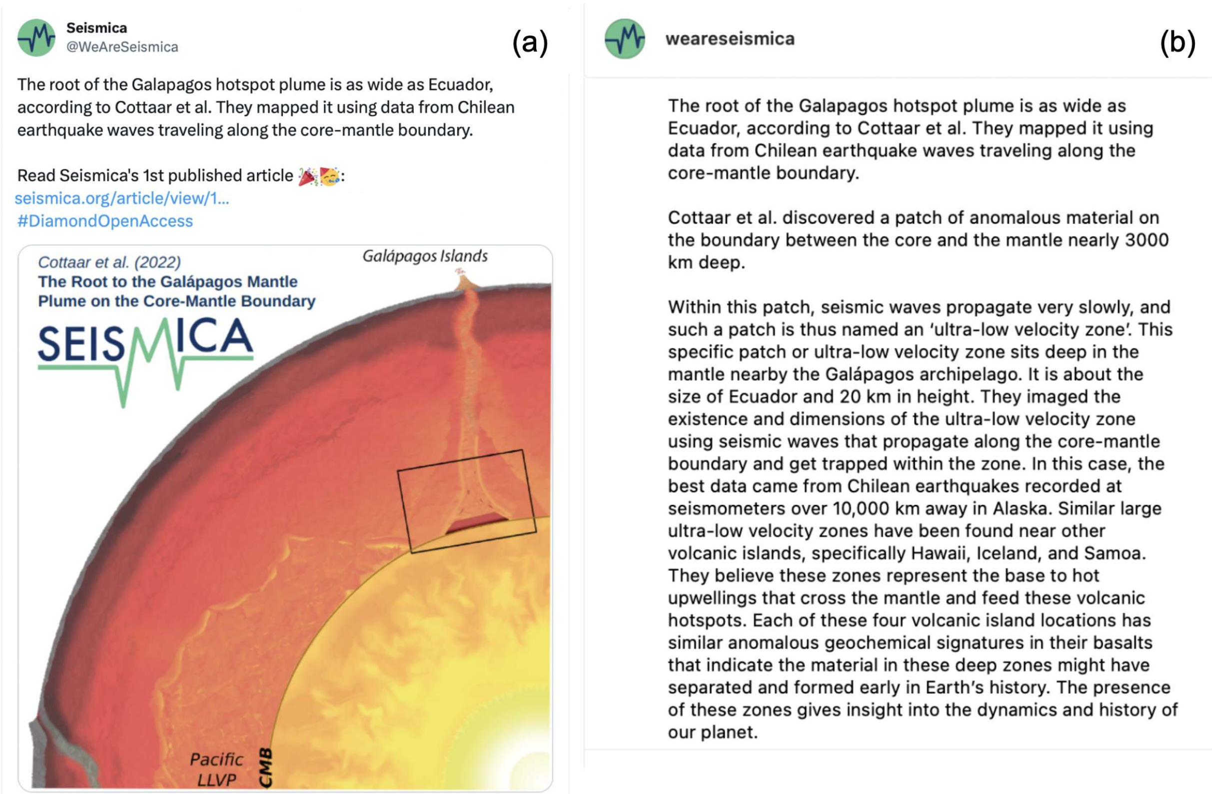

Figure 3 (a) Social media announcement used on Twitter for *Seismica*'s first published paper. (b) Instagram announcement text, where a less restrictive character limit allows for the plain summary of the article to be posted. Both panels advertise Cottaar et al. (2022).

about 4 hours per week. This workload varies over time, depending on how many papers are in production and the timing of upcoming conferences. In the future we hope to do some more detailed workload tracking to better understand how volunteers manage their *Seismica* commitments.

Seismica's volunteers decide to freely give their time to the journal for a variety of reasons. Many are motivated by the opportunity to promote equity in scientific publishing and to bring cutting-edge scientific publishing practices and philosophy to our disciplines. Serving on the editorial side of a journal also gives volunteers the opportunity to keep up with new research. Building community, both within the Editorial Board and in a larger sense that includes reviewers, authors, and readers, can provide tangible benefits to volunteers including expanded professional networks and a shared sense of purpose.

5 Lessons learned so far

With the first few papers submitted to *Seismica*, we quickly learned that the second half of the paper handling process (post-acceptance through production) was, unsurprisingly, much less familiar to everyone on the Editorial Board than the pre-acceptance stage. Practicing with OJS in a sandbox site and developing copy-editing and layout tools before journal launch helped, but not all volunteers had the time to take advantage of training opportunities. As a result, there was a steep on-the-job learning curve for many editors which has begun to level off as most members of the Editorial Board have now had experience completing their roles' core tasks. Below, we describe several key lessons learned during the early weeks and months after *Seismica*'s launch.

We have found that regular communication is crucial at all stages of paper handling: authors and reviewers greatly appreciate regular communication regarding paper status; and HEs, copy/layout editors, and the M&B team have to coordinate article production and promotion. Most of this communication can be kept within OJS using the "discussion" feature. Notably, the OJS dashboard gives minimally detailed automatic updates to authors about submission status, so authors must rely on editors to keep them informed throughout the process.

Maintaining editorial consistency is a crucial task for any journal, and consistency of approach and standards in editorial handling is highly valued at *Seismica* as a mechanism for pursuing our goals of inclusivity and transparency. Toward this end, the entire *Seismica* Editorial Board is invited to virtual meetings (approximately monthly) to discuss policies and values, organizational planning, Open Science principles, and other topics relevant to operations and growth of the journal. Each meeting has two sessions separated by ~12 hours to enable participation by board members in different time zones. This effective line of communication enables adaptability of editorial policies as needed and supports consensus in the management of the journal.

For small, volunteer-run journals similar to *Seismica*, developing robust tools for copy-editing and layout work is important for ensuring that volunteers do not burn out on repetitive tasks. This includes designing production templates that do not require too many modifications for special cases and, if manuscript files will need to be converted between different formats, automating as much of that process as possible. We can't control whether authors use our docx and odt templates correctly, which adds uncertainty to the conversion process. Overall, though, having software tools which automate much of the process has saved *Seismica*'s S&CE team many hours of work already. Providing training and support for copy/layout editors is crucial since their tasks require an especially broad skill set, ranging from strong spelling and grammar skills to using and developing software in multiple coding languages.

The amount of work involved in copy-editing and production spurred us to begin asking HEs to contribute to copy-editing if possible. The HEs already have to read manuscripts in detail, and any corrections that they are able to provide to authors during review and revisions help to share a bit of the burden of the S&CE team. We note that many authors submit very clean files for copy-editing and production that require relatively minimal work, but even then an extra layer of scrutiny is useful for catching as many errors as possible.

Seismica's article promotion process is not standard compared to many other journals in the field, so the M&B team was initially unsure of how authors would respond to questionnaires and how the overall promotion process would work. Encouragingly, M&B has found that authors usually respond to requests for promotion information favorably and in a timely fashion. By establishing practical communication between HEs and authors and setting up internal checklists and guidelines for the article promotion process, M&B has been able to set up an effective routine.

6 Looking forward

Seismica did not need to create an academic publishing process from first principles. However, we have designed the details of our paper-handling workflow to suit the specific requirements of a volunteer-run, community-led, diamond open-access journal – not reinventing the wheel, but building the best possible wheel for our metaphorical cart to roll along.

Designing the paper handling workflow and developing the technical tools described here took a significant amount of effort on the part of the Editorial Board, and we strongly believe that this was a worthwhile investment for the future of *Seismica*. We need credible submissions to sustain and grow *Seismica*, and we need to attract those submissions within a publishing ecosystem where authors have many choices for where to send their work: in other words, we need to build a reputation as a viable (or even preferable) option for publishing (Rindova et al., 2005). Having a robust system for handling papers in line with our values of transparency, credibility, and respect is key to building *Seismica*'s reputation within the seismology and earthquake science community.

Looking to the future, we do not expect our paper-handling workflow to change dramatically, but some aspects may change or evolve as the journal grows, as well as in response to OJS updates. The Executive Editor for Production originally checked and assigned every submission; as our submission rates have increased we now have the Executive Editor for Operations sharing this task. Implementation of different review modes, including double-anonymous review as standard practice for all submissions, is a topic of ongoing conversation on the Editorial Board, and the way that we offer and promote different review options to authors may be updated in the future. Any changes in policy must trigger a workflow review: for example, implementing double-anonymous review would require a check for identifying information in the manuscript before review and in the reviews before sharing with the authors.

As our S&CE team is responsible for design, coding, and implementation of much of the post-acceptance publishing workflow outside of OJS, the process is very agile and changes can role out near instantaneously in response to any issues or new ideas. The workflow has been dynamic in the first year, with continual improvements often made in response to feedback from authors, reviewers, and readers of *Seismica*. We expect future adaptations will be less frequent, but will continue to update our workflow to adapt to policy changes, and arising needs, and to incorporate new tools for efficiency and accessibility as they become available.

Sustaining a volunteer-run journal requires a significant amount of time and effort from the scientific community. We have an enthusiastic and committed Editorial Board at present, but are mindful of the potential for burnout, particularly as we are depending on volunteers to perform tasks that are typically compensated labor (tech support, copy-editing and layout, media promotion) in their spare time. Having volunteers work on these tasks has some tangible benefits, such as that the people who proofread articles and prepare promotional materials have specialized knowledge related to article content and discipline-specific vocabulary, but it also comes with some downsides in terms of the imposed workload. Further, *Seismica* intends to have Editorial Board members rotate off after defined terms a few years in length, so the organization will need a steady supply of new volunteers willing to step in. Establishing processes for onboarding and training new Editorial Board members is important for ensuring that journal operations run smoothly as people rotate on and off the board. *Seismica* has brought on several new Editorial Board members since journal launch: we have added HEs to better balance our portfolio of expertise, and have added members of the S&CE and M&B teams to spread out the workload of the operational teams. New Editorial Board members were found by soliciting applications through *Seismica*'s social media channels, mailing lists, and word of mouth. A committee of current board members reviewed applications and recruited new members based on applicants' scientific expertise, past experience in editorial roles, technical skills, and diversity. The number and enthusiasm of applicants was encouraging, as there will be more calls for new board members in the future.

As we near the one-year mark of post-launch journal operations, there are several open questions surrounding *Seismica*'s future plans and growth: specifically, how far can this workflow scale, and how much do we as an organization want to grow? In theory, we can increase our paper-handling capacity by recruiting additional HEs and members of operational teams (S&CE, M&B), but this approach has limits as it requires training and managing larger editorial boards (Farquharson and Wadsworth, 2018), and intake of papers through initial checks is likely to become a bottleneck. The rate of submissions to *Seismica* has increased from one submission per week in 2022 to more than three per week in 2023, and we are excited to see this sign of support from the research community. At the same time, we have to carefully consider what our limits are as a volunteer organization.

Assuming the rate of submissions continues to increase, we have a few options, including the following: (1) recruit more volunteers to handle papers; (2) limit submissions with paper quotas or limited time windows when submissions are accepted; (3) desk reject more submissions; and (4) hire some paid staff to assist with specific tasks like formatting checks, sending reminder emails, and document format conversions. We do not plan to continue with option (1) indefinitely because, as mentioned above, this adds more work in the form of training and managing a larger Editorial Board and makes it more complicated to maintain the board's consensus-based decision-making practice. The other three options are all possibilities, and the Editorial Board may implement one or more of them in the future, but none of these is an easy or obvious solution – hiring paid staff requires a stable funding source, which we don't have currently, and we don't want to make it so difficult to submit a paper that authors decide to send their work elsewhere.

Seismica is part of a cohort of diamond open access Earth science journals following in the footsteps of *Volcanica* (Farquharson and Wadsworth, 2018), including *Tektonika* (Fernández-Blanco et al., 2023), *Sedimentologika* (Thomas et al., 2023), and *Geomorphica* (Geomorphica, 2023); and more are nascent, including a geochemistry DOAJ. These journals are all independent and unique but have a common philosophy in regards to academic publishing; similarly, they share some common operational needs and challenges that are inherent to running a journal. A group interested in starting a journal following this model could likely make use of most of *Seismica*'s paper-handling workflow with very few modifications. While our processes are designed around OJS, we expect that this workflow could be translated to other journal management systems. The distribution of tasks among people might vary according to how a journal defines different editorial roles, and the exact mechanics of article layout and publication will depend on the publishing formats and platform being used. In general, however, our processes and tools for getting from a manuscript to an open-access, peer-reviewed article are portable to other organizations of similar size and scope.

Acknowledgements

The *Seismica* Editorial Board is grateful to *Volcanica* and the other members of the "Guild of Diamonds" for insights, advice, and diamond open-access fellowship; and to the McGill University Library for support. The authors thank Jamie Farquharson and Mohamed Gouiza for their thoughtful reviews of this manuscript. The authors also thank their colleagues on the Editorial Board for being flexible and willing to learn in real time. Abstract translations benefited from the assistance of AI translation tools via ChatGPT and DeepL.

Data and code availability

The codes discussed in Section 3.2, copies of *Seismica*'s current guidelines, operational team checklists, and HE email resources are available on Zenodo (Mark et al., 2023).

Competing interests

The authors have no competing interests.

References

Baruch, Y., Konrad, A., Aguinis, H., and Starbuck, W. *Opening the black box of editorship*. Springer, 2008.

Brand, A., Allen, L., Altman, M., Hlava, M., and Scott, J. Beyond authorship: attribution, contribution, collaboration, and credit. *Learned Publishing*, 28(2):151–155, 2015. doi: 10.1087/20150211.

Callaghan, S. Preserving the integrity of the scientific record: data citation and linking. *Learned Publishing*, 27(5):S15–S24, 2014. doi: 10.1087/20140504.

Clotworthy, A., Davies, M., Cadman, T. J., Bengtsson, J., Andersen, T. O., Kadawathagedara, M., Vinther, J. L., Nguyen, T.-L., and Varga, T. V. Saving time and money in biomedical publishing: the case for free-format submissions with minimal requirements. *BMC medicine*, 21(1):1–10, 2023. doi: 10.1186/s12916-023-02882-y.

Cottaar, S., Martin, C., Li, Z., and Parai, R. The root to the Galápagos mantle plume on the core-mantle boundary. *Seismica*, 1(1), 2022. doi: 10.26443/seismica.v1i1.197.

Doumont, J.-L. *Trees, Maps, and Theorems: Effective communication for rational minds.*, volume 17/2. Principiae, Belgium, 2009.

European Commission. Consolidated text: Regulation (EU) 2016/679 of the European Parliament and of the Council of 27 April 2016 on the protection of natural persons with regard to the processing of personal data and on the free movement of such data, and repealing Directive 95/46/EC (General Data Protection Regulation), 2016. https://eur-lex.europa.eu/eli/reg/2016/679.

Farquharson, J. and Wadsworth, F. Introducing Volcanica: The first diamond open-access journal for volcanology. *Volcanica*, 1(1), 2018. doi: 10.30909/vol.01.01.i-ix.

Fenton, A., Keli, S., Krtek, J., and Srna, I. Anystyle: Fast and smart citation reference parsing, 2023. https://github.com/inukshuk/anystyle.

Fernández-Blanco, D., Lacassin, R., Gouiza, M., Perez-Diaz, L., Magee, C., McCarthy, D., Doré, T., Péron-Pinvidic, G., Kavanagh, J., Bond, C., and Schmitt, R. Tektonika: The Community-Led Diamond Open-Access Journal for Tectonics and Structural Geology. *тектоніка*, 1(1), July 2023. doi: 10.55575/tektonika2023.1.1.56.

Gebhard, C. and Rosenblum, B. Wrangling math from Microsoft Word into JATS XML workflows. *Learned Publishing*, 29(4): 271–279, 2016. doi: 10.1002/leap.1058.

Geomorphica. Geomorphica journal, 2023. https://journals.psu.edu/geomorphica/index. Last accessed 2023-07-05.

Graf, C., Wager, E., Bowman, A., Fiack, S., Scott-Lichter, D., and Robinson, A. Best Practice Guidelines on Publication Ethics: a Publisher's Perspective. *International Journal of Clinical Practice*, 61:1–26, 2007. doi: 10.1111/j.1742-1241.2006.01230.x.

Hagen, H. LuaTEX: Howling to the moon, 2005.

Hendricks, G., Tkaczyk, D., Lin, J., and Feeney, P. Crossref: The sustainable source of community-owned scholarly metadata. *Quantitative Science Studies*, 1(1):414–427, Feb. 2020. doi: 10.1162/qss_a_00022.

Huh, S. How to Add a Journal to the International Databases, Science Citation Index Expanded and MEDLINE. *Archives of Plastic Surgery*, 43(6):487–490, Nov. 2016. doi: 10.5999/aps.2016.43.6.487.

Kozlov, M. Revealed: the millions of dollars in time wasted making papers fit journal guidelines. *Nature*, June 2023. doi: 10.1038/d41586-023-01846-9.

Mabe, M. A. Scholarly Publishing. *European Review*, 17(1), 2009. doi: 10.1017/S1062798709000532.

MacFarlane, J. Pandoc: a universal document converter, 2006. https://pandoc.org/.

Mark, H., Ragon, T., Hicks, S. P., and The Seismica Editorial Board. Guidelines, policies, checklists, code, and tools for Seismica paper handling, July 2023. doi: 10.5281/zenodo.8147070.

Mittelbach, F. and Rowley, C. LaTeX Tagged PDF—A blueprint for a large project. *TUGboat*, 41(3):292–298, 2020. doi: 10.47397/tb/41-3/tb129mitt-tagpdf.

Ndungu, M. W. Scholarly journal publishing standards, policies and guidelines. *Learned Publishing*, 34(4):612–621, 2021. doi: 10.1002/leap.1410.

Public Knowledge Project. OJS Open Journal Systems: the Public Knowledge Project, Simon Frasier University, 2023. https://pkp.sfu.ca/software/ojs/.

Rindova, V. P., Williamson, I. O., Petkova, A. P., and Sever, J. M. Being Good or Being Known: An Empirical Examination of the Dimensions, Antecedents, and Consequences of Organizational Reputation. *Academy of Management Journal*, 48(6):1033–1049, Dec. 2005. doi: 10.5465/amj.2005.19573108.

Rowe, C., Agius, M., Convers, J., Funning, G., Galasso, C., Hicks, S., Huynh, T., Lange, J., Lecocq, T., Mark, H., Okuwaki, R., Ragon, T., Rychert, C., Teplitzky, S., and van den Ende, M. The launch of Seismica: a seismic shift in publishing. *Seismica*, 1(1), 2022. doi: 10.26443/seismica.v1i1.255.

Staats, M., Aderhold, K., Hafner, K., Dalton, C., Flanagan, M., Lau, H., Simons, F. J., Vallée, M., Wei, S. S., Yeck, W., Frassetto, A., and Busby, R. Inconsistent Citation of the Global Seismographic Network in Scientific Publications. *Seismological Research Letters*, 05 2023. doi: 10.1785/0220230004.

Thomas, C., Privat, A. M.-L. J., Vaucher, R., Spychala, Y., Zuchuat, V., Marchegiano, M., Poyatos-Moré, M., Kane, I., and Chiarella, D. Sedimentologika: a community-driven diamond open access journal in sedimentology. *Sedimentologika*, 1(1), 2023. doi: 10.57035/journals/sdk.2023.e11.1015.

UNESCO. UNESCO Recommendation on Open Science, 2021. doi: 10.54677/MNMH8546. https://unesdoc.unesco.org/ark:/48223/pf0000379949. Last accessed 2023-05-23.

USC. Turkey's next quake: USC research shows where it could happen — but not when, 2023. https://news.usc.edu/207334/turkeys-next-quake-usc-research-shows-where-it-could-happen-but-not-when/. Last Accessed on June 30, 2023.

Volcanica. Volcanica LaTeX Template, 2023. https://www.overleaf.com/latex/templates/volcanica-latex-template/rtbwmkfqwgsb. Last accessed 2023-05-22.

REPORT
doi:10.26443/seismica.v2i2.1031

SEISMICA

Automated shear-wave splitting analysis for single- and multi-layer anisotropic media

Thomas S. Hudson * [1], **Joseph Asplet** [2], **Andrew M. Walker** [1]

[1]Department of Earth Sciences, University of Oxford, Oxford, UK, [2]School of Earth Sciences, University of Bristol, Bristol, UK

Author contributions: *Conceptualization*: T. Hudson. *Methodology*: T. Hudson, J. Asplet. *Software*: T. Hudson, A. Walker. *Formal Analysis*: T. Hudson, J. Asplet, A. Walker. *Writing - original draft*: T. Hudson.

Abstract Shear-wave velocity anisotropy is present throughout the earth. The strength and orientation of anisotropy can be observed by shear-wave splitting (birefringence) accumulated between earthquake sources and receivers. Seismic deployments are getting ever larger, increasing the number of earthquakes detected and the number of source-receiver pairs. Here, we present a new Python software package, SWSPy, that fully automates shear-wave splitting analysis, useful for large datasets. The software is written in Python, so it can be easily integrated into existing workflows. Furthermore, seismic anisotropy studies typically make a single-layer approximation, but in this work we describe a new method for measuring anisotropy for multi-layered media, which is also implemented. We demonstrate the performance of SWSPy for a range of geological settings, from glaciers to Earth's mantle. We show how the package facilitates interpretation of an extensive dataset at a volcano, and how the new multi-layer method performs on synthetic and real-world data. The automated nature of SWSPy and the discrimination of multi-layer anisotropy will improve the quantification of seismic anisotropy, especially for tomographic applications. The method is also relevant for removing anisotropic effects, important for applications including full-waveform inversion and moment magnitude analysis.

Production Editor:
Gareth Funning
Handling Editor:
Lauren Waszek
Copy & Layout Editor:
Hannah F. Mark

Received:
June 6, 2023
Accepted:
September 22, 2023
Published:
October 19, 2023

1 Introduction

Shear-wave velocity anisotropy is present in various media on Earth, from the mantle to the crust and even near-surface structures such as the cryosphere (Crampin and Chastin, 2003; Savage, 1999; Harland et al., 2013). This anisotropy can be measured using the phenomenon of shear-wave splitting, or seismic birefringence (Crampin, 1981; Silver and Chan, 1991). As a shear-wave propagates through a transversely anisotropic medium, it splits into two quasi-shear-waves, the fast and slow shear-waves (see Figure 1). The fast shear-wave propagates parallel to the anisotropic fast axis of the medium and the slow shear-wave is orthogonal to that axis. This anisotropy can be caused by multiple factors, including crystallographic-preferred orientation and shape-preferred orientation anisotropy (Kendall, 2000). Shear-wave splitting can be used to measure the anisotropic orientation of the fabric fast-direction, with the strength of anisotropy quantified by the delay-time between the fast and slow shear-waves.

Shear-wave velocity anisotropy has various applications related to past and present strain, deformation and flow. In the mantle, one can infer mantle flow in both the upper mantle (Hein et al., 2021; Fontaine et al., 2007; Long et al., 2009; Wolfe and Solomon, 1998; Liu et al., 2008; Hall et al., 2000; Fouch et al., 2000) and the lower mantle (Reiss et al., 2019; Creasy et al., 2021; Wolf et al., 2022; Asplet et al., 2023), as well as image shear and mineral transitions (Savage, 1999; Liptai et al., 2022; Wolf et al., 2022; Wookey and Kendall, 2008; Vinnik et al., 1998; Sicilia et al., 2008). In the crust, one can image the orientation of fractures at volcanoes (Savage et al., 2010; Johnson et al., 2011; Bacon et al., 2021; Nowacki et al., 2018; Hudson et al., 2023) and hydrocarbon or CO_2 storage reservoirs (Verdon and Kendall, 2011; Baird et al., 2017), for example. At Earth's surface, anisotropy can be used to infer the accumulation of strain and past deformation in ice streams (Harland et al., 2013; Smith et al., 2017; Kufner et al., 2023; Hudson et al., 2021) and crevasse fracture networks (Gajek et al., 2021). It is also useful to measure shear-wave velocity anisotropy since its effects may need to be compensated for. In full-waveform inversion, if anisotropy is either not adequately modelled or removed then it will not be possible to reconcile phase and amplitude misfit. Similarly, shear-wave splitting may result in spurious/ambiguous S-wave phase arrival time picks, affecting travel-time velocity results. The energy partitioning may also affect earthquake spectra measurements that are used for calculating earthquake moment release. Furthermore, the majority of studies to date assume a single effective layer of anisotropy. However, for many systems there may actually be a number of layers with different anisotropic properties. A means of measuring multi-layer anisotropy is important to more fully describe the physical properties of such systems or if one wishes to more comprehensively re-

*Corresponding author: thomas.hudson@earth.ox.ac.uk

move anisotropic effects.

Various software packages exist for performing shear-wave splitting analysis. A key distinction between packages is the level of autonomy, from considerable manual input from users through to fully automated processing. MFAST (Savage et al., 2010) and SHEBA (Wuestefeld et al., 2010) are two popular packages, both implemented in FORTRAN and utilising SAC for seismic data processing. Both typically require manual input from the user to window the data, for example. Recently, a parallelised wrapper for MFAST, implemented in R, was released (Mroczek et al., 2020), which supports somewhat automated processing. Other packages provide a graphical user interface (GUI), typically optimised for manual analysis of teleseismic data. These GUI-based packages include SplitLab (Wüstefeld et al., 2008; Grund, 2017) and SplitRacer (Reiss and Rümpker, 2017; Link et al., 2022) that are implemented in MATLAB, and Pytheas that is implemented in Python (Spingos et al., 2020). All the above packages perform single-layer splitting measurements only, with the exception of SplitRacer, which can calculate multi-layer splitting given multiple earthquake-receiver pair measurements.

Here, we describe SWSPy, a new, open-source software package for shear-wave splitting analysis, specifically created to accurately and efficiently measure shear-wave velocity anisotropy for individual earthquake-receiver ray-paths. The package is implemented in Python, so that it is familiar to a wide community of users, can easily be implemented into existing workflows, is straight forward to install, and is parallelised so can maximise the potential of modern computers and High Performance Computing (HPC) architecture. SWSPy is specifically designed to be a fully automated method, which can process large seismic datasets of thousands of events at thousands of receivers. This is important since recent advances in seismic instrumentation and data storage now enable datasets comprising orders of magnitude more receivers to be deployed, reducing the magnitude of completeness with a corresponding increase in number of detected earthquakes. Although the package is implemented in Python, the most computationally expensive component is compiled to maximise efficiency. SWSPy also supports a three-dimensional splitting measurement (using the coordinate system of Walsh et al., 2013) and can be applied to analyse shear-wave splitting for multi-layer measurements along individual earthquake-receiver ray-paths in certain instances. SWSPy therefore complements other existing semi-automated, single-layer shear-wave splitting packages. In this study we describe the method and provide a set of examples evidencing the utility and performance of the software.

2 Methods

Shear-wave splitting through an anisotropic medium with a single dominant fabric can be described by two parameters: the delay-time δt between the fast and slow S-wave arrivals; and ϕ, the direction of polari-

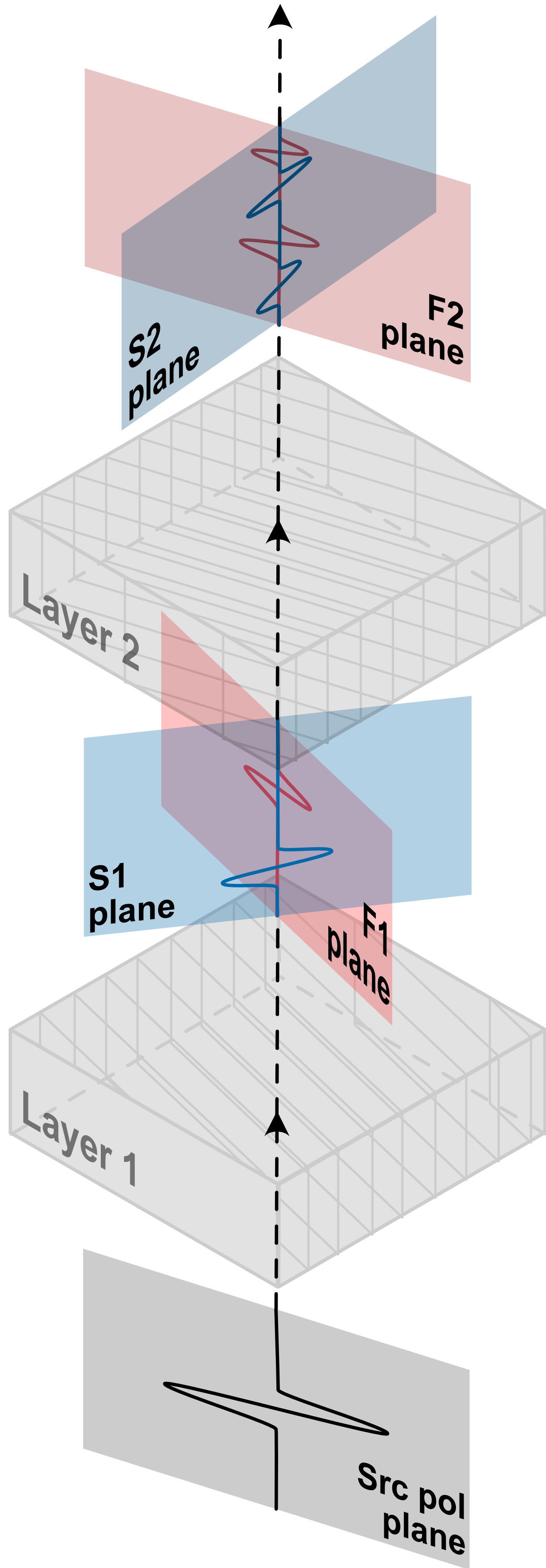

Figure 1 Schematic example of shear-wave splitting through multiple layers with differently oriented fabrics.

sation of the fast S-wave in the plane transverse to propagation (see Figure 2). Various methods exist for measuring these quantities, including cross-correlation (Bowman and Ando, 1987), splitting intensity (Chevrot, 2000), and the eigenvalue method (Silver and Chan, 1991). The cross-correlation method comprises finding the optimal splitting parameters that maximise the cross-correlation of the two rotated and time-shifted ray-perpendicular (typically horizontal) components. The splitting intensity method comprises determining the splitting parameters from the azimuthal dependence of the eigenvector of transverse components of multiple event seismograms at a receiver. It requires the delay-time to be less than the dominant period of the shear-wave (Walsh et al., 2013) and adequate back-azimuth coverage (Long and Silver, 2009). The eigenvalue method comprises rotating and time-shifting the two ray-perpendicular components, searching for splitting parameters associated with a minimum eigenvalue-ratio between the two components. This method is effectively equivalent to the transverse energy minimisation method when the source polarisation is known (Walsh et al., 2013). The method implemented here for shear-wave splitting analysis is the eigenvalue method (Silver and Chan, 1991) with the multi-window clustering of Teanby et al. (2004) and the 3D defined coordinate system implementation of Walsh et al. (2013). The eigenvalue method is chosen because it is typically stable for numerous shear-wave splitting applications and is arguably the most widely adopted method, applicable for a wide range of local to teleseismic seismicity. However, due to the modular nature of the SWSPy Python package, it is straight forward for users/developers to contribute other methods to the package in the future. Below we describe the exact formulation of the eigenvalue method implemented in SWSPy, first for a single anisotropic layer, before expanding the theory to measure shear-wave splitting for multiple layers of anisotropy.

2.1 The eigenvalue method for a single layer

The eigenvalue method used to measure shear-wave splitting in SWSPy comprises the following steps (see Figure 3), for S-wave arrivals at each receiver, for all earthquakes:

1. Load in the data and perform any necessary preprocessing.
2. Rotate data into the LQT (propagation, vertical-transverse, horizontal-transverse) coordinate system.
3. Calculate the ratio of the first and second eigenvalues (λ_1, λ_2), $\frac{\lambda_2}{\lambda_1}$, for all possible fast directions and delay times for the optimal splitting parameters ($\delta t, \phi$).
4. Perform clustering analysis to find optimal splitting parameters corresponding to minimum $\frac{\lambda_2}{\lambda_1}$.
5. Calculate the quality measure, Q_W (Wuestefeld et al., 2010), if desired.
6. Calculate the S-wave source polarisation from the shear-wave splitting corrected particle motions.
7. Convert splitting parameter results from LQT to ZNE coordinate system.

2.1.1 Preprocessing

First the data is preprocessed. This involves detrending the data and performing any desired filtering to remove noise while still preserving the S-wave signal. The data can then be upsampled or downsampled, depending upon the native sampling rate and desired computational efficiency. Upsampling the data allows one to resolve δt more precisely, but comes at a computational cost and will still be fundamentally limited by the sampling-rate of the native data, so should be used with caution. Upsampling is performed using the weighted average slopes method. Conversely, downsampling decreases the precision of δt measurements but decreases the computational cost by reducing the grid-search over the $\delta t - \phi$ space. Instrument response may also be removed at this stage, which is important if S-wave energy falls outside the constant instrument response band of the instrument.

2.1.2 Rotation into the LQT coordinate system

The three-component (ZNE) data are then converted into the LQT coordinate system (see Figure 2). This requires knowledge of the back-azimuth and incidence angle of the ray at the receiver. Rotating the waveforms into the LQT coordinate system allows shear-wave splitting parameters to be measured in 3D and allows one to trivially use borehole as well as surface instruments. Walsh et al. (2013) provide a useful overview of the various coordinate systems that we adopt in this work. SWSPy allows the user to specify to measure splitting in the ZNE coordinate system, which artificially fixes the incidence angle at 0^o from vertical. This assumption is valid for settings where there is a steeply decreasing velocity gradient over multiple wavelengths, typical for the geological setting of most shear-wave splitting studies to date.

2.1.3 Finding optimal splitting parameters

Once the data are rotated, one can perform a grid-search to find the optimal splitting parameters, δt and ϕ, that linearise the data best (energy is maximised in the polarisation (P) plane and minimised in the null (A) plane, see Figure 2). This is the splitting method described in Silver and Chan (1991). For each possible δt-ϕ combination, Q(t) and T(t) are rotated by ϕ clockwise in the QT-plane before Q(t) and T(t) are shifted forward and backward in time, respectively, by $\delta t/2$. We then construct a covariance matrix of the Q(t) and T(t) traces and find the eigenvalues of this matrix. The ratio of the first and second eigenvalues (λ_2/λ_1) describes the linearity of the particle motion in the QT-plane, with smaller ratios indicating greater linearity of the data. The ratio $\frac{\lambda_2}{\lambda_1}$ rather than $\frac{\lambda_1}{\lambda_2}$ is used to maximise stability of the solution (Wuestefeld et al., 2010). The grid-search is the

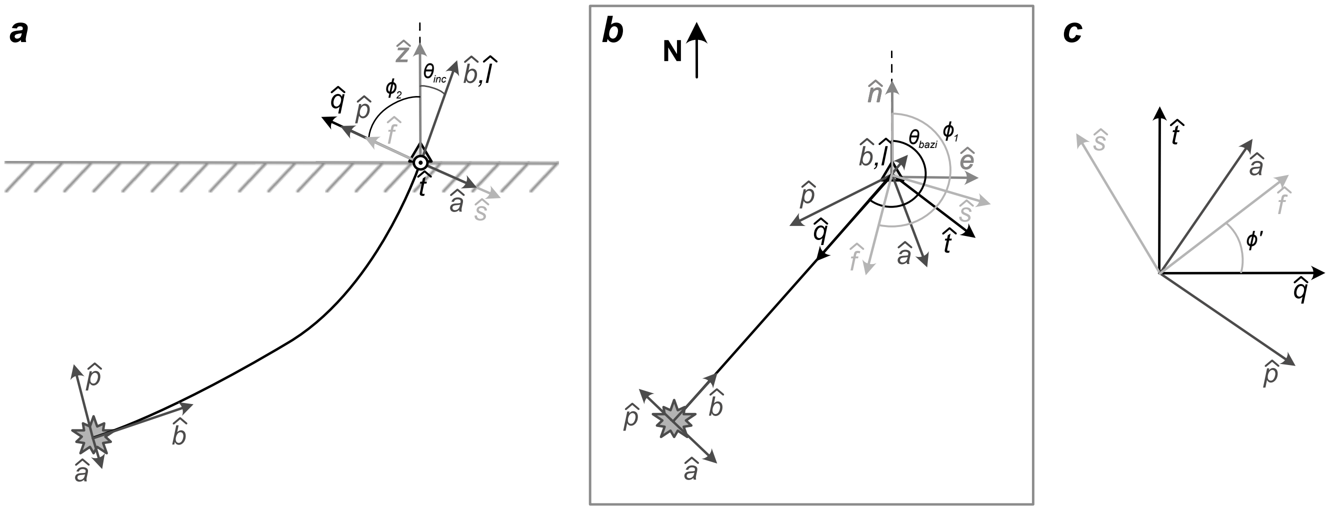

Figure 2 Overview of various coordinate systems. **a.** LQT and BPA coordinate systems in the vertical plane, with the fast ($\hat{f}$) and slow ($\hat{s}$) directions labelled. **b.** LQT and BPA coordinate systems in the horizontal plane, with $\hat{f}$ and $\hat{s}$ labelled as before. **c.** Definition of the various coordinate systems and $\hat{f}$ and $\hat{s}$ in the ray-transverse plane. Various angles are defined as: θ_{inc} is the inclination angle from vertical up of the ray at the receiver; θ_{bazi} is the back-azimuth from North of the ray from the receiver to the source; $\phi_{1,2}$ are the angle of the fast direction relative to North and vertical up, respectively; and ϕ' is the angle of the fast direction from $\hat{q}$. The BPA coordinate system comprises the propagation (B), polarisation (P) and null (A) components. For further details on the coordinate systems, see Walsh et al. (2013).

most computationally intensive step, with the computational cost dependent upon the resolution of both δt and ϕ. To minimise the computational cost, we use the numba compiler (Lam et al., 2015) to wrap the function performing the grid search, allowing it to run as machine code.

2.1.4 Multi-window stability clustering analysis

The selection of the start and end of the window around an S-wave phase can significantly affect the stability of the result. In order to find the most stable result, we implement the clustering approach of Teanby et al. (2004), varying the time of the start and end of the windows and clustering the data to find the most stable result. This involves repeating the grid-search in δt-ϕ space for each window. An example of multiple windows can be seen in Figure 5a, with the window duration, start and end window positions, and number of window combinations all possible to specify by the user (for example, see Figure 4 and Listing 1). For fully automated shear-wave splitting analysis, it is imperative that these parameters are specified prior to processing, in contrast to non-automated methods where the user selects these values ad hoc for each event individually. The user controls the window selection by specifying: the S-wave arrival-time uncertainty/tolerance (t_A, Figure 4); the earliest possible start of the beginning of the any window (t_B, Figure 4); and the earliest possible start of the end of any window (t_C, Figure 4). $t_{A,B,C}$ are all defined relative to the shear-wave phase arrival time. Using the phase arrival time as a reference obviously means that one has to provide SWSPy with adequate approximations of the arrival time of the shear-wave phase to be analysed. The arrival time uncertainty, t_A, is therefore a particularly important parameter for SWSPy's automated windowing procedure. Other methods exist for automatically defining the windowing parameters for specific analyses, for example performing spectral analysis to automatically improve the prediction of teleseismic arrival times (Link et al., 2022). Such methods are not currently implemented in SWSPy, as they are targeted at improving estimates of phase arrival times rather than the splitting analysis itself, which is currently beyond the scope of the SWSPy package. However, future contributors may decide that improving shear-phase arrival times is sufficiently important to add this functionality via an SWSPy submodule in the future.

The optimal splitting parameters, δt and ϕ, for each individual window are clustered using the DBSCAN algorithm (Ester et al., 1996). This is a deviation from the method of Teanby et al. (2004), since we perform the clustering in a new domain that optimally deals with the cyclic nature of ϕ. The clustering domain, $\mathbf{C}$, is defined by,

$$\mathbf{C} = \begin{pmatrix} \tilde{\delta t} \cdot cos(2\phi) \\ \tilde{\delta t} \cdot sin(2\phi) \end{pmatrix}, \tag{1}$$

where $\tilde{\delta t}$ is the normalised lag time and ϕ is the fast-direction polarisation. The optimal overall splitting result for a given source-receiver pair from within all the clusters is defined as the result with the smallest variance within the cluster with the smallest variance, with the within-cluster variance for a given cluster c, $\sigma^2_{cluster,c}$, and the data variance, $\sigma^2_{data,c}$, given by (Teanby et al., 2004),

$$\sigma^2_{cluster,c} = \frac{1}{N_c}\sum_{n=1}^{N_c}(\delta t_n - \bar{\delta t_c})^2 + (\phi_n - \bar{\phi_c})^2, \tag{2}$$

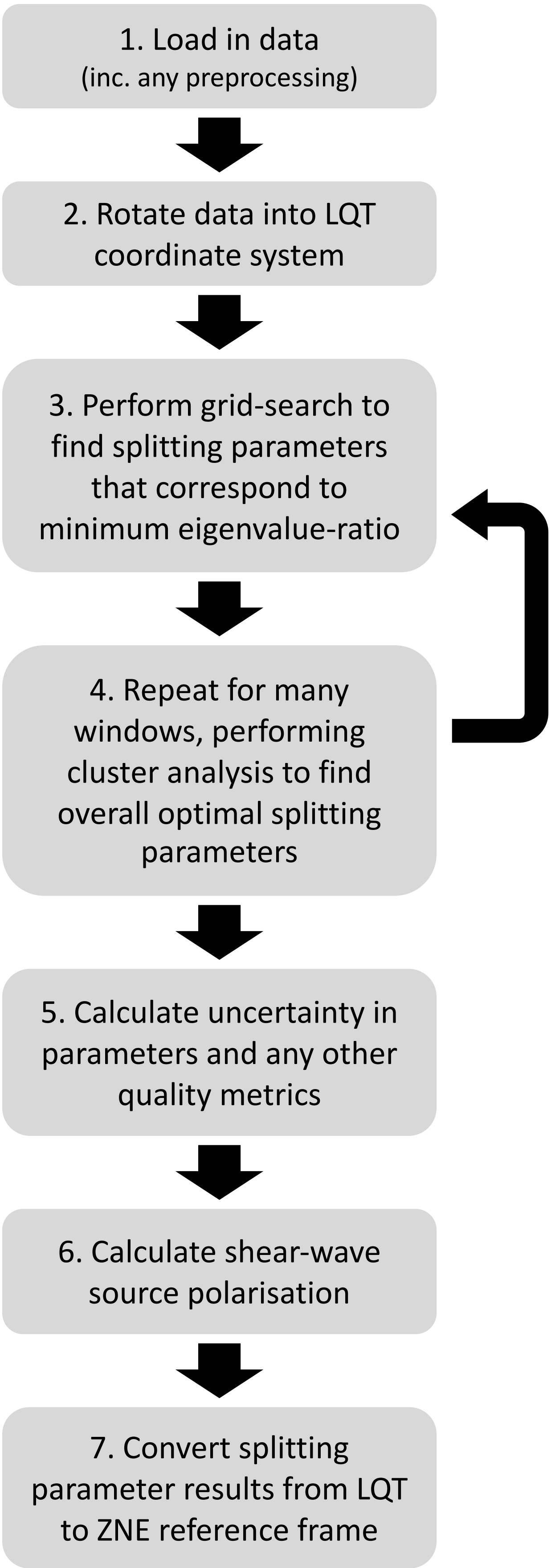

Figure 3 Flow diagram summarising the various shear-wave splitting method steps for single-layer measurements.

$$\sigma^2_{data,c} = \left(\sum_{n=1}^{N_c} \frac{1}{\sigma^2_{\delta t,n}} \right)^{-1} + \left(\sum_{n=1}^{N_c} \frac{1}{\sigma^2_{\phi,n}} \right)^{-1}, \quad (3)$$

where N_c is the number of samples in cluster c, and $\bar{\delta t}_c$, $\bar{\phi}_c$ are the mean values of δt, ϕ, for cluster c respectively (see Teanby et al. (2004) for further details).

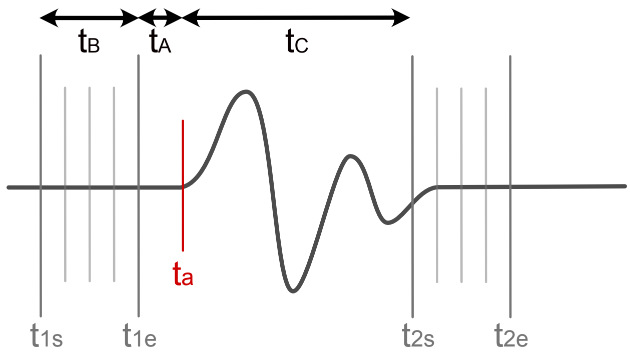

Figure 4 Definition of automated windowing parameters. t_a is the shear-wave arrival time, t_{1s} and t_{1e} are the start and end times of the set of pre-arrival windows, and t_{2s} and t_{2e} are the start and end times of the set post-arrival of windows. t_{A-C} are the user-defined parameters used by SWSPy to specify the range of windows used in the multi-window stability analysis. They are defined by the following variables in SWSPy: t_A = *win_S_pick_tolerance*; t_B = *overall_win_start_pre_fast_S_pick*; t_C = *overall_win_start_post_fast_S_pick*.

2.1.5 Automation for many earthquakes (sources) at many receivers

The clustering method of Teanby et al. (2004) results in stable shear-wave splitting results for a given source-receiver pair, using the eigenvalue method of Silver and Chan (1991). The quality of individual measurements can be generally categorised as: good measurements; poor measurements; and good null measurements (where one can be confident that no splitting is observed). However, typically seismicity studies comprise of tens to hundreds of receivers and catalogues of thousands to hundreds of thousands of earthquakes. A means of automatically quantifying the quality of shear-wave splitting results is therefore desirable. SWSPy contains a class to automatically calculate splitting measurements over entire earthquake catalogues. Three metrics for quantifying the quality of a splitting measurement are: (1) the uncertainty in δt and ϕ ($\alpha_{\delta t}$ and α_ϕ respectively); (2) the linearity of the result, $\frac{\lambda_2}{\lambda_1}$, with smaller $\frac{\lambda_2}{\lambda_1}$ values corresponding to a better result; and (3) the Wuestefeld quality factor, Q_W, which is a measure of the level of agreement between a splitting measurement obtained using the eigenvalue method and the cross-correlation method (Wuestefeld et al., 2010). The cross-correlation method involves cross-correlating the rotated and time-shifted Q and T traces, searching for a maximum similarity between the two waveforms (Wuestefeld et al., 2010). Q_W is given by,

$$Q_W = \begin{cases} -(1 - d_{null}) & \text{for } d_{null} < d_{good} \\ (1 - d_{good}) & \text{for } d_{null} \geq d_{good} \end{cases} \quad (4)$$

where d_{null} and d_{good} are given by,

$$d_{null} = \sqrt{2}\sqrt{\Delta^2 + (\Omega - 1)^2}, \quad (5)$$

$$d_{good} = \sqrt{2}\sqrt{(\Delta - 1)^2 + \Omega^2}, \quad (6)$$

where $\Delta = \delta t_{XC}/\delta t_{EV}$ and $\Omega = (\phi_{EV} - \phi_{XC})/(\pi/4)$. A good measurement with perfect agreement between the eigenvalue and cross-correlation methods should have $\delta t_{EV} = \delta t_{XC}$ and $\phi_{EV} = \phi_{XC}$ ($\Delta = 1, \Omega = 0$), giving $Q_W = 1$, whereas a good null measurement would have $\Delta = 0, \Omega = 1$, giving $Q_W = -1$. Q_W will be near-zero for a poor measurement (see Wuestefeld et al. (2010) for more details). Together, these metrics can be used to identify reliable good and good-null shear-wave splitting measurements in a fully automated way. An example of this is shown in Section 3.3.

2.1.6 S-wave source polarisation

Once an optimal shear-wave splitting result has been obtained, one can remove the effect of shear-wave splitting to retrieve the original S-wave radiated from the earthquake source. The initial S-wave source polarisation can be obtained from the eigenvalues of the anisotropy-removed S-wave particle motions in the QT-plane. The S-wave source polarisation is a useful, yet underused, parameter for seismic analysis since for a double-couple earthquake source, it is the direction of fault slip. We provide an example of how diagnostic source polarisation can be in Section 3.3.

2.1.7 Rotation from the LQT to ZNE coordinate system

Finally, all the results, including the optimal fast direction (ϕ), the various quality metrics, and the S-wave source polarisation are converted from the LQT coordinate system to the ZNE coordinate system (see Figure 2 for definitions of all the relevant angles). The results therefore represent a full 3D result.

2.2 Expanding the method to multi-layer media

The above method has so far only considered the presence of a single anisotropic layer. However, in reality many situations likely exhibit multiple anisotropic layers, potentially with different fast-directions and strengths of anisotropy. Examples might include SKS phases travelling through a mantle layer and a crustal layer (Barruol and Mainprice, 1993), or S-waves originating at the base of an ice stream travelling through a flow-dominated anisotropic layer near the bed and a vertical compressional layer at shallower depths (Kufner et al., 2023). Approximating such systems using a single layer shear-wave splitting method will only allow one to measure the apparent splitting (Silver and Savage, 1994). Obviously this measurement limits the detail to which one can resolve the medium, but it will also result in corrected S-wave arrivals that are not optimally linearised. A multi-layer shear-wave splitting method is thus required to fully describe such systems, providing additional information on the media and optimally linearising the data.

Here, we will refer to measuring shear-wave splitting for two-layers and n-layers somewhat interchangeably. Everything we describe here for a two-layer problem is theoretically possible for $n > 2$ layers, but in practice it is rare that real-world observations would allow for accurate inversion of more than two layers.

Others have developed formulations for solving the multi-layer problem by inverting for two layers simultaneously (Silver and Savage, 1994; Özalaybey and Savage, 1994; Wolfe and Silver, 1998; Reiss and Rümpker, 2017). These methods calculate apparent splitting parameters for a single-layer, using multiple sources arriving at the same receiver combined with theoretical relationships between the apparent splitting parameters and individual layer splitting parameters to invert for the best fitting multi-layer properties (Özalaybey and Savage, 1994). Simply, this can be thought of something akin to a 1D tomography problem. Although evidence of the performance of these methods is limited by the availability of sufficient quality observations, the methods hold theoretically. However, inverting for two layers simultaneously doubles the number of degrees of freedom, which in turn requires multiple source-receiver measurements. Another method, effectively a form of anisotropy tomography, involves splitting the medium a number of box-shaped domains (typically horizontal layers), each with a full anisotropic elastic tensor, and solving the Christoffel equation to find the theoretical splitting parameters (Wookey, 2012; Hammond et al., 2014). These modelled splitting parameters can then be used in combination with observations to form an inversion to find the optimal splitting parameters for each layer. This method is likely more stable than the aforementioned simultaneous method, but requires one to explicitly specify the thickness of anisotropic layers (Wookey, 2012; Hammond et al., 2014; Kufner et al., 2023).

The new method we present here, which is incorporated into SWSPy, originates from the philosophy of measuring multi-layer anisotropy for individual source-receiver pairs, or ray-paths, independently. We choose this philosophy since it can theoretically improve individual splitting measurements that observe multiple anisotropic layers and also because the measurements can then be directly used for anisotropy tomography inversions in a similar framework to that of travel-time velocity tomography inversions. Our method differs from the aforementioned methods in that we measure and remove the multiple anisotropic layers individually, iterating from the shallowest (or final) layer consecutively to the deepest (or first) layer. This method is limited by the criteria that have to be fulfilled in order to enable measurement of multi-layer splitting compared to the simultaneous method of Özalaybey and Savage (1994) and Wolfe and Silver (1998), but allows for constraint of the result even for single measurements because it doesn't increase the number of degrees of freedom when finding the optimal splitting parameters for each layer. Below we describe this new layer-by-layer method for two layers, the assumptions required, and an extended outline for n-layers.

2.2.1 Required assumptions

The layer-by-layer method requires a number of assumptions:

1. n layers split the S-wave n times (Yardley and Crampin, 1991; Silver and Savage, 1994).

2. Each layer has a single effective anisotropy. In other words, this method will only resolve the overall effect of all anisotropic contributions within a given layer, in the same way as the single-layer method.

3. The delay-time of the deepest layer (layer-1), δt_1, must be greater than the longest dominant period component of the S-wave (see Rümpker and Silver (1998b), Figure 1, for a clear example of frequency vs. delay-time effects).

4. The signal dominating an initial apparent single-layer measurement is that of the first layer of splitting. This constraint is likely valid for the majority of scenarios because the first-layer only partitions the energy between two phases (fast and slow, layer-1).

5. The anisotropy of each layer has the same frequency-dependent behaviour (i.e. S-waves are not differentially dispersed by the various layers).

6. The fast directions of each layer (ϕ_1, ϕ_2, ..., ϕ_n) are not parallel or orthogonal to one another in the QT-plane. If they are orthogonal then it will not be possible to differentiate between phases from the two layers as the fast and slow waves will not undergo further splitting, giving a null result for one of the layers (a null result is defined as where anisotropy is indistinguishable).

Although these criteria might appear stringent, it is likely that a number of physical scenarios meet these conditions.

2.2.2 The method for two-layers

The multi-layer splitting method measures the splitting parameters for each individual layer ($\phi_i, \delta t_i$), as well as the apparent splitting parameters using the single-layer method ($\phi_{app}, \delta t_{app}$) so that the significance of the multi-layer result beyond the single-layer result can be quantified. These parameters are measured as follows:

1. The apparent splitting parameters are measured using the single-layer method for a window, win_{init}, containing all the S-wave energy (see Section 2.1).

2. The initial window is partitioned into two windows, one from $t_{win_{init},start}$ to $t_{win_{init},start} + \delta t_{app}$, and another from $t_{win_{init},start} + \delta t_{app}$ to $t_{win_{init},end}$, controlled by the apparent delay-time, δt_{app}.

3. The splitting parameters are measured for each of the these windows, using the eigenvalue method (see Section 2.1), with the most linearised result (smallest λ_2/λ_1) defined as the optimal splitting parameters for the shallowest layer (layer 2 for a two-layer problem).

4. The entire S-wave arrival over win_{init} is then corrected to remove the splitting for layer 2.

5. The splitting parameters are then measured for this corrected data over win_{init}. The optimal splitting parameters measured here correspond to the deepest layer (layer 1).

6. One can then confirm whether the two-layer solution provides a more accurate description of the medium than the single-layer, apparent solution. Here, we define this as a solution where the multi-layer result is: (1) more linear (i.e. $(\lambda_2/\lambda_1)_{multi-layer} < (\lambda_2/\lambda_1)_{single-layer}$); and (2) the fast directions of the two layers have different orientations, after accounting for uncertainty. Here, we define $(\lambda_2/\lambda_1)_{multi-layer}$ in a similar way to Wolfe and Silver (1998), except summing over λ_2/λ_1 rather than λ_2,

$$(\lambda_2/\lambda_1)_{multi-layer} = \sum_{n=1}^{n} \left(\frac{\lambda_2}{\lambda_1}\right)_n , \tag{7}$$

where n denotes the nth layer.

2.2.3 Extension to n-layers

Section 2.2.2 describes the multi-layer method specifically for two layers, for clarity. However, extension of the method for n-layers is theoretically trivial. Steps 2 to 4 in Section 2.2.2 can be repeated for cascading smaller windows, using $\delta t_{2,app}$, $\delta t_{3,app}$, ..., $\delta t_{n,app}$ to partition the windows in each case. However, practically there is a limit to how many layers can be measured independently. Various S-wave phase arrivals are more likely to be indiscernible from one another as the number of layers to solve for becomes greater, since each layer is thinner, which inevitably leads to smaller delay times. Window lengths will also become smaller, leading to less stable solutions. Furthermore, energy partitioning associated with splitting due to each layer will reduce the S-wave amplitudes by $1/2^n$ for n-layers, reducing the SNR of each individual S-wave phase arrival. Therefore, although we include the extension to n-layers for completeness, we only provide examples solving for up to two layers.

2.3 Example of SWSPy usage

SWSPy supports automated measurement of shear-wave splitting for simple single source-receiver pairs to many receivers and many sources. Here, we provide a simple example of how to measure shear-wave splitting for a single source at multiple receivers and an example of how one can perform forward modelling to generate synthetic signals exhibiting shear-wave splitting. A comprehensive set of examples for every result presented in this work are provided within the SWSPy package.

2.3.1 Measuring shear-wave splitting for an earthquake

SWSPy is implemented using a Python class-based structure (see Listing 1), heavily utilising `obspy` for seismic data input and output (Krischer et al., 2015). One creates a `splittingObject`, by passing an `obspy` data stream, `st`, containing seismic traces for all receivers and all components over the earthquake arrival time period. Various parameters defining the windows and parameter search space can then be specified as `splittingObject.parameter`, before performing the shear-wave splitting analysis. The shear-wave splitting analysis in Listing 1 is performed using the function `perform_sws_analysis`, which performs shear-wave splitting for a single layer. To instead use the multi-layer (layer-by-layer) method, one can simply replace this function with the function `perform_sws_analysis_multi_layer`.

Listing 1 Example use of `splittingObject` to perform shear-wave splitting analysis

```
import swspy, obspy

# Create splitting object:
st = obspy.read(<path_to_data>)
splittingObject = swspy.splitting.
    create_splitting_object(st)

# Specify some key parameters...
splittingObject.win_S_pick_tolerance = 0.1
splittingObject.
    overall_win_start_pre_fast_S_pick = 0.3
splittingObject.
    overall_win_start_post_fast_S_pick = 0.2
splittingObject.max_t_shift_s = 1.0

# Perform splitting analysis:
splittingObject.perform_sws_analysis(
    coord_system=‘‘ZNE’’, sws_method=‘‘EV’’)

# Plot and save result:
# (saves splittingObject.sws_result_df to csv
     file)
splittingObject.plot()
splittingObject.save_result()
```

2.3.2 Forward modelling

SWSPy also supports forward modelling, for generating synthetic seismograms passing through anisotropic media. An example of creating a synthetic seismogram for an S-wave with a dominant frequency of 10 Hz travelling through a layer that has a fast direction of 60^o and $\delta t = 0.5\ s$ is shown in Listing 2. Such forward modelling is included for verifying SWSPy performance and solving inversion problems, for example.

Listing 2 Example use of generating a synthetic seismogram `st`

```
import swspy

# Create source-time function:
seismogram_dur_s = 10.0
sampling_rate_hz = 1000.0
st = swspy.splitting.forward_model.
    create_src_time_func(seismogram_dur_s,
    sampling_rate_hz)

# Specify layer anisotropy parameters:
phi_from_N = 60
dt = 0.5
back_azi = 0
event_inclin_angle_at_station = 0

# Apply splitting:
st = swspy.splitting.forward_model.
    add_splitting(st, phi_from_N, dt,
    back_azi, event_inclin_angle_at_station)
```

3 Examples

3.1 Simple icequake example

Here, we use a real-world earthquake at a glacier as an example of S-wave splitting analysis performed using SWSPy, specifically focusing on the key attributes that indicate a reliable measurement. Figure 5 shows a basal stick-slip icequake S-wave arrival at a single receiver from Rutford Ice Stream, Antarctica (Hudson et al., 2020a; Smith et al., 2015). Glacier ice can exhibit a strongly anisotropic fabric, which combined with low noise levels in Antarctica provides an ideal real-world example of S-wave splitting (Smith et al., 2017; Harland et al., 2013; Kufner et al., 2023). Basal stick-slip icequakes also provide an ideal example because their S-wave source polarisations are typically well-constrained, aligned approximately in the direction of ice flow (160^o from North, Smith et al., 2015), in this case confirmed by full-waveform source mechanism inversion (Hudson et al., 2020a).

There are a number of key attributes that represent a well-constrained splitting result. Useful attributes for quantifying the quality of a splitting result are:

1. Checking the raw vs. splitting-removed waveforms in the ZNE coordinate system (see Figure 5a). Firstly, the majority of the S-wave arrival wave packet should lie between the last of the possible window starts and the first of the possible window ends (grey vertical lines, Figure 5a). Secondly, the wave packet of the splitting-removed wave packet should have a shorter duration than the raw data.

2. Maximising and minimising energy on splitting-removed P and A components, respectively (red data, Figure 5b). The amplitude ratio of the P to A components represents the linearity of the splitting-removed particle motions, which is quantified by the ratio of eigenvalues (λ_2/λ_1), with smaller λ_2/λ_1 values representing a more linearised result. For the icequake, $\lambda_2/\lambda_1 = 0.033$, with

the majority of energy contained in the P component, with only a small packet of energy arriving on the A component.

3. Fast and slow S-wave phases should arrive at different times prior to splitting removal and aligned in time post the removal of splitting (see right panel of Figure 5c).

4. Approximately linear particle motion in the North-East plane (see Figure 5d). For the icequake in Figure 5, the particle motion is approximately linearised, except for a small perturbation approximately perpendicular to the dominant strike, with a source polarisation of $\sim 165^o \pm 6^o$ from North, which is in agreement with the ice flow direction and source mechanism inversion (Hudson et al., 2020a).

5. Checking the stability of the clustering analysis (see Figure 5e). At least some of the cluster samples should have small uncertainties, resulting in a stable ϕ and δt solution. If window samples all exhibit significant variation or a clear non-uniform behaviour then the result may be susceptible to effects such as cycle skipping (see Teanby et al. (2004) for further details).

6. A distinct minimum in the eigenvalue ratio within $\phi - \delta t$ space (see Figure 5f). The icequake exhibits a distinct, single global minimum, with the optimal solution indicated by the green point and associated error bars. Note that ϕ is ϕ from Q (ϕ', Figure 2). The $\phi - \delta t$ space plot is useful for interrogating whether cycle skipping occurs. If cycle skipping were dominating the result, then there might be multiple minima, with associated ϕ values separated by 90^o and multiple possible δt values, corresponding to the phase-lag of the cycle skipping. The icequake result shown here is a relatively simple arrival, not exhibiting any significant cycle skipping.

7. Measurement quality parameters λ_2/λ_1 and Q_W. SWSPy outputs multiple parameters that indicate the quality of a S-wave splitting result. The linearity of the result is quantified by the eigenvalue ratio λ_2/λ_1, as discussed above. SWSPy can also calculate the so-called Wuestefeld quality factor, Q_W (Wuestefeld et al., 2010), where $Q_W = 1$ is a good result, $Q_W = 0$ is a poor result, and $Q_W = -1$ is a good null result. Q_W for the icequake in Figure 5 is 0.969, which confirms that the result is consistent using both eigenvalue and cross-correlation methods. However, these measurement quality parameters inevitably are important for automated filtering of many results, for which it is otherwise impractical to check every individual result. For automated analysis, we recommend using quality parameters in combination with uncertainty in ϕ and δt to filter out spurious results (see Section 3.3 for an example).

3.2 Teleseismic shear-wave splitting

Here, we demonstrate the performance of SWSPy for teleseismic shear-wave splitting. Teleseismic shear-wave splitting of SKS, PKS, and SKKS phases is a common technique used to constrain upper mantle deformation patterns (e.g. Silver and Chan, 1991; Kendall et al., 2005; Becker and Lebedev, 2021). These core-refracted phases enable reliable shear-wave splitting measurements of the mantle, due to their near-vertical incidence and radial polarisation caused by a P-to-S conversion when exiting the core (Hall et al., 2004).

Figure 6 shows data from the $M_w 7.1$ 5[th] February 2005 Celebus Sea earthquake, recorded at the station NEE in California, US. Previous shear-wave splitting analysis, using the shear-wave splitting code SHEBA (Wuestefeld et al., 2010), identified discrepant SKS-SKKS shear-wave splitting where SKS was a null result (i.e., no shear-wave splitting) and SKKS exhibited clear shear-wave splitting, with $\phi = 74^o \pm 5^o$, $\delta t = 1.05 \pm 0.07 s$, which is interpreted as a single layer of seismic anisotropy in the lowermost mantle (Asplet et al., 2020). Unlike the ice example, for teleseismic shear-waves $\delta t << T$, the dominant period of the signal, so the fast and slow S-wave arrivals will not be isolated in time nor give the characteristic elliptical particle motion (see Figure 6d). Using SWSPy, we remeasure the shear-wave splitting of the SKKS phase and obtain $\phi = 74.2^o \pm 14.0^o$, $\delta t = 1.05 \pm 0.175 s$ (see Figure 6). These shear-wave splitting parameters agree, within measurement uncertainty, with the SHEBA results (see Table 1). We are also able to retrieve a source polarisation of $115^o \pm 7^o$, which is consistent with the measurement from SHEBA of $115°$ and the observed back-azimuth of 294^o, following the assumption that SKS is radially polarised. When we correct for the measured shear-wave splitting (see Figure 6d) we can see the particle motion has been well linearised, with $\lambda_2/\lambda_1 = 0.018$.

This example only demonstrates a simple teleseismic use case. In reality, modern teleseismic shear-wave splitting studies, particularly those focusing on the lowermost mantle, are more involved. Preprocessing of shear-wave splitting datasets, such as stacking (Deng et al., 2017) and beamforming (Wolf et al., 2023), allow for clearer identification of SKS, SKKS and S3KS phases, especially in noisy datasets. To process large datasets automated approaches for classifying null and split shear-wave splitting using Q_W and λ_2/λ_1 have been developed (Walpole et al., 2014). Advances in modelling plausible anisotropic fabrics from shear-wave splitting measurements (Creasy et al., 2021; Asplet et al., 2023) allow for more quantitative interpretation of observations. The design of SWSPy allows it to be easily integrated into these developing analysis workflows.

3.3 Application of automated S-wave splitting analysis to many earthquakes at a volcano

The previous examples focus on single observations. However, recent advances in the sensitivity and density of instrumentation, combined with computational developments, have resulted in earthquake catalogues containing thousands to millions of events. This

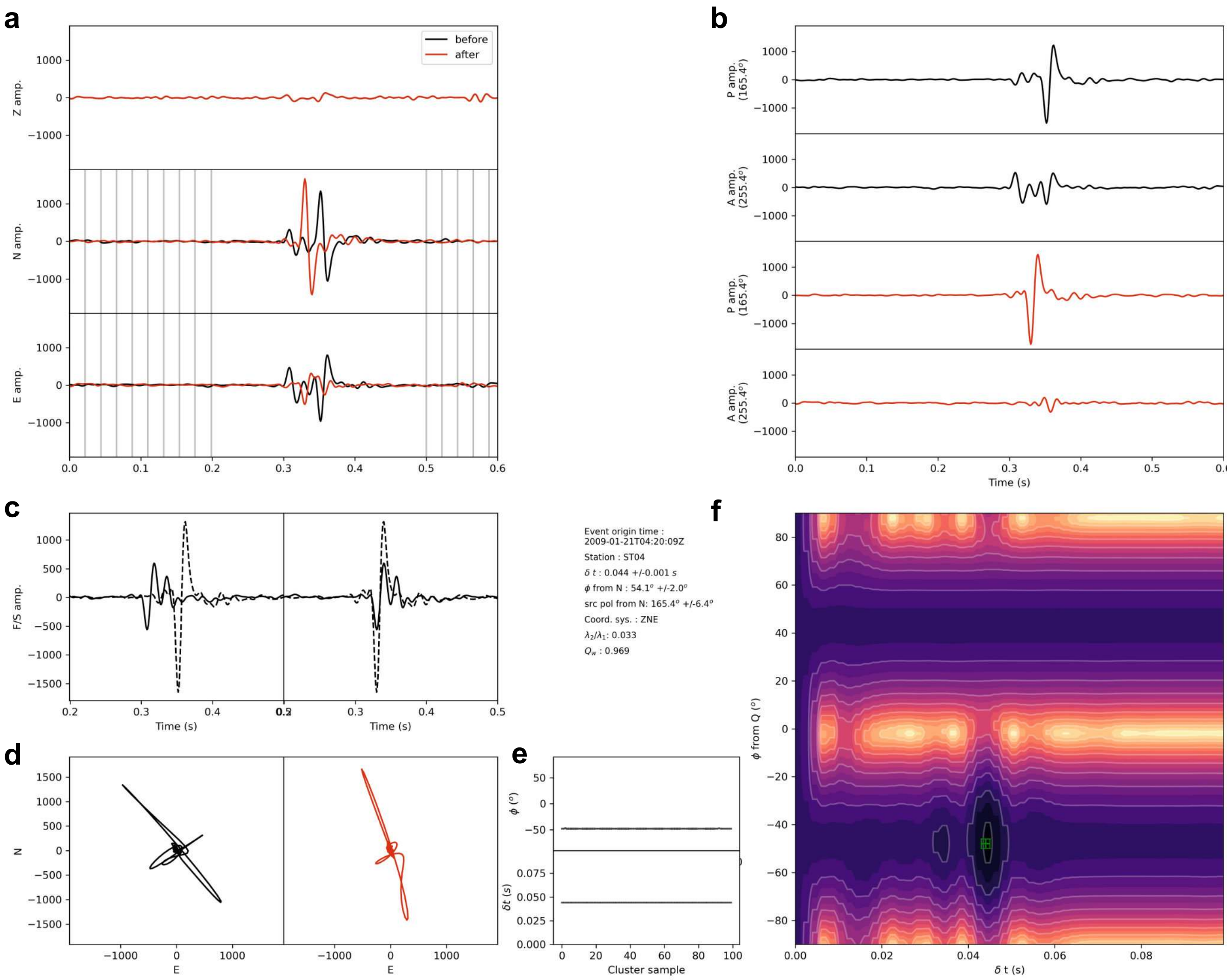

Figure 5 Example of a full output result from SWSPy for an icequake at Rutford Ice Stream, Antarctica, from Hudson et al. (2020a). **a.** Vertical, North and East component seismograms for the S-wave arrival. Black waveforms are the uncorrected data and red are post splitting correction. **b.** P and A component waveforms pre and post splitting. P and A components correspond to the polarisation and null vectors, respectively (see Figure 2). **c.** Fast (solid) and slow (dashed) S-wave arrivals before (left panel) and after (right panel) the delay time shift. **d.** Particle motions in the North-East plane before (left panel) and after (right panel) the splitting correction. **e.** Uncertainty in ϕ and δt for all the clustering samples. **f.** $\phi - \delta t$ space for the optimal cluster result, coloured by eigenvalue ratio. The darker the colour, the smaller the eigenvalue ratio. The optimal splitting result occurs at the global minimum in the $\phi - \delta t$ space, with the optimal solution and its associated uncertainty indicated by the green point and error bars.

presents an opportunity for higher resolution S-wave velocity anisotropy studies. To process such datasets, automation is required. Here, we verify the performance of fully automated S-wave splitting measurements using SWSPy, before showing how this automated S-wave splitting analysis can provide an enhanced picture of the presence of fluids at a volcano.

Results for 1356 earthquakes at Uturuncu volcano, Bolivia, are shown in Figure 7 (Hudson et al., 2023). This earthquake catalogue is derived from a fully automated detection algorithm (Hudson et al., 2022). Figure 7a shows the unfiltered distribution of fast S-wave polarisations for all source-receiver pairs in the entire Uturuncu dataset compared to a filtered subset of the data. The filtered subset that are defined as well-constrained measurements are S-wave splitting results with $Q_W > 0.5$, a fast S-wave polarisation direction uncertainty, $\alpha_\phi < 10^o$, and a delay-time uncertainty, $\alpha_{\delta t} < 0.1\ s$. The filtered subset of fast directions exhibits one dominant direction of anisotropy striking SE-NW. The anisotropy causing these results could be a combination of the crystallographic orientation of the medium and/or fractures. Here, we assume that for a volcano that is actively deforming (Pritchard et al., 2018), the anisotropy is likely dominated by fracturing (a full discussion of the possible mechanisms of anisotropy and justification of this assumption can be found in Hudson et al. (2023)). To verify whether the measured fast directions shown in Figure 7a are truly representing a fractured fabric, we compare the results to independently measured fault strike data, derived from the spatial distribution of microseismicity (see Hudson et al. (2022) for details). The fault strike data shows two orthogonal sets of fractures (Figure 7b). The fast directions from the shear-wave

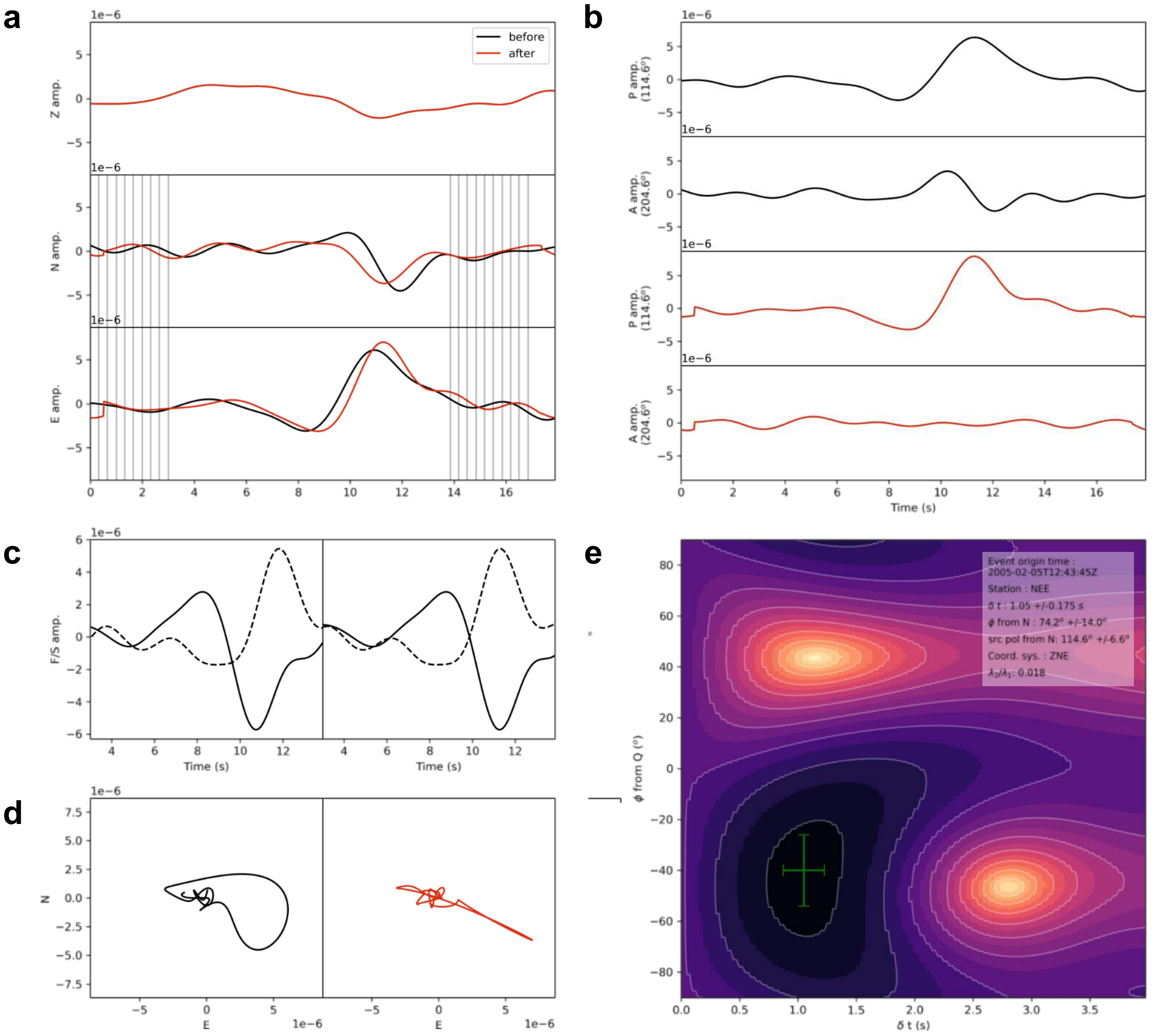

Figure 6 Example of SKKS phase arriving at station NEE from Asplet et al. (2020). **a.** Vertical, North and East component seismograms for the S-wave arrival. **b.** P and A component waveforms pre and post splitting. **c.** Fast and slow S-wave arrivals before and after the delay time shift. **d.** Particle motions in the North-East plane before and after the splitting correction. **e.** $\phi - \delta t$ space for the optimal cluster result. See Figure 5 caption for further labelling details.

splitting align parallel to one set of fault strikes. Attenuation tomography at Uturuncu volcano (Hudson et al., 2023) indicates that fluids are likely present dominantly in faults with this orientation, controlled by the regional stress field of the deforming volcano, which is depicted in Figure 7c. The S-wave anisotropy results are therefore consistent with the interpretation from independent observations, verifying the performance of the automated S-wave splitting approach.

The aforementioned filter criteria are necessarily strict, in order to yield sufficiently high quality measurements to interpret. Such strict criteria have limited analysis of automated S-wave splitting measurements in the past because too many events are discarded (Crampin and Gao, 2006). However, recent developments in the number of earthquakes that can be automatically detected means that, in this example, one still has thousands of observations that meet these criteria. This is likely also the case for other datasets. Fully automated shear-wave splitting methods are the only practical means of processing such large datasets.

Shear-wave splitting analysis also yields S-wave source polarisations, which for double-couple faults is oriented in the direction of fault slip. This is clearly illustrated by comparing the fault strikes to SWSPy derived S-wave source polarisations, which approximately agree for both sets of orthogonal fault strikes. The S-wave source polarisations contain a greater spread, either caused by uncertainty in the measurements or by some of the earthquakes exhibiting a volumetric focal mechanism component. However, S-wave source polarisation data are seldom used in anisotropy or crustal-stress studies. We emphasise these observations in order to encourage others to consider using these data to provide additional information on fracture processes and the stress-state of a medium.

3.4 Multi-layer examples

3.4.1 Forward model example

We first demonstrate the performance of the new multi-layer splitting method on modelled data, before applying it to a real-world example. Figure 8 shows results for a two-layer forward model. Shear-wave splitting is applied twice to a Ricker wavelet with a centre frequency of 10 Hz and a source polarisation of $0^o\ N$ to simulate a wave propagating through a two layer medium ($\phi_{layer1} = 60^o$ and $\phi_{layer2} = 40^o$, $\delta t_{layer1} = 0.5\ s$ and $\delta t_{layer2} = 0.2\ s$). Figure 8 show results for an apparent measurement (assuming a single-layer) and our new explicit layer-by-layer approach.

The apparent shear-wave splitting measurement shown in Figure 8a-d obviously does not find the true result. However, the $\phi - \delta t$ space (see Figure 8d) shows that the apparent measurement is sensitive to both layers, with clearly distinct minima at $\delta t = 0.2\ s$ and $\delta t = 0.5\ s$. The first layer exhibits the stronger splitting signal, as expected theoretically, and so is the result that dominates the solution. The sensitivity of this measurement to both layers theoretically makes sense because rotating the original traces into either of the individual layer planes will typically result in more linearised data, but only minimised for one layer. This exemplifies the findings of Silver and Savage (1994), who describe how apparent single-layer splitting measurements can be used to decipher certain aspects of multi-layered anisotropic media. Incidentally, the $\phi - \delta t$ space also shows a strong cycle-skipping signal, caused by the symmetry of the modelled source-time function and the multiple time-shifts resulting from the two layers. It is this cycle-skipping that would make picking the distinct minima for each layer in $\phi - \delta t$ challenging. If this problem could be overcome, then it may be possible in certain instances to isolate relative splitting properties for each layer. Overall, the corrected waveforms are only linearised for layer-2 (see Figure 8c), and the fast-direction and source polarisation are not correct, due to the remaining effect of the layer-1 splitting.

Results for the new layer-by-layer splitting measurement method presented in this work are more promising (see Figure 8i-l). The anisotropy exhibited by the two layers is well resolved by the method, with all results close to the true values and the majority in agreement, within uncertainty. The corrected waveforms further emphasise the performance of our new layer-by-layer method (see Figure 8g compared to Figure 8c). Overall, these results provide us with confidence that our new multi-layer method can resolve multi-layer anisotropy.

3.4.2 Icequake example

There are few real-world examples of successful multi-layer S-wave velocity anisotropy measurements (Silver and Savage, 1994; Rümpker and Silver, 1998a; Levin et al., 1999), likely primarily due to challenges associated with making such measurements rather than a lack of real-world multi-layered anisotropic media. However, glacier ice can provide a real-world example of multi-layer anisotropy. Typically, previous glacier anisotropy studies assume a single dominant ice fabric caused by crystals in the ice fabric being preferentially aligned by ice flow (Smith et al., 2017; Harland et al., 2013). However, recent observations suggest that Rutford Ice Stream instead has multiple distinguishable layers of anisotropy (Jordan et al., 2022; Kufner et al., 2023). Indications of this can be seen in Figure 5d, where a proportion of the particle motion in the North-East plane is not fully linearised. We therefore use this icequake to demonstrate performance of the multi-layer splitting method applied to real data.

Figure 9 shows the horizontal particle motion for a two-layer S-wave splitting result compared to the single-layer result from Figure 5. The eigenvalue ratio, λ_2/λ_1, indicates that the two-layer result is approximately twice as well linearised compared to the single-layer result. This demonstrates that a two-layer medium describes the observations better than a single-layer medium. The more linear result also allows for greater constraint of the S-wave source polarisation. The two-layer solution includes the delay-time and fast-direction of both layers. The delay-times of the two layers sum to the delay time measured for a single layer, as expected. The two fast directions are distinct from one another, after accounting for uncertainty. This provides us with confidence that the result represents a physical two-layer system, rather than a better fit simply being due to an additional two degrees of freedom of the multi-layer solution. However, the additional degrees of freedom of multi-layer splitting analysis should be treated with caution due to the potential for over-fitting. We suggest that one should reject a higher-order layer solution compared to a lower-order layer solution if consecutive layers have fast directions that are the same within uncertainty. This is also why we favour measuring anisotropic layer properties consecutively rather than all together in a direct inversion, as our consecutive-layer method only has the same number of degrees of freedom per layer measurement as the single-layer method.

The icequake result shown in Figure 9 demonstrates that the method shows promise for interrogating multiple layers of anisotropy that are likely present in numerous real-world scenarios.

3.4.3 Challenges and limitations of multi-layer shear-wave splitting

Although the multi-layer method described above performs well for the synthetic example and the real-world icequake example, the required assumptions mean that it is limited or not applicable for situations that do not exhibit such strong anisotropy relative to signal frequency. We wish to highlight here that it is likely not applicable for the majority of teleseismic shear-wave splitting analyses, or any other situation where δt is less than the dominant period of the S-wave and δt of any crustal layer could conceivably be greater than the magnitude of splitting in the mantle.

The challenges faced by the multi-layer method pre-

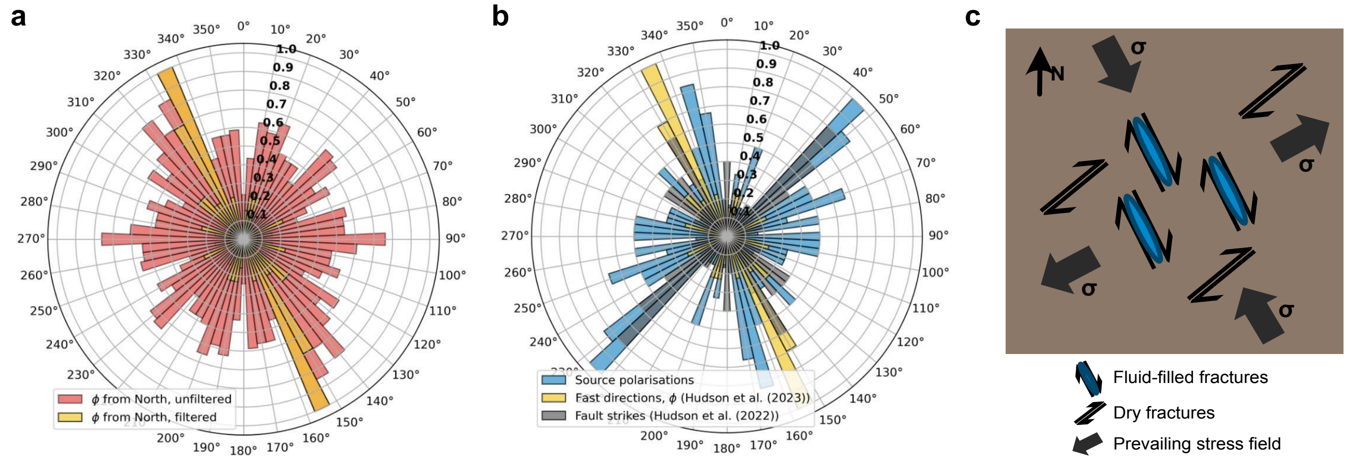

Figure 7 Summary of S-wave splitting analysis for 1356 earthquakes from Uturuncu volcano, Bolivia (Hudson et al., 2023). **a.** Rose histogram of automatically measured S-wave fast directions, before and after filtering (filters applied are: $Q_W > 0.5$; $\alpha_\phi < 10^o$; $\alpha_{\delta t} < 0.1\ s$). **b.** Rose histogram of filtered S-wave fast directions, S-wave source polarisations and fault strikes . Fault strikes are derived from principal component analysis of spatial distribution of clustered microseismicity (Hudson et al., 2022). **c.** Summary of the interpretations of anisotropy combined with source polarisation information.

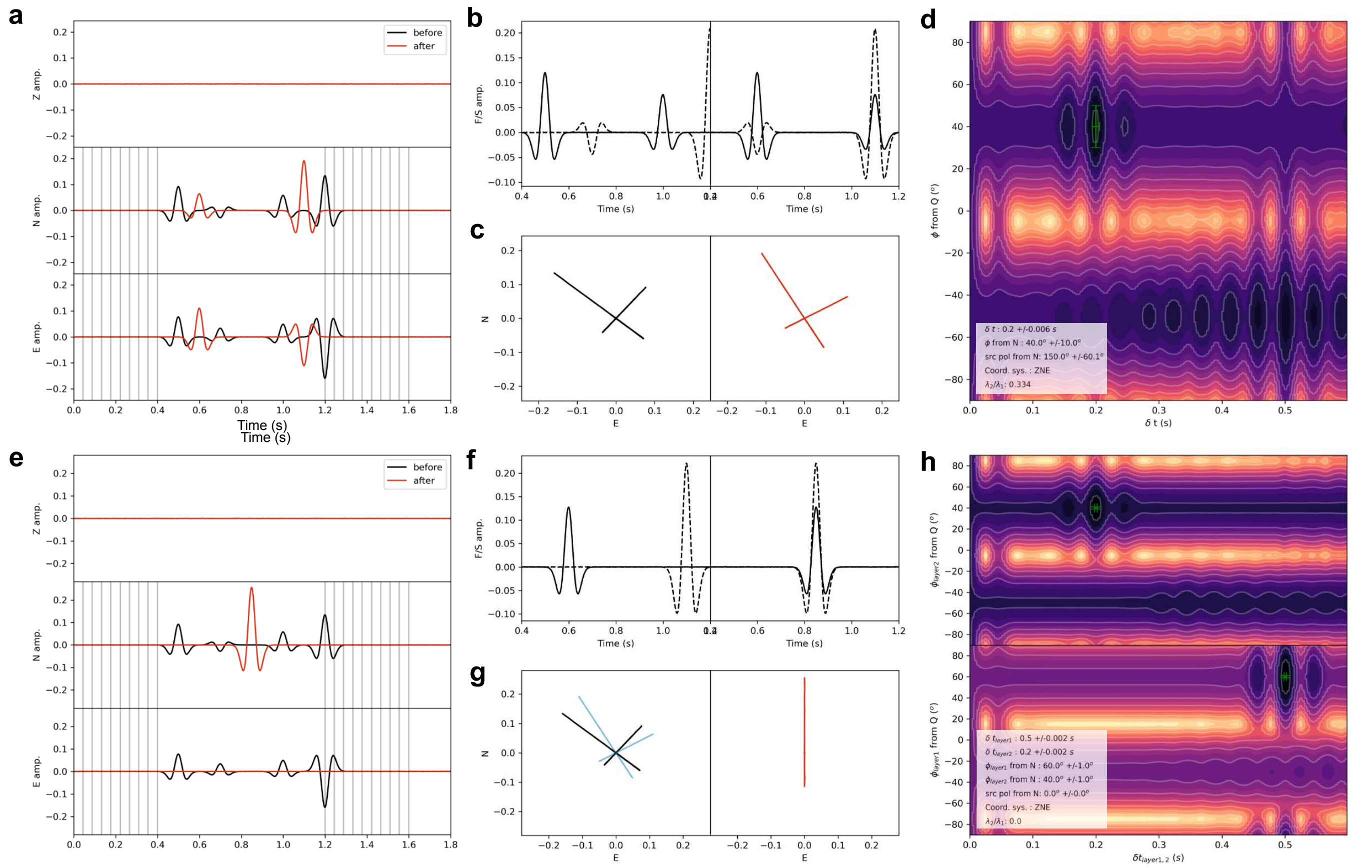

Figure 8 Synthetic, forward model example of multi-layer S-wave splitting analysis, for a medium with two layers of anisotropy ($\phi_{layer1} = 60^o, \phi_{layer2} = 40^o, \delta t_{layer1} = 0.5s, \delta t_{layer2} = 0.2s$) and an S-wave with an initial source polarisation of 0^o from North. **a-d.** Results for an apparent, effective single-layer measurement (see Figure 5 for more details on labelling of subplots). **e-h.** Results for an explicit, layer-by-layer two-layer inversion. Blue data in g. are the particle motions after the intermediate correction for layer-2 only.

sented in this study for teleseismic shear-wave splitting are not unique to this method. Figure 10 exemplifies this issue. Shear-wave splitting analysis is applied to a synthetic seismogram with similar characteristics to an SKS phase arrival that observes a deeper layer with $\delta t_1 = 1.25\ s$, $\phi_1 = 60^o$ and a shallower layer with $\delta t_2 = 0.5\ s$, $\phi_1 = 25^o$. Fast/slow waveforms and particle motions in the horizontal plane are shown for a single-layer effective measurement (Figure 10b) and a two-layer measurement (Figure 10c). The two-

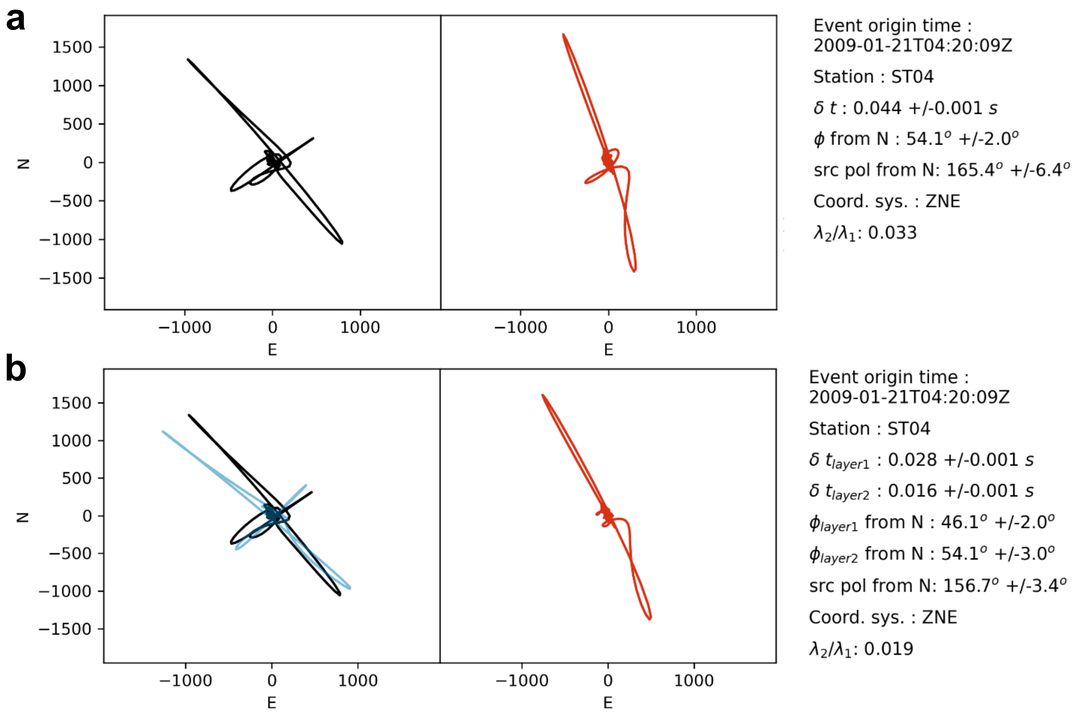

Figure 9 Example of single-layer vs. multi-layer S-wave splitting analysis horizontal particle motions for the icequake in Figure 5. **a.** Single-layer measurement particle motion results before (left) and after (right) the splitting correction. **b.** Multi-layer measurement particle motion results before (left) and after (right) the splitting correction (blue data are initial layer-2 only correction). Text in a. and b. shows key results from the respective S-wave splitting analyses.

layer measurement is made using a single-ray measurement adaptation of Özalaybey and Savage (1994), performing a grid-search over layer-1 and layer-2 parameters to find the values that best agree with the apparent measurements of Figure 10b (see Eq. 1 to 3, Özalaybey and Savage (1994)). Both the effective single-layer measurement of apparent splitting and the multi-layer measurement yield significantly more linearised corrected S-wave arrivals than the original uncorrected waveforms. However, obviously the single-layer measurement does not resolve the anisotropy correctly. The multi-layer measurement does resolve layer-1 with albeit large uncertainties. However, the direction of the layer-2 anisotropy (ϕ_2) is not resolved, disagreeing with the synthetic layer value by exactly 90^o. This is caused by a periodicity in the relationship between apparent splitting parameters ($\alpha_a = 2\phi_a$, $\theta_a = \pi f \delta t_a$, where f is the dominant frequency of the phase arrival). The origin of this behaviour is described in detail in Silver and Savage (1994), with a schematic explanation found in Figure 10c. This periodicity in the relationship between apparent and individual layer parameters results in a non-unique solution for the fast-direction of a given layer (ϕ_i) regardless of orientation and further ambiguity introduced for $\delta t > 1/2f$ (see Figure 10c). Özalaybey and Savage (1994) address such non-unique solutions by combining measurements of multiple SKS phases arriving at many azimuths. Similar approaches have since been implemented by others (Reiss and Rümpker, 2017). We have deliberately not implemented such an algorithm, since the focus of SWSPy here is to be universally applicable to single source-receiver pair measurements rather than specific implementations of 1D or higher-order tomographic methods. Nonetheless, SWSPy could readily comprise part of such a workflow, used to measure apparent splitting parameters before a multi-event inversion.

3.5 Comparison of SWSPy to other shear-wave splitting software packages

For completeness, we compare the results of SWSPy for the two main end-member events in this study, the icequake in Figure 5 and the SKKS arrival in Figure 6. Results of this comparison of SWSPy to MFAST (Savage et al., 2010) and SHEBA (Wuestefeld et al., 2010) are found in Table 1. We do not include results from two other packages, SplitRacer (Reiss and Rümpker, 2017) and Pytheas (Spingos et al., 2020), as these are graphical user interfaces that differ in applicability considerably from our implementation. All the splitting measurements are run using as similar parameters as possible, including the filter properties, duration of data and number of windows used for clustering. The three packages find identical fast-directions (ϕ) and delay-times (δt), within uncertainty. The uncertainty in SWSPy is larger as a result of our definition of uncertainty, which is deliberately a more conservative estimate than the other packages. This is particularly evident for the SKKS example in Table 1. Uncertainties are still only a small fraction of the result for both example events. Where the packages differ is in the source polarisations, where SWSPy and SHEBA agree within uncertainty, while MFAST exhibits significant differences. Given the near-identical performance of SWSPy com-

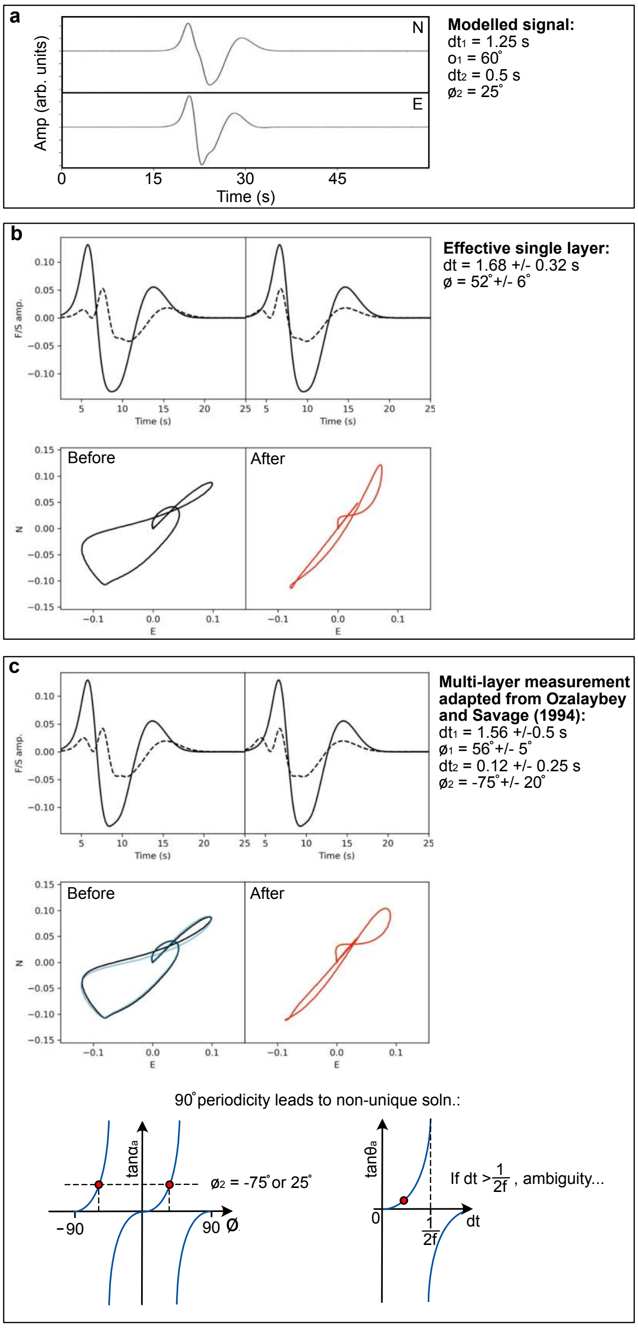

Figure 10 Example of challenges associated with teleseismic multi-layer shear-wave splitting measurements. **a.** Synthetic teleseismic signal with two layers of splitting applied. **b.** Effective single-layer shear-wave splitting measurement. **c.** A multi-layer measurement using a single-ray measurement adaptation of the method of Özalaybey and Savage (1994). Schematic plots of $tan(\alpha_a)$ and $tan(\theta_a)$ in c. show how 90^o periodicity can lead to non-unique fast direction solutions, as is the case in c.

pared to SHEBA and the consistency of source polarisation measurements with the physical settings, we are confident that SWSPy's source polarisation estimates are realistic.

We do not benchmark compute times for SWSPy compared to these other methods since SWSPy is parallelised while SHEBA and MFAST are not. Given the capability of modern computers, it is likely that most users would capitalise on the parallelised nature of SWSPy. This would quickly offset any inefficiency of SWSPy compared to other packages.

4 Discussion

4.1 Benefits and limitations

The aforementioned examples indicate the performance of SWSPy for various shear-wave velocity anisotropy applications. For individual source-receiver measurements, it provides stable measurements as a result of the Teanby et al. (2004) multi-window method combined with the use of more advanced clustering algorithms. 3D splitting measurements are implemented, as defined in Walsh et al. (2013), allowing SWSPy to likely be useful for measuring anisotropy using borehole data or settings without a significant steep velocity gradient that refracts waves towards vertical incidence. For large datasets comprising of many source-receiver pairs, SWSPy includes a fully-automated workflow that can easily be adapted due to the modular nature of the Python package. Parameters that can be used to filter spurious outputs from fully-automated analyses are provided, including quality metrics ($Q_W, \lambda_2/\lambda_1$) and uncertainty measurements ($\alpha_\phi, \alpha_{\delta t}$). The ability to process many thousands to millions of shear-wave splitting measurements will hopefully enable shear-wave velocity anisotropy tomography studies to be performed, with a significant increase in the number of observations reducing the inherently under-constrained nature of the tomography problem (Chevrot et al., 2004). Such anisotropy tomography studies could be useful for imaging mantle dynamics (Chevrot, 2006), imaging deformation at volcanoes (Johnson and Savage, 2012), measuring fracture density at the surface of glaciers (Hudson et al., 2020b; Gajek et al., 2021), and reconciling body-wave and surface wave global tomography models (Becker et al., 2012).

A further advance provided by SWSPy is the ability to measure multi-layer anisotropy under certain conditions. This will enable users to study systems in more detail, as well as attempt to isolate specific layers of interest. While the multi-layer method assumptions (see Section 2.2.1) likely rule out applicability for the majority of teleseismic anisotropy problems, situations allowing for such conditions are likely present at highly anisotropic crustal settings such as volcanoes and hydrocarbon reservoirs, as well as near-surface environments such as glaciers. In such situations, δt is likely smaller than the dominant period, a key assumption due to particle motion effects (Rümpker and Silver, 1998b). Multi-layer measurements could also provide additional observational constraints for anisotropy tomography (Kufner et al., 2023). Furthermore, although we do not implement a teleseismic multi-layer inversion algorithm here, it should also be straight-forward to use SWSPy as part of a multi-layer apparent splitting inversion using multiple sources arriving at the same receiver, as in Özalaybey and Savage (1994), Silver and Savage (1994), and Reiss and Rümpker (2017).

Package	ϕ, IQ (^{o})	δt, IQ (s)	src. pol., IQ (^{o})	ϕ, SKKS (^{o})	δt, SKKS (s)	src. pol., SKKS (^{o})
SWSPy	54.1 ± 2.0	0.044 ± 0.001	165 ± 6	74.2 ± 14.0	1.05 ± 0.18	115 ± 7
MFAST	55.0 ± 1.8	0.044 ± 0.0002	150	74.0 ± 2.8	1.06 ± 0.03	245
SHEBA	55.0 ± 1.8	0.044 ± 0.0001	165 ± 3	74.0 ± 4.8	1.08 ± 0.06	115

Table 1 Comparison of performance of SWSPy to other similar, popular packages. The event IQ is the icequake presented in Figure 5 and the event SKKS is the SKKS phase arrival presented in Figure 6. More details on the packages can be found in the literature (SHEBA: Wuestefeld et al. (2010), MFAST: Savage et al. (2010), and recently parallelised in the version MFASTR: Mroczek et al. (2020)).

SWSPy also has limitations. One limitation is the metrics provided to quantify the quality of a result (Q_W, λ_2/λ_1). While these parameters can prove useful in some instances, we find that they are not universally reliable. We find that the uncertainty measurements provide the most useful way to remove spurious results, at least for the volcanic example provided here (see Figure 7). Link et al. (2022) find that the same metrics also perform well for XKS phase splitting analysis. However, in some cases the stated uncertainty may be an underestimate of the true uncertainty. Areas of further work are therefore better measurement quality metrics and more robustly estimated uncertainty. A further limitation is associated with the layer-by-layer multi-layer anisotropy method presented here. The method requires a specific set of assumptions, and although the data we present here meets these assumptions, it is likely that certain datasets will not. The method should therefore be applied cautiously, considering the assumptions carefully when interpreting any results. A final potential limitation is that SWSPy is written in Python, an inherently slow object-oriented language compared to other languages such as C or julia. To minimise this limitation, SWSPy is accelerated using numba (Lam et al., 2015) to compile and parallelise the computationally heavy functions. Although one could further increase the efficiency by implementing the package in a lower level language, we have not opted to do this, in order to make the package as accessible as possible to users.

4.2 Benefits of shear-wave splitting beyond anisotropy studies

The applications of shear-wave splitting reach beyond imaging subsurface anisotropy. A valuable, yet under utilised parameter is the S-wave source polarisation. Figure 7 shows how source polarisation can provide an independent measurement of fault orientation, at least for double-couple sources (Hudson et al., 2023). Another useful output from shear-wave splitting are anisotropy-corrected waveforms. Correcting for anisotropy is important for performing full-waveform inversions using isotropic models, for example to invert for earthquake source mechanisms (Hudson et al., 2020a). The new multi-layer method presented here will further reduce the misfit when comparing data from seismic waves that propagates through multiple anisotropic layers to isotropic full-waveform models. One final application is the removal of shear-wave splitting effects when calculating earthquake magnitudes. Shear-wave splitting can cause S-wave phases to overlap and interfere with one another, altering the apparent frequency content. This can result in additional uncertainty in moment magnitude calculations (Stork et al., 2014). The ability to easily incorporate shear-wave splitting corrections into moment magnitude workflows may reduce uncertainty in moment magnitude catalogues, relevant for improved seismic monitoring (Schultz et al., 2021).

Acknowledgements

T. Hudson was funded by a Leverhulme Early Career Fellowship from the Leverhulme Trust. We thank M. Kendall for useful discussions. We also thank two reviewers whose input much improved the manuscript. We thank all those who collected data used in this study. The data used in this work is all from publicly available sources, and so we direct readers to the cited publications for proper acknowledgement of these individuals.

Data and code availability

The SWSPy package described in this work is available as an open-source Python package, hosted on GitHub and PyPi, with a snapshot of the exact version released at time of writing available via Zenodo (Hudson, 2023). All data used in the examples are publicly available and are included as example notebooks within the examples directory of the SWSPy package distribution (Hudson, 2023). The Antarctic icequake data and Uturuncu volcano data are available on IRIS under network codes YG (2009, British Antarctic Survey (BAS), 2009), XP (2000-2004, Anandakrishnan et al., 2000), and YS (2009-2013, Pritchard, 2009), respectively, with the data associated with the teleseismic example available from California Institute of Technology and United States Geological Survey Pasadena (1926).

Competing interests

The authors have no competing interests.

References

Anandakrishnan, S., Wiens, D., and Nyblade, A. A Broadband Seismic Investigation of Deep Continental Structure Across the East-West Antarctic Boundary, 2000. https://www.fdsn.org/networks/detail/XP_2000/. doi: 10.7914/SN/XP_2000.

Asplet, J., Wookey, J., and Kendall, M. A potential post-perovskite province in D″ beneath the Eastern Pacific: Evidence from new analysis of discrepant SKSa-SKKS shear-wave splitting. *Geophysical Journal International*, 221(3):2075–2090, 2020. doi: 10.1093/GJI/GGAA114.

Asplet, J., Wookey, J., and Kendall, M. Inversion of shear wave waveforms reveal deformation in the lowermost mantle. *Geophysical Journal International*, 232(1):97–114, 2023. doi: 10.1093/gji/ggac328.

Bacon, C. A., Johnson, J., White, R. S., and Rawlinson, N. On the origin of seismic anisotropy in the shallow crust of the Northern Volcanic Zone , Iceland. *JGR Solid Earth*, 2021. doi: 10.1029/2021JB022655.

Baird, A. F., Kendall, J. M., Fisher, Q. J., and Budge, J. The Role of Texture, Cracks, and Fractures in Highly Anisotropic Shales. *Journal of Geophysical Research: Solid Earth*, 122(12):10,341–10,351, 2017. doi: 10.1002/2017JB014710.

Barruol, G. and Mainprice, D. A quantitative evaluation of the contribution of crustal rocks to the shear-wave splitting of teleseismic SKS waves. *Physics of the Earth and Planetary Interiors*, 78 (3-4):281–300, 1993. doi: 10.1016/0031-9201(93)90161-2.

Becker, T. W. and Lebedev, S. Dynamics of the Upper Mantle in Light of Seismic Anisotropy. In *Geophysical Monograph Series*, pages 257–282. John Wiley & Sons, jul 2021. doi: 10.1002/9781119528609.ch10.

Becker, T. W., Lebedev, S., and Long, M. D. On the relationship between azimuthal anisotropy from shear wave splitting and surface wave tomography. *Journal of Geophysical Research: Solid Earth*, 117(1):1–17, 2012. doi: 10.1029/2011JB008705.

Bowman, J. R. and Ando, M. Shear-wave splitting in the upper-mantle wedge above the Tonga subduction zone. *Geophysical Journal of the Royal Astronomical Society*, 88(March):25–41, 1987. doi: 10.1111/j.1365-246X.1987.tb01367.x.

British Antarctic Survey (BAS). Gauging Rutford Ice Stream Transients (GRIST), 2009. https://www.fdsn.org/networks/detail/YG_2009/.

California Institute of Technology and United States Geological Survey Pasadena. Southern California Seismic Network, 1926. https://www.fdsn.org/networks/detail/CI/. doi: 10.7914/SN/CI.

Chevrot, S. Multichannel analysis of shear wave splitting. *Journal of Geophysical Research: Solid Earth*, 105(B9):21579–21590, 2000. doi: 10.1029/2000jb900199.

Chevrot, S. Finite-frequency vectorial tomography: A new method for high-resolution imaging of upper mantle anisotropy. *Geophysical Journal International*, 165(2):641–657, 2006. doi: 10.1111/j.1365-246X.2006.02982.x.

Chevrot, S., Favier, N., and Komatitsch, D. Shear wave splitting in three-dimensional anisotropic media. *Geophysical Journal International*, 159(2):711–720, 2004. doi: 10.1111/j.1365-246X.2004.02432.x.

Crampin, S. A review of wave motion in anisotropic and cracked elastic-media. *Wave Motion*, 3(4):343–391, 1981. doi: 10.1016/0165-2125(81)90026-3.

Crampin, S. and Chastin, S. A review of shear wave splitting in the crack-critical crust. *Geophysical Journal International*, 155(1): 221–240, 2003. doi: 10.1046/j.1365-246X.2003.02037.x.

Crampin, S. and Gao, Y. A review of techniques for measuring shear-wave splitting above small earthquakes. *Physics of the Earth and Planetary Interiors*, 159(1-2):1–14, 2006. doi: 10.1016/j.pepi.2006.06.002.

Creasy, N., Pisconti, A., Long, M. D., and Thomas, C. Modeling of Seismic Anisotropy Observations Reveals Plausible Lowermost Mantle Flow Directions Beneath Siberia. *Geochemistry, Geophysics, Geosystems*, 22(10), 2021. doi: 10.1029/2021gc009924.

Deng, J., Long, M. D., Creasy, N., Wagner, L., Beck, S., Zandt, G., Tavera, H., and Minaya, E. Lowermost mantle anisotropy near the eastern edge of the Pacific LLSVP : constraints from SKS – SKKS splitting intensity measurements. *Geophysical Journal International*, 210(June):774–786, 2017. doi: 10.1093/gji/ggx190.

Ester, M., Kriegel, H.-P., Sander, J., and Xu, X. A Density-Based Algorithm for Discovering Clusters in Large Spatial Databases with Noise. In *KDD-96 Proceedings*, pages 226–231. Elsevier, 1996.

Fontaine, F. R., Barruol, G., Tommasi, A., and Bokelmann, G. H. Upper-mantle flow beneath French Polynesia from shear wave splitting. *Geophysical Journal International*, 170(3):1262–1288, 2007. doi: 10.1111/j.1365-246X.2007.03475.x.

Fouch, M. J., Fischer, K. M., Parmentier, E. M., Wysession, M. E., and Clarke, T. J. Shear wave splitting, continental keels, and patterns of mantle flow. *Journal of Geophysical Research: Solid Earth*, 105 (3):6255–6275, 2000. doi: 10.1029/1999jb900372.

Gajek, W., Gräff, D., Hellmann, S., Rempel, A. W., and Walter, F. Diurnal expansion and contraction of englacial fracture networks revealed by seismic shear wave splitting. *Communications Earth & Environment*, 2(1):1–8, 2021. doi: 10.1038/s43247-021-00279-4.

Grund, M. StackSplit - a plugin for multi-event shear wave splitting analyses in SplitLab. *Computers and Geosciences*, 105:43–50, 2017. doi: 10.1016/j.cageo.2017.04.015.

Hall, C. E., Fischer, K. M., Parmentier, E. M., and Blackman, D. K. The influence of plate motions on three-dimensional back arc mantle flow and shear wave splitting. *Journal of Geophysical Research: Solid Earth*, 105(B12):28009–28033, 2000. doi: 10.1029/2000jb900297.

Hall, S. A., Kendall, J. M., and van der Baan, M. Some comments on the effects of lower-mantle anisotropy on SKS and SKKS phases. *Physics of the Earth and Planetary Interiors*, 146(3-4):469–481, 2004. doi: 10.1016/j.pepi.2004.05.002.

Hammond, J. O., Kendall, J. M., Wookey, J., Stuart, G. W., Keir, D., and Ayele, A. Differentiating flow, melt, or fossil seismic anisotropy beneath Ethiopia. *Geochemistry, Geophysics, Geosystems*, 15(5):1878–1894, 2014. doi: 10.1002/2013GC005185.

Harland, S., Kendall, J.-M., Stuart, G., Lloyd, G., Baird, A., Smith, A., Pritchard, H., and Brisbourne, A. Deformation in Rutford Ice Stream, West Antarctica: measuring shear-wave anisotropy from icequakes. *Annals of Glaciology*, 54(64):105–114, 2013. doi: 10.3189/2013AoG64A033.

Hein, G., Kolinsky, P., Bianchi, I., and Bokelmann, G. Shear wave splitting in the Alpine region. *Geophysical Journal International*, 227(3):1996–2015, 2021. doi: 10.1093/gji/ggab305.

Hudson, T. S. SWSPy release 1.0.3. *Zenodo*, 2023. doi: 10.5281/zenodo.8006598.

Hudson, T. S., Brisbourne, A. M., Walter, F., Gräff, D., White, R. S., and Smith, A. M. Icequake Source Mechanisms for Studying Glacial Sliding. *Journal of Geophysical Research: Earth Surface*, 125(11), nov 2020a. doi: 10.1029/2020JF005627.

Hudson, T. S., Brisbourne, A. M., White, R. S., Kendall, J. M., Arthern, R., and Smith, A. M. Breaking the Ice: Identifying Hydraulically Forced Crevassing. *Geophysical Research Letters*, 47(21), nov 2020b. doi: 10.1029/2020GL090597.

Hudson, T. S., Baird, A. F., Kendall, J. M., Kufner, S. K., Brisbourne, A. M., Smith, A. M., Butcher, A., Chalari, A., and Clarke, A. Distributed Acoustic Sensing (DAS) for Natural Microseismicity Studies: A Case Study From Antarctica. *Journal of Geophysical Research: Solid Earth*, 126(7):1–19, 2021. doi: 10.1029/2020jb021493.

Hudson, T. S., Kendall, J. M., Pritchard, M. E., Blundy, J. D., and Gottsmann, J. H. From slab to surface: Earthquake evidence for fluid migration at Uturuncu volcano, Bolivia. *Earth and Planetary Science Letters*, 577:117268, 2022. doi: 10.1016/j.epsl.2021.117268.

Hudson, T. S., Kendall, J. M., Blundy, J. D., Pritchard, M. E., MacQueen, P., Wei, S. S., Gottsmann, J. H., and Lapins, S. Hydrothermal Fluids and Where to Find Them: Using Seismic Attenuation and Anisotropy to Map Fluids Beneath Uturuncu Volcano, Bolivia. *Geophysical Research Letters*, 50(5):1–16, mar 2023. doi: 10.1029/2022GL100974.

Johnson, J. H. and Savage, M. K. Tracking volcanic and geothermal activity in the Tongariro Volcanic Centre, New Zealand, with shear wave splitting tomography. *Journal of Volcanology and Geothermal Research*, 223-224:1–10, 2012. doi: 10.1016/j.jvolgeores.2012.01.017.

Johnson, J. H., Savage, M. K., and Townend, J. Distinguishing between stress-induced and structural anisotropy at Mount Ruapehu volcano, New Zealand. *Journal of Geophysical Research: Solid Earth*, 116(12):1–18, 2011. doi: 10.1029/2011JB008308.

Jordan, T. M., Martín, C., Brisbourne, A. M., Schroeder, D. M., and Smith, A. M. Radar Characterization of Ice Crystal Orientation Fabric and Anisotropic Viscosity Within an Antarctic Ice Stream. *Journal of Geophysical Research: Earth Surface*, 127(6):1–24, 2022. doi: 10.1029/2022JF006673.

Kendall, J. M. Seismic anisotropy in the boundary layers of the mantle. *Geophysical Monograph Series*, 117:133–159, 2000. doi: 10.1029/GM117p0133.

Kendall, J.-M., Stuart, G. W., Ebinger, C. J., Bastow, I. D., and Keir, D. Magma-assisted rifting in Ethiopia. *Nature*, 433(7022):146–148, 2005. doi: 10.1038/nature03161.

Krischer, L., Megies, T., Barsch, R., Beyreuther, M., Lecocq, T., Caudron, C., and Wassermann, J. ObsPy: a bridge for seismology into the scientific Python ecosystem. *Computational Science & Discovery*, 8(1):014003, may 2015. doi: 10.1088/1749-4699/8/1/014003.

Kufner, S., Wookey, J., Brisbourne, A. M., Martín, C., Hudson, T. S., Kendall, J. M., and Smith, A. M. Strongly Depth-Dependent Ice Fabric in a Fast-Flowing Antarctic Ice Stream Revealed With Icequake Observations. *Journal of Geophysical Research: Earth Surface*, 128(3):1–25, mar 2023. doi: 10.1029/2022JF006853.

Lam, S. K., Pitrou, A., and Seibert, S. Numba. In *Proceedings of the Second Workshop on the LLVM Compiler Infrastructure in HPC*, pages 1–6, New York, NY, USA, nov 2015. ACM. doi: 10.1145/2833157.2833162.

Levin, V., Menke, W., and Park, J. Shear wave splitting in the Appalachians and the Urals: A case for multilayered anisotropy. *Journal of Geophysical Research: Solid Earth*, 104(B8):17975–17993, 1999. doi: 10.1029/1999jb900168.

Link, F., Reiss, M. C., and Rümpker, G. An automatized XKS-splitting procedure for large data sets: Extension package for SplitRacer and application to the USArray. *Computers and Geosciences*, 158(October 2021):104961, 2022. doi: 10.1016/j.cageo.2021.104961.

Liptai, N., Gráczer, Z., Szanyi, G., Cloetingh, S. A., Süle, B., Aradi, L. E., Falus, G., Bokelmann, G., Timkó, M., Timár, G., Szabó, C., and Kovács, I. J. Seismic anisotropy in the mantle of a tectonically inverted extensional basin: A shear-wave splitting and mantle xenolith study on the western Carpathian-Pannonian region. *Tectonophysics*, 845(October), 2022. doi: 10.1016/j.tecto.2022.229643.

Liu, K. H., Gao, S. S., Gao, Y., and Wu, J. Shear wave splitting and mantle flow associated with the deflected Pacific slab beneath northeast Asia. *Journal of Geophysical Research: Solid Earth*, 113 (1):1–15, 2008. doi: 10.1029/2007JB005178.

Long, M. D. and Silver, P. G. Shear wave splitting and mantle anisotropy: Measurements, interpretations, and new directions. *Surveys in Geophysics*, 30(4-5):407–461, 2009. doi: 10.1007/s10712-009-9075-1.

Long, M. D., Gao, H., Klaus, A., Wagner, L. S., Fouch, M. J., James, D. E., and Humphreys, E. Shear wave splitting and the pattern of mantle flow beneath eastern Oregon. *Earth and Planetary Science Letters*, 288(3-4):359–369, 2009. doi: 10.1016/j.epsl.2009.09.039.

Mroczek, S., Savage, M. K., Hopp, C., and Sewell, S. M. Anisotropy as an indicator for reservoir changes: example from the Rotokawa and Ngatamariki geothermal fields, New Zealand. *Geophysical Journal International*, 220(1):1–17, 2020. doi: 10.1093/gji/ggz400.

Nowacki, A., Wilks, M., Kendall, J. M., Biggs, J., and Ayele, A. Characterising hydrothermal fluid pathways beneath Aluto volcano, Main Ethiopian Rift, using shear wave splitting. *Journal of Volcanology and Geothermal Research*, 356:331–341, 2018. doi: 10.1016/j.jvolgeores.2018.03.023.

Özalaybey, S. and Savage, M. K. Double-layer anisotropy resolved from S phases. *Geophysical Journal International*, 117(3):653–664, 1994. doi: 10.1111/j.1365-246X.1994.tb02460.x.

Pritchard, M. The life cycle of Andean volcanoes:Combining space-based and field studies, 2009. https://www.fdsn.org/networks/detail/YS_2009/. doi: 10.7914/SN/YS_2009.

Pritchard, M. E., de Silva, S. L., Michelfelder, G., Zandt, G., McNutt, S. R., Gottsmann, J., West, M. E., Blundy, J., Christensen, D. H., Finnegan, N. J., Minaya, E., Sparks, R. S., Sunagua, M., Unsworth, M. J., Alvizuri, C., Comeau, M. J., del Potro, R., Díaz, D., Diez, M., Farrell, A., Henderson, S. T., Jay, J. A., Lopez, T., Legrand, D., Naranjo, J. A., McFarlin, H., Muir, D., Perkins, J. P., Spica, Z., Wilder, A., and Ward, K. M. Synthesis: PLUTONS: Investigating the relationship between pluton growth and volcanism in the Central Andes. *Geosphere*, 14(3):954–982, 2018. doi: 10.1130/GES01578.1.

Reiss, M. C. and Rümpker, G. SplitRacer: MATLAB code and GUI for semiautomated analysis and interpretation of teleseismic shear-wave splitting. *Seismological Research Letters*, 88(2):392–409, 2017. doi: 10.1785/0220160191.

Reiss, M. C., Long, M. D., and Creasy, N. Lowermost Mantle Anisotropy Beneath Africa From Differential SKS - SKKS Shear-Wave Splitting. *Journal of Geophysical Research: Solid Earth*, 124 (8):8540–8564, 2019. doi: 10.1029/2018jb017160.

Rümpker, G. and Silver, P. G. Apparent shear-wave splitting parameters in the presence of vertically varying anisotropy. *Geophysical Journal International*, 135(3):790–800, 1998a. doi: 10.1046/j.1365-246X.1998.00660.x.

Rümpker, G. and Silver, P. G. Apparent shear-wave splitting parameters in the presence of vertically varying anisotropy. *Geophysical Journal International*, 135(3):790–800, 1998b. doi: 10.1046/j.1365-246X.1998.00660.x.

Savage, M. K., Wessel, A., Teanby, N. A., and Hurst, A. W. Automatic measurement of shear wave splitting and applications to time varying anisotropy at Mount Ruapehu volcano, New Zealand. *Journal of Geophysical Research: Solid Earth*, 115(12): 1–17, 2010. doi: 10.1029/2010JB007722.

Savage, M. S. Seismic anisotropy and mantle deformation: What have we learned from shear wave splitting? *Reviews of Geophysics*, 37(1):65–106, 1999. doi: 10.1029/98RG02075.

Schultz, R., Beroza, G. C., and Ellsworth, W. L. A risk-based approach for managing hydraulic fracturing–induced seismicity. *Science*, 372(6541):504–507, 2021. doi: 10.1126/science.abg5451.

Sicilia, D., Montagner, J. P., Cara, M., Stutzmann, E., Debayle, E., Lépine, J. C., Lévêque, J. J., Beucler, E., Sebai, A., Roult, G., Ayele, A., and Sholan, J. M. Upper mantle structure of shear-waves velocities and stratification of anisotropy in the Afar Hotspot region. *Tectonophysics*, 462(1-4):164–177, 2008. doi: 10.1016/j.tecto.2008.02.016.

Silver, P. G. and Chan, W. W. Shear Wave Splitting and Sub continental Mantle Deformation. *Journal of Geophysical Research*, 96:429–454, 1991. doi: 10.1029/91JB00899.

Silver, P. G. and Savage, M. K. The Interpretation of shear-wave splitting parameters in the presence of two anisotropic layers. *Geophysical Journal International*, 5(January):689–691, 1994. doi: 10.1111/j.1365-246x.1994.tb04027.x.

Smith, E., Smith, A., White, R., Brisbourne, A., and Pritchard, H. Mapping the ice-bed interface characteristics of Rutford Ice Stream, West Antarctica, using microseismicity. *Journal of Geophysical Research: Earth Surface*, 120(9):1881–1894, 2015. doi: 10.1002/2015JF003587.

Smith, E. C., Baird, A. F., Kendall, J. M., Martin, C., White, R. S., Brisbourne, A. M., and Smith, A. M. Ice fabric in an Antarctic ice stream interpreted from seismic anisotropy. *Geophysical Research Letters*, 44(8):3710–3718, apr 2017. doi: 10.1002/2016GL072093.

Spingos, I., Kaviris, G., Millas, C., Papadimitriou, P., and Voulgaris, N. Pytheas: An open-source software solution for local shear-wave splitting studies. *Computers and Geosciences*, 134(July 2019):104346, 2020. doi: 10.1016/j.cageo.2019.104346.

Stork, A. L., Verdon, J. P., and Kendall, J. M. The robustness of seismic moment and magnitudes estimated using spectral analysis. *Geophysical Prospecting*, 62(4):862–878, 2014. doi: 10.1111/1365-2478.12134.

Teanby, N. A., Kendall, J., and Baan, M. V. D. Automation of Shear-Wave Splitting Measurements using Cluster Analysis. *Bulletin of the Seismological Society of America*, 94(2):453–463, 2004. doi: 10.1785/0120030123.

Verdon, J. P. and Kendall, J. M. Detection of multiple fracture sets using observations of shear-wave splitting in microseismic data. *Geophysical Prospecting*, 59(4):593–608, 2011. doi: 10.1111/j.1365-2478.2010.00943.x.

Vinnik, L., Breger, L., and Romanowicz, B. Anisotropic structures at the base of the Earth's mantle. *Nature*, 393(6685):564–567, jun 1998. doi: 10.1038/31208.

Walpole, J., Wookey, J., Masters, G., and Kendall, J. M. A uniformly processed data set of SKS shear wave splitting measurements: A global investigation of upper mantle anisotropy beneath seismic stations. *Geochemistry, Geophysics, Geosystems*, 15(5):1991–2010, 2014. doi: 10.1002/2014gc005278.

Walsh, E., Arnold, R., and Savage, M. K. Silver and Chan revisited. *Journal of Geophysical Research: Solid Earth*, 118(10):5500–5515, 2013. doi: 10.1002/jgrb.50386.

Wolf, J., Long, M. D., Leng, K., and Nissen-Meyer, T. Constraining deep mantle anisotropy with shear wave splitting measurements: challenges and new measurement strategies. *Geophysical Journal International*, 230(1):507–527, 2022. doi: 10.1093/gji/ggac055.

Wolf, J., Frost, D. A., Long, M. D., Garnero, E., Aderoju, A. O., Creasy, N., and Bozdağ, E. Observations of Mantle Seismic Anisotropy Using Array Techniques: Shear-Wave Splitting of Beamformed SmKS Phases. *Journal of Geophysical Research: Solid Earth*, 128 (1), 2023. doi: 10.1029/2022jb025556.

Wolfe, C. J. and Silver, P. G. Seismic anisotropy of oceanic upper mantle: Shear wave splitting methodologies and observations. *Journal of Geophysical Research: Solid Earth*, 103(1):749–771, 1998. doi: 10.1029/97jb02023.

Wolfe, C. J. and Solomon, S. C. Shear-wave splitting and implications for mantle flow beneath the MELT region of the East Pacific Rise. *Science*, 280(5367):1230–1232, 1998. doi: 10.1126/science.280.5367.1230.

Wookey, J. Direct probabilistic inversion of shear wave data for seismic anisotropy. *Geophysical Journal International*, 189(2):1025–1037, 2012. doi: 10.1111/j.1365-246X.2012.05405.x.

Wookey, J. and Kendall, J. M. Constraints on lowermost mantle mineralogy and fabric beneath Siberia from seismic anisotropy. *Earth and Planetary Science Letters*, 275(1-2):32–42, 2008. doi: 10.1016/j.epsl.2008.07.049.

Wuestefeld, A., Al-Harrasi, O., Verdon, J. P., Wookey, J., and Kendall, J. M. A strategy for automated analysis of passive microseismic data to image seismic anisotropy and fracture characteristics. *Geophysical Prospecting*, 58(5):755–773, 2010. doi: 10.1111/j.1365-2478.2010.00891.x.

Wüstefeld, A., Bokelmann, G., Zaroli, C., and Barruol, G. SplitLab: A shear-wave splitting environment in Matlab. *Computers and Geosciences*, 34(5):515–528, 2008. doi: 10.1016/j.cageo.2007.08.002.

Yardley, G. S. and Crampin, S. Extensive-dilatancy anisotropy: Relative information in VSPs and reflection surveys. *Geophysical Prospecting*, 39(3):337–355, 1991. doi: 10.1111/j.1365-2478.1991.tb00316.x.

REPORT
doi:10.26443/seismica.v2i2.979

SEISMICA

Seismology in the cloud: guidance for the individual researcher

Z. Krauss *[1], **Y. Ni** [2], **S. Henderson** [2,3], **M. Denolle** [2]

[1]School of Oceanography, University of Washington, Seattle, WA, USA, [2]Department of Earth and Space Sciences, University of Washington, Seattle, WA, USA, [3]eScience Institute, University of Washington, Seattle, WA, USA

Author contributions: *Conceptualization*: Z. Krauss, M. Denolle. *Data Curation*: Z. Krauss, Y. Ni. *Formal Analysis*: Z. Krauss, Y. Ni. *Funding Acquisition*: Z. Krauss, Y. Ni, M. Denolle. *Investigation*: Z. Krauss, Y. Ni. *Methodology*: Z. Krauss, Y. Ni, S. Henderson, M. Denolle. *Project Administration*: Z. Krauss, M. Denolle. *Resources*: S. Henderson, M. Denolle. *Software*: Z. Krauss, Y. Ni, S. Henderson. *Supervision*: M. Denolle, S. Henderson. *Validation*: Z. Krauss, Y. Ni, S. Henderson, M. Denolle. *Visualization*: Z. Krauss. *Writing – original draft*: Z. Krauss. *Writing – review & editing*: Z. Krauss, Y. Ni, S. Henderson, M. Denolle.

Abstract The commercial cloud offers on-demand computational resources that could be revolutionary for the seismological community, especially as seismic datasets continue to grow. However, there are few educational examples for cloud use that target individual seismological researchers. Here, we present a reproducible earthquake detection and association workflow that runs on Microsoft Azure. The Python-based workflow runs on continuous time-series data using both template matching and pre-trained machine learning models. We provide tutorials for constructing cloud resources (both storage and computing) through a desktop portal and deploying the code both locally and remotely on the cloud resources. We apply the cloud-based workflow to one year of continuous data from a mid-ocean ridge to demonstrate the construction of two earthquake catalogs, one through template matching and one with a pre-trained machine learning model. We report on scaling of compute times and costs to show that CPU-only processing is generally inexpensive, and can be faster and simpler than using GPUs. Overall, we find that the commercial cloud presents a steep learning curve but is cost-effective. This report is intended as an informative starting point for any researcher considering migrating their own processing to the commercial cloud.

Production Editor:
Gareth Funning
Handling Editor:
Yen Joe Tan
Copy & Layout Editor:
Théa Ragon

Received:
May 22, 2023
Accepted:
August 10, 2023
Published:
August 25, 2023

Glossary for frequently-used terms

Commercial cloud – computational resources that are available for use remotely through a pay-as-you-go system. Cloud providers deliver access to these resources, which are physically maintained in large centers of computing servers, through the internet. Major cloud providers include Microsoft Azure, Amazon Web Services, and Google Cloud Platform.

CPU – "Central Processing Unit". This is the part of a computer that interprets instructions to perform computational tasks. The CPU of a computer typically has multiple "CPU cores", which can each perform one task at a time. In this report, we use the word "CPU" to mean an individual CPU core, such that one CPU can perform one task at a time.

GPU – "Graphics Processing Unit". This is a specialized computing processor that is designed to handle many specific small tasks at once, more efficiently than a CPU. In machine learning, they are commonly used to greatly speed up the training and application of neural networks, which can be applied to earthquake detection.

Parallelization – the act of splitting up a computational task into multiple independent steps, and running these steps on different CPUs or GPUs at the same time, to greatly decrease the overall time needed for computation.

Virtual machine – a resource provided by the commercial cloud that mimics the functionality of a typical computer with chosen amounts of CPUs, GPUs, and memory, but effectively is a barebone operating system which is isolated from the total resources of a larger physical server.

Motivation

Major recent advances in seismological research have been driven by seismic datasets that are dense in both space and time. These include, to name a few, the discovery of slow earthquakes and tectonic tremor (Obara, 2002; Rogers and Dragert, 2003), constraints on the propagation of large earthquakes using back projection (Ishii et al., 2005), and the imaging of shallow Earth properties through the cross-correlation of the ambient seismic field (Shapiro et al., 2005). Recognizing the value of such datasets, community and institutional seismic networks are rapidly increasing the rate and volume of public seismic data. Today, the amount of seismic data available on the IRIS DMC approaches 1 PetaByte, with new technologies able to collect this amount annually (Lindsey et al., 2017). This growth has made seismological research a big-data field that requires methodological advancement and computational infrastructure to maximize discovery (Quinteros et al., 2021).

*Corresponding author: zkrauss@uw.edu

The realization that tectonic events share fundamentally similar physical processes has led seismologists to develop supervised techniques to search the data based on similarity with past events. The technique of template matching, also referred to as matched filter, scans continuous data and detects events using a correlation coefficient with respect to a template (Gibbons and Ringdal, 2006; Turin, 1960). Template matching (TM) is robust at detecting new occurrences of previously seen phenomena and finding events buried in noise (Ross et al., 2019; Shelly et al., 2007). Open-source software to implement TM that makes use of the easily parallelizable nature of the technique is available (Beaucé et al., 2017; Chamberlain et al., 2017), but computational requirements can still be prohibitive when the number of templates is large.

In recent years, seismological research has seen a rapid and massive adoption of statistical and machine learning algorithms in automating seismological research workflows (Mousavi et al., 2020; Perol et al., 2018; Walter et al., 2021; Yoon et al., 2015; Zhu et al., 2023). The focus has largely been on developing and testing workflows on curated earthquake data sets (Michelini et al., 2021; Mousavi et al., 2019; Münchmeyer et al., 2022; Ni et al., 2023). Thus far, only several studies have used machine learning methods to detect new events in continuous seismic records (Tan et al., 2021; Scotto di Uccio et al., 2023). This may be in part because machine-learning models yield inconsistent predictions (Park et al., 2023); however, a more likely barrier to the adoption of machine learning techniques is the high entry cost associated with the computational skills and resources needed to deploy on continuous data.

With the coincident increase in both dataset sizes and the computational cost of state-of-the-art earthquake detection techniques, there is a growing need for seismological workflows to deploy on the cloud (Arrowsmith et al., 2022). Large seismic datasets are well suited for data sharing on cloud object storage, and some institutions such as the USGS and the Southern California Earthquake Data Center have begun migrating raw data and data products to cloud storage permanently (Schovanec et al., 2021; Yu et al., 2021). Despite large archives being on the cloud for a few years, few studies have leveraged them (Clements and Denolle, 2023). Some authors have demonstrated the overall great horizontal scaling performance of cloud computing and developed workflows that stream data using webservices (MacCarthy et al., 2020; Zhu et al., 2023), but the deployment strategies used (e.g., Docker, Dask, Kubernetes) are difficult for researchers to learn and deploy. Most of the seismological community faces a steep learning curve to shifting their functioning local workflows towards cloud computing, limiting its widespread adoption.

This report is distinct from other published seismological cloud-based workflows (Zhu et al., 2023) in that we aim to help the average seismological researcher build their own cloud computing version of their local processing algorithms from the ground up. We demonstrate this through the example of building an earthquake catalog from continuous data. We first develop a workflow to run locally using parallel processing in Python. The workflow applies the two most-used contemporary techniques of supervised earthquake detection: template matching and pre-trained models from machine learning, including earthquake detection, phase picking, and association. Then, we describe what is needed to migrate this workflow to the cloud, including constructing cloud storage, code containers, and cloud computing pools. We use Microsoft Azure because of resources available to us through our home institution, but we report that the core framework is similar to other major cloud providers, provided that researchers adapt for provider-specific storage and compute systems. We describe the workflow in detail and provide Jupyter notebooks and instructional materials through a GitHub page (Krauss et al., 2023a). We attempt to follow the guidelines of FAIR4RS (Barker et al., 2022; Wilkinson et al., 2016), which recommends that published software and metadata be human and machine findable, accessible via GitHub, interoperable, and usable & reusable.

We provide cost and timing context for what users may expect for typical seismic workflows by documenting scaling performance, including a comparison between strategies that use either CPU or GPU computing (see Glossary). We also present results of the earthquake catalog workflow on the tectonically active Endeavour segment of the Juan de Fuca mid-ocean ridge, which act as a proof-of-concept of how template matching and machine learning techniques can be used together construct a detailed earthquake catalog.

Local Workflow

First, we describe how to build the workflow for a local implementation: this represents the first-step case of most individual researchers. We design a workflow to have two separate but operationally equivalent "branches" for the two earthquake detection methods of interest (Figure 1). The format and file structure of the input seismic waveform data is the same for both branches. Both branches produce earthquake detections in the same output format, QuakeML, an XML representation of earthquake metadata widely used by the seismic community (Schorlemmer et al., 2011).

TM is performed using EQcorrscan, an open-source Python toolbox for earthquake detection via the cross-correlation of waveform data with earthquake templates (Chamberlain et al., 2017). Detection parameters including filter bands, template lengths, and the type and magnitude of the detection threshold are specified in the config file as described in Section 2.1. After TM detection, redundant events are removed between templates by identifying events that occur within a given time threshold of each other (e.g., 1 s), and keeping only the event with the highest detection value.

For a comparison to machine learning-based earthquake detection methods, the other branch uses SeisBench, an open-source flexible Python framework for deploying seismological machine learning models (Woollam et al., 2022). Our example workflow uses

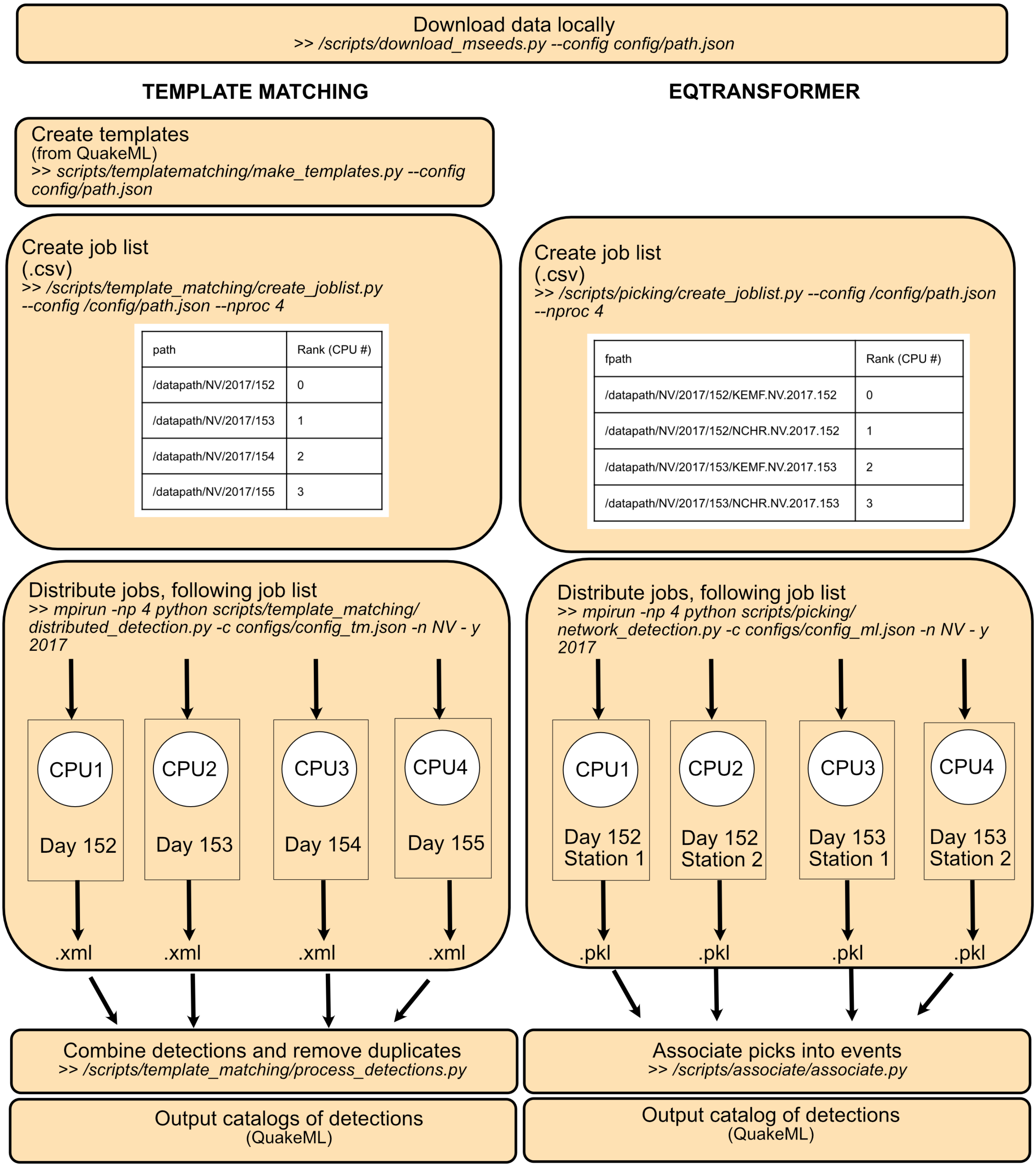

Figure 1 Flowchart of our workflow for performing earthquake detection on seismic waveform data, showing the two branches, TM and EQT, side by side. Each script's name, data format, filename extension, and unix commands are described for transparency and reusability.

EQTransformer (Mousavi et al., 2020) for phase picking and GaMMA (Zhu et al., 2022) for phase association; however, employing a different machine learning model would be straightforward through the flexibility of SeisBench. We do not perform model training, but only model inference: we use the pre-trained EQTransformer model provided by SeisBench, which is identical to the original model weights from Mousavi et al. (2020), to make P- and S-wave picks on all stations. To sweep continuously through the data, we use a sliding window of length 60 s with a step of 30 s and a detection threshold of 0.1 for both P- and S-waves. We then perform phase association using GaMMA, assuming 7.0 and 4.0 km/s as constant velocity for P- and S-waves, respectively, and requiring only one station with picks to form an event. These specifications are made in the config file required for the code execution.

Local set-up

We retrieve seismic waveform data from the IRIS DMC (Trabant et al., 2012) for a given time period using the ObsPy Python toolbox (Beyreuther et al., 2010). Three-component waveform data are resampled to a common sampling rate and stored in day-long chunks for all channels from a single station in the same way they are stored natively within the DMC. We organize these data in a descending folder structure first by network, then year, then day of the year, with individual MiniSEED files saved for each station. The naming of these files is important to parallelization later in the workflow. The data download can be performed using the `/scripts/download_mseeds.py` script (Figure 1), with date limits, network name, station and channel codes, and the output data directory specified within the config file (Notebook S1).

The TM branch requires an input of earthquake templates as an EQcorrscan Tribe object, stored in TAR format. An example script that constructs these templates from waveform data, using a starting earthquake catalog in QuakeML format, can be found at `/scripts/template_matching/make_templates.py`.

Finally, to ensure the portability of the code across machines, we specify all file paths, detection parameters, and machine characteristics in JSON format in a config file in the `/configs/` folder. Notebook S1 details the construction of these files. The config files are referenced in the call to the scripts that execute earthquake detection (Figure 1).

Single-node parallelization

A single computer, or node, typically has several CPU cores (hereafter referred to simply as CPUs) and is the smallest level of parallelization. Earthquake detection can be easily parallelized such that the computation is performed simultaneously for different time periods on different CPUs. For the EQT branch, which performs phase picking on one station at a time, we consider one day of earthquake detection on one station to constitute a single job. For the TM branch, which jointly performs phase picking and association on data from a complete network of stations, we consider one day of earthquake detection on all stations to constitute a single job.

When deploying our workflow locally, we organize the distribution of jobs across available CPUs by first creating a job list in CSV format (Figure 1). The job list is a simple table that ties the file path of MiniSEED data to a CPU number (Figure 1). The script to create this job list, `create_joblist.py`, is different for the TM and EQT branches, and can be found in the `/scripts/template_matching/` and `/scripts/picking/` directories, respectively. The job list CSV file can be created by running the script from the command line with additional arguments that specify how many CPUs to parallelize jobs across, and a path to the JSON config file which contains date limits and the path to the waveform data (Figure 1, Notebook S2).

We then distribute the jobs across CPUs in parallel using Open MPI (O-MPI), an open-source message passing interface (Gabriel et al., 2004). When O-MPI is called at the start of a Unix-style command, the command is simultaneously deployed separately to as many CPUs as specified. In our local workflow, we use O-MPI to run a distributing script `distributed_detection.py` (Figure 1, Notebook S2). As the distributing script runs on each individual CPU, it reads in the created job list and filters the job list to include only those assigned to the current CPU. The distributing script then loops over the filtered list and completes the job by running the script in which the actual detection is performed, `detection.py`, on the specified data path. This operation is the same for both the template matching and machine-learning workflows, with the template matching workflow parallelized over days only and the machine-learning workflow parallelized over both days and stations.

The TM branch outputs a catalog of detected earthquakes with P- and S-wave picks for each day of detection in QuakeML format. These daily catalogs can be converted to a summative earthquake catalog, also in QuakeML format, using `/scripts/template_matching/combine_catalogs.py`, which collates and removes duplicate detections between templates (Notebook S3). The EQT branch outputs a list of P- and S-wave picks for each day of detection in Python Pickle format. These picks can be associated into individual earthquakes using `/scripts/association/associate.py`, which produces an equivalent summative earthquake catalog in QuakeML format (Notebook S3).

Cloud Workflow

The value of the commercial cloud lies in the ability of an individual to pay for the use of computational instances of flexible size at any time in a "pay-as-you-go" structure. However, these virtual machines (VMs) are effectively a blank computer with a user-specified configuration. The configuration of a VM consists of user-specified CPU cores, RAM, and local storage. VMs can be chosen with a range of Operating Systems and environments. We recommend choosing a blank environment and installing only the necessary dependencies.

Using a VM in a way that mimics local workflows requires an ecosystem of cloud resources: a storage container that the VM can read from and write to, a packaged software environment with all desired scripts and their dependencies, and an overarching set of networking permissions that allows all resources to work in tandem (Figure 2). In this section, we describe the construction of an example set of these resources on Microsoft Azure, point to additional materials that further detail how to construct them, and describe how to use the constructed resources to process seismic data in parallel.

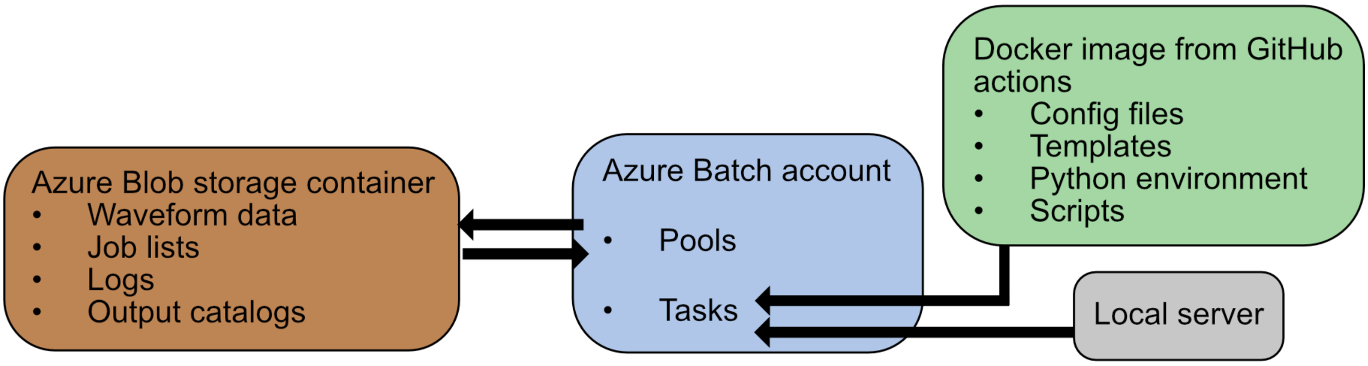

Figure 2 Map of how cloud resources relate to processes run on the local server and the containerized code.

Resource set-up

Containerizing the code base

In order to transition our local research workflow from our computer to the cloud, we first need to encapsulate all dependencies needed for the scripts to successfully execute. Containers are a standard way to define a minimal reproducible computing environment, such that you can guarantee your analysis will run on any other computer. There are various software systems to define and build containers. Docker is a widely-used system of software tools to create, store and execute code as containers. The container image is defined by a Dockerfile, which specifies the operating system software dependencies and command to execute. Images are typically stored on a server that can be accessed over the internet so that any computer can "pull" the image and start the container that executes your code. This allows for a high degree of parallelism because there can be thousands of containers each executing on different cloud-hosted virtual machines.

Because our code is hosted in a GitHub repository named "seismicloud" (https://github.com/Denolle-Lab/seismicloud, Krauss et al., 2023a), we use GitHub Actions continuous integration to build the container. Every time the repository is updated, the script docker.yml rebuilds a container image based on the Dockerfile in the repository. Specifically, the container image installs all Python dependencies (ObsPy, EqCorrscan, etc.) in a basic Linux operating system and copies the current version of the seismicloud codebase, including all scripts and data files. The container image is stored on the publicly-accessible GitHub Container registry. Any machine can create a container of the seismicloud workflow by accessing the URL and corresponding GitHub commit (e.g. `docker run ghcr.io/denolle-lab/seismicloud:latest`).

Initiating an Azure cloud account

Creating a user account on Azure is free, but a form of payment, or "subscription", must be tied to the account in order to create resources. For NSF-funded projects with provisions for cloud computing, this is sometimes done through a supported service, CloudBank (Norman et al., 2021). Once a subscription has been set up and users gain access to the Azure portal, users should begin by creating a budget for their subscription with automatic alerts for when spending has reached a given percent of the allocated funding (Tutorial S1). The next step is to create a "resource group", which will be used to tie the cloud resources users create to the subscription. Finally, a "virtual network" is created, which is a set of permissions that allows you to access the created resources and also allows those resources to access each other. Multiple users on the same subscription who will be carrying out separate processing should create their own separate resource groups and virtual networks. All of these actions are performed on the Azure portal, which is accessed through a web browser (Tutorial S1). We note that we built all of our cloud resources exclusively in the West-US 2 region, which was closest to our local servers in Seattle, Washington.

Storage container

The commercial cloud also provides opportunities for data storage that follow pay-as-you-go pricing. Cloud storage tends to use the model of object storage, which is designed to sustain high frequency data query. In Microsoft Azure, this is called Azure Blob storage. Blob storage containers are easily read from and written to by virtual machines so long as the storage container and virtual machine are under the same virtual network and necessary permissions are specified (see Tutorial S2). The cost of the container is dependent on how much data is actively stored and how frequently data is transferred into or out of the container. For Azure blob storage at the time of writing, the cost to store 1 TB of data is approximately $150 USD per month. Given these costs, typical individual researchers may not want to use Blob as a backup hard drive, but instead use it as temporary storage during computation.

For our workflow, we created one Azure Blob storage container to store raw waveform data and the outputs of processing, including earthquake catalogs, job lists, and processing logs. This choice was driven by our desire to centralize storage for parallelized computation. Tutorial S2 details the creation of the Blob storage container through the Azure portal, including the settings needed to facilitate mounting of the container to virtual machines later in the workflow. To load waveform data to the Blob storage container, we downloaded it on our local servers and then copied it to the storage container using Azure's command line utility AzCopy (see Tutorial S2). Waveform data could also be down-

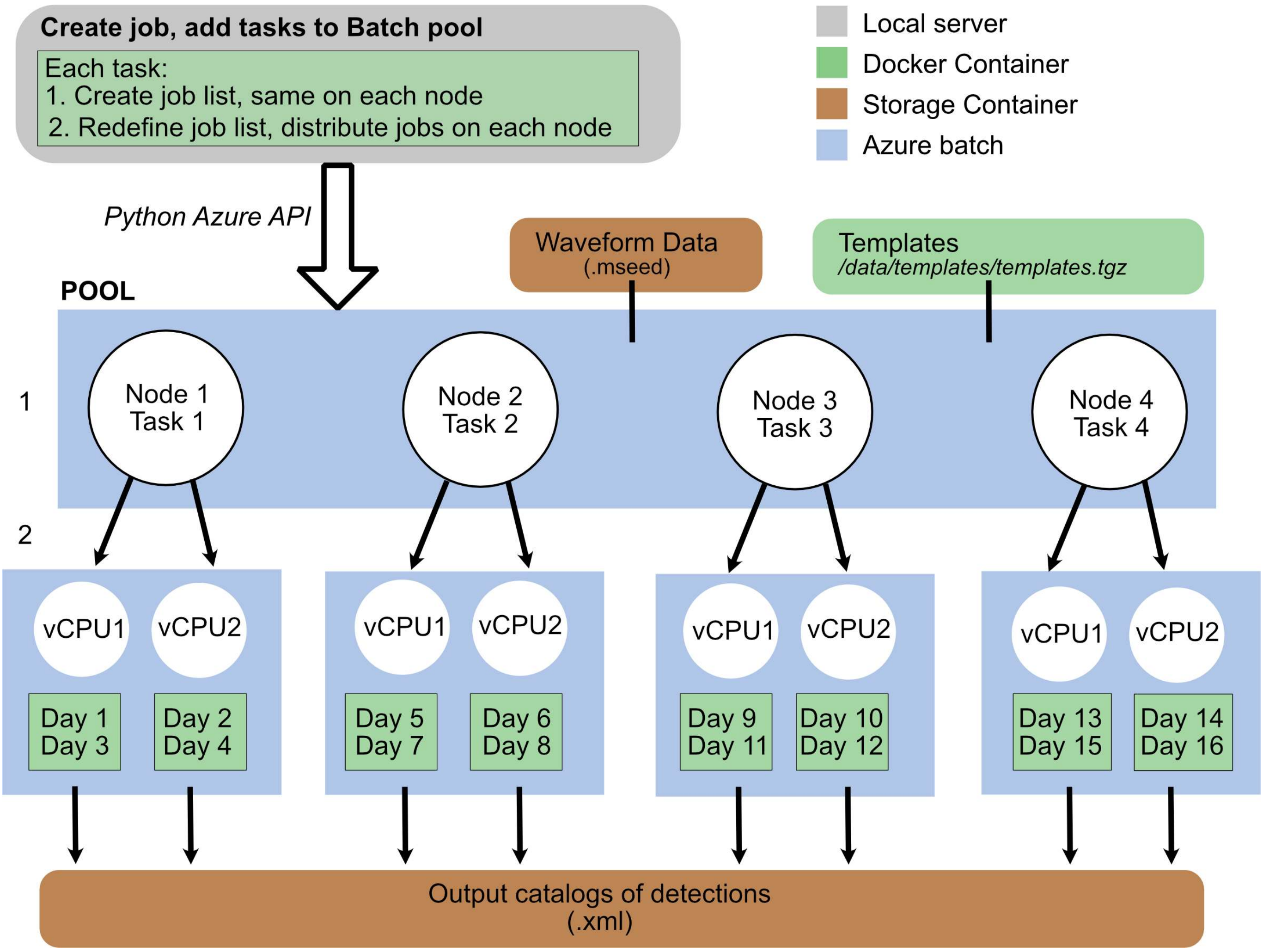

Figure 3 Example flowchart of how Azure cloud Pool-based Parallelization works for the Template Matching workflow, following the color scheme of Figure 2. The EQTransformer workflow is identical, except that the data paths are specific to both the day of the year and the seismic station.

loaded from webservices and stored directly on the storage container by running the `download_waveforms.py` script within the Docker container on a virtual machine with the Blob storage container mounted.

Pool-based parallelization

A powerful option offered by the commercial cloud is the ability to deploy tasks to not just one virtual machine, but pools that can be scaled to include many virtual machines, all managed from one account. In Microsoft Azure, this is performed through a resource called Batch. Batch accounts manage two separate entities: (1) Pools, groups of virtual machines (each called a node when within a Pool), each of which has an identical size and computing environment, and (2) Jobs, sets of commands that are passed to nodes within a Pool, which run with specified settings: inside of a Docker image, for example. Creating a Pool that runs correctly with the user's chosen Docker image and is connected to the user's desired Blob storage container is complicated, but once the Pool has been created, its specifications are saved and you can resize it as needed to run operations on-demand.

Users begin by creating a Batch account which will manage both Pools and Jobs through the Azure portal (see Tutorial S3). A Pool can then be created with a chosen node/virtual machine size, number of nodes, and region. Tutorial S3 details this process. To ensure that the nodes can execute commands within our Docker image, the operating system of the Pool must be specified as Docker compatible. We mount the Blob storage container to each node on the Pool through a start-up command line task. After a Pool has been created, the status of the nodes can be monitored from the Azure portal within the Batch account. The Pool can be resized at any time to contain anywhere from 0 up to the user's given quota of nodes, with all nodes created in the same manner specified when the Pool was created. If quotas, or limits imposed by Azure on how many CPUs can be given to one user in a given region, restrict the Pool the user wants to build, they can be increased through support requests (Tutorial S3). We note that starting quotas for a new user are often quite low, e.g. only 4 vCPUs in a given region.

Once a Pool has been created and the nodes on the Pool have successfully mounted the Blob storage container, we create and send Jobs to the Pool from a local server (e.g., a laptop) using Azure Python libraries.

Notebook S4 details this process. We use the Azure Python libraries to connect to both the Blob storage container and the Batch account using the account names and keys. We then create an empty Job on the Batch account that is tied to the already-created Pool. Next, we decide how many "Tasks" we need to send to the Job based on the number of nodes within the pool, N. Tasks are a single unit of computation, or one command line sent to one node. If all nodes are in use, the Job will keep Tasks in a queue until one becomes free. In our case, we create N Tasks such that the Tasks and nodes are matched 1:1 and there is no queuing. Each Task contains two command line operations: (1) creating a job list in CSV format following Figure 1, and (2) distributing the jobs across CPUs on the node using O-MPI. These commands contain an argument that indicates to the node which index, 1-N, they correspond to. During the creation of each Task, we specify that the commands are run within our Docker image; each node runs a separate Docker container, such that the first task run on each node needs to additionally pull down the container image.

The scripts called in the command lines are found in the `/batch_scripts/` directory of the Docker image. These Batch-specific scripts are very similar to the scripts called during local parallelization and are named in the same way (Figure 1), but are slightly modified to accommodate two levels of parallelization: across nodes, and across CPUs on each node (Figure 3). We avoid the need for inter-node communication by first creating a CSV job list that assigns each job to a node in the Pool rather than an individual CPU, such that each node creates the exact same job list. After the initial job list is created, however, each node then filters the job list following the number, 1-N, of the node, which is specified in the creation of the Task. The filtered, shortened job list is then redefined such that each job on the list is assigned a CPU number instead. The process then runs the same way as the single-instance parallelization, where the jobs on the job list are distributed across CPUs on the nodes using O-MPI (Figure 3). The outputs from all nodes, including job lists, logs, and catalog/pick outputs, are written to the mounted Blob storage container (Figure 3). These outputs can be downloaded locally also using Azure's command line utility AzCopy, as detailed in Tutorial S2.

We choose to use Batch services rather than a workload manager such as SLURM (Yoo et al., 2003), as is typically used in high performance computing (HPC), for several reasons. To use such a system on the cloud would require running a persistent machine to handle orchestrations, which would add cost and complexity. With Batch services, orchestration is instead done by the cloud provider at the time of job submission. Batch services also tend to be focused on independent containerized workflows whereas HPC scheduling systems are designed for non-containerized workflows on closely networked hardware.

Computational Performance

To understand how compute time and costs scale with different Pool sizes and types, we ran both the TM and EQT branches on one year of raw waveform data, ~600 GB in our case. We used data from 2017 for the Ocean Networks Canada NEPTUNE array (network code NV), a cabled 4-station ocean bottom seismometer network on a mid-ocean ridge (Heesemann et al., 2014). These data are locally available from the IRIS DMC. We performed limited preprocessing, only resampling all streams to a common sampling rate of 200 Hz. For the TM branch, we ran detection with a set of 53 templates chosen as a representative sample across the months of 2017 following Krauss and Wilcock (2022).

We constructed two separate Azure Batch Pools for the TM and EQT branches following the steps outlined in Tutorial S3. For the TM Pool, we used a memory-optimized instance type, the `standard_e4_v3`, to accommodate the intensive memory needs of cross-correlation. We found that we needed a minimum memory size of 32 GB, which is paired with 4 CPUs in Azure's virtual machine options, to avoid memory errors from EQcorrscan. For the EQT Pool, we used a compute-optimized instance type, the `standard_f4s`, also with 4 CPUs. The price of equivalent type but larger (more CPUs) virtual machines increases linearly. This is an advantage of using the cloud: it is the same cost to run 60 equivalent machines for one minute as it is to run 1 machine for 60 minutes.

We ran earthquake detection for the entire year of 2017 for both the TM and EQT branches on their corresponding Pools with increasing Pool sizes, from 1-64 nodes, or 4-256 CPUs, and documented compute time and associated costs (Figure 4). The compute times reported in Figure 4 include only the time needed to pull the image once and then run the tasks described in Figure 3, and do not include the additional time needed for waveform download, template construction, Pool start-up, or pick and catalog post-processing. Pool start-up times normally do not exceed 10 minutes, though this varies based on current user traffic in the region. Since start-up processes are run in parallel across nodes on the Pool, overhead start-up times do not tend to increase with number of CPUs or GPUs. The times shown are the mean of the compute time of all Tasks sent to the Pool, which vary slightly due to detections per day and data gaps. The costs associated with each earthquake detection run were calculated by multiplying compute time and number of nodes by Azure's per-hour pricing of the corresponding virtual machine type at the time of writing.

We find that the compute times and costs of both TM and EQT detection scale similarly with numbers of CPUs, with TM detection taking on average 38% of the time needed for EQT detection (Figure 4a). They notably do not scale as one divided by the number of cores despite our distributed memory parallelization scheme, because we do not use inter-node communication. We do not parallelize across all CPUs in the Pool, but only across groups of CPUs. So, if one day of detection takes longer on Node 4 than on Node 5, the next detection

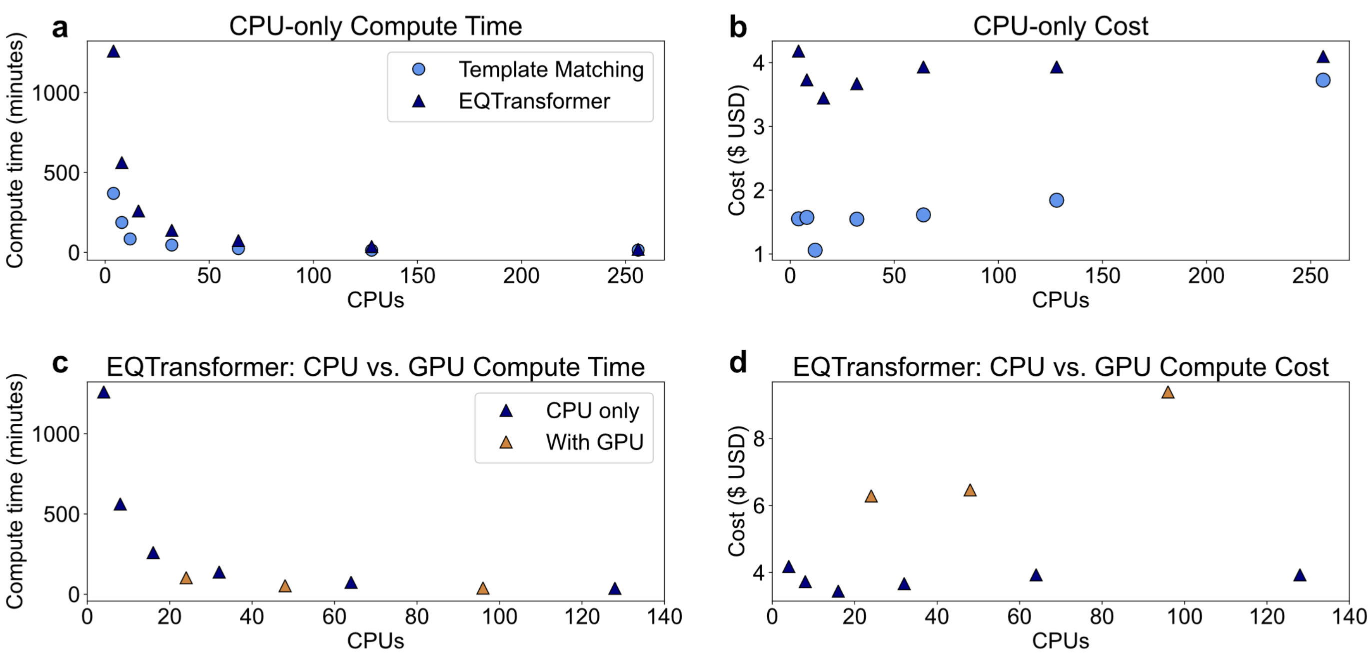

Figure 4 Scaling relationships between compute time, cost, and number of CPUs used for both the Template Matching and EQT workflows.

slated for Node 4 cannot be moved to Node 5 even if Node 5 is idle.

For all Pool sizes tested, we find that the cost of computation is less than $5 USD (Figure 4b). Both the TM and EQT tests show that the minimum cost is associated with a Pool size of 4 nodes, or 16 CPUs, with costs then increasing with increasing Pool size. The cost for the TM tests are lower than the EQT tests due to lower compute times; the virtual machine type used for the TM Pool, `standard_e4_v3`, was slightly more expensive than that used for the EQT pool, the `standard_f4s`, at $0.25 USD/hour and $0.19 USD/hour, respectively.

Constructing our workflow to run only with CPUs and not GPUs was a decision we made to simplify the set-up of our Pools and to minimize the size of our Docker container. By not requiring the CUDA libraries for our Docker container, we reduced the size of the image from 6 GB to 1.4 GB. We also avoided the need for additional complexity in the parallelization method, such that we did not need to distribute tasks across both CPUs and GPUs and manage the communication between them. However, for methods that use deep learning networks such as EQT, GPUs are typically employed during model training to significantly accelerate computation time.

In order to investigate how the speed-up offered by GPUs compares to the lower cost of CPU-only instances, we ran three tests of the EQT branch on an available local server that had 4 A100 GPUs with 80 GB of RAM each. Microsoft Azure has an equivalent virtual machine size, the NC24ads, NC48ads, and NC96ads, with 24, 48, and 96 vCPUs, and 1, 2, and 4 A100 80 GB GPUs, respectively. We evenly distributed the jobs among the GPUs. We recorded the compute time for the 2017 data for three separate tests running locally, using (1) 24 CPUs and 1 A100 GPU, (2) 48 CPUs and 2 A100 GPUs, and (3) 96 CPUs and 4 A100 GPUs (Figure 4c). Using the timing information and pricing information from Azure, we calculated the equivalent cost to run on the cloud using the same computing set-up (Figure 4d). The cost of running on GPU instances is > 3x that of CPU-only instances, with the F4s instance (24 vCPUs) costing $1.19/hour in the West-US 2 region and the NC instance (24 vCPUs) costing $3.80/hour.

For our use case, we find that the same computational speed-up from GPUs can be achieved with only CPUs for a fraction of the cost. For instance, running the EQT branch on one year of data using 128 CPUs from the F4s instance had a compute time of 37 minutes, while the same test ran using 96 CPUs and 4 A100 GPUs took 38 minutes (Figure 4c). These two tests had associated costs of $3.93 USD and $9.38 USD, respectively. While the cost of both of these tests is relatively inexpensive, we point out that the speed-up offered by GPUs is marginal in comparison to the extra time and effort needed to address the complications of parallelizing across GPUs and to increase the size and complexity of the Docker container. It should also be noted that these results are application dependent: we do not attempt to parallelize the TM branch using GPUs with the capabilities of the Fast Matched Filter method (Beaucé et al., 2017) in order to avoid adding CUDA dependencies to the containers.

Example Results

We report results of the TM and EQT detection workflows applied to one year of seismic waveform data. We do not intend for these results to represent a thorough comparison of the two methods because we did not iterate on thresholding parameters for either the TM or EQT branches of detection. This section instead serves as a demonstration of the results of our described workflow.

We apply the TM and EQT detection workflows to waveform data from 2017 for the NV network, a cabled

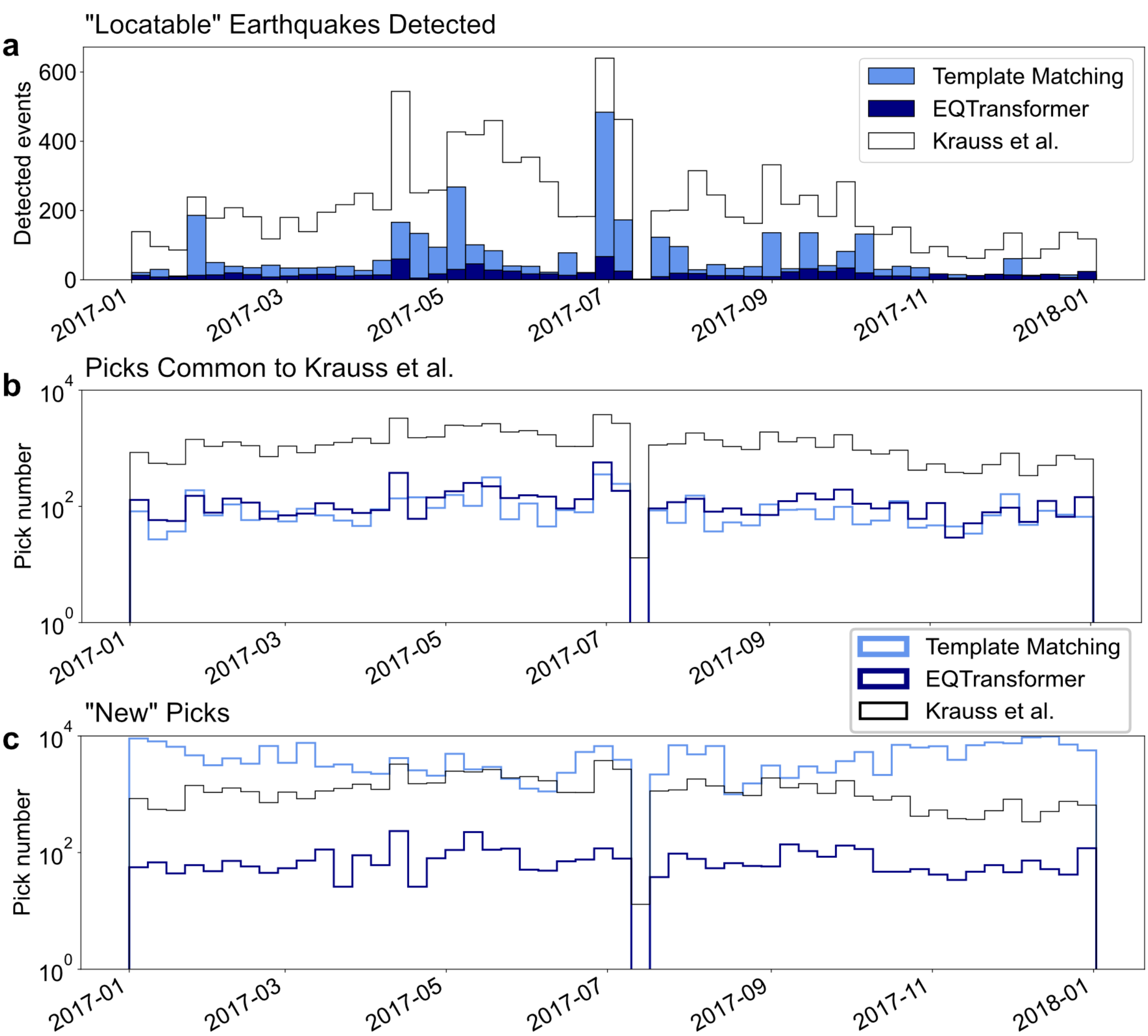

Figure 5 Results of earthquake detection on the NV network for the year of 2017. **(a)** Histogram of earthquakes detected using either TM or EQT in comparison to the catalog of Krauss et al. (2023b), with bin widths of 1 week. The plotted TM events all have absolute cross correlation sums of greater than 3.2, and the plotted EQT events all have at least 6 picks included in the associated event. **(b)** Histogram of how many overall picks were common to the Krauss et al. (2023b) catalog for either TM or EQT at a threshold of 0.5 s pick difference, with bin widths of 1 week. Note that the y-axis is shown in log-scale to improve visual comparison. The data gap in 2017-08 was due to a network outage.

ocean bottom seismometer network that sits within the hydrothermal vent fields of the Endeavour segment on the Juan de Fuca ridge (Heesemann et al., 2014). This area typically experiences at least 10 shallow small earthquakes (Mw < 2.5) per day and frequent swarms. Most recorded earthquakes are located within 40 km of the network. For ground truth comparison of the results of TM and EQT detection, we use the catalog of Krauss et al. (2023b), which was created using traditional STA/LTA methods and has a magnitude of completeness of Mw ~0.5 for earthquakes within the network.

For the TM detection, we use a set of 53 templates that were chosen as representative of the most frequently-occurring families of earthquakes with high waveform similarity during 2017 following Krauss and Wilcock (2022). This is far fewer than the total number of earthquakes (> 11,000) in the Krauss et al. (2023b) catalog for 2017 (Figure 5a), such that we do not expect the TM detection to be able to fully reconstruct the entire catalog. We present the TM detections that have a summed absolute cross correlation across the eight template channels greater than 3.2 (Figure 5), equivalent to a median absolute deviation threshold near 8. For EQT detection, we use the EQT model pretrained on STEAD and required both P- and S-wave thresholds of 0.1, similar to (Jiang et al., 2022; Scotto di Uccio et al., 2023). For EQT, we include earthquakes that contain at least 6 picks after association through GaMMa (Figure 5).

In contrast to the 11,000 located earthquakes in the Krauss et al. (2023b) catalog, the TM and EQT workflows find 3,543 and 924 earthquakes, respectively (Figure 5a). Figure 5 compares the total number of picks made by EQT and TM directly to the Krauss et al. (2023b) catalog, separately classifying those that are common to the catalog (Figure 5b) and those that are "new" picks (Figure 5c). We classify a TM or EQT pick as common to the Krauss et al. (2023b) catalog if it has the same station, phase, and occurs within 0.5 s of a pick in the Krauss et al. (2023b) catalog.

Notably, TM and EQT find comparable numbers of picks that are common to the Krauss et al. (2023b) catalog (Figure 5b), even though TM decisively finds more earthquakes overall (Figure 5a). The picks found by the TM method are mostly “new” picks: only 2% of the TM picks were also in the Krauss et al. (2023b) catalog. This suggests that the picks found by TM are almost entirely just smaller or noisier examples of the template events that went undetected by traditional methods. In contrast, 62% of the picks found by the EQT branch are also in the Krauss et al. (2023b) catalog. Therefore, although EQT finds overall less earthquakes than TM, it likely captures a more complete representation of waveform diversity in the dataset.

These results support the complementary use of template matching and pre-trained machine learning models in constructing earthquake catalogs. Template matching is typically used as a post-processing step to expand catalog completeness after an initial catalog is constructed with machine learning (Shi et al., 2022; Zhang et al., 2022; Zhou et al., 2021; Scotto di Uccio et al., 2023). Our example results, which show that EQT captures a wider range of waveforms while TM detects smaller versions of similar waveforms, support the use of EQT to create a starting catalog and then TM to expand the EQT catalog.

Discussion

We have documented that running seismic workflows on commercial cloud providers can be relatively inexpensive. In our case, costs are < $5 to process one year of continuous data for a small network (Figure 4). This knowledge could significantly expand the ability of the seismic community to perform research at scale: low-cost cloud resources offer a valuable alternative to researchers who do not have institutional access to HPC resources. The pay-as-you-go nature of commercial cloud resources also means that researchers can experiment with different types and sizes of computing resources before committing to the large start-up costs of building a local cluster. This can also mean that fewer machines are plugged in and unused.

However, it is important to reemphasize that working in the cloud can be difficult and unintuitive. Our functioning cloud resource system was only accomplished after months of effort and occasional consultation with data scientists and cloud experts. Much of the workflow we report here relied on skills developed during a week-long “hackathon” with one-on-one help and devoted resources. Our experience suggests that researchers will need access to cloud expertise through their academic institutions to realize the true potential of cloud computing, although we hope the documentation provided here can alleviate some of that need.

Another informative result of our cyberinfrastructure investigation is that the deployment of pre-trained machine-learning workflows on CPU-only set-ups can be as fast as and much easier than a GPU implementation, for the same or lower cost (Figure 4). We attribute this to the large size of the CUDA package in the container and the high speed of prediction using these models on CPU. Traditionally, it is assumed that GPU are better for machine learning workflows, but we suggest that this statement is more strongly true for training these models. In contrast, Yu et al. (2023) report that GPU use for prediction, not training, offers a significant speed up in comparison to CPU-only computation. However, we point out that their timing benchmarks are made using a production-level implementation that directly applies pre-trained machine learning models to discrete non-continuous waveforms. Alternatively, our method uses SeisBench to pre-process waveforms and manage the overlapping of input continuous data prior to application of the machine learning model. Starting from continuous data is very common for many research workflows, and in such cases we have shown that using CPUs can be more cost-effective.

To strengthen the transfer of local workflows to the cloud beyond what we have demonstrated here, researchers could create storage and compute instances through code, referred to as “infrastructure as code”, rather than through desktop portals (e.g., Morris, 2020). We found that this was not feasible with the current permissions settings required with our chosen types of resources, Azure Blob storage and Batch Pools, but we encourage researchers intending to set up large cloud systems that will run long-term to pursue non-portal workflows. Alternatively, point-and-click methods through desktop portals as we have shown here can be an easily understandable way for beginners to get started with cloud resources. It would also be possible for researchers to emulate this workflow on other cloud platforms such as Amazon Web Services or Google Cloud Platform; the codes to interact with the cloud resources (Azure Blob storage, Azure Batch) would need to be adapted to the interface specific to the cloud provider, but no significant changes would need to be made to the code base itself.

Conclusion

The workflow we present provides a basis for individual researchers to adapt their local seismic processing work to the commercial cloud. We have documented how to containerize code repositories using Docker, how to construct and access storage in the Azure cloud, and how to combine these resources to construct and access computing resources in the Azure cloud. For researchers unfamiliar with parallelization techniques in general, we also provide examples for the parallelization of seismic workflows on local machines. The learning curve associated with cloud set-up is steep. But, the results of our scaling tests show that seismic processing in the cloud is both cheap and fast. Since the low cost of cloud computing makes large-scale processing more accessible to the seismic community, the migration of local workflows to the cloud is a worthy endeavor. We hope this work can serve as a useful starting point for other researchers.

Acknowledgements

We thank Naomi Alterman, Jesse Biehl, and Charles Rice for their invaluable knowledge of and assistance with the Azure cloud platform. We also thank two anonymous reviewers for their thoughtful comments which greatly improved the manuscript. Funding was provided by the NSF SCOPED award (EAR-2103701), NSF CyberInfrastructure Award (EAR-2117834), by the University of Washington eScience Institute's inaugural Cloud ReproHackweek, and by a National Defense Science and Engineering Graduate Fellowship to ZK.

Data and code availability

The facilities of IRIS Data Services, and specifically the IRIS Data Management Center, were used for access to waveforms used in this study. IRIS Data Services are funded through the Seismological Facilities for the Advancement of Geoscience (SAGE) Award of the National Science Foundation under Cooperative Support Agreement EAR-1851048. The earthquake catalog for the Endeavour segment that is presented for comparison in this study is available through the Marine Geoscience Data System via 10.26022/IEDA/330498 (Krauss and Wilcock, 2021). The codes referenced in this study, including the Jupyter Notebook tutorials named Notebook S1-S4, are available at https://github.com/Denolle-Lab/seismicloud, stored on Zenodo (Krauss et al., 2023a). Tutorials S1-S3, which are in PDF format, are available as supplementary materials and also in the seismicloud GitHub repository.

References

Arrowsmith, S., Trugman, D., MacCarthy, J., Bergen, K., Lumley, D., and Magnani, M. Big Data Seismology. *Reviews of Geophysics*, 60(2):2021 000769, 2022. doi: 10.1029/2021RG000769.

Barker, M., Chue Hong, N., Katz, D., Lamprecht, A.-L., Martinez-Ortiz, C., Psomopoulos, F., Harrow, J., Castro, L., Gruenpeter, M., Martinez, P., and Honeyman, T. Introducing the FAIR Principles for research software. *Scientific Data*, 9(1):1, 2022. doi: 10.1038/s41597-022-01710-x.

Beaucé, E., Frank, W., and Romanenko, A. Fast Matched Filter (FMF): An Efficient Seismic Matched-Filter Search for Both CPU and GPU Architectures. *Seismological Research Letters*, 89(1): 165–172, 2017. doi: 10.1785/0220170181.

Beyreuther, M., Barsch, R., Krischer, L., Megies, T., Behr, Y., and Wassermann, J. ObsPy: A Python Toolbox for Seismology. *Seismological Research Letters*, 81(3):530–533, 2010. doi: 10.1785/gssrl.81.3.530.

Chamberlain, C., Hopp, C., Boese, C., Warren-Smith, E., Chambers, D., Chu, S., Michailos, K., and Townend, J. EQcorrscan: Repeating and Near-Repeating Earthquake Detection and Analysis in Python. *Seismological Research Letters*, 89(1):173–181, 2017. doi: 10.1785/0220170151.

Clements, T. and Denolle, M. The Seismic Signature of California's Earthquakes, Droughts, and Floods. *Journal of Geophysical Research: Solid Earth*, 128(1):2022 025553, 2023. doi: 10.1029/2022JB025553.

Gabriel, E., Fagg, G., Bosilca, G., Angskun, T., Dongarra, J., Squyres, J., Sahay, V., Kambadur, P., Barrett, B., and Lumsdaine, A. Open MPI: Goals, concept, and design of a next generation MPI implementation. *Recent Advances in Parallel Virtual Machine and Message Passing Interface: 11th European PVM/MPI Users' Group Meeting Budapest, Hungary, September 19-22, 2004*, Proceedings 11:97–104, 2004. doi: 10.1007/978-3-540-30218-6$_1$9.

Gibbons, S. and Ringdal, F. The detection of low magnitude seismic events using array-based waveform correlation. *Geophysical Journal International*, 165(1):149–166, 2006. doi: 10.1111/j.1365-246X.2006.02865.x.

Heesemann, M., Insua, T., Scherwath, M., Juniper, K., and Moran, K. Ocean Networks Canada: From geohazards research laboratories to smart ocean systems. *Oceanography*, 27(2):151–153, 2014. doi: 10.5670/oceanog.2014.50.

Ishii, M., Shearer, P., Houston, H., and Vidale, J. Extent, duration and speed of the 2004 Sumatra–Andaman earthquake imaged by the Hi-Net array. *Nature*, 435(7044):7044, 2005. doi: 10.1038/nature03675.

Jiang, C., Zhang, P., White, M., Pickle, R., and Miller, M. A Detailed Earthquake Catalog for Banda Arc–Australian Plate Collision Zone Using Machine-Learning Phase Picker and an Automated Workflow. *The Seismic Record*, 2(1):1–10, 2022. doi: 10.1785/0320210041.

Krauss, Z. and Wilcock, W. Microseismicity earthquake catalog, Endeavour Segment, Juan de Fuca ridge, 1995–2021 [Dataset. *IEDA*, 2021. doi: 10.26022/IEDA/330498.

Krauss, Z. and Wilcock, W. Investigating microearthquake multiplets using ocean bottom seismometers in a mid-ocean ridge hydrothermal field, 2022.

Krauss, Z., Ni, Y., and Henderson, S. v2.0 Denolle-Lab/seismicloud: Notebooks, Tutorials and Code for "Seismology in the cloud: guidance for the individual researcher", 2023a. doi: 10.5281/zenodo.7948849.

Krauss, Z., Wilcock, W., Heesemann, M., Schlesinger, A., Kukovica, J., and Farrugia, J. A Long-Term Earthquake Catalog for the Endeavour Segment: Constraints on the Extensional Cycle and Evidence for Hydrothermal Venting Supported by Propagating Rifts. *Journal of Geophysical Research: Solid Earth*, 123:2022 025662, 2023b. doi: 10.1029/2022JB025662.

Lindsey, N., Martin, E., Dreger, D., Freifeld, B., Cole, S., James, S., Biondi, B., and Ajo-Franklin, J. Fiber-optic network observations of earthquake wavefields. *Geophysical Research Letters*, 44(23):11–792, 2017. doi: 10.1002/2017GL075722.

MacCarthy, J., Marcillo, O., and Trabant, C. Seismology in the cloud: A new streaming workflow. *Seismological Research Letters*, 91(3):1804–1812, 2020. doi: 10.1785/0220190357.

Michelini, A., Cianetti, S., Gaviano, S., Giunchi, C., Jozinović, D., and Lauciani, V. INSTANCE – the Italian seismic dataset for machine learning. *Earth System Science Data*, 13(12):5509–5544, 2021. doi: 10.5194/essd-13-5509-2021.

Morris, K. *Infrastructure as Code*. O'Reilly Media, Inc, 2020.

Mousavi, S., Sheng, Y., Zhu, W., and Beroza, G. STanford EArthquake Dataset (STEAD): A global data set of seismic signals for AI. *IEEE Access*, 7:179464–179476, 2019. doi: 10.1109/ACCESS.2019.2947848.

Mousavi, S., Ellsworth, W., Zhu, W., Chuang, L., and Beroza, G. Earthquake transformer—An attentive deep-learning model for simultaneous earthquake detection and phase picking. *Nature Communications*, 11(1):3952, 2020. doi: 10.1038/s41467-020-17591-w.

Münchmeyer, J., Woollam, J., Rietbrock, A., Tilmann, F., Lange, D., Bornstein, T., Diehl, T., Giunchi, C., Haslinger, F., and Jozinović, D. Which picker fits my data? A quantitative evaluation of deep learning based seismic pickers. *Journal of Geo-*

physical Research: Solid Earth*, 127(1):2021 023499, 2022. doi: 10.1029/2021JB023499.

Ni, Y., Hutko, A., Skene, F., Denolle, M., Malone, S., Bodin, P., Hartog, R., and Wright, A. Curated Pacific Northwest AI-ready Seismic Dataset. *Seismica*, 2(1):1, 2023. doi: 10.26443/seismica.v2i1.368.

Norman, M., Kellen, V., Smallen, S., DeMeulle, B., Strande, S., Lazowska, E., Alterman, N., Fatland, R., Stone, S., Tan, A., Yelick, K., Dusen, E., and Mitchell, J. CloudBank: Managed Services to Simplify Cloud Access for Computer Science Research and Education. *Practice and Experience in Advanced Research Computing*, page 1–4, 2021. doi: 10.1145/3437359.3465586.

Obara, K. Nonvolcanic deep tremor associated with subduction in southwest Japan. *Science*, 296(5573):1679–1681, 2002. doi: 10.1126/science.1070378.

Park, Y., Beroza, G., and Ellsworth, W. A Mitigation Strategy for the Prediction Inconsistency of Neural Phase Pickers. *Seismological Research Letters*, 94(3):1603–1612, 2023. doi: 10.1785/0220230003.

Perol, T., Gharbi, M., and Denolle, M. Convolutional neural network for earthquake detection and location. *Science Advances*, 4(2): 1700578, 2018. doi: 10.1126/sciadv.1700578.

Quinteros, J., Carter, J., Schaeffer, J., Trabant, C., and Pedersen, H. Exploring Approaches for Large Data in Seismology: User and Data Repository Perspectives. *Seismological Research Letters*, 92(3):1531–1540, 2021. doi: 10.1785/0220200390.

Rogers, G. and Dragert, H. Episodic tremor and slip on the Cascadia subduction zone: The chatter of silent slip. *Science*, 300(5627): 1942–1943, 2003. doi: 10.1126/science.1084783.

Ross, Z., Trugman, D., Hauksson, E., and Shearer, P. Searching for hidden earthquakes in Southern California. *Science*, 364(6442): 767–771, 2019. doi: 10.1126/science.aaw6888.

Schorlemmer, D., Euchner, F., Kästli, P., Saul, J., and Group, Q. QuakeML: Status of the XML-based seismological data exchange format. *Annals of Geophysics*, 54(1), 2011. doi: 10.4401/ag.

Schovanec, H., Haynie, K., and Hearne, M. Development of Cloud Computing Infrastructure for the Automated Creation and Delivery of Near-Real-Time Earthquake Impact Products. *AGU Fall Meeting Abstracts*, page 33 –02, 2021.

Scotto di Uccio, F., Scala, A., Festa, G., Picozzi, M., and Beroza, G. Comparing and integrating artificial intelligence and similarity search detection techniques: Application to seismic sequences in Southern Italy. *Geophysical Journal International*, 233(2): 861–874, 2023. doi: 10.1093/gji/ggac487.

Shapiro, N., Campillo, M., Stehly, L., and Ritzwoller, M. High-resolution surface-wave tomography from ambient seismic noise. *Science*, 307(5715):1615–1618, 2005. doi: 10.1126/science.1108339.

Shelly, D., Beroza, G., and Ide, S. Non-volcanic tremor and low-frequency earthquake swarms. *Nature*, 446(7133):305–307, 2007. doi: 10.1038/nature05666.

Shi, P., Grigoli, F., Lanza, F., Beroza, G., Scarabello, L., and Wiemer, S. MALMI: An Automated Earthquake Detection and Location Workflow Based on Machine Learning and Waveform Migration. *Seismological Research Letters*, 93(5):2467–2483, 2022. doi: 10.1785/0220220071.

Tan, Y., Waldhauser, F., Ellsworth, W., Zhang, M., Zhu, W., Michele, M., Chiaraluce, L., Beroza, G., and Segou, M. Machine-Learning-Based High-Resolution Earthquake Catalog Reveals How Complex Fault Structures Were Activated during the 2016–2017 Central Italy Sequence. *The Seismic Record*, 1(1):11–19, 2021. doi: 10.1785/0320210001.

Trabant, C., Hutko, A., Bahavar, M., Karstens, R., Ahern, T., and Aster, R. Data Products at the IRIS DMC: Stepping Stones for Research and Other Applications. *Seismological Research Letters*, 83(5):846–854, 2012. doi: 10.1785/0220120032.

Turin, G. An introduction to matched filters. *IRE Transactions on Information Theory*, 6(3):311–329, 1960. doi: 10.1109/TIT.1960.1057571.

Walter, J., Ogwari, P., Thiel, A., Ferrer, F., and Woelfel, I. easyQuake: Putting Machine Learning to Work for Your Regional Seismic Network or Local Earthquake Study. *Seismological Research Letters*, 92(1):555–563, 2021. doi: 10.1785/0220200226.

Wilkinson, M., Dumontier, M., Aalbersberg, I. J., Appleton, G., Axton, M., Baak, A., Blomberg, N., Boiten, J.-W., Silva Santos, L., Bourne, P., Bouwman, J., Brookes, A., Clark, T., Crosas, M., Dillo, I., Dumon, O., Edmunds, S., Evelo, C., Finkers, R., and Mons, B. The FAIR Guiding Principles for scientific data management and stewardship. *Scientific Data*, 3(1):1, 2016. doi: 10.1038/sdata.2016.18.

Woollam, J., Münchmeyer, J., Tilmann, F., Rietbrock, A., Lange, D., Bornstein, T., Diehl, T., Giunchi, C., Haslinger, F., Jozinović, D., Michelini, A., Saul, J., and Soto, H. SeisBench—A Toolbox for Machine Learning in Seismology. *Seismological Research Letters*, 93(3):1695–1709, 2022. doi: 10.1785/0220210324.

Yoo, A., Jette, M., and Grondona, M. SLURM: Simple Linux Utility for Resource Management. In Feitelson, D., Rudolph, L., and Schwiegelshohn, U., editors, *Job Scheduling Strategies for Parallel Processing*, page 44–60. Springer, 2003. doi: 10.1007/10968987$_3$.

Yoon, C., O'Reilly, O., Bergen, K., and Beroza, G. Earthquake detection through computationally efficient similarity search. *Science Advances*, 1(11):1501057, 2015. doi: 10.1126/sciadv.1501057.

Yu, E., Bhaskaran, A., Chen, S., Ross, Z., Hauksson, E., and Clayton, R. Southern California Earthquake Data Now Available in the AWS Cloud. *Seismological Research Letters*, 92(5):3238–3247, 2021. doi: 10.1785/0220210039.

Yu, Z., Wang, W., and Chen, Y. Benchmark on the accuracy and efficiency of several neural network based phase pickers using datasets from China Seismic Network. *Earthquake Science*, 36 (2):113–131, 2023. doi: 10.1016/j.eqs.2022.10.001.

Zhang, M., Liu, M., Feng, T., Wang, R., and Zhu, W. LOC-FLOW: An End-to-End Machine Learning-Based High-Precision Earthquake Location Workflow. *Seismological Research Letters*, 93(5): 2426–2438, 2022. doi: 10.1785/0220220019.

Zhou, Y., Ghosh, A., Fang, L., Yue, H., Zhou, S., and Su, Y. A high-resolution seismic catalog for the 2021 MS6.4/MW6.1 Yangbi earthquake sequence. *Earthquake Science*, 34(5):390–398, 2021. doi: 10.29382/eqs-2021-0031.

Zhu, W., McBrearty, I., Mousavi, S., Ellsworth, W., and Beroza, G. Earthquake Phase Association Using a Bayesian Gaussian Mixture Model. *Journal of Geophysical Research: Solid Earth*, 127 (5):2021 023249, 2022. doi: 10.1029/2021JB023249.

Zhu, W., Hou, A., Yang, R., Datta, A., Mousavi, S., Ellsworth, W., and Beroza, G. QuakeFlow: A scalable machine-learning-based earthquake monitoring workflow with cloud computing. *Geophysical Journal International*, 232(1):684–693, 2023. doi: 10.1093/gji/ggac355.

REVIEWED OPINION
doi:10.26443/seismica.v2i2.470

SEISMICA

The need for open, transdisciplinary, and ethical science in seismology

Irina Dallo *[1], **Marcus Herrmann** [2], **Mariano Supino** [3], **José A. Bayona** [4], **Asim M. Khawaja** [5], **Chiara Scaini** [6]

[1]Swiss Seismological Service at ETH Zurich, Switzerland, [2]Università degli Studi di Napoli 'Federico II', Naples, Italy, [3]Istituto Nazionale di Geofisica e Vulcanologia, Rome, Italy, [4]School of Earth Sciences, University of Bristol, Bristol, United Kingdom, [5]GFZ German Research Centre for Geosciences, Potsdam, Germany, [6]National Institute of Oceanography and Applied Geophysics, Trieste, Italy

Author contributions: *Conceptualization*: ID, MH. *Methodology*: ID, MH. *Investigation*: ID, MH, MS, JB, AK, CS. *Resources*: ID, MH, MS, JB, AK, CS. *Writing - original draft*: ID, MH, MS, JB, AK, CS. *Writing - review & editing*: ID, MH, MS, JB, CS. *Visualization*: MH.
ID and MH share first authorship and contributed equally to this opinion paper.

Abstract Reducing the seismic risk for societies requires a bridge between scientific knowledge and societal actions. In recent years, three subjects that facilitate this connection gained growing importance: open science, transdisciplinarity, and ethics. We outline their relevance in general and specifically at the example of 'dynamic seismic risk' as explored in a dedicated workshop. We argue that these reflections can be transferred to other research fields for improving their practical and societal relevance. We provide recommendations for scientists at all levels to make science more open, transdisciplinary, and ethical. Only with a transition can we, as scientists, address current societal challenges and increase societies' resilience to disasters.

Production Editor:
Gareth Funning
Handling Editor:
Samantha Teplitzky
Copy & Layout Editor:
Hannah F. Mark

Signed reviewer(s):
Iryna Kuchma
Carmine Galasso

Received:
10 March 2023
Accepted:
11 July 2023
Published:
1 August 2023

1 Introduction

The devastating 2023 M7.8 Türkiye–Syria earthquake sequence once again highlighted the gap between scientific knowledge and action (e.g., Toomey, 2016): Although the impacted region is known to be at high seismic risk (i.e., highly seismically active, densely populated, and high physical and social vulnerability), the political and societal conditions have complicated and delayed protective measures (e.g., Hussain et al., 2023). To reduce the seismic risk and prepare local communities, experts from different disciplines must collaborate effectively in redesigning the built environment and engaging the construction companies, politicians, residents, etc. in risk education and management (Comfort et al., 2023).

In recent years, three subjects have become increasingly relevant to build that needed bridge between scientific knowledge and societal action, namely open science, transdisciplinarity, and ethics (see Figure 1). These subjects have influenced scientific discussions on how to transition from purely scientific research to practical and societally relevant applications that increase societies' resilience to disasters (e.g., Marti et al., 2022) – just as envisioned by several initiatives around the world, including the EU Horizon 2020 programme, the US National Science Foundation, and the UK Research and Innovation funding agency

We, along with other early career scientists of RISE (Real-time earthquake rIsk reduction for a reSilient Europe; EU Horizon 2020 project), identified these three subjects in several virtual discussions while reflecting on our needs to make our research efforts more societally meaningful and effective. Eventually, together with senior scientists, we discussed and evaluated these subjects during a three-day workshop in Naples (Italy), October 26-28, 2022, under the theme "Bringing research to practical applications that increase society's earthquake resilience" (Supplement 1). This theme resembled RISE's overall goal of advancing the scientific and societal knowledge on dynamic seismic risk, the overarching topic we additionally wanted to explore. First, keynotes from experts gave us a background on the three subjects, and lightning talks by all participants revealed the range of our expertise. Second, we drew a rich picture for the overarching topic and each subject following the Soft Systems Methodology (Pohl, 2020): separate groups sketch and express their ideas as mental models, receive feedback from the other groups, and revise it accordingly (see Supplement S2a-d for the evolution of the rich pictures). This approach allowed us to integrate all our expertise on the topic and subjects.

In the following, we provide the conceptual back-

*Address correspondence to Irina Dallo, ETH Zurich, Swiss Seismological Service, Sonneggstrasse 5, 8092 Zurich, Switzerland, irina.dallo@sed.ethz.ch

ground of the three main subjects, stress their relevance in current research, and illustrate their link to dynamic seismic risk (Figure 1). We believe that these reflections can be transferred to any other research field since the subjects affect various disciplines.

2 The three subjects in the light of dynamic seismic risk

To assess the impact of earthquakes on the built environment and people's well-being, seismic risk combines the knowledge about the potential ground shaking due to future earthquakes (seismic hazard) with the knowledge about the exposure and vulnerability of buildings, infrastructure, and communities. However, seismic risk is not constant but dynamic (varying in time, space, and context) due to changes in short- and long-term temporal variation of the hazard (e.g., occurrence of earthquake sequences, secondary effects such as tsunamis, fires or landslides), exposure (e.g., population growth and displacements, time of the day), and vulnerability (e.g., retrofitting, structural degradation) as well as complex interactions between individual and social vulnerabilities (e.g., Orru et al., 2022). To address these dynamics and related challenges, different approaches are needed in different phases of the disaster cycle (i.e., before, during, and after an earthquake sequence) such as operational earthquake forecasting (Jordan et al., 2011), dynamic exposure and vulnerability modelling (Schorlemmer et al., 2020; Orlacchio et al., 2021; Pittore et al., 2016), earthquake early warning (Allen and Melgar, 2019; Cremen and Galasso, 2020), rapid loss assessment (Erdik et al., 2011), and recovery and rebuilding efforts (Miles and Chang, 2006); see also Supplement S2a.

The data, models, products, and services (hereafter referred to as assets) that have been produced in RISE contribute to all phases of the disaster cycle (Carr, 1932) and, taken together, address dynamic seismic risk (Alexander, 2018). As outlined in the following three sections, these assets can only be combined meaningfully if interdisciplinary research groups openly share and document their inputs and outputs (Section 2.1), actively involve societal stakeholders (Section 2.2), and appropriately consider ethical issues (Section 2.3). For every subject, we dedicate three paragraphs: (§1) the theoretical concepts and advantages, (§2) their specific relevance for dynamic seismic risk, and (§3) solutions and good practices to implement them in future research.

2.1 Open science

Open science envisions transparent and accessible knowledge that is shared and developed collaboratively (UNESCO, 2022). It encompasses practices such as making research outputs open (e.g., open access publications, open data, and open source software), verifiable, and reproducible, as well as openly designing experiments, methods, and analyses. This openness provides many benefits, for instance making it easier to disseminate and communicate scientific knowledge, expedite the scientific process by saving time for re-inventing methods, receive constructive feedback from the scientific community, and promote collaborative, cross-disciplinary, and inclusive research practices. Moreover, open data can help identify systematic data misuse (i.e., a potentially adverse use that was not originally intended), particularly when issues in data analysis arise (e.g., geographical correlation associated with causality; Flaherty et al., 2022). Open science is further guided by the FAIR principles (Wilkinson et al., 2016), ensuring Findability, Accessibility, Interoperability, and Reuse of digital assets. For instance, a Digital Object Identifier (DOI; Paskin, 2010) is key to guarantee correct attribution and access of an asset in the long term (Schymanski and Schymanski, 2023). Moreover, open licenses (see Table 1) ensure an unrestricted use of data, models, or other outputs while appropriately crediting the creator. By complying with these standards and principles, cross-disciplinary efforts are possible (COAR et al., 2021).

Dynamic (seismic) risk assessment requires linking information from different assets and different phases of the disaster cycle, therefore significantly benefiting from an open approach. For example, the European Plate Observing System (EPOS) positioned itself to facilitate the open and FAIR data transfer between institutions and multiple disciplines within solid-earth sciences (Bailo et al., 2022; Marti et al., 2022). The EPOS Thematic Core Service for Seismology (Haslinger et al., 2022) enables homogenized monitoring efforts and collaboration based on seismic waveform data (ORFEUS), rapid earthquake information (EMSC), and expertise in seismic hazard and risk assessments (EFEHR); thus connecting the different assets along the disaster cycle. Also in RISE, some open science assets have been created, such as the pyCSEP toolkit, an open source software for developing and testing probabilistic earthquake forecasts (Savran et al., 2022a,b), so-called reproducibility packages that contain code, data, and other resources to reproduce research outcomes without additional effort (e.g., Bayona et al., 2022, 2023; Khawaja et al., 2023), an open sensor firmware platform that supports creating real-time monitoring networks (quakesaver.net), and a dynamic exposure model based on crowd-sourced/citizen-science building data (Schorlemmer et al., 2020). These developments set an example for making the fundamental assets of dynamic (seismic) risk assessment available. For the 2023 Türkiye–Syria earthquake sequence, in particular, various initiatives (e.g., EERI, 2013; GDACS, 2023; GSLN, 2023) collected open data and reports to facilitate scientific investigation, understanding, and dynamic risk reduction strategies.

To date, several challenges restrict the dissemination and development of open science (see also National Academies of Sciences, Engineering, and Medicine, 2018). Here we emphasize four of them: (i) Open science is not yet fully recognized as a part of science education, therefore authorities (e.g., universities, science ministries, research centers, funding bodies) responsible for overseeing science should put more emphasis on open science; (ii) The tools and technologies being used for open science are either unfamiliar or unavail-

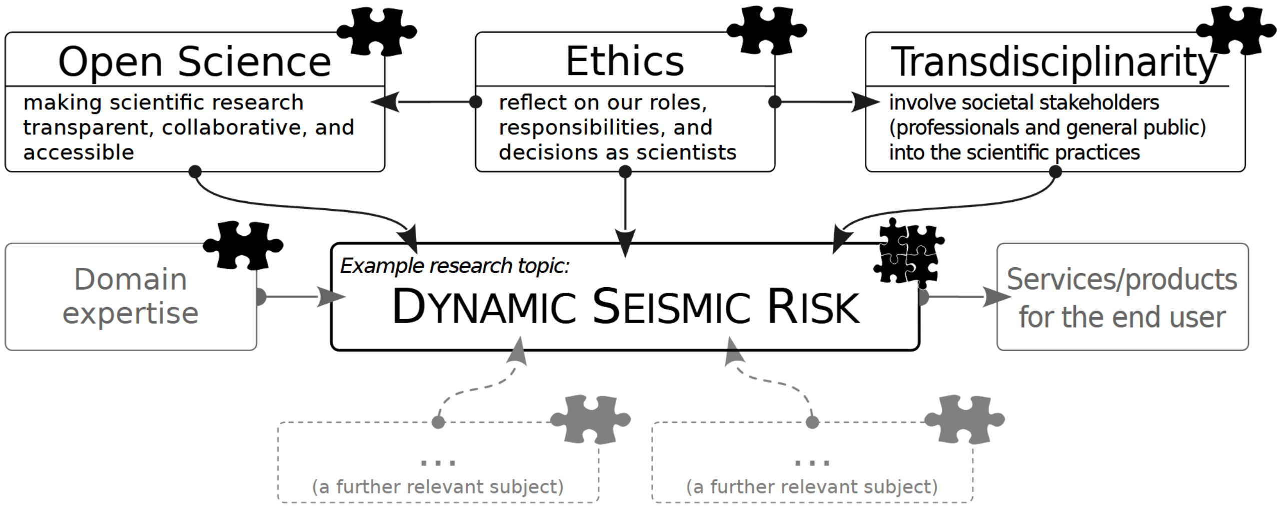

Figure 1 Overview of the three subjects (open science, ethics, and transdisciplinarity) and their relevance in dynamic seismic risk to co-design user-centered services and products. Ethics not only influence dynamic seismic risk, but also open science and transdisciplinarity (see Section 2.3 §2).The two empty dashed boxes at the bottom indicate further important subjects that were not addressed but are similarly relevant (e.g., legality, equity, diversity, inclusivity; Klinkhamer, 2022).

able to many scientists, thereby creating barriers to conducting open science. Training and open tools for the collaborative development of code, data, and methods should be provided to researchers early in their careers; (iii) Open science demands time, which is not yet considered in the researchers' evaluation process. Efforts for open science should be rewarded during the evaluation process of a researcher, for example through qualitative assessments (e.g., Hicks et al., 2015); (iv) The costs of open access publishing are usually high (in particular for journals of repute, which not all research institutions can afford; Sample, 2012), potentially discrediting research, leading to inequity (favoring those who have the funds), and fueling 'predatory' journals (Pourret, 2022); diamond open access journals like this one support a transition in open access publishing (Rowe et al., 2022).

2.2 Transdisciplinarity

Addressing current societal challenges requires transdisciplinary approaches (Peek et al., 2020; Vienni Baptista et al., 2020), that is, integrating knowledge from different scientific disciplines (interdisciplinary) and considering the values, knowledge, and needs of stakeholders in the society, including the public and private sectors, the general public, etc. (stakeholder engagement). Transdisciplinary approaches acknowledge the societal and scientific complexity of a problem (Hirsch Hadorn et al., 2008), co-create knowledge and practices (Pohl et al., 2021), tailor general scientific concepts to the local context (Stablein et al., 2022), and develop user-centered assets to contribute to disaster risk reduction (Dallo, 2022; Raška, 2022). Fostering transdisciplinarity is indispensable because we, as scientists, have a societal responsibility (Di Capua and Peppoloni, 2021) since our scientific outputs can have a direct or indirect impact on people's lives (Marti et al., 2022).

Transdisciplinary efforts to assess risk perception and awareness across communities and stakeholders are essential for disaster risk reduction (UNDRR, 2022a). The dynamic seismic risk framework develops products for different stakeholders who actively participate in all phases of the disaster cycle. In RISE, for example, interdisciplinary groups (consisting of engineers, seismologists, IT specialists, and communication experts) co-designed products and services by involving civil protection, authorities, and the general public through focus groups, interviews, and surveys (Fallou et al., 2022; Marti et al., 2023). It became apparent that a key factor in improving risk mitigation strategies is strengthening the relationship between scientists and stakeholders to better understand societies' needs and concerns.

Transdisciplinarity is not yet fully practiced by scientists involved in disaster risk reduction activities, and is not included in current discipline-specific academic education programs despite the desire of early career scientists (Bridle et al., 2013, Supplement 3). Two main challenges are (i) building interdisciplinary groups and ensuring effective interactions between the disciplinary experts, and (ii) engaging with civil society (a structured and sometimes lengthy process) by building trust between scientists and stakeholders (UNDRR, 2022b). Research infrastructures can foster the development of a transdisciplinary research community in the field of disaster risk (Peek et al., 2020) and provide powerful tools (e.g., data, codes, expertise) to research groups (e.g., Folch et al., 2023; Calatrava et al., 2023; Dañobeitia et al., 2020). Access and interaction with research infrastructures should therefore be promoted and encouraged among the disaster risk community to exploit these opportunities. Further, developing effective risk-related communication, in particular for the general public, is also challenged by potential misinformation, disinformation, and/or misunderstandings. This has been again observed in the 2023 Türkiye–Syria earthquake sequence (e.g., Panjwani, 2023). Thus, communication experts must be aware of these dynamics and continue to provide useful, understandable, and evidence-based recommendations to combat earthquake misinformation (Dallo et al., 2022a), help design and implement strategies for efficiently communicating earthquake early warnings and forecasts (Dryhurst et al., 2021; Freeman et al., 2023), and foster multi-hazard communication among different stakeholders (Dallo, 2022).

2.3 Ethics

Ethics is relevant to data collection, use, and processing, as well as to data-driven decision-making – it must be consciously considered by researchers. In general, experts differentiate between internal and external (research) ethics (ALLEA, 2013). Internal ethics refer to good research practices such as complying with GDPR and FAIR data principles, reflecting on conflicts of interest or embracing the duty to produce open science (Di Capua and Peppoloni, 2021; Wilkinson et al., 2016). External research ethics refer to the relations between science and society such as the potential misuse of information, the responsibility towards society, legal consequences (e.g., L'Aquila trial in 2009), or inclusive research cultures (ALLEA, 2013). These relations have a long history, starting with defined ethical standards after World War II (Evers, 2001). Even though international, European, and national ethical guidelines have been established (e.g., AGU, 2017), their practical implementation is still in its early stages (Di Capua and Peppoloni, 2021).

An assessment of ethical implications is required when personal data (e.g., socio-economic data) are used to assess social vulnerability (Ferreira et al., 2015) and/or consequences of disasters (Mezinska et al., 2016; Louis-Charles et al., 2020). Ethical issues could arise if outcomes of such assessments identify vulnerable or minority groups which can be targeted for other purposes (e.g., insurance plans). Granting public access to data, models, or products of a dynamic risk framework may lead to potential misuse by third parties, which should be considered by the providers and/or scientists beforehand, e.g. by clarifying the responsibility of any consequences. For example, an open earthquake forecasting (or risk) model could either be incorrectly used or its results misinterpreted, which may eventually reduce the trust in those models; or be intentionally manipulated to provide exaggerated forecasts, which may create fear and panic among the public. Ethics also matters when communicating certain information: in the workshop we discussed whether we could simply release probabilistic earthquake short-term forecasts to the public (and if yes, how?). Although those probabilities are produced by several institutions, not every scientist may advocate their public release for ethical reasons (e.g., potential misinterpretation, unintended panic, missing knowledge on translating the probabilities into mitigation actions) – yet, our internal majority voted for an unconditional public release, arguing that some information is more useful for (personal) decision-making than no information. Currently, a few institutions publicly release earthquake forecasts only after a large earthquake occurred (e.g., USGS and GNS). But for making (personal) decisions, people want actionable information, not probabilities (Dallo et al., 2022b).

But ethically, who decides what is actually considered right or wrong? We identified three possible categories: (i) 'agreed upon', where the necessary action to undertake is obvious, such as doing open science, involving more reviewers in the review process to reduce bias, or improving education; (ii) 'subjective', where a consensus is needed (such as publicly releasing forecasts), which can be obtained via voting (democratic) or providing and discussing arguments; and (iii) 'I do not care', where ethical implications are ignored or considered irrelevant (which we think is not a solution, but we have had experiences where scientists had this attitude). For the second category, which is the most difficult one, one may not find a consensus easily and may need to wait for more information or better arguments. Interestingly, a democratic approach to consensus building may in itself be considered unethical because minorities are not adequately represented. Therefore, evaluating ethical implications in practical applications of research results is not trivial – potential unethical situations must be carefully considered and reflected upon.

3 So, what can we do now?

On all levels – individually, within labs, institutionally, nationally, and internationally – more efforts are needed to foster open science, shift from discipline-specific or interdisciplinary research to transdisciplinary research, and jointly discuss the ethical implications of our research. Transdisciplinarity, in particular, is not sufficiently rewarded and encouraged within the academic sector (Müller and Kaltenbrunner, 2019), and all three subjects presented here are, at best, only partially addressed during academic training and career development.

In Table 1 we provide some practical guidelines and general suggestions on how to better address these three subjects. We advocate that research institutes and supervisors integrate them in their training programs for early career scientists, go beyond purely discipline-oriented training, motivate other scientists to consider these subjects in their projects, and bring them up in discussions with colleagues (from other disciplines) or outside academia. Specific programs for short visiting periods or fieldwork might enforce transdisciplinary connections and could be supported financially.

We further suggest that researchers' activities and projects should also be evaluated based on their contributions in terms of transdisciplinarity, openness, and ethical compliance to promote excellence and fairness. Finally, on an university, institutional, or project level, we argue that sessions with practical guidelines are needed to ensure that current and future research excellence considers the three subjects. We are aware that a fixed set of practices and guidelines are not sufficient; for instance, achieving openness in science is also a process of negotiation and dialogue with atten-

The subjects	Practical guidelines	General suggestions
Open Science	• FAIR Principles • OpenAire Open Science Guides • Open Science Training in TRIPLE (Provost et al., 2023) • Ten rules for implementing open and reproducible research practices (Heise et al., 2023) • FOSTER: Open Science Toolkit • Open Science: A Practical Guide for Early-Career Researchers • Open Data Commons Licenses • Creative Commons Licenses • Open Source Initiative – Licenses Overview • EC's Joinup Software License Assistent	• Provide training and use open tools for a collaborative development of code, data, and methods. • Incentives to focus on open science, e.g., publishing software packages should be acknowledged in performance evaluations (Journal of Open Source Software Merow et al., 2023) • Incentives for qualitative evaluations of researcher output, e.g., DORA, Leiden Manifesto, CoARA. • Preferentially publish in (diamond) open access journals
Transdisciplinarity	• td-net toolbox • What is transdisciplinary research? • Ten steps to make your research more relevant • EU action catalogue • Participatory methods • Communication Guide: How to fight misinformation about earthquakes? (Dallo et al., 2022a) • Research Culture – creating an inclusive research environment (e.g., Royal Society)	• Professors should actively share their knowledge about stakeholders' decision-making processes with their junior scientists, e.g., by dedicated seminars. • Training activities (e.g., workshops) where researchers can directly apply transdisciplinarity methods, which they can use for their research. • Real-world laboratories to facilitate the co-production between scientists and stakeholders (Pärli et al., 2022). • Promote more inter- and transdisciplinary interactions (Bridle et al., 2013). • Align incentives (e.g., promotion criteria, tenure, job applications, funding for visiting, and fieldwork). Recognize the value of transdisciplinary journals.
Ethics	• Ethics Education in Science • Artificial Intelligence & Ethics • Code of Conduct for Scientific Integrity • What is Ethics in Research • International Association for Promoting Geoethics	• Claim support for assessing ethical implications of research activities (e.g., ethical review specialists). • Improve review mechanisms to avoid bias and subjectivity. • Build consensus by considering diverse perspectives. • Foster practices and approaches for fieldwork (Ryan-Davis and Scalice, 2022).
All three subjects	• The Turing Way: Practical handbook with focus on reproducible, collaborative, and ethical research • Best practices for transparent, reproducible, and ethical research (de la Guardia and Sturdy, 2019).	• Training courses for early career scientists, seniors, supervisors, etc. (at the institutes) (Nature, 2023). • Project workshops discussing these subjects in the light of the overall project theme or subtasks (as we did, see Supplement S1). • Build reward mechanisms for research that adopts transdisciplinarity, comply with open access principles, and/or covers ethical aspects. • Supervisors should be role models (Haven et al., 2022). • Engage in knowledge transfer and dissemination activities to the society. • Foster interaction with research infrastructures (both at individual level and for research groups).

Table 1 A selection of practical guidelines for each of the three subjects (middle column) and general suggestions to proactively address them (right column). The last row refers to all three subjects.

tion to socio-cultural contexts and diverse perspectives (Leonelli, 2023) – i.e., the interaction of three subjects outlined here. Likewise, open and transdisciplinary approaches can help with a better training in the 'ethical dimension' of science. Only by embracing this open and inclusive system of knowledge production can we, as scientists, help address current societal challenges and ultimately contribute to increasing societies' resilience to disasters.

Acknowledgements

The authors thank Max Werner, the handling editor, and the two reviewers, Carmine Galasso and Iryna Kuchma, for their valuable comments to improve our opinion article. The authors would like to thank all workshop participants for their active contributions: Jedidiah Aguirre, Emanuele Biondini, Laura Cataldi, Marta Han, Marius Paul Isken (and his keynote), Russell Azad Khan, Simone Mancini, Aron Mirwald, Sam Stockman, Nadja Valenzuela, Tara Evaz Zadeh, Paolo Bergamo, Laura Gulia, Valerio Poggi, and Stefan Wiemer (project leader). We sincerely appreciated the keynote talks of Warner Marzocchi, Silvia Peppoloni, and Angelo Strollo for inspiration and valuable insights. We are also grateful to Jamal Dabbeek, Laure Fallou, Pablo Iturrieta, Mabel Orlacchio, Yves Reuland, and Francesco Serafini for the initial virtual brainstorming. This investigation was supported by the 'Real-time Earthquake Risk Reduction for a Resilient Europe' (RISE) project, which received funding from the European Union's Horizon 2020 research and innovation program under grant agreement No 821115. Opinions expressed in this article solely reflect the authors' views; the EU is not responsible for any use that may be made of information it contains.

Data and code availability

The outputs of the RISE ECS Workshop are available in the Supplement (Dallo and Herrmann, 2023).

Competing interests

The authors declare no conflicts of interest.

References

AGU. *The responsibilities and rights of scientists. Position statement*. American Geophysical Union, 2017.

Alexander, D. E. L'Aquila, central Italy, and the "disaster cycle", 2009-2017. *Disaster Prevention and Management: An International Journal*, 28(4):419–433, Aug. 2018. doi: 10.1108/dpm-01-2018-0022.

ALLEA. Ethics education in science. ALL European Academies - Permanent Working Group on Science and Ethics, 2013. https://www.allea.org/wp-content/uploads/2015/07/Statement_Ethics_Edu_web_final_2013_10_10.pd.

Allen, R. M. and Melgar, D. Earthquake Early Warning: Advances, Scientific Challenges, and Societal Needs. *Annual Review of Earth and Planetary Sciences*, 47(1):361–388, May 2019. doi: 10.1146/annurev-earth-053018-060457.

Bailo, D., Jeffery, K. G., Atakan, K., Trani, L., Paciello, R., Vinciarelli, V., Michalek, J., and Spinuso, A. Data integration and FAIR data management in Solid Earth Science. *Annals of Geophysics*, 65 (2):DM210, Apr. 2022. doi: 10.4401/ag-8742.

Bayona, J., Savran, W., Iturrieta, P., Gerstenberger, M., Graham, K., Marzocchi, W., Schorlemmer, D., and Werner, M. Are Regionally Calibrated Seismicity Models More Informative than Global Models? Insights from California, New Zealand, and Italy. *The Seismic Record*, 3(2):86–95, Apr. 2023. doi: 10.1785/0320230006.

Bayona, J. A., Savran, W. H., Rhoades, D. A., and Werner, M. J. Prospective evaluation of multiplicative hybrid earthquake forecasting models in California. *Geophysical Journal International*, 229(3):1736–1753, Jan. 2022. doi: 10.1093/gji/ggac018.

Bridle, H., Vrieling, A., Cardillo, M., Araya, Y., and Hinojosa, L. Preparing for an interdisciplinary future: A perspective from early-career researchers. *Futures*, 53:22–32, Sept. 2013. doi: 10.1016/j.futures.2013.09.003.

Calatrava, A., Asorey, H., Astalos, J., Azevedo, A., Benincasa, F., Blanquer, I., Bobak, M., Brasileiro, F., Codó, L., Cano, L., Esteban, B., Ferret, M., Handl, J., Kerzenmacher, T., Kozlov, V., Křenek, A., Martins, R., Pavesio, M., Rubio-Montero, A., and Sánchez-Ferrero, J. A survey of the European Open Science Cloud services for expanding the capacity and capabilities of multidisciplinary scientific applications. *Computer Science Review*, 49: 100571, Aug. 2023. doi: 10.1016/j.cosrev.2023.100571.

Carr, L. J. Disaster and the Sequence-Pattern Concept of Social Change. *American Journal of Sociology*, 38(2):207–218, Sept. 1932. doi: 10.1086/216030.

COAR, CoreTrustSeal, European University Association, Science Europe, and World Data System. Joint Position Statement on "Data Repository Selection - Criteria That Matter", 2021. https://zenodo.org/record/4649136. doi: 10.5281/ZENODO.4649136.

Comfort, L., Erkan, B., and Gulkan, P. Earthquake in Turkey exposes gap between seismic knowledge and action - but it is possible to prepare, 2023. https://theconversation.com/earthquake-in-turkey-exposes-gap-between-seismic-knowledge-and-action-but-it-is-possible-to-prepare-199379. The Conversation.

Cremen, G. and Galasso, C. Earthquake early warning: Recent advances and perspectives. *Earth-Science Reviews*, 205:103184, June 2020. doi: 10.1016/j.earscirev.2020.103184.

Dallo, I. *Understanding the communication of event-related earthquake information in a multi-hazard context to improve society's resilience*. PhD thesis, ETH Zurich, 2022. http://hdl.handle.net/20.500.11850/535657.

Dallo, I. and Herrmann, M. Supplement of "The need for open, transdisciplinary, and ethical science in seismology", July 2023. doi: 10.3929/ethz-b-000621044.

Dallo, I., Corradini, M., Fallou, L., and Marti, M. How to fight misinformation about earthquakes? A Communication Guide. 2022a. doi: 10.3929/ETHZ-B-000530319.

Dallo, I., Stauffacher, M., and Marti, M. Actionable and understandable? Evidence-based recommendations for the design of (multi-)hazard warning messages. *International Journal of Disaster Risk Reduction*, 74:102917, May 2022b. doi: 10.1016/j.ijdrr.2022.102917.

Dañobeitia, J., Pouliquen, S., Johannessen, T., Basset, A., Cannat, M., Pfeil, B., M.I., F., Materia, P., Gourcuff, C., Magnifico, G., Delory1, E., Rio Fernandez, J., Rodero, I., Beranzoli, L., Nardello, I., Iudicone, D., Carval, T., Gonzalez Aranda, J., Petihakis, G., Blandin, J., Kutsch, W., Rintala, J.-M., Gates, A., and Favali, P. Toward a Comprehensive and Integrated Strategy of the European Marine Research Infrastructures for Ocean Observations. *Frontiers in Marine Science*, 7, Mar. 2020. doi: 10.3389/f-mars.2020.00180.

de la Guardia, F. H. and Sturdy, J. Best Practices for Transparent, Reproducible, and Ethical Research. Technical report, Feb. 2019.

Di Capua, G. and Peppoloni, S. First report on ethical implications of EPOS Services to Society, 2021. https://www.epos-eu.org/sites/default/files/2022-01/First%20report%20on%20ethical%20implications%20of%20EPOS%20Services%20to%20Society.pdf. Deliverable [EPOS SP] 6.1; WP6: Value for Society, Issue 6.1). Instituto Nazionale di Geofisica e Vulcanologia.

Dryhurst, S., Luoni, G., Dallo, I., Freeman, A., and Marti, M. Designing & implementing the seismic portion of dynamic risk communication for long-term risks, variable short-term risks, early warnings, 2021. http://static.seismo.ethz.ch/rise/deliverables/Deliverable_5.3.pdf. Deliverable]. European Horizon-2020 project RISE.

EERI. Earthquake Engineering Research Institute, 2013. https://learningfromearthquakes.org/2023-02-06-nurdagi-turkey.

Erdik, M., Şeşetyan, K., Demircioğlu, M., Hancılar, U., and Zülfikar, C. Rapid earthquake loss assessment after damaging earthquakes. *Soil Dynamics and Earthquake Engineering*, 31(2): 247–266, Feb. 2011. doi: 10.1016/j.soildyn.2010.03.009.

Evers, K. Standards for ethics and responsibility in science, 2001. https://council.science/wp-content/uploads/2017/05/SCRES-Background.pdf. The Standing Committee on Responsibility and Ethics in Science (SCRES), 149.

Fallou, L., Marti, M., Dallo, I., and Corradini, M. How to Fight Earthquake Misinformation: A Communication Guide. *Seismological Research Letters*, 93(5):2418–2422, June 2022. doi: 10.1785/0220220086.

Ferreira, R., Buttell, F., and Ferreira, S. Ethical considerations for conducting disaster research with vulnerable populations. *Journal of Social Work Values and Ethics*, 3:379–384, 2015.

Flaherty, E., Sturm, T., and Farries, E. The conspiracy of Covid-19 and 5G: Spatial analysis fallacies in the age of data democratization. *Social Science & Medicine*, 293:114546, Jan. 2022. doi: 10.1016/j.socscimed.2021.114546.

Folch, A., Abril, C., Afanasiev, M., Amati, G., Bader, M., Badia, R. M., Bayraktar, H. B., Barsotti, S., Basili, R., Bernardi, F., Boehm, C., Brizuela, B., Brogi, F., Cabrera, E., Casarotti, E., Castro, M. J., Cerminara, M., Cirella, A., Cheptsov, A., Conejero, J., Costa, A., de la Asunción, M., de la Puente, J., Djuric, M., Dorozhinskii, R., Espinosa, G., Esposti-Ongaro, T., Farnós, J., Favretto-Cristini, N., Fichtner, A., Fournier, A., Gabriel, A.-A., Gallard, J.-M., Gibbons, S. J., Glimsdal, S., González-Vida, J. M., Gracia, J., Gregorio, R., Gutierrez, N., Halldorsson, B., Hamitou, O., Houzeaux, G., Jaure, S., Kessar, M., Krenz, L., Krischer, L., Laforet, S., Lanucara, P., Li, B., Lorenzino, M. C., Lorito, S., Løvholt, F., Macedonio, G., Macías, J., Marín, G., Montesinos, B. M., Mingari, L., Moguilny, G., Montellier, V., Monterrubio-Velasco, M., Moulard, G. E., Nagaso, M., Nazaria, M., Niethammer, C., Pardini, F., Pienkowska, M., Pizzimenti, L., Poiata, N., Rannabauer, L., Rojas, O., Rodriguez, J. E., Romano, F., Rudyy, O., Ruggiero, V., Samfass, P., Sánchez-Linares, C., Sanchez, S., Sandri, L., Scala, A., Schaeffer, N., Schuchart, J., Selva, J., Sergeant, A., Stallone, A., Taroni, M., Thrastarson, S., Titos, M., Tonelllo, N., Tonini, R., Ulrich, T., Vilotte, J.-P., Vöge, M., Volpe, M., Wirp, S. A., and Wössner, U. The EU Center of Excellence for Exascale in Solid Earth (ChEESE): Implementation, results, and roadmap for the second phase. *Future Generation Computer Systems*, 146:47–61, Sept. 2023. doi: 10.1016/j.future.2023.04.006.

Freeman, A., Dryhurst, S., and Luoni, G. Good practice recommendations: Earthquake forecast communication, 2023. http://rise-eu.org/dissemination/good-practices/oef-communication. European Horizon-2020 project RISE.

GDACS. Global Disaster Alert and Coordination System, 2023. https://www.gdacs.org/report.aspx?eventid=1357372&episodeid=1487096&eventtype=EQ. M 7.8 in Türkiye on 06 Feb 2023 01:17 UTC. Webpage.

GSLN. Geohazard Supersites and Natural Laboratories, 2023. https://geo-gsnl.org/supersites/event-supersites/active-event-supersites/kahramanmaras-event-supersite.

Haslinger, F., Basili, R., Bossu, R., Cauzzi, C., Cotton, F., Crowley, H., Custodio, S., Danciu, L., Locati, M., Michelini, A., Molinari, I., Ottemöller, L., and Parolai, S. Coordinated and Interoperable Seismological Data and Product Services in Europe: the EPOS Thematic Core Service for Seismology. *Annals of Geophysics*, 65 (2):DM213, Apr. 2022. doi: 10.4401/ag-8767.

Haven, T., Bouter, L., Mennen, L., and Tijdink, J. Superb supervision: A pilot study on training supervisors to convey responsible research practices onto their PhD candidates. *Accountability in Research*, pages 1–18, May 2022. doi: 10.1080/08989621.2022.2071153.

Heise, V., Holman, C., Lo, H., Lyras, E. M., Adkins, M. C., Aquino, M. R. J., Bougioukas, K. I., Bray, K. O., Gajos, M., Guo, X., Hartling, C., Huerta-Gutierrez, R., Jindrová, M., Kenney, J. P. M., Kępińska, A. P., Kneller, L., Lopez-Rodriguez, E., Mühlensiepen, F., Richards, A., Richards, G., Siebert, M., Smith, J. A., Smith, N., Stransky, N., Tarvainen, S., Valdes, D. S., Warrington, K. L., Wilpert, N.-M., Witkowska, D., Zaneva, M., Zanker, J., and Weissgerber, T. L. Ten simple rules for implementing open and reproducible research practices after attending a training course. *PLOS Computational Biology*, 19(1):e1010750, Jan. 2023. doi: 10.1371/journal.pcbi.1010750.

Hicks, D., Wouters, P., Waltman, L., de Rijcke, S., and Rafols, I. Bibliometrics: The Leiden Manifesto for research metrics. *Nature*, 520(7548):429–431, Apr. 2015. doi: 10.1038/520429a.

Hirsch Hadorn, G., Hoffmann-Riem, H., Biber-Klemm, S., Grossenbacher-Mansuy, W., Joye, D., Pohl, C., Wiesmann, U., and Zemp, E., editors. *Handbook of transdisciplinary research*. Springer, 2008.

Hussain, E., Kalaycıoğlu, S., Milliner, C., and Çakir, Z. Preconditioning the 2023 Kahramanmaraş (Türkiye) earthquake disaster. *Nature Reviews Earth & Environment*, 4(5):287–289, Apr. 2023. doi: 10.1038/s43017-023-00411-2.

Jordan, T. H., Chen, Y.-T., Gasparini, P., Madariaga, R., Main, I., Marzocchi, W., Papadopoulos, G., Sobolev, G., Yamaoka, K., and Zschau, J. Operational Earthquake Forecasting: State of knowledge and guidelines for implementation. *Annals of Geophysics*, 54(4), Aug. 2011. doi: 10.4401/ag-5350.

Khawaja, A. M., Hainzl, S., Schorlemmer, D., Iturrieta, P., Bayona, J. A., Savran, W. H., Werner, M., and Marzocchi, W. Statistical power of spatial earthquake forecast tests. *Geophysical Journal International*, 233(3):2053–2066, Jan. 2023. doi: 10.1093/gji/ggad030.

Klinkhamer, L. Equity, diversity and inclusivity in open research. *BMJ Open Science*, 2022.

Leonelli, S. Philosophy of open science, 2023. https://philsci-archive.pitt.edu/21986.

Louis-Charles, H. M., Howard, R., Remy, L., Nibbs, F., and Turner, G. Ethical Considerations for Postdisaster Fieldwork and Data Collection in the Caribbean. *American Behavioral Scientist*, 64 (8):1129–1144, July 2020. doi: 10.1177/0002764220938113.

Marti, M., Haslinger, F., Peppoloni, S., Capua, G., Glaves, H., and Dallo, I. Addressing the challenges of making data, products, and services accessible: An EPOS perspective. *Annals of Geophysics*, 65(2):DM212, Apr. 2022. doi: 10.4401/ag-8746.

Marti, M., Dallo, I., Roth, P., Papadopoulos, A., and Zaugg, S. Illustrating the impact of earthquakes: Evidence-based and user-centered recommendations on how to design earthquake scenarios and rapid impact assessments. *International Journal of Disaster Risk Reduction*, 90:103674, May 2023. doi: 10.1016/j.ijdrr.2023.103674.

Merow, C., Boyle, B., Enquist, B. J., Feng, X., Kass, J. M., Maitner, B. S., McGill, B., Owens, H., Park, D. S., Paz, A., Pinilla-Buitrago, G. E., Urban, M. C., Varela, S., and Wilson, A. M. Better incentives are needed to reward academic software development. *Nature Ecology & Evolution*, 7(5):626–627, Feb. 2023. doi: 10.1038/s41559-023-02008-w.

Mezinska, S., Kakuk, P., Mijaljica, G., Waligóra, M., and O'Mathúna, D. P. Research in disaster settings: a systematic qualitative review of ethical guidelines. *BMC Medical Ethics*, 17(1), Oct. 2016. doi: 10.1186/s12910-016-0148-7.

Miles, S. B. and Chang, S. E. Modeling Community Recovery from Earthquakes. *Earthquake Spectra*, 22(2):439–458, May 2006. doi: 10.1193/1.2192847.

Müller, R. and Kaltenbrunner, W. Re-disciplining Academic Careers? Interdisciplinary Practice and Career Development in a Swedish Environmental Sciences Research Center. *Minerva*, 57 (4):479–499, Apr. 2019. doi: 10.1007/s11024-019-09373-6.

National Academies of Sciences, Engineering, and Medicine. *Open Science by Design: Realizing a Vision for 21st Century Research*. National Academies Press, Aug. 2018. doi: 10.17226/25116.

Nature. PhD training is no longer fit for purpose—It needs reform now. *Nature*, 613(7944):414–414, Jan. 2023. doi: 10.1038/d41586-023-00084-3.

Orlacchio, M., Chioccarelli, E., Baltzopoulos, G., and Iervolino, I. State-Dependent Seismic Fragility Functions for Italian Reinforced Concrete Structures: Preliminary Results. In *Proceedings of the 31st European Safety and Reliability Conference (ESREL 2021)*. Research Publishing Services, 2021. doi: 10.3850/978-981-18-2016-8_660-cd.

Orru, K., Klaos, M., Nero, K., Gabel, F., Hansson, S., and Nævestad, T.-O. Imagining and assessing future risks: A dynamic scenario-based social vulnerability analysis framework for disaster planning and response. *Journal of Contingencies and Crisis Management*, Nov. 2022. doi: 10.1111/1468-5973.12436.

Panjwani, A. False social media posts are hindering earthquake relief efforts in Turkey. You can help stop that. *The Guardian*, 2023.

Paskin, N. Digital object identifier (DOI®) system. *Encyclopedia of library and information sciences*, 3:1586–1592, 2010. doi: 10.1081/E-ELIS3-120044418.

Peek, L., Tobin, J., Adams, R. M., Wu, H., and Mathews, M. C. A Framework for Convergence Research in the Hazards and Disaster Field: The Natural Hazards Engineering Research Infrastructure CONVERGE Facility. *Frontiers in Built Environment*, 6, July 2020. doi: 10.3389/fbuil.2020.00110.

Pittore, M., Wieland, M., and Fleming, K. Perspectives on global dynamic exposure modelling for geo-risk assessment. *Natural Hazards*, 86(S1):7–30, June 2016. doi: 10.1007/s11069-016-2437-3.

Pohl, C. Soft systems methodology, 2020. https://zenodo.org/record/3717356. doi: 10.5281/ZENODO.3717356.

Pohl, C., Klein, J. T., Hoffmann, S., Mitchell, C., and Fam, D. Conceptualising transdisciplinary integration as a multidimensional interactive process. *Environmental Science & Policy*, 118:18–26, Apr. 2021. doi: 10.1016/j.envsci.2020.12.005.

Pourret, O. Stop paying to be published Open Access – a French perspective. *European Science Editing*, 48, Aug. 2022. doi: 10.3897/ese.2022.e90113.

Provost, L., Donato, F., Tóth-Czifra, E., Dumouchel, S., Blotière, E., and Chen, Y. Open Science Training in TRIPLE. *Open Research Europe*, 3:39, Feb. 2023. doi: 10.12688/openreseurope.15430.1.

Pärli, R., Stauffacher, M., Seigo, S., Probst, M., and Pearce, B. Designing interventions for sustainable change in a real-world laboratory. *Environment, Development and Sustainability*, Sept. 2022. doi: 10.1007/s10668-022-02659-y.

Raška, P. On Epistemic Dissonance: Contesting the Transdisciplinary Disaster Risk Reduction Education, Research, and Practices. *Frontiers in Earth Science*, 9, Jan. 2022. doi: 10.3389/feart.2021.818361.

Rowe, C., Agius, M., Convers, J., Funning, G., Galasso, C., Hicks, S., Huynh, T., Lange, J., Lecocq, T., Mark, H., Ragon, T., Rychert, C., Teplitzky, S., Den Ende, M., and Okuwaki, R. The launch of Seismica: A seismic shift in publishing. *Seismica*, 1(1), Nov. 2022. doi: 10.26443/seismica.v1i1.255.

Ryan-Davis, J. and Scalice, D. Co-Creating Ethical Practices and Approaches for Fieldwork. *AGU Advances*, 3(6), Dec. 2022. doi: 10.1029/2022av000762.

Sample, I. Harvard University says it can't afford journal publishers' prices. *The Guardian*, 24(1):20–32, 2012.

Savran, W., Bayona, J., Iturrieta, P., Asim, K., Bao, H., Bayliss, K., Herrmann, M., Schorlemmer, D., Maechling, P., and Werner, M. pyCSEP: A Python Toolkit for Earthquake Forecast Developers. *Seismological Research Letters*, 93(5):2858–2870, July 2022a. doi: 10.1785/0220220033.

Savran, W., Werner, M., Schorlemmer, D., and Maechling, P. pyCSEP: A Python Toolkit For Earthquake Forecast Developers. *Journal of Open Source Software*, 7(69):3658, Jan. 2022b. doi: 10.21105/joss.03658.

Schorlemmer, D., Beutin, T., Cotton, F., Ospina, N. G., Hirata, N., Ma, K.-F., Nievas, C., Prehn, K., and Wyss, M. Global Dynamic Exposure and the OpenBuildingMap - A Big-Data and Crowd-Sourcing Approach to Exposure Modeling. Mar. 2020. doi: 10.5194/egusphere-egu2020-18920.

Schymanski, E. L. and Schymanski, S. J. Water science must be Open Science. *Nature Water*, 1(1):4–6, Jan. 2023. doi: 10.1038/s44221-022-00014-z.

Stablein, M., Gonzalez Cruz, J., Fidan, E., Talbot, J., Reed, S., Walters, R., Ogunyiola, A., Fernández Frey, M., Ramirez, M., Rosado Casanova, B., Heemstra, J., Marshall, A., and Rodríguez, L. Compound[ing] disasters in Puerto Rico: Pathways for virtual transdisciplinary collaboration to enhance community resilience. *Global Environmental Change*, 76:102558, Sept. 2022. doi: 10.1016/j.gloenvcha.2022.102558.

Toomey, A. H. What happens at the gap between knowledge and practice? Spaces of encounter and misencounter between environmental scientists and local people. *Ecology and Society*, 21 (2), 2016. doi: 10.5751/es-08409-210228.

UNDRR. *Global Assessment Report on Disaster Risk Reduction 2022: Our World at Risk: Transforming Governance for a Resilient Future*. United Nations, May 2022a. doi: 10.18356/9789210015059.

UNDRR. Prospects and challenges of transdisciplinary research approaches for managing and communicating climate-related risks. In *United Nations Office for Disaster Risk Reduction (UNDRR)*. Geneva, Switzerland, 2022b.

UNESCO. Open Science, 2022. https://www.unesco.org/en/natural-sciences/open-science.

Vienni Baptista, B., Fletcher, I., Maryl, M., Wciślik, P., Buchner, A., Lyall, C., Spaapen, J., and Pohl, C. Final report on understandings of interdisciplinary and transdisciplinary research and factors of success and failure (SHAPE-ID), 2020. https://

zenodo.org/record/3824839.

Wilkinson, M. D., Dumontier, M., Aalbersberg, I. J., Appleton, G., Axton, M., Baak, A., Blomberg, N., Boiten, J.-W., da Silva Santos, L. B., Bourne, P. E., Bouwman, J., Brookes, A. J., Clark, T., Crosas, M., Dillo, I., Dumon, O., Edmunds, S., Evelo, C. T., Finkers, R., Gonzalez-Beltran, A., Gray, A. J., Groth, P., Goble, C., Grethe, J. S., Heringa, J., 't Hoen, P. A., Hooft, R., Kuhn, T., Kok, R., Kok, J., Lusher, S. J., Martone, M. E., Mons, A., Packer, A. L., Persson, B., Rocca-Serra, P., Roos, M., van Schaik, R., Sansone, S.-A., Schultes, E., Sengstag, T., Slater, T., Strawn, G., Swertz, M. A., Thompson, M., van der Lei, J., van Mulligen, E., Velterop, J., Waagmeester, A., Wittenburg, P., Wolstencroft, K., Zhao, J., and Mons, B. The FAIR Guiding Principles for scientific data management and stewardship. *Scientific Data*, 3(1), Mar. 2016. doi: 10.1038/sdata.2016.18.

REVIEWED OPINION
doi:10.26443/seismica.v2i2.242

SEISMICA

A Call to Action for a Comprehensive Earthquake Education Policy in Nepal

G. Hetényi * [1], **S.Subedi** [1,2]

[1]Institute of Earth Sciences, University of Lausanne, Lausanne, Switzerland, [2]Seismology at School in Nepal, Pokhara, Nepal

Author contributions: *Conceptualization*: G. Hetényi, S. Subedi. *Resources*: S. Subedi, G. Hetényi. *Writing - original draft*: G. Hetényi. *Writing - review & editing*: G. Hetényi, S. Subedi.

Production Editor:
Christie Rowe
Handling Editor:
Danielle Sumy
Copy & Layout Editor:
Anant Hariharan

Signed reviewer(s):
Rémy Bossu, Susan Hough, Beth Pratt-Sitaula, Mina Adhikari

Received:
September 16th, 2022
Accepted:
June 16th, 2023
Published:
August 17th, 2023

Abstract Earthquakes in Nepal are among the most damaging natural hazards, claiming many lives and causing more widespread destruction than any other natural hazard. Yet, due to other difficulties and challenges, earthquakes are at the forefront of people's attention only after major events, such as the 1934 or 2015 earthquakes. As a result, current preparedness of the population to earthquakes is far below the optimal level. This calls for an immediate and widespread educational effort to increase awareness and to raise the current young generation responsibly. After describing the current status of earthquake education at various school levels in Nepal, we here propose a series of actions to undertake towards an official education policy, starting from full openness and use of languages, via coordination and teacher's training, to the content, frequency and style of curriculum. We conclude on a timeline of actions, which have various lengths but should start today. We hope that by sharing our researcher and educational experience and thoughts, the actual preparation of the earthquake education policy for Nepal will start being developed under a dedicated team. Elements of the proposal presented here can be used and adapted to other regions at risk around the world.

सारांश **(Nepali)**

नेपाल भौगोलिक रुपमा उच्च भूकम्पीय जोखिममा पर्छ साथै अन्य प्राकृतिक प्रकोपको तुलनामा धेरै ज्यान लिने र धेरै क्षति पुर्याउने प्राकृतिक प्रकोप भूकम्प हो । मानिसहरुको चेतनास्तर, आर्थिक स्थितिलगायत विभिन्न कठिनाइहरुले गर्दा भूकम्प सुरक्षा जनताको प्राथमिकतामा पर्दैन । जव ठुला (वि.स.२०७२ सालको जस्तै) तथा महाभूकम्प (वि.स.१९९० सालको जस्तै) हरु नेपालमा जान्छन तव मानिसहरु यसको बारेमा सचेत भएको जस्तो देखिन्छ । वर्तमान अवस्थामा मानिसहरुले भूकम्प सुरक्षाको लागि गरेको तयारी पर्याप्त छैन । फलस्वरूप, वर्तमान युवा पुस्तालाई भूकम्प सुरक्षामा जागरुक गराउन तथा भूकम्प तयारीमा जिम्मेवार बनाउनको लागि तत्काल र व्यापक शैक्षिक प्रयासको आवश्यकता छ । हामीले नेपालका विभिन्न विद्यालयमा भूकम्प शिक्षाको वर्तमान अवस्थाको बारेमा अध्ययन गरेका छौं साथै उक्त अध्ययनपश्चात भूकम्प सुरक्षाको लागि आधिकारिक शिक्षा नीति निर्माणको लागि आवश्यक योजनाहरु पनि प्रस्ताव गरेका छौं । हाम्रा प्रस्तावहरुमा स्थानीय तथा विभिन्न भाषाको प्रयोग, नि: शुल्क शैक्षिक सामाग्रीको उपलब्धता, सम्बन्धित विषयमा शिक्षकहरुलाई तालिम र तालिमको निरन्तरता, तथा पाठ्यक्रम परिमार्जन र पाठ्यक्रमको शैली आदि छन् । हामीले प्रस्ताव गरेका शैक्षिक नीति निर्माणको लागि गर्नुपर्ने कामहरु फरक फरक समय र अवधिमा सम्पन्न गर्न सकिन्छ । नयाँ योजनाहरु कार्यान्वयन गर्न र प्रतिफल आउन धेरै समय लाग्ने भए पनि उक्त योजनाहरु तत्काल सुरु गर्न सकिने प्रकारका छन् । नेपालको लागि भूकम्प शिक्षा नीति निर्माणको वास्तविक तयारीमा हाम्रा अनुसन्धानका परिणाम, शैक्षिक अनुभव तथा सोचहरु उपयोगी हुनेछन र नीति निर्माणको तयारी एक छुट्टै टोलीले गर्नेछ भन्ने आशा लिएका छौं ।यहाँ प्रस्तुत भूकम्प शिक्षा नीति निर्माण प्रस्तावहरु विश्वमा भूकम्पको जोखिम रहेका अन्य देशहरुमा पनि प्रयोग तथा अनुशरण गर्न सकिन्छ ।

Introduction

Earthquakes in Nepal are the natural hazard with one of the highest rates of casualties and the most powerful and widespread destruction capability (Figure 1; Subedi, 2020). This is not only an observation of the past, but because the collision between the India lithospheric plate and the Tibetan Plateau as well as the related geological processes will continue the same way over millions of years, it is also Nepal's future. However, the preparedness level of Nepal's population to earthquakes is poor, and clearly below the risk represented by earthquakes. This calls for a multitude of actions, among which the introduction of a comprehensive education policy is the one that will reach the entire society.

Earthquake research and information sent to schools and society in Nepal have been ongoing for decades, yet to our knowledge there is no country-wide effort nor policy that would regulate and coordinate actions in this theme. The National Earthquake Monitoring and Research Centre (NEMRC) has been active for more than four decades, and does an excellent job locating earthquakes and sending information to the government and

*Corresponding author: gyorgy.hetenyi@unil.ch

Figure 1 Examples of damage from the 2015 Gorkha earthquake. (a) Gorkha Barpak (epicenter village) before and after the Gorkha earthquake when the earthquake destroyed almost all houses (Adhikari, 2021). (b) Historic Kathmandu tower "Dharahara" before and after the 2015 Gorkha earthquake (Shrestha, 2016).

the public. However, because of the lack of human resources and direction from the government, NEMRC is currently not involved in any earthquake awareness activity. The National Society for Earthquake Technology (NSET) has been working in Nepal to build earthquake-safe schools so that local communities develop their capacities to cope with earthquakes. The School Earthquake Safety Program has been running since 1997 to protect schools against earthquakes. However, these efforts remained primarily focused on the Kathmandu region to assess school buildings' structural and non-structural vulnerability and retrofitting, and have not reached the countryside, which is in dire necessity of development.

Kathmandu Valley has benefited from a few case studies for earthquake risk management and risk mitigation. With the main objectives of formulating a plan for earthquake disaster mitigation and protecting life and property, the Japan International Cooperation Agency (JICA) carried out a study in 2001-2002. Their report suggested establishing an earthquake early warning system, a municipality disaster management institution, building code improvement, and a comprehensive database for earthquake mitigation (Dixit et al., 2000). Similarly, a project in the Kathmandu valley was implemented by NSET in association with GeoHazards International (USA). While a building code has been published, its implementation would need to be at a significantly higher level across the country.

In the meantime, the Government of Nepal has initiated an annual National Earthquake Safety Day (NESD). It was first held in 1999, on the day of the 1934 earthquake: the 2nd day of the Magh month of the Nepali calendar (corresponding to around mid-January), with the goal to raise public awareness about earthquakes (A.D.C.P., 2000). Another project, called SAFER Nepal, led by the University of Bristol (UK), aims to develop a comprehensive scheme for enhancing the seismic safety and resilience of school buildings in Nepal (www.safernepal.net). Kathmandu's students, teachers, and residents benefited from the Nepal Red Cross Society training in essential disaster management planning in 2010 (https://reliefweb.int/report/nepal/training-schoolchildren-earthquake-preparedness).

After the most recent major earthquake in 2015, the Gorkha earthquake Memorial Day has been added to the list of annual events and earthquake-related official programs. The implementation of a revised building code became mandatory for new constructions, mainly in big cities and municipalities. In 2015, the Nepal Academy of Science and Technology (NAST) installed an Earthquake Early Warning system for testing purposes with the support of the Chinese Government. Regarding earthquake education, a minor update in the official curriculum added a new chapter for grade 12 students who chose the optional physics class, entitled "Recent Trends in Physics: Seismology". In general, the theme of earthquakes is widely covered in national and mostly local newspapers, television, and social media if there is an earthquake of felt level.

However, even after the 2015 Gorkha earthquake, when national and international non-governmental organizations tried to initiate earthquake preparedness projects around Kathmandu for local people, the efforts remained geographically rather limited. In 2015, the Government of Nepal established the National Reconstruction Authority to oversee and fast-track reconstruction work, which has now merged with the National Disaster Risk Reduction and Management Authority (NDRRMA). In addition, the Asian Development Bank (ADB) approved the Earthquake Emergency Assistance Project and more stable schools were constructed to meet disaster risk-resilient standards (see at http://dx.doi.org/10.22617/BRF220261-2). USAID and UNICEF also contributed to disaster risk reduction training to establish education in earthquake-affected districts. Many of these projects and programs have a limited duration, however, reflecting the difficulty to secure long-term foreign funding.

In 2018, the Government of Nepal published the National Policy for Disaster Risk Reduction (MoHA, 2018) with the support of the United Nations Development Programme (UNDP). The document is comprehensive, and mentions awareness raising programs. The policy itself (section 7) lists 59 points, among which "education" is mentioned four times. The most prominent and fitting is point 7.1: *"The subject of disaster risk will be incorporated in the curriculum of school and the higher level of education."* This goal is outstanding, but the document gives very little concrete elements describing what is meant, and how it will be implemented. In practice, in the field, we could not find palpable elements reflecting the NPDRR.

Overall, while every project effort towards increased awareness is worthy and laudable, Nepal as a whole still lacks an implementation concept and application scheme of the above policy that would efficiently bring forward the whole society's preparedness. It is to foster the change underlined by the NPDRR that we have written the present document. We have not been responsible for the full development of any legally binding, administrative policy definition so far. However, our intention with this paper is not just mere dreaming: it is based on various backgrounds and experiences. These range from extensive fieldwork in Nepal, especially the initiation and implementation of the Seismology at School in Nepal program (Subedi (2020); www.seismoschoolnp.org), developing Memoranda of Understanding for the scientific cooperation of dozens of research institutions (e.g. Hetényi et al., 2018), and teaching experience at all levels from elementary school (age 6) to university and adults' dedicated training.

This paper begins with describing <u>why</u> earthquake education is needed, with the intention for Nepal to develop its corresponding educational policy and its implementation in a convincing manner. A list of proposals for <u>what</u> to develop is discussed, together with thoughts on <u>how</u>. This development is highly relevant for better preparedness of the public, and for minimizing damage at future earthquakes. As one of our colleagues, Mark Vanstone, rightly said at a workshop: "Earthquake education in the UK is simply a matter of motivation. Proper earthquake education in Nepal is a question of death or life."

1 Data on earthquakes and education

1.1 Earthquakes

It is the same geological processes which have formed the Himalaya that cause earthquakes. These processes have happened for tens of millions of years, and from that point of view even devastating earthquakes happen often. However, compared to a human life's timescale, which is measured in just tens of years, devastating earthquakes occur relatively rarely. This is only an apparent perception. When reading the historical and geological records of the past hundreds to few thousand years, we find numerous large earthquakes that have devastated the region of Nepal (Table 1). Therefore, and because such geological processes repeat in time, we can be 100% sure that similar earthquakes will happen again and again, it is only a question of time. As a consequence, adequate preparation is sorely needed.

For those to whom the above comparison of times is too far-fetched, let us recall the main elements of the 2015 Gorkha earthquake: despite that the magnitude was not the highest of the region (7.8), and that Kathmandu Valley has experienced fairly little damage, nearly 9000 people died (http://drrportal.gov.np/), and the financial damage amounted to 50% of Nepal' annual Gross Domestic Product. Similar or worse events are likely to happen within the next human generations' time span.

1.2 Education in Nepal

We base our assessment on the current education situation in Nepal. This is rooted in the National Cur-

Date	Magnitude (M_w)	Max. intensity	Region	Summary	Source references
2015.05.12	7.2	VII	Kodari	• Destructive landslide in Langtang valley • More damage in Sindhupalchok	U, K15, A16
2015.04.25	7.8	IX	Gorkha	• ∼ 9000 casualties • ∼ 22 000 injured • ∼ 886 000 affected families • ∼ 7 billion USD damage (50% of annual GDP)	A15, P17, M15, U
2011.09.18	6.9	?	Sikkim	• Total of 111 casualties of which 6 deaths in Nepal • Epicenter close to Nepal border	IG
1988.08.20	6.8	?	Udayapur	• >700 casualties • >6000 injured • >20 000 houses destroyed	IG
1980.08.29	6.5	?	Bajhang	• >170 casualties • >10 000 houses destroyed	IG
1936.05.27	6.9	?	Rukum	-	IG
1934.01.15 (became Nepali earthquake safety day)	8.4	IX	Eastern Nepal	• >8500 deaths in Nepal • >7200 deaths in India • >80 000 houses destroyed in Nepal	CM97, S13, S16
1833.08.26	7.6	VIII	Central Nepal	• ∼500 casualties	AD04
1808.06.04	?	?	Kathmandu	• Major destruction	R35, P02
1505.06.06	> 8	XII	Western Nepal	• Epicenter close to Mustang • Felt in India and Tibet	I99, AJ03
1344.09.14	?	XII	Central Nepal	• Major destruction • The King died	P02
1255.06.07	?	XII	Eastern Nepal	• One third of the population killed • The King died • Major destruction	P02

Table 1 Overview of significant earthquakes known to have occurred in Nepal since 1223 A.D. Our records are incomplete and further events occurred earlier in history. Abbreviation of source references: U – USGS, K15 – Kargel et al. (2016), A15 – Adhikari et al. (2015); P17 – Prajapati et al. (2017); M15 – MoHA (2015); IG – ISC-GEM Bondár et al. (2015); CM97 – Chen and Molnar (1977); S13 – Sapkota et al. (2013); S16 – Sapkota et al. (2016); AD04 – Ambraseys and Douglas (2004); R35 – Rana (1935); P02 – Pant (2002); I99 – Iyengar et al. (1999); AJ03 – Ambraseys and Jackson (2003)

riculum, which prescribes the minimum level themes and topics to be taught, in Nepali language (except for English subjects) mostly in public schools, but also in English language in private schools. Nowadays, some public schools have initiated their classes in both languages. This baseline curriculum, however, can be very differently implemented in public and private schools, which often use different books and educational material. Moreover, the implementation of the National Curriculum varies across levels with different bodies intervening in its definition:

- The Curriculum Development Centre (https://moecdc.gov.np/) of the Ministry of Education has the mandate to develop curricula, textbooks, and educational materials for school education (classes 1- 12).
- At the Elementary level (classes 1 to 8), the local governments have explicit authority to develop tailored curricula for local subjects (credit hours: 4

Education level	Grades	Relevant authorities	Seeds of advice
Primary	1-8	• CDC of the Ministry of Education • Local Government	1. Define nation-wide earthquake education curriculum, add content with respect to grade/age of students 2. Introduce regional and local examples
Secondary	9-12	• CDC of the Ministry of Education	1. Add Seismology content/chapter to the Physics class 2. Include earthquakes in a compulsory class, for example social studies
University	Bachelor and above	• CDC of the University	1. Initiate a Department for Earth Sciences 2. Develop an earthquake preparedness plan 3. Include earthquakes in a compulsory subject in all degrees 4. Form teachers' teachers to increase the number of trained teachers in primary and secondary schools

Table 2 Overview of education levels, authorities and seeds of advice for curriculum development. Abbreviation: CDC – Curriculum Development Centre.

out of 32), hence, they can shape the contents. There are 753 local governments, inherently leading to disparities across Nepal.

- At the Secondary level (classes 9 to 12), the Curriculum Development Centre can shape the curricula. Therefore, we can expect more similarity between schools.
- At the University level, it is each university's Curriculum Development Centre (for example, https://tucdc.edu.np/, https://pu.edu.np/academics/cdc/) or special committee formed by the university who can develop, modify and execute the curriculum, which can lead to rather homogeneous teaching provided there is agreement on the source of contents.

These information are summarized by education level in Table 2, together with seeds of advice for curriculum development.

Compared to the administration hierarchy of Nepal, one can observe that the Province Governments are not directly involved in the curriculum shaping. We find that the overall organization landscape is rather complex, and that the introduction of new educational content requires coordination between these different bodies. We anticipate this is better done as early as possible in the process, and holds not only on the content, but also on the frequency of teaching a given topic in the classroom.

2 Methodology

The rationale we present in this paper to suggest key elements for developing an educational policy is based on: a broad, personal experience of growing up in Nepal and following the entire educational pathway there for the second author; extensive field experience in scientific research for the first author; and in-depth exchanges with teachers and students in the frame of the Seismology at School in Nepal educational program we have initiated and carried out together since 2017. These latter efforts have not only covered purely educational aspects, but we have also investigated the Hindu religious perspective on earthquakes (Subedi and Hetényi, 2021), we have triggered and worked across the disciplines to develop and to broadcast the Nepali Earthquake Awareness Song (YouTube link: https://youtu.be/ymE-lrAK0TI; Figure 2), and recently inspired the realization of a new card game (Figure 3) to sensitize students to the importance of earthquake preparedness.

Beyond these experiences in Nepal, we have also gathered relevant inputs from around the world, through publications (e.g., "The Power of Citizen Seismology: Science and Social Impacts" special volume, available at https://www.frontiersin.org/research-topics/10854/the-power-of-citizen-seismology-science-and-social-impacts#articles), other online information, and personal discussions with experts in this domain, mainly the UK, France, Switzerland, the USA, Hungary, and Italy. It is based on all this information that we have discussed and developed the proposals for a modern earthquake education policy tailored to Nepal.

3 Proposals for and Discussion on an Education Policy

3.1 Openness

We put a large emphasis on full and immediate openness of all educational material. Part of the research community, including seismologists, still employs closed or embargoed data, as well as publications that are only available based on subscription. This is not only unnecessary but also counterproductive in the educational context. The education policy, all educational material and anything that helps efficient knowledge transfer should be publicly, freely, and immedi-

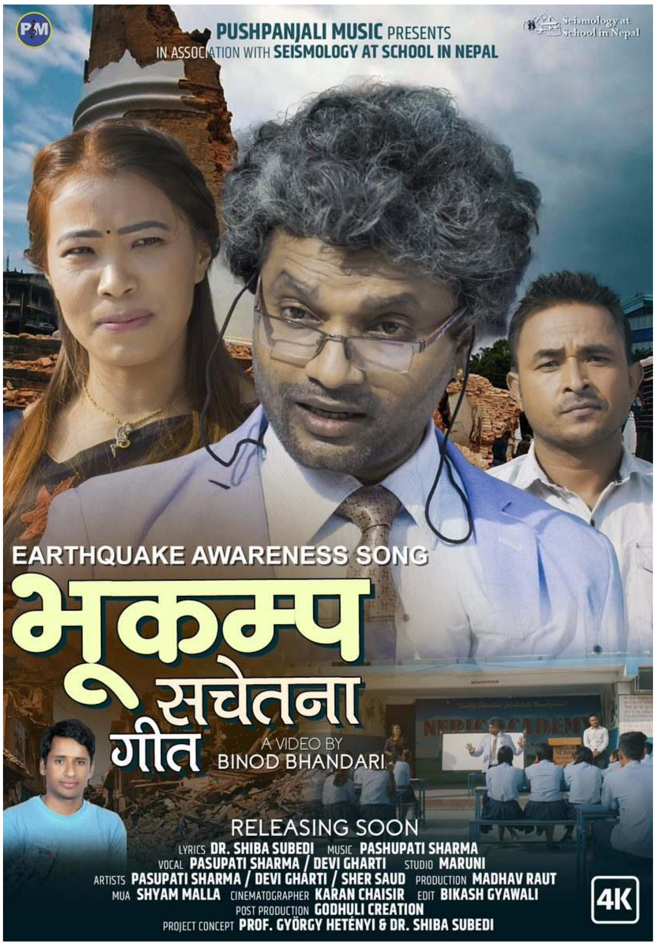

Figure 2 Poster of the Earthquake Awareness Song, an audio-video document to increase earthquake preparedness in Nepal. Lyrics in Nepali and in English are available in the video's description (https://youtu.be/ymE-lrAK0TI).

ately available in locations where users find it without obstacles. We recommend a central website with high-quality, digital and searchable information at least in Nepali and English languages.

3.2 Language

Although the official language is Nepali, we recommend maintaining English as the second language in which the policy and the curriculum are prepared and published. The English version of the policy will facilitate its future update by international experts. For greater inclusivity, we also propose that the main elements of earthquake preparedness, e.g. the "Drop – Cover – Hold" principle, are prepared in every written language and dialect in Nepal (there are 17 with minimum 100 000 speakers each (Central Bureau of Statistics, 2012)). For all other non-written languages and dialects (over 100), we propose that local teachers spread the information orally, or through the radio, TV, and voice messages if these are technically possible and available for the target population.

3.3 Coordination and teacher's training

As described under Data (section 1), education coordination in Nepal involves several actors and layers of hierarchy, such as local government, Curriculum Development Centre, etc. The introduction of a new education theme (earthquakes) in a comprehensive way therefore requires efficient coordination between these groups. Since the topic is in some ways new, and could be initially regarded as out of the ordinary, it is extremely important that the right experts are involved in the coordination. But how can these experts be identified if there is currently no deep-reaching earthquake education in Nepal?

We see this current proposal as the first step to resolve this apparent chicken-or-egg problem. There exists sufficient information on earthquakes to make the first step, to create the policy and to prepare the educational material. However, a very important second step must follow to ensure a sustainable system: the training of teachers, who are able to teach the new theme at every level and in each school. A one-time training of elementary and secondary school teachers is not sufficient. Training should be regular, and for that to be implementable, a large number of expert teachers are required across the country. This calls for the introduction of earthquake science as a proper program at the university level. The current Geology curriculum and the current Physics curriculum are insufficient and unable to fulfill this goal, as earthquake science (seismology) is part of geophysics, which falls between the two. Therefore, for the sustainable implementation of earthquake education policy, a university level geophysics program is desired.

Ultimately, this requires active researchers and teachers to be hired at the University level, to serve as teachers' teachers. This is how most teachers in Western countries are formed: they follow higher level studies at Pedagogical Schools or Teacher Education programs. This idea is not new; for example it has already been employed – in very different contexts – at the end of the 18th century in France (see the *École Normale Supérieure*), and in the 19th century in Hungary (the *József Eötvös Collegium*). The difference to an entire teacher's training curriculum for the current goal of earthquake education in Nepal would be that teachers follow short upgrades or block course to familiarize themselves with the topic and how it can be taught in various classes. In other words, it could become teachers' professional development to attend such trainings, just as they could attend such events on climate change, geopolitics etc. In our experience with workshops organized for teachers in the frame of the Seismology-at-School-in-Nepal program, 1-2 days for 40-100 attendees can be efficient, and also provide a useful venue for teachers to exchange between them. In Nepal, such an effort should be aided by the National Earthquake Monitoring and Research Centre and the Nepal Academy of Science and Technology, but because neither of these are educational institutions nor can they host large number of students, it remains the Universities' role to lead higher education training.

3.4 Introduction to the curriculum, diffusion of information, and frequency

The primary way of spreading relevant earthquake and preparedness information to the society should remain the schools. We think that it is not the amount, but the frequency and regularity of teaching that will make a difference. Practically, the amount of material to teach to make an impact is not enormous, but whether the students are exposed to it once a year or once a month does make a huge difference. Teachers participating in our Seismology at School in Nepal program confirm this; a survey taken with hundreds of students before the start of the program as well as 2 years after show that the teaching program has already made a positive impact (Subedi et al., 2020b).

A step in the program-building process will be a comprehensive review of existing programs, practice and effective strategies. Nevertheless, a few points can already be put forward here. In the Elementary levels 1-4, we propose monthly or bi-monthly activities, in a subject that connects to the environment or geography. Any kind of game, for example our educational card game on earthquakes (Figure 3) could be included. In levels 5-8, the frequency could become monthly, and history and social science classes could also include topics related to earthquakes. In the Secondary level (levels 9-12), the compulsory Sciences or Social sciences class could lead, possibly helped by computer science, for example for the search and visualization of earthquake information, or a hands-on exercise of simple earthquake location using the tutorial provided by Subedi et al. (2021). The University level teaching should encompass the full spectrum of information, ideally combined with some computer programming exercises.

At all levels, the students should be shown where the Emergency Meeting Point (Figure 4) of their building/school campus is, and regular earthquake evacuation drills should be performed: run outside if on the ground floor, "Drop-Cover-Hold" if on upper floors. Schools that have the opportunity to use a low-cost seismometer can develop various activities for all age classes around those (Subedi et al., 2020a).

Beyond the school frame, numerous other pathways exist to inform the entire society. Obviously, a selection needs to be made, so that this information forms an official, recognized channel, not too frequently, but in a focused, to-the-point manner. These pathways include social media (e.g., Facebook, Twitter, Instagram), governmental television channel (Nepal TV), radio, private televisions, GSM mobile voice message, as well as internationally used and acknowledged information distribution such as "Recent Earthquake Teachable Moments" by the EarthScope Consortium (Bravo and Hubenthal, 2016) and the "@LastQuake" Twitter bot by EMSC (Chen et al., 2020; Bossu et al., 2023). Here again, the emphasis is on regularity. Finally, all relevant information should be available digitally in an open website.

Figure 3 Some of the cards from the earthquake card game "Beat the Quake". The game was developed in 2021 for the Seismology at School in Nepal program (initial ideas and support: György Hetényi and Shiba Subedi, development and testing: Gergely Szakács, graphics: Levente Forgács).

Figure 4 Emergency assembly point sign in Nepali and English, developed and implemented by the Seismology at School in Nepal program.

3.5 Respect of religious and traditional beliefs, social context

Although we have anticipated this topic before starting our Seismology at School in Nepal, we have encountered a broader range of questions in the field regarding the scientific approach to earthquakes, and how they compare with local beliefs. Although most school students (and people in general) can likely be convinced about the geological approach to earthquakes, one should avoid any conflicts with those who strongly believe in other explanations of earthquakes. Teachers should be aware of this potential source of confrontation, and instead of contrasting scientific and traditional interpretations, they could present both and initiate discussion. A description of how Hindu texts mention earthquake phenomena is presented in Subedi and Hetényi (2021). Adapting this point to other religious contexts around the worlds requires some research and discussion with historians, theologists and sociologists. Furthermore, the perception of hazard and risk in the local communities can be researched further to improve preparedness (e.g. Adhikari et al., 2018).

3.6 Alerting

In Nepal the authority to observe earthquakes and to report them to the government is the National Earthquake Monitoring and Research Centre. Alerts are issued to government institutions once a noteworthy earthquake is identified and confirmed. Public alert is currently not implemented, as it requires the preparation, implementation, and technical testing of an adequate earthquake early warning system. This is a long-term undertaking falling outside the scope of an educational policy; however, the types of alert systems could already be mentioned at school so that future generations are familiar with those. Alert pathways include dedicated sirens, voice messages, television and radio broadcast interruption, SMS through mobile phone, and dedicated smartphone apps. They can be issued nationally, regionally, or locally. It is highly important to discuss the available time to react after receiving an alert, and what false alerts and missed alerts are.

3.7 Proposed timeline

The compilation and implementation of an earthquake education policy requires numerous steps, which, in duration, range between very short to very long.

The initiation of policy making would ideally start very shortly. A dedicated group should dress a more detailed picture of the Nepali education landscape, based on this paper but with further input across the country and the authorities.

The development of the curriculum content can be established in the timescale of a year for the pilot ideas. Likewise, the first implementation could follow relatively shortly, with the most important elements provided to all teachers.

Three tasks take longer than one or two years. Practically, to prepare, print and distribute the updated schoolbooks, with information on earthquake science and practical steps to increase preparedness. Then, the establishment of successful organizational unit within the University frame, to provide research capacity and teachers' teachers, is a multi-year process. Finally, to rigorously test and adapt an effective educational strategy, which may require years and perseverance.

Nevertheless, there is no time to delay the beginning of the process. Earthquakes are unpredictable and institutional preparation and education in this matter should have already started.

3.8 Considerations of HOW to proceed

It is certainly easier to summarize <u>why</u> and <u>what</u> is needed in front of a given challenge, compared to the way it should be implemented. Indeed, many of our colleagues – and the Reviewers – wondered <u>how</u> such goals can be achieved, especially with limited resources. Our rationale below is based on two main observations:

- Projects and programs led from abroad are almost exclusively limited in time. This is because it is incredibly difficult, even for relatively rich countries, to obtain long-term financial support flowing to another region on Earth.

- Adapting educational plans is relatively cheap. It does not require much money to update and improve what is regularly taught in the classroom. Coordination between authorities and schools, as well as updating the teaching material does require manpower, but the Full-Time-Employee need to cover these tasks is negligible compared to the number of administrators or teachers.

Therefore, we argue that the development and implementation of educational policy is not a question of financial resources, but of political and personal will. Moreover, since it has to be a long-term effort in Nepal, it is best led by a Nepali authority or institution. For example (and not a recommendation): the Ministry of Education could take the lead and develop the policy and suggest overall implementation steps together with Nepal Policy Institute. Then, the Ministry of Education could invite provincial and local government representatives, University Rectors/Presidents, representatives of NEMRC, NAST, NSET and of the Seismology-at-School-in-Nepal program, to form a council where further steps of implementation are defined. Foreign help for well-defined tasks with a clear timeline, whether it is for adding up-to-date content, or to bring educational tools to schools, can be solicited, and has good chances to go through as one-time proposals with development agencies once education is under the spotlight of a dedicated educational policy. This should be relatively straightforward to advertise under UN's Sustainable Development Goals, especially #4 "Quality Education".

4 Conclusions

Considering the tragic history and the great threat of devastating earthquakes in Nepal, as well as the poor level of preparedness, we urge the development of an earthquake education policy. The theme of earthquakes should be added to regular teaching activities as soon as possible. The main challenge is not the development of an overly detailed program, but the frequency of mentioning earthquakes and protective measures at school. A small but regular effort will lead to long-term and broad-reaching preparedness of the population. In this paper we gathered information and proposals on why such a policy is needed, and what we recommend to be included. The "how", or the practical implementation, should go hand in hand with the actual development of the earthquake education policy by a dedicated commission or institution. Our general experience in earthquakes and in teaching led us to draft this paper, with the intention for it to serve as the baseline for the corresponding policy formulation for Nepal. This work will certainly benefit from the experience of countries that have advanced in this domain (e.g., Japan), and elements of a successful Nepali earthquake education policy can be adapted to other regions of high seismic hazard around the world.

A bullet-point summary for policymakers closes this work:

- There is a current policy void in terms of earthquake education in Nepal.
- Earthquake education should be comprehensive, fully open and accessible.
- Actors of curriculum definition and implementation across Nepal should coordinate efficiently.
- The need for teachers' teachers is best realized as an organizational unit within a University.
- Regular and frequent teaching of short but diverse, age-adapted activities are recommended.
- Religious and traditional beliefs should be respected.
- Information should be diffused to the entire society, not only to schools.
- The definition of the main actors in leading this policy writing should start now.

Acknowledgements

We are grateful to teachers who shared their real-life experiences with us throughout the years of the Seismology at School in Nepal program. We thank all reviewers for the advice and opinions: Mina Adhikari, Rémy Bossu, Beth Pratt-Sitaula as well as Susan Hough, those feedbacks have improved the content and presentation of this publication. We are grateful to Danielle Sumy for her editorial handling and the entire Seismica team for their work and commitment.

Competing interests

The authors declare having no competing or conflicting interest of any kind.

References

A.D.C.P. Project Completion Report of the Kathmandu Valley Earthquake Risk Management Project. Asian Disaster Preparedness Center, 2000. https://www.adpc.net/igo/category/ID187/doc/2013-lPGs38-ADPC-Kathmandu_Valley_Earthquake_Risk_Management_Project.pdf.

Adhikari, L. Seismicity associated with the April 25, 2015, Gorkha earthquake in Nepal: Probing the Himalayan Seismic Cycle. PhD thesis, University of Paris, France, 2021.

Adhikari, L., Gautam, U., Koirala, B., Bhattarai, M., Kandel, T., Gupta, R., Timsina, C., Maharjan, N., Majarjan, K., Dahal, T., Hoste-Colomer, R., Cano, Y., Dandine, M., Guilhem, A., Merrer, A., Roudil, P., and Bollinger, L. The aftershock sequence of the 2015 April 25 Gorkha–Nepal earthquake. *Geophysical Journal International*, 203(3):2119–2124, 2015. doi: 10.1093/gji/ggv412.

Adhikari, M., Paton, D., Johnston, D., Prasanna, R., and McColl, S. Modelling predictors of earthquake hazard preparedness in Nepal. *Procedia Engineering*, 212:910–917, 2018. doi: 10.1016/j.proeng.2018.01.117.

Ambraseys, N. and Douglas, J. Magnitude calibration of north Indian earthquakes. *Geophysical Journal International*, 159(1): 165–206, 2004. doi: 10.1111/j.1365-246X.2004.02323.x.

Ambraseys, N. and Jackson, D. *A note on early earthquakes in northern India and southern Tibet*. Current Science, 2003.

Bondár, I., Engdahl, E., Villaseñor, A., Harris, J., and Storchak, D. ISC-GEM: Global Instrumental Earthquake Catalogue (1900-2009): II. *Location and seismicity patterns. Physics of the Earth and Planetary Interiors*, 239:2–13, 2015. doi: 10.1016/j.pepi.2014.06.002.

Bossu, R., Corradini, M., Cheny, J., and Fallou, L. A social bot in support of crisis communication:-years of @LastQuake experience on Twitter. *Frontiers in Communication*, 8:992654, 2023. doi: 10.3389/fcomm.2023.992654.

Bravo, T. and Hubenthal, M. Using Earthquakes as "Teachable Moments". *Science Teacher*, 83:3, 2016.

Central Bureau of Statistics. *National population and housing census-2011*. Central Bureau of Statistics, National Planning Commission (NPC), Kathmandu, 2012.

Chen, K., Liang, W., Lin, C., and Wu, L. Citizen Seismology in Taiwan: Development, Outreach, and Formative Assessment of Near-Real Time Earthquake Game Competition Activities. *Frontiers in Earth Science*, 8:154, 2020. doi: 10.3389/feart.2020.00154.

Chen, W. and Molnar, P. Seismic moments of major earthquakes and the average rate of slip in central Asia. *Journal of Geophysical Research*, 82(20):2945–2969, 1977. doi: 10.1029/JB082i020p02945.

Dixit, A., Dwelley-Samant, L., Nakarmi, M., Pradhanang, S., and Tucker, B. The Kathmandu Valley earthquake risk management project: an evaluation, 2000. http://www.iitk.ac.in/nicee/wcee/article/0788.pdf,.

Hetényi, G., Molinari, I., Clinton, J., Bokelmann, G., Bondár, I., Crawford, W. C., Dessa, J.-X., Doubre, C., Friederich, W., Fuchs, F., et al. The AlpArray seismic network: a large-scale European experiment to image the Alpine Orogen. *Surveys in Geophysics*, 39:1009–1033, 2018. doi: 10.1007/s10712-018-9472-4.

Iyengar, R., Sharma, D., and Siddiqui, J. Earthquake history of India in medieval times. *Indian Journal of History of Science*, 34: 181–238, 1999.

Kargel, J., Leonard, G., Shugar, D., Haritashya, U., Bevington, A., Fielding, E., and Young, N. Geomorphic and geologic controls of geohazards induced by Nepal's 2015 Gorkha earthquake. *Sci-*

ence, 351(6269), 2016. doi: 10.1126/science.aac8353.

MoHA. Nepal disaster report 2015. The Government of Nepal, Ministry of Home Affairs and Disaster Preparedness Network-Nepal, 2015.

MoHA. National Policy for Disaster Risk Reduction. In *The Government of Nepal, Ministry of Home Affairs*. Kathmandu, Nepal, 2018.

Pant, M. A step toward a historical seismicity of Nepal. *Adarsa*, 2: 29–60, 2002.

Prajapati, S., Dadhich, H., and Chopra, S. Isoseismal map of the 2015 Nepal earthquake and its relationships with ground-motion parameters, distance and magnitude. *Journal of Asian Earth Sciences*, 133:24–37, 2017. doi: 10.1016/j.jseaes.2016.07.013.

Rana, B. Nepal ko Maha Bhukampa (The Great Earthquake of Nepal). Kathmandu, Nepal, 1935. (in Nepali).

Sapkota, S., Bollinger, L., Klinger, Y., Tapponnier, P., Gaudemer, Y., and Tiwari, D. Primary surface ruptures of the great Himalayan earthquakes in 1934 and 1255. *Nature Geoscience*, 6(1):71–76, 2013. doi: 10.1038/ngeo1669.

Sapkota, S., Bollinger, L., and Perrier, F. Fatality rates of the Mw 8.2, 1934, Bihar–Nepal earthquake and comparison with the April 2015 Gorkha earthquake. *Earth, Planets and Space*, 68(1):1–9, 2016. doi: 10.1186/s40623-016-0416-2.

Shrestha, N. *Rebuilding Nepal After Earthquake*. European Press Photo Agency, 2016.

Subedi, S. Seismology at school in Nepal: Building an operational low-cost seismic network to establish an educational seismology program. PhD thesis, University of Lausanne, Switzerland., 2020.

Subedi, S. and Hetényi, G. The representation of earthquakes in Hindu religion: a literature review to improve educational communications in Nepal. *Frontiers in Communication*, 6:668086, 2021. doi: 10.3389/fcomm.2021.668086.

Subedi, S., Hetényi, G., Denton, P., and Sauron, A. Seismology at school in Nepal: A program for educational and citizen seismology through a low-cost seismic network. *Frontiers in Earth Science*, 8:73, 2020a. doi: 10.3389/feart.2020.00073.

Subedi, S., Hetényi, G., and Shackleton, R. Impact of an educational program on earthquake awareness and preparedness in Nepal. *Geoscience Communication*, 3(2):279–290, 2020b. doi: 10.5194/gc-3-279-2020.

Subedi, S., Denton, P., Michailos, K., and Hetényi, G. Making seismology accessible to the public in Nepal: an earthquake location tutorial for education purposes. *Bulletin of Nepal Geological Society*, 38:149–162, 2021.